Geophysical Monograph Series

175 **A Continental Plate Boundary: Tectonics at South Island, New Zealand** *David Okaya, Tim Stem, and Fred Davey (Eds.)*
176 **Exploring Venus as a Terrestrial Planet** *Larry W. Esposito, Ellen R. Stofan, and Thomas E. Cravens (Eds.)*
177 **Ocean Modeling in an Eddying Regime** *Matthew Hecht and Hiroyasu Hasumi (Eds.)*
178 **Magma to Microbe: Modeling Hydrothermal Processes at Oceanic Spreading Centers** *Robert P. Lowell, Jeffrey S. Seewald, Anna Metaxas, and Michael R. Perfit (Eds.)*
179 **Active Tectonics and Seismic Potential of Alaska** *Jeffrey T. Freymueller, Peter J. Haeussler, Robert L. Wesson, and Göran Ekström (Eds.)*
180 **Arctic Sea Ice Decline: Observations, Projections, Mechanisms, and Implications** *Eric T. DeWeaver, Cecilia M. Bitz, and L.-Bruno Tremblay (Eds.)*
181 **Midlatitude Ionospheric Dynamics and Disturbances** *Paul M. Kintner, Jr., Anthea J. Coster, Tim Fuller-Rowell, Anthony J. Mannucci, Michael Mendillo, and Roderick Heelis (Eds.)*
182 **The Stromboli Volcano: An Integrated Study of the 2002–2003 Eruption** *Sonia Calvari, Salvatore Inguaggiato, Giuseppe Puglisi, Maurizio Ripepe, and Mauro Rosi (Eds.)*
183 **Carbon Sequestration and Its Role in the Global Carbon Cycle** *Brian J. McPherson and Eric T. Sundquist (Eds.)*
184 **Carbon Cycling in Northern Peatlands** *Andrew J. Baird, Lisa R. Belyea, Xavier Comas, A. S. Reeve, and Lee D. Slater (Eds.)*
185 **Indian Ocean Biogeochemical Processes and Ecological Variability** *Jerry D. Wiggert, Raleigh R. Hood, S. Wajih A. Naqvi, Kenneth H. Brink, and Sharon L. Smith (Eds.)*
186 **Amazonia and Global Change** *Michael Keller, Mercedes Bustamante, John Gash, and Pedro Silva Dias (Eds.)*
187 **Surface Ocean–Lower Atmosphere Processes** *Corinne Le Quèrè and Eric S. Saltzman (Eds.)*
188 **Diversity of Hydrothermal Systems on Slow Spreading Ocean Ridges** *Peter A. Rona, Colin W. Devey, Jérôme Dyment, and Bramley J. Murton (Eds.)*
189 **Climate Dynamics: Why Does Climate Vary?** *De-Zheng Sun and Frank Bryan (Eds.)*
190 **The Stratosphere: Dynamics, Transport, and Chemistry** *L. M. Polvani, A. H. Sobel, and D. W. Waugh (Eds.)*
191 **Rainfall: State of the Science** *Firat Y. Testik and Mekonnen Gebremichael (Eds.)*
192 **Antarctic Subglacial Aquatic Environments** *Martin J. Siegert, Mahlon C. Kennicut II, and Robert A. Bindschadler*
193 **Abrupt Climate Change: Mechanisms, Patterns, and Impacts** *Harunur Rashid, Leonid Polyak, and Ellen Mosley-Thompson (Eds.)*
194 **Stream Restoration in Dynamic Fluvial Systems: Scientific Approaches, Analyses, and Tools** *Andrew Simon, Sean J. Bennett, and Janine M. Castro (Eds.)*
195 **Monitoring and Modeling the Deepwater Horizon Oil Spill: A Record-Breaking Enterprise** *Yonggang Liu, Amy MacFadyen, Zhen-Gang Ji, and Robert H. Weisberg (Eds.)*
196 **Extreme Events and Natural Hazards: The Complexity Perspective** *A. Surjalal Sharma, Armin Bunde, Vijay P. Dimri, and Daniel N. Baker (Eds.)*
197 **Auroral Phenomenology and Magnetospheric Processes: Earth and Other Planets** *Andreas Keiling, Eric Donovan, Fran Bagenal, and Tomas Karlsson (Eds.)*
198 **Climates, Landscapes, and Civilizations** *Liviu Giosan, Dorian Q. Fuller, Kathleen Nicoll, Rowan K. Flad, and Peter D. Clift (Eds.)*
199 **Dynamics of the Earth's Radiation Belts and Inner Magnetosphere** *Danny Summers, Ian R. Mann, Daniel N. Baker, and Michael Schulz (Eds.)*
200 **Lagrangian Modeling of the Atmosphere** *John Lin (Ed.)*
201 **Modeling the Ionosphere-Thermosphere** *Jospeh D. Huba, Robert W. Schunk, and George V Khazanov (Eds.)*
202 **The Mediterranean Sea: Temporal Variability and Spatial Patterns** *Gian Luca Eusebi Borzelli, Miroslav Gacic, Piero Lionello, and Paola Malanotte-Rizzoli (Eds.)*
203 **Future Earth - Advancing Civic Understanding of the Anthropocene** *Diana Dalbotten, Gillian Roehrig, and Patrick Hamilton (Eds.)*
204 **The Galápagos: A Natural Laboratory for the Earth Sciences** *Karen S. Harpp, Eric Mittelstaedt, Noémi d'Ozouville, and David W. Graham (Eds.)*
205 **Modeling Atmospheric and Oceanic Flows: Insightsfrom Laboratory Experiments and Numerical Simulations** *Thomas von Larcher and Paul D. Williams (Eds.)*
206 **Remote Sensing of the Terrestrial Water Cycle** *Venkat Lakshmi (Eds.)*
207 **Magnetotails in the Solar System** *Andreas Keiling, Caitríona Jackman, and Peter Delamere (Eds.)*
208 **Hawaiian Volcanoes: From Source to Surface** *Rebecca Carey, Valerie Cayol, Michael Poland, and Dominique Weis (Eds.)*
209 **Sea Ice: Physics, Mechanics, and Remote Sensing** *Mohammed Shokr and Nirmal Sinha (Eds.)*
210 **Fluid Dynamics in Complex Fractured-Porous Systems** *Boris Faybishenko, Sally M. Benson, and John E. Gale (Eds.)*
211 **Subduction Dynamics: From Mantle Flow to Mega Disasters** *Gabriele Morra, David A. Yuen, Scott King, Sang Mook Lee, and Seth Stein (Eds.)*
212 **The Early Earth: Accretion and Differentiation** *James Badro and Michael Walter (Eds.)*
213 **Global Vegetation Dynamics: Concepts and Applications in the MC1 Model** *Dominique Bachelet and David Turner (Eds.)*
214 **Extreme Events: Observations, Modeling and Economics** *Mario Chavez, Michael Ghil, and Jaime Urrutia-Fucugauchi (Eds.)*
215 **Auroral Dynamics and Space Weather** *Yongliang Zhang and Larry Paxton (Eds.)*
216 **Low-Frequency Waves in Space Plasmas** *Andreas Keiling, Dong-Hun Lee, and Valery Nakariakov (Eds.)*
217 **Deep Earth: Physics and Chemistry of the Lower Mantle and Core** *Hidenori Terasaki and Rebecca A. Fischer (Eds.)*
218 **Integrated Imaging of the Earth: Theory and Applications** *Max Moorkamp, Peter G. Lelievre, Niklas Linde, and Amir Khan (Eds.)*
219 **Plate Boundaries and Natural Hazards** *Joao Duarte and Wouter Schellart (Eds.)*
220 **Ionospheric Space Weather: Longitude and Hemispheric Dependences and Lower Atmosphere Forcing** *Timothy Fuller-Rowell, Endawoke Yizengaw, Patricia H. Doherty, and Sunanda Basu (Eds.)*
221 **Terrestrial Water Cycle and Climate Change: Natural and Human-Induced Impacts** *Qiuhong Tang and Taikan Oki (Eds.)*

Geophysical Monograph 222

Magnetosphere-Ionosphere Coupling in the Solar System

Charles R. Chappell
Robert W. Schunk
Peter M. Banks
James L. Burch
Richard M. Thorne
Editors

This Work is a co-publication between the American Geophysical Union and John Wiley and Sons, Inc.

AGU
American Geophysical Union

WILEY

This Work is a co-publication between the American Geophysical Union and John Wiley & Sons, Inc.

Published under the aegis of the AGU Publications Committee

Brooks Hanson, Director of Publications
Robert van der Hilst, Chair, Publications Committee

Published by John Wiley & Sons, Inc., Hoboken, New Jersey
Published simultaneously in Canada

Library of Congress Cataloging-in-Publication Data is available.

ISBN: 978-1-119-06677-4

Cover Images:

—Photograph by Charles R. Chappell of Yosemite National Park California taken from Inspiration Point. Yosemite has been the location of two important AGU conferences on Magnetosphere-Ionosphere Coupling at Earth and the planets.

—A schematic drawing by Charles R. Chappell of the outflow of the Earth's ionosphere as it moves outward to become a source of plasma for the magnetosphere.

—A simulation model image of the magnetosphere of Saturn showing the effect of its ionosphere on the shape of the magnetic field and the concentrations of different ions trapped in the magnetosphere (*Jia et. al.*, this volume)

Printed in the United States of America

10 9 8 7 6 5 4 3 2 1

CONTENTS

Part III The Effect of Low-energy Plasma on the Stability of Energetic Plasmas

Part IV Unified Global Modeling of Ionosphere and Magnetosphere at Earth

CONTRIBUTORS

Takumi Abe
Associate Professor
Institute of Space and Astronautical Science
Japan Aerospace Exploration Agency
Sagamihara, Kanagawa, Japan

M. André
Swedish Institute of Space Physics
Uppsala, Sweden

T. F. Averkamp
Engineering Specialist
Department of Physics and Astronomy
University of Iowa, Iowa City, IA, USA

L. Baddeley
Birkeland Centre for Space Science
The University Centre in Svalbard
Longyearbyen, Norway

Peter M. Banks
Professor University of Michigan (Retired)
Santa Rosa, CA, USA

Abdallah R. Barakat
Research Associate Professor
Center for Atmospheric and Space Sciences
Utah State University
Logan, UT, USA

J. W. Bonnell
Project Physicist
Space Sciences Laboratory
University of California, Berkeley
Berkeley, CA, USA

Jacob Bortnik
Professor
Department of Atmospheric and
Oceanic Sciences
University of California Los Angeles (UCLA)
Los Angeles, CA, USA

S. R. Bounds
Associate Research Scientist
Department of Physics and Astronomy
University of Iowa
Iowa City, IA, USA

Kevin S. Brenneman
NASA Goddard Space Flight Center
Greenbelt, MD, USA

James L. Burch
Vice President
Space Science and Engineering Division
Southwest Research Institute
San Antonio, TX, USA

Charles R. Chappell
Research Professor
Department of Physics and Astronomy
Vanderbilt University
Nashville, TN, USA

Lunjin Chen
Professor
Department of Physics
W. B. Hanson Center for Space Sciences
University of Texas, Dallas
Richardson, TX, USA

James H. Clemmons
Principal Director
Space Science Applications Laboratory
Aerospace Corporation
El Segundo, CA, USA

Andrew J. Coates
Professor of Physics and Deputy Director
(Solar System) MSSL
University College London
Mullard Space Science Laboratory
Dorking, Surrey, UK

Glyn A. Collinson
NASA Goddard Space Flight Center
Greenbelt, MD, USA

Thomas E. Cravens
Professor
Department of Physics and Astronomy
University of Kansas
Lawrence, KS, USA

Geoff Crowley
CEO and Chief Scientist
Atmospheric & Space Technology Research Associates (ASTRA) LLC
Boulder, CO, USA

Christopher Cully
Department of Physics and Astronomy
University of Calgary
Calgary, AB, Canada

Richard E. Denton
Research Professor
Department of Physics and Astronomy
Dartmouth College
Hanover, NH, USA

Eric Donovan
Department of Physics and Astronomy
University of Calgary
Calgary, AB, Canada

Douglas P. Drob
Research Physicist
Space Science Division
Naval Research Laboratory
Washington, DC, USA

Gregory D. Earle
Department of Physics
Virginia Technical University
Blacksburg, VA, USA

J. Vincent Eccles
Professor of Physics
Center for Atmospheric and Space Sciences
Utah State University
Logan, UT, USA

A. Eriksson
Swedish Institute of Space Physics
Uppsala, Sweden

Keiichiro Fukazawa
Professor
Academic Center for Computing and Media Studies
Kyoto University
Yoshidahonmachi, Sankyo-ku
Kyoto, Japan

Andrew J. Gerrard
Professor
Center for Solar-Terrestrial Research, New Jersey Institute of Technology
Newark, NJ, USA

Alex Glocer
Research Astrophysicist
Geospace Physics Laboratory
NASA Goddard Space Flight Center
Greenbelt, MD, USA

Tamas I. Gombosi
Professor
Department of Climate and Space Sciences and Engineering
University of Michigan
Ann Arbor, MI, USA

Daniel J. Gershman
NASA Goddard Space Flight Center
Greenbelt, MD, USA

D. A. Gurnett
James A. Van Allen/Roy J. Carver Professor of Physics
Department of Physics and Astronomy
University of Iowa
Iowa City, IA, USA

S. Haaland
Birkeland Centre for Space Science
University of Bergen
Norway; *and*
Max-Planck Institute for Solar Systems Research
Göttingen
Germany

R. A. Heelis
Director, William B. Hanson Center for Space Sciences
University of Texas at Dallas
Richardson, TX, USA

Thomas W. Hill
Professor Emeritus
Physics and Astronomy Department
Rice University
Houston, TX, USA

George B. Hospodarsky
Associate Research Scientist
Department of Physics and Astronomy
University of Iowa
Iowa City, IA, USA

Joseph D. Huba
Section Head, Space Physics
Plasma Physics Division
Naval Research Laboratory (NRL)
Washington, DC, USA

Xianzhe Jia
Associate Professor
Department of Climate and Space Sciences and Engineering
University of Michigan
Ann Arbor, MI, USA

Ying-Dong Jia
Assistant Research Geophysicist
Department of Earth, Planetary and Space Sciences
University of California at Los Angeles
Los Angeles, CA, USA

C. Johnsen
Department of Physics
University of Oslo
Norway

Robert E. Johnson
Professor
University of Virginia
Charlottesville, VA, USA; *and*
Professor
New York University
New York City, NY, USA

Vania K. Jordanova
Senior Research Scientist
Space Science and Applications Group
Los Alamos National Laboratory
Los Alamos, NM, USA

Larry Kepko
NASA Goddard Space Flight Center
Greenbelt, MD, USA

George Khazanov
NASA Goddard Space Flight Center
Greenbelt, MD, USA

Lynn M. Kistler
Professor
Department of Physics and Space Science Center
University of New Hampshire
Durham, NH, USA

Naritoshi Kitamura
Aerospace Project Research Associate
Institute of Space and Astronautical Science
Japan Aerospace Exploration Agency
Sagamihara, Kanagawa, Japan

Margaret G. Kivelson
Professor Emerita
Research Professor
Department of Climate and Space Sciences and Engineering
University of Michigan
Ann Arbor, MI, USA; *and*
Department of Earth, Planetary, and Space Sciences
University of California at Los Angeles
Los Angeles, CA, USA

C. A. Kletzing
F. Wendell Miller Professor
Department of Physics and Astronomy
University of Iowa
Iowa City, IA, USA

David J. Knudsen
Department of Physics and Astronomy
University of Calgary
Calgary, AB, Canada

Jonathan Krall
Research Physicist
Plasma Physics Division
Naval Research Laboratory (NRL)
Washington, DC, USA

Atsushi Kumamoto
Associate Professor
Department of Geophysics
Graduate School of Science
Tohoku University
Sendai, Japan

W. S. Kurth
Research Scientist
Department of Physics and Astronomy
University of Iowa
Iowa City, IA, USA

Louis J. Lanzerotti
Professor
Center for Solar-Terrestrial Research, New Jersey
Institute of Technology
Newark, NJ, USA

Stephen A. Ledvina
Space Sciences Laboratory
University of California Berkeley
Berkeley, CA, USA

J. S. Leisner
Senior Scientist
Department of Physics and Astronomy
University of Iowa,
Iowa City, IA, USA;
Current affiliation:
Arctic Slope Technical Services
Beltsville, MD, USA

Marc Lessard
Space Science Center
University of New Hampshire
Durham, NH, USA

K. Li
Max-Planck Institute for Solar Systems Research
Göttingen, Germany

Wen Li
Research Scientist
Department of Atmospheric and Oceanic Sciences
University of California Los Angeles (UCLA)
Los Angeles, CA, USA

Michael W. Liemohn
Professor
Department of Climate and Space Sciences and Engineering
University of Michigan
Ann Arbor, MI, USA

William Longley
Graduate Student
Department of Physics and Astronomy
Rice University
Houston, TX, USA

Gang Lu
Senior Scientist
High Altitude Observatory
National Center for Atmospheric Research
Boulder, CO, USA

Janet G. Luhmann
Senior Fellow
Space Sciences Laboratory
University of California Berkeley
Berkeley, CA, USA

B. Lybekk
Department of Physics
University of Oslo
Norway

Qianli Ma
Postdoctoral Fellow
Department of Atmospheric and Oceanic Sciences
University of California Los Angeles (UCLA)
Los Angeles, CA, USA

Elizabeth A. MacDonald
NASA Goddard Space Flight Center
Greenbelt, MD, USA

L. Maes
Royal Belgian Institute for Space Aeronomy
Brussels, Belgium

Donald G. Mitchell
Principal Professional Staff Physicist
Applied Physics Laboratory
Johns Hopkins University
Laurel, MD, USA

J. D. Menietti
Research Scientist
Department of Physics and Astronomy
University of Iowa
Iowa City, IA, USA

Thomas E. Moore
Senior Project Scientist for MMS
Heliophysics Science Division
NASA Goddard Space Flight Center
Greenbelt, MD, USA

Binbin Ni
Professor
Department of Space Physics
Wuhan University
Wuhan, Hubei, China

Michael J. Nicolls
Center for Geospace Studies
SRI International
Menlo Park, CA, USA

H. Nilsson
Swedish Institute of Space Physics
Kiruna, Sweden

Yukitoshi Nishimura
Assistant Researcher
Department of Atmospheric and Oceanic Sciences
University of California, Los Angeles
Los Angeles, CA, USA

Nikolai Østgaard
Professor
Department of Physics and Technology
University of Bergen
Bergen, Norway

A. Pedersen
Department of Physics
University of Oslo
Norway

A. M. Persoon
Research Specialist
Department of Physics and Astronomy
University of Iowa,
Iowa City, IA, USA

William K. Peterson
Research Scientist
Laboratory of Atmospheric and
Space Physics
University of Colorado
Boulder, CO, USA

Robert Pfaff
Space Weather Laboratory
NASA Goddard Space Flight Center
Greenbelt, MD, USA

D. Píša
Postdoctoral Research Scientist
Department of Physics and Astronomy
University of Iowa, Iowa City, IA, USA;
Current affiliation:
Department of Space Physics Institute of Atmospheric Physics, Czech Academy of Science Prague,
Czech Republic

Craig J. Pollock
NASA Goddard Space Flight Center
Greenbelt, MD, USA

Patricia Reiff
Professor
Department of Physics and Astronomy
Rice University
Houston, TX, USA

Jone Peter Reistad
Graduate Student
Department of Physics and Technology
University of Bergen
Bergen, Norway

Matthew S. Richard
Assistant Professor
Department of Physics and Astronomy
Benedictine College
Atchison, KS, USA

Aaron J. Ridley
Professor
Department of Climate and Space Sciences and Engineering
University of Michigan
Ann Arbor, MI, USA

Douglas E. Rowland
NASA Goddard Space Flight Center
Greenbelt, MD, USA

Christopher T. Russell
Professor
Department of Earth, Planetary and Space Sciences
University of California at Los Angeles
Los Angeles, CA, USA

Ennio Sanchez
Center for Geospace Studies
SRI International
Menlo Park, CA, USA

O. Santolík
Professor
Department of Space Physics
Institute of Atmospheric Physics
The Czech Academy of Sciences
Prague, Czech Republic; *and*
Faculty of Mathematics and Physics
Charles University
Prague, Czech Republic

S. Sazykin
Senior Faculty Fellow
Department of Physics and Astronomy
Rice University
Houston, TX, USA

R. W. Schunk
Director, Center for Atmospheric and Space Sciences
Professor of Physics
Center for Atmospheric and Space Sciences
Utah State University
Logan, UT, USA

Atsuki Shinbori
Researcher
Research Institute for Sustainable Humanosphere
Kyoto University
Uji, Japan

Kanako Seki
Professor
Department of Earth and Planetary Science
Graduate School of Science
The University of Tokyo
Tokyo, Japan

Joshua Semeter
Physics and Astronomy Department
Boston University
Boston, MA, USA

Ilkka Sillanpää
Research Scientist
Finnish Meteorological Institute
Helsinki, Finland

Sven Simon
Assistant Professor
Earth and Atmospheric Sciences
Georgia Institute of Technology
Atlanta, GA, USA

R. W. Spiro
Adjunct Professor
Department of Physics and Astronomy
Rice University, Houston, TX, USA

Darci Snowden
Assistant Professor
Central Washington University
Ellensburg, WA, USA

Robert J. Strangeway
Institute for Geophysics and Planetary Physics
University of California at Los Angeles
Los Angeles, CA, USA

Jeffrey Thayer
Aerospace Engineering
University of Colorado
Boulder, CO, USA

Richard M. Thorne
Distinguished Research Professor,
Department of Atmospheric and Oceanic Sciences
University of California Los Angeles (UCLA)
Los Angeles, CA, USA

F. R. Toffoletto
Professor
Department of Physics and Astronomy
Rice University
Houston, TX, USA

J. Hunter Waite, Jr.
Program Director
Space Science and Engineering
Southwest Research Institute
San Antonio, TX, USA

Raymond J. Walker
Professor Emeritus
Department of Earth Planetary and Space Sciences
University of California at Los Angeles
Los Angeles, CA, USA

Shigeto Watanabe
Professor
Space Information Center
Hokkaido Information University
Ebetsu, Japan

Daniel T. Welling
Assistant Research Scientist
Department of Climate and Space Sciences and Engineering
University of Michigan
Ann Arbor, MI, USA

Hanying Wei
Assistant Research Geophysicist
Department of Atmospheric Science
University of California at Los Angeles
Los Angeles, CA, USA

Joseph H. Westlake
Senior Staff Scientist
Applied Physics Laboratory
Johns Hopkins University
Laurel, MD, USA

Adam K. Woodson
Postdoctoral Researcher
Laboratory for Atmospheric and Space Physics
University of Colorado
Boulder, CO, USA

R. A. Wolf
Research Professor
Department of Physics and Astronomy
Rice University, Houston, TX, USA

J. R. Wygant
Professor
School of Physics and Astronomy
University of Minnesota
Minneapolis, MN, USA

Manabu Yamada
Associate Staff Scientist
Planetary Exploration Research Center
Chiba Institute of Technology
Narashino, Japan

J. Yang
Research Scientist
Department of Physics and Astronomy
Rice University
Houston, TX, USA

Andrew W. Yau
Professor
Department of Physics and Astronomy
University of Calgary
Calgary, Alberta, Canada

Shasha Zou
Associate Professor
Department of Climate and Space Sciences and Engineering
University of Michigan
Ann Arbor, MI, USA

PROLOGUE

The Earth and other planets in the solar system have atmospheres that vary in chemical composition and density depending on the processes that have taken place during the origin and evolution of the planet. As the different wavelengths of sunlight shine on the atmosphere, the atoms and molecules can be ionized, becoming electrically charged particles that can be energized further and moved upward away from the planet. This ionized layer, the ionosphere, is guided dynamically by electric and magnetic fields that are present at the planet. The strength and shape of the planetary magnetic field are influenced by the internal structure of the planet itself, and these factors can vary from the weakest intrinsic magnetic field at Mercury to the strongest at Jupiter.

As the outer atmosphere of the Sun is accelerated away as an ionized gas, it becomes the solar wind that streams outward through the solar system and affects the different planets. This highly variable solar wind interacts with the magnetic fields of the planets and creates electric fields that influence the motion of the charged ionospheric particles and that can accelerate them to much higher energies, thrusting them upward into the magnetic envelope that surrounds the planet. This process establishes the ionosphere as a very important source of the energetic charged particles that can be found around the different planets. At Earth, this magnetic envelope containing charged particles is called the magnetosphere.

Early studies of the Earth's magnetosphere measured these energetic particles and found that they were of similar energies to the protons, alpha particles, and electrons of the solar wind. This led to an initial conclusion that the energetic particles of planetary magnetospheres came from the solar wind and not from the planet itself. With the subsequent development of particle instrumentation that could determine the mass of these energetic particles, it was found, surprisingly, that there were significant amounts of particles with masses typical of the atmosphere and ionosphere of the planet and not of the solar wind, e.g., oxygen, nitrogen, and even molecular ions. This discovery in the 1970s established a new way of thinking about the processes by which the magnetospheres of the Earth and the planets were filled. These magnetic "buckets" can be filled from the inside out as well as the outside in.

Our early ideas about how things work, however, often form paradigms that are hard to change. This has been the case with the Earth's magnetosphere, where a large segment of the research community has not yet adjusted to the idea that the ionosphere may be a significant and oftentimes dominant source of the energetic plasma that is found in the Earth's space environment. The same is true for the planetary environments. Over the 40-year period of study of the Earth and planetary space environments, the confluence of new measurement techniques, extraordinary planetary missions, and coupled dynamic models has opened the door for a dramatic new paradigm-changing understanding. This history set the stage for the 2014 Yosemite Chapman Conference on Magnetosphere-Ionosphere Coupling in the Solar System. This resulting monograph is at the center of this exciting discovery and new scientific knowledge.

The first step needed was to bring together the space scientists who study the ionosphere with those who study the magnetosphere, and let them learn from each other. This had been the goal of the first Yosemite conference, four decades earlier. That conference started a movement toward a different awareness of the coupled nature of the system, but there was at that early time, no inclination that the ionosphere could actually be supplying charged particles, or plasma, to form the energetic regions of the magnetosphere where particles had energies up to a million times that of the ionospheric particles.

The second step needed was to bring together scientists who study the Earth's space environment with scientists who study the other planetary environments. This had begun in a limited way, but the 2014 Yosemite conference was intentionally designed to create this cross-discipline interaction, teaching, and learning. It was very successful in doing this, and this monograph captures this knowledge and makes it available to the broader international heliophysics and planetary science communities.

In addition to the cross-discipline merger of the scientists, the conference was designed to feature the history of this research. This was captured through the unique use of video that was made at the first Yosemite conference in 1974. This video was digitized for use at the 2014 meeting. Excerpts of the 1974 video were used to introduce each session, showing "the way we were" in 1974 and its

implied comparison with "the way we now are" in terms of our understanding of the coupling of the ionosphere with the magnetosphere, not just at Earth but also at other planets. Many of the video excerpts were of renowned scientists in our field who are no longer alive.

For many of the young researchers who were at the 2014 meeting, it was the first time that they had ever seen and heard some of these amazing pioneers in their field. These excerpts are made available to the reader through URL links given throughout this monograph**.** The full video of the 1974 meeting, which was digitized by the Television Archive at Vanderbilt University, is available online in the digital library at Utah State University in connection with their Center for Space Science and can be found at http://digitalcommons.usu.edu/yosemite_chapman/1974/.

In addition to the original video, arrangements were made to have the 2014 Yosemite conference recorded in HD color video. This video includes all of the talks from the 2014 conference and is also available at the Utah State University online digital library. It is found at http://digitalcommons.usu.edu/yosemite_chapman/2014/. This monograph contains URL links to videos of the original talks related to each of the chapters. The uniqueness of this video cannot be overemphasized. The viewer can watch a space scientist at the 2014 meeting in his eighties watching and commenting on a video of himself in his forties or the video of a very special PhD advisor of 40 years ago being watched and remembered by his previous PhD student! These are amazing scenes, not only for the comments related to what we have learned over this career-long four decades, but also the way we looked and talked in the early 1970s, near post-Woodstock era, as contrasted to today. This video element of the monograph adds unique supplemental value to this entire endeavor. These two online videos bring tremendous personal depth to the monograph. I am certain that nothing like this exists in our field of research, and I would be surprised if it exists in any other fields of space science. It is a most significant time capsule of ambience that has brought much more significance to the Yosemite conference and to this monograph.

The flow of the monograph chapters has been set up in the same way that the Yosemite Chapman Conference was arranged. The rationale for the flow had two themes. In the larger sense, more measurement and modeling of magnetosphere-ionosphere coupling has been done at Earth than at the planets. Because of this, the monograph begins with a look at the research that has been done at the Earth. Since the Earth-centered research forms the foundation for both measurements and modeling at the other planets, the relative number of papers has been weighted toward research that has been done in the Earth's space environment.

Within this larger theme, the chapters have been arranged in order to build up our understanding of each environment based on a progression of processes that follow the dynamics of the ionospheric source and its movement upward into the magnetosphere with its resulting effects. Hence, the monograph chapters begin with the ionospheric source, followed by the upward movement of the particles, then the influence of the low energy ionospheric particles in creating/affecting the higher energy particle populations of the magnetosphere and finally the modeling that has been has been carried out to predict the ionospheric outflow and its merger into the overall magnetospheric models.

Following the foundation established by the research in the terrestrial environment, the chapters turn to the planets and begin with the relevant measurements that have been made followed by the modeling of ionosphere-magnetosphere coupling that is now being done at the planets, much of it based on earlier modeling at the Earth. The monograph is completed with an assessment of where we stand in our understanding and a look at a future mission that would address the very important areas where more measurement and study are needed.

In conclusion, the reader/viewer is in for a treat with this monograph. It chronicles the advancement of knowledge in this interdisciplinary field and brings together the work of space scientists from around the world. It is an intellectual and visual journey though our exploration and discovery of the role that the ionosphere plays in determining the filling and dynamics of the space environments of the Earth and the planets. It covers a career-long experience that begins with the earliest ideas about this topic that came on the scene in the early 1970s and ends with an explanation of the new paradigm for the role of the ionosphere at the Earth and other planets of our solar system.

So sit back, enter the first URL given in the Table of Contents into your laptop, and watch an excerpt of the talk given by Jim Burch in 1974. Then read his introductory chapter from the 2014 conference and, if you desire, enter the URL given in his chapter and watch Jim give the 2014 talk himself. Then proceed through the video/chapter parade and enjoy seeing special people from our past in combination with the new discoveries and knowledge of the present—all done in the magnificence of Yosemite National Park, one of the most beautiful places on spaceship Earth!

Rick Chappell, *Vanderbilt University*
February 2016

Images from the 1974 and 2014 Yosemite Conferences

ACKNOWLEDGMENTS

I would like to thank my many colleagues whose ideas and contributions made this conference and monograph possible. First, thanks to the members of the Conference Organizing Committee: Robert Schunk, Utah State University; Andrew Nagy, University of Michigan; Peter Banks, University of Michigan, Retired; James Burch, Southwest Research Institute; and Daniel Baker, University of Colorado. Second, thanks to the Conference Program Committee: Thomas Moore, NASA Goddard Space Flight Center; Daniel Welling, University of Michigan; Margaret Kivelson, University of California, Los Angeles; Hunter Waite, Southwest Research Institute; Mary Hudson, Dartmouth University; Roderick Heelis, University of Texas at Dallas, Emma Bunce, University of Leicester; James Spann, NASA Marshall Space Flight Center; Andrew Coates, University College London; and Michael Mendillo, Boston University.

I am particularly indebted to Dr. Richmond Hoch and to the Battelle Northwest Laboratory whose foresight, commitment, and support led to the videotaping of the original 1974 Yosemite conference. I would also like to thank the National Aeronautics and Space Administration and the National Science Foundation whose support made the conference and the digitization of the original 1974 videotapes possible. We are also indebted to the American Geophysical Union, the Vanderbilt University Television Archive, Utah State University with its Digital Commons Archive, and the University of Michigan Atmospheric, Oceanic and Space Sciences Department.

Finally, thanks to my colleagues who brought their knowledge and insights to the creation of this monograph, co-editors Robert Schunk, Utah State University; Peter Banks, University of Michigan, Retired; Richard Thorne, University of California, Los Angeles; and James Burch, Southwest Research Institute.

Part I
Introduction

1

Magnetosphere-Ionosphere Coupling, Past to Future

James L. Burch

Video of Yosemite Talk, URL: http://dx.doi.org/10.15142/T3J01P

ABSTRACT

Prior to the 1970s, magnetospheric physics and upper atmospheric/ionospheric physics were separate scientific disciplines with separate space missions and separate theory and modeling programs. This situation led to a certain labeling (of scientific programs, scientific society sections, conferences, and even scientists), and this labeling was limiting scientific advances. Although some of this labeling still persists, it has largely become recognized that the upper atmosphere, ionosphere, magnetosphere, and the nearby solar wind comprise a single coupled system of geospace that must be studied together. This review traces some of the early concepts of magnetosphere-ionosphere (M-I) coupling through the past four decades and makes suggestions for future progress.

1.1. INTRODUCTION

The 1974 Yosemite Conference on Magnetosphere-Ionosphere Coupling was a unique event during which leading scientists in both magnetospheric and ionospheric physics met together in a remote location to examine in a unique way not only the overlap but also the interrelationships of their previously quite separate disciplines. Since M-I coupling as a research field has progressed greatly over the past 40 years, it is perhaps informative to trace some of the instances in which coupled magnetospheric and ionospheric phenomena were just beginning to be appreciated in a meaningful way and describe how these ideas have evolved to the present and into the future.

Early models of the interaction between the solar wind and the Earth's magnetosphere included the ionosphere but mainly as a footprint of conductivity for magnetospheric convection [e.g., *Axford and Hines*, 1961; *Wolf*, 1970]. During this same time somewhat controversial theories for the production of a polar wind, which populates the magnetosphere with ionospheric plasma, were developed and ultimately became widely accepted [e.g., *Banks and Holzer*, 1968]. In this same era, *Vasyliunas* [1970] developed a mathematical theory of M-I coupling that formed the basis for many theoretical advances in the field [*e.g., Wolf*, 1975].

Starting in the early 1970s, satellite measurements began to show that cold ionospheric particles (mainly H^+ and He^+) are important constituents of the inner and middle magnetosphere [*Chappell et al.*, 1970] and that energetic heavy ions (mainly O^+) precipitate into the low-altitude auroral zone during geomagnetic storms [*Sharp et al.*, 1972]. While H^+ ions, which dominate magnetospheric plasmas at all energies, can have their origins both in the solar wind and the ionosphere, the widespread prevalence of O^+ ions, which are almost exclusively from the ionosphere, suggested that the ionospheric plasma source is important and capable of supplying most if not all of magnetospheric plasma [*Chappell et al.,* 1987].

Southwest Research Institute, San Antonio, TX, USA

Magnetosphere-Ionosphere Coupling in the Solar System, Geophysical Monograph 222, First Edition.
Edited by Charles R. Chappell, Robert W. Schunk, Peter M. Banks, James L. Burch, and Richard M. Thorne.

New data sets and discoveries in that epoch were mainly responsible for the advent of M-I coupling science. One new data set that came on line was generated by the Chatanika Radar facility, which pioneered the use of the incoherent scatter technique to derive large-scale plasma convection patterns [*Brekke et al.*, 1974]. These convection patterns can be mapped into the magnetosphere to help gauge and visualize global magnetospheric dynamics. Another landmark discovery was auroral kilometric radiation (AKR), which was originally referred to as terrestrial kilometric radiation (TKR) [*Gurnett*, 1974; *Alexander and Kaiser*, 1976]. Since AKR beams outward from the auroral regions, it was only first observed many years after the discovery of radio emissions from Saturn and Jupiter [*Kaiser and Stone*, 1975]. In the case of Jupiter, the frequencies are much higher so that the so-called decametric radiation can be observed from the Earth's surface.

By far the strongest channel for coupling between the magnetosphere and ionosphere is the auroral oval and its extension into space. In the early 1970s, auroral particles first began to be observed from orbing spacecraft [e.g., *Frank and Ackerson*, 1971; *Winningham et al.*, 1973]. Sounding rocket measurements of auroral electrons had shown earlier that their energy spectra were monoenergetic and hence consistent with acceleration by an electric field component aligned along the magnetic field [*McIlwain*, 1960]. Subsequent measurements, however, showed that lower-energy electrons also precipitated into the aurora along with the monoenergetic beams [*Frank and Ackerson*, 1971]. Some controversy therefore arose about the source of the low-energy electrons, and this controversy was resolved by *Evans* [1974], who showed that they were backscattered and secondary electrons trapped between the parallel potential drop and the ionosphere. The possibility of Alfvén-wave acceleration of auroral electrons was investigated by *Hasegawa* [1976]. Later on, measurements from the FAST spacecraft showed that Alfvén-wave acceleration is an important phenomenon especially near the polar-cap boundary [e.g., *Chaston et al.*, 2003].

Another auroral phenomenon associated with M-I coupling is the stable auroral red (SAR) arc, which appears at mid-latitudes during magnetic storms. These arcs are produced either by Coulomb collisions between ring current particles and plasmaspheric electrons, electron acceleration by resonant wave interactions along magnetic field lines, or possibly precipitation of energetic electrons [*Hoch*, 1973]. These possibilities started to be examined closely during the early 1970s, and later satellite measurements combined with auroral imaging triggered further work in the 1980s, but research on the source of SAR arcs is still ongoing [*Kozyra et al.*, 1997].

Starting from these early observations, the following sections trace progress and consider future directions in a subset of important M-I coupling phenomena. Related M-I coupling phenomena are also described that are observed at other planets, particularly Saturn, which, while vastly different, may in fact be the closed analog to Earth's magnetosphere.

1.2. STABLE AURORAL RED ARCS

In his review of ground-based observations of SAR arcs, *Hoch* [1973] noted that a few hours after the Earth's magnetic field has been disturbed by a strong increase in the solar plasma flux, two glowing red zones are often detected, occurring approximately along lines of constant geomagnetic latitude in mid-latitude regions. These glowing zones, which occur simultaneously, one in each hemisphere, are caused by emission from the neutral atomic oxygen atom. He noted further that the arcs are subvisual and are detected only at night with photometric and photographic equipment. Based on the spatial occurrence of SAR arcs approximately along the plasmapause and their temporal relationship with large geomagnetic storms, Hoch suggested the ring current as the energy source and the interaction of the ring current with the plasmasphere as the energy transfer mechanism. Mechanisms suggested by *Hoch* [1973] included the following:

1. heat flow: transfer of kinetic energy by Coulomb collisions
2. transfer of ring current proton kinetic energy to hydromagnetic waves, which are damped by the electrons in the SAR arc region
3. direct influx of energetic electrons into the SAR arc region

Later measurements from spacecraft confirmed his observations based on global imaging as shown in Figure 1.1 and allowed further research to be done regarding the three possible mechanisms suggested in his review. The most current review of SAR arc formation is by *Kozyra et al.* [1997], who showed modeling results consistent with the energy source being Coulomb drag energy losses from ring-current O^+ ions (Figure 1.2). The mechanism for transferring this energy downward along field lines is still not settled. Even though heated electron inflow into a SAR arc was observed by *Gurgiolo et al.* [1982], the transport mechanism of the electrons from the ring current to the ionosphere is still to be determined. Because of the relative rarity of SAR arcs and their subvisual nature, imaging from orbiting spacecraft with sensitive wave and electric field measurements will be needed for an eventual understanding of this fascinating phenomenon that populates one of the important interfaces between the ionosphere and the magnetosphere.

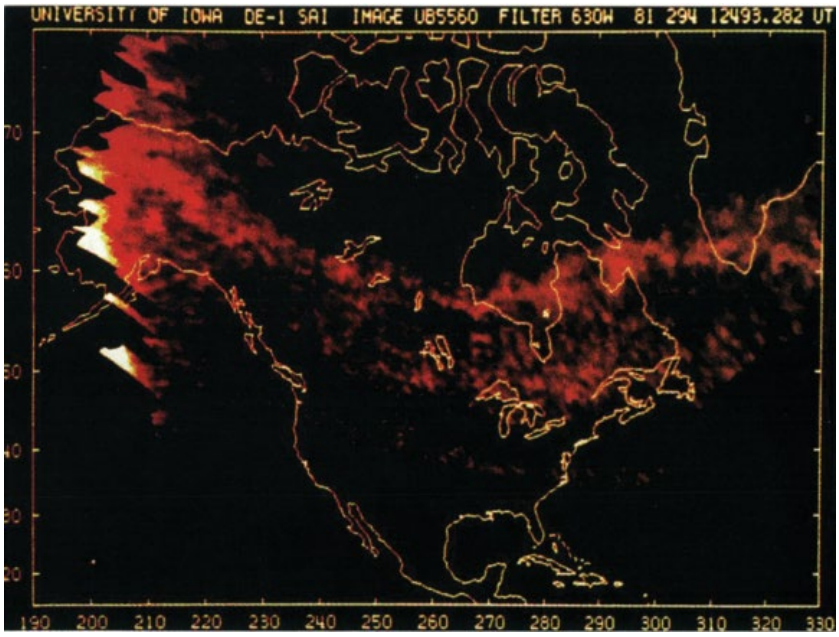

Figure 1.1 Image of SAR arc on October 21, 1981 taken at a wavelength of 630.0 nm from the Dynamics Explorer 1 spacecraft. Geographic latitude and longitude in degrees are shown on the vertical and horizontal axes, respectively [*Craven et al.*, 1982].

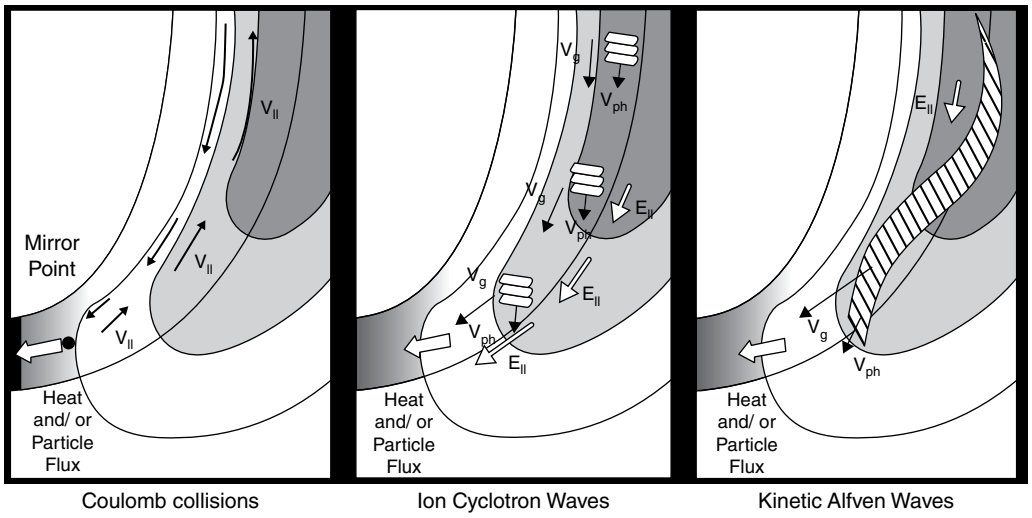

Figure 1.2 Candidate magnetospheric energy sources for SAR arc formation [*Kozyra et al.*, 1997].

1.3. PLASMASPHERE DRAINAGE PLUMES

The early 1970s saw the first synoptic satellite measurements of cold plasma in the equatorial region of the inner and middle magnetosphere. Comprehensive studies of the morphology and dynamics of the plasmasphere, which is produced by filling of magnetic flux tubes by ionospheric plasma via diffusive equilibrium, were reviewed by *Chappell* [1972]. Erosion of the plasmasphere during magnetic storms, a typical bulging of the plasmasphere into the dusk hemisphere, and detached blobs of plasma in the afternoon sector were some of the prominent features discovered in the equatorial region by the OGO-5 spacecraft. During the same time, models of the response of the plasmapause to geomagnetic activity as reflected by changes in the convection electric field in a dipole magnetic field were described by *Grebowsky* [1970] and *Chen and Wolf* [1972]. Examples of the results are shown in Figures 1.3 and 1.4. The Chen and Wolf model (Figure 1.4) predicts that the plume will wrap around the

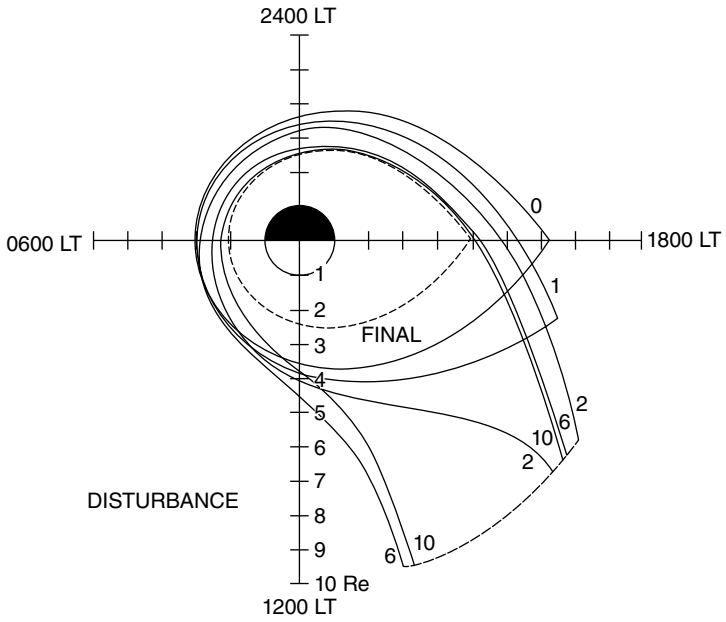

Figure 1.3 Early stages of formation of a plasma drainage plume in the afternoon sector [from *Grebowsky*, 1970]. The numbers are hours following an approximate doubling of the dawn-dusk convection electric field.

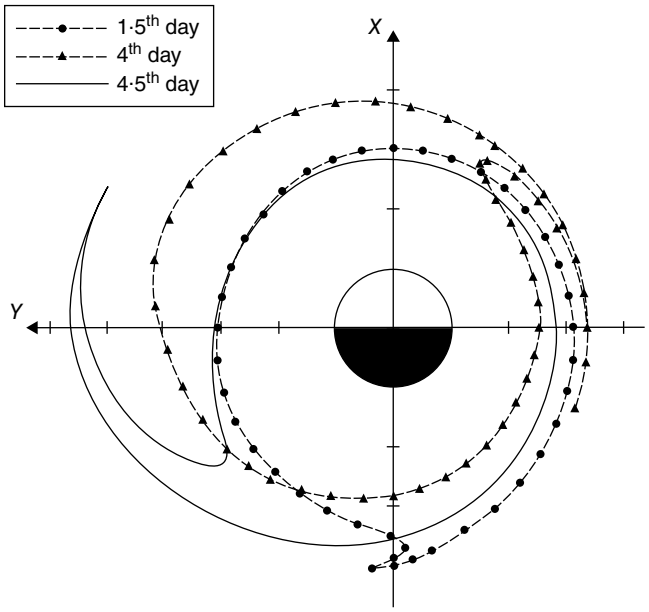

Figure 1.4 Full development of a plasmasphere drainage plume from the model of *Chen and Wolf* [1972]. Plasmapause positions are shown for the 1.5th day, 4th day, and 4.5th day after a sudden decrease in the convection electric field after a disturbed day.

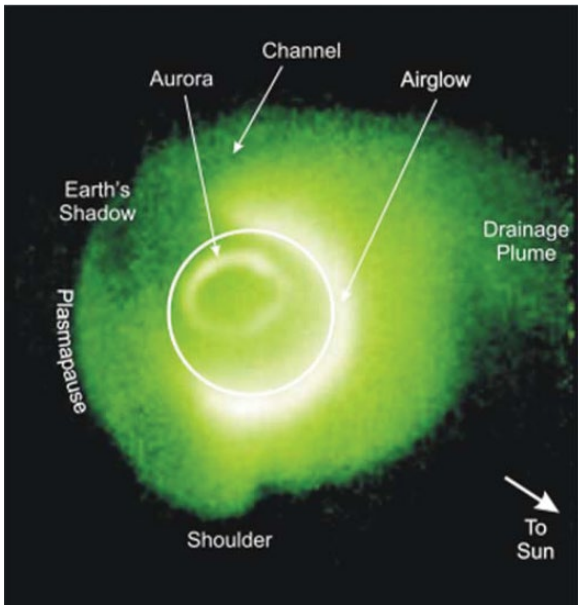

Figure 1.5 Image taken from about 8 R_E geocentric of the plasmasphere in 30.4 nm by the IMAGE EUV instrument [*Burch*, 2005; *Sandel et al.*, 2003].

Earth if, after a period of intensification the convection electric field drops to a lower value and remains there for an extended period of time. *Chen and Wolf* [1972] referred to this predicted evolution as the "wrapping up of the plasmasphere."

The presence of the predicted drainage plumes could not be confirmed until plasmasphere imaging became available with the Imager for Magnetopause-to-Aurora Global Explorer (IMAGE) mission [*Burch et al.*, 2001]. An image of the plasmasphere taken in 30.4 nanometer (nm) extreme ultraviolet (EUV) light is shown in Figure 1.5. This emission is caused by resonant scattering

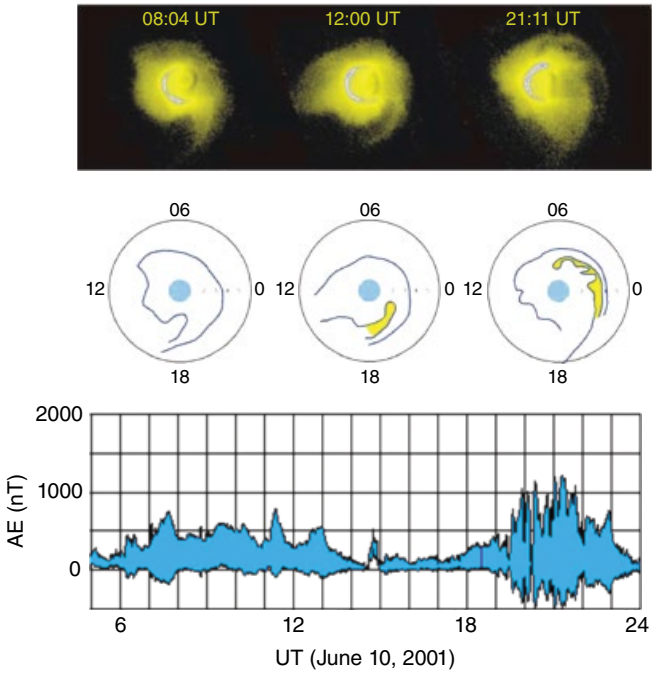

Figure 1.6 On June 10, 2001, a channel formed in the premidnight sector when a drainage plume wrapped around the main body of the plasmasphere. *Top panel*: EUV images with the Sun to the left. *Middle panel*: Mapping of the prominent brightness gradients to the plane of the magnetic equator in [L, MLT] space. *Bottom panel*: AE index. Over time the plume wraps to form a channel marked by the yellow fill [*Sandel et al.*, 2003].

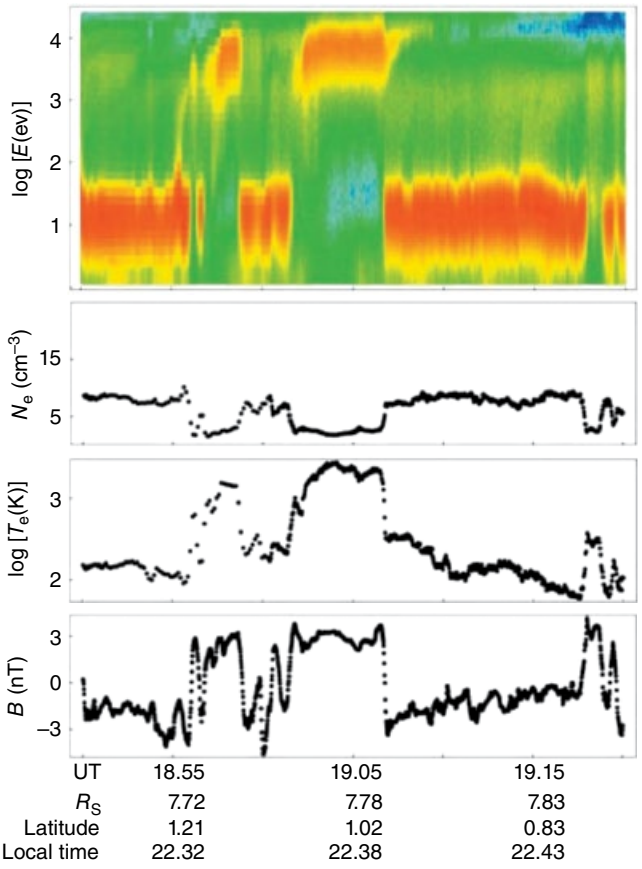

Figure 1.7 Electron and magnetic field data obtained by Cassini near the equatorial plane of Saturn on 28 October 2004. *Top panel:* Spectrogram of energy E versus time in Universal Time (UT) of electron counts from the CAPS Electron Spectrometer instrument. The pitch angle of the particles is near 90. *Second panel:* Electron density Ne integrated over 1 eV to 26 keV after subtraction of spacecraft photoelectrons. *Third panel:* Log of electron temperature. *Fourth panel:* Deviation of the magnetic field magnitude B from the ambient values [*Burch et al.*, 2007].

of sunlight by helium ions, which comprise about 15% of the plasmasphere density. Also noted in Figure 1.5 are other features that appear at or near this wavelength including the aurora and the helium geocorona. The shoulder feature noted in Figure 1.5, which was discovered by IMAGE-EUV, is caused by northward turnings of the interplanetary magnetic field (IMF) [*Goldstein et al.*, 2002].

Figure 1.6 shows the evolution of the drainage plume as observed by IMAGE-EUV during a period of multiple substorms on June 10, 2001 [*Sandel et al.*, 2003]. As noted in Figure 1.6, the plume wraps around the Earth in the manner predicted by *Chen and Wolf* [1972] creating a channel, which is often observed in the global images (Figure 1.5).

It is interesting to compare plasmasphere dynamics at Earth with similar phenomena at rotation-dominated planets such as Jupiter and Saturn. Saturn is roughly ten times as large as Earth and rotates more than twice as fast (10.7-hour rotation period). It has a spin-aligned dipole magnetic field that is much weaker than Jupiter's but nevertheless about 580 times stronger than Earth's. Except for a magnetotail, Saturn's magnetosphere is essentially a plasmasphere but with internal plasma sources (predominantly Enceladus) and ubiquitous interchange instabilities [*Burch et al.*, 2005, 2007; *Hill et al.*, 2005]. An example of interchange events observed within the E ring of Saturn is shown in Figure 1.7. Colder high-density plasma is replaced by much hotter but lower density plasma from the outer magnetosphere. This process is important at Saturn because of the planet's rapid rotation with centrifugal force taking the place of gravity in the closely related Rayleigh-Taylor instability on Earth.

1.4. RING CURRENT DECAY

As the cause of global magnetic disturbances during geomagnetic storms, the ring current is one of the most powerful of magnetospheric phenomena, involving ions

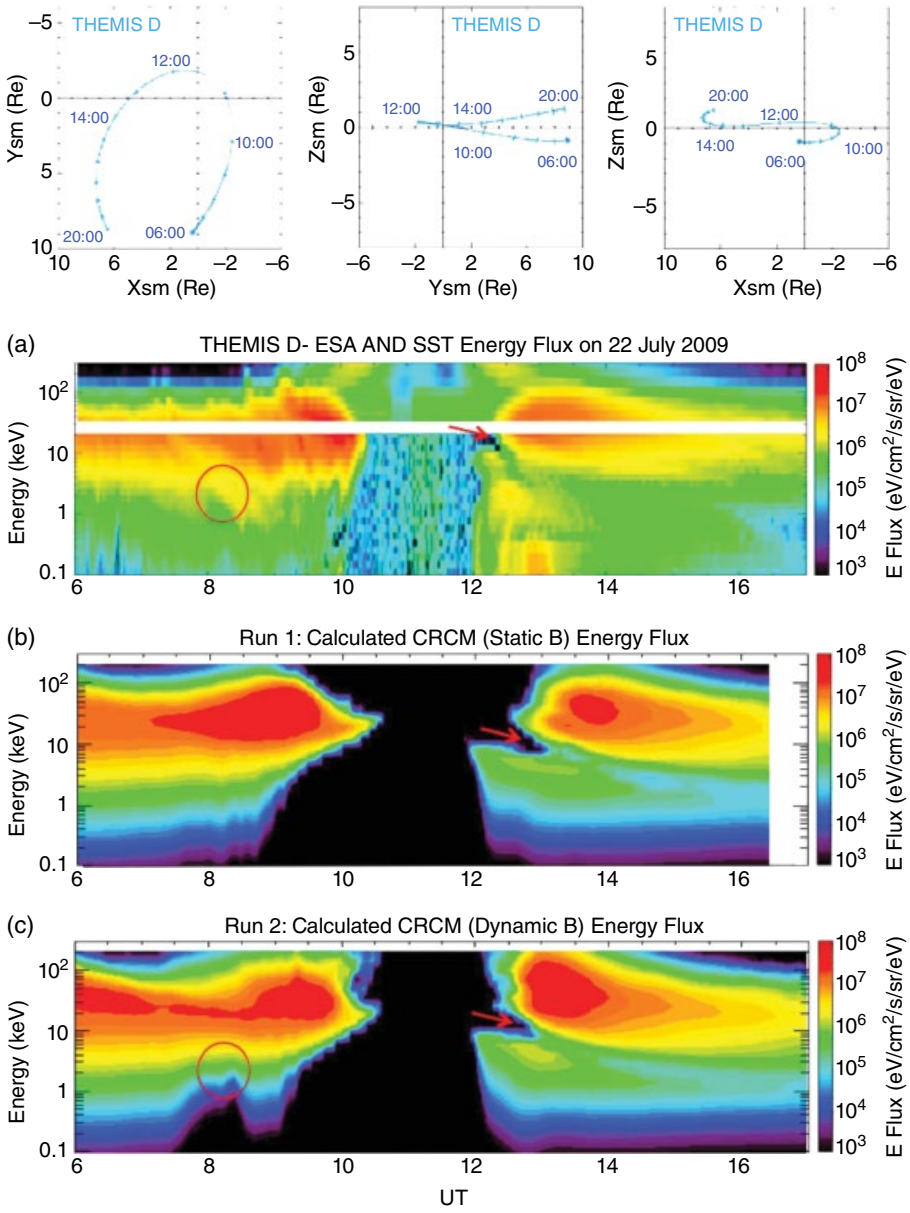

Figure 1.8 (top) The orbits of THEMIS D (blue) and E (red) projected on SM X-Y, Y-Z, and X-Z planes on 22 July 2009. (a) ESA and SST spectrogram from THEMIS-D. (b and c) CRCM calculated spectrogram from Run 1 and Run 2, respectively. Red arrows indicate "drift-holes" [*Fok et al.*, 2010].

with energies of 10s of kiloelectron-volt (keV). Nevertheless, the ring current is strongly mediated and eventually lost by interactions with the upper atmosphere and ionosphere. Resonant interactions with whistler-mode waves were shown to be important for the precipitation of ring current ions, particularly near the plasmapause, where the ring current and plasmasphere overlap [*Williams and Lyons*, 1974]. On a global basis, however, charge exchange with exospheric hydrogen atoms and Coulomb collisions within the loss cone of the ring-current ions have been shown perhaps to be more important.

As shown in Figure 1.8, recent comprehensive models of the loss of ring-current ions due to charge exchange and Coulomb collisions have produced results that are consistent with both in situ measurements and imaging of ring-current ions [*Fok et al.*, 2010]. Nevertheless, there still is strong evidence for the importance of wave-particle interactions as an ion precipitation agent in regions of overlap between the ring current and plasmapause. One of these regions is associated with the detached proton auroral arcs that were sometimes observed by IMAGE in the afternoon sector as shown in Figure 1.9 from *Burch*

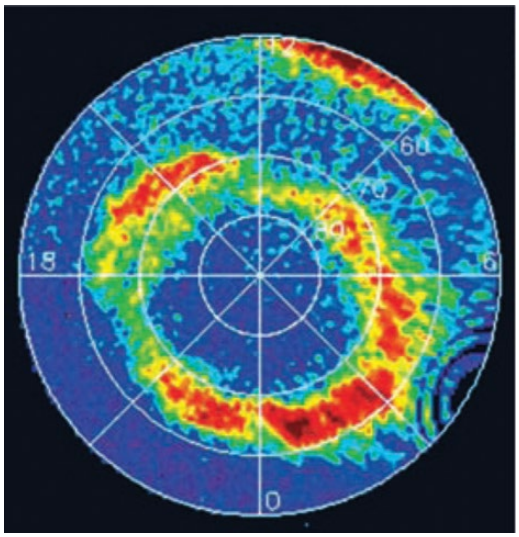

Figure 1.9 Ultraviolet auroral image mapped to invariant latitude and magnetic local time. A detached arc is centered on 15:00 MLT. Selected from Figure 6 of *Burch et al*. [2002].

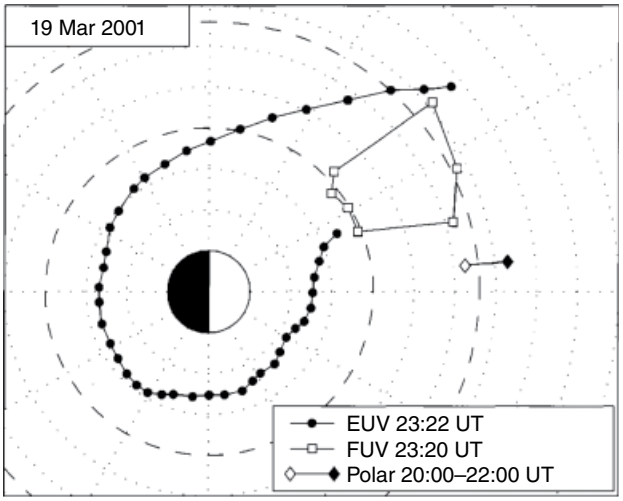

Figure 1.10 EUV plasmapause locations (black dots) are shown along with the mapped proton precipitation region (open squares) from ultraviolet images like the one shown in Figure 1.4. The diamonds show the track of the Polar spacecraft over which strong electromagnetic ion cyclotron waves were observed [*Spasojevic et al*., 2005].

et al. [2002]. *Spacojevic* et al. [2005] investigated a number of the detached proton auroras and found that they were spatially associated with plasmasphere drainage plumes. In the event shown in Figure 1.10, measurements from the Polar spacecraft, which was located in a nearby region, showed the presence of intense electromagnetic ion cyclotron waves of the type that are predicted to grow in regions of enhanced cold plasma density.

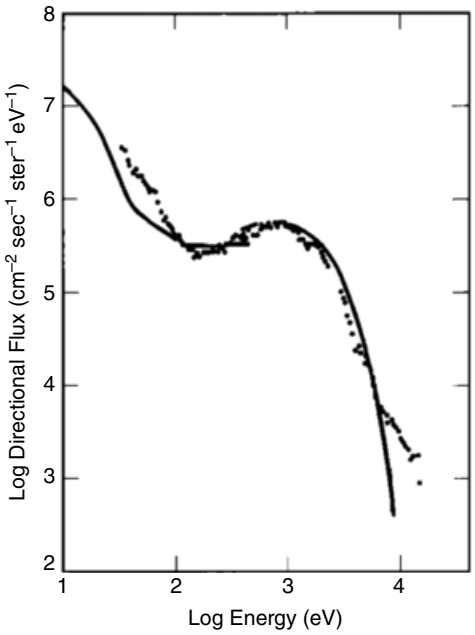

Figure 1.11 Model electron energy spectrum computed by assuming a 400-V potential difference along a magnetic field line and an unenergized Maxwellian electron distribution of temperature of 800 eV and density of 5 cm^{-3} [*Evans*, 1974]. The data represent an electron spectrum observed by *Frank and Ackerson* [1971].

1.5. INVERTED VS AND DISPERSIVE ALFVÉN WAVES

Sounding-rocket measurements of nearly monoenergetic keV electrons focused attention on an electrostatic acceleration mechanism in the topside ionosphere [*McIlwain*, 1960]. Further sounding-rocket measurement showed that the spectrum extended to low energies of a few tens of eV [*Westerlund*, 1968]. These low-energy electron measurements began to cast doubt on the electrostatic acceleration mechanism because if all of the auroral electrons originated in the magnetosphere they should all arrive at the beam energy, and this doubt persisted until 1974. By that time orbiting satellites had shown the monoenergetic beams to have a characteristic inverted-V shape in energy and latitude [*Frank and Ackerson*, 1971]. Using energy spectra from the Frank and Ackerson publication, *Evans* [1974] produced a model of the acceleration of auroral electrons with a field-aligned electrostatic potential drop and the interaction of the electrons with the upper atmosphere. Elegant in its simplicity, this model was able to fit the observed electron energy spectrum with the low energy electrons being auroral backscattered and secondary electrons, which are trapped between a magnetic mirror point in the atmosphere and the electrostatic potential at high altitudes (see Fig. 1.11). "The possibility

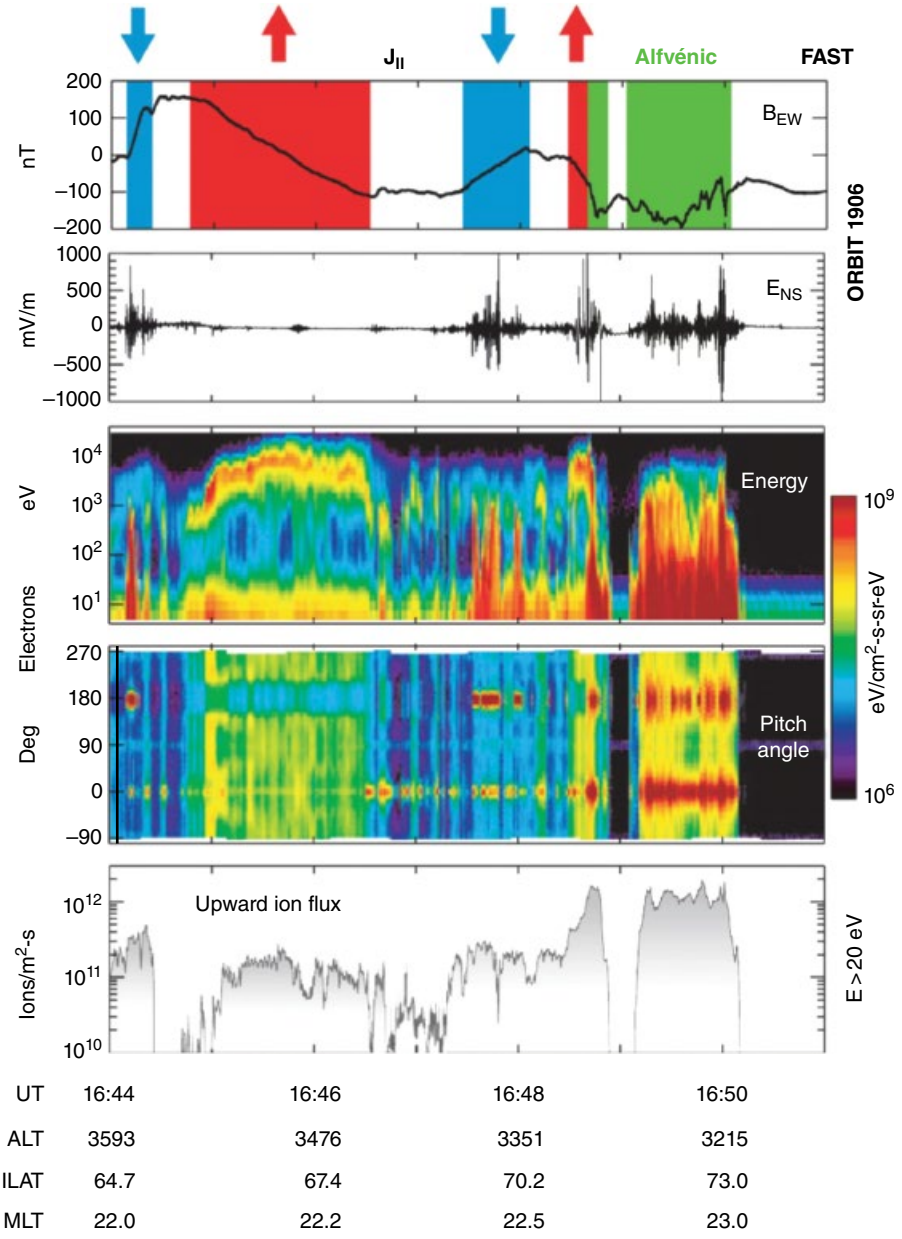

Figure 1.12 FAST satellite pass across the premidnight auroral zone showing (top to bottom *B* and *E*-field variations, electron energy and pitch-angle distribution and outflowing ion flux in the three characteristic acceleration regions: (1) Alfvénic region just equatorward of the polar cap boundary, (2) upward-current (inverted-V) regions, and (3) downward-current regions (adapted from Figure 4.2 of *Paschmann et al.*, 2002).

that upward-going backscattered and secondary electrons, produced by a primary beam incident upon the atmosphere, would reappear as precipitating electrons was not appreciated" [*Evans*, 1974].

Further measurements of auroral particles by orbiting spacecraft showed that not all the electrons appear in inverted-V structures. In some regions of the auroral oval often, but not exclusively, near the polar-cap boundary, field-aligned and counterstreaming electrons, with broad energy distributions (<10 eV up to a few keV) are observed as shown in Figure 1.12. The broad energy range and bi-directionality suggest stochastic acceleration by Alfvénic parallel E-fields [*Chaston et al.* 2003a, 2003b], but other observations indicate that resonant Landau acceleration by inertial Alfvén waves propagating downward from high altitudes is also at play (*Wygant et al.* 2002). Field-aligned currents in the downward-current acceleration region are carried by upflowing superthermal electrons

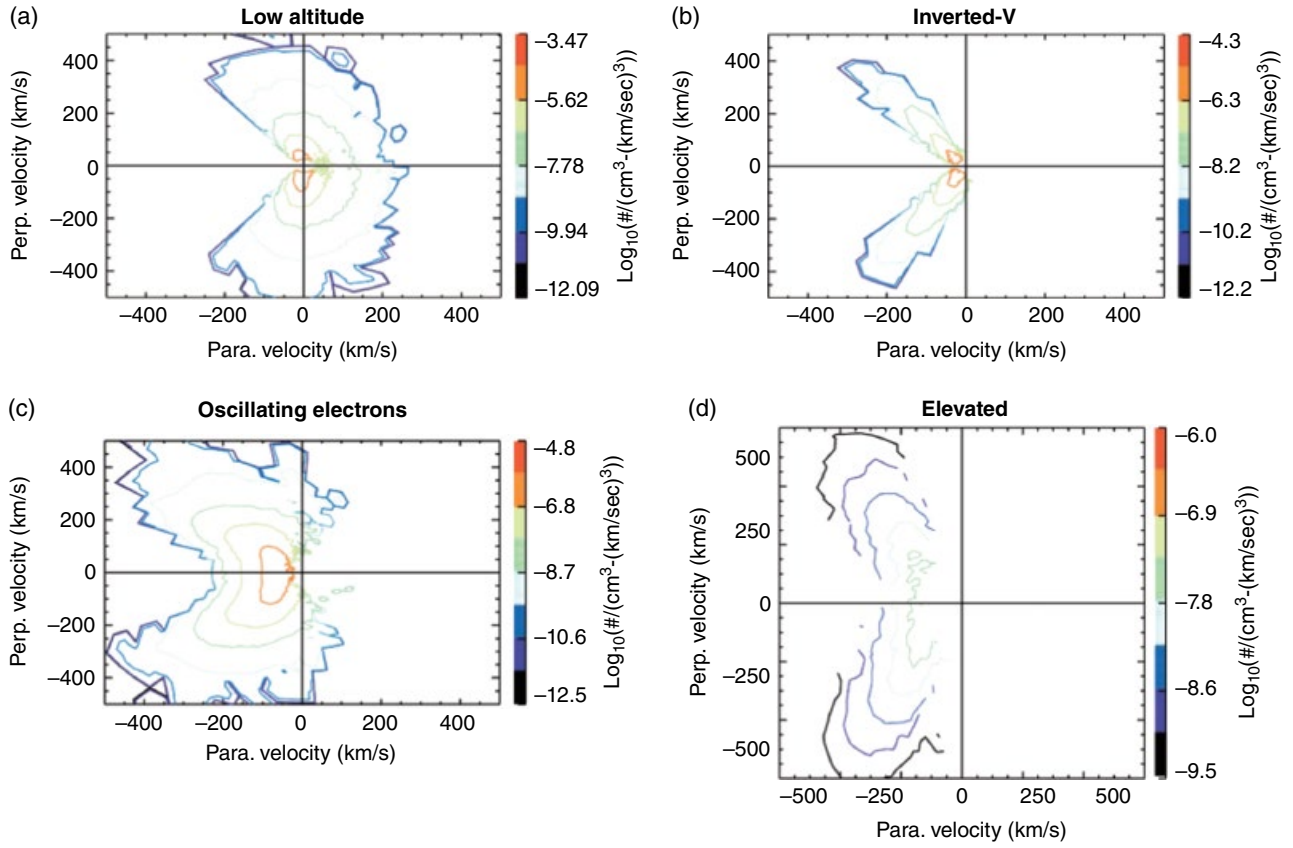

Figure 1.13 H^+ ion distribution function contours as functions of v_{perp} and $v_{parallel}$, taken from various pre-midnight auroral conditions: (a) low altitude, (b) inverted-V, (c) oscillating electron flux region, and (d) nongyrotropic example [*Lynch et al.*, 2002].

(up to a few keV), which are thought to be energized by electric double layers (*Andersson et al.* 2002) and other wave-particle interactions. The flux of ion outflows (bottom panel) is highest in the region of Alfvénic turbulence.

1.6. ION OUTFLOW

One of the great surprises in 1970s magnetospheric physics was the discovery of precipitating keV-range oxygen ions by *Shelley et al.* [1972], but what comes down also must have gone up. This was confirmed by *Shelley et al.* [1976], who discovered copious amounts of keV-range oxygen and hydrogen ions flowing out of the ionosphere along magnetic field lines. This result was followed by the discovery by *Sharp et al.* [1977] of ion conics, particles moving out of the ionosphere at pitch angles of 130° to 140°, which were interpreted to have been accelerated in a direction normal to the magnetic field at a lower altitude with the magnetic mirror force and magnetic moment conservation accounting for the "folding up" of the distribution toward the magnetic field direction. Although this interpretation is probably correct for some of the ion conics, it has been difficult to find the presumed source region where the pitch angles would be near 90°. Also the observation of conics over a wide range of altitudes shows similar conic angles, suggesting that the acceleration is not limited to a narrow altitude range but instead occurs all along magnetic field lines.

Together, the field-aligned energetic ions (ion beams) and ion conics add up to a massive outflow of particles into the magnetosphere. While hydrogen cannot be used as a tracer of the solar wind and ionospheric sources, O^+ surely can. The fact the O^+ ions are observed throughout the magnetosphere over a wide range of energies leads to the conclusion that the ionosphere is a very important source of plasma to the magnetosphere [e.g., *Chappell et al.*, 1987].

Prior to 1972 a common assumption in magnetospheric physics was that all of the energetic plasma came from the solar wind and that it was only the cold plasma of the plasmasphere that originated in the ionosphere. This notion was so strong that for many years no keV range mass spectrometers were ever designed into

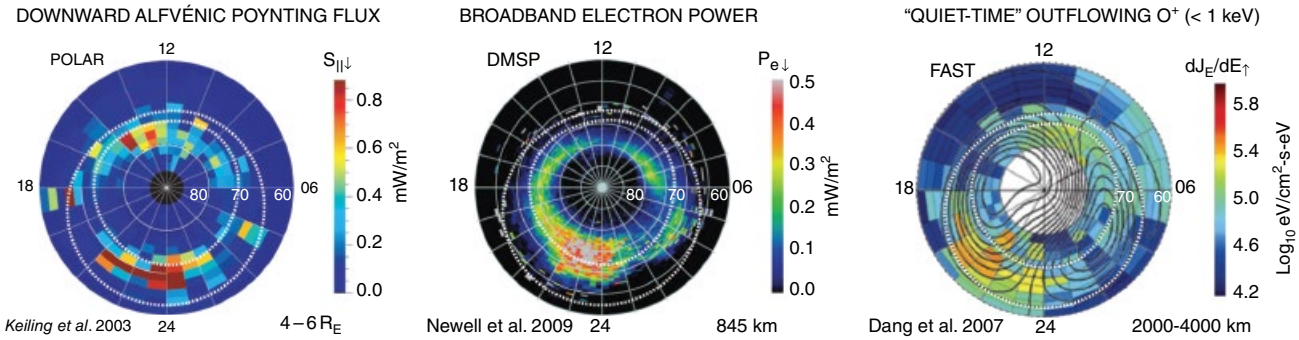

Figure 1.14 Observed statistical distributions of Alfvénic Poynting flux flowing toward Earth at 4–6 R_E geocentric altitude [*Keiling et al.*, 2003], broadband electron power precipitating at 845-km altitude [*Newell et al.*, 2009], and differential energy flux of outflowing O^+ at 2000–4000 km [*Dang et al.*, 2007]. Qualitative comparison suggests correlation between all three observables, particularly in the nightside "convection throat."

magnetospheric missions. It is interesting that the breakthroughs on the ionospheric keV ion source were made from rather obscure low-altitude defense department satellites rather than from mainstream magnetospheric physics missions. The lesson is always to be trying something new and different even if it is against the conventional wisdom, but it is usually not possible on expensive missions that are designed by committees and must guarantee results.

The science of ion beams and conics has progressed very rapidly and by now is a science discipline of its own. Recent data and modeling results by *Lynch et al.* [2002] show how various types of conical ion distributions occur in various auroral conditions, illustrating the complexity of this field of study and the many unsolved problems that still exist. Figure 1.13 shows four different H^+ distribution functions, which all fall into the general description of ion conics. Only Figure 1.13(b) fits the original concept of conical distributions while the others contain mixtures of parallel and perpendicular acceleration and wave heating.

The global nature of ion outflow is illustrated in Figure 1.14, which shows outflowing <1 keV O^+ ions (right panel) along with electron precipitation power (center panel) and downward Alfvénic Poynting flux (left panel). These three parameters are generally correlated, especially in the pre-midnight region of ionospheric flow reversal (the Harang discontinuity), indicating that ion energization is closely coupled to convection especially in fast flow channels.

1.7. AURORAL KILOMETRIC RADIATION

That the Earth is a powerful radio source was surprisingly unknown prior to the observations made from outside the magnetosphere by *Gurnett* [1974], *Kaiser and Stone* [1975], and *Alexander and Kaiser* [1976]. The generation and beaming of AKR was explained by a comprehensive theory published by *Wu and Lee* [1979]. The cyclotron maser theory of Wu and Lee has been successful in predicting the X-mode radiation, the beaming of waves upward from an auroral plasma density cavity, and the polarization of the waves, which is opposite in the northern and southern hemispheres. The predictions of the theory have been confirmed in the case of Saturn kilometric radiation (SKR) as well as for Jupiter's decametric radiation, which by virtue of its much higher frequency was discovered through ground-based observations in 1955 [*Burke and Franklin*, 1955].

The cyclotron maser theory is based on electron velocity-space gradients that occur in the auroral regions. These gradients were originally identified with the well-known loss cone, which is caused by atmospheric absorption of energetic particles but has since been associated with electron "hole" distributions that develop in the downgoing auroral electron population. An example of the simultaneous occurrence of both of these gradient regions is shown in Figure 1.15 from *Menietti et al.* [1993]. A schematic representation of the cyclotron maser interaction is shown in Figure 1.16, in which a flux tube depleted of plasma by a field-aligned electric field forms a resonant cavity for Doppler resonance of electromagnetic waves with auroral electrons. The density gradients that occur at the ionosphere and at the walls of the cavity both trap the waves and allow them to escape upward. The electron interaction explains the right- and left-hand polarizations that occur in the two hemispheres of Earth, Saturn, or Jupiter.

1.8. SATURN MAGNETOSPHERIC PERIODICITY

Although SKR and its periodicity of about 10.7 hours was observed by the Pioneer and Voyager spacecraft, it was not until the Cassini orbital mission that the evolution of the periodicity and its appearance in all plasma,

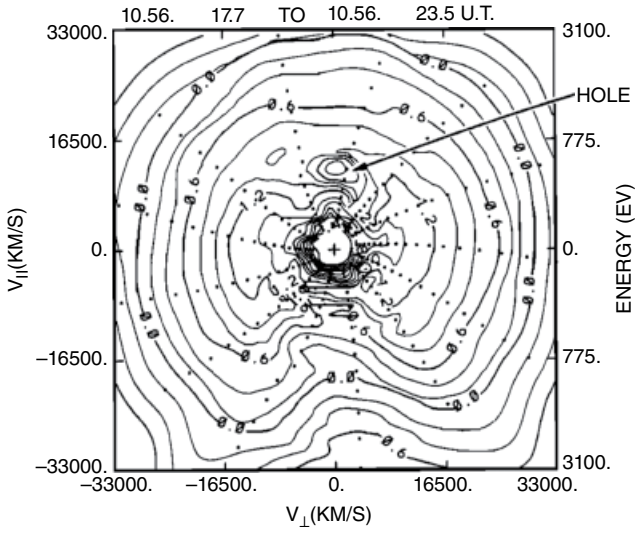

Figure 1.15 Example contour plot of electron distribution functions measured on September 27, 1981, show loss cone and hole distributions, both of which can contain free energy for the growth of AKR emissions [*Menietti et al.*, 1993].

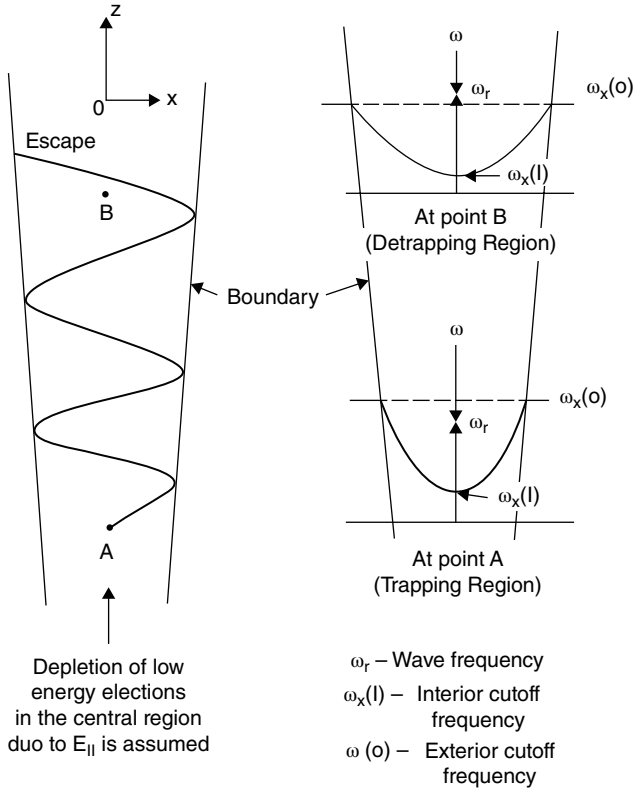

Figure 1.16 Schematic of wave trapping and escape in an auroral density depletion, which forms a resonant cavity for the production of S-mode waves by Doppler resonance with auroral electrons [*Wu and Lee*, 1979].

energetic particle, and magnetic field measurements began to be observed. Figure 1.17 shows the evolution of the periodicity of the northern and southern hemisphere components of SKR for the first six years after Cassini's orbital insertion. Prior to the Cassini mission the SKR periodicity was taken as the best measurement of Saturn's rotation rate. However, the discovery of two periodicities, both of which are slower than measurements based on the gravity field [*Anderson and Schubert*, 2007] and cloud motions [*Read et al.*, 2009], raised new questions. The rotation deficit was associated with slippage between the ionosphere and magnetosphere, which varied in a seasonal manner since initially the slower rotation occurred in the summer (southern) hemisphere and the more rapid rotation in the northern (winter) hemisphere. Numerous ideas and models have been proposed for the periodicity of SKR and the many other plasma and field phenomena observed in the Saturn magnetosphere (Figure 1.18). Some of the ideas have involved magnetospheric phenomena such as magnetic cams [*Southwood and Kivelson*, 2007], plasma cams [*Burch et al.*, 2009], plasma tongues [*Goldreich and Farmer*, 2007], or interchange modes [*Gurnett et al.*, 2007], while others have involved ionospheric sources such as long-lived vorticities [*Jia and Kivelson*, 2012]. The search has been complicated by the fact that the clear hemispheric separation between the two periodicity modes has not been re-established since the apparent crossover in 2010.

Although the cause of the SKR and magnetospheric periodicity at Saturn remains a mystery, it is nonetheless one of the most dramatic manifestations of M-I coupling in the solar system. Future missions to Saturn that are designed to investigate these specific phenomena, most likely with multiple spacecraft and enhanced atmospheric and magnetospheric imaging, will be needed.

1.9. FUTURE CAPABILITIES: MODELING AND NEW MISSIONS

Progress in understanding the geospace environment is dependent not only on new measurements but on accurate modeling, which only recently began to include M-I coupling phenomena such as ion outflow. Figure 1.19 illustrates the results of a model of magnetospheric sawtooth oscillations both with and without ionospheric outflow [*Brambles et al.*, 2013]. Inclusion of the outflow is clearly necessary for the sawtooth events to appear in the model.

Much progress has been made in the assimilation of data into ionospheric models [e.g., *Schunk et al.*, 2004] but much less so in magnetospheric models. With the dramatic advances in the accuracy of magnetospheric models, the role of data has to evolve from something to be explained, to targeted inputs, to models that establish boundary conditions and end states.

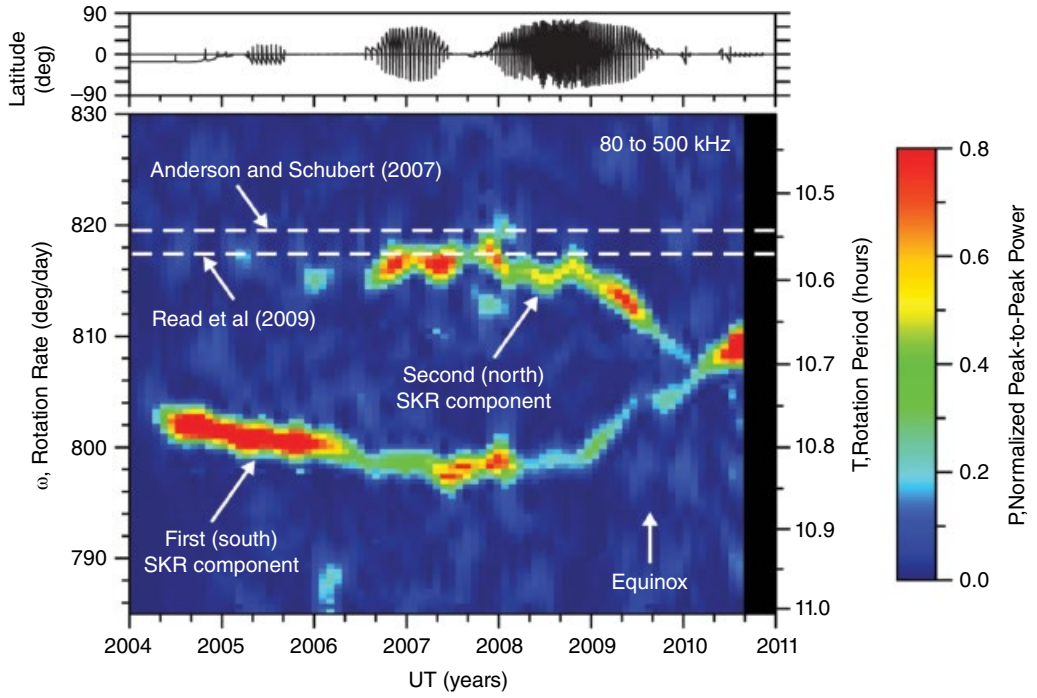

Figure 1.17 The top panel shows the latitude of Cassini, and the bottom panel shows a frequency-time spectrogram of the normalized peak-to-peak power of the SKR modulation as a function of UT and the rotational modulation rate, ω. The white dashed horizontal lines are the internal rotation rates of Saturn inferred by *Anderson and Schubert* [2007] and *Read et al*. [2009]. Note that the rotational modulation rates are all less than the inferred internal rotation rate, which implies that the magnetospheric is slipping with respect to the rotation of Saturn's interior [*Gurnett et al*., 2010].

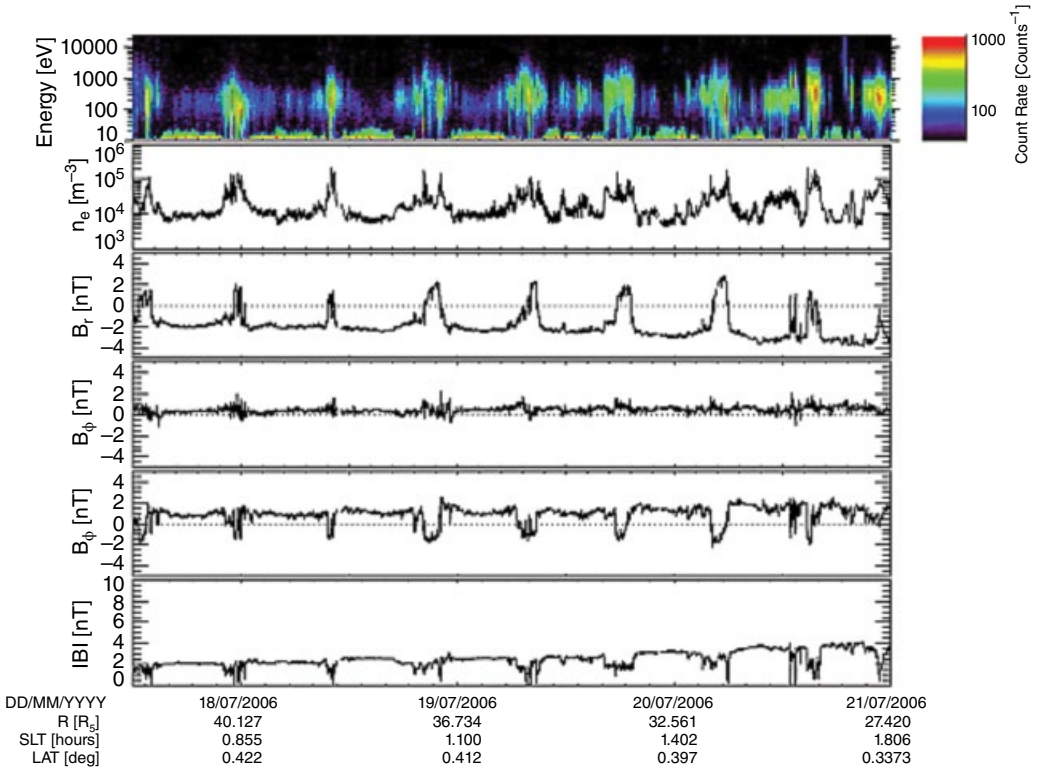

Figure 1.18 The fluxes and number densities of low-energy electrons (first and second plots) and magnetic field (third through sixth plots) measured by the Cassini spacecraft during 17 July 2006 to 21 July 2006 [*Khurana et al*., 2009].

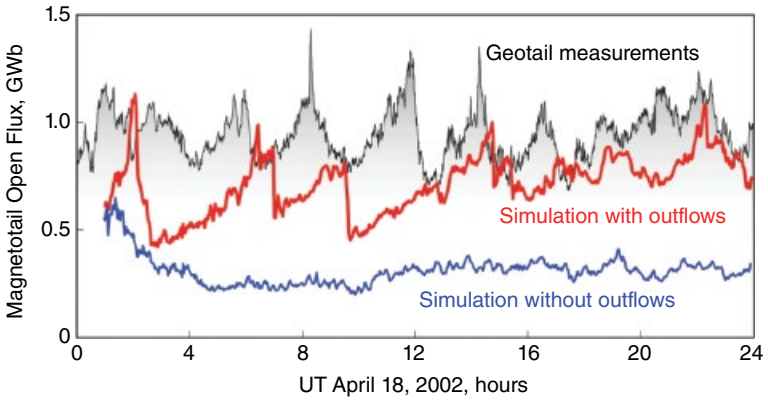

Figure 1.19 Magnetic flux derived from observations (black), baseline simulation (blue), and outflow simulation (red) calculated at the (top) polar cap and (bottom) magnetotail during the 18 April 2002 sawtooth event. Red vertical dashed lines show substorm onsets in the outflow simulation. Black vertical dashed lines show observed substorm onsets. Adapted from Figure 4 of *Brambles et al*. [2013].

The first Jupiter polar orbiter mission, Juno, is set to arrive at the planet on July 4, 2016. With auroral imaging and a full set of plasma, energetic particle, and wave and magnetic field measurements, Juno is equipped to investigate M-I coupling in the Jovian environment. In the case of Earth, the Magnetospheric Multiscale (MMS) mission is now performing a detailed experiment on magnetic reconnection in the outer magnetosphere. While not specifically designed to investigate M-I coupling, MMS will nevertheless obtain the first detailed measurement of the process that transmits solar-wind energy into the magnetosphere and ionosphere.

Future proposed magnetospheric and ionospheric missions generally involve clusters or constellations of spacecraft equipped to map out the flow of mass, energy, and momentum throughout geospace with both imaging and in situ measurements. Because of the shear size and dynamic behavior of geospace, such missions will have to involve intrinsic modeling components because it will not be possible to measure everything on a closely spaced grid but instead will require a computational web to connect many of the measurement points.

While the challenge for M-I coupling at the Earth is to obtain global and dynamic coverage of geospace, full understanding of M-I coupling requires further exploration of its occurrence in other planetary environments. Up until now magnetospheric and ionospheric measurements have been carried upon planetary missions, but the time is coming when the traditional boundaries of heliophysics need to be expanded toward their natural limits.

1.10. CONCLUSIONS

As summarized in this review, the early 1970s clearly was a watershed period for M-I coupling. The many new measurements that were made over only about half a decade resulted in the realization of the importance of M-I interactions. The discussions held at the 1974 Yosemite Conference on Magnetosphere-Ionosphere Coupling led eventually to the implementation of a dedicated space mission, Dynamics Explorer, which resulted in vast new knowledge of how the polar magnetosphere and ionosphere behave as one coupled system.

But now there is a crossroads, with measurement requirements expanding while resources are mostly stagnant. More now than before, the relevance and excitement of M-I coupling and other important heliophysics phenomena need to be demonstrated in the context of a mature science rather than a new science, which is clearly more difficult. There is no easy answer, but the lessons from the past often illuminate paths to the future, and the lesson of the birth of M-I coupling research four decades ago is that a large and diverse scientific community working together while appreciating each other's science can lead to great success.

REFERENCES

Alexander, J. K., and M. L. Kaiser (1976), Terrestrial kilometric radiation, I - Spatial, structure studies, *J. Geophys. Res.*, *81*, 5948–5956, doi:10.1029/JA081i034p05948.

Anderson, J. D., and G. Schubert (2007), Saturn's gravitational field, internal rotation, and interior, *Science*, *307*, 1384–1387, doi:10.1126/science.1144835.

Andersson L, et al. (2002) Characteristics of parallel electric fields in the downward current region of the aurora, *Phys. Plasmas*, *9*(8), 3600–3609, doi:10.1063/1.1490134.

Axford, W. I., and C. O. Hines (1961), A unifying theory of high-latitude geophysical phenomena and geomagnetic storms, *Can. J. Phys.*, *39*, 1433–1464, doi:10.1139/p61–172.

Banks, P. M., and T. E. Holzer (1968), The polar wind, *J. Geophys, Res*., *73*, 6846, doi:10.1029/JA073i021p06846.

Brambles, O. J., et al. (2013), The effects of ionospheric outflow on ICME and SIR driven sawtooth events, *J. Geophys. Res.*, *118*, 6026–6041, doi:10.1002/jgra.50522.

Brekke, A., et al. (1974), Incoherent scatter measurements of E region conductivities and currents in the auroral zone, *J. Geophys.Res.*, *79*, 3773–3790, doi:10.1029/JA079i025p03773.

Burch, J. L. (2005), Magnetospheric imaging: Promise to reality, *Rev. Geophys.*, *43*, RG3001, doi:10.1029/2004RG000160.

Burch, J. L., et al. (2001), Views of Earth's magnetosphere with the IMAGE satellite, *Science*, *291*, 619–624, doi:10.1126/science.291.5504.619.

Burch, J. L., et al. (2002), Interplanetary magnetic field control of afternoon-sector detached proton auroral arcs, *J. Geophys. Res.*, *107*(A9), 1251, doi:10.1029/2001JA007554.

Burch, J. L., et al. (2005), Properties of local plasma injections in Saturn's magnetosphere, *Geophys. Res. Lett.*, *32*, L14S02, doi:10.1029/2005GL022611.

Burch, J. L., et al. (2007), Tethys and Dione as sources of outward-flowing plasma in Saturn's magnetosphere, *Nature*, *447*, doi:10.1038/nature05906.

Burch, J. L., et al. (2009), Periodicity in Saturn's magnetosphere: Plasma cam, *Geophys. Res. Lett.*, *36*, L14203, doi:10.1029/2009GL039043.

Burke, B. F., and K. L. Franklin (1955), Observations of a variable radio source associated with the planet Jupiter, *J. Geophys. Res.*, *60*, 213–217, doi:10.1029/JZ060i002p00213.

Chappell, C. R. (1972), Recent satellite measurements of the morphology and dynamics of the plasmasphere, *Rev. Geophys.*, *10*, 951–979, doi:10.1029/RG010i004p00951.

Chappell, C. R., et al. (1970), The morphology of the bulge region of the plasmasphere, *J. Geophys. Res.*, *75*, 3848, doi:0.1029/JA075i019p03848.

Chappell, C. R., et al. (1971), Ogo 5 measurements of the plasmasphere during observations of stable auroral red arcs, *J. Geophys. Res.*, *76*, 2357, doi:10.1029/JA076i010p02357.

Chappell, C. R., et al. (1987), The ionosphere as a fully adequate source of plasma for the earth's magnetosphere, *J. Geophys. Res.*, *92*, 5896, doi:10.1029/JA092iA06p05896.

Chaston, C. C., et al. (2003a), Kinetic effects in the acceleration of auroral electrons in small scale Alfvén waves: A FAST case study, *Geophys. Res. Lett.*, *30*, 1289, doi:10.1029/2002GL015777.

Chaston, C. C., et al. (2003b) The width and brightness of auroral arcs driven by inertial Alfvén waves, *J. Geophys. Res.*, *108*, 1091, doi:10.1029/2001JA007537.

Chen, A. J., and R. A. Wolf, Effects on the plasmasphere of a time-varying convection electric field, *Planet. Space Sci.*, *20*, 483–509, doi:10.1016/0032–0633(72)90080–3.

Craven, J. D., et al. (1982), Global observations of a SAR arc, *Geophys. Res. Lett.*, *9*, 961–964, doi:10.1029/GL009i009p00961.

Dang, G., et al. (2007) Morphology of polar ionospheric O^+ ion upflow: FAST observations during quiet time, *Chinese Sci. Bull.*, *52*(24), 3403–3415, doi:10.1007/s11434-007-0444-1.

Fok, M.-C., et al. (2010), Simulation and TWINS observations of the 22 July 2009 storm, *J. Geophys. Res.*, *115*, A12231, doi:10.1029/2010JA015443.

Frank, L. A., and K. L. Ackerson (1971), Observations of Charged Particle Precipitation into the Auroral Zone, *J. Geophys. Res.*, *76*, 3612–3643, doi:10.1029/JA076i016p03612.

Goldreich, P., and A. J. Farmer (2007), Spontaneous axisymmetry breaking of the external magnetic field at Saturn, *J. Geophys. Res.*, *112*, doi:10.1029/2006JA012163.

Goldstein, J. et al. (2002), IMF-driven overshielding electric field and the origin of the plasmaspheric shoulder of May 24, 2000, *Geophys. Res. Lett.*, *29*(16), 1819, doi:10.1029/2001GL014534.

Grebowsky, J. M. (1970), Model study of plasmapause motion, *J. Geophys. Res.*, *75*(22), 4329–4333, doi:10.1029/JA075i022p04329.

Gurgiolo, C., et al. (1982), Observation of a heated electron population associated with the 6300 Å SAR arc emission, *Geophys. Res. Lett.*, *9*, 965–968, doi: 10.1029/GL009i009p00965.

Gurnett, D. A. (1974), The Earth as a radio source: Terrestrial kilometric radiation, *J. Geophys. Res.*, *79*, 4227–4238, doi:10.1029/JA079i028p04227.

Gurnett, D. A., et al. (2007), The rotation of the inner region of Saturn's plasma disk, *Science*, *316*, 442–445, doi:10.1126/science.1138562.

Gurnett, D. A., et al. (2010), The reversal of the rotational modulation rates of the north and south components of Saturn kilometric radiation near equinox, *Geophys. Res. Lett.*, *37*, L24101, doi:10.1029/2010GL045796.

Hasegawa, A. (1976), Particle acceleration by MHD surface wave and formation of aurora, *J. Geophys. Res.*, *81*, 5083–5090, doi:10.1029/JA081i028p05083.

Hill, T. W., et al. (2005), Evidence for rotationally driven plasma transport in Saturn's magnetosphere, *Geophys. Res. Lett.*, *32*, L14S10, doi:10.1029/2005GL022620.

Hoch, R. J. (1973), Stable auroral red arcs, *Rev. Geophys.*, *11*, 935–949, doi:10.1029/RG011i004p00935.

Jia, X., and M. G. Kivelson (2012), Driving Saturn's magnetospheric periodicities from the upper atmosphere/ionosphere: Magnetotail response to dual sources, *J. Geophys. Res.*, *117*, A11219, doi:10.1029/2012JA018183.

Kaiser, M. L., and R. G. Stone (1975), Earth as an Intense Planetary Radio Source: Similarities to Jupiter and Saturn, *Science*, *189*, 285–287, doi:10.1126/science.189.4199.285.

Keiling, A. (2003), The global morphology of wave Poynting flux: powering the aurora, *Science*, *299*, 383–386, doi:10.1126/science.1080073.

Khurana, K. K., et al. (2009), Sources of rotational signals in Saturn's magnetosphere, *J. Geophys. Res.*, *114*, A02211, doi:10.1029/2008JA013312.

Kozyra, J. U., et al. (1997), High-altitude energy source(s) for stable auroral red arcs, *Rev. Geophys.*, *35*, 155–190, 10.1029/96RG03194.

Lynch, K. A., et al. (2002), Return current region aurora: E-parallel, j_z, particle energization, and broadband ELF wave activity, *J. Geophys. Res.*, *107*, doi:10.1029/2001JA900134.

McIlwain, C. E. (1960), Direct measurement of particles producing visible auroras, *J. Geophys. Res.*, *65*, 2727–2747, doi:10.1029/JZ065i009p02727.

Menietti, J. D., et al. (1993), DE 1 particle and wave observations in auroral kilometric radiation (AKR) source regions, *J. Geophys. Res.*, *98*, 5865–5879, doi:10.1029/92JA02340.

Newell, P. T., et al. (2009), Diffuse, monoenergetic, and broadband aurora: The global precipitation budget, *J. Geophys. Res.*, *114*, A09207, doi:10.1029/2009JA014326.

Paschmann, G., et al. (2002), Auroral Plasma Physics, *Space Sci. Rev*., *103*, doi:10.1023/A:1023030716698.

Read, P. L., et al. (2009), Saturn's rotation period from its atmospheric planetary-wave configuration, *Nature*, *460*, 608–610, doi:10.1038/nature08194.

Sandel, B. R., et al. (2003), Extreme ultraviolet imager observations of the structure and dynamics of the plasmasphere, *Space Sci. Rev*., *109*, 25–46, 10.1023/B:SPAC.0000007511.47727.5b.

Schunk, R. W., et al. (2004), Global Assimilation of Ionospheric Measurements (GAIM), *Radio Sci*., *39*, RS1S02, doi:10.1029/2002RS002794.

Sharp, R. D., et al. (1977), Observation of an ionospheric acceleration mechanism producing energetic (keV) ions primarily normal to the geomagnetic field direction, *J. Geophys. Res.*, *82*, 3324–3328, doi:10.1029/JA082i022p03324.

Shelley, E. G., et al. (1972), Satellite Observations of Energetic Heavy Ions during a Geomagnetic Storm, *J. Geophys. Res.*, *77*, 6104, doi:10.1029/JA077i031p06104.

Shelley, E. G., et al. (1976), Satellite observations of an ionospheric acceleration mechanism, *Geophys. Res. Lett.*, *3*, 654–656, doi:10.1029/GL003i011p00654.

Southwood, D. J., and M. G. Kivelson (2007), Saturnian magnetospheric dynamics: Elucidation of a camshaft model, *J. Geophys. Res.*, *112*, A12222, doi:10.1029/2007JA012254.

Spasojević, M., et al. (2005), Afternoon subauroral proton precipitation resulting from ring current-plasmasphere interaction, in *Inner Magnetosphere Interactions: New Perspectives from Imaging* (eds. J. Burch, M. Schulz, and H. Spence), American Geophysical Union, Washington, D. C., doi:10.1029/159GM06.

Treumann, R. A., et al. (2011), Electron-cyclotron maser radiation from electron holes: upward current region, *Ann. Geophys.*, *29*, 1885–1904, doi:10.5194/angeo-29-1885-2011.

Vasyliunas, V. M. (1970), Mathematical Models of Magnetospheric Convection and Its Coupling to the Ionosphere, in *Particles and Field in the Magnetosphere*, ed. by B. M. McCormac and A. Renzini, Astrophysics and Space Science Library, *17*, 60, Reidel, Dordrecht.

Westerlund, L. H. (1969), The auroral electron energy spectrum extended to 45 ev, *J. Geophys. Res.*, *74*(1), 351–354, doi:10.1029/JA074i001p00351.

Williams, D. J., and L. R. Lyons (1974), Further aspects of the proton ring current interaction with the plasmapause: Main and recovery phases, *J. Geophys. Res.*, *79*(31), 4791–4798, doi:10.1029/JA079i031p04791.

Winningham, J. D., et al. (1973), Simultaneous Observations of Auroras from the South Pole Station and of Precipitating Electrons by Isis I, *J. Geophys. Res.*, *78*, 6579–6594, doi:10.1029/JA078i028p06579.

Wolf, R. A. (1970), Effects of ionospheric conductivity on convective flow of plasma in the magnetosphere, *J. Geophys. Res.*, *75*, 4677, doi:10.1029/JA075i025p04677.

Wolf, R. A. (1975), Ionosphere-magnetosphere coupling, *Space Sci. Rev*., *17*, 537–562, doi:0.1007/BF00718584.

Wu, C. S., and L. C. Lee (1979), A theory of the terrestrial kilometric radiation, *Astrophys. J.*, *230*, 621–626, doi:10.1086/157120.

Wygant, J. R., et al. (2002), Evidence for kinetic Alfvén waves and parallel electron energization at 4–6 R_E altitudes in the plasma sheet boundary layer, *J. Geophys. Res.*, *107*, doi:10.1029/2001JA900113.

Part II
The Earth's Ionosphere as a Source

2

Measurements of Ion Outflows from the Earth's Ionosphere

Andrew W. Yau[1], William K. Peterson[2], and Takumi Abe[3]

Video of Yosemite Talk, URL: http://dx.doi.org/10.15142/T34S3N

ABSTRACT

Our current view of ion outflows and their important role in magnetosphere-ionosphere-thermosphere coupling has been shaped principally by satellite, sounding-rocket, and ground-based radar observations over the past four decades, and by polar wind and related theoretical models dating back to the 1960s. The variety of ion outflows may be grouped into two categories: thermal outflows, including the polar wind and auroral bulk ion up-flow, and suprathermal outflows, including ion beams, ion conics, transversely accelerated ions, and upwelling ions. Both categories of outflows are strongly influenced by the solar extreme ultraviolet (EUV) irradiance and solar wind energy input and the state of the magnetosphere-ionosphere-thermosphere. This review focuses on the thermal outflows and their role as an important source of plasma for the suprathermal outflows at higher altitudes.

2.1. INTRODUCTION

The variety of observed ion outflows in the high-latitude ionosphere may be grouped into two categories: thermal outflows (bulk ion flows) with energies up to a few electron-volts (eV) in which all the ions acquire a bulk flow velocity, and suprathermal outflows in which in general a fraction of the ions are energized to much higher energies. The category of bulk ion flows includes the polar wind and auroral bulk O^+ up-flow from the topside auroral and polar cap ionosphere. The category of suprathermal ion outflows includes ion beams, ion conics, transversely accelerated ions (TAI), and upwelling ions (UWI).

[1]*University of Calgary, Calgary, Alberta, Canada*

[2]*Laboratory of Atmospheric and Space Physics, University of Colorado, Boulder, CO, USA*

[3]*Institute of Space and Astronautical Science, Japan Aerospace Exploration Agency, Sagamihara, Kanagawa, Japan*

In this review, we will focus on ion outflow measurements from satellites, rockets, and ground-based radars over the past four decades since the pioneering work of *Shelley et al.* [1976], in the context of our current perspectives on ion outflows and their important role in magnetosphere-ionosphere-thermosphere coupling.

Figure 2.1 is a schematic summary of these measurements, which were in general acquired in different phases in the 11-year solar cycle, and covered different altitude and ion energy ranges. For example, the measurements with the Chatanika and the European incoherent scatter (EISCAT) radars and the EISCAT Svalbard radar (ESR) were confined to thermal outflows in the topside ionosphere below 1000 kilometer (km) altitude, as were those on DE-2. In contrast, the measurements on S3-3, Viking, Freja, and Fast Auroral Snap-shoT (FAST) were confined to suprathermal outflows, while those on several other satellites covered both thermal and suprathermal outflows, notably DE-1, Akebono, Polar, and Cluster.

As chronicled in the historical review of *Lemaire et al.* [2007], the early polar wind measurements were preceded

Magnetosphere-Ionosphere Coupling in the Solar System, Geophysical Monograph 222, First Edition.
Edited by Charles R. Chappell, Robert W. Schunk, Peter M. Banks, James L. Burch, and Richard M. Thorne.

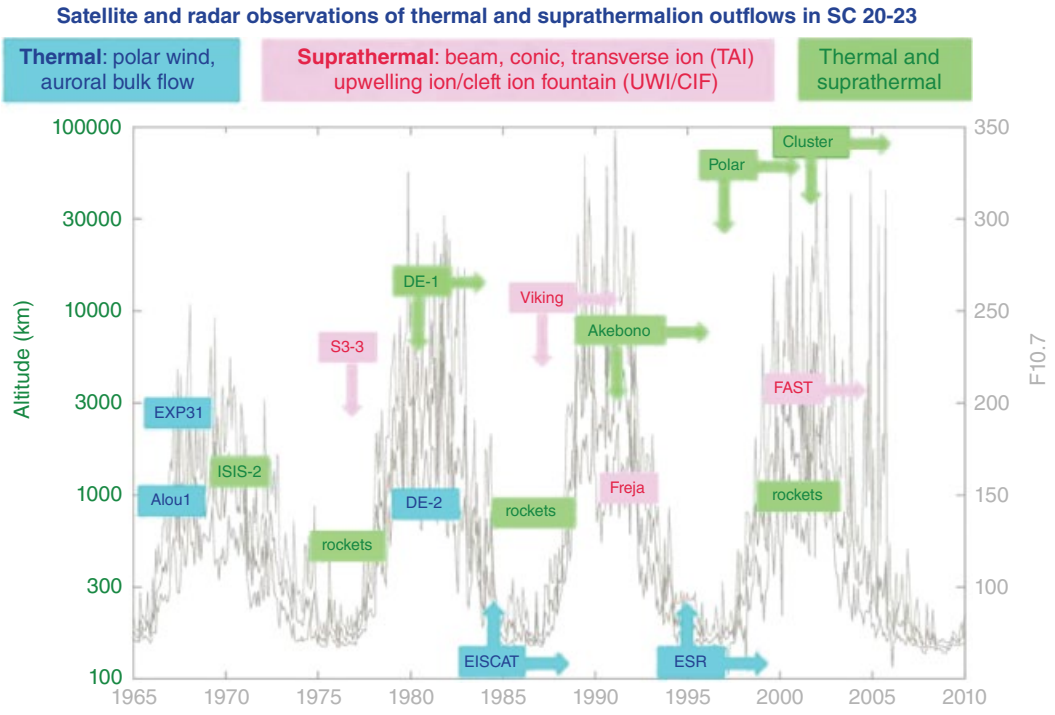

Figure 2.1 Schematic summary of satellite, rocket, and ground-based radar observations of ion outflows in different altitude regions and different phases of Solar Cycle 20-23. Cyan = thermal; magenta = suprathermal; green = thermal and suprathermal outflow observations; Left axis: altitude; right axis and gray traces: Monthly minimum, mean, and maximum $F_{10.7}$.

by hydrodynamic [*Banks and Holzer*, 1968; *Marubashi*, 1970] and kinetic polar wind models [*Lemaire and Scherer*, 1971] in the 1960s. These early models laid the conceptual foundation for subsequent semi-kinetic and transport-equations based models and recent three-dimensional time-dependent models [cf. the review of Schunk 2007], and continue to shape our approach to ion outflow measurements to this day. It is important to take into account the relative phase in the solar cycle and the relative altitude and ion energy coverage between different measurements. In general, the occurrence morphology of ion outflows is a function of the state of the magnetosphere, including the timing, location, and strength of auroral substorms and geomagnetic storms and the degree of filling of the plasmasphere. Many ion outflow characteristics have strong energy, altitude, and local time dependences, and exhibit significant long-term variations as well as variability on the time scale of days within a solar rotation near solar maximum that are a result of the strong dependence of thermospheric temperature on solar EUV flux.

2.2. THERMAL OUTFLOWS

At both auroral and polar cap latitudes, a plasma flux tube undergoes a circulation cycle that begins with stretching in length, from ~10 to ~100 R_E. During the stretch part of the cycle, the ionospheric plasma can expand freely into the upper reaches of the flux tube where the plasma pressure is reduced or negligible, and the plasma pressure gradient and a number of other forcing [cf. *Banks and Kockarts*, 1973] act in concert and result in the formation of the polar wind. In particular, the spatial separation between the heavier ions and the electrons due to the Earth's gravitation produces a polarization electric field that acts to accelerate the ions in the upward direction; additional acceleration mechanisms give rise to the so-called "non-classical" polar wind [*Schunk*, 2007].

Polar wind ion observations have been made on a number of polar-orbiting satellites, including ISIS-2, DE-1, Akebono, and Polar; polar wind electron observations have also been made on DE-1 and Akebono. These observations spanned different phases of Solar Cycle 20 to 23, and a wide range of altitudes from ~1000 to ~50,500 km (8 R_E) altitude [*Yau et al.*, 2007]. A composite picture of the polar wind emerges from these observations.

The observed polar wind is regularly present at all local times and polar latitudes, and is composed primarily of electrons and H^+, He^+, and O^+ ions. The ion composition varies with the solar cycle, and is dominated in density by O^+ ions up to 4000–7000 km. The dayside and the nightside velocity profiles are qualitatively similar for all three

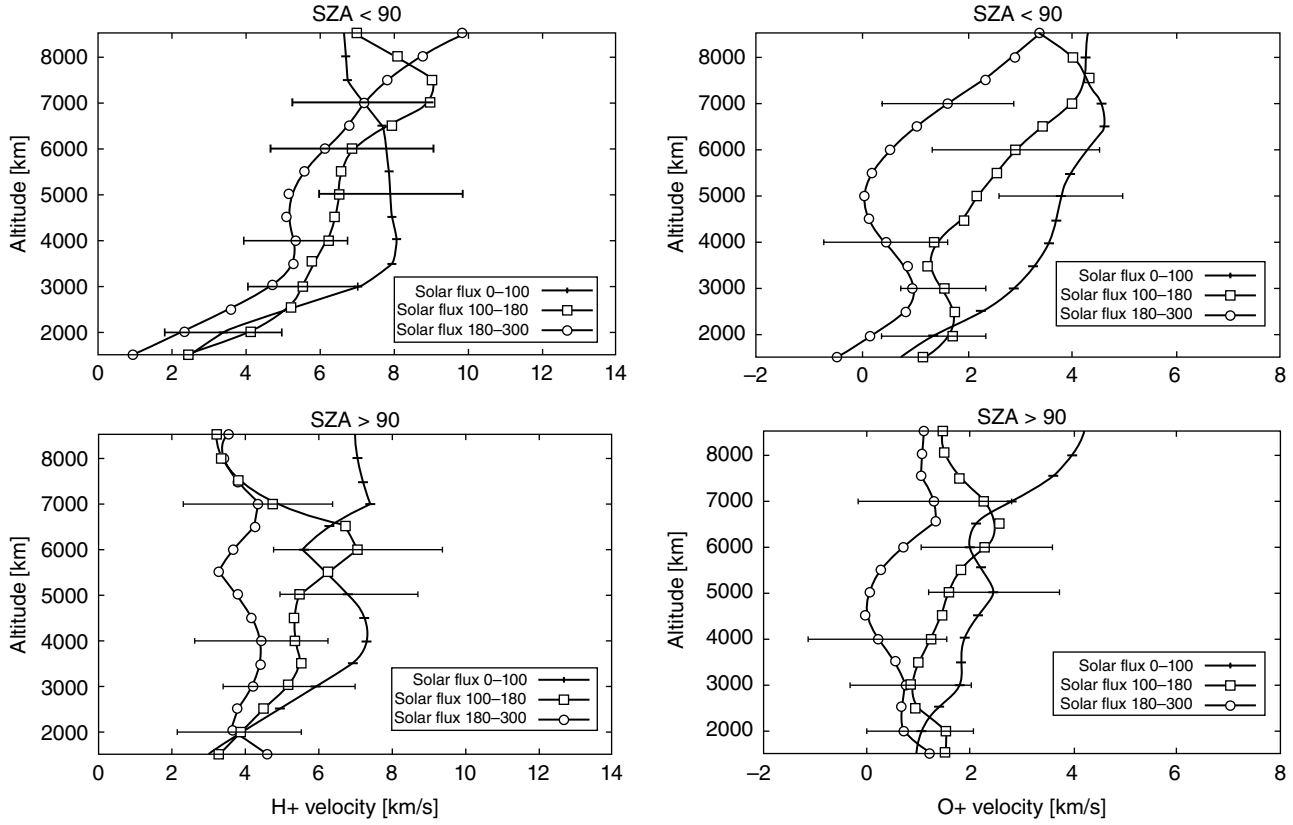

Figure 2.2 Averaged H^+ (left) and O^+ (right) velocity observed on Akebono versus altitude for different solar flux ($F_{10.7}$) levels: (top) SZA < 90°; (bottom) SZA > 90°. [From *Abe et al.*, 2004]

species. Both exhibit an approximately monotonic increase in velocity with altitude, mass dependence on the magnitude of the velocity, and the largest acceleration (increase of velocity with altitude) of the H^+ velocity below 4000 km.

Near solar maximum on the dayside, the H^+ velocity typically reaches 1 km/second (s) near 2000 km, the He^+ and O^+ velocities near 3000 and 6000 km. For all three species, the average velocity on the dayside is about 12, 6, and 4 km/s at 10,000 km, respectively, which is larger compared with ~7, 4, and 3 km/s on the nightside [*Abe et al.*, 1993a]. The larger velocity is suggestive of possible enhancement in the ambipolar electric field amplitude or presence of additional ion acceleration on the dayside due to escaping atmospheric photoelectrons [*Tam et al.*, 2007]. The averaged O^+ velocity begins to increase near 5000 km. This suggests that the O^+ ions above this altitude are predominantly upward; on the nightside, the averaged O^+ velocity starts to increase from zero at 7000 km.

The magnitude of ion acceleration at a given altitude is found to correlate strongly with the electron temperature [*Abe et al.*, 1993b]. The ion velocity to electron temperature ratio also increases with altitude. This increase is consistent with the cumulative increase in ion velocity due to acceleration via ambipolar electric field along the field line. The variability (standard deviation) of the ion velocity during active times ($K_P \geq 3$) is as much as 50% of the mean, and larger than at quiet times ($K_P \leq 2$). The mean velocity appears only weakly dependent on K_P for all three species.

Figure 2.2 shows the averaged H^+ and O^+ polar wind velocity at different solar flux levels ($F_{10.7}$) as a function of altitude in the sunlit (SZA < 90°) and shadow (non-sunlit; SZA > 90°) regions, respectively. In the sunlit region, the H^+ velocity increases with altitude at all altitudes for all solar flux levels, except at low solar flux ($F_{10.7} < 100$) where it remains almost constant above 4000 km. However, the velocity gradient in different altitude regions varies with solar flux. At high solar flux ($F_{10.7} > 180$), the velocity increases continuously from 1500 km to 8500 km. In comparison, at low solar flux, the velocity increase with altitude is much larger below 3600 km and much smaller above 4000 km; as a result, the averaged velocity is about 50–60% larger at 4000 km and comparable at ~7000 km.

The O^+ velocity in the sunlit region remains less than 1 km s^{-1} below 6000 km but increases with altitude above at high solar flux. Similar transition in the velocity is

observed at 4000 km at medium solar flux. At low solar flux, the velocity increases gradually with altitude from 1500 to 7000 km, reaching 4 km s^{-1} at 5000 km. In other words, the altitudinal gradients of both H^+ and O^+ velocity have very similar solar flux dependence and altitude variations (i.e., larger gradient below 5000 km and smaller gradient above 7000 km at low solar flux than at high solar flux), resulting in generally higher H^+ and O^+ velocities below 7000 km and 8500 km, respectively, at low solar flux.

The observed ion outflow rate of H^+ and O^+ is also only weakly dependent on K_p, the O^+ rate at 6000–9000 km altitude increasing by a factor of 1.7 as K_p increases from 1 to 6 [*Abe et al.*, 1996]. The outflow rate of both species exhibits very similar interplanetary magnetic field (IMF) B_Z dependence, and increased with B_Z under northward IMF conditions.

The magnetic local time (MLT) dependence of the polar wind ion flux strongly resembles that of the observed ion velocity: the ion flux is largest in the noon quadrant and smallest in the midnight quadrant. This is consistent with the larger ambipolar electric field in the sunlit polar wind. The polar wind H^+ flux (normalized to 2000 km altitude) in the noon quadrant is in the range of $1–20 \times 10^7$ cm^{-2} s^{-1}. The corresponding O^+ flux is typically a factor of 1.5–2.0 smaller. The fluxes of the different polar wind ion species have markedly different seasonal dependences in general. In the case of He^+, the flux has a winter-to-summer ratio of ~20, which is attributed to the seasonal variations of neutral atmospheric helium and molecular nitrogen associated with the "winter helium bulge" [*Liu et al.*, 2014] and the corresponding helium photo-ionization rate and He^+–N_2 charge-exchange rate.

As the polar wind ions flow upward along open magnetic field lines to higher altitudes and undergo generally anti-sunward convection in the dayside cusp and the polar cap, they may be subject to a number of "non-classical" polar wind ion acceleration mechanisms [*Yau et al.*, 2007]. Examples of such mechanisms include centrifugal acceleration in the parallel direction due to strong $E \times B$ convection in regions of curved magnetic field at high altitudes above a few R_E. The result of this is that ions continue to increase in both drift speed and temperature. Figure 2.3 shows the occurrence distributions of polar wind H^+ and O^+ ions near Polar apogee at 50,500 km altitude, where the H^+ density averages ~0.3 cm^{-3} and the H^+ parallel velocity averages 45 km s^{-1} near solar minimum [*Su et al.*, 1998]. The corresponding O^+ density and velocity are about a factor of 6 and 2.7 smaller (i.e., ~0.05 cm^{-3} and ~17 km s^{-1}), respectively.

The observed velocity ratio between ion species on both Akebono and Polar spans a wide range of values and on average lies between unity and the inverse square root mass ratio of the species (i.e., $1 < V_{\|,H^+}/V_{\|,O^+} < \sqrt{m_{O^+}/m_{H^+}} = 4$). This suggests that a number of processes of comparable energy gain may be contributing to the overall ion acceleration.

The term "auroral bulk ion flow" (see for example *Yau and André* [1997]) refers to the thermal ion flow in the auroral ionosphere, which is typically dominated by O^+ ions. The term "up-flow" is used instead of "outflow" to emphasize the very low, and below escape, energy nature of bulk ion flows in the topside ionosphere. Ion up-flows at velocities exceeding 1 km/s have been observed in both the nightside auroral zone and the dayside cleft on low-altitude polar-orbiting satellites, including DE-2 [*Loranc et al.*, 1991] and Defense Meteorological Satellite Program (DMSP) [*Redmon et al.*, 2010], and from radars, including Chatanika [*Bates*, 1974], EISCAT [*Foster et al.*, 1998], and ESR [*Ogawa et al.*, 2009]. The observed up-flow is highly variable in time and location, and generally is confined to narrow latitude regions. Large upward ion flows often occur in regions of large ion convection velocities, and are dominated by O^+ and at times enhanced in molecular NO^+.

On DE-2 at 600–1000 km, the occurrence probability of up-flow is generally larger than that of down-flow in the auroral zone but smaller in the polar cap on both the dayside and the nightside. The peak probability spans the convection reversal on the dayside, and is more extended in latitude and located at lower latitude on the nightside. The probability for flows exceeding 100 m s^{-1} increases and moves equatorward with increasing K_p, from about 0.25 near 78° invariant at $K_p \leq 3$– to about 0.35 near 70° at $K_p \geq 6$ on the dayside. In the polar cap (<78° invariant), the probability of up-flow is several times larger during northward IMF than during southward IMF, and it is generally greater in the pre-noon sector than in the pre-midnight sector.

On the DMSP satellites at ~850 km, *Redmon et al.* [2010] extended the up-flow observations of *Coley et al.* [2003] in the dawn-dusk sector to other (pre-noon to noon and pre-midnight to midnight) MLT sectors, and used dynamic auroral boundary coordinates to characterize the location of ion up-flows with respect to the auroral oval. The ion flow was found to be mostly upward in the auroral zone, with peak ion-flux in the noon and midnight sectors, and to be mostly downward in the polar cap except around 09 MLT, where strong upward fluxes were regularly observed.

However, the region of peak ion up-flow does not exactly match the auroral particle precipitation boundaries. Instead, the observed ion-flux peaks at the polar cap edge in the pre-midnight sector irrespective of geomagnetic activity level, and at the equatorward edge of the auroral zone in the dusk sector particularly during moderate and active times.

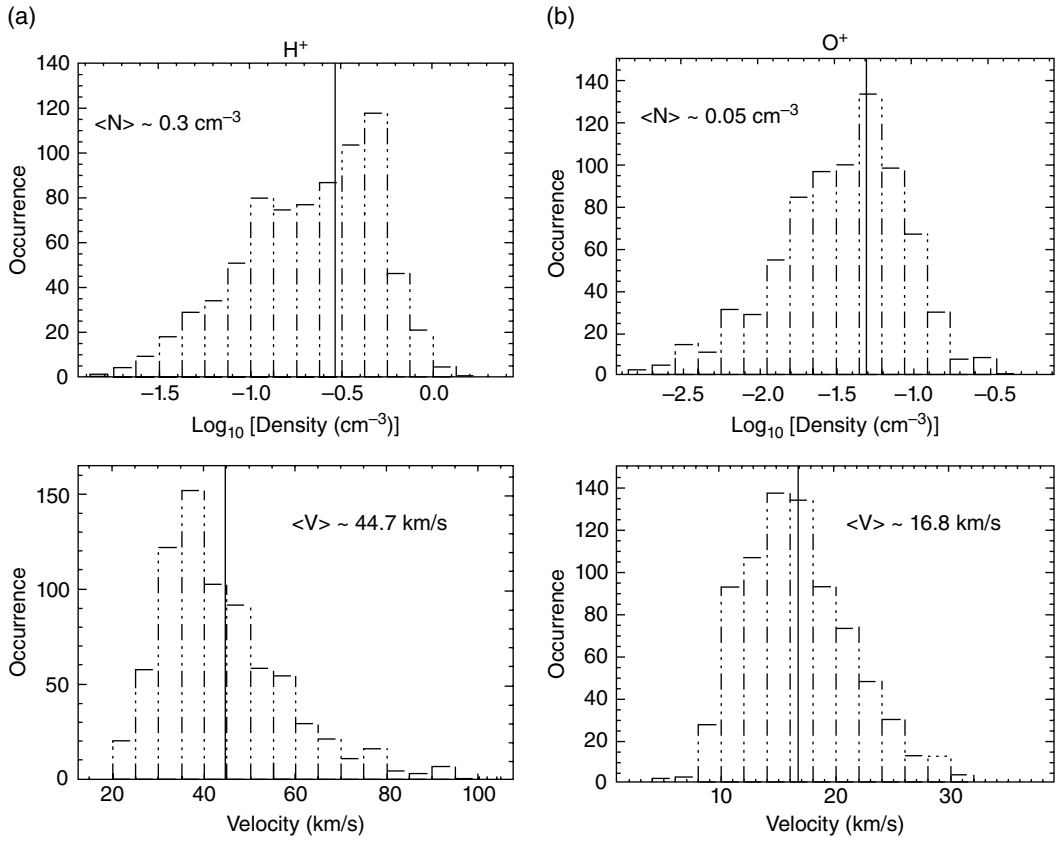

Figure 2.3 Occurrence histograms of (a) H^+ and (b) O^+ polar wind density (top) and parallel velocity (bottom) on Polar at 50,500 km near solar minimum. [Adapted from *Su et al.,* 1998]

The up-flow observed by EISCAT (at 66.2° invariant) generally falls into two types. The type-1 up-flow is associated with strong electric fields in regions of downward field-aligned currents and very low F-region electron densities adjacent to auroral arcs, and it is characterized by ion temperature enhancements and by perpendicular ion temperature anisotropy ($T_\perp > T_{//}$). The latter is indicative of frictional heating of ions drifting through neutrals and production of strong pressure gradients, which push the ions upward. The type-2 up-flow is typically observed above auroral arcs and is characterized by electron temperature enhancement, weak to moderate convection electric fields, and stronger ion flux. All of these features are indicative of auroral electron precipitation and resulting electron ionization. Type-2 up-flow seems to occur more frequently compared with type-1 up-flow [*Wahund et al.*, 1992].

On average, the occurrence probability of up-flow at 500 km altitude is higher on the duskside than on the dawnside and peaks at ~23% in the pre-midnight sector. The up-flow velocity increases monotonically with altitude starting from about 300 km, to values exceeding 100 m/s at 500 km in the majority (~55%) of times [*Foster et al.*, 1998]. Roughly 50–60% of the observed up-flow events occur during intervals of enhanced ion temperature.

The occurrence probability of ion up-flow is significantly larger at all altitudes during disturbed times ($K_P \geq 4$) compared with quiet times [*Liu et al.*, 2001]. Furthermore, the starting altitude of up-flow is lower (200–250 km), and the increase of occurrence probability with geomagnetic activity is much more pronounced on the dawnside than on the duskside, resulting in a higher probability on the dawnside. The increase in probability with altitude is also stronger. The observed magnetic activity dependence of ion up-flow is consistent with ion acceleration in the F-region and topside ionosphere receiving important contributions from both $E \times B$-driven ion frictional heating and precipitating soft electron-driven electron heating.

At ESR (75.4° invariant), the up-flow on the dayside starts or reaches an observable velocity at higher altitudes, and has a larger occurrence probability than on the nightside above 400 km [*Liu et al.*, 2001] as well as a dawn-dusk asymmetry that increases with altitude in favor of the dawnside over the duskside. The starting altitude of ion up-flow increases with solar activity level, with approximately 25% and 16% of the dayside up-flow

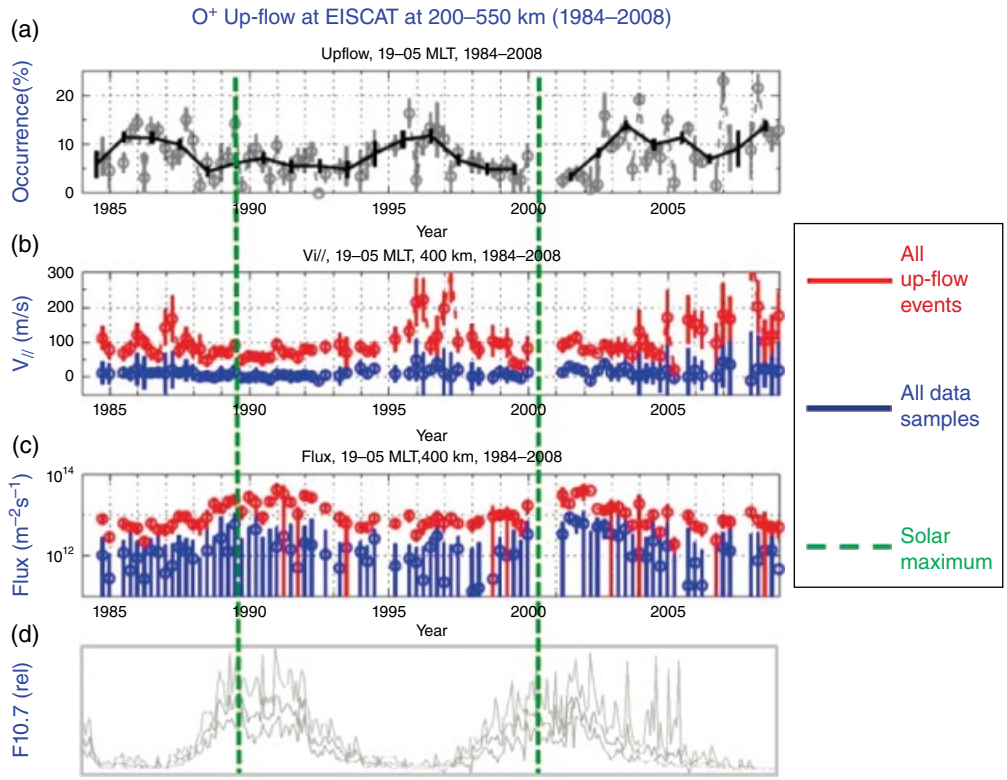

Figure 2.4 Nightside (19–05 MLT) ion up-flow at EISCAT from 1984 to 2008: (a) averaged occurrence probability at 200–550 km, (b) field-aligned ion velocity, and (c) ion flux at 400 km; (d) monthly minimum, mean, and maximum $F_{10.7}$. [Adapted from *Ogawa et al.*, 2010]

events below 400 km (55% and 34% below 450 km) altitude in period of low and high solar activity ($F_{10.7} < 140$ and $F_{10.7} > 140$), respectively.

The up-flow occurrence probability at 500 km altitude increases with K_p, and peaks around geomagnetic noon at ~11–21%, where the averaged ion flux reaches 2×10^9 cm^{-2} s^{-1}, and it is relatively independent of geomagnetic activity level (K_p). During quiet and moderately active periods, the down-flow probability peaks in the dawn sector (03–09 MLT) at ~5–6%. During disturbed periods, the down-flow probability peaks in the noon sector (10–15 MLT) at ~25%, which exceeds the up-flow probability and is indicative of ESR being equatorward of most of the up-flow events.

Ogawa et al. [2009] found the ion up-flow occurrence probability to increase with both solar wind density (above 30 cm^{-3}) and solar wind velocity (up to 700 m s^{-1}), and to peak in value inside the cusp, while the upward ion flux increases with solar wind density and decreases with solar wind velocity. Both IMF B_Y and B_Z are found to affect the up-flow occurrence probability, which increases with increasing magnitude of B_Y and peaks at $B_Z \sim -5$ nT. The apparent movement of the dayside ion up-flow region may be understood in terms of the influence of solar wind velocity and density and the IMF B_Y and B_Z on the shape, size, and location of the up-flow region, since the location of the dayside cusp is known to move equatorward with decreasing IMF B_Z or increasing solar wind dynamic pressure.

The contrast in up-flow occurrence probability distribution between EISCAT and ESR, the probability being higher in the dusk and midnight sectors at EISCAT but higher in the dawn and noon sectors at ESR, is believed to reflect the combined effects of both MLT and latitudinal variations of up-flow at the respective locations of the two radars.

The observed ion up-flows at both EISCAT and ESR exhibit seasonal as well as solar cycle variation [*Foster et al.*, 1998]. Above 300 km altitude at EISCAT, the occurrence probability of up-flow is greater during the winter months, and its nightside maximum is more pronounced near solar maximum [*Liu et al.*, 2001], when the ion flux is also larger and the ion velocity smaller. Figure 2.4a shows the average observed occurrence probability of ion up-flows on the nightside (19–05 MLT) at EISCAT between 200 and 550 km, from 1984 to 2008 when the monthly average of $F_{10.7}$ varied from ~70 to 250 (Figure 2.4d). Figure 2.4b and 2.4c show the

corresponding field-aligned ion velocity and ion flux at 400 km, respectively. On average, the upward ion velocity in up-flow events was a factor of 2 higher at low solar flux than at high solar flux ($F_{10.7} > 140$), when the upward ion flux was a factor of 4 higher. The larger flux at high solar flux (i.e., near solar maximum) is attributed to the stronger solar EUV flux, and the resulting increase in thermospheric temperature, oxygen density, and ionization in the F-region. The smaller velocity is attributed to the higher ion-neutral collision frequency due to the higher exospheric temperature and neutral oxygen density in the thermosphere.

Ogawa et al. [2010] found the average starting altitude of ion up-flow to track the measured electron density profile, and to be typically 100–150 km higher than the latter. At low solar flux, the distribution of starting altitude exhibits a broad peak that starts at ~300 km, peaks near 450 km, and extends to ~520 km. At high solar flux, the distribution shifts to higher altitude, starting near ~350 km, peaking more sharply near 450 km, and extending to at least 540 km. The variation of the starting height with solar activity level can be attributed to the increased atmospheric density and ion-neutral collision frequency at a given altitude near solar maximum: the neutral atomic oxygen density at the starting height of 300 km is $\sim 3 \times 10^8$ cm^{-3} near solar minimum, compared with the corresponding density value of $\sim 3.3 \times 10^8$ cm^{-3} at the (increased) starting height of ~450 km near solar maximum. This is consistent with the fact that the atmospheric density and ion-neutral collision frequency at the starting up-flow altitude are comparable at solar minimum and maximum, respectively.

Both the satellite and the radar observations demonstrate the significant role of both soft electron-driven electron heating and convection-driven ion heating in auroral ion up-flow production. Frictional heating of O^+ ions enhances the ion temperature in the F-region and increases the preexisting parallel pressure gradient, and the ions respond by flowing to higher altitude to attain a new equilibrium scale height distribution [*Bates*, 1974; *Schunk*, 2007]. Although the increase of the scale height is a transient feature, the up-flow can remain if new plasma is horizontally convected into the heating region. The effect of ion frictional heating is expected to increase with K_P and to be stronger on the duskside and in the winter. This explains the higher occurrence probability on the duskside at EISCAT latitude and the increase in occurrence probability with geomagnetic activity at both ESR and EISCAT.

Likewise, soft precipitating electrons deposit their energy in the F-region via electron impact ionization of the neutrals and collisional energy transfer with the neutrals, and thereby increase the average thermal electron energy (i.e., electron temperature) and enhance the ambipolar electric field. The effect of soft electron precipitation is expected to be stronger during disturbed times, particularly in the dusk sector, and to play a more dominant role on the dayside where the precipitating electrons tend to be softer. This explains the higher dayside occurrence probability at ESR compared with EISCAT at both quiet and disturbed times, and the higher probability on the duskside during disturbed times. It also suggests that soft electron-driven electron heating may be more efficient than convection-driven ion heating in driving ion up-flow.

The composition of thermal ion outflows is in general highly variable, not only in the O^+/H^+ ratio but also in the relative abundance of minor ion species, particularly at active times. Figures 2.5a and 2.5b show examples of significant fluxes of upflowing molecular ions in storm-time orbit passes from DE-1 and Akebono, respectively. Figure 2.5a shows the distinct presence of N_2^+, NO^+, and O_2^+ ions on DE-1 above 1 R_E altitude throughout the post-midnight to morning sector in the storm of September 8, 1982. Figure 2.5b shows the presence of N^+ and O^{++} ions at enhanced abundance ($O^{++}/O^+ \approx 0.3$, $N^+/O^+ \approx 1$) as well as the presence of molecular N_2^+ and NO^+ ions on Akebono at 1.4 R_E altitude on the dayside in the storm of March 12, 1990.

The presence of molecular ions at high altitude is a signature of fast ion acceleration in the F-region and topside ionosphere, where they have much shorter recombination lifetimes (~1–10 minutes) compared with atomic O^+ ions due to their fast dissociative recombination rate, as well as higher gravitational escape energy due to their larger mass. In other words, in order to reach higher altitudes, molecular ions from the F-region and topside ionosphere must gain more energy and do so at a faster rate compared with H^+ and O^+ ions.

2.3. SUPRATHERMAL OUTFLOWS

In the category of suprathermal outflows, the occurrence and morphological characteristics of ion beams, conics, and upwelling ions in the different altitude regions were the subject of a number of statistical studies of upflowing ions (UFI) using S3-3, DE-1, Viking, Akebono, Freja, FAST, and Polar data, which were the focus of previous reviews by *Yau and André* [1997], *Moore et al.* [1999], and *Yau et al.*, [2011].

Ion beams are generally observed above 5000 km altitude but are occasionally present down to about 2000 km during active aurora. The occurrence probability of both H^+ and O^+ ion beams increases with altitude at both quiet and active times. The increase is most prominent for the lower-energy (<1 keV) ions. In contrast, ion conics are observed down to sounding rocket altitudes (1000 km or below) [*Yau et al.*, 1983] and up to several Earth radii and

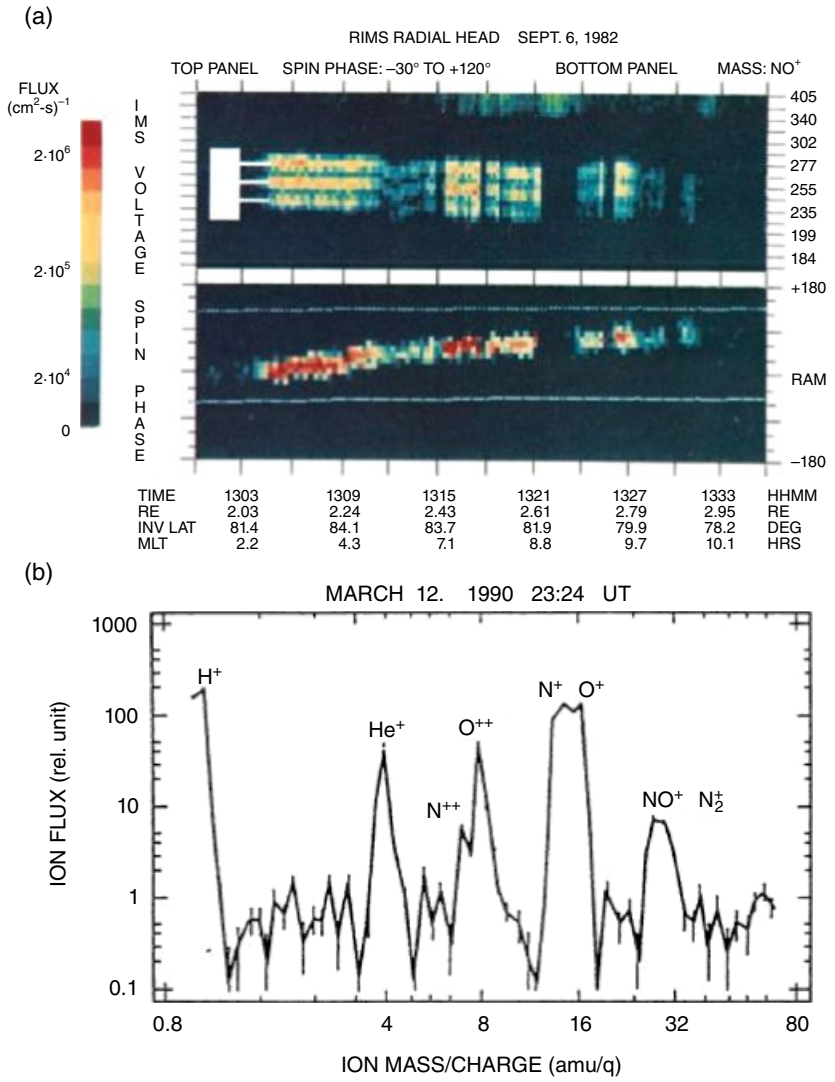

Figure 2.5 Observation of upflowing molecular ions in magnetic storms (a) on DE-1 on September 6, 1982 and (b) on Akebono on March 12, 1990. [Adapted from *Craven et al.*, 1985 and *Yau et al.*, 1993]

beyond [*Hultqvist*, 1983; *Bouhram et al.*, 2004], with decreasing occurrence probability at low energy (<1 keV) with increasing altitude above ~10,000 km. Both ion beams and ion conics are a common phenomenon, with occurrence frequencies sometimes higher than 50% above 1 R_E altitude, and are dominated by H^+ and O^+ ions in the 10 eV to a few keV range; UFI of a few tens of keV energy occasionally occur.

TAI are present regularly down to about 3000 km [*Whalen et al.*, 1991] on the dayside and to 1400–1700 km [*Klumpar*, 1979; *André et al.*, 1994] on the nightside, and occasionally down ~400 km during active aurora [*Yau et al.*, 1983; *Arnoldy et al.*, 1992]. Upwelling ions are observed exclusively in the morning sector of the auroral oval and the lower latitudes of the polar cap, with parallel (upward) and perpendicular energization to energies from one to tens of eV [*Pollock et al.*, 1990]. They are dominated by O^+ ions and are the most persistent suprathermal ion outflow feature in the cleft region, hence the term "cleft ion fountain."

The occurrence probability of both H^+ and O^+ upflowing ions is fairly independent of magnetic activity (K_P index). However, compared with H^+, the intensity distribution of O^+ UFI exhibits a much stronger dependence on magnetic activity as well as much larger seasonal and long-term variations, which are attributed to changes in the incident solar EUV flux on the atmosphere in different seasons of the year and at different phases of the 11-year solar cycle.

Yau et al. [1988] reported net ion outflow rates of both H^+ and O^+ on DE-1 integrated over all MLT and invariant latitudes above 56°, as a function of the K_P index and $F_{10.7}$. The O^+ rate increased exponentially with K_P, by a factor of 20 from $K_P = 0$ to 6, and exceeded 3×10^{26} ions s^{-1}

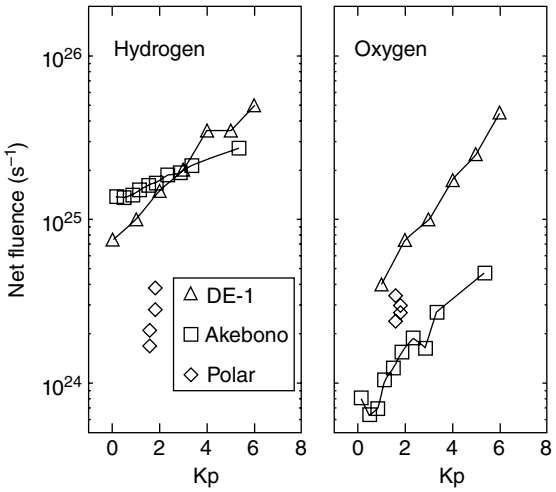

Figure 2.6 H^+ and O^+ ion outflow rates near solar minimum as a function of K_p: (squares) thermal rate on Akebono below 9000 km, (triangles) suprathermal rate on DE-1 above 16000 km, (diamonds) suprathermal rate on Polar below 9000 km. [From *Cully et al.*, 2003]

at times of high solar and magnetic activity. The rate at low solar activity was about a factor of 4 smaller than that at high activity. In contrast, the H^+ rate was very similar across each of the three $F_{10.7}$ ranges. In all three $F_{10.7}$ ranges, the dependence of the O^+ rate on K_P was similar. In comparison, the H^+ rate increased with K_P more moderately, by a factor of 4 from $K_P = 0$ to 6.

Peterson et al. [2008] analyzed the observed ion outflow flux and energy distributions near Polar perigee in dynamic boundary-related coordinates [*Andersson et al.*, 2004], and found that for all three ion species (H^+, O^+, and He^+), the observed energetic UFI is predominantly in the midnight quadrant of the auroral zone, including ~50% of the total H^+ and He^+ flux and ~30% of the O^+ flux, compared with ~37% of O^+ flux in the noon quadrant where most of the flux was on cusp field lines (see e.g., *Zheng et al.*, 2005).

Only a very small fraction (~2–3%) of the observed energetic UFI was in the polar cap. However, their presence confirms that not only are energetic ions being transported by prevailing convection electric fields to the high-altitude polar cap, but they are also produced by ion acceleration events in the polar cap ionosphere [*Shelley et al.*, 1982; *Maggiolo et al.*, 2011], likely in connection with polar cap arcs during northward IMF and quiet geomagnetic conditions.

Figure 2.6 compares the observed low-energy ion outflow rates observed on Akebono below 9000 km near solar minimum with the corresponding suprathermal rates on Polar at the same altitudes (15 eV–16 keV) and on DE-1 above 16,000 km (10 eV–16 keV), respectively. The rate of low-energy H^+ on Akebono is comparable with the suprathermal rate on DE-1 and a factor of 4–10 higher than the suprathermal rate on Polar. This indicates that significant acceleration of H^+ occurs above 9000 km in the high-latitude ionosphere. In contrast, the rate of low-energy O^+ below 9000 km is less than the corresponding suprathermal rate above this altitude, which is in turn less than the corresponding suprathermal rate above 16,000 km. This means that a significant fraction of O^+ is accelerated below 9000 km, and that the acceleration continues between 9000 and 16,000 km. In other words, a significant fraction of low-energy ions at low altitudes in the high-latitude ionosphere, including polar wind ions and auroral ion up-flows, is accelerated to suprathermal energies at higher altitudes, where it "loses its identity" as thermal-energy ions. Thus, it is important to consider both thermal and suprathermal ion outflow in the high-latitude ionosphere as an integrated entity.

2.4. SUMMARY AND DISCUSSION

A brief review is presented above of ion outflow observations over the past four decades. A composite view that emerges from these observations is that the system of ionospheric ion outflows constitutes an important response of the ionosphere-thermosphere to solar and magnetospheric energy input, and is constrained by the structure of the thermosphere and the variability of this energy input in an 11-year Solar Cycle. In other words, the different thermal and suprathermal ion outflow populations exhibit significant variability in occurrence, energy, composition, and intensity distributions.

The body of observations to date suggests that (a) the thermal outflows are the source of low-energy plasma for the suprathermal outflows at higher altitudes, (b) parallel, perpendicular, and centrifugal acceleration processes all contribute to the production of suprathermal outflows, with centrifugal acceleration playing a crucial role at quiet times, (c) cold ionospheric ions are the "rule" rather than the "exception" in the magnetosphere, given the substantial fraction of such ions that are often "hidden" in the sunlit magnetosphere, and (d) the presence of low fluxes of ionospheric O^+ ions "in the pipeline" between the ionosphere and the plasma sheet at quiet times may have a non-negligible influence on the dynamics of the inner magnetosphere at active times.

ACKNOWLEDGMENTS

We acknowledge the support for this research from the Canadian Space Agency and the Natural Science and Engineering Research Canada (NSERC) to A. W. Yau, from National Aeronautics and Space Administration (NASA) to W. K. Peterson, and from Institute of Space

and Astronautical Sciences (ISAS), Japan Aerospace Exploration Agency (JAXA) to T. Abe.

REFERENCES

Abe, T., B. A. Whalen, A. W. Yau, R. E. Horita, S. Watanabe, and E. Sagawa (1993a), EXOS-D (Akebono) SMS observations of the polar wind, *J. Geophys. Res.*, *98*, 11191–11203.

Abe, T., B. A. Whalen, A. W. Yau, S. Watanabe, E. Sagawa, and K. I. Oyama (1993b), Altitude profile of the polar wind velocity and its relationship to ionospheric conditions, *Geophys. Res. Lett.*, *20*, 2825–2828.

Abe, T., S. Watanabe, B. A. Whalen, A. W. Yau, and E. Sagawa (1996), Observations of polar wind and thermal ion outflow by Akebono/SMS, *J. Geomag. Geoelectr. 48*, 319–325.

Abe, T., A. W. Yau, S. Watanabe, M. Yamada, and E. Sagawa (2004), Long-term variation of the polar wind velocity and its implication for the ion acceleration process: Akebono/suprathermal ion mass spectrometer observations, *J. Geophys. Res.*, *109*, doi:10.1029/2003JA010223.

Andersson, L., W. K. Peterson, and K. M. McBryde (2004), Dynamic coordinates for auroral ion outflow, *J. Geophys. Res.*, *109*, A08201, doi:10.1029/2004JA010424.

André, M., P. Norqvist, A. Vaivads, et al. (1994), Transverse ion energization and wave emissions observed by the Freja satellite, *Geophys. Res. Lett. 21*, 1915–1918.

Arnoldy, R.L., K.A. Lynch, P.M. Kintner, et al. (1992), Bursts of transverse ion acceleration at rocket altitudes, *Geophys. Res. Lett. 19*, 413–416.

Banks, P. M., and G. Kockarts (1973), Aeronomy, Part B, Academic Press, New York, NY, USA.

Banks, P. M., and T. E. Holzer (1968), The polar wind, *J. Geophys. Res.*, *73*, 6846–6854 doi:10.1029/JA073i021p06846.

Bates, H. F. (1974), Atmospheric expansion from Joule heating, *Planet. Space Sci., 22*, 925.

Bouhram, M., B. Klecker, W. Miyake, et al. (2004), On the altitude dependence of transversely heated O^+ distributions in the cusp/cleft, *Ann. Geophys.*, *22*, (380) 1787–1798.

Coley, W. R., R. A. Heelis, and M. R. Hairston (2003), High-latitude plasma outflow as measured by the DMSP spacecraft, *J. Geophys. Res.*, *108*, 1441, doi:10.1029/2003JA009890.

Craven, P. D., R. C. Olsen, C. R. Chappell, and L. Kakani (1985), Observations of molecular ions in the earth's magnetosphere, *J. Geophys. Res.*, *90*, 7599–7605.

Cully, C. M., E. F. Donovan, A. W. Yau, and G. G. Arkos (2003), Akebono suprathermal mass Spectrometer observations of low-energy ion outflow: dependence on magnetic activity and solar wind conditions, *J. Geophys. Res.*, *108*, 1093, doi:10.1029/2001JA009200.

Foster, C., M. Lester, and J. A. Davies (1998), A statistical study of diurnal, seasonal and solar cycle variations of F-region and topside auroral upflows observed by EISCAT between 1984 and 1996, *Ann. Geophys. 16*, 1144–1158.

Hultqvist, B. (1983), On the origin of the hot ions in the disturbed dayside magnetosphere, *Planet. Space Sci.*, *31*, 173–184.

Klumpar, D. M. (1979), Transversely accelerated ions: an ionospheric source of hot magnetospheric ions, *J. Geophys. Res. 84*, 4229–4237.

Lemaire, J., and M. Scherer (1971), Simple model for an ion-exosphere in an open magnetic field, *Phys. Fluids*, *14*, 1683–1694.

Lemaire, J., W. K. Peterson, T. Chang, R. W. Schunk, A. R. Barakat, H. G. Demars, and G. V. Khazanov (2007), History of kinetic polar wind models and early observations, *J. Atmos. Solar Terr. Phys.*, *69*, 1901–1935.

Liu, H. X., S. Y. Ma, K. Schlegel (2001), Diurnal, seasonal, and geomagnetic variations of large field-aligned ion upflows in the high-latitude ionospheric F-region, *J. Geophys. Res. 106*, 14651–14661.

Liu, X., W. Wang, J. P. Thayer, et al. (2014), The winter helium bulge revisited, *Geophys. Res. Lett.*, *41*, 6603–6609, doi:10.1002/2014GL061471.

Loranc, M., W. B. Hanson, R. A. Heelis, and J. P. St.-Maurice (1991), A morphological study of vertical ionospheric flows in the high-latitude F region, *J. Geophys. Res. 96*, 3627–3646.

Marubashi, R. (1970), Escape of the polar ionospheric plasma into the magnetospheric tail, *Rep. Ionos. Sp. Res. Japan*, *24*, 322–340.

Maggiolo, R., M. Echim, J. De Keyser, D. Fontaine, C. Jacquey, and I. Dandouras (2011), Polar cap ion beams during periods of northward IMF: Cluster statistical results, *Ann. Geophys.*, *29*, 771–787, doi:10.5194/angeo-29-771-2011.

Moore, T. E., R. Lundin, D. Alcayde, et al. (1999), Source processes in the high-latitude ionosphere. *Space Sci. Rev. 88*, 7–84.

Ogawa, Y., S. C. Buchert, R. Fujii, S. Nozawa, and A. P. van Eyken (2009), Characteristics of ion upflow and downflow observed with the European Incoherent Scatter Svalbard radar, *J. Geophys. Res. 114*, A05305, doi:10.1029/2008JA013817.

Ogawa, Y., S. C. Buchert, A. Sakurai, S. Nozawa, and R. Fujii (2010), Solar cycle dependence of ion upflow in the polar ionosphere observed with the EISCAT Tromso UHF radar. *J. Geophys. Res. 115*, A07310, doi:10.1029/2009JA014766.

Peterson, W. K., L. Andersson, B. C. Callahan, H. L. Collin, J. D. Scudder, and A. W. Yau (2008), Solar-minimum quiet time ion energization and outflow in dynamic boundary related coordinates, *J. Geophys. Res.*, *113*, A07222, doi:10.1029/2008JA013059.

Pollock, C. J., M. O. Chandler, T. E. Moore, J. H. Waite, Jr., C. R. Chappell, and D. A. Gurnett (1990), A survey of upwelling ion event characteristics, *J. Geophys. Res.*, *95*, 18969–18980.

Redmon, R. J., W. K. Peterson, L. Andersson, E. A. Kihn, W. F. Denig, M. Hairston, and R. Coley (2010), Vertical thermal O^+ flows at 850 km in dynamic auroral boundary coordinates, *J. Geophys. Res.*, *115*, A00J08, doi:10.1029/2010JA015589.

Schunk, R. W. (2007), Time-dependent simulations of the global polar wind, *J. Atmos. Solar Terr. Phys. 69*, 2028–2047.

Shelley, E. G., R. D. Sharp, and R. G. Johnson (1976), Satellite observations of an ionospheric acceleration mechanism, *Geophys. Res. Lett.*, *3*, 654–657.

Shelley, E. G., W. K. Peterson, A. G. Ghielmetti, and J. Geiss (1982), The polar ionosphere as a source of energetic magnetospheric plasma, *Geophys. Res. Lett.*, *9*, 941–944.

Su, Y. J., J. L. Horwitz, T. E. Moore, B. L. Giles, M. O. Chandler, P. D. Craven, M. Hirahara, and C. J. Pollock (1998), Polar wind survey with the thermal ion dynamics experiment/plasma source instrument suite aboard POLAR, *J. Geophys. Res.*, *103*, 29305–29337.

Tam, S. W. Y., T. Chang, and V. Pierrard (2007), Kinetic modeling of the polar wind, *J. Atmos. Solar Terr. Phys. 69*, 1984–2027.

Wahlund, J. E., H. J. Opgenoorth, I. Haggstrom, K. J. Winser, and G. O. L. Jones (1992), EISCAT observations of topside ionospheric ion outflows during auroral activity: Revisited, *J. Geophys. Res.*, *97*, 3019–3037.

Whalen, B. A., S. Watanabe, and A. W. Yau (1991), Thermal and suprathermal ion observations in the low altitude transverse ion energization region. *Geophys. Res. Lett. 18*, 725–728.

Yau, A. W., and M. André (1997), Source processes in the high latitude ionosphere, *Space Sci. Rev., 80*, 1–25.

Yau, A. W., B. A. Whalen, A. G. McNamara, P. G. Kellogg, and W. Bernstein (1983), Particle and wave observations of low-altitude ionospheric ion acceleration events, *J. Geophys. Res.*, *88*, 341–355.

Yau, A. W., W. K. Peterson, and E. G. Shelley (1988), Quantitative parameterization of energetic ionospheric ion outflow, in *Modeling Magnetospheric Plasma, Geophysical Monograph 44*, American Geophysical Union, Washington, DC. pp. 211–217.

Yau, A. W., B. A. Whalen, C. Goodenough, E. Sagawa, and T. Mukai (1993), EXOSD (Akebono) observations of molecular NO^+ and N_2^+ upflowing ions in the high-altitude auroral ionosphere. *J. Geophys. Res. 98*, 11205–11224.

Yau, A. W., T. Abe, and W. K. Peterson (2007), The polar wind: recent observations, *J. Atmos. Solar Terr. Phys.*, *69*, 1936–1983.

Yau, A.W., T. Abe, and W.K. Peterson (2011), Influences of the ionosphere, thermosphere and magnetosphere on ion outflows, in W. Liu, M. Fujimoto (eds.), *The Dynamic Magnetosphere*, IAGA Special Sopron Book Series 3, pp. 283–314, Springer B.V., doi:10.1007/978-94-007-0501-2_16.

Zheng, Y., T. E. Moore, F. S. Mozer, C. T. Russell, and R. J. Strangeway (2005), Polar study of ionospheric ion outflow versus energy input, *J. Geophys. Res.*, *110*, A07210, doi:10.1029/2004JA010995.

3

Low-energy Ion Outflow Observed by Cluster: Utilizing the Spacecraft Potential

S. Haaland[1,2], M. André[3], A. Eriksson[3], K. Li[2], H. Nilsson[4], L. Baddeley[5], C. Johnsen[6], L. Maes[7], B. Lybekk[8], and A. Pedersen[8]

Video of Yosemite Talk, URL: http://dx.doi.org/10.15142/T3MS30

ABSTRACT

A significant amount of mass is lost from the Earth's atmosphere through ions escaping from the polar ionosphere. Due to spacecraft charging effects, in situ measurements using traditional plasma instruments are typically not able to detect the low energy part of the outflow. Recent advances in instrumentation and methodology, combined with comprehensive data sets from the Cluster constellation of spacecraft have provided far better opportunities to assess the role of the low energy ions. With this new technique, it is possible to bypass detection problems caused by spacecraft charging effects, and provide quantitative, in situ estimates of cold ion density and outflow velocity. In this chapter, we give an overview of these advances and highlight some of the key results based on this methodology. The results corroborate earlier findings that polar rain and the open polar cap is the primary source of cold outflow, but we also find enhanced cold outflow from the cusp and auroral zone though, in particular during disturbed geomagnetic conditions. The transport of cold ions is mainly governed by the convection, and most of the outflowing ions are transported to the nightside plasma sheet and recirculated in the magnetosphere. Transport times are of the order of two to four hours from the ionosphere to the nightside magnetospheric plasma sheet. Direct loss along open field lines downtail into the solar wind only takes place during quiet magnetospheric conditions with low or stagnant convection. Only about 10% of the total cold outflow is directly lost downtail into the solar wind.

[1]*Birkeland Centre for Space Science, University of Bergen, Norway*
[2]*Max-Planck Institute for Solar Systems Research, Göttingen, Germany*
[3]*Swedish Institute of Space Physics, Uppsala, Sweden*
[4]*Swedish Institute of Space Physics, Kiruna, Sweden*
[5]*Birkeland Centre for Space Science, The University Centre in Svalbard, Longyearbyen, Norway*
[6]*Department of Geophysics, University of Oslo, Norway*
[7]*Royal Belgian Institute for Space Aeronomy, Brussels, Belgium*
[8]*Department of Physics, University of Oslo, Norway*

3.1. INTRODUCTION

Every day, the Earth loses a significant amount of mass through escape of atmospheric material into space. Much of the loss is made up by ionized material, and the outflow of low energy ions of ionospheric origin is believed to be a significant contributor to the magnetospheric plasma population [*Horwitz*, 1982; *Chappell et al.*, 1987; *André and Cully*, 2012].

Escape from the atmosphere, whether neutral or ionized, can be understood by considering the forces acting

Magnetosphere-Ionosphere Coupling in the Solar System, Geophysical Monograph 222, First Edition.
Edited by Charles R. Chappell, Robert W. Schunk, Peter M. Banks, James L. Burch, and Richard M. Thorne.

on the thermospheric constituents. If the total upward forces exceed downward forces, ions are accelerated upward and can potentially escape. Gravity is usually the main downward force and acts on both neutrals and ions, and depends on mass and altitude. For neutrals, pressure gradients due to thermal effects constitute the dominant upward force. For ions, the picture is more complicated, and additional electromagnetic forces must be taken into account. Some of these forces (which may be directed either upward or downward) depend on the mass of the particle; others do not. Charge (and charge state) also play a role for electromagnetic forces.

It is often convenient to cast the force balance picture into an energy balance analogy. In this description, the Earth's gravitational potential energy balanced against the ions' upward directed kinetic energy. For particles at rest, minimum escape energies for protons and oxygen from the Earth are around 0.6 and 10 electron-volt (eV), respectively.

Above the open polar cap regions, where no hydrostatic equilibrium can be established, low energy electrons, due to their low mass, can easily escape the Earth's gravitational potential [e.g., *Dessler and Michel*, 1966]. As a consequence, an ambipolar electric field arises due to the charge separation. This ambient electric field acts as a force on charged particles and decelerates electrons and accelerates ions [see e.g., *Kitamura et al.*, 2017, (this volume) and references therein for more details here]. Simulations by *Su* [1998] suggest a resulting total potential drop on the order of a few 10s of volts over an altitude of several Earth radii (R_E 6371 kilometer [km]). This ambient electric field, although very small, is sufficient to maintain a flow of plasma from the ionosphere into the magnetosphere. This outflow, the polar wind, was first predicted by models [*Axford*, 1968; *Banks and Holzer*, 1968]. Experimental observations of the polar wind from were first reported by *Hoffman* [1970] and later in other sources [e.g., *Hoffman et al.*, 1974; *Chandler et al.*, 1991; and *Abe et al.*, 1993]. See also *Yau et al.* [2017] (this volume) for a comprehensive overview. All these observations were taken below 1 R_E altitude.

At higher altitudes (above a few R_E), it becomes notoriously difficult to measure the low energy part of the outflowing plasma population. In the tenuous plasma polar cap and lobe regions of the Earth's magnetosphere, the spacecraft voltage often reaches several tens of volts positive due to photo emissions. This spacecraft potential will shield low energy ions from reaching the spacecraft sensors. Unless the effects of spacecraft charging can be eliminated, cold ions therefore remain invisible for particle detectors. Attempts to bypass this problem has so far typically involved some form of active spacecraft potential control. A notable example utilizing this kind of neutralization is the study by *Su et al.* [1998], which used particle measurements from the Polar spacecraft. During a limited time period the onboard Plasma Source Instrument (PSI) was operating, and was able to keep the spacecraft voltage at a few volts. *Su et al.* [1988] were then able to observe and characterize polar wind outflow at high altitudes.

The Cluster spacecraft [*Escoubet et al.*, 1997; *Escoubet and Schmidt*, 2000], forming the basis for most of the results discussed in the present paper, also has an active spacecraft potential control [Active Spacecraft Potential Control (ASPOC), see *Riedler et al.*, 1997] but to our knowledge no specific study focusing on polar wind or ion outflow has systematically utilized this. Furthermore, active spacecraft control typically works by emitting metallic ions from a finite reservoir. Continuous operation over an extended time is therefore not feasible. The last ASPOC instrument on Cluster ceased working in 2006 when this reservoir was depleted [*Torkar and Jeszenszky*, 2010].

Engwall et al. [2006] presented a completely different approach to cold ion outflow detection. By utilizing data from two independent electric field instruments, they were able to exploit spacecraft charging to derive densities and outflow velocities of cold plasma. Basically, a supersonic flow of low-energy ions forms a wake behind the charged spacecraft. The electric field caused by this wake, combined with a functional dependence between the ambient plasma density and the spacecraft potential, is then used to determine the cold ion outflow. This technique has been applied by a number of follow-up studies, e.g., *Engwall, et al.* [2009a]; *Nilsson et al.* [2010]; *Haaland, et al.* [2012a, b]; *Li et al.* [2012, 2013]; *André et al.* [2014]; *Haaland et al.* [2015]; *Li et al.* [2016].

The purpose of this chapter is to give an overview of the methodology and some of the key results obtained from this new technique. The chapter is organized as follows: In Section 2, we explain why cold ion measurements are difficult and how the instrumentation onboard Cluster is used to bypass these difficulties. Thereafter, in Section 3, we present a description of the Cluster cold ion data set and its characteristics. Section 4 presents some of the results based on this methodology. Finally, Section 5 is a summary of the results.

3.2. THE COLD ION DETECTION CHALLENGE

So why are measurements of cold ion so difficult, and why are low energy ions sometimes referred to as *invisible* or *hidden* [e.g., *Olsen*, 1982; *Olsen et al.*, 1985; *Chappel et al.*, 1987, 2000; *André and Cully*, 2012]? To answer these question, we have to take a closer look at the environment in which spacecraft operate.

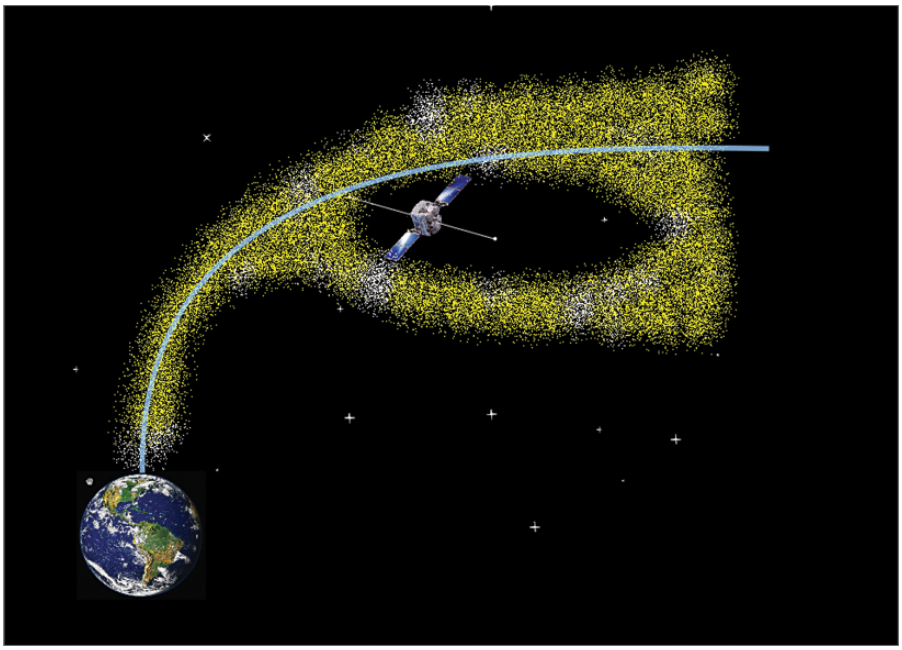

Figure 3.1 Illustration of shielding due to spacecraft charging. Low energy ions emanating from the polar cap region travel upward along the magnetic field lines. Due to a positive spacecraft charge, ions with energies below the spacecraft potential energy will not reach particle detectors onboard the satellite; they remain 'invisible.' A wake, void of ions, but filled with electrons, will be formed downstream of the spacecraft.

Spacecraft traversing the high altitude polar cap and the magnetically connected lobe regions spend most of their time in sunlight. Solar radiation, in particular the ultraviolet (UV) and extreme ultraviolet (EUV) range, corresponding to 2 to 20 nanometer (nm) wavelengths, causes photoelectron emissions from the surface of the spacecraft. In low density plasma regions like the high altitude polar cap regions and in the magnetotail lobes, this electron loss cannot be compensated. The result is a current imbalance, with a net electron current away from the spacecraft. In the lobe and polar cap, where the tenuous plasma is insufficient to replenish the electron loss, the spacecraft will end up with an excess of positive charges. Consequently, the spacecraft can end positively charged to several 10s of volts [see e.g., *Lybekk et al.*, 2012]. Unless this charging can be prevented or circumvented, this will cause problems for low energy plasma measurements.

Typically, there are no strong heating or field aligned acceleration mechanisms above the polar cap region or in the lobes, and the outflowing ions will not gain significant energy as they move outward. Ions of ionospheric origin are therefore characterized (and identified) by low energies. If the energy of the ions is below the spacecraft potential energy (eV_{SC}, where e is elementary charge and V_{SC} is the spacecraft charge relative to the ambient plasma), these ions will be deflected away from the positively charged spacecraft. Unless the ions have sufficient energy to overcome this deflection, they will not be able to reach particle detectors on the spacecraft. They are "invisible" as illustrated in Figure 3.1.

In the following, we will refer to these ions as "cold," where the term cold implies that the total energy of the ions is below the spacecraft potential energy. Note that this inability to measure cold ions is completely independent of particle sensor properties such as sensitivity, noise levels, and energy thresholds. Spacecraft charging implies that the particles to be measured simply do not reach the sensors. A completely different approach is therefore required.

Remote sensing of cold ion outflow is also difficult. Ground-based measurements (e.g., incoherent scatter radars) can only measure up to about 1000 km altitude. Vertical upward motion at these altitudes, sometimes termed upwelling, is is often associated with a significant downward vertical motion. It is thus difficult to assess how much plasma actually reaches escape velocity and eventually escapes the Earth's gravitational field. Given that the ambipolar electric field responsible for the escape can span several Earth radii in altitude, low orbit satellites, although often less affected by spacecraft charging due to higher ambient plasma densities, have similar issues.

3.2.1. Utilizing Spacecraft Potential and Wake

A unique feature of the Cluster satellite mission is the combination of two complementary electric field experiments, the Electron Drift Instrument (EDI) [see

Paschmann et al., 1997; *Quinn et al.*, 2001] and the Electric Field and Wave (EFW) experiment [see *Gustafsson et al.*, 2001]. This combination is the key element for the new technique to estimate cold ion flux.

EFW is a classic double probe experiment, consisting of two pairs of equally shaped spherical probes, each mounted on a wire boom approximately 40 meters (m) away from the spacecraft body. Only the spin plane electric field can be measured by EFW, but by assuming no or negligible electric potential drop along the magnetic field, $E_{\perp} >> E_{\parallel}$, the full three-dimensional electric field can sometimes be estimated.

EDI is based on the drift of an electron gyro center in the presence of external forces. Each Cluster spacecraft is equipped with two EDI gun/detector units. Each gun emits a modulated electron beam with a fixed beam energy. The beam energy can be switched between 500 eV and 1 keV to measure the effects of magnetic gradients, but because these are usually small compared to the local electron gyro radius, the beam is typically kept fixed at 1 keV. The direction of this beam is continuously controlled through a servo loop so that the beam returns to the detector unit. The gyro center position and motion can then be determined from triangulation (or, in some regions, from the time of flight of the emitted electrons). For a known magnetic field with negligible gradients, the gyro center drift of the emitted beam is proportional to the convective electric field. The measurement principle of EDI does not allow for a continuous operation in all plasma regimes, but in regions with fairly stable magnetic field, and low electron background plasma, EDI provides the full three-dimensional convective electric field with very high accuracy.

3.2.1.1. Cold Plasma Density

The spacecraft charge can be used to our advantage, however. Regarding spacecraft charge, the voltage difference between the probes is assumed to be at or close to the ambient plasma potential and the electric potential of the spacecraft body.

Spacecraft charging depends on solar irradiance, spacecraft surface material, spacecraft surface area, and the ambient plasma density. With the former parameters known, it is possible to use the spacecraft potential to estimate the ambient electron density, and thus the plasma density [e.g., *Pedersen et al.*, 2001, and references therein]. In general, a relation of the form

$$N_e = Ae^{-BV_{SC}} + Ce^{-DV_{SC}} \tag{3.1}$$

exists. N_e is the sought after electron density, V_{SC} is the spacecraft potential relative to the ambient plasma. The coefficients A, B, C, and D are determined from calibrations against other measurements, and implicitly contain information about solar illumination and spacecraft surface properties. In *Lybekk et al.* [2012], the charge effect caused by the EDI electron emission was also taken into account and incorporated into the above calibration coefficients.

3.2.1.2. Cold Ion Bulk Velocity

The bulk flow of the plasma can be obtained by combining measurements from the EDI and EFW instruments onboard Cluster.

If the bulk energy, E_{Ki} of the cold ions flowing across the spacecraft is larger than their thermal energy, kT_i, i.e., the following inequality exists:

$$kT_i < E_{Ki} < eV_{SC}, \tag{3.2}$$

a wake void of ions will be formed downstream of the spacecraft. Electrons, however, with their higher mobility (typically $kT_e >> E_{Ke}$), will be able to fill the wake. Consequently, an electric field, $\vec{E}^W$ along the bulk flow direction, $\vec{u}$ will arise:

$$\vec{E}^W = g\vec{u} \tag{3.3}$$

where the scaling factor, g, is a function of the local plasma parameters, and can be experimentally determined [*Engwall et al.*, 2006].

The size of the wake is comparable to the boom-to-boom scale size of the spacecraft but much smaller than the gyro radius of the 1 keV electron beam emitted by EDI. Thus, EFW will be influenced by the artificial electric field, whereas EDI is not affected. The wake electric field can therefore expressed as a deviation between the electric field measured by EFW, $\vec{E}^{EFW}$ and the real, unperturbed ambient electric field $\vec{E}^{EDI}$

$$\vec{E}^W = \vec{E}^{EFW} - \vec{E}^{EDI} = g\vec{u} \tag{3.4}$$

Note that the perpendicular part of the bulk flow, $\vec{u}_{\perp}$, is obtained directly from the EDI measurements; $\vec{u}_{\perp} = \vec{E}^{EDI} \times \vec{B}/B^2$. The parallel component of u is then obtained by first decomposition $\vec{E}^W$ into two spin plane component, E_x^W and E_x^W. An explicit expression for the parallel bulk velocity of the cold ions is thereafter obtained from:

$$u_{\parallel} = \frac{E_x^W u_{\perp}, y + -E_y^W u_{\perp}, x}{E_y^W B_x - E_x^W By} \tag{3.5}$$

where B is the magnetic field.

Note that wake formation as such is not exclusive to the polar cap or lobe regions [e.g., *Whipple et al.*, 1974 and references therein], but the combination of the two electric field measurements onboard Cluster has made determination of the bulk velocity possible for the first time.

3.2.1.3. Flux of Cold Ions

From the above equations (1) and (5), the flux of cold ions at the spacecraft position can now be determined:

$$f_{\parallel} = N_e * u_{\parallel} \tag{3.6}$$

We shall refer to the above $f_{\parallel}$ as local flux, noting that it is the in situ flux at Cluster, taken anywhere between 4 and 19 R_E altitudes. To facilitate comparison with other ion outflow measurements, and to estimate the total outflow, it is useful to normalize the outflow to a certain altitude, typically the topside ionosphere or exobase. Using flux conservation considerations and magnetic flux tube cross section from a magnetic field model, we can now scale this flux to ionospheric altitudes (here 1000 km). We shall later refer to this as *mapped flux*. The total outflow can then be obtained by integrating this mapped flux over the source area.

3.2.2. Estimating Total Outflow Rates

In the outflow estimates given in *Engwall et al*. [2009a, 2009b], it was assumed that the source area was the open polar cap region, simply defined as the area above 70° invariant latitude at 1000 km altitude. They also made no provisions for any time dependent or disturbance dependent variations of the total polar cap area, and also assumed identical areas in the Northern and Southern Hemisphere. *Haaland et al*. [2012a, 2012b], used a slightly more realistic approach based on a model by *Storelis et al*. [1998], which took into account variation in polar cap size. Later, *Li et al.* [2012], using the same data set, confirmed that the open polar cap was the source region. These results also demonstrated large variation in the source area with disturbance levels; the source area was significantly larger during disturbed conditions, consistent with an expanding and contraction polar cap.

3.2.3. Constraints and Limitations in Data and Method

It is fair to say that the above methodology and the Cluster cold ion data set can only provide a partial view of the total escape of ionized material from the Earth's atmosphere.

From the above derivation, one notes that it is not possible to distinguish between different ion species. Nor is any distinction between ion charge state possible. The wake method is more sensitive to lighter ions, as these are more affected by the wake, however. Observations by *Su et al.* [1998] indicate that hydrogen is the dominant species in low-energy outflow from the polar cap region. Nevertheless, in *Engwall et al.* [2009a] and *André et al.* [2014] the derived densities were lowered by a factor of 0.8 to account for the presence of heavy ions. In reality, the abundance of heavier ions, typically oxygen, varies both with geomagnetic activity and source location. Oxygen is more likely to emanate from the cusp and auroral zone [e.g., *Yau and Andre*, 1997; *Lockwood et al.*, 1985a, 1985b], though.

Equation (2) puts limits on temperature and bulk energy of the ions possible to detect. Also, since the velocity determination rests on the identification of a downstream wake (which is not always observed, even in the polar cap and lobe regions), the data set is not continuous in time. The bulk flow direction should have a significant component along the spin plane of the spacecraft. Otherwise, the EFW probes will not be able to measure the wake field. This is usually no issue in the lobes, where the magnetic field is stretched out, but can be an issue closer to Earth.

Also, as with any collection of experimental data, there are uncertainties related to both measurements, methodology, and the underlying assumptions. *Engwall et al.* [2009a] estimated that error due to methodology is of the order of ± 40% or less for velocity calculations and of the order of 20% for electron density calculations. The statistical spread in the observations is much larger than this.

3.3. THE CLUSTER COLD ION DATA SET

Cluster consists of four identical spacecraft flying in formation with varying separation distance. The orbit is an approximately 4 x 19 R_E polar orbit with a duration of about 57 hours. The spacecraft traverses the lobe region from July to October, so the cold ion observations are limited to this season. In the community, the four spacecraft are conveniently referred to as C1, C2, C3, and C4. The instrumentation is identical, but not all instruments work on all spacecraft. In particular, EDI data are available from C1 and C3 throughout the time period 2001 to 2010 relevant for the present paper. EDI data from C2 are available until early 2004 but has not been used to derive cold ion data. No EDI data are available from C4. Data from EFW are available from all four spacecraft, with limitations as described in *André et al*. [2014]. In particular, EFW data from C3 are less useful during much of 2006 due to mismatch between instrument bias current settings and actual photoemissions.

Two large data sets based on Cluster observations and the above wake method have been compiled. The first data set, derived and presented in *Engwall et al*. [2009a], consists of approximately 170,000 records with cold ion density and bulk outflow velocity. This data set is based on C3 measurements for the years 2001 to 2005.

In 2013, the EFW team in Uppsala started a project to update and extend the Cluster cold ion data set. This involved analysis also of data from the Cluster C1 spacecraft, and also for later years. This new data set presently

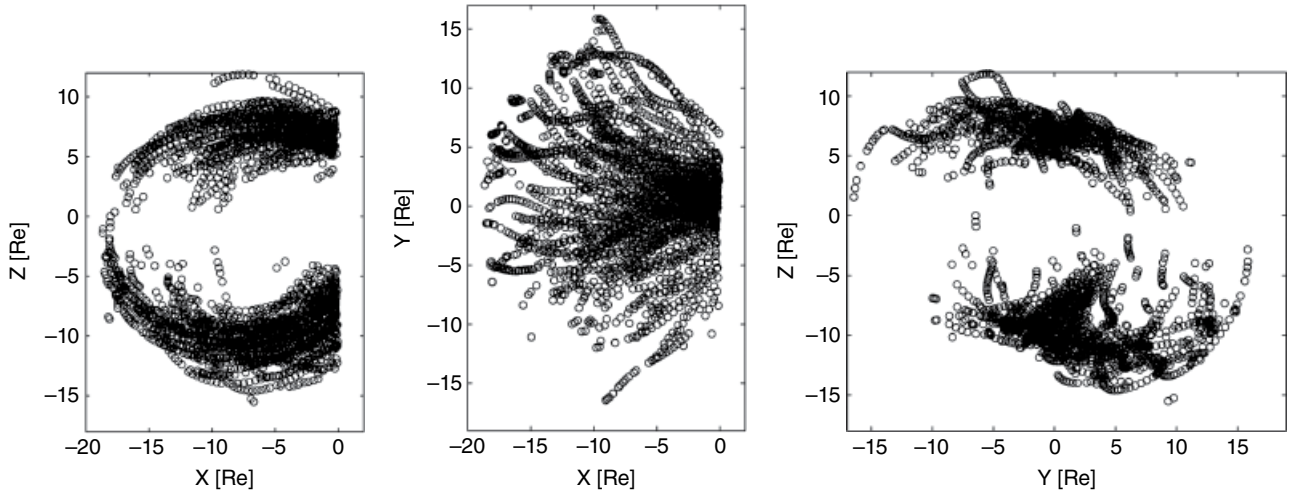

Figure 3.2 Illustration of data coverage for the current Cluster cold ion data set. Each black dot represents the position of an individual wake detection from which the flux could be determined. From left to right, the coverage as projected into the XZ_{GSM}, XY_{GSM}, and ZY_{GSM} planes, respectively.

consists of data from C1 and C3 for 2001 to 2010, although the lower solar activity means that there are less data from later years. In total, this dataset contains approximately 320,000 records from which reliable cold ion fluxes could be determined. Details and characteristics of this data can be found in *André et al.* [2014]. The spatial coverage for this combined set, illustrated in Figure 3.2, is similar to the earlier data set, but the larger number of records and the extended time interval opens for new studies, e.g., effects of solar cycle variations.

3.4. RESULTS

In the following section, we highlight some of the main results based on Cluster measurements of cold ions. At the time of writing (2015), the extended cold data set and the publication by *André et al.* [2014] had just been released. With a few exceptions, most of the results discussed below are therefore based on the original cold ion dataset as described in *Engwall et al.* [2009a].

3.4.1. Characteristic Cold Ion Densities and Velocities

Initial cold ion outflow rates were established by *Engwall et al.* [2009a] and found to be comparable to earlier estimates based on particle instruments (and thus higher energies). Integrated over the whole polar cap, outflow rates of the order of 10^{26} ions/s were reported. *André et al.* [2014] obtained similar rates using the extended data set. In large parts of geospace, for example the lobe regions, little or no heating or acceleration takes place, and cold ions seem to dominate the plasma population [*André and Cully*, 2012].

Figure 3.3 shows the distribution of measured outflow velocities (panel a) and densities (panel b) but is based on the full data set prepared by *André et al.* [2014]. We have removed records with negative velocities, because these suggest motion into the ionosphere. Values shown are taken from both hemispheres.

The locally measured mean and median densities of the full data set (i.e., no subsetting according geomagnetic activity, solar activity, or similar) are 0.21 and 0.13 centimeter $(cm)^{-3}$, respectively. Mean and median outflow velocities are 27 and 23 km/s^{-1}, respectively, once again based on the full data set. Panel c of Figure 3.3 shows the velocity and density as a function of altitude. Each point in this panel represents the average (mean) velocity within the given altitude range. Velocities increase with increasing radial distance, indicating acceleration, presumably due to centrifugal forces [*Cladis*, 1986; *Nilsson et al.*, 2010]. Densities decrease with radial distance as expected from the expanding flux tubes.

3.4.2. Identifying the Source Region

As mentioned above, the fundamental cause of the polar wind is the lack of hydrostatic equilibrium above the open polar cap, which causes escape of electrons and consequently an ambipolar electric field that extracts low energy ions. In their estimation of total outflow rates, *Engwall et al.* [2009a] assumed that the source was the polar cap region, simply defined as the area above 70° geomagnetic latitude.

Haaland et al. [2012b] also assumed the open polar cap as the primary source region for their estimations. They used a polar cap area given by an empirical model by

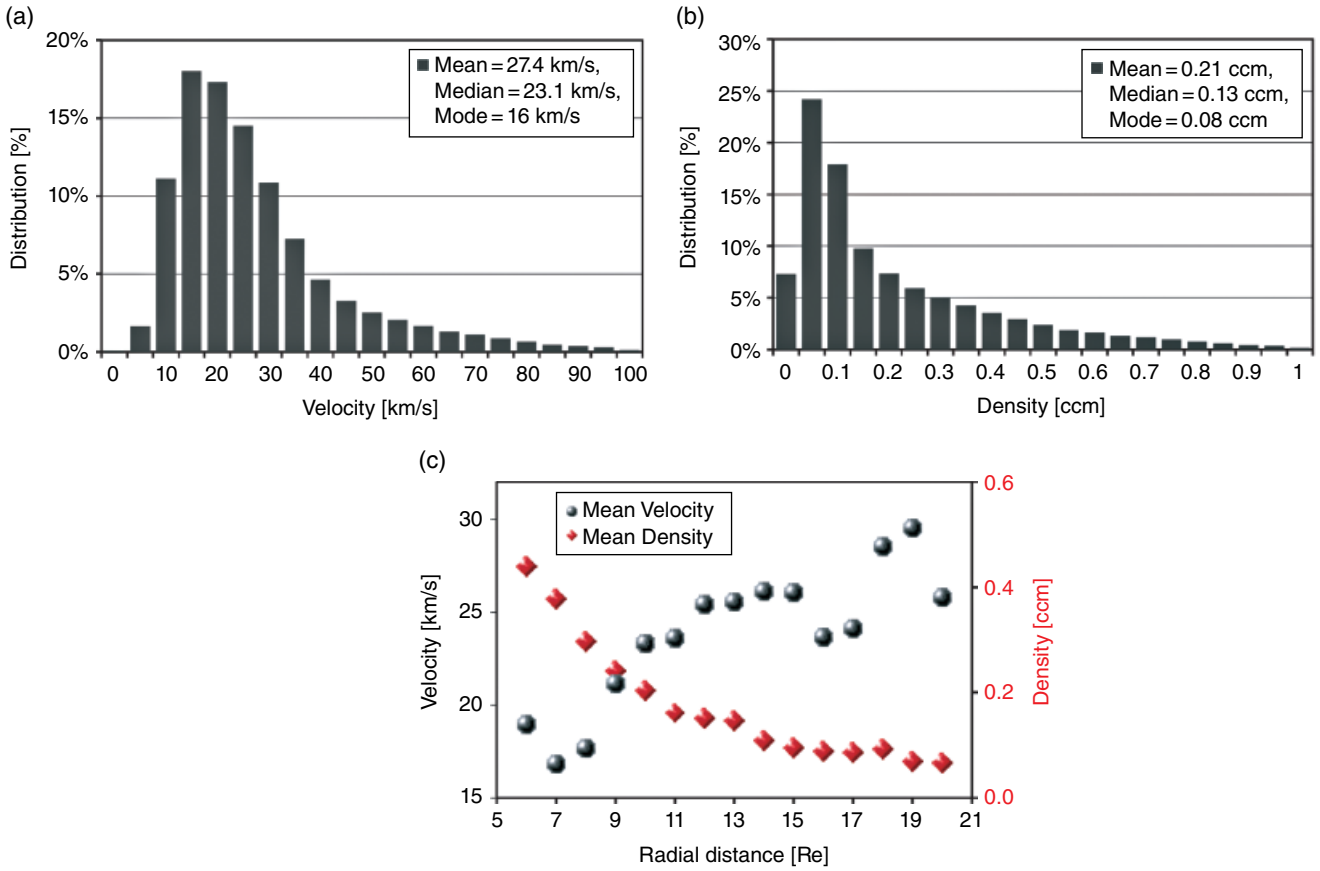

Figure 3.3 Panels a and b: Distribution of velocity and density, respectively. Panel c: Radial distance dependence of density (red color; values given by right vertical axis) and velocity (black color, left vertical axis).

Sotirelis et al. [1998]. This approach took into account that the polar cap region size can vary significantly with geomagnetic activity. For prolonged periods with northward interplanetary magnetic field (IMF) conditions, the polar cap area, and thus the source area of the polar wind can shrink to less than half than its average size.

An even more elaborate determination of the source area was undertaken by *Li et al.* [2012]. They used particle tracing [*Northrop and Scott*, 1964], taking all relevant forces into account, traced the ion transport path back to the ionosphere, and generated maps of the source regions for various disturbance levels and solar wind conditions. The overall results, reproduced in Figure 3.4, largely corroborated the *Haaland et al.* [2012b], findings in terms of source region and source area.

An interesting result of the *Li et al.* [2012] study was the identification of enhanced outflow from the cusp region and from the vicinity of the nightside auroral region. These regions are normally associated with ion outflow of more ions with higher energies, and also often with a larger abundance of heavier ions due to the additional acceleration potentials in these regions. One possible explanation for the cold outflow from these regions is enhanced production of secondary electrons due to impact ionization of the neutral atmosphere. These secondary electrons behave in much the same way as photoelectrons in enhancing the electric field as well as the electron temperature.

The apparent north-south asymmetry in Figure 3.4 is an artifact of the Cluster orbit. Southern hemisphere measurements are on average taken 1 R_E higher than in the northern hemisphere. Southern hemisphere data will therefore be biased toward data from the dayside/cusp region whereas northern hemisphere measurements will contain a larger fraction of ions that can be traced back to the nightside and the auroral region.

3.4.3. The Role of Solar Irradiance and the Solar Wind

Solar irradiance is the most important driver of ionization in the polar cap region. The $F_{10.7}$ index, a proxy for the total emission (in units of 10^{-2}Wsm^{-2}) from the solar disc at 10.7 cm wavelength, is frequently used to characterize solar irradiance. Figure 3.5 shows the in situ measured density and outflow velocity and the calculated

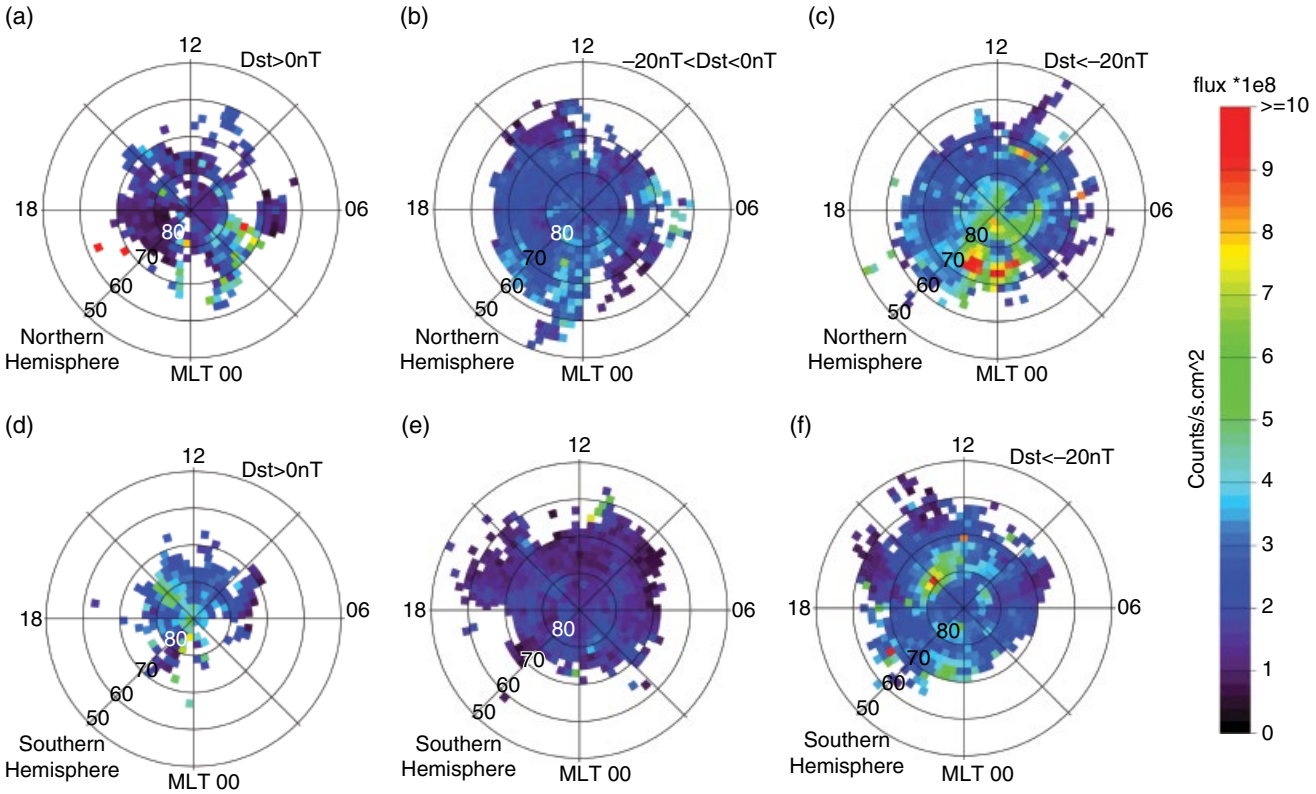

Figure 3.4 Maps of the source regions for cold ion outflow. Color indicates flux values. Panel a to c: Average ionospheric outflow fluxes in the northern hemisphere for quiet, moderate, and disturbed geomagnetic conditions. Panel d to e: Corresponding fluxes for southern hemisphere. After *Li et al.* [2012].

flux, mapped to 1000 km in the topside thermosphere, as a function of the $F_{10.7}$ index.

We note from Figure 3.5, which is essentially a reproduction of Figure 3.5 in *André et al.* [2014], that the outflow velocity does not seem to vary significantly with solar irradiance. All values in this binned distribution are in the range of 20 to 30 kms^{-1}, and there is no significant systematic increase in velocity with increasing solar activity. The density, however, varies more than a factor of 2 between low and high solar activity, consistent with the Cluster results reported in *Svenes et al.* [2008] and *Lybekk et al.* [2012]. The mapped flux also shows a marked increase with increasing solar activity.

In addition to the long time solar cycle variation of solar irradiance, there is also a seasonal and daily variation in the solar illumination. Since the Cluster orbit is only suitable for cold ion detection using the above methodology during the period around equinox, we are not able to address seasonal effects. Interestingly, the source maps shown in Figure 3.4 do not reveal any significant differences between the sunlit and the dark ionosphere in terms of mapped flux, although such a day/night asymmetry would be expected from models [e.g., *Glocer et al.*, 2012].

Solar wind-magnetosphere interaction, and in particular dayside reconnection, is a significant driver for magnetospheric circulation. Secondary effects of this interaction, in particular particle precipitation, is another significant mechanism for ionization, but is most prominent in the auroral zone and cusp regions and to a lesser degree in the open polar cap regions.

Some caution is necessary when interpreting the role of the solar wind dynamic pressure on ion outflow. An enhanced solar wind pressure leads to a compression of the whole magnetosphere. To the first order, this will be manifested as higher plasma density throughout the magnetosphere, but the actual supply of ionospheric material does not necessarily increase.

There are also other conceivable correlations of the cold ion flux. For example, the polar wind flux depends on the thermosphere neutral hydrogen density, which varies with solar cycle, as well as the O^+ density, which varies in response to a number of effects [e.g., *Yau et al.*, 2011].

In summary, however, results based on the Cluster cold ion data set suggest that solar illumination primarily controls ionization and outflow flux, whereas solar wind-magnetosphere interaction mainly affects transport.

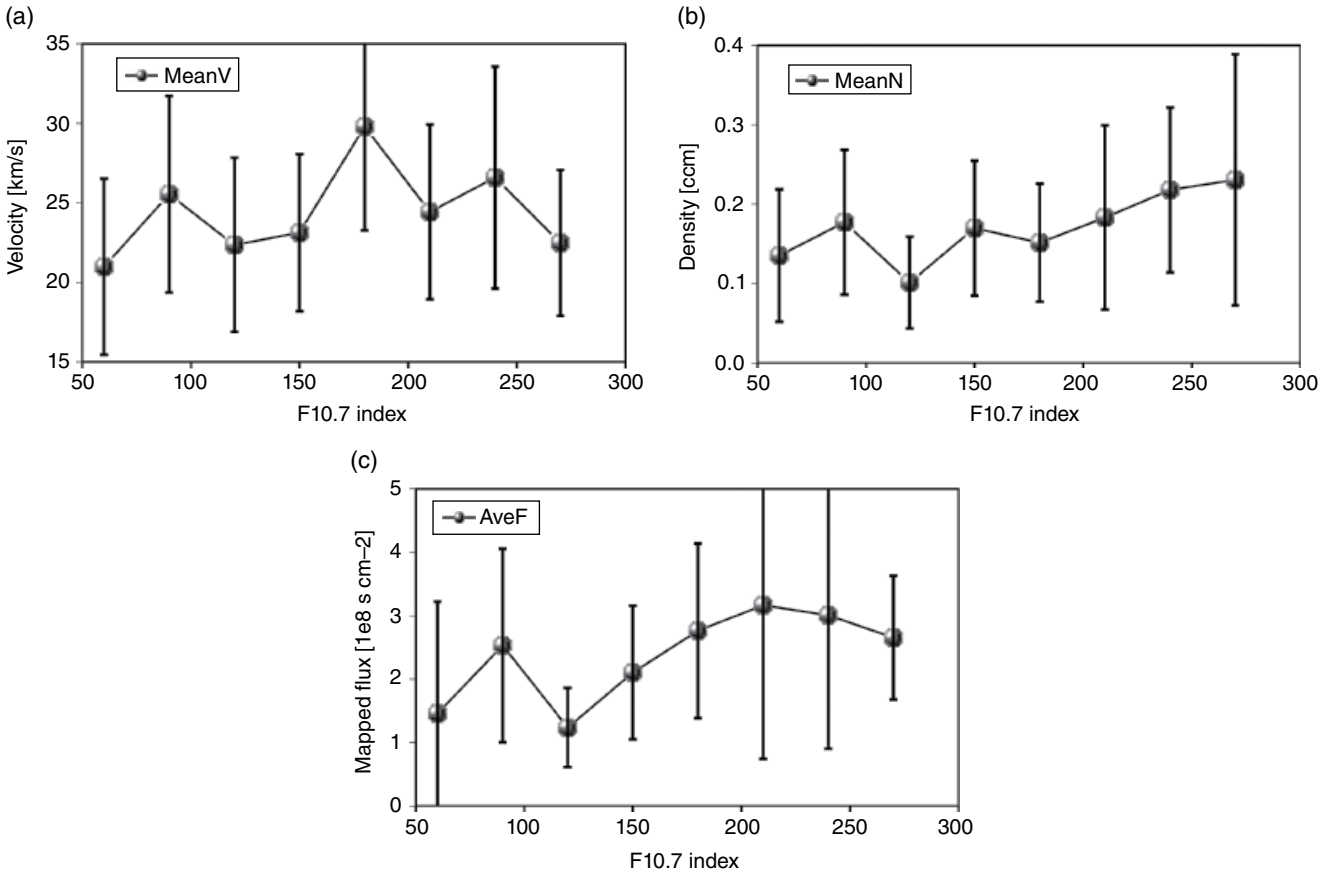

Figure 3.5 Panel a: In situ (e.g., measured at 4–19 Re) cold ion velocity (black) as function of solar irradiance as expressed by the $F_{10.7}$ index (see text for details). Panel b: Density as a function of solar irradiance. Panel c: Mapped flux as a function of solar irradiance. Error bars indicate statistical spread (standard deviation) of the measurements. [See also Figure 3.5 in *André et al.,* 2014].

The latter, and in particular the role of the IMF and convection, will be discussed further in the sections below.

3.4.4. Transport of Cold Ions to the Magnetosphere

The motion of the outflowing ions consists of a combination of parallel velocity and convection. Figure 3.6a schematically illustrates the motion of an individual ion from a given location in the ionosphere during moderately disturbed conditions with some convection.

At time t_1, the ion has escaped the Earth's gravitation potential and moves upward along an open field line (red lines in Figure 3.6a). At time t_2, the ion has moved further outward along the same field line, but this field line has now convected toward the plasma sheet, and will eventually be closed (i.e., reconnected in the tail) before the ion reaches the reconnection line. Thus, despite starting out on open field lines, this ion will be transported to the nightside plasma sheet where it contributes to plasma sheet refilling and plasma sheet dynamics.

From Figure 3.6a it is apparent that the initial position of the ion also plays a role. Ions escaping on from the dayside ionosphere and cusp region will be on field lines that will have to be convected a longer distance before reaching the plasma sheet. By the same token, ions escaping from the nightside ionosphere will have a shorter transport path to the magnetosphere. With parallel outflow velocities of the order of 20 to 30 kms^{-1}, the transport times from the ionospheric source to the nightside plasma sheet is in the order of several hours [see e.g., Table 1 in *Li et al.*, 2013].

Recent results from *Li et al.* [2016] indicates a region of stagnant outflow motion, and thus enhanced density near the high altitude dayside cusp region. These indications stem from the tracing results of *Li et al.* [2012], in which a number of tracing results suggested a parallel velocity close to zero in this region. The implications of this finding are not yet fully understood. One hypothesis is that the outward transport becomes stagnant in the transition region between the domain of the ambient

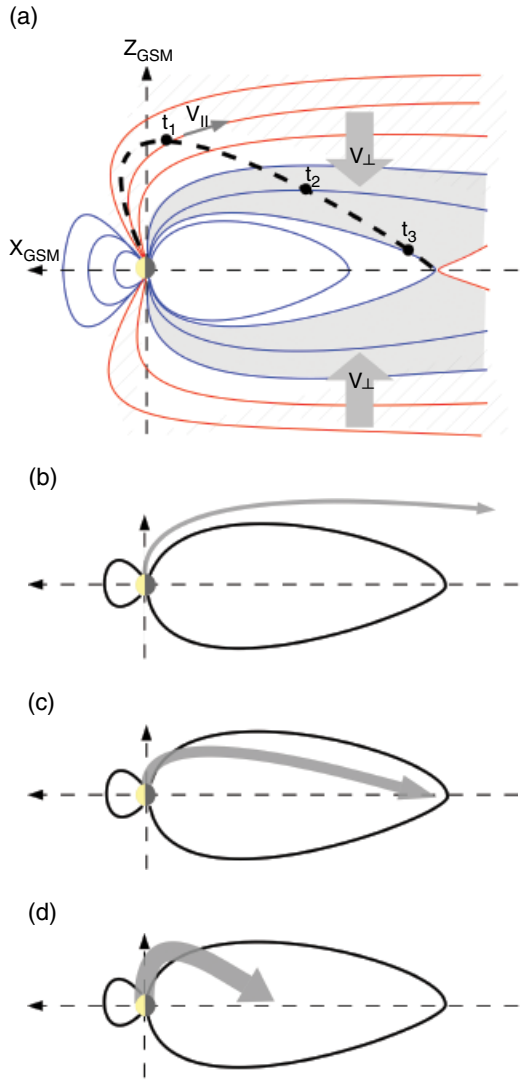

Figure 3.6 Panel a: Schematic trajectory of an individual ion from the ionosphere to the magnetosphere (dashed solid line). The motion consists of a field aligned and a convective part. If convection is sufficiently large compared to the parallel velocity, an ion initially on open field lines (t_1) will eventually be convected to the plasma sheet (t_3). Panel b to d: Effect of disturbance levels. For stagnant convection (panel a), the outflow is low and most ions escape on open field lines downtail. For intermediate geoactivity, there is more outflow but still slow convection. The ions are transported further tailward. During strong geomagnetic activity, the total outflow is higher, mainly due to the expanded polar cap area. The convection is also stronger, transporting more material to the near-Earth plasma sheet.

electric field responsible for extracting the ions in the first place, and a region at slightly higher altitudes where centrifugal acceleration becomes active. In this region, an equilibrium between upward and downward forces may be established under certain conditions. Unless there are any strong convection, cold ions would then pile up in this region.

3.4.4.1. Acceleration

The ambipolar electric field responsible for the extraction of the ions probably reach up to a few R_E altitudes [cf. the simulations by *Su*, 1998, mentioned above]. Above this, there is probably no significant electric field. However, due to centrifugal acceleration [e.g., *Cladis*, 1986], the ions will continue to increase their parallel velocity as they travel outward. The local acceleration is probably very small, but since it works over long distances, the total parallel velocity increase can be significant between the ionosphere and the far tail.

Nilsson et al. [2010] used data based on the wake method to quantify the acceleration due to centrifugal forces, and found averages local acceleration of the order of $5\,ms^{-2}$, which on average gave the ions an additional 5 to 10 km/s velocity over the 5 to 20 R_E range Cluster covers. Figure 3.3c, derived from the new complete data set seem to corroborate these numbers. Centrifugal acceleration becomes less effective further downtail, where the magnetic field becomes more stretched out.

3.4.4.2. Loss Versus Recirculation

Most of the low energy ion escape takes place on open magnetic field lines. However, as illustrated in Figure 3.6, it does not necessarily mean that these ions are lost into interplanetary space.

Haaland et al. [2012b] combined outflow velocities from *Engwall et al.* [2009a] with lobe convection results from *Haaland et al.* [2008] to estimate the loss versus circulation. They found that the largest direct downtail losses occurred under northward IMF conditions with stagnant convection. Except from effects of centrifugal acceleration discussed above, the field aligned velocity of the cold ions does not seem to vary significantly with IMF or geomagnetic disturbance. Convection, largely controlled by the dayside reconnection, on the other hand, is strongly dependent on IMF direction. Consequently, the transport of cold ions from the ionosphere into the magnetosphere is essentially controlled by convection, as illustrated in panels b, c, and d in Figure 3.6.

Table 3.1, compiled from Tables 2 and 3 in *Haaland et al.* [2012a], shows average velocities, densities, and fluxes for different IMF orientations and geomagnetic disturbance levels.

A more detailed study about the fate of the cold ions was conducted by *Li et al.* [2013]. As in the construction of the source maps shown in Figure 3.4, they used a full particle tracing of the measured outflow velocity and density, combined it with the measured convection and a model magnetic field [*Tsyganenko*, 2002] to estimate the

Table 3.1 Measured and calculated key parameters based on the cold ion data set of *Engwall et al.* [2009a]. We have divided the full dataset into subsets containing three different disturbance levels (first rows) and four different orientation of the interplanetary magnetic field (lower rows). This table is based on Tables 2 and 3 in *Haaland et al.* [2012b]. For each subset of disturbance levels and IMF directions, the different columns indicate the following: B: Average Dst.; C: Average IMF By value; D: Average IMF Bz value; E: Average plasma density; F: Average outflow velocity; G: Average mapped flux; H: Average convection velocity based on the *Haaland et al.* [2008] data set; I: Total outflow. (Based on the mapped flux [column G] and the polar cap arcs (estimated from *Sotirelis et al.* [1998]); J: Direct downtail loss, i.e., ions unable to convect to plasma sheet before passing distant X-line

A	B	C	D	E	F	G	H	I	J
	Averages taken from *Engwall et al.* [2009a]						Calculated values		
Activity/conditions	Dst	IMF By	IMF Bz	Ne	$V_{\|\|}$	Flux	$V_{\perp}$	Outflow	Loss
	[nT]	[nT]	[nT]	[cm]	[km s^{-1}]	[s^{-2} cm^{-1}]	[km s^{-2}]	[s^{-1}]	[$^{-1}$]
Quiet (Dst > 0 nT)	−43.0	1.4	−1.4	0.184	23.1	1.21e8	4.5	2.6e25	2.5e25
Moderate (−20 < Dst < 0)	−10.4	−0.5	−0.5	0.127	23.3	0.87e8	6.9	2.1e25	7.4e24
Storm (Dst < −20 nT)	7.5	−1.2	0.5	0.209	28.1	1.48e8	10.1	4.2e25	1.7e24
IMF By+	−29.8	4.6	0.0	0.172	25.8	1.22e8	8.0	2.6e25	1.0e24
IMF By −	−19.8	−5.4	−0.9	0.141	25.2	0.99e8	7.9	2.1e25	1.8e24
IMF Bz+	−39.2	−0.4	−4.6	0.196	24.6	1.35e8	1.7	1.1e25	7.2e24
IMF Bz −	−21.9	0.7	3.7	0.233	26.9	1.48e8	12.2	6.4e25	0

fate of the ions. Each individual observation was traced from the spacecraft position to a position slightly above the plasma sheet (no tracing was done inside the estimated plasma sheet, as the tracing assumptions break down here).

Figure 3.7 (based on Figures 5 and 6 in *Li et al.* [2013]) shows maps of the plasma sheet landing regions for the cold ions. During quiet and moderate conditions, the supply to the plasma sheet is typically below $10^5 s^{-1}$ (dark blue color) and spread out over a wide region. Some of the ions end up more than 60 R_E downtail. During disturbed conditions, fluxes are generally higher (green and red color, corresponding to fluxes above $10^5 s^{-1}$) and also deposited closer to Earth, with the majority of the deposition on between 20 to 30 R_E downtail.

Another interesting result from the *Li et al.* [2013] study, and also seen in Figure 3.7, is the dawn dusk asymmetry in the deposition. For disturbed conditions there seems to be a larger deposition on the duskside. The reason for this asymmetry is not fully clear, but external effects such as a bias in the interplanetary magnetic field can not fully explain the asymmetry [*Walsh et al.*, 2014a].

3.5. SUMMARY AND OUTLOOK

The unique combination of two complementary electric field techniques onboard the Cluster spacecraft and a novel technique has made it possible to estimate ion outflow velocities and densities of low energy ions. The novel technique is based on the detection of a wake forming of the positively charged spacecraft in a supersonic ion bulk flow region, and a functional dependence between the ambient plasma density and the spacecraft potential. The method is most sensitive to protons with energies up to a few tens of eV.

3.5.1. Summary of Experimental Results

The Cluster observations of cold plasma has provided us with new opportunities to study outflow and transport of cold ions from the ionosphere to the magnetosphere. In particular, it has been possible to quantify velocities, densities, and fluxes and their dependence on external drivers such as solar activity, solar wind-magnetosphere interaction, and geomagnetic activity.

The main experimental results from Cluster cold ion data set and studies thereof so far can be summarized in the following points:

- Typical field aligned outflow velocities measured in situ by Cluster in the high altitude polar cap and lobe regions (8–14 R_E altitude) are around 20 kms^{-1}. Typical plasma densities are around 0.1 cm^{-3}.
- Mapped to the ionosphere, the outflow rate is of the order of 1e-8 s^{-1}cm^{-2}. Integrated over the total polar cap area, the total outflow is of the order 1e26 s^{-1}.
- The outflow velocity is not very much affected by solar irradiance, but the density, and thus outflow rate vary almost a factor 3 between low solar irradiance and high irradiance.
- Outflow velocity or density do not vary significantly with geomagnetic activity or solar wind-magnetosphere interaction, but the convection and thus the fate of the

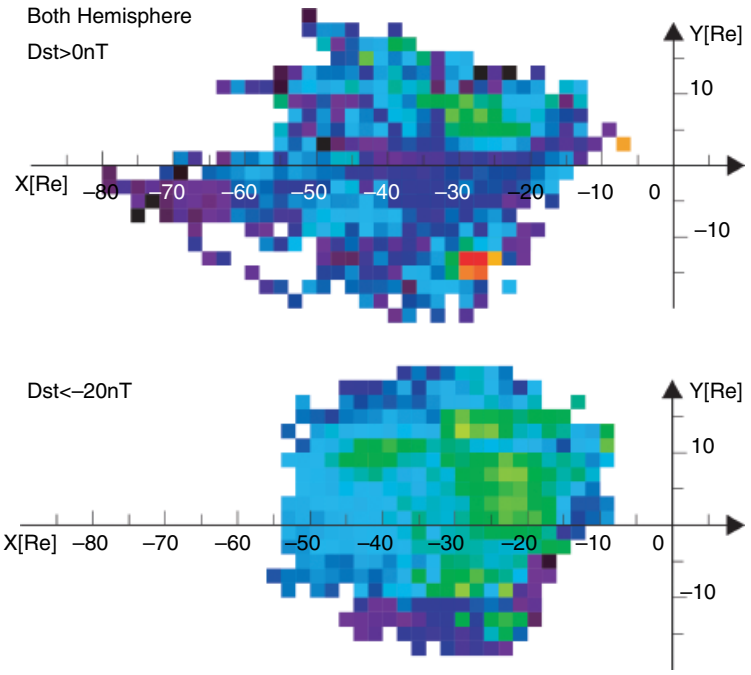

Figure 3.7 Maps of landing regions in the plasma sheet for the cold ions for quiet (top panel) and disturbed geomagnetic conditions. To construct these maps, individual ions from both hemispheres were mapped to a position slightly above the plasma sheet, and grouped into a 2x2 R_E bins. Colors indicate average fluxes within these bins. [Adapted from Figures 5 and 6 in *Li et al.*, 2013].

ions are strongly dependent on IMF direction and geomagnetic activity.

• Transport times from the ionosphere to the plasmasheet in the nightside magnetosphere is on the order of 2 to 4 hours. There seems to be a larger deposition in the duskside plasma sheet.

• The fate of the outflowing ions are largely controlled by the convection. Overall, only about 10%, or 1e25 s^{-1} cold ions are directly lost downtail. The rest are recirculated within the magnetosphere where they eventually contribute to the formation of the plasma sheet and ring current population.

• As pointed out by *André and Cully* [2012], low-energy ions typically dominate the density in large regions of the magnetosphere on the nightside and in the polar regions. These ions also often dominate in the dayside magnetosphere, and can alter the dynamics of processes like magnetic reconnection [e.g., *Walsh et al.*, 2014b; *Toledo-Redondo et al.*, 2015].

3.5.2. Outlook and Open Questions

At the time of writing, there are also ongoing projects to incorporate the Cluster cold ion dataset into polar wind models [see e.g., *Glocer*, 2017; *Welling*, 2017; and other papers of this volume] and to use the data to study specific intervals or phenomena [e.g., *Haaland et al.*, 2015; *Li et al.*, 2016].

Most of the studies discussed in the present paper are concerned with high latitude and lobe regions. But new results, for example from the dayside magnetopause [e.g., *Walsh et al.*, 2014b; *Toledo-Redondo et al.*, 2015; *Sonnerup et al.*, 2015], taking cold plasma into account, indicate that cold ions can play a significant role for fundamental plasma properties, and significantly alter the dynamics also in other regions of space.

The Cluster cold ion data set has also left a few puzzling questions that deserve some attention. These questions follow:

Cold ions in the cusp and auroral zone: The main source of the cold ions detected by Cluster seems to be the open polar cap. The mapping results of *Li et al.* [2012] revealed an interesting feature, though. As seen in Figure 3.4, there seems to be enhanced outflow from the cusp and auroral regions. The peak fluxes are almost an order of magnitude higher than the more homogeneous regions in the central polar cap area.

The conventional view is that additional energy in the form of Poynting flux and/or additional acceleration due to field aligned potential drops is available in these regions. The cusp and auroral zone is therefore known to be the source of various types of outflow [see e.g., reviews

by *Yau and André*, 1997; *André and Yau*, 1997], but typically at higher energies and at times with a significant fraction of oxygen. It is unclear whether the enhanced fluxes of cold ions is a result of higher ionization and thus a larger source reservoir, or whether the enhanced energy input also favors mechanisms enabling the cold ions to escape (e.g., the impact of enhanced production of secondary electrons discussed above).

Dawn-dusk asymmetries: *Li et al.* [2013] and *Walsh et al.* [2014a] noted a persistent dawn-dusk asymmetry in the deposition of cold ions to the plasma sheet (see also Figure 3.7). There seems to be an overall larger deposition on dusk. This asymmetry is not very apparent in the source maps (Figure 3.4) and may be a result of an overall dawn-dusk asymmetry in the transport between the ionosphere and magnetosphere rather than an inherent asymmetry in the polar cap source region. Modulation by IMF By cannot fully explain the asymmetry. A similar asymmetry was also noted by *Howarth and Yau* [2008] and *Yau et al.* [2012] in studies of oxygen outflow, but they related the asymmetry to IMF By effects during the transit from the ionosphere to the magnetosphere.

A stagnant region of cold ions in the high altitude dayside cusp/cleft region: In their attempts to trace the cold ions from the Cluster spacecraft to its source region, *Li et al.* [2012] noted that a significant fraction of the tracing result suggested zero parallel velocity around the high altitude dayside cusp/cleft region. Presently, no complete explanations for these stagnation regions exist [*Li et al.*, 2016].

ACKNOWLEDGMENTS

Work at the University of Bergen is supported by the Norwegian Research Council under grant 216872/F50 and the Fritjof Nansen Fund for Scientific Research. Computer code used for the calculations in this paper has been made available as part of the QSAS science analysis system. Solar wind data were obtained from the Coordinated Data Analysis Web (CDAWeb, see http://cdaweb.gsfc.nasa.gov/about.html). We also thank the International Space Science Institute, Bern, Switzerland, for providing computer resources and infrastructure for data exchange.

REFERENCES

Abe, T., B. A. Whalen, A. W. Yau, R. E. Horita, S. Watanabe, and E. Sagawa (1993), EXOS D (Akebono) suprathermal mass spectrometer observations of the polar wind, *J. Geophys. Res.*, *98*, 11,191, doi:10.1029/92JA01971.

André, M., and C. M. Cully (2012), Low-energy ions: A previously hidden solar system particle population, *Geophys. Res. Lett.*, *39*, L03101, doi:10.1029/2011GL050242.

André, M., and A. Yau (1997), Theories and Observations of Ion Energization and Outflow in the High Latitude Magnetosphere, *Space Sci. Rev*, *80*, 27–48, doi:10.1023/A:1004921619885.

André, M., K. Li, and A. Eriksson (2014), Outflow of low-energy ions and the solar cycle, *J. Geophys. Res.*, *33*, doi:10.1002/2014JA020714.

Axford, W. I. (1968), The Polar Wind and the Terrestrial Helium Budget, *J. Geophys. Res., 73*, 6855–6859, doi:10.1029/JA073i021p06855.

Banks, P. M., and T. E. Holzer (1968), The polar wind, *J. Geophys. Res.*, *73*(21), 6846–6854, doi:10.1029/JA073i021p06846.

Chandler, M. O., T. E. Moore, and J. H. Waite, Jr. (1991), Observations of polar ion outflows, *J. Geophys. Res.*, *96*, 1421–1428, doi:10.1029/90JA02180 .

Chappell, C. R., T. E. Moore, and J. H. Waite, Jr. (1987), The ionosphere as a fully adequate source of plasma for the earth's magnetosphere, *J. Geophys. Res.*, *92*, 5896–5910, doi:10.1029/JA092iA06p05896 .

Chappell, C. R., B. L. Giles, T. E. Moore, D. C. Delcourt, P. D. Craven, and M. O. Chandler (2000), The adequacy of the ionospheric source in supplying magnetospheric plasma, *Journal of Atmospheric and Solar-Terrestrial Physics*, *62*, 421–436, doi:10.1016/S1364-6826(00)00021-3.

Cladis, J. B. (1986), Parallel acceleration and transport of ions from polar ionosphere to plasma sheet, *Geophys. Res. Lett., 13*, 893–896, doi:10.1029/GL013i009p00893.

Dessler, A. J., and F. C. Michel (1966), Plasma in the geomagnetic tail, *J. Geophys. Res., 71*, 1421–1426, doi:10.1029/JZ071i005p01421.

Engwall, E., A. I. Eriksson, M. André, I. Dandouras, G. Paschmann, J. Quinn, and K. Torkar (2006), Low-energy (order 10 eV) ion flow in the magnetotail lobes inferred from spacecraft wake observations, *Geophys. Res. Lett.*, *33*, L06110, doi:10.1029/2005GL025179.

Engwall, E., A. I. Eriksson, C. M. Cully, M. André, P. A. Puhl-Quinn, H. Vaith, and R. Torbert (2009a), Survey of cold ionospheric outflows in the magnetotail, *Annales Geophysicae*, *27*, 3185–3201, doi:10.5194/angeo-27-3185-2009.

Engwall, E., A. I. Eriksson, C. M. Cully, M. André, R. Torbert, and H. Vaith (2009b), Earth's ionospheric outflow dominated by hidden cold plasma, *Nature Geoscience*, *2*, 24–27, doi:10.1038/ngeo387.

Escoubet, C. P., and R. Schmidt (2000), Cluster II: Plasma Measurements in Three Dimensions, *Advances in Space Research*, *25*, 1305–1314.

Escoubet, C. P., R. Schmidt, and M. L. Goldstein (1997), Cluster - Science and Mission Overview, *Space Sci. Rev*, *79*, 11–32, doi:10.1023/A:1004923124586.

Glocer, A. (2015), *Coupling Ionospheric outflow to magnetospheric models*, chap. 15, p. 195, this volume, AGU Geophysical Monograph Series, Wiley.

Glocer, A., N. Kitamura, G. Toth, and T. Gombosi (2012), Modeling solar zenith angle effects on the polar wind, *J. Geophys. Res.*, *117*, A04318, doi:10.1029/2011JA017136.

Gustafsson, G., M. André, T. Carozzi, A. I. Eriksson, C. G. Fälthammar, R. Grard, G. Holmgren, J. A. Holtet, N. Ivchenko, T. Karlsson, Y. Khotyaintsev, S. Klimov, H. Laakso, P. A. Lindqvist, B. Lybekk, G. Marklund,

F. S. Mozer, K. Mursula, A. Pedersen, B. Popielawska, S. Savin, K. Staziewicz, P. Tanskanen, A. Vaivads, and J. E. Wahlund (2001), First results of electric field and density measurements by Cluster EFW based on initial months of operation, *Annales Geophysicae*, *19*, 1219.

Haaland, S., G. Paschmann, M. Förster, J. Quinn, R. Torbert, H. Vaith, P. Puhl-Quinn, and C. Kletzing (2008), Plasma convection in the magnetotail lobes: statistical results from Cluster EDI measurements, *Annales Geophysicae*, *26*, 2371–2382, doi:10.5194/angeo-26-2371-2008.

Haaland, S., A. Eriksson, E. Engwall, B. Lybekk, H. Nilsson, A. Pedersen, K. Svenes, M. André, M. Förster, K. Li, C. Johnsen, and N. Østgaard (2012a), Estimating the capture and loss of cold plasma from ionospheric outflow, *J. Geophys. Res.*, *117*, A07311, doi:10.1029/2012JA017679.

Haaland, S., K. Svenes, B. Lybekk, and A. Pedersen (2012b), A survey of the polar cap density based on Cluster EFW probe measurements: Solar wind and solar irradiation dependence, *J. Geophys. Res.*, *117*, A01216, doi:10.1029/2011JA017250.

Haaland, S., A. Erikson, L. Maes, M. André, L. Baddeley, A. Barakat, R. Chappell, V. Eccles, C. Johnsen, K. Li, B. Lybekk, A. Pedersen, R. Schunk, and D. Welling (2015), Estimation of cold plasma outflow during geomagnetic storms, *J. Geophys. Res.,* p. in review.

Hoffman, J. H. (1970), Studies of the composition of the ionosphere with a magnetic deflection mass spectrometer, Int. J. Mass Spectrom. Ion Phys, pp. 315–322, doi:10.1016/0020-7381(70)85047-1.

Hoffman, J. H., W. H. Dodson, C. R. Lippincott, and H. D. Hammack (1974), Initial ion composition results from the Isis 2 satellite, *J. Geophys. Res.*, *79*, 4246–4251, doi:10.1029/JA079i028p04246.

Horwitz, J. L. (1982), The ionosphere as a source for magnetospheric ions, *Reviews of Geophysics and Space Physics*, *20*, 929–952, doi:10.1029/RG020i004p00929.

Howarth, A., and A. W. Yau (2008), The effects of IMF and convection on thermal ion outflow in magnetosphere-ionosphere coupling, *Journal of Atmospheric and Solar-Terrestrial Physics*, *70*, 2132–2143, doi:10.1016/j.jastp.2008.08.008.

Kitamura, N., K. Seki, and Y. Nishimura (2015), *Thermal and low-energy outflows in an through the polar cap*, chap. 7, p. 91, this volume, AGU Geophysical Monograph Series, Wiley.

Li, K., S. Haaland, A. Eriksson, M. André, E. Engwall, Y. Wei, E. A. Kronberg, M. Fränz, P. W. Daly, H. Zhao, and Q. Y. Ren (2012), On the ionospheric source region of cold ion outflow, *Geophys. Res. Lett.*, *39*, L18102, doi:10.1029/2012GL053297 .

Li, K., S. Haaland, A. Eriksson, M. André, E. Engwall, Y. Wei, E. A. Kronberg, M. Fränz, P. W. Daly, H. Zhao, and Q. Y. Ren (2013), Transport of cold ions from the polar ionosphere to the plasma sheet, *J. Geophys. Res.*, *118*, 5467–5477, doi:10.1002/jgra.50518.

Li, K., S. Haaland, P. W. Daly, E. A. Kronberg, M. André, A. Eriksson, A. Pedersen, B. Lybekk, and Y. Wei (2016), On the dayside high altitude stagnant region of cold ion outflow, *J. Geophys. Res.*, *120*, in review.

Lockwood, M., J. H. Waite, Jr., T. E. Moore, C. R. Chappell, and J. F. E. Johnson (1985a), A new source of suprathermal O(+) ions near the dayside polar cap boundary, *J. Geophys. Res., 90*, 4099–4116, doi:10.1029/JA090iA05p04099.

Lockwood, M., J. H. Waite, Jr., T. E. Moore, C. R. Chappell, and M. O. Chandler (1985b), The cleft ion fountain, *J. Geophys. Res.*, *90*, 9736–9748, doi:10.1029/JA090iA10p09736.

Lybekk, B., A. Pedersen, S. Haaland, K. Svenes, A. N. Fazakerley, A. Masson, M. G. G. T. Taylor, and J.-G. Trotignon (2012), Solar cycle variations of the Cluster spacecraft potential and its use for electron density estimations, *J. Geophys. Res.*, *117*, A01217, doi:10.1029/2011JA016969.

Nilsson, H., E. Engwall, A. Eriksson, P. A. Puhl-Quinn, and S. Arvelius (2010), Centrifugal acceleration in the magnetotail lobes, *Annales Geophysicae*, *28*, 569–576, doi:10.5194/angeo-28-569-2010.

Northrop, T. G., and F. R. Scott (1964), The Adiabatic Motion of Charged Particles, *American Journal of Physics*, *32*, 807–807, doi:10.1119/1.1969867.

Olsen, R. C. (1982), The hidden ion population of the magnetosphere, *J. Geophys. Res., 87*, 3481–3488, doi:10.1029/JA087iA05p03481.

Olsen, R. C., C. R. Chappell, D. L. Gallagher, J. L. Green, and D. A. Gurnett (1985), The hidden ion population, Revisited, *J. Geophys. Res.*, *90*, 12,121, doi:10.1029/JA090iA12p12121.

Paschmann, G., F. Melzner, R. Frenzel, H. Vaith, P. Parigger, U. Pagel, O. H. Bauer, G. Haerendel, W. Baumjohann, N. Scopke, R. B. Torbert, B. Briggs, J. Chan, K. Lynch, K. Morey, J. M. Quinn, D. Simpson, C. Young, C. E. McIlwain, W. Fillius, S. S. Kerr, R. Mahieu, and E. C. Whipple (1997), The Electron Drift Instrument for Cluster, *Space Sci. Rev*, *79*, 233–269.

Pedersen, A., P. Décréau, C. Escoubet, G. Gustafsson, H. Laakso, P. Lindqvist, B. Lybekk, A. Masson, F. Mozer, and A. Vaivads (2001), Four-point high time resolution information on electron densities by the electric field experiments (EFW) on Cluster, *Ann. Geophys.*, *19*, 1483–1489, doi:10.5194/angeo-19-1483-2001.

Quinn, J. M., G. Paschmann, R. B. Torbert, H. Vaith, C. E. McIlwain, G. Haerendel, O. Bauer, T. M. Bauer, W. Baumjohann, W. Fillius, M. Foerster, S. Frey, E. Georgescu, S. S. Kerr, C. A. Kletzing, H. Matsui, P. Puhl-Quinn, and E. C. Whipple (2001), Cluster EDI convection measurements across the high-latitude plasma sheet boundary at midnight, *Ann. Geophys.*, *19*, 1669–1681.

Riedler, W., K. Torkar, F. Rudenauer, M. Fehringer, A. Pedersen, R. Schmidt, R. J. L. Grard, H. Arends, B. T. Narheim, J. Troim, R. Torbert, R. C. Olsen, E. Whipple, R. Goldstein, N. Valavanoglou, and H. Zhao (1997), Active Spacecraft Potential Control, *Space Sci. Rev*, *79*, 271–302, doi:10.1023/A:1004921614592.

Sonnerup, B., G. Paschmann, S. Haaland, T. Phan, and S. Eriksson (2015), Reconnection layer bounded by switch-off shocks: Magnetopause crossing by themis d on 03 august 2008, *J. Geophys. Res., 121*, 3310–3332, doi:10.1002/2016JA022362.

Sotirelis, T., P. T. Newell, and C. Meng (1998), Shape of the open-closed boundary of the polar cap as determined from observations of precipitating particles by up to four DMSP satellites, *J. Geophys. Res.*, *103*, 399–406, doi:10.1029/97JA02437.

Su, Y.-J. (1998), The photoelectron-driven polar wind: Coupled fluid- semikinetic simulations and measurements by the

thermal ion dynamics experiment on the POLAR spacecraft, Ph.D. thesis, University of Alabama in Huntsville.

Su, Y.-J., J. L. Horwitz, T. E. Moore, B. L. Giles, M. O. Chandler, P. D. Craven, M. Hirahara, and C. J. Pollock (1998), Polar wind survey with the Thermal Ion Dynamics Experiment/Plasma Source Instrument suite aboard POLAR, *J. Geophys. Res.*, *103*, 29, 305–329, 338, doi:10.1029/98JA02662.

Svenes, K. R., B. Lybekk, A. Pedersen, and S. Haaland (2008), Cluster observations of near-Earth magnetospheric lobe plasma densities a statistical study, *Annales Geophysicae*, *26*, 2845–2852, doi:10.5194/angeo-26-2845-2008.

Toledo-Redondo, S., A. Vaivads, M. André, and Y. V. Khotyaintsev (2015), Modification of the Hall physics in magnetic reconnection due to cold ions at the Earth's magnetopause, *Geophys. Res. Lett., 42*, 6146–6154, doi:10.1002/2015GL065129.

Torkar, K., and H. Jeszenszky (2010), *ASPOC Data Products in the Cluster Active Archive*, pp. 39–49.

Tsyganenko, N. A. (2002), A model of the near magnetosphere with a dawn-dusk asymmetry 1. Mathematical structure, *J. Geophys. Res.*, *107*, 1179, doi:10.1029/2001JA000219.

Walsh, A. P., S. Haaland, C. Forsyth, A. M. Keesee, J. Kissinger, K. Li, A. Runov, J. Soucek, B. M. Walsh, S. Wing, and M. G. G. T. Taylor (2014a), Dawn-dusk asymmetries in the coupled solar wind-magnetosphere-ionosphere system: a review, *Annales Geophysicae*, *32*, 705–737, doi:10.5194/angeo-32-705-2014.

Walsh, B. M., T. D. Phan, D. G. Sibeck, and V. M. Souza (2014b), The plasmaspheric plume and magnetopause reconnection, *Geophys. Res. Lett.*, *41*, 223–228, doi:10.1002/2013GL058802.

Welling, D. T. (2015), *Recent advances in magnetosphere mass coupling in global models*, chap. 14, p. 179, AGU Geophysical Monograph Series, Wiley.

Whipple, E. C., J. M. Warnock, and R. H. Winkler (1974), Effect of satellite potential on direct ion density measurements through the plasmapause, *J. Geophys. Res.*, *79*, 179–186, doi:10.1029/JA079i001p00179.

Yau, A., W. K. Peterson, and T. Abe (2011), *Influences of the Ionosphere, Thermosphere and Magnetosphere on Ion Outflows*, chap. 3, pp. 283–314, IAGA Special Sopron Book Series, Springer Netherlands, doi:10.1007/978-94-007-0501-2-16.

Yau, A., W. K. Peterson, and T. Abe (2015), *Measurements of ion outflow from the Earth's ionosphere*, chap. 2, p. 21, this volume, AGU Geophysical Monograph Series, Wiley.

Yau, A. W., and M. André (1997), Sources of Ion Outflow in the High Latitude Ionosphere, *Space Sci. Rev*, *80*, 1–25, doi:10.1023/A:1004947203046.

Yau, A. W., A. Howarth, W. K. Peterson, and T. Abe (2012), Transport of thermal-energy ionospheric oxygen (O^+) ions between the ionosphere and the plasma sheet and ring current at quiet times preceding magnetic storms, *J. Geophys. Res.*, *117*, A07215, doi:10.1029/2012JA017803.

4

Advances in Understanding Ionospheric Convection at High Latitudes

R. A. Heelis

Video of Yosemite Talk, URL: http://dx.doi.org/10.15142/T3QG6Z

ABSTRACT

The many advances in understanding high latitude ionospheric convection over the last 40 years are briefly reviewed. During this period a specification of the ionospheric convection pattern has evolved from a static distribution of electrostatic potential contours that describe the paths along which plasma moves, to a dynamic pattern of potential contours that are valid instantaneously but evolve in time under the changing influences of the solar wind on the dayside, and the magnetotail on the nightside. Incorporating our new understanding of the convection pattern, which may change on spatial scales up to 5 degrees in latitude and on temporal scales of a few minutes to a few hours, into physical and mathematical descriptions that may be used in ionospheric and thermospheric models, is a significant challenge that remains to be addressed.

4.1. INTRODUCTION

Over the last 40 years our understanding of ionospheric convection at high latitudes has advanced significantly with the aid of sophisticated observational techniques and ever improving computational models. In the relatively small area of the ionosphere near 400 km altitude and above 50° magnetic latitude, the plasma motion responds to a multitude of processes in the inner magnetosphere and at the magnetopause. These responses take place over spatial scales ranging from one kilometer to thousands of kilometers and over temporal scales ranging from minutes to many hours. Despite the rapid increase in the sophistication and quality of our observations and the capability of our numerical models, the connections between the ionosphere and the magnetosphere remain challenged by the presence of induced fields in one location and not in the other, by the variable Alfvén wave travel time through the system and by the scale size dependence in the electromagnetic coupling between the two regions. Here we briefly review the advances that have been made in describing the properties of the ionospheric convection pattern and its relationship to processes occurring in the inner and outer magnetosphere.

4.2. OBSERVATIONAL CAPABILITIES

Measurements of electric fields from low-earth orbiting satellites were among the first to provide a nearly instantaneous signature of the ionospheric convection pattern [*Cauffman and Gurnett*, 1972]. They clearly established the notion of a two-cell convection pattern that was consistent with expectations based on the interaction of the magnetosphere and the solar wind described by *Axford and Hines* [1961] and by *Dungey* [1961] when the interplanetary magnetic field (IMF) was directed to the south. During this same period, a simple model for a

William B. Hanson Center for Space Sciences, University of Texas at Dallas, Dallas, Richardson, TX, USA

Magnetosphere-Ionosphere Coupling in the Solar System, Geophysical Monograph 222, First Edition.
Edited by Charles R. Chappell, Robert W. Schunk, Peter M. Banks, James L. Burch, and Richard M. Thorne.

two-cell convection pattern appropriate for times of southward IMF was put forward by *Volland* [1978] and is still used today in many sophisticated models of ionospheric density, temperature, and composition [e.g., *Sojka et al.*, 1981]. The region of anti-sunward convection is frequently referred to as the polar cap, and the polar cap potential difference is a parameter that is frequently used to describe the magnitude of the convective flows. However, it should be emphasized that the polar cap defined in this way does not specifically describe the topology (open or closed) of the magnetic field.

During times of southward IMF, subsequent analysis of ionospheric convection signatures revealed that the plasma flow in the region of anti-sunward convection identified as the polar cap was not distributed uniformly but rather showed a distinct dawn-dusk asymmetry that was organized by the sign of the IMF B_y component [*Heppner*, 1972]. This asymmetry, previously recognized in ground-based magnetic variations in the polar cap [*Svalgaard*, 1973; *Mansurov*, 1970], led to the first empirical models of the ionospheric convection pattern [*Heppner*, 1977]. Direct observations of the plasma drift were also made during this period, which produced a more detailed description of shear and rotational flows across the transition from sunward to anti-sunward convection [*Heelis et al.*, 1976]. In particular it was noted that shear flows tend to define the reversal boundary across the dayside and that rotational flows are generally confined to a narrow local time region near noon. Within this narrow region called the cusp, the flow direction toward dawn or toward dusk is determined by the sign of the IMF B_y component [*Heelis et al.*, 1984].

Figure 4.1 shows the principal differences in the polar cap flows that are produced when the IMF has a southward component and the IMF B_y component makes a transition from negative to positive. These passes, made by the Defense Meteorological Satellite Program, show the sunward and anti-sunward plasma drift speed as the satellite traverses the high latitude northern hemisphere from dusk to dawn. In the upper panel B_y is negative and the anti-sunward flows in the polar cap are stronger on the duskside. Examining the spatial extent of the convection cells reveals that the dawn and dusk cells are comparable. By contrast in the lower panel, when B_y is positive, the flows in the polar cap are stronger in the dawnside, and the duskside convection cell occupies a significantly larger spatial extent than the dawn cell. This asymmetry in the spatial extent and magnitude of the convective flows has the opposite dependence on B_y in the southern hemisphere.

Satellite measurements are certainly not the only tool to contribute to the collection of knowledge of plasma flows in the auroral zone and polar cap. Incoherent scatter radars bring a powerful technique to the problem allowing altitude profiles of plasma flows, density, and

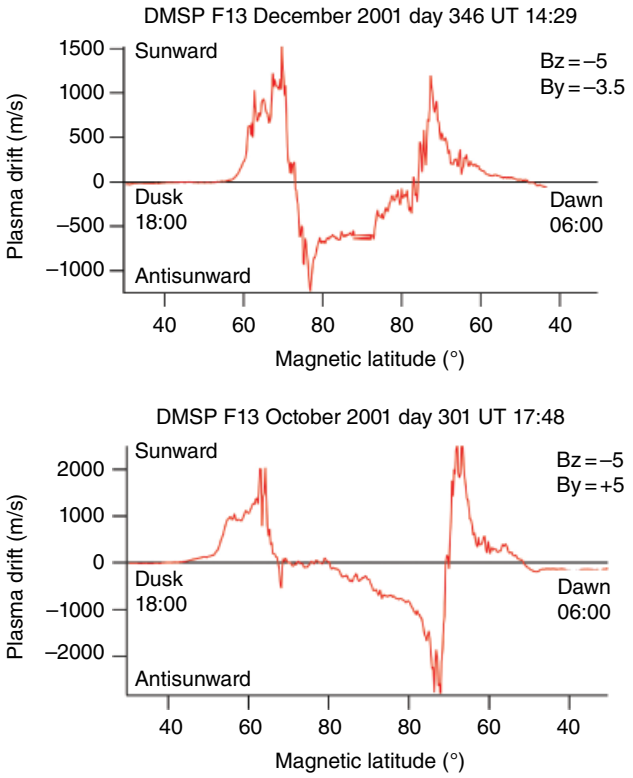

Figure 4.1 Signatures of the sunward and anti-sunward plasma flows across the high latitude northern hemisphere show a distinct asymmetry in the magnitude of the flow across the polar cap that is dependent on the IMF B_y component.

temperature to be obtained locally with a temporal cadence of a few minutes. Since the initial measurements made by the Chatanika radar [*Banks and Doupnik*, 1975], this technique is now utilized at locations around the world and is capable of examining microscale processes over limited latitude ranges in addition to capitalizing on the rotation of the observing station to examine larger scale local time variations. *Peymirat and Fontaine* [1997] extend auroral zone measurements made by the European Incoherent Scatter (EISCAT) radar into the polar cap by completing a description of the electric potential distribution in the region and more recently a description of time variable flow enhancements and their effects on plasma transport through the cusp [*Moen et al.*, 2004; *Carlson,* 2012] and through the nightside [*Lyons et al.*, 2015] have fundamentally changed our vision of the nature of ionospheric convection.

More global views of the ionospheric convection pattern have also been obtained by the inversion of ground-based magnetometer data [*Richmond and Kamide*, 1988], and these studies have established the connections between the dayside and nightside convective flows, albeit on spatial scales that are quite large and may not accurately describe the flow across convection reversal boundaries

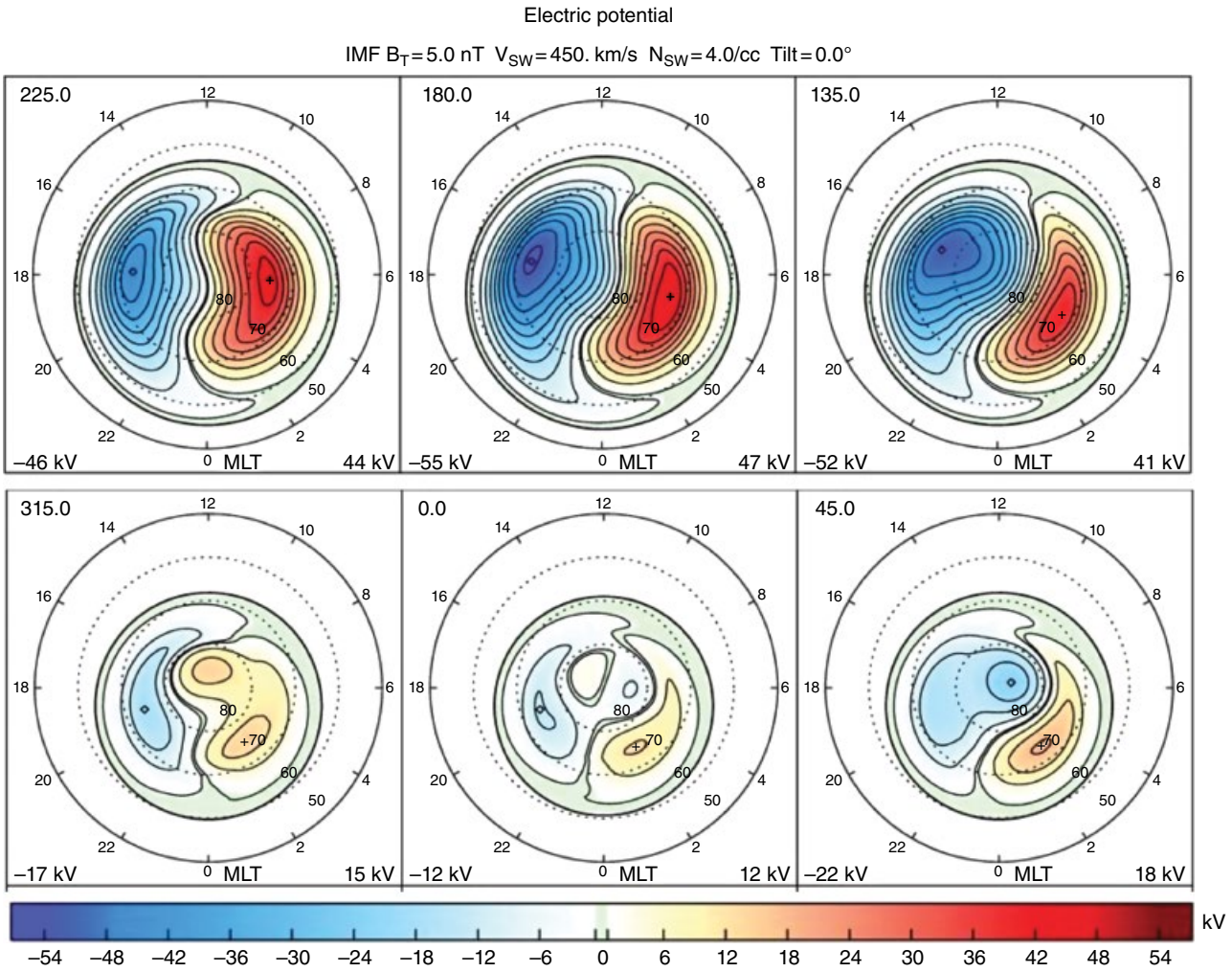

Figure 4.2 The top panels show the average convective flows seen in the northern hemisphere when the IMF is southward with B_y negative (left) and B_y positive (right). The lower panels show the average flows seen when the IMF has a northward component with B_y negative (left) and B_y positive (right). [after *Weimer,* 2005]

[*Ridley and Clauer*, 1996]. Such studies have, however, allowed the response of the convection pattern to changes in the IMF to be examined and indicated the temporal scales over which these responses occur [*Ridley et al.*, 1998]. The development of ground-based high-frequency (HF) radar detection of plasma flows from multiple overlapping beams [*Greenwald et al.*, 1985] has also contributed immensely to a description of the convective flow in restricted regions and to the development of global models that connect the regional flows by enforcing the condition for a curl-free electric field [*Cousins and Shepherd*, 2010]. During the mid-1980s, the Dynamics Explorer data provided a quasi-continuous database of electric field measurements from which a comprehensive empirical model of the high latitude convection pattern was first constructed [*Weimer*, 2005]. Since that time, the almost continuous collection of satellite and ground-based measurements of electric fields have improved our confidence in the model, as representative of the largest climatological scales over which the electric potential distribution can be specified. Figure 4.2 is adapted from a now commonly used model [*Weimer*, 2005] that represents the average observed convection pattern and its major dependencies on the IMF magnitude and direction. The top row illustrates the two-cell convection pattern that prevails when the IMF is directed to the south and the spatial asymmetry in the pattern that evolves in the northern hemisphere as B_y changes from negative (left) to positive (right). In the bottom row, the pattern shows the development of convection cells at the highest latitudes that circulate in the opposite sense to those seen at lower latitudes when the IMF has a northward component. It is important to note that these representations are temporal and spatial averages of individual satellite

passes such as those shown previously. Thus, they show features that may not be recognized in individual observations or assimilations of data over short time periods.

4.3. OBSERVATIONS AND INTERPRETATION

The extreme sensitivity of the high latitude convection pattern to the IMF configuration is strong evidence that an important driver for the observed convection arises from direct connection between the IMF and the geomagnetic field as originally proposed by *Dungey* [1961]. While observations of the resultant ionospheric plasma flows were being assembled, predictions of the nature of these flows were also produced by consideration of the requirements for interconnection between the draped IMF in the magnetosheath and the geomagnetic dipole field [*Crooker*, 1988]. These requirements for interconnection between the magnetic fields of different origin and the electromagnetic forces imposed on the plasma produce asymmetries in the cusp flows and the electric fields across the polar cap that are consistent with observations. More recently the forces imposed on the plasma during the interaction of the magnetosphere with the solar wind are reproduced in magnetohydrodynamic (MHD) models that more accurately describe the configuration of the convective flows in the ionosphere that are observed [*Lopez et al.*, 1999].

Coupled with observations of the ionospheric plasma flows and electric fields are measurements of precipitating energetic particles from the magnetosphere, which originally identified a signature of the cusp [*Heikilla and Winningham*, 1971] and subsequently signatures of the central plasma sheet and the low latitude boundary layer of the magnetosphere [*Winningham et al.*, 1975]. These measurements have been combined to examine the spatial relationships between the particle and convection boundaries in the high latitude ionosphere. *Heelis et al.* [1980] found that during times of southward IMF, the convection reversal boundary lies equatorward of a sharp poleward boundary in the precipitating energetic electron flux identified with the equatorial boundary layer of the magnetosphere. Figure 4.3 from the work of *Drake et al.* [2009] describes the average location of the convection reversal boundary and the poleward edge of the auroral precipitation as a function of local time. It shows that, in the ionosphere, this region occupies about 2° in latitude, and a quantitative analysis by *Sundberg et al.* [2008] suggests that the anti-sunward flow in this region rarely contributes more than 5 kilovolts (kV) to the total potential drop across the polar cap. Thus, during times of southward IMF, when the total potential drop across the convection reversal boundary is greater than 50 kV, the contribution from the boundary layer is quite small. However, during times of northward IMF this small boundary layer driver can represent a significant contribution to the sunward flow that is seen at lowest latitudes at all times.

Typically then, there are two drivers associated with the circulation of the ionospheric plasma at high latitudes, and they are shown schematically for southward and northward IMF in Figure 4.4. When the IMF is southward, the oppositely directed magnetic fields at the magnetopause allow the flow of plasma on closed magnetic flux tubes, associated with the geomagnetic field in the magnetosphere, to move to open magnetic flux tubes associated with the IMF in the magnetosheath. This process, referred to as merging, produces ionospheric flows

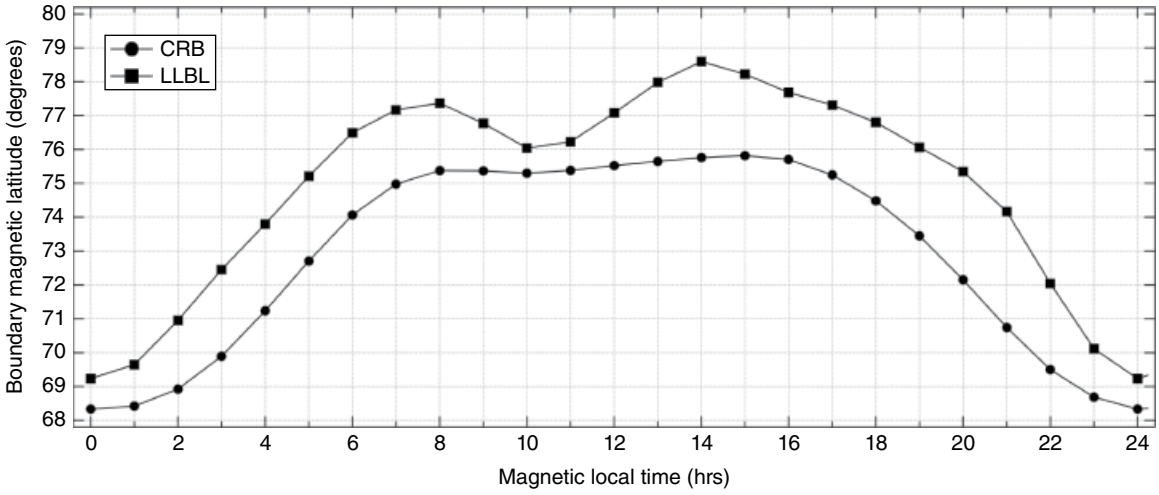

Figure 4.3 The location of the poleward boundary of the auroral precipitation, indicated by squares, and the convection reversal boundary, indicated by circles, shows that auroral precipitation consistently extends poleward of the convection reversal; boundary in a region termed the boundary layer. [after *Drake et al.*, 2009]

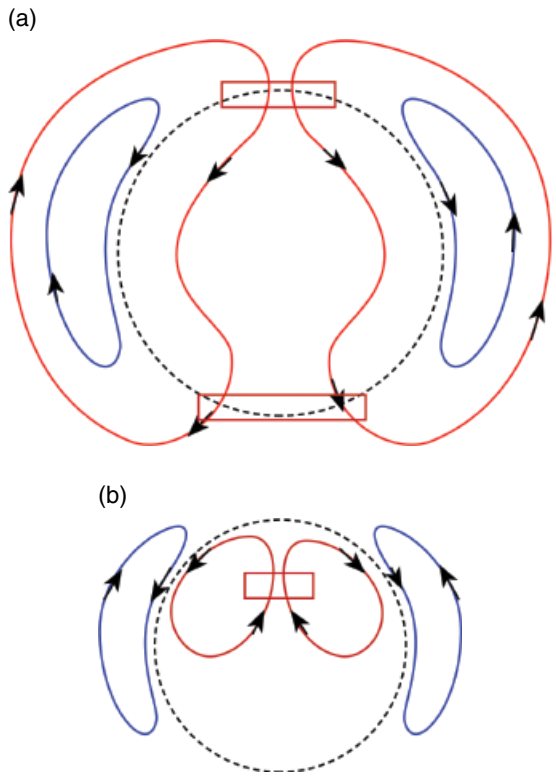

Figure 4.4 Schematic illustration of convection cells driven by viscous interaction in the boundary layer (blue) and direct connection with the IMF (red). The configuration for (a) southward IMF and (b) northward IMF is indicated.

with an anti-sunward (poleward) component across the polar cap boundary near local noon (as indicated by the red box in Figure 4.4a) and a dawn to dusk potential difference across the region of open magnetic flux enclosed inside the dashed circle. Near local midnight, the stretched field-line geometry in the magnetotail creates conditions that allow the plasma on open magnetic flux tubes in the tail lobes to flow onto the closed magnetic flux tubes of the plasma sheet. This process is referred to as reconnection and produces anti-sunward (equatorward) ionospheric flows across the polar cap boundary near midnight in the region indicated by another red box. The resulting two-cell circulation of plasma and magnetic flux is shown in red in Figure 4.4. So-called viscous-like interaction also drives a two-cell circulation, with sunward flow at the lowest latitude and anti-sunward flow at higher latitudes. These cells lie within the region of closed magnetic flux and are shown in blue in Figure 4.4 equatorward of the region of open magnetic flux. Presently the factors that affect the magnitude of this driver are not well documented but are associated with processes affecting the magnitude and extent of the anti-sunward flow in the equatorial magnetospheric boundary layer [*Farrugia et al.*, 2001].

When the IMF is northward, the boundary layer driver continues to drive a two-cell circulation of closed magnetic flux (as shown in Figure 4.4b), while the merging mechanism drives the recirculation of plasma and open magnetic flux on ionspheric convection cells that are sometimes referred to as lobe cells [*Crooker*, 1992]. In this case the merging/reconnection regions are the same (as indicated by the single red box in Figure 4.4b), and are accessed by the magnetosheath field that is draped over the magnetosphere. The configuration of the magnetotail during northward IMF remains an area of study related to the appearance of discrete auroral forms at the highest latitudes [*Cumnock*, 2005].

Given the picture of convection drivers that we have described, the challenge now remains to reconcile these drivers with the observed behavior of the convecting plasma in the ionosphere. Here, there are some significant difficulties associated with the temporal and spatial scales over which the drivers operate such that individual observations rarely display the average features that we have described [*Bekerat et al.*, 2003].

4.4. SPATIAL AND TEMPORAL VARIATIONS IN CONVECTION

In 1979, *Russell and Elphic* [1979] demonstrated that a significant contribution to the conversion of closed magnetic flux to open magnetic flux near the nose of the magnetopause took place sporadically and in patches termed flux transfer events. Since that time, the ionospheric signatures of these events have been well documented in plasma flows [e.g., *Pinnock et al.*, 1995], optical emissions [*Skjaevland et al.*, 2011], and ground magnetic perturbations [*Clauer and Petrov*, 2002]. Figure 4.5, extracted from *Skjaevland et al.* [2011], shows signatures of poleward-moving emissions apparently associated with the addition of open magnetic flux to the dayside. Seen here are periodic latitudinal extensions of the emissions associated with cusp electron precipitation, with the extensions originating from successively lower latitudes. Such observations suggest that plasma flows into the polar cap on the dayside occur sporadically in universal time and in restricted local time intervals. Plasma flow bursts associated with such emissions are directly observed by ground-based radar and satellite measurements [*Rinne et al.*, 2010], and are directed to the east or west in accord with the polarity of the IMF B_y component, as revealed in the average climatological patterns shown previously. Thus, the accumulation of evidence for rapidly varying convection in the cusp region is consistent with the early work on the addition of open magnetic flux to the polar cap put forward by *Cowley and Lockwood* [1992]. These ideas have since been expanded to include associated increases and decreases in the polar cap area

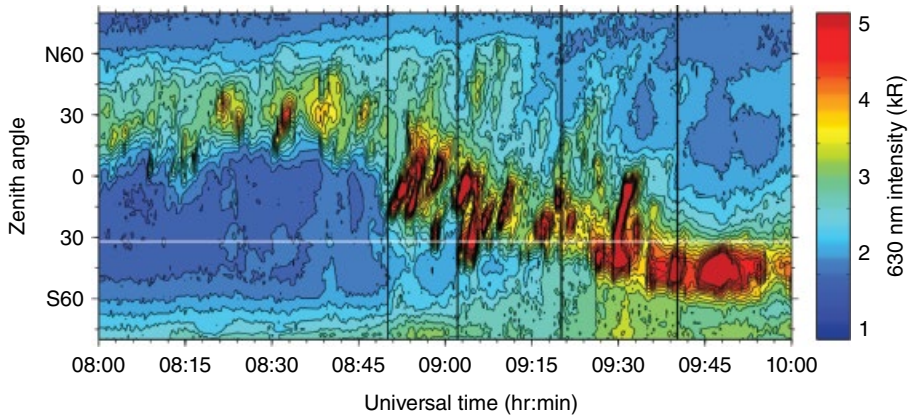

Figure 4.5 Poleward convecting plasma, which is temporally activated in spatially confined regions, is suggested by the appearance of optical emissions that extend poleward from and equatorward moving cusp location. [after *Skjaeveland et al.*, 2010]

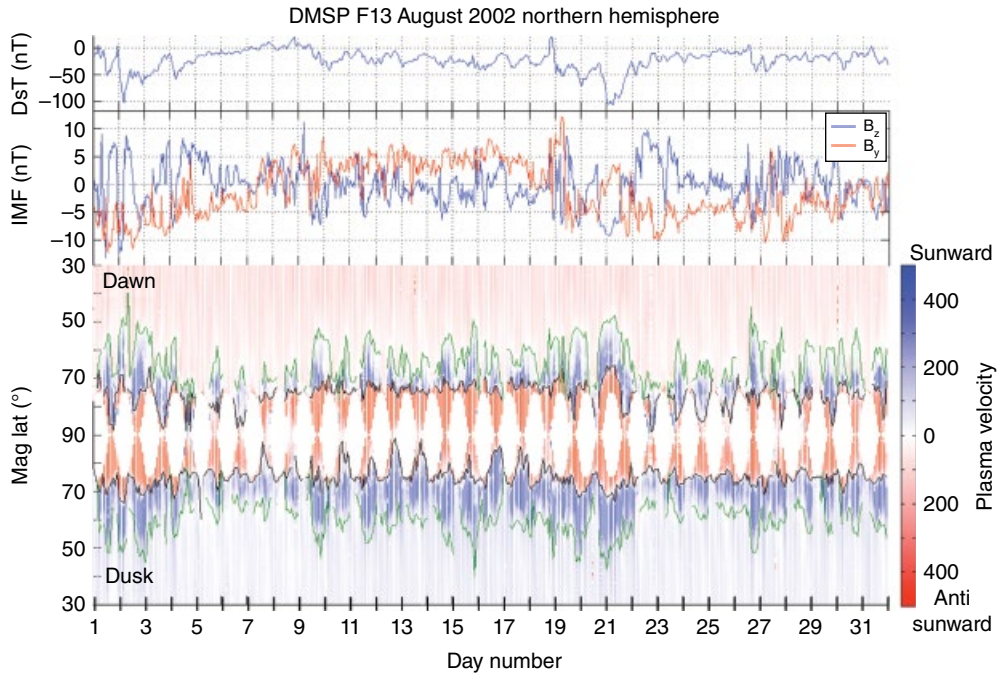

Figure 4.6 Sequential passes of the DMSP satellite across the high-latitude northern hemisphere from dusk to dawn show a highly variable polar cap boundary that expands and contracts in response to changes in IMF B_z and moves laterally in response to change in IMF B_y.

[*Milan et al.*, 2009] that would result from an imbalance between the dayside and nightside reconnection rates at the magnetopause [*Siscoe and Huang*, 1985]. At this time, a so-called expanding contracting polar cap model is a paradigm that embraces most of the temporal variations in the high latitude convection pattern [*Morley and Lockwood*, 2006].

The bottom panel in Figure 4.6 shows a sequence of Defense Meteorological Satellite Program (DMSP) passes over the northern hemisphere for a period of one month. The passes cross the high latitude region along the dawn-dusk meridian, and the anti-sunward and sunward flows are shown in red and blue, respectively. The latitude variations in those flows make it straightforward to identify the convection reversal boundary and the low latitude extent of the auroral zone flows. The black and green lines show the temporal variations in these boundaries, which can be related to variations in the driver, specified by the IMF shown in the middle panel and by the magnetospheric response described by the

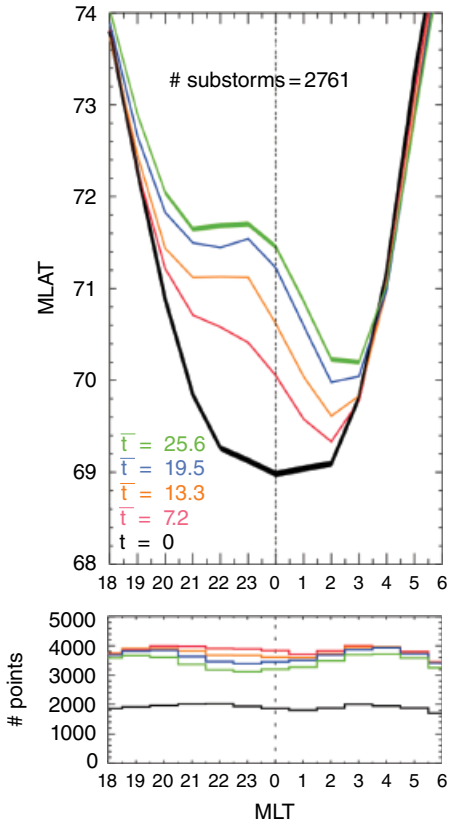

Figure 4.7 Observations of the polar cap boundary across midnight show that it changes location by as much as 3° during the course of as substorm. [after *Laundal et al.,* 2010]

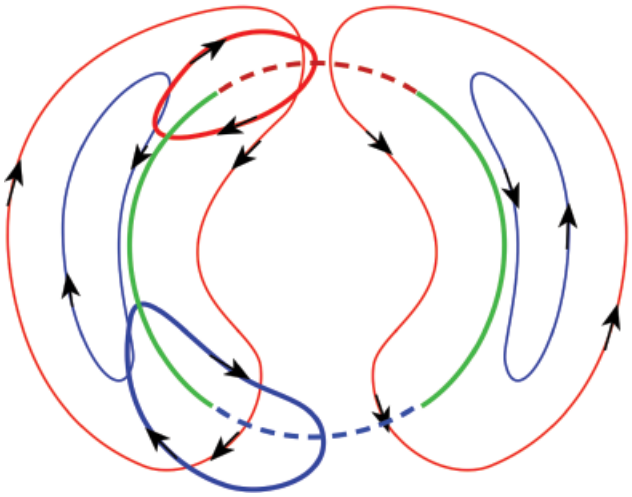

Figure 4.8 Schematic illustration of the components of the ionospheric convection pattern that comprise those from a background driven by quasi-steady state dayside merging and nightside reconnection (thin red) and viscous interaction (thin blue) and additional features that are responsive to sporadic changes in the dayside merging rate (thick red) and the nightside reconnection rate (thick blue).

Dst index shown in the top panel. It is easy to see three key features of the convection pattern. First, the polar cap boundary, which defines the region of open magnetic flux, moves by as much as 5 degrees in latitude at a given location, as seen on day 21 for example. The boundary expands and contracts at both the dawn and dusk sides. These motions of the boundary are well correlated with the z-component of the IMF, shown in blue in the middle panel, and consistent with the expectations of the expanding/contracting polar cap that have been well documented by *Milan et al.* [2009]. Expansion of the region occupied by the auroral zone flows also occurs in both the dawn and dusk sectors. It is also well correlated with the IMF B_z and consistent with the breakdown in shielding by the ring current during a magnetic storm growth phase [*Jaggi and Wolf*, 1973]. Finally, a latitude displacement of one convection reversal boundary with respect to the other is easily seen on days 4 and5 and days 17 and 18, for example. These displacements are well correlated with IMF B_y and indicate the reorientation of the convection pattern that is produced by a change in the direction of the IMF B_y, even when the rate of change of magnetic flux across the polar cap boundary does not change. It should be clear from these data that both the plasma velocity and convection speed near dawn and dusk are highly variable parameters that are responsive to changes in the IMF.

Figure 4.7, reproduced from the work of *Laundal et al.* [2010], shows the location of the polar cap boundary across midnight obtained from a superposed epoch analysis of its position during a substorm. It also illustrates the spatial variability of the polar cap boundary near midnight that may change in latitude by 3 degrees over a period of 20 minutes. Taken in total, these observations and many other studies suggest that the convection pattern may be described well by the existence of one driver on the dayside, which modulates the transfer of magnetic flux across the polar cap boundary due to changes in the solar wind and another on the nightside that modulates the transfer of magnetic flux across the polar cap boundary due changes in substorm activity.

Based on the convincing evidence for temporal variations in the flows across the polar cap boundary, we amend the description of the instantaneous convection pattern that we described earlier. Figure 4.8 shows a schematic illustration of the polar cap boundary displayed with three colors representing projections of a dayside merging region at the magnetopause in red, a region of the boundary across which there is no flow near dawn and dusk in green, and a nightside reconnection region in blue. Also shown are instantaneous electric potential contours representing a background circulation as in Figure 4.4 and additional flows that exist on smaller spatial scales and shorter time

scales associated with modulation of the magnetic flux across the polar cap boundary on the dayside in red and on the nightside in blue. Together these features serve to change the orientation of instantaneous convection trajectories observed at any given time, and create the imbalances in magnetic flux transfer across the polar cap boundary that lead to expansions and contractions in the polar cap area. Note that spatial relocations of the polar cap boundary occur where the convection trajectories cross the boundary that is green, since at these locations the plasma motion and the boundary motion are the same.

It is now clear that not only are the convective flow speeds variable in time and space, but so too are the boundaries that describe the latitudinal extent of the convection pattern and the open/closed field line boundary [*Chen et al.*, 2015]. Understanding, and accurately representing, the dynamics of the high latitude convection pattern is now the foremost challenge to describing the motion of plasma packets in the ionosphere at high latitudes and the effects of the momentum and energy exchange with the neutral thermosphere.

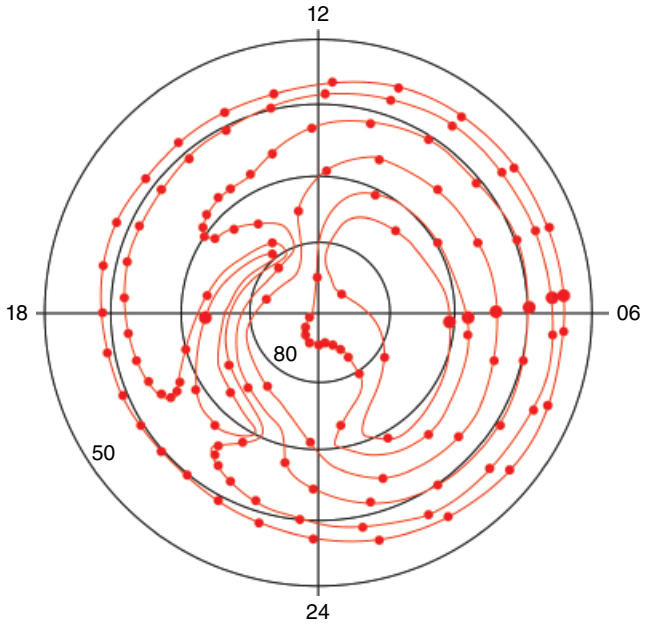

Figure 4.9 A common two-cell convection pattern when added with the planetary corotation produces regions where the residence time of plasma packets is very long. Red dots indicate the position of plasma packets every hour. Long times in daylight produces enhanced plasma densities and in darkness produces large plasma depletions.

4.5. EFFECTS IN THE IONOSPHERE AND THERMOSPHERE

Large convective velocities in the high latitude ionosphere result in significant frictional heating that modify the horizontal and vertical motions of both the ion and neutral gases. The heating takes place predominantly in the auroral zones and in the dayside cusp region in response to the spatial and temporal enhancements in plasma drift that have been discussed previously. The resultant heating gives rise to upward flows in the ion and neutral gases [*Deng et al.*, 2013; *Horwitz and Lockwood*, 1995] with the upflowing ionospheric plasma having a significant impact on the dynamics of the hotter magnetospheric plasma [*Lotko*, 2007]. As the ionospheric plasma subsequently flows across the polar cap and out of the region of enhanced frictional heating, the plasma returns to its previous state with downward ion fluxes being dominant. During times of southward IMF, the bulk motion of the ionosphere can be viewed as a three-dimensional circulation with sunward and upward flows in the auroral zone, anti-sunward and upward flows in the cusp, and anti-sunward and downward flows in the polar cap [*Heelis et al.*, 1992].

When considering the ionospheric plasma density distribution at high latitudes, there are several major considerations. We first note that it is the convection trajectories with respect to the Earth-Sun line that determine the state of the plasma. Thus, it is important to consider the corotation of the plasma in addition to the influence of the convective paths we have discussed previously. Figure 4.9 shows the convective paths for a simple two-cell convection pattern that also includes corotation. Here the solid dots along each path in the panel to the right represent one-hour intervals in universal time, in order to emphasize that it is the direction of the flow and the residence time in sunlight that largely determines the magnitude of the plasma density. Thus, for example, plasma near 0900 local time and 70° latitude has a large residence time in sunlight while moving poleward. These conditions provide the maximum possible increase in plasma density [*Heelis et al.*, 2009]. By contrast the plasma near midnight local time and 85° latitude has a maximum residence time in darkness, thus leading to the lowest possible observed plasma density [*Brinton et al.*, 1978; *Sojka et al.*, 1981].

Finally, it is important to recognize that no plasma will circulate along the trajectories shown in Figure 4.9 or any of the instantaneous convection cells shown in previous figures. Typically it will take many hours to trace such a flow path, and it is now well established that the flow may significantly change on time scales less than one hour. How the plasma responds to such changes in the convection pattern is a significant challenge that has yet to be incorporated in the models of the ionosphere and thermosphere. Step-wise changes in the convection pattern that are instantaneously imposed on the plasma are not appropriate, since plasma near the dawn and

dusk convection reversal boundaries may find itself instantaneously making a transition from closed to open magnetic flux. In fact, at these locations the plasma may move poleward or equatorward as the boundary itself moves, as described in the expanding/contracting model put forward by *Morley and Lockwood* [2006]. As the boundary expands and contracts, it will not retain the nominally circular geometry that is generally displayed in convection patterns. The boundary is in fact continuously distorted in a manner determined by the potential distribution itself. This dynamic reconfiguration of the convection pattern is the next step in accurately specifying the plasma motion in the high-latitude ionosphere.

4.6. SUMMARY

Over the past 40 years, significant progress has been made in describing the convective motions of the plasma in the high latitude ionosphere. In addition to a phenomenological description of the convection pattern and its dependencies on conditions in the solar wind, we have also improved our understanding of the physical links between the ionosphere, the magnetosphere, and the solar wind that give rise to the observed convective motions. Many features of the observations are now captured in the large-scale MHD models that describe the overall behavior of the ionosphere-magnetosphere-solar wind system. With our expanded observational and modeling capabilities, additional challenges have emerged related largely to identifying the spatial and temporal scales that provide the variability to the system and accommodating this variability in our description of ionospheric variability. The path forward will require additional observational capability to capture the appropriate scale sizes for the electromagnetic energy inputs, the associated plasma convective paths, and the particle energy inputs. This information will in turn drive a requirement for adaptation of the models to accommodate a dynamic convection pattern that evolves self consistently in accord with the electric potential described by dayside merging rates, nightside reconnection rates, and viscous-like interactions at the magnetopause.

ACKNOWLEDGMENTS

This work is supported by NASA grant NNH-13ZDA001N to the University of Texas at Dallas. The author is grateful for the many interactions with colleagues who have contributed to the advancements made over the last 40 years, in particular to the late William B. Hanson who pioneered the plasma drift measurements that added significantly to our knowledge and provided this author with an unprecedented career opportunity.

REFERENCES

Axford, W. I. (1961), and Hines, C. O, A unifying theory of high latitude geophysical phenomena and magnetic storms, *Can. J. Phys*., *39*, 1433.

Banks, P. M, and J. R. Doupnik (1975), A review of auroral zone electrodynamics deduced from incoherent scatter radar observations, *J. Atmos. Terr. Phys.*, *37*, 951.

Bekerat, H. A., R. W. Schunk, and L. Scherliess (2003), Evaluation of statistical convection patterns for real-time ionospheric specifications and forecasts, *J. Geophys. Res*., *108*, 1413, doi:10.1029/2003JA009945, A12.

Brinton, H. C., J. M. Grebowsky, and L. H. Brace (1978), The high-latitude winter *F* region at 300 km: Thermal plasma observations from AE-C, *J. Geophys. Res.*, *83*(A10), 4767–4776, doi:10.1029/JA083iA10p04767.

Carlson, H. C. (2012), Sharpening our thinking about polar cap ionospheric patch morphology, research and mitigation techniques. *Radio Sci*. *47*, RS0L21, doi:10.1029/2011RS004946.

Cauffman, D. P., and. D. A. Gurnett (1972), Satellite measurements of high latitude convection electric fields, *SpaceSci. Rev.*, *13*, 369.

Chen, Y.-J., R. A. Heelis, and J. A. Cumnock (2015), Response of the ionospheric convection reversal boundary at high latitudes to changes in the interplanetary magnetic field. *J. Geophys. Res. Space Physics*, *120*, 5022–5034. doi: 10.1002/2015JA021024.

Clauer, C. R., and V. G. Petrov (2002), A statistical investigation of traveling convection vortices observed by the west coast Greenland magnetometer chain, *J. Geophys. Res*., *107*(A7), doi:10.1029/2001JA000228,.

Cousins, E. D. P., and S. G. Shepherd (2010), A dynamical model of high-latitude convection derived from SuperDARN plasma drift measurements, *J. Geophys. Res.*, *115*, A12329, doi:10.1029/2010JA016017.

Cowley, S. W. H., and M. Lockwood (1992), Excitation and decay of solar wind driven flows in the magnetosphere–ionosphere system, *Annales Geophys.*, *I0*, 103–115.

Crooker, N. U. (1992), Reverse convection, *J. Geophys. Res.*, *97*(A12), 19363–19372, doi:10.1029/92JA01532.

Crooker, N. U. (1988), Mapping the merging potential from the magnetopause to the ionosphere through the dayside cusp, *J. Geophys. Res.*, *93*(A7), 7338–7344, doi:10.1029/JA093iA07p07338.

Crooker, N. U., and G. L. Siscoe (1990), On mapping flux transfer events to the ionosphere, *J. Geophys. Res.*, *95*(A4), 3795–3799, doi:10.1029/JA095iA04p03795.

Cumnock, J. A. (2005), High-latitude aurora during steady northward interplanetary magnetic field and changing IMF *By*, *J. Geophys. Res.*, *110*, A02304, doi:10.1029/2004JA010867.

Deng, Y., T. J. Fuller-Rowell, A. J. Ridley, D. Knipp, and R. E. Lopez (2013), Theoretical study: Influence of different energy sources on the cusp neutral density enhancement, *J. Geophys. Res. Space Physics*, *118*, 2340–2349, doi:10.1002/jgra.50197.

Drake, K. A., R. A. Heelis, M. R. Hairston, and P. C. Anderson (2009), Electrostatic potential drop across the ionospheric signature of the low-latitude boundary layer, *J. Geophys. Res.*, *114*, A04215, doi:10.1029/2008JA013608.

Dungey, J. W. (1961), Interplanetary Magnetic Field and the Auroral Zones, *Phy Rev. Lett*., *6*, 47.

Farrugia, C. J., F. T. Gratton, and R. B. Torbert (2001), The role of viscous-type processes in solar wind-magnetosphere interactions, *Space Sci. Rev*., *95*, 443–456, doi:10.1023/A:1005288703357.

Greenwald, R. A., K. B. Baker, R. A. Hutchins, and C. Hanuise (1985), An HF phased-array radar for studying small-scale structure in the high-latitude ionosphere, *Radio Sci.*, *20*, 63–79.

Heelis, R. A. (1984), The effects of interplanetary magnetic field orientation on dayside high-latitude ionospheric convection, *J. Geophys. Res.*, *89*(A5), 2873–2880, doi:10.1029/JA089iA05p02873.

Heelis, R. A., W. R. Coley, M. Loranc, and M. R. Hairston (1992), Three-dimensional ionospheric plasma circulation, *J. Geophys. Res.*, *97*(A9), 13903–13910, doi:10.1029/92JA00872.

Heelis, R. A., J. J. Sojka, M. David, and R. W. Schunk (2009), Storm time density enhancements in the middle-latitude dayside ionosphere, *J. Geophys. Res.*, *114*, A03315, doi:10.1029/2008JA013690.

Heelis, R. A., W. B. Hanson, and J. L. Burch (1976), Ion convection velocity reversals in the dayside cleft, *J. Geophys. Res.*, *81*(22), 3803–3809, doi:10.1029/JA081i022p03803.

Heelis, R., J. Winningham, W. Hanson, and J. Burch (1980), The relationships between high-latitude convection reversals and the energetic particle morphology observed by Atmosphere Explorer, *J. Geophys. Res.*, *85*(A7), 3315–3324, doi:10.1029/JA085iA07p03315.

Heikkila, W. J., and J. D. Winningham (1971), Penetration of magnetosheath plasma to low altitudes through the dayside magnetospheric cusps, *J. Geophys. Res.*, *76*(4), 883–891, doi:10.1029/JA076i004p00883.

Heppner, J. P. (1972), Polar-cap electric field distributions related to the interplanetary magnetic field direction. *Journal of Geophysical Research 77*, doi: 10.1029/JA077i025p04877.

Heppner, J. P. (1977), Empirical models of high-latitude electric fields, *J. Geophys. Res.*, *82*(7), 1115–1125, doi:10.1029/JA082i007p01115.

Horwitz, J. L., and M. Lockwood (1985), The cleft ion fountain: A two-dimensional kinetic model, *J. Geophys. Res.*, *90*(A10), 9749–9762, doi:10.1029/JA090iA10p09749.

Jaggi, R. K., and R. A. Wolf (1973), Self-consistent calculation of the motion of a sheet of ions in the magnetosphere, *J. Geophys. Res.*, *78*(16), 2852–2866, doi:10.1029/JA078i016p02852.

Laundal, K. M., N. Østgaard, H. U. Frey, and J. M. Weygand (2010), Seasonal and interplanetary magnetic field–dependent polar cap contraction during substorm expansion phase, *J. Geophys. Res.*, *115*, A11224, doi:10.1029/2010JA015910.

Lopez, R. E., M. Wiltberger, J. G. Lyon, C. C. Goodrich, and K. Papadopoulos (1999), MHD simulations of the response of high-latitude potential patterns and polar cap boundaries to sudden southward turnings of the interplanetary magnetic field, *Geophys. Res. Lett*., *26*(7), 967–970, dio:10.1029/1999GL900113.

Lotko, W. (2007), The magnetosphere ionosphere system from the perspective of plasma circulation: A tutorial, *J. Atmos. Solar Terr. Phys*., *69*(3), 191–211, doi:10.1016/j.jastp.2006.08.011.

Lyons, L. R., Y. Nishimura, B. Gallardo-Lacourt, M. J. Nicolls, S. Chen, D. L. Hampton, W. A. Bristow, J. M. Ruohoniemi, N. Nishitani, E. F. Donovan, and V. Angelopoulos (2015), Azimuthal flow bursts in the inner plasma sheet and possible connection with SAPS and plasma sheet earthward flow bursts. *J. Geophys. Res. Space Physics*, *120*, 5009–5021. doi:10.1002/2015JA021023.

Mansurov, S. M. (1970), New evidence of the relationship between magnetic field in space and on the earth, *Geomagn. Aeron.*, *9*, 622.

Milan, S. E., J. Hutchinson, P. D. Boakes, and B. Hubert (2009), Influences on the radius of the auroral oval, *Ann. Geophys.*, *27*, 2913–2924, doi:10.5194/angeo-27-2913-2009.

Moen, J., M. Lockwood, K. Oksavik, H. C. Carlson, W. F. Denig, A. P. van Eyken, and I. W. McCrea (2004), The dynamics and relationships of precipitation, temperature and convection boundaries in the dayside auroral ionosphere, *Ann. Geophys.*, *22*, 1973–1987, doi:10.5194/angeo-22-1973-2004.

Morley, S. K., and M. Lockwood (2006), A numerical model of the ionospheric signatures of time-varying magnetic reconnection: III. Quasi-instantaneous convection responses in the Cowley-Lockwood paradigm, *Ann. Geophys*., *24*, 961–972, doi:10.5194/angeo-24-961-2006, 2006.

Peymirat, C., and D. Fontaine (1997), Polar cap convection patterns inferred from EISCAT observations, *Ann. Geophys.*, *15*, 403–411, doi:10.1007/s00585-997-0403-9.

Pinnock, M., A. S. Rodger, J. R. Dudeney, F. Rich, and K. B. Baker (1995), High spatial and temporal resolution observations of the ionospheric cusp, *Ann. Geophys.*, *13*, 919–925, doi:10.1007/s00585-995-0919-9.

Richmond, A. D., and Y. Kamide (1988), Mapping electrodynamic features of the high-latitude ionosphere from localized observations: Technique, *J. Geophys. Res.*, *93*(A6), 5741–5759, doi:10.1029/JA093iA06p05741.

Ridley, A. J., G. Crowley, and C. Freitas (2000), An empirical model of the ionospheric electric potential., *Geophys. Res. Lett*., *27*, 22, 3675–3678, doi: 10.1029/1999GL011161.

Ridley, A. J., G. Lu, C. R. Clauer, and V. O. Papitashvili (1998), A statistical study of the ionospheric convection response to changing interplanetary magnetic field conditions using the assimilative mapping of ionospheric electrodynamics technique, *J. Geophys. Res.*, *103*(A3), 4023–4039, doi:10.1029/97JA03328.

Ridley, A. J., and C. R. Clauer (1996), Characterization of the dynamic variations of the dayside high-latitude ionospheric convection reversal boundary and relationship to interplanetary magnetic field orientation, *J. Geophys. Res*.

Rinne, Y., J. Moen, H. C. Carlson, and M. R. Hairston (2010), Stratification of east-west plasma flow channels observed in the ionospheric cusp in response to IMF BY polarity changes, *Geophys. Res. Lett.*, *37*, L13102, doi:10.1029/2010GL043307.

Russell, C. T., and R. C. Elphic (1979), ISEE observations of flux transfer events at the dayside magnetopause, *Geophys. Res. Lett.*, *6*(1), 33–36, doi:10.1029/GL006i001p00033.

Siscoe, G. L., and T. S. Huang (1985), Polar cap inflation and deflation, *J. Geophys. Res.*, *90*(A1), 543–547, doi:10.1029/JA090iA01p00543.

Skjæveland, Å., J. Moen, and H. C. Carlson (2011), On the relationship between flux transfer events, temperature

enhancements, and ion upflow events in the cusp ionosphere, *J. Geophys. Res.*, *116*, A10305, doi:10.1029/2011JA016480.

Sojka, J. J., W. J. Raitt, and R. W. Schunk (1981a), A theoretical study of the high-latitude winter F region at solar minimum for low magnetic activity, *J. Geophys. Res.*, *86*(A2), 609–621, doi:10.1029/JA086iA02p00609.

Sundberg, K. Å. T., L. G. Blomberg, and J. A. Cumnock (2008), Statistical analysis of the sources of the cross-polar potential for southward IMF, based on particle precipitation characteristics, *Geophys. Res. Lett.*, *35*, L08103, doi:10.1029/2008GL033383.

Svalgaard, L. (1973), Polar cap magnetic variations and their relationship with the interplanetary magnetic sector structure, *J. Geophys. Res.*, *78*(13), 2064–2078, doi:10.1029/JA078i013p02064.

Volland, H. (1975), Models of the global electric fields within the magnetosphere, *Ann. Geophys.*, *31*, 159–173.

Volland, H. (1978), A model of the magnetospheric electric convection field, *J. Geophys. Res.*, *83*(A6), 2695–2699, doi:1 0.1029/JA083 iA06p026 95.

Weimer, D. R. (2005), Improved ionospheric electrodynamic models and application to calculating Joule heating rates, *J. Geophys. Res.*, *110*, A05306, doi:10.1029/2004JA010884.

Winningham, J. D., F. Yasuhara, S.-I. Akasofu, and W. J. Heikkila (1975), The latitudinal morphology of 10-eV to 10-keV electron fluxes during magnetically quiet and disturbed times in the 2100–0300 MLT sector, *J. Geophys. Res.*, *80*(22), 3148–3171, doi:10.1029/JA080i022p03148.

5

Energetic and Dynamic Coupling of the Magnetosphere-Ionosphere-Thermosphere System

Gang Lu

Video of Yosemite Talk, URL: http://dx.doi.org/10.15142/T3T88K

ABSTRACT

This paper illustrates several important energetic and dynamic processes taking place within the magnetosphere-ionosphere-thermosphere system during the October 2003 geomagnetic storms. Numerical simulations based on the National Center for Atmospheric Research - Thermosphere Ionosphere Mesosphere Electrodynamics General Circulation Model (NCAR-TIMEGCM) were carried out to assess the relative impact of various solar and magnetospheric forcings. The model showed a significant increase of thermospheric temperature in response to Joule heating dissipation during the storms, from about 30% (or 400°K) above 400 kilometers (km) to about 10% (or ~100°K) at 150 km. Thermospheric mass density exhibited similar altitude dependence in its storm-time response, with an increase of more than 150% above 400 km to about 30% at 150 km. Around 100 km, thermospheric storm effects became indiscernible. Intense auroral and Joule heating dissipation altered the *F*-region peak density NmF_2 and raised the peak height hmF_2. Energetic particle precipitation not only increases the *E*- and *D*-region conductivity but also enhances Joule and particle heating in these regions. The NO_X enhancement and ozone (O_3) destruction resulting from solar energetic protons (SEP) were seen throughout the rest of year 2003 following the Halloween storms. Significant hemispheric asymmetry was found, in that the SEP-related NO_X and O_3 changes were more pronounced in the northern hemisphere than in the southern hemisphere.

5.1. INTRODUCTION

The Earth's ionosphere and thermosphere are influenced by several geophysical forcings. Solar ultraviolet (UV) and extreme ultraviolet (EUV) radiation is the main energy source for heating, ionization, and photochemical reactions in the thermosphere and ionosphere. Energetic particles from the Sun and the magnetosphere penetrate into the ionosphere/thermosphere and even down to the upper stratosphere where they produce additional ionization and heating to affect the chemistry and dynamics of these regions. Electric fields and currents are transmitted between the magnetosphere and the ionosphere, providing an important source of energy and momentum for the coupled magnetosphere-ionosphere-thermosphere system. While each of the solar and magnetospheric forcings produces a unique set of effects on the ionosphere and thermosphere, jointly, they can cause rather complex global responses due to the interplay of the various chemical, photochemical, dynamical, and electrodynamical processes within this highly coupled system. To understand and elucidate the effects of the different forcings on the thermosphere and ionosphere, it is necessary to resort to physics-based models that have the fully compatible neutral atmosphere and ionosphere, together

High Altitude Observatory, National Center for Atmospheric Research, Boulder, CO, USA

Magnetosphere-Ionosphere Coupling in the Solar System, Geophysical Monograph 222, First Edition.
Edited by Charles R. Chappell, Robert W. Schunk, Peter M. Banks, James L. Burch, and Richard M. Thorne.

with self-consistent treatments of various physical processes. The NCAR-TIMEGCM is one such model, which allows us to delineate and understand how various solar and magnetospheric forcings affect the upper atmosphere.

Energetic particles, namely electrons and protons, released from the magnetosphere cover a wide range of energies from a few electron volt (eV) to hundreds of million electron volts (MeV). Precipitating electrons of several kiloelectron-volts (keV) are deposited in the 90–150 km altitude range, and they are mostly responsible for producing auroras and creating the *E*-region ionosphere. Though protons with energies less than 30 keV also produce auroral emission at higher altitudes, they contribute less than 20% of the total energy input in the auroral zone [*Fuller-Rowell and Evans*, 1987]. More energetic electrons of a few hundred keV can penetrate to the lower thermosphere and mesosphere. Modeling studies have demonstrated that these energetic particles can significantly enhance the *D*-region electron density and also alternate the chemical compositions between 70 and 80 km altitudes [e.g., *Codrescu et al*., 1997; *Fang et al.,* 2007]. SEPs, particularly those with energies >1 MeV, penetrate even deeper into the atmosphere, and their effects have been seen down to the upper stratosphere [e.g., *Solomon et al*., 1982; 1983; *Reid, et al*., 1991; *Jackman et al*., 2005, 2008, 2009; *Randall et al*., 2007; *Seppälä et al*., 2007]. While auroral energetic electrons with energies <30 keV are commonly included in global circulation models such as the TIMEGCM, the Coupled Thermosphere-Ionosphere-Plasmasphere (CTIP) [*Fuller-Rowell et al*., 1996], and the Global Ionosphere-Thermosphere Model (GTIM) [*Ridley et al.*, 2006], treatments of more energetic (e.g., >30 keV) magnetospheric particles have only been experimented using the TIMEGCM [e.g., *Codrescu et al.,* 1997]. Furthermore, the specification of energetic particles in these studies was based on empirical models rather than real-time data. So far there are no studies that involve all types of energetic particles, namely, auroral precipitating electrons (<30 keV), magnetospheric energetic particles (>30 keV), and SEPs (>1 MeV), in a single investigation.

This paper discusses thermospheric and ionospheric response to major geomagnetic storms taking place in October 2003, commonly referred as the Halloween storms. The storms featured several concurrent solar and magnetospheric disturbances, including intense geomagnetic storms triggered by fast-moving coronal mass ejections (CME), a large SEP event, and intense energetic particle precipitation from the magnetosphere. This is therefore an ideal case to assess the relative contributions of the different external drivers on the coupled magnetosphere-ionosphere-thermosphere system. This paper is organized as follows: Section 5.2 describes the data inputs and the models used in the study. Section 5.3 presents and discusses the various energetic and dynamic properties of the ionosphere and thermosphere in response to the solar and magnetospheric forcings. The main findings of the study are summarized in Section 5.4.

5.2. DATA AND MODEL DESCRIPTION

5.2.1. Energetic Particles Data from Polar Orbiting Environment Satellite and Geostationary Operational Environmental Satellite

The Medium Energy Proton and Electron Detector (MEPED) instrument, which is a component of the second-generation Space Environment Monitor (SEM-2) detector onboard the Polar Orbiting Environment Satellite (POES) spacecraft, measures the influx of electrons between 30 and 1000 keV in three energy ranges (e.g., >30 keV, >100 keV, and >300 keV), and the influx of protons between 30 and 6900 keV in six energy ranges (e.g., 30–80 keV, 80–240 keV, 240–800 keV, 800–2500 keV, 2500–6900 keV, and >6900 keV). More detailed information on SEM-2 can be found in *Evans and Greer* [2002]. For this case study, the MEPED data were available from three National Oceanic and Atmospheric Administration (NOAA)-POES satellites (e.g., N15, 16, and 17) operating in sun-synchronous orbit at ~830 km altitude with an orbital period of ~100 mins. Global maps of the MEPED electron and proton fluxes were obtained by combining all satellite measurements over a three-hour interval, and linear interpolation was applied to bin the data into two-dimensional arrays with 1° in latitude and 2° in longitude. Electron and proton energy spectra were constructed by fitting an exponential distribution function to the MEPED electrons and protons separately. Energy flux and characteristic energy in each latitude-longitude bin were derived based on least squares fitting at a three-hour cadence. As noted by several recent investigations [e.g., *Roger et al.*, 2010; *Lam et al*., 2010; *Asikainen and Mursula*, 2013], the MEPED instrument suffers from cross-contamination between electrons and protons. We suspect that the MEPED measurement error due to the cross-contamination is probably smaller than the errors associated with averaging and interpolating the data to construct the three-hourly two-dimensional maps. Also, the overestimate of the MEPED electron and proton fluxes from the cross-contamination may be partially compensated by the underestimate resulting from the smoothing process for the two-dimensional maps. Nevertheless, we caution readers that the effects by the MEPED data (MEPED electrons in particular) presented here should be considered only as semi-quantitative. More importantly, the emphasis of this investigation is on the relative contributions by the different energetic particles.

Besides POES, the Geostationary Operational Environmental Satellite (GOES) at geosynchronous orbit measures energetic protons at seven energy ranges: >1 MeV, >5 MeV, >10 MeV, >30 MeV, >50 MeV, >60 MeV, and >100 MeV. Similar to the MEPED data, the GOES MeV proton fluxes are fitted to an exponential function. While recognizing that a fraction of the GOES MeV protons may originate from the magnetosphere, we have assumed the GOES protons as SEPs for the purpose of this investigation. Figure 5.1 shows the characteristic energy and energy flux of SEPs measured by GOES-11 from 25 October to 8 November 2003. There were three episodes of SEP intensification over this 14-day period. The most intense SEP precipitation occurred around 06 universal time (UT) on 29 October, which was preceded by a relatively weak SEP event on 26–27 October and followed by another modest SEP event centered on 3 November. When simulating the SEP effects in the TIMEGCM, the SEP influx is uniformly applied over both the northern and southern polar regions above |60°| magnetic latitude as suggested by *Jackman et al*. [2008].

5.2.2. Assimilative Mapping of Ionospheric Electrodynamics

The assimilative mapping of ionospheric electrodynamics (AMIE) data assimilation algorithm was first developed at High Altitude Observatory (HAO)/NCAR in 1988 [*Richmond and Kamide*, 1988], and it has since been undergoing continuous improvement in terms of its spatial resolution and its ability to ingest new types of data [e.g., *Lu et al*., 1998, 2001]. The objective of the AMIE procedure is to obtain optimal estimates of high-latitude ionospheric electrodynamic fields by combining various direct and indirect observations of these fields. For this case study, the data input to AMIE includes magnetic field perturbations at 166 ground magnetometer stations worldwide (37 of them in the southern hemisphere), ion drift measurements from three Defense Meteorological Satellite Program (DMSP) satellites (e.g., F13, 14, and 15), from the Super Dual Auroral Radar Network (SuperDARN) high-frequency coherent scatter radars (8 in the northern hemisphere and 1 in the southern hemisphere), and from the Sondrestrom incoherent scatter radar, along with auroral precipitating electrons measured by the DMSP and POES satellites. The Total Energy Detector (TED) onboard POES is part of the SEM-2 instrument suite. TED is designed to measure auroral energy flux carried by auroral electrons and protons in energies from 50 eV to 20 keV in 16 energy bands, and the Maxwellian mean energy and energy flux of precipitating particles are derived [*Fuller-Rowell and Evans*, 1987]. For DMSP, auroral precipitating particles between 30 eV and 30 keV are measured in 19 logarithmically spaced energy steps. A Maxwellian distribution function is applied to the differential fluxes to obtain the

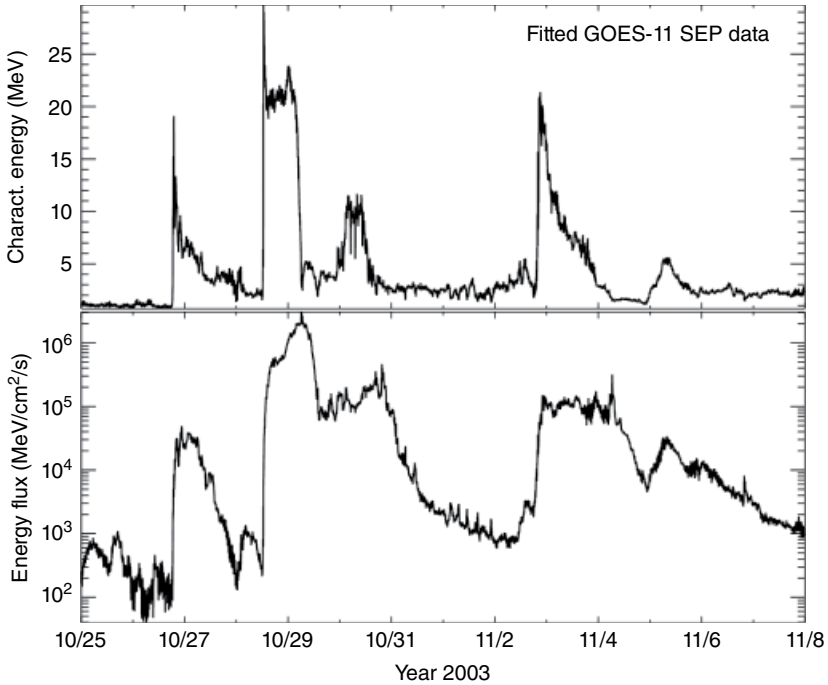

Figure 5.1 (top) Characteristic energy and (bottom) energy flux of solar energetic protons derived from an exponential fitting to the GOES-11 data.

mean energy and energy flux of auroral particles [*Rich et al*., 1987]. Indirect information from ground magnetometer data is also used to infer auroral conductance based on the empirical formula of *Ahn et al*. [1983]. Note that only auroral precipitating electrons are considered in AMIE analysis since precipitating protons contribute less than 20% of total auroral energy flux [*Fuller-Rowell and Evans*, 1987]. Northern and southern hemispheric patterns of auroral precipitating electron energy flux and mean energy, electric potential, height-integrated Joule heating, together with other electrodynamics fields are derived from AMIE in a five-min cadence.

5.2.3. TIMEGCM

The NCAR-TIMEGCM [*Roble and Ridley*, 1994; *Roble*, 1995] is a global model specifically designed for the mesosphere-thermosphere-ionosphere system. It extends from approximately 30 km to 500 to 700 km, depending on solar activity. The model includes all of the important aeronomical, dynamical, and electrodynamical processes that are appropriate for these regions. It solves self-consistently the fully coupled, nonlinear, hydrodynamic, thermodynamic, and continuity equations of the neutrals, together with ion and electron energy and momentum equations, ion continuity equations, and the neutral wind dynamo from the stratosphere to the upper thermosphere. The model has a horizontal resolution of $5° \times 5°$ in latitude and longitude and a vertical resolution of one-half-scale height, with a total of 49 constant pressure levels. A high-resolution version of the model is also available now, which has a grid size of 2.5° in latitude and longitude and one-fourth scale height vertically. The lower boundary of the TIMEGCM is specified by climatological diurnal and semi-diurnal tides based on the Global Scale Wave Model (GSWM) [*Hagan and Forbes*, 2002, 2003]. In addition, daily averaged temperature as well as zonal and meridianal winds from the National Center for Environmental Predictions (NCEP) reanalysis are used in this study to represent other long-period waves generated below the TIMEGCM lower boundary. The upper boundary inputs to the TIMEGCM include energetic particle precipitation based on real-time POES-MEPED and GOES SEP measurements, and auroral electron precipitation and ionospheric electric field from the AMIE outputs. Furthermore, the one-min solar fluxes from the flare irradiance spectral model (FISM) [*Chamberlin et al*., 2007, 2008] are also used as input to drive the TIMEGCM. FISM is an empirical model based on measurements from the Solar EUV Experiment (SEE) instrument [*Woods et al*., 2005] on board the thermosphere-ionosphere-mesosphere energetics and dynamics (TIMED) satellite. The high-cadence FISM solar flux data are necessary to simulate thermospheric response to solar flares. However, we will not discuss the solar flare effects specifically in this paper since they have been described in detail by *Qian et al*. [2010]. Rather, the main emphasis of this study is on the relative effects of storm-time Joule heat energy dissipation as well as various energetic particles on the thermosphere and ionosphere. The model ran in a one-min time step, and the model inputs were linearly interpolated to the model times.

5.3. RESULTS

The solar wind and geophysical conditions for the period of 28 to 31 October 2003 are plotted in Figure 5.2. The solar wind bulk speed (top panel) and the interplanetary magnetic field (IMF) (second panel) were measured by the Advanced Composition Explorer (ACE) spacecraft located at (231, 41, −20) R_E in GSE (X, Y, Z) coordinates, and are time-shifted by 24 mins to account for solar wind propagation from the spacecraft location to the dayside magnetospause. A large CME was released from the Sun around 11:30 UT on 28 October with a speed greater than 2000 km/s [*Gopalswamy et al*., 2005], and arrived at Earth in less than a day at 11:00 UT on 29 October [*Richardson and Cane*, 2010]. A second large CME reached the Earth on 30 October, which had a peak speed of ~1700 km/s. Prior to the arrival of the fast CMEs, the IMF B_Z component was rather weak, with a magnitude of about 5 nT. When the fast CMEs encounter the slow background solar wind, interplanetary shocks are formed. Between the shock front and the leading edge of the CME are the compressed sheath regions, which are highlighted in gray. Inside the sheath region, B_2 was highly fluctuating, especially in the early portion of the sheath region on 29 October when B_2 oscillated between ±50 nT.

Figure 5.2c shows the *Dst* index derived from 43 ground magnetometer stations located below |40°| magnetic latitude at a one-min cadence. The interplanetary shock prompted a storm sudden commencement (SSC) as manifested by the positive excursion in *Dst* at 06:12 UT on 29 October, followed by rapid decrease in *Dst* until about 09:45 UT when B_2 became northward prior to the arrival of the first CME. The leading edge of the first CME was northward so that *Dst* remained relatively flat until ~18:00 UT when B_2 turned southward in the trailing edge of the CME flux tube. The first CME produced a major storm with a minimum *Dst* value of −405 nT. Before the *Dst* index recovered to its prestorm value after the passage of the first CME, the arrival of the second CME on 30 October caused *Dst* to dip again, producing a second, even more intense geomagnetic storm with a minimum *Dst* value of −455 nT. It is worth of mentioning that the B_2 values associated with these two *Dst* dips were about

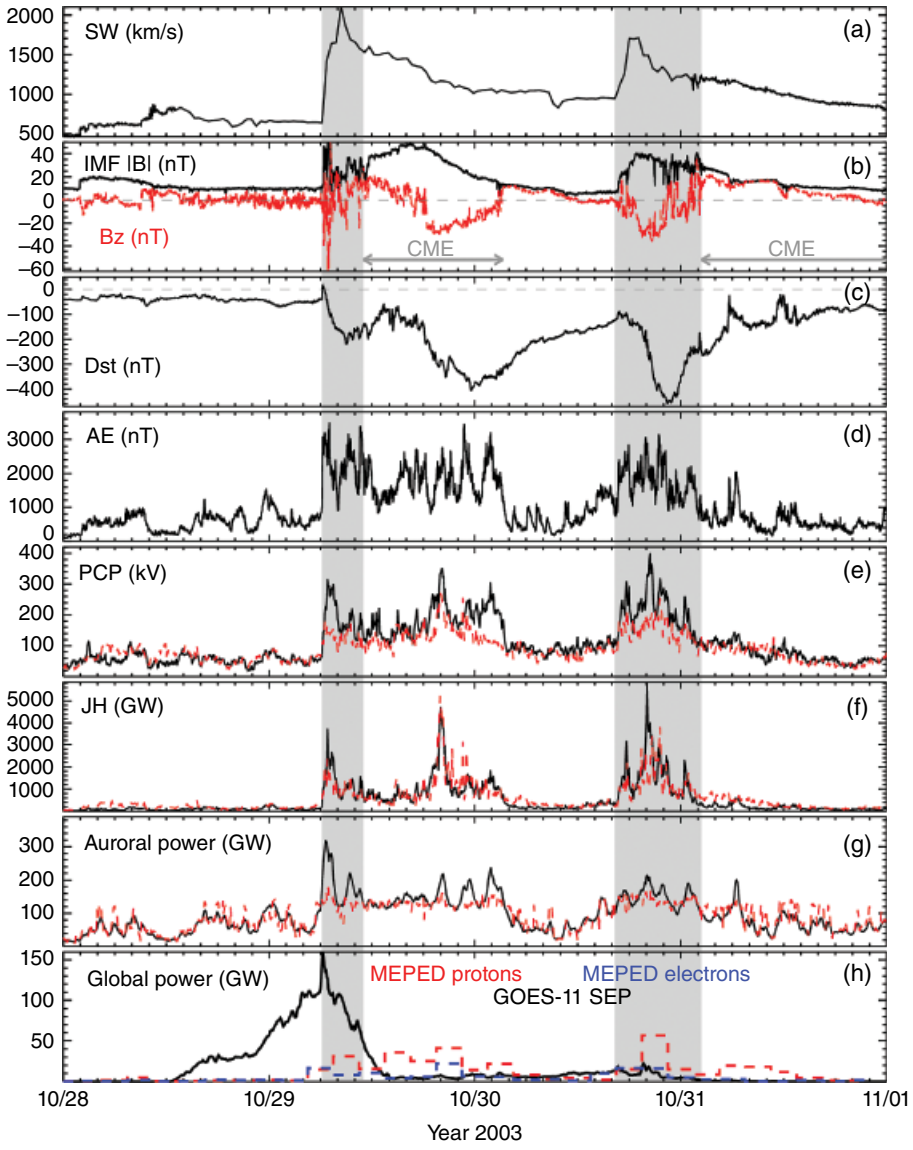

Figure 5.2 Solar wind and geophysical parameters for the period of 28–31 October 2003. (a) ACE solar wind speed, (b) IMF and the B_z component, (c) the one-min *Dst* index derived from 43 mid- and low-latitude stations, (d) the one-min *AE* index derived from 75 auroral stations, (e) the polar cap potential drop in the northern (black solid line) and southern (red dashed line) hemisphere, (f) hemispheric integrated Joule heating rate over the northern (black) and southern (red) hemisphere, (g) hemispheric integrated auroral power over the northern (black) and southern (red) hemisphere, and (h) globally integrated power by SEPs (black solid line), MEPED electrons (blue histogram) and MEPED protons (red histogram).

the same (both around −30 nT), and the duration of the B_z southward phase for the second CME (~seven hours) was even shorter than that for the first CME (~nine hours). Yet, the second storm was more intense as gauged by the *Dst* value, which may indicate the importance of the pre-conditioning of the magnetosphere.

Figure 5.2d shows the one-min auroral electrojet (*AE*) index, which was derived from 75 magnetometer stations located between 55° and 76° magnetic latitudes north and south. There are extensive auroral activities throughout the 3-day period from 29 to 31 October, with the maximum *AE* value exceeding 3000 nT. Intense auroral activities are accompanied by enhanced electric field or plasma convection. Figure 5.2e shows the distributions of the polar cap potential (PCP) drop over the northern (black solid line) and southern hemisphere (red dashed line), respectively. PCP varies from tens kilovolts (kV) prior to the storms to ~400 kV during the storm on 30 October.

There are some differences in PCP between the two hemispheres, with the southern hemispheric PCP values somewhat smaller than those in the northern hemisphere. This is partially because of the difference in data coverage because there are many fewer data available in the southern hemisphere so that the fitted electric potentials rely more on the underlying empirical model in regions where there are no data [*Lu et al.*, 2001].

The storms led to intense energy dissipation into the ionosphere in terms of Joule heating and energetic particle precipitation. Figures 5.2f and 5.2g show the hemispheric integrated Joule heating rate and auroral electron energy flux over the northern and southern hemispheres. The highest hemispheric Joule heating reaches about 5500 gigawatts (GW) (or 5.5 terawatts [TW]) whereas the highest hemispheric auroral power is about 300 GW. However, the magnitude of Joule heating and auroral power are about the same during quiet times, both around a few tens GW. The globally integrated power by various energetic particles is shown in Figure 5.2h, in which the black line corresponds to SEPs with energies greater than 1 MeV, and the blue and red histograms correspond to the MEPED electrons and protons in the energy range from 30 keV to 2.5 MeV that are primarily injected from radiation belts and the ring current. The peak SEP power is about 160 GW, which is roughly one-half of the peak hemispheric auroral power. Thus, despite being the fourth largest SEP event in the past 50 years [*Jackman et al.*, 2008], the total energy dissipation by SEPs is much less than the storm-time auroral energy dissipation. The total energy dissipation by MEPED electrons and protons is somewhat smaller, with a maximum value of 131 GW for MEPED protons and 91 GW for MEPED electrons. When averaged over the 3-day storm interval of 29 to 31 October, the globally integrated Joule heating is 1276 GW, the globally integrated auroral power is 210 GW, the mean MEPED electron power is about 25 GW, and the mean MEPED proton power 47 GW. For SEPs, a 3-day average over the period of 28 to 30 October yields a mean power of 23 GW. As we will show below, the different energetic particles affect the upper atmosphere in their unique ways.

5.3.1. Effects of Auroral Precipitation and Joule Heating

Joule heating and auroral precipitation are the two main forms of magnetospheric energy input to the ionosphere and thermosphere. Figure 5.3 compares the distributions of height-integrated Joule heating (top row) and auroral electron energy flux (bottom row) over the northern hemisphere at quiet time (left) and at active time (right). The contours in the top row represent electric potentials, with dashed contours for negative potentials (clockwise plasma convection) and solid contours for positive potentials (counter clockwise convection). At quiet time, the hemispheric integrated Joule heating (50 GW) is about the same as the hemispheric integrated auroral electron energy flux (53 GW). During storm time, Joule heating (2393 GW) exceeds auroral precipitation (194 GW) by more than one order of magnitude.

Intense Joule energy dissipation can have a drastic impact on the thermosphere and ionosphere. Figure 5.4 shows the globally averaged thermospheric response to the storms. The top panel plots the time series of the reversed *Dst* index in black and the hemispheric integrated Joule heating rate in red. A good correlation is found between the reversed *Dst* index and the three-hour smoothed Joule heating, with a correlation coefficient of 0.90 and a time lag of two hours. The second panel of Figure 5.4 shows the percent change of global mean neutral temperature at selected altitudes. The differences are derived from the TIMEGCM calculations for the period of 28 October to 1 November with respect to the global mean values at the corresponding altitudes at 00 UT on 28 October. Note that the small bump around 11 UT on October 28 is associated with thermospheric response to an X-class flare rather than geomagnetic activity. A detailed investigation of the flare effects on the thermosphere and ionosphere has been carried out by *Qian et al.* [2010]. Here we focus our attention on the storm effects. The slanted gray arrows connect the peaks between the smoothed Joule heating and the difference neutral temperature, indicating a delay time of two to three hours between the peak Joule heating dissipation and the maximum global thermospheric response. It is interesting to note that this time delay is similar to the time lag of the reversed *Dst* index with respect to Joule heating. This similarity, however, does not imply a causal relationship between the thermosphere and the inner magnetosphere; in fact, we anticipate the relationship between them is far more complex as the physical processes driving the ring current intensification are totally different from the dynamical and chemical processes responsible for the storm-time thermospheric variations. Enhanced Joule energy dissipation heats up neutral gases causing the global mean temperature to increase by ~30% in the upper thermosphere above 400 km. The percent change in neutral temperature decreases as altitude decreases. The storm-induced temperature increase drops to ~10% at 150 km, and becomes negligible around 100 km.

Heating from auroral and Joule energy dissipation causes the thermosphere to expand upward, bringing heavier molecular-rich air to higher altitudes and thus increasing mean mass density at a fixed altitude. Figure 5.4c shows the percent change of global mean mass density and the N_2/O ratio at selected altitudes. The percent change of neutral mass density (the N_2/O ratio)

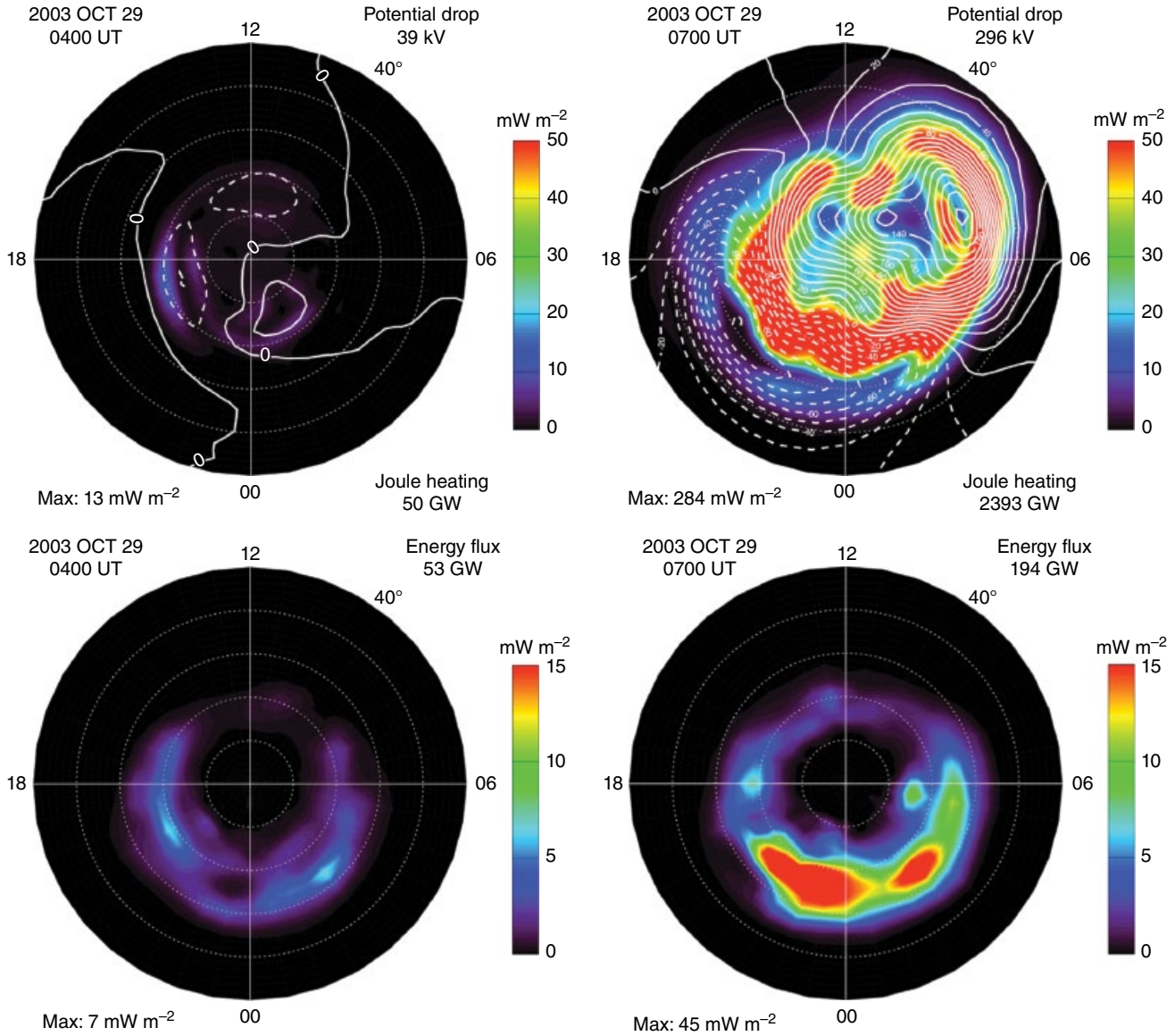

Figure 5.3 Distributions of (top row) height-integrated Joule heating and (bottom row) auroral electron energy flux in the northern hemisphere. The overlain contours in the top row are electric potentials, and the contour interval is 10 kV. The hemispheric integrated Joule heating rate is shown in the lower right corner of the patterns in the top row, and the hemispheric integrated auroral power shown in the upper right corner of the patterns in the bottom row. The left column corresponds to a quiet time at 04 UT on 29 October, and the right column for an active time at 07 UT on 29 October. All patterns are plotted in magnetic latitude and magnetic local time.

during the Halloween storms is quite impressive, varying from over 150% (300%) in the upper thermosphere to ~25% (50%) in the lower thermosphere at 150 km. Again, no discernible changes in mass density and the N_2/O ratio can been seen at 100 km altitude.

Among the most observed ionospheric variables during geomagnetic storms are variations of the *F* layer peak electron density NmF_2 and the peak height hmF_2. An increase (decrease) of NmF_2 is referred as a positive (negative) storm phase. Change in NmF_2 is subject to several chemical and dynamical processes. Higher molecular concentration due to thermospheric upwelling contributes to more rapid recombination between electrons and ions, resulting in a reduction in NmF_2 [*Rishbeth*, 1989; *Burns et al.*, 1991, 1995]. Equatorward disturbance winds in form of traveling atmospheric disturbances (TAD), on

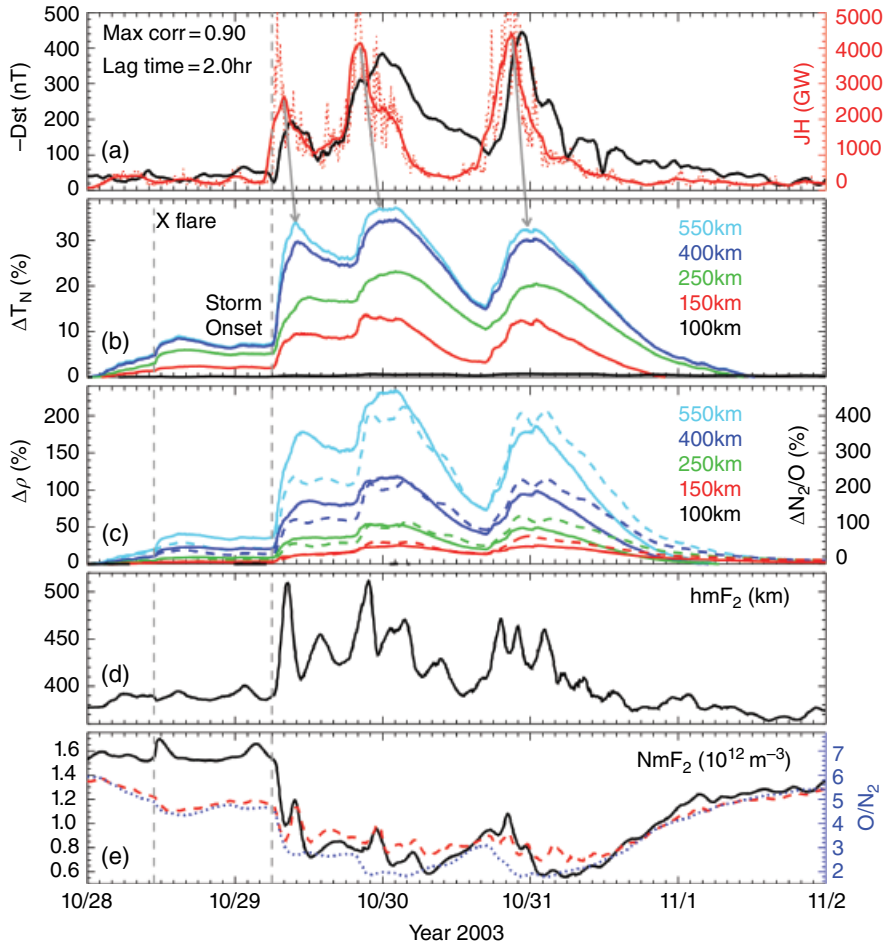

Figure 5.4 Distributions of (a) the reversed Dst index (black) and globally integrated Joule heating rate (red), with the five-min Joule heating shown by the red dotted line and the three-hour running average by the solid red line, (b) percent change of global mean temperature at selected altitudes, (c) percent change of neutral mass density (solid lines) and the N_2/O ratio (dashed lines) at selected altitudes, (d) global mean hmF_2, and (e) global mean NmF_2 (solid line), the O/N_2 ratio (blue dotted line), and the O/N_2 plus modulations from hmF_2 (red dashed line). See text for detail.

the other hand, lift the *F* layer to higher altitude at mid-latitudes where the recombination rate becomes smaller, resulting in an increase in NmF_2 [*Prölss*, 1993]. Figure 5.4d shows the response of globally averaged hmF_2 to the storms. Like the thermosphere, the excess storm-time Joule heating raises the *F* layer peak altitude by 50 to 100 km. Unlike the thermosphere, change in hmF_2 exhibits large modulations with a period of five to six hours, which is approximately the travel time of TADs from the auroral zone in one hemisphere to another with a typical phase speed of 750 m/s. Variations of NmF_2 are plotted in Figure 5.4e, which shows an overall reduction during the storm interval. The large-scale NmF_2 variations closely resemble the O/N_2 ratio at hmF_2 shown as the blue dotted line, indicating that composition change is the main cause of the NmF_2 reduction during the storms. To understand the small-scale variations in NmF_2, the red dashed line in Figure 5.4e represents the O/N_2 ratio plus 1.5% of hmF_2 variations that is time-shifted by one and one-half hours and unit-less. Though far from perfect, the red dashed line does capture most of the small-scale variations in NmF_2, impling that the small-scale variations in NmF_2 are caused by dynamical process related to the rise and fall of hmF_2 due to TADs.

5.3.2. Effects of Energetic Particles on the Ionosphere

Besides solar radiation, precipitation of energetic electrons and protons is another important source of ionization and heating in the upper atmosphere. Since precipitating particles originated from the Sun and from the magnetosphere possess different characteristics, it is

important to assess the relative contributions they have on the ionosphere in terms of ionization, conductivity, and heating.

Figure 5.5 shows the distributions of energy flux and mean energy of auroral precipitating electrons as well as MEPED electrons and protons at 07 UT in the northern hemisphere. Note that different color scales are applied to the different energetic particles. There are several notable differences between auroral electrons and MEPED particles: (1) the auroral electron energy flux is about 10 times larger than the MEPED electron energy flux; (2) the intense MEPED electron and proton fluxes are located near the equatorward edge of auroral electron flux; (3) the MEPED electron flux peaks in the post-midnight sector (with two peaks at about 01:30 and 03 local time [LT], respectively); and (4) the MEPED proton flux peaks at earlier local times compared to the MEPED electrons (the proton flux peaks at about 21 LT and 01 LT, respectively). The latitude difference between auroral precipitating electrons and the MEPED energetic particles implies that they map to the different magnetospheric source regions, with auroral precipitating electrons originating from the plasma sheet [*Newell and Meng*, 1994] and the MEPED particles from the ring current and radiation belts in the inner magnetosphere [e.g., *Meredith et al.*, 2011; *Lam et al.*, 2010]. The local time separation between the MEPED electrons and protons is attributed to the fact that energetic electrons move toward dawn and energetic protons toward dusk in the inner magnetosphere owing to magnetic gradient-curvature forces. At this particular UT, the mean energy of auroral precipitating electrons is around 4 to5 keV, and the mean energy of the MEPED protons around 70 to 80 keV. The mean energy of MEPED electrons shows a wide range of variations, but the most intense MEPED electron influx is carried by those with energies between 80 to 90 keV.

While the ionization rate is proportional to the energy flux of precipitating particles, how deep they penetrate into the upper atmosphere is dependent on the particles' energies. The top row of Figure 5.6 shows the vertical distributions of ionization rates at local midnight by the different energetic particles at 07 UT on 29 October. Ionization rates by precipitating electrons are calculated using the analytic expression described by *Roble and Ridley* [1987], whereas ionization rates by MEPED protons and SEPs are derived using the parameterization of *Lummerzheim* [1992]. Ionization by auroral precipitating electrons mostly takes place in the 100–200 km altitude

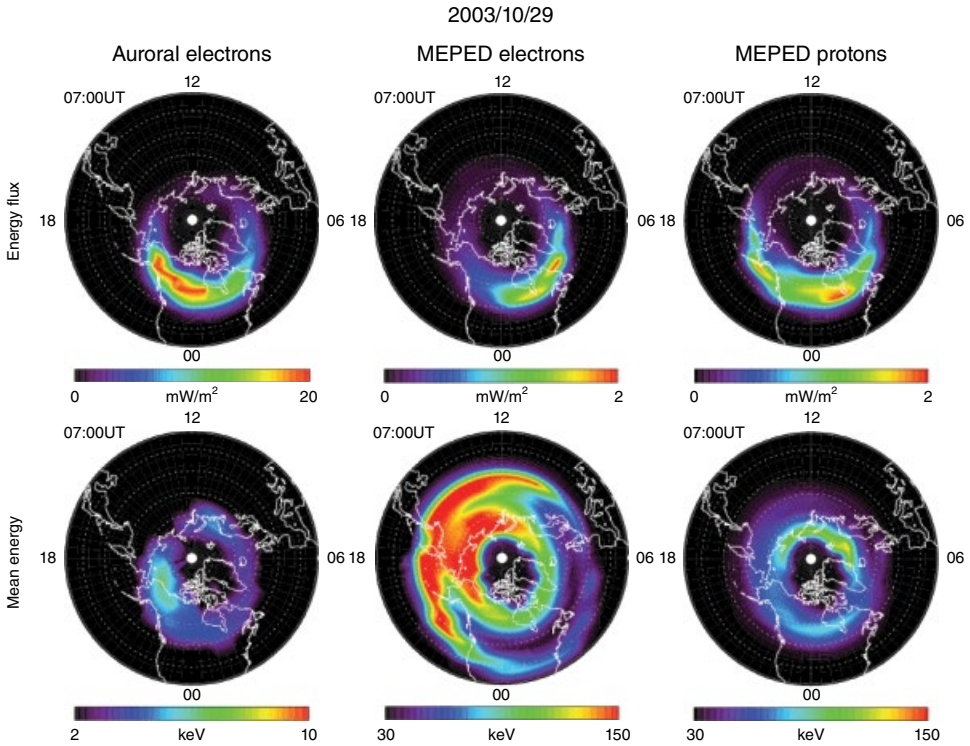

Figure 5.5 Distributions of (top row) energy flux and (bottom row) mean energy of auroral electrons (left panels), MEPED electrons (middle panels), and MEPED protons (right panels) at 07 UT on 29 October. Note that color scales are different for the different energetic particles. All patterns are plotted in geographic latitude and local time.

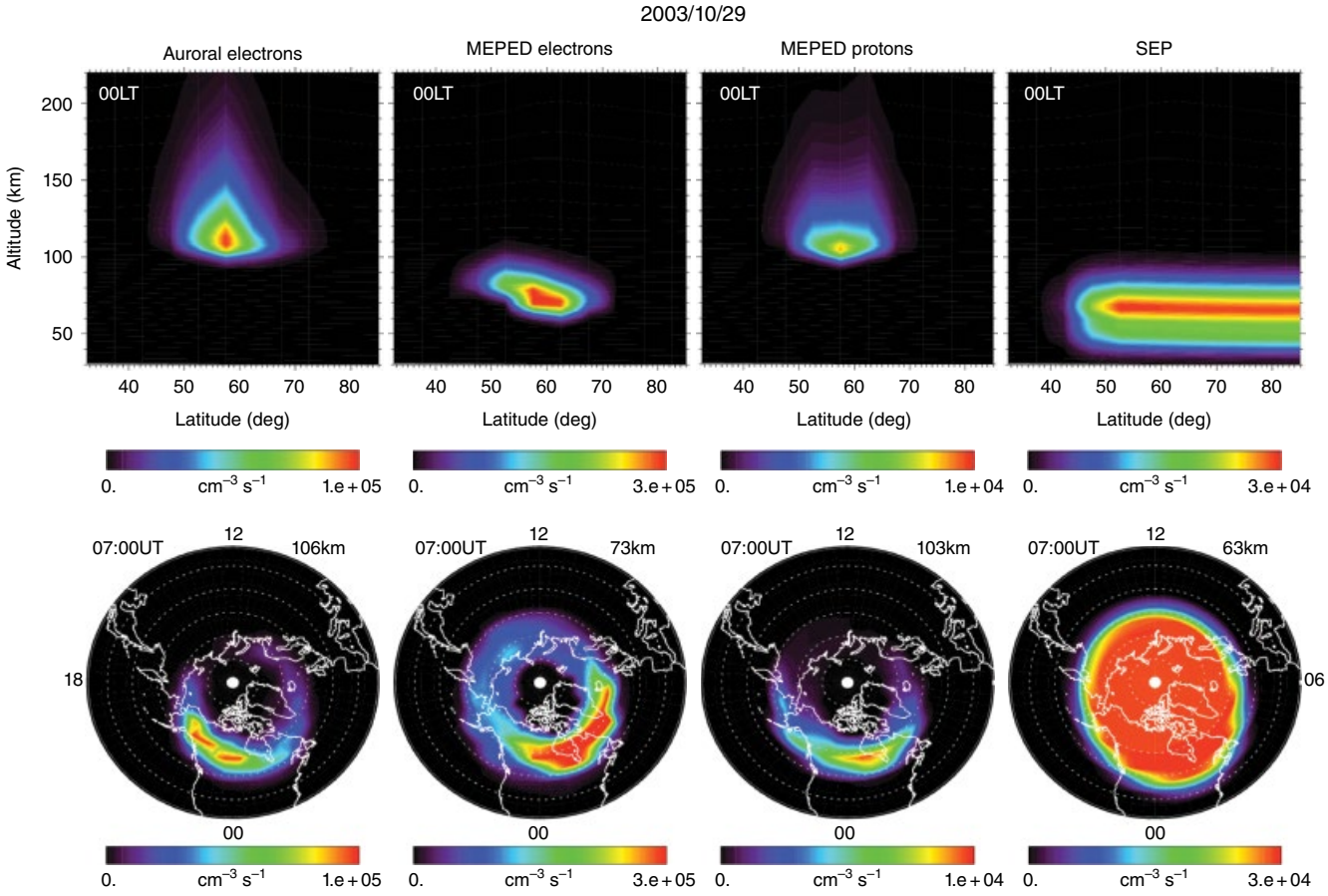

Figure 5.6 (top row) Vertical distributions of the ionization rate by the different energetic particles. (bottom row) Horizontal distributions of ionization rate at the altitude where the corresponding ionization shown in the top row peaks. Note that color scales are different for the different energetic particles.

range but peaks at around 106 km. Ionization by MEPED electrons is mostly between 60 and 100 km, with a peak ionization at around 73 km. Ionization by MEPED protons is concentrated in the altitude range between 95 and 160 km but peaks at around 103 km, very similar to that of the auroral electrons in the same LT sector. SEP's deposition altitude extends from 40 to 80 km, and the corresponding ionization rate peaks at 63 km. The bottom row of Figure 5.6 presents the horizontal distributions at altitudes where the ionization rates by the different energetic particles peak. The horizontal distributions of the ionization rates closely resemble the energy fluxes by the corresponding energetic particles shown in Figure 5.5. SEP precipitation is specified over the polar region above 60° magnetic latitude (MLAT), which appears as an oval shape when plotted in geographic coordinates in Figure 5.6.

Figure 5.7 compares ionospheric conductivity as well as Joule and particle heating rates associated with the different energetic particles. The top row of Figure 5.7 corresponds to auroral precipitating electrons. Pedersen conductivity produced by auroral electrons peaks around 120 km whereas Hall conductivity peaks at 110 km. Joule heating is calculated from $\sigma_p E^2$, where σ_p is Pedersen conductivity and E is electric field. Thus, Joule heating has similar altitude dependence as Pedersen conductivity since the electric field does not change with altitude within the TIMEGCM vertical domain below 800 km. Heating by precipitating particles on ambient neutral gases is calculated by multiplying the corresponding ionization rate by 35 eV per ion pair and by assuming a heating efficiency of 50% [*Rees, et al.*, 1983; *Roble and Ridley* 1987]. The peak Joule heating rate in the auroral zone is about 1.7×10^{-3} mW/m^3, and the peak auroral particle heating is 3×10^{-4} mW/m^3. Therefore, Joule frictional heating is more than 5 times of auroral particle heating for the given UT and LT.

The middle row of Figure 5.7 illustrates the effects of MEPED particles. There are two altitude peaks in ionospheric conductivity and heating, with the high-altitude peak corresponding to auroral electrons and the low-altitude peak to MEPED electrons. As shown

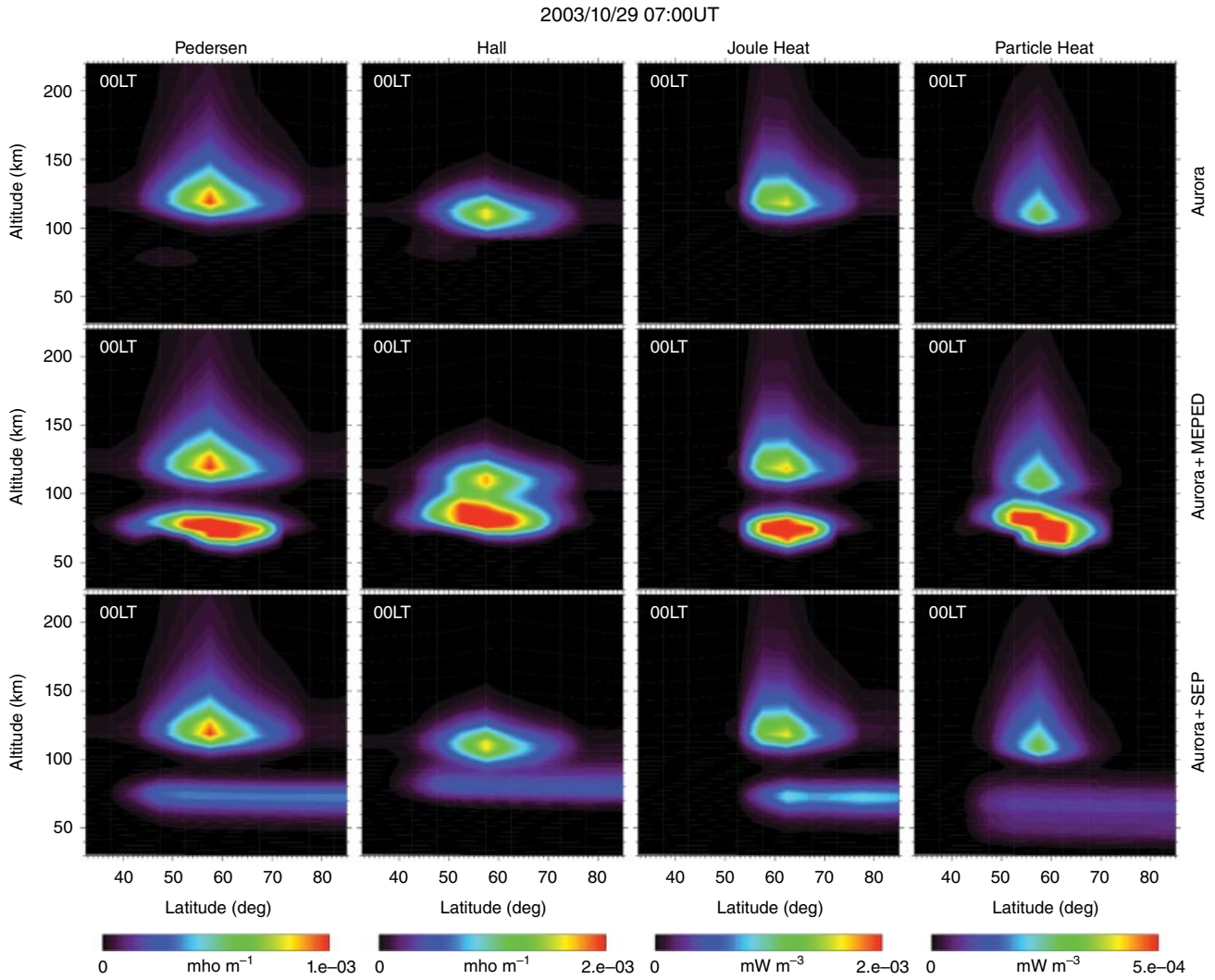

Figure 5.7 (top row) Vertical distributions of Pedersen and Hall conductivity, Joule heating, and particle heating associated with auroral electrons. (middle row) Similar vertical distributions but for auroral plus MEPED particles. (bottom row) Similar vertical distribution but for auroral electrons plus SEPs. All plots correspond to local midnight at 07 UT on 29 October.

in Figure 5.6, the ionization rate by MEPED protons is distributed in the similar altitude range as auroral electrons, but its value is about an order of magnitude smaller so that the contributions by MEPED protons to conductivity and heating are very small compared to auroral electrons at the given UT and LT sector. In contrast, conductivity and heating by MEPED electrons are larger than those of auroral electrons. The MEPED electron-produced Pedersen (Hall) conductivity have a maximum value of 2×10^{-3} mho/m (3×10^{-3} mho/m), which is about twice of the auroral electron-induced conductivity. The MEPED Joule heating has a peak value of 4×10^{-3} mW/m^3 and the MEPED particle heating reaches about 1×10^{-3} mW/m^3, both are more than 3 times of the auroral-induced heating.

The effects of SEPs on the ionosphere are shown in the bottom row of Figure 5.7. The SEP-induced Pedersen conductivity peaks around 70 km and Hall conductivity at 80 km. However, the SEP-induced conductivity is nearly an order of magnitude smaller than the MEPED electron produced conductivity. The resulting Joule heating due to SEPs centers around 70 km, with a peak magnitude of 9×10^{-4} mW/m^3. The SEP particle heating is about 8×10^{-5} mW/m^3, almost negligible compared to the MEPED particle heating for the selected UT and LT. It should be pointed out that the relative contributions to ionospheric conductivity and Joule and particle heating by the various energetic particles may differ at different LT sectors and/or different UT since energetic particle precipitation is highly dynamic.

5.3.3. Effects of Energetic Particles on the Upper Atmosphere

Precipitation of energetic particles not only ionizes the neutral gases but also alters atmospheric composition. To assess the effects of various solar and magnetospheric energetic particles on the upper atmosphere, a series of numerical experiments is carried out by including one particular source of energetic particles at a time.

Figure 5.8 shows the difference plots of zonally averaged electron density N_E, odd hydrogen HO_X ($H+OH+HO_2$), odd nitrogen NO_X ($NO+NO_2$), and ozone O_3 at 62.5°N. The differences are between the TIMEGCM runs with and without the MEPED data while using the same auroral precipitation and no SEPs for the two sets of runs. Enhanced MEPED electron precipitation ionizes neutral gases and increases N_E above 60 km. Once this ionization source is gone, charged particles quickly vanish due to very large recombination rate in the mesosphere and lower thermosphere regions. MEPED electrons also enhance the production of HO_X. Since HO_X has a short lifetime of a few hours [*Solomon et al.*, 1982, 1983], it returns to its pre-storm state shortly after the MEPED precipitation has subsided. NO_X, on the other hand, has a much longer lifetime. Once formed, NO_X can last from days to months, depending on its altitude of formation and its transport after formation [*Solomon et al.*, 1982; *Jackman and Meade*, 1988]. Consequently, enhanced NO_X lasts for many days after the storm while being transported downward in the winter northern hemisphere due to mesospheric circulation. NO_X produced by MEPED electrons catalytically destroys O_3 in the lower mesosphere between 45 and 60 km. The depletion of O_3 persists for as long as NO_X is elevated though the maximum O_3 reduction appears about 5 km

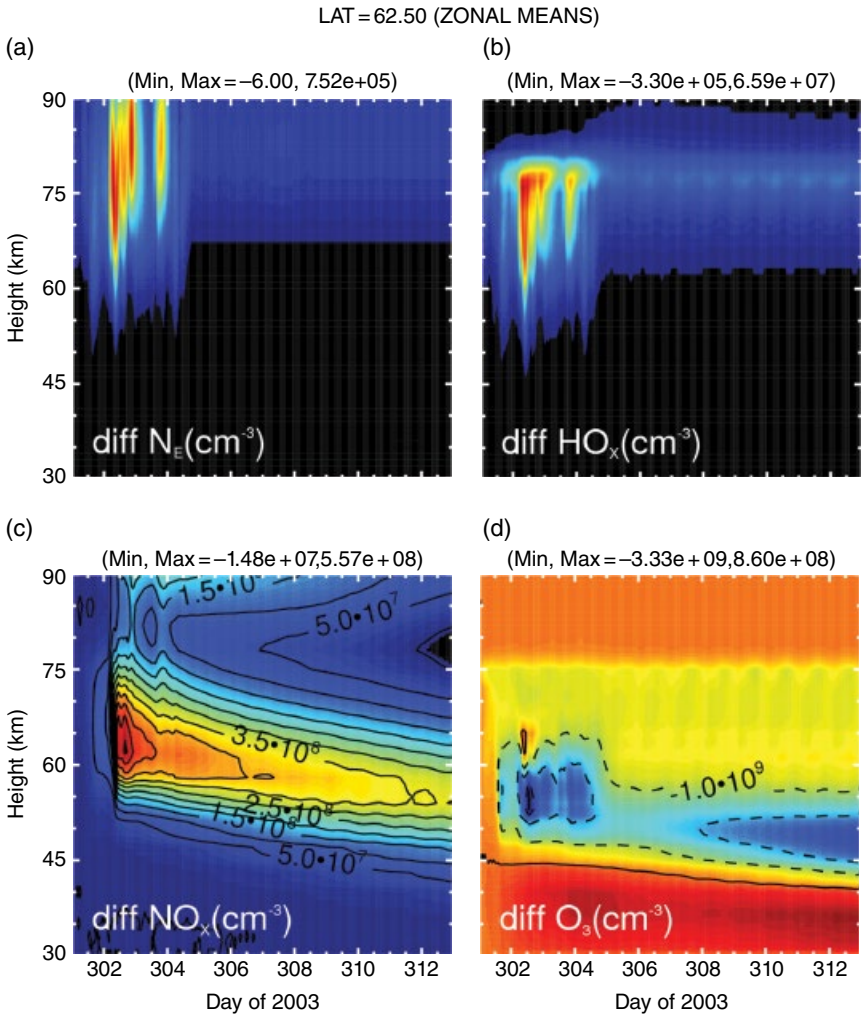

Figure 5.8 Difference plots between simulations with and without MEPED data. (a) Electron density N_E, (b) HO_X ($H+OH+HO_2$), (c) NO_X ($NO+NO_2$), and (d) ozone O_3. The values are zonal averages at 62.5°N, and the maximal and minimal values are given on the top of each panel.

below the maximum NO_X enhancement. This altitude difference is attributed to the difference in scale height between NO_X and O_3 in the mesosphere region.

Compared to MEPED electrons, SEPs penetrate even deeper into the atmosphere. Figure 5.9 shows the difference plots of HO_X, NO_X and O_3 over Eureka in northern Canada and over McMurdo in Antarctic. The differences are between the TIMEGCM runs with and without the GOES-11 SEP data input while auroral precipitation is kept the same and MEPED data are excluded in the two runs. Again, the increase in HO_X by SEPs is short lived due to its short lifetime, and is concentrated between 40 to 60 km in the northern polar region, about 20 km lower than the MEPED-produced HO_X shown in Figure 5.8. The vertical distribution of the SEP-produced HO_X in the southern polar cap extends to a broader altitude range

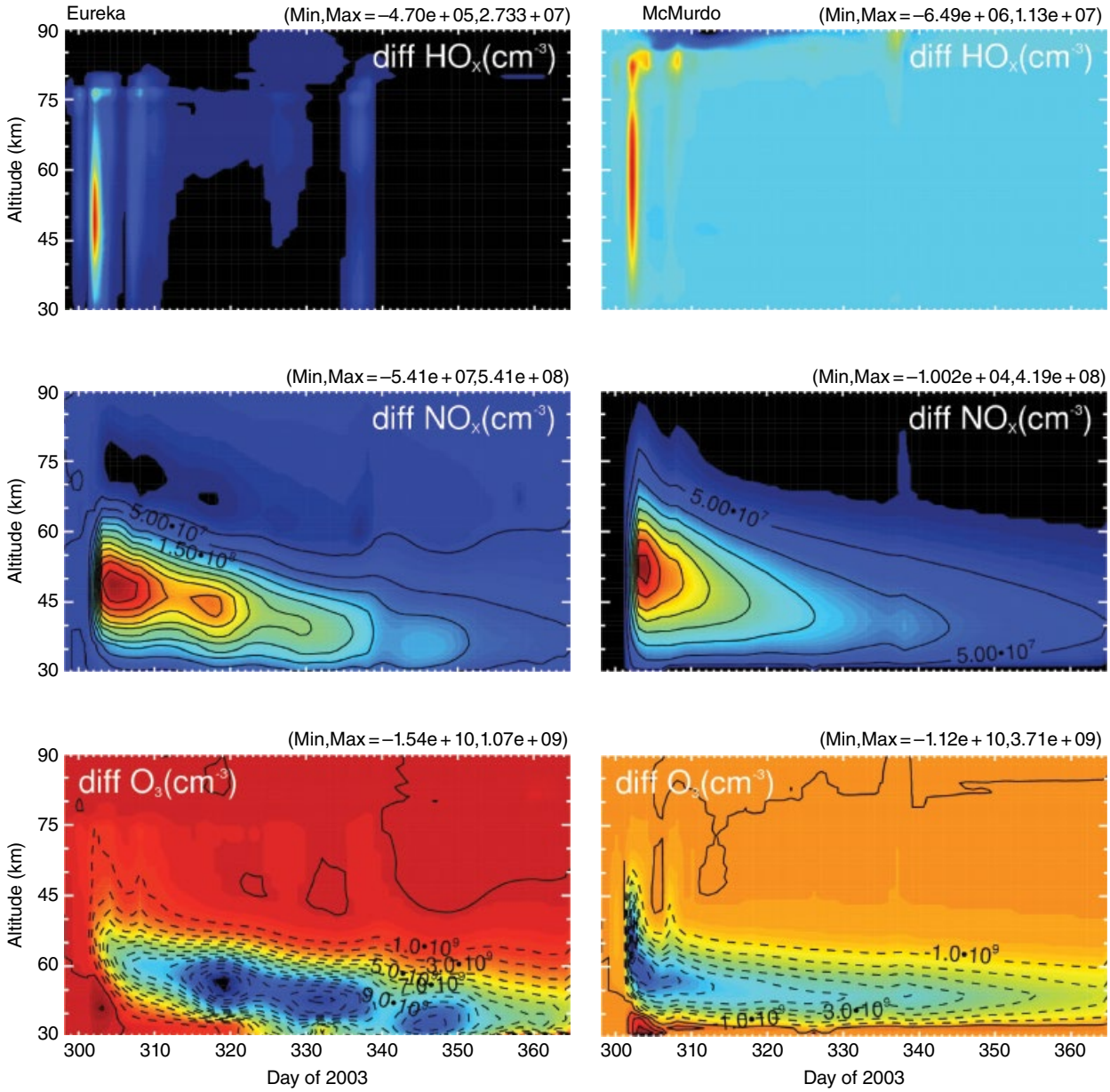

Figure 5.9 Difference plots between simulations including and excluding SEPs. (left column) Difference HO_X, NO_X, and O_3 over Eureka in northern Canada and (right column) difference HO_X, NO_X and O_3 over McMurdo in Antarctic from 25 October to 31 December 2003. The maximal and minimal values are indicated in the upper right corner of each panel.

from 40 km up to 80 km. This hemispheric difference is largely a result of the seasonal difference between the winter northern polar cap and the summer-like southern polar cap. Though the enhanced SEPs last only a few days in duration, their impact on the upper atmosphere can be seen over several months after the storms. Precipitating SEPs cause significant increase in NO_X in the altitude range of 35–70 km initially over both polar regions, which then slowly diminish while being transported downward in the northern hemisphere due to mesospheric circulation. By the end of the year, the remnant of increased NO_X can still be seen in the upper stratosphere around 35–40 km in the northern polar cap. The vertical distribution of the difference NO_X in the southern polar cap lies about 5 km higher than that in the northern polar cap, and the magnitude of the southern NO_X change is also smaller. This hemispheric difference is again a seasonal effect. NO_X is one of the most important consitituents that catalytically destroy ozone. Indeed, significant O_3 reduction is found below 55 km that persists throughout the rest of the year and even into early 2004. The difference O_3 by SEPs also depicts large hemispheric asymmetry, with the O_3 reduction being much larger in the northern polar cap than in the southern polar cap and also the downward transport being more prominent in the north. The hemispheric asymmetry in the NO_X, and O_3 response shown in Figure 5.9 is consistent with observations during the same event. For example, *López-Puertas et al*. [2005] reported that the NO_X increase in the northern polar region was about twice of that in the southern polar region based on observations from the Michelson Interferometer for Passive Atmospheric Sounding (MIPAS) instrument. Large hemispheric difference in O_3 reduction was also observed by a number of independent instruments, including the Scanning Imaging Absorption Spectrometer for Atmospheric Chartography (SCIAMACHY) instrument onboard the Environmental Satellite (Envisat) spacecraft [*Rohen et al*., 2005] and by MIPAS [*López-Puertas et al*., 2005]. These observations revealed a nearly double O_3 reduction in the northern polar cap compared to the southern polar cap.

5.4. SUMMARY AND CONCLUSIONS

We have investigated in this paper the thermospheric and ionospheric responses to the well-known Halloween storm in October 2003. Using realistic specification of high-latitude ionospheric electric field and auroral precipitation derived from AMIE, together with real-time input of various energetic particles, the TIMEGCM simulation revealed some important effects of solar and magnetospheric forcings on the ionosphere and thermosphere. The main findings of the study are summarized below:

1. By combining a comprehensive set of observations from both ground- and space-based instruments using the AMIE procedure, it was found that Joule heating is the most significant form of magnetospheric energy input to the upper atmosphere. Averaged over the 3-day storm interval of 29 to 31 October, the globally integrated Joule heating is 1276 GW, followed by the globally integrated auroral power of 210 GW by precipitating electrons with energies less than 30 keV. The more energetic (>30 keV) magnetospheric precipitating particles are also important source of energy input, with a 3-day average power input of 25 GW by MEPED electrons and 47 GW by MEPED protons. The Halloween storms were accompanied by a large SEP event, which has a peak power of ~160 GW and a 3-day (28 to 30 October 2003) average power of 23 GW when integrated above |60°| magnetic latitude in both northern and southern polar regions.

2. Enhanced Joule heating dissipation drives significant increase of thermospheric temperature, which varies from ~10% (or ~100°K) at 150 km to more than 30% (or 400°K) above 400 km. The excess heat causes thermospheric upwelling such that molecular-rich neutrals are brought to higher altitudes, resulting in substantial increase in mean mass density and the N_2/O ratio during the storms. The percent change in mass density decreases as altitude decreases, varying from over 150% at 400 km to ~30% at 150 km. The percent increase in the N_2/O is double of the mass density change, and has a similar downward trend in terms of altitude dependence. No measurable change is found around 100 km, implying that the effects of Joule heating diminish in the lower thermosphere where neutral density is so large compared to ion density that energy transfer between ions and neutrals through frictional collision becomes ineffective.

3. Though enhanced Joule heating raises the *F* layer to higher altitudes, change in hmF_2 displays strong modulations with a period of five to six hours, which is similar to the inter-hemisphere travel time of TADs. The large-scale NmF_2 exhibits an overall reduction that is proportional to the reduction of the O/N_2 ratio during the storms, indicating that composition change is the dominant factor of negative storm phases. Smaller-scale NmF_2 variations, on the other hand, are closely related to the hmF_2 variations with a time-shift of one and one-half hours.

4. Energetic particle precipitation can have significant influence on the ionosphere. Because of difference in mean energy, the different energetic particles are dissipated at various altitudes affecting the *E* and *D* regions in terms of conductivity and heating. Ionization by auroral electrons with a mean energy of 4 to 5 keV peaks around 106 km, and ionization by MEPED protons of 70 to 80 keV peaks at 103 km. MEPED electrons of 80 to 90 keV are mostly deposited between 60 and 100 km, with

ionization peaking at 73 km. SEPs with energies of a few MeV penetrate as low as 40 km, and the resulting ionization rate peaks around 63 km. The local *D* region conductivity and heating by MEPED electrons are about twice as large as the local *E* region conductivity and heating by auroral electrons. By comparison, the effects of SEPs on the ionosphere are an order of magnitude smaller than those by auroral and MEPED electrons for the given UT and LT.

5. Both MEPED electrons and SEPs have profound impacts on the upper atmosphere during the Halloween storms. Our simulations show dramatic increase in NO_X, which in turn cause catalytically destruction of O_3. The O_3 reduction associated with MEPED electrons is confined in the lower mesosphere between 45 and 60 km in the northern hemisphere, whereas the O_3 reduction associated with SEPs is found below 55 km. Because of the seasonal effect, the impact of energetic particles on NO_X and O_3 is more pronounced in the northern hemisphere than in the southern hemisphere. This hemispheric asymmetry was evident in several satellite observations.

ACKNOWLEDGMENTS

I wish to acknowledge the International Real-time Magnetic Observatory Network for the INTERMAGNET magnetometer network, the Geophysical Institute of the University of Alaska for the Alaska magnetometer stations, the Solar-Terrestrial Environment Laboratory of the Nagoya University for the 210 magnetic meridian chain, the Finnish Meteorological Institute for the IMAGE chain, the Canadian Space Agency for CARISMA magnetometer network, and the Space Plasma Environment and Radio Science (SPEARS) in the Department of Communication Systems at the Lancaster University for the SAMNET magnetometer chain, and the Danish Meteorological Institute for the Greenland magnetometer stations. J. Posch at Augsburg College, A. Weather at Siena College, and O. Troshichev at the Arctic and Antarctic Research Institute in Russia provided additional ground magnetometer data used in the study. The SuperDARN radar data were provided by J. M. Ruohoniemi of the Virginia Tech SuperDARN group that is supported by the National Science Foundation (NSF) under awards AGS-0946900 and AGS-0838219. The DMSP particle data were prepared by Fred Rich at Air Force Research Laboratory, and the DMSP ion drift data were provided online by the University of Texas at Dallas at http://cindispace.utdallas.edu/DMSP/dmsp_data_at_utdallas.html. The POES data were processed and provided by Dr. Dave Evans at NOAA Space Weather Prediction Center. The ACE solar wind and IMF key parameters were obtained from the NASA CDAW website (http://cdaweb.gsfc.nasa.gov).

This work was supported in part by the Heliophysics Guest Investigators program under NASA grant NNH09AK621, by the Living With a Star Program under NASA grant NNX14AE08G, and by the U.S. Participating Investigator (USPI) Program under NASA Grant NNX12AD26G. NCAR is sponsored by the NSF. I would like to acknowledge high performance computing support from Yellowstone (ark:/85065/d7wd3xhc) provided by NCAR's Computational and Information Systems Laboratory and sponsored by the NSF. TIMEGCM and AMIE results used in this study are archived on NCAR's High Performance Storage System, and are available on request.

REFERENCES

Ahn, B.-H., R. M. Robinson, Y. Kamide, and S. I. Akasofu (1983), Electric conductivities, electric fields and auroral particle energy injection rate in the auroral ionosphere and their empirical relations to the horizontal magnetic disturbances, *Planet. Space Sci.*, *31*, 641–653.

Asikainen, T., and K. Mursula (2013), Correcting the NOAA/MEPED energetic electron fluxes for detector efficiency and proton contamination, *J. Geophys. Res. Space Physics*, *118* 6500–6510, doi:10.1002/jgra.50584.

Burns, A. G., T. L. Killeen, and R. G. Roble (1991), A theoretical study of thermospheric composition perturbations during an impulsive geomagnetic storm, *J. Geophys. Res.*, *96*(A8), 14153–14167, doi:10.1029/91JA00678.

Burns, A. G., T. L. Killeen, G. R. Carignan, and R. G. Roble (1995), Large enhancements in the O/N_2 ratio in the evening sector of the winter hemisphere during geomagnetic storms, *J. Geophys. Res.*, *100*(A8), 14661–14671, doi:10.1029/94JA03235.

Chamberlin, P. C., T. N. Woods, and F. G. Eparvier (2007), Flare irradiance spectral model (FISM): Daily component algorithms and results, *Space Weather*, *5*, S07005, doi:10.1029/2007SW000316.

Chamberlin, P. C., T. N. Woods, and F. G. Eparvier (2008), Flare irradiance spectral model (FISM): Flare component algorithms and results, *Space Weather*, *6*, S05001, doi:10.1029/2007SW000372.

Codrescu, M. V., T. J. Fuller-Rowell, R. G. Roble, and D. S. Evans (1997), Medium energy particle precipitation influences on the mesosphere and lower thermosphere, *J. Geophys. Res.*, *102*(A9), 19977–19987, *doi:*10.1029/97JA01728.

Evans, D. S., and M. S. Greer (2002), Polar Orbiting Environmental Satellite Space Environment Monitor, 2: Instrument Descriptions and Archive Data Documentation, *NOAA Technical Memorandum 1.2*, Space Environment Center, Boulder, Colorado, http://satdat.ngdc.noaa.gov/sem/poes/docs/sem2_docs/2003/SEM2v1.2.pdf.

Fang, X., A. J. Ridley, M. W. Liemohn, J. U. Kozyra, and D. S. Evans (2007), Global 30–240 keV proton precipitation in the 17–18 April 2002 geomagnetic storms: 3. Impact on the ionosphere and thermosphere, *J. Geophys. Res.*, *112*, A07310, doi:10.1029/2006JA012144.

Fuller-Rowell, T. J., and D. S. Evans (1987), Height-integrated Pedersen and Hall conductivity patterns inferred from the TIROS-NOAA satellite data, *J. Geophys. Res.*, *92*(A7), 7606–7618, doi:10.1029/JA092iA07p07606.

Fuller-Rowell, T. J., R. J. Moffett, S. Quegan, D. Rees, M. V. Codrescu, and G. H. Millward (1996), *A coupled thermosphere-ionosphere Model (CTIM), in STEP Handbook on Ionospheric Models*, Ed. R. W. Schunk, Utah University, Logan, UT.

Gopalswamy, N., et al. (2005), Coronal mass ejections and other extreme characteristics of the 2003 October–November solar eruptions, *J. Geophys. Res.*, *110*, A09S15, doi:10.1029/2004JA010958.

Hagan, M. E., and J. M. Forbes (2002), Migrating and nonmigrating diurnal tides in the middle and upper atmosphere excited by tropospheric latent heat release, *J. Geophys. Res., 107*(D24), 4754, doi:10.1029/2001JD001236.

Hagan, M. E., and J. M. Forbes (2003), Migrating and nonmigrating semidiurnal tides in the upper atmosphere excited by tropospheric latent heat release, *J. Geophys. Res.*, *108*, 1062, doi:10.1029/2002JA009466.

Jackman, C. H., and P. E. Meade (1988), Effect of solar proton events in 1978 and 1979 on the odd nitrogen abundance in the middle atmosphere, *J. Geophys. Res.*, *93*(D6), 7084–7090, doi:10.1029/JD093iD06p07084.

Jackman, C. H., M. T. DeLand, G. J. Labow, E. L. Fleming, D. K. Weisenstein, M. K. W. Ko, M. Sinnhuber, and J. M. Russell (2005), Neutral atmospheric influences of the solar proton events in October–November 2003, *J. Geophys. Res.*, *110*, A09S27, doi:10.1029/2004JA010888.

Jackman, C. H., D. R. Marsh, F. M. Vitt, R. R. Garcia, E. L. Fleming, G. J. Labow, C. E. Randall, M. López-Puertas, T. von Clarmann, and G. P. Stiller (2008), Short- and medium-term atmospheric constituent effects of very large solar proton events, *Atmos. Chem. Phys.*, *8*, 765–785.

Jackman, C. H., D. R. Marsh, F. M. Vitt, R. R. Garcia, C. E. Randall, E. L. Fleming, *and* S. M. Frith (2009), Long-term middle atmospheric influence of very large solar proton events, *J. Geophys. Res.*, *114, D11304, doi:*10.1029/2008JD011415.

Lam, M. M., R. B. Horne, N. P. Meredith, S. A. Glauert, T. Moffat-Griffin, and J. C. Green (2010), Origin of energetic electron precipitation >30 keV into the atmosphere, *J. Geophys. Res.*, *115, A00F08, doi:*10.1029/2009JA014619.

López-Puertas, M., B. Funke, S. Gil-López, T. von Clarmann, G. P. Stiller, M. Höpfner, S. Kellmann, H. Fischer, and C. H. Jackman (2005), Observation of NO_X enhancement and ozone depletion in the Northern and Southern Hemispheres after the October–November 2003 solar proton events, *J. Geophys. Res.*, *110*, A09S43, doi:10.1029/2005JA011050.

Lu, G., *et al.* (1998), Global energy deposition during the January 1997 magnetic cloud event, *J. Geophys. Res.*, *103*(A6), 11685–11694, doi:10.1029/98JA00897.

Lu, G., A. D. Richmond, J. M. Ruohoniemi, R. A. Greenwald, M. Hairston, F. J. Rich, and D. S. Evans (2001), An investigation of the influence of data and model inputs on assimilative mapping of ionospheric electrodynamics, *J. Geophys. Res., 106*, 417–433, doi:10.1029/2000JA000606.

Lummerzheim, D. (1992), Comparison of energy dissipation functions for high energy auroral electron and proton precipitation, Rep. *UAG-R-318, Geophys. Inst.*, University of Alaska-Fairbanks, Fairbanks.

Meredith, N. P., R. B. Horne, M. M. Lam, M. H. Denton, J. E. Borovsky, and J. C. Green (2011), Energetic electron precipitation during high-speed solar wind stream driven storms, *J. Geophys. Res.*, *116*, A05223, doi:10.1029/2010JA016293.

Newell, P. T., and C.-I. Meng (1994), Ionospheric projections of magnetospheric regions under low and high solar wind pressure conditions, *J. Geophys. Res.*, *99*(A1), 273–286, doi:10.1029/93JA02273.

Prölss, G. W. (1993), On explaining the local time variation of ionospheric storm effects, *Ann. Geophysicae*, *11*, 1–9.

Qian, L., A. G. Burns, P. C. Chamberlin, and S. C. Solomon (2010), Flare location on the solar disk: Modeling the thermosphere and ionosphere response, *J. Geophys. Res.*, *115*, A09311, doi:10.1029/2009JA015225.

Randall, C. E., V. L. Harvey, C. S. Singleton, S. M. Bailey, P. F. Bernath, M. Codrescu, H. Nakajima, and J. M. Russell III (2007), Energetic particle precipitation effects on the Southern Hemisphere stratosphere in 1992–2005, *J. Geophys. Res.*, *112, D08308,* doi:10.1029/2006JD007696.

Rees, M. H., B. A. Emery, R. G. Roble, and K. Stamnes (1983), Neutral and ion gas heating by auroral electron precipitation, *J. Geophys. Res.*, *88*(A8), 6289–6300, doi:10.1029/JA088iA08p06289.

Reid, G. C., S. Solomon, and R. R. Garcia (1991), Response of the middle atmosphere to the solar proton events of August–December 1989, *Geophys. Res. Lett.*, *18*, 1019–1022.

Rich, F. J., M. S. Gussenhoven, and M. E. Greenspan (1987), Using simultaneous particle and field observations on a low altitude satellite to estimate Joule heat energy flow into the high latitude ionosphere, *Ann. Geophys.*, *5A*, 527–534.

Richardson, I. G., and H. V. Cane (2010), Near-Earth Interplanetary Coronal Mass Ejections During Solar Cycle 23 (1996–2009): Catalog and Summary of Properties, *Solar Phys.*, *264*, doi:/10.1007/s11207-010-9568-6.

Richmond, A. D., and Y. Kamide (1988), Mapping electrodynamic features of the high-latitude ionosphere from localized observations: Technique, *J. Geophys. Res.*, *93*(A6), 5741–5759, doi:10.1029/JA093iA06p05741.

Ridley, A. J., Y. Deng, and G Tóth (2006), The global ionosphere-thermosphere model, *Journal of Atmospheric and Solar-Terrestrial Physics*, *68*, 839–864, doi:10.1016/j.jasp.2006.01.008.

Rishbeth, H. (1989), *F*-region storms and thermospheric circulation, in *Electromagneti Coupling in the Polar Cleft and Caps*, edited by P. E. Sandholt and A. England, pp. 393–406, Kluwer Acad. Norwell, MA.

Roble, R. G., and E. C. Ridley (1987), An auroral model for the NCAR thermospheric general circulation model (TGCM), *Ann. Geophys.*, *5A*(6), 369–382.

Roble, R. G., and E. C. Ridley (1994), A thermosphere-ionosphere-mesosphere-electrodynamics general circulation model (time-GCM): Equinox solar cycle minimum simulations (30–500 km), *Geophys. Res. Lett.*, *21*, doi:10.1029/93GL03391.

Roble, R. G. (1995), Energetics of the mesosphere and thermosphere, in *The Upper Mesosphere and Lower Thermosphere: A review of Experiment and Theory, Geophys. Monogr. Ser., 87*, pp. 1–21, AGU, Washington D.C.

Rodger, C. J., M. A. Clilverd, J. C. Green, and M. M. Lam (2010), Use of POES SEM-2 observations to examine radiation belt dynamics and energetic electron precipitation into the atmosphere, *J. Geophys. Res.*, *115*, A04202, doi:10.1029/2008JA014023.

Rohen, G., et al. (2005), Ozone depletion during the solar proton events of October/November 2003 as seen by SCIAMACHY, *J. Geophys. Res.*, *110*, A09S39, doi:10.1029/2004JA010984.

Seppälä, A., M. A. Clilverd, and C. J. Rodger (2007), NO_X enhancements in the middle atmosphere during 2003–2004 polar winter: Relative significance of solar proton events and the aurora as a source, *J. Geophys. Res.*, *112*, D23303, doi:10.1029/2006JD008326.

Solomon, S., P.J. Grutze, and R.G. Roble (1982), Photochemical coupling between the thermosphere and the lower atmosphere I. Odd nitrogen from 50 to 120 km, J. *Geophys. Res.*, *87*, 7206.

Solomon, S., G. C. Reid, D. W. Rusch, R. J. Thomas (1983), Mesospheric ozone depletion during the Solar Proton Event of July 13, 1982 Part II. Comparison between theory and measurements. *Geophysical Research Letters*, *10*: 257–260. doi: 10.1029/GL010i004p00257.

Woods, T. N., F. G. Eparvier, S. M. Bailey, P. C. Chamberlain, J. Lean, G. J. Rottman, S. C. Solomon, W. K. Tobiska, and D. Woodraska (2005), The Solar EUV Experiment (SEE): Mission overview and first results, *J. Geophys. Res.*, *110*, A01312, doi:10.1029/2004JA010765.

6

The Impact of O^+ on Magnetotail Dynamics

Lynn M. Kistler

Video of Yosemite Talk, URL: http://dx.doi.org/10.15142/T3D303

ABSTRACT

The O^+ abundance in the magnetotail is significantly enhanced during solar and geomagnetic active times. Adding O^+ to the normally H^+ dominated plasma significantly changes the plasma mass density, and O^+ has a larger gyroradius than H^+ at the same energy or velocity. It has been suggested that these differences will have an effect on the magnetotail dynamics. In this paper, we summarize the observational results on the impacts that increased heavy ions may have in the magnetotail region on current sheet stability, reconnection rate, and current sheet and reconnection region structure. The observations indicate that O^+ does not increase the instability of the current sheet to reconnection. The effect on the local reconnection rate has not been determined definitively, but there is no large-scale evidence that it decreases the reconnection rate. The O^+ does add a third scale, larger than the electron and proton scales, to the current sheet and the reconnection region. Theoretical research into how this third scale changes magnetotail dynamics is only just beginning.

6.1. INTRODUCTION

The contribution of heavy ions, particularly O^+, to the plasma sheet is highly variable [*Young et al.*, 1982; *Mouikis et al.*, 2010]. These studies show that statistically, while the H^+ plasma sheet density is relatively constant, the O^+, and therefore the O^+/H^+ ratio, both increase with greater solar extreme ultraviolet (EUV) input and geomagnetic activity. There are even times when O^+ is the dominant ion [e.g., *Kistler et al.*, 2005]. However, although we know that O^+ can be a significant fraction of the plasma mass and density, it is not clear what impact the high O^+ has on the magnetosphere.

There are a number of differences between O^+ and H^+ that may be important to magnetospheric dynamics. First, because the mass is 16 times higher, additional O^+ increases the mass density. As noted by *Lennartsson et al.*, [1993], a 50%/50% admixture of O^+ and H^+ ions, which has been observed in the storm-time plasma sheet, will have an order of magnitude higher mass density than a pure H^+ plasma. If the O^+ behaves as a fluid, moving with the H^+, the higher mass density will decrease the Alfvén speed. This would have the effect of decreasing the reconnection rate [*Shay and Swisdak*, 2004].

However, this is not the only difference. The O^+ gyroradius is 4 times larger than H^+ at the same energy, or 16 times larger at the same velocity. Thus, the regions of the plasma sheet in which the ion no longer satisfies the frozen in condition, and/or shows the effects of its finite gyroradius, are larger for O^+. Because of this, the motion of O^+ may be significantly different from H^+ in the plasma sheet, leading to effects different from those predicted just by assuming a higher mass density.

Finally, the transport of O^+ to the plasma sheet will be different from H^+. The transport from the cusp outflow

Department of Physics and Space Science Center, University of New Hampshire, Durham, NH, USA

Magnetosphere-Ionosphere Coupling in the Solar System, Geophysical Monograph 222, First Edition.
Edited by Charles R. Chappell, Robert W. Schunk, Peter M. Banks, James L. Burch, and Richard M. Thorne.

region through the lobe is governed by the "velocity filter effect" [*Horwitz and Lockwood*, 1985; *Horwitz*, 1986]. All ions convect over the polar cap and into the lobe with the same ExB velocity perpendicular to the field. However, their velocity parallel to the field increases with energy. Thus, in the time that it takes the field line to convect from the dayside into the tail, higher velocity ions go further down the tail than lower velocity ions. Because this process filters by velocity, it implies that H^+ and O^+ at the same position in the lobe will have energies different by a factor of 16 and gyroradii that are different by a factor of 16. Thus, the O^+ that enters the plasmasheet at a particular location will be much more likely to show kinetic effects than the H^+. Ion outflow from the nightside aurora, which has direct access to the plasmasheet, will behave similarly. The O^+ outflow at the same energy as H^+ will move more slowly up the field line, and, since the plasma sheet convection is earthward, it will end up closer to the earth than the H^+ when it reaches the neutral sheet. The H^+ outflow observed at the same equatorial location as the O^+ outflow will be much lower in energy.

How these differences might impact magnetospheric dynamics was first addressed using the ion composition instruments on the International Sun-Earth Explorer (ISEE) and Active Magnetospheric Particle Tracer Explorer (AMPTE) missions. In more recent years, the measurements from Cluster and the long-term Geotail measurements have allowed further progress to be made. In the following section, we discuss what the observations have determined about the impact of O^+ in the nightside magnetosphere, addressing the following questions:

1. Does O^+ affect the triggering of reconnection in the magnetotail?
2. Does O^+ impact the reconnection rate?
3. Does O^+ impact the current sheet and reconnection region structure?

6.2. DOES O^+ AFFECT THE TRIGGERING OF RECONNECTION

The most common effect suggested for O^+ is that it decreases the stability of the plasma sheet. *Baker et al.* [1982] proposed that the linear ion tearing instability would be enhanced by O^+ in the plasma sheet. This instability is triggered when the ions become unmagnetized in the thin plasma sheet. Because the growth rate is proportional to the ion gyroradius, heavier ions could increase the instability.

Lakhina [1995], *Lakhina and Tsurutani* [1997], and *Lakhina* [2001] have studied the effect of cold and hot O^+ beams on the plasma sheet instability. They find that these beams could give rise to helicon waves in the plasma sheet. The localized minima in Bz,which result from the fluctuations in this mode, are likely to be sites for the excitation of the tearing mode instability. In addition, the low frequency turbulence could scatter electrons and further enhance the growth of the instability. Thus, these models would predict that the substorms would be most likely to trigger during times when O^+ beams are present.

Other researchers have concentrated on the effect that O^+ may have in the near-earth plasma sheet. *Rothwell et al.* [1988, 1991] have used a two-circuit model to describe the auroral current structure. Because the magnetospheric current in this model is proportional to the mass density, a higher mass density shifts the conditions that are favorable to breakup toward L-shells as low as 5–6 Re. *Cladis and Francis* [1992] modeled the trajectories of cusp ions to the near-earth plasma sheet and calculated the pressure from the resulting distribution. They concluded that the O^+ pressure in that region could build up to high enough values to trigger a velocity shear instability.

Magnetohydrodynamic (MHD) modeling has shown some support for the idea that increased O^+ will impact the triggering of reconnection. *Wiltberger et al.* [2010], using a multi-fluid model, found that in the model that included O^+ outflow, a second substorm occurred that was not seen in the no-outflow case. *Brambles et al.* [2011] proposed that a feedback mechanism may be responsible for the occurrence of strong periodic substorms, called sawtooth events. They show, using a multi-fluid model, that the outflowing O^+ fills the plasma sheet, which distended the tail into a highly stretched configuration. When the pressure can no longer be contained, a substorm occurs, a plasmoid is ejected, and the field dipolarizes. The energy release from this substorm drives more outflow, which starts the cycle over again. *Yu and Ridley* [2013] examined whether the source of the O^+ makes a difference. They found that O^+ from the cusp that enters through tail reconnection does make the tail more unstable. However, in contrast to the *Brambles et al.* [2011] result, they found that O^+ from the nightside aurora that enters directly into the plasma sheet earthward of the reconnection line has the opposite effect, suppressing substorm onset.

Since the suggestion of *Baker et al.* [1982], researchers have looked to confirm or refute that O^+ plays a substorm triggering role using three observational methods. The first is to look at timing: Is there any indication that O^+ increases prior to substorm onset, indicating that it is a trigger? The second is to look for evidence that more substorms are triggered when and where there is more O^+. The final method is to look at differences in the loading during the growth phase of a substorm. If the tail is more unstable, onset should occur with less loading. In the following, we go through the results from these three methods.

6.2.1. Timing

Daglis et al. [1990] used AMPTE/Charge Composition Explorer (CCE) data to observe the change in 1–300 kiloelectron-volt (keV) O^+ energy density in the near-earth (~8 Re) plasma sheet during one substorm. They found that during the growth phase, the fractional energy density increase was largest for the O^+, with the energy density increasing to 5 times its quiet-time density. After substorm onset, the O^+ increases by another factor of 5. However, although O^+ showed the largest increase, the absolute contribution of O^+ to the pressure was only ~15–25% of the H^+ contribution. Thus, if there was a significant effect due to O^+, it was not due to a large pressure. They suggest that O^+ contributes to the curvature current in this region, accelerating the tail stretching during the growth phase. This result was only shown for one event.

Lennartsson et al. [1993] addressed this question statistically using 0.1–17 keV ion composition data from ISEE 3 (inside 23 Re) and AMPTE/High Performance Capillary Electrophoresis (HPCE) (at ~8 Re). They noted that there are many observations of substorms where O^+ does not increase until after substorm onset. To test whether a high O^+/H^+ ratio ever functions as a trigger, they identified time periods where the O^+/H^+ ratio increased from <20% to >30%, and checked whether these increases were associated with a following or simultaneous increase in auroral electrojet (AE). They found no examples where the hourly AE increased in the hour succeeding the O^+/H^+ increase. They also performed statistical correlations between the hour averaged AE and average ion mass both before the AE measurement and after. They found that the best correlation was between AE and the ion mass two hours later, with essentially no correlation with the ion mass before. Thus, they concluded that there was no evidence that O^+ played an important role in triggering substorms. *Daglis and Sarris* [1998] commented on the Lennartson paper, arguing that the long-time averages used in the Lennartson study would mask the effects of O^+, if they were from short-lived localized enhancements. Additionally, it is possible that the increase occurs at energies below or above the energy range of the ISEE instrument.

Kistler et al. [2006] addressed the timing question with Cluster/Composition and Distribution Function (CODIF) data in the mid-tail region (15–19 Re) using a superposed epoch analysis. They divided the dataset into non-storm and storm-time substorms, and determined how the composition changes relative to substorm onset time. They examined the changes in density, pressure (energy density), and temperature. They found that while the O^+/H^+ ratio was about a factor of 5 higher during storm times than non-storm times, there was no systematic change in the O^+/H^+ ratio during the growth phase of the substorms during either activity level. The densities and pressure of both H^+ and O^+ did increase during the growth phase. However, they both increased by the same factor. This is most likely due to compression of the tail during the growth phase, in order to maintain pressure balance, not due to an increased source population with the same relative composition. Thus, there was no indication from timing that additional O^+ was triggering the events. *Liao et al.* [2014] further divided the substorm events into sawtooth events and isolated substorms. As discussed above, it has been proposed that sawtooth events specifically are driven by an increased O^+ input during the growth phase. Figure 6.1 shows the results of the superposed epoch analysis where the data are divided into three different activity levels: non-storm times, storm main phase, and storm recovery phase. The green lines indicate sawtooth events, and the red lines are isolated substorms. They found that the O^+/H^+ ratio does increase during the growth phase of sawtooth events. However, the difference between sawtooth events and isolated substorms is greater during non-storm (Figure 6.1a) and recovery-phase events (Figure 6.1c) than during storm main-phase events (Figure 6.1b), where the increase is relatively small. During isolated substorms, the ratio stays the same, or even decreases, consistent with the *Kistler et al.* [2006] results. Thus, there is some indication that during sawtooth events, O^+ may play a role, but not during other substorms.

To summarize, there is some indication that in the near-earth region, there is an increase in O^+ during the growth phase prior to onset, but this is based on one event. A larger study in this region would be welcome. In the mid-tail region, where reconnection onset is thought to occur, the vast majority of substorms show no increase in O^+ during the growth phase. Only sawtooth events, which occur predominantly during storms, show an increase of O^+ during the growth phase.

6.2.2. Are There More Substorm Onsets Where There Is More O^+?

A second way to address the question is to determine if more substorms occur when more O^+ is present. The original [*Baker et al.*, 1982] paper suggested that the asymmetries observed in substorm onset location, i.e., that onset occurs preferentially on the duskside, may be related to an asymmetry in the O^+ in the tail. This suggestion was based on the best observations of the time, i.e., observations by *Sharp et al.* [1981], that showed a clear duskside preference for the occurrence of "ion streams," cold field-aligned beams of ions, in the plasma sheet. However, *Sharp et al.* [1981] were only considering this limited population, not the overall O^+ composition of the plasma sheet. Subsequent statistical studies, including

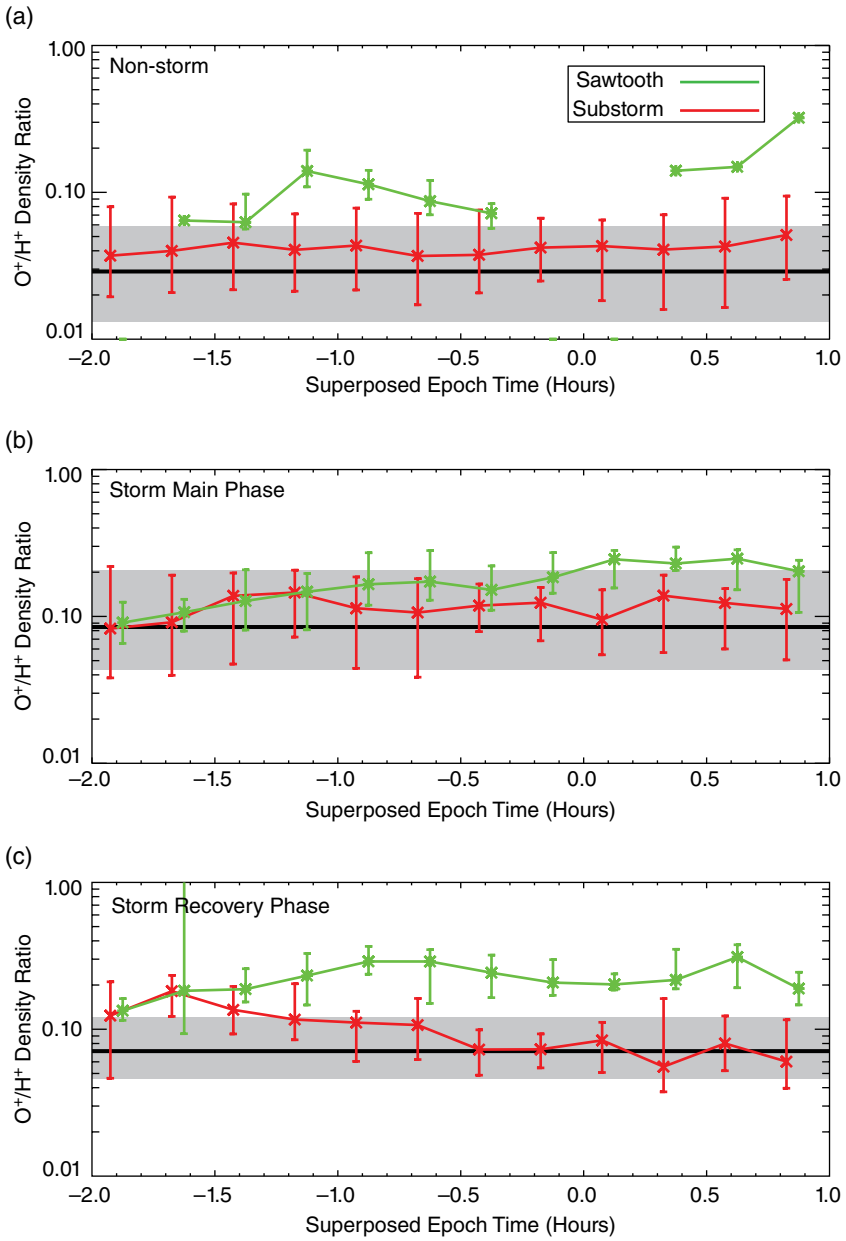

Figure 6.1 Superposed epoch analysis of the O^+/H^+ density ratio as a function of time relative to substorm onset time for three different activity levels: (a) non-storm times, (b) storm main phase, and (c) storm recovery phase. [From *Liao et al.*, 2014]

Lennartsson and Shelley [1986], using ISEE data, and *Mouikis et al.* [2010], using Cluster data, showed no dawn-dusk asymmetry for the O^+/H^+ ratio in the mid-tail plasma sheet. *Maggiolo and Kistler* [2014] confirmed the *Mouikis et al.* [2010] result and also found no dawn-dusk asymmetry in the O^+/H^+ ratio at 7–8 Re. Thus, the reason for the overall asymmetry in substorm onset location must have some other explanation.

Baker et al. [1985] looked for evidence that the O^+ made the plasmasheet more unstable to reconnection in a case study, the Coordinated Data Analysis Workshop (CDAW) 6 event. This event consisted of two substorms. The first one was localized in the 0200–0300 LT sector and occurred when the plasma sheet was predominantly composed of H^+ and He^{++}. This first substorm resulted in significant O^+ being added to the plasma sheet. The second substorm occurred much farther westward than the original substorm. They interpreted this as an example where the increased O^+ abundance in the plasma sheet may have affected the location of the substorm onset. Thus, they

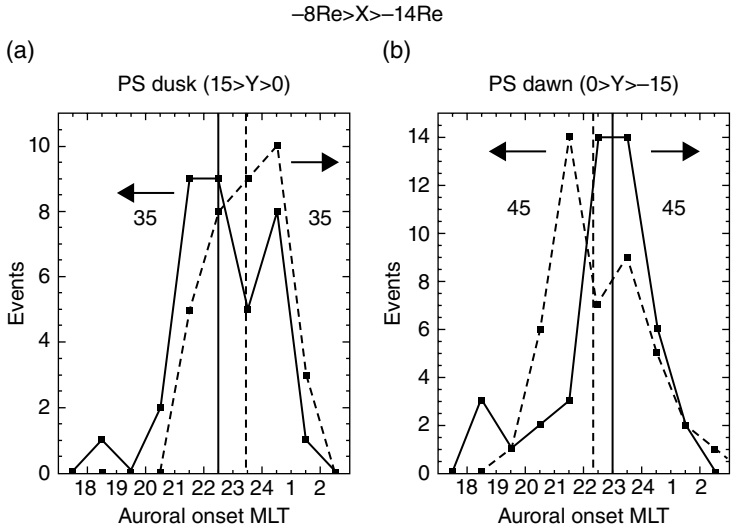

Figure 6.2 Distribution of substorm onset MLT for time periods when the O^+/H^+ ratio is high (solid) or low (dashed) on the (a) duskside and on the (b) dawnside in the -8Re>X>-14 Re region. [From *Ono et al.,* 2010]

proposed a feedback mechanism in which one substorm creates more outflow, which then makes the tail more unstable in some region, leading to a second substorm.

Ono et al. [2010] used the long-term Geotail/Supra-Thermal Ion Composition Spectrometer (STICS) data set to determine if substorm onset was more likely to occur in a particular local time region if the O^+/H^+ ratio were high in that region. They calculated the O^+/H^+ density ratio before each substorm onset. Then, for the set of pre-onset Geotail measurements on the duskside, they sorted the data set by O^+/H^+ ratio and plotted the substorm onset location for the top and bottom halves of the O^+/H^+ ratio distribution. The results for the near-earth (-8Re>X>-14 Re) region are shown in Figure 6.2. They found that the median onset location for the duskside high O^+/H^+ dataset was an hour further duskward than the low O^+/H^+ half (22.5 versus 23.5 magnetic local time [MLT]). They performed the same analysis with data from the dawnside, and found that the onset was further dawnward when the O^+/H^+ ratio was high (23:00 versus 22:15). Note that in all cases the median is still on the duskside, but the high O^+/H^+ is correlated with a shift toward the high O^+/H^+ region. This difference was only true for the near-earth subset of Geotail data (-8Re>X>-14 Re). For locations further down the tail, the amount of O^+ in the plasma sheet makes no difference to the onset location.

Another way to assess whether O^+ is a trigger is to measure if there are more substorms when there is more O^+ in the plasma sheet overall. The average plasma sheet mass increases significantly with increased solar EUV, often measured using the F10.7 index. *Lennartsson et al.* [1993] showed that the average O^+/H^+ ratio in the plasma sheet increases and decreases along with F10.7, but substorm activity, as measured by AE or kilopond (Kp), does not show a similar increase, either in frequency or in peak value. *Nosé et al.* [2009] performed a similar analysis with the long-term Geotail data set. They also showed the strong correlation between the average O^+/H^+ ratio and F10.7. Using the number of substorms determined from Pi2 pulsations, they found no correlation between the O^+/H^+ ratio and the frequency of substorms over the solar cycle. When they normalized, their substorm frequency by the *Kan and Lee* [1979] coupling function, they found that, in fact, the normalized frequency of substorms is lower when the O^+/H^+ ratio is higher. Thus, if anything, the O^+ has the effect of suppressing substorms.

6.2.3. O^+ Effect on Loading

A final method for testing if O^+ makes the plasma sheet unstable is to examine the loading itself. The classic signature of loading in the plasma sheet is an increase in the total pressure during the growth phase. The increased lobe flux increases the tail-flaring angle, and so a larger component of the solar wind dynamic pressure is normal to the magnetopause [*Coroniti and Kennel*, 1972]. This increases the tail pressure. After reconnection is triggered, the lobe flux decreases, which decreases the flaring angle, and the pressure decreases. Thus, the increase in pressure during the growth phase is an indication of how much loading has occurred before reconnection onset. If the plasma sheet is more unstable, we would expect that there would be less loading

before onset occurs. *Kistler et al.* [2006] had observed in their superposed epoch analysis that the amount of loading during storm time substorms was in fact greater than during non-storm substorms. Since the O^+/H^+ ratio is higher during storms, this would indicate that the O^+ is making the tail more stable. *Liu et al.* [2013] examined this in more detail using a statistical study. In order to compare events that occur under different external conditions, the tail pressure must be normalized by the solar wind pressure so that only the pressure due to loading is considered. The normalized pressure is equivalent to $\sin^2\alpha$, where α is the flaring angle. In addition, to compare events measured at different distances down the tail, an additional normalization is required to take into account the variation of the flaring angle with distance. The empirical magnetopause of *Petrinec and Russell* [1996] is used to determine the final normalized pressure, $\sin^2\alpha^*$. *Liu et al.* [2013] determined the correlation between the maximum value of $\sin^2\alpha^*$, an indicator of the amount of loading during the substorms, and various plasma sheet parameters prior to onset including the proton density, the O^+ density, the density ratio and the mass density. Figure 6.3, panels (a) – (d) show the results. The best correlation is with the O^+ density, and the correlation is positive; more O^+ leads to greater loading, implying that O^+ actually makes the tail more stable.

6.3. DOES O^+ IMPACT THE TAIL RECONNECTION RATE?

Because the reconnection rate is expected to scale as a fraction of the Alfvén speed, enhanced O^+, which increases the mass density, is expected to slow the reconnection rate. Three-fluid simulations by *Shay and Swisdak* [2004] showed that adding a third heavy ion fluid does reduce the reconnection rate but not as much as expected because the aspect ratio of the reconnection region also changes. *Hesse and Birn* [2004] examined the impact of a background (lobe) population of either cold protons or cold O^+ entering the reconnection region in kinetic particle in cell (PIC) simulations. They found that the cold protons actually had a larger impact on the reconnection rate than O^+, because the protons were more coupled with the reconnecting system. Thus, there are some indications from simulations that the reduction in reconnection rate from O^+ is not as large as expected from the simple fluid picture.

The impact of O^+ on the tail reconnection rate is difficult to measure simply because the reconnection rate in the tail is difficult to measure. There have only been a handful of measurements of the local rate [*Xiao et al.*, 2007; *Pu et al.*, 2010], and the error bars tend to be large, so performing a statistical study has not yet been possible. However, it is possible to measure the rate of unloading in

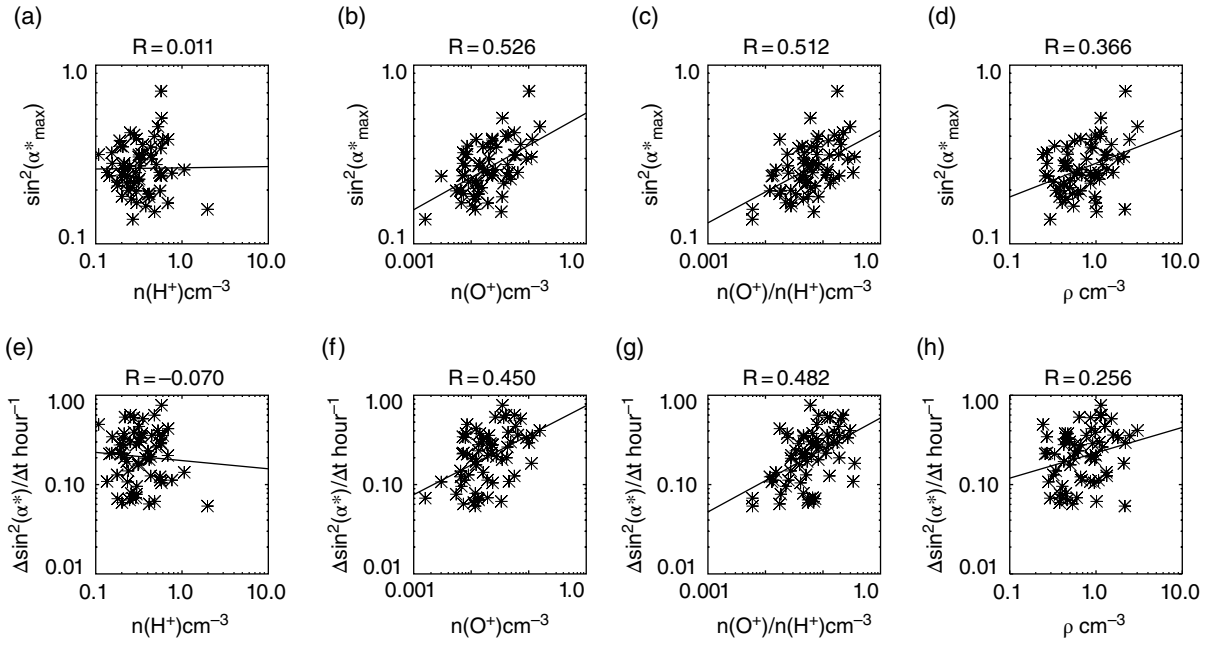

Figure 6.3 Dependence of the maximum pressure, normalized for solar wind pressure and tail distance effects, on plasma sheet parameters (a) H^+ density, (b) O^+ density, (c) O^+ to H^+ density ratio, and (d) mass density. Dependence of normalized pressure decrease rate during substorm expansion on (e) H^+ density, (f) O^+ density, (g) O^+ to H^+ density ratio, and (h) mass density. [From *Liu et al.*, 2013]

the tail. Unloading is due to reconnection of lobe flux over some width of the tail. Thus, the unloading rate is determined by both the local rate of reconnection and the width of the tail that is able to reconnect. *Liu et al.* [2013] correlated the unloading rate with a number of plasma sheet parameters. The change in the normalized pressure discussed above, $\sin^2\alpha^*$, is used to measure the unloading. The results, panels (e)–(h) shown in Figure 6.3, indicate that the unloading rate is faster when the O^+ density and the O^+/H^+ ratio are higher. If the faster unloading is due to a change in the reconnection rate, it would be counter to the expectation that O^+, by decreasing the Alfvén speed, would make the reconnection rate slower. The other possibility is that during high O^+ events, reconnection is occurring across a greater width of the tail. There is some indirect evidence that this might be the case. Sawtooth events are known to occur over a broader region of the tail [*Cai et al.*, 2006]; *Liao et al.* [2014] showed that sawtooth events are associated with a higher O^+ content. Thus, it is possible that high O^+ events are also broader. However, this result would need to be confirmed with additional study.

6.4. HOW DOES O+ INFLUENCE THE CURRENT SHEET AND TAIL RECONNECTION REGION

In addition to understanding the impacts on a large scale, work has also been done to understand the O^+ impacts on the small scales. As the current sheet thickness is thought to scale as the ion gyroradius, or ion inertial length, O^+ may increase the current sheet thickness. *Zelenyi et al.* [2006] developed a model of a current sheet consisting of electrons, H^+ and O^+. They showed that the self-consistent solution had a nested structure, with an electron current sheet inside a proton current sheet that is inside a broad O^+ current sheet, as shown in Figure 6.4. They found that in this multi-species current sheet, as the O^+/H^+ ratio increased from 0.25 to 1, the contribution of O^+ to the fraction of the current carried by the O^+ increased from 18% to ~30%, where the 30% is an upper limit, depending on the flux and the temperature. *Kistler et al.* [2005] measured the O^+ contribution to the current using Cluster/CODIF measurements and found that O^+ carried on the order of 10% of the current during O^+-rich events, which is of the same order as the Zelenyi calculation.

To determine whether the current sheet thickness depends on the composition of the plasma sheet, *Liu et al.* [2014] measured the current sheet thickness using the four Cluster spacecraft during nine reconnection events from 2001, when the spacecraft spacing was ~1000 km, and 2003, when the spacing was ~300 km. Three methods were used to determine the thickness: fitting to a Harris sheet, fitting to a time-dependent Harris sheet, and the

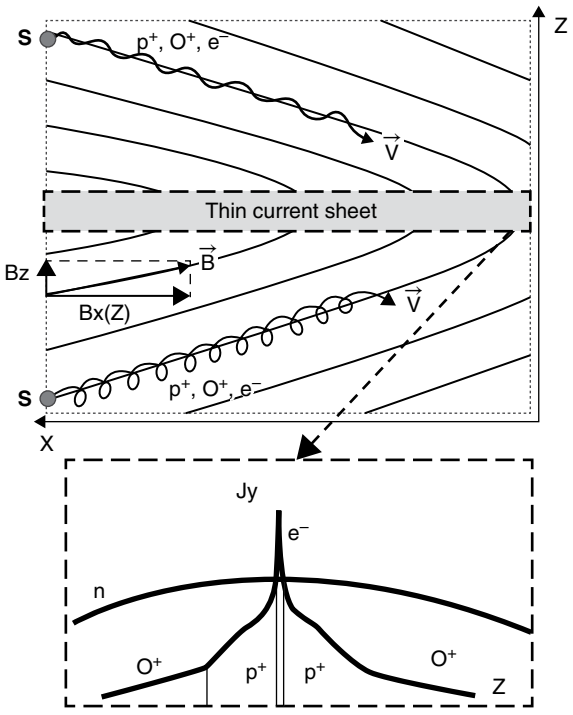

Figure 6.4 Model of a thin current sheet containing H^+, O^+, and e-. The bottom panel shows the multi-scale structure. [From *Zelenyi et al.*, 2006]

magnetic field gradient estimation method [*Shen et al.*, 2008]. These methods only give one current sheet thickness; if the current sheet has a multiscale structure, as suggested by Zelenyi, only the dominant component will be found. Figure 6.5 from *Liu et al.* [2014] shows the current sheet thickness plotted as a function of the proton gyroradius in the central plasma sheet. The events are color coded to indicate whether they are high O^+ (solid) or low O^+ (open). The current sheet thickness has the scale of the proton gyroradius, independent of the amount of O^+ in the plasma sheet. This result is consistent with the result of *Zelenyi et al.* [2006] in that even when there is significant O^+ in the plasma sheet, the proton scale remains, and provides the dominant inner current sheet structure. A broader O^+ structure may be there as well, but it is more difficult to extract from the observations. *Artemyev et al.* [2008] used fast current sheet crossings to attempt to do this by fitting the data to the three-species Zelenyi model. These crossings were not necessarily examples close to a reconnection line. They were able to reasonably fit the observed current sheet structure using the Zelenyi model, also confirming the multi-scale nature of the current sheet.

To examine the three-species reconnection region in more detail, *Liu et al.* [2015] compared the H^+ and O^+ distribution functions from a three-species PIC simulation of reconnection with observations in the H^+ and O^+

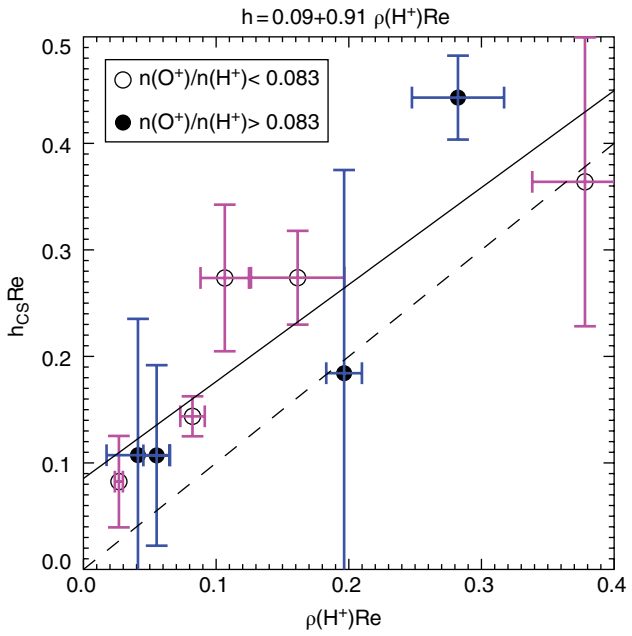

Figure 6.5 The half current sheet thickness as a function of the H^+ gyroradius [From *Liu et al.*, 2014, Figure 4a].

diffusion regions in the tail. Figure 6.6 shows the regions of agyrotropy for each species in the vicinity of the reconnection region from the simulation. The three-scale nested structure of the reconnection region is clearly apparent. The electrons are agyrotropic over a narrow region (Figure 6.6a), the H^+ over a wider region (Figure 6.6b), and the O^+ agyrotropy (Figure 6.6c) extends over a good fraction of the plasma sheet.

Also identified by black boxes are the regions where the distribution functions are determined, and compared with distribution functions from two events from Cluster, an event on 15 September 2001, and an event on 21 August 2002. Good agreement was found between the simulated and observed distribution functions in the different regions indicated in Figure 6.6. Figure 6.7 shows an example. The four panels on the left show distributions from the region marked (e) from the PIC simulation, while the four panels on the right show observations from the 15 September 2001 event, when the Cluster spacecraft is in a similar region. This region is outside the H^+ diffusion region, in the H^+ exhaust flow, but still in the O^+ diffusion region. The four panels in each case show cuts in the V_x–V_y plane and the V_x–V_z plane for the two species, H^+ and O^+. One difference between the simulation and the observation coordinate system is that the x-axis is reversed, so positive x is tailward for the simulations, while negative x is tailward for the observations. The red box in the O^+ simulation distributions indicates the approximate velocity limits of the observational distributions on the right. The H^+ simulated distribution is broad and streaming tailward. The O^+ simulated distribution shows a bouncing motion in the X-Z plane, along with both tailward (−x) and duskward (+y) motion. The observations show a similar pattern. The H^+ is broad and streaming tailward, while the O^+ is bouncing in Z, and moving both tailward (−x) and duskward (+y). The difference in the motion of the two species again confirms the picture of the multi-scale reconnection region, with the O^+ diffusion region extending further downstream than the H^+ diffusion region.

6.5. DISCUSSION AND SUMMARY

One thing that is abundantly clear from the studies is that if the relative abundance of O^+ does impact the stability of the tail, the effect is relatively minor, and often outweighed by other factors. The evidence for an O^+ effect is slightly higher in the near Earth plasma sheet. In this region, for example, *Daglis et al.* [1990] did observe an increase in the O^+/H^+ ratio prior to substorm onset in one event, and *Ono et al.* [2010] found that the composition in this region has a small impact on the location of onset. In the mid-tail, which is where reconnection onset most often occurs, there is no evidence that O^+ has an impact on substorm onset, except in the special case of sawtooth events. *Liao et al.* [2014] did find evidence that the O^+/H^+ ratio increased prior to substorm onset for this particular type of substorms. All other studies have found that, if anything, O^+ may suppress onset. Thus, at this point, there is some evidence that O^+ may have an impact on current disruption in the near Earth region but does not make the tail more unstable to reconnection onset.

The abovementioned observational studies have predominantly looked at the effects of an enhanced O^+/H^+ ratio on the magnetotail, not an absolute increase in O^+ itself. Some of the mechanisms proposed that affect the tail dynamics actually depend on the total mass density, while others depend on the larger scale of the O^+, compared to H^+. For example, the reconnection rate in the fluid picture depends on the mass density, so the rate could be affected by either enhanced O^+ or a dense population of H^+. The MHD modeling of *Brambles et al.* [2011] points to an enhanced overall particle pressure leading to the instability, and this could be due either to O^+ or H^+. Thus, future work needs to be done to ascertain whether enhanced pressure or density, independent of species, is the governing factor in controlling the reconnection onset and the rate. If so, this may be one reason that an O^+ effect is not so clear.

These studies have also shown that it is not sufficient to treat the mixed H^+ and O^+ ions in the plasma sheet as just a heavier fluid, or as a plasma with a larger "average" gyroradius. The consequences based on this model, that for example, the plasma sheet should be more

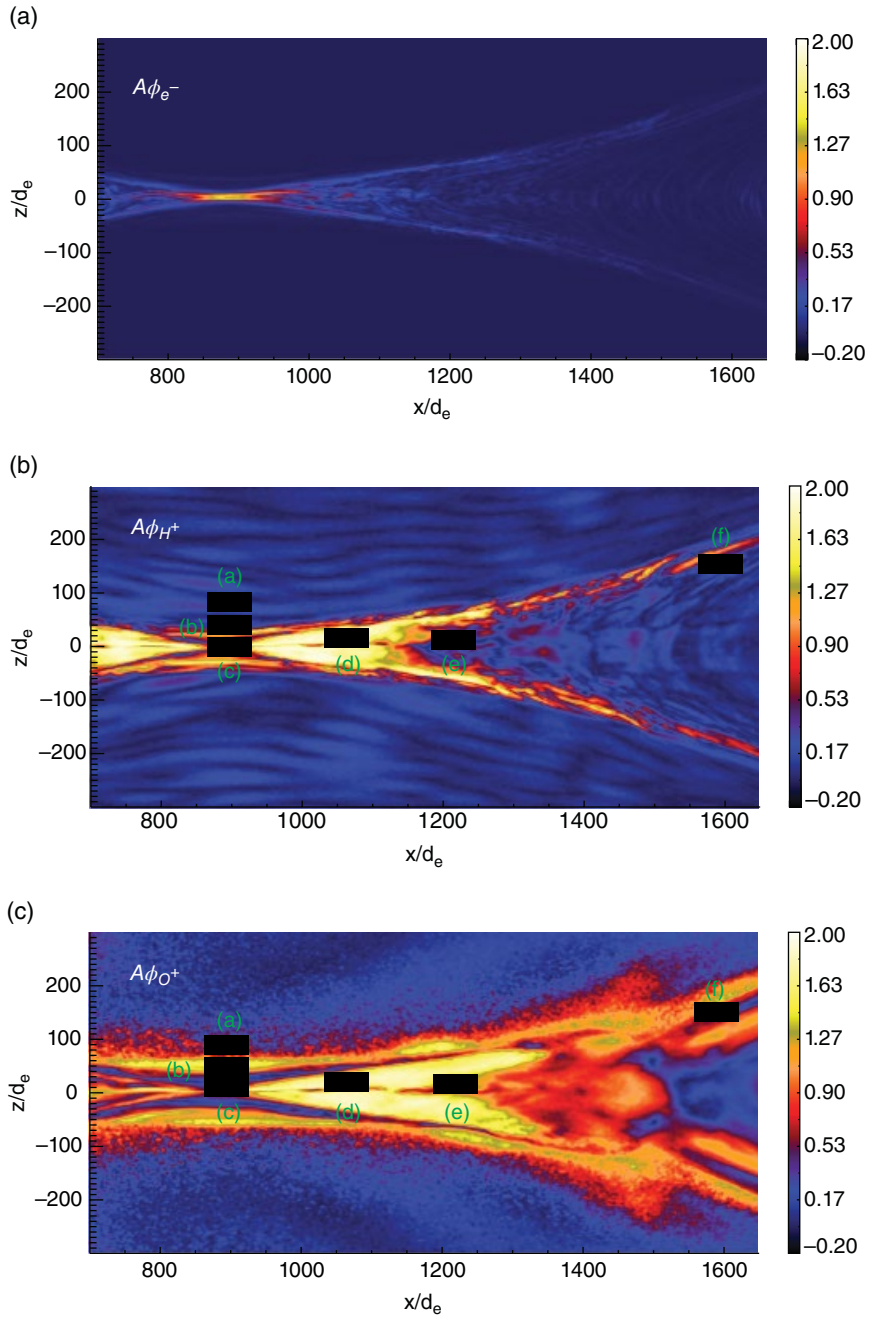

Figure 6.6 The agyrotropy of (a) electrons, (b) H^+, and (c) O^+ in the vicinity of the reconnection region in a two-dimensional PIC simulation. [From *Liu et al.*, 2015]

unstable with more O^+ due to the larger gyroradius, or that the reconnection rate will be lower due to the reduced Alfvén speed, have not been found. Instead, the O^+ introduces an additional scale to the plasma, and so the physics must be addressed as a multi-scale problem. Theoretical work in understanding the effects of the larger scale using fully kinetic simulations [e.g., *Karimabadi et al.*, 2011; *Markidis et al.*, 2011; *Liu et al.*, 2015] is only just beginning. With the launch of the Magnetospheric Multiscale Mission, and the associated theoretical work that will take place, we expect new insights on this problem in the near future.

ACKNOWLEDGMENTS

Work at UNH was supported by National Aeronautics and Space Administration (NASA) under grants NNX11AB65G, NNX10AQ42G, and NNX12AD16G.

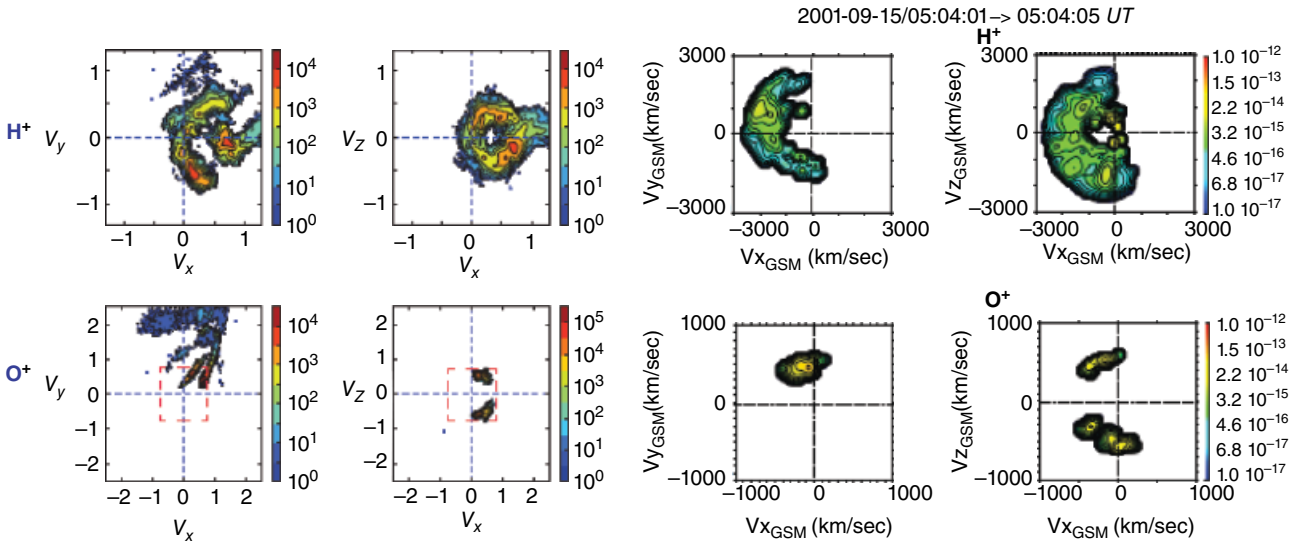

Figure 6.7 Comparison of cuts of the distribution functions from simulation (left four panels) and observation during one event (right four panels). [From *Liu et al.*, 2015]

REFERENCES

Artemyev, A. V., A. A. Petrukovich, L. M. Zelenyi, H. V. Malova, V. Y. Popov, R. Nakamura, A. Runov, and S. Apatenkov (2008), Comparison of multi-point measurements of current sheet structure and analytical models, *Annales Geophysicae*, *26*(9), 2749–2758, doi:10.5194/angeo-26-2749-2008.

Baker, D. N., E. W. J. Hones, D. T. Young, and J. Birn (1982), The possible role of ionospheric oxygen in the initiation and development of plasma sheet instabilities, *Geophys. Res. Lett.*, *9*, 1337–1340, doi:10.1029/GL009i012p01337.

Baker, D. N., T. A. Fritz, J. Birn, W. Lennartsson, B. Wilken, and H. W. Kroehl (1985), The role of heavy ionospheric ions in the localization of substorm disturbances on March 22, 1979, CDAW 6, *J. Geophys. Res.*, *90*, 1273–1281, doi:10.1029/JA090iA02p01273.

Brambles, O. J., W. Lotko, B. Zhang, M. Wiltberger, J. Lyon, and R. J. Strangeway (2011), Magnetosphere Sawtooth Oscillations Induced by Ionospheric Outflow, *Science*, *332*(6), 1183–1186, doi:10.1126/science.1202869.

Cai, X., M. G. Henderson, and C. R. Clauer (2006), A statistical study of magnetic dipolarization for sawtooth events and isolated substorms at geosynchronous orbit with GOES data, *Annales Geophysicae*, *24*(1), 3481–3490, doi:10.5194/angeo-24-3481-2006.

Cladis, J. B., and W. E. Francis (1992), Distribution in magnetotail of O(+) ions from cusp/cleft ionosphere, A possible substorm trigger, *J. Geophys. Res.*, *97*, 123–130, doi:10.1029/91JA02376.

Coroniti, F. V., and C. F. Kennel (1972), Changes in magnetospheric configuration during the substorm growth phase, *J. Geophys. Res.*, *77*(1), 3361, doi:10.1029/JA077i019p03361.

Daglis, I. A., and E. T. Sarris (1998), Comment on "Experimental investigation of possible geomagnetic feedback from energetic (0.1 to 16 keV) terrestrial O+ ions in the magnetotail current sheet" by O. W. Lennartsson, D. M. Klumpar, E. G. Shelley and J. M. Quinn, *J. Geophys. Res.*, *103*(A), 29545–29548, doi:10.1029/98JA02268.

Daglis, I. A., E. T. Sarris, and G. Kremser (1990), Indications for ionospheric participation in the substorm process from AMPTE/CCE observations, *Geophysical Research Letters (ISSN0094-8276)*, *17*, 57–60, doi:10.1029/GL017i001p00057.

Hesse, M., and J. Birn (2004), On the cessation of magnetic reconnection, *Annales Geophysicae*, *22*(2), 603–612, doi:10.5194/angeo-22-603-2004.

Horwitz, J. L. (1986), The tail lobe ion spectrometer, *J. Geophys. Res.*, *91*, 5689–5699, doi:10.1029/JA091iA05p05689.

Horwitz, J. L., and M. Lockwood (1985), The cleft ion fountain, A two-dimensional kinetic model, *J. Geophys. Res.*, *90*, 9749–9762, doi:10.1029/JA090iA10p09749.

Kan, J. R., and L. C. Lee (1979), Energy coupling function and solar wind-magnetosphere dynamo, *Geophys. Res. Lett.*, *6*, 577–580, doi:10.1029/GL006i007p00577.

Karimabadi, H., V. Roytershteyn, C. G. Mouikis, L. M. Kistler, and W. Daughton (2011), Flushing effect in reconnection: Effects of minority species of oxygen ions, *Planetary and Space Science*, *59*(7), 526–536, doi:10.1016/j.pss.2010.07.014.

Kistler, L. M., C. G. Mouikis, X. Cao, H. Frey, B. Klecker, I. Dandouras, A. Korth, M. F. Marcucci, R. Lundin, M. McCarthy, R. Friedel, and E. Lucek (2006), Ion composition and pressure changes in storm time and nonstorm substorms in the vicinity of the near-Earth neutral line, *J. Geophys. Res.*, *111*(A), 11222, doi:10.1029/2006JA011939.

Kistler, L. M., C. Mouikis, E. Möbius, B. Klecker, J. A. Sauvaud, H. Rème, A. Korth, M. F. Marcucci, R. Lundin, G. K. Parks, and A. Balogh (2005), Contribution of nonadiabatic ions to the cross-tail current in an O+ dominated thin current sheet, *J. Geophys. Res.*, *110*(A), 06213, doi:10.1029/2004JA010653.

Lakhina, G. S. (1995), Excitation of plasma sheet instabilities by ionospheric O+ ions, *Geophys. Res. Lett.*, *22*(2), 3453–3456, doi:10.1029/95GL03427.

Lakhina, G. S. (2001), Role of helicon modes in the injection of oxygen ions in the ring current, *Journal of Atmospheric and Solar-Terrestrial Physics*, *63*(5), 481–487.

Lakhina, G. S., and B. T. Tsurutani (1997), Helicon modes driven by ionospheric O+ ions in the plasma sheet region, *Geophys. Res. Lett.*, *24*(1), 1463–1466, doi:10.1029/97GL01208.

Lennartsson, O. W., D. M. Klumpar, E. G. Shelley, and J. M. Quinn (1993), Experimental investigation of possible geomagnetic feedback from energetic (0.1 to 16 keV) terrestrial O(+) ions in the magnetotail current sheet, *J. Geophys. Res.*, *98*, 19443, doi:10.1029/93JA01991.

Lennartsson, W., and E. G. Shelley (1986), Survey of 0.1- to 16-keV/e plasma sheet ion composition, *J. Geophys. Res.*, *91*, 3061–3076, doi:10.1029/JA091iA03p03061.

Liao, J., X. Cai, L. M. Kistler, C. R. Clauer, C. G. Mouikis, B. Klecker, and I. Dandouras (2014), The relationship between sawtooth events and O+ in the plasma sheet, *Journal of Geophysical Research (Space Physics)*, *119*(3), 1572–1586, doi:10.1002/2013JA019084.

Liu, Y. H., C. G. Mouikis, L. M. Kistler, S. Wang, V. Roytershteyn, and H. Karimabadi (2015), The heavy ion diffusion region in magnetic reconnection in the Earth's magnetotail, *Journal of Geophysical Research (Space Physics)*, *120*(5), 3535–3551, doi:10.1002/2015JA020982.

Liu, Y. H., L. M. Kistler, C. G. Mouikis, V. Roytershteyn, and H. Karimabadi (2014), The scale of the magnetotail reconnecting current sheet in the presence of O+, *Geophys Res Lett*, *41*(1), 4819–4827, doi:10.1002/2014GL060440.

Liu, Y., L. M. Kistler, C. G. Mouikis, B. Klecker, and I. Dandouras (2013), Heavy ion effects on substorm loading and unloading in the Earth's magnetotail, *Journal of Geophysical Research (Space Physics)*, *118*(5), 2101–2112, doi:10.1002/jgra.50240.

Maggiolo, R., and L. M. Kistler (2014), Spatial variation in the plasma sheet composition: Dependence on geomagnetic and solar activity, *Journal of Geophysical Research (Space Physics)*, *119*(4), 2836–2857, doi:10.1002/2013JA019517.

Markidis, S., G. Lapenta, L. Bettarini, M. Goldman, D. Newman, and L. Andersson (2011), Kinetic simulations of magnetic reconnection in presence of a background O+ population, *J. Geophys. Res.*, *116*, doi:10.1029/2011JA016429.

Mouikis, C. G., L. M. Kistler, Y. H. Liu, B. Klecker, A. Korth, and I. Dandouras (2010), H+ and O+ content of the plasma sheet at 15–19 Re as a function of geomagnetic and solar activity, *J. Geophys. Res.*, *115*, A00J16, doi:10.1029/2010JA015978.

Nosé, M., A. Ieda, and S. P. Christon (2009), Geotail observations of plasma sheet ion composition over 16 years: On variations of average plasma ion mass and O+ triggering substorm model, *J. Geophys. Res.*, *114*(A), 07223, doi:10.1029/2009JA014203.

Ono, Y., S. P. Christon, H. U. Frey, and A. T. Y. Lui (2010), Distribution of O+ ions in the plasma sheet and locations of substorm onsets, *J. Geophys. Res.*, *115*(A), A09220, doi:10.1029/2009JA015138.

Petrinec, S. M., and C. T. Russell (1996), Near-Earth magnetotail shape and size as determined from the magnetopause flaring angle, *J. Geophys. Res.*, *101*(A), 137–152, doi:10.1029/95JA02834.

Pu, Z. Y., X. N. Chu, X. Cao, V. Mishin, V. Angelopoulos, J. Wang, Y. Wei, Q.-G. Zong, S. Y. Fu, L. Xie, K.-H. Glaßmeier, H. Frey, C. T. Russell, J. Liu, J. McFadden, D. Larson, S. Mende, I. Mann, D. Sibeck, L. A. Sapronova, M. V. Tolochko, T. I. Saifudinova, Z. H. Yao, X. G. Wang, C. J. Xiao, X. Z. Zhou, H. Rème, and E. Lucek (2010), THEMIS observations of substorms on 26 February 2008 initiated by magnetotail reconnection, *J. Geophys. Res.*, *115*(A), A02212, doi:10.1029/2009JA014217.

Rothwell, P. L., Block, L. P., C. G. Falthammar, and M. B. Silevitch (1988), A new model for substorm onsets, The prebreakup and triggering regimes, *Geophysical Research Letters (ISSN 0094-8276)*, *15*, 1279–1282, doi:10.1029/GL015i011p01279.

Rothwell, P. L., M. B. Silevitch, Block, L. P., and C. G. Falthammar (1991), Prebreakup arcs - A comparison between theory and experiment, *J. Geophys. Res.*, *96*, 13967, doi:10.1029/91JA01268.

Sharp, R. D., D. L. Carr, W. K. Peterson, and E. G. Shelley (1981), Ion streams in the magnetotail, *J. Geophys. Res.*, *86*, 4639–4648, doi:10.1029/JA086iA06p04639.

Shay, M. A., and M. Swisdak (2004), Three-Species Collisionless Reconnection: Effect of O+ on Magnetotail Reconnection, *Physical Review Letters*, *93*(1), 175001, doi:10.1103/PhysRevLett.93.175001.

Shen, C., Z. J. Rong, X. Li, M. Dunlop, Z. X. Liu, H. V. Malova, E. Lucek, and C. Carr (2008), Magnetic configurations of the tilted current sheets in magnetotail, *Annales Geophysicae*, *26*(1), 3525–3543, doi:10.5194/angeo-26-3525-2008.

Wiltberger, M., W. Lotko, J. G. Lyon, P. Damiano, and V. Merkin (2010), Influence of cusp O+ outflow on magnetotail dynamics in a multifluid MHD model of the magnetosphere, *J. Geophys. Res.*, *115*(1), doi:10.1029/2010JA015579.

Xiao, C. J., Z. Y. Pu, X. G. Wang, Z. W. Ma, S. Y. Fu, T. D. Phan, Q.-G. Zong, Z. X. Liu, M. W. Dunlop, K.-H. Glaßmeier, A. Balogh, H. Rème, I. Dandouras, and C. P. Escoubet (2007), A Cluster measurement of fast magnetic reconnection in the magnetotail, *Geophys. Res. Lett.*, *34*(1), 1101, doi:10.1029/2006GL028006.

Young, D. T., H. Balsiger, and J. Geiss (1982), Correlations of magnetospheric ion composition with geomagnetic and solar activity, *J. Geophys. Res.*, *87*, 9077–9096, doi:10.1029/JA087iA11p09077.

Yu, Y., and A. J. Ridley (2013), Exploring the influence of ionospheric O+ outflow on magnetospheric dynamics: dependence on the source location, *Journal of Geophysical Research (Space Physics)*, *118*(4), 1711–1722, doi:10.1029/2012JA018411.

Zelenyi, L. M., H. V. Malova, V. Y. Popov, D. C. Delcourt, N. Y. Ganushkina, and A. S. Sharma (2006), "Matreshka" model of multilayered current sheet, *Geophys. Res. Lett.*, *33*(5), L05105, doi:10.1029/2005GL025117.

7

Thermal and Low-energy Ion Outflows in and through the Polar Cap: The Polar Wind and the Low-energy Component of the Cleft Ion Fountain

Naritoshi Kitamura[1], Kanako Seki[2], Yukitoshi Nishimura[3], Takumi Abe[1], Manabu Yamada[4], Shigeto Watanabe[5], Atsushi Kumamoto[6], Atsuki Shinbori[7], and Andrew W. Yau[8]

Video of Yosemite Talk, URL: http://dx.doi.org/10.15142/T33K51

ABSTRACT

Using long-term Akebono satellite data, we show that during geomagnetically quiet periods the O^+ ion velocity is approximately zero, on average, and that there is no apparent stable upward acceleration under sunlit conditions below ~7000 km altitude, even at solar maximum when the effect of photoelectrons is expected to be maximal. Thus, only a very limited O^+ ion flux can be expected during geomagnetically quiet periods. The flux of polar wind H^+ ions is likely controlled by the reaction rate for the production of H^+ ions. A field-aligned potential drop develops at high altitudes so as to equilibrate the net escape photoelectron flux with the polar wind H^+ ion flux. During geomagnetically active periods, the low-energy component of the cleft ion fountain would be of the greatest importance for O^+ ions in the high altitude polar cap. The large spatial scale (on the order of 1000 km, mapped to the ionosphere), large ion fluxes (~10^9 cm^{-3} s^{-1} mapped to 1000 km altitude), and long duration (comparable to that of the main phase of geomagnetic storms) indicate a significant supply of very-low-energy O^+ ions to the near-Earth plasma sheet through the dayside polar cap during the main phase of geomagnetic storms.

[1]*Institute of Space and Astronautical Science, Japan Aerospace Exploration Agency, Sagamihara, Kanagawa, Japan*
[2]*Department of Earth and Planetary Science, Graduate School of Science, The University of Tokyo, Tokyo, Japan*
[3]*Department of Atmospheric and Oceanic Sciences, University of California, Los Angeles, Los Angeles, CA, USA*
[4]*Planetary Exploration Research Center, Chiba Institute of Technology, Narashino, Japan*
[5]*Space Information Center, Hokkaido Information University, Ebetsu, Japan*
[6]*Department of Geophysics, Graduate School of Science, Tohoku University, Sendai, Japan*
[7]*Research Institute for Sustainable Humanosphere, Kyoto University, Uji, Japan*
[8]*Department of Physics and Astronomy, University of Calgary, Calgary, Alberta, Canada*

7.1. THERMAL AND LOW-ENERGY ION OUTFLOWS IN AND THROUGH THE POLAR CAP

Since magnetic field lines in the polar cap open up to interplanetary space, energy input to the ionosphere, responsible for driving ion outflows, is small compared with the inputs in the cusp and the auroral zone. However, significant ion fluxes have been detected in the high altitude polar cap and the lobe regions [e.g., *Lockwood et al.*, 1985; *Waite et al.*, 1985; *Kitamura et al.*, 2010b, 2012b; *Liao et al.*, 2012]. Although recent indirect measurements indicate that low-energy ions usually dominate the density and outward flux [*André et al.*, 2015], it is difficult to measure such thermal-energy ions directly. Only a small number of polar orbiting magnetospheric satellites

Magnetosphere-Ionosphere Coupling in the Solar System, Geophysical Monograph 222, First Edition.
Edited by Charles R. Chappell, Robert W. Schunk, Peter M. Banks, James L. Burch, and Richard M. Thorne.

(above ~1000 km altitude) were equipped with instruments to measure such ions (which are characterized by energies of ~1 electron volt [eV]). Moreover, since spacecraft are charged positively in tenuous plasma under sunlit conditions, such ions are retarded, and at least a faction cannot reach the detectors. Thus, measurements of thermal-energy ions at high altitudes may be biased toward high-density cases.

The polar wind is the dominant outflow process in the polar cap during geomagnetically quiet periods, while low-energy ions that are supplied by the cleft ion fountain drift into the polar cap during geomagnetically active periods [e.g., *Lockwood et al.*, 1985; *Waite et al.*, 1985]. Since it becomes difficult to distinguish polar wind ions from this latter population during geomagnetically active periods, geomagnetically quiet periods are more suitable to investigate the characteristics of polar wind ions, although these measurements are more difficult because of the prevailing low densities compared with those during active periods.

In Section 7.2.1, the polar wind is briefly reviewed with particular focus on sunlit conditions. Additional analyses mainly using thermal ion data obtained by the Akebono satellite during geomagnetically quiet periods are described in Sections 7.2.2 and 7.2.3. A discussion is presented in Section 7.2.4. In Section 7.3, we briefly review the main features of low-energy ion outflows measured in the polar cap during geomagnetically active periods, when the low-energy component of the cleft ion fountain flows into the polar cap. Brief overall conclusions are given in Section 7.4.

7.2. ION OUTFLOWS IN QUIET TIME: THE POLAR WIND

7.2.1. The Impact of Photoelectrons on the Polar Wind

The ambipolar ion outflow, which is referred to as the 'polar wind,' is one of the most fundamental terrestrial plasma outflow processes [e.g., *Lemaire et al.*, 2007; *Schunk*, 2007; *Tam et al.*, 2007; *Yau et al.*, 2007, and references therein]. Ions on open field lines (such as those found in the polar cap) can escape along these field lines. Under sunlit conditions, both thermal-energy ions and ionospheric photoelectrons, which are generated by ionization of the atmosphere by solar extreme ultraviolet radiation, escape along the open field lines in the polar cap. Although the classical polar wind theory expect that only light ions (H^+ and He^+) can escape by this process [e.g., *Axford*, 1968; *Banks and Holzer*, 1968], observations by the Akebono satellite [*Abe et al.*, 1993, 2004] and the photoelectron driven polar wind model of *Tam et al.* [1995] indicate that thermal energy O^+ ions can also escape. In contrast, polar wind models that take into account the effects of photoelectrons developed by *Wilson et al.* [1997] and *Su et al.* [1998] have demonstrated that O^+ ion acceleration at low altitudes is weak, and a large field-aligned potential drop (~10–60 volts [V]) occurs at high altitudes (~6 Earth radii [R_E]). *Khazanov et al.* [1997] indicate that thermal electron inflows compensate for photoelectron escape and contribute zero net field-aligned current conditions without ion outflows with large fluxes. As described above, controversy has ensued regarding whether the polar wind mechanism can cause significant steady O^+ ion outflows as well as regarding the impact of photoelectrons on the polar wind acceleration.

Statistical analyses using observations by the Fast Auroral Snap-shoT (FAST) satellite in the polar cap have demonstrated that a large fraction of upward traveling photoelectrons are reflected back onto the ionosphere by a field-aligned potential drop (typically 10–25 V for small field-aligned current cases) during geomagnetically quiet periods [*Kitamura et al.*, 2012a, 2015]. *Kitamura et al.* [2015] also suggested that it is the source region of H^+ ions in the topside ionosphere and not the photoelectron flux that controls the terrestrial polar wind outflow, since the polar wind ion flux estimated from photoelectron outflows does not change with increasing photoelectron production caused by increasing solar activity as schematically indicated by Figures 7.1a and 7.1b. These authors stated that the magnitude of the field-aligned potential drop at high altitudes is likely determined to equilibrate electron fluxes with ion fluxes regulated by the production rate of H^+ ions, which is not expected to increase with increasing solar activity [*Richards and Torr*, 1985; *Barakat et al.*, 1987]. However, whether or not the contribution of thermal-energy O^+ ions to the ion flux is negligible is not yet clear because of a lack of mass-separated thermal-energy ion measurements.

Here we investigate the parallel velocity of polar wind ions in the polar cap during geomagnetically quiet periods using long-term thermal ion data obtained by the Akebono satellite at solar maximum, when the impact of photoelectrons is expected to be maximal.

7.2.2. Dataset and Analysis Method

The Akebono satellite was launched on 22 February 1989 with an initial perigee, apogee, and inclination of 274 km, 10,500 km, and 75°, respectively. The spin axis was directed toward the Sun. We analyzed the parallel ion velocity profile obtained by the suprathermal ion mass spectrometer (SMS) aboard the Akebono satellite, which is a modified Bennett-type radio frequency mass spectrometer that measures the thermal (0.1–25 eV q^{-1}) and suprathermal (<4 keV q^{-1}) ion distributions in the 0.9–67 amu q^{-1} mass-per-charge range [*Whalen et al.*, 1990]. The data in this study were acquired in fast scan

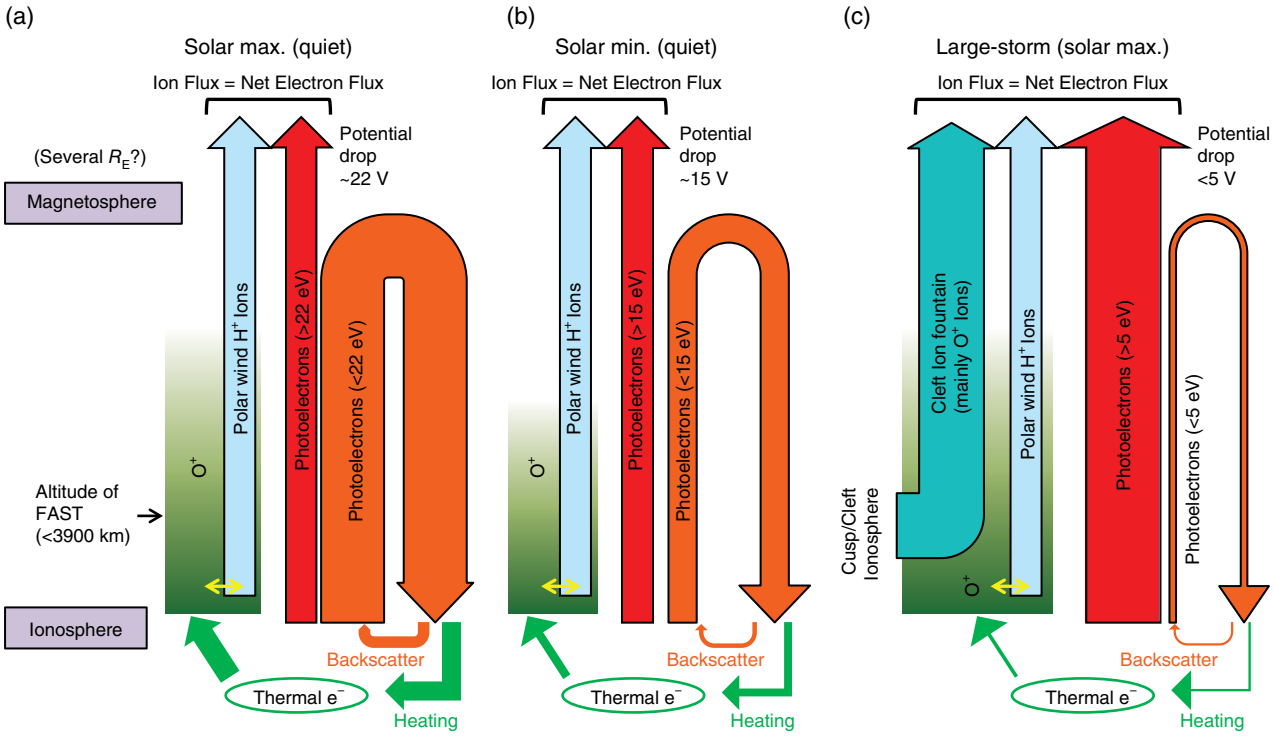

Figure 7.1 Schematic of the polar wind system under sunlit conditions with zero net field-aligned current conditions at (a) solar maximum (quiet), and (b) solar minimum (quiet), and (c) during large geomagnetic storms (solar maximum). During geomagnetically quiet periods, ion fluxes are dominated by polar wind H^+ ions that are regulated by the production rate of H^+ ions (thin yellow arrows: the accidentally resonant charge exchange between O^+ ions and neutral H), which is not expected to increase with increasing solar activity. The magnitude of the field-aligned potential drop at high altitudes is likely determined to equilibrate net escape electron fluxes (red arrows) with ion fluxes (blue arrows). During geomagnetically quiet periods, O^+ ions are almost in hydrostatic equilibrium, and the scale height of O^+ ions is strongly controlled by solar radiation incident onto the ionosphere by changing the ion and electron temperatures in the ionosphere. The reflected photoelectrons (orange arrows) also contribute to electron heating and affect the scale height of O^+ ions (green arrows). The field-aligned potential drop almost disappears during large geomagnetic storms to let a larger fraction of photoelectrons escape and to equilibrate the escape photoelectron flux with the enhanced total ion flux as a result of additional ions coming from the cleft ion fountain.

mode in the large aperture setting. In this mode, the thermal ion distribution function was obtained every 16 s (corresponding to two spin periods). Moments of thermal H^+, He^+, and O^+ ions, and spacecraft potential were estimated following the procedure described by *Watanabe et al.* [1992].

If the plasma density is too low, ions cannot be detected, while the ion count will saturate if the plasma density is too high. Thus, for example, cases where the thermal ion moments are available may be biased toward high densities at high altitudes. To check for the presence of bias related to the plasma density, we selected only cases where thermal ion and electron density observations [*Kitamura et al.*, 2011] are available simultaneously. In situ electron densities were obtained from plasma wave data (i.e., from the upper hybrid resonance frequency or the electron plasma frequency) measured by the plasma wave and sounder (PWS) experiments, which were designed to measure AC electric fields over a frequency range from 20 kilohertz (kHz) to 5.1 megahertz (MHz) [*Oya et al.*, 1990]. The detailed derivation method of the electron density and examples of the plasma wave data were presented by *Kitamura et al.* [2009]. In this analysis, electron densities (with a time resolution of 2 s in most cases) were averaged over 8-s intervals to match the temporal resolution of the SMS.

We used data obtained in the polar cap during geomagnetically quiet periods (*Kp* index ≤2+ for the preceding 3 h and −10 nT ≤ *SYM-H* index ≤40 nT) to focus on the polar wind at solar maximum (monthly mean $F_{10.7}$ index >170). These definitions are identical to those used by *Kitamura et al.* [2011, 2012a, 2015]. In a same manner as the study on the electron density by *Kitamura et al.* [2011], the polar cap is defined based on an empirical model

(only in ranges of 0000–0800 magnetic local time (MLT) and 1400–2400 MLT were included) [*Carbary*, 2005].

Since the SMS can only detect ions near the spin plane (within ~30° in the large aperture setting), the number of ions detected by the SMS strongly depends on both the plasma density and the relation between the direction of motion of the plasma and that of the satellite. For example, if the ram direction (the direction of the velocity vector of the satellite) is close to the spin axis and the horizontal plasma velocity is almost zero, the peak of the distribution function remains outside of the field of view, except when the parallel ion velocity is large (a factor of ~2 compared with the velocity of the satellite). In cases where most of the ions are not detected, moments cannot be obtained using this method [*Watanabe et al.*, 1992]. Since we identified that this significantly affects the analysis of the parallel ion velocity, in the present analysis we only used those datasets for which the angle between the direction to the Sun (spin axis) and the velocity vector of the satellite was 60°–120°. Since horizontal ion transport due to ionospheric convection in the polar cap is likely weak during geomagnetically quiet periods, we neglected the effects of plasma motion in the direction of the spin axis (noon-midnight direction).

We attempted to minimize the contribution of heated populations (e.g., ions of cleft ion fountain origin) by excluding measurements in which the O^+ ion temperature exceeded 30,000 K. This is the same threshold as adopted by *Abe et al.* [2004].

7.2.3. Parallel Ion Velocities

Figure 7.2 shows altitude profiles of ion velocities under sunlit conditions (solar zenith angle [SZA] <90°). Observed electron densities (N_{e_obs}) are normalized using an empirical electron density model (N_{e_model}) [*Kitamura et al.*, 2011]. Different levels of the normalized electron density are shown using different colors. Under sunlit conditions, the upper quartile levels of the electron density are approximately twice the median values for an altitude range of 3000–7000 km [*Kitamura et al.*, 2011]. Thus, $N_{e\_obs}/N_{e\_model} > 5$ is very rare. A significant number of such data is only available around 4000 km altitude (Figure 7.2). For the altitude range of 3000–7000 km, the medians of the parallel ion velocities of each species are almost constant (H^+: ~5 km s^{-1}, He^+: ~1 km s^{-1}, O^+: ~0 km s^{-1}). As expected, the parallel ion velocity decreases with increasing ion mass. The O^+ ion velocity is approximately zero, on average, at least below ~7000 km altitude. This is consistent with the photoelectron driven polar wind models of *Wilson et al.* [1997] and *Su et al.* [1998] that take the field-aligned potential drop at high altitudes into account. This near-zero O^+ ion velocity is also consistent with the model of *Khazanov et al.* [1997], although the model does not take the potential drop at high altitude into account. Since their model allows thermal electron inflows to compensate for outflowing photoelectron fluxes, the inflowing thermal electrons probably behave similarly to the reflected photoelectrons that do not exist in the model.

Figure 7.3 shows medians and quartiles of the parallel ion velocities for $0.5 \le N_{e\_obs}/N_{e\_model} \le 2$ (normal density) and $N_{e\_obs}/N_{e\_model} > 2$ (high density) separately. The velocity of H^+ ions shown in Figure 7.3a tends to become low for the high density cases around 4000 km altitude (above ~1×10^3 cm^{-3}). Although the reason for this is unclear, the low velocity of H^+ ions is similar to the reduction in the velocity of the H^+ ions in regions of electron density enhancements [*Ichikawa et al.*, 2002; *Abe et al.*, 2005; *Kitanoya et al.*, 2011]. The velocity of the He^+ ions is not significantly affected by density variations (Figure 7.3b). The medians of the O^+ ion velocity are higher for high-density cases than for normal density cases (Figure 7.3c). Thus, density enhancements are likely associated with enhancements of O^+ ion upflows. A further detailed assessment of such unusual cases is beyond the scope of this paper. To understand the ground state of the polar wind, measuring thermal-energy ions down to the normal density level is important. Where thermal ion data are only available in enhanced density cases, the O^+ ion velocity would be overestimated, and the H^+ ion velocity may also differ from the ground state.

Although the upward H^+ and O^+ ion velocities may start to increase around 7000 km altitude (Figures 7.2 and 7.3), it is difficult to definitively conclude this because of a bias favoring high-density cases, which are associated with larger velocities (Figures 7.3a and 7.3c); the medians for the altitude range of 7000–8000 km (Figures 7.2a and 7.2c) are similar to those pertaining to the high density cases (Figures 7.3a and 7.3c). Since even the medians of the normal density case were biased to $N_{e\_model}/N_{e\_model} > 1.0$, ion velocities may be slightly overestimated even for the normal density case. The typical electron density in this altitude range is lower than ~100 cm^{-3} [*Kitamura et al.*, 2011]. Future routine observations of thermal energy ions in such density environments will be needed to further investigate the parallel O^+ ion acceleration in the polar wind.

Figure 7.4 shows the SZA distribution of the data and the O^+ ion velocities at an altitude range of 3000–7000 km, where the velocity is not strongly dependent on altitude (Figure 7.2). O^+ ion velocities do not strongly depend on the SZA at least for SZA <100°. H^+ and He^+ ion velocities are also not dependent on SZA (not shown). Very few data for the normal electron density level ($0.5 \le N_{e\_obs}/N_{e\_model} \le 2$) are available for SZA >100°. This is likely due to the drastic decrease in the electron density with increasing SZA at SZA ~110° [*Kitamura et al.*, 2011].

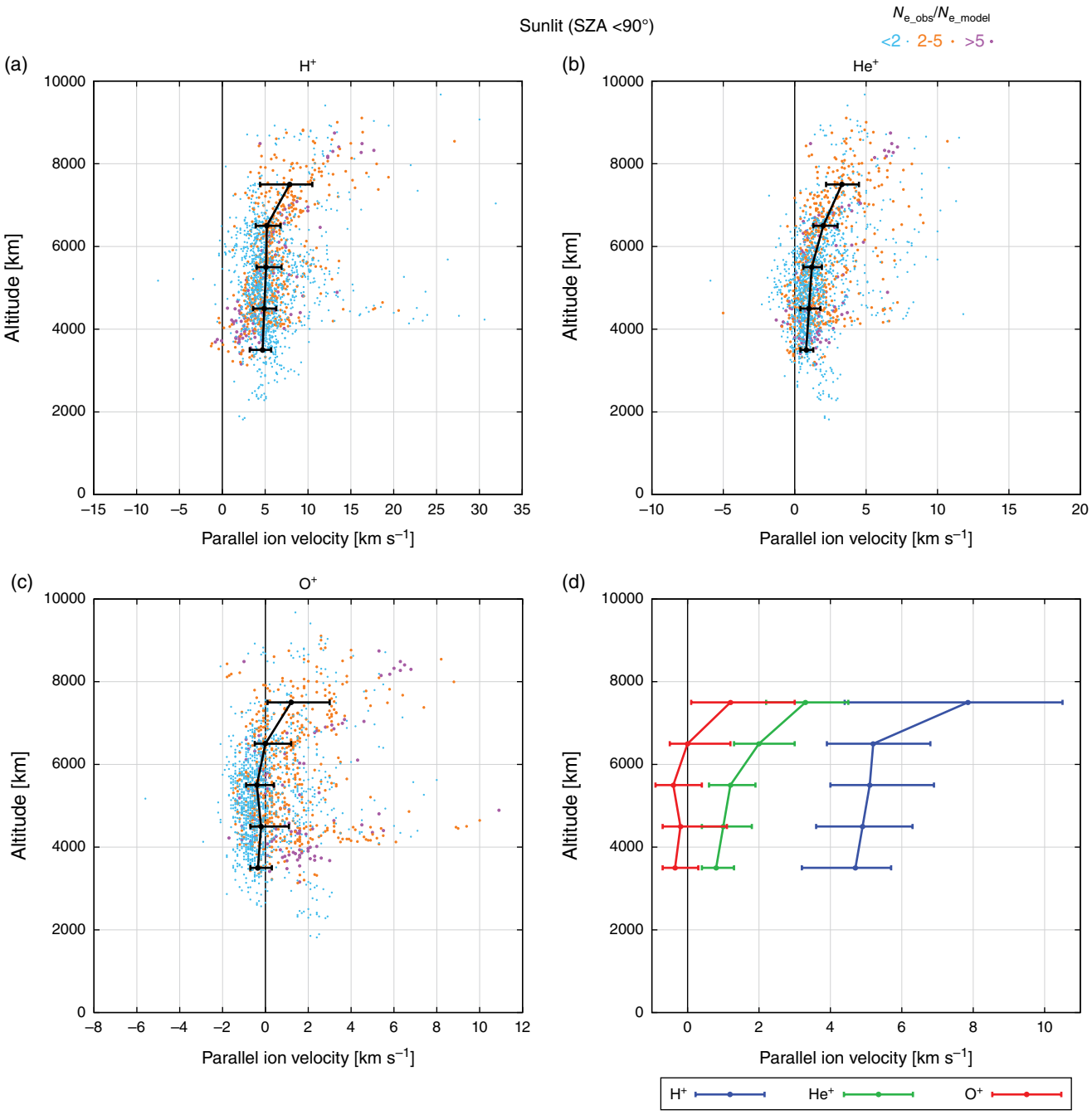

Figure 7.2 Altitude profiles of (a) H^+, (b) He^+, (c) O^+, and (d) all ion velocities under sunlit conditions (SZA <90°). Median and quartiles are plotted only when the number of data points in a given bin is larger than 100.

7.2.4. The Polar Wind Under Sunlit Conditions

The approximately zero O^+ ion velocity, on average, at least below ~7000 km altitude, supports the expectation that these O^+ ions are almost in hydrostatic equilibrium [*Kitamura et al.*, 2011]. Heating of the sunlit ionosphere by reflected photoelectrons contributes to determining the scale height of O^+ ions [*Varney et al.*, 2014] (green arrows in Figure 7.1). *Kitamura et al.* [2011] indicate that O^+ ions may be dominant up to the apogee of the Akebono satellite (10,500 km altitude) under sunlit conditions at solar maximum because there is no apparent transition of the altitudinal electron density profile.

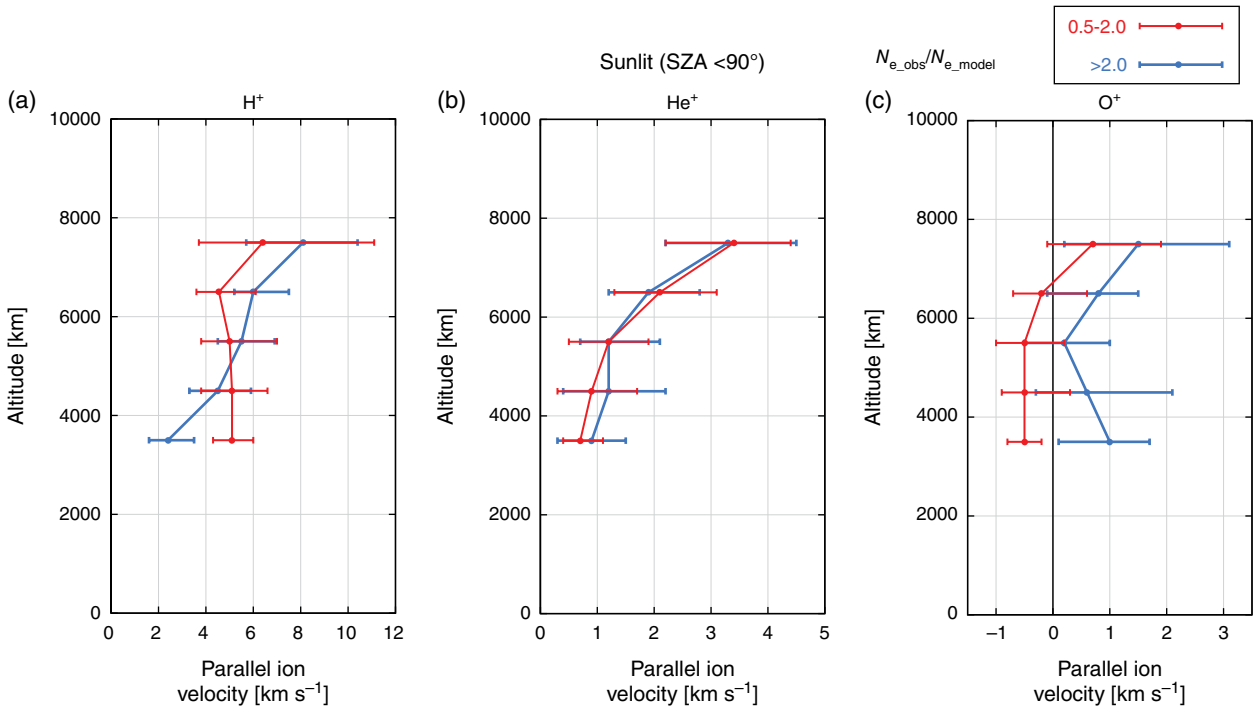

Figure 7.3 Altitude profiles of (a) H^+, (b) He^+, and (c) O^+ ion velocities under sunlit conditions (SZA <90°). Medians and quartiles for normal density cases (red lines, 0.5 ≤N_{e_obs}/N_{e_model} ≤2) and high density cases (blue lines, N_{e_obs}/N_{e_model} >2) are plotted separately only when the number of data points in a given bin is larger than 50.

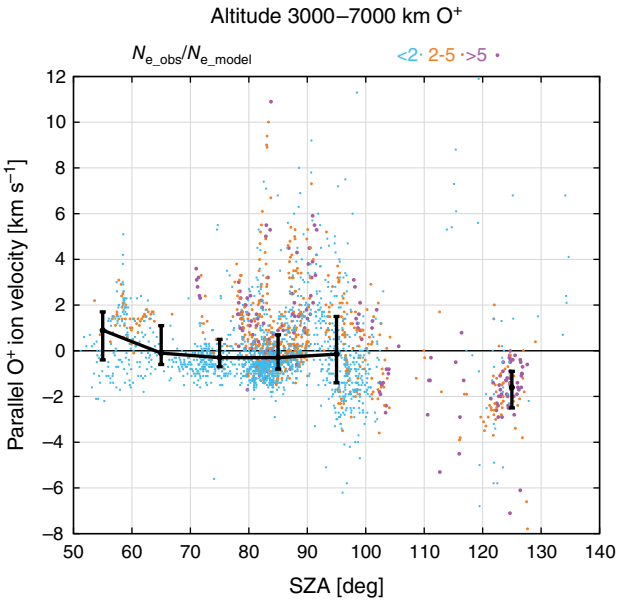

Figure 7.4 SZA distribution of O^+ ion velocities at an altitude range of 3000–7000 km. Median and quartiles are plotted only when the number of data points in a given bin is larger than 100.

To provide a balance with the median of the net escaping electron number flux (1.7×10^8 cm^{-2} s^{-1} during geomagnetically quiet periods at solar maximum [*Kitamura et al.*, 2012]) based on only using H^+ ions with a velocity of ~5 km s^{-1} at 2 R_E (Figure 7.2a), the density of H^+ ions should be ~65 cm^{-3} at 2 R_E. Note that this is an estimated upper limit, since contributions from all other ion species have been neglected. This density is almost of the same order of magnitude as the electron density under sunlit conditions at 2 R_E (~50–200 cm^{-3} [*Kitamura et al.*, 2011]). Thus, a transition from the altitude where O^+ ions are dominant to that where H^+ ions dominate may occur around 2 R_E under sunlit conditions during geomagnetically quiet periods.

Using the typical electron density (~100 cm^{-3} for SZA ~70° at 7500 km altitude [*Kitamura et al.*, 2011]) as a typical upper limit to the O^+ ion density and an upward velocity of ~0.7 km s^{-1} (Figure 7.3c for the normal density case at ~7500 km altitude), the typical upper limit to the O^+ ion flux is, on average, ~5×10^7 cm^{-2} s^{-1} (mapped to 1000 km altitude). This typical upper limit is only about one third of the polar wind ion flux estimated from photoelectron measurements [*Kitamura et al.*, 2012a, 2015]. Thus, the contribution of O^+ ions to the total ion flux in the polar cap would be limited, on average, even at solar maximum. The flux of polar wind ions is likely controlled by the reaction rate for the production of H^+ ions (i.e., the accidentally resonant charge exchange between O^+ ions and neutral H in the topside ionosphere), at least under sunlit conditions [*Richards and Torr*, 1985; *Barakat et al.*, 1987; *Kitamura et al.*, 2015].

The magnitude of the field-aligned potential drop at high altitudes would be determined mostly by the balance between the polar wind H^+ ion flux and the escape photoelectron flux [*Kitamura et al.*, 2015]. The magnitude of the potential drop controls the fraction and amount of reflected photoelectrons that precipitate to and heat the ionosphere (Figure 7.1). If this heating impacts positively on the production rate of H^+ ions (yellow arrows in Figure 7.1), negative feedback occurs, as suggested by *Kitamura et al.* [2012]. Modeling by *Richards and Torr* [1985] indicated that an increase in the scale height of O^+ ions impacts positively on the production rate of H^+ ions, while an increase in the O^+ ion density in the topside ionosphere impacts negatively on the production rate as a result of an increase in the starting altitude of H^+ ion diffusion because of a decrease in the neutral H density at the increased start altitude. Which of these impacts is stronger and whether or not the effect is significant should be studied in the future to gain a more detailed understanding of the polar wind system under sunlit conditions.

Although modeling by *Wilson et al.* [1997] and *Su et al.* [1998] indicated that an abrupt potential drop occurs at ~4–7 R_E, the location and shape of the potential drop have not been clearly determined observationally. *Moore et al.* [1999] (their Plate 2) reported sudden increases and decreases in the energy of outflowing ions at ~6–8 R_E in the polar cap. This would support the existence of an abrupt potential drop and, correspondingly, ion acceleration by this potential drop. For further confirmation, in situ measurements of electrons in the loss cone and ions with mass analysis around the potential drop will be important. If a satellite crosses an abrupt potential drop from the bottom side, the reflected photoelectron component should suddenly disappear, and all ion species should attain the same energy in the parallel direction.

The field-aligned potential drop at high altitudes is expected to cause significant outward acceleration of H^+ ions. If some O^+ ions are present around the potential drop, they will also be accelerated. This outward acceleration increases ion loss toward the distant tail and complicates trajectory calculations of outflowing ions, which are usually performed assuming equipotential field lines [e.g., *Huddleston et al.*, 2005; *Ebihara et al.*, 2006; *Haaland et al.*, 2012; *Yau et al.*, 2012].

Modeling studies predict that the H^+ ion flux decreases with increasing activity as a result of suppression of the neutral H density [*Richards and Torr*, 1985; *Barakat et al.*, 1987], although such a decrease is not identified by recent indirect measurements of the polar wind [*André et al.*, 2015; *Kitamura et al.*, 2015]. More detailed discussion about the difference between the modeling studies and observations was performed by *Kitamura et al.* [2015]. Very precise long-term direct measurements of the polar wind H^+ ion flux, which have not been available yet, are essential to identify the cause of the difference between the predictions by modeling studies and measurements, and to further assess how important the regulation by the production rate of H^+ ions is in the polar wind system. If the H^+ ion flux decreases with increasing activity as predicted, increase in the O^+ ion flux may compensate for the decrease. However, the limited O^+ ion flux from the polar cap at solar maximum that is estimated in the present study indicates that such compensation, if any, is insignificant.

A polar wind-like process, which is called the plasmaspheric refilling, also occurs in the subauroral zone (trough region). The lack of O^+ ions in the polar wind flux is consistent with the lack of O^+ ions in the plasmasphere proper [*Chappell et al.*, 1970], except for the O^+ torus, which is associated with high ionospheric electron temperature [*Horwitz et al.*, 1985]. However, on the closed magnetic field lines in the subauroral zone, thermal energy electrons and/or photoelectrons can be supplied from the opposite hemisphere. Since these electrons can compensate for photoelectron fluxes from the hemisphere, a large field-aligned potential drop, which is observed in the polar cap (on open field lines), would not be developed.

7.3. ION OUTFLOWS IN ACTIVE TIME: THE CLEFT ION FOUNTAIN

Low-energy ions that are supplied by the cleft ion fountain, which is thought to be caused by soft electron precipitation and waves in the cusp/cleft region, drift into the polar cap during geomagnetically active periods [e.g., *Lockwood et al.*, 1985; *Waite et al.*, 1985; *Kitamura et al.*, 2010a, 2010b, 2012b]. Thus, it is difficult to distinguish the effect of the polar wind from the cleft ion fountain during active periods. However, the field-aligned potential drop at high altitudes decreases in magnitude or almost disappears during large geomagnetic storms to let a larger fraction of the photoelectrons escape and to equilibrate the escape photoelectron flux with the enhanced total ion flux [*Kitamura et al.*, 2013] (Figure 7.1c). This means that the ambipolar electric field, which is the driving force of the polar wind, decays. In addition, the decrease in the magnitude of the potential drop causes a decrease in the reflected photoelectron flux, which is one of the energy inputs into the ionosphere. This would impact negatively on the development of the ambipolar electric field at low altitudes, since this causes a decrease in the ionospheric temperature. Thus, the polar wind type parallel acceleration is likely suppressed. This suppression mitigates the effect of the field-aligned acceleration on the particle trajectory calculations in active conditions, in contrast to the situation during quiet periods as discussed in Section 7.2.4.

A case study by *Kitamura et al.* [2012b] of a large geomagnetic storm reported that the perpendicular ion

temperature in the polar cap was very low (~0.03–3 eV) below ~7 R_E. Thus, the effect of local wave heating of O^+ ions in the polar cap would be weak at these altitudes.

During geomagnetically active periods, enhanced magnetospheric convection causes centrifugal acceleration [e.g., *Cladis*, 1986] in the high altitude polar cap and the lobe region to become more important, especially along field lines in the fast flow channels in the polar cap [*Nishimura et al.*, 2010, 2014; *Zou et al.*, 2014]. Since the centrifugal acceleration becomes effective at high altitudes, where the $\mathbf{E} \times \mathbf{B}$ drift velocity becomes large, during active periods, ions traveling through the polar cap are accelerated mainly by this centrifugal force, in contrast to the situation during quiet periods, when the field-aligned acceleration by electric fields would be dominant.

As discussed above, since polar wind type parallel acceleration is likely suppressed, O^+ ion supply from the polar cap ionosphere is further less likely to occur during active periods compared with quiet periods. Almost all upflowing O^+ ions observed in the high altitude polar cap and the lobe region likely come from the cleft ion fountain during active periods [e.g., *Lockwood et al.*, 1985; *Waite et al.*, 1985; *Kitamura et al.*, 2010b, 2012b; *Liao et al.*, 2012]. The plasma density in the polar magnetosphere (at a few R_E) tends to increase with increasing geomagnetic activity [e.g., *Laakso et al.*, 2002; *Nsumei et al.*, 2008; *Kitamura et al.*, 2010a, 2010b, 2012b]. The regions of the density enhancement, which correspond to the lowest energy component of the cleft ion fountain, are widely spread (on the order of 1000 km, mapped to the ionosphere) throughout the polar cap, and the duration of these density enhancements is comparable to that of the main phase of geomagnetic storms [*Kitamura et al.*, 2010a, 2010b, 2012b]. In the region of the density enhancement in the dayside polar cap at ~9000 km altitude, the very low-energy (below ~10 eV) O^+ ion flux can reach ~10^9 cm^{-2} s^{-1} (mapped to 1000 km altitude) [*Kitamura et al.*, 2010b, 2012b]. Although observations of very low-energy ions are limited, the large spatial scale, large ion fluxes, and long duration indicate a significant supply of very low-energy O^+ ions to the magnetosphere through this region. This low-energy component of the cleft ion fountain can reach the equatorial near-Earth tail region under strong convection [*Kitamura et al.*, 2010b]. Since recent observations in the plasma sheet indicate that an enhancement of the O^+/H^+ density ratio is more pronounced within ~15 R_E [*Ohtani et al.*, 2011; *Maggiolo and Kistler*, 2014], this population would be an important source of O^+ ions in the plasma sheet if this is a common feature during geomagnetic storms. Note that the ion outflow from the nightside auroral zone is another source of O^+ ions in the near-Earth plasma sheet. The fact that Earthward fast flows tend to be less O^+ rich than the surrounding plasmas [*Ruan et al.*, 2005] and fast tailward flows [*Ohtani et al.*, 2015] are also consistent with the idea that direct O^+ ion supply to the near-Earth tail region is more important compared with O^+ ion supply through the mid-tail region (i.e., the higher energy component of the cleft ion fountain).

7.4. CONCLUSIONS

We have investigated the parallel velocity of the polar wind ions in the polar cap during geomagnetically quiet periods using long-term data obtained by the Akebono satellite at solar maximum, when the impact of photoelectrons is expected to be maximal. The O^+ ion velocities were approximately zero, on average, and there is no clear apparent stable upward acceleration under sunlit conditions below ~7000 km altitude. This result supports the expectation of hydrostatic equilibrium of O^+ ions and that the scale height of O^+ ions in the polar cap is strongly controlled by solar radiation incident onto the ionosphere by changing the ion and electron temperatures in the ionosphere [*Kitamura et al.*, 2011].

In contrast, the flux of polar wind H^+ ions is likely controlled by the reaction rate for the production of H^+ ions (i.e., the accidentally resonant charge exchange between O^+ ions and neutral H in the topside ionosphere), at least under sunlit conditions. Since the upward velocity of O^+ ions are approximately zero, on average, a very limited flux of O^+ ions can be expected during geomagnetically quiet periods. The magnitude of the field-aligned potential drop at high altitudes is likely determined mostly by the balance between the escape photoelectron flux and the polar wind H^+ ion flux.

During geomagnetically active periods, the driving force of the polar wind (the potential drop) weakens so that the low-energy component of the cleft ion fountain will be of most importance for O^+ ions in the high altitude polar cap. The large spatial scale, large ion fluxes, and long duration of electron density enhancements, which likely correspond to the low-energy component of the cleft ion fountain, indicate a significant supply of very low-energy O^+ ions to the near-Earth plasma sheet through the dayside polar cap during the main phase of geomagnetic storms.

ACKNOWLEDGMENTS

The Akebono satellite project was managed by Institute of Space and Astronautical Science (ISAS), Japan Aerospace Exploration Agency (JAXA). The *Kp* and *SYM-H* indices were provided by the World Data Center (WDC) for Geomagnetism, Kyoto. The monthly mean $F_{10.7}$ solar radio flux index was provided by the National

Geophysical Data Center (NGDC) (http://www.ngdc.noaa.gov/stp/space-weather/solar-data/solar-features/solar-radio/noontime-flux/penticton/penticton_observed/listings/listing_drao_noontime-flux-observed_monthly.txt). N. K. was supported by a Research Fellowship of the Japan Society for the Promotion of Science (JSPS), JSPS KAKENHI Grant Number 24·5283. N. K. and K. S. were supported by the Geospace Environment Modeling System for Integrated Studies (GEMSIS) project of Solar-Terrestrial Environment Laboratory (STEL), Nagoya University. A. S. was supported by the Inter-university Upper atmosphere Global Observation NETwork (IUGONET) project, which is funded by the Ministry of Education, Culture, Sports, Science and Technology (MEXT), Japan.

REFERENCES

Abe, T., B. A. Whalen, A. W. Yau, R. E. Horita, S. Watanabe, and E. Sagawa (1993), EXOS D (Akebono) suprathermal mass spectrometer observations of the polar wind, *J. Geophys. Res.*, *98*, 11,191–11,203, doi:10.1029/92JA01971.

Abe, T., A. W. Yau, S. Watanabe, M. Yamada, and E. Sagawa (2004), Long-term variation of the polar wind velocity and its implication for the ion acceleration process: Akebono/suprathermal ion mass spectrometer observations, *J. Geophys. Res.*, *109*, A09305, doi:10.1029/2003JA010223.

Abe, T., Y. Ichikawa, and A. W. Yau (2005), Generation of high-density plasma in the polar cap observed by the Akebono satellite, *Adv. Space Res.*, *36*, 1872–1877, doi:10.1016/j.asr.2004.06.024.

André, M., K. Li, and A. I. Eriksson (2015), Outflow of low-energy ions and the solar cycle, *J. Geophys. Res. Space Physics*, *120*, 1072–1085, doi:10.1002/2014JA020714.

Axford, W. I. (1968), The polar wind and the terrestrial helium budget, *J. Geophys. Res.*, *73*, 6855–6859, doi:10.1029/JA073i021p06855.

Banks, P. M., and T. E. Holzer (1968), The polar wind, *J. Geophys. Res.*, *73*, 6846–6854, doi:10.1029/JA073i021p06846.

Barakat, A. R., R. W. Schunk, T. E. Moore, and J. H. Waite Jr. (1987), Ion escape fluxes from the terrestrial high-latitude ionosphere, *J. Geophys. Res.*, *92*, 12,255–12,266, doi:10.1029/JA092iA11p12255.

Carbary, J. F. (2005), A *Kp*-based model of auroral boundaries, *Space Weather*, *3*, S10001, doi:10.1029/2005SW000162.

Chappell, C. R., K. K. Harris, and G. W. Sharp (1970), A study of the influence of magnetic activity on the location of the plasmapause as measured by OGO 5, *J. Geophys. Res.*, *75*, 50–56, doi:10.1029/JA075i001p00050.

Cladis, J. B. (1986), Parallel acceleration and transport of ions from polar ionosphere to plasma sheet, *Geophys. Res. Lett.*, *13*, 893–896, doi:10.1029/GL013i009p00893.

Ebihara, Y., M. Yamada, S. Watanabe, and M. Ejiri (2006), Fate of outflowing suprathermal oxygen ions that originate in the polar ionosphere, *J. Geophys. Res.*, *111*, A04219, doi:10.1029/2005JA011403.

Horwitz, J. L., L. H. Brace, R. H. Comfort, and C. R. Chappell (1986), Dual-spacecraft measurements of plasmasphere-ionosphere coupling, *J. Geophys. Res.*, *91*, 11,203–11,216, doi:10.1029/JA091iA10p11203.

Huddleston, M. M., C. R. Chappell, D. C. Delcourt, T. E. Moore, B. L. Giles, and M. O. Chandler (2005), An examination of the process and magnitude of ionospheric plasma supply to the magnetosphere, *J. Geophys. Res.*, *110*, A12202, doi:10.1029/2004JA010401.

Khazanov, G., M. Liemohn, and T. Moore (1997), Photoelectron effects on the self-consistent potential in the collisionless polar wind, *J. Geophys. Res.*, *102*, 7509–7521, doi:10.1029/96JA03343.

Kitamura, N., A. Shinbori, Y. Nishimura, T. Ono, M. Iizima, and A. Kumamoto (2009), Seasonal variations of the electron density distribution in the polar region during geomagnetically quiet periods near solar maximum, *J. Geophys. Res.*, *114*, A01206, doi:10.1029/2008JA013288.

Kitamura, N., Y. Nishimura, T. Ono, A. Kumamoto, A. Shinbori, M. Iizima, A. Matsuoka, and M. R. Hairston (2010a), Temporal variations and spatial extent of the electron density enhancements in the polar magnetosphere during geomagnetic storms, *J. Geophys. Res.*, *115*, A00J02, doi:10.1029/2009JA014499.

Kitamura, N., et al. (2010b), Observations of very-low-energy (<10 eV) ion outflows dominated by O^+ ions in the region of enhanced electron density in the polar cap magnetosphere during geomagnetic storms, *J. Geophys. Res.*, *115*, A00J06, doi:10.1029/2010JA015601.

Kitamura, N., Y. Ogawa, Y. Nishimura, N. Terada, T. Ono, A. Shinbori, A. Kumamoto, V. Truhlik, and Jan. Smilauer (2011), Solar zenith angle dependence of plasma density and temperature in the polar cap ionosphere and low-altitude magnetosphere during geomagnetically quiet periods at solar maximum, *J. Geophys. Res.*, *116*, A08227, doi:10.1029/2011JA016631.

Kitamura, N., K. Seki, Y. Nishimura, N. Terada, T. Ono, T. Hori, and R. J. Strangeway (2012a), Photoelectron flows in the polar wind during geomagnetically quiet periods, *J. Geophys. Res.*, *117*, A07214, doi:10.1029/2011JA017459.

Kitamura, N., Y. Nishimura, M. O. Chandler, T. E. Moore, N. Terada, T. Ono, A. Shinbori, and A. Kumamoto (2012b), Storm-time electron density enhancement in the cleft ion fountain, *J. Geophys. Res.*, *117*, A11212, doi:10.1029/2012JA017900.

Kitamura, N., K. Seki, Y. Nishimura, T. Hori, N. Terada, T. Ono, and R. J. Strangeway (2013), Reduction of the field-aligned potential drop in the polar cap during large geomagnetic storms, *J. Geophys. Res. Space Physics*, *118*, 4864–4874, doi:10.1002/jgra.50450.

Kitamura, N., K. Seki, Y. Nishimura, and J. P. McFadden (2015), Limited impact of escaping photoelectrons on the terrestrial polar wind flux in the polar cap, *Geophys. Res. Lett.*, *42*, 3106–3113, doi:10.1002/2015GL063452.

Kitanoya, Y., T. Abe, A. W. Yau, T. Hori, and N. Nishitani (2011), Localized electron density enhancements in the high-altitude polar ionosphere and their relationships with storm-enhanced density (SED) plumes and polar tongues of

ionization (TOI), *Ann. Geophys.*, *29*, 367–375, doi:10.5194/angeo-29-367-2011.

Ichikawa, Y., T. Abe, and A. W. Yau (2002), Plasama density enhancements in the high-altitude polar cap region observed on Akebono, *Geophys. Res. Lett.*, *29*, 1327, doi:10.1029/2001GL013723.

Laakso, H., R. Phaff, and R. Janhunen (2002), Polar observations of electron density distribution in the Earth's magnetosphere. 1. Statistical results, *Ann. Geophys.*, *20*, 1711–1724, doi:10.5194/angeo-20-1711-2002.

Lemaire, J. F., W. K. Peterson, T. Chang, R. W. Schunk, A. R. Barakat, H. G. Demars, and G. V. Khazanov (2007), History of kinetic polar wind models and early observations, *J. Atmos. Sol. Terr. Phys.*, *69*, 1901–1935, doi:10.1016/j.jastp.2007.08.011.

Liao, J., L. M. Kistler, C. G. Mouikis, B. Klecker, and I. Dandouras (2012), Solar cycle dependence of the cusp O^+ access to the near-Earth magnetotail, *J. Geophys. Res.*, *117*, A10220, doi:10.1029/2012JA017819.

Lockwood, M., J. H. Waite Jr., T. E. Moore, J. F. E. Johnson, and C. R. Chappell (1985), A new source of suprathermal O^+ ions near the dayside polar cap boundary, *J. Geophys. Res.*, *90*, 4099–4116, doi:10.1029/JA090iA05p04099.

Maggiolo, R., and L. M. Kistler (2014), Spatial variation in the plasma sheet composition: Dependence on geomagnetic and solar activity, *J. Geophys. Res. Space Physics*, *119*, 2836–2857, doi:10.1002/2013JA019517.

Moore, T. E., M. O. Chandler, C. R. Chappell, R. H. Comfort, P. D. Craven, D. C. Delcourt, H. A. Elliott, B. L. Giles, J. L. Horwitz, C. J. Pollock, and Y.-J, Su (1999), Polar/TIDE Results on Polar Ion Outflows, in *Sun-Earth Plasma Connections, Geophys. Monogr. Ser*., *109*, edited by J. L. Burch, R. L. Carovillano, and S. K. Antiochos, AGU, Washington, D. C. doi: 10.1029/GM109p0087.

Nishimura, Y., et al. (2010), Preonset time sequence of auroral substorms: Coordinated observations by all-sky imagers, satellites, and radars, *J. Geophys. Res*., *115*, A00I08, doi:10.1029/2010JA015832.

Nishimura, Y., et al. (2014), Day-night coupling by a localized flow channel visualized by polar cap patch propagation, *Geophys. Res. Lett.*, *41*, 3701–3709, doi:10.1002/2014GL060301.

Nsumei, P. A., B. W. Reinisch, P. Song, J. Tu, and X. Huang (2008), Polar cap electron density distribution from IMAGE radio plasma imager measurements: Empirical model with the effects of solar illumination and geomagnetic activity, *J. Geophys. Res.*, *113*, A01217, doi:10.1029/2007JA012566.

Ohtani, S., M. Nosé, S. P. Christon, and A. T. Y. Lui (2011), Energetic O^+ and H^+ ions in the plasma sheet: Implications for the transport of ionospheric ions, *J. Geophys. Res.*, *116*, A10211, doi:10.1029/2011JA016532.

Ohtani, S., M. Nosé, Y. Miyashita, and A. T. Y. Lui (2015), Responses of different ion species to fast plasma flows and local dipolarization in the plasma sheet, *J. Geophys. Res. Space Physics*, *120*, 187–200, doi:10.1002/2014JA020517.

Richards, P. G., and D. G. Torr (1985), Seasonal, diurnal, and solar cyclical variations of the limiting H^+ flux in the Earth's topside ionosphere, *J. Geophys. Res.*, *90*, 5261–5268, doi:10.1029/JA090iA06p05261.

Ruan, P., S. Y. Fu, Q.-G. Zong, Z. Y. Pu, X, Cao, W. L. Liu, X. Z. Zhou, and P. W. Daly (2005), Ion composition variations in the plasma sheet observed by Cluster/RAPID, *Geophys. Res. Lett.*, *32*, L01105, doi:10.1029/2004GL021266.

Schunk, R. W. (2007), Time-dependent simulations of the global polar wind, *J. Atmos. Sol. Terr. Phys.*, *69*, 2028–2047, doi:10.1016/j.jastp.2007.08.009.

Su, Y.-J., J. L. Horwitz, G. R. Wilson, P. G. Richards, D. G. Brown, and C. W. Ho (1998), Self-consistent simulation of the photoelectron-driven polar wind from 120 km to 9 R_E altitude, *J. Geophys. Res.*, *103*, 2279–2296, doi:10.1029/97JA03085.

Tam, S. W. Y., F. Yasseen, T. Chang, and S. B. Ganguli (1995), Self-consistent kinetic photoelectron effects on the polar wind, *Geophys. Res. Lett.*, *22*, 2107–2110, doi:10.1029/95GL01846.

Tam, S. W. Y., T. Chang, and V. Pierrard (2007), Kinetic modeling of the polar wind, *J. Atmos. Sol. Terr. Phys.*, *69*, 1984–2027, doi:10.1016/j.jastp.2007.08.006.

Varney, R. H., S. C. Solomon, and M. J. Nicolls (2014), Heating of the sunlit polar cap ionosphere by reflected photoelectrons, *J. Geophys. Res. Space Physics*, *119*, 8660–8684, doi:10.1002/2013JA019378.

Waite Jr., J. H., T. Nagai, J. F. E. Johnson, C. R. Chappell, J. L. Burch, T. L. Killeen, P. B. Hays, G. R. Carignan, W. K. Peterson, and E. G. Shelley (1985), Escape of suprathermal O^+ ions in the polar cap, *J. Geophys. Res.*, *90*, 1619–1630, doi:10.1029/JA090iA02p01619.

Watanabe, S., B. A. Whalen, and A. W. Yau (1992), Thermal ion observations of depletion and refilling in the plasmaspheric trough, *J. Geophys. Res.*, *97*, 1081–1096, doi:10.1029/91JA02818.

Whalen, B. A., J. R. Burrows, A. W. Yau, E. E. Budzinski, A. M. Pilon, I. Iwamoto, K. Marubayashi, S. Watanabe, H. Mori, and E. Sagawa (1990), The suprathermal ion mass spectrometer (SMS) onboard the Akebono (EXOS-D) satellite, *J. Geomag. Geoelectr*., *42*, 511–536.

Wilson, G. R., G. Khazanov, and J. L. Horwitz (1997), Achieving zero current for polar wind outflow on open flux tubes subjected to large photoelectron fluxes, *Geophys. Res. Lett.*, *24*, 1183–1186, doi:10.1029/97GL00923.

Yau, A. W., T. Abe, and W. K. Peterson (2007), The polar wind: Recent observations, *J. Atmos. Sol. Terr. Phys.*, *69*, 1936–1983, doi:10.1016/j.jastp.2007.08.010.

Yau, A. W., A. Howarth, W. K. Peterson, and T. Abe (2012), Transport of thermal-energy ionospheric oxygen (O^+) ions between the ionosphere and the plasma sheet and ring current at quiet times preceding magnetic storms, *J. Geophys. Res.*, *117*, A07215, doi:10.1029/2012JA017803.

Zou, Y., Y. Nishimura, L. R. Lyons, E. F. Donovan, J. M. Ruohoniemi, N. Nishitani, and K. A. McWilliams (2014), Statistical relationships between enhanced polar cap flows and PBIs, *J. Geophys. Res. Space Physics*, *119*, 151–162, doi:10.1002/2013JA019269.

8

Ionospheric and Solar Wind Contributions to Magnetospheric Ion Density and Temperature throughout the Magnetotail

Michael W. Liemohn and Daniel T. Welling

Video of Yosemite Talk, URL: http://dx.doi.org/10.15142/T3D596

ABSTRACT

The coupled codes within the Space Weather Modeling Framework are used to assess the relative contributions of solar wind and ionospheric origin protons to geospace. The study employs both the multispecies and multifluid versions of the magnetohydrodynamic (MHD) model to investigate this issue. During southward interplanetary magnetic field (IMF), the central plasma sheet is dominated by ionospheric material entering near the midnight meridian, with only a small and hot contribution from the solar wind. During northward IMF, solar wind entry on the dayside flanks allows for this population to dominate the magnetospheric ion density and provide a cold, dense population to near-Earth space. However, the ionosphere still supplies a significant minority fraction to the magnetotail density. For both IMF conditions, the multispecies simulation has similar total density (n) and temperature (T) values, but the species-dependent properties are quite different. The multifluid result reveals distinct characteristics, which could be used by observational studies to identify source regions. The timing to reach steady state is very quick when the turning is southward, removing the preexisting configuration in the tail within 2 hours, but takes ~8 hours to reach a quasi-steady-state situation after a northward turning.

8.1. INTRODUCTION

The balance between solar wind entry and ionospheric outflow at supplying the magnetosphere with plasma has been investigated for many years. *Moore et al.* [1995] provide a clear review of early understanding of these relative contributions, defining the term geopause for the boundary between ion populations dominated by the Earth's upper atmosphere (inside the geopause) and the solar wind (beyond this surface). Note that the geopause is not the same as the magnetopause, which is the magnetic boundary between the Earth's field and the IMF. The two can be very different, with solar wind entry causing the geopause to shrink well inside of the magnetopause or, conversely, lobal winds from the ionosphere raining onto the plasma sheet beyond the tail reconnection line and extending the geopause far beyond the magnetopause.

Regarding ionospheric ions, the amount of O^+, which is distinctly of ionospheric and not solar wind origin, within the plasma sheet has been shown to change with magnetic activity [e.g., *Young et al.*, 1982; *Lennartson and Shelley*, 1986; *Daglis et al.,* 1993]. Outflow from the high latitude ionosphere changes with solar wind dynamic pressure [e.g., *Moore et al.*, 1997], solar wind electric field [*Cully et al.*, 2003], IMF B_z polarity [*Lennartsson et al.*, 2004], and Poynting flux into the ionosphere [*Strangeway et al.*, 2005], and the amount of capture of ionospheric

Department of Climate and Space Sciences and Engineering, University of Michigan, Ann Arbor, MI, USA

Magnetosphere-Ionosphere Coupling in the Solar System, Geophysical Monograph 222, First Edition.
Edited by Charles R. Chappell, Robert W. Schunk, Peter M. Banks, James L. Burch, and Richard M. Thorne.

material within the plasma increases with activity [e.g., *Liemohn et al.*, 2005, 2007; *Moore et al.,* 2005b].

Several studies, however, show that the solar wind can dominate the plasma sheet composition, with He^{++} serving as a unique solar origin tracer within the magnetosphere [e.g., *Phan et al*., 2000; *Lennartsson*, 2001]. The density in the plasma sheet has been strongly correlated with solar wind density [e.g., *Borovsky et al*., 1998; *McComas et al.*, 2002], especially during northward IMF when superdense plasma sheet conditions arise [e.g., *Thomsen et al*. 2003; *Lavraud et al.*, 2005]. Solar wind capture into the magnetosphere on the dayside during northward IMF conditions has been documented in several observational studies [e.g., *Song and Russell*, 1992; *Le et al.*, 1996; *Onsager et al*., 2001; *Lavraud et al.*, 2006a, 2006b].

Numerical modeling has been used to examine the physical processes leading to these observational findings of plasma sheet composition. *Walker et al.* [1999] provides a thorough review of the early studies, for which the dominant view was that solar wind entry through the lobes controlled plasma sheet density. Other studies challenged this view, however, in particular with the development of multi-species and multifluid MHD models. The former treatment has separate continuity equations for each ion species but a single set of momentum and energy equations, while the latter uses a full set of Euler equations for each ion species. *Winglee* [1998, 2003] and *Winglee et al.* [2002] showed that ionospheric outflow was a large contributor to the plasma content in the magnetosphere, presenting the changes to the geopause, defined either by density or pressure contribution, as a function of outflow and solar wind conditions. These breakthrough studies were followed by others that used test particle tracing through dynamically varying but single-fluid MHD results [e.g., *Moore et al.*, 2005a, 2005b; *Peroomian et al*., 2007], revealing the specific ionospheric locations supplying the plasma sheet with H^+ and O^+ (a location that shifts tailward with higher outflow initial energy) as well as the ubiquitous nature of the solar wind entry into the magnetotail.

Many MHD simulations have used and still employ a passive inner boundary condition, for which the density is nonzero, but the radial velocity is set to zero (see *Welling and Liemohn* [2014] for a complete discussion). MHD models have become more sophisticated in their treatment of the ionospheric outflow boundary conditions. For instance, *Glocer et al.* [2009a] described a hydrodynamic polar wind outflow model (PWOM) that provides a spatially and temporally varying ionospheric outflow source to the magnetosphere. *Welling et al.* [2011] and *Ilie et al*. [2015] showed that PWOM outflow calculations have a huge influence on the resulting near-Earth ion composition and can explain the observed increase in inner magnetospheric O^+ during storms. *Wiltberger et al.* [2010] injected low-energy O^+ from the dayside cusp region, showing that it had significant effects on the magnetospheric configuration by bringing the tail reconnection line Earthward and lowering the cross polar cap potential. *Brambles et al.* [2010] employed the empirical *Strangeway et al.* [2005] relationship between Poynting flux and outflow, finding that steady driving can cause oscillatory magnetospheric behavior due to this causally driven ionospheric boundary condition. As a final example, *Damiano et al.* [2010] and *Welling and Liemohn* [2014] demonstrated that solar wind pressure can drive ionospheric outflow, as seen in the *Moore et al.* [1997] measurements.

The study by *Welling and Ridley* [2010] conducted a series of numerical experiments to explore the development of the plasma sheet composition under a variety of solar wind driving conditions. That study used multi-species MHD (separate continuity equations but a combined momentum and energy equation set) with two proton populations, one from the solar wind and another from the ionosphere, confirming that the ionospheric source dominates the plasma sheet density for southward IMF but that the solar wind source is the most prevalent source for northward IMF. This approach, however, could not fully explain temperature dependencies in the tail because of the combined energy equation. This is an important and unresolved question, though, because gradient-curvature drift is directly proportional to particle energy [e.g., *Ejiri*, 1978]. The delivery of the material to the inner magnetosphere, therefore, depends greatly on the temperature of the near-Earth plasma sheet [e.g., *Thomsen et al.*, 1998, 2003; *Garner,* 2000; *Ebihara and Ejiri*, 2000; *Liemohn et al*., 2008], with the formation of nose structures in the tens of keV range by those particles convecting farthest inward [e.g., *Smith and Hoffman*, 1974; *Ejiri et al.*, 1980; *Ganushkina et al.*, 2001; *Lavraud and Jordanova*, 2007]. Moreover, the use of multispecies MHD does not allow for coincident but counterstreaming ion populations, which was shown to be a limitation for the development of plasma in the mantle [e.g., *Welling and Liemohn*, 2014]. It is useful, therefore, to further explore this question and resolve the dependence on near-Earth velocity and temperature with respect to plasma source.

The present study continues the theme of *Welling and Ridley* [2010] by using a multi-fluid MHD approach to model the magnetosphere. Identical idealized driving conditions are used here, with the resulting plasma sheet differentiated not only in density but also in velocity and temperature. These results are examined and discussed and placed into the context of previous studies, especially those of *Welling and Ridley* [2010].

8.2. METHODOLOGY

This study follows the methodology of *Welling and Ridley* [2010] in that it employs the Space Weather Modeling Framework (SWMF) [*Toth et al*., 2005], a code

structure that couples together distinct scientific numerical tools into a unified simulation. Specifically, only two models are used in this calculation set, the Block Adaptive Tree Solar Wind Roe-type Upwind Scheme (BATS-R-US) MHD code [*Powell et al.*, 1999] and an ionospheric electric potential solver [*Ridley and Liemohn*, 2002; *Ridley et al.*, 2004].

In addition to using the multispecies version of BATS-R-US in which several ion species are calculated with different continuity equations but a single set of momentum and energy equations [e.g., *Ma et al.*, 2002], this study will also use the multifluid version of the code that uses distinct sets of the Euler equations for each ion species [e.g., *Glocer et al.*, 2009b; *Dalal et al.*, 2011]. Results from these two versions of the BATS-R-US code will be compared and discussed in the following sections. Only two ion species will be included in the simulations: protons of solar wind origin and protons of ionospheric origin. The former is set with a boundary condition flowing into the simulation domain from the +X boundary while the latter is defined with a density value at the inner boundary of the simulation domain, which is a sphere of radius 2.5 R_E centered on the Earth. The first is a driven boundary condition in that there is an imposed velocity with a large and negative X component (i.e., the upstream solar wind flow) while the second is a passive boundary condition requiring diffusion across one or more grid cells before field-aligned flows extract the ions into other parts of the simulation domain. *Welling and Liemohn* [2014] showed that this passive outflow roughly resembles a physically driven ionospheric outflow as forces within the MHD simulation domain create large outflows in certain spatial locations and suppress outflow in other regions. Several studies have used the passive inner boundary condition with high success in explaining observed geospace phenomena, using the single-fluid [e.g., *Zhang et al.*, 2007; *Ilie et al.*, 2010a, 2010b; *Ridley et al.*, 2010], multispecies [e.g., *Glocer et al.*, 2009a; *Welling and Ridley*, 2010; *Welling et al.*, 2011], and multifluid [e.g., *Glocer et al.*, 2009b; *Yu and Ridley*, 2013; *Ilie et al.*, 2015] versions of the BATS-R-US code within the SWMF. It should be noted that ionospheric oxygen ions are not included in this study.

The rest of the numerical set up for the simulations is exactly the same as that described by *Welling and Ridley* [2010]. The runs use a Rusanov solver with the monotonized central limiter, which is a blend between the minmod and superbee flux limiters. The minmod limiter is robust but diffusive and is used near shocks and other steep gradients in the state variables while the superbee limiter is nondiffusive but less stable and is used everywhere else in the simulation domain. The grid resolution varies from 1/8 R_E near the Earth and in regions of interest all the way up to 8 R_E grid cells a large negative X values far from the central tail region. See Figure 1 of *Welling and Ridley* [2010] for a schematic of the grid resolution as a function of spatial location. The resulting grid set up yields a total of 1.9 million grid cells. The time step is allowed to vary to maintain explicit time stepping stability, usually in the 1–5 s range throughout the simulations conducted for this study in order to focus the comparison on the two H^+ sources and their fate within the magnetosphere.

The boundary conditions to be used in these simulations follow. All simulations will have a solar wind density and velocity of 8.7 cm^{-3} and 450 km s^{-1} and an inner boundary density held constant at 28 cm^{-3}. The first run to be discussed starts with a southward IMF of $B_Z = -10$ nT for 4 hours and then flips it northward to $B_Z = +10$ nT for an additional 8 hours. A second simulation will reverse this process, starting with northward IMF for 8 hours and then instantaneously flipping the IMF to a southward configuration and holding it there for 4 hours.

8.3. RESULTS

Figures 8.1 and 8.2 show the results of using the multispecies (lower row) and multifluid (upper row) MHD models in the SWMF for northward IMF (left column) and southward IMF (right column). The color quantity shown in these plots is the percent of the density attributable to the solar wind source term, with red indicating high solar wind relative content and blue showing regions dominated by the ionospheric H^+ source. The values are shown at the end of the simulation intervals for each of the IMF conditions (i.e., at or close to steady state values). For Figure 8.1, the values are shown in the equatorial plane. The black lines on the plots are flow traces, connecting the components of these vectors in the equatorial plane, and the arrows indicate flow direction along these lines (with the arrow size indicating relative flow speed). For Figure 8.2, the values are shown in the noon-midnight meridional plane. The black and white lines show magnetic field traces in this plane, connecting the components of these vectors in the Y = 0 plane, with the black lines indicating IMF or open field lines and the while lines showing closed field lines with both ends connecting to Earth.

There are several key features to notice in these plots. For southward IMF, the key feature is that the magnetosphere is dominated by the ionospheric source. In particular, near-Earth space and the central plasma sheet region contain mostly ionospheric ions, while the solar wind dominates near the flanks. In the central meridian of the magnetotail, only a small percentage of the total plasma density is from the solar wind as a bit of solar wind enters the magnetosphere from the mantle through nightside reconnected field lines.

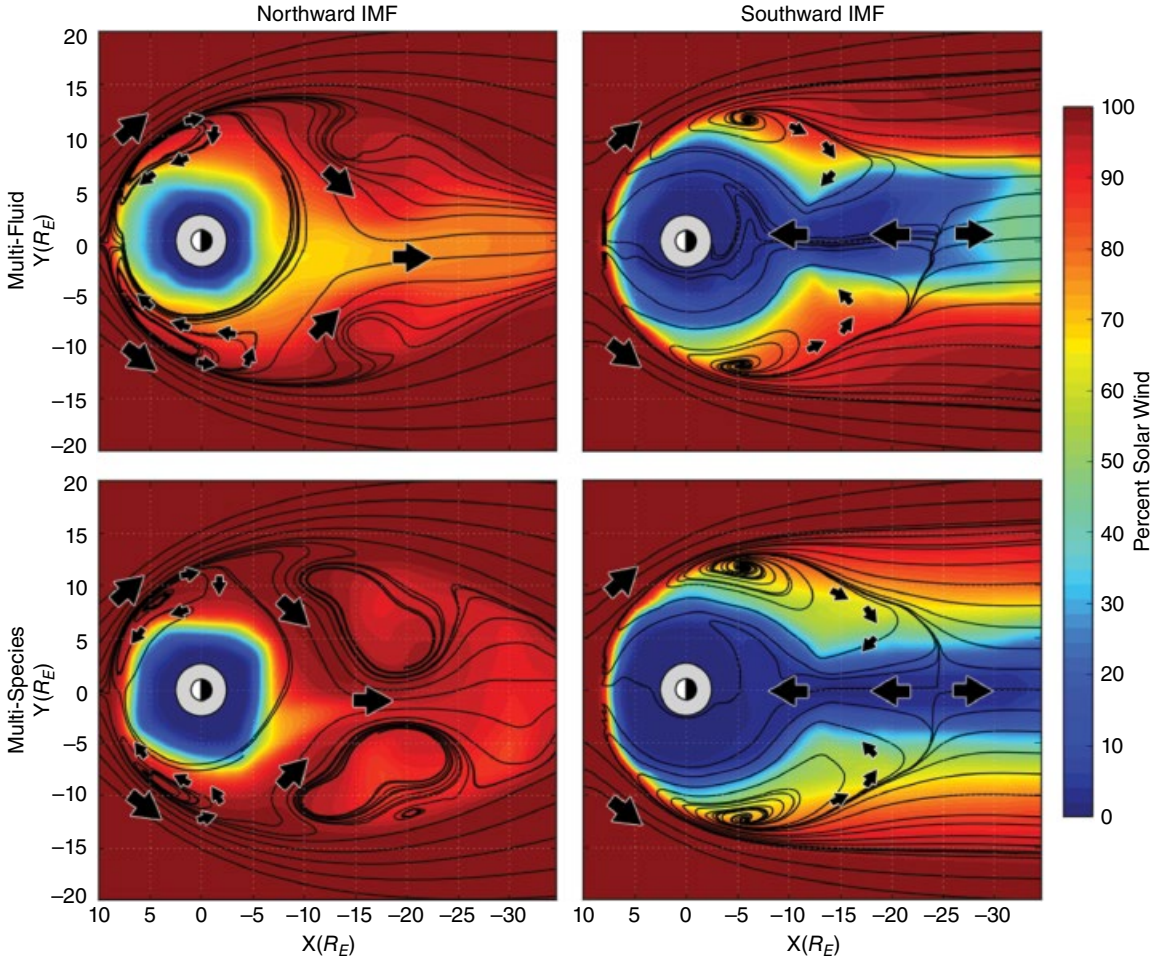

Figure 8.1 Equatorial plane (x-y in GSM) maps of percent solar wind during northward IMF (left column) and southward IMF (right column) with the multifluid MHD model (top row) and multispecies MHD model (bottom row). The view is from over the North Pole with the Sun to the left. Blue represents ionospheric source dominance, and red signifies dominance by the solar wind source. The black links are flow streamtraces with the arrows indicating flow direction. The origin of the axes is the Earth and a gray region inside the MHD simulation domain.

For northward IMF, the magnetosphere is dominated by the solar wind source. Entry into the magnetosphere is on the dayside, circulating into the plasma sheet from the flank regions between X = 0 and -10 R_E, as seen in the streamlines in Figure 8.1. This flow then bifurcates, with most of the plasma flowing tailward but a significant fraction circulating sunward or lingering in the near-Earth nightside region. The central meridian in the tail is mostly flowing downtail away from Earth, with some ionospheric source contribution to the total plasma density.

In comparing the multifluid results with those from the multispecies run, the southward IMF figures look quite similar. The multifluid setup produces a bit more ionospheric contribution to the magnetotail flank regions (yellow instead of red color) than the multispecies result but also more solar wind contribution to the central meridian densities (green-yellow instead of blue color).

For the northward IMF case, there are also similarities and differences between the multifluid and multispecies results. The main difference is that the multifluid simulation has more ionospheric contribution in the central meridian of the magnetotail (yellow instead of red color). The inner magnetospheric region and high-latitude magnetosphere, however, are quite similar between the two simulations.

To investigate the timing of how these steady state scenarios arise, Figures 8.3 and 8.4 show percent solar wind values as a function of time for several locations in the near-Earth magnetotail (X values from -5 to -15 R_E). Each panel shows values in the equatorial plane for Y values between -10 and +10 R_E. Time runs along

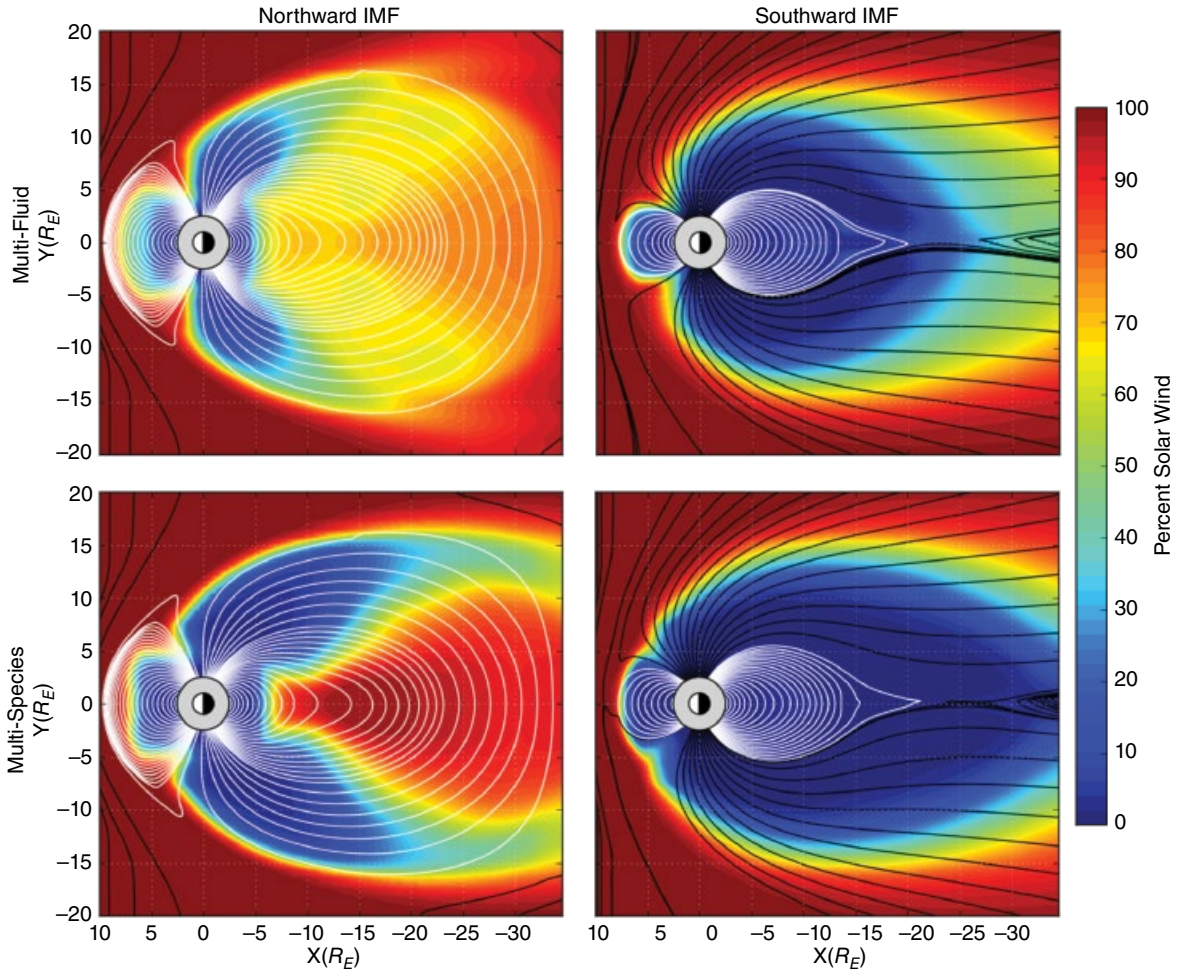

Figure 8.2 Noon-midnight meridian (x-z plane in GSM) values of percent solar wind. The layout and color scheme are the same as in Figure 8.1, except that the view is from dusk with the Sun to the left. The lines are magnetic field traces in the plane, with white designating closed field lines and black indicating open or purely IMF field lines.

the x-axis in hours with the vertical white dashed line showing the IMF turning. In Figure 8.3, this is the south-to-north IMF turning occurring at t = 4 h, while in Figure 8.4, this is the north-to-south IMF turning at t = 8 h. Initialization transients in the simulation make the first few hours of each simulation meaningless, so the timelines of the two figures start close to the steady state solution for the first IMF value and then show the transition to the other IMF setting.

There are several noteworthy features of the south-to-north IMF turning (Figure 8.3). One is that there are transient features of the northward IMF turning that greatly influence the compositional nature of the near-Earth plasma sheet but that do not last more than about an hour, for instance, the sudden appearance of solar wind dominance at X = -15, Y = 0 (last panel), about 40 minutes after the IMF turning. This burst of solar wind material only lasts for 20 minutes and then it is gone. The longer-lasting change of composition from ionospheric to solar wind dominance fills in slowly from the flanks. This solar wind infiltration takes hours, reaching a quasi steady state after perhaps 5 hours, with slow and subtle changes still occurring many hours after this. By the end of the simulation interval, the solar wind source reaches ~60% contribution at geosynchronous location near midnight (X = -6.6, Y = 0). Also note that there is an asymmetry to the ionospheric contribution, with the southward IMF causing a slightly post-midnight skew to the region of ionospheric dominance while the northward IMF driving has a slight pre-midnight skew to the ionospheric contribution to the tail density.

The north-to-south transition (Figure 8.4) shares some features with the S-to-N turning but has important distinctions. As in Figure 8.3, there are transient features in the compositional maps that last about an hour after the IMF turning. Once these transients are cleared, however,

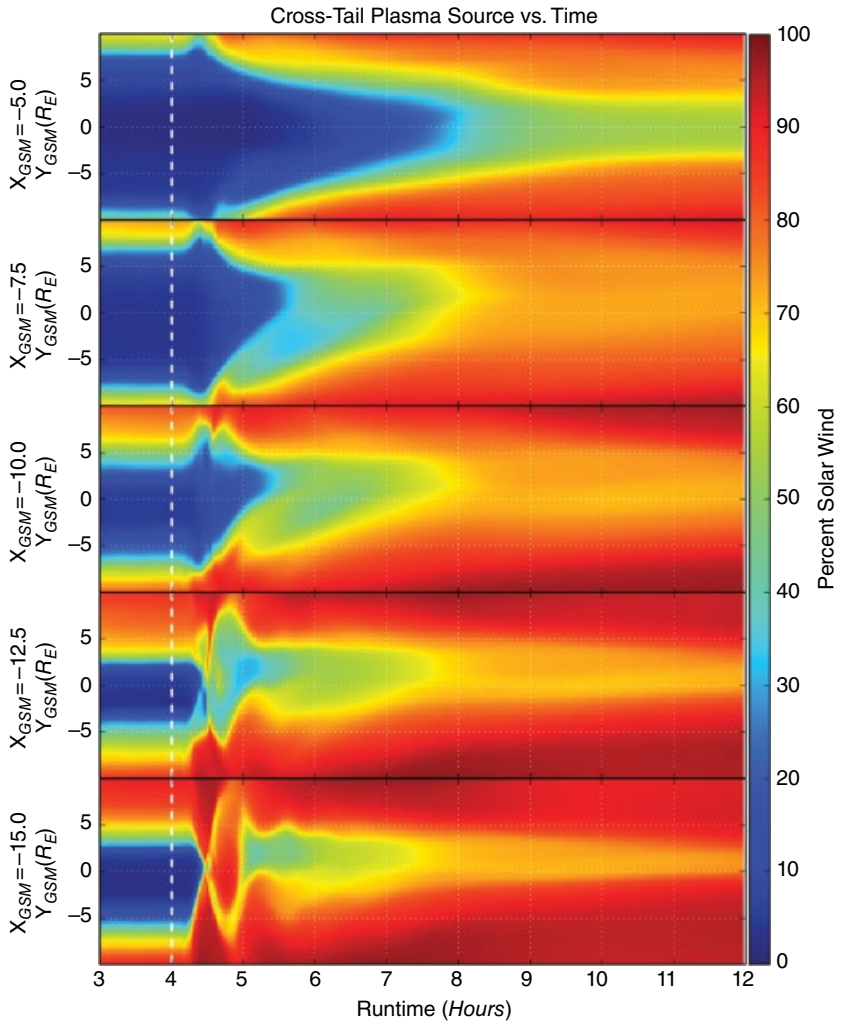

Figure 8.3 Percent solar wind at several downtail XGSM locations as a function of time and YGSM (all values taken in the equatorial plane at ZGSM=0). The IMF turns from south to north at t=4 h.

the steady state source composition is attained much faster than for the northward turning. A steady-state scenario is reached within 2 hours after the southward turning.

Another result to consider is the temperature in the equatorial plane. Figure 8.5 shows the temperature in units of keV in the Z = 0 plane for the north IMF (left column) and south IMF (right column) steady state scenarios. The top two rows are for the multifluid simulation, showing T for the solar wind-origin and ionosphere-origin plasma populations, respectively. The bottom row shows T from the multispecies simulation. Note that the color bar is on a logarithmic scale ranging from 10 eV to 20 keV.

There are several very interesting features to point out in the panels of Figure 8.5. The first thing to note is the similarity between the three plots within a column. For north IMF (left column), all three plots show the same basic features, with very cold T upstream of the bow shock, higher values of 100 s of eV in the magnetosheath region, and even higher T within the magnetosphere, regardless of the origin of the ions or the simulation setup. Within the magnetosphere, T decreases with distance away from Earth, but this gradient is not that large, changing from T values in the inner magnetosphere, around geosynchronous orbit distance, of 1–2 keV and dropping to a few 100 eV in the midtail region at X = -20 R_E. For south IMF (right column), again, all three panels show a similar overall temperature trend. They all have very cold T in the upstream region, then a hotter T of 100 s of eV in the magnetosheath, a T gradient with |Y| across the tail peaking in hot region of several keV along the Y ~ 0 central meridian of the magnetotail, and a very hot inner magnetospheric region with T values above 5 keV. For both the northward and southward IMF cases, the multispecies temperature values throughout the equatorial

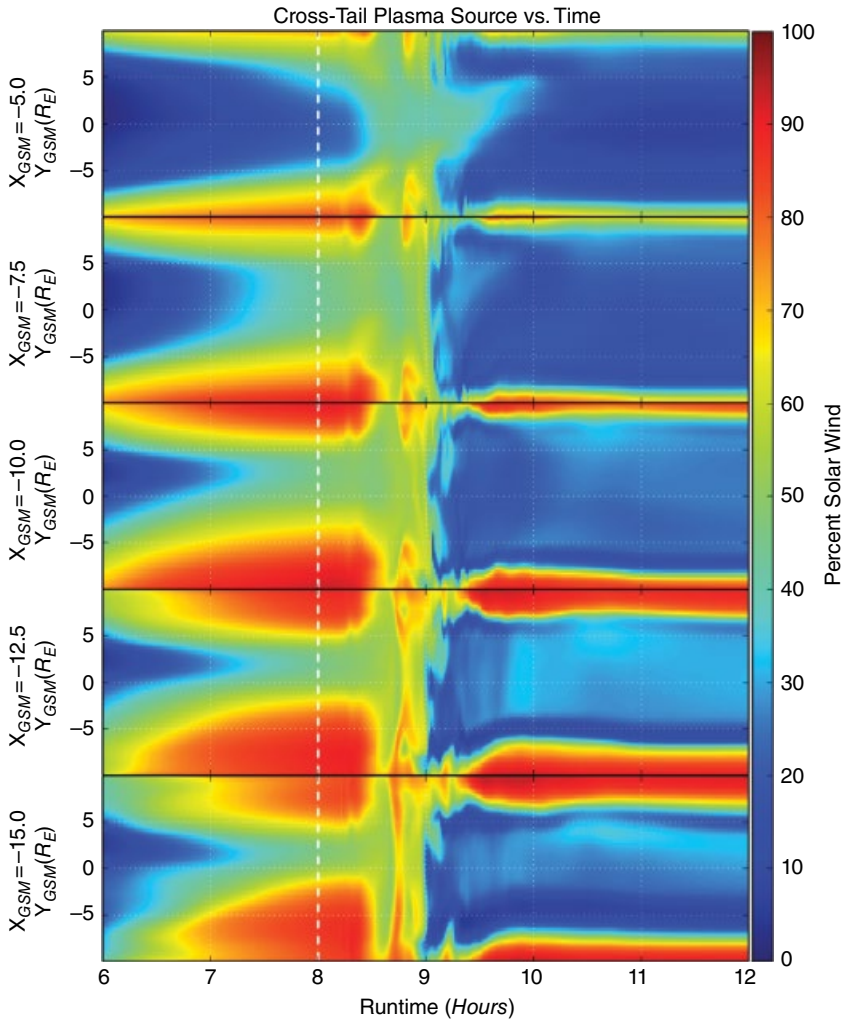

Figure 8.4 Same as Figure 8.3 except for a simulation with a north-to-south IMF turning at t=8 h.

plane (lower panels) are between the temperatures of the two species in the multifluid results.

In addition to the above-mentioned similarities, Figure 8.5 shows that the temperature of the ions from the two sources can be rather different. For northward IMF, the solar wind-origin plasma within the magnetosphere is cooler than the ionospheric-origin plasma. For southward IMF, though, the opposite is true, with the solar wind-origin plasma reaching much higher temperatures than the ionosphere-origin ions.

There are also similarities and differences between the two IMF driving conditions. For instance, both runs yield temperatures that increase closer to the Earth, as expected from adiabatic energization. Another similarity is the upstream and magnetosheath temperatures. As for differences, the magnetospheric temperatures are significantly lower in the north IMF result than the south IMF case.

To get a more quantitative analysis of the compositional and temperature changes in the tail, Figure 8.6 shows line plots of the n and T at $X=-7$, $Y=0$ R_E as a function of time for the south-to-north IMF turning simulation. In Figure 8.6a, the results for the two ion species are shown in color, with blue indicating the ionospheric source fluid and red showing the solar wind source results at this location. Also plotted are the combined density and temperature from the two simulations (total and weighted average, respectively) in the gray lines. The multifluid results are shown as solid lines, and the multispecies densities are given with the dashed lines. For the temperature plot in Figure 8.6b, the color and line style scheme is the same, except there are not separate temperatures for the two sources from the multispecies simulation.

These line plots clearly show the switch from ionospheric to solar wind dominance in near-Earth space. It also shows a profound influence on temperature. During southward IMF, both n and T are dominated by the ionospheric source, with very little solar wind source at this

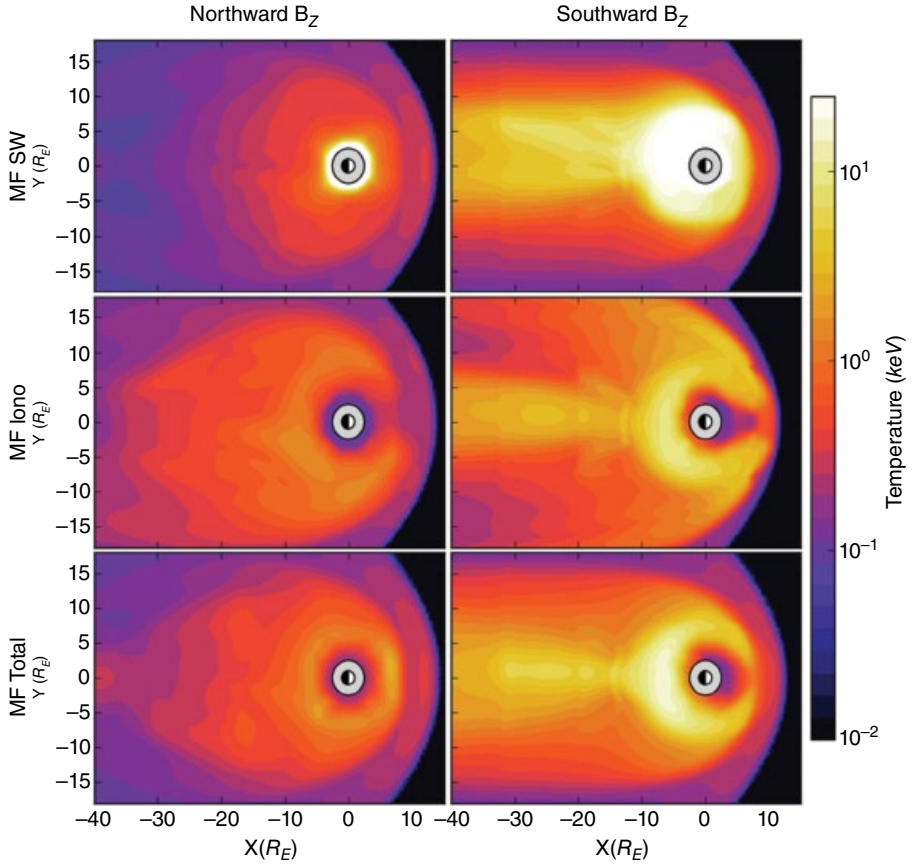

Figure 8.5 Equatorial plane temperatures for northward IMF (left panel) and southward IMF (right panel). The top two rows are from the multifluid simulation, showing the T values for the solar wind-origin and ionospheric-origin populations, respectively, while the lowest row shows the temperature from the multispecies simulation. The view is from over the North Pole with the Sun to the right. Note that the color bar is logarithmic and in units of keV.

location at the inner edge of the nightside plasma sheet. During northward IMF, n and T are dominated by the solar wind source; there is still a significant amount of ionospheric material but now even more solar wind ions are present.

Figure 8.6 shows that the ionospheric ion density is rather constant throughout the simulation, regardless of IMF orientation. There are small variations, especially after the IMF turning, but the ionospheric density at this location hovers between 1.5 and 2 cm^{-3} for the multifluid run and 0.8 to 1.2 cm^{-3} for the multispecies run. The ionospheric-origin temperature in the multifluid result is not constant across the IMF turning, however, dropping from ~8 keV during the southward IMF interval to ~2 keV after the switch to northward IMF.

The changes seen in the solar wind values in Figure 8.6 are more dramatic, with large differences in both n and T with the IMF turning. With the switch from south to north IMF, the solar wind-source density at this location rises from less than 0.1 cm^{-3} to several cm^{-3}, and in fact is still steadily rising at the t = 8 h end of the graph. Conversely, the solar wind-source population temperature (in the multifluid run) plunges from 25–30 keV down to ~1 keV and then hovers at this value for the remainder of the simulation.

In comparing the multifluid to multispecies simulation results, the same general features are seen during this IMF turning interval. For instance, the density steadily rises and the temperature steadily falls after the switch to northward IMF. There are some key differences, however. One is that there is consistently less density in the multispecies simulation results than from the multifluid simulation. Another difference is that the average temperature is higher in the multispecies results than in the multifluid calculation.

8.4. DISCUSSION

As expected from previous studies, it is clear that the plasma sheet is profoundly different under southward and northward IMF conditions and that the relaxation time for the plasma sheet to reach a steady state is very

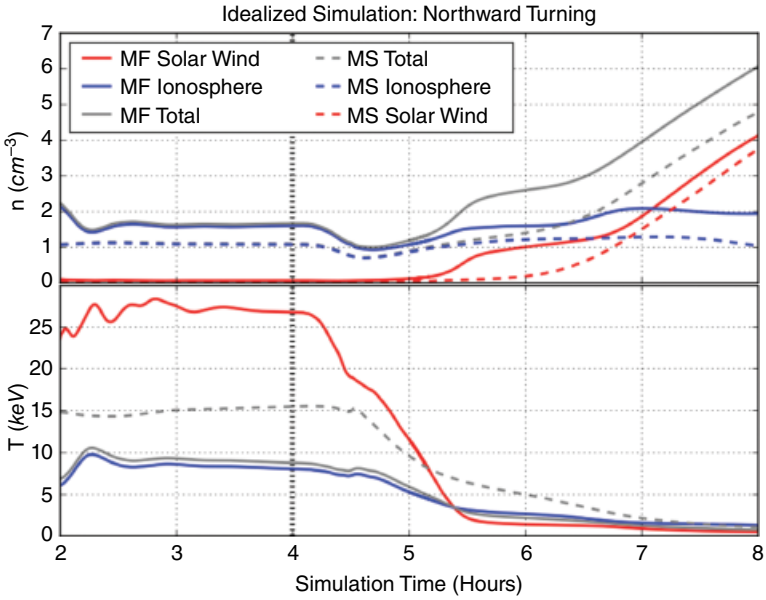

Figure 8.6 Density and temperature at x=-7 R_E along the X_{GSM} axis as a function of time from both the multifluid and multispecies MHD simulations. The red and blue curves are solar wind and ionospheric source values, respectively, from the multifluid (solid lines) and multispecies (dashed lines) runs, and the gray lines are the combined values from the multifluid (solid) and multispecies (dashed) simulations. The northward turning of the IMF occurs at t=4 h, as indicated by the vertical dotted line.

different between the two driving scenarios. Under southward IMF (set to $B_Z = -10$ nT for these simulations), the ionospheric source of H^+ dominates the composition of the central meridian of the magnetotail and the temperatures are relatively hot (above 5 keV). The plasma is convected relatively fast toward the Earth, with subsequent adiabatic energization occurring along the way. The dearth of H^+ ions of solar wind origin in the near-Earth plasma sheet is because only a small fraction of the plasma in the mantle convects across the magnetopause boundary or is captured onto closed field lines after reconnection in the tail. It should be noted that the multifluid approach allows for counterstreaming velocities for the two ion populations in the cusp, so the solar wind ions penetrate more deeply in this region and therefore more robustly fill the mantle just beyond the magnetotail lobes. The multispecies simulation does not allow for this intermixing in the cusp region and inhibits the solar wind from filling the mantle. Similarly, while some solar-origin plasma enters the plasma sheet on the flanks, it circulates at large |Y| values and does not easily reach the inner magnetosphere. The mantle protons that enter the magnetosphere at the nightside reconnection line, however, are dramatically energized by the long drift path through the magnetotail toward the Earth. The ionospheric-origin plasma, in contrast, joins the Earthward flow at essentially all locations and downtail distances of the plasma sheet, resulting in a broad mixture of attained energization for this population. Therefore, the solar-origin component of the plasma near geosynchronous orbit is very hot relative to the dominant ionospheric-origin plasma.

During northward IMF (set to $B_Z = +10$ nT in these simulations), the solar wind H^+ source dominates the composition everywhere in the plasma sheet, and the temperatures are much cooler (below 2 keV). The reduced convection in the magnetotail means that particles are not pushed across magnetic field isocontours and adiabatically energized, so the temperatures remain quite low. For the solar-origin plasma near geosynchronous orbit seen in Figure 8.6, this material enters the magnetosphere on the dayside and drifts inward from the flanks toward the Y = 0 meridian in the region from X = 0 to −10 R_E. This drift is along magnetic field isocontours, shown clearly by the streamtraces in Figure 8.1, and so the plasma drifts without much additional energy gain and retains its magnetosheath temperature of ~1 keV.

In the simulations presented here, the geophysical and solar wind driving conditions are steady and idealized, with the dipole aligned with the Z axis and the IMF directed purely southward or northward (± 10 nT). The resulting entry mechanism for this condition is double lobe reconnection, which has been observationally shown to occur regularly for such configurations [e.g., *Song and Russell*, 1992; *Fuselier et al.*, 1997; *Øieroset et al.*, 2005; *Lavraud et al.*, 2006a, 2006b]. It is also very similar to the

finding of double-lobe reconnection in global MHD simulations by *Li et al.* [2005]. This does not preclude the possibility of Kelvin-Helmholtz instabilities causing solar wind entry along the flanks during northward IMF [e.g., *Fujimoto et al.*, 1998; *Hasegawa et al.*, 2004]. Both mechanisms result in solar-origin plasma inside the magnetopause in the plasma sheet flanks between $X = 0$ and $-10\ R_E$. From this location, the plasma drifts azimuthally to the near-Earth nightside plasma sheet and forms the cold, dense plasma sheet.

It is interesting to note that the density of the ionospheric-origin H^+ in the near-Earth plasma sheet (seen in Figure 8.6a) is relatively constant regardless of IMF direction. In the southward IMF case, the ionospheric material drifts farther downtail before reaching the plasma sheet and eventually drifting back toward the Earth. For northward IMF, this downtail flow within the lobes is much weaker, resulting in more ionospheric-origin plasma entering the plasma sheet closer to Earth. Even though the flow paths are very different, they yield about the same number of ions to the nightside geosynchronous region. Although the difference in the drift path has little effect on the density, it causes a large change (at least a factor of 4) in the temperature of these particles because of the different cumulative amount of acceleration experienced.

Let us summarize the connection to drift physics. First, the cross-tail electric field energizes ions on their entry to the plasma sheet. This is how the ionospheric-origin plasma attains 1–2 keV temperature during northward IMF. Subsequently, there either is or is not additional acceleration within the plasma sheet. If the electric field is strong, then the plasma will drift toward Earth, crossing magnetic field isocontours and being further energized. If the electric field is weak, then drift is dominated by magnetic gradient-curvature drift and corotation, so less heating is experienced by the plasma. In these conditions, to reach the near-Earth nightside, ionospheric material has to locally rain down on the plasma sheet, and the solar material drifts to this location from the flanks near $X \sim 0$.

The timing difference to reach steady state after an IMF turning matches expectations. There are transient features that last an hour or so followed by a progression toward the steady state situation. This steady state is reached very fast for southward IMF because convection is strong and the plasma moves quickly, flushing out the preexisting plasma conditions and bringing in new populations throughout the tail. During northward IMF, convection is much slower and the relaxation time to achieve a steady result is much longer.

A key finding of this study is the multifluid versus multispecies comparison. From Figures 8.1 and 8.2, it is clear that mixing of the two H^+ populations occurs throughout the magnetosphere, and the distinct velocities in the multifluid simulation better allow for this mixing. The compositional results for the multifluid simulations are not as extreme as those for the multispecies result. Furthermore, the temperature differences between the two proton populations seen in Figure 8.5 allows for the possibility of their distinct identification and separation of the origin location of otherwise identical particles in the magnetosphere.

In addition to the distinct velocities of multifluid MHD allowing for mixing and compositional differences relative to multispecies results, the use of a multifluid equation set for the MHD simulations have significant impact on the resulting densities and temperatures. As seen in Figure 8.6, the multispecies simulations yield essentially the same total density and averaged temperature in the near-Earth nightside. The multifluid result, however, allows for a compositional analysis of these changes. During southward IMF, it is seen that the plasmas of ionospheric and solar wind origin have vastly different temperatures (by a factor of 3). This difference is explained by the plasma sheet entry locations of these populations and their unique drift paths and subsequent adiabatic energization. For northward IMF, the cold, dense plasma sheet is dominated by solar-origin protons but contains a minor but still substantial population of ionospheric-origin plasma. Both populations experienced very little adiabatic acceleration in the plasma sheet and are thus relatively lower in temperature.

This partitioning of the plasma into components has implications for observational studies of the Earth's magnetosphere. The idealized input simulations conducted for this study provide a basic understanding of the difference in density, temperature, and relative composition contributions between the ions from the two sources for northward and southward IMF. In particular, the ions of solar and ionospheric origin have two distinct temperatures, which vary as a function of IMF and location within the plasma sheet, and this knowledge can be used to diagnose the relative contribution of each ion source. This study considered only two fluids, both protons, yet, because of the different entry processes to the plasma sheet, temperature can serve as a unique identifier between the two otherwise identical populations.

This study only considered a single setting for the MHD inner boundary mass density setting (28 amu cm^{-3}). It should be noted that the variation across solar cycle for ionospheric H^+ outflow can be significant, with observations showing up to an order of magnitude difference [e.g., *Demars and Schunk*, 2001; *Liu et al.*, 2001; *Yau et al.*, 2007; *Peterson et al.*, 2008]. The influence of this density change could have substantial influences on the plasma sheet morphology presented here. Similarly, the inclusion of O^+ as a third species in the multifluid simulation will

also have consequences for the structure and dynamics of the plasma sheet. Both of these influences will be explored in future studies.

The partitioning of the H^+ sources with the multifluid approach will also have significant impact on the development of magnetic storms. Specifically, the source of keV ions to the inner magnetosphere will vary greatly depending on the temporal evolution of the IMF, including that preceding the initial phase of the storm. The delivery of cold, dense solar-origin ions to the near-Earth plasma sheet prior to storm onset preconditions the magnetosphere for a more intense ring current development during the subsequent southward IMF interval. Conversely, brief intervals of northward IMF during a magnetic storm will not flood the near-Earth plasma sheet with cold, dense solar-origin ions; it takes many hours for that population to develop and reach this location deep within the magnetosphere. The ~hour-long transient feature phenomenon seen in Figures 8.3 and 8.4 is further evidence of the magnetosphere acting as a low-pass filter of solar wind fluctuations [e.g., *Tsurutani et al.,* 1990; *Murr and Hughes*, 2007; *Ilie et al.*, 2010a].

8.5. CONCLUSIONS

This study used numerical simulations to assess the relative contribution of solar wind and ionospheric material in the Earth's magnetosphere. The SWMF was used to couple the BATS-R-US MHD model to an ionospheric potential solver with steady, idealized driving conditions to explore the timing and characteristics of solar wind entry and ionospheric outflow during northward and southward IMF. Two versions of the BATS-R-US code were used: the multispecies version, which has separate continuity equations for each ion species but a single set of momentum and energy equations for all ion species combined; and the multifluid version, which uses a full set of Euler equations for each ion species. Key similarities and differences between these model configurations were compared and discussed.

The basic results are as follows. It was shown that for southward IMF, the plasma sheet is dominated by ionospheric material with hot and tenuous characteristics. For northward IMF, the plasma sheet is dominated by the solar wind with cold and dense properties. During a turning of the IMF from south to north, initial transient features last about an hour and then a slow conversion toward a steady state configuration builds over the course of many hours throughout the magnetotail. A turning from north to south IMF has similar transient features during the first hour, but the progression toward a steady state level is very quick, taking just another hour or so to achieve.

Several important implications of these findings have been discussed here. Perhaps the biggest conclusion to draw is that the ions of solar wind and ionospheric origin have unique entry locations and drift paths through the plasma sheet, therefore they have distinct temperatures throughout this region. Single-fluid or multispecies approaches that use a unified momentum equation cannot resolve these independent entry paths to the plasma sheet; multifluid simulations reveal the distinct entry processes and drift paths through the magnetotail and therefore offer insight toward identifying sources of magnetospheric plasma populations. Observational studies should carefully examine the proton velocity space distribution for a dual temperature distribution. Under southward IMF, the protons of solar wind origin should have a smaller density but a much hotter temperature than protons from the ionosphere. This situation is reversed for northward IMF, however, with the protons of solar wind origin being denser and cooler than those from the ionosphere.

Another implication from the results presented above is that the timing for the magnetotail to adjust to a turning of the IMF is very different depending on the IMF polarity. If the turning is southward, the adjustment time is very quick, and the preexisting material for the prior northward IMF conditions is quickly flushed out of the plasma sheet. The magnetotail is dominated by ionospheric-origin ions for southward IMF, and these ions are already present in the tail lobes and plasma sheet. Therefore, it does not take 4+ hours to reach a steady state, but rather the cool, dense solar wind material leaves within an hour and new steady state is reached soon after that.

If the turning is northward, however, the situation is very different. The adjustment time is much longer, with places in the tail, like the near-Earth nightside region around geosynchronous altitude, taking 6–8 hours to reach a steady state scenario. The very slow convection under northward IMF does not sweep away the preexisting ionospheric material, and it takes a long time for the solar wind ions to leak into the magnetosphere through the flanks and azimuthally drift toward the inner magnetosphere. This slow timescale for reconfiguration of the magnetosphere needs to be taken into account when analyzing magnetospheric observations and making inferences about geospace dynamics.

ACKNOWLEDGMENTS

This work was supported by National Science Foundation (NSF) grant AGS-1202984 and National Aeronautics and Space Administration (NASA) grants NNX11AO60G and NNX13AD69G. The SWMF code used for this study is freely available from the Center for Space Environment Modeling website at http://csem.

engin.umich.edu or can be run from the Community Coordinated Modeling Center at http://ccmc.gsfc.nasa.gov. In addition, the simulation set up configurations and output files used to produce the plots in this study can be obtained upon request to the authors.

REFERENCES

Borovsky, J. E., M. F. Thomsen, and R. C. Elphic (1998), The driving of the plasma sheet by the solar wind, *J. Geophys. Res.*, *103*, 17,617.

Brambles, O. J., W. Lotko, P. A. Damiano, B. Zhang, M. Wiltberger, and J. Lyon (2010), Effects of causally driven cusp O^+ outflow on the storm time magnetosphere-ionosphere system using a multifluid global simulation, *J. Geophys. Res.*, *115*, A00J04, doi:10.1029/2010JA015469.

Cully, C. M., E. Donovan, A. W. Yau, and G. G. Arkos (2003), Akebono/Suprathermal Mass Spectrometer observations of low-energy ion outflow: Dependence on magnetic activity and solar wind conditions, *J. Geophys. Res.*, *108*(A2), 1093, doi:10.1029/2001JA009200.

Daglis, I. A., E. T. Sarris, and B. Wilken (1993), AMPTE/CCE CHEM observations of the ion population at geosynchronous altitudes, *J. Geophys. Res.*, *98*, 685.

Damiano, P. A., O. J. Brambles, W. Lotko, B. Zhang, M. Wiltberger, and J. Lyon (2010), Effects of solar wind dynamic pressure on the ionospheric O^+ fluence during the 31 August 2005 storm, *J. Geophys. Res.*, *115*, A00J07, doi:10.1029/2010JA015583.

Demars, H. G., and Schunk, R. W. (2001), Seasonal and solar cycle variations of the polar wind, *J. Geophys. Res.*, *106*, 8157–8168.

Ebihara, Y., and M. Ejiri (2000), Simulation study on fundamental properties of the storm-time ring current, *J. Geophys. Res.*, *105*, 15,843.

Ejiri, M. (1978), Trajectory traces of charged particles in the magnetosphere, *J. Geophys. Res.*, *83*, 4798.

Ejiri, M., R. A. Hoffman, and P. H. Smith (1980), Energetic particle penetrations into the inner magnetosphere, *J. Geophys. Res.*, *85*, 653.

Ganushkina, N., M. Liemohn, M. Kubyshkina, R. Ilie, and H. Singer (2010), Distortions of the magnetic field by storm-time current systems in Earth's magnetosphere, *Ann. Geophys.*, *28*, 123–140.

Garner, T. W. (2003), Numerical experiments on the inner magnetospheric electric field, *J. Geophys. Res.*, *108*(A10), 1373, doi:10.1029/2003JA010039.

Glocer, A., G. Toth, T. Gombosi, and D. Welling (2009a), Modeling ionospheric outflows and their impact on the magnetosphere, initial results, *J. Geophys. Res.*, *114*, A05216, doi:10.1029/2009JA014053.

Glocer, A., G. Toth, T. Ma, Y. Gombosi, J. Zhang, and L. Kistler (2009b), Multi-fluid BATS-R-US: Magnetospheric composition and dynamics during geomagnetic storms, initial results, *J. Geophys. Res.*, *114*, A12203, doi:10.1029/2009JA014418.

Gombosi, T. I., G. Tóth, D. L. De Zeeuw, K. C. Hansen, K. Kabin, and K. G. Powell (2002), Semirelativistic magnetohydrodynamics and physics based convergence acceleration, *J. Comput. Phys.*, *177*, 176–205.

Ilie, R., M. W. Liemohn, and A. Ridley (2010a), The effect of smoothed solar wind inputs on global modeling results, *J. Geophys. Res.*, *115*, A01213, doi:10.1029/2009JA014443.

Ilie, R., M. W. Liemohn, J. U. Kozyra, and J. E. Borovsky (2010b), An investigation of the magnetosphere-ionosphere response to real and idealized co-rotating interaction region events through global magnetohydrodynamic simulations, *Proc. R. Soc. A*, *466*(2123): 3279–3303, doi:10.1098/rspa.2010.0074.

Ilie, R., M. W. Liemohn, and G. Toth, (2015), The effect of ionospheric outflow and magnetospheric composition on ring current formation and evolution, *J. Geophys. Res. Space Physics*, submitted, ms # 2014JA019794.

Lavraud, B., and V. K. Jordanova (2007), Modeling the effects of cold-dense and hot-tenuous plasma sheet on proton ring current energy and peak location, *Geophys. Res. Lett.*, *34*, L02102, doi:10.1029/2006GL027566.

Lavraud, B., M. H. Denton, M. F. Thomsen, J. E. Borovsky, and R. H. W. Friedel (2005), Superposed epoch analysis of dense plasma access to geosynchronous orbit, *Ann. Geophys.*, *23*(7), 2519–2529.

Lavraud, B., M. F. Thomsen, B. Lefebvre, S. J. Schwartz, K. Seki, T. D. Phan, Y. L. Wang, A. Fazakerley, H. Rème, and A. Balogh (2006a), Evidence for newly closed magnetosheath field lines at the dayside magnetopause under northward IMF, *J. Geophys. Res.*, *111*, A05211, doi:10.1029/2005JA011266.

Lavraud, B., M. F. Thomsen, J. E. Borovsky, M. H. Denton, and T. I. Pulkkinen (2006b), Magnetosphere preconditioning under northward IMF: Evidence from the study of coronal mass ejection and corotating interaction region geoeffectiveness, *J. Geophys. Res.*, *111*, A09208, doi:10.1029/2005JA011566.

Le, G., C. T. Russell, J. T. Gosling, and M. F. Thomsen (1996), ISEE observations of low-latitude boundary layer for northward interplanetary magnetic field: Implications for cusp reconnection, *J. Geophys. Res.*, *101*(A12), 27,239–27,249.

Lennartsson, W. (1992), A scenario for solar wind penetration of Earth's magnetic tail based on ion composition data from the ISEE 1 spacecraft, *J. Geophys. Res.*, *97*, 19,221.

Lennartsson, W., and E. G. Shelley (1986), Survey of 0.1- to 16-keV/e plasma sheet ion composition, *J. Geophys. Res.*, *91*, 3061.

Lennartsson, O. W., H. L. Collin, and W. K. Peterson (2004), Solar wind control of Earth's H+ and O+ outflow rates in the 15-eV to 33-keV energy range, *J. Geophys. Res.*, *109*(A12), A12212, doi:10.1029/2004JA010690.

Liemohn, M. W., T. E. Moore, P. D. Craven, W. Maddox, A. F. Nagy, and J. U. Kozyra (2005), Occurrence statistics of cold, streaming ions in the near-Earth magnetotail: Survey of Polar-TIDE observations, *J. Geophys. Res.*, *110*, A07211, doi:10.1029/2004JA010801.

Liemohn, M. W., T. E. Moore, and P. D. Craven (2007), Geospace activity dependence of cold, streaming ions in the near-Earth magnetotail, *J. Atmos. Solar-Terr. Phys.*, *69*, 135.

Liemohn, M. W., J.-C. Zhang, M. F. Thomsen, J. E. Borovsky, J. U. Kozyra, and R. Ilie (2008), Superstorms at geosynchronous

orbit: how different are they?, *Geophys. Res. Lett*., *35*, L06S06, doi:10.1029/2007GL031717.

Liemohn, M. W., D. L. De Zeeuw, R. Ilie, and N. Yu. Ganushkina (2011), Deciphering magnetospheric cross-field currents, *Geophys. Res. Lett.*, *38*, L20106, doi:10.1029/2011GL049611.

Liemohn, M. W., D. L. De Zeeuw, N. Y. Ganushkina, J. U. Kozyra, and D. T. Welling (2013), Magnetospheric cross-field currents during the January 6-7, 2011, high-speed stream-driven interval, *J. Atmos. Solar-Terr. Phys*., *99*, 78–84, doi: 10.1016/j.jastp.2012.09.007.

Liu, H., S.-Y. Ma, and K. Schlegel (2001), Diurnal, seasonal, and geomagnetic variations of large field-aligned ion upflows in the high-latitude ionospheric F region, *J. Geophys. Res.*, *106*(A11), 24651, doi:10.1029/2001JA900047.

McComas, D. J., P. Valek, J. L. Burch, C. J. Pollack, R. M. Skoug, and M. F. Thomsen, Filling and emptying of the plasma sheet: Remote observations with 1–70 keV energetic neutral atoms, *Geophys. Res. Lett*., *29*(22), 2079, doi:1029/2002GL016153, 2002.

Moore, T. E., et al. (1997). High-altitude observations of the polar wind, *Science 277*, 349.

Moore, T. E., M.-C. Fok, M. O. Chandler, C. R. Chappell, S. Christon, D. Delcourt, J. Fedder, M. Huddleston, M. Liemohn, W. Peterson, and S. P. Slinker, Plasma sheet and (non-storm) ring current formation from solar and polar wind sources, *J. Geophys. Res.*, *110*, A02210, doi:10.1029/2004JA010563, 2005a.

Moore, T. E., M.-C. Fok, M. O. Chandler, S.-H. Chen, S. P. Christon, D. C. Delcourt, J. Fedder, M. Liemohn, W. K. Peterson, and S. Slinker (2005b), Solar and ionospheric plasmas in the ring current, in *Inner Magnetosphere Interactions: New Perspectives from Imaging*, *AGU Monogr. Ser*., vol. *159*, ed. by J. L. Burch, M. Schulz, and H. Spence, p. 179, Am. Geophys. Un., Washington, D. C.

Murr, D. L., and W. J. Hughes (2007), The coherence between the IMF and high-latitude ionospheric flows: The dayside magnetosphere-ionosphere low-pass filter, *J. Atmos. Sol. Terr. Phys.*, *69*(3), 223–233.

Onsager, T. G., J. D. Scudder, M. Lockwood, and C. T. Russell (2001), Reconnection at the high latitude magnetopause during northward interplanetary magnetic field conditions, *J. Geophys. Res.*, *106*(A11), 25,467–25,488.

Peroomian, V., M. El-Alaoui, M. A. Abdalla, and L. M. Zelenyi (2007), A comparison of solar wind and ionospheric plasma contributions to the September 24–25, 1998 magnetic storm, *J. Atmos. Sol. Terr. Phys.*, *69*, 212–222, doi:10.1016/j.jastp.2006.07.025.

Peterson, W. K., L. Andersson, B. C. Callahan, H. L. Collin, J. D. Scudder, and A. W. Yau (2008), Solar-minimum quiet time ion energization and outflow in dynamic boundary related coordinates, *J. Geophys. Res.*, *113*(A7), 07222, doi:10.1029/2008JA013059.

Phan, T. D., R. P. Lin, S. A. Fuselier, and M. Fujimoto (2000), Wind observations of mixed magnetosheath-plasma sheet ions deep inside the magnetosphere, *J. Geophys. Res.*, *105*, 5497.

Ridley, A. J., and M. W. Liemohn (2002), A model-derived description of the penetration electric field, *J. Geophys. Res.*, *107*(A8), 1151, doi:10.1029/2001JA000051.

Ridley, A. J., T. I. Gombosi, and D. L. De Zeeuw (2004), Ionospheric control of the magnetosphere: Conductance, *Ann. Geophys.*, *22*, 567.

Smith, P.H., and R. A. Hoffman (1974), Direct observations in the dusk hours of the characteristics of the storm time ring current particles during the beginning of magnetic storms, *J. Geophys. Res.*, *79*, 966.

Song, P., and C. T. Russell (1992), Model of the formation of the lowlatitude boundary layer for strongly northward interplanetary magnetic field, *J. Geophys. Res.*, *97*(A2), 1411–1420.

Strangeway, R. J., R. E. Ergun, Y.-J. Su, C. W. Carlson, and R. C. Elphic (2005), Factors controlling ionospheric outflows as observed at intermediate altitudes, *J. Geophys. Res.*, *110*, A03221, doi:10.1029/2004JA010829.

Toth, G., D. L. De Zeeuw, T. I. Gombosi, W. B. Manchester, A. J. Ridley, I. V. Sokolov, and I. I. Roussev (2007), Sun-to-thermosphere simulation of the 28 to 30 October 2003 storm with the Space Weather Modeling Framework, *Space Weather*, *5*, S06003, doi:10.1029/2006SW000272.

Toth. G. et al. (2012), Adaptive numerical algorithms in space weather modeling, *J. Comput. Phys.*, *231*, 870.

Thomsen, M. F., J. E. Borovsky, D. J. McComas, and M. R. Collier, Variability of the ring current source population, *Geophys. Res. Lett.*, *25*, 3481, 1998.

Thomsen, M. F., J. E. Borovsky, R. M. Skoug, and C. W. Smith (2003), Delivery of cold, dense plasma sheet material into the near-Earth region, *J. Geophys. Res.*, *108*(A4), 1151, doi:10.1029/2002JA009544.

Tsurutani, B. T., M. Sugiura, T. Iyemori, B. E. Goldstein, W. D. Gonzalez, S. I. Akasofu, and E. J. Smith (1990), The nonlinear response of AE to the IMF BS driver: A spectral break at 5 hours, *Geophys. Res. Lett.*, *17*(3), 279–282.

Walker, R., et al. (1999), Source and loss processes in the magnetotail, in *Magnetospheric Plasma Sources and Losses*, edited by B. Hultqvist et al., p. 346, Kluwer Acad., Norwell, Mass.

Welling, D. T., and A. J. Ridley (2010), Exploring sources of magnetospheric plasma using multispecies MHD, *J. Geophys. Res.*, *115*, A04201, doi:10.1029/2009JA014596.

Welling, D. T., and M. W. Liemohn (2014), Outflow in global magnetohydrodynamics as a function of a passive inner boundary source, *J. Geophys. Res. Space Physics*, *119*, 2691–2705, doi: 10.1002/2013JA019374.

Welling, D. T., V. K. Jordanova, S. G. Zaharia, A. Glocer, and G. Toth (2011), The effects of dynamic ionospheric outflow on the ring current, *J. Geophys. Res.*, *116*, A00J19, doi:10.1029/2010JA015642.

Wiltberger, M., W. Lotko, J. G. Lyon, P. Damiano, and V. Merkin (2010), Influence of cusp O^+ outflow on magnetotail dynamics in a multifluid MHD model of the magnetosphere, *J. Geophys. Res.*, *115*, A00J05, doi:10.1029/2010JA015579.

Winglee, R. M. (1998), Multi-fluid simulations of the magnetosphere: The identification of the geopause and its variation with IMF, *Geophys. Res. Lett.*, *25*, 4441.

Winglee, R. M. (2003), Circulation of ionospheric and solar wind particle populations during extended southward interplanetary magnetic field, *J. Geophys. Res.*, *108*(A10), 1385, doi:10.1029/2002JA009819.

Winglee, R. M., D. Chua, M. Brittnacher, G. K. Parks, and G. Lu (2002), Global impact of ionospheric outflows on the dynamics of the magnetosphere and cross-polar cap potential, *J. Geophys. Res.*, *107*(A9), 1237, doi:10.1029/2001JA000214.

Yau, A.W., T. Abe, W.K. Peterson (2007), The polar wind: Recent observations, *J. Atmos. Solar-Terr. Phys.*, *69*(16), 1936–1983, doi:10.1016/j.jastp.2007.08.010.

Yu, Y., and A. J. Ridley (2013), Exploring the influence of ionospheric O^+ outflow on magnetospheric dynamics: Dependence on the source location, *J. Geophys. Res. Space Physics*, *118*, 1711–1722, doi:10.1029/2012JA018411.

Zhang, J.-Ch., M. W. Liemohn, D. L. De Zeeuw, J. E. Borovsky, A. J. Ridley, S. Sazykin, M. F. Thomsen, J. U. Kozyra, T. I. Gombosi, and R. A. Wolf (2007), Understanding storm-time ring current sources through data-model comparisons of a moderate storm, *J. Geophys. Res.*, *112*, A04208, doi:10.1029/2006JA011846.

Part III
The Effect of Low-energy Plasma on the Stability of Energetic Plasmas

9

How Whistler-Mode Waves and Thermal Plasma Density Control the Global Distribution of the Diffuse Aurora and the Dynamical Evolution of Radiation Belt Electrons

Richard M. Thorne[1], Jacob Bortnik[1], Wen Li[1], Lunjin Chen[2], Binbin Ni[3], and Qianli Ma[1]

Video of Yosemite Talk, URL: http://dx.doi.org/10.15142/T38G6X

ABSTRACT

Intense non-linear chorus emissions are generated in the low-density region outside the plasmasphere during the convective injection of plasma sheet electrons into the inner magnetosphere. A small portion of chorus emissions are able to propagate to high latitudes and are refracted into the plasmasphere to provide an embryonic source for plasmaspheric hiss. A third class of whistler-mode wave, the equatorial magnetosonic wave, is generated by ion ring distributions, which develop mostly on the dayside following ion injection into the ring current. All three classes of whistler-mode waves play a role in storm-time electron dynamics. Specifically, chorus provides the major mechanism for the scattering of low-energy electrons into the atmosphere and is responsible for the global distribution of the diffuse aurora. Chorus is also primarily responsible for the stochastic acceleration of electrons to relativistic energies, over a timescale comparable to or less than a day, leading to local peaks in electron phase space density in the outer radiation zone. Equatorial magnetosonic waves can also contribute to electron acceleration but only over a much longer timescale (~10 days). During the recovery phase of a storm, the plasmasphere refills causing the plasmapause to move outward, leaving accelerated electrons trapped within the relatively benign dense plasmasphere, where they are slowly removed by scattering loss into the atmosphere due to interactions with plasmaspheric hiss and electromagnetic ion cyclotron (EMIC) waves.

9.1. INTRODUCTION

The Earth's radiation belts are essentially collisionless, implying that dynamical changes in the energetic electron population are primarily controlled by interactions with magnetospheric plasma waves [*Thorne*, 2010]. Important waves responsible for the electron dynamics are generated by natural instabilities in the magnetosphere following the injection of plasma sheet ions and electrons into the inner magnetosphere during enhanced convection events. The global distribution of magnetospheric waves, generated during periods when the magnetosphere is strongly coupled to the solar wind, is illustrated in Figure 9.1. Injected ions and electrons responsible for the wave excitation typically have energies below 50 kiloelectron-volt (keV), and many of these particles are on open drift trajectories, which ultimately carry them into the dayside magnetopause. However, more energetic electrons (>100 keV to a few million electron volts [MeV]) are subject to rapid

[1]*Department of Atmospheric and Oceanic Sciences, University of California Los Angeles (UCLA), Los Angeles, CA, USA*

[2]*Department of Physics, University of Texas, Dallas, Richardson, TX, USA*

[3]*Department of Space Physics, Wuhan University, Wuhan, Hubei, China*

Magnetosphere-Ionosphere Coupling in the Solar System, Geophysical Monograph 222, First Edition.
Edited by Charles R. Chappell, Robert W. Schunk, Peter M. Banks, James L. Burch, and Richard M. Thorne.

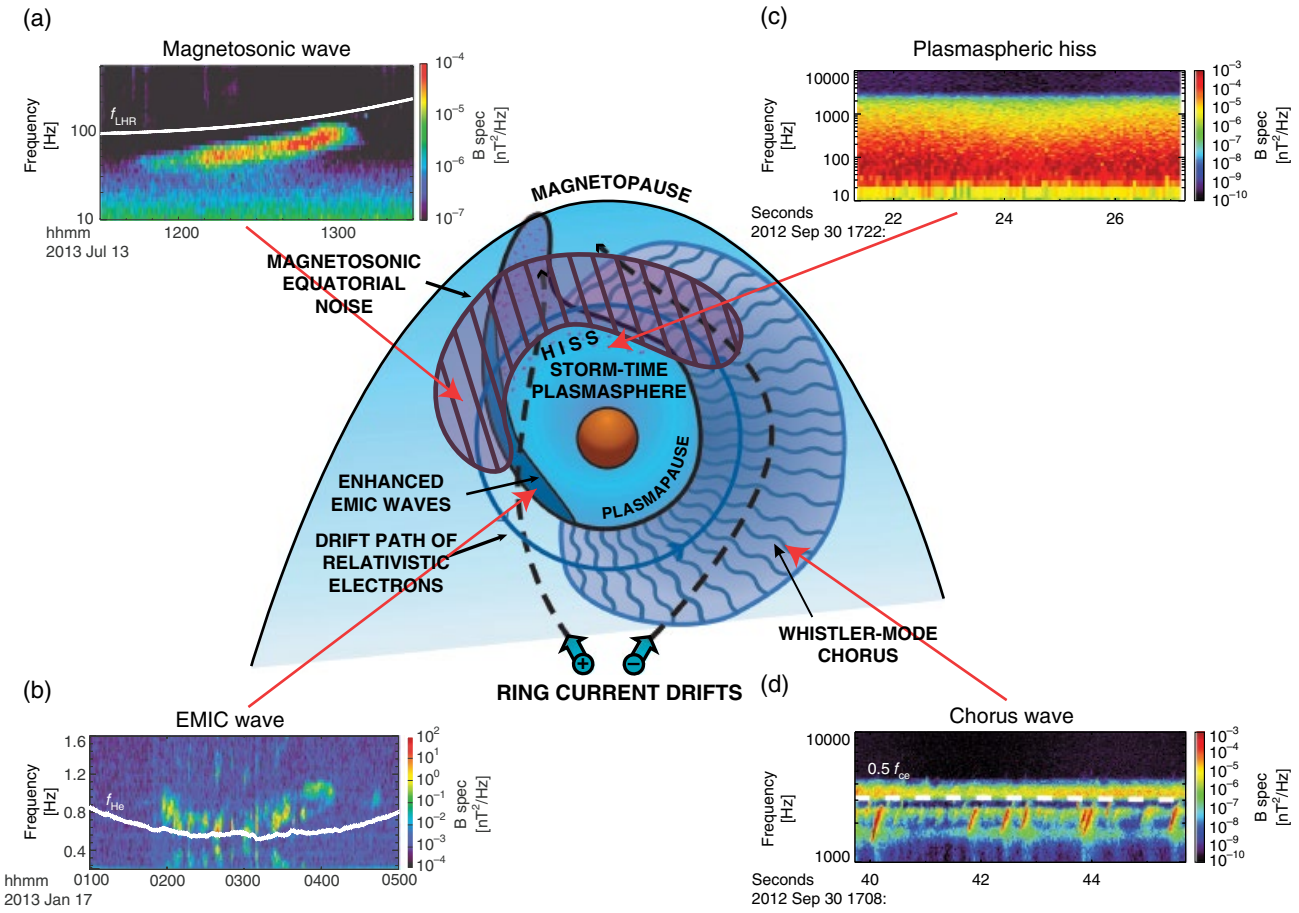

Figure 9.1 The spatial distribution of important waves in the inner magnetosphere, in relation to the plasmasphere and the drift-paths of ring-current (10–100 keV) electrons and ions and relativistic (≥0.3 MeV) electrons.

magnetic gradient drifts and are constrained to move on roughly circular drift orbits, where they can interact with different waves. During such interactions, whistler-mode chorus and equatorial magnetosonic waves cause net electron acceleration [*Horne and Thorne*, 2003; *Horne et al.*, 2007], while plasmaspheric hiss and EMIC waves primarily lead to pitch angle scattering and ultimate loss to the atmosphere [*Li et al.*, 2007; *Summers et al.*, 2007]. The energetic electrons can also be transported radially during interactions with ultra low frequency (ULF) waves, which act as either a source or a sink of the energetic electron population, dependent on the radial gradients of the energetic particle phase space density [*Chen et al.*, 2007]. The solar wind ultimately provides the source of free energy for wave excitation in the magnetosphere, but whether the resulting wave-particle interaction leads to a net enhancement or loss of the energetic electron population during any specific solar induced event is delicately controlled by the relative strength of various source and loss processes. The ambient plasma density within the magnetosphere also plays a key role in both the wave excitation and propagation process, and in determining resonant electron energies. In this chapter, we review some of the major advances that have recently been made in our current understanding of electron acceleration and loss during geomagnetically active periods.

9.2. ORIGIN AND GLOBAL DISTRIBUTION OF MAGNETOSPHERIC WHISTLER-MODE EMISSIONS

Three of the waves illustrated in Figure 9.1 propagate in the whistler-mode, but their properties are distinctly different, as are their roles in energetic electron dynamics, as discussed in the following paragraphs.

Chorus emissions are generated by a cyclotron resonant instability in the low-density region outside the plasmapause following the injection of medium energy (~1–30 keV) electrons into the inner magnetosphere during periods of enhanced convection or substorms [*Li et al.*, 2008]. As plasma sheet electrons are transported into lower L, they both gain energy and develop the pitch angle anisotropy required for rapid linear wave growth. Subsequent wave growth is determined by non-linear

processes [e.g., *Omura et al.*, 2008], and the waves are observed as discrete "chirps" in two frequency bands below and above one half the electron gyro-frequency [*Tsurutani and Smith*, 1974]. Lower band chorus, which plays a major role in the acceleration of energetic radiation belt electrons (Section 9.4), is generally much stronger than waves in the upper band [*Li et al.*, 2011; *Meredith et al.*, 2012]. As injected electrons drift eastward toward dawn, they are rapidly scattered in pitch-angle during resonant interactions with the excited chorus. The injected electron population is maintained close to marginal stability [*Kennel and Petschek*, 1966], which allows chorus excitation over a broad spatial region on the dawnside. The global distribution and spectral characteristics of chorus emissions under different levels of geomagnetic activity have been obtained statistically using numerous in situ satellite wave observations [*Li et al.*, 2009, 2011; *Meredith et al.*, 2012]. More recently, a dynamic model for the global intensity and temporal variability of chorus has been obtained using the ratio between the precipitated and trapped electron flux measured on low-altitude Polar Orbiting Environment Satellite (POES) spacecraft [*Li et al.*, 2013; *Ni et al.*, 2014a]. The properties of chorus and their global distribution have been used to simulate the role of chorus in both diffuse auroral precipitation (Section 9.3) and in electron acceleration to relativistic energies (Section 9.4).

Plasmaspheric hiss is an unstructured whistler-mode wave, which is confined to the region inside the dense plasmasphere or dayside drainage plumes. It has long been established that hiss is primarily responsible for the slow decay of energetic electrons injected into the outer radiation belt and slot region during magnetic storms [*Lyons et al.*, 1972; *Abel and Thorne*, 1998; *Meredith et al.*, 2006; *Ni et al.*, 2013, 2014b; *Li et al.*, 2014b]. However, the origin of this broadband emission remained a mystery for four decades until it was demonstrated that chorus emissions propagating into the plasmasphere could provide the embryonic source for hiss [*Bortnik et al.*, 2008a, 2009, 2011; *Li et al.*, 2015a], which together with modest local cyclotron resonant amplification just inside the plasmapause [*Chen et al.*, 2012] can account for the dominant properties of hiss.

Equatorial magnetosonic (MS) waves are highly oblique whistler-mode waves propagating below the lower hybrid frequency and generally confined within a few degrees of the magnetic equatorial plane [e.g., *Russell et al.*, 1970; *Nemec et al.*, 2005]. The waves are generated near or outside the plasmapause by ion ring distributions [*Horne et al.*, 2000; *Ma et al.*, 2014a], which develop on the dayside following the injection of ring current ions into the inner magnetosphere [*Chen et al.*, 2010; *Jordanova et al.*, 2012]. In addition, MS waves are able to propagate over a considerable distance from the local source and are observed deep inside the plasmasphere [*Ma et al.*, 2014b]. The global distribution of MS waves has been obtained from satellite observations [*Ma et al.*, 2013] and has recently been used to evaluate the role of such waves in radiation belt electron dynamics [*Li et al.*, 2014a; *Ma et al.*, 2015a]. Most important is their ability to contribute to the acceleration of electrons to relativistic energies due to Landau resonance [*Horne et al.*, 2007], the transit time electron scattering over a broad region of momentum space due to the equatorial wave confinement [*Bortnik and Thorne*, 2010; *Bortnik et al.*, 2015], the formation of butterfly pitch angle distribution [*Ma et al.*, 2015a], and the effect on the dynamics of equatorially mirroring electrons during bounce resonance [*Chen et al.*, 2015].

9.3. GLOBAL DISTRIBUTION OF DIFFUSE AURORAL PRECIPITATION

During active geomagnetic conditions, diffuse auroral precipitation provides up to 80% of the ionizing energy input over a broad range of latitude (~60°–70°) into the nightside upper atmosphere [*Newell et al.*, 2009], and is consequently a dominant source of ionospheric high latitude conductivity. Enhanced conductivity influences the coupling between the magnetosphere and ionosphere and hence the penetration of the convection electric field into the inner magnetosphere. An accurate specification of the global pattern of diffuse auroral precipitation is therefore required to model convective transport during active geomagnetic conditions. The main source of diffuse auroral energy input into the atmosphere is from electrons between a few hundred electron-volts (eV) and a few tens of keV. Such electrons are essentially collisionless, and their precipitation into the atmosphere is caused by pitch-angle scattering during resonant interactions with plasma waves. Early theoretical modeling of the diffuse auroral precipitation considered the role of either electrostatic Electron Cyclotron Harmonic (ECH) waves [*Kennel et al.*, 1970; *Lyons*, 1974] or electromagnetic chorus [*Villalon and Burke*, 1995]. Both waves are able to interact with electrons in the correct energy range, and both waves have a spatial distribution and dependence on geomagnetic activity similar to the observed global distribution of diffuse auroral precipitation [*Petrinec et al.*, 1999]. However, detailed modeling of the rate of electron scattering, using more recent statistical models for the scattering waves obtained from the Combined Release and Radiation Effects Satellite (CRRES) [*Meredith et al.*, 2009], has demonstrated that a combination of upper and lower band chorus provides the dominant process for diffuse auroral precipitation at $L < 8$ [*Thorne et al.*, 2010]. The scattering by chorus also accounts for the observed resulting pitch-angle distribution of the trapped electron left behind in space [*Tao et al.*, 2011], namely strong pancake distributions below a few keV and increased anisotropy above ~10 keV, as electrons gradient drift toward the dayside. Such anisotropic electrons can provide a source of free energy for sustained whistler instability over the entire dawn sector.

The scattering by chorus can exceed the strong diffusion rate during intense geomagnetic activity [*Ni et al.*, 2008, 2011b] leading to rapid precipitation into the atmosphere and significant depletion of injected electrons before they are able to drift to the dayside. This accounts for the overall global distribution of the precipitation fluxes. Even though chorus emissions are considered to be the principal cause of the most intense diffuse aurora at L <8, recent statistical models for the distribution of chorus obtained from the Time History of Events and Macroscale Interactions during Substorms (THEMIS) spacecraft indicate that such waves are rarely excited at higher L shells [*Li et al.*, 2009, 2011] because the ambient injected electron population is relatively isotropic and has insufficient anisotropy for whistler-mode instability [*Li et al.*, 2010]. In contrast, ECH instability is driven by small gradients in the pitch angle distribution in the vicinity of the loss cone, and indeed ECH waves are present at L <8 during intense injection events [*Ni et al.*, 2011c; *Zhang et al.*, 2014]. Recent modeling has shown that scattering by ECH waves can account for the global distribution of the diffuse aurora observed at high invariant latitudes [*Ni et al.*, 2011a, 2012; *Zhang et al.*, 2015].

9.4. ELECTRON ACCELERATION BY CHORUS EMISSIONS

Detailed analysis of energetic radiation belt electron data during periods of outer zone enhancement has identified the development of local peaks in electron phase space density [*Green and Kivelson*, 2004; *Chen et al.*, 2007; *Turner et al.*, 2013; *Reeves et al.*, 2013], which provides direct evidence for electron acceleration in the heart of the outer radiation belt (L~4–6). These observations are inconsistent with acceleration caused by inward radial diffusive transport, which would lead to a monotonic gradient in phase space density that increases with increasing L. Earlier theoretical modeling indicated that chorus could be a potential candidate for local electron acceleration [*Horne and Thorne*, 1998; *Summers et al.*, 1998; *Summers et al.*, 2002; *Horne et al.*, 2005], but a definitive resolution of the importance of chorus for radiation belt acceleration was not possible due to limitations in the energy range and resolution of the electron observations and a lack of a dynamic model for the global distribution and variability of chorus waves. The launch of the Van Allen Probes spacecraft in 2012 provided unique high-resolution energetic electron data together with simultaneous in situ plasma wave and density measurements. In addition, a time-varying physics-based model for the global distribution of chorus emissions has recently been developed based on low-altitude electron measurements from the suite of POES spacecraft [*Li et al.*, 2013; *Ni et al.*, 2014a]. This event-specific global wave model has been used to evaluate drift and bounce averaged rates of electron energy and pitch-angle scattering for subsequent use in a Fokker-Planck simulation of electron dynamical evolution during specific magnetic storms [*Thorne et al.*, 2013b; *Li et al.*, 2014c]. The two-dimensional modeling agrees well with the observed temporal evolution of both the energy spectrum and angular distribution of the relativistic electron flux, at locations near the developing peaks in high-energy electron phase space density [*Reeves et al.*, 2013]. Similar three-dimensional event-specific wave modeling, together with the inclusion of radial diffusive transport, has demonstrated the importance of accurate specification of the variable low-energy seed electron population, and the need to account for outward radial diffusion and loss to the magnetopause boundary [*Shprits et al.*, 2006; *Tu et al.*, 2014].

Previous modeling of radiation belt electron dynamics employed statistical models for the global distribution of chorus waves based on observations from numerous satellites during different levels of geomagnetic activity [e.g., *Meredith et al.*, 2012]. Unfortunately, while the statistical wave models provide a realistic measure of the increase in wave intensity with geomagnetic activity, they are not able to capture the rapid dynamic variability and intensity of the global distribution of wave amplitudes during strong magnetic storms [*Tu et al.*, 2014]. In addition, statistical models for the distribution of plasma density [e.g., *Sheeley et al.*, 2001] tend to overestimate the density and thus underestimate both the electron resonant energies and also the rate of energy diffusion (which depends sensitively on the ratio between the electron plasma frequency and electron gyrofrequency [*Horne et al.*, 2005]) during periods of intense convection [*Thorne et al.*, 2013b]. Scaling the statistical plasma density to accurate in situ satellite observation values, and the adoption of event-specific global wave models tend to provide a much better estimate of bounce and drift averaged electron scattering rates during more extreme events and should probably be the gold standard for future diffusion modeling.

Over the three years of operation of the Van Allen Probes, there have been numerous observations of rapid electron acceleration to energies ~ MeV, all of which have been associated with enhanced levels of chorus activity, but relatively few storms have led to acceleration to energies near 10 MeV. The special solar wind conditions leading to the highly relativistic acceleration require a relatively weak solar wind pressure with the magnetopause boundary outside 10 R_E (thus minimizing loss to the boundary), and an extended period of strongly southward-directed interplanetary magnetic field [e.g., *Thorne et al.*, 2013b; *Li et al.*, 2014c, 2015b]. The latter can both maintain enhanced convection of plasma sheet electrons into the inner magnetosphere leading to continual chorus excitation, and also produce significantly reduced plasma

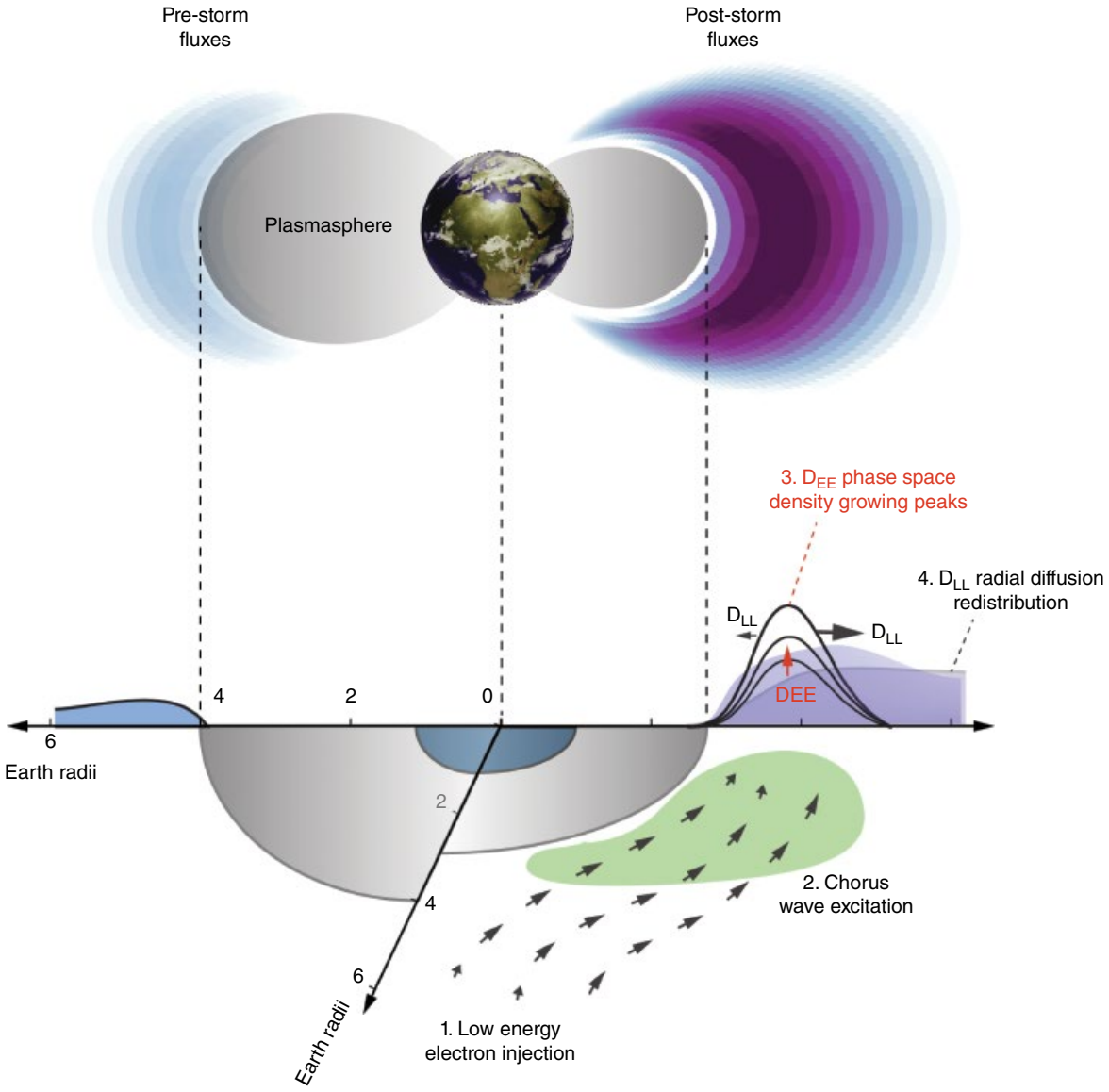

Figure 9.2 Schematic illustration of local electron acceleration by chorus. The injection of low-energy plasma sheet electrons into the inner magnetosphere causes chorus wave excitation in the low-density region outside the cold plasmasphere. Local energy diffusion associated with wave scattering leads to the development of strongly enhanced phase space density just outside the plasmapause. Subsequently, radial diffusion can redistribute the accelerated electrons inward or outward from the developing peak.

density, which is conducive to more efficient local momentum diffusion. The acceleration process described above, and schematically depicted in Figure 9.2, involves the transfer of energy between the injected thermal electrons and the high-energy tail population using waves as an intermediary. It is a universal physical process, which should also be effective in the magnetospheres of Jupiter, Saturn, and other magnetized plasma environments in the cosmos.

9.5. LONG-TERM RELATIVISTIC ELECTRON DECAY BY PLASMASPHERIC HISS AND EMIC WAVES

Once electrons have been accelerated to relativistic energies during a storm by the processes described above, and after convective injection subsides and the plasmapause moves outward, much of the newly formed electron belt is engulfed by and confined within the relatively benign plasmasphere where losses are controlled by scattering due

to plasmaspheric hiss and EMIC waves. During extended periods of weak geomagnetic activity, the timescale for such scattering loss is very long (weeks to months dependent on the electron energy) and radial diffusive transport is even slower inside L ~3. As a consequence, isolated rings of relativistic electrons can persist near L ~3.0–3.5 for months until some new solar induced events cause a disruption [*Baker et al.*, 2013, 2014]. At energies below a few MeV, the dominant scattering loss is controlled by the ambient intensity of plasmaspheric hiss [*Thorne et al.*, 2013a; *Ni et al.*, 2013], but an additional loss by EMIC scattering is required to explain the observed decay of more relativistic electrons [*Ma et al.*, 2015b].

9.6. CONCLUDING REMARKS

Significant advances in our understanding of energetic electron acceleration and decay have been made over the last few years, due in large part to the unprecedented high-resolution data from the Van Allen Probes. Much of the dynamic variability of the radiation belts involves interactions with magnetospheric plasma waves, which are naturally generated following the convective injection of plasma sheet electrons and ions into the inner magnetosphere. The injected electron population is unstable to the generation of whistler-mode chorus emissions and ECH waves, which cause rapid pitch angle scattering into the atmosphere and thus control the global distribution of the diffuse aurora. Chorus is also responsible for energy transfer to the more energetic radiation belt population, and such stochastic energy diffusion can lead to the observed enhancement of highly relativistic electrons and the development of peaks in the radial profile of phase space density in the outer radiation belt during magnetic storms. The local acceleration process is most efficient in the low-density region just outside the plasmapause [*Horne et al.*, 2005; *Thorne et al.*, 2013b], which for strong storms leads to orders of magnitude increases in energetic electron flux for L >3, and a partial refilling of the slot between the inner and outer radiation belts. As geomagnetic activity subsides, the accelerated electrons find themselves engulfed within the expanding plasmasphere. Because of their rapid gradient drift timescales (~10 mins), the rate of radial diffusion of relativistic electrons due to drift resonance with penetrating substorm electric fields [*Cornwall*, 1968] is extremely small [*Lyons and Thorne*, 1973] and the injected electrons remain essentially confined to the L shell of injection. Here they are only subject to slow pitch-angle scattering loss to the atmosphere due to interactions with weak but persistent plasmaspheric hiss. At energies < MeV, the scattering by hiss causes a slow exponential decay on timescales less than a few days [*Meredith et al.*, 2006; *Thorne et al.*, 2013a; *Ni et al.*, 2013]. However, the lifetime of the injected electrons increases dramatically with energy and can exceed a month for electrons above 5 MeV. Such long lifetimes account for the existence of long-lived storage rings of highly relativistic electrons following certain magnetic storms [*Baker et al.*, 2013; *Thorne et al.*, 2013a].

Theoretical modeling of radiation belt electron dynamics has up till now been mostly based on a remarkably successful quasi-linear formulation of the rates of pitch angle, energy, and radial diffusion. However, many of the plasma waves involved in the dynamic variability of the radiation belts attain amplitudes where non-linear effects need to be included [*Cattell et al.*, 2008; *Bortnik et al.*, 2008b; *Albert et al.*, 2012]. Incorporating such non-linear effects in three-dimensional and four-dimensional modeling codes will be an important challenge in future modeling efforts.

ACKNOWLEDGMENTS

This work was supported by Johns Hopkins University/Applied Physics Laboratory (JHU/APL) contracts 967399 and 921647 under the National Aeronautics and Space Administration's (NASA)'s prime contract NAS5-01072. The analysis at UCLA was supported by the EMFISIS sub-award 1001057397:01 and by the ECT sub-award 13-041, NASA grants of NNX11AR64G, NNX13AI61G, NNX14AI18G, NNX15AF61G, and NNX15AI96G, and the National Science Foundation (NSF) grant PLR-1341359 and AGS 1405054, and the AFOSR award FA9550-15-1-0158. BN thanks the support by the NSFC grants 41204120 and 41474141. LC acknowledges the support of NSF AGS-1405041 and NASA NNX15AF55G. The authors thank the entire Van Allen Probes team for providing such excellent data for the reported work.

REFERENCES

Abel, R. W., and R. M. Thorne (1998), Electron scattering loss in Earth's inner magnetosphere,1: Dominant physical processes, *J. Geophys. Res.*, *103*, 2385–2396.

Albert, J. M., Tao, X. and Bortnik, J. (2012) Aspects of Nonlinear Wave-Particle Interactions, in Dynamics of the Earth's Radiation Belts and Inner Magnetosphere (eds D. Summers, I. R. Mann, D. N. Baker and M. Schulz), American Geophysical Union, Washington, D. C.. doi:10.1029/2012GM001324.

Baker, D. N., et al. (2013), A Long-lived Relativistic Electron Storage Ring Embedded in Earth's Outer Van Allen Belt, *Science*, *340*, 186–190, doi:10.1126/science.1233518.

Baker, D. N., et al. (2014), An impenetrable barrier to ultra-relativistic electrons in the Van Allen radaition belt, *Nature*, *515*, 531–534, doi:10.1038/nature13956.

Bortnik, J., R. M. Thorne, and N. P. Meredith (2008a), The unexpected origin of plasmaspheric hiss from discrete chorus emissions, *Nature*, *452*, 62–66, doi:10.1038/nature06741.

Bortnik, J., R. M. Thorne, and U. S. Inan (2008b), Nonlinear interaction of energetic electrons with large amplitude chorus, *Geophys. Res. Lett.*, *35*, L21102, doi:10.1029/2008GL035500.

Bortnik, J., et al. (2009), First observation linking the origin of plasmaspheric hiss to discrete chorus emissions, *Science*, *324*, 775–778, doi:10.1126/science.1171273.

Bortnik, J., and R. M. Thorne (2010), Transit time scattering of energetic electrons due to equatorially confined magnetosonic waves, *J. Geophys. Res.*, *115*, A07213, doi:10.1029/2010JA015283.

Bortnik, J., L. Chen, W. Li, and R. M. Thorne (2011), Modeling the evolution of chorus waves into plasmaspheric hiss, *J. Geophys. Res.*, *116*, A08221, doi:10.1029/2011JA016499.

Bortnik, J., Thorne, R. M., Ni, B. and Li, J. (2015), Analytical approximation of transit time scattering due to magnetosonic waves, *Geophys. Res. Lett*., *42*, 1318–1325, doi:10.1002/2014GL062710.

Cattell, C., et al. (2008), Discovery of very large amplitude whistler-mode waves in Earth's radiation belts, *Geophys. Res. Lett.*, *35*, L01105, doi:10.1029/2007GL032009.

Chen, L., R. M. Thorne, V. K. Jordanova, and R. B. Horne (2010), Global simulation of magnetosonic wave instability in the storm time magnetosphere, *J. Geophys. Res.*, *115*, A11222, doi:10.1029/2010JA015707.

Chen, L., W. Li, J. Bortnik, and R. M. Thorne (2012), Amplification of whistler-mode hiss inside the plasmasphere, *Geophys. Res. Lett.*, *38*, L08111, doi:10.1029/2012GL051488.

Chen, L., A. Maldonado, J. Bortnik, R. Thorne, J. Li, L. Dai, and X. Zhan (2015), Nonlinear Bounce Resonances between Magnetosonic Waves and Equatorially Mirroring Electrons, *J. Geophys. Res.*, doi:10.1002/2015JA021174.

Chen, Y., G. D. Reeves, and R. H. W. Friedel (2007), The energization of relativistic electrons in the outer Van Allen belt, *Nature Physics*, *3*, 614.

Cornwall, J. M. (1968), Diffusion processes influenced by conjugate point wave phenomena, *Radio Sci.*, *3*, 740.

Green, J. C., and M. G. Kivelson (2004), Relativistic electrons in the outer radiation belt: Differentiating between acceleration mechanisms, *J. Geophys. Res.*, *109*, A03213, doi:10.1029/2003JA010153.

Hardy, D. A., M. S. Gussenhoven, and E. Holeman (1985), A Statistical Model of Auroral Electron Precipitation, *J. Geophys. Res.*, *90*(A5), 4229–4248.

Horne, R. B., and R. M. Thorne (1998), Potential wave modes for electron scattering and stochastic acceleration to relativistic energies during magnetic storms, *Geophys. Res., Lett*., *25*, 3011–3014, doi:10.1029/98GL01002.

Horne, R. B., and R. M. Thorne (2003), Relativistic electron acceleration and precipitation during resonant interactions with whistler-mode chorus, *Geophys. Res., Lett*., *30*, (10), 1527, doi:10.1029/2003GL016973.

Horne, R. B., et al. (2005), Timescales for radiation belt electron acceleration by whistler mode chorus waves, *J. Geophys. Res.*, *110*, A03225, doi:10.1029/2004JA010811.

Horne, R. B., et al. (2007), Electron acceleration in the Van Allen belts by fast magnetosonic waves, *Geophys. Res. Lett.*, *34*, L17107, doi:10.1029/2007GL030267.

Horne, R. B., et al. (2008), Gyro-resonant electron acceleration at Jupiter, *Nature Phys.*, *4*, 301.

Jordanova, V. K., R. M. Thorne, W. Li, and Y. Miyoshi (2010), Excitation of whistler-mode chorus from global ring current simulations, *J. Geophys. Res*., *115*, A00F10, doi:10.1029/2009JA014810.

Jordanova, V., D. Welling, S. Zaharia, L. Chen, and R. Thorne (2012), Modeling ring current ion and electron dynamics and plasma instabilities during a high-speed stream driven storm, *J. Geophys. Res*., *117*, A00L08, doi:10.1029/2011JA017433.

Kennel, C. F., F. L. Scarf, R. W. Fredricks, J. H. McGehee, and F. V. Coroniti (1970), VLF electric field observations in the magnetosphere, *J. Geophys. Res.*, *75*(31), 6136–6152.

Li, J., et al. (2014a), Interactions between magnetosonic waves and radiation belt electrons: Comparisons of quasi-linear calculations with test particle simulations, *Geophys. Res. Lett.*, *41*, 4828–4834, doi:10.1002/2014GL060461.

Li, W., Y. Y. Shprits, and R. M. Thorne (2007), Dynamical evolution of energetic electrons due to wave-particle interactions during storms, *J. Geophys. Res.*, *112*, A10220, doi:10.1029/2007JA012368.

Li, W., R. M. Thorne, N. P. Meredith, R. B. Horne, J. Bortnik, Y. Y. Shprits, and B. Ni (2008), Evaluation of whistler-mode chorus amplification during an injection event observed on CRRES, *J. Geophys. Res.*, *113*, A09210, doi:10.1029/2008JA013129.

Li, W., R. M. Thorne, V. Angelopoulos, J. Bortnik, C. M. Cully, B. Ni, O. LeContel, A. Roux, U Auster, and W. Magnes (2009), Global distribution of whistler-mode chorus observed on the THEMIS spacecraft, *Geophys. Res. Lett.*, *36*, L09104, doi:10.1029/2009GL037595.

Li, W., et al. (2010), THEMIS analysis of observed electron distributions responsible for chorus excitation, *J. Geophys. Res*., *115*, A00F11, doi:10.1029/2009JA014845.

Li, W., J. Bortnik, R. M. Thorne, Y. Nishimura. V. Angelopoulos, O. Le Contel, and J. B. Bonnell (2011), Global distribution of wave amplitudes and wave normal distributions of chorus waves with high-resolution THEMIS wave observations, *J. Geophys. Res.*, *116*, A12205, doi:10.1029/2011JA017035.

Li, W., J. Bortnik, Y Nishimura, R. M. Thorne, and V. Angelopoulos (2012), The origin of pulsating aurora: Modulated whistler-mode chorus waves, in *Auroral Phenomenology and Magnetospheric Processes: Earth and Other Planets*, *Geophys. Monogr. Ser*., vol. *197*, edited by A. Keiling, E. Donovan, F. Bagenal, and T. Karlson, pp. 379–388, AGU, Washington, D. C.

Li, W., B. et al. (2013), Constructing the global distribution of chorus waves intensity using measurements of electrons by the POES satellites and waves by the Van Allen probes, *Geophys. Res., Lett*., *40*, 4526–4532, doi:10.1002/grl.50920.

Li, W., et al. (2014b), Quantifying hiss-driven energetic electron precipitation: A detailed conjunction event analysis, *Geophys. Res. Lett.*, *41*, 1085–1092, doi:10.1002/2013GL059132.

Li, W., et al. (2014c), Radiation belt electron acceleration by chorus waves during the 17 March 2013 storm, *J. Geophys. Res. Space Physics*, *119*, 4681–4693, doi:10.1002/2014JA019945.

Li, W., L. Chen, J. Bortnik, R. M. Thorne, V. Angelopoulos, C. A. Kletzing, W. S. Kurth, and G. B. Hospodarsky (2015a), First evidence for chorus at a large geocentric distance as a source of plasmaspheric hiss: Coordinated THEMIS and Van Allen Probes observation, *Geophys. Res. Lett*., *42*, 241–248, doi:10.1002/2014GL062832.

Li, W., R. M. Thorne, J. Bortnik, D. N. Baker, G. D. Reeves, S. G. Kanekal, H. E. Spence, and J. C. Green (2015b), Solar wind conditions leading to efficient radiation belt electron

acceleration: A superposed epoch analysis, *Geophys. Res. Lett.*, *42*, 6906–6915, doi:10.1002/2015GL065342.

Lyons, L. R. (1974), Electron diffusion driven by magnetospheric electrostatic waves, *J. Geophys. Res.*, *79*, 575–580.

Lyons, L. R., R. M. Thorne and C. F. Kennel (1972), Pitch-angle diffusion of radiation belt electrons within the plasmasphere, *J. Geophys. Res.*, *77*, 3455–3474.

Ma, Q., W. Li, R. M. Thorne, and V. Angelopoulos (2013), Global distribution of magnetosonic waves observed by THEMIS spacecraft, *Geophys. Res. Lett.*, *40*, 1895–1901, doi:10.1002/grl50434.

Ma, Q., W. Li, L. Chen, R. M. Thorne, and V. Angelopoulos (2014a), Magnetosonic wave excitation by ion ring distributions in the Earth's inner magnetosphere, *J. Geophys. Res. Space Physics*, *119*, 844–852. doi:10.1002/2013JA019591.

Ma, Q., et al. (2014b), The trapping of equatorial magnetosonic waves in the Earth's outer plasmasphere, *Geophys. Res. Lett.*, *41*, 6307–6313, doi:10.1002/2014GL061414.

Ma, Q., W. Li, R. M. Thorne, J. Bortnik, C. A. Kletzing, W. S. Kurth, and G. B. Hospodarsky (2015a), Electron scattering by magnetosonic waves in the inner magnetosphere, *J. Geophys. Res. Space Physics*, *120*, doi:10.1002/2015JA021992.

Ma, Q., et al. (2015b), Modeling inward diffusion and slow decay of energetic electrons in the Earth's outer radiation belt, *Geophys. Res. Lett.*, *42*, 987–995, doi:10.1002/2014GL062977.

Meredith, N. P., et al. (2006), Energetic outer-zone electron lifetimes during low geomagnetic activity, *J. Geophys. Res.*, *111*, A05212, doi:10.10292005A011516.

Meredith, N. P., R. B. Horne, R. M. Thorne, & R. R. Anderson (2009), Survey of upper band chorus and ECH waves: Implications for the diffuse aurora, *J. Geophys. Res.*, *114*, A07218, doi:1029/2009JA14230.

Meredith, N. P., et al. (2012), Global models of lower band and upper band chorus from multiple satellite observations, *J. Geophys. Res.*, *117*, A10225, doi:10.1029/2012JA017978.

Nemec, F., et al. (2005), Initial results of a survey of equatorial noise emissions observed by the Cluster spacecraft, *Planet. & Space Sci.*, *53*, 291–298.

Newell, P. T., Sotirelis, T. & Wing, S. Diffuse, monoenergetic, and broadband aurora: The global precipitation budget (2009), *J. Geophys. Res.*, *114*, A09207, doi:10.1029/2006JA012237.

Ni, B., R. M. Thorne, Y. Y. Shprits, and J. Bortnik (2008), Resonant scattering of plasma sheet electrons by whistler-mode chorus: Contribution to diffuse auroral precipitation, *Geophys. Res. Lett.*, *35*, L11106, doi:10.1029/2008GL034032.

Ni, B., et al. (2011a), Resonant scattering of plasma sheet electrons leading to diffuse auroral precipitation: 1. Evaluation for electrostatic electron cyclotron harmonic waves, *J. Geophys. Res.*, *116*, A04218, doi:10.1029/2010JA016232.

Ni, B., R. M. Thorne, N. P. Meredith, R. B. Horne, and Y. Y. Shprits (2011b), Resonant scattering of plasma sheet electrons leading to diffuse auroral precipitation: 2. Evaluation for whistler mode chorus waves, *J. Geophys. Res.*, *116*, A04219, doi:10.1029/2010JA016233.

Ni, B, et al. (2011c), Global distribution of electrostatic electron cyclotron harmonic waves observed on THEMIS, *Geophys. Res. Lett.*, *38*, L17105, doi:10.1029/2011GL048793.

Ni, B., et al. (2012), Efficient diffuse auroral electron scattering by electrostatic electron cyclotron harmonic waves in the outer magnetosphere: A detailed case study, *J. Geophys. Res.*, *117*, A01218, doi:10.1029/2011JA017095.

Ni, B., J. Bortnik, R. M. Thorne, Q. Ma, and L. Chen (2013), Resonant scattering and resultant pitch angle evolution of relativistic electrons by plasmaspheric hiss, *J. Geophys. Res. Space Physics*, *118*, 7740–7751, doi:10.1002/2013JA019260.

Ni, B., et al. (2014a), A novel technique to construct the global distribution of whistler-mode chorus wave intensity using low-altitude POES electron data, *J. Geophys. Res. Space Physics*, *119*, 5685–5699, doi:10.1002/2014JA019935.

Ni, B., et al. (2014b), Resonant scattering of energetic electrons by unusual low-frequency hiss, *Geophys. Res. Lett.*, *41*, 1854–1861, doi:10.1002/2014GL059389.

Nishimura, Y., et al. (2010), Identifying the driver of pulsating aurora, *Science*, *330*, 81–84, doi:10.1126/science.1193186.

Omura, Y., Y. Katoh, and D. Summers (2008), Theory and simulation of the generation of whistler-mode chorus, *J. Geophys. Res.*, *113*, A04223, doi:10.1029/2007JA012622.

Petrinec, S. M., D. L. Chenette, J. Mobilia, M. A. Rinaldi, and W. L. Imhof (1999), Statistical X ray auroral emissions – PIXIE observations, *Geophys. Res. Lett.*, *26*(11), 1565–1568.

Reeves, G. D., et al. (2013), Electron Acceleration in the heart of the Van Allen radiation belts, *Science*, *341*, 991–994, doi:10.1126/science.1237743.

Russell, C.T., Holzer, R.E., Smith, E.J. (1970), OGO 3 observations of ELF noise in the magnetosphere 2. The nature of the equatorial noise. *J. Geophys. Res*. *73*, 755–768.

Shprits, Y. T., et al. (2006), Outward radial diffusion driven by losses at magnetopause, *J. Geophys. Res.*, *111*, A11214, doi:10.1029/2006JA011657.

Summers, D., R. M. Thorne, and F. Xiao (1998), Relativistic theory of wave-particle resonant diffusion with application to electron acceleration in the magnetosphere, *J. Geophys. Res.*, *103*, 20,487–20,500.

Summers, D., et al. (2002), Model of the energization of outer-zone electrons by whistler-mode chorus during the October 9, 1990 geomagnetic storm, *Geophys. Res., Lett.*, *29*, (24). 2174, doi:10.1029/2001GL016039.

Summers, D., B. Ni, and N. P. Meredith (2007), Timescales for radiation belt electron acceleration and loss due to resonant wave-particle interactions: 2. Evaluation for VLF chorus, ELF hiss, and electromagnetic ion cyclotron waves, *J. Geophys. Res.*, *112*, A04207, doi:10.1029/2006JA011993.

Tao, X., et al. (2011), Evolution of electron pitch-angle distributions following injection from the plasma sheet, *J. Geophys. Res.*, *116*, A04229, doi:10.1029/2010JA016245.

Thorne, R. M. (2010), Radiation belt dynamics: The importance of wave-particle interactions, *Geophys. Res. Lett.*, *37*, L22107, doi:10.1029/2010GL044990.

Thorne, R. M., B. Ni, X. Tao, R. B. Horne, and N. P. Meredith (2010), Scattering by chorus waves as the dominant cause of diffuse auroral precipitation, *Nature*, *467*, 943–946, doi:10.1038/nature09467.

Thorne, R. M., et al. (2013a), Evolution and slow decay of an unusual isolated ring of relativistic electrons near L~ 3.2

following the September 2012 magnetic storm, *Geophys. Res., Lett*., *40*, 3507–3511, doi:10.1002/grl.50627.

Thorne, R. M., et al. (2013b), Van Allen probe evidence of relativistic radiation belt electron acceleration by magnetospheric chorus, *Nature*, *504*, 411–414, doi:10.1038/nature12889.

Tsurutani, B. T., and E. J. Smith (1974), Postmidnight Chorus: A Substorm Phenomenon, *J. Geophys. Res.*, *79*(1), 118–127.

Tu, W., et al. (2014), Event- specific chorus wave and electron seed population models in DREAM3D using the Van Allen Probes, *Geophys. Res. Lett.*, *41*, 1359–1366, doi:10.1002/2013GL058819.

Turner, D. L., et al. (2013), On the storm-time evolution of relativistic electron phase space density in Earth's outer radiation belt, *J. Geophys. Res. Space Physics*, *118*, 2196–2212, doi:10.1002/jgra.50151.

Villalon, E., and W. J. Burke (1995), Pitch angle scattering of diffuse auroral electrons by whistler mode waves, *J. Geophys. Res.*, *100*, 19,361–19,369.

Zhang, X., V. Angelopoulos, B. Ni, R. M. Thorne, and R. B. Horne (2014), Extent of ECH waves emissions in Earth's magnetotail, *J. Geophys. Res., Space Physics*, *119*, 5561–5574, doi:10.1002/2014JA019931.

Zhang, X., V. Angelopoulos, B. Ni, and R. M. Thorne (2015), Predominance of ECH wave contribution to diffuse aurora in Earth's outer magnetosphere, *J. Geophys. Res. Space Phys*., *120*, 295–309, doi:10.1002/2014JA020455.

10

Plasma Wave Measurements from the Van Allen Probes

George B. Hospodarsky[1], W. S. Kurth[1], C. A. Kletzing[1], S. R. Bounds[1], O. Santolík[2,3], Richard M. Thorne[4], Wen Li[4], T. F. Averkamp[1], J. R. Wygant[5], and J. W. Bonnell[6]

Video of Yosemite Talk, URL: http://dx.doi.org/10.15142/T3W886

ABSTRACT

The twin Van Allen Probes spacecraft were launched on 30 August 2012 to study the Earth's Van Allen radiation belts. The Electric and Magnetic Field Instrument Suite and Integrated Science (EMFISIS) investigation includes the Waves instrument that simultaneously measures three orthogonal components of the wave magnetic field from ~10 hertz (Hz) to 12 kilohertz (kHz) and, with the support of the Electric Fields and Waves (EFW) sensors, three components of the wave electric field from ~10 Hz to 12 kHz, and a single electric component up to ~500 kHz. Since launch, a variety of plasma waves have been detected that are believed to play a role in the dynamics of the radiation belts, including whistler mode chorus, plasmaspheric hiss, and magnetosonic equatorial noise. Lightning produced whistlers, electron cyclotron harmonic emission, quasi-periodic (QP) whistler mode emission, and the upper hybrid resonance (UHR) are also often detected. The UHR is used to determine the local electron plasma density (an important parameter of the plasma required for various modeling and simulation studies). Measuring all six components simultaneously allows the wave propagation parameters of these plasma wave emissions, including the Poynting flux, wave normal vector, and polarization, to be obtained. We will summarize the EMFISIS wave observations and discuss their role in the Van Allen radiation belt dynamics.

10.1. INTRODUCTION

Plasma waves play an important role in the dynamics of Earth's Van Allen radiation belts [*Thorne*, 2010; *Hospodarsky et al*., 2012; and references within]. Wave-particle interactions produce both acceleration and loss of radiation belt particles [*Kennel and Petschek*, 1966; *Omura and Summers*, 2006; *Thorne et al*., 2013a]. The Van Allen Radiation Belt Storm Probes (RBSP) mission consists of two identical spacecraft with a comprehensive suite of field and particle instruments, providing a rich new data set for studies of wave-particle interactions in Earth's radiation belts. This paper will summarize some of the RBSP plasma wave observations and discuss their role in radiation belt dynamics.

The twin RBSP spacecraft were launched on 30 August 2012 into nearly identical ~9 hour orbits, which are inclined to the geographic equator by about 10°, with apogee near 5.8 Earth radii (R_E) and perigee near 1.1 R_E. The two spacecraft lap each other every 60 to 70 days, and they completed their first complete coverage of Magnetic

[1]*Department of Physics and Astronomy, University of Iowa, Iowa City, IA, USA*

[2]*Department of Space Physics, Institute of Atmospheric Physics, The Czech Academy of Sciences, Prague, Czech Republic*

[3]*Faculty of Mathematics and Physics, Charles University, Prague, Czech Republic*

[4]*Department of Atmospheric and Oceanic Sciences, University of California, Los Angeles (UCLA), Los Angeles, CA, USA*

[5]*School of Physics and Astronomy, University of Minnesota, Minneapolis, MN, USA*

[6]*Space Sciences Laboratory, University of California, Berkeley, Berkeley, CA, USA*

Magnetosphere-Ionosphere Coupling in the Solar System, Geophysical Monograph 222, First Edition.
Edited by Charles R. Chappell, Robert W. Schunk, Peter M. Banks, James L. Burch, and Richard M. Thorne.

Local Time (MLT) in May 2014. Each spacecraft contains five instrument suites designed to measure the waves and particles found in the Earth's Van Allen radiation belts [*Mauk et al.*, 2013]. The EMFISIS suite [*Kletzing et al.,* 2013] includes a triaxial magnetometer (MAG) and a plasma wave instrument (Waves). Waves contains a six-channel WaveForm Receiver (WFR) that simultaneously measures at 35,000 samples per second the three magnetic and three electric components of plasma waves in the frequency range of ~10 Hz to ~12 kHz using triaxial search coils (magnetic search coil [MSC]) and the Electric Fields and Waves (EFW) [*Wygant et al.*, 2013] triaxial electric field sensors. By measuring all six components of the plasma waves simultaneously, wave propagation parameters such as the wave normal and Poynting vectors can be determined. Survey WFR spectral matrices are returned continuously with a typical cadence of six seconds by collecting onboard 16,384 samples (0.468 s waveform) simultaneously in each of the six channels, performing a fast Fourier transform (FFT), calibrating in frequency space, and averaging into 65 frequency bins between 2.14 Hz and 11.2 kHz. A number of higher resolution burst modes are also available, including one that obtains simultaneous 208,896 samples (5.968 seconds) waveform data from each of the six channels (see *Kletzing et al.* [2013] for more details on the EMFISIS survey and burst modes). The Waves instrument also contains a High Frequency Receiver (HFR) that measures a single electric field component in the frequency range of ~10 kHz to ~500 kHz, with a typical survey cadence of 0.5 second. The primary objective of the HFR is to allow the determination of the electron density (n_e) by measuring the frequency of the upper hybrid resonance emission (f_{UHR}) [*Kurth et al.,* 2015].

Figure 10.1 shows time-frequency spectrograms of the EMFISIS survey wave data for one orbit (orbit 2100) of spacecraft B (SCB). The top panel (a) shows the HFR data (attached to the Eu antenna), the second panel (b) shows the sum of the two spin plane (Eu and Ev) electric field channels, and the third panel (c) shows the sum of the three magnetic channels. The white lines show the electron cyclotron frequency (f_{ce}), 0.5 f_{ce}, the lower hybrid frequency (f_{LHR}), and the proton cyclotron frequency (f_{cp}) as determined from the magnitude of the background magnetic field as measured by MAG. During this orbit, a wide range of plasma wave emissions are detected in the WFR, panels (b) and (c), including whistler mode chorus, plasmaspheric hiss, electrostatic cyclotron harmonic (ECH) emissions, magnetosonic equatorial noise emission, and lightning whistlers. Furthermore, the HFR detects (top panel) the UHR and ECH emissions, along with auroral kilometric radiation (AKR) [*Gurnett* 1974; *Ergun et al.,* 1998] and non-thermal continuum radiation [*Gurnett,* 1975]. The abrupt changes in the frequency of the UHR frequency are an indication of the spacecraft exiting (~00:25) and reentering (~06:00) the plasmasphere [*Kurth et al.*, 2015]. The bottom two panels of Figure 10.1 show the polar angle of the wave normal angle, panel (d), and Poynting vector angle, panel (e), with respect to the background magnetic field as determined with the Single Value Decomposition (SVD) method [*Santolík et al.,* 2003a]. To more easily see the wave propagation properties of the emissions, a plotting filter has been applied to the data so that only angles corresponding to emissions with a magnetic field spectral density greater than 10^{-7} nT^2/Hz are plotted. The value of 10^{-7} nT^2/Hz for the plotting filter was chosen to be well above the noise level of the instrument for the frequency range of most of the emissions detected during this period, but not so large as to exclude the plotting of the emissions of interest. The next sections will discuss the wave emissions detected by RBSP and summarize some of the early the results concerning radiation belt dynamics.

10.2. LIGHTNING WHISTLERS

Radio emissions from lightning can penetrate through the ionosphere and travel along geomagnetic field lines into the magnetosphere, where the higher frequency components propagate faster than the lower frequencies, producing the well-known dispersed lightning whistler emission often detected by orbiting spacecraft [*Helliwell,* 1969]. A number of previous studies have investigated the role of lightning whistlers in radiation belt dynamics [e.g., *Lauben et al.*, 2001; *Rodger et al.*, 2003; *Meredith et al.*, 2007] and as a possible source of plasmaspheric hiss [*Draganov et al.*, 1992; *Green et al.,* 2005; 2006; *Thorne et al.,* 2006; *Meredith et al.,* 2006].

EMFISIS detects lightning whistlers during most orbits, both as sporadic bursty emissions detected in the survey data near perigee, e.g., speckled emission in panels (b) and (c) of Figure 10.1 observed from about 22:45 and 06:30 UT above ~1 kHz, and as fully resolved dispersed whistler emissions in the burst waveform data. Figure 10.2 shows an example of lightning whistlers as detected in the six-channel burst waveform data in which the spacecraft encounters multiple reflections as the initial lightning whistler "bounces" back and forth between each hemisphere. The top panel of Figure 10.2 shows the sum of the three magnetic field components of the WFR, the middle panel shows the wave normal polar angle with respect to the background magnetic field (plotted from 50° to 90° to emphasize the increase in wave normal angle with each bounce), and the bottom panel shows the direction of the Poynting vector dotted with the background field (blue for the Poynting vector direction parallel to the magnetic field, red for antiparallel). As expected from cold plasma dispersion theory, each bounce of the reflected lightning whistlers shows increased dispersion

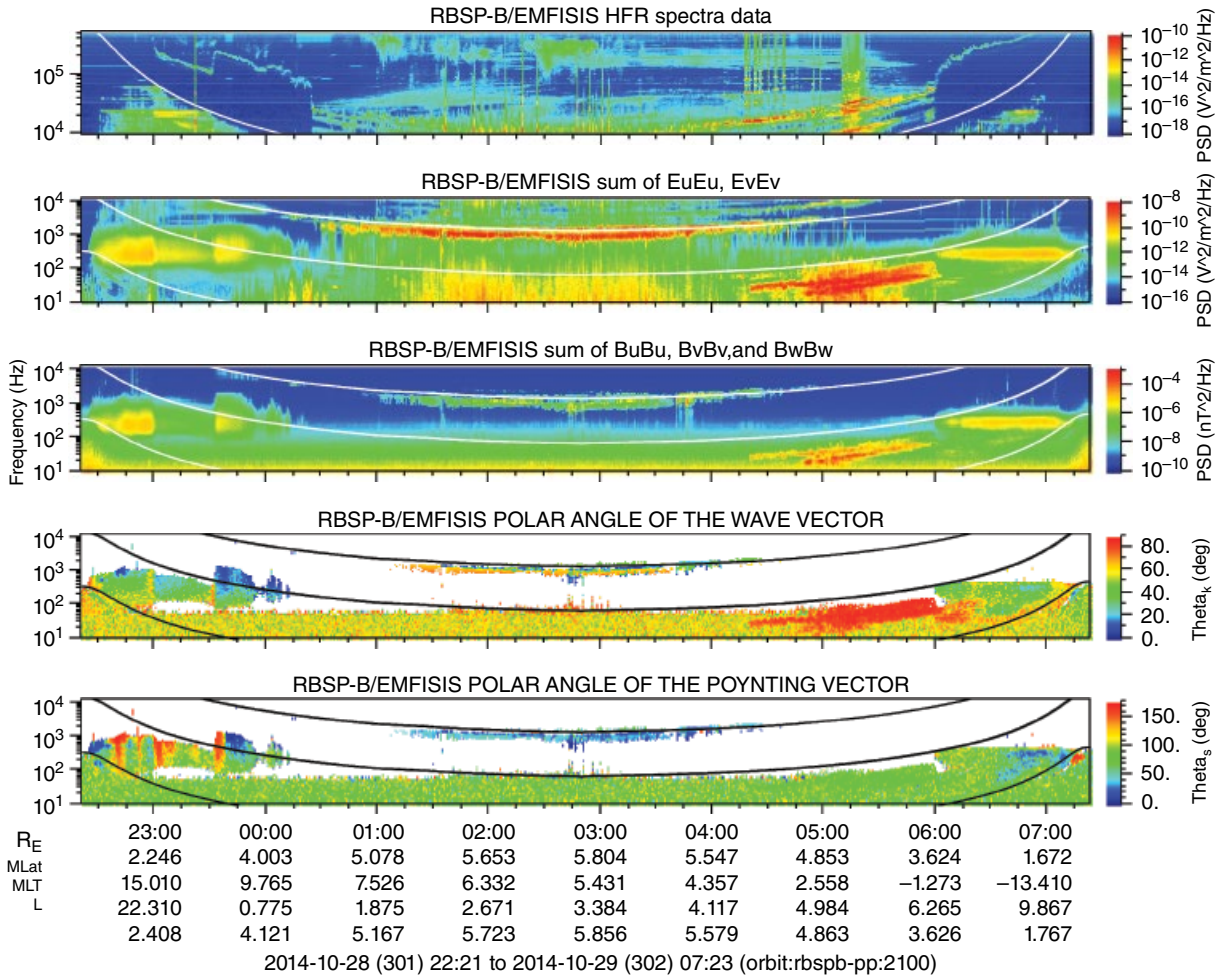

Figure 10.1 Time-frequency spectrograms of the EMFISIS survey wave data for orbit 2100 of spacecraft B showing plasma waves that are believed to be important for radiation belt dynamics. The top panel shows the HFR data (attached to the Eu antenna), the second panel shows the sum of the two spin plane (Eu and Ev) electric field channels, the third panel shows the sum of the three magnetic channels, and the fourth and fifth panels show the polar angle of the wave normal angle and the Poynting vector angle with respect to the background magnetic field as determined with the SVD method [*Santolík et al.,* 2003a]. For the fourth and fifth panel, a plotting filter has been applied to the data so that only results corresponding to emissions with a magnetic field spectral density greater than 10^{-7} nT^2/Hz are plotted. The lines show various frequencies of the plasma as determined from the magnitude of the background magnetic field as measured by MAG.

(top panel), the wave normal angle increases (middle panel), and the direction of the whistlers changes with each pass over the spacecraft (bottom panel).

Zheng et al. [2015] investigated the relationship between lightning strokes detected by the ground-based World Wide Lightning Location Network (WWLLN) [*Dowden et al.,* 2002] and lightning whistlers detected by RBSP. Examining periods the RBSP spacecraft were on magnetic field lines that connected to the ionosphere close to a region where lightning was detected on the ground by the WWLLN, they found that about 30 to 50% of the spacecraft detected whistlers could be directly associated with specific lightning strokes. Further analysis investigating the relation between specific lightning strokes and the propagation properties of the whistlers is ongoing.

10.3. WHISTLER MODE CHORUS

Chorus is an electromagnetic, right-hand polarized whistler mode emission generated by nonlinear interactions with energetic electrons [*Storey*, 1953; *Allcock*, 1957; *Helliwell,* 1969]. Chorus is usually detected outside of Earth's plasmasphere during periods of disturbed magnetospheric conditions in two distinct frequency bands separated by a gap at one-half of the electron cyclotron frequency, with the lower band ranging from

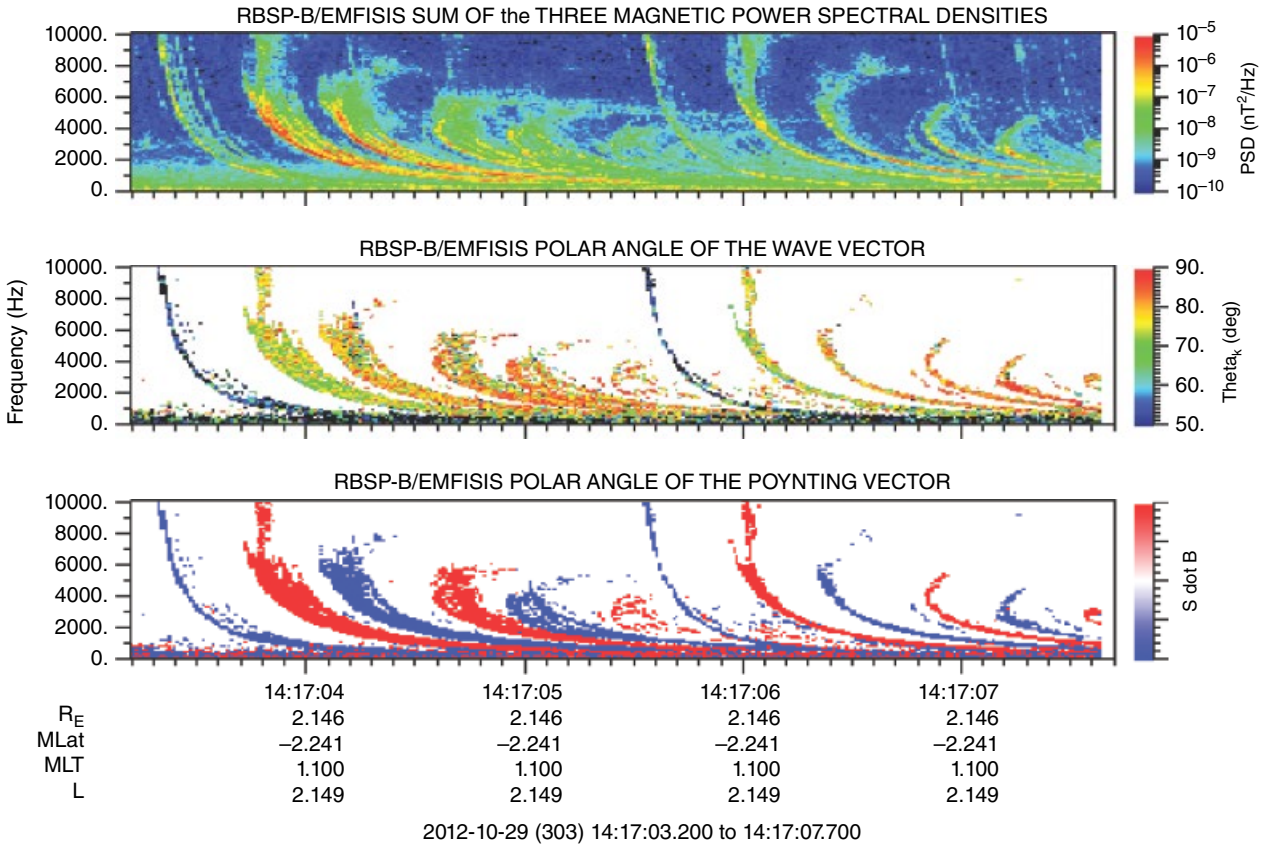

Figure 10.2 Time-frequency spectrograms of lightning whistlers as detected in the six-channel burst waveform data. The top panel shows the sum of the three magnetic field components of the WFR, the middle panel shows the wave normal polar angle with respect to the background magnetic field, and the bottom panel shows the direction of the Poynting vector dotted with the background field (blue for the Poynting vector direction parallel to the magnetic field, red for antiparallel).

about 0.1 to 0.5 f_{ce}, and the upper band from about 0.5 to 0.8 f_{ce} [*Tsurutani and Smith*, 1974, 1977; *Meredith et al.*, 2001; *Sigsbee et al.,* 2008]. High time resolution measurements of chorus often show complicated fine structures, including rising and falling tones (often called chorus elements), and short impulsive bursts, all with time scales of much less than a second [*Gurnett and O'Brien*, 1964; Sazhin and *Hayakawa*, 1992; *Santolík et al.*, 2003b, 2004a]. The origin of this fine structure and its relationship to the source of chorus is an active area of research [*Katoh and Omura*, 2011; *Omura et al.,* 2008; *Tao et al.,* 2012; *Summers et al.,* 2013; and references therein].

Chorus emission is detected on many orbits by RBSP. Figure 10.1 includes an example of chorus emissions as observed in the EMFISIS survey data on SCB. During this orbit, chorus is detected from about 01:00 to 05:00 UT in the frequency range of about 1 to a few kHz. Two frequency bands of chorus are detected, with a gap at ~0.5 f_{ce}, as shown by the white line in panels (b) and (c). The bottom two panels of Figure 10.1 show that the majority of the chorus detected on this orbit has large (>20°) wave normal angles, panel (d), and is propagating parallel to the background magnetic field, panel (e), away from the likely source region near the magnetic equator [*Ledocq et al.*, 1998]. Large wave normal angles for chorus are not uncommon in the RBSP data and are not unexpected since observations from other missions have reported similar large values in the source region of chorus [e.g., *Santolík et al.*, 2009; *Li et al.*, 2011].

The high-resolution burst data from RBSP EMFISIS shows a wide range of chorus fine structure. Figure 10.3 shows examples of time-frequency spectrograms of chorus emission fine structure from the WFR Bu channel six-second waveform burst data. Panel (a) of Figure 10.3 shows an example of "typical" chorus with two emission bands with a gap at ~0.5 f_{ce}. The lower band in this example contains a number of rising tone elements while the upper band is more hiss like (structureless). Panel (b) shows an example of upper band chorus with no lower band chorus present. Panel (c) shows an example of lower band chorus with an individual element that initially falls in frequency (~20:07:24.5 to ~20:07:26.5 UT)

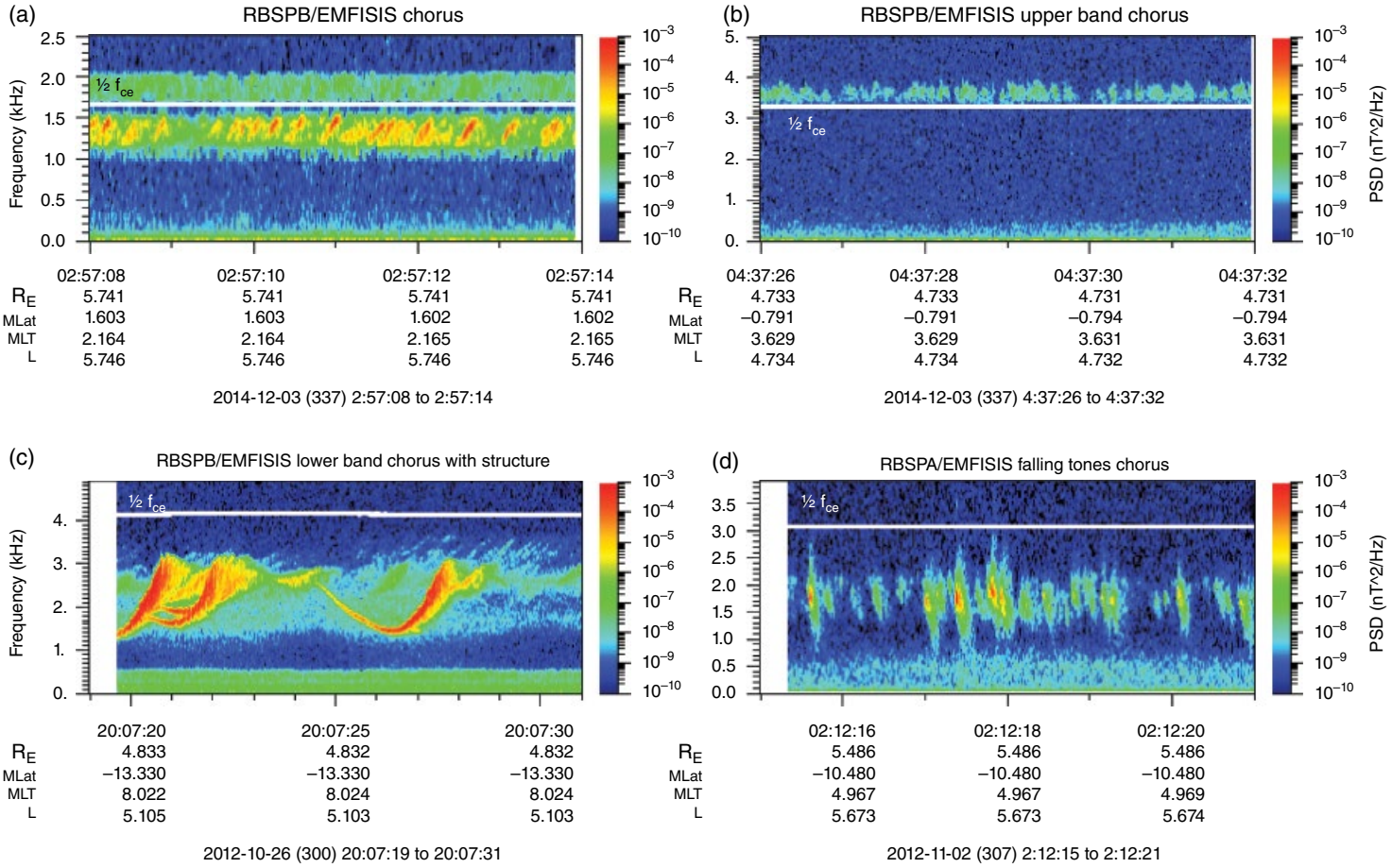

Figure 10.3 Time-frequency spectrograms showing four examples of chorus emission fine structure from the WFR Bu channel six-second waveform burst data.

and then rises in frequency (~20:07:26.5 to ~20:07:28 UT), while panel (d) shows an example of lower band chorus with falling tones. The high sampling rate of the EMFISIS instrument allows detailed examination of the individual wave packets associated with chorus and investigations into possible nonlinear processes and generation mechanisms.

Santolík et al. [2014] examined the fine structure for large-amplitude, lower band chorus wave packets similar to those found in panel (a) of Figure 10.3. Using the full three-dimensional WFR burst wave magnetic field data, they directly determined the intensity and wave propagation parameters of individual chorus wave subpackets. Peak amplitudes of these subpackets were found to range from a few tens of pT to ~3 nT, large enough for nonlinear processes to be important. Furthermore, they found that the wave vector direction can change by many tens of degrees within a single chorus subpacket and also over a chorus element. Work is ongoing to determine the reason for this variation and to determine the possible implications for radiation belt particle dynamics.

A number of studies have also investigated the role of chorus and the dynamics of the Van Allen radiation belts during specific events or storms [*Thorne et al.,* 2013a; *Li et al.,* 2013a; *Foster et al.,* 2014; *Fennell et al.,* 2014; *Li et al.,* 2014a; *Su et al.,* 2014; *Xiao et al*., 2014; *Liu et al.*, 2015]. For example, *Thorne et al*. [2013a] showed that local stochastic acceleration by chorus waves was the dominant process for the development of the peaks in electron phase space densities reported by *Reeves et al*. [2013] during the 9 October 2012 storm.

Direct wave-particle interactions of chorus emissions and source population of keV electrons in the postmidnight sector following a plasma injection have been reported by *Fennell et al.* [2014]. They found simultaneous occurrences of QP bursts of 17 to 26 keV electrons and chorus emissions, with the electron angular distribution changing dramatically during the burst events. Using the measured values of f_{ce}, the frequency of the chorus emissions, n_e determined from the UHR [*Kurth et al.,* 2015], and the pitch angles of the peak electron flux, the expected resonance electron energy was estimated to be ~15 to 35 keV for the upper band chorus detected during this event, very similar to the observed strong and rapid changes in the electron fluxes from 17 to 26 keV.

Although the twin RBSP spacecraft, along with other spacecraft such as Time History of Events and Macroscale Interactions during Substorms (THEMIS) [*Angelopoulos*, 2008] and Cluster [Escoubet et al., 1997] provide multipoint measurements of wave properties in multiple locations in the magnetosphere, it is still difficult at times to determine the instantaneous global distribution of whistler mode chorus and hiss amplitudes that are needed to determine the global rate of transport, loss, and acceleration of radiation belt particles. In an attempt to overcome this problem, *Li et al*. [2013a] developed a technique to infer the chorus wave intensity from the low altitude 30 to 100 keV electron observations from the National Oceanic and Atmospheric Administration's Polar-orbiting Operational Environmental Satellites (POES) by using the measured Van Allen Probes data of chorus wave intensity to "calibrate" the technique. This technique to determine global chorus wave intensity has been further refined [*Ni et al*., 2014a], and applied to estimate the electron acceleration due to chorus during the March 17, 2013 storm [*Li et al.,* 2014a]. Further work has also expanded this technique to provide reasonable estimates of plasmaspheric hiss intensity [*Li et al.,* 2014b].

A number of other studies involving Van Allen Probe chorus observations include attempts to explain the gap at 1/2 f_{ce} [*X. Fu et al*., 2014], comparing cold plasma dispersion theory to actual measured wave magnetic field intensities [Hartley et al., 2015], and comparing RBSP measurements to high altitude balloon measurements above Antarctica by the Balloon Array for Radiation belt Relativistic Electron Losses (BARREL) mission [*Millan et al.,* 2013; *Halford et al., 2015*].

10.4. PLASMASPHERIC HISS

Plasmaspheric hiss is a broadband, structureless whistler mode emission usually found in Earth's plasmasphere [*Dunckel and Helliwell,* 1969; *Thorne et al.,* 1973] and in high-density plumes [*Chan and Holzer*, 1976; *Parrot and Lefeuvre*, 1986]. Plasmaspheric hiss is believed to be responsible for generating the slot region between the inner and outer Van Allen radiation belts by causing electron precipitation into the upper atmosphere through pitch angle scattering [*Lyons et al.,* 1972; *Lyons and Thorne,* 1973; *Abel and Thorne*, 1998; *Meredith et al.,* 2004], and to be important for the scattering of outer zone electrons due to the intense hiss in plasmaspheric plumes [*Summers et al.,* 2007, 2008].

There are three main theories proposed for the origin of plasmaspheric hiss: (1) growth from pre-existing waves due to free energy of unstable electron populations [*Thorne et al.,* 1973; *Church and Thorne*, 1983]; (2) accumulation of lightning whistler waves [*Draganov et al.,* 1992; *Green et al*., 2005; 2006; *Thorne et al.,* 2006; *Meredith et al.,* 2006]; and (3) propagation into the plasmasphere of chorus emissions produced near the magnetic equator outside of the plasmasphere [*Chum and Santolík*, 2005; *Santolík et al.,* 2006; *Bortnik et al*., 2008, 2009a, 2009b].

Figure 10.1 shows examples of plasmaspheric hiss detected from about 22:20 to 00:30 UT and 06:00 to 07:10 UT by SCB in the frequency range of ~100 Hz to ~2 kHz. RBSP detects plasmaspheric hiss on most orbits, and a number of studies have investigated the properties of hiss [*Li et al.,* 2013b; *Li et al.,* 2015a], the role hiss plays in radiation belt dynamics and electron precipitation

[*Thorne et al.,* 2013b; *Li et al*., 2014b; *Ni et al.,* 2014b; *Y. Chen et al*., 2014; *Breneman et al.,* 2015; *Zhu et al.*, 2015; *Li et al.,* 2015a], and the possible sources of plasmaspheric hiss [*L. Chen et al*., 2014; *Li et al*., 2015b]. We will briefly discuss some of these results below.

Previous results, primarily from the Combined Release and Radiation Effects Satellite (CRRES), found that plasmaspheric hiss was usually detected between ~100 Hz to 2 kHz [*Meredith et al*., 2004]. However RBSP, with better resolution at the lower frequencies, often detects plasmaspheric hiss associated with substorm injected electrons at frequencies below 100 Hz, sometimes down to ~20 Hz [*Li et al*., 2013b]. *Ni et al.* [2014b] showed that this lower frequency hiss can scatter ~50 to 200 keV electrons much more rapidly than the "normal" higher frequency hiss, and also changes scattering rates at other energies. *Li et al.* [2015a] determined the global distribution of plasmaspheric hiss for different levels of substorm activity as detected by RBSP. This result showed that the hiss wave power frequently extends below 100 Hz, and using this new statistical hiss wave frequency spectrum in electron pitch angle diffusion coefficients calculations leads to a difference in electron pitch angle scattering rates up to a factor of ~5 depending on energy and L-shell compared to the frequently used Gaussian wave frequency spectrum. These results strongly suggest that realistic hiss wave spectra are critical in accurate predictions of radiation belt electron dynamics. *L. Chen et al.* [2014] examined possible sources of these low frequency hiss waves and found that although the low frequency hiss is only weakly unstable due to the newly injected electrons, multiple passes through the amplification region could produce a sufficient wave gain (>40 dB) out of background noise, and that the cyclic ray paths of the waves were stable over a range of initial wave normal angles (<20°), consistent with observations.

As mentioned earlier, the source of plasmaspheric hiss has been debated for over 40 years. Recent results from RBSP have suggested that the source is likely a combination of two of the proposed origins (local growth from unstable electrons and chorus propagating into the plasmasphere). *Li et al*. [2013b] suggested that the low frequency hiss (<100 Hz) observed by RBSP is most likely created locally from injected energetic electrons, primarily because chorus at these frequencies would have to originate from unrealistic large L shells. Furthermore, *L. Chen et al.* [2014] showed from a ray tracing study that locally generated low frequency hiss can encounter the amplification region multiple times, resulting in the observed wave intensities. However, they also found that the higher frequency (>500 Hz) hiss didn't follow these cyclic amplification trajectories, suggesting that local generation cannot explain the higher frequency hiss, leaving chorus as the likely source as proposed by *Bortnik et al*. [2008]. To further investigate the possibility of chorus as a source for the hiss, a coordinated campaign between THEMIS and RBSP was performed in the first half of 2014 while the apogee of both spacecraft were on the dayside. *Li et al.* [2015b] reports on an event during this campaign in which chorus was detected by THEMIS at an L of ~9.8 that was highly correlated with the hiss detected by RBSP inside the plasmasphere at L of ~5.8. Ray tracing results showed that the chorus could propagate from the THEMIS location to RBSP on a timescale similar to the time delay of chorus and hiss that was observed between the two spacecraft, providing strong evidence that at least a portion of plasmaspheric hiss originated from chorus at higher L shells propagating into the plasmasphere.

Narrowband emissions that appear to be triggered and rise out of the top of plasmaspheric hiss bands are often detected on the ground [*Smith and Nunn*, 1998] and in space [*Helliwell*, 1965; *Picket et al.,* 2005]. These emissions have many of the same characteristics as chorus elements, including rising and falling tones. The RBSP spacecraft often detects these emissions near the plasmapause boundary in the dusk sector. Figure 10.4 shows four examples of these emissions from the WFR magnetic field burst data. These emissions are primarily detected below 1/2 f_{ce}, but are sometimes observed crossing 1/2 f_{ce}, as shown in panels (a) and (d) in Figure 10.4. A more detailed survey of the occurrence and wave properties of these emissions, plus their relationship to chorus, is under way and will be reported in a future work.

10.5. MAGNETOSONIC EQUATORIAL NOISE EMISSION

Low-frequency electromagnetic emissions propagating in the fast magnetosonic mode perpendicular to the ambient magnetic field, $\mathbf{B}_0$, are frequently detected in Earth's inner magnetosphere within about 10 degrees of the geomagnetic equator [*Russell et al.,* 1970; *Santolík et al.,* 2004b; *Meredith et al*., 2008]. These emissions are usually observed between the local f_{cp} and f_{LHR}, and often contain a great deal of fine structures consisting of a complex superposition of bands with frequency spacing from a few Hertz to several tens of Hertz, similar to the proton and ion cyclotron frequencies [*Gurnett*, 1976; *Perraut et al.*, 1982]. The source of the waves is believed to be low energy proton shell distributions [*Perraut et al.,* 1982; *Boardsen et al*., 1992; *L. Chen et al*., 2011; *Thomsen et al*., 2011; *Ma et al.,* 2014a], and a number of authors have examined the importance of these waves on radiation belt dynamics [*Horne et al.,* 2000, 2007; *L. Chen et al.,* 2010; *Bortnik and Thorne*, 2010].

RBSP provides a new opportunity to examine the characteristics of the magnetosonic equatorial emissions and their role in radiation belt dynamics. Two recent studies have used the RBSP wave and particle data to examine at

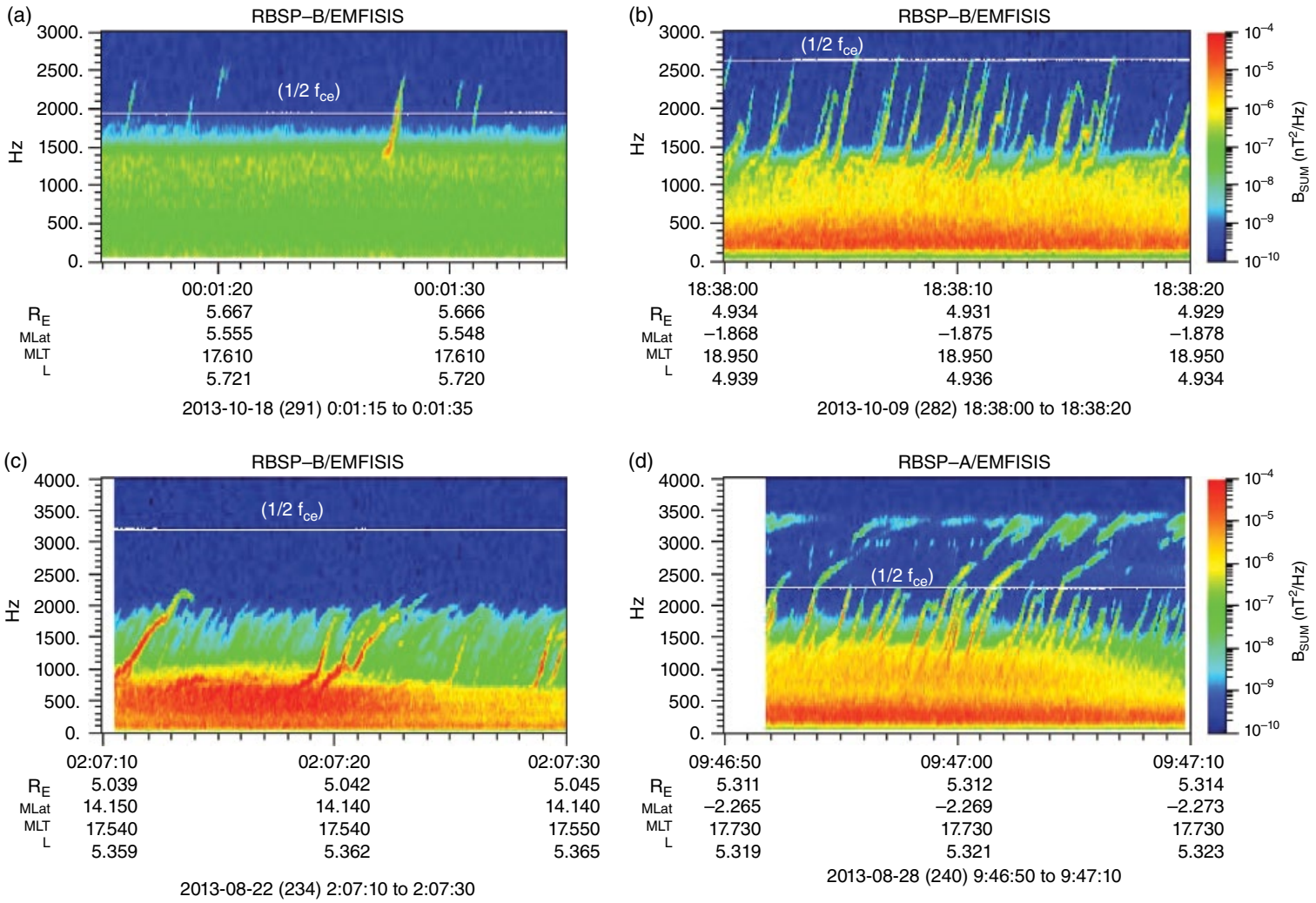

Figure 10.4 Time-frequency spectrograms showing four examples of narrowband emissions that appear to be triggered and rise out of the top of plasmaspheric hiss bands from the WFR Bu channel six-second waveform burst data.

the properties of these waves and the role of the proton ring distributions to excite the waves and their propagation [*Ma et al.,* 2014b; *Zhou et al*., 2014]. *Ma et al.* [2014b] found that for the events they analyzed, the waves were locally excited by an ion ring distribution near the equatorial plasmapause, propagated inward to lower L shells, and became trapped in a limited radial region in the outer plasmasphere. *Zhou et al*. [2014] found that the proton ring provides the source of free energy for the growth of the waves and that the growth rates peaked at harmonics of f_{cp}. They also found that the waves were excited at larger L shells and could propagate toward lower L shells, suggesting that the proton ring in one region can produce equatorial noise emissions in other regions.

Another study by *Boardsen et al.* [2014] examined the properties of the waves, specifically the QP enhancement of the intensities that are sometimes observed by RBSP. Figure 10.1 shows an example of magnetosonic equatorial emissions detected by RBSP from about 04:15 to 06:00 UT and between f_{LHR} and f_{cp}. These emissions are often one of the most intense (~10^{-4} nT^2/Hz) emissions detected in the magnetosphere, and since their wave normal angles are near 90°, they are easy to see in polar wave normal angle spectrograms, as shown in panel (d) of Figure 10.1. The high resolution burst data capability of the EMFISIS instrument allows the fine structure of these emissions to also be examined. Panels (a) and (c) of Figure 10.5 show a 20-minute period of continuous burst data from the event shown in Figure 10.1. The top left panel (a) shows a time-frequency spectrogram of the sum of the three search coil channels of the WFR, and the bottom left panel (c) shows the wave normal angle with respect to the background magnetic field. Two types of fine structure are observed in this event. The first structure, starting at about 40 Hz and going up in frequency, is narrowband lines of nearly constant frequency with spacing similar to the local f_{cp}. This structure is very similar to the structure detected by earlier spacecraft [e.g., *Gurnett*, 1976] and is very commonly associated with equatorial noise emissions. The second type of fine structure observed during this event is QP enhancements in intensity with a period of less than a minute that rise in frequency. This QP structure of equatorial noise has not been reported in earlier spacecraft studies, probably due to the lower time and frequency resolution of earlier wave receivers. However, it has been detected in the THEMIS [*H. S. Fu et al., 2014*], RBSP [*Boardsen et al., 2014*], and Cluster [*Nemec et al.,* 2015] data.

Panels (b) and (d) of Figure 10.5 show another example from the EMFISIS survey data of magnetosonic equatorial emissions that contains QP dispersive intensity enhancements with a period of ~1.5 mins. A preliminary survey of the RBSP data from 1 September 2012 to 10 November 2014 has found over 100 QP equatorial noise events, with typical periods of about one to a few minutes. These events tend to occur on the dayside and are primarily seen between L shells of ~3.5 to 5.5. Although these emissions have some similar characteristics to the QP whistler mode emissions discussed in the next section, there are also many differences, and it is not clear if or how they are related. A more detailed survey of the occurrence and wave properties of these emissions is under way and will be reported in a future work.

10.6. QUASI-PERIODIC WHISTLER MODE EMISSION

QP whistler mode emissions are electromagnetic waves observed in the inner magnetosphere in the frequency range of a few hundred Hz to a few kHz that exhibit a longer periodic time modulation (tens of seconds to many minutes) of the wave intensity, much longer than the sub-second structure often observed with whistler mode chorus. These waves were first reported from observations at high latitude ground-based stations [*Carson et al.,* 1965; *Smith et al.*, 1998], and have been characterized from the ground-based observations as Type 1 (correlated with Ultra Low Frequency (ULF) geomagnetic pulsations) and Type 2 (not correlated with ULF pulsations) [*Kitamura et al*., 1969; *Sato et al.,* 1974]. QP emissions have also been detected by a number of spacecraft, including Freja and Magion 5 [*Pasmanik, et al.,* 2004], DEMETER [*Hayosh et al*., 2013; *Němec et al*., 2013a], and Cluster [*Němec et al.,* 2013b, 2014]. Although the specific generation mechanism of QP emissions and their possible role in radiation belt dynamics is still not well understood [*Tixier and Cornilleau-Wehrlin*, 1986; *Sazhin and Hayakawa*, 1994], one possible candidate is ULF pulsations of the magnetic field modulating the resonant conditions of wave growth in the wave generation region [*L. Chen*, 1974; *Sazhin*, 1987]. A very similar emission with similar spectral properties of the QP emission has been detected at Saturn by the Cassini spacecraft [*Hospodarsky et al.,* 2008]. These whistler mode emissions at Saturn tend to have ~5-minute periods, and are referred to as "rising whistler mode emission" and sometimes as "worms" [*Leisner et al.,* 2015]. However, it is currently unclear if the same type of source generation can explain the Earth and Saturn emissions.

The RBSP mission provides new opportunities to examine the QP emissions, first by examining the characteristics of the waves when the two spacecraft (or other spacecraft such as Cluster) are in different locations in the magnetosphere, and second by examining joint observations between RBSP and ground-based observatories [*Titova et al.,* 2015]. Figure 10.6 shows four examples of QP emissions as detected by RBSP using the WFR MSC survey data. The top two panels of Figure 10.6 show the

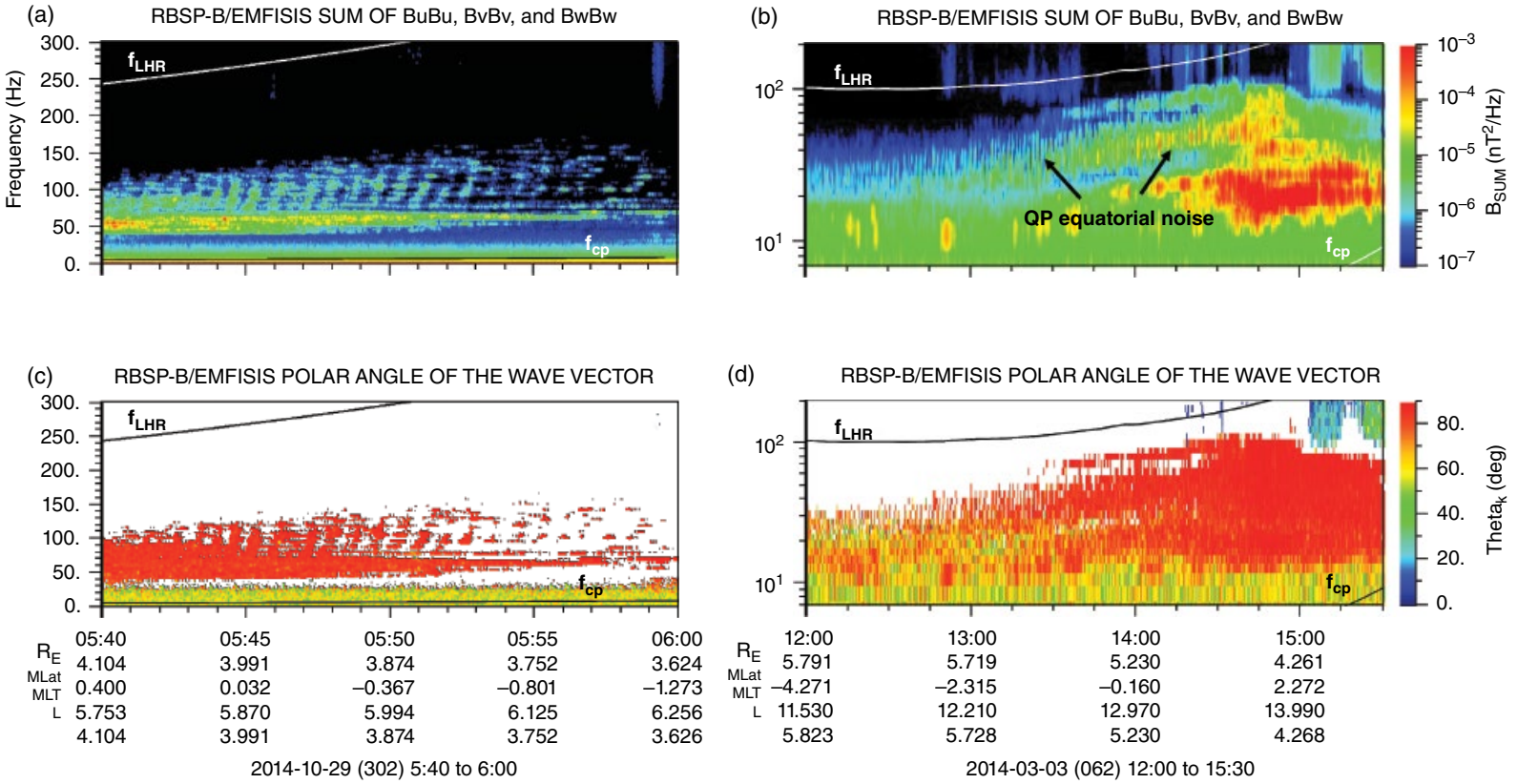

Figure 10.5 The left two panels show time-frequency spectrograms of continuous burst data from the magnetosonic equatorial noise emission event shown in Figure 10.1. The top left panel shows the sum of the three magnetic components of the WFR, and the bottom left panel shows the wave normal angle with respect to the background magnetic field. The right two panels show time-frequency spectrograms of EMFISIS survey data of magnetosonic equatorial emissions that contains QP, dispersive intensity enhancements with a period of ~1.5 mins. The top right panel shows the sum of three search coil channels of the WFR, and the bottom right panel shows the wave normal angle with respect to the background magnetic field.

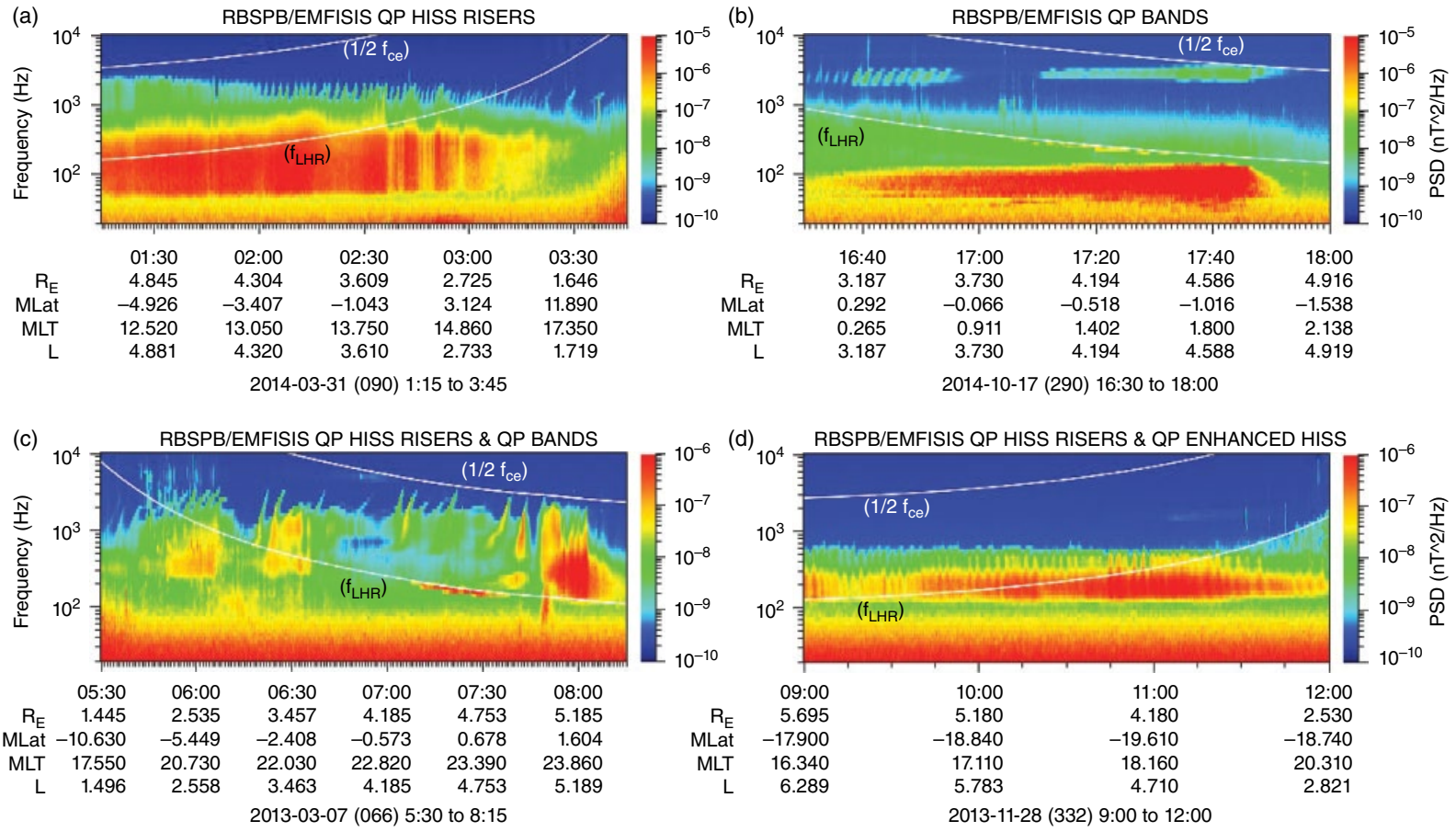

Figure 10.6 Time-frequency spectrograms showing four examples of QP whistler mode emissions as detected by RBSP using the WFR MSC survey data.

two main types of QP structure, QP emissions that rise out of a band of hiss (called QP hiss risers), and QP emissions observed in a band, either separated from the lower frequency hiss or detected when no hiss is present (called QP bands). Panel (c) of Figure 10.6 shows a more complicated period when both QP hiss risers and QP bands are detected. Panel (d) of Figure 10.6 shows an example when the QP hiss risers extend down into the hiss bands and the hiss itself has a periodic intensity enhancement. An initial examination of the Van Allen Probe EMFISIS Survey data has been performed for the period from 1 September 2012 to 10 October 2014 to search for QP events. A total of 292 QP events have been detected between both spacecraft, with 143 events detected by SCA and 149 by SCB. It should be noted that an "event" was defined as a "continuous" series of QP emissions, so each event is usually made up of many tens of QP intensity enhancement elements. Most events lasted less than one hour, but a few lasted for over six hours. Banded QP emissions made up 80 of the events, QP Hiss Risers (included QP enhanced hiss) made up 191, and 21 events contained both QP Banded and QP Hiss Risers. The period of the QP enhancements ran from about 1 to 16 minutes, with most being around 2 to 4 minutes. It should be noted that the sampling period of the survey data makes it difficult to detect periodicities below about 1 minute. This initial survey found that RBSP detected QP emissions at all MLT and at all magnetic latitudes that RBSP sampled (−20° to +20°). Many events were also detected on successive orbits when the spacecraft returned to the same region, suggesting a source process lasting for many hours. Furthermore, many events were detected on both spacecraft at the same time, even during large spacecraft separations, suggesting global events. Further evidence of the global nature of some QP events is the detection of QP emissions by RBSP at the same time as QP events reported by the Cluster spacecraft [*Nemec et al., 2014*]. These initial results and a comparison to the Cluster events will be part of a future work.

10.7. CONCLUSION

The Van Allen Probe mission is returning outstanding particle and wave data, resulting in major advances in our understanding of the role of plasma waves in the dynamics of Earth's Van Allen belts. Numerous studies have advanced our understanding of whistler mode chorus, plasmaspheric hiss, magnetosonic equatorial noise, lightning produced whistlers, and QP whistler mode emission. The ability to measure all six components simultaneously has provided high resolution wave propagation parameters of plasma wave emissions, especially relating to chorus, allowing better characterization of the role the waves play in particle acceleration and loss. Studies of plasmaspheric hiss have found evidence of hiss produced locally and also from chorus. The magnetosonic equatorial noise emission was found to often contain a QP intensity enhancement. The use of the UHR to determine the local electron plasma density has also been invaluable in a number of investigations, including modeling and simulation studies.

The Van Allen Probes have been in orbit for over three years, are roughly halfway through their second orbital coverage of MLT, and have recently been approved for an extended mission phase lasting into 2017. Since the launch of RBSP, the solar cycle has exited solar maximum and is extending through its declining phase. Conditions during a declining phase are historically different from those that prevail during solar maximum, sometimes leading to higher energization for relativistic electrons. The extended mission phase of RBSP provides an excellent opportunity to investigate these changing conditions and evolution of the Van Allen radiation belts. The Van Allen Probes will also coordinate with new assets that have recently launched spacecraft (e.g., the National Aeronautics and Space Administration's (NASA) Magnetospheric Multiscale), and with upcoming missions such as the Japanese Exploration of Energization and Radiation in Geospace mission, the Department of Defense DSX mission, and several upcoming relevant CubeSat missions, providing new opportunities to globally investigate the Earth's Van Allen Radiation Belts.

ACKNOWLEDGMENTS

The research at The University of Iowa was supported by Johns Hopkins University/Applied Physics Laboratory (JHU/APL) contract no. 921647 under NASA Prime contract no. NAS5-01072. The analysis at UCLA was supported by the NASA grants NNX14AI18G, NNX11AR64G, NNX13AI61G, and NNX15AI96G. The EMFISIS data are open and available to the public at http://emfisis.physics.uiowa.edu/data/index.

REFERENCES

Abel, B., and R. M. Thorne (1998), Electron scattering loss in Earth's inner magnetosphere: 1. Dominant physical processes, *J. Geophys. Res.*, *103*, 2385–2396, doi:10.1029/97JA02919.

Allcock, G. M. (1957), A study of the audio-frequency radio phenomenon known as "dawn chorus," *Aust. J. Phys.*, *10*, 286.

Angelopoulos, V. (2008), The THEMIS Mission, *Space Science Reviews 141*(1–4), 5–34, doi:10.1007/s11214-008-9336-1.

Boardsen, S. A., D. L. Gallagher, D. A. Gurnett, W. K. Peterson, and J. L. Green (1992), Funnel-shaped low-frequency equatorial waves, *J. Geophys. Res.*, *97*, 14,967–14,976.

Boardsen, S. A., G. B. Hospodarsky, C. A. Kletzing, R. F. Pfaff, W. S. Kurth, J. R. Wygant, and E. A. MacDonald (2014), Van Allen Probe observations of periodic rising frequencies of the fast magnetosonic mode, *Geophys. Res. Lett.*, *41*, 8161–8168, doi:10.1002/2014GL062020.

Bortnik, J., R. M. Thorne, and N. P. Meredith (2008), The unexpected origin of plasmaspheric hiss from discrete chorus emissions, *Nature*, *452*, 62–66, doi:10.1038/nature06741.

Bortnik, J., R. M. Thorne, and N. P. Meredith (2009a), Plasmaspheric hiss overview and relation to chorus, *J. Atmos. Sol. Terr. Phys.*, *71*, 1636, doi:10.1016/j.jastp.2009.03.023.

Bortnik, J., et al. (2009b), First observation linking the origin of plasmaspheric hiss to discrete chorus emissions, *Science*, *324*, 775–778, doi:10.1126/science.1171273.

Bortnik, J., and R. M. Thorne (2010), Transit time scattering of energetic electrons due to equatorially confined magnetosonic waves, *J. Geophys. Res.*, *115*, A07213, doi:10.1029/2010JA015283.

Breneman, A. W., A. Halford, R. Millan, M. McCarthy, J. Fennell, J. Sample, L. Woodger, G. B. Hospodarsky, J. R. Wygant, C. A. Cattell, J. Goldstein, D. Malaspina, and C. A. Kletzing (2015), Observations of a Global Coherence Scale Modulating Electron Loss Due to Plasmaspheric Hiss, *Nature, submitted*.

Carson, W. B., J. A. Koch, J. H. Pope, and R. M. Gallet (1965), Long-period very low frequency emission pulsations, *J. Geophys. Res.*, *70*(17), 4293–4303, doi:10.1029/JZ070i017p04293.

Chan, K. W., and R. E. Holzer (1976), ELF hiss associated with plasma density enhancements in the outer magnetosphere, *J. Geophys. Res.*, *81*(13), 2267–2274, doi:10.1029/JA081i013p02267.

Chen, L. (1974), Theory of ULF modulation of VLF emissions, *Geophys. Res. Lett.*, *1*(2), 73–75, doi: 10.1029/GL001i002p00073.

Chen, L., R. M. Thorne, V. K. Jordanova, and R. B. Horne (2010), Global simulation of magnetosonic wave instability in the storm time magnetosphere, *J. Geophys. Res.*, *115*, A11222, doi:10.1029/2010JA015707.

Chen, L., R. M. Thorne, V. K. Jordanova, M. F. Thomsen, and R. B. Horne (2011), Magnetosonic wave instability analysis for proton ring distributions observed by the LANL magnetospheric plasma analyzer, *J. Geophys. Res.*, *116*, A03223, doi:10.1029/2010JA016068.

Chen, L., R. M. Thorne, J. Bortnik, W. Li, R. B. Horne, G. D. Reeves, C. A. Kletzing, W. S. Kurth, G. B. Hospodarsky, H. E. Spence, J. B. Blake and J. F. Fennell (2014), Generation of unusually low frequency plasmaspheric hiss, *Geophys. Res. Lett.*, *41*, 5702–5709, doi:10.1002/2014GL060628.

Chen, Y., G. D. Reeves, R. H. W. Friedel, and G. S. Cunningham (2014), Global time-dependent chorus maps from low-Earth-orbit electron precipitation and Van Allen Probes data, *Geophys. Res. Lett.*, *41*, 755–761, doi:10.1002/2013GL059181.

Chum, J. and Santoík, O. (2005), Propagation of whistler-mode chorus to low altitudes: divergent ray trajectories and ground accessibility, *Ann. Geophys.*, *23*, 3727–3738, doi:10.5194/angeo-23-3727-2005.

Church, S. R., and R. M. Thorne (1983), On the Origin of Plasmaspheric Hiss: Ray Path Integrated Amplification, *J. Geophys. Res.*, *88*(A10), 7941–7957, doi:10.1029/JA088iA10p07941.

Dowden, R. L., J. B. Brundell, and C. J. Rodger, Vlf lightning location by time of group arrival (toga) at multiple sites, *Journal of Atmospheric and Solar-Terrestrial Physics*, *64*(7), 817–830, 2002.

Draganov, A. B., U. S. Inan, V. S. Sonwalkar, and T. F. Bell (1992), Magnetospherically reflected whistlers as a source of plasmaspheric hiss, *Geophys. Res. Lett.*, *19*(3), 233–236, doi:10.1029/91GL03167.

Dunckel, N., and R. A. Helliwell (1969), Whistler mode emissions on the OGO-1 satellite, *J. Geophys. Res.*, *74*, 6371–6385, doi:10.1029/JA074i026p06371.

Escoubet, C. P., R. Schmidt and M. L. Goldstein (1997), CLUSTER – Science and Mission Overview, *Space Science Reviews 79*(1–2), 11–32, doi:10.1023/A:1004923124586.

Ergun, R. E., et al. (1998), FAST satellite wave observations in the AKR source region, *Geophys. Res. Lett.*, *25*, 2061–2064, doi:10.1029/98GL00570.

Fennell, J. F., et al. (2014), Van Allen Probes observations of direct wave-particle interactions, *Geophys. Res. Lett.*, *41*, 1869–1875, doi:10.1002/2013GL059165.

Foster, J. C., P. J. Erickson, D. N. Baker, S. G. Claudepierre, C. A. Kletzing, W. S. Kurth, G. D. Reeves, S. A. Thaller, H. E. Spence, Y. Y. Shprits, and J. R. Wygant (2014), Prompt Energization of Relativistic and Highly Relativistic Electrons During a Substorm Interval: Van Allen Probes Observations, *Geophys. Res. Lett.*, *41*, 20–25, doi:10.1002/2013GL058438.

Fu, H. S., J. B. Cao, Z. Zhima, Y. V. Khotyaintsev, V. Angelopoulos, O. Santolík, Y. Omura, U. Taubenschuss, L. Chen, and S. Y. Huang (2014), First observation of rising-tone magnetosonic waves, *Geophys. Res. Lett.*, *41*, 7419–7426, doi:10.1002/2014GL061867.

Fu, X., M. M. Cowee, R. H. Friedel, H. O. Funsten, S. P. Gary, G. B. Hospodarsky, C. Kletzing, W. Kurth, B. A. Larsen, K. Liu, E. A. MacDonald, K. Min, G. D. Reeves, R. M. Skoug, and D. Winsk (2014), Whistler anisotropy instabilities as the source of banded chorus: Van Allen Probes observations and particle-in-cell simulations, *J. Geophys. Res. Space Physics*, *119*, 8288–8298, doi:10.1002/2014JA020364.

Green, J. L., S. Boardsen, L. Garcia, W. W. L. Taylor, S. F. Fung, and B. W. Reinisch (2005), On the origin of whistler mode radiation in the plasmasphere, *J. Geophys. Res.*, *110*, A03201, doi:10.1029/2004JA010495.

Green, J. L., S. Boardsen, L. Garcia, S. F. Fung, and B. W. Reinisch (2006), Reply to "Comment on 'On the origin of whistler mode radiation in the plasmasphere' by Green et al.", *J. Geophys. Res.*, *111*, A09211, doi:10.1029/2006JA011622.

Gurnett, D. A. (1974), The Earth as a radio source: Terrestrial kilometric radiation, *J. Geophys. Res.*, *79*(28), 4227–4238, doi:10.1029/JA079i028p04227.

Gurnett, D. A. (1975), The Earth as a radio source: The non-thermal continuum, *J. Geophys. Res.*, *80*, 2751–2763, doi:10.1029/JA080i019p02751.

Gurnett, D. A. (1976), Plasma wave interactions with energetic ions near the magnetic equator, *J. Geophys. Res.*, *81*, 2765–2770, doi:10.1029/JA081i016p02765.

Gurnett, D. A., and B. J. O'Brien (1964), High-latitude geophysical studies with satellite Injun 3: 5. Very-low-frequency electromagnetic radiation, *J. Geophys. Res.*, *69*(1), 65–89, doi:10.1029/JZ069i001p00065.

Halford, A. J., S. L. McGregor, K. R. Murphy, R. M. Millan, M. K. Hudson, L. A. Woodger, C. A. Cattel, A. W. Breneman, I. R. Mann, W. S. Kurth, G. B. Hospodarsky, M. Gkioulidou, and J. F. Fennell (2015), BARREL observations of an ICME-Shock impact with the magnetosphere and the resultant radiation belt electron loss, *J. Geophys. Res.*, in press.

Hartley D. P., Y. Chen, C. A. Kletzing, M. H. Denton, and W. S. Kurth (2015), Applying the cold plasma dispersion relation to whistler mode chorus waves: EMFISIS wave measurements from the Van Allen Probes, *J. Geophys. Res. Space Physics*, *120*, doi:10.1002/2014JA020808.

Hayosh, M., D. L. Pasmanik, A. G. Demekhov, O. Santolík, M. Parrot, and E. E. Titova (2013), Simultaneous observations of quasi-periodic ELF/VLF wave emissions and electron precipitation by DEMETER satellite: A case study, *J. Geophys. Res. Space Physics*, *118*, 4523–4533, doi:10.1002/jgra.50179.

Helliwell, R. A. (1965), *Whistlers and Related Ionospheric Phenomena*, Stanford University Press, Stanford, California.

Helliwell, R. A. (1969), Low-frequency waves in the magnetosphere, *Rev. Geophys.*, *7*, 281–303, doi:10.1029/RG007i001p00281.

Horne, R. B., G. V. Wheeler, and H. St. C. K. Alleyne (2000), Proton and electron heating by radially propagating fast magnetosonic waves, *J. Geophys. Res.*, *105*, 27,597–27,610.

Horne, R. B., R. M. Thorne, S. A. Glauert, N. P. Meredith, D. Pokhotelov, and O. Santolík (2007), Electron acceleration in the Van Allen radiation belts by fast magnetosonic waves, *Geophys. Res. Lett.*, *34*, L17107, doi:17110.11029/12007GL030267.

Hospodarsky, G. B., T. F. Averkamp, W. S. Kurth, D. A. Gurnett, J. D. Menietti, O. Santolík, and M. K. Dougherty (2008), Observations of chorus at Saturn using the Cassini Radio and Plasma Wave Science instrument, *J. Geophys. Res.*, *113*, A12206, doi:10.1029/2008JA013237.

Hospodarsky, G. B., J. S. Leisner, K. Sigsbee, J. D. Menietti, W. S. Kurth, D. A. Gurnett, C. A. Kletzing, and O. Santolík (2012), Plasma Wave Observations at Earth, Jupiter, and Saturn, *Dynamics of Earth's Radiation Belts and Inner Magnetosphere*, ed. by D. Summers, I.R. Mann, D.N. Baker, and M. Schulz, Geophys. Monogr. Ser., Vol. *199*, pp. 415–430, doi:10.1029/2012GM001342.

Katoh, Y., and Y. Omura (2011), Amplitude dependence of frequency sweep rates of whistler mode chorus emissions, *J. Geophys. Res.*, *116*, A07201, doi:10.1029/2011JA016496.

Kennel, C. F., and H. E. Petschek (1966), Limit on stably trapped particle fluxes, *J. Geophys. Res.*, *71*(1), 1–28, doi:10.1029/JZ071i001p00001.

Kitamura, T., J. A. Jacobs, T. Watanabe, and R. B. Flint Jr. (1969), An investigation of quasi-periodic VLF emissions, *J. Geophys. Res.*, *74*(24), 5652–5664, doi:10.1029/JA074i024p05652.

Kletzing, C. A., W. S. Kurth, M. Acuna, R. J. MacDowall, R. B. Torbert, T. Averkamp, D. Bodet, S. R. Bounds, M. Chutter, J. Connerney, D. Crawford, J. S. Dolan, R. Dvorsky, G. B. Hospodarsky, J. Howard, V. Jordanova, R. A. Johnson, D. L. Kirchner, B. Mokrzycki, G. Needell, J. Odom, D. Mark, R. Pfaff, Jr., J. R. Phillips, C. W. Piker, S. L. Remington, D. Rowland, O. Santolík, R. Schnurr, D. Sheppard, C. W. Smith, R. M. Thorne, and J. Tyler (2013), The Electric and Magnetic Field Instrument Suite and Integrated Science (EMFISIS) on RBSP, *Space Science Reviews 179*(1-4): 127–181, doi:10.1007/s11214-013-9993-6.

Kurth, W.S., S. DePascuale, J.B. Faden, C.A. Kletzing, G.B. Hospodarsky, S. Thaller, and J.R. Wygant (2015), Electron Densities Inferred from Plasma Wave Spectra Obtained by the Waves Instrument on Van Allen Probes, *J. Geophys. Res.*, in press, doi:10.1002/2014JA020857.

Lauben, D. S., U. S. Inan, and T. F. Bell (2001), Precipitation of radiation belt electrons induced by obliquely propagating lightning-generated whistlers, *J. Geophys. Res.*, *106*(A12), 29745–29770, doi:10.1029/1999JA000155.

LeDocq, M. J., D. A. Gurnett, and G. B. Hospodarsky (1998), Chorus source location from VLF Poynting flux measurements with the Polar spacecraft, *Geophys. Res. Lett.*, *25*, 4063–4066, doi:10.1029/1998GL900071.

Leisner, J, S., G. B. Hospodarsky, J. D. Menietti, U. Taubenschuss, and D. A. Gurnett (2015), Rising Whistler-Mode Emissions in Saturn's Inner Magnetosphere, *J. Geophys. Res.*, submitted.

Li, W., J. Bortnik, R. M. Thorne, and V. Angelopoulos (2011), Global distribution of wave amplitudes and wave normal angles of chorus waves using THEMIS wave observations, *J. Geophys. Res.*, *116*, A12205, doi:10.1029/2011JA017035.

Li, W., B. Ni, R. M. Thorne, J. Bortnik, J. C. Green, C. A. Kletzing, W. S. Kurth, and G. B. Hospodarsky (2013a), Constructing the global distribution of chorus wave intensity using measurements of electrons by the POES satellites and waves by the Van Allen Probes, *Geophys. Res. Lett.*, *40*, 4526–4532, doi:10.1002/grl.50920.

Li, W., R. M. Thorne, J. Bortnik, G. D. Reeves, C. A. Kletzing, W. S. Kurth, G. B. Hospodarsky, H. E. Spence, J. B. Blake, J. F. Fennell, S. G. Claudepierre, J. R. Wygant, and S. A. Thaller (2013b), An unusual enhancement of low-frequency plasmaspheric hiss in the outer plasmasphere associated with substorm-injected electrons, *Geophys. Res. Lett.*, *40*, 3798–3803, doi:10.1002/grl.50787.

Li, W., R. M. Thorne, Q. Ma, B. Ni, J. Bortnik, D. N. Baker, H. E. Spence, G. D. Reeves, S. G. Kanekal, J. C. Green, C. A. Kletzing, W. S. Kurth, G. B. Hospodarsky, J. B. Blake, J. F. Fennell, and S. G. Claudepierre (2014a), Radiation belt electron acceleration by chorus waves during the 17 March 2013 storm, *J. Geophys. Res. Space Physics*, *119*, 4681–4693, doi:10.1002/2014JA019945.

Li, W., B. Ni, R. M. Thorne, J. Bortnik, Y. Nishimura, J. C. Green, C. A. Kletzing, W. S. Kurth, G. B. Hospodarsky, H. E. Spence, G. D. Reeves, J. B. Blake, J. F. Fennell, S. G. Claudepierre, and X. Gu (2014b), Quantifying hiss-driven energetic electron precipitation: A detailed conjunction event analysis, *Geophys. Res. Lett.*, *41*, 1085–1092, doi:10.1002/2013GL059132.

Li, W., Q. Ma, R. M. Thorne, J. Bortnik, C. A. Kletzing, W. S. Kurth, G. B. Hospodarsky, and Y. Nishimura (2015a), Statistical properties of plasmaspheric hiss derived from Van Allen Probes data and their effects on radiation belt electron dynamics. *J. Geophys. Res. Space Physics*, *120*, 3393–3405. doi:10.1002/2015JA021048.

Li, W., L. Chen, J. Bortnik, R. M. Thorne, V. Angelopoulos, C. A. Kletzing, W. S. Kurth, and G. B. Hospodarsky (2015b), First evidence for chorus at a large geocentric distance as a source of plasmaspheric hiss: Coordinated THEMIS and Van Allen Probes observation, *Geophys. Res. Lett.*, *42*, 241–248, doi:10.1002/2014GL062832.

Liu, S., F. Xiao, C. Yang, Y. He, Q. Zhou, C. A. Kletzing, W. S. Kurth, G. B. Hospodarsky, H. E. Spence, G. D. Reeves, H. O. Funsten, J. B. Blake, D. N. Baker and J. R. Wygant (2015), Van Allen Probes observations linking radiation belt electrons to chorus waves during 2014 multiple storms, *J. Geophys. Res. Space Physics*, *120*, doi:10.1002/2014JA020781.

Lyons, L. R., R. M. Thorne, and C. F. Kennel (1972), Pitch-Angle Diffusion of Radiation Belt Electrons within the Plasmasphere, *J. Geophys. Res.*, *77*(19), 3455–3474, doi:10.1029/JA077i019p03455.

Lyons, L. R., and R. M. Thorne (1973), Equilibrium structure of radiation belt electrons, *J. Geophys. Res.*, *78*, 2142–2149, doi:10.1029/JA078i013p02142.

Ma, Q., W. Li, L. Chen, R. M. Thorne, and V. Angelopoulos (2014a), Magnetosonic wave excitation by ion ring distributions in the Earth's inner magnetosphere, *J. Geophys. Res. Space Physics*, *119*, 844–852, doi:10.1002/2013JA019591.

Ma, Q., W. Li, L. Chen, R. M. Thorne, C. A. Kletzing, W. S. Kurth, G. B. Hospodarsky, G. D. Reeves, M. G. Henderson, and H. E. Spence (2014b), The trapping of equatorial magnetosonic waves in the Earth's outer plasmasphere, *Geophys. Res. Lett.*, *41*, 6307–6313, doi:10.1002/2014GL061414.

Mauk, B. H., N. J. Fox, S. G. Kanekal, R. L. Kessel, D. G. Sibeck and A. Ukhorskiy (2013), Science Objectives and Rationale for the Radiation Belt Storm Probes Mission, *Space Science Reviews 179*(1–4), 3–27, doi: 10.1007/s11214-012-9908-y.

Meredith, N. P., R. B. Horne, and R. R. Anderson (2001), Substorm dependence of chorus amplitides: Implications for the acceleration of electrons to relativistic energies, *J. Geophys. Res.*, *106*, 13,165–13,178, doi:10.1029/2000JA900156.

Meredith, N. P., R. B. Horne, R. M. Thorne, D. Summers, and R. R. Anderson (2004), Substorm dependence of plasmaspheric hiss, *J. Geophys. Res.*, *109*, A06209, doi:10.1029/2004JA010387.

Meredith, N. P., R. B. Horne, M. A. Clilverd, D. Horsfall, R. M. Thorne, and R. R. Anderson (2006), Origins of plasmaspheric hiss, *J. Geophys. Res.*, *111*, A09217, doi:10.1029/2006JA011707.

Meredith, N. P., R. B. Horne, S. A. Glauert, and R. R. Anderson (2007), Slot region electron loss timescales due to plasmaspheric hiss and lightning-generated whistlers, *J. Geophys. Res.*, *112*, A08214, doi:10.1029/2007JA012413.

Meredith, N. P., R. B. Horne, and R. R. Anderson (2008), Survey of magnetosonic waves and proton ring distributions in the Earth's inner magnetosphere, *J. Geophys. Res.*, *113*, A06213, doi:10.1029/2007JA012975.

Millan, R. M., M. P. McCarthy, J. G. Sample, D. M. Smith, L. D. Thompson, D. G. McGaw, L. A. Woodger, J. G. Hewitt, M. D. Comess, K. B. Yando, A. X. Liang, B. A. Anderson, N. R. Knezek, W. Z. Rexroad, J. M. Scheiman, G. S. Bowers, A. J. Halford, A. B. Collier, M. A. Clilverd, R. P. Lin, and M. K. Hudson (2013), The Balloon Array for RBSP Relativistic Electron Losses (BARREL), *Space Science Reviews 179*, 503–530, doi:10.1007/s11214-013-9971-z.

Němec, F., O. Santolík, M. Parrot, J. S. Pickett, M. Hayosh, and N. Cornilleau-Wehrlin (2013a), Conjugate observations of quasi-periodic emissions by Cluster and DEMETER spacecraft, *J. Geophys. Res. Space Physics*, *118*, 198–208, doi:10.1029/2012JA018380.

Němec, F., O. Santolík, J. S. Pickett, M. Parrot, and N. Cornilleau-Wehrlin (2013b), Quasiperiodic emissions observed by the Cluster spacecraft and their association with ULF magnetic pulsations, *J. Geophys. Res. Space Physics*, *118*, 4210–4220, doi:10.1002/jgra.50406.

Němec, F., J. S. Pickett, and O. Santolík (2014), Multispacecraft Cluster observations of quasiperiodic emissions close to the geomagnetic equator, *J. Geophys. Res. Space Physics*, *119*, 9101–9112, doi:10.1002/2014JA020321.

Němec, F., O. Santolík, Z. Hrbackova, J. S. Pickett, and N. Cornilleau-Wehrlin (2015), Equatorial noise emissions with quasiperiodic modulation of wave intensity, *J. Geophys. Res. Space Physics*, *120*, 2649–2661, doi:10.1002/2014JA020816.

Ni, B., W. Li, R. M. Thorne, J. Bortnik, J. C. Green, C. A. Kletzing, W. S. Kurth, G. B. Hospodarsky, and M. de Soria-Santacruz Pich (2014a), A novel technique to construct the global distribution of whistler mode chorus wave intensity using low-altitude POES electron data, *J. Geophys. Res. Space Physics*, *119*, 5685–5699, doi:10.1002/2014JA019935.

Ni, B., W. Li, R. M. Thorne, J. Bortnik, Q. Ma, L. Chen, C. A. Kletzing, W. S. Kurth, G. B. Hospodarsky, G. D. Reeves, H. E. Spence, J. B. Blake, J. F. Fennell, and S. G. Claudepierre (2014b), Resonant scattering of energetic electrons by unusual low-frequency hiss, *Geophys. Res. Lett.*, *41*, 1854–1861, doi:10.1002/2014GL059389.

Omura, Y., and D. Summers (2006), Dynamics of high-energy electrons interacting with whistler mode chorus emissions in the magnetosphere, *J. Geophys. Res.*, *111*, A09222, doi:10.1029/2006JA011600.

Omura, Y., Y. Katoh, and D. Summers (2008), Theory and simulation of the generation of whistler-mode chorus, *J. Geophys. Res.*, *113*, A04223, doi:10.1029/2007JA012622.

Parrot, M., and F. Lefeuvre (1986), Statistical study of the propagation characteristics of ELF hiss observed on GEOS 1, inside and outside the plasmasphere, *Ann. Geophys.*, *4*, 363–384.

Pasmanik, D. L., E. E. Titova, A. G. Demekhov, V. Y. Trakhtengerts, O. Santolík, F. Jiricek, K. Kudela, and M. Parrot (2004), Quasi-periodic ELF/VLF wave emissions in the Earth's magnetosphere: Comparison of satellite observations and modelling, *Ann. Geophys.*, *22*, 4351–4361.

Perraut, S., A. Roux, P. Robert, R. Gendrin, J. A. Savaud, J. M. Bosqued, G. Kremser, and A. Korth (1982), A systematic study of ULF waves above fH+ from GEOS 1 and 2 measurements and their relationship with proton ring distributions, *J. Geophys. Res.*, *87*, 6219–6236, doi:10.1029/JA087iA08p06219.

Pickett, J. S., O. Santolík, S. W. Kahler, A. Masson, M. L. Adrian, D. A. Gurnett, T. F. Bell, H. Laakso, M. Parrot, P. Décréau, A. Fazakerley, N. Cornilleau-Wehrlin, A. Balogh and M. André (2005), Multi-Point Cluster Observations of

VLF Risers, Fallers and Hooks at and Near the Plasmapause, *Multiscale Processes in the Earth's Magnetosphere: From Interball to Cluster*, ed. by J.-A. Sauvaud and Z. Němeček, Springer Netherlands. *178*: 307–328, doi: 10.1007/1-4020-2768-0_17.

Reeves, G. D., H. E. Spence, M. G. Henderson, S. K. Morley, H. W. Friedel, H. O. Funsten, D. N. Baker, S. G. Kanekal, J. B. Blake, J. F. Fennell, S. G. Claudepierre, R. M. Thorne, D. L. Turner, C. A. Kletzing, W. S. Kurth, B. A. Larsen, and J. T. Niehof (2013), Electron Acceleration in the Heart of the Van Allen Radiation Belts, *Science 341*, 991–994 doi:10.1126/science.1237743.

Rodger, C. J., M. A. Clilverd, and R. J. McCormick (2003), Significance of lightning-generated whistlers to inner radiation belt electron lifetimes, *J. Geophys. Res*., *108*, 1462, doi:10.1029/2003JA009906, A12.

Russell, C. T., R. E. Holzer, and E. J. Smith (1970), OGO 3 observations of ELF noise in the magnetosphere 2. The nature of equatorial noise, *J. Geophys. Res.*, *75*, 755–768.

Santolík, O., M. Parrot, and F. Lefeuvre (2003a), Singular value decomposition methods for wave propagation analysis, *Radio Sci. 38*(1), 1010, doi:10.1029/2000RS002523.

Santolík, O., D. A. Gurnett, J. S. Pickett, M. Parrot, and N. Cornilleau-Wehrlin (2003b), Spatio-temporal structure of storm-time chorus, *J. Geophys. Res.*, *108*(A7), 1278, doi:10.1029/2002JA009791.

Santolík, O., D. A. Gurnett, J. S. Pickett, M. Parrot, and N. Cornilleau-Wehrlin (2004a), A microscopic and nanoscopic view of storm-time chorus on 31 March 2001, *Geophys. Res. Lett*., *31*, L02801, doi:10.1029/2003GL018757.

Santolík, O., F. Nemec, K. Gereova, E. Macusova, Y. de Conchy, and N. Cornilleau-Wehrlin (2004b), Systematic analysis of equatorial noise below the lower hybrid frequency, *Ann. Geophys.*, *22*, 2587–2595.

Santolík, O., J. Chum, M. Parrot, D. A. Gurnett, J. S. Pickett, and N. Cornilleau-Wehrlin (2006), Propagation of whistler mode chorus to low altitudes: Spacecraft observations of structured ELF hiss, *J. Geophys. Res.*, *111*, A10208, doi:10.1029/2005JA011462.

Santolík, O., D. A. Gurnett, J. S. Pickett, J. Chum, and N. Cornilleau-Wehrlin (2009), Oblique propagation of whistler mode waves in the chorus source region, *J. Geophys. Res*., *114*, A00F03, doi:10.1029/2009JA014586.

Santolík, O., C. A. Kletzing, W. S. Kurth, G. B. Hospodarsky, and S. R. Bounds (2014), Fine structure of large-amplitude chorus wave packets, *Geophys. Res. Lett.*, *41*, 293–299, doi:10.1002/2013GL058889.

Sato, N., K. Hayashi, S. Kokubun, T. Oguti, and H. Fukunishi (1974), Relationships between quasi-periodic VLF emission and geomagnetic pulsations; *J. Atmos. Terr. Phys. 36*, 1515–1526, doi:10.1016/0021-9169(74)90229-3.

Sazhin, S. S. (1987), An analytical model of quasiperiodic ELF-VLF emissions, *Planet. Space Sci.*, *35*(10), 1267–1274, doi:10.1016/0032-0633(87)90111-5.

Sazhin, S. S., and M. Hayakawa (1992), Magnetospheric chorus emissions: A review, Planet. *Space Sci*., *40*, 681–697, doi:10.1016/0032-0633(92)90009-D.

Sazhin, S. S., and M. Hayakawa (1994), Periodic and quasiperiodic VLF emissions, *J. Atmos. Terr. Phys.*, *56*, 735–753, doi: 10.1016/0021-9169(94)90130-9.

Smith, A. J., and D. Nunn (1998), Numerical simulation of VLF risers, fallers, and hooks observed in Antarctica, *J. Geophys. Res.*, *203*(A4), 6771–6784, doi:10.1029/97JA03396.

Smith, A. J., M. J. Engebretson, E. M. Klatt, U. S. Inan, R. L. Arnoldy, and H. Fukunishi (1998), Periodic and quasiperiodic ELF/VLF emissions observed by an array of Antarctic stations, *J. Geophys. Res.*, *103*(A10), 23611–23622, doi:10.1029/98JA01955.

Sigsbee, K., J. D. Menietti, O. Santolík, and J. B. Blake (2008), Polar PWI and CEPPAD observations of chorus emissions and radiation belt electron acceleration: Four case studies, *J. Atmos. Sol. Terr. Phys.*, *70*(14), 1774–1788, doi:10.1016/j.jastp.2008.02.005.

Storey, L. R. O. (1953), An investigation of whistling atmospherics, *Philos. Trans. R. Soc. London, Ser. A*, *246*, 113–141, doi:10.1098/rsta.1953.0011.

Su, Z., H. Zhu, F. Xiao, H. Zheng, Y. Wang, Z. He, C. Shen, C. Shen, C. B. Wang, Rui Liu, Min Zhang, Shui Wang, C. A. Kletzing, W. S. Kurth, G. B. Hospodarsky, H. E. Spence, G. D. Reeves, H. O. Funsten, J. B. Blake, D. N. Baker, and J. R. Wygant (2014), Intense duskside lower band chorus waves observed by Van Allen Probes: Generation and potential acceleration effect on radiation belt electrons, *J. Geophys. Res. Space Physics*, *119*, 4266–4273, doi:10.1002/2014JA019919.

Summers, D., B. Ni, and N. P. Meredith (2007), Timescales for radiation belt electron acceleration and loss due to resonant wave-particle interactions: 2. Evaluation for VLF chorus, ELF hiss, and electromagnetic ion cyclotron waves, *J. Geophys. Res*., *112*, A04207, doi:10.1029/2006JA011993.

Summers, D., B. Ni, N. P. Meredith, R. B. Horne, R. M. Thorne, M. B. Moldwin, and R. R. Anderson (2008), Electron scattering by whistler mode ELF hiss in plasmaspheric plumes, *J. Geophys. Res.*, *113*, A04219, doi:10.1029/2007JA012678.

Summers, D., R. Tang, Y. Omura, and D.-H. Lee (2013), Parameter spaces for linear and nonlinear whistler-mode waves. *Phys. Plasmas*, *20*, 072110, doi:10.1063/1.4816022.

Tao, X., J. Bortnik, R. M. Thorne, J. M. Albert, and W. Li (2012), Effects of amplitude modulation on nonlinear interactions between electrons and chorus waves, *Geophys. Res. Lett.*, *39*, L06102, doi:10.1029/2012GL051202.

Thomsen, M. F., M. H. Denton, V. K. Jordanova, L. Chen, and R. M. Thorne (2011), Free energy to drive equatorial magnetosonic wave instability at geosynchronous orbit, *J. Geophys. Res.*, *116*, A08220, doi:10.1029/2011JA016644.

Thorne, R. M., E. J. Smith, R. K. Burton, and R. E. Holzer (1973), Plasmaspheric Hiss, *J. Geophys. Res.*, *78*(10), 1581–1596, doi:10.1029/JA078i010p01581.

Thorne, R. M., R. B. Horne, and N. P. Meredith (2006), Comment on "On the origin of whistler mode radiation in the plasmasphere" by Green et al., *J. Geophys. Res.*, *111*, A09210, doi:10.1029/2005JA011477.

Thorne, R. M. (2010), Radiation belt dynamics: The importance of wave-particle interactions, *Geophys. Res. Lett.*, *37*, L22107, doi:10.1029/2010GL044990.

Thorne, R. M., W. Li, B. Ni, Q. Ma, J. Bortnik, L. Chen, D. N. Baker, H. E. Spence, G. D. Reeves, M. G. Henderson, C. A. Kletzing, W. S. Kurth, G. B. Hospodarsky, J. B. Blake, J. F. Fennell, S. G. Claurepierre, and S. G. Kanekal (2013a), Rapid Local Acceleration of Relativistic Radiation-Belt Electrons

by Magnetospheric Chorus, *Nature*, *504*, pp. 411–414, doi:10.1038/nature12889.

Thorne, R. M., W. Li, B. Ni, Q. Ma, J. Bortnik, D. N. Baker, H. E. Spence, G. D. Reeves, M. G. Henderson, C. A. Kletzing, W. S. Kurth, G. B. Hospodarsky D. Turner, and V. Angelopoulos (2013b), Evolution and slow decay of an unusual narrow ring of relativistic electrons near L~3.2 following the September 2012 magnetic storm, *Geophys. Res. Lett.*, *40*, 3507–3511, doi:10.1002/grl.50627.

Titova, E. E., B. V. Kozelov, A. G. Demekhov, J. Manninen, O. Santolík, C. A. Kletzing, and G. Reeves (2015), Identification of the source of quasiperiodic VLF emissions using ground-based and Van Allen Probes satellite observations, *Geophys. Res. Lett.*, *42*, 6137–6145, doi:10.1002/2015GL064911.

Tixier, M., and N. Cornilleau-Wehrlin (1986), How are the VLF quasi-periodic emissions controlled by harmonics of field line oscillations? The results of a comparison between ground and Geos satellites measurements, *J. Geophys. Res.*, *91*(A6), 6899–6919, doi:10.1029/JA091iA06p06899.

Tsurutani, B. T., and E. J. Smith (1974), Postmidnight chorus: A substorm phenomenon, *J. Geophys. Res.*, *79*, 118–127, doi:10.1029/JA079i001p00118.

Tsurutani, B. T., and E. J. Smith (1977), Two types of magnetospheric ELF chorus and their substorm dependences, *J. Geophys. Res.*, *82*(32), 5112–5128, doi:10.1029/JA082i032p05112.

Wygant, J. R., J. W. Bonnell, K. Goetz, R. E. Ergun, F. S. Mozer, S. D. Bale, M. Ludlam, P. Turin, P. R. Harvey, R. Hochmann, K. Harps, G. Dalton, J. McCauley, W. Rachelson, D. Gordon, B. Donakowski, C. Shultz, C. Smith, M. Diaz-Aguado, J. Fischer, S. Heavner, P. Berg, D. M. Malsapina, M. K. Bolton, M. Hudson, R. J. Strangeway, D. N. Baker, X. Li, J. Albert, J. C. Foster, C. C. Chaston, I. Mann, E. Donovan, C. M. Cully, C. A. Cattell, V. Krasnoselskikh, K. Kersten, A. Brenneman, and J. B. Tao (2013), The electric field and waves instruments on the Radiation Belt Storm Probes Mission, *Space Sci. Rev.*, *179*, 183–220, doi:10.1007/s11214-013-0013-7.

Xiao, F., C. Yang, Z. He, Z. Su, Q. Zhou, Y. He, C. A. Kletzing, W. S. Kurth, G. B. Hospodarsky, H. E. Spence, G. D. Reeves, H. O. Funsten, J. B. Blake, D. N. Baker, and J. R. Wygant (2014), Chorus acceleration of radiation belt relativistic electrons during March 2013 geomagnetic storm, *J. Geophys. Res. Space Physics*, *119*, 3325–3332, doi:10.1002/2014JA019822.

Zheng, H., R. H. Holzworth, J. B. Brundell, J. R. Wygant, G. B. Hospodarsky, F. S. Mozer, A. R. Jacobson, and J. Bonnell (2015), Possible relation between lightning detected by WWLLN and whistler waves observed by Van Allen Probes (RBSP), *J. Geophys. Res.,* submitted.

Zhou, Q., et al. (2014), Excitation of nightside magnetosonic waves observed by Van Allen Probes, *J. Geophys. Res. Space Physics*, *119*, 9125–9133, doi:10.1002/2014JA020481.

Zhu H., Z. Su, F. Xiao, H. Zheng, Y. Wang, C. Shen, T. Xian, S. Wang, C. A. Kletzing, W. S. Kurth, G. B. Hospodarsky, H. E. Spence, G. D. Reeves, H. O. Funsten, J. B. Blake, and D. N. Baker (2015), Plasmatrough exohiss waves observed by Van Allen Probes: Evidence for leakage from plasmasphere and resonant scattering of radiation belt electrons, *Geophys. Res. Lett.*, *42*, doi:10.1002/2014GL062964.

11

Ring Current Ions Measured by the RBSPICE Instrument on the Van Allen Probes Mission

Louis J. Lanzerotti and Andrew J. Gerrard

Video of Yosemite Talk, URL: http://dx.doi.org/10.15142/T31011

ABSTRACT

Earth's ring current has been a subject of interest and considerable study for nearly a century, from the days of ground-based geomagnetism to the satellite era. Protons, helium ions, and oxygen ions are known to contribute to the ring current species population and energy density content, and this is the population that produces equatorial-region depressions in Earth's magnetic field during large geomagnetic disturbances associated with the Dst index. These ion species are also important in understanding ion transport and charge exchange processes in the inner magnetosphere. However, measurements of such ions are relatively rare. In this paper we report on ion flux measurements of the ring current population made by the Radiation Belt Storm Probe Ion Composition Experiment (RBSPICE) instruments on the National Aeronautics and Space Administration (NASA) Van Allen Probes spacecraft. Proton (~45-kiloelectron-volt [keV] to ~518-keV), He ion (~65-keV to ~520-keV), and O ion (~140-keV to ~1130-keV) integral and differential flux measurements from approximately two years of observations, coving all magnetic local times, are reported. These contemporary data at energies >100-keV are a unique resource that can provide verifications of, and improvements to, models of ring current ion energization and losses in Earth's magnetosphere, including their roles in plasma processes for producing instabilities and wave generation.

11.1. INTRODUCTION

The existence of a possible ring current around Earth has been a topic of considerable discussion and research for nearly a century. These considerations were stimulated by observations of the global depression in the dominantly north-south component of the magnetic field at near equatorial magnetic observation sites at the time of a geomagnetic disturbance (e.g., extensive discussion and history in *Chapman and Bartels* [1941]). This depression is now associated with the often used Dst index. Indeed, *Chapman and Ferraro* [1933] postulated that a cloud of solar particles, after impacting Earth's magnetic field and causing the sudden increase or "sudden commencement" in the field, could then set up a ring of particles that would provide the depression in the geomagnetic field that was generally measured following the initiation of a large magnetic disturbance. Measurement of the ring current was an early objective of space research once rocketry was available for placing instruments into the near-space environment and following Van Allens discovery of the magnetosphere.

Dessler [1970], in his discussion of the award of the 1970 Nobel Prize in physics to Hannes Alfvén, wrote that Alfvén had introduced the concept of a ring current formed from quasi-trapped radiation in a 1939 paper in an "obscure" journal after it was rejected by *Terrestrial*

Center for Solar-Terrestrial Research, New Jersey Institute of Technology, Newark, NJ, USA

Magnetosphere-Ionosphere Coupling in the Solar System, Geophysical Monograph 222, First Edition.
Edited by Charles R. Chappell, Robert W. Schunk, Peter M. Banks, James L. Burch, and Richard M. Thorne.

Magnetism and Atmospheric Electricity. Prior to the discovery of trapped radiation in Earth's geomagnetic field, S. Fred Singer had also discussed the trapping of charged particles in the dipole field, and the formation of a ring current [*Singer,* 1957, 1958].

Davis and Williamson [1966] suggested that the proton fluxes >100-keV at ~3.5 Earth radii measured by an instrument on the Explorer 14 satellite had sufficient energy density to produce the magnetic field depressions in magnetic storms. They suggested that these particles might be the principal cause of the ring current [*Van Allen*, 2002]. *Cahil* [1966], using measurements from his magnetometer instrument on Explorer 26, provided the first in situ measurements of the depressed magnetic field in the ring current region.

The first measurements of the ion composition of the ring current [*Gloeckler et al*., 1985] was made possible by the CHEM instrument on the Active Magnetospheric Particle Tracer Explorer/Charge Composition Explorer (AMPTE/CCE) mission (of which one of the principal objectives was to study particle access to the magnetosphere by the release of lithium ions upstream of the magnetopause and detecting them inside the geomagnetic cavity). *Hamilton et al*. [1988] reported that during a very large geomagnetic storm, a sizable component (order 60 to 80%) of the ring current density could be of ionosphere origin. Further studies of ring current composition was made possible by the Magnetospheric Ion Composition Spectrometer (MICS) instrument on the CRRES mission, which was aimed principally at studies of the dynamics of the radiation belts. For example, *Daglis et al*. [1999] examined in considerable detail the relative importance of ionosphere oxygen to the magnetic field depressions during the main phases of large geomagnetic storms. Much of our understanding of ring current dynamics and morphology came from the AMPTE and CRRES measurements [e.g., *Sheldon and Hamilton*, 1993; *Sheldon*, 1994; *Milillo et al*., 2001; *Milillo et al.*, 2003].

The ring current was first imaged via energetic neutral atom (ENA) measurements by IMP 7/8 and ISEE-1 [*Roelof et al*., 1985], and then later by instruments on the the Polar spacecraft [*Henderson et al*., 1997] and the IMAGE satellite [*Burch*, 2000, 2005]. Such observations used neutral particle imaging "cameras" [e.g., *Mitchell et al.*, 2000] to provide high time resolution measurements of the ring current dynamics from high latitudes [e.g., *Brandt et al*., 2002; *Roelof et al*., 2004; *Lui et al*., 2005].

Because of its historical importance in the field of geomagnetism, and its continued importance for the dynamics of the magnetosphere, numerous reviews of measurements and of the theoretical aspects of the ring current have been published. These include those of *Daglis et al.* [1999], *Ebihara and Ejiri* [2003], and *Daglis* [2006].

This particular paper presents an overview of the most recent ring current species measurements made by the RBSPICE on the NASA Van Allen Probes B spacecraft for more than one-and-one-half years after instrument commissioning following launch on 30 August 2012. These data are unique in that much of the particle energy reported here is >100-keV, an energy range that was difficult to measure in past instruments for a variety of reasons. Similar data have been made on Van Allen Probes A (not shown herein) and match the gross features of the data reported here in most every detail, though small-scale differences (i.e., intra-orbit variations) do exist and are beyond the scope of this report. These data also provide a comprehensive view of the near-equatorial population of ring current energy ions (i.e., protons, He ions, and O ions, hereafter referred to simply as protons, He, O) as the spacecraft precessed through all magnetic local times.

11.2. INSTRUMENT

The details of the RBSPICE instrument can be found in *Mitchell et al*. [2013]. The data presented herein are all based on Level 2 (i.e., differential flux) measurements made with the time-of-flight by energy (TOFxE) operation mode. Thus, for each particle (i.e., energy) detection made by the solid-state detector (SSD), a corresponding time-of-flight measurement is recorded from the microchannel plate (MCP), which records secondary electrons ejected from start and stop foils. This data product dramatically reduces possible contamination associated with flying through the heart of the radiation belts due to the required coincidence of the measurements made by the SSD and MCP. These measurements are Poisson distributed and the data reported herein are all statistically significant.

We note that the TOF x pulse height (i.e., TOFxPH) data, which uses the pulse height values measured by the MCPs to differentiate species, were not used in this study. This capability can be used to infer proton and O ions at lower energies than the TOFxE product (i.e., at energies lower than which the SSD can record particle detections), but requires very careful consideration of potential background contamination sources that was beyond the scope of the lengthy data set presented herein.

We also note that the RBSPICE instruments have defined pre- and post-perigee operation times. These operation windows have varied throughout the course of the Van Allen Probes mission, and changes are evident in low L-shell data. The windows are chosen to avoid the triggering of anomalous high voltage alarms, whose root cause is unknown (i.e., the high voltage alarms would shut down the RBSPICE instrument and prevent data collection).

11.3. L-SHELL VERSUS TIME OBSERVATIONS

An overview of RBSPICE integral flux [particles/(s · cm²)] measurements of protons (45-keV to 518-keV) from just after instrument commissioning (11 November 2012) following launch to 18 August 2014 are shown in the second panel of Figure 11.1. The top panel of this figure shows the hourly Dst data from the World Data Center for Geomagnetism, Kyoto University. The proton data are binned into 30-min, 0.1 L-shell realizations (where L is determined by a dipole L model). The measurements below L~2.5 (just following commissioning) and for some 20 days were made in the original spatial window for acquiring RBSPICE data; this window was subsequently reduced in spatial extent because of the aforementioned instrument operational constraints.

Inspection of these top panels shows the expected close connection between Dst index, which unto itself is taken as a measure of change in the ring current, to proton injection into the inner magnetosphere [*Gerrard et al.*,

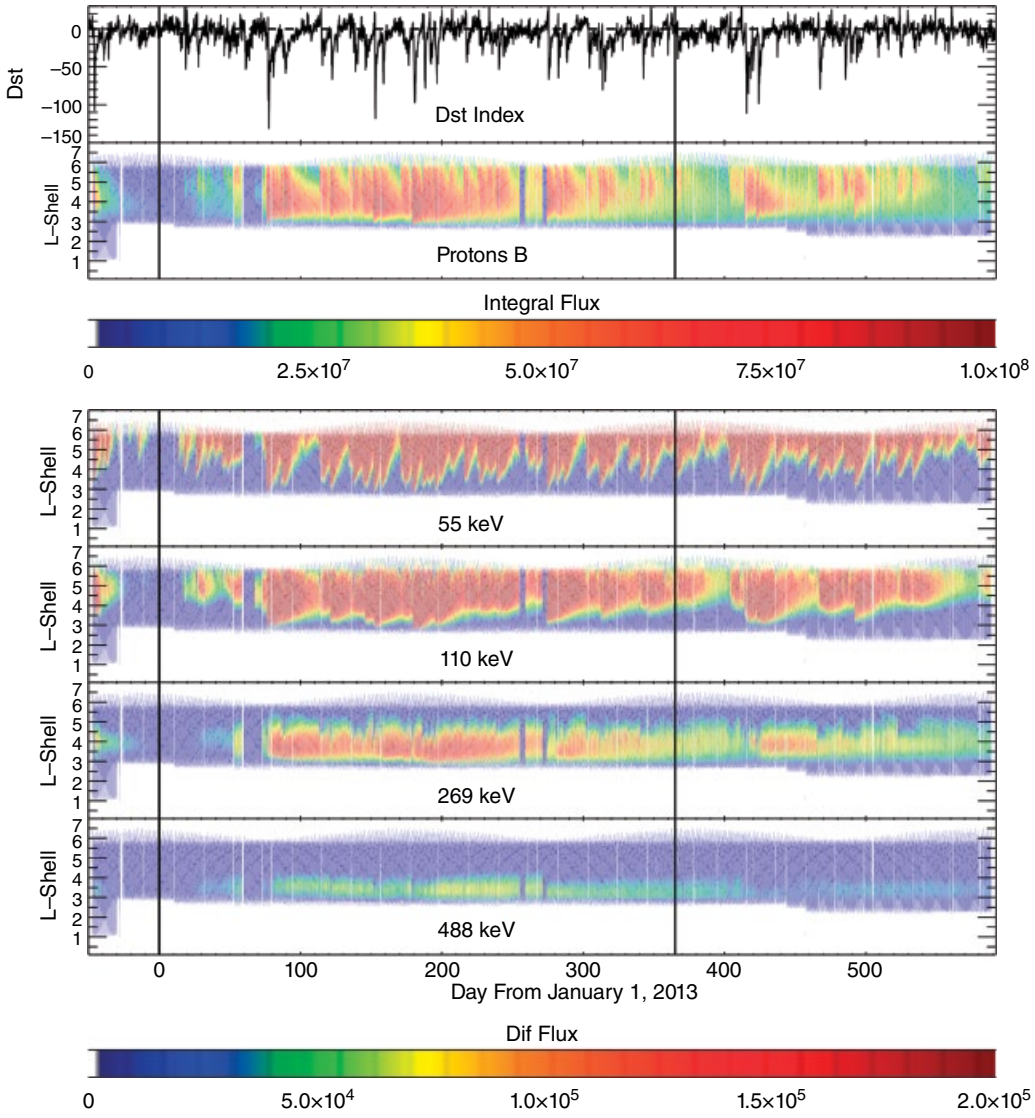

Figure 11.1 (top) Hourly Dst values as reported from the WDC for Geomagnetism, Kyoto, Japan. Time is measured in days from January 1, 2013. The vertical back lines denote the transition from 2012–2013 and 2013–2014, respectively. (second panel) Proton integral flux [particles/(s · cm²)], between the 45-keV to 518-keV energy range, as measured by the RBSPICE instrument aboard the Van Allan Probes spacecraft B, binned into 30-min, 0.1 L-shell realizations. L here is determined by a dipole L model. The measurements below L~2.5 early in the mission demonstrate the original data window of RBSPICE, which was subsequently reduced due to instrument constraints. (bottom four panels) Proton differential flux [particles/(s · cm² · keV)] for 55-keV, 110-keV, 269-keV, and 488 keV particles, respectively.

2014a]. This close connection is valid for both weak injections (indicated by small decreases in Dst) and much stronger storm-time events (indicated by larger decreases in the Dst index). Furthermore, the second panel shows the loss of high L-shell protons before lower L-shell populations. This is opposite to what would be expected from charge exchange loss rates, which indicate that protons, as well as for He and O, have longer lifetimes at higher L-shells [*Ebihara and Ejiri*, 2003]. This apparent loss of high L-shell protons before low L-shell protons is tied to the cross-field radial diffusion of low energy/high L-shell particles to lower L-shell and subsequent energization via conservation of the first adiabatic invariant [e.g., *Schulz and Lanzerotti*, 1974], as was also shown for He in *Gerrard et al*. [2014b]. The violation of the third adiabatic invariant that produces the inward radial diffusion can arise from a variety of operative mechanisms over the course of time: sudden geomagnetic impulses, ultra low frequency (ULF) waves, sudden geomagnetic commencements, etc.

The lower four panels plot the measurements of the differential fluxes [particles/(s·cm²·keV)] of RBSPICE protons at four separate energies: 55-keV, 110-keV, 269-keV, and 488-keV, respectively. Inspection of these panels shows that there is a strong association with the increase in flux of the lower energy protons (e.g., the 55- and 110-keV particles) with initial decreases in Dst. At the higher energies, namely the 269-keV energies, which we later call "medium" ring current energies, such initial decreases in Dst are associated with decreases in proton flux. An example is shown in Figure 11.2 (denoted vertical lines). We speculate these decreases are caused by a combination of convective electric fields, magnetopause shadowing, or field-line curvature losses that are induced during the onset of storm activity associated with the Dst decrease. The highest of the proton energies (i.e., 488-keV and above) from Figure 11.1 shows a long term persistence that only mildly fluctuates in intensity [also shown in Figure 11.2]. These particles are likely produced from the lower energies/high L-shell populations through radial transport and adiabatic energization, and are largely unaffected by storm-time induced changes. At L~3 there is a general decrease in the proton flux that suggests that there are fewer protons at lower L-shells, which would correspond with the slot region.

Plotted in Figure 11.3 are He and O ion integral fluxes (middle and bottom panels, respectively) for the same time interval as the proton data of Figure 11.1. The He data cover the ~65-keV to ~520-keV energy range and the O data

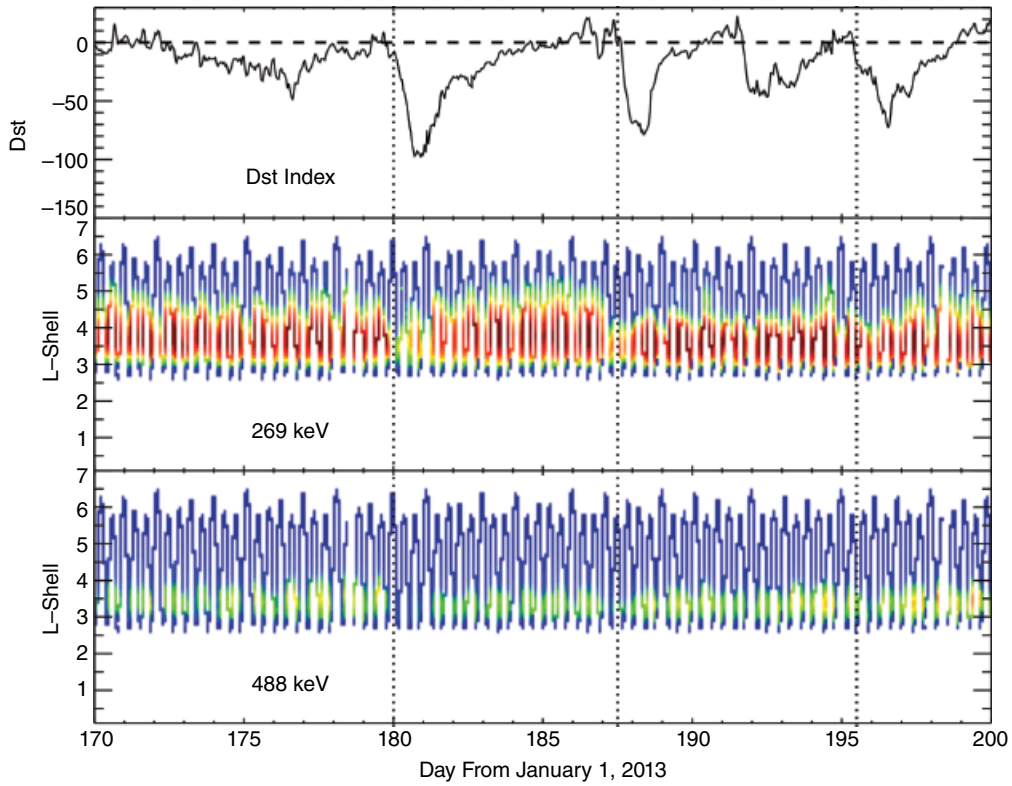

Figure 11.2 Zoom of a specific time period from Figure 11.1. (top) Hourly Dst values. (middle and bottom) Proton differential flux [particles/(s · cm² · keV)] for 269-keV and 488-keV particles, respectively. The color scale is the same as that in Figure 11.1. The vertical dashed lines show three examples when, at storm onset, the 269-keV and higher energy protons are reduced in flux.

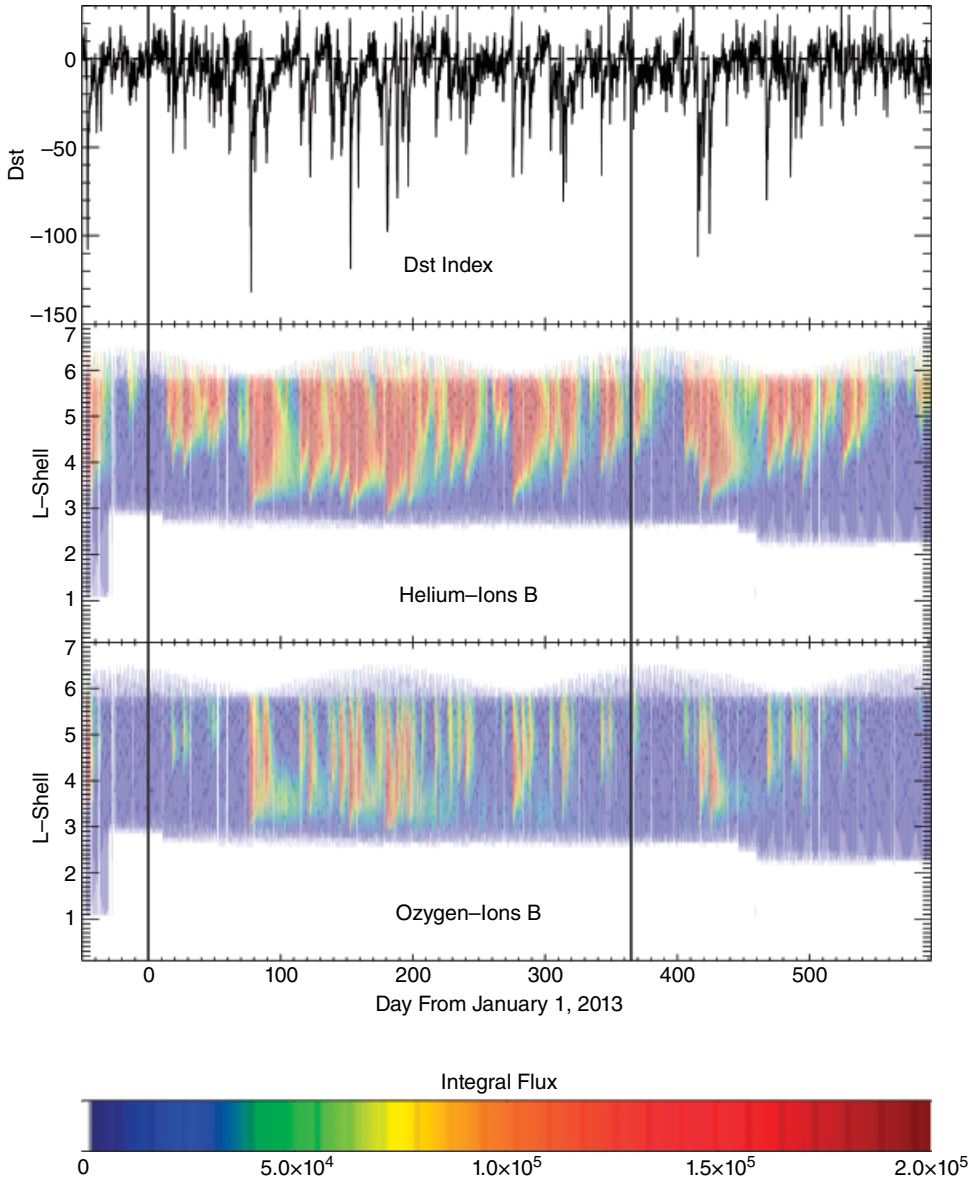

Figure 11.3 (top) Hourly Dst values as from Figure 11.1. (middle) He-ion integral flux [particles/(s · cm^2)], between the ~65-keV to ~520-keV)energy range, as measured by the RBSPICE instrument aboard the Van Allan Probes spacecraft B, binned into 30-min, 0.1 L-shell realizations. L here is determined by a dipole L model. (bottom) O-ion integral flux [particles/(s · cm^2)], between the 140-keV to 1130-keV energy range in the same manner as the He-ions. Vertical lines represent the yearly transition between 2012 to 2013 and 2013 to 2014, respectively.

cover the ~140-keV to ~1130-keV energy range. The time and L-shell bins are the same as for the H data in Figure 11.1 (the integral flux scale is different than Figure 11.1).

Inspection of Figure 11.3 shows that the He and O flux values are approximately a factor of 100 lower than the protons, as was shown in *Gerrard et al.* [2014a]. Furthermore, many of the temporal and intensity features observed in the proton fluxes are also observed in the heavier ions. For example, as was observed with the protons, the lower energy He and O are tightly associated with Dst decreases while the medium energies are anti-correlated [not shown]. In addition, these He and O data (particularly the O as seen in Figure 11.3) also show the persistence of fluxes in the L~3-3.5 region.

Comparisons of Figures 11.1 and 11.3, however, show that the decay rates of the various species after a decrease in Dst vary dramatically relative to each other. As was reported in *Gerrard et al.* [2014a], the lifetimes of the O are shortest, followed by He, and then protons (which seem to persist the longest).

11.4. SPATIAL OBSERVATIONS

During the long time interval covered by the fluxes in Figures 11.1 and 11.3, the Van Allen Probes precessed through all local magnetic times, with some overlap for the early morning/post midnight sector. Thus, for this late 2012 to mid 2014 time interval, the near equatorial orbit of the Van Allen Probes makes it possible to describe the distribution of ring current energy particles around Earth. Of course, such a description is time dependent in that the data cover only one complete orbital precession. Nevertheless, this type of description is useful for ring current models and for global descriptions of the ring current plasma environment.

Plotted in Figure 11.4 are the global equatorial (i.e., SM $Z=0$, projected along the field line to the $Z=0$ plane) distributions of differential fluxes for four of the RBSPICE proton energy channels (55-keV, 110-keV, 269-keV, and 488-keV, respectively) during the "quiet time" periods in Figures 11.1. That is, data here are only for Dst values ranging from $10 < \text{Dst} < +10$, and only for periods not identified as storm initial phase or main phase. The positive SM z-axis points out of the figure of each quadrant. The solar direction is to the left of each quadrant. Though Dst fundamentally measures the net flux of charged particles into and out of the Earth's ring current/inner magnetospheric system, we note that its use as a measure of "quiet time" is not perfect because substorm processes or dayside compression-induced geomagnetic variability, for example, may not lead to large particle injection into the inner magnetosphere and thus not be reflected in Dst variations. Thus, our steady Dst definition of "quiet time" here is somewhat unique.

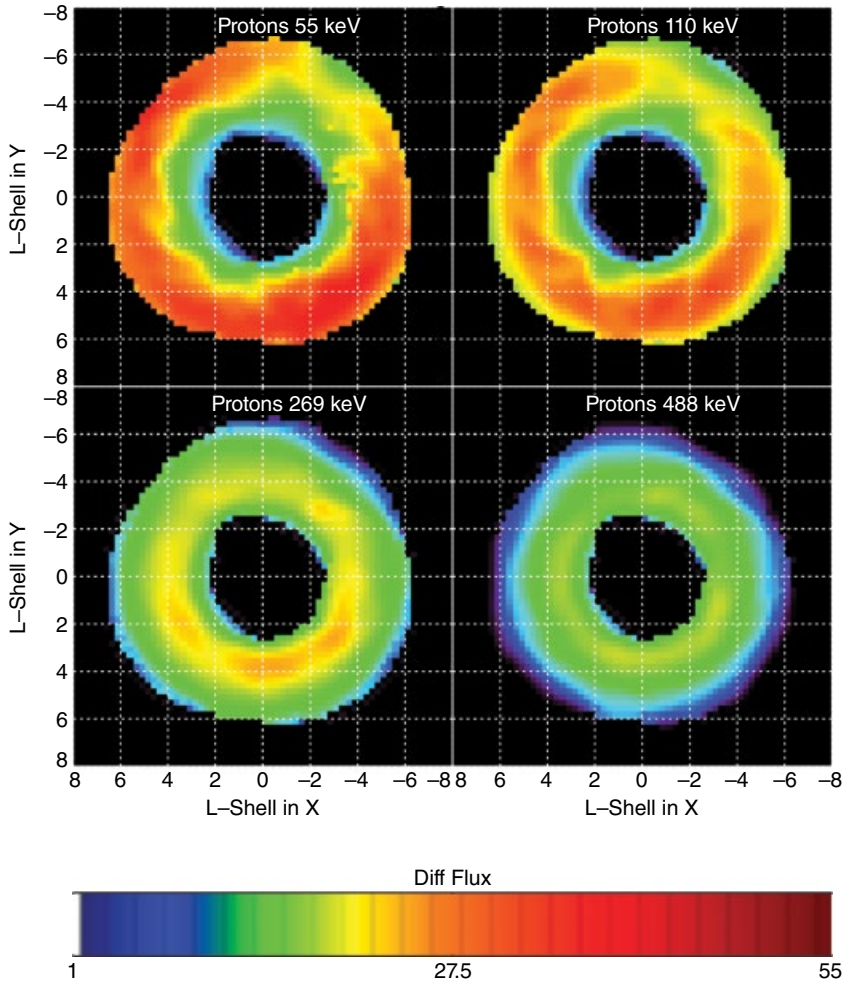

Figure 11.4 X-Y SM spatial distributions of differential flux [particles/(s·cm²·keV)] for protons at energies of (a) 55-keV, (b) 110-keV, (c) 269-keV, and (d) 488-keV. Only "quiet time" data are used here (see text for definition). The flux values are given in decibels (i.e., in dB). The radial distance is the L-shell, as determined by a simple dipole model, and the SM z-axis points out of the figure.

The most striking aspect of these Figure 11.4 distributions is that the higher energy protons are found at lower L-shells compared to the distributions of the lower energies, as was also seen in Figure 11.1. The lowest energy (55-keV; upper left quadrant) protons are located in the outer region of the Van Allen Probes orbit, L~5, while the higher energy distributions (with lower intensities) are located at L~3. Again, the obvious explanation for this radial energy distribution is that in the course of time the lower energy protons are radially diffused inward, gaining energy by conservation of the first adiabatic invariant. The lower intensities of the higher energy ions at the lower L-values, in comparison to the lower energies at the higher L-values, suggest that particle loss also occurs during the radial diffusion process.

The azimuthal distributions of He and O ions for the same time interval (i.e., the nearly two years of data at quiet time) of Figure 11.4 are shown in Figure 11.5. Again, the SM z-axis points out of the figure, and the solar direction is to the left in each quadrant. The upper two quadrants show He ions at 110-keV and 518-keV. The lower two quadrants show O ions for the same corresponding energies.

As was the case for the proton distributions in Figure 11.4, the lower energy He and O ions are concentrated at the higher L-values, L~5 to L~6, while the higher energy ions are found deeper into the magnetosphere, near L~3. Again, the differences in the energy distributions between high and low energy ions can be attributed to inward radial diffusion of the ring current-energy ions, conserving the first adiabatic invariant. The lower intensities of the higher energy He and O at the lower L-values, in comparison to the lower energy intensities at the higher L-values, suggests He and O loss during the radial diffusion process.

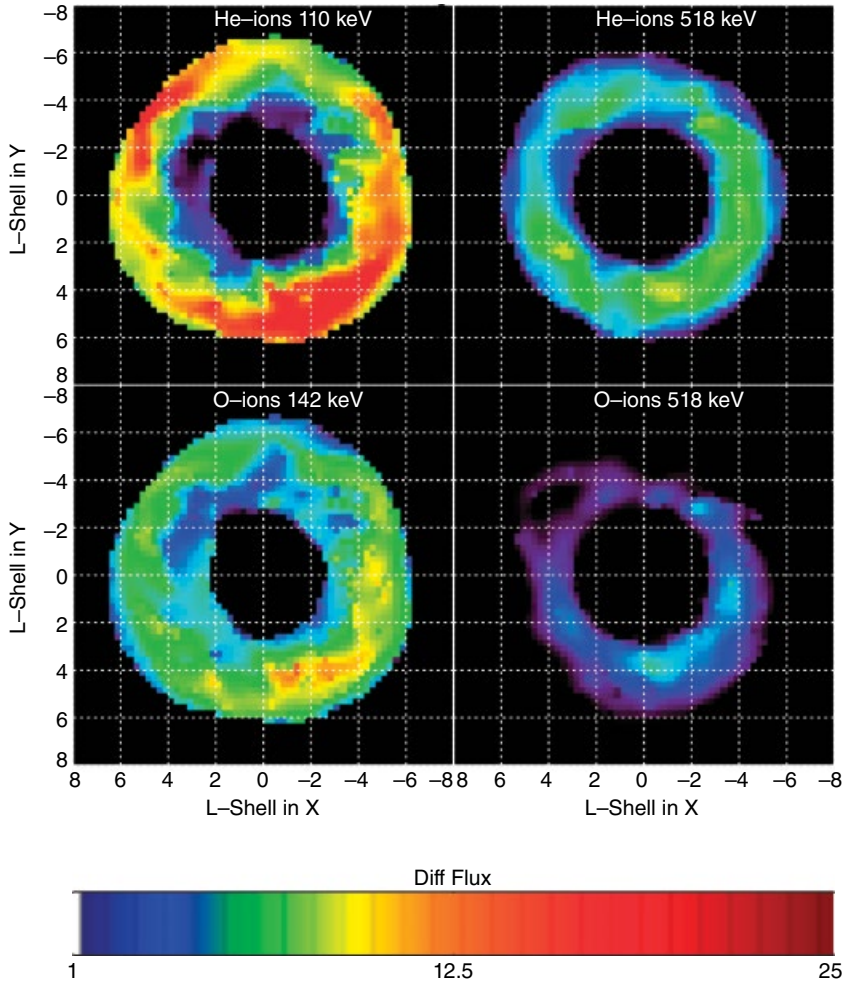

Figure 11.5 X-Y SM spatial distributions of differential flux [particles/(s · cm² · keV)] for helium-ions, at energies of (a) 110 keV and (b) 518 keV, and oxygen-ions, at energies of (c) 142 keV and (d) 518 keV. Only "quiet time" data are used here (see text for definition). The flux values are given in decibels (i.e., in dB). The radial distance is the L-shell, as determined by a simple dipole model, and the SM z-axis points out of the figure.

11.5. DISCUSSIONS

Of particular note from Figures 11.1, 11.2, and 11.3 is the close association of the ions to the decreases in the Dst index, and the resultant spatial and temporal evolution of each species. The level of Dst decrease is generally correlated to L-shell extent (i.e., penetration into lower L-shells) and increase in flux of the ions. As noted, this relationship is energy dependent, with the lower energy particles being the most strongly correlated to Dst and the medium to higher energy particles being anti-correlated or uncorrelated, depending upon the energy range and species. In fact, the highest energy particles seem almost independent of the injection intensity as recorded by the magnitude of the Dst change. There is no readily apparent time delay (i.e., apparent at this temporal binning) between the Dst and said correlation(s). In terms of recovery, the lower energy O are lost first, followed by the He, and then the protons. This species-dependent removal, caused by the varying loss rates, is likely tied to the structure of the Dst recovery phase, with a full "three-phase" recovery due to loss of O, then He, then protons after a relatively major injection/storm event. Other types of recoveries would then be tied to the nature of the injection and the amount of heavy ions injected into the ring current. (See, for example,*Aguado et al.*, [2010] and references therein.)

The global distributions of the ring current ions as illustrated in Figures 11.4 and 11.5 show that the ring current in the different energy manifestations is not symmetric around Earth. A portion of the azimuthal asymmetry in these figures very likely arises from the fact that the data are more than a years worth, with small variations of geomagnetic activity with local time as the satellite precessed through all local times (even though only "quiet time ion data, defined above, were used). Yet the observations are not inconsistent with the first report of *Frank* [1967] that the actual ring current, whose particles had just been measured, was indeed asymmetric. Furthermore, these observations are not inconsistent with other observations at lower energies [e.g., *Roeder et al.*, 2005] or with the importance that has been placed on the asymmetric ring current in establishing magnetosphere dynamics [e.g., *Liehmon et al.*, 2001].

Acknowledging the fact that the sampling in local time can be aliased by geomagnetic activity during the precession interval, the protons, He, and O appear to be most abundant in the post-dusk/pre-midnight sector. This might be expected due to the westward drift associated with ions accessing the magnetosphere from the magnetotail region. By the time the ions azimuthally drift around the Earth and enter the post-midnight/dawn sector, their flux has been reduced due to various loss processes or open drift shells. Another possibility is that there is quasi-episodic injection of magnetotail ions even during "quiet" geomagnetic activity, providing a continual source of ions that circulates around the inner magnetosphere. The He and O spatial distributions are more complex than the proton data, even though this spatial map has been created during quiet intervals. That is, He and O flux "clumps" are seen in certain regions (e.g, in the post-dawn/pre-noon sector). The cause(s) for such He and O structure is still unclear, and such data should serve as a nice test for current ring current models.

11.6. CONCLUSIONS

The RBSPICE instrument gives a contemporary view, at high spatial and spectral resolution, of ring current protons, He, and O around Earth between energies of ~ 50-keV to ~500-keV. This capability, coupled with the broader suite of instruments on the NASA Van Allen Probes spacecraft, which no previous mission had, enable the community to obtain fundamental data on the inner magnetosphere. Such data will allow us to better understand a number of, as of yet open, physical mechanisms (e.g., charge exchange rates, injection dynamics, particle energization) during both quiet and active periods. As demonstrated herein, the RBSPICE data from both Van Allen Probes spacecraft A and B are both providing closure on current questions and simultaneously opening new puzzles for the current and future generations of geospace scientists.

Furthermore, these data can be used in the quest to better understand the interactions between the highly complex, nonlinear ionosphere-inner magnetosphere-magnetotail system and the various feedback routes. Now that such ring current data are available, questions involving 1) the role of ring current closure on the ionosphere, 2) the role of impulsive electric fields, 3) the role of ULF, electromagnetic ion cyclotron (EMIC), chorus, and hiss waves on ion populations (especially for transport and loss), 4) the impact of terrestrial outflow returning to the inner magnetosphere, 5) the mixing of magnetosheath and magnetotail/lobe plasmas, 6) small-scale plasma physics, and a host of others, can now be addressed much more productively.

ACKNOWLEDGMENTS

The authors thank team discussions with the larger RBSPICE and Van Allan Probes teams. The RBSPICE instrument was supported by Johns Hopkins University/Applied Physics Laboratory (JHU/APL) Subcontract No. 937836 to the New Jersey Institute of Technology

under NASA Prime Contract No. NAS5-01072. The Dst hourly data came from the WDC for Geomagnetism, Kyoto, Japan.

REFERENCES

Aguado, J., C. Cid, E. Saiz, and Y. Cerrato (2010), Hyperbolic decay of the Dst Index during the recovery phase of intense geomagnetic storms, *J. Geophys. Res*, *115*, A07220, doi:10.1029/2009JA014658.

Brandt, P. C., D. G. Mitchell, Y. Ebihara, B. R. Sandel, E. C. Roelof, J. L. Burch, and R. Demajistre (2002), IMAGE/high-energy energetic neutral atom: Global energetic neutral atom imaging of the plasma sheet and ring current during substorms, *J. Geophys. Res.*, *07*, A12, doi: 10.1029/2002JA009307.

Burch, J. L. (2000), IMAGE mission overview, *Space Sci. Rev.*, *91*, 1–4.

Burch, J. L. (2005), Magnetospheric Imaging: Promise to reality, *Rev. Geophys*, *43*, 3, RG3001.

Cahill, L. J., Jr. (1966), Inflation of the inner magnetosphere during a magnetic storm, *J. Geophys. Res.*, *71*, 4505.

Chapman, S., and J. Bartels (1941), Geomagnetism. Vol. I. Geomagnetic and related phenomena, and Vol. II. Analysis and physical interpretation of the phenomena, *Quarterly Journal of the Royal Meteorological Society*, The International Series of Monographs on Physics, London (Sir Humphrey Milford, Oxford University Press), 67.

Chapman, S., and V. C. A. Ferraro (1933), A new theory of magnetic storms, *Terrestrial Magnetism and Atmospheric Electricity (Journal of Geophysical Research)*, *38*, 79, doi:10.1029/TE038i002p00079.

Daglis, I. A., R. Thorne, W. Baumjohann, and S. Orsini (1999), The terrestrial ring current: Origin, formation, and decay, *Reviews of Geophysics*, *37*,4, doi:8755-1209/99/1999 RG900009.

Daglis, I. A. (2006), Ring current dynamics, *Space Sci. Rev.*, *124*, 183.

Dessler, A. J. (1970), Swedish scientist recognized after many years of rejection and obscurity, *Science*, *170*, 604.

Davis, L. R., and J. M. Williamson (1966), Outer Zone Protons, *Radiation Trapped in the Earth's Magnetic Field*, Astrophysics and Space Science Library, B. M. McCormac, ed., 5.

Ebihara, Y., and M. Ejiri (2003), Numerical simulation of the ring current: Review, *Space Sci. Rev.*, *105*, 377–452.

Frank, L. A. (1967) On the extraterrestrial ring current during geomagnetic storms, *J. Geophys. Res.*, *72*, doi:10.1029/JZ072i015p03753.

Gerrard, A., L. Lanzerotti, M. Gkioulidou, D. Mitchell, J. Manweiler, J. Bortnik, and K. Keika (2014), Initial measurements of O-ion and He-ion decay rates observed from the Van Allen Probes RBSPICE instrument, *J. Geophys. Space Res.*, *119*, 88138819, doi:10.1002/2014JA020374.

Gerrard, A., L. Lanzerotti, M. Gkioulidou, D. Mitchell, J. Manweiler, and J. Bortnik (2014), Quiet time observations of He ions in the inner magnetosphere as observed from the RBSPICE instrument aboard the Van Allen Probes mission, *Geophys. Res. Lett*, *41*, doi:10.1002/2013GL059175.

Gloeckler, G., F. M. Ipavich, B. Wilken, W. Stuedemann, and D. Hovestadt (1985), First composition measurement of the bulk of the storm-time ring current (1 to 300 KeV/e) with AMPTE-CCE, *Geophys. Res. Lett.*, *12*, 325–328, doi:10.1029/GL012i005p00325.

Hamilton, D. C., G. Gloeckler, F. M. Ipavich, W. Studemann, B. Wilken, and G. Kremser (1988), Ring current development during the great geomagnetic storm of February 1986, *J. Geophys. Res.*, *93*, 14,343–14,355, doi:10.1029/JA093iA12p14343.

Henderson, M. G., G. D. Reeves, H. E. Spence, R. B. Sheldon, A. M. Jorgensen, J. B. Blake, and J. F. Fennell (1997), First energetic neutral atom images from Polar, *Geophys. Res. Lett.*, *24*, 11671170, doi:10.1029/97GL01162.

Liehmon, M. W., J. U. Kozyra, M. F.Thomsen, J. L.Roeder, G. Lu, J. E. Borovsky, and T. E. Cayton (2001), Dominant role of the asymmetric ring current in producing the stormtime Dst, *J. Geophys. Res.*, *106*, 10883–10904, doi:10.1029/2000JA000326.

Lui, A.T.Y., et al., (2005), Observations of energetic neutral oxygen by IMAGE/HENA and GEOTAIL/EPIC, *Geophys. Res. Lett.*, *32*, 13, L13104, doi:10.1029/2005GL022851.

Mauk, B. H., N. J. Fox, S. G. Kanekal, R. L. Kessel, D. G. Sibeck, and A. Ukhorskiy (2012), Science Objectives and Rationale for the Radiation Belt Storm Probes Mission, *Space Science Reviews* 10.1007/s11214-012-9908-y.

Milillo, A., S. Orsini, and I. A. Daglis (2001), Empirical model of proton fluxes in the equatorial inner magnetosphere: Development, *J. Geophys. Res.*, *106*(A), 2571325730, doi:10.1029/2000JA900158.

Milillo, A., S. Orsini, D. C. Delcourt, A. Mura, S. Massetti, E. de Angelis, and Y. Ebihara (2003), Empirical model of proton fluxes in the equatorial inner magnetosphere: 2. Properties and applications, *J. Geophys. Res.*, *108*(A), 1165, doi:10.1029/2002JA009581.

Mitchell, D. G., S. E. Jaskulek, C. E. Schlemm, E. P. Keath, R. E. Thompson, B. E. Tossman, J. D. Boldt, J. R. Hayes, G. B. Andrews, N. Paschalidis, D. C. Hamilton, R. A. Lundgren, E. O. Tums, P. Wilson, IV, H. D. Voss, D. Prentice, K. C. Hsieh, C. C. Curtis, and F. R. Powell (2000), High energy neutral atom (HENA) imager for the IMAGE mission, *Space Science Reviews*, *91*.

Mitchell, D., L. J. Lanzerotti, C. K. Kim, M. Stokes, G. Ho, S. Cooper, A. Ukhorskiy, J. W. Manweiler, S. Jaskulek, D. K. Haggerty, P. Brandt, M. Sitnov, K. Keika, J. R. Hayes, L. E. Brown, R. S. Gurnee, J. C. Hutcheson, K. S. Nelson, N. Paschalidis, E. Rossano, S. Kerem (2013), Radiation Belt Storm Probes Ion Composition Experiment (RBSPICE), *Space Science Reviews*, *179*, doi:10.1007/s11214-013-9965-x.

Roeder, J. L., M. W. Chen, J. F. Fennell, and R. Friedel (2005), Empirical models of the low-energy plasma in the inner magnetosphere, *Space Weather*, *3*(1), S12B06, doi:10.1002/2005SW000161.

Roelof, E. C., D. G. Mitchell, and D. J. Williams (1985), Energetic neutral atoms (E~50keV) from the ring current IMP 7/8 and ISEE-1, *J. Geophys. Res.*, *90*, 10,991–11,008, doi:10.1029/JA090iA11p10991.

Roelof, E.C. (2004), Derivation of currents and diamagnetic effects from global plasma pressure distributions obtained by IMAGE/HENA, *Adv. Space Res.*, *33* (5), 747–751.

Schulz, M., and L. Lanzerotti (1974), *Particle Diffusion in the Radiation Belts*, Physics and Chemistry in Space, Berlin, Springer.

Sheldon, R. B. and D. C. Hamilton (1993), Ion transport and loss in the earth's quiet ring current. I - Data and standard model, *J. Geophys. Res.*, *98*, 13491, doi:10.1029/92 JA02869.

Sheldon, R. B. (1994), Ion transport and loss in the Earth's quiet ring current. 2: Diffusion and magnetosphere-ionosphere coupling, *J. Geophys. Res.*, *99*, 5705–5720, doi:10.1029/93 JA02769.

Singer, S. F. (1957), A new model of magnetic storms and aurora, *Trans. Am. Geophys. Union*, *38*, 175.

Singer, S. F. (1958), Role of ring current in magnetic storms, *Trans. Am. Geophys. Union*, *39*, 532.

van Allen, J.A. (2002), *Magnetospheric Physics*, The Century of Space Science, Volume I, J. A. Bleeker, J. Geiss, and M. C. E. Huber, eds., Kluwer Academic Publishers.

12

Global Modeling of Wave Generation Processes in the Inner Magnetosphere

Vania K. Jordanova

Video of Yosemite Talk, URL: http://dx.doi.org/10.15142/T3RG68

ABSTRACT

Plasma waves play a fundamental role in the energization and loss of charged particles in the inner magnetosphere. Numerical modeling is a powerful tool to specify their global time-dependent distribution beyond sparsely available in situ satellite measurements. To investigate the generation of two dominant emissions, whistler mode chorus and electromagnetic ion cyclotron (EMIC) waves on a global scale, we perform storm simulations with our ring current-atmosphere interactions model with self-consistent magnetic field (RAM-SCB). We find increased anisotropies in the ion and electron velocity distributions due to fresh particle injections from the plasma sheet and subsequent energy dependent drifts and losses in realistic electric and magnetic fields. These unstable distributions induce the growth of plasma waves in the equatorial magnetosphere with high spatial and temporal variability; chorus wave growth maximizes at larger radial distances outside the plasmasphere in the morning sector, while EMIC waves intensify in the afternoon sector where energetic protons drift westward through high-density plasmaspheric regions. The EMIC wave-induced proton precipitation predicted with RAM-SCB reproduces well the temporal and spatial evolution of Imager for Magnetopause-to-Aurora Global Explorer (IMAGE) observations of detached subauroral proton arcs. Further studies are needed to quantify the integrated global effect of these waves on the near-Earth radiation environment.

12.1. INTRODUCTION

The near-Earth space environment is a highly dynamic and coupled system through a complex set of physical processes over a large range of scales. It responds nonlinearly to driving by the time-varying solar wind, with important feedback from many parts of the system, and is also far from benign: magnetospheric dynamics result in "space weather," which are conditions that can damage or disable orbiting satellites [e.g., *Gubby and Evans*, 2002]. The most important space weather events, geomagnetic storms, are triggered by plasma eruptions on the Sun slamming into Earth one to four days later [e.g., *Burch*, 2001]. Conditions in space may turn from quiet to destructive in minutes, and storms may last up to several days. Storms intensify the ring current, the magnetically trapped charged particles (tens kiloelectron-folt [keV]) circling Earth between ~2 to 5 Earth radii (R_E). The mechanisms for particle injection, trapping, and loss have been studied since the beginning of space exploration [e.g., *Frank*, 1967; *Cornwall et al.*, 1970], however, their theoretical evaluation and implementation in numerical models of geomagnetic storms remain challenging.

An important consequence of particle injections is the generation of plasma waves that transfer energy from

Space Science and Applications Group, Los Alamos National Laboratory, Los Alamos, NM, USA

Magnetosphere-Ionosphere Coupling in the Solar System, Geophysical Monograph 222, First Edition.
Edited by Charles R. Chappell, Robert W. Schunk, Peter M. Banks, James L. Burch, and Richard M. Thorne.

the fields back to the particles. Charged particles can be accelerated to very high energies becoming "killer" electrons that damage spacecraft, or can be precipitated into the Earth's atmosphere producing the spectacular aurora. These extremely complex feedback mechanisms regulate the intensity and distribution of particle populations as a delicate balance between sources and losses. A long-standing unresolved problem since the discovery of the radiation belts in 1958 [*Van Allen et al.*, 1958] is how the particles get accelerated to relativistic energies. Is it by radial transport from an outside source or is it in situ local acceleration by plasma waves? Recent data from the National Aeronautics and Space Administration (NASA) Van Allen Probes [*Reeves et al.*, 2013; *Thorne et al.*, 2013] identify local acceleration as the main driver, highlighting the importance of understanding how these waves are generated and how the acceleration takes place.

From the variety of plasma waves observed in the magnetosphere, the acceleration and loss of "killer" electrons are associated mostly with whistler mode chorus emissions, plasmaspheric hiss, and EMIC waves. Whistler mode chorus is a naturally occurring emission in the very low frequency (VLF) range with a power minimum at ~0.5 f_{ce} (where f_{ce} is the local electron gyrofrequency) separating the emissions into lower and upper bands [*Tsurutani and Smith*, 1974]. Its source region is located near the geomagnetic equator [e.g., *Santolik et al.*, 2003], and chorus waves are most frequently observed outside of the plasmasphere with intensities strongly dependent on geomagnetic conditions. A recent statistical survey using a comprehensive set of data from five satellite missions [*Meredith et al.*, 2012] indicates that the largest intensities of equatorial lower band chorus are seen between 23 and 12 magnetic local time (MLT) from about 4 to 9 R_E. The peak intensities of equatorial upper band chorus are smaller and occur between 23 and 11 MLT from about 3 to 7 R_E. Although upper band chorus is confined to the magnetic equator, lower band chorus can propagate to mid and high latitudes on the dayside [e.g., *Horne et al.*, 2005; *Bunch et al.*, 2012] where peak intensities are observed between 07 and 14 MLT from about 4 to 9 R_E. The generation mechanism of chorus emissions contains both linear and nonlinear growth, however, the specifics are not yet well understood. Chorus waves are initially excited by cyclotron resonant interaction with anisotropic low-energy (tens of keV) electrons [e.g., *Kennel and Thorne*, 1967; *Gary and Wang*, 1996; *Li et al.*, 2009]. The linear growth plays a dominant role in the early stage, and a growth rate larger than 40 dB/s was shown as a requirement for nonlinear instability [*Nunn et al.*, 1997]. It has been also demonstrated that the inhomogeneity in the background magnetic field is important for the production of nonlinear discrete chorus elements [*Katoh and Omura*, 2007; *Omura et al.*, 2008]. Both theoretical and observational studies have suggested that chorus waves may propagate into the plasmasphere and evolve into plasmaspheric hiss [e.g., *Bortnik et al.*, 2008; *Meredith et al.*, 2013]. Plasmaspheric hiss is largely responsible for the formation of the slot region between the inner and outer radiation belts [*Lyons and Thorne*, 1973; *Meredith et al.*, 2009]. It also contributes to the loss of outer radiation belt electrons during the main and recovery phases of geomagnetic storms [*Summers et al.*, 2007] and the quiet time decay of energetic electrons in the outer radiation belt [*Meredith et al.*, 2006].

EMIC waves are observed in the inner magnetosphere in the ultra low frequency (ULF) range in three distinct frequency bands: hydrogen (between the proton and helium gyrofrequency), helium (between the helium and oxygen gyrofrequency), and oxygen (below the oxygen gyrofrequency). The hydrogen band EMIC waves are usually observed outside the plasmapause, the helium band is observed both inside and outside the plasmapause [*Fraser and Nguyen*, 2001], and the oxygen band EMIC waves are rarely observed [*Bräysy et al.*, 1998]. Statistical studies examining the occurrence of EMIC waves [e.g., *Anderson et al.*, 1992; *Erlandson and Ukhorskiy*, 2001; *Usanova et al.*, 2012] have found that although these waves are observed over a wide range of radial distances, from about 3 to 10 R_E, their occurrence maximizes in the afternoon sector and their intensity increases with geomagnetic activity. The detailed radial and MLT spatial structure of EMIC waves, however, is not well known. Analyzing the global morphology and spectral characteristics of EMIC waves derived from Combined Release and Radiation Effects Satellite (CRRES) observations. *Meredith et al.* [2014] found that the helium band waves are more frequently observed than the hydrogen band in the afternoon sector, and the average intensity of the helium band (in that sector) between 4 and 7 R_E was 2 nT^2, while that of the proton band was 0.5 nT^2. Comparing Van Allen Probes measurements with ground-based observations of EMIC waves, *Mann et al.* [2014] found that although an extended interval (>18 h) of continuous EMIC waves was observed on ground, both Van Allen Probes A and B observed very narrow (0.1 to 0.4 R_E) EMIC emission confined to the outer edge of the plasmasphere. The narrow width could explain the relative rarity of space-based EMIC occurrence compared to ground-based observations. EMIC waves are excited by anisotropic (tens of keV) ring current ions injected in the inner magnetosphere during geomagnetic storms and substorms [*Cornwall et al.*, 1970; *Jordanova et al.*, 2001]. Theoretical predictions that EMIC waves are generated in the equatorial plane are supported by CRRES observations indicating a source region within 11° of the equator [*Loto'aniu et al.*, 2005] and by the absence of reflected wave packet energy [e.g., *Mursula*, 2007].

Chorus emissions outside the plasmapause are important for the local acceleration of ~100 keV electrons to million electron volts (MeV) energies [e.g., *Horne and Thorne*, 1998; *Summers et al.*, 1998; *Miyoshi et al.*, 2003]. On the other hand, pitch angle scattering by EMIC waves may cause the precipitation and loss of ring current ions [e.g., *Cornwall et al.*, 1970; *Jordanova et al.*, 2001; *Yahnin and Yahnina*, 2007] as well as relativistic electrons [e.g., *Thorne*, 1974; *Albert*, 2003; *Jordanova et al.*, 2008; *Kersten et al.*, 2014; *Usanova et al.*, 2014]. Intense relativistic electron precipitation to the atmosphere has been observed by a number of low-Earth orbiting satellites [e.g., *Lorentzen et al.*, 2001; *Bortnik et al.*, 2006] and with both ground-based and balloon experiments [e.g., *Clilverd et al.*, 2007; *Millan et al.*, 2007]. Observed proton precipitation has been associated with detached subauroral proton arcs [*Immel et al.*, 2002; *Spasojevic et al.*, 2004], dayside subauroral proton flashes [*Hubert et al.*, 2003; *Yahnina et al.*, 2008], and subauroral morning proton spots [*Frey et al.*, 2004; *Yahnin et al.*, 2007]. This paper presents global patterns of whistler mode chorus and EMIC wave generation and particle precipitation calculated with a kinetic ring current model and comparisons with observations. Development of accurate numerical models is important to assess the role of these two dominant plasma waves in geomagnetic storm dynamics, as well as for the prediction of hazardous space weather events.

12.2. KINETIC MODEL OF THE RING CURRENT

To study the transport, acceleration, and loss of energetic particles in the inner magnetosphere, several global four-dimensional models that average out the gyration and bounce motion of a charged particle about the magnetic field line, but not its drift motion around the Earth, have been developed. The RAM solves the bounce-averaged kinetic equation for energetic particles including all pitch angles, derived theoretically and implemented numerically by *Jordanova* [1995]. RAM was originally developed with an emphasis on the study of wave-particle interactions in the inner magnetosphere [*Jordanova et al.*, 1996; 1997], using energy and pitch angle as independent variables for the phase space distribution function. Therefore, RAM differs from the models of *Fok et al.* [1995] and *Chen et al.* [1998], which employ the first and second adiabatic invariants as independent variables. The two spatial variables, radial distance from Earth and MLT, are the same in all three of these ring current models. RAM has been used successfully to study various aspects of ring current dynamics over the past decades [e.g., *Jordanova et al.*, 2001, 2006; *Kozyra et al.*, 2002; *Liemohn et al.*, 1999; *Khazanov et al.*, 2002]. In the relativistic case, the kinetic equation for the phase space distribution function $Q_l(R_o, \phi, E, \mu_o, t)$ for species l becomes:

$$\frac{\partial Q_l}{\partial t} + \frac{1}{R_o^2}\frac{\partial}{\partial R_o}\left(R_o^2\left\langle\frac{dR_o}{dt}\right\rangle Q_l\right) + \frac{\partial}{\partial \phi}\left(\left\langle\frac{d\phi}{dt}\right\rangle Q_l\right) + \frac{1}{\gamma p}\frac{\partial}{\partial E}\left(\gamma p\left\langle\frac{dE}{dt}\right\rangle Q_l\right) + \frac{1}{h\mu_o}\frac{\partial}{\partial \mu_o}\left(h\mu_o\left\langle\frac{d\mu_o}{dt}\right\rangle Q_l\right) = \left\langle\left(\frac{\partial Q_l}{\partial t}\right)_{loss}\right\rangle \tag{12.1}$$

Here the brackets $\langle\ \rangle$ denote averaging between the mirror points and the index o refers to the quantities in the magnetic equatorial plane: R_o is the radial distance from 2 R_E to 6.5 R_E, ϕ is the geomagnetic east longitude, p is the relativistic momentum of the particle, γ is the relativistic factor, and E is the kinetic energy, typically from ~0.1 keV to ~400 keV. The equatorial pitch angle α_o varies from 0° to 90° and $\mu_o = \cos(\alpha_o)$. The field-geometric function h is related to the half-bounce path length S_B by the formula $h = S_B/(2R_o)$. The three major ring current ion species H^+, O^+, He^+, and electrons are included in our model.

The left-hand side of equation (1) describes the transport and acceleration of charged particles along adiabatic drift paths in time-dependent electric and magnetic fields. At first RAM used simple analytical expressions that approximated the Earth's magnetic field as a dipole and the magnetospheric electric field as the gradient of a *Kp*-dependent convection potential [*Volland*, 1973; *Stern*, 1975; *Maynard and Chen*, 1975] plus a corotation potential. For a self-consistent calculation of the magnetic field, RAM was later coupled with a three-dimensional Euler potential-based plasma equilibrium code (SCB), which calculates the magnetic field in force balance with the plasma pressure from the ring current particles [*Jordanova et al.*, 2006, 2010b; *Zaharia et al.*, 2006]. Further studies investigated one-way [*Zaharia et al.*, 2010; *Welling et al.*, 2011] and two-way [*Yu et al.*, 2014] coupling of RAM-SCB with the magnetohydrodynamic (MHD) code Block Adaptive Tree Solar Wind Roe-type Upwind Scheme (BATS-R-US) through the Space Weather Modeling Framework (SWMF) [*Tóth et al.*, 2005]. In the two-way coupling study, the ionospheric potential solver of *Ridley et al.* [2004] was used to establish the self-consistency in the electric field for RAM-SCB. These studies demonstrated that the self-consistent feedback significantly affects the global magnetic and electric fields and the subsequent redistribution of ring current particles in the inner magnetosphere.

All important particle loss processes are included in the right-hand side of equation (1). For ring current ions, these are charge exchanges with neutral hydrogen from the geocorona resulting in the generation of high energy neutrals and low energy protons, scattering by EMIC waves toward the loss cone, and particle precipitation and absorption

in the atmosphere at low altitudes. For energetic (keV) electrons, the most important loss processes are scattering by lightning whistler, hiss, and VLF transmitters inside the plasmasphere and by whistler mode chorus outside the plasmasphere, and electron precipitation to the atmosphere. The loss cone in RAM-SCB corresponds to an altitude of 200 kilometers (km). A simulation run typically starts about 10 hours before storm commencement with initial conditions specified after quiet time satellite measurements and evolves into storm time. The boundary conditions are taken either from energetic particle data from Los Alamos National Laboratory (LANL) geosynchronous spacecraft or from physics-based (e.g., BATS-R-US) or empirical models [e.g., *Tsyganenko and Mukai*, 2003] and are usually updated every 5 min. The input ion flux at the nightside boundary is typically divided among the three ion species using statistical studies [*Young et al.*, 1982; *Mouikis et al.*, 2010] that correlate the ion composition with geomagnetic and solar activity.

12.3. GLOBAL MODELING OF EMIC WAVE GENERATION

The RAM-SCB model calculates in a self-consistent manner the growth rate of EMIC waves from the evolving ring current ion population by solving the linearized dispersion relation [e.g., *Gomberoff and Neira*, 1983; *Kozyra et al.*, 1984] in the equatorial plane, where the density, parallel energy, and temperature anisotropy of the ring current H^+, O^+, and He^+ ion species are calculated by taking moments of the distribution functions Q_l obtained from equation (1). The cold plasma densities are obtained with a coupled time-dependent plasmasphere model [*Rasmussen et al.*, 1993]. The superposition of the growth or damping rates due to each individual ring current ion species determines whether waves are excited in the multi-ion plasma. The convective growth rates are integrated along field-aligned wave paths to obtain the wave gain, and the wave amplitudes are calculated with a semi-empirical model [*Jordanova et al.*, 2001] since neither the background noise level from which the waves grow is well known nor the linear calculations provide a saturation mechanism. The effect of plasma wave scattering on the ring current distributions is treated following quasi-linear theory as a diffusive process. Diffusion coefficients that consider the presence of heavy ions in the plasma [*Jordanova et al.*, 1996] and thus reduce significantly the proton lifetimes at lower energies (~10–100 keV) are used. The average flux in the loss cone is calculated for given energy ranges and global images of precipitating fluxes are obtained as the storm develops.

Mechanisms causing the proton precipitation during detached subauroral arcs were investigated by *Jordanova et al.* [2007]. Signatures of subauroral precipitation were observed by the IMAGE Far Ultra Violet (FUV) instrument in the afternoon sector beginning around 2100 UT on 23 January 2001 [*Immel et al.*, 2002; *Burch et al.*, 2002]. The proton aurora brightened significantly around 2300 UT and separated from the main auroral arc, which receded toward the pole. The detached proton arc was observed until the spacecraft could image the northern auroral oval at ~0025 UT on 24 January. The Fast Auroral SnapshoT (FAST) ion spectrometer measured proton fluxes at energies less than 30 keV in the same local time sector, conjugate to the IMAGE observations. Significant proton precipitation was observed equatorward of −69° MLAT at the time of the detached proton arc observation by IMAGE while there was no enhancement in the electron precipitation at these latitudes. Figure 12.1 shows results from a RAM simulation [*Jordanova et al.*, 2007] using a Volland-Stern type electric field driven by a high-time resolution effective *Kp* (dashed line) derived from the Auroral Boundary Index (ABI), and a dipolar magnetic field. Geoeffective He^+ band EMIC waves (wave gain above ~20 dB) were preferentially excited along the plasmapause or in regions of enhanced plasmaspheric densities occurring within dayside drainage plumes. The wave gain (Figure 12.1a) reached a maximum in the postnoon MLT sector between hours 47 and 48; it decreased below the geoeffective level (~20 dB) by hour 49 due to the wave scattering feedback and isotropization of the proton ring current. Precipitating proton fluxes integrated over 10–40 keV energies are shown in Figures 12.1b and 12.1c. To isolate the effects of wave-particle interactions, we show fluxes calculated without (Figure 12.1b) and with (Figure 12.1c) EMIC wave scattering included. The subauroral precipitation region observed with IMAGE FUV is mapped to the equatorial plane and plotted with a diamond line. When there was not a distinct subauroral arc (hour 47), the line shows the equatorward edge of the proton oval. It is evident that plasma wave scattering significantly enhanced the ion precipitation within localized regions in the afternoon sector where EMIC wave instability developed, matching very well the temporal and spatial evolution of FUV observations. This indicates that cyclotron resonant wave-particle interactions are a viable mechanism for the generation of subauroral proton arcs. These results are confirmed by a more recent study [*Chen et al.*, 2014] of EMIC wave modeling during the 8 to 11 June 2001 geomagnetic storm. Simulations using RAM-SCB and a ray tracing code showed that the EMIC wave gain was predominantly in the He^+ band, and EMIC wave distributions agreed with proton aurora observations from IMAGE satellite at subauroral latitudes during this storm period.

One limitation of our previous studies of EMIC wave generation and proton precipitation is the confinement of the outer model boundary to geosynchronous orbit while

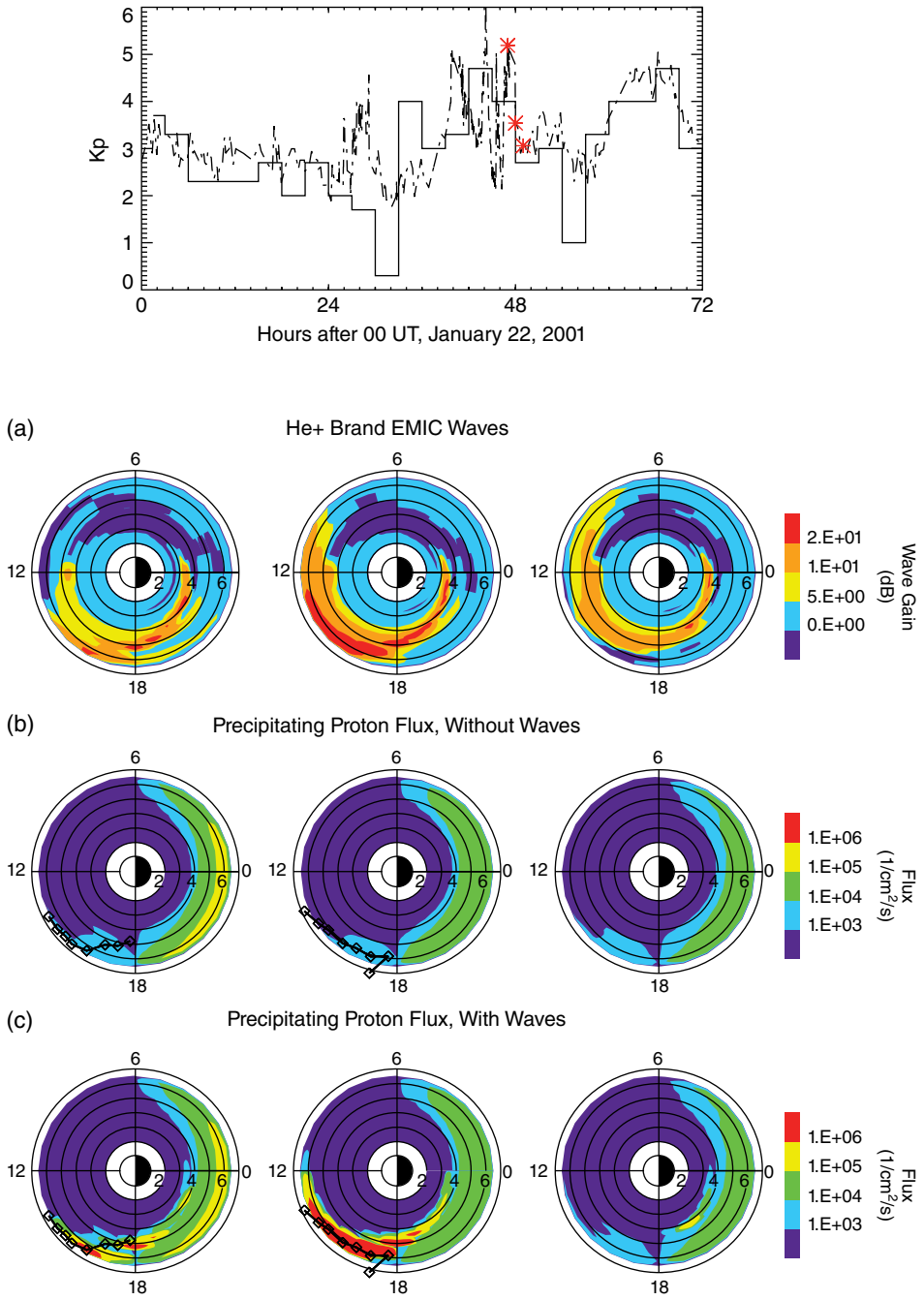

Figure 12.1 Planetary (solid line) and effective (dashed line) *Kp* index and (a) calculated EMIC wave gain as a function of radial distance in the equatorial plane and MLT at hours 47, 48, and 49 after 00 UT on 22 January 2001 indicated with stars on the *Kp* plot. (b) Precipitating 10–40 keV proton number flux considering drift and collisional losses. (c) Same as (b), but adding pitch angle scattering by EMIC waves. The diamond line indicates the low-latitude boundary of FUV images of proton precipitation mapped to the SM equatorial plane. [after *Jordanova et al.*, 2007]

IMAGE observations clearly show that the proton precipitation extends to larger radial distances. Therefore, we have expanded RAM-SCB from 6.5 to 9 R_E by specifying the plasma boundary conditions after the empirical plasma sheet model TM03 [*Tsyganenko and Mukai*, 2003] based on Geotail data. Another development of RAM-SCB is its coupling with the upgraded electric field model W05 [*Weimer*, 2005], which has more accurate field values and a better reproduction of nonlinear saturation effects in the solar wind-magnetosphere coupling. *Jordanova et al.* [2014]

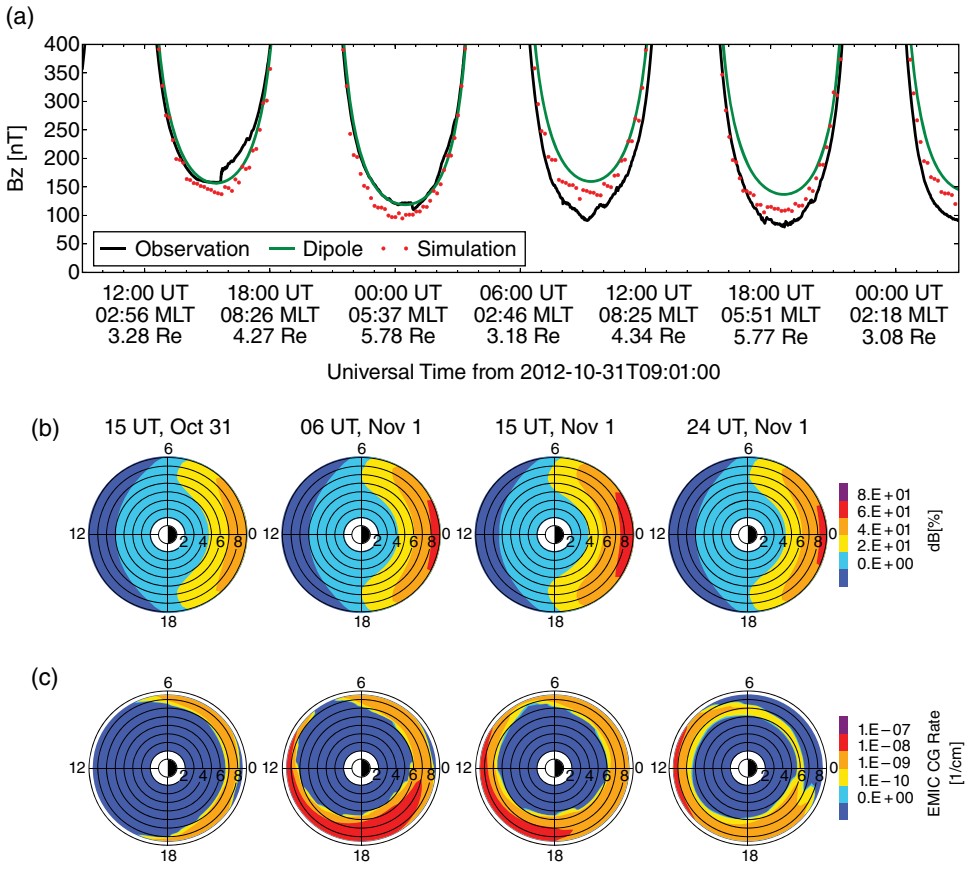

Figure 12.2 (a) The B_z magnetic field component measured with EMFISIS (black line) on RBSP-B, compared with RAM-SCB simulations (red dotted line), and with the Earth dipolar field (green line). (b) The relative difference between the intensity of the Earth dipolar field and the magnetic field calculated with RAM-SCB. (c) the EMIC convective growth rate in the SM equatorial plane at four representative times during the investigated storm. [after *Jordanova et al.*, 2014]

used this improved model to investigate the dynamics of the ring current during the moderate storm of 1 November 2012 with $Dst \approx -60$ nT and $Kp = 5^-$. Comparisons with high-resolution data from the instruments on the Van Allen Probes showed that the expanded RAM-SCB model reproduced reasonably well the initial ring current buildup caused by the simultaneous increase of the plasma sheet source population and the convective electric field. Model results reproduced MagEIS observations at higher energies ($E > 50$ keV) including dispersed ion injections, however, underestimated HOPE observations at lower energies ($E < 10$ keV). Several reasons for this disagreement like proper representation of initial and boundary conditions are currently under investigation. RAM-SCB calculations of all three components of the large-scale magnetic field were in good agreement with measurements from the Electric and Magnetic Field Instrument Suite and Integrated Science (EMFISIS) magnetometer. The calculated B_z component (Figure 12.2a) showed significant depression compared to the Earth dipolar field near apogee ($R_o > 4.5R_E$) during even this moderate storm, although it did not completely capture the magnitude of the observed depression. The relative difference between the intensity of the Earth dipolar field and the self-consistently calculated RAM-SCB magnetic field in the equatorial plane became larger than 60% at $R_o \geq 8R_E$ (Figure 12.2b). The convective growth rate of He^+ band EMIC waves maximized during the storm main phase (0600 UT 1 November) on the duskside at $R_o > 6R_E$, extending to ~9 R_E (Figure 12.2c). These results demonstrated that previous studies limited to regions inside geosynchronous orbit may have underestimated the effect of EMIC wave scattering on the energetic particle populations.

12.4. GLOBAL MODELING OF WHISTLER MODE CHORUS GENERATION

In order to quantify the effect of whistler mode wave scattering on energetic particle dynamics, knowledge of the global wave distribution is needed. Empirical wave

distributions derived from a statistical wave database [e.g., *Meredith et al.*, 2012] for a range of geomagnetic indices are typically used in radiation belt diffusion codes. However, during active times, the geomagnetic indices may reach values much higher than the cutoff used in the empirical models. Strong chorus waves with amplitudes larger than the ones predicted by the empirical model were observed in situ by the EMFISIS instrument on the Van Allen Probes during both dips of the 8 to 9 October 2012 major geomagnetic storm [*Tu et al.*, 2014]. Therefore, event-specific models that provide the global distribution of chorus waves inferred from precipitating electron fluxes (30–100 keV) measured by Polar Orbiting Environmental Satellites (POES) have been developed recently [*Li et al.*, 2013; *Chen et al.*, 2014]. The multiple low-altitude POESs cover a broad range of *L*-shells and MLT with reasonably good spatial and temporal resolution, contrary to the limited in situ data provided by equatorial satellites along their orbits. These new models have been validated by analyzing conjunction events, and it was found that the correlation between measured and inferred chorus wave amplitudes was reasonably high (~0.6 to 0.8). Using these event-specific chorus wave models, the local acceleration of seed electrons to relativistic energies observed during several storms by the Van Allen Probes instruments was well reproduced [*Li et al.*, 2014; *Tu et al.*, 2014].

Another approach adopted in our studies is to numerically compute the generation of whistler mode waves driven by the free energy in the anisotropic ring current electron population. Under the assumption that the waves propagate parallel to the magnetic field in uniform plasma immersed in a strong magnetic field, the rate of wave growth or damping depends mainly on the pitch angle anisotropy and the number of resonating particles. We have thus implemented in RAM [*Jordanova et al.*, 2010a] the computation of the linear growth rate in the equatorial plane with a dispersion relation using the effective anisotropy *A* [*Kennel and Petschek*, 1966]:

$$A(V_R) = \left[\frac{\int_0^\infty v_\perp dv_\perp \left(v_\parallel \frac{\partial Q_l}{\partial v_\perp} - v_\perp \frac{\partial Q_l}{\partial v_\parallel} \right) \frac{v_\perp}{v_\parallel}}{2\int_0^\infty Q_l v_\perp dv_\perp} \right]_{v_\parallel = V_R} \qquad (12.2)$$

Here $v_\perp$ is the electron velocity perpendicular to the ambient magnetic field, while $v_\parallel = V_R$ is the electron parallel velocity obtained from the resonance condition. This algorithm integrates arbitrary distribution functions and removes the need of fitting the particle distributions with bi-Maxwellian functions. These calculations were updated in RAM-SCB to use nondipolar magnetic field, and the model was used to simulate the high-speed stream driven storm of 23 to 26 October 2002 [*Jordanova et al.*, 2012]. It was found that the anisotropy of ring current velocity distributions increased significantly at large distances from Earth on the dayside due to particle transport and drift-shell splitting in the nondipolar magnetic field. As a result, the growth rate of chorus waves increased significantly in a self-consistent magnetic field compared to a dipolar magnetic field.

To investigate further, the theoretical prediction of plasma wave generation on a global scale, we use the updated RAM-SCB driven by the solar wind-dependent W05 electric field to simulate ring current and plasma wave dynamics during the 7 to 9 October 2012 major magnetic storm when Van Allen Probes data are available for comparison. In these simulations, the plasma inflow from the magnetotail is specified after spin-averaged flux measurements from LANL geosynchronous spacecraft; data are excluded when the satellites are in the magnetosheath and interpolated in MLT to fill the gaps. Representative growth rate of lower-band chorus (with frequency 0.45 f_{ce}) calculated at hours 30, 38, and 44, are plotted together with the effective anisotropy *A* as defined in equation (2) in Figures 12.3a and 12.3b, respectively. The corresponding cold plasma density, ratio of plasma frequency (f_{pe}) to cyclotron frequency (f_{ce}), and parallel energy of resonant particles are shown in Figure 12.4. Initially (hour 30), the ring current electron distribution is isotropic at large radial distances and stable to whistler mode wave excitation. Although the distribution is anisotropic at small radial distances, the electron fluxes are considerably reduced due to losses inside the plasmasphere [e.g., *Jordanova et al.*, 2010a] so that there is no significant wave growth prediction at this time. Big anisotropy ($A > 1$) develops with storm progression (hour 38) at $R_o > 4\ R_E$ as the plasma sheet electrons penetrate inside of geosynchronous orbit and drift eastward and, in agreement with previous studies, the maximum growth rate occurs on the dawnside outside of the plasmasphere. The intense chorus growth expands to other MLT as the ring current becomes more symmetric (hour 44). The f_{pe}/f_{ce} ratio ranges from ~2 to ~5 and the resonant electrons have parallel energy from ~4 to ~15 keV. The strong linear growth predicted by these RAM-SCB simulations should be sufficient to excite further nonlinear growth. These results are in agreement with the strong chorus waves (>100 pT wave amplitude) observed in situ by the Van Allen Probes on 8 October 2012 near dawn from ~4 to 6 R_E and with POES observations of 30–100 keV electron precipitation [*Chen et al.*, 2014]. These refined global theoretical predictions of chorus wave generation will be used to calculate the wave-induced scattering effects on radiation belt electrons in future extensions of this work.

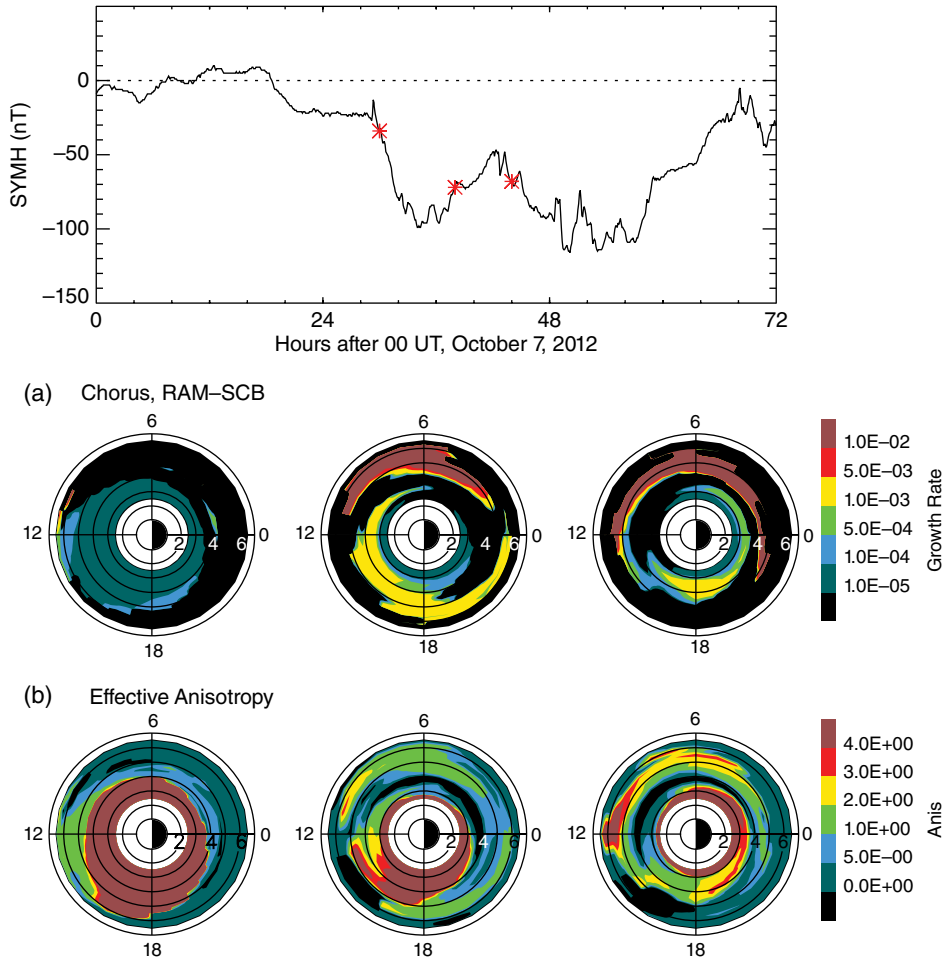

Figure 12.3 (a) Normalized growth rate of whistler mode chorus obtained in the equatorial plane with RAM-SCB at hours 30, 38, and 44 after 00 UT 7 October 2012 indicated with stars on the *SYM-H* plot. (b) Corresponding effective anisotropy of ring current electrons.

12.5. CONCLUSIONS

The Earth's ring current is a very dynamic region that couples the magnetosphere and the ionosphere in several ways: (1) ring current pressure buildup affects the large-scale inner magnetospheric electric and magnetic fields, and (2) anisotropic ring current ion and electron distributions generate diverse wave modes. In return, these processes affect the redistribution of charged particles, making the near-Earth space environment a very complex and highly coupled system. An outstanding question is to determine the temporal evolution and spatial extent of geoeffective plasma waves during storm time. This paper presents a brief summary of recent observations and modeling efforts of the global distributions of two dominant plasma waves, whistler mode chorus and EMIC, that are generated in the inner magnetosphere.

Empirical models for chorus wave distributions have been developed on the basis of satellite observations. They indicate that the wave intensity increases during active times, and chorus waves are mostly observed on the dawnside outside of the plasmasphere. Although these models have improved with the increase of available multi-satellite data, they still have crude temporal and spatial variability due to the statistical averaging and binning of the data. Higher resolution is provided from recently developed event-specific models that infer chorus wave intensities from precipitating electron fluxes observed with multiple POES satellites. The radiation belt electron dynamics were much better reproduced with these event-specific models. Yet another approach under development is the numerical modeling of chorus wave generation from the anisotropic ring current electron distributions. Results from such simulations of chorus wave growth during a large magnetic storm showed good qualitative agreement with the temporal and spatial wave distribution inferred from POES data and with in situ chorus observations from the Van Allen Probes.

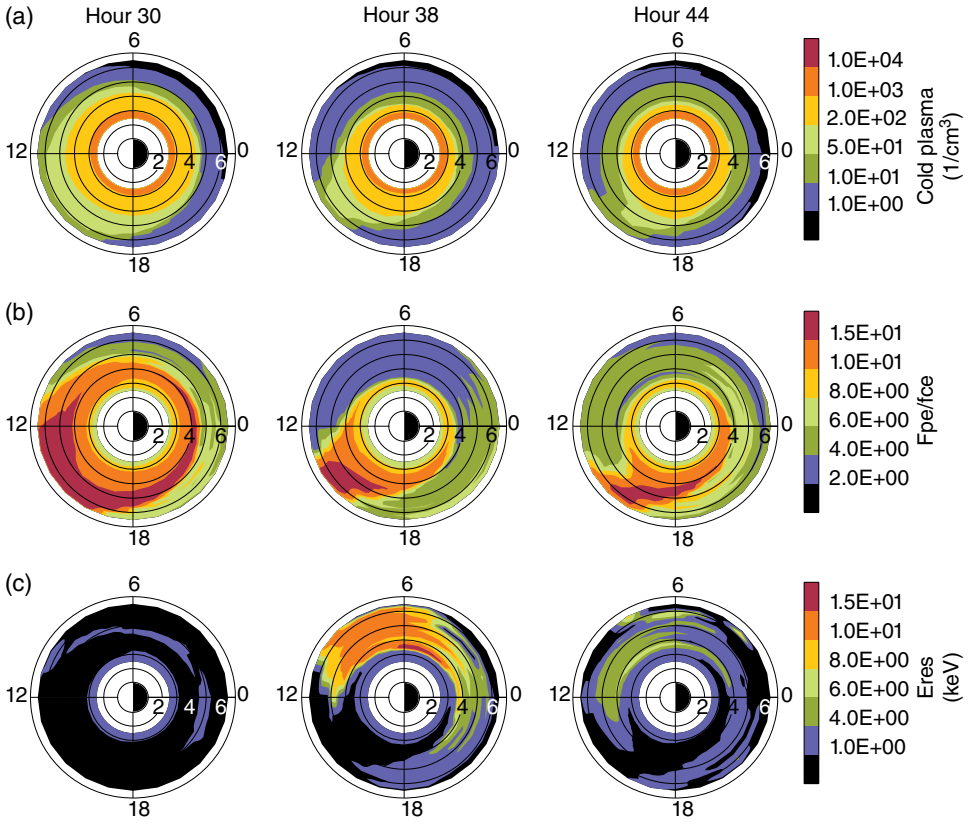

Figure 12.4 (a) Plasmaspheric electron density, (b) normalized frequency, and (c) resonant energy of ring current electrons as a function of radial distance in the equatorial plane and MLT at selected hours after 00 UT 7 October 2012.

The global distribution of EMIC waves is less well known. An empirical model of the global occurrences of these waves was recently developed from CRRES data as a function of geomagnetic activity divided into three levels based on the *AE* index. It was found that EMIC waves are most prevalent during active conditions in the afternoon sector between 4 and 7 R_E. While satellite observations indicate that EMIC waves are confined to narrow regions, ground-based instruments provide measurements over extended intervals and may be used for further model refinement and better estimates of the global EMIC wave occurrence. Numerical models that calculate the generation of EMIC waves based on the anisotropic ring current ion population provide global distributions with much higher temporal and spatial resolution. The localized proton precipitation simulated with these models shows good agreement with IMAGE observations of subauroral proton arcs. Obtaining the wave amplitudes from the theoretical calculation of linear growth rates however is challenging; an improvement of existing numerical models that use semi-empirical relations will be to employ direct correlations between the linear growth and the saturated wave amplitude. Future research is needed in this direction to achieve a full physical coupling between the plasma and the fields necessary for the development of predictive space weather models.

ACKNOWLEDGMENTS

This work was conducted under the auspices of the U. S. Department of Energy through the Los Alamos National Laboratory Directed Research and Development (LDRD) program, with partial support from NASA under NNG13PJ05I and NNH14AX90I and National Science Foundation (NSF) under AGS1203460.

REFERENCES

Albert, J. M. (2003), Evaluation of quasi-linear diffusion coefficients for EMIC waves in a multispecies plasma, *J. Geophys. Res.*, *108*, 1249, doi:10.1029/2002JA009792.

Anderson, B. J., R. E. Erlandson, and L. J. Zanetti (1992), A statistical study of Pc 1–2 magnetic pulsations in the equatorial magnetosphere: 1. Equatorial occurrence distributions, *J. Geophys. Res.*, *97*, 3075–3088.

Bortnik, J., R. M. Thorne, T. P. OBrien, J. C. Green, R. J. Strangeway, Y. Y. Shprits, and D. N. Baker (2006), Observation of two distinct, rapid loss mechanisms during the 20 November 2003 radiation belt dropout event, *J. Geophys. Res.*, *111*, A12216, doi:10.1029/2006JA011802.

Bortnik, J., R. M. Thorne, and N. P. Meredith (2008), The unexpected origin of plasmaspheric hiss from discrete chorus emissions, *Nature*, *452*, 62–66, doi:10.1038/nature06741.

Bräysy, T., K. Mursula, and G. Markland (1998), Ion cyclotron waves during a great geomagnetic storm observed by Freja double-probe electric field instrument, *J. Geophys. Res.*, *103*, 4145–4155.

Bunch, N. L., M. Spasojevic, and Y. Y. Shprits (2012), Off-equatorial chorus occurrence and wave amplitude distributions as observed by the Polar Plasma Wave Instrument, *J. Geophys. Res.*, *117*, A04205, doi:10.1029/2011JA017228.

Burch, J. L. (2001), The fury of space storms, *Sci. American*, *284*, p. 86, doi:10.1038/scientificamerican0401-86.

Burch, J. L., W. S. Lewis, T. J. Immel, P. C. Anderson, H. U. Frey, S. A. Fuselier, J.-C. Gerard, S. B. Mende, D. G. Mitchell, and M. F. Thomsen (2002), Interplanetary magnetic field control of afternoon-sector detached proton auroral arcs, *J. Geophys. Res.*, *107*, 1251, doi:10.1029/2001JA007554.

Chen, L., V. K. Jordanova, M. Spasojevic, R. M. Thorne, and R. B. Horne (2014), Electromagnetic ion cyclotron wave modeling during the geospace environment modeling challenge event, *J. Geophys. Res.*, *119*, 2963–2977, doi:10.1002/2013JA019595.

Chen, M. W., M. Schulz, J. L. Roeder, J. F. Fennell, and L. R. Lyons (1998), Simulations of ring current proton pitch-angle distributions, *J. Geophys. Res.*, *103*, 165.

Chen, Y., G. D. Reeves, R. H. W. Friedel, and G. S. Cunningham (2014), Global time-dependent chorus maps from low-Earth-orbit electron precipitation and Van Allen Probes data, *Geophys. Res. Lett.*, *41*, 755–761, doi:10.1002/2013GL059181.

Clilverd, M. A., C. J. Rodger, R. M. Millan, J. G. Sample, M. Kokorowski, M. P. McCarthy, T. Ulich, T. Raita, A. J. Kavanagh, and E. Spanswick (2007), Energetic particle precipitation into the middle atmosphere triggered by a coronal mass ejection, *J. Geophys. Res.*, *112*, A12206, doi:10.1029/2007JA012395.

Cornwall, J. M., F. V. Coroniti, and R. M. Thorne (1970), Turbulent loss of ring current protons, *J. Geophys. Res.*, *75*, 4699.

Erlandson, R. E., and A. J. Ukhorskiy (2001), Observations of electromagnetic ion cyclotron waves during geomagnetic storms: Wave occurrence and pitch angle scattering, *J. Geophys. Res.*, *106*, 3883–3895, doi:10.1029/2000JA000083.

Fok, M.-C., T. Moore, J. Kozyra, G. Ho, and D. Hamilton (1995), Three-Dimensional Ring Current Decay Model, *J. Geophys. Res.*, *100*, 9619.

Frank, L. A. (1967), On the extraterrestrial ring current during geomagnetic storms, *J. Geophys. Res.*, *72*, 3753.

Fraser, B. J., and T. S. Nguyen (2001), Is the plasmapause a preferred source region of electromagnetic ion cyclotron waves in the magnetosphere? *J. Atmos. Terr. Phys.*, *63*, 1225–1247.

Frey, H. U., G. Haerendel, S. B. Mende, W. T. Forrester, T. J. Immel, and N. Østgaard (2004), Subauroral morning proton spots (SAMPS) as a result of plasmapause-ring-current interaction, *J. Geophys. Res.*, *109*, A10305, doi:10.1029/2004JA010516.

Gary, S. P., and J. Wang (1996), Whistler instability: Electron anisotropy upper bound, *J. Geophys. Res.*, *101*, 10,749–10,754, doi:10.1029/96JA00323.

Gomberoff, L., and R. Neira (1983), Convective growth rate of ion cyclotron waves in a H^+-He^+ and H^+-He^+-O^+ plasma, *J. Geophys. Res.*, *88*, 2170.

Gubby, R., and Evans, J. (2002). Space environment effects and satellite design, *J. Atm. Sol.-Terr. Physics*, *64*, 1723–1733, doi:10.1016/S1364-6826(02)00122-0.

Horne, R. B., and R. M. Thorne (1998), Potential waves for relativistic electron scattering and stochastic acceleration during magnetic storms, *Geophys. Res. Lett*, *25*, 3011.

Horne, R. B., R. M. Thorne, S. A. Glauert, J. M. Albert, N. P. Meredith, and R. R. Anderson (2005), Timescales for radiation belt electron acceleration by whistler mode chorus, *J. Geophys. Res.*, *110*, A03225, doi:10.1029/2004JA010811.

Hubert B., J. C. Gérard, S. A. Fuselier, and S. B. Mende (2003), Observation of dayside subauroral proton flashes with the IMAGE-FUV imagers, *Geophys. Res. Lett.*, *30*, 1145, doi:10.1029/2002GL016464.

Immel T. J., S. B. Mende, H. U. Frey, L. M. Peticolas, C. W. Carlson, J.-C. Gerard, B. Hubert, S. A. Fuselier, and J. L. Burch (2002), Precipitation of auroral protons in detached arcs, *Geophys. Res. Lett.*, *29*, doi:10.1029/2001GL013847.

Jordanova, V. K. (1995), Kinetic model of the terrestrial ring current, Ph. D. thesis, University of Michigan, Ann Arbor, USA, December.

Jordanova, V. K., J. U. Kozyra, and A. F. Nagy (1996), Effects of heavy ions on the quasi-linear diffusion coefficients from resonant interactions with EMIC waves, *J. Geophys. Res.*, *101*, 19771–19778, doi:10.1029/96JA01641.

Jordanova, V. K., J. U. Kozyra, A. F. Nagy, and G. V. Khazanov (1997), Kinetic model of the ring current-atmosphere interactions, *J. Geophys. Res.*, *102*, 14,279–14,292, doi:10.1029/96JA03699.

Jordanova, V. K., C. J. Farrugia, R. M. Thorne, G. V. Khazanov, G. D. Reeves, and M. F. Thomsen (2001), Modeling ring current proton precipitation by electromagnetic ion cyclotron waves during the May 14–16, 1997, storm, *J. Geophys. Res.*, *106*, 7–22, doi:10.1029/2000JA002008.

Jordanova, V. K., Y. S. Miyoshi, S. Zaharia, M. F. Thomsen, G. D. Reeves, D. S. Evans, C. G. Mouikis, and J. F. Fennell (2006), Kinetic simulations of ring current evolution during the Geospace Environment Modeling challenge events, *J. Geophys. Res.*, *111*, A11S10, doi:10.1029/2006JA011644.

Jordanova, V. K., M. Spasojevic, and M. F. Thomsen (2007), Modeling the electromagnetic ion cyclotron wave-induced formation of detached subauroral proton arcs, *J. Geophys. Res.*, *112*, A08209, doi:10.1029/2006JA012215.

Jordanova, V. K., J. Albert, and Y. Miyoshi (2008), Relativistic electron precipitation by EMIC waves from self-consistent global simulations, *J. Geophys. Res.*, *113*, A00A10, doi:10.1029/2008JA013239.

Jordanova, V. K., R. M. Thorne, W. Li, and Y. Miyoshi (2010a), Excitation of whistler mode chorus from global ring current simulations, *J. Geophys. Res.*, *115*, A00F10, doi:10.1029/2009JA014810.

Jordanova, V. K., S. Zaharia, and D. T. Welling (2010b), Comparative study of ring current development using empirical,

dipolar, and self-consistent magnetic field simulations, *J. Geophys. Res.*, *115*, A00J11, doi:10.1029/2010JA015671.

Jordanova, V. K., D. T. Welling, S. G. Zaharia, L. Chen, and R. M. Thorne (2012), Modeling ring current ion and electron dynamics and plasma instabilities during a high-speed stream driven storm, *J. Geophys. Res.*, *117*, A00L08, doi:10.1029/2011JA017433.

Jordanova, V. K., Y. Yu, J. T. Niehof, R. M. Skoug, G. D. Reeves, C. A. Kletzing, J. F. Fennell, and H. E. Spence (2014), Simulations of inner magnetosphere dynamics with an expanded RAM-SCB model and comparisons with Van Allen Probes observations, *Geophys. Res. Lett.*, *41*, 26872694, doi:10.1002/2014GL059533.

Katoh, Y., and Y. Omura (2007), Computer simulation of chorus wave generation in the Earth's inner magnetosphere, *Geophys. Res. Lett.*, *34*, L03102, doi:10.1029/2006GL028594.

Kennel, C. F., and H. Petschek (1966), Limit on stably trapped particle fluxes, *J. Geophys. Res.*, *71*, 128.

Kennel, C. F., and R. M. Thorne (1967), Unstable growth of unducted whistlers propagating at an angle to the geomagnetic field, *J. Geophys. Res.*, *72*, 871.

Kersten, T., R. B. Horne, S. A. Glauert, N. P. Meredith, B. J. Fraser, and R. S. Grew (2014), Electron losses from the radiation belts caused by EMIC waves, *J. Geophys. Res.*, *119*, 88208837, doi:10.1002/2014JA020366.

Khazanov, G. V., K. V. Gamayunov, V. K. Jordanova, and E. N. Krivorutsky (2002), A self-consistent model of interacting ring current ions and electromagnetic ion cyclotron waves, initial results: Waves and precipitating fluxes, *J. Geophys. Res.*, *107*, 1085, doi:10.1029/2001JA000180.

Kozyra, J. U., T. E. Cravens, A. F. Nagy, E. G. Fontheim, and R. S. B. Ong (1984), Effects of energetic ions on electromagnetic ion cyclotron wave generation in the plasmapause region, *J. Geophys. Res.*, *89*, 2217.

Kozyra, J. U., M. W. Liemohn, C. R. Clauer, A. J. Ridley, M. F. Thomsen, J. E. Borovsky, J. L. Roeder, V. K. Jordanova, and W. D. Gonzalez (2002), Multistep Dst development and ring current composition changes during the 4–6 June 1991 magnetic storm, *J. Geophys. Res.*, *107*, 1224, doi:10.1029/2001JA00023.

Li, W., R. M. Thorne, V. Angelopoulos, J. W. Bonnell, J. P. McFadden, C. W. Carlson, O. LeContel, A. Roux, K. H. Glassmeier, and H. U. Auster (2009), Evaluation of whistler-mode chorus intensification on the nightside during an injection event observed on the THEMIS spacecraft, *J. Geophys. Res.*, *114*, A00C14, doi:10.1029/2008JA013554.

Li, W., B. Ni, R. M. Thorne, J. Bortnik, J. C. Green, C. A. Kletzing, W. S. Kurth, and G. B. Hospodarsky (2013), Constructing the global distribution of chorus wave intensity using measurements of electrons by the POES satellites and waves by the Van Allen Probes, *Geophys. Res. Lett.*, *40*, 45264532, doi:10.1002/grl.50920.

Li, W., et al. (2014), Radiation belt electron acceleration by chorus waves during the 17 March 2013 storm, *J. Geophys. Res.*, *119*, 46814693, doi:10.1002/2014JA019945.

Liemohn, M., J. Kozyra, V. Jordanova, G. Khazanov, M. Thomsen, and T. Cayton (1999), Analysis of Early Phase Ring Current Recovery Mechanisms during Geomagnetic Storms, *Geophys. Res. Lett.*, *26*, 2845–2848.

Lorentzen, K. R., J. B. Blake, U. S. Inan, and J. Bortnik (2001), Observations of relativistic electron microbursts in association with VLF chorus, *J. Geophys. Res.*, *106*, 6017–6027, doi:10.1029/2000JA003018.

Loto'aniu, T. M., B. J. Fraser, and C. L. Waters (2005), Propagation of electromagnetic ion cyclotron wave energy in the magnetosphere, *J. Geophys. Res.*, *110*, A07214, doi:10.1029/2004JA010816.

Lyons, L. R., and R. M. Thorne (1973), Equilibrium structure of radiation belt electrons, *J. Geophys. Res.*, *78*, 2142–2149.

Mann, I. R., M. E. Usanova, K. Murphy, M. T. Robertson, D. K. Milling, A. Kale, C. Kletzing, J. Wygant, S. Thaller, and T. Raita (2014), Spatial localization and ducting of EMIC waves: Van Allen Probes and ground-based observations, *Geophys. Res. Lett.*, *41*, 785–792, doi:10.1002/2013GL058581.

Maynard, N. C., and A. J. Chen (1975), Isolated cold plasma regions: Observations and their relation to possible production mechanisms, *J. Geophys. Res.*, *80*, 1009.

Meredith, N. P., R. B. Horne, S. A. Glauert, R. M. Thorne, D. Summers, J. M. Albert, and R. R. Anderson (2006), Energetic outer zone electron loss timescales during low geomagnetic activity, *J. Geophys. Res.*, *111*, A05212, doi:10.1029/2005JA011516.

Meredith N.P., R. B. Horne, S. A. Glauert, D. N. Baker, S. G. Kanekal, and J. M. Albert (2009), Relativistic electron loss timescales in the slot region, *J. Geophys. Res.*, *114*, A03222, doi:10.1029/2008JA013889.

Meredith, N. P., R. B. Horne, A. Sicard-Piet, D. Boscher, K. H. Yearby, W. Li, and R. M. Thorne (2012), Global model of lower band and upper band chorus from multiple satellite observations, *J. Geophys. Res.*, *117*, A10225, doi:10.1029/2012JA017978.

Meredith, N. P., R. B. Horne, J. Bortnik, R. M. Thorne, L. Chen, W. Li, and A. Sicard-Piet (2013), Global statistical evidence for chorus as the embryonic source of plasmaspheric hiss, *Geophys. Res. Lett.*, *40*, 2891–2896, doi:10.1002/grl.50593.

Meredith, N. P., R. B. Horne, T. Kersten, B. J. Fraser, and R. S. Grew (2014), Global morphology and spectral properties of EMIC waves derived from CRRES observations, *J. Geophys. Res.*, *119*, 5328–5342, doi:10.1002/2014JA020064.

Millan, R. M., R. P. Lin, D. M. Smith, and M. P. McCarthy (2007), Observation of relativistic electron precipitation during a rapid decrease of trapped relativistic electron flux, *Geophys. Res. Lett.*, *34*, L10101, doi:10.1029/2006GL028653.

Miyoshi, Y., A. Morioka, T. Obara, H. Misawa, T. Nagai, and Y. Kasahara (2003), Rebuilding process of the outer radiation belt during the 3 November 1993 magnetic storm: NOAA and Exos-D observations, *J. Geophys. Res.*, *108*, 1004, doi:10.1029/2001JA007542.

Mouikis, C. G., L. M. Kistler, Y. H. Liu, B. Klecker, A. Korth, and I. Dandouras (2010), H+ and O+ content of the plasma sheet at 15–19 Re as a function of geomagnetic and solar activity, *J. Geophys. Res.*, *115*, A00J16, doi:10.1029/2010JA015978.

Mursula, K. (2007), Satellite observations of Pc1 pearl waves: The changing paradigm, *J. Atmos. Sol. Terr. Phys.*, *69*, 1623–1634, doi:10.1016/j.jastp.2007.02.013.

Nunn, D., Y. Omura, H. Matsumoto, I. Nagano, and S. Yagitani (1997), The numerical simulation of VLF chorus and discrete

emissions observed on the Geotail satellite using a Vlasov code, *J. Geophys. Res.*, *102*, 27,083–27,098, doi:10.1029/97JA02518.

Omura, Y., Y. Katoh, and D. Summers (2008), Theory and simulation of the generation of whistler-mode chorus, *J. Geophys. Res.*, *113*, A04223, doi:10.1029/2007JA012622

Rasmussen, C. E., S. M. Guiter, and S. G. Thomas (1993), Two-dimensional model of the plasmasphere: Refilling time constants, *Planet. Space Sci.*, *41*, 35.

Reeves, G. D., et al. (2013), Electron acceleration in the heart of the Van Allen radiation belts, *Science*, *341*, 991, doi: 10.1126/science.1237743.

Ridley, A. J., T. I. Gombosi, and D. L. De Zeeuw (2004), Ionospheric control of the magnetosphere: Conductance, *Ann. Geophys.*, *22*, 567.

Santolik O., D. A. Gurnett, J. S. Pickett, M. Parrot, and N. Cornilleau-Wehrlin (2003), Spatio-temporal structure of storm-time chorus, *J. Geophys. Res.*, *108*, 1278, doi:10.1029/2002JA009791.

Spasojevic, M., H. U. Frey, M. F. Thomsen, S. A. Fuselier, S. P. Gary, B. R. Sandel, and U. S. Inan (2004), The link between a detached subauroral proton arc and a plasmaspheric plume, *Geophys. Res. Lett.*, *31*, L04803, doi:10.1029/2003GL018389.

Summers, D., R. M. Thorne, and F. Xiao (1998), Relativistic theory of wave-particle resonant diffusion with application to electron acceleration in the magnetosphere, *J. Geophys. Res.*, *103*, 20487.

Summers, D., B. Ni, and N. P. Meredith (2007), Timescales for radiation belt electron acceleration and loss due to resonant wave-particle interactions: 2. Evaluation for VLF chorus, ELF hiss, and electromagnetic ion cyclotron waves, *J. Geophys. Res.*, *112*, A04207, doi:10.1029/2006JA011993.

Stern, D. P. (1975), The motion of a proton in the equatorial magnetosphere, *J. Geophys. Res.*, *80*, 595.

Thorne, R. M. (1974), A possible cause of dayside relativistic electron precipitation events, *J. Atmos. Terr. Phys.*, *36*, 635–645.

Thorne, R. M., et al. (2013), Rapid local acceleration of relativistic radiation-belt electrons by magnetospheric chorus, *Nature*, *504*, 411, doi:10.1038/nature12889.

Téth, G., et al. (2005), Space Weather Modeling Framework: A new tool for the space science community, *J. Geophys. Res.*, *110*, A12226, doi: 10.1029/2005JA011126.

Tsurutani, B., and E. Smith (1974), Postmidnight Chorus: A Substorm Phenomenon, *J. Geophys. Res.*, *79*, 118–127.

Tsyganenko, N. A., and T. Mukai (2003), Tail plasma sheet models derived from geotail particle data, *J. Geophys. Res.*, *108*, 1136, doi:10.1029/2002JA009707.

Tu, W., G. S. Cunningham, Y. Chen, S. K. Morley, G. D. Reeves, J. B. Blake, D. N. Baker, and H. Spence (2014), Event-specific chorus wave and electron seed population models in DREAM3D using the Van Allen Probes, *Geophys. Res. Lett.*, *41*, 1359–1366, doi:10.1002/2013GL058819.

Usanova, M. E., I. R. Mann, J. Bortnik, L. Shao, and V. Angelopoulos (2012), THEMIS observations of electromagnetic ion cyclotron wave occurrence: Dependence on AE, SYM-H, and solar wind dynamic pressure, *J. Geophys. Res.*, *117*, A10218, doi:10.1029/2012JA018049.

Usanova, M. E., et al. (2014), Effect of EMIC waves on relativistic and ultrarelativistic electron populations: Ground-based and Van Allen probes observations, *Geophys. Res. Lett.*, *41*, 13751381, doi:10.1002/2013GL059024.

Van Allen, J. A., G. H. Ludwig, E. C. Ray, and C. E. McIlwain (1958), Observation of high intensity radiation by satellites 1958 Alpha and Gamma, *Jet Propulsion*, *28*, 9, pp. 588, doi: 10.2514/8.7396.

Volland, H. (1973), A semiempirical model of large-scale magnetospheric electric fields, *J. Geophys. Res.*, *78*, 171.

Weimer, D. R. (2005), Improved ionospheric electrodynamic models and application to calculating Joule heating rates, *J. Geophys. Res.*, *110*, A05306, doi:10.1029/2004JA010884.

Welling, D. T., V. K. Jordanova, S. G. Zaharia, A. Glocer, and G. Tóth (2011), The effects of dynamic ionospheric outflow on the ring current, *J. Geophys. Res.*, *116*, A00J19, doi:10.1029/2010JA015642.

Yahnin, A. G., and T. A. Yahnina (2007), Energetic proton precipitation related to ion-cyclotron waves, *J. Atmos. Sol. Terr. Phys.*, *69*, 1690–1706.

Yahnin, A. G., T. A. Yahnina, and H. U. Frey (2007), Subauroral proton spots visualize the Pc1 source, *J. Geophys. Res.*, *112*, A10223, doi:10.1029/2007JA012501.

Yahnina, T. A., H. U. Frey, T. Bsinger, and A. G. Yahnin (2008), Evidence for subauroral proton flashes on the dayside as the result of the ion cyclotron interaction, *J. Geophys. Res.*, *113*, A07209, doi:10.1029/2008JA013099.

Young, D. T., H. Balsiger, and J. Geiss (1982), Correlations of magnetospheric ion composition with geomagnetic and solar activity, *J. Geophys. Res.*, *87*, 9077.

Yu, Y., V. Jordanova, D. Welling, B. Larsen, S. G. Claudepierre, and C. Kletzing (2014), The role of ring current particle injections: Global simulations and Van Allen Probes observations during 17 March 2013 storm, *Geophys. Res. Lett.*, *41*, 1126–1132, doi:10.1002/2014GL059322.

Zaharia, S., V. K. Jordanova, M. F. Thomsen, and G. D. Reeves (2006), Self-consistent modeling of magnetic fields and plasmas in the inner magnetosphere: Application to a geomagnetic storm, *J. Geophys. Res.*, *111*, A11S14, doi:10.1029/2006JA011619.

Zaharia, S., V. K. Jordanova, D. Welling, and G. Tóth (2010), Self-consistent inner magnetosphere simulation driven by a global MHD model, *J. Geophys. Res.*, *115*, A12228, doi:10.1029/2010JA015915.

Part IV
Unified Global Modeling of Ionosphere and Magnetosphere at Earth

13

Modeling Magnetosphere-Ionosphere Coupling via Ion Outflow: Past, Present, and Future

R. W. Schunk

Video of Yosemite Talk, URL: http://dx.doi.org/10.15142/T3C88J

ABSTRACT

Ion outflow from the Earth's ionosphere was first proposed in the mid 1960s. Since then, a myriad of measurements and numerical simulations have clearly established that ion outflow (O^+, H^+) is an important ionosphere-magnetosphere coupling mechanism. The heavy O^+ ions have been observed in several regions of the magnetosphere, including the plasma sheet, lobe, and distant tail, and they have been shown to significantly affect magnetospheric processes. To fully understand the effect of ion outflow on the magnetosphere, it is important to establish the conditions under which the outflow is possible, the spatial distribution of the outflow, and the energy distribution of the escaping ions. These issues have been extensively studied during the last four decades, and the results appear in an extensive literature. Here, the focus is on the modeling associated with plasma outflow from the Earth's ionosphere. The paper is based on a Yosemite 2014 presentation and covers past (Classical Polar Wind), present (Generalized Polar Wind), and future (anticipated) ion outflow modeling efforts.

13.1. INTRODUCTION

Significant progress has been made during the last 40 years in identifying the processes that couple the magnetosphere and ionosphere. The progress was achieved with the aid of new measurement techniques, enhanced data coverage, sophisticated global models, and extensive model-data comparisons. It is now clear that the magnetosphere-ionosphere system exhibits a significant amount of spatial structure and rapid temporal variations. This variability is associated with magnetic storms and substorms, nonlinear processes that operate over a range of spatial scales, time delays, and feedback mechanisms between the two domains. The variability and resultant structure of the ionosphere can appear in the form of propagating plasma patches, polar wind jets, pulsing of the ion and neutral polar winds, auroral and boundary blobs, and ionization channels associated with sun-aligned polar cap arcs, discrete auroral arcs, and storm-enhanced densities (SED). The variability and structure of the thermosphere can appear in the form of propagating atmospheric holes, neutral gas fountains, neutral density patches, transient neutral jets, and supersonic winds.

Significant advances have been made during the last 40 years in modeling the variability and structure associated with magnetosphere-ionosphere coupling [*Schunk and Nagy,* 2009 and references therein]. However, this brief article focuses on the modeling associated with plasma outflow from the Earth's ionosphere. The other topics are covered in the additional articles included in this monograph and important review articles on ion

Center for Atmospheric and Space Sciences, Utah State University, Logan, UT, USA

Magnetosphere-Ionosphere Coupling in the Solar System, Geophysical Monograph 222, First Edition.
Edited by Charles R. Chappell, Robert W. Schunk, Peter M. Banks, James L. Burch, and Richard M. Thorne.

outflow measurements are provided by *Peterson et al.* [2006, 2008] and *Yau et al.* [2007].

13.2. CLASSICAL POLAR WIND

The existence of the magnetosphere was deduced in the early 1960s [*Axford and Hines,* 1961; *Dungey,* 1961]. Shortly after this deduction, it was suggested that there should be a continuous outflow of plasma (H^+ and He^+) along polar cap field lines because they extend deep into space (Figure 13.1). The early models used to support this suggestion were based on a thermal evaporation process [*Dessler and Michel*, 1966; *Bauer*, 1966]. However, it was later argued that the ionospheric plasma outflow should be supersonic like the solar wind, and it was called the 'polar wind' [*Axford*, 1968]. Subsequently, a simple one-dimensional hydrodynamic formulation was used that emphasized the supersonic character of the plasma outflow and the basic features of the classical polar wind were elucidated [*Banks and Holzer*, 1968, 1969]. For these classical polar wind simulations, it was assumed that the outflow was driven by the pressure gradient between the ionosphere and deep space.

The early polar wind modeling involved one-dimensional steady-state daytime simulations for fixed locations. A sample from this type of hydrodynamic simulation is given in Figure 13.2 [*Raitt et al.*, 1975]. The simulation is based on a solution of the H^+ and O^+ continuity, momentum, and energy equations assuming that O^+ is gravitationally bound. The different sets of H^+ density and drift velocity profiles shown in the figure correspond to different assumed H^+ escape velocities at the upper boundary of 3000 kilometers (km). The light H^+ ions are produced by the resonant charge exchange reaction $O^+ + H \Leftrightarrow O + H^+$ and then the H^+ ions drift to higher altitudes. As the H^+ escape, velocity at 3000 km is increased, the upward H^+ velocity increases, and the H^+ density decreases at altitudes above 600–700 km. Curve (a) is basically a diffusive equilibrium profile; curves (b–e) correspond to subsonic outflow, curve (f) is transonic flow; and curves (g–h) correspond to supersonic outflow. Simulations like this have shown that the H^+ escape 'flux' increases to a saturation limit as the H^+ escape velocity at the upper boundary increases.

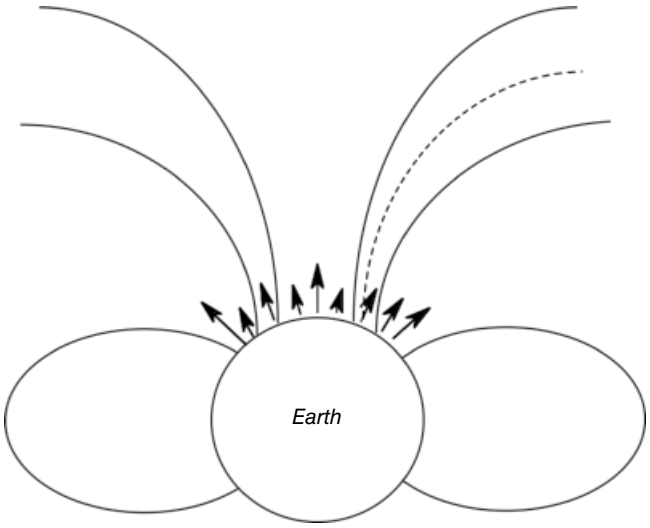

Figure 13.1 Schematic diagram that shows the outflow of thermal plasma (polar wind) from the topside ionosphere along geomagnetic field lines in the northern hemisphere. A similar plasma up-flow also occurs on closed plasmaspheric field lines during refilling after geomagnetic storms, but this topic is covered in other chapters of the monograph.

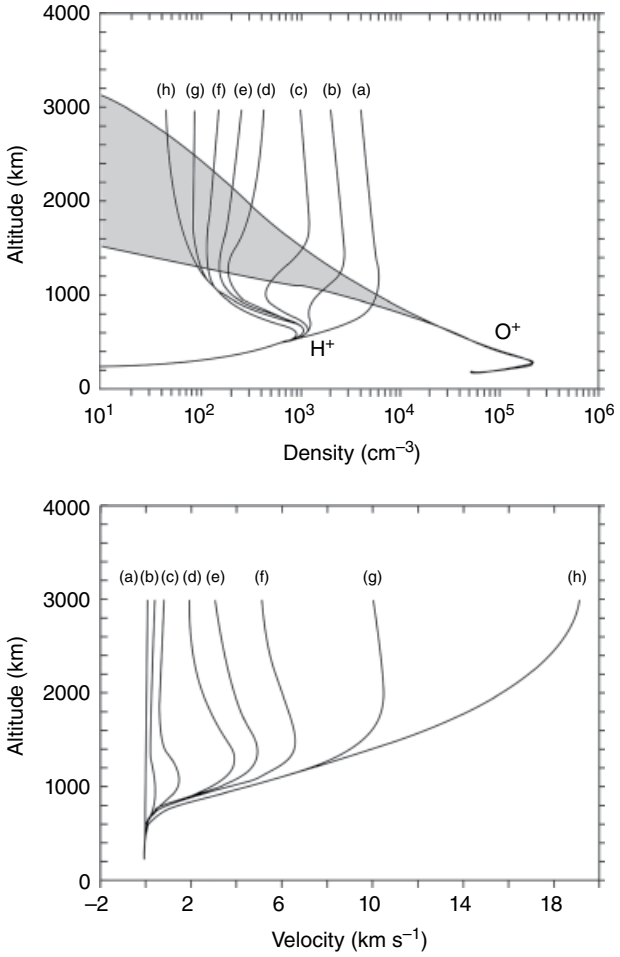

Figure 13.2 Calculated H^+ density (top) and field-aligned outflow velocity (bottom) profiles for the daytime terrestrial ionosphere at high latitudes. The different profiles correspond to different assumed H^+ outflow velocities at 3000 km; (a) 0.06, (b) 0.34, (c) 0.75, (d) 2.0, (e) 3.0, (f) 5.0, (g) 10.0, and (h) 20 km s^{-1}. The range of O^+ density profiles is shown by the shaded region, with the upper O^+ curve associated with high H^+ outflow and vice versa [*Raitt et al.*, 1975].

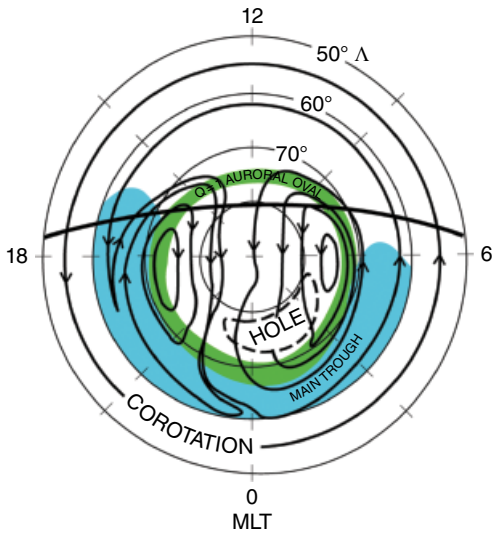

Figure 13.3 Schematic diagram showing the various processes and features that occur in the Earth's high-latitude region in a magnetic local time (MLT), invariant latitude reference frame. The solid lines with arrows are the plasma convection trajectories at 300 km, and the curved solid line is the terminator location. The features shown are the quiet-time auroral oval, the polar ionization hole, and the main electron density trough [*Brinton et al.*, 1978].

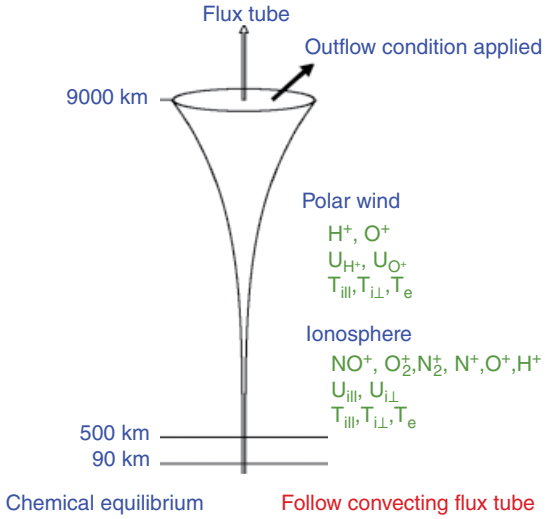

Figure 13.4 Schematic diagram showing a flux tube of plasma [*Schunk and Sojka*, 1997].

In addition to the steady-state hydrodynamic solutions discussed above, some one-dimensional time-dependent polar wind solutions were obtained for a 'fixed' location, with the time variations driven by imposed energy inputs. However, the plasma at high latitudes is continually drifting across the polar region (Figure 13.3). For a southward Interplanetary Magnetic Field (IMF), the plasma drifts in an anti-sunward direction across the polar cap, and then there is a return flow equatorward of the auroral oval. Hence, the plasma continually moves into and out of sunlight, the polar cap, nocturnal oval, and main electron density trough.

In order to take account of this motion, *Schunk and Sojka* [1989, 1997] constructed a global ionosphere-polar wind model. The model extends from 90 to 9000 km for latitudes greater than 50° magnetic. In the E and F regions, the model calculated time-dependent three-dimensional distributions for the electron and ion (NO^+, O_2^+, N_2^+, N^+, O^+) densities, field-aligned drift velocities, and temperatures from diffusion and heat conduction equations. In the topside ionosphere, the time-dependent, nonlinear, hydrodynamic equations for H^+ and O^+ are solved self-consistently with the lower ionosphere equations. The transport equations are solved as a function of altitude for convecting plasma flux tubes (Figure 13.4). The three-dimensional nature of the model is obtained by following numerous plasma flux tubes. This global ionosphere-polar wind model takes account of ion-neutral frictional heating, particle hearing, anisotropic ion temperatures, the magnetic mirror force, supersonic ion outflow, shock formation, ion energy increase during plasma expansions, as well as a myriad of E and F region processes.

The initial global ionosphere-polar wind simulations were conducted for an idealized geomagnetic storm. In these simulations, empirical models were used for the plasma convection [*Heppner and Maynard*, 1987] and particle precipitation [*Hardy et al.*, 1985] patterns. The empirical models were varied in time to mimic a Kp = 6 geomagnetic storm. The idealized storm contained growth, main, and decay phases. During increasing magnetic activity, the particle precipitation and plasma convection patterns expanded, the particle precipitation became more intense, and the convection speeds increased. The reverse occurred during declining magnetic activity. First, a diurnally reproducible, global, ionosphere- polar wind system was simulated for quiet conditions (Kp = 1). Then, from 4–5 Universal Time (UT) there was an exponential increase in magnetic activity (growth phase), from 5–6 UT the magnetic activity was held constant (main phase), from 6–10 UT there was an exponential decrease in magnetic activity back to quiet conditions (decay phase), and then the global simulation was continued for several more hours. Note that the particle precipitation and plasma convection patterns varied continuously and smoothly during this idealized storm.

The idealized storm was used in four geophysical cases (winter and summer solstices for solar maximum and minimum). For each case, the simulation with the best spatial resolution contained 1000 convecting plasma flux

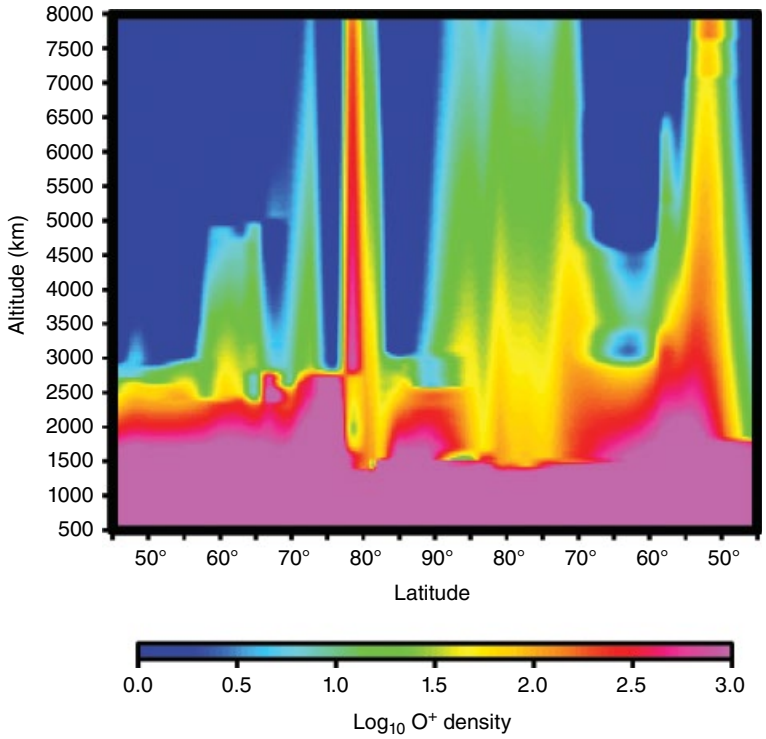

Figure 13.5 Snapshot of the O^+ density distribution versus altitude and latitude across the polar cap from noon to midnight. The snapshot is at the end of the idealized storm's main phase (0600 UT), and the conditions are winter and solar maximum. Densities greater than 10^3 cm^{-3} are colored pink, and densities less than 1 cm^{-3} are dark blue [*Schunk and Sojka*, 1997; *Schunk*, 1999].

tubes, which provided a 130–200 km horizontal spatial resolution in the polar cap. Figures 13.5 and 13.6 show, respectively, snapshots of the O^+ and H^+ density distributions versus altitude and latitude across the polar cap at the end of the storm's main phase (6 UT) for the winter, solar maximum case. The most striking feature in the O^+ and H^+ density distributions is the spatial structure, both with latitude and altitude. Note the 'bite-out' in the H^+ density at altitudes from 1400–2000 km on the night side at latitudes between 80°–65°.

The main results obtained from the *Schunk and Sojka* [1989, 1997] global ionosphere-polar wind 'storm' simulations follow:

- The polar wind outflow is similar to a campfire with flickering flames.
- O^+ becomes the dominant ion to altitudes as high as 9000 km in the polar region.
- H^+ 'bite-outs' with altitude can occur throughout the storm.
- H^+ 'blowouts' can occur throughout the polar region after the storm commencement.
- The polar wind exhibits a day-night asymmetry (solar zenith effect) due to T_e.
- Propagating and stationary polar wind jets typically occur.
- The temporal variation of the polar wind at high and low altitudes can be opposite.
- Ion counter-streaming vertical flows can occur in the polar cap.

13.3. GENERALIZED POLAR WIND

Shortly after the early hydrodynamic polar wind studies, the research focus shifted to non-classical polar wind outflow mechanisms [*Banerjee and Gavrishchaka*, 2007; *Barakat et al.*, 2003; *Gombosi and Nagy*, 1989; *Horwitz et al.*, 1994; *Khazanov et al.*, 2012; *Lemaire, et al.*, 2007; *Schunk*, 2007; *Schunk and Nagy*, 2009; *Tam et al.*, 2007; and the extensive reference lists given in these papers]. Figure 13.7 is a schematic diagram that shows the various non-classical processes that have been found to affect ion outflow (Generalized Polar Wind [GPW]). On the dayside, elevated electron temperatures and escaping photoelectrons are important energy sources for escaping ions. In the cusp and aurora, unstable field-aligned currents can excite waves over a range of altitudes that can then accelerate ions both parallel and perpendicular to **B**. The resulting ion beams and conics have sufficient energy to escape the ionosphere. The convection of the ion beams and conics into the polar cap can then lead to unstable

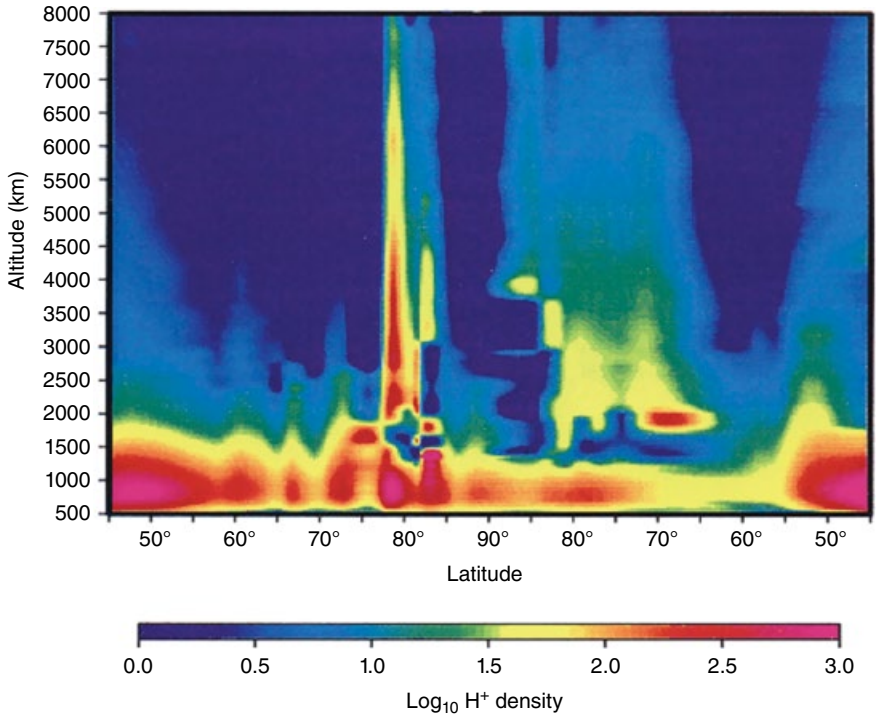

Figure 13.6 Snapshot of the H^+ density distribution versus altitude and latitude across the polar cap from noon to midnight. The snapshot is at the end of the idealized storm's main phase (0600 UT), and the conditions are winter and solar maximum. Densities greater than 10^3 cm^{-3} are colored pink, and densities less than 1 cm^{-3} are dark blue [*Schunk and Sojka*, 1997; *Schunk*, 1999].

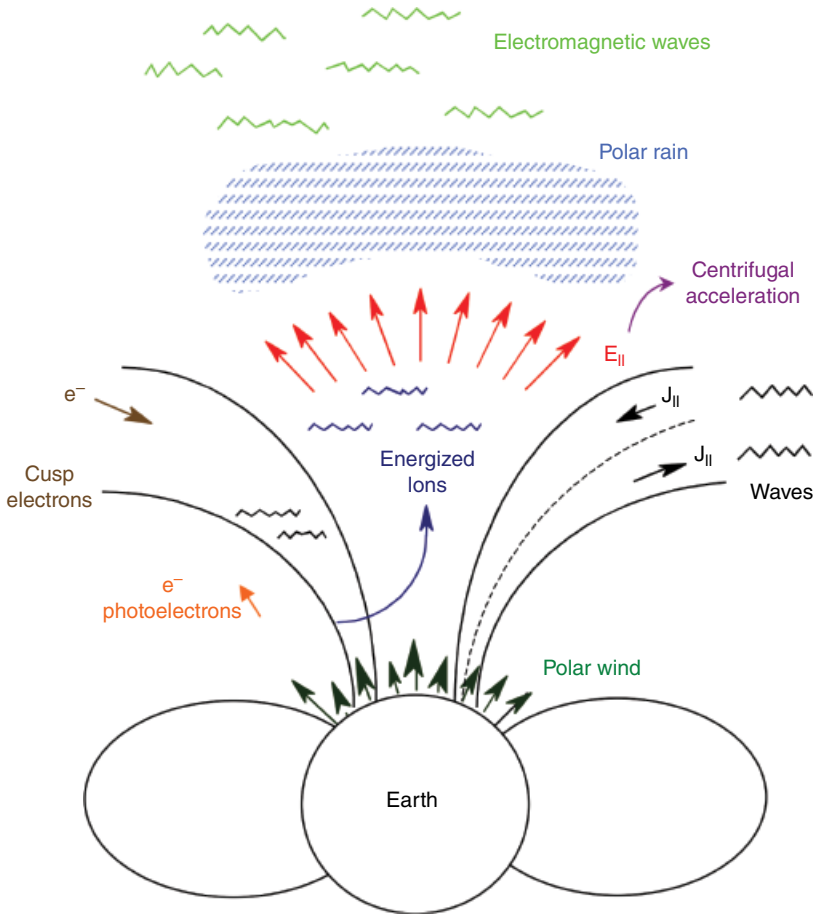

Figure 13.7 Schematic diagram showing the non-classical processes that affect ion outflow from the high-latitude ionosphere [*Schunk and Sojka*, 1997].

plasma conditions as they pass through the slower moving background polar wind. Also, the interaction of the cold polar wind electrons with the hot polar rain electrons can result in field-aligned double-layer electric fields in the polar cap (~4000 km), which can energize the escaping ions. At higher polar cap altitudes (~6000 km), electromagnetic wave turbulence can significantly affect the ion outflow through the perpendicular wave heating that is associated with Wave-Particle Interactions (WPI). In addition, centrifugal acceleration acts to increase ion outflow velocities as the plasma flux tubes convect across the polar cap.

13.3.1. Global GPW Simulations

At first, the various non-classical ion outflow processes were modeled separately using Particle In Cell (PIC) or kinetic formulations. The simulations were either for a fixed location with time-varying energy inputs or for a single convecting plasma flux tube. Subsequently, *Barakat and Schunk* [2006] constructed a 'global' GPW model. The GPW model is a fluid-PIC hybrid model, with a standard ionosphere model at low altitudes (90–1200 km) and PIC ions/fluid electrons at high altitudes (1200 km to several Earth radii). The solutions are obtained as a function of altitude for convecting plasma flux tubes, taking into account both classical and non-classical processes. Typically, 1000 convecting plasma flux tubes are followed as they drift across the high-latitude region, and each flux tube contains 1 million ions, so a global simulation contains 1 billion particles.

The global GPW model includes H^+ and O^+ ions, classical polar wind processes, self collisions and H^+-O^+ collisions, centrifugal acceleration, body forces (electrostatic, gravity, magnetic mirror), wave-particle interactions, low-altitude auroral energy sources, cold ionosphere and hot magnetosphere electrons, photoelectrons, plasma instabilities, etc. The global GPW model not only calculates ion and electron densities, drift velocities, and temperatures but ion velocity distributions as well.

The first set of global GPW simulations that were conducted corresponds to reruns of the idealized geomagnetic storm for the four geophysical cases (summer and winter at solar maximum and minimum) discussed in Section 13.2. Figure 13.8 shows snapshots of the O^+/H^+ density ratio just before the commencement of the idealized storm (4 UT; left panel) and in the middle of the storm's main phase (5.5 UT; right panel), and at altitudes of 1500, 2500, and 18,000 km. The important results obtained from the set of global GPW simulations follow:

1. During geomagnetic storms, there are large upward O^+ fluxes throughout the polar region, and O^+ becomes the dominant ion at basically all altitudes.

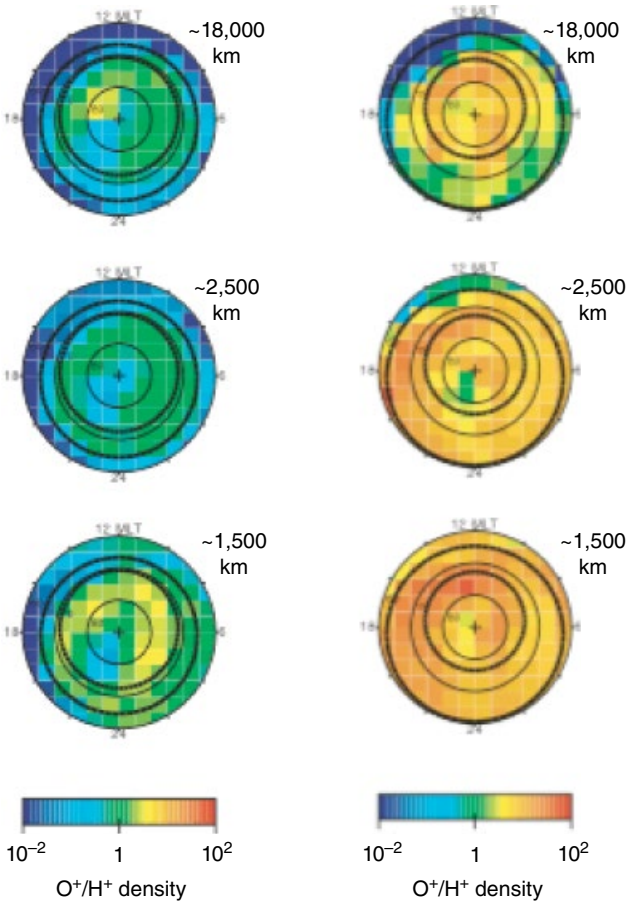

Figure 13.8 Snapshots of the O^+/H^+ density ratio just before the commencement of the idealized storm (4 UT; left panel) and in the middle of the storm's main phase (5.5 UT; right panel), and at altitudes of 1500, 2500, and 18,000 km. The coordinates of the dial plots are MLT and magnetic latitude (greater than 60°) in the northern hemisphere. The thick black lines show the boundaries of the auroral oval. [from *Barakat and Schunk*, 2006]

2. The non-classical processes supply sufficient energy to the O^+ ions so that they continue to flow upward and eventually they escape into the magnetosphere. This is in contrast to the results from the hydrodynamic polar wind simulations, where during the storm the O^+ ions flow upward and become the dominant ion at high altitudes, but then flow downward and return to the ionosphere when the storm subsides. The classical polar wind ions (O^+) have insufficient energy to escape.

3. Basically, all of the O^+ ions that reach 4000–5000 km acquire sufficient energy from non-classical processes to escape the ionosphere.

4. The escaping ionospheric ions have non-Maxwellian velocity distributions, with the shape and severity depending on location, altitude, and storm phase. The non-Maxwellian ion velocity distributions that are obtained

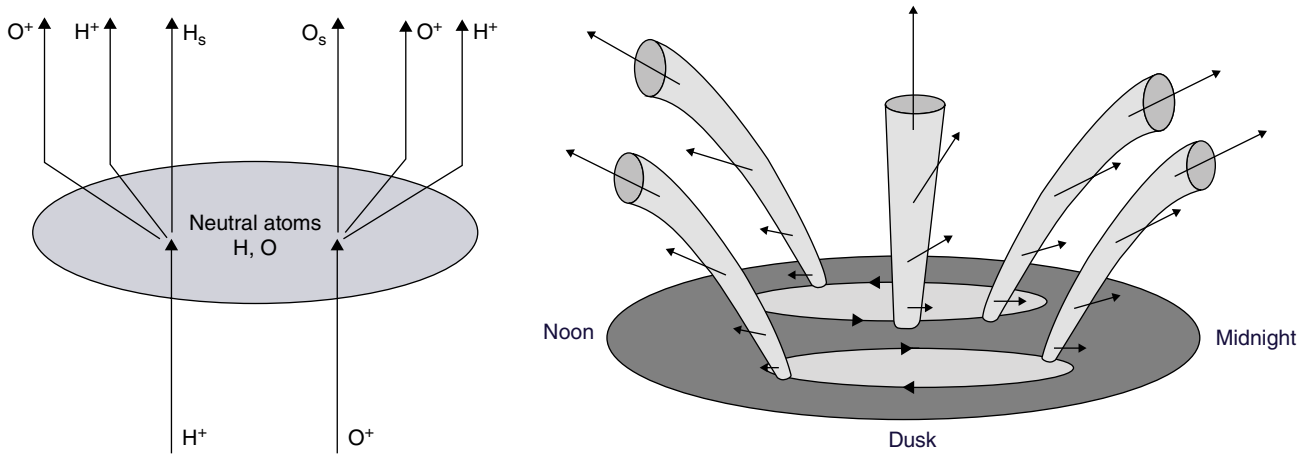

Figure 13.9 Diagram showing the production of neutral particles as the polar wind ions traverse the neutral upper atmosphere (left) and the three-dimentional nature of the neutral polar wind, with super-thermal neutral moving in all directions (right). [from *Gardner and Schunk*, 2004]

in the global storm simulations include beam, pancake, conic, torus, bi-Maxwellian, double-peaked, counter-streaming, and asymmetric with elongated tails along B distributions.

13.3.2. Neutral Polar Wind

The National Aeronautics and Space Administration (NASA) Imager for Magnetopause-to-Aurora Global Explorer (IMAGE) spacecraft measured large escape fluxes (~$1-4 \times 10^9$ cm^{-2} s^{-1}) of neutral atoms from the high-latitude ionosphere [*Wilson et al.*, 2003, 2005], and this was in conflict with previous simulations that predicted small neutral particle escape fluxes [*Tinsley et al.*, 1986; *Hodges*, 1994]. However, the real surprise was that the measurements indicated the neutrals appeared to be coming from all directions, and at that time, this was a perplexing result. On the other hand, more recent global ionosphere-polar wind simulations had indicated that the H^+ and O^+ escape fluxes increase markedly during geomagnetic storms, and that they are time-dependent and spatially non-uniform. This implied that during geomagnetic storms and substorms, substantial fluxes of super-thermal neutral particles (H and O) could be created via charge exchange between polar wind ions and the neutrals in the upper atmosphere. Subsequent simulations by *Gardner and Schunk* [2004, 2005] that modeled both the ions and charge exchange neutrals were able to explain the surprising neutral particle measurements and established the existence of a Neutral Polar Wind.

The escaping H^+ and O^+ ions in the polar wind execute three characteristic motions. They spiral about the geomagnetic field, flow up and out of the topside ionosphere, and drift horizontally across the polar region in response to magnetosphere electric fields, moving into and out of sunlight, the cusp, polar cap, nocturnal auroral oval, and main electron density trough. During this motion, the ions can undergo charge exchange reactions with the neutral upper atmosphere, which is composed of thermal neutrals and hot geo-coronal neutrals (Figure 13.9). Specifically, the up-flowing O^+ and H^+ ions can have charge exchange reactions with both the H and O atmospheric neutrals, and this would yield up-flowing super-thermal O and H atoms. These reactions would also produce non-flowing H^+ and O^+ ions, which would then be accelerated upward by the field-aligned ambipolar electric field in the polar wind. The initial velocities of the neutral particles created by charge exchange in the polar wind are equal to the velocities of the H^+ or O^+ parent ions just before the charge exchange reactions. Therefore, at high altitudes, neutral streams of H and O are created that predominantly flow in the vertical direction (the neutral polar wind), while at low altitudes the neutrals tend to 'move in all directions' as a result of ion gyration, ion up-flow, and plasma convection [*Gardner and Schunk*, 2004, 2005].

13.4. FUTURE DEVELOPMENTS

It is now well known that O^+ outflow has a significant effect on the magnetosphere, and O^+ has been observed in several regions of the magnetosphere, including the plasma sheet, lobe, and distant tail. Consequently, there have been several developments aimed at incorporating multiple ion species in global magnetohydrodynamic (MHD) models of the magnetosphere [e.g., *Brambles et al.*, 2011; *Garcia and Merkin*, 2010; *Glocer et al.*, 2009; *Wiltberger et al.*, 2010; *Winglee et al.*, 2002]. From these and other studies, it appears that O^+ can reduce the cross-tail potential, affect dayside reconnection, induce substorms, and modify the plasma sheet. To date,

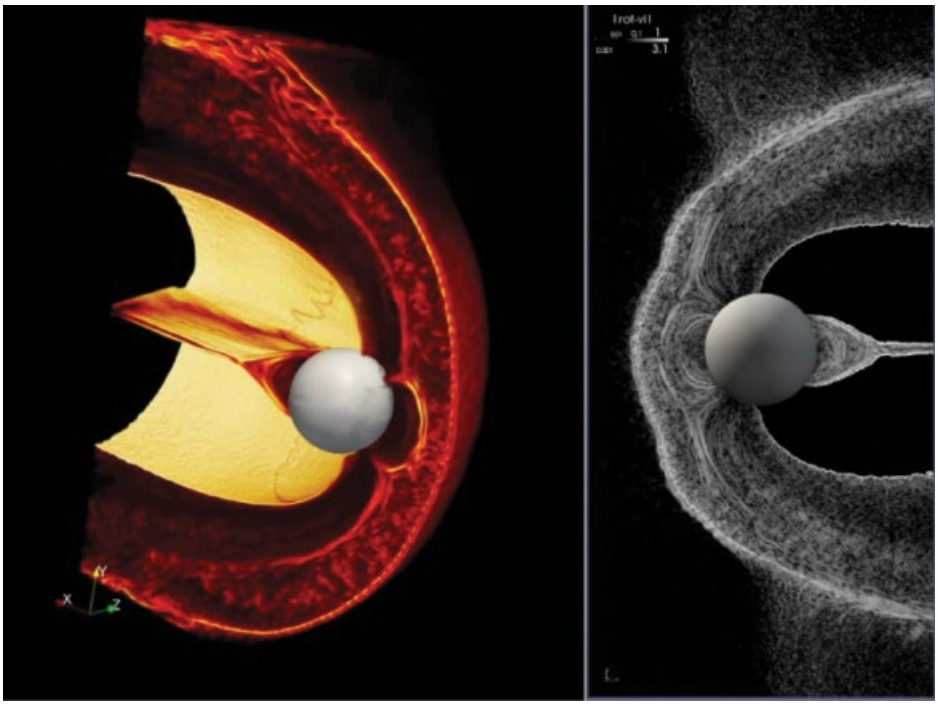

Figure 13.10 Results from a three-dimensional global hybrid simulation. Ion foreshock and plasma instability in the magnetotail are shown. [adapted from *Karimabadi et al.,* 2013]

however, primarily simple 'fluid' outflow models have been used in association with the global MHD magnetosphere models, and it is expected that this work will continue during the next decade with the use of better ionosphere outflow models. Efforts are also under way to include kinetic processes in MHD magnetosphere models in local magnetospheric regions.

An alternative approach that, no doubt, will be vigorously pursued during the next decade is the development of a kinetic model of the coupled ionosphere, plasmasphere, polar wind, and magnetosphere. It is clear that kinetic processes play a major role in each of these regions, and a coupled kinetic model will allow the coupling physics to evolve self-consistently. As noted above, the ion velocity distributions in the polar wind are highly non-Maxwellian, and these distributions cannot be taken into account in the 'fluid' MHD magnetosphere models. However, a physics-based global Ionosphere-Plasmasphere-Polar Wind (IPPW) model is being developed that includes kinetic ions and fluid electrons. Also, a kinetic model for super-thermal electrons (SE) is being developed for the ionosphere, plasmasphere, and polar wind [*Khazanov et al.*, 2012, 2013]. Efforts are under way to couple these models.

A global hybrid model of the magnetosphere (HYPERS), which contains kinetic ions and fluid electrons, is being developed in parallel with the above efforts [*Karimabadi et al.*, 2010, 2011; *Omelchenko and Karimabadi*, 2012]. There have been a few two-dimensional and three-dimensional global hybrid simulations that model the interaction of the solar wind with the magnetosphere, and Figure 13.10 shows an example of a recent three-dimensional global hybrid simulation. Because of petascale computers and other improvements, the authors can conduct global hybrid simulations with 2048 cells in each dimension. The ultimate goal is to couple the kinetic models of the magnetosphere, ionosphere, plasmasphere, and polar wind, and if successful, this should lead to a significant advance in modeling near-Earth space.

REFERENCES

Axford, W. I. (1968), The polar wind and the terrestrial helium budget, *J. Geophys. Res.*, *73*, 6855–6859.

Axford, W. I., and C. O. Hines (1961), A unifying theory of high-latitude geophysical phenomena and geomagnetic storms, *Can. J. Phys.*, *39*, 1433–1464.

Banerjee, S., and V. V. Gavrishchaka (2007), Multimoment convecting flux tube model of the polar wind system with return current and microprocesses, *J. Atmos. Solar-Terr. Phys.*, *69*, 2071.

Banks, P. M., and T. E. Holzer (1968), The polar wind, *J. Geophys. Res.*, *73*, 6846–6854.

Banks, P. M., and T. E. Holzer (1969), Features of plasma transport in the upper atmosphere, *J. Geophys. Res.*, *74*, 6304.

Barakat, A. R., R. W. Schunk, and H. G. Demars (2003), Seasonal and solar cycle dependence of the generalized polar

wind with low-altitude auroral ion energization, *J. Geophys. Res.*, *108* (A11), 1405.

Barakat, A. R., and R. W. Schunk (2006), A 3-dimensional model of the generalized polar wind, *J. Geophys. Res.*, *111*, A12314, doi:10.1029/2006JA011662.

Bauer, S. J. (1966), The structure of the topside ionosphere, in *Electron Density Profiles in the Ionosphere and Exosphere*, ed. by J. Frihagen, 387–397, North-Holland, New York.

Brambles, O. J., W. Lotko, B. Zhang, M. Wiltberger, J. Lyon, and R. J. Strangeway (2011), Magnetosphere sawtooth oscillations induced by ionospheric outflow, *Science*, *332*(6), 1183, doi:10.1126/science.1202869.

Brinton, H. C., et al. (1978), The high-latitude winter F-region at 300 km: thermal plasma observations from AE-C, *J. Geophys. Res.*, *83*, 4767.

Dessler, A. J., and F. C. Michel (1966), Plasma in the geomagnetic tail, *J. Geophys. Res.*, *71*, 1421–1426.

Dungey, J. W. (1961), Interplanetary magnetic field and the auroral zones, *Phys. Review Letters*, *6*, 47–48.

Garcia, K., and V. G. Merkin (2010), Effects of nightside O^+ outflow on magnetospheric dynamics: Results of multi-fluid MHD modeling, *J. Geophy.s Re.s*, *115*, A00J09.

Gardner, L. C., and R. W. Schunk (2004), Neutral polar wind, *J. Geophys. Res.*, *109*, A05301, doi:10.1029/2003JA010291.

Gardner, L. C., and R. W. Schunk (2005), Global neutral polar wind model, *J. Geophys. Res.*, *110*, A10302, doi:10.1029/2005JA011029.

Gombosi, T. I. and A. F. Nagy (1989), Time-Dependent modeling of field-aligned current-generated ion transients in the polar wind, *J. Geophys. Res.*, *94*, A1, 359–369.

Glocer, A., G. Tóth, T. Gombosi, and D. Welling (2009), Modeling ionospheric outflows and their impact on the magnetosphere, initial results, *J. Geophys. Res.*, *114*, Issue A5, 5216.

Hardy, D. A., M. S. Gussenhoven, and E. Holeman (1985), A statistical model of auroral electron precipitation, *J. Geophys. Res.*, *90*, 4229–4248.

Heppner, J.-P., and N. C. Maynard (1987), Empirical high-latitude electric field models, *J. Geophys Res.*, *92*, 4467–4489.

Hodges, R. R. Jr. (1994), Monte Carlo simulation of the terrestrial hydrogen exosphere, *J. Geophys. Res.*, *99*(A12), 23229–23248, 10.1029/94JA02183.

Horwitz, J. L., C. W. Ho, H. D. Scarbro, G. R. Wilson, and T. E. Moore (1994), Centrifugal acceleration of the polar wind, *J. Geophys. Res.*, *99*, A8, 15051–15064.

Karimabadi, H., H. X. Vu, B. Loring, Y. Omelchenko, M. Tatineni, A. Muhamdar, and B. Geveci (2010), Petascale global kinetic simulations of the magnetosphere and visualization strategies for analysis of very large multi-variate datasets, *ASP Conference Series*, vol. *444*, pp. 281–2910.

Karimabadi, H., J. Dorelli, H. X. Vu, B. Loring, and Y. Omelchenko (2011), Is quadrupole structure of out-of-plane magnetic field evidence for Hall reconnection?, *Modern Challenges in Nonlinear Plasma Physics: a Festschrift Honoring the Career of Dennis Papadopoulos*, Halkidiki, Greece, 15–19 June 2010, AIP Conference Proceedings, vol. *1320*, pp. 137–143.

Karimabadi, H., P. O'Leary, M. Tatineni, B. Loring, A. Majumdar, and B. Geveci (2013), In-situ visualization for global hybrid simulations, *ACM 978-1-4503-2170-9/13/07.*

Khazanov, G. V., I. Khabibrakhmanov, and A. Glocer (2012), Kinetic description of ionospheric outflows based on the exact form of Fokker-Planck collision operator: Electrons, *J. Geophys. Res.*, *117*, No. A11, A11203, doi:10.1029/2012JA018082.

Khazanov, G. V., A. Glocer, M. W. Liemohn, and E. W. Himwich (2013), Superthermal electron energy interchange in the ionosphere-plasmasphere system, *J. Geophys. Res.*, *118*, 110, doi:10.1002/jgra.50127.

Lemaire, J. F., et al. (2007), History of kinetic polar wind models and early observations, *J. Atmos. Solar-Terr. Phys.*, *69*, 1901.

Omelchenko, Y. A., and H. Karimabadi, HYPERS: A Unidimensional asynchronous framework for multiscale hybrid imulations (2012), *J. Comp. Phys. 231*, 1766–1780.

Peterson, W. K., L. Andersson, B. C. Callahan, H. L. Collin, J. D. Scudder, and A. W. Yau (2008), Solar-minimum quiet time ion energization and outflow in dynamic boundary related coordinates, *J. Geophys. Res.*, *113*, A07222, doi:10.1029/2008JA013059.

Peterson, W. K., H. L. Collin, O. W. Lennartsson, and A. W. Yau (2006), Quiet time solar illumination effects on the fluxes and characteristic energies of ionospheric outflow, *J. Geophys. Res.*, *111*, A11S05, doi:10.1029/2005JA011596.

Raitt, W. J., R. W. Schunk, and P. M. Banks (1975), A comparison of the temperature and density structure in high and low speed thermal proton flows, *Planet. Space Sci.*, *23*, 1103–1117.

Schunk, R. W. (1999), Ionospheric Outflow, in Sun-Earth Plasma Connections, *Geophys. Monograph*, *109*, 195–206.

Schunk, R. W. (2007), Time-dependent simulations of the global polar wind, *J. Atmos. Solar-Terr. Phys.*, *69*, 2028–2047.

Schunk, R. W., and A. F. Nagy (2009), *Ionospheres*, Second Addition, Cambridge University Press, Cambridge, U.K.

Schunk, R. W., and J. J. Sojka (1989), A three-dimensional time-dependent model of the polar wind, *J. Geophys. Res.*, *94*, 8973–8991.

Schunk, R. W., and J. J. Sojka (1997), Global ionosphere-polar wind system during changing magnetic activity, *J. Geophys. Res.*, *102*, 11625–11651.

Tam, S. W. Y., T. Chang, and V. Pierrard (2007), Kinetic modeling of the polar wind, *J. Atmos. Solar-Terr. Phys.*, *69*, 1984.

Tinsley, B. A., et al. (1986), Monte Carlo models for the Terrestrial Exosphere over a solar cycle, *J. Geophys. Res.*, *91*, 13631.

Wilson, G. R., T. E. Moore, and M. R. Collier (2003), Low-energy neutral atoms observed near the Earth, *J. Geophys. Res.*, *108* (A4), 1142, doi:10.1029/2002JA009643.

Wilson, G. R., and T. E. Moore (2005), Origins and variation of terrestrial energetic neutral atoms outflow, *J. Geophys. Res.*, *110*, A02207, doi:10.1029/2003JA010356.

Wiltberger, M., W. Lotko, J. G. Lyon, P. Damiano, and V. Merkin (2010), Influence of cusp O^+ outflow on magnetotail dynamics in a multifluid MHD model of the magnetosphere, *J. Geophys. Res. 115*, A00J05, doi:10.1029/2010JA015579.

Winglee R. M., D. Chua, B. Brittnacher, and G. K. Parks (2002), Global impact of ionospheric outflows on the dynamics of the magnetosphere and cross-polar potential, *J. Geophys. Res. 107* (A9), 1237.

Yau, A. W., A. Takumi, and W. K. Peterson (2007), The polar wind: Recent observations, *J. Atmos. Sol-Terr Phys.*, *69*, 1936–1983.

14

Coupling the Generalized Polar Wind Model to Global Magnetohydrodynamics: Initial Results

Daniel T. Welling[1], Abdallah R. Barakat[2], J. Vincent Eccles[3], R. W. Schunk[2], and Charles R. Chappell[4]

Video of Yosemite Talk, URL: http://dx.doi.org/10.15142/T3V88W

ABSTRACT

A growing number of global magnetohydrodynamic (MHD) simulations of the Earth's magnetosphere have included some form of ionospheric outflow at the inner boundary. This has been done either using a classical polar wind approach, where only pressure gradient and ambipolar forces are considered, or with a subset of the non-classical polar wind, where a plethora of acceleration mechanisms create a faster, more oxygen-rich polar wind. This study is the first to couple a robust, complete treatment of the classical and non-classical polar wind to a global magnetosphere model. The Generalized Polar Wind (GPW) model is used to drive oxygen and hydrogen outflow in the Block Adaptive Tree Solar wind Roe-type Upwind Scheme (BATS-R-US) model. A synthetic storm is simulated, and results are compared to simulations using classic polar wind approximations. It is found that the additional oxygen outflow provided by GPW has a number of important effects on storm dynamics, ranging from ring current energization to tail mass-loading prior to substorm onset. These results are discussed in the context of other approaches to include outflow in global models. It is found that the geoeffectiveness of outflowing subpopulations, such as dayside cusp or nightside auroral outflow, is dependent on the others, leading to a more complex magnetospheric response compared to previous studies that used idealized outflow prescriptions from only a single source region.

14.1. INTRODUCTION

In accordance with the growing number of observations of ionospheric plasma throughout the magnetosphere [see recent reviews by *Kronberg et al.*, 2014 and *Welling et al.*, 2015a], there has been an increasing number of global-scale numerical simulations that include the ionospheric source of magnetospheric plasma [*Wiltberger*, 2015]. Often, these simulations have used an outflow specification that represents the "classical" polar wind [*Axford*, 1968; *Banks and Holzer*, 1968; *Ganguli*, 1996], either by leveraging simple inner boundary conditions [*Winglee*, 1998; *Winglee*, 2000; *Siscoe et al.*, 2001; *Walker et al.* 2003; *Zhang et al.*, 2007; *Welling and Liemohn*, 2014] or by using a first-principles-based approach to better capture ambipolar and pressure gradient acceleration of cold plasma [*Glocer et al.*, 2009a, 2009b; *Welling et al.*, 2011]. The resulting outflow is cold and dense, and

[1]*Department of Climate and Space Sciences and Engineering, University of Michigan, Ann Arbor, MI, USA*

[2]*Center for Atmospheric and Space Sciences, Utah State University, Logan, UT, USA*

[3]*Center for Atmospheric and Space Sciences, Utah State University, Logan, UT, USA*

[4]*Vanderbilt University, Nashville, TN, USA*

Magnetosphere-Ionosphere Coupling in the Solar System, Geophysical Monograph 222, First Edition.
Edited by Charles R. Chappell, Robert W. Schunk, Peter M. Banks, James L. Burch, and Richard M. Thorne.

extends across the polar cap. Each of these studies has found that the classical polar wind is a critical component of magnetospheric dynamics.

Other studies have attempted to examine the role of the "non-classical" or "generalized" polar wind [*Schunk and Sojka*, 1997; *Barakat and Schunk*, 2006] on magnetospheric dynamics. Generalized polar wind is outflow that results not only from the classical acceleration mechanisms but from a plethora of effects that are capable of increasing the outflowing fluxes, especially of heavy ions. Such non-classical acceleration mechanisms include wave-particle transverse heating [e.g., *Chaston et al.*, 2004, 2007], centrifugal acceleration [e.g., *Cladis*, 1986; *Horwitz et al.*, 1994], and effects of hot electron populations [e.g., *Barakat and Schunk*, 1983, *Barakat et al.*, 1998; *Khazanov et al.*, 1997]. Because of the difficulty of capturing this glut of processes, inclusion of non-classical outflow in global models has, to date, come in two varieties. The first is to use empirical functions to capture a subset of additional acceleration [e.g., *Brambles et al.*, 2010; *Brambles et al.*, 2011; *Ouellette et al.*, 2013]. The second is to artificially impose outflow rates of given densities and velocities to determine the influence of non-classical polar wind originating from a certain region or energy range [e.g., *Wiltberger et al.*, 2010; *Garcia et al.*, 2010; *Yu and Ridley*, 2013a, 2013b]. These studies have demonstrated the importance of including more realistic outflows in global models.

Despite these important advances, clear drawbacks exist in these studies that limit our understanding of the full impact of the generalized polar wind on magnetospheric dynamics. Each of the abovementioned studies found that the magnetosphere responds differently to outflow resulting from different acceleration mechanisms, originating from different regions, or traveling at different velocities. It is also evident that the outflow-magnetosphere system is highly non-linear [*Brambles et al.*, 2011; *Welling et al.*, 2015b]. A comprehensive approach to including polar wind outflow in global models would certainly yield results different to those of limited scope. However, no such approach exists to date.

This study presents new results of global MHD magnetospheric simulations that include outflow from the GPW model [*Barakat and Schunk*, 2006]. This model is a comprehensive model of the polar wind that includes all known classical and non-classical acceleration mechanisms acting on light and heavy ions. Using the combined MHD and GPW approach, a synthetic storm is simulated, and the results are compared to two control cases: a simulation without driven outflow and a simulation with classical polar wind outflow from the Polar Wind Outflow Model (PWOM) [*Glocer et al.*, 2009a, 2009b; *Welling et al.*, 2011]. These new results emphasize the need for expanded polar wind modeling and represent a new capability for the space science community.

14.2. METHODOLOGY

14.2.1. Model Description

The global MHD model used in this study is the single fluid, multi-species version of the BATS-R-US [*Powell et al.*, 1999; *De Zeeuw et al.*, 2000; *Ma et al.*, 2004]. The model domain stretches from 32 R_E in the upstream direction to 224 R_E downstream and 128 R_E in each other direction. A defining characteristic of this model is its flexible grid. For this study, the code configuration and grid layout follows that of *Welling et al.* [2011] and *Welling et al.* [2015b]. The grid layout yields 1.9 million grid cells with the highest resolution (1/8 R_E) about the inner boundary and 1/4 R_E in areas of interest (near-Earth lobes and central plasma sheet). See Figure 1 of *Welling and Ridley* [2010] for more details. Upstream solar wind and interplanetary magnetic field (IMF) conditions serve as the only input for the model.

The inner boundary of BATS-R-US is paramount to studies of ionospheric outflow. It is a sphere of radius 2.5 R_E. In the absence of externally imposed outflow, radial velocity is set to zero, and the mass density is 28 cm^{-3}. These simple conditions result in de facto outflow of mass into the global domain [*Welling and Liemohn*, 2014]. Though this source of plasma displays realistic dynamics, it is much lower in magnitude than fluxes set by ionospheric models and assumes a purely proton outflow population.

Velocity tangent to the inner boundary is set using electric potential values from a height-integrated ionospheric electrodynamics solver, the Ridley Ionosphere Model (RIM) [*Ridley and Liemohn*, 2002; *Ridley et al.*, 2004]. This model receives field-aligned currents (FAC) from BATS-R-US and uses them, along with an empirically based conductance pattern, to calculate the electric potential. The potential values are then used to set the tangential velocity about the MHD inner boundary. An important input to this model is the $F_{10.7}$ radio flux, a proxy for solar extreme ultraviolet irradiance, which scales the conductance.

The classical polar wind is modeled by PWOM [*Glocer et al.*, 2007; *Glocer et al.*, 2009a, 2009b; *Welling et al.*, 2011]. This model solves the gyrotropic transport equations of O^+, He^+, H^+, and e^{-1} along many non-interacting one-dimensional radial flux tubes stretching from 250 *km* to the inner boundary of BATS-R-US model (~ 9500*km*). Each flux tube is allowed to drift horizontally using the local $E \times B$ velocity. Again, model setup closely follows that of similar recent studies [*Welling et al.*, 2011; *Welling et al.*, 2015b]. A key difference in this study is that the number of modeled flux tubes has been increased from 126 to 468, greatly improving the horizontal spatial resolution.

Finally, the non-classical polar wind is simulated using the GPW model. The GPW model is a fluid/particle

hybrid model that includes both classical and non-classical polar wind processes. The model extends from 90 *km* to 8 R_E and takes account of plasma convection and auroral precipitation. In the ionosphere and low-altitude polar wind (90–1200 *km*), the continuity, momentum, and energy equations are solved for six ion species (NO^+, O^{2+}, N^{2+}, O^+, He^+, H^+) and electrons [*Schunk and Sojka,* 1989; *Sojka and Schunk*, 1997]. The equations are solved along **B** for individual convecting flux tubes of plasma, and the three-dimensional nature of the model is obtained by following a large number of flux tubes. This low-altitude model takes account of diffusion and supersonic ion outflow, cross-field electrodynamic drifts, neutral winds and composition changes, chemical reactions, ion production (due to solar ultraviolet/extreme ultraviolet [UV/EUV] radiation, star light, and precipitation), thermal conduction, and a myriad of local heating and cooling processes. Above 1200 *km*, the ions are treated as individual particles (particle in cell [PIC]) while the electrons are a fluid [*Barakat and Schunk*, 2006]. The PIC model properly accounts for (1) O^+ and H^+; (2) cold (ionospheric) and hot (magnetospheric) electrons; (3) self-collisions and inter-species ion collisions; (4) wave-particle interactions in the aurora and polar cap; (5) gravitational, electrostatic, and magnetic mirror forces; (6) centrifugal acceleration; and (7) low-altitude auroral ion energization processes. The GPW output includes ion velocity distributions and the associated densities, drift velocities, temperatures, etc. Hence, the GPW model can account for exotic ion velocity distributions (beams, conics, double-humped, bi-Maxwellian, toroidal, etc.). The GPW model can be driven by empirical, physics-based, or data assimilation convection and precipitation models.

For this study, the empirical inputs and configuration follow that of *Barakat and Schunk* [2006]. A total of 1565 flux tubes are followed with 1 million ions per tube in each polar region (2 billion particles). The formulation of the high-altitude WPI is similar to *Barakat and Schunk* [2001], where the wave spectrum level is based on an empirical formula given by *Barghouthi et al*. [1998]. The position and size of the polar cap and the cusp/auroral oval regions are similar to that of *Barakat and Schunk* [2006], and the low-altitude ion heating occurs within the altitude range of 1,600 to 1,800 *km*. The rest of the parameters are similar to those in *Barakat et al.* [2003]. The effects of the polar rain are taken into account in a manner similar to *Barakat et al.* [1998].

14.2.2. Model Coupling

All model couplings are handled by the Space Weather Modeling Framework (SWMF) [*Tóth et al.*, 2005; *Tóth et al.*, 2012], a flexible tool for performing complex simulations of the multi-scale space environment. The SWMF executes, synchronizes, and couples each of the models integrated within its domain. The coupling setup closely follows that of the previous studies listed above. BATS-R-US shares FAC information to both RIM and PWOM. RIM uses this as input to its potential solver and to empirically set ionospheric conductance. RIM then returns the electric potential to set the BATS-R-US tangential inner boundary velocity. PWOM uses FACs from BATS-R-US to set the electron velocity based on current conservation with ion flow. FACs are also used as a proxy for precipitating topside electron heat flux. The resulting H^+ and O^+ densities and velocities are passed to BATS-R-US to set the radial velocity and species-specific density at the MHD inner boundary. These couplings are performed every 10 seconds of simulation time.

Coupling between the GPW and the other models is strictly one-way; GPW is run independently, and its results at the MHD inner boundary altitude are used as input to BATS-R-US instead of PWOM. The reason for this approach is the intense resources required to run GPW. In stand-alone mode, each GPW flux tube can be run independently on a super computing cluster. A full, two-way coupled simulation that includes the other models would require all GPW flux tubes to be simulated simultaneously, making such a simulation prohibitively expensive.

When either outflow model is coupled to the MHD model, the outflow values must be collapsed to fit the physical restrictions of MHD. First, the results are interpolated to the MHD grid. Because this is far coarser than the horizontal resolution of either GPW or PWOM, both outflow codes are using an acceptable number of flux tubes. Further, in the case of GPW, the moments of the full outflow velocity distribution are calculated and handed to BATS-R-US. Therefore, some information is lost in the conversion from the kinetic GPW to the fluid BATS-R-US codes.

14.2.3. Simulation Setup

A simple, synthetic storm is first simulated using the GPW in stand-alone mode. For ionospheric purposes, the storm is defined by the K_P index, shown in the top frame of Figure 14.1. K_P begins at quiet-time levels then ramps up over a one-hour period to a value of 6, representing a moderate to strong geomagnetic storm. K_P remains elevated for one hour before relaxing back down to quiet levels over the course of four hours. This K_P curve serves as input to the many empirical models leveraged by the GPW. In addition, $F_{10.7}$ solar radio flux is required. A value of 70.0 is used, representing solar minimum-type conditions.

BATS-R-US requires upstream solar wind conditions and not K_P index as input. It is therefore necessary to

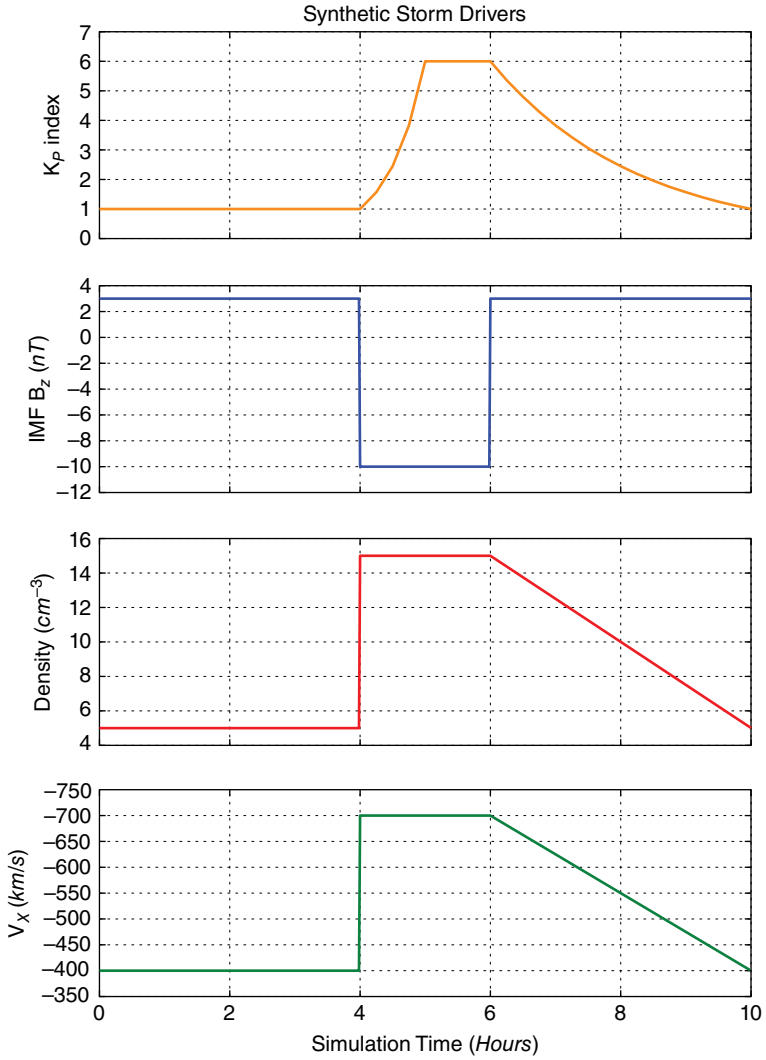

Figure 14.1 Input K_p for the GPW model (top frame) and input values for the coupled models (remaining frames). From the top frame downward: K_p index, IMF $B_{Z'}$ solar wind number density, and solar wind Earthward velocity.

obtain synthetic solar wind drivers that correspond to the geomagnetic response parameterized by the K_p shown in Figure 14.1 in order to ensure that the models are not inconsistent. To do this, a set of BATS-R-US and GPW runs were performed with different upstream conditions. Virtual magnetometer output [*Yu et al.*, 2010] was used to create a synthetic K_p curve to compare against the curve used to drive GPW. In addition, the simulated cross polar cap potential (CPCP) from the RIM model was compared to that used internally by GPW. The z-component of the IMF, solar wind number density, and Earthward velocity curves shown in Figure 14.1 yielded good agreement between input values for GPW and output values from the coupled models. The SWMF's ability to successfully reverse-engineer upstream conditions is supported by its history of successfully reproducing ground-based magnetometer observations [*Yu et al.*, 2010; *Pulkkinen et al.*, 2013] and in situ and remote observations of ionospheric currents [*Wang et al.*, 2008; *Korth et al.*, 2011].

All analysis of model results is performed using the SpacePy software library [*Morley et al.*, 2010].

14.3. RESULTS

14.3.1. Ionospheric Outflow

Figure 14.2 characterizes the pre-storm (0:00–4:00 universal time [UT]) outflowing oxygen from PWOM (left column) and GPW (right column) in terms of number density (top row) and radial velocity (middle row). These are the values that are directly fed to the global MHD model. In the bottom row of Figure 14.2, the radial flux of oxygen is shown in units of $cm^{-2}s^{-1}$. The altitude slices are taken at the interface between the

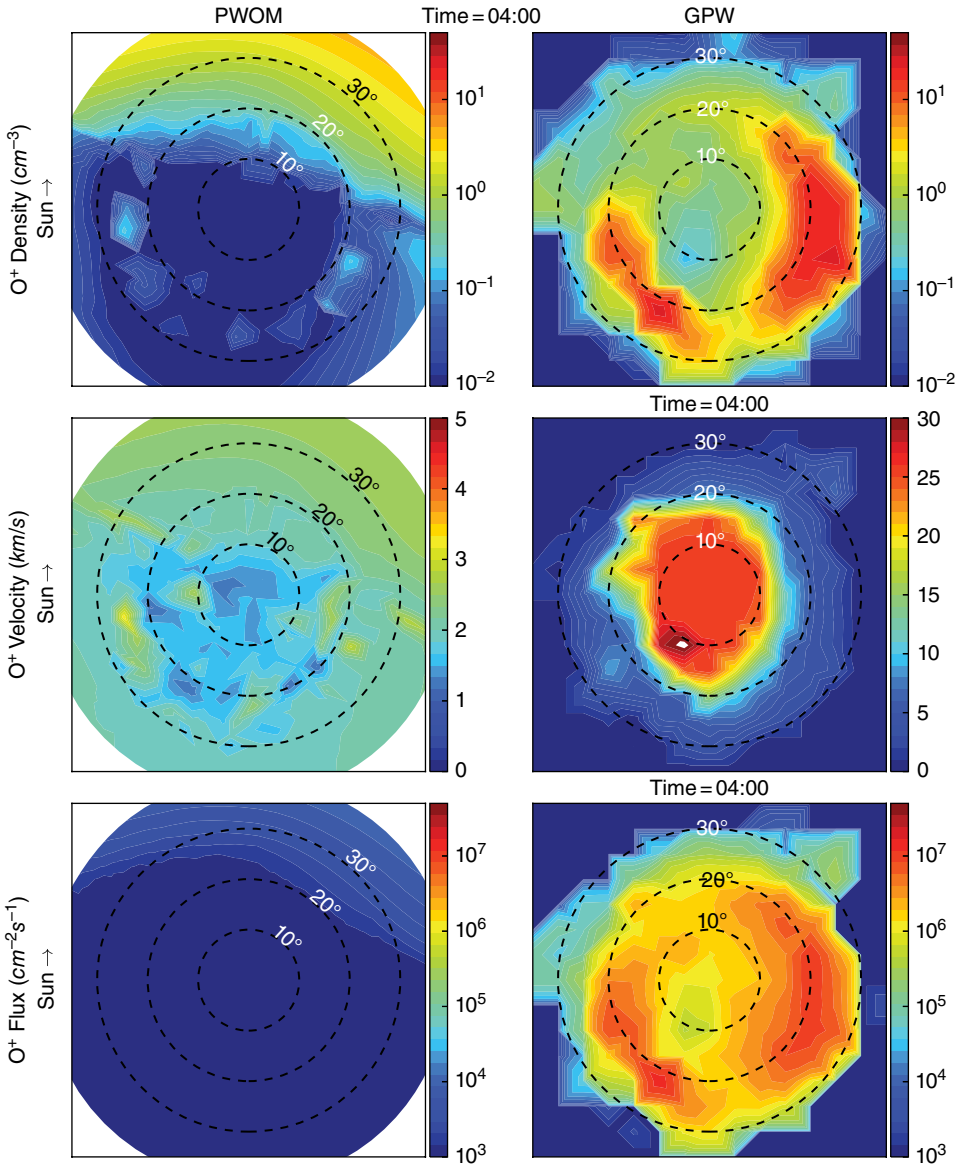

Figure 14.2 Pre-storm oxygen density (top row), radial velocity (center row), and radial flux (bottom row) at the interface between the PWOM (left column) or GPW (right column) and the MHD model. Densities are shown on a log scale. Note the different scales for the PWOM and GPW velocity plots. Concentric dashed circles show colatitude from the north magnetic pole.

ionospheric outflow models and the global MHD code; these are the values that are handed to BATS-R-US at its 2.5 R_E inner boundary. These plots illustrate that even under quiet conditions, the additional acceleration mechanisms included in the generalized (non-classical) polar wind drives stronger heavy ion outflow. In PWOM, most of the high-altitude oxygen is located on the daylight portion of the hemisphere. Though some localized patches exist on the nightside, the densities are below 1 cm^{-3}. The upward velocity is spatially uniform with a magnitude around 2 km/s. In stark contrast, the GPW results show enhanced oxygen about the quiet time auroral region reaching as much as 10 cm^{-3}. In the polar regions, densities of around 1 cm^{-3} are present. The difference is large enough that a different color scale is necessary between the two simulations (maximum value of 5 and 30 cm^{-3} for PWOM and GPW, respectively). Over the pole, non-classical acceleration of oxygen drives radial velocities to an order-of-magnitude higher than the PWOM-derived values (note the different color scale). At 10° colatitude in the midnight sector, a localized region of very fast (> 30 km/s) outflow is found.

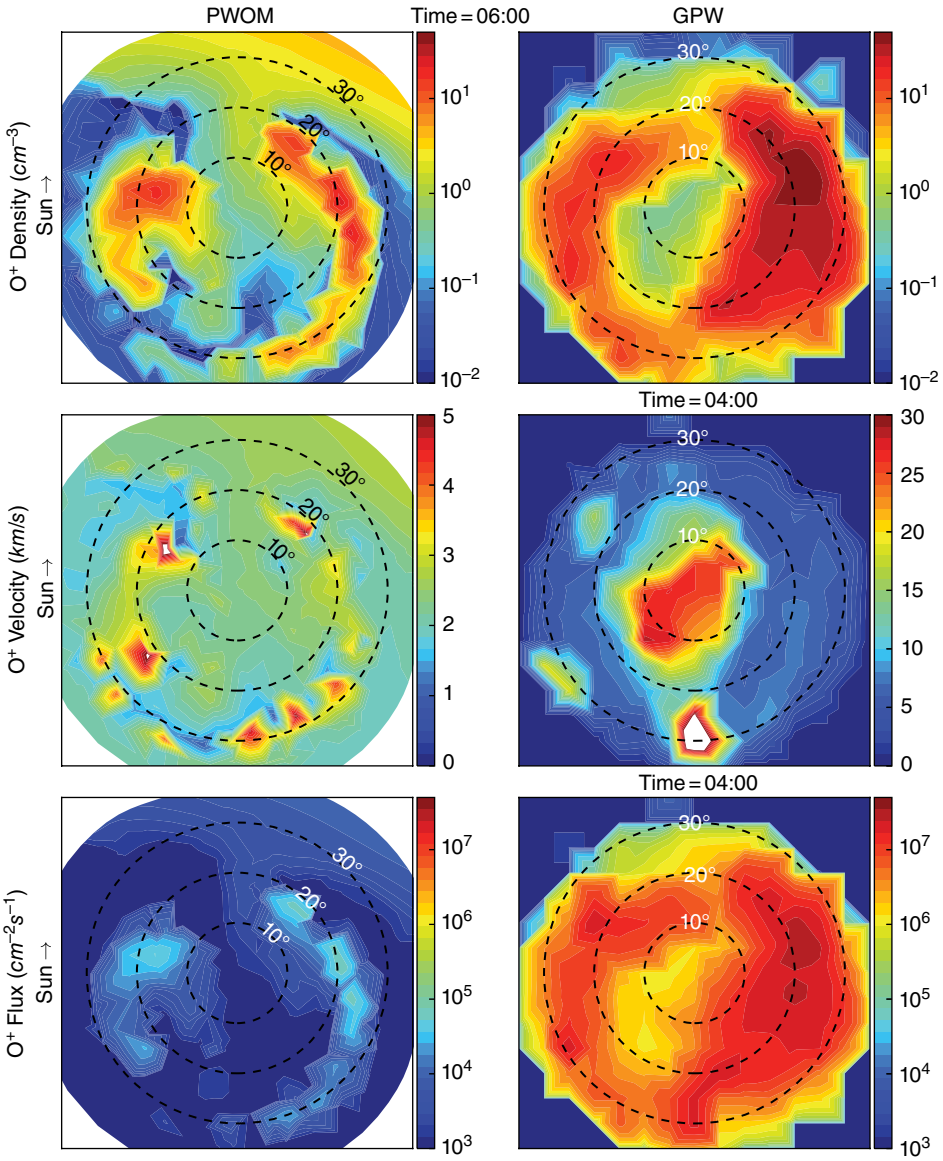

Figure 14.3 The same as Figure 14.2 but during the storm activity peak.

This feature is one of many short-lived transient flows found in the GPW results, consistent with previous studies demonstrating the highly structured and dynamic nature of non-classical outflow [*Schunk and Sojka*, 1997; *Demars and Schunk*, 2002]. These transients are not relegated to the nightside. Outside of the pole, background velocities between the two models are similar.

In terms of fluxes, the magnitudes and spatial distribution produced by the GPW roughly matches expectations based on statistics of observations [e.g., *Lennartsson et al.*, 2004; *Peterson et al.*, 2008]. A notable exception is the cusp region, where fluxes are under-predicted by the GPW. In contrast, the PWOM produces very weak quiet time O^+ fluxes that do not resemble observed patterns.

Figure 14.3 shows the same values, but at the end of the storm peak (6:00 UT). Although both models show an increase in oxygen density and velocity, the GPW model values still eclipse those of its counterpart. PWOM shows an increase in both density (up to ~10 cm^{-3}) and velocity (~5 *km/s*). The density increase comes in two varieties: advective, as photoions from the sunlit portion of the hemisphere $E \times B$ drift over the pole, and upwelling flows associated with FACs [*Glocer et al.*, 2009a; *Welling et al.*, 2015a]. The fastest upflows are associated with the latter. The GPW results show a broad increase in oxygen density about the now-active auroral oval. The densities regularly surpass that of the PWOM results, reaching as much as 50 cm^{-3} in some regions. Velocity is broadly but weakly

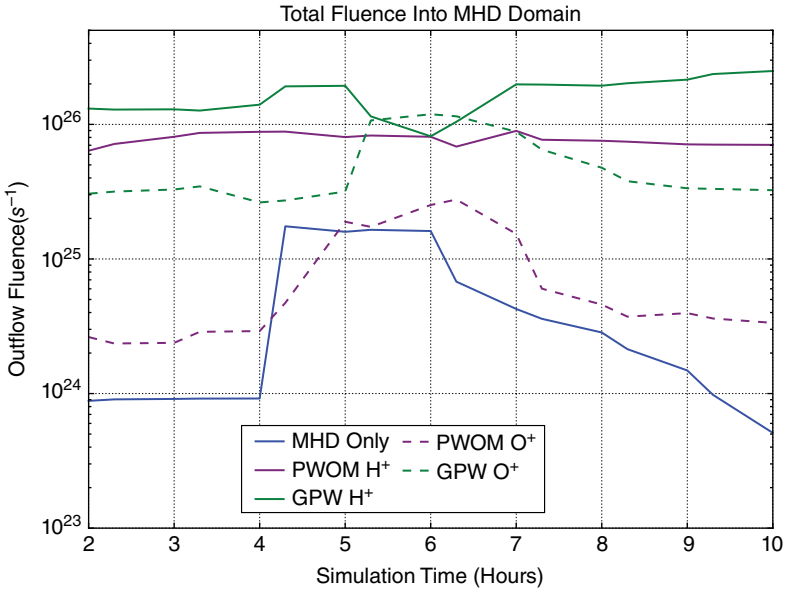

Figure 14.4 Total number fluence of H^+ (solid lines) and O^+ (dashed lines) entering the MHD domain for all three simulations: MHD only (blue lines), MHD and PWOM (purple lines), and MHD and GPW (green lines).

increased, with a typical flow of $5-10\ km/s$. The isolated fast-flow transients appear more frequently during active times.

H^+ fluxes (not shown) display a greater degree of similarity across models and exhibit less variability. During quiet periods, PWOM density ranges from a few cm^{-3} rising to about 10 cm^{-3} in the sunlit regions. Velocity is uniform with a magnitude of 15 *km/s*. Over the polar cap, GPW has a similar H^+ density but a higher velocity (~ 20 *km/s*); at lower latitudes, GPW density is higher (20–30 cm^{-3}), but velocity is slightly lower (10 *km/s*). During storm peak, these patterns and magnitudes change only marginally. The biggest difference is in GPW densities, which drop down to PWOM-type levels.

Figure 14.4 quantifies the total contribution each model makes to the global magnetosphere. Each line shows the total fluence, or the total ions per second passing through the MHD inner boundary, as a function of time. Solid lines show H^+ fluence; dashed lines show O^+ fluence. PWOM results are shown as purple lines, and GPW results as green lines. For comparison, the total fluence generated when constant, uniform inner boundary conditions are used and an all-hydrogen plasma is assumed is shown in blue.

For PWOM-obtained fluence, the total outflow reaches expected values of 10^{25} to 10^{26} *ions/s* [*Yau et al.*, 1988; *Moore et al.*, 1997; *Cully et al.*, 2003]. H^+ fluence is almost constant throughout the entire event. O^+ fluence increases by nearly an order-of-magnitude during strong driving but never surpasses the total H^+ fluence. The increase in oxygen fluence is coincident with the start of the storm but does not reach peak values until two hours later, just as the IMF turns northward again. It takes two hours for oxygen to return to quiet time levels.

The GPW fluence shows several unique features compared to the PWOM results. First, the magnitude of the outflow for both species is stronger, especially for oxygen, where GPW-derived values are an order-of-magnitude larger. The GPW H^+ fluence is also more dynamic; it increases during the first hour of the storm before decreasing during the second hour, then returning to quiet time levels during the recovery phase. GPW oxygen fluence shows an inverse pattern, decreasing very slightly at first, then increasing by a factor of 5 to surpass the total H^+ contribution. This is in contrast to the PWOM results, where oxygen increases immediately with storm onset but remains well below the H^+ fluence. Overall, this figure shows what is intimated by Figures 14.2 and 14.3: the GPW accelerates far more mass into the magnetosphere than PWOM.

14.3.2. Magnetospheric Response

Figure 14.5 summarizes the impact each outflow specification has on magnetospheric dynamics in terms of the D_{ST} index. The index is calculated via a Biot-Savart integral centered at GSM origin (the center of the Earth) and includes all currents inside the entire MHD domain. The sub-MHD currents (i.e., ionospheric currents), are not included in this calculation. As is the case with observed D_{ST}, this value is most indicative of the strength of the ring current [*Mayaud*, 1980].

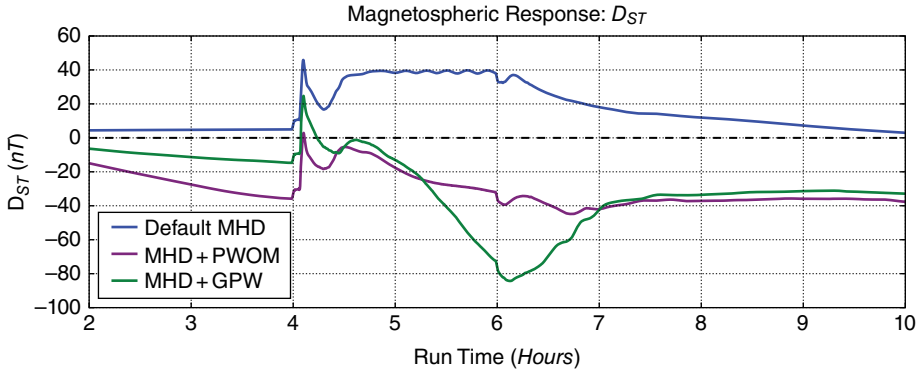

Figure 14.5 D_{ST} as calculated from BATS-R-US for the three simulations. Line colors are the same as in Figure 14.4.

The blue line shows the D_{ST} index when no outflow model is included in the calculation. The storm sudden commencement (SSC) manifests as a sharp up-tick in D_{ST} resulting from increased magnetopause currents. Without strong mass driving or a dedicated inner magnetosphere model to accurately capture the magnetically drifting hot population, very little pressure builds up in the MHD model. As such, the magnetopause currents continue to dominate D_{ST} dynamics throughout the manufactured event, yielding very unrealistic results. This is similar to other MHD simulation results when a ring current model is not included [*Rastätter et al.*, 2013]. At 6:00 UT, as the IMF and solar wind drivers return to their nonstorm values, the D_{ST} index returns to zero over several hours.

The purple and green curves show the D_{ST} values when either the PWOM or GPW models are included, respectively. Both show the same SSC signature as the MHD-only result, but then quickly drop to strongly negative values, indicating the buildup of an appreciable ring current. The values continue to drop over the two-hour storm period, signaling that there is continual mass and energy build up in the magnetosphere until IMF turns northward at 6:00 UT. At this point, both simulations have slight recoveries to new equilibrium values. The sustained negative values are likely due to the trapping of plasma in absence of non-advective losses (e.g., charge exchange) as the corotation field takes over from the diminished convection field. Both of these curves resemble real D_{ST} curves far better than their MHD-only counterpart.

The two outflow-case curves in Figure 14.5 differ from each other in an important way: the maximum storm strength. After the SSC, the PWOM-case D_{ST} reaches a minimum of –44.9 nT, which would be considered a fairly weak storm event. In contrast, the GPW D_{ST} (green line) reaches –84.3 nT, almost double the classical outflow situation. Additionally, at the time of the northward turning (6:00 UT), D_{ST} is decreasing at a far greater rate for the GPW case than the PWOM case; the magnitude of the slope of the GPW line is about a factor of 5 greater than the PWOM line. The simple D_{ST} curves reveal that the increased outflow from the non-classical polar wind is a critical value for building a realistic ring current population.

To investigate the dynamics behind the D_{ST} curves, Figures 14.6 and 14.7 show the magnetospheric conditions during pre-storm (2:00 UT) and storm maximum (6:00 UT), respectively. Each panel is a cut through the noon-midnight meridian of the MHD domain. Each row presents results from a different simulation: the MHD-only case (top row), the MHD and PWOM case (center row), and the MHD and GPW case (bottom row). Each column shows a different variable: the log of total number density (left column), the log of the thermal pressure (center column), and composition as the log of the percent oxygen by number (rightmost column). The center row also shows the magnetic field configuration with the last-closed field line shown in red.

Before storm onset (Figure 14.6), the three simulations have already begun to diverge. The MHD only simulation includes almost no subpolar outflow, as evidenced by the lowest number density in that region of any simulation. The inner magnetosphere is truly a cavity, with almost no thermal pressure buildup. In contrast, the PWOM outflow is concentrated on the dayside, as shown previously in Figure 14.2. The mid-latitude outflow contribution populates the inner magnetosphere and is accelerated by the corotational electric field and by the weak convection electric field driven by reverse convection and flank viscous interactions. A moderate pressure of a few *nPa* is able to accrue before the storm begins. Because outflow at polar latitudes is weak, the lobes are less populated than the MHD case. Finally, the GPW case displays unique features not observed in the other simulations. The lobe number density is on par with the MHD-only case, but the population is oxygen-rich, meaning that the mass density is far higher than the other two simulations. Subpolar outflow has populated the inner magnetosphere but not the extent that is seen in the PWOM-coupled simulation.

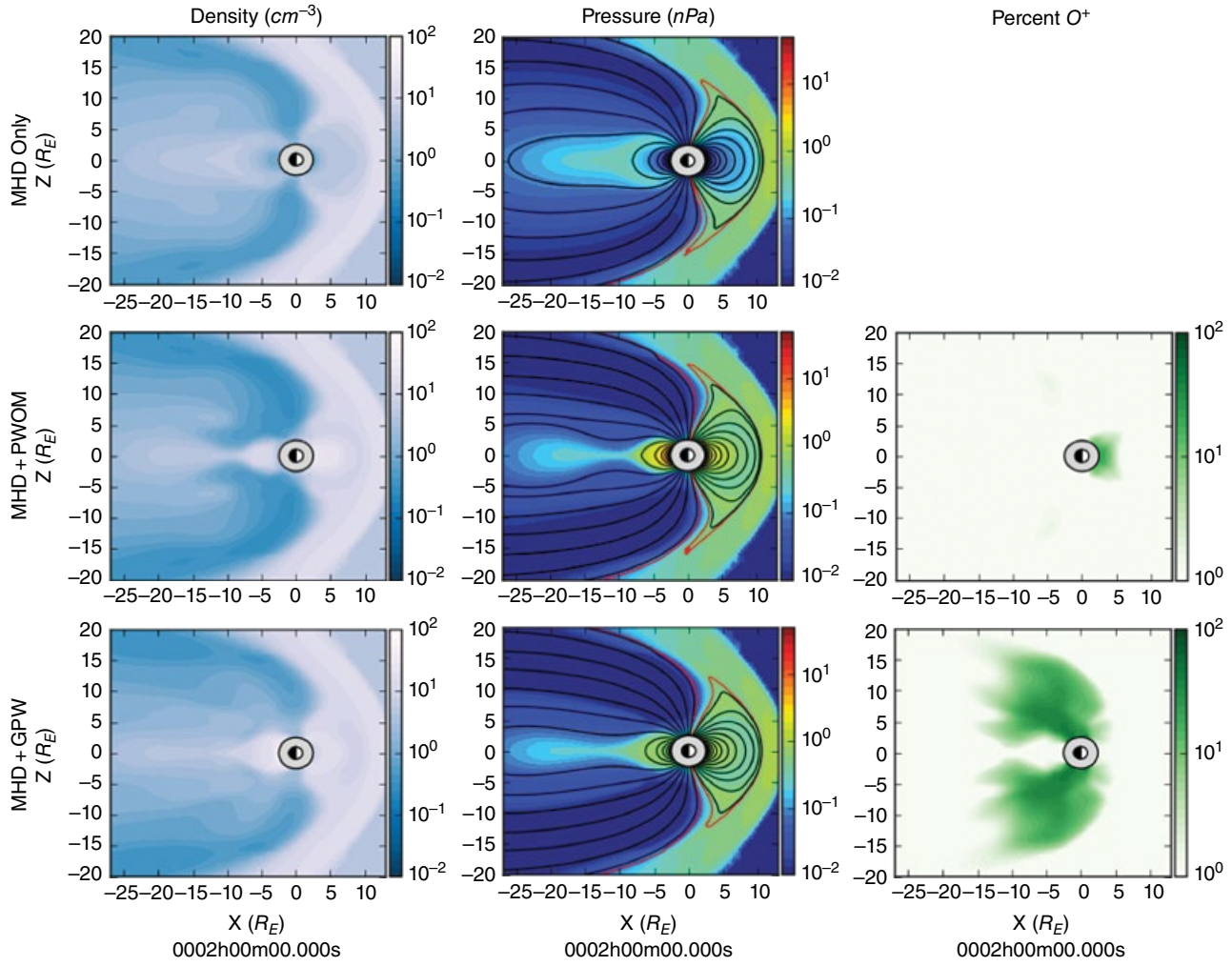

Figure 14.6 Magnetospheric conditions in the X-Z GSM plane for MHD without driven outflow (top row), MHD with PWOM (center row), and MHD with GPW (bottom row). The leftmost column shows the logarithm of total number density. The center column shows the logarithm of total plasma thermal pressure and the closed magnetic field lines (last closed line shown in red). The rightmost column shows the logarithm of percent oxygen by number. Results during pre-storm conditions (2:00 UT) are shown.

At storm peak (Figure 14.7), the three simulations yield completely different magnetospheres. The MHD-only simulation now shows increased number density around the cusps and mantle; however, it is apparent that only a small fraction is populating the near-Earth plasma sheet and inner magnetosphere. As a result, only a few *nPa* of pressure builds up on the nightside, and the magnetotail is short and quite dipolar in shape. When PWOM-driven outflow is included, total number density increases in almost every region. With additional mass feeding the plasma sheet, ring current pressure builds to tens of *nPa*. This stretches the tail and distorts the dayside magnetosphere. Oxygen comprises tens of percent of the total plasma number density. The situation becomes more extreme when GPW is included. There is more outflow, more plasma, and a greater buildup of inner magnetosphere pressure. The magnetotail now stretches twice as far as in the PWOM case. Oxygen is dominating the composition, especially over the poles and in the lobes.

At 6:00 UT, IMF turns northward, and the magnetosphere in all simulations undergoes reconfigurations as it adjusts to the post-storm conditions. This manifests as the development and release of plasmoids. For the MHD only simulation (not shown), the plasmoids are very small (only a few R_E in diameter). For the simulations that include outflow from either the PWOM or GPW simulations, however, the plasmoid releases are major events, as shown in Figure 14.8. This figure shows the conditions through the tail at 6:45 UT. At this time, large plasmoids are about to be released in both the MHD with PWOM

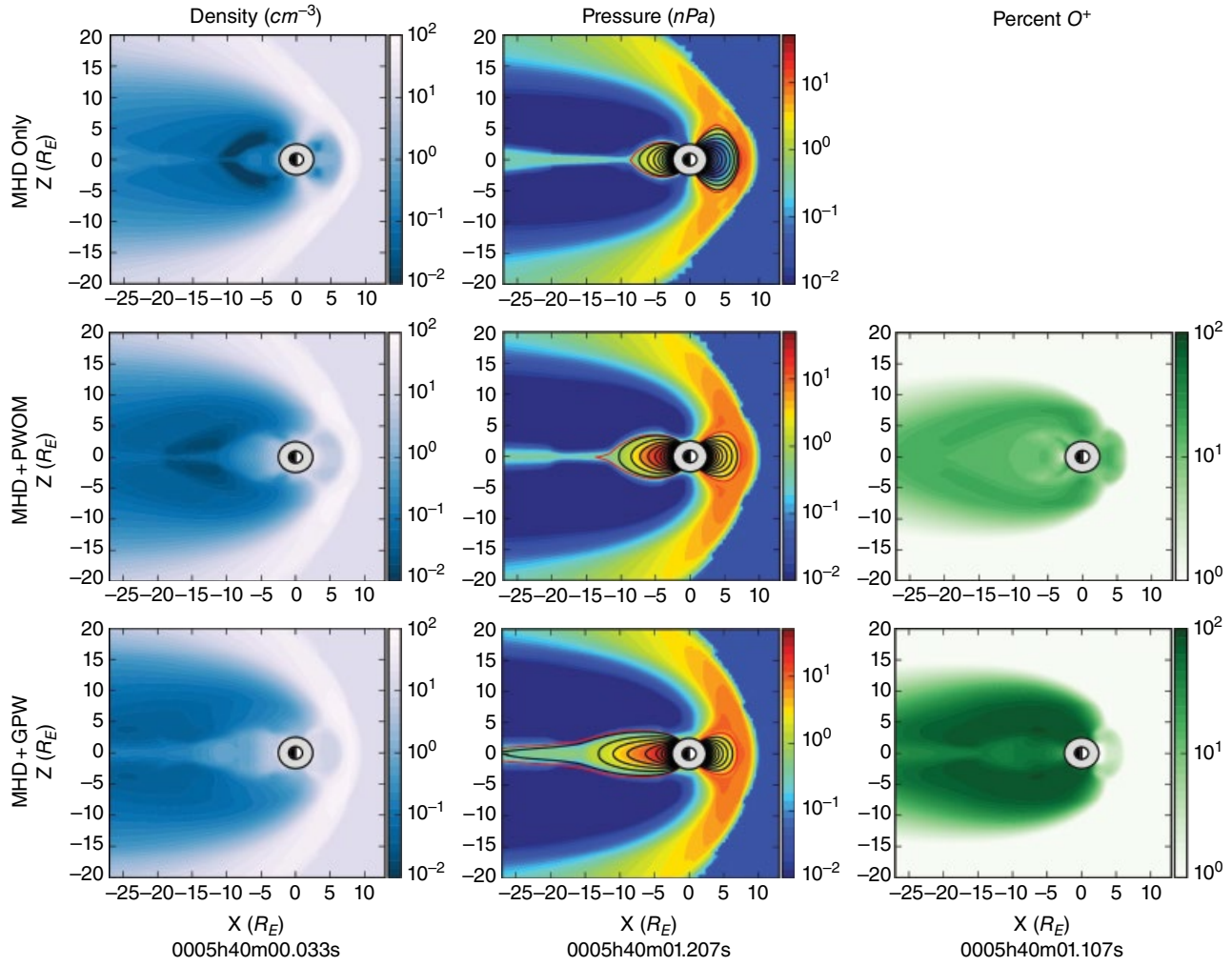

Figure 14.7 Same as Figure 14.6 but for storm peak (6:00 UT).

(top frame) and MHD with GPW (bottom frame) simulations. Near-Earth neutral lines have developed in both simulations at ~12 R_E down tail. However, due to the greater pressure build up and field stretching in the MHD with GPW simulation, the distant neutral line is deep down tail, whereas the PWOM case is ~ 33 R_E down tail. The GPW-case substorm contains greater magnetic flux, as evidenced by the higher latitude of its last-closed magnetic field line (shown in red). Contained in these plasmoids is a considerable amount of thermal pressure that is about to be exhausted down tail from the near-Earth plasma sheet (Figure 14.8, shaded contours). Although the peak pressure values in each simulation are comparable, higher pressure values are found in a broad region in the GPW-case simulation, indicating that more thermal energy is being shed compared to the PWOM-case simulation. The additional outflow provided by the GPW is driving stronger substorm-like events in the MHD.

Finally, Figure 14.9 summarizes the ionospheric electrodynamics for all three simulations via the CPCP. Previous studies have shown that inclusion of global outflow can lower CPCP precipitously [*Winglee et al.*, 2002; *Glocer et al.*, 2009a; *Brambles et al.*, 2010, etc.]. This effect manifests clearly in the present study. The maximum CPCP for the MHD-only simulation (Figure 14.9, blue line) is 286.3 *kV*. When either PWOM or GPW is included, this value drops to 181.9 or 178.3 *kV*, respectively, a relative decrease of 36.5%. This decrease is in line with previous studies.

14.4. DISCUSSION

The immediate conclusion that can be drawn from these simulations is that while inclusion of dynamic, classical polar wind outflow increases the total energy density of the storm-time magnetosphere, the inclusion

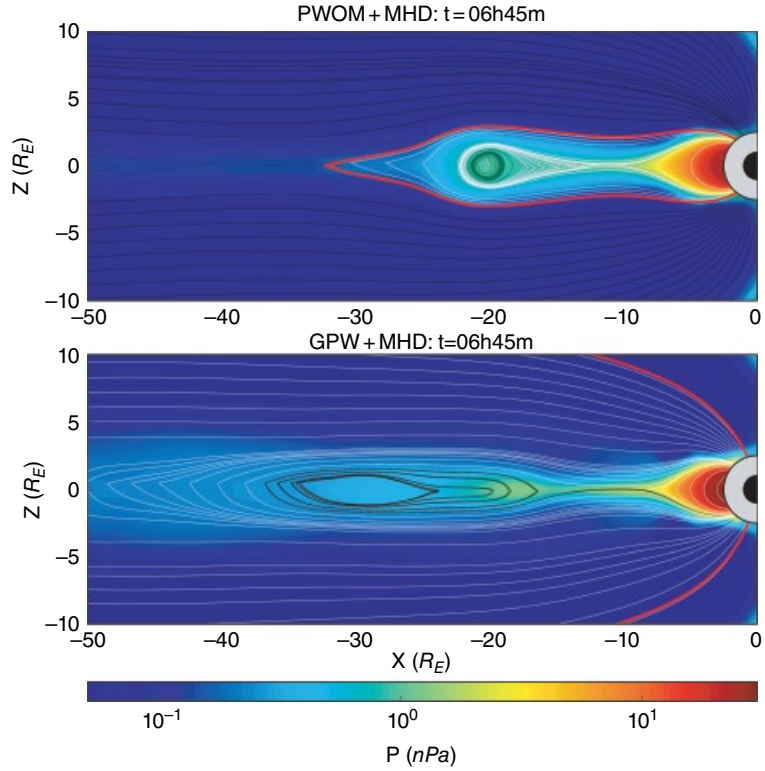

Figure 14.8 Plasmoid formation and release in the X-Z GSM plane for the MHD with PWOM simulation (top frame) and the MHD with GPW simulation (bottom frame). Contours show total plasma thermal pressure. White (black) lines show closed (open) magnetic field lines. Thick red lines mark the last-closed field lines.

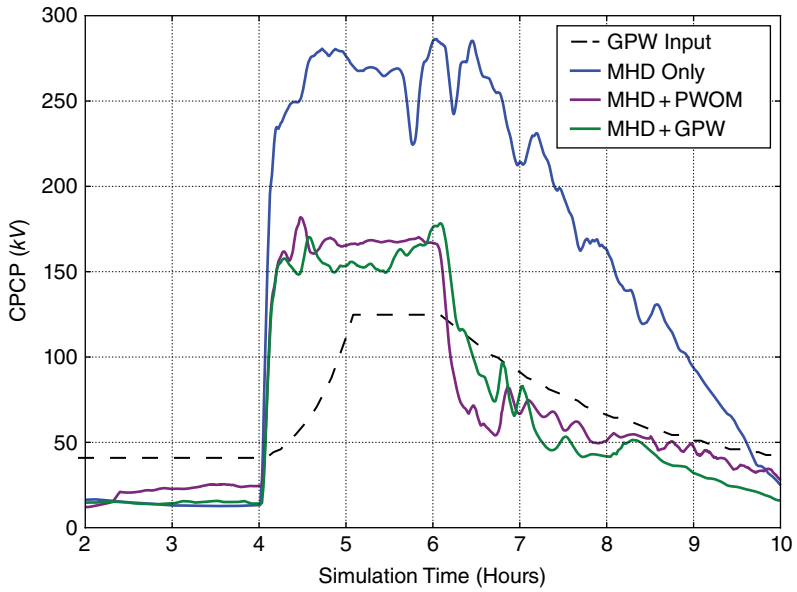

Figure 14.9 Cross polar cap potential as calculated from ionospheric electrodynamics model. The black dashed line shows the CPCP derived from the electric potential model used to drive the GPW. Other line colors are the same as in Figure 14.4.

of non-classical acceleration mechanisms increases the energy density further. The GPW model yields greater total flux of ions, especially oxygen, compared to the PWOM model results. A large fraction of this additional outflow is captured in the magnetotail, energized, and contributes to the inner magnetosphere.

This outcome may appear intuitively obvious, but other contemporary studies show that this result was not guaranteed. *Glocer et al.* [2009a, 2009b] showed that inclusion of classical polar wind outflow would indeed increase the inner magnetosphere energy density. *Brambles et al.* [2010] demonstrated that a fast, tenuous outflow would travel past the tail neutral line and escape down tail, having little effect on magnetospheric dynamics. Conversely, a denser, slower outflow (i.e., one that is more like the classical polar wind) would find its way to the plasma sheet and fuel the ring current. *Yu and Ridley* [2013a] explored the dependence of magnetospheric dynamics on outflow from different source regions. It was found that cusp-region plasma was far more effective at energizing the ring current than nightside auroral outflow. *Garcia et al.* [2010] found that nightside auroral outflow could enhance inner magnetosphere pressure but only if outflowing fluxes were increased past realistic values. These studies show the complexity inherent in attempting to forecast the fate of ionospheric outflow once in the magnetosphere.

Non-classical outflow is a conglomeration of all of these effects. The additional acceleration mechanisms act to change the outflow velocity and the total number flux in different ways at different source regions. Increased cusp outflow velocity may cause a portion of cusp outflow to escape down tail, but this loss of mass may be compensated for by an intensification of slow polar cap outflow or nightside auroral outflow. The net sum is an increase in energy density within the plasma sheet and ring current compared to a classical polar wind outflow.

The fate of a particular outflow population is also dependent on the fate of other populations. Suppose, for example, outflow from either the PWOM or the GPW was only allowed to pass into the MHD domain from a limited dayside sector. Because the outflow from the GPW is much faster than that of the PWOM (Figure 14.2), the GPW outflow could easily escape the magnetosphere while the PWOM outflow would be captured, and these conclusions would be reversed. However, GPW outflow from the polar cap and nightside is contributing to the plasma sheet, and as this population builds in the inner magnetosphere, the tail is stretched far down tail. Now, even the faster dayside populations are likely to be captured because the distance it must travel to escape has increased substantially. In this way, the true role of each outflowing population is a non-linear function of whole-system dynamics.

Magnetospheric preconditioning is also playing a role in these results. The non-classical acceleration mechanisms in the GPW results provide more quiet-time fluxes to BATS-R-US, resulting in mass-loaded lobes (Figure 14.6). During pre-storm conditions, this material blows down tail and is lost. When IMF turns southward, this material quickly advects into the plasma sheet, and can quickly contribute to the ring current. Observational evidence exists for this effect [*Peterson et al.*, 2009].

Previous studies have found that inclusion of ionospheric outflow can affect the development and timing of magnetospheric substorm events [*Wiltberger et al.*, 2010; *Brambles et al.*, 2011; *Ouellette et al.*, 2013]. In this study, it is found that the magnitude of the outflow determines the magnitude (in terms of magnetic flux and thermal energy encapsulated within the plasmoid) of the substorm. These events serve to shed excess thermal energy that builds within the MHD magnetosphere during the storm, in agreement with other studies [e.g., *Ouellette et al.* [2013]. Naturally, it follows that if ionospheric outflow is feeding the plasma sheet and ring current, intensifying this outflow will increase the available energy density that will be shed during substorm events.

A final observation from these results is the effect, or rather, lack of effect on CPCP when a generalized rather than a classical polar wind is used. As stated previously, both the PWOM and GPW cases yield lower CPCP values than the MHD-only case. However, the CPCP between the two outflow cases is nearly identical. These results suggest that there is a saturation effect with outflow-related CPCP reductions; the addition of far more heavy ion outflow from the GPW calculation (as evidenced in Figure 14.4) does not lower the polar cap potential any further than the PWOM case. This seems to support the conclusions of *Welling and Zaharia* [2012]; the additional inflation of the magnetosphere in the GPW case does not result in further reduction of the CPCP, as suggested by *Brambles et al.* [2010].

Previous studies have shown that there are complicating factors to this effect, including the source location, density, and radial velocity of the outflow. *Brambles et al.* [2010] showed a slow, dense outflow was effective at reducing CPCP, while fast flowing outflow would exhaust down tail, having little effect. *Garcia et al.* [2010], in contrast to the results shown here, demonstrated that increasing the magnitude of an artificially imposed nightside auroral region outflow would increase the magnitude of the CPCP reduction. *Yu and Ridley* [2013b], using constant polar-cap oxygen outflow, showed that an increase in outflow density could increase CPCP by lowering the Kelvin-Helmholtz stability criteria along the flanks of the magnetopause. *Yu and Ridley* [2013a] showed that cusp-source outflow results in a stronger reduction of

CPCP versus nightside outflow. The use of GPW here, which increases outflow density and velocity over many regions dynamically, likely combines many of these factors in a way that leaves the CPCP at similar values as the PWOM case. Further investigation is required, especially because there is no consensus as to the root cause of the outflow-related CPCP reductions in global models [*Welling and Zaharia*, 2012].

There are several outstanding issues with this study. First is the lack of self-consistency between the GPW and BATS-R-US. Lack of self-consistency means that features in the ionosphere and magnetosphere may become incongruent. For example, cusp outflow in the GPW may not map to the cusp in the magnetosphere, and regions of outflow intensifications may not align with regions of energy deposition from the magnetosphere. It can also mean that the PWOM outflow model is being driven differently than the GPW model, though the dominant physical mechanisms in each are so different that this is likely a second order effect. Self-consistency between outflow and magnetosphere/ionosphere dynamics can also lead to the development of mass-energy feedback loops, discussed by *Moore et al.* [2014] and demonstrated by *Brambles et al.* [2010], *Brambles et al.* [2013], *Ouellette et al.* [2013], and most recently by *Welling et al*. [2015b]. Solving these problems requires full two-way coupling between the outflow model and the global magnetosphere code. Another complication is the lack of a coupled inner magnetosphere model, which creates issues from the other direction. Accurate inner magnetosphere pressure distributions are necessary to accurately capture magnetic field geometry [*Zaharia et al.*, 2006, 2010], which effects the transport of outflow into the magnetosphere and plasma sheet. Recent work has shown that these two problems are deeply intertwined through relationships between outflow and ring current dynamics [*Welling et al.*, 2015b]. Finally, a lack of comprehensive physics in the magnetosphere model can play a limiting role. When the distribution of outflowing ions is collapsed to a single fluid, the particles cannot disperse by mass or energy as they traverse the lobe. Multi-fluid MHD is one way to help address this and will be leveraged in future outflow-MHD coupling efforts.

14.5. CONCLUSIONS

This study presents initial results of coupling a generalized polar-wind model to a global MHD model. A synthetic storm is simulated using MHD only, MHD and a classical polar wind model, and MHD with outflow supplied by the generalized polar wind model. The three cases are compared to examine how the additional outflow acceleration mechanisms affect global magnetospheric dynamics.

The non-classical polar wind model is able to drive faster and denser outflows of oxygen and hydrogen in the MHD domain, affecting magnetospheric dynamics in several ways. The additional outflow feeds the plasma sheet, resulting in an increased inner magnetosphere energy density. The additional energy density affected substorm development during the end of the storm by increasing the pressure and magnetic flux contained within the plasmoid.

These results illustrate the need for a comprehensive approach to polar wind outflow in global magnetosphere models. Similar studies have explored subsets of non-classical outflow by limiting either the energization mechanism, flux of outflowing particles, or the spatial region of the outflow. The results attained in this work stand in contradiction to many of the independent conclusions shown by other works. This is a function of the sensitivity of the global system to outflow dynamics. Compared to previous studies, these results also demonstrate that the geoeffectiveness of one ionospheric outflow subpopulation is dependent on others. Therefore, obtaining accurate and detailed outflow fluxes is critical for producing realistic magnetosphere results.

ACKNOWLEDGMENTS

This work was supported by National Science Foundation (NSF) award Atmostpheric and Geospace Sciences (AGS) 1202984 and National Aeronautics and Space Administration (NASA) award NNX13AD69G to the University of Michigan and NSF grant AGS 1203725 to Utah State University. Models housed at the University of Michigan (SWMF, BATS-R-US, and PWOM) can be freely obtained from http://csem.engin.umich.edu. Simulation data can be obtained by contacting the authors.

REFERENCES

Axford, W. I. (1968), The Polar Wind and the Terrestrial Helium Budget, *J. Geophys. Res.*, *73*, 6855–6859, doi:10.1029/JA073i021p06855.

Banks, P. M., and T. E. Holzer (1968), The Polar Wind, *J. Geophys. Res.*, *73*, 6846–6854, doi:10.1029/JA073i021p06846.

Barakat, A., and R. Schunk (2001), Effects of waveparticle interactions on the dynamic behavior of the generalized polar wind, *Journal of Atmospheric and Solar-Terrestrial Physics*, *63*(1), 75–83, doi:10.1016/S1364-6826(00)00106-1.

Barakat, A. R., and R. W. Schunk (1983), O+ ions in the polar wind, *Journal of Geophysical Research*, *88*(A10), 7887, doi:10.1029/JA088iA10p07887.

Barakat, A. R., and R. W. Schunk (2006), A three-dimensional model of the generalized polar wind, *Journal of Geophysical Research*, *111*(A12), A12, 314, doi:10.1029/2006JA011662.

Barakat, A. R., H. G. Demars, and R. W. Schunk (1998), Dynamic features of the polar wind in the presence of hot

magnetospheric electrons, *Journal of Geophysical Research*, *103*(A12), 29,289, doi:10.1029/98JA02827.

Barakat, A. R., R. W. Schunk, and H. G. Demars (2003), Seasonal and solar activity dependence of the generalized polar wind with low-altitude auroral ion energization, *Journal of Geophysical Research*, *108*(A11), 1405, doi:10.1029/2002JA009360.

Barghouthi, I., A. Barakat, and A. Persoon (1998), *Astrophysics and Space Science*, *259*(2), 117–140, doi:10.1023/A:1001569207346.

Brambles, O. J., W. Lotko, P. A. Damiano, B. Zhang, M. Wiltberger, and J. Lyon (2010), Effects of causally driven cusp O^+ outflow on the storm time magnetosphere-ionosphere system using a multifluid global simulation, *Journal of Geophysical Research (Space Physics)*, *115*, A00J04, doi:10.1029/2010JA015469.

Brambles, O. J., W. Lotko, B. Zhang, M. Wiltberger, J. Lyon, and R. J. Strangeway (2011), Magnetosphere sawtooth oscillations induced by ionospheric outflow., *Science (New York, N.Y.)*, *332*(6034), 1183–1186, doi:10.1126/science.1202869.

Brambles, O. J., W. Lotko, B. Zhang, J. Ouellette, J. Lyon, and M. Wiltberger (2013), The effects of ionospheric outflow on ICME and SIR driven sawtoothevents, *Journal of Geophysical Research: Space Physics*, *118*(10), 6026–6041, doi:10.1002/jgra.50522.

Chaston, C. C., J. W. Bonnell, C. W. Carlson, J. P. McFadden, R. E. Ergun, R. J. Strangeway, and E. J. Lund (2004), Auroral ion acceleration in dispersive Alfvén waves, *Journal of Geophysical Research (Space Physics)*, *109*, A04205, doi:10.1029/2003JA010053.

Chaston, C. C., C. W. Carlson, J. P. McFadden, R. E. Ergun, and R. J. Strangeway (2007), How important are dispersive Alfvén waves for auroral particle acceleration?, *Geophys. Res. Lett.,, 34*, L07101, doi:10.1029/2006GL029144.

Cladis, J. B. (1986), Parallel acceleration and transport of ions from polar ionosphere to plasma sheet, *grl, 13,* 893–896, doi:10.1029/GL013i009p00893.

Cully, C. M., E. Donovan, A. W. Yau, and G. G. Arkos (2003), Akebono/Suprathermal Mass Spectrometer observations of low-energy ion outflow: Dependence on magnetic activity and solar wind conditions, *Journal of Geophysical Research*, *108*(A2), 1093, doi:10.1029/2001JA009200.

De Zeeuw, D. L., T. I. Gombosi, C. P. T. Groth, K. G. Powell, and Q. F. Stout (2000), An adaptive MHD method for global space weather simulations, *IEEE Trans. Plasma Sci.*, *28*, 1956–1965.

Demars, H. G., and R. W. Schunk (2002), Three-dimensional velocity structure of the polar wind, *Journal of Geophysical Research: Space Physics*, *107*(A9), 1250, doi:10.1029/2001JA000252.

Ganguli, S. B. (1996), The polar wind, *Reviews of Geophysics*, *34*, 311–348, doi:10.1029/96RG00497.

Garcia, K. S., V. G. Merkin, and W. J. Hughes (2010), Effects of nightside O^+ outflow on magnetospheric dynamics: Results of multifluid MHD modeling, *Journal of Geophysical Research (Space Physics)*, *115*, A00J09, doi:10.1029/2010JA015730.

Glocer, A., T. Gombosi, G. Toth, K. Hansen, A. Ridley, and A. Nagy (2007), Polar wind outflow model: Saturn results, *J. Geophys. Res.*, p. 112, doi:10.1029/2006JA011755.

Glocer, A., G. Tóth, T. Gombosi, and D. T. Welling (2009a), Modeling ionospheric outflows and their impact on the magnetosphere, initial results, *Journal of Geophysical Research (Space Physics)*, *114*, 5216–+, doi:10.1029/2009JA014053.

Glocer, A., G. Tóth, T. Ma, Y. Gombosi, J. Zhang, and L. Kistler (2009b), Multi-fluid BATS-R-US: Magnetospheric composition and dynamics during geomagnetic storms, initial results, *Journal of Geophysical Research (Space Physics)*, *114*, 12,203–+, doi:10.1029/2009JA014418.

Horwitz, J. L., C. W. Ho, H. D. Scarbro, G. R. Wilson, and T. E. Moore (1994), Centrifugal acceleration of the polar wind, *Journal of Geophysical Research*, *99*(A8), 15,051, doi:10.1029/94JA00924.

Khazanov, G. V., M. W. Liemohn, and T. E. Moore (1997), Photoelectron effects on the self-consistent potential in the collisionless polar wind, *Journal of Geophysical Research*, *102*(A4), 7509, doi:10.1029/96JA03343.

Korth, H., L. Rastätter, B. J. Anderson, and A. J. Ridley (2011), Comparison of the observed dependence of large-scale Birkeland currents on solar wind parameters with that obtained from global simulations, *Annales Geophysicae*, *29*(10), 1809–1826, doi:10.5194/angeo-29-1809-2011.

Kronberg, E. A., et al. (2014), Circulation of Heavy Ions and Their Dynamical Effects in the Magnetosphere: Recent Observations and Models, *Space Science Reviews*, *184*(1–4), 173–235, doi:10.1007/s11214-014-0104-0.

Lennartsson, O. W., H. L. Collin, and W. K. Peterson (2004), Solar wind control of Earth's H^+ and O^+ outflow rates in the 15-eV to 33-keV energy range, *Journal of Geophysical Research*, *109*(A12), A12, 212, doi:10.1029/2004JA010690.

Ma, Y., A. Nagy, I. Sokolov, and K. Hansen (2004), Three-dimensional, multispecies, high spatial resolution MHD studies of the solar wind interaction with Mars, *J. Geophys. Res., 109*, doi:A07211,10.1029/2003JA010367.

Mayaud, P. N. (1980), *Derivation, Meaning, and Use of Geomagnetic Indices, Geophysical Monograph Series*, vol. *22*, American Geophysical Union, Washington, D. C., doi:10.1029/GM022.

Moore, T., M.-C. Fok, and K. Garcia-Sage (2014), The ionospheric outflow feedback loop, *Journal of Atmospheric and Solar-Terrestrial Physics*, *115–116*, 59–66, doi:10.1016/j.jastp.2014.02.002.

Moore, T. E., et al. (1997), High-Altitude Observations of the Polar Wind, *Science*, *277*(5324), 349–351, doi:10.1126/science.277.5324.349.

Morley, S. K., J. Koller, D. T. Welling, and B. A. Larsen (2010), Spacepy, A Python-based library of tools for the space sciences, in *Proceedings of the 9th Python in Science Conference*, edited by S. van der Walt and J. Millman, pp. 39–45.

Ouellette, J. E., O. J. Brambles, J. G. Lyon, W. Lotko, and B. N. Rogers (2013), Properties of outflow-driven sawtooth substorms, *Journal of Geophysical Research: Space Physics*, *118*(6), 3223–3232, doi:10.1002/jgra.50309.

Peterson, W., L. Andersson, B. Callahan, S. Elkington, R. Winglee, J. Scudder, and H. Collin (2009), Geomagnetic activity dependence of O+ in transit from the ionosphere, *Journal of Atmospheric and Solar-Terrestrial Physics*, *71*(16), 1623–1629, doi:10.1016/j.jastp.2008.11.003.

Peterson, W. K., L. Andersson, B. C. Callahan, H. L. Collin, J. D. Scudder, and A. W. Yau (2008), Solar-minimum quiet time ion energization and outflow in dynamic boundary related coordinates, *Journal of Geophysical Research*, *113*(A7), A07,222, doi:10.1029/2008JA013059.

Powell, K., P. Roe, T. Linde, T. Gombosi, and D. L. De Zeeuw (1999), A solution-adaptive upwind scheme for ideal magnetohydrodynamics, *J. Comp. Phys.*, *154*, 284–309.

Pulkkinen, A., et al. (2013), Community-wide validation of geospace model ground magnetic field perturbation predictions to support model transition to operations, *Space Weather*, *11*(6), 369–385, doi:10.1002/swe.20056.

Rastätter, L., et al. (2013), Geospace environment modeling 2008–2009 challenge: Dst index, *Space Weather*, *11*(4), 187–205, doi:10.1002/swe.20036.

Ridley, A., T. Gombosi, and D. L. De Zeeuw (2004), Ionospheric control of the magnetospheric configuration: Conductance, *Ann. Geophys.*, *22*, 567–584.

Ridley, J. A., and M. W. Liemohn (2002), A model-derived storm time asymmetric ring current driven electric field description, *J. Geophys. Res., 107*(A8), doi:10.1029/2001JA000,051.

Schunk, R. W., and J. J. Sojka (1989), A three-dimensional time-dependent model of the polar wind, *Journal of Geophysical Research*, *94*(A7), 8973, doi:10.1029/JA094iA07p08973.

Schunk, R. W., and J. J. Sojka (1997), Global ionosphere-polar wind system during changing magnetic activity, *Journal of Geophysical Research*,*102*(A6),11,625,doi:10.1029/97JA00292.

Siscoe, G. L., G. M. Erickson, B. U. O. Sonnerup, N. C. Maynard, K. D. Siebert, D. R. Weimer, and W. W. White (2001), Relation between cusp and mantle in MHD simulation, *Journal of Geophysical Research*, *106*(A6), 10,743, doi:10.1029/2000JA000385.

Sojka, J., and R. Schunk (1997), Simulations of high latitude ionospheric climatology, *Journal of Atmospheric and Solar-Terrestrial Physics*, *59*(2), 207–229, doi:10.1016/S1364-6826(96)00037-5.

Tóth, G., et al. (2005), Space weather modeling framework: A new tool for the space science community, *J. Geophys. Res.*, *110*, A12,226, doi:10.1029/2005JA011126.

Tóth, G., et al. (2012), Adaptive numerical algorithms in space weather modeling, *Journal of Computational Physics*, *231*(3), 870–903, doi:10.1016/j.jcp.2011.02.006.

Walker, R. J., M. Ashour-Abdalla, T. Ogino, V. Peroomian, and R. L. Richard (2003), Modeling Magnetospheric Sources, *Geophysical Monograph Series*, *133*, doi:10.1029/133GM03.

Wang, H., A. J. Ridley, and H. Luhr (2008), Validation of the Space Weather Modeling Framework using observations from CHAMP and DMSP, *Space Weather*, *6*(S03001), doi:10.1029/2007SW000355.

Welling, D. T., and M. W. Liemohn (2014), Outflow in global magnetohydrodynamics as a function of a passive inner boundary source, *Journal of Geophysical Research: Space Physics*, pp. 2691–2705, doi:10.1002/2013JA019374.

Welling, D. T., and A. J. Ridley (2010), Exploring sources of magnetospheric plasma using multispecies MHD, *Journal of Geophysical Research (Space Physics)*, *115*(A14), 4201–+, doi:10.1029/2009JA014596.

Welling, D. T., and S. G. Zaharia (2012), Ionospheric outflow and cross polar cap potential: What is the role of magnetospheric inflation?, *Geophys. Res. Lett.*, *39*, L23101, doi:10.1029/2012GL054228.

Welling, D. T., V. K. Jordanova, S. G. Zaharia, A. Glocer, and G. Tóth (2011), The effects of dynamic ionospheric outflow on the ring current, *Journal of Geophysical Research (Space Physics)*, *116*, doi:10.1029/2010JA015642.

Welling, D. T., et al. (2015a), The Earth: Plasma Sources, Losses, and Transport Processes, *Space Science Reviews, Under Review*.

Welling, D. T., V. K. Jordanova, A. Glocer, G. Tóth, M. W. Liemohn, and D. R. Weimer (2015b), The two-way relationship between ionospheric outflow and the ring current, *Journal of Geophysical Research: Space Physics*, pp. 4338–4353, doi:10.1002/2015JA021231.

Wiltberger, M. (2015), Review of Global Simulation Studies of Effect of Ionospheric Outflow on Magnetosphere-Ionosphere System Dynamics, in *Magnetotails in the Solar System*, chap. 22, pp. 373–392, John Wiley & Sons, Inc., Hoboken, NJ, doi:10.1002/978111884232.

Wiltberger, M., W. Lotko, J. G. Lyon, P. Damiano, and V. Merkin (2010), Influence of cusp O^+ outflow on magnetotail dynamics in a multifluid MHD model of the magnetosphere, *Journal of Geophysical Research (Space Physics)*, *115*, A00J05, doi:10.1029/2010JA015579.

Winglee, R. M. (1998), Multi-fluid simulations of the magnetosphere: The identification of the geopause and its variation with IMF, *Geophys. Res. Lett.*, *25*, 4441–4444.

Winglee, R. M. (2000), Mapping of ionospheric outflows into the magnetosphere for varying IMF conditions., *J. Atmos. and Terr. Phys., 62*, 527.

Winglee, R. M., D. Chua, M. Brittnacher, G. K. Parks, and G. Lu (2002), Global impact of ionospheric outflows on the dynamics of the magnetosphere and cross-polar cap potential, *Journal of Geophysical Research (Space Physics)*, *107*, 1237–+, doi:10.1029/2001JA000214.

Yau, A. W., W. K. Peterson, and E. G. Shelley (1988), Quantitative parametrization of energetic ionospheric ion outflow, Washington DC *American Geophysical Union Geophysical Monograph Series*, pp. 211–217.

Yu, Y., and A. J. Ridley (2013a), Exploring the influence of ionospheric O^+ outflow on magnetospheric dynamics: dependence on the source location, *Journal of Geophysical Research (Space Physics)*, *118*, 1711–1722, doi:10.1029/2012JA018411.

Yu, Y., and A. J. Ridley (2013b), Exploring the influence of ionospheric O+ outflow on magnetospheric dynamics: The effect of outflow intensity, *Journal of Geophysical Research: Space Physics*, *118*(9), 5522–5531, doi:10.1002/jgra.50528.

Yu, Y., A. J. Ridley, D. T. Welling, and G. Tóth (2010), Including gap region field-aligned currents and magnetospheric currents in the MHD calculation of ground-based magnetic field perturbations, *Journal of Geophysical Research (Space Physics)*, *115*(A14), A08, 207, doi:10.1029/2009JA014869.

Zaharia, S., V. K. Jordanova, M. F. Thomsen, and G. D. Reeves (2006), Self-consistent modeling of magnetic fields and

plasmas in the inner magnetosphere: Application to a geomagnetic storm, *Journal of Geophysical Research (Space Physics)*, *111*(A10), 11–+, doi:10.1029/2006JA011619.

Zaharia, S., V. K. Jordanova, D. T. Welling, and G. Tóth (2010), Self-consistent inner magnetosphere simulation driven by a global MHD model, *Journal of Geophysical Research (Space Physics)*, *115*(A14), A12,228, doi:10.1029/2010JA015915.

Zhang, J., et al. (2007), Understanding storm-time ring current development through data-model comparisons of a moderate storm, *J. Geophys. Res.*, *112*, A04, 208, doi:10.1029/2006JA011,846.

15

Coupling Ionospheric Outflow into Magnetospheric Models: Transverse Heating from Wave-Particle Interactions

Alex Glocer

Video of Yosemite Talk, URL: http://dx.doi.org/10.15142/T33S3B

ABSTRACT

We discuss current approaches to coupling ionospheric outflows into global models of the magnetosphere and demonstrate their inability to adequately include transverse heating due to wave-particle interactions. As the wave heating region extends over spatial regions covering both outflow and magnetosphere domains, acceleration from this process cannot be left solely to the outflow calculation but must be included in the magnetosphere calculation as well. A magnetosphere model that can include these effects must, at a minimum, account for pitch-angle anisotropy. Therefore, the anisotropic magnetohydrodynamic (MHD) equations are the minimum set of equations that a magnetosphere model can use for this problem and still use the fluid description. Using anisotropic MHD, we present a new coupling paradigm that accounts for transverse acceleration when merging ionospheric outflows into the global magnetosphere. A basic demonstration of the approach is provided illustrating its feasibility and resulting in additional acceleration and anisotropy development in the magnetosphere when wave heating is included in the coupling.

15.1. INTRODUCTION

Magnetosphere-ionosphere (M-I) coupling is a critical process in understanding the near-Earth space environment. In recent years, M-I coupling has been increasingly represented in global models of the magnetosphere to great effect. This coupling takes many forms but can be loosely thought of as consisting of two categories: electromagnetic coupling and ionospheric outflows.

Electromagnetic coupling in global magnetosphere models has largely coalesced around a single common approach. Current densities are calculated near the inner boundary of the magnetosphere model and mapped down to ionospheric altitudes along magnetic field lines. Those currents are then combined with a model of the ionospheric conductivity using a potential solver to obtain the ionospheric potential. The potential is mapped back to the inner boundary of the magnetosphere model where it is used to set the convection velocities at that altitude. This general approach is used by the Block Adaptive Tree Solar-wind Roe Upwind Scheme (BATS-R-US) code in the Space Weather Modeling Framework (SWMF) [*Ridley et al.*, 2004], the Lyon-Fedder-Mobbary (LFM) [*Wiltberger et al.*, 2004], OpenGGCM [*Raeder et al.*, 2001], and GUMICS [*Janhunen et al.*, 2012] codes. Although these models all follow the same general approach, there are significant differences in how the underlying conductance models are set.

Geospace Physics Laboratory, NASA Goddard Space Flight Center, Greenbelt, MD, USA

Magnetosphere-Ionosphere Coupling in the Solar System, Geophysical Monograph 222, First Edition.
Edited by Charles R. Chappell, Robert W. Schunk, Peter M. Banks, James L. Burch, and Richard M. Thorne.

Ionospheric outflows refer to the escape of ionospheric plasma into the magnetosphere. Compared to solar wind plasma, which primarily consists of protons, the ionosphere is capable of supplying both light and heavy ions. O^+ in particular is a clear marker of an ionospheric source and is seen to be a major factor in magnetospheric composition during geomagnetic storms [*Lennartsson et al.*, 1981; *Nosé et al.*, 2003]. The presence of O^+ in the magnetosphere has many system-wide consequences for the space environment. It can dominate the energy density and pressure in the ring current [*Moore et al.*, 2001; *Daglis et al.*, 1993; *Daglis et al.*, 1999; *Nosé et al.*, 2005], affect the ElectroMagnetic Ion Cyclotron (EMIC) wave growth rates and stop bands [*Kozyra et al.*, 1984; *Jordanova et al.*, 1996; *Thorne and Horne*, 1997], and can affect the reconnection rate [*Shay and Swisdak*, 2004]. Intriguingly, recent simulations by *Brambles et al.* [2011] indicate that ionospheric plasma could induce sawtooth oscillations. Clearly ionospheric outflows play an important role in understanding magnetospheric dynamics, but global models have neglected this critical source of plasma for many years. *Winglee* [1998] introduced the first model capable of tracking O^+ as a separate magnetospheric population, but it was more than a decade before other magnetospheric models introduced similar capabilities [*Glocer et al.*, 2009; *Wiltberger et al.*, 2010].

Approaches vastly differ when it comes to including ionospheric outflows, in contrast to the uniformity of approach seen in the electromagnetic coupling. The most straightforward approach is to define a density at the inner boundary of the magnetosphere model and rely on diffusion and subsequent acceleration by centrifugal, $J \times B$, and pressure gradient to further accelerate the plasma. This is the approach used by *Winglee* [1998]. *Welling and Liemohn* [2014] study this "de-facto outflow" in detail and demonstrate that it can reproduce a reasonable spatial distribution and overall fluence. A more comprehensive approach is to use a first-principles based model of the ionospheric outflow and use the result of that model to set the density and velocity boundary conditions for each species in the magnetosphere model. Such an approach was first used by *Glocer et al.* [2009a] and in subsequent studies by *Welling et al.* [2011] and *Ilie et al.* [2013]. First-principles based models of ionospheric outflow operate in the so-called "gap region" between the ionosphere and magnetosphere. This region spans the altitude range between the upper boundary of most ionospheric codes (around 500 kilometers [km]) and the inner boundary of most magnetospheric codes (1.5Re).

Another approach is to use an empirical specification for including ionospheric outflows that accounts for spatial and temporal variations but dispenses with the challenges inherent in modeling the underlying physical processes. This approach takes an empirical specification relating either soft electron precipitation or Poynting flux and ionospheric outflow fluxes [e.g., *Zheng et al.*, 2005; *Strangeway, et al.*, 2005] and then makes a decision about how to partition the flux into density and velocity to use as magnetospheric boundary conditions for the ion species [e.g., *Fok et al.*, 2006; *Gagne*, 2005; *Brambles et al.*, 2011]. Both of these methods for including ionospheric outflow into a model of the global magnetosphere have one thing in common: each method treats the outflow as a problem that ultimately requires only specification of a density and velocity on the inner boundary of the magnetosphere. Most critically, there are currently no attempts to include pitch-angle anisotropy, a direct consequence of transverse heating by wave-particle interactions, when merging representations of ionospheric outflow into magnetospheric models.

In this paper we describe a new approach to account for the neglected role of transverse heating due to wave-particle interactions in M-I coupling. In Section 14.2, we describe the issues related to including this physical process. We then suggest a new paradigm for including outflow into global models of the magnetosphere that accounts for the heating, the associated pitch-angle anisotropy, and the consequences for acceleration. We further demonstrate a proof of concept of this approach. Finally, Section 14.3 discusses the benefits and shortcomings of the proposed approach.

15.2. INCLUDING WAVE-PARTICLE INTERACTIONS WHEN MERGING OUTFLOW WITH A MAGNETOSPHERE MODEL

Wave-particle interactions play a role in the acceleration of plasma in the high-latitude, high-altitude polar region. For example, waves affect the outflow solution through the ponderomotive force of Alfvén waves [*Li and Temerin*, 1993; *Guglielmi et al.*, 1996; *Khazanov et al.*, 1998]. Ponderomotive forces are intrinsically included in the MHD equations used in most magnetosphere models of Earth as well as some models of ionospheric outflow. Resonant wave-particle interactions with intense low-frequency auroral zone turbulence can cause heating transverse to the magnetic field and leading to ion conics [e.g., *Retterer et al.*, 1987; *Crew et al.*, 1990; *Barghouthi*, 1997; *Bouhram et al.*, 2003; *Waara et al.*, 2011]. Unlike ponderomotive forces, there is currently no global coupled M-I model that accounts for resonant wave-particle interactions as part of a first-principles outflow calculation.

Although transverse heating due to wave-particle interactions is not accounted for in magnetosphere models, they are treated by some models of the ionospheric outflow. In particular, *Barakat and Schunk* [2001] use a hybrid modeling approach to treat outflow along

individual field lines convecting through the polar region (with macroscopic ion as particles and a Boltzmann relation for electrons). They include the transverse heating due to wave-particle interactions using a Monte Carlo approach, which randomly perturbs the perpendicular velocity at a rate consistent with the quasi-linear diffusion approximation given by *Retterer et al.* [1987]. Appropriate diffusion rates are determined for each outflow region (polar cap, aurora, and cusp) by estimating the spectral density for each region based on Dynamics Explorer data [*Barghouthi*, 1997]. In their study, *Barakat and Schunk* [2001] found that transverse heating is very large and grows with altitude. Indeed, the majority of the heating manifests itself above an altitude of 1.5 Earth radii (Re), the nominal inner boundary used in most magnetosphere models.

The transverse heating spans altitudes covered by both ionospheric outflow and magnetosphere models. Therefore, the process cannot be left to only the ionospheric outflow calculation but must be included in the magnetosphere model. However, MHD models of the magnetosphere are isotropic and therefore ill-equipped to incorporate such heating terms; there is only a scalar pressure and no equivalent of the mirror force in the ideal MHD momentum equations. The inclusion of wave-particle heating terms in the magnetosphere therefore requires an approach that includes pitch-angle anisotropy. Hybrid or particle in cell (PIC) models of the magnetosphere can naturally handle pitch-angle anisotropy but are currently too computationally expensive for regular simulations of an Earth-sized magnetosphere. Anisotropic MHD [*Meng et al.*, 2012] is perhaps the minimum set of physical equations that can be used to model the magnetosphere and still include transverse heating resulting from wave-particle interactions. In this case, a wave heating term must be added to the perpendicular pressure equation to reflect the effect of the wave-particle interactions. The excess random perpendicular motion is converted into organized parallel motion via the following term in the momentum equation:

$$\nabla \cdot \left[\left(p_{\parallel} - p_{\perp} \right) \mathbf{bb} \right] \tag{15.1}$$

where $p_{\parallel}$ is the parallel pressure, $p_{\perp}$ is the perpendicular pressure, and **b** is the magnetic field unit vector. This term acts like a mirror force and approximates the folding and acceleration of a perpendicularly heated distribution. It should be noted that there is no similar term in the ideal MHD equations.

There is still the problem of how to specify the appropriate wave heating rate. Unfortunately, there is no known way to compute the plasma heating rate from magnetospheric conditions using a physical model. Short of a physical model that includes the turbulence that results in heating, we have to rely on an empirical specification; the latter was done in the study of *Barakat and Schunk* [2001] detailed above. A similar approach can be used in a fluid model of the magnetosphere by averaging the perpendicular perturbation resulting from quasi-linear diffusion. This yields:

$$\langle \delta p_{\perp} / \delta t \rangle = \rho \langle (\Delta v_{\perp})^2 \rangle \approx 4 \rho D \tag{15.2}$$

$\langle \delta p_{\perp} / \delta t \rangle$ is the source term for the perpendicular pressure equation that represents the effect of the waves, ρ is the mass density, $\langle (\Delta v_{\perp})^2 \rangle$ is the average of the square of the perpendicular velocity perturbation over velocity space due to the effect of waves, and D is the quasilinear diffusion rate. Values of D are given for each region in *Barakat and Schunk* [2001]. To apply this term in the magnetosphere requires knowledge of the magnetic connectivity at each grid point (connected to polar cap, aurora, or cusp). Because the empirical specification is only valid for points magnetically connected to these three regions, the wave heating region must be restricted spatially to avoid including regions where the empirical specification is not valid. This means that every point in the magnetosphere domain must be frequently traced to determine if it is magnetically connected to the polar cap, aurora, or cusp. Frequent tracing of every magnetospheric grid point to determine connectivity is a daunting proposition given that magnetospheric simulations frequently have tens of millions of computational cells. Fortunately, this part of the problem has already been solved; many global magnetosphere models are coupled with ring inner magnetosphere model coupling to the global MHD code [*Glocer et al.*, 2009] can be directly applied to determining magnetic connectivity for setting the wave heating. The same parallel field line tracing algorithms used in the SWMF to handle the ring current coupling [*Glocer et al.*, 2009b] can be directly applied to determining magnetic connectivity for setting the wave heating.

From this discussion we draw two important conclusions:

1. Transverse heating due to wave-particle interactions is a process that spans spatial domains of the gap region in which ionospheric outflow models operate and the magnetospheric model domain. Therefore, the current paradigms which rely on the outflow model to only specify densities and velocities at the magnetosphere boundary are insufficient to correctly account for this process.

2. A magnetosphere model that can include the associated wave-heating terms, and accept transversely accelerated populations from the outflow model, must account for pitch-angle anisotropy.

Given these conclusions, we propose a new coupling paradigm.

15.2.1. A New Paradigm for M-I Coupling With Outflow: Including Transverse Heating

The fundamental features of the new coupling approach follow: (1) Pitch-angle anisotropy should be captured, 2) The entire domain over which transverse heating from wave-particle interactions occurs is captured, and 3) Transverse heating is included over a three-dimensional domain that includes the magnetosphere.

The coupling paradigm is described in the following steps:

- The chosen outflow model provides density, velocity, and parallel and perpendicular pressures to set the inner boundary condition of the anisotropic MHD model (or an alternate model that accounts for pitch-angle anisotropy).
- If the outflow model does not include pitch-angle anisotropy, or does not include wave-particle interactions, the anisotropic MHD boundary is moved down to an altitude below where the main heating occurs (<1 Re).
- Each point in the magnetosphere would need to trace along the magnetic field back to the ionosphere to determine the type of heating terms to apply locally (cusp, polar cap, aurora).
- The heating term is then applied to each point.

Figure 15.1 summarizes the above algorithm showing the values that must be passed from the outflow model to the magnetosphere model, and how a point in the magnetosphere (the red dot) is traced back to the ionosphere to determine the heating type to be used. One method is given in the previous section for specifying the heating term, but the basic coupling idea works for terms with different forms. Note, a consistent heating term should be used in both the outflow model and the magnetosphere code.

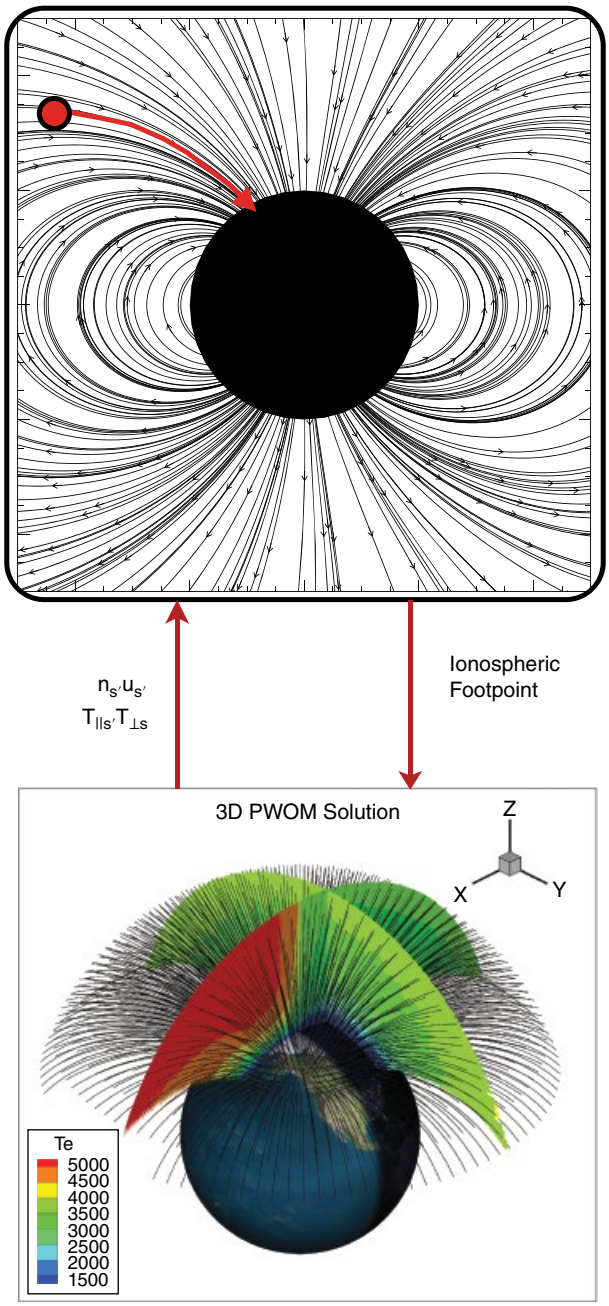

Figure 15.1 A schamic depiction of the proposed coupling paradigm. The outflow model provides boundaries for the magnetosphere, and then each point in the magnetosphere model must determine the appropriate wave heating description by mapping along magnetic field lines back to the ionosphere to determine if heating values appropriate to cusp, polar cap, or aurora should be used.

15.2.2. Proof of Concept

We demonstrate the feasibility of the proposed coupling approach using the following simplified configuration. The most basic outflow model is assumed, that is, setting a constant density and zero velocity at the inner boundary (see discussion in the introduction). The anisotropic MHD version of BATS-R-US simulation is used with the inner boundary moved down to 1 Re altitude to better capture the wave acceleration region. The simulation applies the transverse heating terms from wave-particle interactions (discussed earlier) in the red region shown in Figure 15.2. Heating terms appropriate for the cusp are used everywhere in this region in order to demonstrate maximum effectiveness of the waves. A grid resolution of 1/16 Re is used in this region to better capture the heating. Nominal solar wind conditions with a density of $5\,cm^{-3}$, a velocity of 400 km/s, and an IMF of constant southward magnetic field of 5 nT is used. This simulation is the most basic implementation of the proposed coupling paradigm and serves as a proof of concept that the proposed approach can successfully include the transverse heating missing from previous approaches of coupling ionospheric outflows with global magnetosphere models.

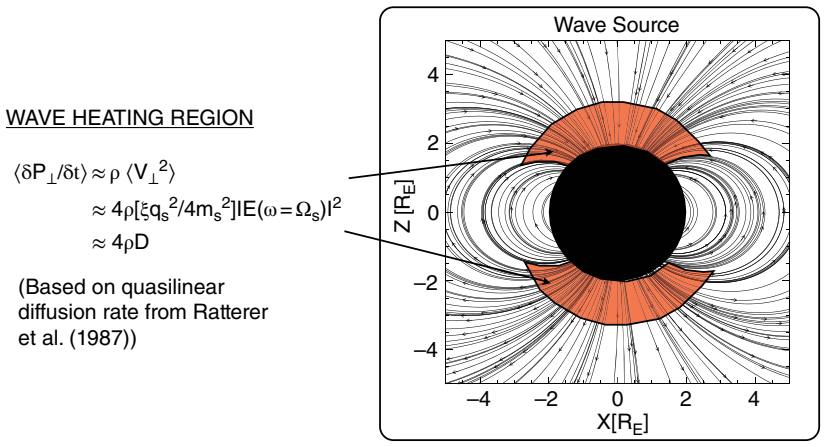

Figure 15.2 A depiction of the wave heating region imposed in our proof of concept test.

We note that the wave acceleration region is often below 1 Re altitude, but lowering the inner boundary further while maintaining an adequate spatial resolution and reasonable time step is challenging for the three-dimensional magnetospheric model. A more complete test would be to include an outflow model with both anisotropy and wave-particle interactions to handle the region below 1 Re. Nevertheless, the current test is sufficient to demonstrate that the proposed approach enables the magnetosphere model to participate in including the effects of wave-particle interactions, and what the general effects of those interactions would look like.

Figure 15.3 presents the results from two simulations. The left panels show a control case when wave heating is not included, and the right panels show the case when wave heating is included. The $y = 0$ Geocentric Solar Magnetospheric (GSM) plane is shown. The top plots present the pressure anisotropy defined by

$$\frac{p_{\parallel} - p_{\perp}}{p_{\parallel} + p_{\perp}}$$

The bottom plots present the field-aligned velocity. As expected, significant pressure anisotropy forms over the poles, and large outflow velocities are generated by the mirror force when the transverse heating is included. Further from the planet, where the outflow velocities are greatest, the anisotropy relaxes to isotropy as the mirror force folds the distribution function. We note that the velocities at 2 Re altitude in the control case are significantly higher than those typically observed; however, the purpose of the control run is to provide a basis for comparison for our concept that is qualitatively valid but not necessarily quantitatively accurate.

The effect of the waves is clearly exaggerated in this case as we chose heating terms most appropriate to cusp, where the waves are strongest, and imposed them over the entire polar region. In reality, the anisotropy would be weaker, more localized, and generate weaker outflow velocities. Specifically, the wave-particle interactions should be included in the aurora, cusp, and polar cap [*Barakat and Schunk*, 2001] with the strongest wave heating in the cusp and aurora. The simulation presented covers those regions together with the strongest heating term applied throughout. As a result, this demonstration shows the maximum conceivable effectiveness of the waves. Choosing such strong transverse heating terms demonstrates that the code can withstand very strong wave terms, and further illustrates how the solution is expected to respond to the inclusion of wave-particle interactions. Most importantly, the results show the wave-particle interactions need not be relegated to the outflow calculation but can be included in the magnetosphere model as well.

15.3. CONCLUSION

The existence of outflows of ionospheric plasma to the magnetosphere along open magnetic field lines was first suggested by *Axford* [1968] and *Banks and Holzer* [1968]. Later observations by the Explorer 31 and Instrument Suite and Integrated Science (ISIS) 2 satellites [*Hoffman*, 1970; *Brinton et al.*, 1971; *Hoffman et al.*, 1974] confirmed those predictions. The presence of O^+ outflows seen by DE-1 [*Nagai et al.*, 1984; *Waite et al.*, 1985] is an important indicator that processes beyond the classical polar wind mechanism, such as the effects of superthermal electrons [e.g., *Tam et al.*, 1995], field-aligned currents (FAC) [*Gombosi and Nagy*, 1989], ponderomotive interaction with waves [e.g., *Khazanov et al.*, 2000], and transverse heating due to wave-particle interactions [e.g., *Retterer et al.*, 1987] are at work. Determining the relative effectiveness of these competing pathways is a significant challenge that coupled models of the magnetosphere and ionosphere have only just begun to grapple with.

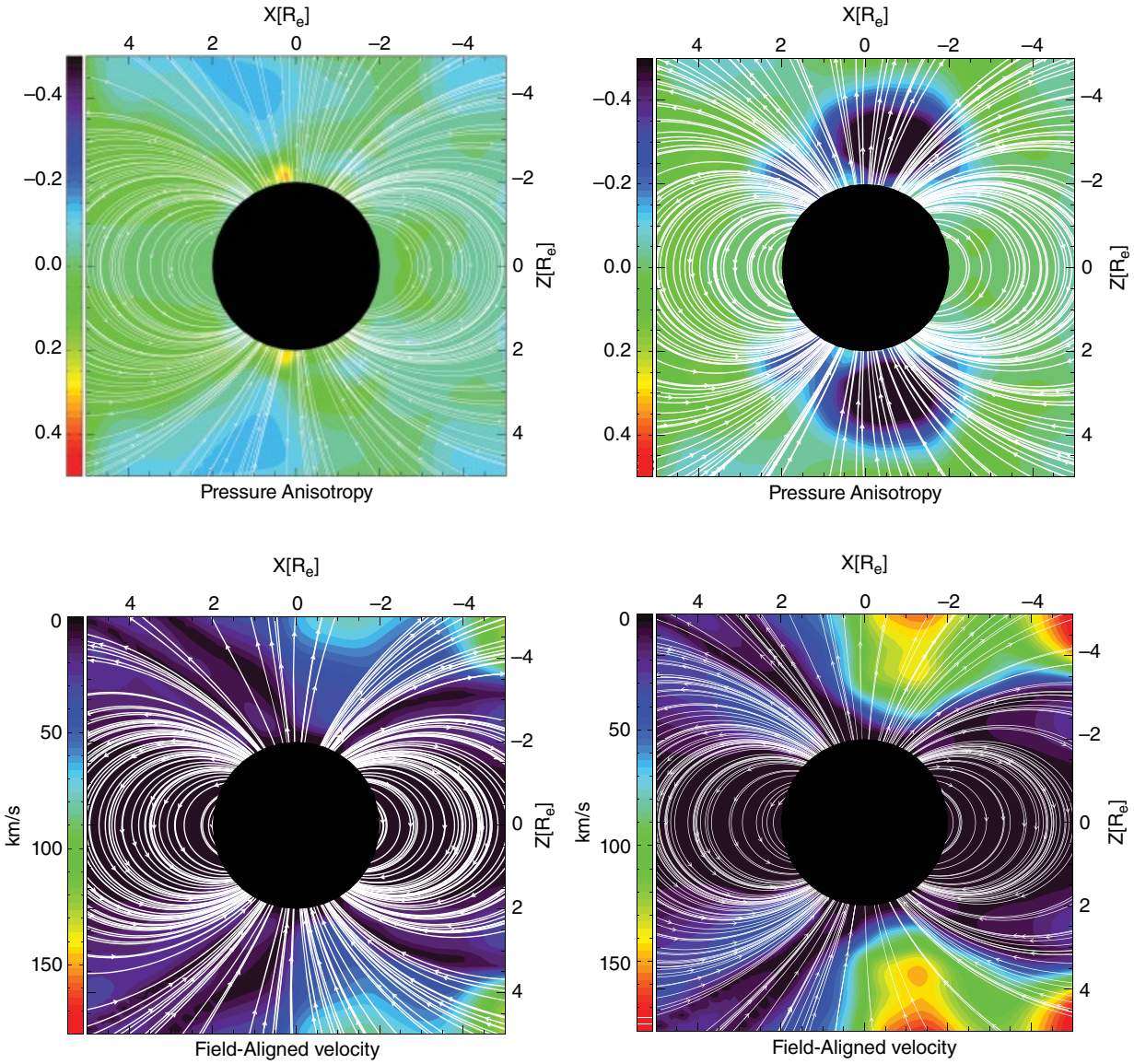

Figure 15.3 Results of our proof of concept with the control case (no wave heating) on the left, and with wave heating on the right. The top plots are pressure anisotropy (0 is isotropic, positive tends towards parallel, and negative tends toward perpendicular). The bottom plots depict the field aligned velocities. Inclusion of wave heating creates strong anisotropies and outflow velocities.

This paper focused on the treatment of transverse heating due to wave-particle interactions when merging ionospheric outflows with global models of the magnetosphere. DE observations show that the spectral density of the waves is constant or increases with altitude [*Gurnett et al.*, 1984]. Applying the associated transverse heating in models gives heating at altitudes extending well into the magnetosphere domain *Barakat and Schunk* [2001]. We therefore conclude that the inclusion of this type of wave-particle interaction cannot be left solely to the model or representation of ionospheric outflow, but the magnetospheric model must include the interaction as well. Magnetosphere models based on MHD or multifluid MHD are inherently unable to account for this physical process as they assume isotropic pitch-angle distributions and so cannot include a perpendicular heating term or a mirror force. Moreover, the coupling paradigm, where all that is needed is to set the state variables at the inner boundary of the magnetosphere model, is insufficient because a consistent wave representation needs to be incorporated.

We presented a new coupling paradigm that incorporates transverse wave heating into merged models of ionospheric outflow as well and presented a proof of concept. Our demonstration using an extreme representation of the waves showed that the approach is feasible. Where the wave heating terms are strong, significant anisotropies will form, and a mirror force will generate strong flows and isotropize the distribution away from the heating region. This approach can work for a wide variety of wave representations and for any outflow representation either empirical or first principles.

The coupling paradigm we describe is a step toward a more complete representation of ionospheric outflows in coupled models of the magnetosphere and ionosphere, but there is still much to do. In our demonstration we only use anisotropic MHD, which has the advantage that it includes pitch-angle anisotropy, but is actually a step backward in that it cannot track ion species independently as multifluid MHD can do. Anisotropic MHD can only be used to look at the combined outflow, but future work would have to move to multifluid anisotropic MHD.

The most glaring issue in our coupling approach is the lack of reliable wave heating representations. We proposed using the representation from *Barakat and Schunk* [2001] adapted to a fluid description. That relies ultimately on an empirical representation of the spectral density that may not be appropriate in every case. One path forward is the generation of new empirical representations, however no empirical representation of the waves can ever complete the physical model of magnetosphere-ionosphere coupling as the waves generated would not be consistent with plasma parameters calculated by the model. An alternative way forward involves bringing to bear a local plasma physics model that derives the wave spectral density and spatial distribution from the plasma conditions calculated by a global model. This problem has an interesting analogy with the approach used to calculate EMIC wave amplitudes in the inner magnetosphere. In that situation there is a ring current model capable of calculating the pressure anisotropy that provides the free energy for EMIC wave generation but does not include physics required to calculate the wave amplitudes without relying on an empirical relationship [e.g., *Kozyra et al.*, 1997]. It is possible, however, to use a hybrid model to conduct local physics simulations to derive relationships between the parameters calculated the ring current model and the ultimate wave amplitudes generated [*Bortnik et al.*, 2011]. Future investigations could employ a similar approach to attempt to connect the local parameters calculated by global model with wave growth. Fortunately, new representations of the waves can be incorporated into the proposed coupling approach as they become available from either improved empirical specification or from a more physics based approach.

ACKNOWLEDGMENTS

Resources supporting this work were provided by the NASA High-End Computing (HEC) Program through the NASA Advanced Supercomputing (NAS) Division at Ames Research Center and the NASA Center for Climate Simulation (NCCS) at Goddard Space Flight Center. A. Glocer was supported by the NASA Geospace Supporting Research and Technology (SR&T) Program.

REFERENCES

Axford, W. I. (1968), The polar wind and the terrestrial helium budget, *J. Geophys. Res.*, *73*, 68,55.

Banks, P. M., and T. E. Holzer (1968), The Polar Wind, *J. Geophys. Res.*, *73*, 6846–6854, doi:10.1029/JA073i021p06846.

Barakat, A. R., and R. W. Schunk (2001), Effects of wave-particle interactions on the dynamic behavior of the generalized polar wind, *Journal of Atmospheric and Solar-Terrestrial Physics*, *63*, 75–83, doi:10.1016/S1364-6826(00)00106-1.

Barghouthi, I. A. (1997), Effects of wave-particle interactions on H^+ and O^+ outflow at high latitude: A comparative study, *J. Geophys. Res.*, *102*, 22,065–22,076, doi:10.1029/96JA03293.

Bortnik, J., N. Omidi, L. Chen, R. M. Thorne, and R. B. Horne (2011), Saturation characteristics of electromagnetic ion cyclotron waves, *Journal of Geophysical Research (Space Physics)*, *116*, A09219, doi:10.1029/2011JA016638.

Bouhram, M., M. Malingre, J. R. Jasperse, and N. Dubouloz (2003), Modeling transverse heating and outflow of ionospheric ions from the dayside cusp/cleft. 1 A parametric study, *Annales Geophysicae*, *21*, 1753.

Brambles, O. J., W. Lotko, B. Zhang, M. Wiltberger, J. Lyon, and R. J. Strangeway (2011), Magnetosphere Sawtooth Oscillations Induced by Ionospheric Outflow, *Science*, *332*(6034), 1183–1186.

Brinton, H. C., J. M. Grebowsky, and H. G. Mayr (1971), Altitude Variation of Ion Composition in the Midlatitude Trough Region: Evidence for Upward Plasma Flow, *J. Geophys. Res.*, *76*, 3738–3745, doi:10.1029/JA076i016p03738.

Crew, G. B., T. Chang, J. M. Retterer, W. K. Peterson, and D. A. Gurnett (1990), Ion cyclotron resonance heated conics - Theory and observations, *J. Geophys. Res.*, *95*, 3959.

Daglis, I. A., E. T. Sarris, and B. Wilken (1993), AMPTE/CCE CHEM observations of the energetic ion population at geosynchronous altitudes, *Annales Geophysicae*, *11*, 685–696.

Daglis, I. A., R. M. Thorne, W. Baumjohann, and S. Orsini (1999), The terrestrial ring current: Origin, formation, and decay, *Reviews of Geophysics*, *37*, 407, doi:10.1029/1999RG900009, (c) 1999: American Geophysical Union.

Fok, M., T. E. Moore, P. C. Brandt, D. C. Delcourt, S. P. Slinker, and J. A. Fedder (2006), Impulsive enhancements of oxygen ions during substorms, *Journal of Geophysical Research (Space Physics)*, *111*, 10,222−+, doi:10.1029/2006JA011839.

Gagne, J. (2005), Implementation of ionospheric outflow in the lfm global mhd magnetospheric simulation, Ph.D. thesis, Dartmouth College.

Glocer, A., G. Téth, Y. Ma, T. Gombosi, J.-C. Zhang, and L. M. Kistler (2009), Multifluid Block-Adaptive-Tree Solar wind

Roe-type Upwind Scheme: Magnetospheric composition and dynamics during geomagnetic storms, Initial results, *Journal of Geophysical Research (Space Physics)*, *114* (A13), A12203, doi:10.1029/2009JA014418.

Glocer, A., G. Téth, T. Gombosi, and D. Welling (2009a), Modeling ionospheric outflows and their impact on the magnetosphere, initial results, *J. Geophys. Res.*, *114* (A05216), doi:10.1029/2009JA014053.

Glocer, A., G. Toth, M. Fok, T. Gombosi, and M. Liemohn (2009b), Integration of the radiation belt environment model into the space weather modeling framework, *Journal of Atmospheric and Solar-Terrestrial Physics*, *71*, 1653–1663, doi:10.1016/j.jastp.2009.01.003.

Glocer, A., M. Fok, X. Meng, G. Toth, N. Buzulukova, S. Chen, and K. Lin (2013), CRCM + BATS-R-US two-way coupling, *Journal of Geophysical Research (Space Physics)*, *118*, 1635–1650, doi:10.1002/jgra.50221.

Gombosi, T. I., and A. Nagy (1989), Time-dependent modeling of field aligned current-generated ion transients in the polar wind, *J. Geophys. Res.*, *94*, 359–369.

Guglielmi, A., J. Kangas, K. Mursula, T. Pikkarainen, O. Pokhotelov, and A. Potapov (1996), Pc 1 induced electromagnetic lift of background plasma in the magnetosphere, *J. Geophys. Res.*, *101*, 21,493–21,500, doi:10.1029/96JA01750.

Gurnett, D. A., R. L. Huff, J. D. Menietti, J. L. Burch, J. D. Winningham, and S. D. Shawhan (1984), Correlated low-frequency electric and magnetic noise along the auroral field lines, *J. Geophys. Res.*, *89*, 8971–8985, doi:10.1029/JA089iA10p08971.

Hoffman, J. H. (1970), Studies of the composition of the ionosphere with a magnetic deflection mass spectrometer, *Int. J. Mass Spectrom. Ion Phys.*, *4* (315).

Hoffman, J. H., W. H. Dodson, C. R. Lippincott, and H. D. Hammack (1974), Initial ion composition results from the Isis 2 satellite, *J. Geophys. Res.*, *79*, 4246–4251, doi:10.1029/JA079i028p04246.

Ilie, R., R. M. Skoug, P. Valek, H. O. Funsten, and A. Glocer (2013), Global view of inner magnetosphere composition during storm time, *Journal of Geophysical Research (Space Physics)*, *118*, 7074–7084, doi:10.1002/2012JA018468.

Janhunen, P., M. Palmroth, T. Laitinen, I. Honkonen, L. Juusola, G. Facskó, and T. I. Pulkkinen (2012), The GUMICS-4 global MHD magnetosphere-ionosphere coupling simulation, *Journal of Atmospheric and Solar-Terrestrial Physics*, *80*, 48–59, doi:10.1016/j.jastp.2012.03.006.

Jordanova, V., L. Kistler, J. Kozyra, G. Khazanov, and A. Nagy (1996), Collisional losses of ring current ions, *J. Geophys. Res.*, *101*, 111.

Khazanov, G. V., M. W. Liemohn, E. N. Krivorutsky, and T. E. Moore (1998), Generalized kinetic description of a plasma in an arbitrary field-aligned potential energy structure, *J. Geophys. Res.*, *103*, 6871–6890, doi:10.1029/97JA03436.

Khazanov, G. V., I. K. Khabibrakhmanov, and E. N. Krivorutsky (2000), Interaction between an Alfvén wave and a particle undergoing acceleration along a magnetic field, *Physics of Plasmas*, *7*, 1.

Kozyra, J. U., T. E. Cravens, A. F. Nagy, E. G. Fontheim, and R. S. B. Ong (1984), Effects of energetic heavy ions on electromagnetic ion cyclotron wave generation in the plasmapause region, *J. Geophys. Res.*, *89*, 2217–2233, doi:10.1029/JA089iA04p02217.

Kozyra, J. U., V. K. Jordanova, R. Horne, and R. M. Thorne (1997), Modeling of the contribution of electromagnetic ion cyclotron (EMIC) waves to stormtime ring current erosion, *American Geophysical Union Geophysical Monograph Series*, *98*, 187.

Lennartsson, W., R. D. Sharp, E. G. Shelley, R. G. Johnson, and H. Balsiger (1981), Ion composition and energy distribution during 10 magnetic storms, *J. Geophys. Res.*, *86*, 4628–4638, doi:10.1029/JA086iA06p04628.

Li, X., and M. Temerin (1993), Ponderomotive effects on ion acceleration in the auroral zone, *Geophys. Res. Lett.*, *20*, 13–16, doi:10.1029/92GL03011.

Meng, X., G. Téth, M. W. Liemohn, T. I. Gombosi, and A. Runov (2012), Pressure anisotropy in global magnetospheric simulations: A magnetohydrodynamics model, *Journal of Geophysical Research (Space Physics)*, *117*, 8216, doi:10.1029/2012JA017791.

Moore, T. E., M. O. Chandler, M.-C. Fok, B. L. Giles, D. C. Delcourt, J. L. Horwitz, and C. J. Pollock (2001), Ring Currents and Internal Plasma Sources, *Space Science Reviews*, *95*, 555–568.

Nagai, T., J. H. Waite, Jr., J. L. Green, C. R. Chappell, R. C. Olsen, and R. H. Comfort (1984), First measurements of supersonic polar wind in the polar magnetosphere, *Geophys. Res. Lett*, *11*, 669–672, doi:10.1029/GL011i007p00669.

Nosé, M., R. W. McEntire, and S. P. Christon (2003), Change of the plasma sheet ion composition during magnetic storm development observed by the Geotail spacecraft, *Journal of Geophysical Research (Space Physics)*, *108*, 1201, doi:10.1029/2002JA009660.

Nosé, M., S. Taguchi, K. Hosokawa, S. P. Christon, R. W. McEntire, T. E. Moore, and M. R. Collier (2005), Overwhelming O^+ contribution to the plasma sheet energy density during the October 2003 superstorm: Geotail/EPIC and IMAGE/LENA observations, *Journal of Geophysical Research (Space Physics)*, *110*, 9, doi:10.1029/2004JA010930.

Raeder, J., et al. (2001), Global simulation of the Geospace Environment Modeling sub-storm challenge event, *J. Geophys. Res.*, *106*, 281.

Retterer, J. M., T. Chang, G. B. Crew, J. R. Jasperse, and J. D. Winningham (1987), Monte Carlo modeling of ionospheric oxygen acceleration by cyclotron resonance with broad-band electromagnetic turbulence, *Physical Review Letters*, *59*, 148–151, doi: 10.1103/PhysRevLett.59.148.

Ridley, A. J., T. I. Gombosi, and D. L. De Zeeuw (2004), Ionospheric control of the magnetosphere: Conductance, *Ann. Geophys.*, *22*, 567–584.

Shay, M. A., and M. Swisdak (2004), Three-Species Collisionless Reconnection: Effect of O^+ on Magnetotail Reconnection, *Physical Review Letters*, *93*(17), 175,001−+, doi:10.1103/PhysRevLett.93.175001.

Strangeway, R. J., R. E. Ergun, Y.-J. Su, C. W. Carlson, and R. C. Elphic (2005), Factors controlling ionospheric outflows as observed at intermediate altitudes, *Journal of Geophysical Research (Space Physics)*, *110*, 3221, doi:10.1029/2004JA010829.

Tam, S. W. Y., F. Yasseen, T. Chang, and S. B. Ganguli (1995), Self-consistent kinetic photoelectron effects on the polar wind, *Geophys. Res. Lett.*, *22*, 2107–2110, doi: 10.1029/95GL01846.

Thorne, R. M., and R. B. Horne (1997), Modulation of electromagnetic ion cyclotron instability due to interaction with ring current O^+ during magnetic storms, *J. Geophys. Res.*, *102*, 14,155–14,164, doi:10.1029/96JA04019.

Waara, M., R. Slapak, H. Nilsson, G. Stenberg, M. André, and I. A. Barghouthi (2011), Statistical evidence for O^+ energization and outflow caused by wave-particle interaction in the high altitude cusp and mantle, *Annales Geophysicae*, *29*, 945–954, doi: 10.5194/angeo-29-945-2011.

Waite, J. H., Jr., et al. (1985), Escape of suprathermal O^+ ions in the polar cap, *J. Geophys. Res.*, *90*, 1619–1630, doi:10.1029/JA090iA02p01619.

Welling, D. T., and M. W. Liemohn (2014), Outflow in global magnetohydrodynamics as a function of a passive inner boundary source, *Journal of Geophysical Research (Space Physics)*, *119*, 2691–2705, doi:10.1002/2013JA019374.

Welling, D. T., V. K. Jordanova, S. G. Zaharia, A. Glocer, and G. Toth (2011), The effects of dynamic ionospheric outflow on the ring current, *Journal of Geophysical Research (Space Physics)*, *116*, A00J19, doi:10.1029/2010JA015642.

Wiltberger, M., W. Wang, A. Burns, S. Solomon, J. Lyon, and C. Goodrich (2004), Initial results from the coupled magnetosphere ionosphere thermosphere model: magnetospheric and ionospheric responses, *Journal of Atmospheric and Solar-Terrestrial Physics*, *66*, 1411–1423.

Wiltberger, M., W. Lotko, J. G. Lyon, P. Damiano, and V. Merkin (2010), Influence of cusp O^+ outflow on magnetotail dynamics in a multifluid MHD model of the magnetosphere, *Journal of Geophysical Research (Space Physics)*, *115*, A00J05, doi: 10.1029/2010JA015579.

Winglee, R. M. (1998), Multi-fluid simulations of the magnetosphere: The identification of the geopause and its variation with IMF, *Geophys. Res. Lett.*, *25*, 4441–4444, doi: 10.1029/1998GL900217.

Zheng, Y., T. E. Moore, F. S. Mozer, C. T. Russell, and R. J. Strangeway (2005), Polar study of ionospheric ion outflow versus energy input, *Journal of Geophysical Research (Space Physics)*, *110*, 7210−+, doi:10.1029/2004JA010995.

16

Modeling of the Evolution of Storm-Enhanced Density Plume during the 24 to 25 October 2011 Geomagnetic Storm

Shasha Zou and Aaron J. Ridley

Video of Yosemite Talk, URL: http://dx.doi.org/10.15142/T37G6M

ABSTRACT

The global ionosphere and thermosphere model (GITM) has been used to study the formation of the storm-enhanced density (SED) plume during the 24 to 25 October 2011 geomagnetic storm. Simulation results suggest that plasmas originating from both dawn and dusk sectors are able to contribute to the formation of the SED plume. However, the ionospheric plasmas originating from different local time sectors have very different properties, such as the F-layer peak density N_mF_2 and the peak height h_mF_2. Plasmas originating from the dawn sector exhibit slow but steady increase in h_mF_2, N_mF_2, and the total electron content (TEC), while those from the dusk sector experience more steep increase and decrease in h_mF_2 and TEC. This suggests that the h_mF_2 together with the TEC value might provide a means for understanding the origin of the plasmas that contribute to formation of the SED plumes. In addition, the simulation results show that the pressure gradient below the F-layer peak increases within the plumes, and the thermospheric wind significantly increases during the plume decay phase, consistent with the previous explanation of the plume decay based on incoherent scatter radar measurements.

16.1. INTRODUCTION

During enhanced convection periods, in particular geomagnetic storms, a ridge of enhanced ionospheric density can form at the dayside subauroral and auroral latitudes as part of a much larger scale density increase, the so-called storm-enhanced density (SED) [e.g., *Foster,* 1993]. This ridge of high ionospheric density is often referred to as an SED plume, and is an important means of transporting high-density solar extreme ultraviolet (EUV) produced ionospheric plasmas into the polar cap and the nightside aurora region, where they might serve as a source of intense ion upflow/outflow [e.g., *Semeter et al.,* 2004; *Yuan et al.,* 2008; *Lotko,* 2007]. In recent years, our understanding of the formation of SEDs and associated SED plumes has been significantly deepened, largely benefitting from the global-scale ground-based TEC observations [e.g., *Mannucci et al.,* 2005; *Coster and Skone,* 2009; *Immel and Mannucci,* 2013], incoherent scatter radars [e.g., *Foster et al.,* 2005; *Huang et al.,* 2005; *Zou et al.,* 2013, 2014] as well as numerical simulations [e.g., *Heelis et al.,* 2009; *Sojka et al.,* 2012; *David et al.,* 2011].

The formation of SED and SED plumes during several recent intense geomagnetic storms has been studied in detail through analysis of data from multiple instruments, including ground-based incoherent scatter radar at Poker Flat (PFISR), GPS TEC, and Super Dual Auroral Radar Network (SuperDARN) [*Zou et al.,* 2013, 2014]. *Zou et al.* [2013] carried out a detailed case study of the 24 to 25 October 2011 storm and found that the SED plume formed during this event consisted of two

Department of Climate and Space Sciences and Engineering, University of Michigan, Ann Arbor, MI, USA

Magnetosphere-Ionosphere Coupling in the Solar System, Geophysical Monograph 222, First Edition.
Edited by Charles R. Chappell, Robert W. Schunk, Peter M. Banks, James L. Burch, and Richard M. Thorne.

parts with very different plasma characteristics. The first part was associated with northward convection flows with speeds of a couple of hundred m/s while the second part was associated with much larger northwestward convection flows with speeds close to ~2 km/s. In both parts, the convection flows had a large and persistent northward component, which lift the plasma to higher altitudes, due to the non-vertical geometry of the field line (~78° inclination angle at PFISR), where the charge exchange and recombination rates become smaller. In addition, the production was still ongoing in the sunlit regions. Both processes contributed to the TEC increase. This TEC increase mechanism has been studied using numerical models by *Heelis et al.* [2009] and *David et al.* [2011]. In a following study, *Zou et al.* [2014] found for the first time large downward field-aligned flows within the SED plume during the plume decay phase. It was suggested that both ambipolar diffusion and enhanced northward thermospheric wind contributed to the large downward field-aligned flows, and the plasma loss rate would increase at lower altitudes because of larger charge exchange and recombination rate.

Because of the long lifetime due to slow recombination and charge exchange processes, characteristics of the F-layer plasma observed by a ground-based radar at a certain time reflects not only the electrodynamics simultaneously occurring at that time but also that experienced by the plasma before reaching the radar's field-of-view. Therefore, a time-dependent ionosphere and thermosphere model is required to understand the origin of the plasma contributing to the SED plume. In this study, we apply GITM to study the formation of the SED plumes during the 24 to 25 October 2011 geomagnetic storm with focus on the plasma characteristics within the SED plume and their origins.

16.2. MODEL DESCRIPTION

GITM is a three-dimensional spherical code that models the Earth's thermosphere and ionosphere system using a stretched grid in latitude and altitude [*Ridley et al.,* 2006; *Deng et al.,* 2008a, 2008b; *Pawlowski and Ridley,* 2008, 2009]. GITM explicitly solves for the densities of various neutral species including $O(^3P)$, $O(^1D)$, O_2, $N(^2D)$, $N(^4S)$, N_2, and NO, the densities of different ion species including $O^+(^4S)$, $O^+(^2D)$, $O^+(^2P)$, O^+_2, N^+, N^+_2, and NO^+, three-dimensional neutral and ion velocities, and neutral, ion, and electron temperatures. One of the major differences between GITM and other models of the upper atmosphere is that altitude is used as the vertical coordinate as opposed to pressure. The altitude spacing is set to be approximately 1/3 of the neutral scale height, and the vertical domain is specified by setting the lower boundary and the number of grid points (50 in the present case). GITM has been run with a resolution of 1° in latitude and 2.5° in longitude uniform over the entire globe with 50 vertical levels, resulting in an altitude domain from ~100 to ~700 km. This high spatial resolution is particularly useful for the study of the SED plume, which could be quite narrow in its cross section. In this study, the *Weimer* [1996] electrodynamic potential pattern is used to drive the high-latitude ionospheric convection, and the auroral dynamics is specified using the Ovation-SM electron precipitation pattern [*Mitchell et al.,* 2013].

16.3. MODEL RESULTS

The solar wind and interplanetary magnetic field (IMF) observations from the ACE spacecraft during the 24 to 25 October 2011 geomagnetic storm are shown in Figure 16.1, together with the *Sym-H* index, which is an indicator of the ring current strength. The *Sym-H* minimum dipped below −150 nT, indicating that it is an intense geomagnetic storm. The solar wind and IMF observations have been dynamically propagated to the Earth's magnetopause based on the distance between the satellite and the magnetopause and the solar wind speed. The simulation was initiated from 21 October 2011, several days before the storm onset, allowing the model to relax to a quasi-steady state before the commencement of the storm.

Figure 16.2 shows a comparison of the TEC value between the storm time (red) and the quiet time (green) at the PFISR location. In Figure 16.2a, the GITM TEC values are averaged over three grid points (~7.5° in longitude) around PFISR and are shown by dots with the standard deviation of TEC denoted by the gray error bars. TEC values in GITM are calculated by integrating the electron density between ~100 to ~700 km. The quiet time GITM results (green dots) are saved every 30 min and are linearly interpolated to 5-minute time resolution in order to calculate the ratio shown in Figure 16.2c. The storm time GITM results (red dots) are saved every 5 min. In Figure 16.2b, the TEC values obtained from the madrigal database [*Rideout and Coster,* 2006] are also averaged over 6° longitudes around PFISR and are shown in red (green) with uncertainties denoted by light gray (darker gray) error bars. They are calculated using ground-based dual-frequency GPS receivers and represent the integrated electron densities from the ground to the GPS satellite altitude (~20,200 km). The ratios between the modeled TEC over the observed TEC during both quiet and storm times are shown in Figure 16.2b.

Overall, the modeled TEC values are of smaller magnitude than the observed ones as indicated by the less than unity ratios in Figure 16.2b. The averaged ratio over the plotting time period is ~0.78 during the quiet time and ~0.61 during the storm time, while the standard deviation of the ratio is ~0.08 during the quiet time and ~0.17 during the storm time. Underestimation of TEC values in GITM is partially due to the altitude of the GITM upper

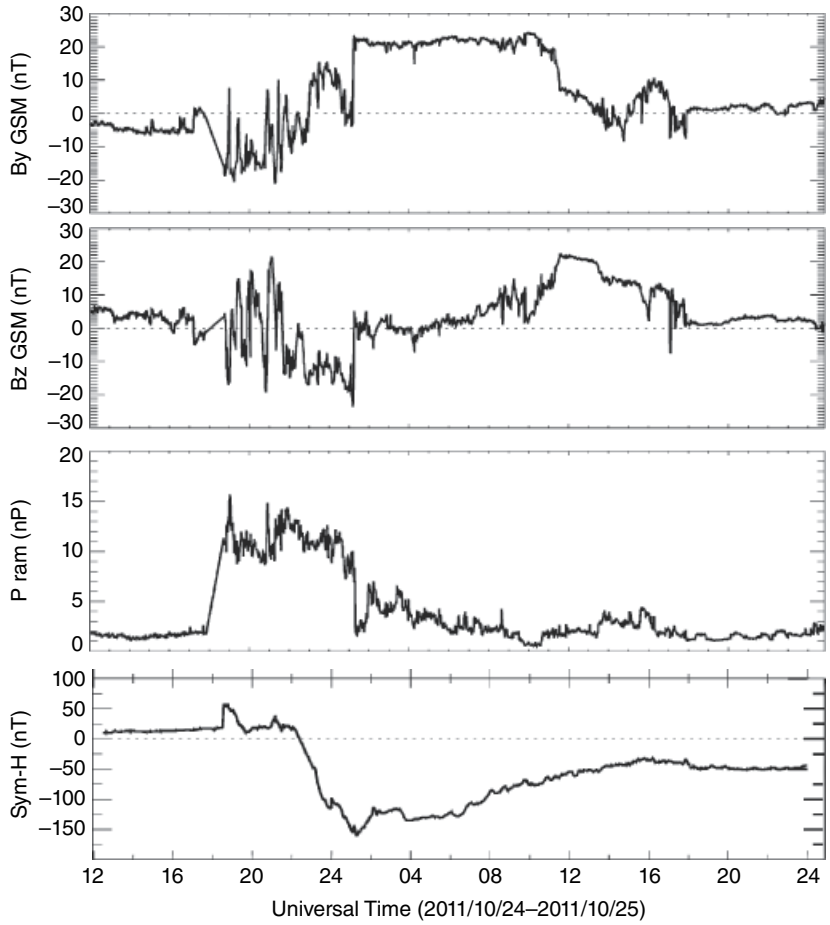

Figure 16.1 The IMF B_y, B_z in GSM coordinates and solar wind dynamic pressure observations from 12 UT on 24 October to 24 UT on 25 October 2011. The *Sym-H* index is also shown at the bottom panel.

boundary at ~700 km. The underestimation is particularly severe during storm time, that is, strong driving conditions, because the lifting of the ionosphere results in a large amount of plasmas moving out of the GITM simulation domain. However, GITM captured the basic quiet time diurnal variation and storm time TEC increase at the SED plume around 23 universal time (UT) on 24 October 2011, which is the focus of this paper.

GITM is a three-dimensional time-dependent fluid model driven, in part, by the high-latitude convection pattern. The contribution to the SED plume at a given time and given location can be studied by tracing a column of plasma backward in time. In addition, because the ion velocity within a column is altitude dependent due to decreased collisional frequencies between neutrals and plasmas at higher altitudes, the cumulative effect is that a selected column would become stretched over time and may no longer be a well-defined column if tracing backward for long periods of time. Therefore, in this study, we only trace the plasma backward for two hours.

The plasma characteristics of five columns near the center of the SED plume have been selected for detailed investigation. Their locations at 2320 UT, when the TEC within the plume reached its peak value, are shown as black filled diamonds in Figure 16.3a, and their locations about two hours earlier are shown in Figure 16.3b. In both plots, the background colors and contours represent the TEC values in the northern hemisphere above 40° latitude in geographic coordinates. Comparing the starting and ending locations of the plasma columns between the two plots clearly indicates that plasmas contributing to the SED plume can come from a wide range of latitudes and local times.

Time histories of the plasma characteristics, including TEC, the F-layer peak density (N_mF_2) and the F-layer peak density height (h_mF_2), of three selected columns, that is, from dusk, noon, and dawn sectors, are shown in Figure 16.4, respectively. The solid vertical lines at 2140 UT denote the time when the IMF turned southward, and the dotted vertical lines at 2220 UT mark the time when the IMF turned to weakly southward for about 20 min until 2240 UT. Plasmas originating from the dawn sector (right column) show slow but steady increase

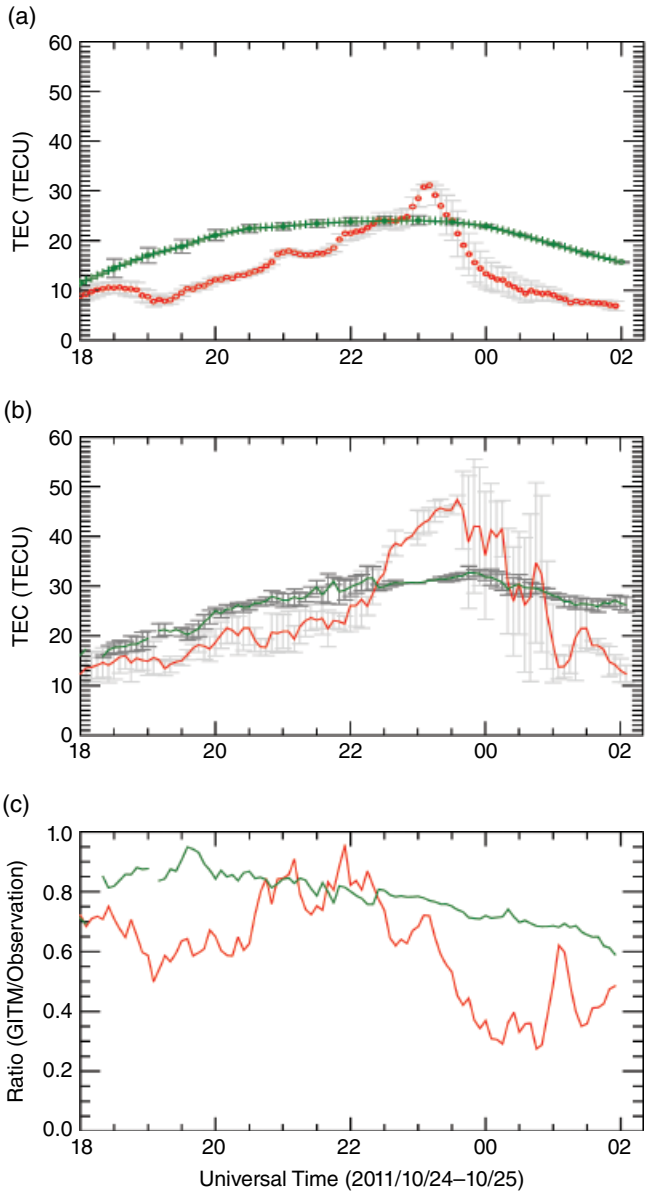

Figure 16.2 Comparisons between modeled and observed TEC values at PFISR location. Green and red curves indicate quiet and storm times, respectively. (a) TEC calculated using GITM results, which is the integration of electron density between ~100 to ~700 km. Error bars indicate the standard deviations of TECs within the three simulation grid points around PFISR longitude. (b) TEC values based on ground-based dual-frequency GPS receivers. Error bars indicate the standard deviations of TECs within 6° longitude around PFISR longitude. (c) The ratio between the modeled and the observed TEC values.

in N_mF_2, h_mF_2, and TEC. In contrast, the plasmas originating from the dusk sector (left column) exhibit much larger variations in those key parameters, including ~33% h_mF_2 change from ~300 to ~400 km within 15 mins and ~25% TEC change from ~24 to 30 TECU (1 TECU = 10^{16} m^{-2}) within 30 mins. Simulation results show that the initiation of the h_mF_2 variations on the duskside responds to the expansion and contraction of the convection pattern driven by the IMF B_z variations very rapidly. Plasmas coming from the noon sector have the largest N_mF_2, but exhibit no significant variations in h_mF_2 and TEC. TEC increases within a fluxtube originating from the dawn sector have been previously modeled using the Utah State University Time Dependent Ionospheric Model (TDIM) [*Schunk and Walker,* 1973; *Schunk et al.,* 1975, 1976; *Sojka et al.,* 1981a, 1981b] driven by the Defense Meteorological Satellite Program (DMSP) observations [*Heelis et al.,* 2009] and by the University of Michigan's

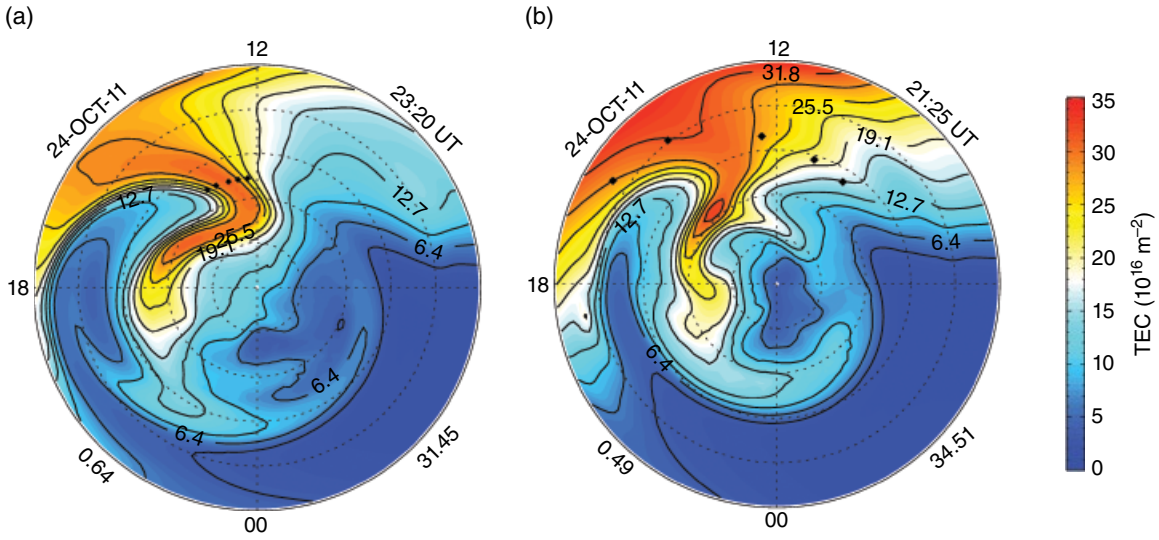

Figure 16.3 TEC contours with the starting and ending locations of five plasma columns denoted. The starting and ending times for particle tracing are 2320 UT and 2125 UT on 24 October 2011.

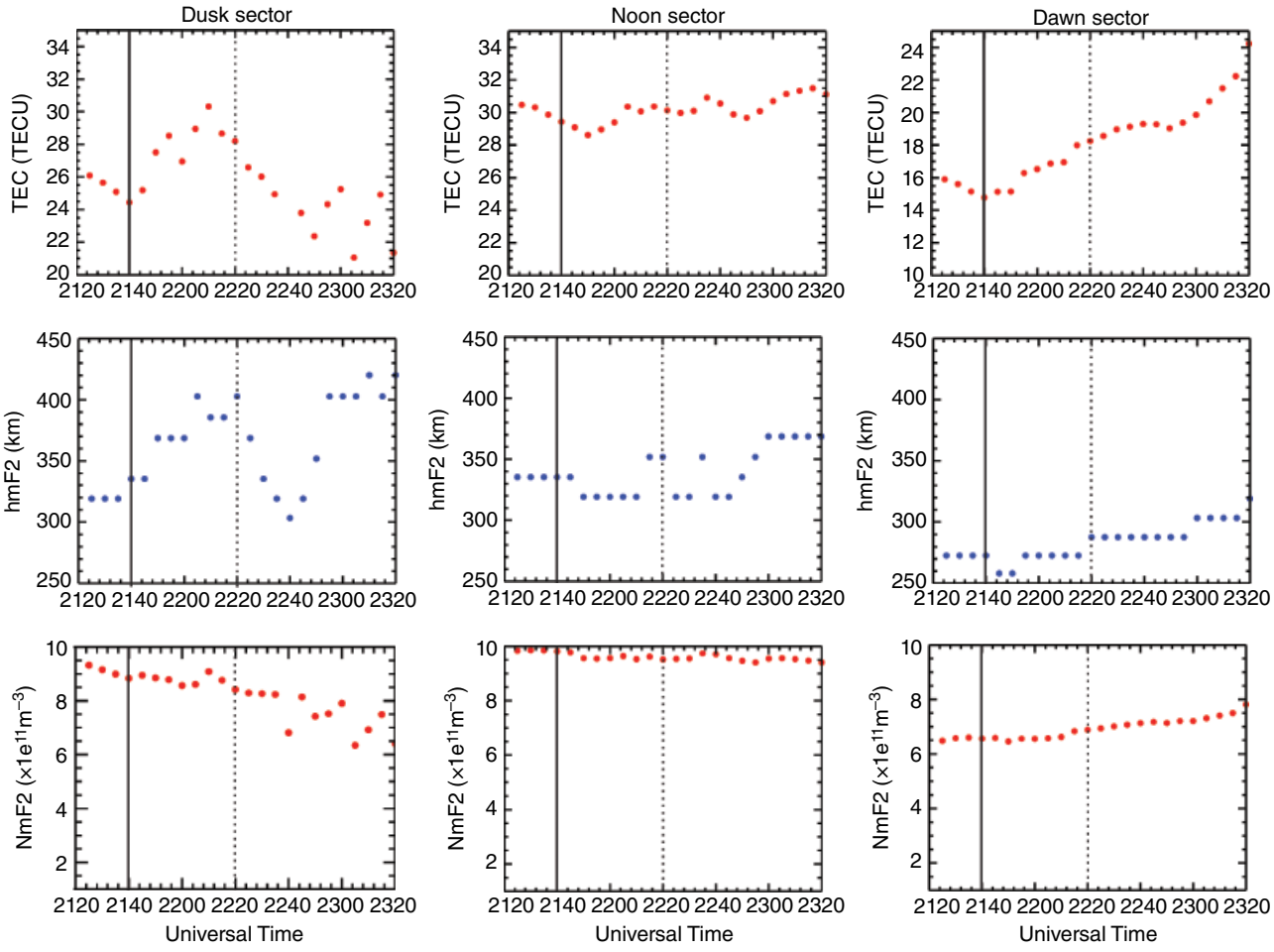

Figure 16.4 Time history of TEC, the F-layer peak density N_mF_2 and the peak height h_mF_2 of the three selected simulation columns. The solid and dotted vertical lines indicate the time of IMF B_z southward and northward turnings. From left column to right column are plasmas originating from the dusk, noon and dawn sectors, respectively.

Hot Electron and Ion Drift Integrator (HEIDI) model [*Liemohn et al.,* 2004, 2006] in *David et al.* [2011]. Both models show that the TEC increase can be as large as 20 to 30 TECU in less than three hours. The TEC increase in GITM is of smaller magnitude partly because of the GITM's limited upper boundary altitude at ~700 km. In this study, the Weimer model of high-latitude convection pattern is used, while in the previous modeling studies, DMSP observations and the output from the HEIDI model were used. Differences in the driver may also contribute to the discrepancies in the TEC values.

The characteristics of the plasma coming from the dusk sector are described in detail in Figure 16.5. Figure 16.5a shows the electron density vertical profiles at 2140 UT (black) and 2210 UT (blue), after the southward turning, and Figure 16.5b shows a representative electron density change at 2145 UT during one GITM iteration (~3 s) due to vertical (black) and horizontal (blue) transport as well as chemistry (red) within this 30-min period. During this interval, the TEC increases ~6 TECU in the entire simulation domain. One can see that the TEC increase is mainly due to the topside ionospheric density increase, which results from the upward vertical transport above ~350 km.

Similarly, Figure 16.5c shows the electron density vertical profiles at 2220 UT (black) and 2235 UT (blue), during the 20 min weakening of the southward IMF. The TEC decrease is mainly due to the topside electron density decrease. Figure 16.5d, which is in the same format as

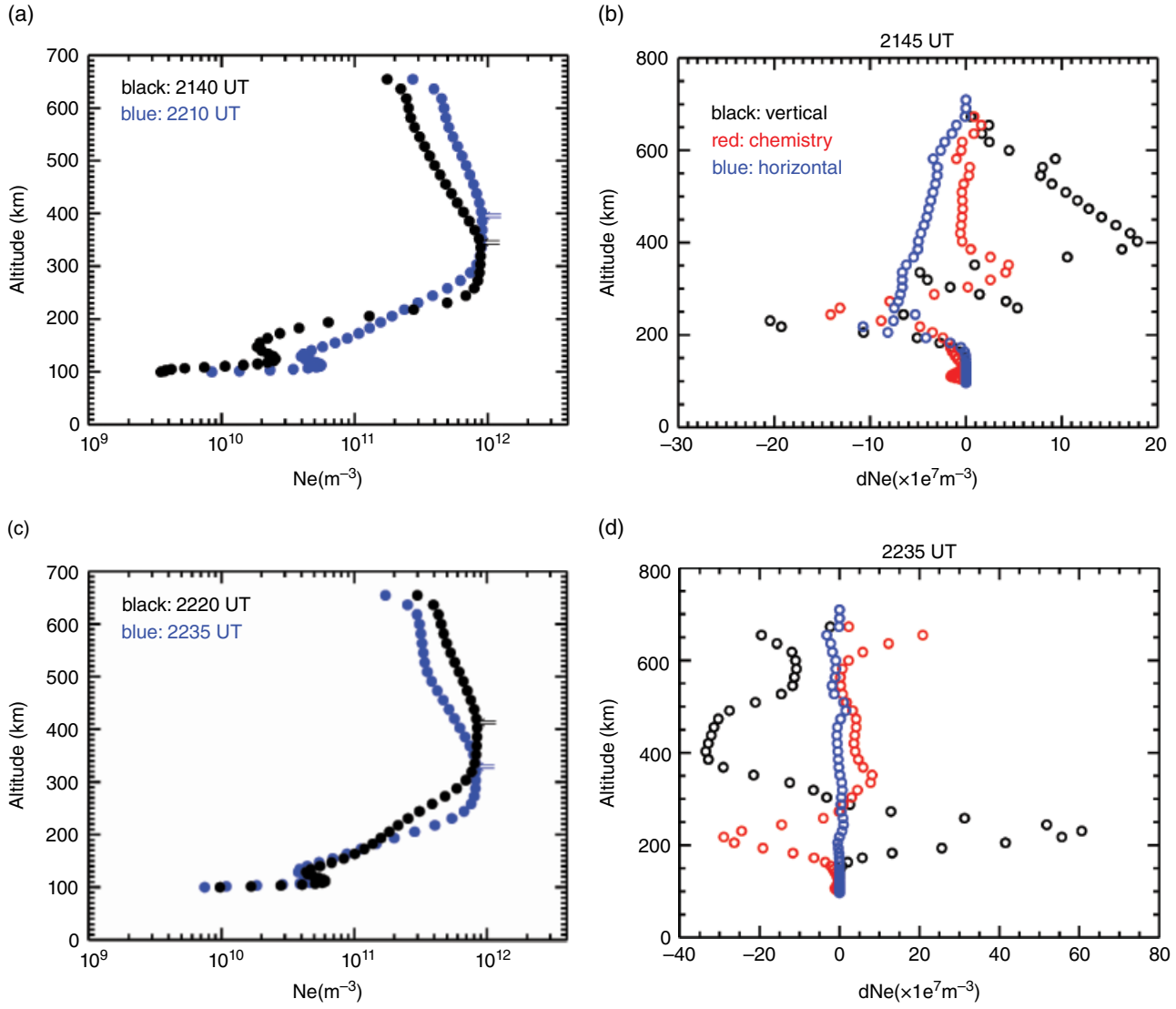

Figure 16.5 Selected ionospheric electron density profiles (a, c) and the electron density changes due to vertical, horizontal transports and chemistry (b, d). The starting location of the column is 65.4° in latitude and 217.0° in longitude in geographic coordinates.

Figure 16.5b, suggests that the topside electron density decrease is a result of downward vertical transport above ~300 km. These plasmas are transported to lower altitudes where the recombination rates and charge exchange are much higher because of higher neutral densities. The ionospheric electron density profiles and the electron density changes for the noon and the dawn sectors are not shown because they resemble those in the dusk sector and are less representative.

Zou et al. [2014] used PFISR measurements to investigate in detail the formation and decay of the SED plumes due to the combined effects of convection and thermospheric winds during intense storms. They found that the formation of the high density was mainly due to the lift of plasma to higher altitudes in sunlit regions produced by convection flows, and the decay of the plume was caused by enhanced downward field-aligned flows as a result of enhanced ambipolar diffusion and thermospheric wind. In Figure 16.6, we analyze the GITM simulation output at the location of PFISR (~78° magnetic field inclination angle and ~20° declination angle) to examine whether the modeling results confirm this picture. From top to bottom, Figure 16.6 shows the TEC, the average ion velocity between ~220 and 560 km in the geographic vertical direction, the average thermospheric wind between ~200 and 560 km in the geomagnetic north direction, and the ion pressure gradient below the F-layer peak between ~200 and 350 km (positive means upward in the geographic coordinates). The averaged vertical ion velocity in Figure 16.6b was mainly positive after the IMF turned southward at 2140 UT, which leads to the sharper increase of TEC (highlighted by arrows) and is consistent with the h_mF_2 increase shown in Figures 16.4 and 16.5. In addition, the averaged northward thermospheric wind speed in Figure 6c shows a rapid increase shortly after 2300 UT, at the same time as the initiation of the TEC decrease. This result suggests that the enhanced northward thermospheric wind pushes the plasma to lower altitudes where the charge exchange and recombination rates are higher, thereby leading to TEC decrease. The pressure gradient below the F-layer peak in Figure 16.6d closely follows the trend of the TEC curve in Figure 16.6a. Positive pressure gradient in the vertical direction indicates a downward pressure gradient force and thus enhanced downward ambipolar diffusion within the SED plume. All of the simulation results shown above are consistent with the observations shown in *Zou et al.* [2013, 2014].

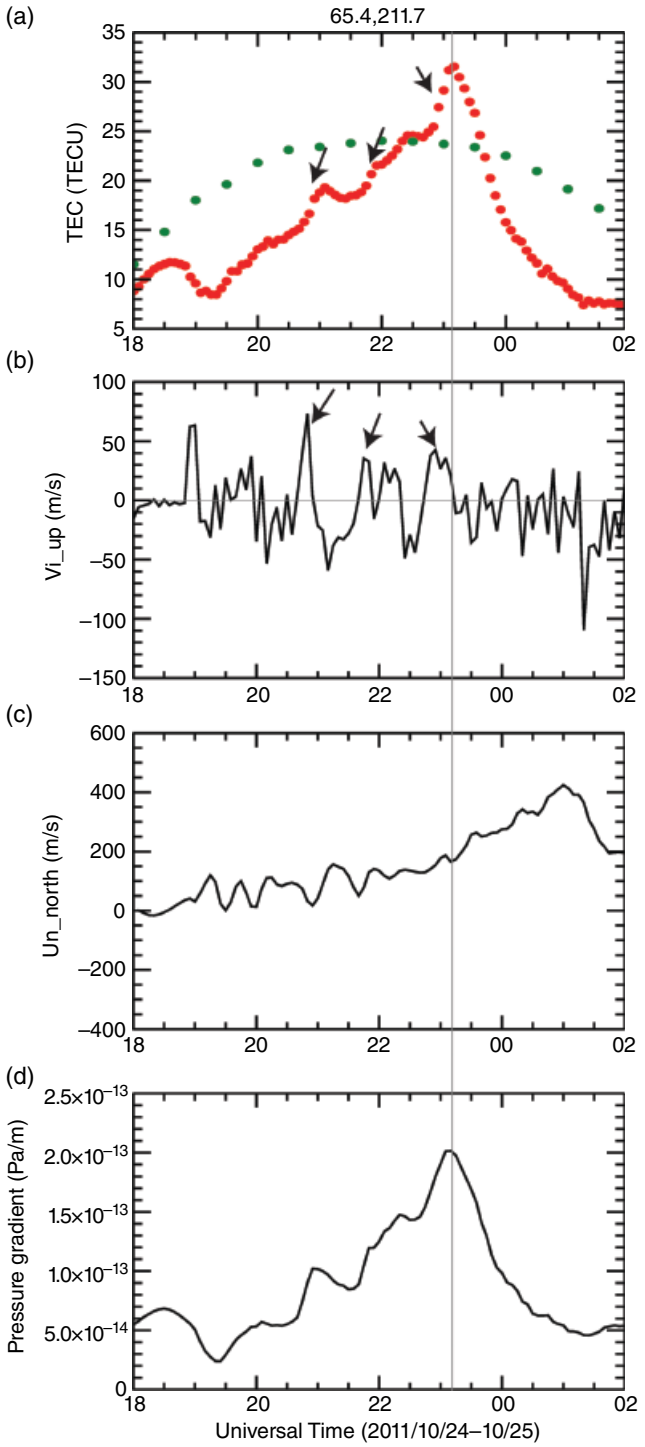

Figure 16.6 Time series of modeled TEC (red for storm time and green for quiet time) at the location of PFISR (a), upward ion drift averaged between ~200 and 560 km at the same location (b), thermospheric wind in the geomagnetic north direction averaged between ~200 and 560 km (c), and pressure gradient in the geographic vertical direction averaged between ~200 and 350 km (d). The vertical line indicates the time when peak TEC value was reached.

16.4. SUMMARY AND CONCLUSIONS

In this study, we have used the GITM model to investigate the dynamics of the SED plume during the 24 to 25 October 2011 intense geomagnetic storm. Simulation

results suggest that plasma originating from a wide range of latitudes and local times are able to contribute to the formation of SED plumes. However, the ionospheric key parameters, such as the F-layer peak density N_mF_2 and the peak height h_mF_2, can be very different for plasmas of different origins. In particular, we find that plasmas originating from the dawn sector showed slow but steady increase in h_mF_2, N_mF_2 and TEC, while those from the dusk sector experience larger variations with steep changes in h_mF_2 and TEC. This simulation result suggests that the h_mF_2 together with the TEC value might provide a useful means for understanding the origin of the plasma that supplies the SED plume. The h_mF_2 and the TEC are highly sensitive to the high-latitude convection pattern, which is in turn driven by the solar wind and IMF conditions. Therefore, accurate forecast of the formation of SED and SED plume would require a high-fidelity model of high-latitude convection.

In addition, the simulation results show that the averaged pressure gradient force below the F-layer peak increases within the plumes, and the northward thermospheric wind is also enhanced during the plume decay phase, consistent with observations previously obtained from ground-based radars.

Based on both observations and simulation results, the formation and decay of the SED and associated SED plumes can be summarized as follows:

• The high-latitude convection pattern expands equatorward, and the convection speed increases mainly due to IMF southward turning. In the presence of a non-vertical magnetic field, the increased convection flows lift the F-layer ionospheric plasma to higher altitudes where the charge exchange and recombination rates are lower but the solar EUV production is still ongoing in sunlit regions, thereby resulting in TEC increases.

• While the F-layer ionospheric density continues to increase, the pressure gradient force driven by the density gradient pushes plasma to lower altitudes where the charge exchange and recombination rates are higher.

• At the same time, the expanded and enhanced ionospheric convection pattern would induce thermospheric winds with a similar flow pattern. Near the dayside SED plume, the northward component of the wind increases significantly, and it can also act to push plasma to lower altitudes through ion-neutral collisions.

The above sequence suggests that self-regulating processes in the coupled high-latitude ionosphere and thermosphere play a vital role in determining the fate of the SED plume.

ACKNOWLEDGMENTS

The solar wind and IMF data used in this study are obtained from the Advanced Composition Explorer (ACE) spacecraft and have been dynamically propagated to the Earth's magnetopause. The *SYM-H* index is from the World Data Center (WDC) for Geomagnetism, Kyoto. The GPS TEC data are from the Madrigal database. The research by S. Zou is supported by National Aeronautics and Space Administration (NASA) grant NNX14AF31G and National Science Foundation (NSF) grant AGS1342968.

REFERENCES

Coster, A., and S. Skone (2009), Monitoring storm-enhanced density using IGS reference station data, *J. Geod.*, *83*(3–4), 345–351.

David, M., J. J. Sojka, R. W. Schunk, M. W. Liemohn, and A. J. Coster (2011), Dayside midlatitude ionospheric response to storm time electric fields: A case study for 7 September 2002, *J. Geophys. Res.*, *116*, A12302, doi:10.1029/2011JA016988.

Deng, Y., A. D. Richmond, A. J. Ridley, and H. Liu (2008a), Assessment of the non-hydrostatic effect on the upper atmosphere using a general circulation model (GCM), *Geophys. Res. Lett.*, *35*, L01104, doi:10.1029/2007GL032182.

Deng, Y., A. J. Ridley, and W. Wang (2008b), Effect of the altitudinal variation of the gravitational acceleration on the thermosphere simulation, *J. Geophys. Res.*, *113*, A09302, doi:10.1029/2008JA013081.

Foster, J. C. (1993), Storm Time Plasma Transport at Middle and High Latitudes, *J. Geophys. Res.*, *98*(A2), 1675–1689, doi:10.1029/92JA02032.

Foster, J. C., et al. (2005), Multiradar observations of the polar tongue of ionization, *J. Geophys. Res.*, *110*, A09S31, doi:10.1029/2004JA010928.

Heelis, R. A., J. J. Sojka, M. David, and R. W. Schunk (2009), Storm time density enhancements in the middle-latitude dayside ionosphere, *J. Geophys. Res.*, *114*, A03315, doi:10.1029/2008JA013690.

Huang, C.-S., J. C. Foster, L. P. Goncharenko, P. J. Erickson, W. Rideout, and A. J. Coster (2005), A strong positive phase of ionospheric storms observed by the Millstone Hill incoherent scatter radar and global GPS network, *J. Geophys. Res.*, *110*, A06303, doi:10.1029/2004JA010865.

Immel, T. J., and A. J. Mannucci (2013), Ionospheric redistribution during geomagnetic storms, *J. Geophys. Res. Space Physics*, *118*, 7928–7939, doi:10.1002/2013JA018919.

Liemohn, M. W., A. J. Ridley, D. L. Gallagher, D. M. Ober, and J. U. Kozyra (2004), Dependence of plasmaspheric morphology on the electric field description during the recovery phase of the 17 April 2002 magnetic storm, *J. Geophys. Res.*, *109*, A03209, doi:10.1029/2003JA010304.

Liemohn, M. W., A. J. Ridley, J. U. Kozyra, D. L. Gallagher, M. F. Thomsen, M. G. Henderson, M. H. Denton, P. C. Brandt, and J. Goldstein (2006), Analyzing electric field morphology through data-model comparisons of the Geospace Environment Modeling Inner Magnetosphere/Storm Assessment Challenge events, *J. Geophys. Res.*, *111*, A11S11, doi:10.1029/2006JA011700.

Lotko, W. (2007), The magnetosphere–ionosphere system from the perspective of plasma circulation: a tutorial, *J. Atmos. Sol. Terr. Phys.*, *69* (2007), pp. 191–211.

Mannucci, A. J., B. D. Wilson, D. N. Yuan, C. H. Ho, U. J. Lindqwister, and T. F. Runge (1998), A global mapping technique for GPS-derived ionospheric total electron content measurements, *Radio Sci.*, *33*(3), 565–582, doi:10.1029/97RS02707.

Mannucci, A. J., B. T. Tsurutani, B. A. Iijima, A. Komjathy, A. Saito, W. D. Gonzalez, F. L. Guarnieri, J. U. Kozyra, and R. Skoug (2005), Dayside global ionospheric response to the major interplanetary events of October 29–30, 2003 "Halloween Storms," *Geophys. Res. Lett.*, *32*, L12S02, doi:10.1029/2004GL021467.

Mitchell, E. J., P. T. Newell, J. W. Gjerloev, and K. Liou (2013), OVATION-SM: A model of auroral precipitation based on SuperMAG generalized auroral electrojet and substorm onset times, *J. Geophys. Res. Space Physics*, *118*, doi:10.1002/jgra.50343.

Pawlowski, D. J., and A. J. Ridley (2008), Modeling the thermospheric response to solar flares, *J. Geophys. Res.*, *113*, A10309, doi:10.1029/2008JA013182.

Pawlowski, D., and A. Ridley (2009), Quantifying the effect of thermospheric parameterization in a global model, *J. Atmos. Sol-Terr. Phys.*, *71*, 2017, doi:10.1016/j.jastp.2009.09.007.

Rideout, W., and A. Coster (2006), Automated GPS processing for global total electron content data, *GPS Solut.*, *10*(3), 219–228, doi:10.1007/s10291-006-0029-5.

Ridley, A. J., Y. Deng, and G. Tóth (2006), The global ionosphere–thermosphere model, *J. Atmos. Sol. Terr. Phys.*, *68*, 839–864, doi:10.1016/j.jastp.2006.01.008.

Schunk, R. W., and J. C. G. Walker (1973), Theoretical ion densities in the lower ionosphere, *Planet. Space Sci.*, *21*, 1875–1896, doi:10.1016/0032-0633(73)90118-9.

Schunk, R. W., W. J. Raitt, and P. M. Banks (1975), Effect of electric fields on the daytime high-latitude E and F regions, *J. Geophys. Res.*, *80*, 3121–3130, doi:10.1029/JA080i022p03121.

Schunk, R. W., P. M. Banks, and W. J. Raitt (1976), Effects of electric fields and other processes upon the nighttime high-latitude F layer, *J. Geophys. Res.*, *81*(19), 3271–3282.

Semeter, J., C. J. Heinselman, J. P. Thayer, R. A. Doe, and H. U. Frey (2003), Ion upflow enhanced by drifting F-region plasma structure along the nightside polar cap boundary, *Geophys. Res. Lett.*, *30*, 2139, doi:10.1029/2003GL017747, 22.

Sojka, J. J., W. J. Raitt, and R. W. Schunk (1981a), A theoretical study of the high-latitude winter F region at solar minimum for low magnetic activity, *J. Geophys. Res.*, *86*, 609–621, doi:10.1029/JA086iA02p00609.

Sojka, J. J., W. J. Raitt, and R. W. Schunk (1981b), Theoretical predictions for ion composition in the high-latitude winter F-region for solar minimum and low magnetic activity, *J. Geophys. Res.*, *86*, 2206–2216, doi:10.1029/JA086iA04p02206.

Sojka, J. J., M. David, R. W. Schunk, and R. A. Heelis (2012), A modeling study of the longitudinal dependence of storm time midlatitude dayside total electron content enhancements, *J. Geophys. Res.*, *117*, A02315, doi:10.1029/2011JA017000.

Weimer, D. (1996), A flexible, IMF dependent model of high-latitude electric potential having "space weather" applications, *Geophys. Res. Lett.*, *23*, 2549, doi:10.1029/2000JA000604.

Yuan, Z.-G., X.-H. Deng, and J.-F. Wang (2008), DMSP/GPS observations of intense ion upflow in the midnight polar ionosphere associated with the SED plume during a super geomagnetic storm, *Geophys. Res. Lett.*, *35*, L19110, doi:10.1029/2008GL035462.

Zou, S., A. J. Ridley, M. B. Moldwin, M. J. Nicolls, A. J. Coster, E. G. Thomas, and J. M. Ruohoniemi (2013), Multi-instrument observations of SED during 24–25 October 2011 storm: Implications for SED formation processes, *J. Geophys. Res. Space Physics*, *118*, 7798–7809, doi:10.1002/2013JA018860.

Zou, S., M. B. Moldwin, A. J. Ridley, M. J. Nicolls, A. J. Coster, E. G. Thomas, and J. M. Ruohoniemi (2014), On the generation/decay of the storm-enhanced density plumes: Role of the convection flow and field-aligned ion flow, *J. Geophys. Res. Space Physics*, *119*, 8543–8559, doi:10.1002/2014JA020408.

17

Forty-Seven Years of the Rice Convection Model

R. A. Wolf, R. W. Spiro, S. Sazykin, F. R. Toffoletto, and J. Yang

Video of Yosemite Talk, URL: http://dx.doi.org/10.15142/T3001Q

ABSTRACT

The 1974 version of the Rice Convection Model (RCM) got some important things right: It predicted that the inner edge of the plasma sheet would tend to shield the inner magnetosphere and low-latitude ionosphere from the full force of convection, and it predicted the region-2 currents before they were observed. However, it tended to overestimate the efficiency of the shielding. The 1974 RCM also had some major latent defects that only became evident later, after the model had been upgraded so that it could be compared with more observations. One involved the duration of events in which the shielding was violated. A second and more major problem was that RCM-computed plasma-sheet pressures were systematically inconsistent with data-based magnetic field models. Only in the last few years has this difficulty been partially resolved within the context of the RCM. The model now presents a far more complex picture of how plasma moves through the magnetosphere than the 1974 model did. Whereas the 1974 RCM showed plasma flowing nearly uniformly sunward through most of the plasma sheet, the modern picture has much of the transport in the form of mesoscale bubbles (bursty bulk flows) that flow rapidly earthward through a slow-moving background.

17.1. INTRODUCTION

Work on the RCM began 47 years ago in 1968, though it was much later before it became clear that the model was significant enough to deserve a name. The code originally represented an attempt to mathematize the picture of convection of plasma through the closed-field-line part of the ionosphere and magnetosphere that was presented qualitatively in a paper by *Schield et al*. [1969]. The first publication on the new code [*Wolf*, 1970] described a calculation of ionospheric and magnetospheric potential patterns in the closed-field-line region as well as some features of the associated magnetospheric particle distribution. The calculation included a complicated model of ionospheric conductance, including the day-night effect and auroral enhancement, but no field-aligned currents. By the time of the 1974 Yosemite meeting, an ion plasma sheet and its associated Birkeland currents had been added to the model [*Jaggi and Wolf*, 1973], allowing it to begin to make more interesting predictions. However, all ions were assumed to have the same magnetic moment, with drifts confined to the equatorial plane.

This paper summarizes what we got right in 1974 and what we got wrong. It also discusses latent problems with the model that became apparent only when it was upgraded so that it could be compared with more observational data. In fact, we are just now producing runs that appear to resolve one of those difficulties.

Department of Physics and Astronomy, Rice University, Houston, TX, USA

Magnetosphere-Ionosphere Coupling in the Solar System, Geophysical Monograph 222, First Edition.
Edited by Charles R. Chappell, Robert W. Schunk, Peter M. Banks, James L. Burch, and Richard M. Thorne.

17.2. RICE CONVECTION MODEL LOGIC AND FORMULATION

Since about 1976, the RCM has assumed that the magnetospheric particles have an isotropic pitch-angle distribution, and the energy spectrum has been divided up into channels characterized by different values of the isotropic energy invariant $\lambda = W_K V^{2/3}$, where W_K is the kinetic energy in gyro and bounce motion, and $V = \int ds / B$ is the volume of a unit magnetic flux tube. The bounce-averaged drift velocity for species s, recorded on an ionospheric grid, is given by

$$\mathbf{v}_{D,s} = \frac{\mathbf{B} \times \nabla \left(q_s \Phi_m + \lambda_s V^{-2/3} \right)}{q_s B^2} \tag{17.1}$$

where Φ_m is the potential on an ionospheric grid that does not rotate with the Earth. The magnetospheric particle distribution evolves according to

$$\left(\frac{\partial}{\partial t} + \mathbf{v}_{D,s} \cdot \nabla \right) \eta_s = -L_s \tag{17.2}$$

where η_s is the number of particles of species s per unit magnetic flux, and L_s = loss rate (precipitation + charge exchange). The parameter η_s is the distribution function multiplied by a constant that depends on the range of λ covered by species s. The total particle pressure is given by

$$p = \frac{2V^{-5/3}}{3} \sum_s \eta_s \lambda_s \tag{17.3}$$

The density of Birkeland current, which controls ionosphere-magnetosphere coupling, is given by the famous equation of *Vasyliunas* [1970]:

$$J_{\parallel} = \frac{1}{2} \hat{b} \cdot \nabla_i V \times \nabla_i p \tag{17.4}$$

where the subscript i refers to the ionosphere, and we have assumed north-south symmetry. The RCM neglects effects of inertial currents, which prevents it from representing waves and limits its applicability to time scales much longer than magnetohydrodynamic (MHD)-wave travel times.

Until about 1975, the magnetospheric particles were all assumed to be equatorially mirroring, so the second term of the right side of the equation analogous to (1) just represented gradient drift and was proportional to the magnetic moment [*Jaggi and Wolf*, 1973]. Electrons were assumed cold, and all ions were assumed to have the same magnetic moment.

For most RCM runs, the equation for conservation of current at the ionosphere has been

$$\nabla_i \cdot \left(\Sigma \cdot \nabla_i \Phi_i \right) = -J_{\parallel} \sin I \tag{17.5}$$

where I is the magnetic dip angle, Σ is the ionospheric-conductance tensor, and Φ_i is the potential in a frame that rotates with the Earth. It differs from Φ_m by a corotation potential. The modern code includes a neutral-wind term in (5). For a full derivation of equations (1) through (5), see *Harel et al*. [1981] or *Wolf* [1983].

Figure 17.1 shows the basic logic of the RCM. In its essence, the diagram applies from 1974 all the way to the present. Starting with an initial plasma distribution (top box), and a magnetic field model, the code uses (4) to derive the distribution of magnetic-field-aligned (Birkeland) currents down into the ionosphere from the divergence of the gradient/curvature-drift current. Given an ionospheric conductance model and appropriate boundary conditions, the code calculates the potential distribution in the ionosphere from (5). Using the magnetic field model, the potential is mapped back to the equatorial plane, usually assuming no field-aligned potential drop. The particle distribution is then advanced one time step using (2). The cycle then repeats.

Over the past 45 years, the model has evolved dramatically. The 1973–1974 code used a 560-point two-dimensional grid, while we now run with up to 150,000 grid points. The representation of the plasma sheet has changed from a sheet of equatorially mirroring ions with the same magnetic moment to isotropic pitch-angle distributions of H^+, O^+, and e^-, each represented by ~100 invariant-energy channels. The invariant energy $\lambda = W_K V^{2/3}$, where W_K is kinetic energy, and $V = \int ds / B$ is the flux tube volume [*Harel et al*., 1981]. A related model, the Comprehensive Ring Current Model (CRCM), calculates full pitch-angle distributions, conserving the first two adiabatic invariants but including estimated pitch-angle scattering [*Fok et al*, 2001]. The plasma boundary conditions, once held constant, now vary with both position and time. The magnetic field model now depends on time using a statistical model driven by solar wind data (this version is called RCM), an equilibrium model that is in force balance with RCM-computed pressure (this version is RCM-E), or a three-dimensional MHD code [*DeZeeuw et al*., 2004; *Toffoletto et al*., 2004; *Hu et al*., 2010]. The basic RCM conductance model is now based on the IRI-1990 empirical ionosphere [*Bilitza et al*., 1993] and MSIS 90 neutral density model [*Hedin et al*., 1990]. The auroral conductance enhancement is now computed by assuming a fixed fraction of strong pitch-angle scattering and the formulae of *Robinson et al*. [1987]. The RCM has also been two-way coupled to a full dynamic ionosphere [*Huba and Sazykin*, 2014] and a dynamic thermosphere-ionosphere [*Maruyama et al*., 2007]. For a more complete review of how the RCM and RCM-E work, see *Toffoletto et al.* [2003].

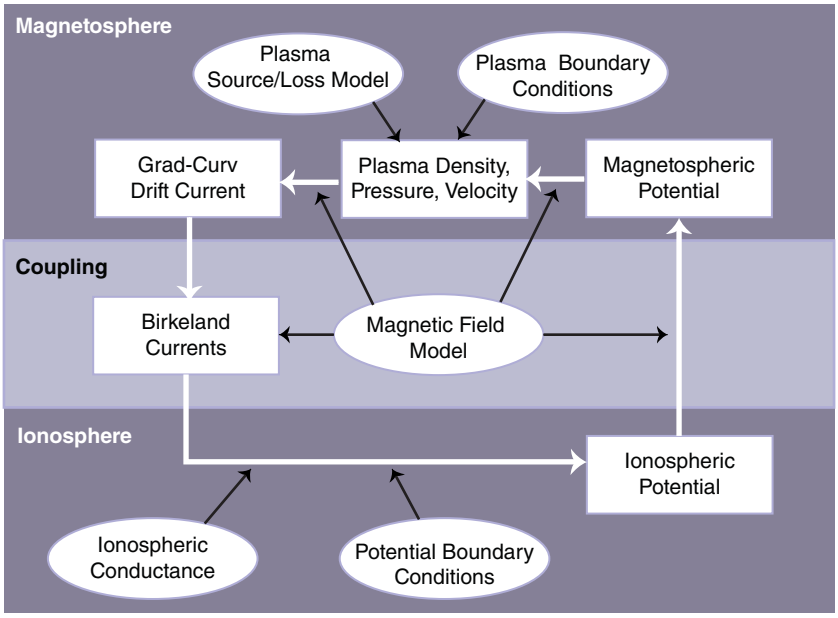

Figure 17.1 Logic diagram of the Rice Convection Model. The five boxes connected by white arrows represent the primary calculations and originated from *Vasyliunas* [1970]. The ovals represent input models.

17.3. WHAT THE 1974 RCM GOT RIGHT AND WHAT IT GOT WRONG

17.3.1. Things We Got Right

Before the observational identification of region-1 and region-2 Birkeland currents [*Zmuda and Armstrong*, 1974], RCM simulations were predicting the same kind of two-ring pattern [*Wolf*, 1974]. Figure 17.2 compares figures from those publications. The idea of the two-ring pattern of Birkeland currents was first clearly expressed in the paper by *Schield et al.* [1969], which was the paper that provided the original motivation for development of the RCM. V. M. Vasyliunas and R. A. Wolf both set out to mathematize the qualitative *Schield et al.* [1969] paper at about the same time, with Vasyliunas developing an elegant analytic theory [*Vasyliunas*, 1970, 1972] and Wolf pursuing a computer-simulation approach [*Wolf,* 1970; *Jaggi and Wolf*, 1973; *Wolf*, 1974]. The RCM's early contribution to the understanding of the Birkeland current pattern lay in showing that Vasyliunas's basic results were still valid even if various simplifying assumptions were relaxed. Figure 17.2b shows few equipotentials extending equatorward of the lower-latitude ring of currents, indicating that the mid- and low-latitude ionosphere was well shielded from the magnetospheric convection electric field. Figure 17.3 shows results of a computer experiment in which the RCM was run for 15 hours magnetosphere time so that it came to approximately steady state with a polar cap potential drop of 33.4 kilovolt (kV), after which the potential drop was suddenly increased by a factor of four and held steady again. The figure shows the result of mapping the ionospheric potential out in the magnetospheric equatorial plane (in the rest frame of the rotating Earth so that the convection potential is displayed, but the corotation potential is not). In Figure 17.3a, which shows the steady-state configuration, the inner magnetosphere is very well shielded from the convection electric field. Figure 17.3b, which shows the pattern right after the potential drop was suddenly increased by a factor of four, shows that strong electric fields now penetrate into the inner magnetosphere. In Figure 17.3c, which shows the potential pattern 10 minutes later, it can be seen that shielding has by now been substantially reasserted on the nightside but not so much on the dayside. Figure 17.3d shows the pattern 1:50 later, by which time the shielding has largely reasserted itself everywhere.

The tendency of the inner edge of the plasma sheet to shield the inner magnetosphere from the convection electric field, which had also been predicted by *Schield et al.* [1969] and *Vasyliunas* [1972], has been repeatedly confirmed by observations, but mostly indirectly. It is difficult to test shielding theory directly based on observational-average electric field profiles, because shielding is often violated and also because it is difficult to distinguish observationally between electric fields that result from direct penetration from high latitudes and fields that result from neutral winds. Consequently, the most convincing observational confirmation of the theory of shielding has been through the agreement between the observed and predicted violation of the

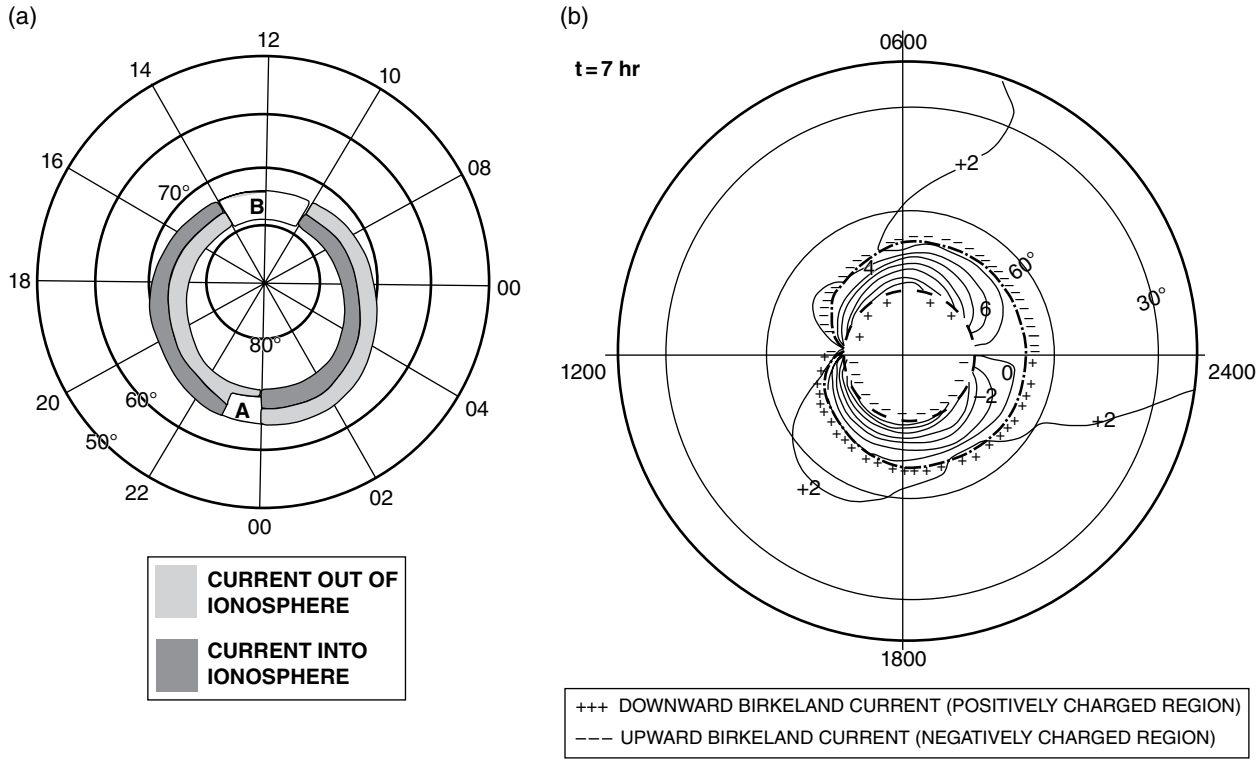

Figure 17.2 (a) Diagram of region-1 and region-2 currents, adapted from the original discovery paper of *Zmuda and Armstrong* [1974]. The view is from high above the northern ionosphere, with the Sun at the top. (b) RCM-based plot of ionospheric equipotentials after the model had been run 7 hours with steady inputs, adapted from *Wolf* [1974]; the Sun is to the left in (b); the + and – signs indicate downward and upward Birkeland currents, respectively. The poleward ring of currents was estimated by neglecting ionospheric currents in the polar cap.

shielding. The theory says that violation of the shielding should respond in minutes to a change in solar-wind driver, whereas neutral winds should take an hour or more to respond. The first convincing confirmation of the shielding idea was the observation of the overshielding phenomenon [*Kelley et al.*, 1979], namely the occurrence of backward (antisunward) convection in response to a sharp northward turning of the interplanetary magnetic field (IMF). There have also been many observations of undershielding, where sunward convection penetrates to low latitudes after a sharp southward turning of the IMF [see the review by *Fejer*, 1991]. In addition to individual event studies, *Fejer and Scherliess* [1997] found a clever statistical way to demonstrate both overshielding and undershielding responses to northward and southward turnings, using many years of incoherent backscatter radar measurements.

17.3.2. Something We Got Wrong

Modern RCM runs still exhibit shielding and region-2 currents. However, the steady-state shielding is typically not as strong in the new runs as in the old. The main reason is related to plasma sheet temperature. In the 1970s, there were no statistical studies of plasma sheet temperature, and we were forced to base our boundary-condition temperatures on published data from a few events. When the first statistical studies came out [*Huang and Frank*, 1986], it became apparent that we had underestimated plasma sheet ion temperature substantially, and correcting that error decreased predicted shielding efficiency in steady state.

17.3.3. Something Else We Got Wrong

Careful comparison of RCM calculations of prompt-penetration electric fields with observations showed that the observed duration of the events was longer than expected [*Spiro et al.*, 1988]. The discrepancy can largely be resolved if the reaction of the magnetospheric magnetic field to a sharp change in IMF is included in the calculation. The early calculations of prompt-penetration effects (e.g., Figure 17.3 and *Spiro et al.* [1988]) assumed a time-independent magnetic field, but the magnetospheric magnetic field actually changes systematically in response to changes in the

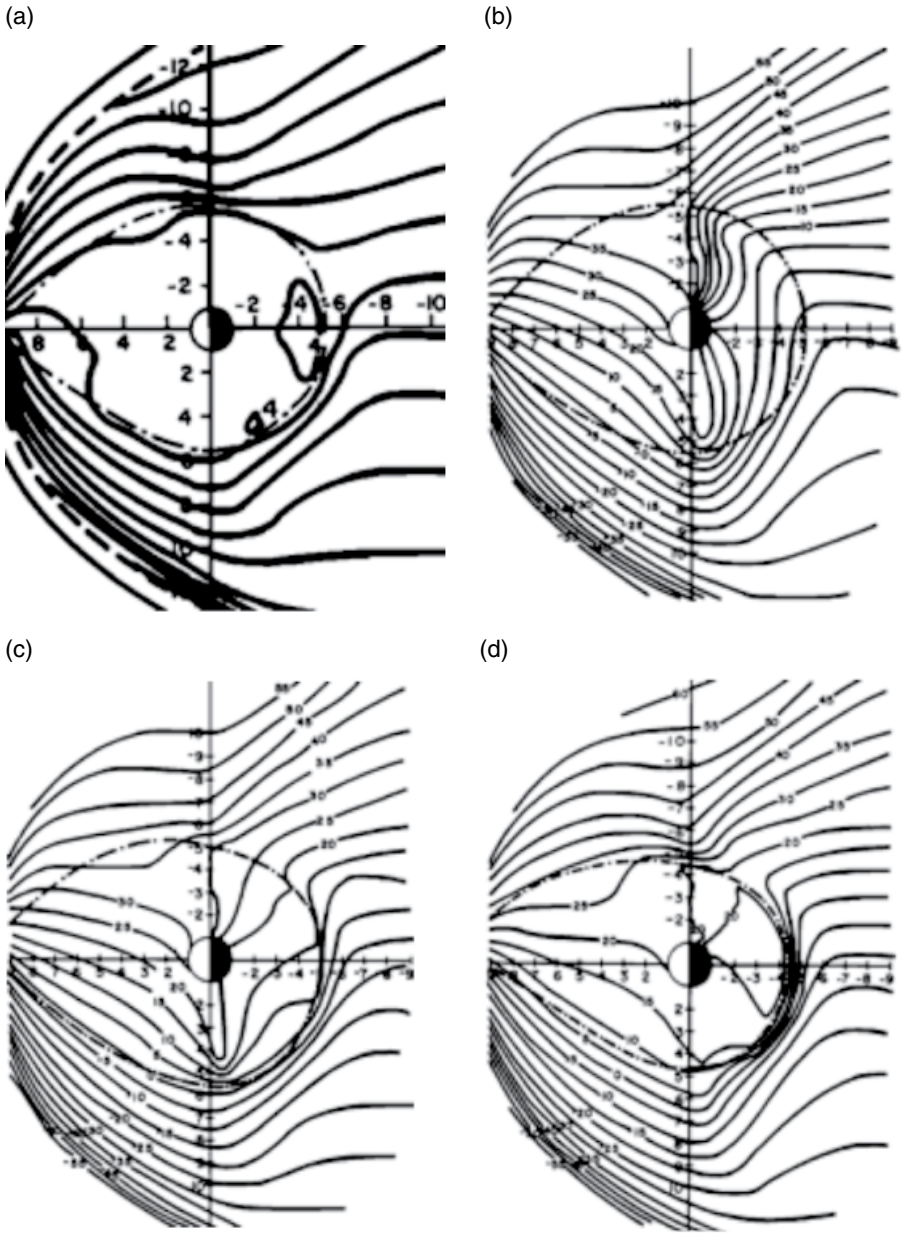

Figure 17.3 Equatorial equipotential diagrams (a) after a 15-hour RCM run with a steady 33.4-kV potential drop; (b) Immediately after a factor-of-four increase in potential drop; (c) 10 minutes later; (d) 2 hours after the increase. The corotation is not displayed, though it was included in the calculation [from *Jaggi and Wolf*, 1973].

solar-wind driver. For example, the overall response of the nightside plasma sheet to a northward turning is for plasma sheet magnetic field lines to become less stretched, which implies a westward induction electric field in the near-equatorial magnetosphere. That induction field moves the inner edge of the plasma sheet earthward. It does not map to the ionosphere, but it strengthens the overshielding effect and increases its duration. (For a detailed discussion, see *Fejer et al.*, 1990.)

17.3.4. State of the Art in Calculating Electric Fields in the Low-latitude Ionosphere

Observational testing of predicted magnetospherically generated electric fields is difficult, because low-latitude ionospheric electric fields are driven by three processes: neutral winds due to solar heating of the dayside atmosphere, prompt penetration electric fields, and disturbance-dynamo neutral winds caused by magnetospheric activity. Observationally, it is often difficult to sort out what

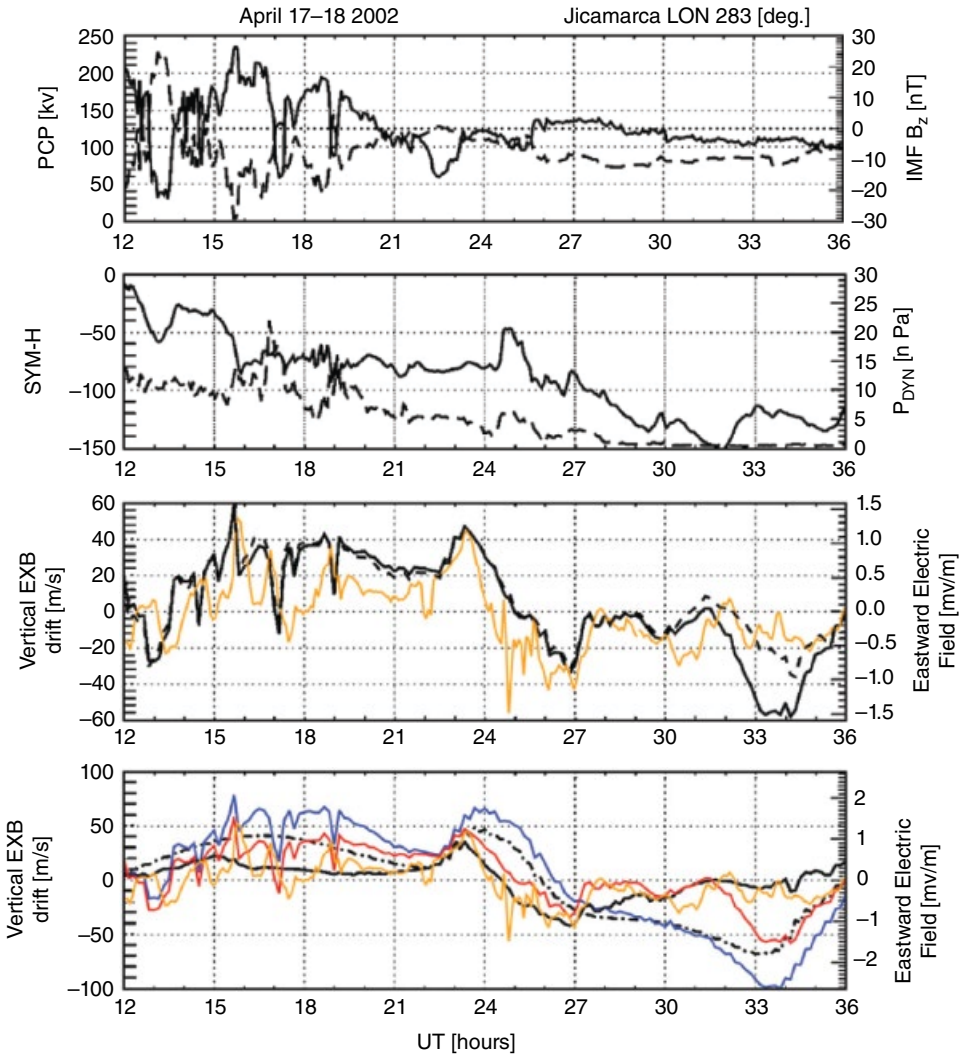

Figure 17.4 The top panel shows IMF B_z as a function of time (dashed curve), based on Advanced Composition Explorer (ACE) data, as well as the polar cap potential estimated from those data (solid curve). The second panel shows the Sym H index (solid) and solar wind ram pressure (dashed). The third panel compares vertical drifts measured at Jicamarca (orange curve) with drifts calculated at that location based on two Coupled Thermosphere-Ionosphere-Plasmasphere Electrodynamics-Rice Convection Model (CTIPe-RCM) runs, one (solid black) in which the plasma boundary condition varied as a function of time following the solar-wind-driven *Tsyganenko-Mukai* [2003] empirical model and the other (dashed) using a time-independent plasma boundary condition. The bottom panel compares vertical drifts from four different model runs: a quiet-time reference run (dash-dot), a run with disturbance dynamo winds but no penetration (black solid), a run with prompt penetration but no disturbance dynamo (blue solid), and a run with both dynamo and disturbance dynamo (red solid). Local time at Jicamarca, which is at the magnetic equator, is UT 5 hr. [From *Maruyama et al.*, 2007]

mechanisms are dominant at any given time. Nowadays, some theoretical calculations of low-latitude electric fields include all of these effects in disturbed times. Figure 17.4 shows results from coupling the RCM to the CTIP-e ionosphere-thermosphere model [*Maruyama et al.*, 2007]. The figure compares Jicamarca radar measurements of upward velocity above the Earth's magnetic equator with results from coupled-model runs. Figure 17.4 shows some clear instances of prompt penetration, for example, response to a brief strong southward excursion of the IMF (near 16 Universal Time [UT]) and responses to brief northward excursions (near 17 and 19 UT). However, the model-computed penetration electric field (blue curve) was substantial for extended periods, and that seems characteristic of major storms [e.g., *Basu et al.*, 2001; *Mannucci et al.*, 2008]. Both disturbance dynamo and penetration electric fields seem to have been important in the April 2002 storm. Overall, the coupled model, with both

penetration and dynamo effects included, does a decent job of representing the overall time variation of the zonal electric field at the equator.

17.4. LATENT DEFECT IN THE 1974 MODEL AND PARTIAL RESOLUTION

In the 1973–1974 version of RCM, there was no way to calculate the plasma-sheet pressure distribution, because the distribution function was assumed to be pancake-like (zero second invariant), which meant infinite pressure in the equatorial plane, zero elsewhere. When we switched to assuming isotropic pitch angles and could calculate pressure, we encountered a major problem, which we called the pressure balance inconsistency [*Erickson and Wolf*, 1980]. The problem is best illustrated in terms of the entropy parameter $pV^{5/3}$. Though flux tube volume V cannot be measured, V and $pV^{5/3}$ can be derived from statistical models. As shown in Figure 17.5, the statistics-based $pV^{5/3}$ systematically increases tailward, with an increase that is typically a factor of four to five between $x = -10$ and -30 R_E. If loss by precipitation and charge exchange is neglected, then adiabatic drift theory for an isotropic pitch-angle distribution implies that $p_k V^{5/3}$ is conserved along a drift path, where p_k is the partial pressure for particles of given chemical species and given energy invariant λ_k (e.g., *Wolf et al*., 2009). As a result, the traditional RCM, which solved the equations of adiabatic drift, usually predicted that $pV^{5/3}$ was nearly constant throughout the plasma sheet, except for the inner edge region, but this result conflicts with Figure 17.5 and results from many other similar studies [e.g., *Xing and Wolf*, 2007]. Key long-term questions for our group follow: What physical mechanism, not included in the RCM of the 1980s, is responsible for resolving the pressure balance inconsistency? Can the RCM be modified to represent that physics?

Pontius and Wolf [1990] pointed out that a plasma-sheet flux tube that has lower $pV^{5/3}$ than its neighbors will experience an earthward buoyancy force, accelerating toward regions where the background plasma has lower $pV^{5/3}$. Low-$pV^{5/3}$ flux tubes are termed "bubbles," and high-$pV^{5/3}$ flux tubes are called "blobs." A bubble, which contains less plasma than the background, cannot carry as much westward cross-tail current as the background. The east side of the bubble charges positive, the west side negative, and current is diverted along field lines to the ionosphere, west across the ionosphere, and back along the magnetic field to the west side of the bubble. *Pontius and Wolf* [1990] estimated that the earthward speed of a substantially depleted bubble could be quite fast, possibly approaching the Alfvén speed.

If flux tubes are created with a range of values of $pV^{5/3}$, the earthward motion of bubbles and tailward motion of blobs tends to stratify the plasma sheet into a configuration with a tailward gradient in $pV^{5/3}$, consistent with the results shown in Figure 17.5. *Pontius and Wolf* [1990] suggested that the bubble-blob interchange activity might be capable of resolving the pressure balance inconsistency, but it was not clear whether that mechanism was strong enough to stratify the plasma sheet, in the presence of the observed overall earthward convection.

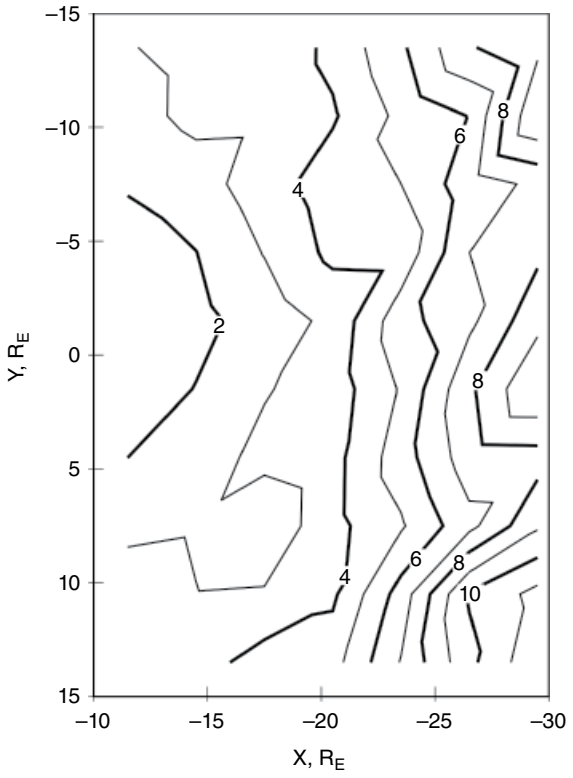

Figure 17.5 Equatorial contour plot of average $PV^{5/3}$, in 10^{16} SI units ($Jm^{-4/3}/T^{5/3}$) [from *Kaufmann et al.,* 2004].

Almost immediately after the *Pontius and Wolf* [1990] paper came out, *Baumjohann et al*. [1990] announced the discovery of bursty bulk flows (BBF), which were regions of enhanced, mostly earthward, transport that contained flow bursts that reached speeds above 400 km/s. *Angelopoulos et al.* [1994] established the statistical properties of BBFs. *Chen and Wolf* [1993] suggested that the flow bursts were bubbles, an identification confirmed by *Sergeev et al*. [1996], *Kauristie et al.* [2000], and others. Many simulations have demonstrated the action of bubbles within various approximations and boundary conditions, including global MHD simulations [e.g., *Pembroke et al*., 2012], tail MHD [e.g., *Birn et al.*, 2004, 2013], particle in cell (PIC) [e.g., *Pritchett et al*., 2014], RCM [*Zhang et al*., 2009], and Rice Convection Model - Equilibrium (RCM-E) [*Yang et al*., 2011].

With improvements in grid resolution, we can now begin to represent BBFs within the RCM-E in an effort to

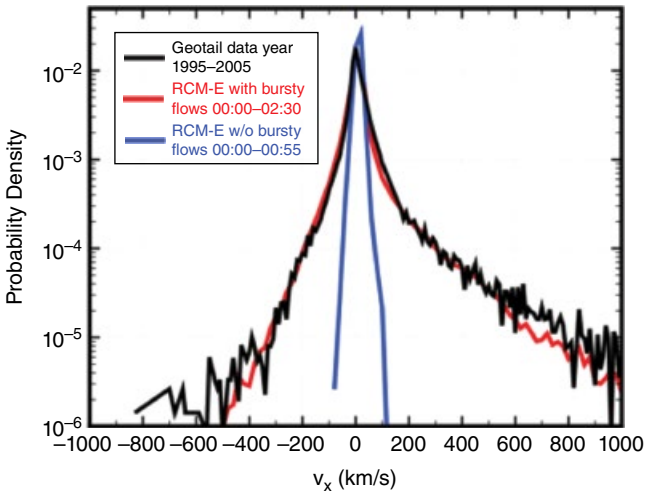

Figure 17.6 Velocity probability distributions for $-19<x<-10$. The black curve is based on Geotail data for 1995 to 2005. The blue curve is for an RCM-E run with a uniform, time-independent distribution function on the tailward boundary. The red curve is for an RCM-E run in which bubbles were introduced at the tailward boundary, with the level of variations set to fit the observed probability distribution [from *Yang et al.*, 2014].

investigate whether the observed bubble-blob activity is strong enough to resolve the pressure-balance inconsistency. Because $pV^{5/3}$ can't be measured, we can't construct an observation-based probability distribution for values of $pV^{5/3}$ in the plasma sheet. However, flow velocity is relatively easy to measure, and velocity probability distributions have been constructed for various conditions [*Guild et al.*, 2008]. One such distribution is shown as the black curve in Figure 17.6. Note that while the peak of the distribution is very near zero velocity, there is a substantial probability of flows with $V_x > 400$ km/s but a much smaller probability of flows with $V_x < -400$ km/s. Most of the average earthward velocity is due to the difference between the earthward and tailward flows on the wings of the distribution.

We performed two RCM-E runs, both of which had steady total polar cap potentials of 50 kV. In one case (blue curve in Figure 17.6), the distribution function was fixed to be UT-independent on the tailward boundary, and the electric field along the boundary was approximately uniform; the reason for showing results at 55 minutes for this run is that, after that time, the inner plasma sheet was so stretched that the equilibrium solver could not find a solution. In the second case, random fluctuations were introduced in $pV^{5/3}$ at the tailward boundary with the level of the fluctuations adjusted so that the overall average fluctuation level in V_x (red curve) matched the observed distribution (black curve), over the same range of x. Regions of the boundary with reduced $pV^{5/3}$ had stronger westward potential electric field than regions with higher $pV^{5/3}$. *Yang et al.* [2014] describe the details of the simulation.

Figure 17.7a shows the equatorial distribution of $pV^{5/3}$ at the end of the 2-1/2 hour run with bubbles. Notice how the channel of strong earthward flow and reduced $pV^{5/3}$ in the pre-midnight sector, that is, the model's representation of a BBF, has made its way to the geosynchronous-orbit region, while the high- $pV^{5/3}$ plasma does not penetrate deep into the magnetosphere. Movie S1, which is attached as a supplement to this paper, provides a picture of how BBFs are introduced sporadically at the boundary and make their way to the inner plasma sheet.

Figure 17.7b addresses the question of whether introduction of these bubbles at the tailward boundary at a rate that is consistent with the observed velocity statistics resolves the pressure balance inconsistency. The difference between the black and blue curves illustrates the classic pressure-balance inconsistency. The black curve, representing the statistical average, shows an almost uniform gradient between 8 and 19 R_E. The blue curve, representing the model run with steady inputs, shows a weak gradient in $pV^{5/3}$ beyond 12 R_E, but a strong gradient between 8 and 10 R_E. (The boundary conditions on the runs were set so that there would be approximate agreement at 19 R_E.) The red curve, representing the result of averaging over the run with bubble injections, is much closer to the data-based black curve than the blue curve, though there is still a significant difference between 8 and 12 R_E. The fact that some difference remains is not surprising, since a 2-1/2 hour run with constant total polar-cap potential may not be a good approximation to an average over $Kp = 3$ intervals in many years of data. However, it is clear that including a realistic level of bubble/BBF activity in the model calculation goes a long way toward eliminating the pressure-balance inconsistency.

17.5. CONCLUDING COMMENTS

The 1974 model got some important things right, but the RCM-based picture of how the closed-field-line magnetosphere works has changed considerably over the past 45 years, as can be seen by comparing Figure 17.3a with Figure 17.7a. Both of these plots show potential patterns computed after a long period with a constant polar-cap potential drop. Movie S1, from *Yang et al.* [2014], gives a fuller view of the complexity of the present picture, which includes plasma bubbles coursing through the plasma sheet.

17.6. SUPPLEMENTARY DIGITAL DATA

The following data item, Movie S1 from Yang et al. [2014], is available online at https://youtu.be/5gNxTk1zPXk.

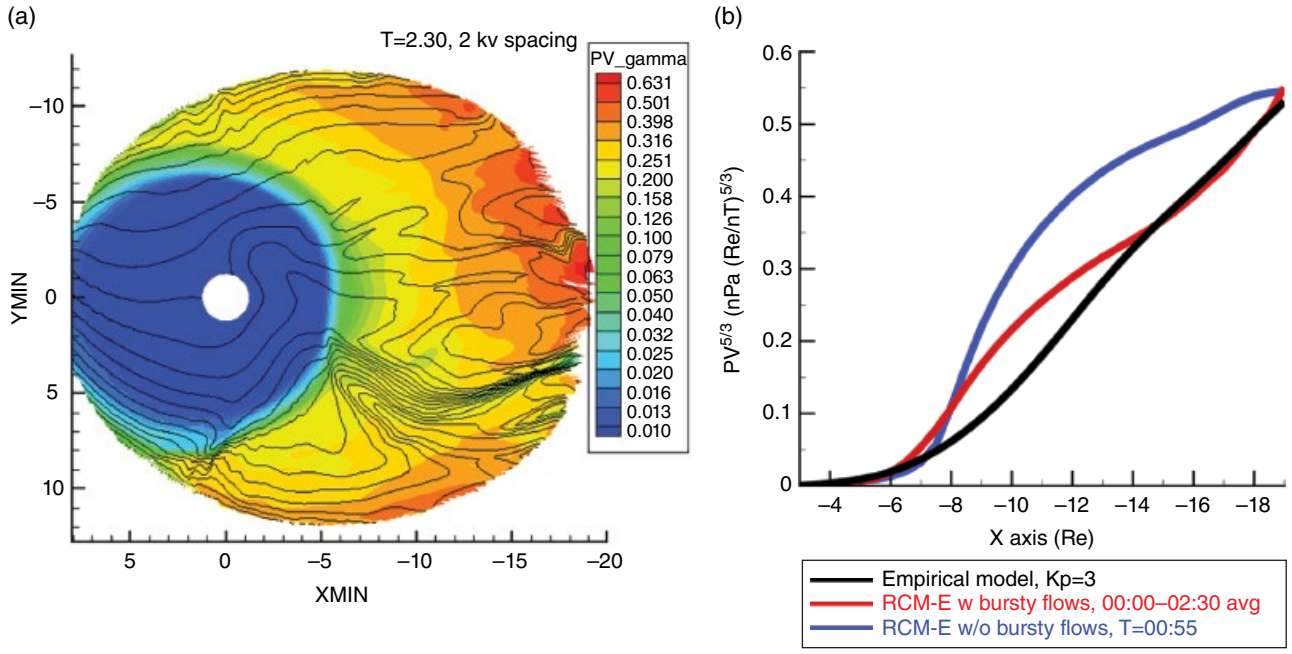

Figure 17.7 (a) Colors show the equatorial distribution of $PV^{5/3}$ at the end of the 2-1/2 hour run with bubbles injected sporadically through the tailward boundary. Black contours are the equatorial map of ionospheric potentials. (b) $PV^{5/3}$ along the $-x$ axis, calculated three ways: from an observation-based $Kp = 3$ *Tsyganenko* [1989] model relaxed to equilibrium (black), end of RCM-E run with steady boundary conditions (blue), and average over the 2-1/2-hour run with bubble injection at the tailward boundary (red) [adapted from *Yang et al.*, 2014].

ACKNOWLEDGMENTS

The authors are grateful to many people who have contributed to the RCM over the years, particularly R. K. Jaggi and M. Harel. This work was supported by National Aeronautics and Space Administration (NASA) Living With a Star (LWS) grant NNX13AF92G and NASA H-GCR grant NNX14AN55G.

REFERENCES

Angelopoulos, V., C. F. Kennel, F. V. Coroniti, R. Pellat, M. G. Kivelson, R. J. Walker, C. T. Russell, W. Baumjohann, W. C. Feldman, and J. T. Gosling (1994), Statistical characteristics of bursty bulk flow events, *J. Geophys. Res.*, *99*, 21257–21280.

Basu, S., S. Basu, K. M. Groves, H.-C. Yeh, S.-Y. Su, F. J. Rich, P. J. Sultan, and M. J. Keskinen (2001), Response of the equatorial ionosphere in the South Atlantic region to the great magnetic storm of July 15, 2000, *Geophys. Res. Lett.*, *28*, 3577–3580.

Baumjohann, W., G. Paschmann, and H. Lühr (1990), Characteristics of high-speed ion flows in the plasma sheet, *J. Geophys. Res.*, *95*, 3801–3809.

Bilitza, D., K. Rawer, L. Bossy, and T. Gulyaeva (1993), International Reference Ionosphere - Past, Present, and Future .1. Electron-Density, *Adv. Space Res.*, *13*, 3–13.

Birn, J., J. Raeder, Y. L. Wang, R. A. Wolf, and M. Hesse (2004), On the propagation of bubbles in the geomagnetic tail, *Ann. Geophys.*, *22*, 1773–1786.

Birn, J., R. Nakamura, and M. Hesse (2013), On the propagation of blobs in the magnetotail: MHD simulations, *J. Geophys. Res.*, *118*, 5497–5505, doi: 10.1002/jgra.50521.

Chen, C. X., and R. A. Wolf (1993), Interpretation of high speed flows in the plasma sheet, *J. Geophys. Res.*, *98*, 21409-21419.

DeZeeuw, D. L., S. Sazykin, R. A. Wolf, T. I. Gombosi, A. J. Ridley, and G. Tóth (2004), Coupling of a global MHD code and an inner magnetosphere model: Initial results, *J. Geophys. Res.*, *109*, A12219, doi:10.1029/12003JA010366.

Erickson, G. M., and R. A. Wolf (1980), Is steady convection possible in the Earth's magnetotail?, *Geophys. Res. Lett.*, *7*, 897–900.

Fejer, B. G. (1991), Low latitude electrodynamic plasma drifts: A review, *J. Atmos. Terr. Phys.*, *53*, 677.

Fejer, B. G., and L. Scherliess (1997), Empirical models of storm time equatorial zonal electric fields, *J. Geophys. Res.*, *102*, 24047–24056.

Fejer, B. G., R. W. Spiro, R. A. Wolf, and J. C. Foster (1990), Latitudinal variation of perturbation electric fields during magnetically disturbed periods: 1986 SUNDIAL observations and model results, *Ann. Geophys.*, *8*, 441–454.

Fok, M.-C., R. A. Wolf, R. W. Spiro, and T. E. Moore (2001), Comprehensive computational model of Earth's ring current, *J. Geophys. Res.*, *106*, 8417–8424.

Guild, T. B., H. E. Spence, E. L. Kepko, V. Merkin, J. G. Lyon, M. Wiltberger, and C. C. Goodrich (2008), Geotail and LFM comparisons of plasma sheet climatology: Flow variability, *J. Geophys. Res.*, *113*, A04217, doi:10.1029/2007JA012613.

Harel, M., R. A. Wolf, P. H. Reiff, R. W. Spiro, W. J. Burke, F. J. Rich, and M. Smiddy (1981), Quantitative simulation of a magnetospheric substorm 1, Model logic and overview, *J. Geophys. Res.*, *86*, 2217–2241.

Hedin, A. E., M. A. Biondi, R. G. Burnside, G. Hernandez, R. M. Johnson, T. L. Killeen. C. Mazaudier, J. W. Meriwether, J. E. Salah, R. J. Sica, R. W. Smith, N. W. Spencer, V. B. Wickwar, and T. S. Virdi (1991), Revised global model of thermosphere winds using satellite and ground-based observations, *J. Geophys. Res*, *96*, 7657–7688.

Hu, B., F. R. Toffoletto, R. A. Wolf, S. Sazykin, J. Raeder, D. Larson, and A. Vapirev (2010), One-way coupled OpenGGCM/RCM simulation of the March 23, 2007 substorm event, *J. Geophys. Res.*, *115*, A12205, doi:10.1029/2010JA015360.

Huang, C. Y., and L. A. Frank (1986), A statistical study of the central plasma sheet: Implications for substorm models, *Geophys. Res. Lett.*, *13*, 652–655.

Huba, J. D., and S. Sazykin (2014), Storm time ionosphere and plasmasphere structuring: SAMI3-RCM simulation of the 31 March 2001 geomagnetic storm, *Geophys. Res. Lett.*, *43*, doi:10.1002/2014GL062110.

Jaggi, R. K., and R. A. Wolf (1973), Self-consistent calculation of the motion of a sheet of ions in the magnetosphere, *J. Geophys. Res.*, *78*, 2852–2866.

Kaufmann, R. L., W. R. Paterson, and L. A. Frank (2004), Pressure, volume, and density relationships in the plasma sheet, *J. Geophys. Res.*, *109*, A08204, doi:10.1029/2003JA010317.

Kauristie, K., V. A. Sergeev, M. Kubyshkina, T. I. Pulkkinen, V. Angelopoulos, T. Phan, R. P. Lin, and J. A. Slavin (2000), Ionospheric current signatures of transient plasma sheet flows, *J. Geophys. Res.*, *105*, 10677–10690.

Kelley, M. C., B. G. Fejer, and C. A. Gonzales (1979), An explanation for anomalous ionospheric electric fields associated with a northward turning of the interplanetary magnetic field, *Geophys. Res. Lett.*, *6*, 301–304.

Mannucci, A. J., B. T. Tsurutani, M. A. Abdu, W. D. Gonzalez, A. Komjathy, E. Echer, B. A. Iijima, G. Crowley, and D. Anderson (2008), Superposed epoch analysis of the dayside ionospheric response to four intense geomagnetic storms, *J. Geophys. Res.*, *113*, A00a02, doi 10.1029/2007ja012732.

Maruyama, N., S. Sazykin, R. W. Spiro, B. G. Fejer, R. Wolf, D. Anderson, A. Anghel, F. R. Toffoletto, T. J. Fuller-Rowell, M. Codrescu, A. D. Richmond, and G. H. Millward (2007), Modeling storm-time electrodynamics of the low-latitude ionosphere-thermosphere system: Can long lasting disturbance electric fields be accounted for?, *J. Atm. Solar-Terrest. Phys.*, *69*, 1182–1199.

Pembroke, A., F. Toffoletto, S. Sazykin, M. Wiltberger, J. G. Lyon, V. Merkin, and P. Schmitt (2012), Initial results from a dynamic coupled magnetosphere-ionosphere-ring current-model, *J. Geophys. Res.*, *117*, A02211, doi:10.1029/2011JA016979.

Pontius, D. H., Jr., and R. A. Wolf (1990), Transient flux tubes in the terrestrial magnetosphere, *Geophys. Res. Lett.*, *17*(1), 49–52.

Pritchett, P. L., F. V. Coroniti, and Y. Nishimura (2014), The kinetic ballooning/interchange instability as a source of dipolarization fronts and auroral streamers, *J. Geophys. Res.*, *119*(6), 4723–4739, doi:10.1002/2014JA019890.

Robinson, R. M., R. R. Vondrak, K. Miller, T. Dabbs, and D. Hardy (1987), On calculating ionospheric conductances from the flux and energy of precipitating electrons, *J. Geophys. Res.*, *92*, 2565–2569.

Schield, M. A., J. W. Freeman, Jr., and A. J. Dessler (1969), A source for field-aligned currents at auroral latitudes, *J. Geophys. Res.*, *74*, 247–256.

Sergeev, V. A., V. Angelopoulos, J. T. Gosling, C. A. Cattell, and C. T. Russell (1996), Detection of localized, plasma-depleted flux tubes or bubbles in the midtail plasma sheet, *J. Geophys. Res.*, *101*, 10817-10826.

Spiro, R. W., R. A. Wolf, and B. G. Fejer (1988), Penetration of high-latitude-electric-field effects to low latitudes during SUNDIAL 1984, *Ann. Geophys.*, *6*, 39–50.

Toffoletto, F., S. Sazykin, R. Spiro, and R. Wolf (2003), Inner magnetospheric modeling with the Rice Convection Model, *Space Sci. Rev.*, *107*, 175–196.

Toffoletto, F., J. Lyon, S. Sazykin, R. Spiro, and D. Wolf (2004), RCM meets LFM: Initial results of one-way coupling, *J. Atm. Solar Terrest. Phys.*, *66*, 1361–1370.

Tsyganenko, N. A. (1989), A magnetospheric magnetic field model with a warped tail current sheet, *Planet. Space Sci.*, *37*, 5–20.

Tsyganenko, N. A., and T. Mukai (2003), Tail plasma sheet models derived from Geotail particle data, *J. Geophys. Res.*, *108*(A3), doi:10.1029/2002JA009707.

Vasyliunas, V. M. (1970), Mathematical models of magnetospheric convection and its coupling to the ionosphere, in *Particles and Fields in the Magnetosphere*, edited by B. M. McCormac, pp. 60–71, D. Reidel, Hingham, MA.

Vasyliunas, V. M. (1972), The interrelationship of magnetospheric processes, in *The Earth's Magnetospheric Processes*, edited by B. M. McCormac, pp. 29–38, D. Reidel, Dordrecht.

Wolf, R. A. (1970), Effects of ionospheric conductivity on convective flow of plasma in the magnetosphere, *J. Geophys. Res.*, *75*, 4677.

Wolf, R. A. (1974), Calculations of magnetospheric electric fields, in *Magnetospheric Physics*, edited by B. M. McCormac, pp. 167–177, D. Reidel, Dordrecht, Netherlands.

Wolf, R. A. (1983), The quasi-static (slow-flow) region of the magnetosphere, in *Solar Terrestrial Physics*, edited by R. L. Carovillano and J. M. Forbes, pp. 303–368, D. Reidel, Hingham, MA.

Wolf, R. A., Y. F. Wan, X. Xing, J. C. Zhang, and S. Sazykin (2009), Entropy and plasma sheet transport, *J. Geophys. Res.*, *114*, A00d05, doi:10.1029/2009ja014044.

Xing, X., and R. A. Wolf (2007), Criterion for interchange instability in a plasma connected to a conducting ionosphere, *J. Geophys. Res.*, *112*, A12209, doi:10.1029/2007JA012535.

Yang, J., F. R. Toffoletto, R. A. Wolf, and S. Sazykin (2011), RCM-E simulation of ion acceleration during an idealized plasma-sheet bubble injection, *J. Geophys. Res.*, *116*, A05201, doi:10.1029/2010JA16346.

Yang, J., R. A. Wolf, F. R. Toffoletto, S. Sazykin, and C.-P. Wang (2014), RCM-E simulation of bimodal transport in the plasma sheet, *Geophys. Res. Lett.*, *41*, 1817–1822, doi:10.1002/2014GL059400.

Zhang, J.-C., R. A. Wolf, R. W. Spiro, G. M. Erickson, S. Sazykin, F. R. Toffoletto, and J. Yang (2009), Rice Convection Model simulation of the injection of an observed bubble into the inner magnetosphere: 2. Simulation results, *J. Geophys. Res.*, *114*, A08219, doi:10.1029/02009JA014131.

Zmuda, A. J., and J. C. Armstrong (1974), The diurnal flow pattern of field-aligned currents, *J. Geophys. Res.*, *79*, 4611–4619.

18

Magnetospheric Model Performance during Conjugate Aurora

William Longley[1], Patricia Reiff[1], Jone Peter Reistad[2], and Nikolai Østgaard[2]

Video of Yosemite Talk, URL: http://dx.doi.org/10.15142/T3H01C

ABSTRACT

On 17 August 2001, the Imager for Magnetopause-to-Aurora Global Explorer (IMAGE) satellite viewed the Northern aurora, while the POLAR satellite observed the Southern aurora. Unlike typical cases where the aurora is conjugate, the large Y-component of the Interplanetary Magnetic Field (IMF) makes the polar cap shift toward the dusk in one hemisphere and toward the dawn in the other. Using the satellite images, we identified the Polar Cap Boundary (PCB) in both hemispheres, and determined the Dawn-Dusk Offset, ΔL, which ranged from 0° to 15° latitude. We found correlations of 0.90 in the North and 0.83 in the South between ΔL and IMF By. We then computed PCBs using four magnetohydrodynamic (MHD) models. None of the models accurately reproduced the observations, with Block Adaptive Tree Solar Wind Roe-type Upwind Scheme (BATS-R-US) producing boundaries that are too symmetric, Open Geospace General Circulation Model (OpenGGCM) producing boundaries that are too distorted, and the LFM-MIX model giving the best average offset but did not match the observed variation with solar wind parameters.

18.1. INTRODUCTION

The aurora is a highly visible indicator of magnetosphere-ionosphere coupling. We use the auroral response of a coronal mass ejection (CME) to test magnetospheric MHD models. The purpose of this study is not to perform a careful optimization of the models but instead to take the "standard" versions of the Community Coordinated Modeling Center (CCMC) models, which are in heavy use among the community and challenge them with unusual input conditions, to see which performs best. The CME carried a strong magnetic field, with a y-component (By) averaging 25 nT for nearly 12 hours and a z-component (Bz) varying from 0 nT to −20 nT. During this time span, the Kp index peaked at 7, and aurora were simultaneously observed by IMAGE in the northern hemisphere, and by POLAR in the southern hemisphere.

In 1996 POLAR was launched in a highly elliptical polar orbit with an 18-hour period, spending 13 hours of the orbit imaging the aurora in one hemisphere [*Frank et. al,* 1995]. By 2001, the apogee of the orbit was above the equator and allowed POLAR to start observing the aurora in the southern hemisphere for several hours at a time. The IMAGE satellite was launched in early 2000 and placed into a highly elliptical polar orbit, spending 10 hours of its 14.2-hour orbital period high above the northern hemisphere [*Burch,* 2000]. The precession of each satellite's orbit from the northern hemisphere to the southern led to a brief window from 2001 to 2002 where each satellite was able to concurrently observe a different hemisphere.

[1]*Department of Physics and Astronomy, Rice University, Houston, TX, USA*

[2]*Department of Physics and Technology, University of Bergen, Bergen, Norway*

Magnetosphere-Ionosphere Coupling in the Solar System, Geophysical Monograph 222, First Edition.
Edited by Charles R. Chappell, Robert W. Schunk, Peter M. Banks, James L. Burch, and Richard M. Thorne.

Trapped particles in Earth's magnetic field will follow field lines and bounce between the north and south hemispheres, eventually precipitating into the atmosphere and creating the aurora when the particles are scattered or accelerated into the "loss cone" [*Reiff et al.,* 1988]. *Østgaard et al.* [2005] used simultaneous conjugate aurora events observed by POLAR and IMAGE to identify shared features of the aurora in each hemisphere. The distinct features were found to be shifted in longitude, an effect present in runs of the Tsyganenko 96 and 02 models during the same events. *Liou and Newell* [2010] used POLAR data to determine the longitude of 2539 auroral breakups, which were found to correlate well with the By component of the IMF and the dipole tilt angle. Similarly, *Stubbs et al.* [2005] found effects of the IMF on non-conjugacy of auroral images.

18.2. DATA ANALYSIS

18.2.1. Coordinate Systems

Our examination of the aurora requires two different coordinate systems: one three-axis Cartesian system to measure components of the IMF, and one latitude and longitude system to create polar plots of the aurora. To measure the IMF, we use the Geocentric Solar Magnetospheric (GSM) coordinate system defined by the x-axis lying along the Sun-Earth line, the z-axis containing the projection of the magnetic dipole orthogonal to the x-axis, and the y-axis completing the right-handed orthogonal triad [*Hapgood,* 1992].

The raw data from IMAGE and POLAR capture whatever the camera is pointing at. To make these data comparable between satellites, and even successive time steps of the same satellite, we map it to a latitude- and longitude-based polar map. The Apex coordinate system is well suited for mapping where the aurora occur, and is based on magnetic shells, where each magnetic shell has an apex of a given height above the Earth's surface [*VanZandt et al.,* 1972]. The latitude in the Apex coordinate system specifies the magnetic shell the point lies on, and the longitude specifies the Magnetic Local Time (MLT) of the particular field line. The third Apex coordinate specifies the height above the Earth, and we take that coordinate to be the 100 km ionosphere boundary when mapping the aurora.

18.2.2. Auroral Imaging Data

The IMAGE satellite was in position to capture the 17 August 2001 event in the northern hemisphere from 16:41 Universal Time (UT) to 19:01 UT. The Far Ultra Violet Imager/Wideband Imaging Camera (FUV/WIC) instrument is used to view the aurora in the 140 nm to 190 nm ultraviolet band, capturing several Nitrogen emission lines in the Lyman-Birge-Hopfield band and a few atomic Nitrogen lines [*Mende et al.,* 2000]. WIC has an angular resolution of 0.1 degrees and a temporal resolution of 123 seconds [*Burch,* 2000]. The POLAR satellite was able to fully capture the event in the southern hemisphere from 17:00 UT to 18:13 UT and captured the nightside of the event during the remainder of the 16:41 UT to 19:01 UT window. The visible (VIS) Earth instrument measures the 130.4 nm Oxygen emission line with a spatial resolution of 0.12 degrees [*Frank et. al,* 1995]. POLAR-VIS has a temporal resolution of 54 seconds, but the 2-min temporal resolution of IMAGE is used instead, matched to the closest POLAR image. Figure 18.1 shows a snapshot at 18:38 UT of the dataset used, with a lobe cell convection pattern overlaid onto the northern hemisphere [*Reiff et al.,* 1985].

We identify the PCB in the images by using an operational definition of a 2.0 kR (1300 counts on the detector) precipitation threshold for IMAGE data, and a 6.0 kR (27 counts on the detector) precipitation threshold for POLAR data. The Dawn-Dusk Offset, ΔL, is then computed by subtracting the colatitude of the PCB at 6:00 MLT from the colatitude of the PCB at 18:00 MLT. Positive ΔL values signify a polar cap that is shifted to the dusk, and negative ΔL values signify a polar cap shifted to the dawn. For instances where a satellite does not completely capture the aurora at 6:00 or 18:00 MLT, we estimate the location of the PCB and place an appropriately sized error bar on that point. For all points a minimum error of $\pm$0.3 degrees latitude is used to account for the pixel width of the data. For the 67 image frames we use, 1 of the frames from IMAGE does not capture the 18:00 MLT boundary, 3 of the frames from POLAR fail to capture both the 6:00 MLT boundary and the 18:00 MLT boundary, and 24 of the POLAR frames only capture the 6:00 boundary. Note that using a higher value of the auroral brightness for the operational definition of the PCB will yield a lower (and more circular) PCB. This will be explored in a second paper in progress.

18.2.3. Models

The results from the IMAGE and POLAR observations are compared to the outputs of the Space Weather Modeling Framework (SWMF)/BATS-R-US model both with and without the Comprehensive Ring Current Model (referred to as BATS-R-US and BATS-CRCM from here on) [*Glocer et al.,* 2013; *Tóth et al.,* 2012], the OpenGGCM model [*Raeder et al.,* 2001; *Fuller-Rowell et al.,* 1996], and the CMIT/LFM-MIX model (referred to as LFM) [*Lyon et al.,* 2004; *Merkin and Lyon,* 2010]. All models were run from the CCMC website, using the measured solar wind plasma and

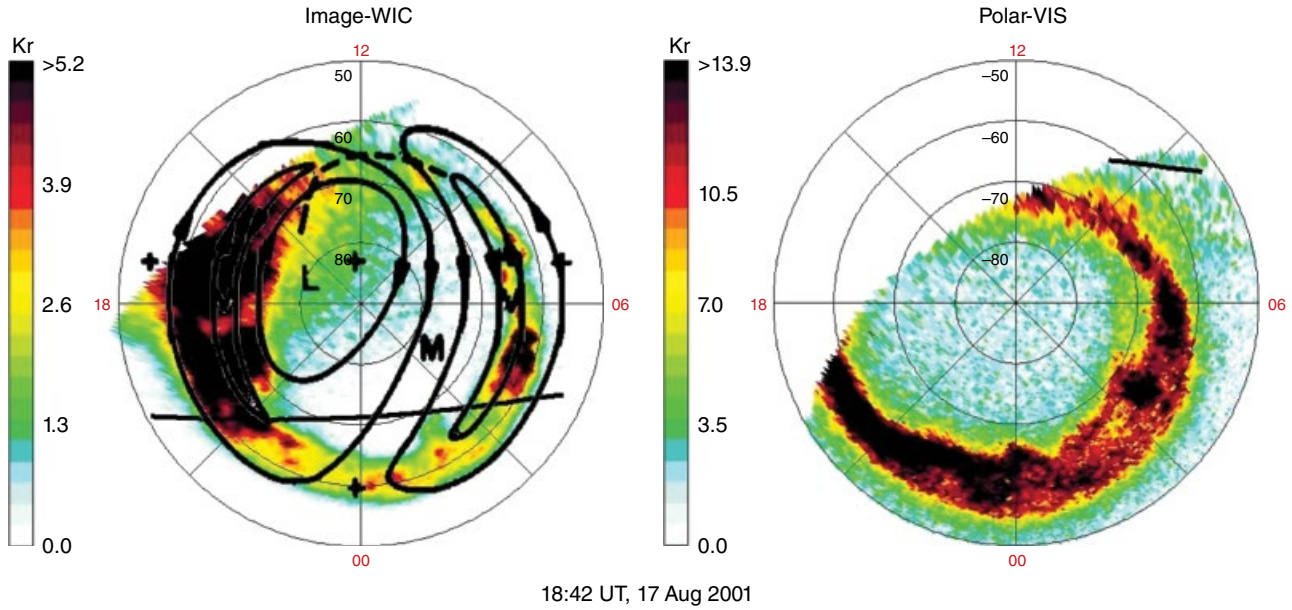

Figure 18.1 The aurora observed by IMAGE in the northern hemisphere and by POLAR in the southern hemisphere at 18:38 UT. The northern polar cap shows a shift toward dawn, and the southern hemisphere shows a clear shift toward dusk. In these images looking down on the Apex pole, noon is at the top and dawn is at the right. A lobe cell convection pattern [adapted from *Reiff et al.*, 1985] has been overlaid on the northern hemisphere auroral image.

magnetic field as inputs to solve three-dimensional MHD equations. Each model approximates the Earth's magnetic field as a dipole, with the BATS-R-US models allowing the dipole tilt angle to update throughout the simulation, and the OpenGGCM and LFM models keeping a fixed dipole tilt angle for the duration of the run. The BATS-R-US, BATS-CRCM, and OpenGGCM models use a 5.4 nT average Bx over the course of the model run, while the LFM model only allows 0 Bx. The BATS-CRCM and LFM models are coupled to inner magnetosphere models (CRCM and MIX, respectively). Both the BATS-R-US and the BATS-CRCM were run in higher resolution mode for the inner boundary. The models were run from 16:15 to 19:15 UT to minimize the effects of a fixed dipole tilt in the OpenGGCM and LFM models. *Pulkkinen et al.* [2013] provides more in-depth comparisons and descriptions of the models used.

The PCB is an output of each model run, and is obtained by tracing field lines to determine the open-closed boundary in the model. The boundary is plotted on the ionosphere map, which can be seen in Figure 18.2. For each frame of the ionosphere the Dawn-Dusk Offset, ΔL, is computed in the same way we computed ΔL for the IMAGE and POLAR data. Some of the outputs of the OpenGGCM and LFM models have multi-valued boundaries at a fixed MLT. We handle this in two ways. The first way is to locate and record each distinct value of the PCB at the desired MLT, and to then independently examine each point's evolution in time. The second way is to average all the locations together, compute the standard deviation, and then use that standard deviation as an error bar for our analysis.

18.2.4. Solar Wind Data

We use the "OMNI 1 minute IMF and Plasma data" dataset from CDAWeb for our IMF and solar wind data. The IMF and solar wind data are already time shifted to account for propagation to the Earth's bow shock and are averaged over 1-min intervals. The key parameters used for plots are the IMF By and Bz components in GSM coordinates; the IMF Clock Angle, $\theta_C = \text{Arctan}(By/Bz)$; and the Epsilon parameter, $\varepsilon = vB^2\,\text{Sin}^4(\theta_C/2)$. Figure 18.3 shows By, Bz, and θ_C parameters during the event, as well as one hour prior to the event.

18.3. RESULTS

The computed Dawn-Dusk Offset observed by the IMAGE and POLAR satellites is plotted against the solar wind parameters By, θ_C, and ε (not shown). We perform a least squares fit to account for the error bar, σ, associated with each point ΔL, and then compute the standard correlation coefficient r. We use the ΔL and σ values from each frame of data to calculate the fit; therefore, a ΔL value with a large error will be unimportant to the fit line.

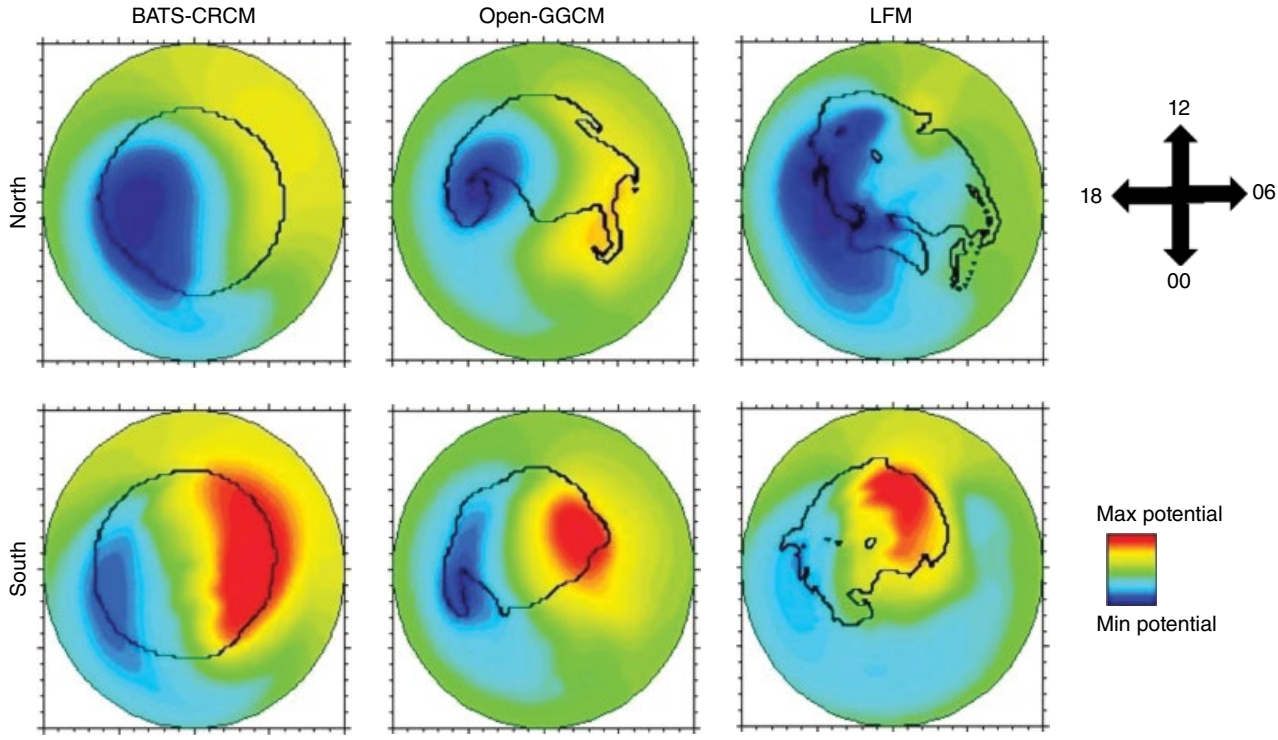

Figure 18.2 Ionosphere and polar cap boundary at 18:41 UT for various models. The color indicates the ionospheric potential, and the solid circle indicates the polar cap boundary (which is distorted for some of the models at certain times). The blue area is convection flowing clockwise, and the red area is convection flowing counterclockwise. In steady state, flow lines are equipotentials. Not shown is the BATS-R-US plot, which is nearly identical to the BATS-CRCM plot.

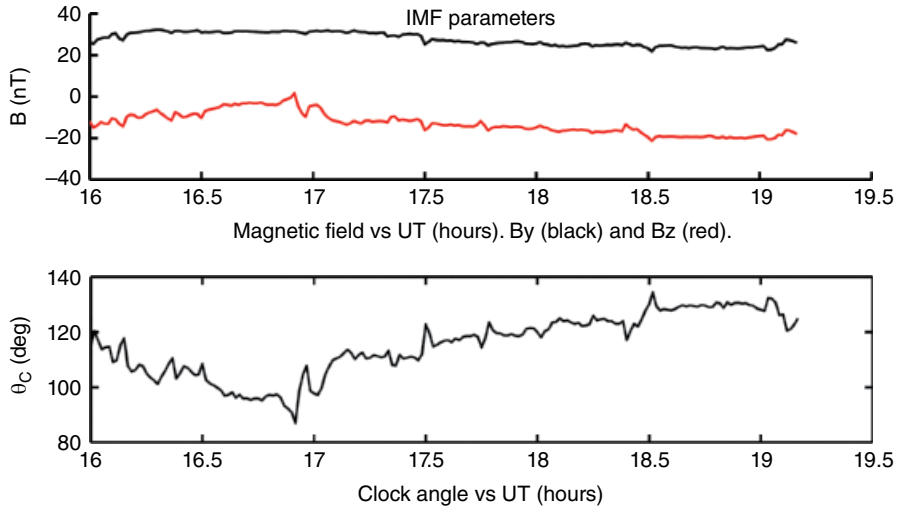

Figure 18.3 Top, IMF B_y (black) and B_z (red). Bottom, Clock Angle (θ_C) on 17 August 2001.

When calculating the correlation coefficient, we only include ΔL values where σ is less than 2 degrees of latitude (which excludes 5 of the 67 data points). Taking the 1-min averaged solar wind parameters, we find the Dawn-Dusk Offset, ΔL, correlates best with By in both hemispheres, with $r = 0.84$ in the north and $r = 0.81$ in the south. Table 18.1 shows the correlations of ΔL with θ_C and ε.

The Earth's magnetosphere has been shown to reconfigure over a 30- to 60-min window in response to changes in the solar wind. To explore this expectation we use time

Table 18.1 Correlations (r) of various solar wind parameters against the observed Dawn-Dusk Offset from the IMAGE and POLAR satellites. Correlations listed as Northern Hemisphere, (Southern Hemisphere). For each function, the time shown in the second column is for the best correlation

	1 min By	30 min $<B_y>$	1 min θ_C	45 min $<\theta_C>$	1 min ε	50 min $<\varepsilon>$
ΔL	0.84 (0.81)	0.90 (0.83)	−0.79 (−0.68)	−0.88 (−0.85)	0.73 (0.56)	−0.85 (−0.87)

Table 18.2 Correlations (r) of 30 min averaged B_y against the Dawn-Dusk Offset (ΔL) as determined by each of the models. Correlations (r) of a 45 min averaged θ_C against ΔL also shown in parentheses for comparison

	BATS-R-US	BATS-CRCM	OpenGGCM Poleward	OpenGGCM Equator	LFM Poleward	LFM Equator
ΔL in North	−0.75 (0.75)	−0.91 (0.92)	−0.42 (0.45)	0.44 (−0.43)	−0.29 (0.21)	−0.30 (−0.35)
ΔL in South	0.11 (−0.11)	0.31 (−0.32)	0 (0)	0.24 (−0.27)	0.48 (−0.49)	0.11 (−0.05)

Table 18.3 Minimum and maximum Dawn-Dusk Offsets from every satellite and model (in degrees of latitude)

Northern Hemisphere	IMAGE	BATS-R-US	BATS-CRCM	OpenGGCM Poleward	OpenGGCM Equator	LFM Poleward	LFM Equator
Average ΔL	−7.6°	−2.2°	−0.6°	−6.1°	−4.4°	−10.4°	1.7°
(Min, Max) ΔL	(−15°, 0°)	(−4°, −1°)	(−4°, 1°)	(−15°, 12°)	(−18°, 20°)	(−21°, −5°)	(−2°, 8°)
Southern Hemisphere	POLAR	BATS-R-US	BATS-CRCM	OpenGGCM Poleward	OpenGGCM Equator	LFM Poleward	LFM Equator
Average ΔL	10.2°	2.5°	5°	3.7°	14.4°	14.5°	15.3°
(Min, Max) ΔL	(5°, 14°)	(2°, 3°)	(4°, 7°)	(−10°, 21°)	(2°, 31°)	(8°, 19°)	(13°, 19°)

averages of By, θ_C, and ε. A constant weighted average of the parameters over the previous *t* minutes works best, and by trying different values of *t* we can improve the correlations of ΔL against each of the three solar wind parameters. For By, we find a 30-min constant average produces the best correlations, with r = 0.90 in the northern hemisphere and r = 0.83 in the southern hemisphere. Table 18.1 shows the correlations of all the time-averaged parameters.

18.4. MODEL RESULTS

Using the same methods from Section 18.3, we check the correlation of ΔL as calculated by the MHD models against the solar wind parameters By, and θ_C. The correlation coefficients from these plots are listed in Table 18.2. Since the OpenGGCM and LFM models have PCBs that are often multivalued along a given meridian, we have tracked the polar cap at both the lowest (listed as equator, since this is the most equatorward boundary) and highest (listed as poleward, as this is the most poleward boundary) latitudes that it crosses the dawn-dusk meridian. Both BATS models show strong correlations with ΔL in the northern hemisphere, with the CRCM inner magnetosphere model improving the correlations in all cases. However, the BATS models disagree with the satellite data in the northern hemisphere on the sign of the correlation; when ΔL is increasing in the data, it is decreasing in the models.

What is more useful, and more interesting, is comparing the plot trends between each model. Table 18.3 lists the ranges and average of ΔL in each hemisphere for all the models and the satellite data. Both BATS-R-US models have very small Dawn-Dusk Offsets, whereas the POLAR/IMAGE data, the LFM model, and the OpenGGCM model all have abs(ΔL) > 10° at times, and a large range of ΔL over the course of the event. Finally, the slope of the fit lines to ΔL varies between the data, with the northern hemisphere plots of By having a positive slope for the IMAGE data and the equatorward OpenGGCM boundary but a negative slope for all of the other models. The slopes of the ΔL versus By plots in the southern hemisphere are positive for all models and the satellite data (except for 0 correlation fits).

18.5. DISCUSSION

ΔL measured from POLAR and IMAGE correlated best with a 30-min average of By, a 45-min average of θ_C, and a 50-min average of ε. An initial conclusion is to think the magnetosphere responds to each of these variables

on those time scales, but a deeper look into the solar wind data shows this is not the case. The first thing to note is how high the By component is, ranging from 22 nT to 32 nT, with an average of 28 nT over the course of the event. In comparison, the only other studies of conjugate aurora captured by POLAR and IMAGE occurred during events with By between −10 nT and 10 nT [*Reistad et al.,* 2013]. This abnormally high By, coupled with the fact that we only examined 67 images taken over a 2-1/2-hour interval means we do not have a firm basis for drawing broad conclusions.

We also do not have evidence to support ΔL responding specifically to one parameter. When looking at 45-min averaged solar wind parameters, we find By, Bz, θ_C, and the ε parameter all show high correlations ($0.8 < r < 0.9$) with ΔL. However, the 1-min and 45-min averaged parameters are all highly collinear for this event. To draw any conclusions about which solar wind parameter has the strongest effect on the Dawn-Dusk Offset, we would need to add to our study other events where the solar wind data have a larger range of values. Additionally, the dipole tilt angle influences auroral symmetry but is not observed in a two-hour long event [*Østgaard,* 2005; *Liou and Newell,* 2010]. Future studies would greatly benefit from examining several events, and thus, looking at a larger parameter space.

18.5.1. Lobe Cells

The largest source of error in locating the satellite imaged PCB occurs at dusk in the northern hemisphere near the end of the event (Figure 18.1). The difficulty arises from weak precipitation occurring well inside the main auroral oval. If we look at the ionosphere computed by BATS-CRCM (Figure 18.2), we see a southern hemisphere with two convection cells of comparable strength, and the PCB running through the middle of each cell. However, the northern hemisphere has a dominant dusk convection cell sitting inside the polar cap boundary. BATS-R-US has similar ionospheric convection, and the LFM and OpenGGCM models also show dominant dusk convection cells sitting inside the PCB. A convection pattern like this in the summer hemisphere during a strong + By period is best explained by a lobe cell circulating within the dusk convection cell [*Burch et al.,* 1985].

A lobe cell arises when the IMF merges not with a dayside closed magnetic field line but with a field line in the tail that is already open, leading to a "stirring" of open field lines [*Reiff et al.,* 1985]. A lobe cell can be completely open, or partially open and partially closed, depending on the tilt of the dipole and the x-component of the IMF [*Crooker and Rich,* 1993]. This process may be fundamentally unstable, thus, the difficulty in the models in successfully tracing the open/closed boundary could be related to the existence of these lobe cells. However, it is also possible the difficulties the models had could be due to the grid size they were run on, as shown in *Ridley et al.* [2010], or by other features inherent to the models. Another potential source of disagreement may be the use of a relatively low precipitation flux as the operational definition of the PCB in the images. Using a significantly higher flux level as the operational definition of PCB can move it to lower latitudes, below the area we have tentatively identified as lobe cells. However, with that definition, the correlation of those boundaries with the IMF is not as good. These will be examined in a follow-up paper.

18.5.2. Model Validity

The unusually high By during this event allows us to test the robustness of the models used. While ΔL measured by IMAGE and POLAR correlated well with all the time-averaged solar wind parameters, only the northern hemisphere of the BATS-R-US and BATS-CRCM models showed comparable correlations. In the southern hemisphere, the observed correlation with By was opposite to that expected from any model, and is likely to be strongly aliased by the time variation of Bz along with By. The LFM model was also the only model to calculate average ΔL values in the same range as IMAGE and POLAR, with the ranges of BATS-R-US and BATS-CRCM being too narrow, and the range of OpenGGCM showing strong variability.

The BATS-R-US and BATS-CRCM generated outputs that are too symmetric compared to the satellite observations. The LFM model generated polar cap boundaries that are distorted and asymmetric but generally in line with the observed polar cap measurement. The OpenGGCM model predicted highly irregular polar cap boundaries. The most critical zero-level predictions are the average Dawn-Dusk Offset and the range of the offsets during the event, which clearly show the LFM model producing an average polar cap offset closest to the observed polar cap offset (Table 18.3). The BATS-CRCM and LFM models are coupled with an inner magnetosphere model, which could explain the better performance of BATS-CRCM compared to the BATS-R-US model, and the overall better performance of the LFM model.

18.6. SUMMARY

Using the Dawn-Dusk Offset as a proxy measurement of auroral conjugacy, we have found each hemisphere responds differently to changes in the solar wind. The northern (summer) hemisphere develops a lobe cell within the dusk convection cell, creating a moderate amount of precipitation not seen in the southern hemisphere. Even before the lobe cell occurs, we see a trend where the Dawn-Dusk Offset decreases with time in each hemisphere, causing the southern hemisphere to become more symmetric

about the pole but leading to a greater asymmetry of the northern polar cap. Our observations were compared to several MHD model outputs, with no model yielding an accurate depiction of the event. Most of the disagreement between the models and the satellite data, and between the models themselves, results from the way each model depicted a lobe cell developing throughout the event.

ACKNOWLEDGMENTS

This work was carried out using the SWMF/BATS-R-US tools developed at The University of Michigan Center for Space Environment Modeling (CSEM) and made available through the CCMC. POLAR-VIS data are available from The University of Iowa, and IMAGE WIC data are available from The University of California, Berkley. This research was partially supported by the Magnetospheric Multiscale Mission (MMS) mission under grant 599790Q. More detail can be found in the M.S. thesis of William Longley, [https://scholarship.rice.edu/handle/1911/77212], upon which this paper is based. Videos of the entire auroral conjunction event, and with overlays of the model predicted boundaries, can be seen at http://space.rice.edu/IMAGE/conjunction.

REFERENCES

Burch, J. L., P. H. Reiff, J. D. Menietti, R. A. Heelis, W. B. Hanson, S. D. Shawhan, E. G. Shelley, M. Sugiura, D. R. Weimer, and J. D. Winningham (1985), IMF B_y-dependent plasma flow and Birkeland currents in the dayside magnetosphere: 1. Dynamics Explorer observations, *J. Geophys. Res.*, *90*(A2), 1577–1593, doi:10.1029/JA090iA02p01577.

Burch, J. L. (2000), Image mission overview, *Space Science Reviews*, *91*, 1–14.

Crooker, N. U., and F. J. Rich (1993), Lobe cell convection as a summer phenomenon, *J. Geophys. Res.*, *98*(A8), 13,403–13,407, doi:10.1029/93JA01037.

Frank, L. A., J. B. Sigwarth, J. D. Craven, J. P. Cravens, J. S. Dolan, M. R. Dvorsky, P. K. Hardebeck, J. D. Harvey, and D. W. Muller (1995), The visible imaging system (VIS) for the Polar Spacecraft, *Space Science Reviews*, *71*, 297–328.

Fuller-Rowell, T. J., et al. (1996), A coupled thermosphere ionosphere model (CTIM), in: STEP Report, R. W. Schunk, ed., Scientific Committee on Solar Terrestrial Physics, NOAA/NGDC, Boulder, CO, *239*.

Glocer, A., M. Fok, X. Meng, G. Tóth, N. Buzulukova, S. Chen, and K. Lin, (2013). CRCM + BATSRUS two-way coupling. *Journal of Geophysical Research: Space Physics*, *118* (4), 1635–1650. doi:10.1002/jgra.50221.

Hapgood, M. A. (1992), Space physics coordinate transformations: A user guide. *Planetary and Space Science*, Vol. *40*, No. 5, pp. 711–717.

Liou, K., and P. T. Newell (2010), On the azimuthal location of auroral breakup: Hemispheric asymmetry, *Geophys. Res. Lett.*, *37*, L23103, doi:10.1029/2010GL045537.

Lyon, J. G., J. A. Fedder, and C. M. Mobarry (2004), The Lyon-Fedder-Mobarry (LFM) global MHD magnetospheric simulation code, *J. Atmos. Solar-Terr. Phys.*, *66*, 1333.

Mende, S. B., et al. (2000), Far ultraviolet imaging from the IMAGE spacecraft. 2. Wideband FUV imaging, *Space Science Reviews*, *91*, 271–285.

Merkin, V. G., and J. G. Lyon (2010), Effects of the low-latitude ionospheric boundary condition on the global magnetosphere, *JGR*, *115*, A10202, doi:10.1029/2010JA015461.

Østgaard, N., N. A. Tsyganenko, S. B. Mende, H. U. Frey, T. J. Immel, M. Fillingim, L. A. Frank, and J. B. Sigwarth (2005), Observations and model predictions of substorm auroral asymmetries in the conjugate hemispheres, *Geophys. Res. Lett.*, *32*, L05111, doi:10.1029/2004GL022166.

Powell, K. G., P. L. Roe, T. J. Linde, T. I. Gombosi, and D. L. De Zeeuw (1999), A Solution-Adaptive Upwind Scheme for Ideal Magnetohydrodynamics Journal of Computational Physics, Volume 154, Issue 2, 20 September, Pages 284–309, 10.1006/jcph.1999.6299.

Pulkkinen, A., L. Rastätter, M. Kuznetsova, H. Singer, C. Balch, D. Weimer, G. Tóth, A. Ridley, T. Gombosi, M. Wiltberger, J. Raeder, and R. Weigel (2013), Community-wide validation of geospace model ground magnetic field perturbation predictions to support model transition to operations. *Space Weather*, *11*(6), 369–385. doi:10.1002/swe.20056.

Raeder, et al. (2001), Global simulation of the geospace environment modeling substorm challenge event, *JGR*, *106*, 381.

Reiff, P. H., and J. L. Burch (1985), IMF B_y-dependent plasma flow and Birkeland currents in the dayside magnetosphere: 2. A global model for northward and southward IMF, *J. Geophys. Res.*, *90*(A2), 1595–1609, doi:10.1029/JA090iA02p01595.

Reiff, P. H., H. L. Collin, J. D. Craven, J. L. Burch, J. D. Winningham, E. G. Shelley, L. A. Frank, and M. A. Friedman (1988), Determination of auroral electrostatic potentials using high- and low-altitude particle distributions, *J. Geophys. Res.*, *93*(A7), 7441–7465, doi:10.1029/JA093iA07p07441.

Reistad, J. P., N. Østgaard, K. M. Laundal, and K. Oksavik (2013), On the non-conjugacy of nightside aurora and their generator mechanisms, J. Geophys. Res. *Space Physics*, *118*, 3394–3406, doi:10.1002/jgra.50300.

Ridley, A. J., Gombosi, T. I., Sokolov, I. V., Tóth, G., and Welling, D. T. (2010). Numerical considerations in simulating the global magnetosphere. *Annales Geophysicae*, *28*(8), 1589–1614. doi:10.5194/angeo2815892010.

Stubbs, T.J., R. R. Vondrak, N. Østgaard, J. B. Sigwarth, and L. A. Frank (2005), Simultaneous observations of the auroral oval in both hemispheres under varying conditions., *Geophys. Res. Lett*., Vol *32*, L03103, doi:10.1029/2004GL021199.

Tóth, G., B. van der Holst, I. V. Sokolov, D. L. De Zeeuw, T. I. Gombosi, F. Fang, W. B. Manchester, X. Meng, D. Najib, K. G. Powell, Q. F. Stout, A. Glocer, Y.-J. Ma, M. Opher (2012), Adaptive numerical algorithms in space weather modeling. *Journal of Computational Physics*, *231* (3), 870–903. doi:10.1016/j.jcp.2011.02.006.

VanZandt, T. E., W. L. Clark, and J. M. Warnock (1972), Magnetic apex coordinates: A magnetic coordinate system for the ionospheric F_2 layer, *J. Geophys. Res.*, *77*(13), 2406–2411, doi:10.1029/JA077i013p02406.

19

Day-to-Day Variability of the Quiet-Time Plasmasphere Caused by Thermosphere Winds

Jonathan Krall[1], Joseph D. Huba[1], Douglas P. Drob[2], Geoff Crowley[3], and Richard E. Denton[4]

Video of Yosemite Talk, URL: http://dx.doi.org/10.15142/T3KS3P

ABSTRACT

Simulations using the NRL SAMI3 (Sami3 is Also a Model of the Ionosphere) ionosphere/plasmasphere code have recently shown that the shape of the quiet-time plasmasphere varies significantly with the thermospheric wind pattern. Results are shown using winds from the Horizontal Wind Model 93 (HWM93), 07 (HWM07), and the Thermosphere Ionosphere Mesosphere Electrodynamics General Circulation Model (TIMEGCM). Because the differences in winds from these models are consistent with day-to-day variability in measured winds, we find that our SAMI3 results represent effects in the plasmasphere that could result from day-to-day variability in the thermosphere. We conclude that day-to-day variability in thermospheric wind patterns leads to day-to-day variability in the inner magnetosphere.

19.1. INTRODUCTION

The plasmasphere affects the magnetosphere by affecting, for example, electromagnetic waves and particle energization [*Singh et al.*, 2011]. During a geomagnetic storm, the plasmasphere, a tenuous plasma trapped by the Earth's magnetic field, is shaped by magnetospheric convection [*Liemohn et al.*, 2004]. At the onset of a storm, the plasmasphere erodes rapidly [*Carpenter*, 1966; *Goldstein et al.*, 2003], shrinking in radius by 2–3 R_E in a matter of hours.

During quiet times, the plasmasphere is often considered to have a "teardrop" shape, resulting from a combination of corotation and quiet-time, steady magnetospheric convection [*Doe et al.*, 1992]. However, even the earliest measurements of the duskside "bulge" showed slight day-to-day variation in the position of the bulge; this was attributed to moderate geomagnetic activity [*Carpenter*, 1966]. Later observations, in the form of extreme ultraviolet (EUV) images from the Imager for Magnetopause-to-Aurora Global Exploration (IMAGE) spacecraft [*Burch*, 2000], show plasmasphere features such as shoulders, fingers, notches, crenulation, and channels [*Darrouzet et al.*, 2009; *Singh et al.*, 2011].

In a recent study, we found that the shape of the plasmasphere can be affected by thermosphere winds [*Krall et al.*, 2014]. Focusing on a geomagnetically quiet post-storm refilling period, 1 to 5 February 2001, and using the NRL SAMI3 ionosphere/plasmasphere model, we found that results varied with respect to varying thermosphere winds.

Below we review the SAMI3 simulations of *Krall et al.* [2014], in which the model ionosphere is coupled to each of three wind models: the HWM93 empirical wind model [*Hedin*, 1991], the more-recent HWM07 model [*Drob and*

[1]*Plasma Physics Division, Naval Research Laboratory (NRL), Washington, DC, USA*

[2]*Space Sciences Division, Naval Research Laboratory, Washington, DC, USA*

[3]*Atmospheric & Space Technology Research Associates (ASTRA) LLC, Boulder, CO, USA*

[4]*Department of Physics and Astronomy, Dartmouth College, Hanover, NH, USA*

Magnetosphere-Ionosphere Coupling in the Solar System, Geophysical Monograph 222, First Edition.
Edited by Charles R. Chappell, Robert W. Schunk, Peter M. Banks, James L. Burch, and Richard M. Thorne.

et al., 2008], and the first-principles TIMEGCM [*Roble and Ridley*, 1994; *Crowley et al.*, 1999]. We next consider the hypothesis that differences between these three model results can serve as a proxy for differences that might arise due to day-to-day variability. Based on these findings, we consider the hypothesis that thermospheric winds are a source of day-to-day variability in the shape of the plasmasphere.

19.2. SAMI3

The NRL SAMI3 code [*Huba et al.*, 2008; *Huba and Krall*, 2013], which is based on the SAMI2 (Sami2 is Another Model of the Ionosphere) code [*Huba et al.*, 2000], was used in this study. SAMI3 includes the wind-driven dynamo electric field, solving a two-dimensional electrostatic potential equation that is based on current conservation ($\nabla \cdot \mathbf{J} = 0$). In SAMI3, thermospheric composition and winds are specified. Composition can be specified using the NRLMSISE00 model [*Picone et al.*, 2002] or using values from the TIMEGCM thermosphere model, which we have coupled to SAMI3. For wind velocities, we use TIMEGCM or either of the HWM07 or HWM93 empirical wind models.

For dynamics along field lines, SAMI3 solves the continuity and momentum fluid equations for seven ion species. The temperature equation is solved for three atomic ion species and the electrons. Transport across field lines is included as $\mathbf{E} \times \mathbf{B}$ drifts. These include the corotation potential, if needed, the wind-driven dynamo potential, and the high-latitude magnetospheric potential, which are simply added together. The magnetospheric potential is provided by the Weimer05 [*Weimer*, 2005] empirical model, which is driven by solar wind quantities B_y, B_z, V_x, and n_p.

Below we present simulation results that first appeared in *Krall et al.* [2014, further modeling details given therein], where we simulated a post-storm period. We will focus on days 33 to 36 of 2001, during which time the SAMI3 plasmasphere is refilling with plasma from the well-tested SAMI3 ionosphere [*Shim and et al.*, 2011].

19.3. SAMI3 RESULTS

Figure 19.1 shows color contours of the base 10 logarithm of the electron density ($\log_{10}\ n_e$) in the magnetic equatorial plane, plotted every 8 hours during 3 days of refilling for a simulation using the HWM07 wind model. Plots in any one column are separated by one day of simulated time.

Of interest is the plasmasphere morphology, which might be assumed to be the same as the plasmapause morphology. During an extended quiet period of refilling, however, the plasmapause becomes ill defined. We instead consider two measures of the plasmasphere shape. First, a single white contour line in each plot at a fixed density value 100 cm^{-3} highlights the shape of the model plasmasphere. Second, density profiles versus magnetic local time (MLT) at fixed $L = 4.4$ and at the magnetic equator are shown in the bottom row. The three density profiles in each such plot correspond to the three contour plots in the same column; these profiles show clear evidence of refilling, with later profiles having higher density.

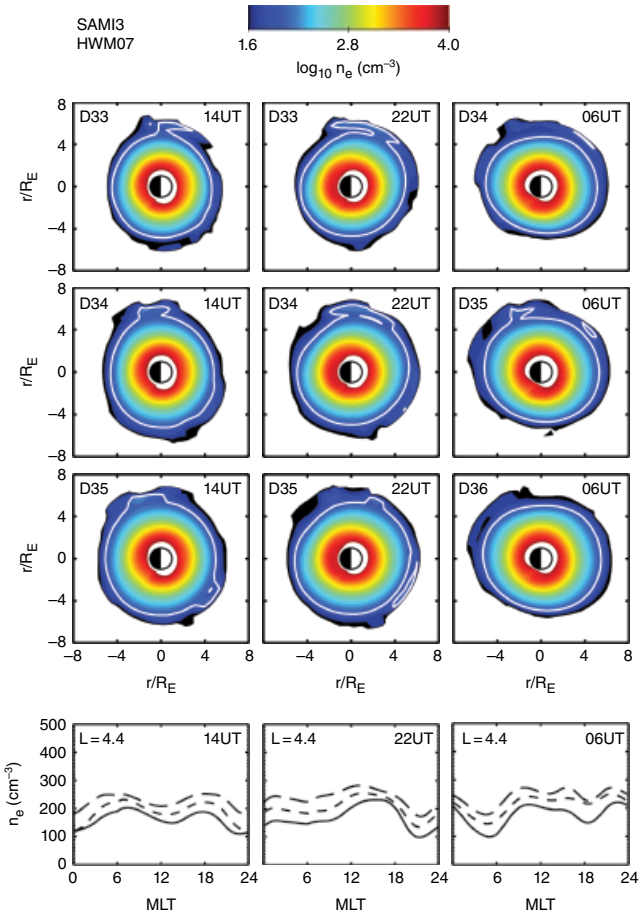

Figure 19.1 Color-contours of n_e (log scale) in the equatorial plane, plotted every 8 hours during 3 days of refilling. A single white contour line in each plot indicates density 100 cm^{-3}. Below each column is a plot of n_e versus MLT at $L = 4.4$ for the top contour plot (solid curve), middle plot (dashed), and bottom plot (long-dashed) in that column. The HWM07 wind model is used in this case.

Given that the plasmasphere is a three-dimensional object, it is possible that a tilt in the plasmasphere out of the equatorial plane would appear to be a change in its shape. In this version of SAMI3, however, the magnetic and geographic axes are aligned in such a way that there

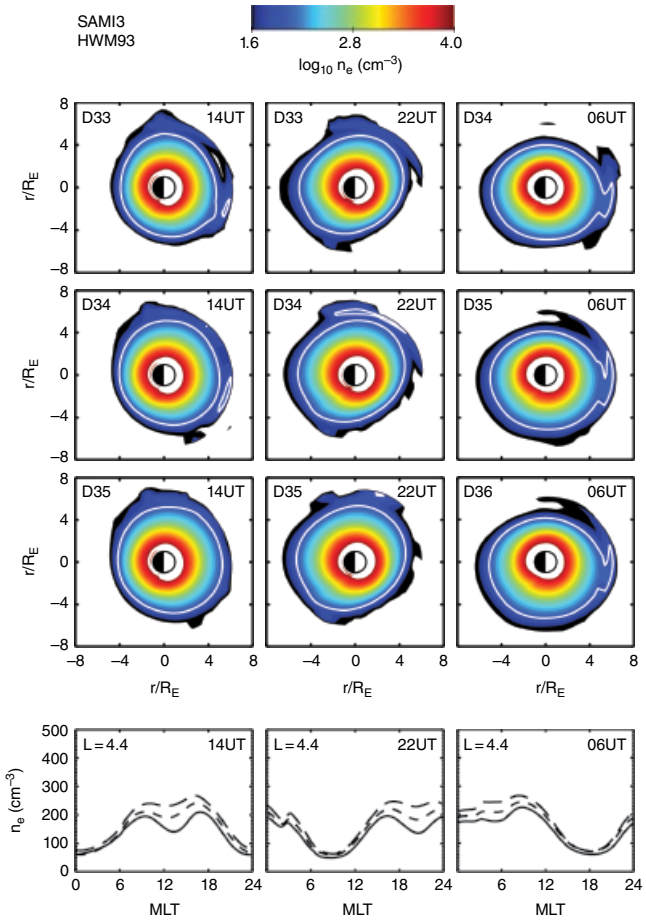

Figure 19.2 Same as Figure 19.1 but with HWM93 winds.

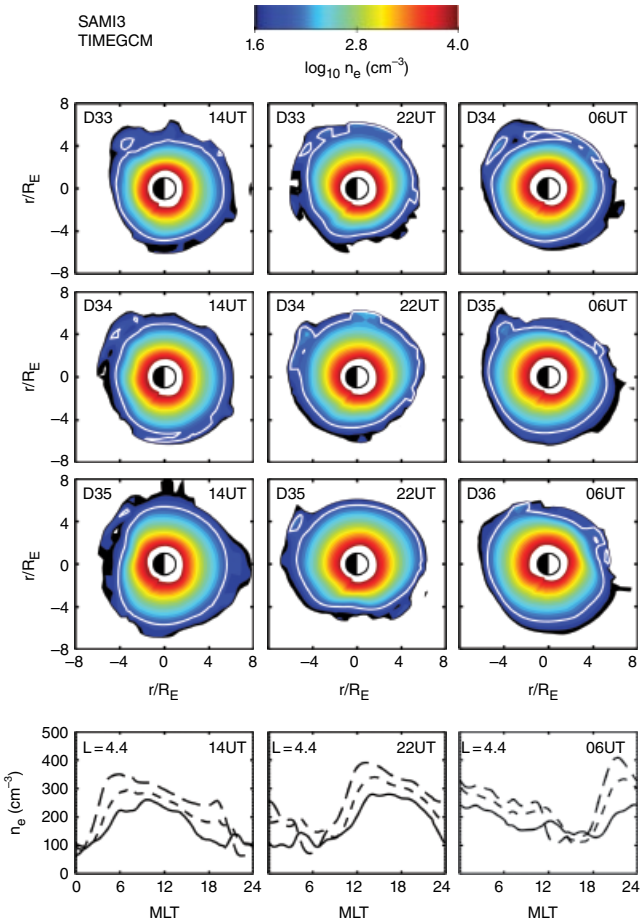

Figure 19.3 Same as Figure 19.1 but with TIMEGCM thermospheric winds and composition values.

is no significant tilting. As used here, "shape" effectively refers to the shape of the plasmapause.

Figure 19.2 shows color contours of the electron density for a simulation using the HWM93 wind model in the same format as Figure 19.1. Results are similar to the HWM07 case, except that the shape is different and the refilling, as seen in the density profiles (lower row of plots), is less uniform than in the HWM07 case.

In the HWM07 and HWM93 results, we see that the morphology of the plasmasphere repeats at one day intervals. For example, the three plots in the middle column of Figure 19.2 have a similar, slightly-elongated shape. Profiles versus MLT at $L = 4$, shown in the bottom row, confirm the similarity in the density profiles within each column. In *Krall et al.* [2014, see Figure 19.2 therein] we show that this repetition disappears when the simulation is run with no winds.

Noting that the HWM07 and HWM93 empirical wind models include seasonal trends, but no day-to-day variability, we can interpret the lack of day-to-day variability here in light of our previous result, that the thermosphere can shape the quiet-time plasmasphere. Specifically, we interpret the lack of day-to-day variability in these results as evidence that the influence of the model thermosphere (no day-to-day variability) is stronger than the influence (via the Weimer05 model) of the solar wind stream, which does vary from day to day. Our current hypothesis, that thermospheric winds are a source of day-to-day variability in the shape of the plasmasphere, suggests that the daily repetition in Figures 19.1 and 19.2 may be unphysical.

Figure 19.3 shows color contours of the electron density for a simulation using the TIMEGCM thermosphere in the same format as Figure 19.1. Here we expect to see some degree of day-to-day variability, which enters the model through the high-latitude potential and through tidal boundary conditions at the low-altitude boundary (at about 30 km). Results show that, while the day-to-day repetition of plasmasphere shape is perhaps less striking than in the HWM93 case, it is clearly present in the

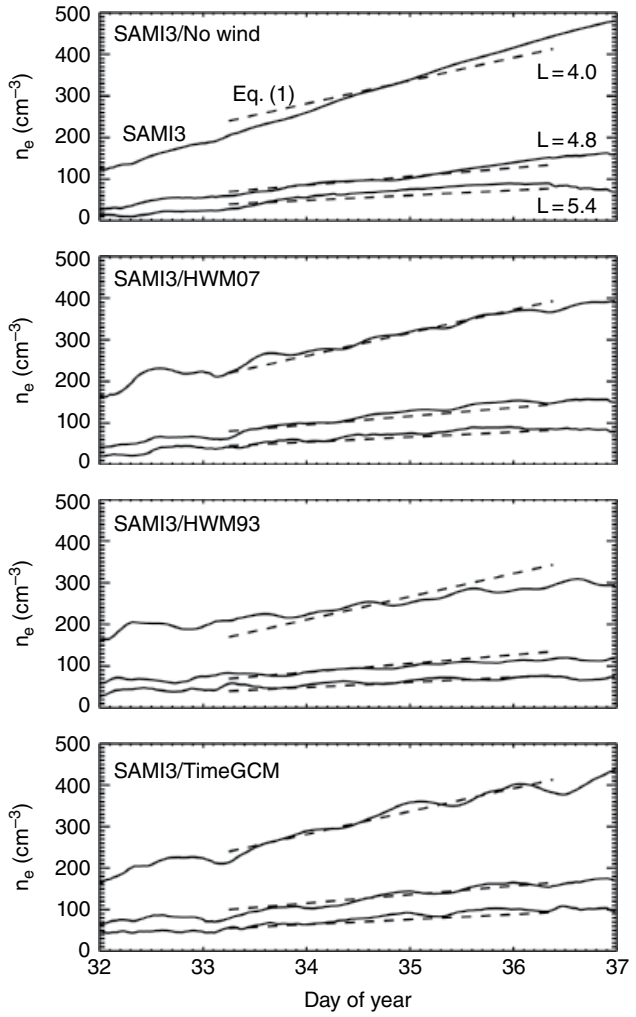

Figure 19.4 Electron density averaged over longitude in the equatorial plane plotted versus time for $L = 4.0$, 4.8 and 5.4 (solid curves) for SAMI3/No Wind, SAMI3/HWM07, SAMI3/HWM93, and SAMI3/TIMEGCM. Dashed lines in each plot indicate rates from *Krall et al.* [2014, see equation 1 therein].

density profiles (bottom row). As with the comparison of HWM07 to HWM93 results, we see that the shape of the plasmasphere at any given time differs from any corresponding result using a different wind model.

These results show plasmaspheric features that co-rotate with Earth. Specifically, the density profiles of Figures 19.2 and 19.3 (see lowest row of each figure) show a similar shape in each panel, with the shape moving by about 8 hours in local time as universal time advances by 8 hours.

Refilling curves for the three wind models, and for a run with no winds, are shown in Figure 19.4. In each case, n_e from SAMI3 is averaged over longitude at the magnetic equator and plotted versus time at $L = 4.0$, 4.8, and 5.4. For comparison, rates from equation (1) of *Krall et al.* [2014] are plotted as dashed lines. These rates are based on in situ measurements and are identical in each plot. Among the SAMI3 results, refilling is fastest for the No Wind case. Model-data agreement generally improves as we go from HWM93 to HWM07 and then to TIMEGCM.

19.4. VARIABILITY IN WINDS

In *Krall et al.* [2014], we found that winds affect the plasmasphere in two specific ways. First, the winds shape the ionosphere through vertical/meridional $\mathbf{E}\times\mathbf{B}$ drifts, affecting the source of the plasmasphere. As a result, the refilling rate changes with the winds.

Second, winds affect zonal $\mathbf{E}\times\mathbf{B}$ drifts, affecting the shape of the plasmasphere. As illustrated in Figures 19.1, 19.2, and 19.3, the plasmasphere is shaped by the combined effects of high-latitude convection potential, the wind-driven dynamo potential, and corotation. Even during a moderate storm, the wind-driven dynamo potential distorts potential contours out to about $L = 4$ [*Krall et al.*, 2014, see Figure 15 therein]. By contrast, wind-driven ion dynamics along the geomagnetic field were found to have little effect on either the refilling rate or the shape.

Wave coupling from below is a major source of the observed day-to-day variability of the thermosphere and ionosphere [*Fang et al.*, 2013; *Siskind et al.*, 2014]. This variability is illustrated in Figure 19.5, which shows a comparison of individual zonal wind observations between 225 and 300 km within approximately ±7.5° latitude of the Renior Fabry-Perot Interferometer (FPI), located at 6.89°S, 38.56° W [*Makela et al.*, 2013]. The observations from the Renior FPI (blue), the Jicamarca FPI (cyan), the European Space Agency, Gravity Field and Steady State Ocean Circulation Explorer (GOCE) satellite (magenta), the wind imaging interferometer (WINDII) 557.7-nm measurements (green), and the WATS instrument on the Dynamics Explorer 2 (DE2) satellite (red) are shown [for details, please see Table 1 in *Drob et al.*, 2015]. In addition to being localized in latitude, these satellite data are, except for DE2, confined in longitude to ±90° for WINDII and ±10° for GOCE.

In Figure 19.5 there is general agreement among the various data sets where they overlap and/or are adjacent. The interannual self-consistency of local time variations is demonstrated by the fact that DE2 observations, obtained from 1981 to 1983, WINDII measurements between 1992 to 1997, GOCE observations from 2009 to 2012, and FPI measurements from 2009 to 2013, all align well. This shows that inter-annual variability is not strong, even across a solar cycle [*Drob et al.*, 2015]. However, the scatter in the data points shows that there is significant

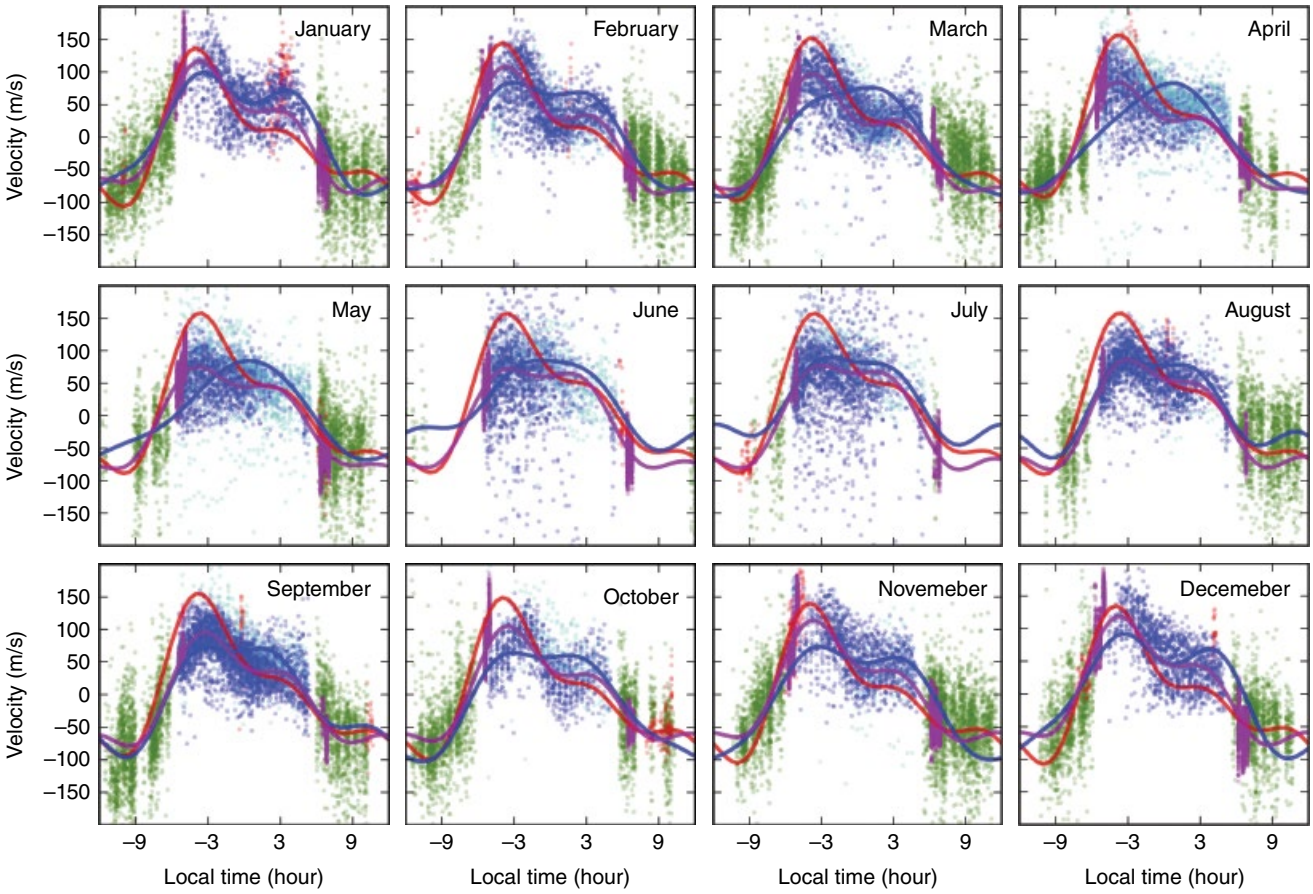

Figure 19.5 HWM model winds and the zonal wind observations. The observations are shown as data points for the Renior FPI (blue), the Jicamarca FPI (cyan), GOCE (magenta), WINDII 557.7-nm measurements (green), and DE2 WATS (red). The model results are plotted as curves for HWM93 (red), HWM07 (blue), and HWM14 (magenta) at 250 km.

variability, with the average of the hourly standard deviations for all of the data shown being 36.7 m/s.

The curves plotted in Figure 19.5 show model results from HWM93 (red), HWM07 (blue), and the recently developed HWM14 [*Drob et al.*, 2015] model (magenta) at 250 km. We see that the HWM93 and HWM07 curves generally lie within the bounds of the data, meaning that the difference between SAMI/HWM07 and SAMI/HWM93 results above are consistent with differences that could arise due to day-to-day variability.

19.5. CONCLUSIONS

We have reviewed SAMI3 plasmasphere simulations showing that the plasmasphere shape and post-storm refilling rate depend significantly on thermosphere winds. However, we do not yet know the degree to which day-to-day variability in thermosphere winds affects the inner magnetosphere via the plasmasphere. In the case of TIMEGCM, there is day-to-day variability in the winds but only as a result of the high latitude forcing driven by the solar wind variability and assimilative mapping of ionospheric electrodynamics (AMIE) high latitude electric fields [*Crowley and Meier*, 2008; *Crowley et al.*, 2008, 2010]. The TIMEGCM variability is expected to be more realistic than that of the HWM models because the HWM models, by design, lack day-to-day variability.

We conclude that the differences seen in SAMI3 results using winds from the HWM07, HWM93, and TIMEGCM models represent differences that might arise from day-to-day variability in the thermospheric winds. That is, if all three wind models are valid, then properly included day-to-day variability could produce a result that looks like the HWM93 result on one day, the HWM07 result on the next day, and the TIMEGCM result on the day after that.

ACKNOWLEDGMENTS

This research was supported by NRL Base Funds and the National Aeronautics and Space Administration (NASA) Living With a Star (LWS) Program. The Dartmouth College work was supported by NASA grant NNX10AQ60G (Living with a Star Targeted Research Plasmasphere focused science topic) and National Science Foundation (NSF) grant AGS-1105790. The ASTRA work was funded in part by NSF grants AGS-1354574 and AGS-1144062 and the NASA Ionospheric Connection Explorer (ICON) mission NNG12FA45C (Subcontract 00008210 to ASTRA).

REFERENCES

Burch, J. L. (2000), Image mission overview, *Space Sci. Rev.*, *91*, 1–14.

Carpenter, D. L. (1966), Whistler studies of the plasmapause in the magnetosphere, 1, temporal variations in the position of the knee and some evidence on plasma motions near the knee, *J. Geophys. Res.*, *71*, 693–709.

Crowley, G., and R. R. Meier (2008), Disturbed O/N2 ratios and their transport to middle and low latitudes, in *Midlatitude Ionospheric Dynamics and Disturbances*, edited by P. M. Kintner, A. J. Coster, T. Fuller-Rowell, A. J. Mannucci, M. Mendillo, and R. Heelis, pp. 221–234, American Geophysical Union, Washington, DC, doi:10.1029/181GM20.

Crowley, G., C. Freitas, A. Ridley, D. Winningham, R. G. Roble, and A. D. Richmond (1999), *Next generation space weather specification and forecasting model*, Ionospheric Effects Symposium, Alexandria, VA

Crowley, G., A. Reynolds, J. P. Thayer, J. Lei, L. J. Paxton, A. B. Christensen, Y. Zhang, R. R. Meier, and D. J. Strickland (2008), Periodic modulations in thermospheric composition by solar wind high speed streams, *Geophysical Research Letters*, *35*(21), doi:10.1029/2008GL035745, l21106.

Crowley, G., D. J. Knipp, K. A. Drake, J. Lei, E. Sutton, and H. Lühr (2010), Thermospheric density enhancements in the dayside cusp region during strong by conditions, *Geophysical Research Letters*, *37*(7), doi:10.1029/2009GL042143, l07110.

Darrouzet, F., D. L. Gallagher, N. Andre, D. L. Carpenter, I. Dandouras, P. M. E. Decreau, J. D. Keyser, R. E. Denton, J. C. Foster, J. Goldstein, M. B. Moldwin, B. W. Reinisch, B. R. Sandel, and J. Tu (2009), Plasmaspheric density structures and dynamics: properties observed by the CLUSTER and IMAGE missions, *Space Sci. Rev.*, *145*, 55–106, doi:10.1007/s11214-008-9438-9.

Doe, R. A., M. B. Moldwin, and M. Mendillo (1992), Plasmapause morphology determined from an empirical ionospheric convection model, *Journal of Geophysical Research: Space Physics*, *97*(A2), 1151–1156, doi:10.1029/91JA01649.

Drob, D. P., and et al. (2008), An empirical model of the Earth's horizontal wind fields: HWM07, *J. Geophys. Res.*, *113*, A12304, doi:doi:10.1029/2008JA013668.

Drob, D. P., J. T. Emmert, J. W. Meriwether, J. J. Makela, E. Doornbos, M. Conde, G. Hernandez, J. Noto, K. A. Zawdie, S. E. McDonald, J. D. Huba, and J. H. Klenzing (2015), An update to the Horizontal Wind Model (HWM): The quiet time thermosphere, *Earth and Space Science*, pp. 301–319 doi:10.1002/2014EA000089.

Fang, T.-W., R. Akmaev, T. Fuller-Rowell, F. Wu, N. Maruyama, and G. Millward (2013), Longitudinal and day-to-day variability in the ionosphere from lower atmosphere tidal forcing, *Geophysical Research Letters*, *40*(11), 2523–2528, doi:10.1002/grl.50550.

Goldstein, J., B. R. Sandel, W. T. Forrester, and P. H. Reiff (2003), IMF-driven plasmasphere erosion of 10 July 2000, *Geophys. Res. Lett.*, *30*, 1146, doi:10.1029/2002GL016478.

Hedin, A. E. (1991), Revised global model of thermosphere winds using satellite and ground-based observations, *J. Geophys. Res.*, *96*(A5), 7657–7688, doi:10.1029/91JA00251.

Huba, J. D., and J. Krall (2013), Modeling the plasmasphere with SAMI3, *Geophys. Res. Lett.*, *40*, 6–10, doi:10.1029/2012GL054300.

Huba, J. D., G. Joyce, and J. A. Fedder (2000), SAMI2 (Sami2 is another model of the ionosphere): A new low-latitude ionosphere model, *J. Geophys. Res.*, *105*(A10), 23,035–23,053, doi:10.1029/2000JA000035.

Huba, J. D., G. Joyce, and J. Krall (2008), Three-dimensional equatorial spread *F* modeling, *Geophys. Res. Lett.*, *35*, L10102, doi:10.1029/2008GL033509.

Krall, J., J. D. Huba, R. E. Denton, G. Crowley, and T.-W. Wu (2014), The effect of the thermosphere on quiet time plasmasphere morphology, *Journal of Geophysical Research: Space Physics*, *119*(6), 5032–5048, doi:10.1002/2014JA019850.

Liemohn, M. W., A. J. Ridley, D. L. Gallagher, D. M. Ober, and J. U. Kozyra (2004), Dependence of plasmaspheric morphology on the electric field description during the recovery phase of the 17 April 2002 magnetic storm, *Journal of Geophysical Research: Space Physics*, *109*(A3), n/a–n/a, doi:10.1029/2003JA010304.

Makela, J. J., D. J. Fisher, J. W. Meriwether, R. A. Buriti, and A. F. Medeiros (2013), Near-continual ground-based nighttime observations of thermospheric neutral winds and temperatures over equatorial brazil from 2009 to 2012, *Journal of Atmospheric and Solar-Terrestrial Physics*, *103*, 94–102, doi:10.1016/j.jastp.2012.11.019.

Picone, J. M., A. Hedin, D. Drob, and A. Aikin (2002), NRLMSISE-00 empirical model of the atmosphere: Statistical comparisons and scientific issues, *J. Geophys. Res.*, *107*, doi:10.1029/2002JA009430.

Roble, R. G., and E. C. Ridley (1994), A thermosphere-ionosphere-mesosphere-electrodynamics general circulation model (time-GCM): Equinox solar cycle minimum simulations (30–500 km), *Geophysical Research Letters*, *21*(6), 417–420, doi:10.1029/93GL03391.

Shim, J. S., and et al. (2011), CEDAR electrodynamics thermosphere ionosphere (ETI) challenge for systematic assessment of ionosphere/thermosphere models: NmF2, hmF2, and vertical drift using ground-based observations, *Space Weather*, *9*, S12003, doi:10.1029/2011SW000727.

Singh, A. K., R. P. Singh, and D. Siingh (2011), State studies of Earth's plasmasphere: A review, *Planet. Space Sci.*, *59*, 810–834, doi:10.1016/j.pss.2011.03.013.

Siskind, D. E., D. P. Drob, K. F. Dymond, and J. P. McCormack (2014), Simulations of the effects of vertical transport on the thermosphere and ionosphere using two coupled models, *Journal of Geophysical Research: Space Physics*, *119*(2), 1172–1185, doi:10.1002/2013JA019116.

Weimer, D. R. (2005), Predicting surface geomagnetic variations using ionospheric electrodynamic models, *J. Geophys. Res.*, *110*, A12307, doi:10.1029/2005JA011270.

Part V
The Coupling of the Ionosphere and Magnetosphere at Other Planets and Moons in the Solar System

20

Magnetosphere-Ionosphere Coupling at Planets and Satellites

Thomas E. Cravens

Video of Yosemite Talk, URL: http://dx.doi.org/10.15142/T32S31

ABSTRACT

An important topic in solar system plasma physics is the linkage and coupling of denser, colder ionospheric plasma of planets and satellites with more energetic external plasma such as in the solar wind, magnetospheres, and ionospheres. How energy and momentum are exchanged between different plasma regions obviously depends on the characteristics of the body, and in particular on the presence of, or lack of, a significant intrinsic magnetic field. Field-aligned electrical currents play an important role in these processes. The strong magnetic fields at Earth, Jupiter, and Saturn carve out large magnetospheres, within which the electrodynamical force balance is enforced by current systems, some of which close in the ionosphere. Auroral emission from planetary or satellite upper atmospheres often, but not always, accompanies the field-aligned currents. Objects like Venus, and Saturn's satellite Titan, have ionospheres, but lack significant intrinsic magnetic fields. The external plasma, solar wind plus associated induced magnetospheres, still couples with the ionospheres and upper atmospheres of such bodies. A broad review of magnetosphere-ionosphere (M-I) coupling at other planets will be given in this chapter.

20.1. INTRODUCTION

20.1.1. Plasmas

Different regions of the space environment such as surfaces, neutral atmospheres, ionospheres, magnetospheres, and the solar wind are linked in several ways including (1) mass and particles (governed by a fluid continuity equation), (2) momentum (governed by an equation of motion or momentum equation), and (3) energy (governed by an energy equation). The electric and magnetic fields obey Maxwell's equations. A key characteristic of plasmas is high electrical conductivity, so that electrical currents easily flow and induce magnetic fields. Magnetic fields often connect different plasma regions. M-I coupling in its broadest sense includes the "induced" magnetospheres of Venus and Mars as well as the intrinsic magnetic field cases of Mercury, Earth, Jupiter, and Saturn. For a more thorough treatment of this subject, the reader is referred to textbooks such as, but not limited to, *Cravens* [1997], *Kivelson and Russell* [1985], and *Schunk and Nagy* [2000].

20.1.2. Interaction of the Solar Wind with Solar System Bodies

The Sun is the source of extreme ultraviolet and soft X-ray radiation that generates planetary ionospheres via the photoionization of the neutral atmospheres. The solar corona is the source of the solar wind, which can inject momentum and energy into planetary magnetospheres and ionospheres.

Department of Physics and Astronomy, University of Kansas, Lawrence, KS, USA

Magnetosphere-Ionosphere Coupling in the Solar System, Geophysical Monograph 222, First Edition.
Edited by Charles R. Chappell, Robert W. Schunk, Peter M. Banks, James L. Burch, and Richard M. Thorne.

One way to organize the types of interaction is as follows [*Cravens*, 1989, 1997; *Kivelson and Russell*, 1995]:

1. Earth-like (strong intrinsic magnetic field acts as obstacle to solar wind flow)
2. Venus-like (ionospheric thermal pressure)
3. Comet-like (ion pick-up and mass-loading)
4. Moon-like (direct impact with surface)

Note that "real" interactions are a "mixture" of the above prototypical interaction types. For example, 1. through 3. shown above are all relevant to Mars, which in its southern hemisphere, has strong crustal magnetic fields, although no global field.

20.1.3. Earth-like Interactions

The definition of the magnetosphere is relatively clear-cut for Earth-like interactions, that is, the region where the intrinsic magnetic field organizes the plasma morphology and dynamics [*Hill*, 1983; *Mauk et al.*, 2002]. A brief summary of the Earth-like interaction is now given, but this topic is mostly left to other papers in this volume.

Figure 20.1 is a schematic of the Earth's magnetosphere, showing the magnetopause (i.e., boundary between the solar wind plasma and magnetospheric plasma), the cusp (where newly opened magnetic field lines connect the Earth to the solar wind), and the magnetotail. Magnetic pressure in the magnetosphere balances the solar wind dynamic pressure at the magnetopause boundary, which is typically 10 R_E (Earth radii) from Earth, although the size depends on solar wind conditions. The solar wind is supersonic and superAlfvénic, and a bow shock is present upstream of the magnetosphere (not shown in Figure 20.1). Magnetic reconnection at the dayside magnetopause "opens" the magnetosphere, allowing some magnetic field lines to connect the Earth to the interplanetary medium. Magnetic flux is convected tailward past the cusp regions and into the tail lobes.

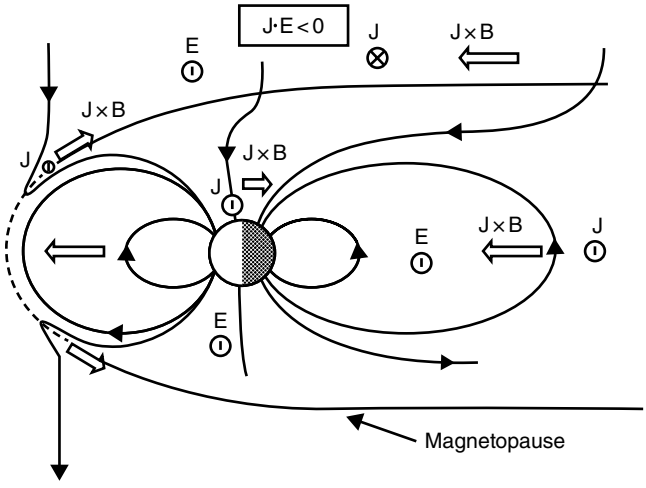

Figure 20.1 Schematic of the terrestrial magnetosphere, as viewed from the side. Electrical currents are shown as well as where large magnetic stresses (J × B) are present. Field-aligned currents linking to the ionosphere ($J_{||}$) are also indicated. The magnetic reconnection diffusion region on the subsolar magnetopause is shown for a case in which the interplanetary magnetic field is southward. The Sun is to the left of the diagram. The bow shock, located outside the magnetopause, is not shown. [from *Cravens*, 1997, Cambridge University Press, © 1997, used with permission]

Electrical current also flows in the plasmasheet (or neutral sheet), a layer of enhanced plasma density and pressure. This current is responsible for inducing the magnetic field of the tail. Sporadic reconnection takes place in the plasmasheet, thus removing magnetic flux and energizing the plasma. Electrical currents flow along magnetic field lines (field-aligned or "Birkeland" currents) and link different regions. Aurorae can be associated with these field-aligned currents. Electrons can be accelerated to several kiloelectron-volt (keV) energies at the plasmasheet, during events called substorms. The electrons are guided by the magnetic field toward Earth and precipitate into the atmosphere where they deposit energy in the ionosphere in the form of heat, ionization, and optical emissions [*Mauk et al.*, 2002; *Galand and Chakrabati*, 2002].

20.1.4. The Solar Wind Interaction with Non-Magnetic Planets (Venus-like and Comet-like)

External plasmas interact with non-magnetic bodies via the atmospheres and ionospheres. For example, the thermal pressure of dense ionospheric plasma acts as an obstacle to the magnetized solar wind at Venus. When the solar wind dynamic pressure is relatively low, the ionosphere is largely field-free, and the interplanetary magnetic field piles up just outside the ionospheric boundary (called the ionopause). For high solar wind dynamic pressure, magnetic fields are induced throughout the ionosphere, in which case the ionopause becomes a broad transition region. Solar wind dynamic pressure is "converted" into magnetic pressure in the magnetic pile-up region (or magnetic barrier), and this pressure is balanced by thermal pressure of the ionosphere. This pressure balance was first confirmed by in situ measurements made by instruments onboard the Pioneer Venus Orbiter [*Russell and Vaisberg*, 1983; *Luhmann and Cravens*, 1991]. Figure 20.2 illustrates this type of interaction. The magnetic field drapes around the planet and extends into an induced magnetotail.

Another process affecting the dynamics is the addition of mass to the flow, which by conservation of momentum causes the flow to slow down. The "mass-loading" process

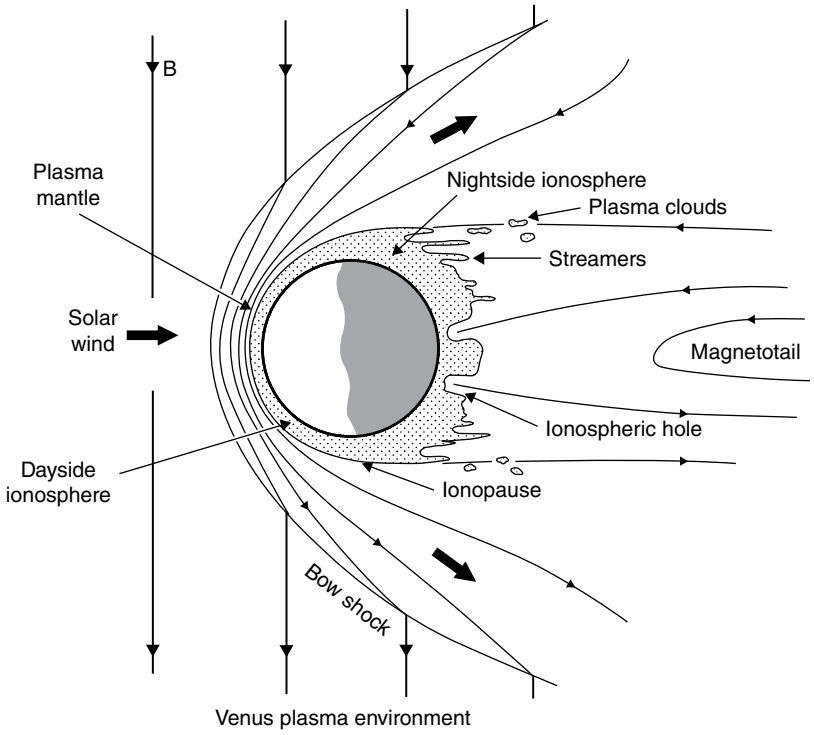

Figure 20.2 Schematic of the solar wind interaction with Venus. The Sun is to the left of the diagram. Magnetic field lines are shown as well as the direction of the solar wind flow around the ionosphere, which is also indicated. The ionopause is the upper boundary of the ionosphere, and for the case shown the ionosphere is field-free (not always the case). [from *Cravens*, 1997, Cambridge University Press, © 1997, used with permission]

is especially important for the solar wind interaction with comets. The nucleus of a comet is typically only a few kilometers across and consists of frozen volatiles (mostly water but some carbon dioxide and other species) [cf. *Mumma and Charnley*, 2011] and dust. As the comet moves into the inner solar system, the ice heats up and sublimates, with the vapor cloud extending great distances into the surrounding interplanetary space (and solar wind). Dust is carried out with the gas. When solar radiation ionizes the neutral molecules, cometary ions are created and respond to the Lorentz force associated with the interplanetary magnetic field (IMF) and the associated motional electric field ($\mathbf{E} = -\mathbf{u} \times \mathbf{B}$, where $\mathbf{u}$ is the solar wind velocity and $\mathbf{B}$ is the magnetic field). Cometary ions are said to be "picked-up" by the solar wind flow, thus affecting the dynamics and energetics of the overall flow. The slowing down of the mass-loaded plasma flow near the comet is associated with the build-up and draping of the magnetic field (i.e., induced currents flow) and the formation of a magnetotail.

Mass loading of external flow via ionization of neutral gas also takes place for other solar system bodies that have extensive exospheres, including Mars, Saturn's satellites Titan and Enceladus, and Jupiter's satellite Io.

20.2. MHD PROCESSES AND MI COUPLING TUTORIAL

20.2.1. Kinetic Description of Plasmas

The appropriate description of space plasmas (e.g., corona, solar wind, magnetosphere, ionosphere) depends on what one wants to know about the plasma, and on the computational and analytical tools at one's disposal. The basic equation is Boltzmann's equation (or Vlasov equation in the absence of collisions) [*Krall and Trivelpiece*, 1973], which describes the time evolution of particle distribution functions as functions of position and velocity. Maxwell's equations are also needed to describe the electric and magnetic fields. A fluid description is often sufficient, and then the fluid conservation equations (i.e., continuity, momentum, and energy) apply.

20.2.2. MHD Theory

For a magnetized plasma, magnetohydrodynamic (MHD) theory is an appropriate description of many aspects of a plasma environment [see *Krall and Trivelpiece*,1973; see many references in *Cravens*, 1997]. In this short review, we will emphasize the

momentum/force balance using MHD theory. The momentum equation is:

$$\rho\left(\frac{\partial \mathbf{u}}{\partial t}+\mathbf{u}\cdot\nabla\mathbf{u}\right)=-\nabla\left(p_e+p_i\right)+\mathbf{J}\times\mathbf{B}+\rho\mathbf{g}-\rho\nu_{in}\left(\mathbf{u}-\mathbf{u}_n\right) \tag{20.1}$$

where ρ is the mass density, **u** is the bulk flow velocity, p_e and p_i are electron and ion pressures, respectively, **J** is the current density, $\mathbf{u}_n$ is the neutral flow velocity, and ν_{in} is the ion-neutral collision frequency. $p_e=n_e k_B T_e$ and $p_i=n_e k_B T_i$ where n_e is the electron density (assumed to be equal to the ion density by quasi-neutrality) and T_e and T_i are the electron and ion temperatures, respectively. Energy equations (not shown here) are needed to find the pressure or temperatures.

For many situations and particularly when there is no large intrinsic magnetic field, the current density is found using Ampere's law, without the displacement current. The magnetic force term in the momentum equation becomes:

$$\mathbf{J}\times\mathbf{B}=-\nabla\left(B^2/2\mu_0\right)+\frac{1}{\mu_0}\mathbf{B}\cdot\nabla\mathbf{B} \tag{20.2}$$

The first term is the gradient of a magnetic pressure ($p_B=B^2/2\mu_0$), and the second term is a magnetic tension force. At the ionopause of Venus, adopting $\mathbf{u}\approx 0$, the force balance equation (1) across the layer becomes $p_B+p_e+p_i\approx$ constant. Thermal pressure on the ionosphere side balances magnetic pressure on the solar wind side of the ionopause:

$$n_e k_B\left(T_e+T_i\right)(\text{ionosphere})\approx B^2/2\mu_0\,(\text{magnetic barrier}) \approx \rho_{sw}u_{sw}{}^2\text{solar wind}). \tag{20.3}$$

See *Russell and Vaisberg* [1983] or *Luhmann and Cravens* [1991]. The evolution of the magnetic field in MHD theory is found using the electric field specified by a generalized Ohm's law ($\mathbf{E}\approx -\mathbf{u}\times\mathbf{B}+\eta\mathbf{J}$ for simple situations) plus Faraday's law, which gives a magnetic convection/diffusion equation:

$$\frac{\partial \mathbf{B}}{\partial t}=\nabla\times\left(\mathbf{u}\times\mathbf{B}\right)-\nabla\times\left(D_B\nabla\times\mathbf{B}\right) \tag{20.4}$$

$D_B=\eta/\mu_0$ is the magnetic diffusion equation where η is the resistivity. For a plasma with very high electrical conductivity, $D_B\approx 0$ and the first term on the right-hand side dominates, in which case it can be demonstrated that thinking of magnetic field lines as "frozen into" the fluid flow is a useful abstraction (this is "ideal" MHD). However, if the plasma co-exists with a sufficiently dense neutral gas so that D_B is finite then magnetic flux can "thaw" and field lines disconnect from specific fluid parcels (see references in *Cravens* [1997]).

20.2.3. Electrical Current Description of Plasma Dynamics

When a large intrinsic magnetic field with sources is present, then the pure "MHD" approach becomes problematic since the induced field is much smaller than the total magnetic field. Furthermore, several ion species, as well as electrons, can contribute to the ionospheric conductivity. In this case, it is better to "book-keep" the electrical current plus use the steady-state charge continuity equation: $\nabla\cdot\mathbf{J}=0$.

The magnetosphere (or other external environment) is usually handled separately from the ionosphere for this approach. Parallel (or field-aligned) electrical currents associated with the magnetospheric dynamics are determined on an "inner" boundary at the top of the ionosphere. The current density in the ionosphere must satisfy the charge continuity law:

$$J_{\parallel}=-\nabla\cdot\mathbf{K}_{\perp} \tag{20.5}$$

where $J_{\parallel}$ is the boundary current density and $\mathbf{K}_{\perp}$ is the horizontal current integrated over the vertical extent of the ionosphere. $\mathbf{K}_{\perp}$ is related to the electric field imposed on the ionospheric plasma by an Ohm's law that includes all the plasma species and the effects of the intrinsic magnetic field: $\mathbf{K}_{\perp}=\Sigma_P\mathbf{E}_{\perp}+\Sigma_H\mathbf{E}_{\perp}\times\mathbf{b}$, where Σ_P and Σ_H, are the height-integrated Pederson and Hall electrical conductivities, respectively, in the ionosphere, and **b** is a unit vector in the magnetic field direction. Expressions for these conductivities can be found in many places [e.g., *Volland*, 1984; *Kelley*, 1989], and they depend on electron and ion collision frequencies and gyrofrequencies. The field-aligned currents allow the dynamics, or force balance, between different regions to be linked.

A simple schematic of the linkage of different plasma regions using field-aligned currents instead of a MHD approach is given in Figure 20.3. The top slab can be considered to be some region with high conductivity in which the field lines are tied to a moving plasma and hence "bent" (this slab represents the "magnetosphere" or "solar wind"). A **J** X **B** force develops that impedes the flow of this plasma as long as field-aligned currents can flow through the "ionosphere." The current flows into the higher resistivity lower slab from the upper slab along the magnetic field. The **J** X **B** force in the lower slab tries to get the plasma moving even though it is impeded by collisions with the neutrals. The linkage of the dynamics of the two slabs is via the field-aligned currents, $J_{\parallel}$.

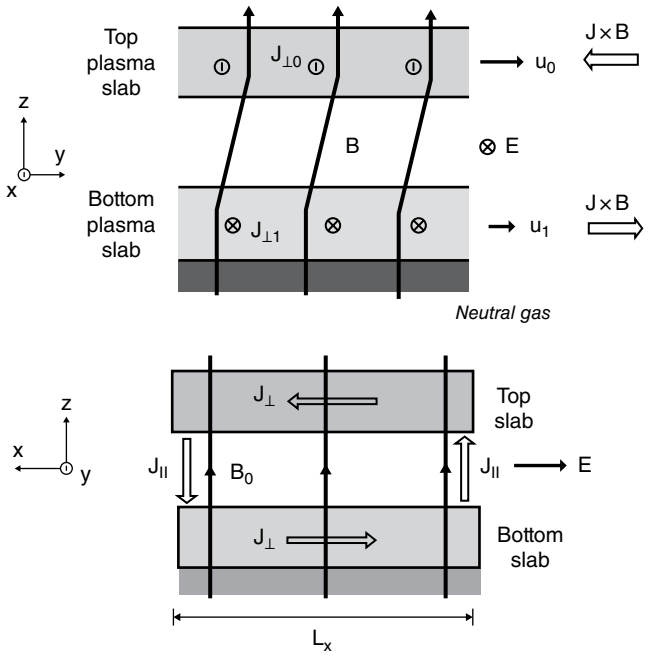

Figure 20.3 Simple slab model for two plasma regions linked by magnetic field lines and field aligned electrical currents. Both side views are shown as well as flow velocities and the J × B forces. [from *Cravens*, 1997, Cambridge University Press, © 1997, used with permission]

20.2.4. Magnetic Reconnection

Magnetic reconnection in space plasmas is an important process not easily described in terms of pure fluid theory. Consider two adjacent magnetized plasma regions in which the magnetic field directions are at least partially opposed, thus representing a current sheet. If the external flows exert pressure on this sheet tending to make it thinner, the plasma in a portion of the sheet can become subject to plasma instabilities and the effective resistivity can become large enough that magnetic diffusion takes place (in the "diffusion region") and the magnetic field lines lose their attachment to fluid parcels, thus changing the magnetic topology [*Hesse et al.*, 1999]. Key regions for reconnection for Earth-like solar wind interactions are the subsolar magnetopause, where interplanetary field lines connect to planetary field lines, and in the plasmasheet where sporadic reconnection takes place [*Angelopoulos et al.*, 2008]. The dayside magnetospheric reconnection process is much more efficient for southward interplanetary magnetic field, which allows a larger electrical potential to be imposed across the magnetosphere and a more vigorous plasma convection to take place. Magnetic flux is added to the tail lobes, and the plasmasheet current intensifies for this situation. Magnetic reconnection in the magnetotail, taking place sporadically in the form of magnetic substorms, is needed to conserve magnetic flux over the long run. This tail region magnetic reconnection is associated with enhanced field-aligned currents and the aurora associated with this. National Aeronautics and Space Administration's (NASA) recently launched Magnetic Multiscale Mission (MMS) is designed to study the reconnection regions.

20.2.5. Field-Aligned Currents and the Aurora

In an aurora, energetic particles from an external region (e.g., a magnetosphere) enter, or "precipitate," into an atmosphere resulting in ionization, heating, and optical emissions in the target atmosphere [cf. *Galand and Chakrabarti*, 2002]. In the usual case of charged particle aurorae, the particles are guided by magnetic field lines and also carry electrical current (that is, $J_\parallel$). Auroral emission is an important diagnostic of field-aligned currents and MI coupling [*Iijima and Potemra*, 1978; *Mauk and Bagenal,* 2012].

Diffuse aurora is when the velocity distribution functions of the external particle population(s) remain relatively unaltered, usually remaining "thermal" or Maxwellian, and these populations carry the electrical current. A diffuse aurora is often found in the terrestrial polar cap for both proton and electron precipitation. However, there are regions in the M-I current system for which the $J_\parallel$ required for the momentum balance significantly exceeds the current that can be carried along the magnetic field line by the ambient/thermal particle populations ($I_{therm\parallel} \approx -e\, n_e\, v_{therme} \approx -e\, n_e\, \{k_B T_e/m_e\}^{1/2}$). This situation arises in the Earth's magnetotail during magnetic substorms. Part of the problem is the large magnetic field strength difference between the external region and the planetary ionosphere (e.g., a "mirror ratio" of $\approx 10^3$ for Earth). Magnetic mirroring of charged particles in converging magnetic field lines results in most particles being reflected. Only particles whose pitch-angles (i.e., angle with respect to the magnetic field) are within the "loss cone" reach the atmosphere. However, if the particles are accelerated along the magnetic field direction, by a field-aligned electric field for example, the loss cone can be filled with more particles and a larger $J_\parallel$ carried. One early treatment of this topic was by *Knight* [1973], who demonstrated that for some range of field-aligned electrical potentials ($\Delta V_\parallel$) and particle fluxes the current enhancement was linearly proportional to the potential difference ($J_\parallel \approx J_{therm\parallel}$ $(e\,\Delta V_\parallel)/k_B T_{therme}$). Other forms of current-voltage relations have been derived.

Alfvénic aurora can also contribute to magnetosphere-ionosphere coupling [*Mauk et al.*, 2002]. Alfvén waves in ideal MHD propagate only along the background magnetic field, and they are not associated with any parallel wave electric field. However, Alfvén waves (i.e., kinetic Alfvén waves) found in space can have a perpendicular

component to the wave vector and have a parallel component of the wave electric field, thus allowing electron acceleration [*Goertz*, 1984; *Watt and Rankin*, 2012].

20.3. M-I COUPLING AT JUPITER

Jupiter has a large intrinsic magnetic field, with a surface field 20 times Earth's surface field. Jupiter rapidly rotates with a 10-hour rotation period. These two characteristics plus the existence of an internal plasma source from Io's volcanoes determine the magnetospheric dynamics at this planet. The magnetospheric plasma tends to co-rotate with Jupiter, and M-I current systems are set up to accomplish this. The SO_2 from Jupiter's satellite Io, at an orbital distance of 5 Jovian radii (R_j), is dissociated and ionized in the Io Plasma Torus (IPT) [cf. *Mauk and Bagenal,* 2012]. Newly born oxygen and sulfur ions are "picked up" by the magnetic field and the co-rotation (or convection) electric field ($\mathbf{E}_{co} \approx - \mathbf{u}_{cor} \times \mathbf{B}$). These ions also begin to corotate, albeit as hot, heavy ions. J × B forces are required to add the needed momentum to the flow, and these currents are associated with field-aligned currents linking the magnetosphere to the ionosphere [*Hill*, 2001; *Cowley and Bunce*, 2001].

Figure 20.4 is a Hubble Space Telescope (HST) image of Jupiter's north aurora [*Clarke et al*., 1998]. The main auroral oval is obvious, as are the auroral footprints of the Galilean satellites (at lower latitudes with magnetic field lines linking the ionosphere to the satellites) [*Clarke et al*., 1998]. Polar cap emissions are also present (ultraviolet [UV] in the image, but X-ray emission also exists, as will be discussed later). Figure 20.5 is a schematic (not to scale) of the type of electrical current system present at Jupiter, either for the satellites or for the middle magnetosphere. The field-aligned currents associated with magnetospheric stresses close in the resistive ionosphere.

The interaction of Jupiter's magnetospheric plasma with its satellites is an interesting topic in its own right [*Kivelson et al.*, 2004; *Hess et al*., 2011], but space precludes much discussion here. The auroral satellite footprints on Jupiter of these interactions are clear (Figure 20.4). The Io auroral footprint is associated with about 1 MA of current generated by "induction" at Io, carried along the field lines (and Alfvén wings), through the Io Plasma Torus, and to the Jovian ionosphere where the currents close [*Hill and Vasyliunas*, 2002; *Kivelson et al*., 2004; *Bonford*, 2012; *Hess et al.*, 2011]. Ganymede's magnetospheric interaction is particularly interesting because this satellite has its own magnetic field, thus allowing magnetic reconnection to be a key part of the interaction [*Kivelson et al*., 2004; *Bonford*, 2012; *Jia et al*., 2010; *Paty and Winglee*, 2004].

An important dynamical imperative for Jupiter is that all the ions created near the IPT must be removed from the magnetosphere, either being carried out to the magnetopause or down the tail [cf. *Mauk et al*., 2002]. The angular momentum per unit mass increases with radial distance so that the J × B force term must also increase, as

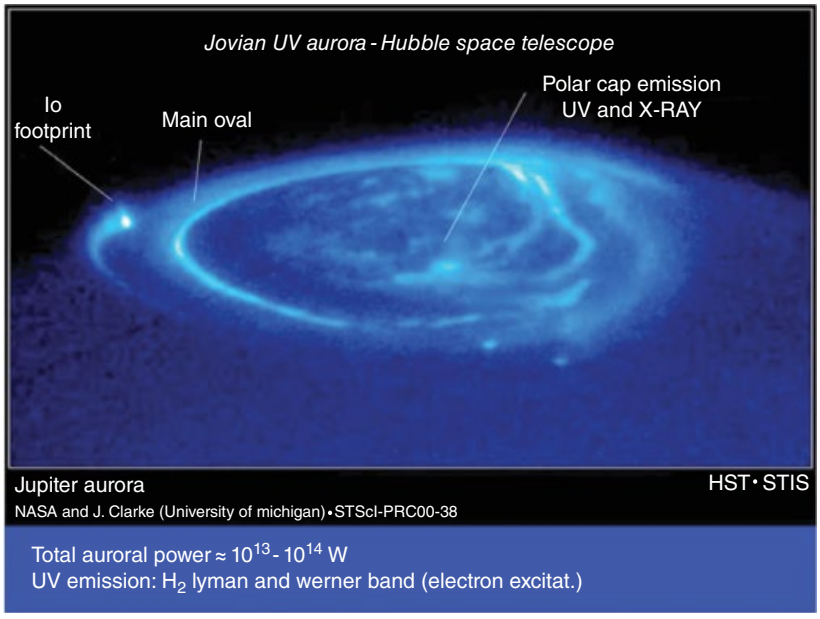

Figure 20.4 HST image of Jupiter's aurora including the main oval, the polar cap aurora, and satellite footprints. [from Cravens and Ozak, Auroral Ion Precipitation and Acceleration at the Outer Planets, in Auroral Phenomenology and Magnetospheric Processes: Earth and Other Planets, Geophys. Monogr. Ser., vol. 197, edited by A. Keiling et al., 2012. Used with permission. © American Geophysical Union]

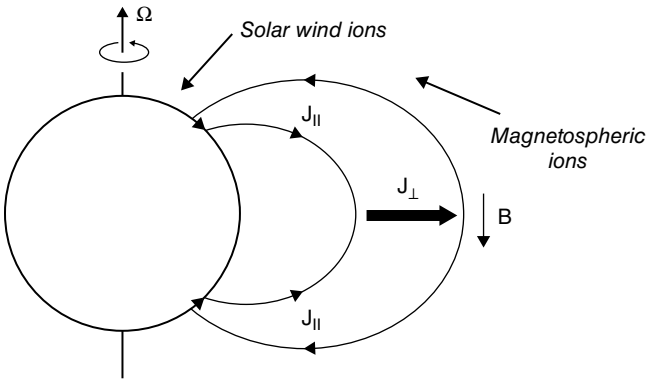

Figure 20.5 Schematic of current system for a rotational magnetosphere. [from *Cravens et al.,* 2003, Implications of Jovian X-ray emission for magnetosphere-ionosphere coupling, Journal of Geophysical Research, used with permission, © American Geophysical Union]

must the field-aligned current needed to complete the equivalent circuit. This happens near a radial distance of ≈ 30 R_J, beyond which the coupling cannot maintain co-rotation, and a lag in the corotation takes place. Note that Jupiter's magnetopause is located at radial distances of 50 to 100 R_J. The peak auroral currents occur at the radial position where the departure from corotation begins [*Hill*, 2001]. Another interpretation is that corotation lag takes place where the momentum carried by Alfvén waves from the ionosphere is no longer sufficient to maintain corotation [*Vasyliunas*, 1983].

The main auroral currents at Jupiter (≈100 MA) originate in the middle magnetosphere and link via field-aligned currents to the Jovian polar ionosphere near a latitude of about 70° (Figure 20.4). The auroral emissions are mainly from the H_2 Lyman and Werner bands and thought to be produced by 100 keV electrons [cf. *Grodent et al.*, 2003]. This requires considerable acceleration from the thermal energies of the ambient magnetospheric plasma near 30 R_J. The main auroral oval emission is relatively steady. The total auroral power is ≈ 10^{13} to 10^{14} W, which is 100 times the solar extreme ultraviolet (EUV) input for Jupiter. The field-aligned current associated with the co-rotation lag (and main oval) was estimated from the M-I coupling by *Hill* [2001].

Precipitation of energetic electrons from the middle magnetosphere is responsible for the main auroral oval at Jupiter (currents out of the ionosphere), but both energetic electron and ion precipitation are thought to be taking place in the polar caps. Auroral emission has been observed in the infrared, visible, ultraviolet, and X-ray parts of the spectrum [*Elsner et al.,* 2005; *Gladstone et al.*, 2002]. The polar cap emission is more time variable [*Waite et al.*, 2001] and must also connect to particle populations located near the magnetopause and/or deep in the magnetotail. Plasmoid formation in the magnetotail is thought to be an important process that can produce an aurora at higher latitudes.

The X-ray emission observed from Jupiter's polar cap probably comes from precipitation of energetic (million electron volts [MeV]) heavy sulfur and oxygen ions from the outer magnetosphere and/or magnetopause regions [*Cravens et al.*, 2003; *Ozak et al.*, 2010]. *Bunce et al.* [2004] suggested that magnetic reconnection at the dayside magnetopause could be responsible for the downward currents. The MeV energies are required for the incident ions to lose their electrons during collisions with atmospheric molecular hydrogen, resulting in charge oxygen and sulfur charge states high enough to emit X-rays. Charge exchange collisions of the highly stripped ions then produce excited ions that emit X-rays. *Ozak et al.* [2010 and references therein] used a Monte Carlo code to study the ion precipitation process, including the altitude-dependence of the energy deposition and the X-ray production from charge-exchange collisions. The large field-aligned potentials suggested are also needed to provide the field-aligned current associated with the reconnection at the magnetopause [*Bunce et al.*, 2004] according to the Knight mechanism mentioned earlier. The spectrum of secondary electrons produced in the atmosphere and the field-aligned currents (few MA) were also calculated [*Ozak et al.*, 2013]. Escaping secondary electrons are accelerated upward to MeV energies by the same field-aligned potentials responsible for the downward ion acceleration. Evidence exists for relativistic electrons in the outer magnetosphere [*MacDowell et al.,* 1993]. The upcoming NASA Juno mission to Jupiter will shed much light on Jovian M-I coupling.

20.4. M-I COUPLING AT SATURN

Saturn also has a bright UV aurora with a power intermediate between Earth and Jupiter (10^{11} W; *Gombosi and Ingersoll*, 2010; *Clarke,* 2012). Like Jupiter, the emissions are mainly from the H_2 Lyman and Werner bands as indicated by HST and by Cassini observations [*Badman and Cowley*, 2007; *Clarke,* 2012]. Saturn's main aurora is more time variable than the Jovian main aurora, and it also strongly depends on solar wind conditions, unlike Jovian auroral emission. The fact that Saturn's magnetospheric interaction depends on solar wind conditions was recognized by *Desch* [1982] in a study of radio emission from this planet. More recent studies using Cassini data have provided more information on this relationship [*Carbary et al.*, 2009; *Badman et al.*, 2008].

Saturn's magnetosphere has a radial extent of ≈ 25 R_S, although this distance depends on solar wind conditions. A key feature of Saturn's magnetosphere is that neutral water vapor is a key species in the inner magnetosphere.

The water mainly comes from vents (i.e., tiger stripes) found in the southern hemisphere of Saturn's icy satellite Enceladus [*Waite et al.*, 2006]. Volatiles (mainly H_2O and CO_2) and ice grains escape from these vents forming a plume. Saturn's rings also supply some water to the magnetosphere. The water group species (H_2O, OH, O, H) are ionized by solar radiation and/or electron impact ionization and are then picked up by the motional electric field (i.e., the co-rotation electric field) and magnetic field [*Tokar et al.*, 2008]. Electrical currents should be associated with the ion pick-up, although little auroral emission is evident at the latitudes linking to the Enceladus torus.

Saturn's magnetospheric plasma flows past, and interacts with, Saturn's satellites. The next section will consider the plasma interaction with Titan, but brief discussion of the interaction with Enceladus and its plume will now be given [e.g., *Tokar et al.*, 2006]. Plasma flows into the plume region at a speed of about 25 km/s and mainly consists of H_2O^+, OH^+, and O^+ ions, as mentioned above. Charge exchange collisions between the H_2O^+ ions and the water in the plume remove momentum from the flow, which slows the plasma in the plume down to much lower speeds of less than a few km/s [*Kriegel et al.*, 2009]. In this slower region, ion-neutral chemistry is possible, and H_3O^+ ions are formed from reaction of H_2O^+ with H_2O [cf. *Cravens et al.*, 2009a]. Much of the negative charge in the plume has been shown to be charged nanograins and not just electrons [*Hill et al.*, 2012]. The interaction with Enceladus produces Alfvén wings in which field-aligned currents, with their associated magnetic perturbations, link to Saturn [*Kriegel et al.*, 2011].

The magnetosphere beyond about 6 R_J is more dynamic, and the interchange instability is thought to play an important role in driving plasma transport [*Hill et al.*, 2005; *Rymer et al.,* 2009a]. More energetic electron populations are present and are associated with plasma injection events that exchange plasma between the outer and inner magnetosphere [*Young et al.,* 2007*; Rymer et al.,* 2007]. In this same region, more energetic ion populations (10 keV) are present and are linked to a "ring" current [*Krimigis et al.*, 2005; *Young et al.*, 2005; *Mitchell et al.*, 2009]. These ions have been observed by in situ instruments onboard the Cassini Orbiter. The Cassini MIMI (Magnetospheric Imaging Instrument) experiment has

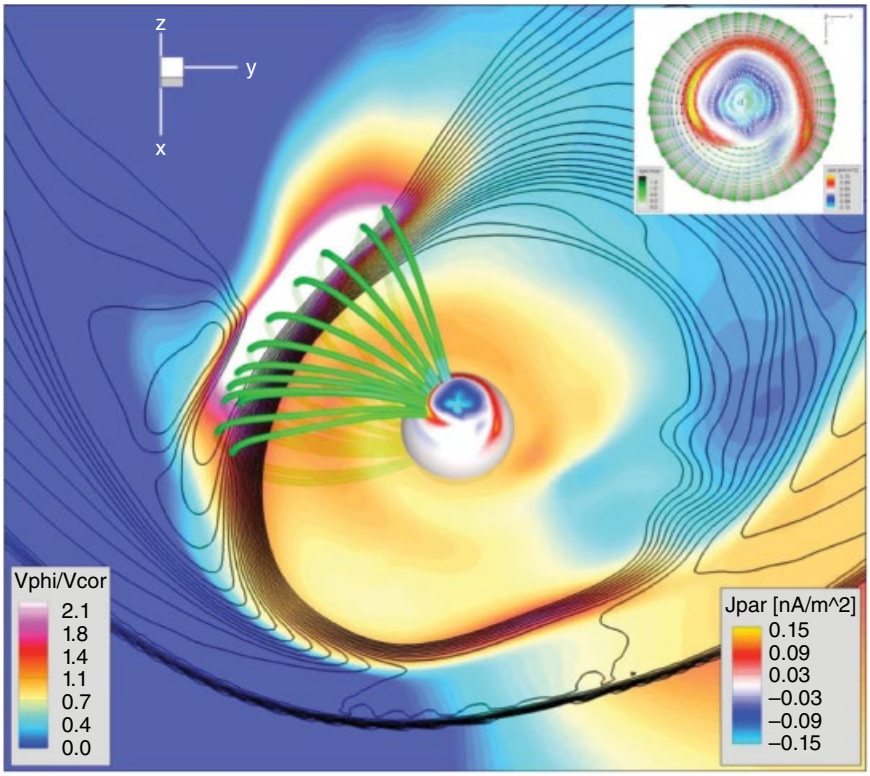

Figure 20.6 Results from a MHD model of Saturn's magnetosphere. The main figure shows flow velocities in the equatorial plane and some magnetic field lines linking the dawnside magnetopause region to the polar ionosphere. The inset figure shows field aligned current densities in the polar cap. The auroral emission is assumed to correlate with these currents. [from *Jia et al.*, 2012, Magnetospheric configuration and dynamics of Saturn's magnetosphere: A global MHD simulation, Journal of Geophysical Research, used with permission, © American Geophysical Union]

also imaged the energetic neutral atoms (ENA) from the charge exchange of the fast ring current ions with neutrals [*Mitchell et al*., 2009].

Saturn's auroral oval links to the dynamic outer magnetospheric dynamics just mentioned. Particularly intense auroral emission takes place near the dawnside of the oval, and it appears to be associated with the outer dawnside magnetosphere [*Badman and Cowley*, 2007*; Bunce et al.,* 2008*; Jia et al.*, 2012]. Dawnside enhancements in detected ENA fluxes could be related to this [*Mitchell et al*., 2009]. This emission brightens when the solar wind dynamic pressure increases. Global MHD models of Saturn's magnetospheric dynamics [*Jia et al*., 2012] help to interpret the Cassini observations of the magnetosphere and aurora (see Figure 20.6). The MHD calculations suggest that the magnetic stresses are especially large near the dawnside magnetopause as co-rotating plasma (moving sunward at this local time) is squeezed inside the magnetopause, which has moved inward with increasing solar wind pressure. A shear layer with large currents is generated (Figure 20.6), and this links to the bright auroral region on the dawnside. Interestingly, the main auroral oval at Jupiter also has a sharper boundary on the dayside than on the nightside, possibly associated with sunward flow from the near tail [cf. *Badman et al*., 2007].

20.5. M-I COUPLING AT TITAN: AN EXAMPLE OF A NON-MAGNETIC SATELLITE INTERACTION

A number of planetary natural satellites interact in interesting ways with the external plasma environment. With the exception of Jupiter's satellite Ganymede, which has a small intrinsic magnetic field, the interactions are moon-like (i.e., with surface), Venus-like, or comet-like. The nature of the interaction depends on how much of an atmosphere or exosphere the satellite has and also on where in the planetary magnetosphere the satellite's orbit is. Due to space limitations, only the Titan case will be discussed in this paper. The chapter by *Westlake et al.* in this volume also considers the Titan interaction.

Titan orbits Saturn at a distance of 20 R_S (Saturn radii). Most of the time this places Titan inside Saturn's magnetosphere, but occasionally, when solar wind conditions push the magnetopause inward, Titan can find itself in Saturn's magnetosheath, or rarely even in the upstream solar wind. The location of Titan in the magnetosphere is also important to the interaction. For example, electron fluxes are much lower in the lobes than in the plasmasheet [*Rymer et al*., 2009b]. The magnetospheric plasma (density ≈ 0.3 cm^{-3}, ion temperature ≈ 5 keV for O^+ and 1 keV for H^+) is moving at subcorotation speeds (100 km/s).

Titan is not your typical moon, having an atmosphere with a surface pressure of 1.5 bars, mainly consisting of molecular nitrogen but with a couple percent methane and other hydrocarbon or nitrile species such as HCN, C_2H_2, and C_2H_4 [*Waite et al.,* 2007]. Ionization of the atmosphere by solar radiation and by precipitating electrons (i.e., M-I coupling) creates a chemically complex ionosphere with many ion species including $HCNH_+$, $C_2H_5^+$, $C_3H_5^+$, $CHNH_2^+$, etc. [*Cravens et al.*, 2006; *Vuitton et al*., 2014].

Voyager 1 made the first measurements of the plasma environment [e.g., *Hartle et al*., 1982, 2006]. The copious data returned from instruments on the NASA-European Space Agency (ESA) Cassini Orbiter has greatly improved our understanding of Titan's linkage to Saturn's magnetosphere. The external plasma flow is typically submagnetosonic but superAlfvénic, so a bow shock is not expected and is not observed [*Wahlund et al*., 2014]. The interaction has both Venus-like and comet-like aspects in that the pressure of the thermal ionospheric pressure and mass loading both contribute to making Titan an obstacle to the external flow. The external pressure is high enough that the ionosphere is magnetized (like that of Venus or Mars for high solar wind pressure). Ion-neutral collisions take up some of the momentum carried into the ionosphere. Given Titan's extensive exosphere, the topside ionosphere transition region between the main ionosphere and the rapidly moving external flow is $\approx R_T/2$. Some of the more energetic ions can penetrate below the main ionosphere and generate lower altitude ionospheric layers [*Cravens et al*., 2008].

The Titan interaction can be described using MHD theory [*Ma et al*., 2006, 2009; *Ledvina and Cravens*, 1998] or with hybrid models (particle ions and fluid electrons) [*Ledvina et al.,* 2012*; Silanpaa et al.,* 2011; *Simon et al.*, 2010; and see *Wahlund et al.* [2014] review] rather than with the "electrical current approach" since the fields are induced rather than intrinsic. Magnetometer data and models indicate that magnetic field lines appear to be draped around the Titan obstacle for altitudes above about 1500 km [cf. *Wahlund et al*., 2014; *Edberg et al*., 2010], but the magnetic structure at lower altitudes is puzzling [*Luhmann et al.,* 2012; *Cravens et al.,* 2010]. For example, the magnetic field near the main ionosphere (1000–1300 km) seems to reflect external conditions that existed about 30 minutes previously rather than present conditions, that is, the ionosphere has a magnetic memory [*Bertucci et al*., 2008].

The magnetic field permeating the ionosphere and linking to Saturn's magnetosphere provides a conduit for plasma and energy exchange between the ionosphere and the external medium. Such a possibility was recognized before the Cassini mission [e.g., *Hartle et al*., 1982; *Gan et al*., 1992; *Westlake et al.*, 2012] but has been confirmed by Cassini data. For example, electron and ion populations from Saturn's outer magnetosphere [*Rymer et al*., 2009b] can precipitate into the atmosphere and

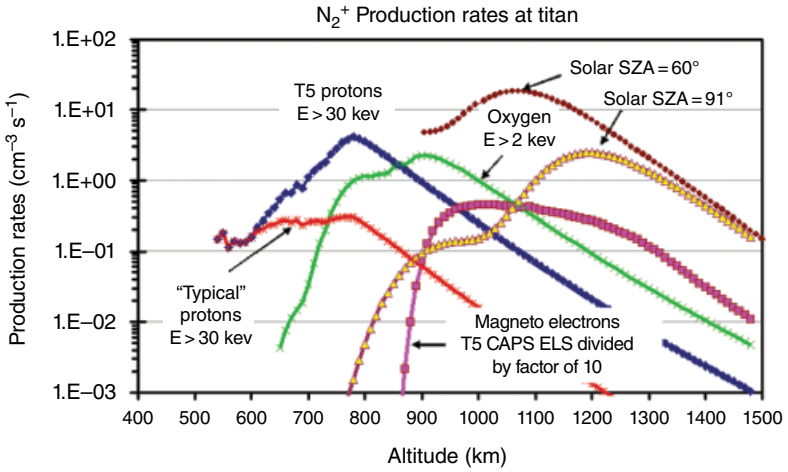

Figure 20.7 Ion production rates versus altitude in Titan's upper atmosphere from several sources including magnetospheric energetic protons and oxygen ions, from energetic electrons, and from solar EUV radiation. [from *Cravens et al.*, 2008, Energetic ion precipitation at Titan, Journal of Geophysical Research, used with permission, © American Geophysical Union]

produce ionospheric plasma on the nightside of Titan [*Richard et al.*, 2015; *Agren et al.*, 2007; *Cravens et al.*, 2009b; *Wahlund et al.*, 2014; *Galand et al.*, 2014). Figure 20.7 shows ion production rates in Titan's atmosphere due to the precipitation of magnetospheric electrons and ions.

20.6. SUMMARY

Magnetosphere-ionosphere coupling at solar system bodies manifests itself in many ways. This paper has provided a brief review of the main types of plasma interactions, and the associated M-I coupling, found in the solar system. Our knowledge of the M-I coupling at other planets and satellites has been advanced by the many spacecraft sent to these bodies and by the theoretical and numerical models developed to interpret the data obtained during these missions.

ACKNOWLEDGMENTS

Support from NASA's Cassini project via a subcontract from Southwest Research Institute, and from NASA contracts NNX13AG04G and NNX14AG79G is gratefully acknowledged.

REFERENCES

Agren, K., et al. (2007), On magnetospheric electron impact ionization and dynamics in Titan's ram-side and polar ionosphere, a Cassini case study, *Annales Geophysicae*, *25*, 2359–2369.

Angelopoulos, V., et al. (2008), Tail reconnection triggering substorm onset, *Science*, *321*, 931–935, DOI:*10.1126/science.116045*.

Badman, S. V., and S. W. H. Cowley (2007), Significance of Dungey-cycle flows in Jupiter's and Saturn's magnetospheres, and their identification on closed equatorial field lines, *Ann. Geophys*, *25*, 941–951.

Badman, S. V., S.W.H. Cowley, L. Lamy, B. Cecconi, and P. Zarka (2008), Relationship between solar wind corotating interaction regions and the phasing and intensity of Saturn kilometric radiation bursts, *Ann. Geophys.*, *26*, 3641–3651.

Bertucci, C., N. Achilleos, M. K. Dougherty, R. Modolo, A. J. Coates, K. Szego, A. Masters, Y. Ma, F. M. Neubauer, P. Garnier, J.-E. Wahlund, and D. T. Young (2008), The magnetic memory of Titan's ionized atmosphere, *Science*, *321*, 1475.

Bonford, B. (2012), When moons create aurora: The satellite footprints on giant planets, pp. 133–140 in *Auroral Phenomenology and Magnetospheric Processes: Earth and Other Planets*, eds. A. Keiling, E. Donovan, F. Bagenal, and T. Karlsson, Geophys. Mono. **197**, American Geophysical Union, Washington, D.C..

Bunce, E. J., S. W. H. Cowley, and T. K. Yeoman (2004), Jovian cusp processes: Implications for the polar aurora, *J. Geophys. Res.*, *109*, A09513, doi:10.1029/2003JA010280.

Bunce, E. J., et al. (2008), Origin of Saturn's aurora: Simultaneous observations by Cassini and the Hubble Space Telescope, *J. Geophys. Res.*, *113*, A09209, doi:10.1029/2008JA01257.

Carbary, J. F., E. C. Roelof, D. G. Mitchell, S. M. Krimigis, and N. Krupp (2009), Solar wind periodicity in energetic electrons at Saturn, *Geophys. Res. Lett.*, *36*, L22104, doi:10.1029/2009GL041086.

Clarke J. T. (2012), Auroral Processes at Jupiter and Saturn, *Auroral Phenomenology and Magnetospheric Processes: Earth and Other Planets*, eds. A. Keiling, E. Donovan, F. Bagenal, and T. Karlsson, Geophys. Mono. **197**, p. 113, American Geophysical Union, Washington, D.C..

Clarke, J. T., et al. (1998), Hubble Space Telescope imaging of Jupiter's UV aurora during the Galileo orbiter mission, *J. Geophys. Res.*, *103*, 20217.

Cowley, S. W. H., and E. J. Bunce (2001), Origin of the main auroral oval in Jupiter's coupled magnetosphere-ionosphere system, *Planet. Space. Sci.*, *49*, 1067–1088.

Cravens, T. E. (1989), Solar wind interactions with non-magnetic planets, *Solar System Plasma Physics*, eds. J. H. Waite, Jr., J. L. Burch, and R. L. Moore, Geophysical Mono. **54**, p. 352, American Geophysical Union, Washington, D.C..

Cravens, T. E. (1997), *Physics of Solar System Plasmas*, Cambridge Univ. Press, Cambridge.

Cravens, T. E., J. H. Waite, T. I. Gombosi, N. Lugaz, G. R. Gladstone, B. H. Mauk, and R. J. MacDowall (2003), Implications of Jovian X-ray emission for magnetosphere-ionosphere coupling, *J. Geophys. Res.*, *108* (A12), 1465, doi:10.1029/2003JA010050.

Cravens, T. E., I. P. Robertson, J. H. Waite Jr., R. V. Yelle, W. T. Kasprzak, C. N. Keller, S. A. Ledvina, H. B. Niemann, J. G. Luhmann, R. L. McNutt, W.-H. Ip, V. De La Haye, I. Mueller-Wodarg, J.-E. Wahlund, V. A. Anicich, and V. Vuitton (2006), The composition of Titan's ionosphere, *Geophys. Res. Lett.*, *33*, L07105, doi:10.1029/2005GL025575.

Cravens, T. E., et al. (2008), Energetic ion precipitation at Titan, *Geophys. Res. Lett.*, *35*, doi:10.1029/2007GL032451.

Cravens, T. E., R. L. McNutt, J. H. Waite, Jr., I. P. Robertson, J. G. Luhmann, W. Kasprzak, and W.-H. Ip (2009a), Plume ionosphere of Enceladus as seen by the Cassini ion and neutral mass spectrometer, *Geophys. Res. Lett.*, *36*, L08106, doi:10.1029/2009GL037811.

Cravens, T. E., I. P. Robertson, J. H. Waite Jr., R. V. Yelle, V. Vuitton, A. J. Coates, J.-E. Wahlund, et al. (2009b), Model-data comparisons for Titan's nightside ionosphere, *Icarus*, *199*, 174–88. doi:10.1016/j.icarus.2008.09.005.

Cravens, T. E., M. Richard, Y.-J. Ma, C. Bertucci, J. Luhmann, S. Ledvina, I. P. Robertson, J.-E. Wahlund, K. Agren, J. Cui, I. Muller-Wodarg, J. H. Waite, M. Dougherty, J. Bell, and D. Ulusen (2010), Dynamical and magnetic field time constants for Titan's ionosphere, Empirical estimates and comparisons with Venus, *J. Geophys. Res.*, *115*, A08319, doi:10.1029/2009JA015050.

Cravens, T. E., and Ozak, N. (2012), Auroral Ion Precipitation and Acceleration at the Outer Planets, in Auroral Phenomenology and Magnetospheric Processes: Earth and Other Planets, Geophys. Monogr. Ser., vol. 197, A. Keiling et al. (eds.). Used with permission. Copyright American Geophysical Union.

Desch, M. D. (1982), Evidence for solar wind control of Saturn radio emission, *J. Geophys. Res.*, *97*, 4549–4754, doi:10.1029/JA087iA06p04549.

Edberg, N. J. T., J.-E. Wahlund, K. Ågren, M. W. Morooka, R. Modolo, C. Bertucci, and M. K. Dougherty (2010), Electron density and temperature measurements in the cold plasma environment of Titan: Implications for atmospheric escape, *Geophys. Res. Lett.*, *37*, L20105, doi:10.1029/2010GL044544.

Elsner, R. F., et al. (2005), Simultaneous Chandra X-ray, Hubble Space Telescope ultraviolet, and Ulysses radio observations of Jupiter 's aurora, *J. Geophys. Res.*, *110*, A01207, doi:10.1029/2004JA010717.

Galand, M., and S. Chakrabarti (2002), Auroral processes in the solar system, *Atmospheres in the Solar System: Comparative Aeronomy*, edited by M. Mendillo, A. Nagy, and J. H. Waite, Geophys. Monogr. **130**, p. 55, American Geophysical Union, Washington, D.C..

Galand, M., A. J. Coates, T. E. Cravens, and J.-E. Wahlund (2014), Titan's ionosphere, *Titan: Interior, Surface, Atmosphere, and Space Environment*, eds. I. Muller-Wodarg, C. A. Griffith, E. Lellouch, and T. E. Cravens, p. 376, Cambridge Univ. Press, Cambridge.

Gan, L., C. N. Keller, and T. E. Cravens (1992), Electrons in the ionosphere of Titan, *J. Geophys. Res.*, *97*, 12136.

Gladstone, G. R., et al. (2002), A pulsating auroral x-ray hot spot on Jupiter, *Nature*, *415*, 1000–1003.

Goertz, C. (1984), Kinetic Alfvén waves on auroral field lines, *Planet. Space Sci.*, *32*, 1387–1392.

Gombosi, T. I., and A. P. Ingersoll (2010), Saturn: Atmosphere, ionosphere, and magnetosphere, *Science*, *327*, 1476.

Grodent, D., J. T. Clarke, J. Kim, J. H. Waite, and S. W. H. Cowley (2003), Jupiter's main auroral oval observed with HST-STIS, *J. Geophys. Res.*, *108*(A11), 1389, doi:10.1029/2003JA009921.

Hartle, R. E., E. C. Sittler, Jr., K. Ogilvie, J. D. Scudder, A. J. Lazarus, and S. K. Atreya (1982), Titan's ion exosphere observed from Voyager 1, *J. Geophys. Res.*, *87*, 1383.

Hartle, R. E., et al. (2006), Initial interpretation of Titan plasma interaction as observed by the Cassini Plasma Spectrometer: Comparisons with Voyager 1, *Planet. Space Sci.*, *54*, 1211.

Hess, S. L. G., P. A. Delamere, V. Dols, and E. C. Ray (2011), Comparative study of the power transferred from satellite-magnetospheric interactions to auroral emissions, *J. Geophys. Res.*, *116*, A01202, doi:10.1029/2010JA015807.

Hesse, M., K. Schindler, J. Birn, and M. Kuznetsova (1999), The diffusion region in collisionless magnetic reconnection, *Phys. Plasma*, *6*, 1781–1795.

Hill, T. W. (1983), Solar wind magnetosphere coupling, p. 261 in *Solar-Terrestrial Physics: Principles and Theoretical Foundations*, eds. R. L. Carovillano and J. M. Forbes, D. Reidel Publ., Dordrech, The Netherlands.

Hill, T. W. (2001), The Jovian auroral oval, *J. Geophys. Res.*, *106*, 8101–8108, doi:10.1029/2000JA000302.

Hill, T. W., and V. M. Vasyliunas (2002), Jovian auroral signatures of Io's corotational wake, *J. Geophys. Res.*, *107* (A12), 1464, doi:1029/2002JA009514m.

Hill, T. W., et al. (2005), Evidence for rotationally-driven plasma transport in Saturn's magnetophere, *Geophys. Res. Lett.*, *32*, L14510.

Hill, T. W., et al. (2012), Charged nanograins in the Enceladus plume, *J. Geophys. Res.*, *117*, A05209, doi:10.1029/2011JA017218.

Iijima, T., and T. A. Potemra (1978), Large-scale characteristics of field-aligned currents associated with substorms, *J. Geophys. Res.*, *83*, 599.

Jia, X. R., R. J. Walker, M. G. Kivelson, K. K. Khurana, and J. A. Linker (2010), Dynamics of Ganymede's magnetopause: Intermittent reconnection under steady external conditions, *J. Geophys. Res.*, *115*, A12202, doi:10.1029/2010JA015771.

Jia, X., K. C. Hansen, T. I. Gombosi, M. G. Kivelson, G. Tóth, D. L. DeZeeuw, and A. J. Ridley (2012), Magnetospheric configuration and dynamics of Saturn's magnetosphere: A

global MHD simulation, *J. Geophys. Res.*, *117*, A05225, doi:10.1029/2012JA017575.

Kelley, M. C. (1989), *The Earth's Ionosphere*, *Plasma Physics and Electrodynamics*, Academic Press, San Diego.

Kivelson, M. G., and C. J. Russell, eds. (1995), *Introduction to Space Physics*, Cambridge Univ. Press, Cambridge.

Kivelson, M. G., F. Bagenal, W. S. Kurth, F.M. Neubauer, C. Paranicas, and J. Saur (2004), Magnetopheric interactions with satellites, pp. 513–536 in *Jupiter: The Planet, Satellites, and Magnetosphere*, eds. F. Bagenal, T. E. Dowling, and W. B. McKinnon, Cambridge Univ. Press, Cambridge, UK.

Knight, S. (1973), Parallel electric fields, *Planet. Space Sci.*, *21*, 741–750, doi:10.1016/0032-0633(73)90093-7.

Krall, N. A., and A. W. Trivelpiece (1973), *Principles of Plasma Physics*, McGraw-Hill, New York.

Kriegel, H., S. Simon, J. Müller, U. Motschmann, J. Saur, K.-H. Glassmeier, and M. K. Dougherty (2009), The plasma interaction of Enceladus: 3D hybrid simulations and comparison with Cassini MAG data, *Planet. Space Sci.*, *57*, 2113–2122, doi:10.1016/j.pss.2009.09.025.

Kriegel, H., S. Simon, U. Motschmann, J. Saur, F. M. Neubauer, A. M. Persoon, M. Dougherty, and D. A. Gurnett (2011), Influence of negatively charged plume on the structure of Enceladus' Alfvén wings: Hybrid simulations versus Cassini magnetometer data, *J. Geophys. Res.*, *116*, A10223, doi:10.1029/2011JA016842.

Krimigis, S. M., et al. (2005), Dynamics of Saturn's magnetosphere from MIMI during Cassini's orbital insertion, *Science*, *307*(5713), 1270.

Ledvina, S. A., and T. E. Cravens (1998), A three-dimensional MHD model of plasma flow around Titan, *Planet. Space Sci.*, *46*, 1175.

Ledvina, S. A., S. H. Brecht, and T. E. Cravens (2012), The orientation of Titan's dayside ionosphere and its effect on Titan's plasma interaction, *Earth Planets Space*, *64*, 231–236.

Luhmann, J. G., and T. E. Cravens (1991), Magnetic fields in the ionosphere of Venus, *Space Sci. Rev.*, *55*, 201.

Luhmann, J. G., D. Ulusen, S. A. Ledvina, K. Mandt, B. Magee, J. H. Waite, J. Westlake, et al. (2012), Investigating magnetospheric interaction effects on Titan's ionosphere with the Cassini orbiter Ion Neutral Mass Spectrometer, Langmuir Probe and Magnetometer observations during targeted flybys, *Icarus*, *219*, 534–55, doi:10.1016/j.icarus.2012.03.015.

Ma, Yingjuan, A. F. Nagy, T. E. Cravens, I. V. Sokolov, K. C. Hansen, Jan-Erik Wahlund, F. J. Crary, A. J. Coates, and M. K. Dougherty, Comparisons between MHD model calculations and observations of Cassini flybys of Titan, *J. Geophys. Res.: Space Physics*, *111*, A05207. doi:10.1029/2005JA011481, 2006.

Ma, Y.-J., C. T. Russell, A. F. Nagy, G. Tóth, et al. (2009), Time-dependent global MHD simulations of Cassini T32 Flyby: From magnetosphere to magnetosheath, *J. Geophys. Res.*, *114*, 3204, doi:10.1029/2008JA013676.

MacDowall, R. J., M. L. Kaiser, M. D. Desch, W. M. Farrell, R. A. Hess, and R. G. Stone (1993), Quasiperiodic Jovian radio bursts: Observations from the Ulysses radio and plasma wave experiment, *Planet. Space Sci.*, *41*, 1059–1072, doi:10.1016/0032-0633(93)90109-F.

Mauk, B. H., B. J. Anderson, and R. M. Thorne (2002), Magnetosphere-ionosphere coupling at Earth, Jupiter, and beyond, in *Atmospheres in the Solar System: Comparative Aeronomy*, edited by M. Mendillo et al., vol. *130*, pp. 97–114, American Geophysical Union, Washington, D.C.

Mauk, B., and F. Bagenal (2012), Comparative Auroral Physics: Earth and Other Planets, *Auroral Phenomenology and Magnetospheric Processes: Earth and Other Planets*, eds. A. Keiling, E. Donovan, F. Bagenal, and T. Karlsson, Geophysical Mon. 197, p. 3, American Geophysical Union, Washington D.C.

Mitchell, D. G., J. F. Carbary, S. W. H. Cowley, T. W. Hill, and P. Zarka (2009), The dynamics of Saturn's Magnetosphere, Chapter 10, in *Saturn from Cassini-Huygens*, edited by M. K. Dougherty et al., p. 257, Springer Science+Business media, doi:10.1007/978-1-4020-9217-6_10.

Mumma, M. J., and S. B. Charnley (2011), The chemical composition of comets, Emerging taxonomies and natal heritage, *Ann. Rev. Astron. Astrophys.*, vol. *49*, 471–524, doi: 10.1146/annrev-astro-081309-130811.

Ozak, N., D. R. Schultz, T. E. Cravens, V. Kharchenko, and Y.-W. Hui (2010), Auroral x-ray emission at Jupiter: Depth effects, *J. Geophys. Res.*, *115*, A11306, doi:10.1029/2010JA015635.

Ozak, N., T. E. Cravens, and D. R. Schultz (2013), Auroral ion precipitation at Jupiter: Predictions for Juno, *Geophys. Res. Lett.*, *40*, doi:10.1002/grl.50812.

Paty, C., and R. Winglee (2004), Multi-fluid simulations of Ganymede's magnetosphere, *Geophys. Res. Lett.*, *31*, L24806, doi:10.1029/2004GL021220.

Richard, M., T. E. Cravens, C. Wylie, D. Webb, Q. Chediak, K. Mandt, J. H. Waite Jr., A. Rymer, C. Bertucci, A. Wellbrock, A. Windsor, and A. J. Coates (2015), An empirical approach to modeling ion production rates in Titan's ionosphere II: Ion production rates on the nightside, *J. Geophys. Res.*, *120*, 1281, doi:10.1002/2014JA020343.

Russell, C. T., and O. Vaisberg (1983), The interaction of the solar wind with Venus, *Venus*, eds. D. M Hunten, L. Colin, T. M. Donahue, and V. I. Moroz, p. 873, Univ. Arizona Press, Tucson.

Rymer, A.M., et al. (2007), Electron sources in Saturn's magnetosphere, *J. Geophys. Res.*, *112*, A02201, doi:10.1002/2014JA020343.

Rymer, A. M., et al. (2009a), Cassini evidence of rapid interchange transport at Saturn, *Planet. Space Sci.*, *57*, 1779–1784.

Rymer, A. M., H. T. Smith, A. Wellbrock, A. J. Coates, and D. T. Young (2009b), Discrete classification and electron energy spectra of Titan's varied magnetospheric environment, *Geophys. Res. Lett.*, *36*, L15109, doi:10.1029/2009GL039427.

Schunk, R. W., and A. F. Nagy (2000), *Ionospheres*, Cambridge Univ. Press, Cambridge.

Silanpaa, I., D. T. Young, F. Crary, M. Thomsen, et al. (2011), Cassini Plasma Spectrometer and hybrid model study on Titan's interaction: Effect of oxygen ions, *J. Geophys. Res.*, *116*, 7223, doi:10.1029/2011JA016443.

Simon, S., A. Wennmacher, F. M. Neubauer, C. L. Bertucci, et al. (2010), Titan's highly dynamic magnetic environment: A systematic survey of Cassini magnetometer observations from flybys TA – T62, *Planet Space Sci.*, *58*, 1230–1251, doi:10.1016/j.pss.2010.04.021.

Tokar, R. L., R. E. Johnson, T. W. Hill, D. H. Pontius, W. S. Kurth, F. J. Crary, D. T. Young, M. F. Thomsen, D. B. Reisenfeld, A. J. Coates, G. R. Lewis, E. C. Sittler, and D. A. Gurnett (2006), The interaction of atmosphere of Enceladus with Saturn's plasma, *Science*, *311*, 1409–1412, doi:10.1126/science.1121061.

Tokar, R. L., R. J. Wilson, R. E. Johnson, M. G. Henderson, M. F. Thomsen, M. M. Cowee, E. C. Sittler Jr., D. T. Young, F. J. Crary, H. J. McAndrews, and H. T. Smith (2008), Cassini detection of water-group pick-up ions in the Enceladus torus, *Geophys. Res. Lett.*, *35*, L14202, doi:10.1029/2008GL034749.

Vasyliunas, V. M. (1983), Plasma distribution and flow, in *Physics of the Jovian Magnetosphere*, edited by A. J. Dessler, Cambridge Univ. Press, Cambridge, UK, p. 395.

Volland, H. (1984), *Atmospheric Electrodynamics*, Springer-Verlag, Berlin.

Vuitton, V., O. Dutuit, M. A. Smith, and N. Balucani (2014), Chemistry of Titan's atmosphere, p. 224 in *Titan: Interior, Surface, Atmosphere, and Space Environment*, eds. I. Muller-Wodarg, C. A. Griffith, E. Lellouch, and T. E. Cravens, Cambridge Univ. Press, Cambridge.

Wahlund, J.-E., R. Modolo, C. Bertucci, and A. J. Coates (2014), Titan's magnetospheric and plasma environment, *Titan: Interior, Surface, Atmosphere, and Space Environment*, eds. I. Muller-Wodarg, C. A. Griffith, E. Lellouch, and T. E. Cravens, p. 419, Cambridge Univ. Press, Cambridge.

Waite, J. H., et al. (2001), An auroral flare at Jupiter, *Nature*, *410* (6830), 787–789.

Waite Jr., J. H., M. R. Combi, W.-H. Ip, T. E. Cravens, R. L. McNutt Jr., W. Kasprzak, R. Yelle, J. G. Luhmann, H. Niemann, D. Gell, B. Magee, G. Fletcher, J. Lunine, and W.-L. Tseng (2006), Cassini Ion and Neutral Mass Spectrometer: Enceladus plume composition and structure, *Science*, *311*, 1419.

Waite, J. H., D. T. Young, T. E. Cravens, A. J. Coates, et al. (2007), The process of tholin formation in Titan's upper atmosphere, *Science*, *316*, 870-875, doi:10.1126/Science. 1139727.

Watt, C. E. J., and R. Rankin (2012), Alfvén wave acceleration of auroral electrons in warm magnetospheric plasma, *Auroral Phenomenology and Magnetospheric Processes: Earth and Other Planets*, eds. A. Keiling, E. Donovan, F. Bagenal, and T. Karlsson, Geophysical Mon. **197**, pp. 251–260American Geophysical Union, Washington D.C.

Westlake, J. H., C. P. Paranicas, T. E. Cravens, J. G. Luhmann, K. E. Mandt, H. T. Smith, D. G. Mitchell, A. M. Rymer, M. E. Perry, J. H. Waite Jr., and J.-E. Wahlund (2012), The observed composition of ions outflowing from Titan, *Geophys. Res. Lett.*, *39*, L19104, doi:10.1029/2012GL 053079.

Young, D. T., et al. (2005), Composition and dynamics of plasma in Saturn's magnetosphere, *Science*, *307*, 1262–1266.

Young, D. T., S. J. Bolton, M. F. Thomsen, and M. K. Dougherty (2007), Electron sources in Saturn's magnetosphere, *J. Geophys. Res.*, *112*, A02201, doi:10.1029/2006JA012017.

21

Plasma Measurements at Non-Magnetic Solar System Bodies

Andrew J. Coates

Video of Yosemite Talk, URL: http://dx.doi.org/10.15142/T3B887

ABSTRACT

The solar system includes a number of non-magnetic objects. These include comets, Venus, Mars, and the moon, as well as moons of Saturn, Jupiter, and beyond. The plasma interaction depends on upstream conditions, whether that is the solar wind or a planetary magnetosphere, and whether the object itself has any atmosphere. Several space missions have explored these objects so far, with many carrying plasma and field instrumentation, and have revealed some similarities and differences in the interactions. Processes such as ion pickup are the key to the cometary interaction, but pickup is also present in many other locations, and ionospheric processes are important when an atmosphere or exosphere is present. In all cases plasma interacting with the surface or atmosphere can cause escape and modification over time. Here we will review plasma measurements at non-magnetic objects from the various missions, and summarize information about the key processes including plasma escape at these objects.

21.1. INTRODUCTION

The interaction of plasma with non-magnetic solar system bodies started with early exploration of Earth's moon, Mars, and Venus in the 1960s. Spacecraft have since additionally visited comets and the moons of Jupiter, Saturn, and briefly Uranus and Neptune, as well as Mars, Venus, and the moon. New Horizons arrived at Pluto in 2015. The data interpretation and analysis from all of these objects have provided important comparisons to the magnetized objects. In Figure 21.1, we summarize the missions that have visited un-magnetized objects carrying suitable instrumentation. The mission names are superimposed on a comparison of interaction scales for both magnetized and unmagnetized solar system objects.

University College London, Mullard Space Science Laboratory, Dorking, Surrey, UK

In this paper we will summarize some of the results on plasma interactions from non-magnetized objects. First we will highlight the importance of the environment of the objects as well as the nature of the body, including whether it has an atmosphere or not. We will then review some of the key plasma processes, including ion pickup, ionospheric processes, and plasma escape.

21.2. TYPES OF INTERACTION

The types of interaction are strongly dependent on the upstream conditions and the nature of the object. We now consider these in turn.

21.2.1. Upstream Conditions

The plasma environment of any object is a key feature in determining the plasma interaction. Some objects interact with the solar wind (including the Moon for

Magnetosphere-Ionosphere Coupling in the Solar System, Geophysical Monograph 222, First Edition.
Edited by Charles R. Chappell, Robert W. Schunk, Peter M. Banks, James L. Burch, and Richard M. Thorne.

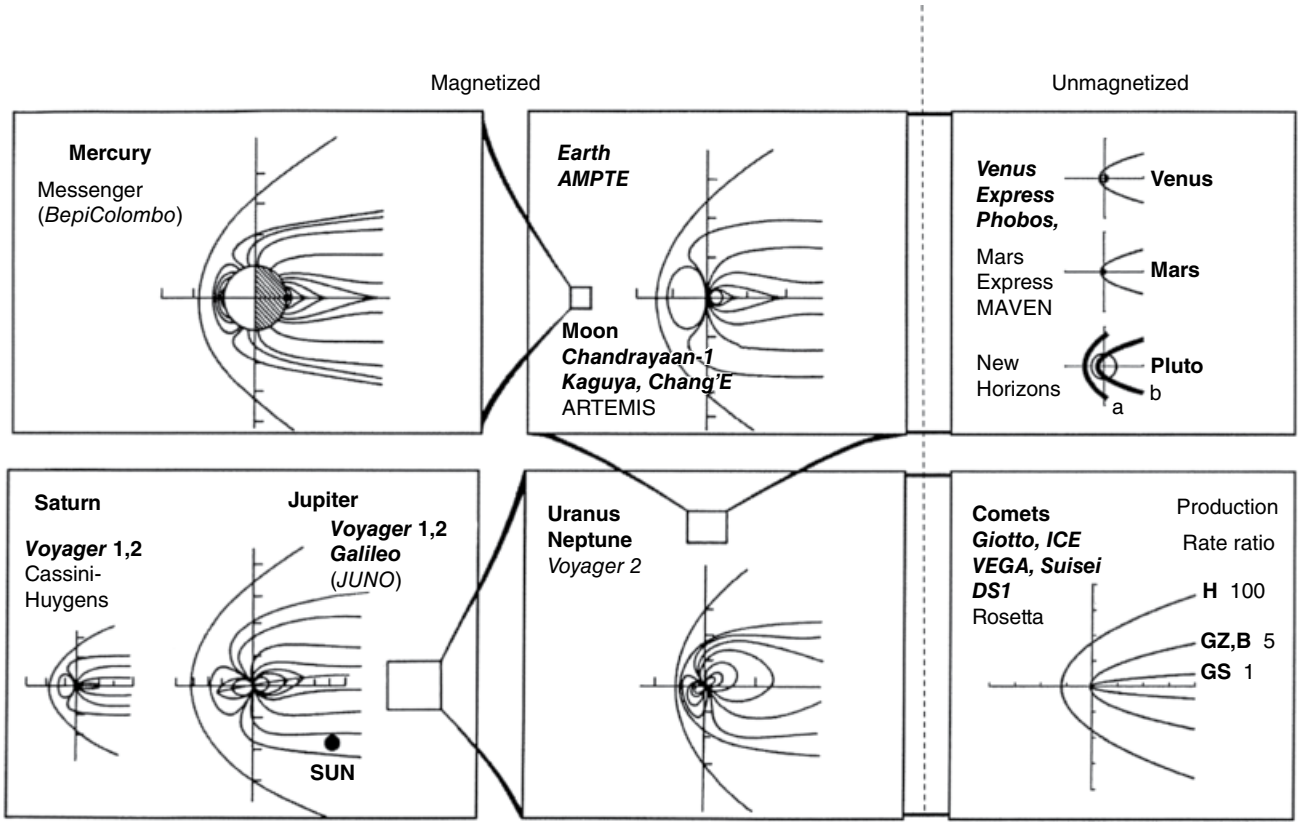

Figure 21.1 Comparison of scales for magnetized and unmagnetized objects in the solar system. [adapted by *Coates*, 1999, 2001 from *Russell and Walker*, 1995] Object names are in **bold**, missions carrying relevant instrumentation within the last 30 years are in ***bold italics***, the last 10 years are in normal font, and approved future missions are in (*bracketed italics*).

much of its orbit, Venus, Mars, comets, asteroids, distant outer planet moons, and trans-Neptunian objects), while others are immersed in planetary magnetospheres (e.g., the Moon in the magnetotail, Phobos, Deimos, and the principal moons of Jupiter and Saturn).

The solar wind conditions vary with distance from the Sun. For example, the solar wind density N_{sw} and the radial magnetic field component B_r are both controlled on average by the inverse square law and are $\propto R_{AU}^{-2}$, while the azimuthal magnetic field component $B_\varphi \propto R_{AU}^{-2}$ [*Parker*, 1958; *Hundhausen*, 1995]. On average the Mach number increases with distance from the Sun, while the plasma β peaks near the orbits of Earth and Mars [*Russell et al.*, 1990]. The actual solar wind conditions are highly variable and permeated by impulsive features such as interplanetary shocks, interplanetary coronal mass ejections (ICME), and corotating interaction regions (CIR). This clearly has an impact on the interaction geometry, and on escape rates for example, as will be discussed in Section 21.4.

21.2.2. Nature of Obstacle

Although Mars has crustal magnetic fields [*Acuna et al.*, 1998; *Connerney et al.*, 2001, 2005], it lacks a global dipole field and is thus classed as an unmagnetized object. In other cases, the presence or absence of an atmosphere and/or significant outgassing, and subsequent ionization, is important in determining the nature of the interaction. In Table 21.1, we summarize the unmagnetized objects in the solar system.

Luhmann [1995] summarized the stages of plasma interaction with an ionosphere. The sunlit atmosphere of a body will ionise and become an ionosphere. Production by photoionization is balanced by recombination. A flow of plasma upstream, such as the solar wind, would naturally create a wake behind the object. If the upstream plasma is magnetized, this ultimately leads to a magnetic barrier or ionopause forming, where the inside thermal pressure balances the upstream magnetic pressure, and magnetic field draping around the obstacle results in an

Table 21.1 Neutral gas production rates for comets and other solar system objects visited by spacecraft with plasma instrumentation. Where appropriate, ion loss rate estimates are indicated by *

Object	Atmosphere/exosphere composition	Production rate (s^{-1})	
Venus	CO_2, N_2, O, CO	*2.2 x 10^{23}–10^{25}	*Coates et al.*, 2015a; *Brace*, 1987; *Barabash*, 2007a
Earth	N_2, O_2	10^{24}–10^{26}	*Haaland*, 2013
Moon	Na, K		
Mars	CO_2, CO, O	*10^{23}–10^{25}	*Barabash*, 2007b; *Lundin*, 2008; *Lundin*, 2013; *Lundin*, 1989; *Ramstad*, 2013
Comet Giacobini-Zinner	H_2O, CO, CO_2	4x10^{28}	*Mendis*, 1986
Comet Halley	H_2O, CO, CO_2	6.9x10^{29}	*Krankowsky*, 1986
Comet Grigg-Skjellerup	H_2O, CO, CO_2	7.5x10^{27}	*Johnstone*, 1993
Comet Borrelly	H_2O, CO, CO_2	3.5x10^{28}	*Young*, 2004
Comet Churyumov-Gerasimenko	H_2O, CO, CO_2	3x10^{24}–5x10^{27}	*Hansen*, 2007; *Motschmann*, 2006
Io	SO_2, SO, S, O, Na, Cl	3x10^{28}	*Bagenal*, 1994
Europa	O_2, O_3, O, Na	2x10^{27}	*Smyth*, 2006
Ganymede	O_2, O_3, O	1.3x10^{27}	*Marconi*, 2007
Callisto	O_2, O_3, O		
Titan	N_2, CH_4, hydrocarbons	*4x10^{24}–10^{25}	*Coates*, 2012; *Wahlund*, 2005
Enceladus	H_2O	3x10^{27} –1–2x10^{28}	*Tokar*, 2006; *Smith*, 2010
Rhea	H_2O	2.45x10^{24}	*Teolis*, 2010
Dione	H_2O	9.6x10^{25}	*Tokar*, 2012
Pluto	N_2, CH_4	10^{25}–10^{27}	*McNutt*, 1989

induced magnetotail. This picture is valid while the upstream magnetic field varies and the field does not have time to diffuse through the object, as in the solar wind interaction with Mars, Venus, and Titan (upstream of Saturn's magnetopause).

When inside Saturn's magnetosphere, Titan's interaction is complicated by Saturn's corotating plasma, which sweeps past Titan creating a different angle with the solar wake depending on Titan's position in local time. In addition, magnetospheric electrons add to photoionization as a source of ionization. Titan also has no bow shock when the upstream flow is subsonic and sub-Alfvénic.

21.3. OBJECTS

21.3.1. Comets and Ion Pickup

As a comet approaches the Sun, neutral water (and other) molecules sublime from the nucleus and drift away as neutrals. When a neutral particle is ionized in a magnetized plasma, it feels an electric field $\boldsymbol{E} = -\boldsymbol{v} \times \boldsymbol{B}$ where $\boldsymbol{v}$ is the plasma velocity and $\boldsymbol{B}$ the magnetic field. It then gyrates around the magnetic field, producing a cycloid in real space (illustrated schematically in Figure 21.2). In velocity space this corresponds to a ring. The ring is unstable, and waves are produced, and wave-particle interactions produce pitch angle scattering of the pickup ions, leading to a shell in velocity space.

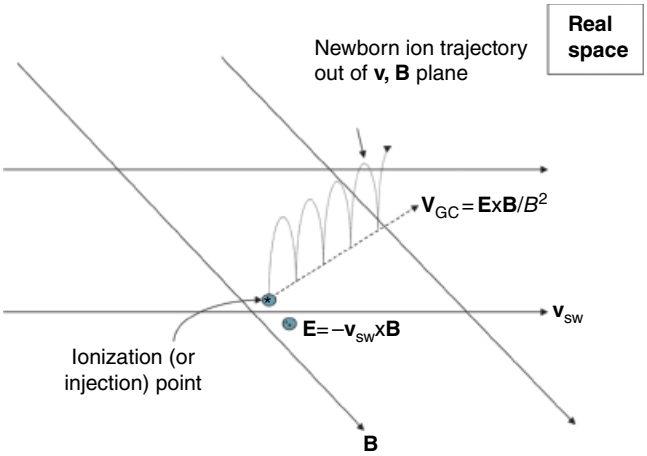

Figure 21.2 Schematic diagram showing the early stages of the pickup of ionized neutrals. The cycloid in real space corresponds to a ring in velocity space.

The interacting waves move parallel and antiparallel to the magnetic field, producing a bispherical shell [see reviews by *Coates*, 2010; *Coates and Jones*, 2009; and references therein].

With respect to the neutral particles, the maximum energy of the ring can be written:

$$E_{max,ring} = 2mv_{sw}^2 \sin^2 \vartheta_{vB} = 4m_{amu}E_{sw} \sin^2 \vartheta_{vB}$$

where θ_{vB} is the angle between the flow velocity v_{sw} and the magnetic field. Similarly, the maximum (simple) shell velocity is:

$$E_{max,shell} = 4m_{amu}E_{sw}$$

This can reach ~70 kiloelectron-volt (keV) for a water group ion in the solar wind. This is clearly seen in the cometary data and in data from other objects [e.g., from Giacobini-Zinner [*Hynds et al.*, 2006]; Halley [*Johnstone et al.*, 1986a; *Neugebauer et al.*, 1989; *Coates et al.*, 1989; *Terasawa et al.*, 1986]; Grigg-Skjellerup [*Johnstone et al.*, 1993; *Coates et al.*, 1993a, 1993b]; Borrelly [*Young et al.*, 2004); and Churyumov-Gerasimenko [*Nilsson et al.*, 2015]. Figure 21.3 shows some examples of pickup water group ion ring and shell distributions seen on the inbound trajectory at comet Halley [*Coates et al.*, 1989]. Each plot is a V_{perp}-$V_{parallel}$ representation of the pickup water ion distribution functions in the solar wind frame, with a ring indicated by a * and a simple shell shown by a dashed

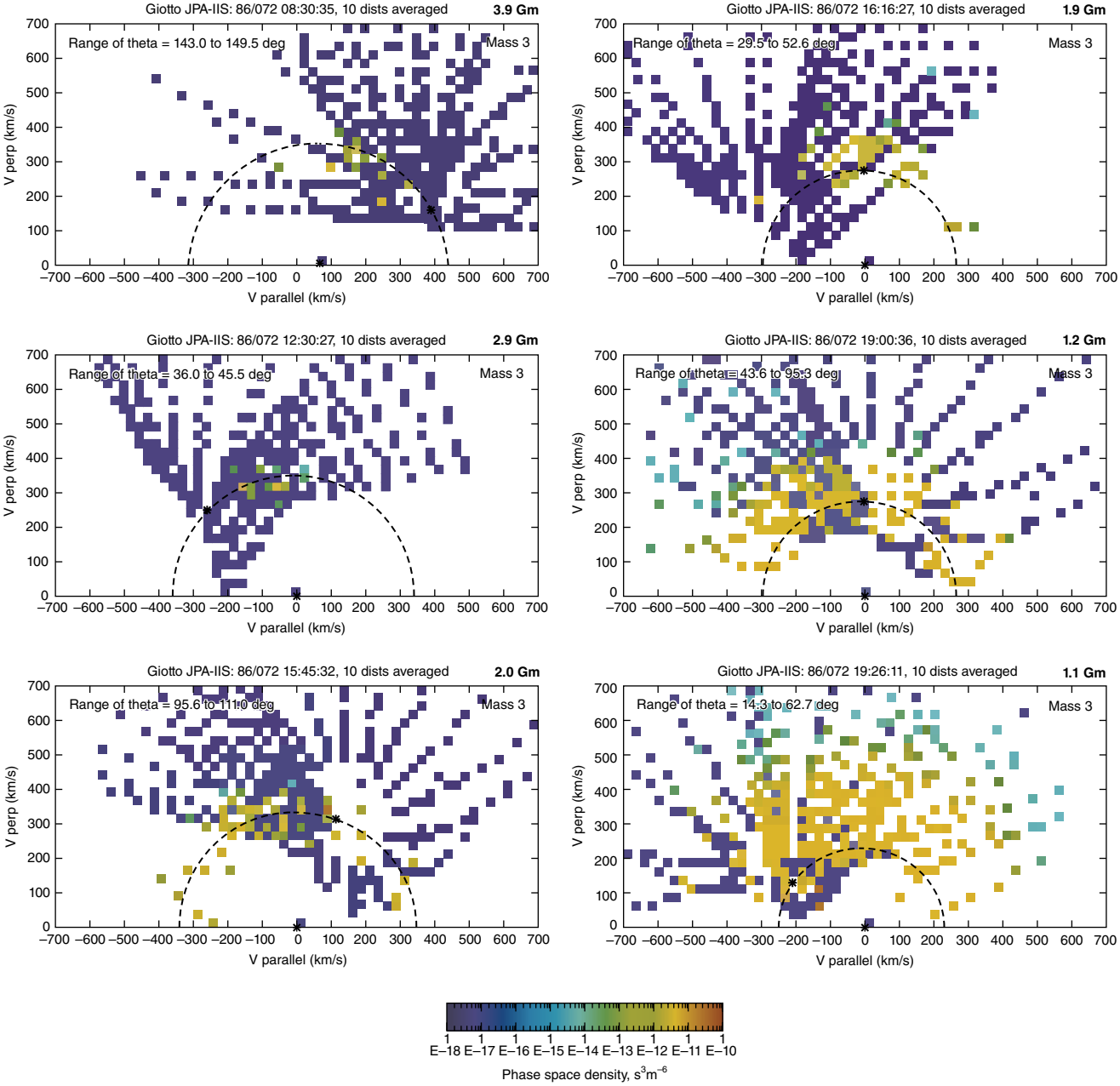

Figure 21.3 Examples of pickup water group ion ring and shell distributions seen at comet Halley [see *Coates et al.*, 1989].

semicircle. At large distances (3.9, 2.9 Gm), the distributions are ring-like, closer (2.0 and 1.9 Gm) pitch angle scattering has occurred and they are fairly shell-like, while each side of the bow shock (1.2 and 1.1 Gm) significant energy scattering is seen.

Using the Halley data, *Coates et al.* [1990] showed evidence for bispherical shell distributions by estimating the water group ion bulk speed in a magnetic field-aligned solar wind frame. The early Rosetta data show ions in the early phase of pickup [*Nilsson et al.*, 2015; *Goldstein et al.*, 2015], with some similarities to the Active Magnetospheric Particle Tracer Explorer (AMPTE) releases [*Coates et al.*, 1986; *Johnstone et al.*, 1986b; *Coates et al.*, 1988] and to non-gyrotropic ions seen at comet GS [*Coates et al.*, 1993b]. In Figure 21.4, we illustrate the change in the comet-solar wind interaction as a comet approaches the Sun. Far from the Sun, the interaction is asteroidal with additional ion pickup increasing with decreasing heliocentric distance, and close to the Sun the interaction is developed with a contact surface and bow shock.

Following these initial stages of pickup, additional acceleration (and deceleration) may be provided by the Fermi I and/or II mechanisms [see *Coates*, 1991 for a review].

21.3.2. Mars

Mars has no global magnetic field; instead Mars has a network of crustal remanent fields mainly associated with the older Southern highlands, left over from when the planet was magnetized 3.8 billion years ago [e.g., *Acuna et al.*, 1998; *Connerney et al.*, 2001, 2005]. However, Mars has an exosphere larger than its ionosphere, and ionization and ion pickup can occur above the ionopause [*Luhmann and Brace*, 1991; *Luhmann et al.*, 1992; *Lundin et al.*, 1989 and references therein]. Also, direct pickup from the upper atmosphere as well as the extended exosphere is possible.

At the orbit of Mars, the gyroradius of pickup heavy (e.g., O^+) ions is larger than the planetary radius, and solar wind scavenging has been observed [*Barabash et al.*, 2007]. The estimated loss rate based on Phobos data was ~10^{25} s^{-1} [*Lundin et al.*, 1989]; this is significant on the timescale of the solar system, corresponding to a loss of ~tens of % of Earth's atmospheric mass.

However, recent measurements of loss rate from Mars Express were a factor 100 lower [*Barabash et al.*, 2007]. This is thought to be due to a lack of coverage of low energy (~10 electron-volt [eV]) ions. The instrumental settings have since been changed and the rates are now being revised upward [e.g., *Lundin et al.*, 2008; *Kallio et al.*, 2010] to ~10^{25} s^{-1}, though solar wind forcing is also important, making the loss rate higher towards solar maximum [*Kallio et al.*, 2010]. In addition, thermal hydrogen escape is higher at Mars [*Lammer et al.*, 2008].

As at a comet, field draping and an 'induced magnetosphere' form a barrier, upstream of which a bow shock forms. It was also anticipated that asymmetric pickup would be the result of reabsorption by the planet, producing further pickup ions. These are also seen by ASPERA-3 on Mars Express [*Lundin et al.*, 2008, 2009; *Kallio et al.*, 2010]. Recent work has also highlighted the interplanetary electric field orientation, and this organizes the interaction region [e.g., *Fedorov et al.*, 2008]. See Figure 21.5, which shows oxygen ions escaping along the Martian tail, and their intensity is controlled by the electric field direction.

Effects from pickup protons are also seen due to the extended hydrogen exosphere at Mars. The Martian bow shock is different to the cometary bow shock in that it is not caused by mass loading, although the effects of mass loading start to be significant near the shock location [*Dubinin et al.*, 1993]. Pickup protons have been observed directly and form additional evidence for an extended exosphere [*Dubinin et al.*, 2006]. An asymmetry controlled by the interplanetary electric field orientation is observed in related proton cyclotron wave emissions [*Wei et al.*, 2006]. The magnetic field orientation has been inferred from pickup proton observations [*Yamauchi et al.*, 2006].

Pickup may be augmented by other processes, such as ambipolar outflow due to the escape of ionospheric electrons [*Coates et al.*, 2011a]. Photoelectrons are seen in the tail of Mars well away from their production region in the dayside ionosphere [*Frahm et al.*, 2006a, 2006b; *Liemohn et al.*, 2006; *Frahm et al.*, 2010] as well as at other objects such as Titan [*Coates et al.*, 2007a], and Venus [*Coates et al.*, 2008]. See also *Coates et al.*, 2011a. Figure 21.6(a) shows ionospheric photoelectrons, identified by their distinctive energy peaks in the 20–30 eV region, seen in the Martian tail at distances up to 10,000 km [from *Frahm et al.*, 2006b]. Observations in the tail of the objects has highlighted the possible role of a polar wind mechanism, as the energetic photoelectron may travel along the magnetic field relatively easily, to enhance plasma escape [e.g., *Coates et al.*, 2011, 2015a].

The Mars aurora was one of the important discoveries by the Mars Express mission. *Bertaux et al.* [2005] used the SPICAM ultraviolet spectrometer to find concentrated areas of emission at the foot of magnetic cusps caused by the crustal fields on Mars. This interesting discovery was followed up by *Leblanc et al.* [2006], who found that the precipitating electrons were electrons with tens of eV, by *Lundin et al.* [2006], who likened the electron signatures to inverted 'V's at Earth, and by *Leblanc et al.* [2008], who found additional examples and studied the morphology in greater detail. This will be one of the interesting features for MAVEN to study, as well as looking at escape processes in more detail.

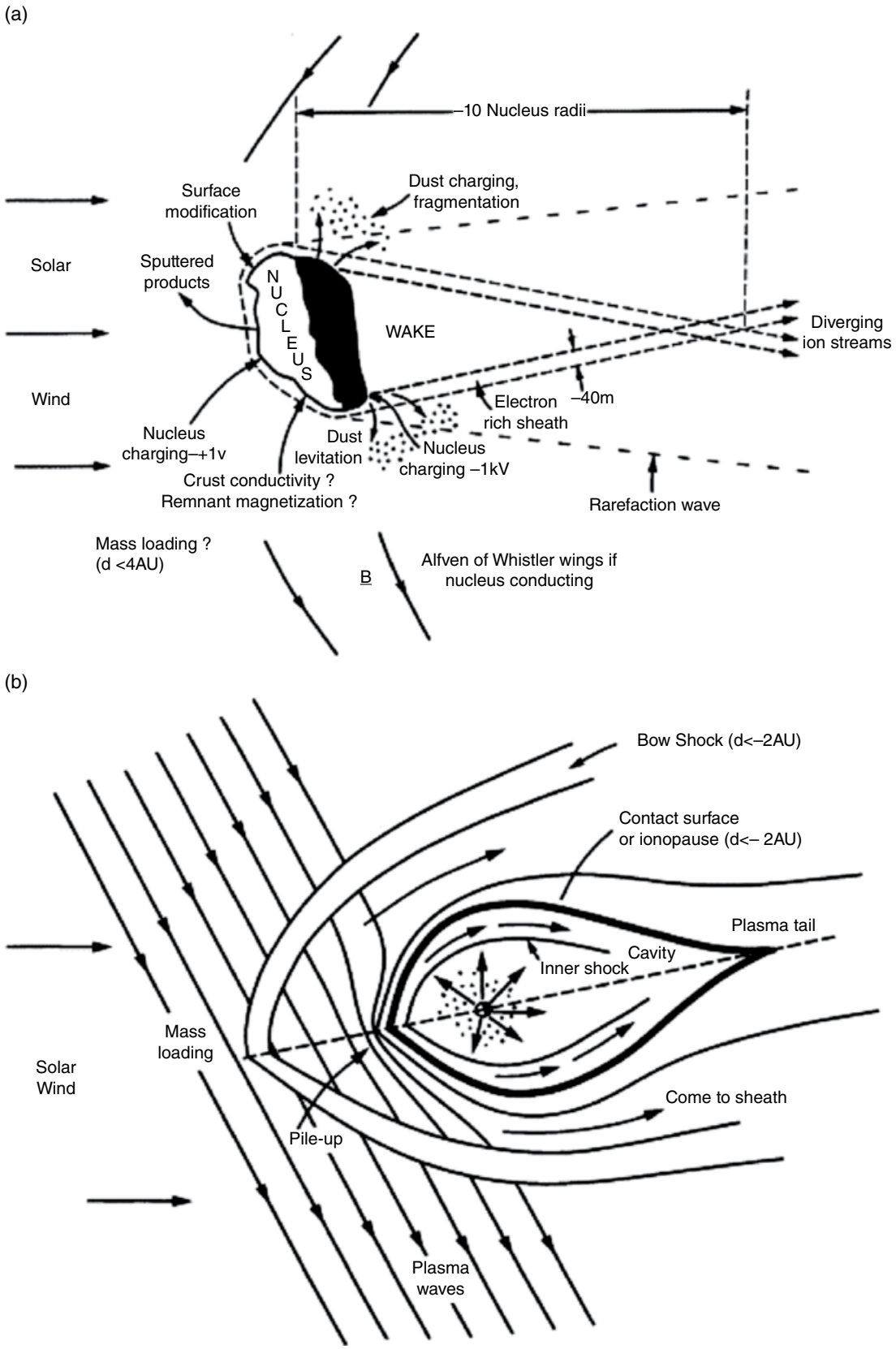

Figure 21.4 Change in the comet-solar wind interaction as a comet approaches the Sun.

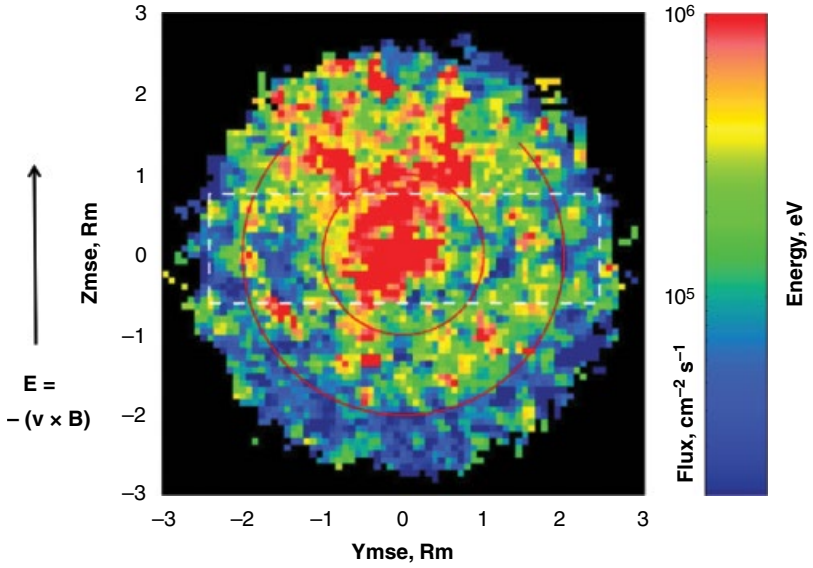

Figure 21.5 Organization of the Mars Express ion escape data by the interplanetary electric field [*Fedorov et al.*, 2008].

21.3.3. Venus

Venus has no magnetic field. It has a thick atmosphere and ionosphere. The ionopause position is governed by a pressure balance between the ionospheric thermal pressure and the magnetic field pressure immediately outside, which is ultimately related to the solar wind dynamic pressure upstream (modified by pickup) [*Brace et al.*, 1987; *Russell et al.*,,2006 and references therein]. Outside the ionosphere, ionized neutrals may again be picked up. The pickup ion gyroradius is smaller than the planetary radius in this case. Again, solar wind 'scavenging' plays a role in the evolution of the atmosphere. Pickup ions (O^+) were seen escaping Venus from Pioneer Venus Orbiter (PVO) [*Brace et al.*, 1987] although they play little role in shaping the overall interaction unlike at comets [*Russell et al.*, 2006]. Venus Express, which has mass discrimination capability, measures hydrogen and oxygen as the dominant escaping species along the tail, with a stoichiometric ratio of 2, indicating loss of water [*Barabash et al.*, 2007].

The estimated loss based on PVO data was ~10^{24} s^{-1}, a steady loss down the tail. However, solar wind intensifications were suggested to increase the average by a factor ~50 [*Brace et al.*, 2007]. Initial Venus Express measurements indicated a rate of ~10^{25} s^{-1} via the tail, with approximately 10% via pickup [*Barabash et al.*, 2007]. Again, ambipolar diffusion caused by ionospheric photoelectrons may augment or even feed the pickup and tail loss processes [*Coates et al.*, 2011a].

Fedorov et al. [2008] compared the light and heavy ion losses at Mars and Venus. At both objects, hydrogen escape occurred on the flanks within, and somewhat planet-ward of, the magnetosheath, while the heavy ion escape was predominantly in the tail. The data were also ordered by the interplanetary electric field, showing an enhancement of oxygen escape in the positive E_{sw} sector. This indicates that the ion escape is controlled by the magnetic field [*Fedorov et al.*, 2008]. Some of these may be pickup ions, but other processes of ionospheric escape are also present.

Recent observations of proton cyclotron waves in the solar wind near Venus [*Delva et al.*, 2008a, 2008b, 2009] indicate that their source may be ion pickup-produced waves from an extended neutral hydrogen exosphere there. As yet, no direct particle observations have been made to confirm this.

In situ measurements of the Venus ionosphere have been made by Venus Express. Some interesting observations include the expansion of the ionosphere to a 'teardrop' shape during low solar wind activity [*Wei et al.*, 2012], cross-terminator ion flow [*Szego et al.*, 2009; *Wood et al.*, 2012], and the magnetization of the Venus ionosphere [*Angsmann et al.*, 2011]. In addition, ionospheric photoelectrons were characterized in detail in the sunlit ionosphere for the first time [*Coates et al.*, 2008]. As at Mars, such electrons are seen in the tail at up to 2.3 R_V along the tail, away from the production point [*Tsang et al.*, 2015; *Coates et al.*, 2011a; *Coates et al.*, 2015a]. The escape rate at Venus was also estimated from the ionospheric plasma observation in the tail and compared with that of other solar system objects [*Coates et al.*, 2015a]. See Section 21.4.

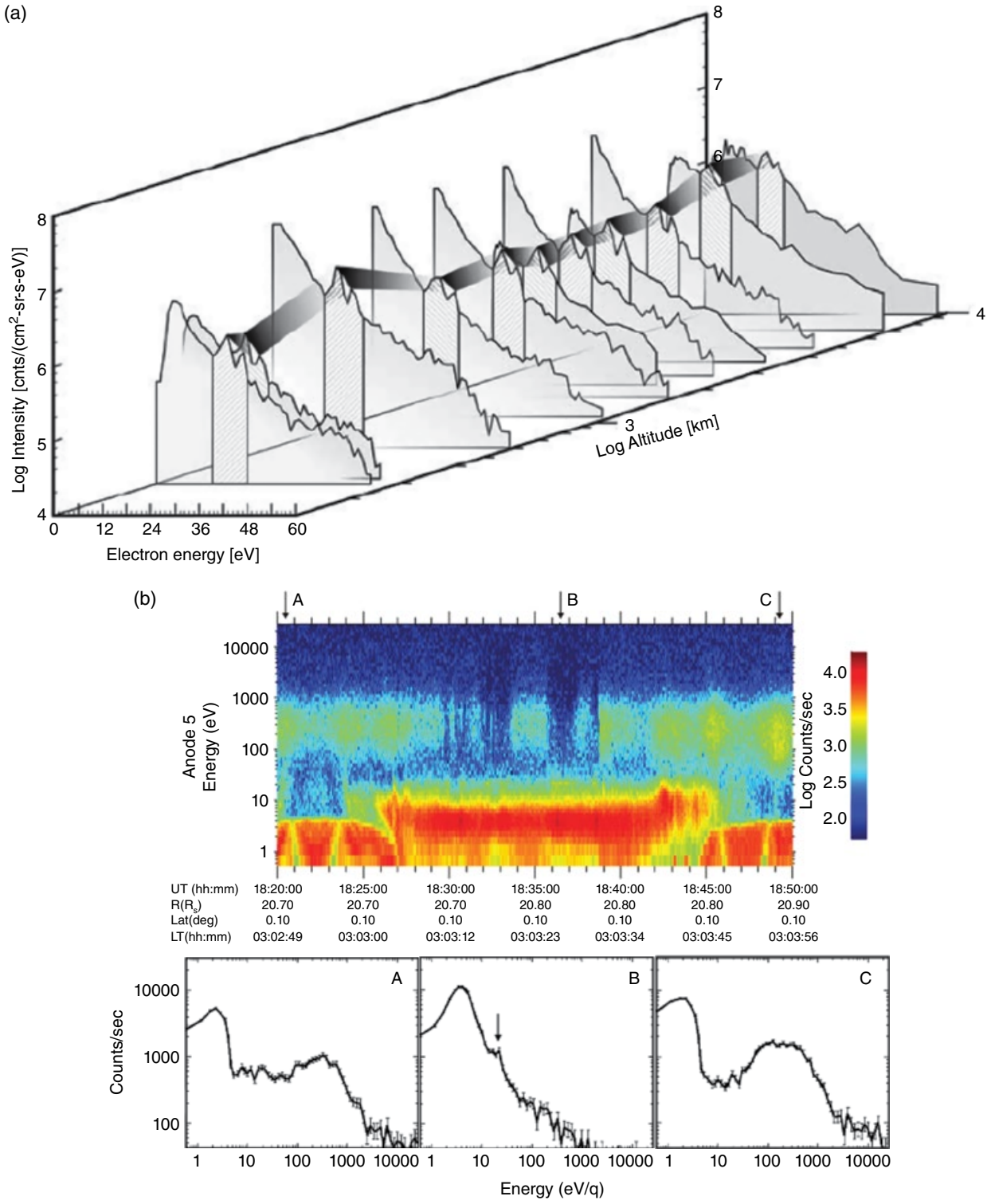

Figure 21.6 Ionospheric plasma in the tails of: (a) Mars at up to 10,000 km [from *Frahm et al.*, 2006b], and (b) Titan [from *Coates et al.*, 2007].

Some recent observations were presented on magnetic reconnection in the tail of Venus [*Zhang et al.*, 2012], the first time this process has been seen in situ at an unmagnetized object. Although seen in the Martian tail [*Eastwood et al.*, 2008], the presence of crustal fields may be relevant in that case. In addition, hot flow anomalies were studies at Venus [*Collinson et al.*, 2012]; this is an effect seen at Earth where the bow shock may bulge during interaction with solar wind discontinuities. Also, it was shown that the escape rate from Venus increases by almost a factor of 2 during a CIR event in the solar wind [*Edberg et al.*, 2011] and up to a factor 100 during a coronal mass ejection (CME) [*Luhmann et al.*, 2007].

21.3.4. Saturn's Moons

Some features of the plasma interaction conditions at Saturn's moons are summarized in Table 21.2. Clearly, upstream conditions and presence of an atmosphere are important.

21.3.4.1. Titan

At Titan, a strong local interaction with Saturn's magnetosphere forms a complex plasma tail [e.g., *Coates*, 2009; *Coates et al.*, 2011b and references therein]. Titan's orbital position at 20 Saturn radii means that it can encounter a range of conditions in the magnetosphere [e.g., *Rymer et al.*, 2009; *Simon et al.*, 2013; *Arridge et al.*, 2011a] and sometimes encounters the magnetosheath [*Bertucci et al.*, 2008] and also the solar wind [*Bertucci et al.*, 2015]. Early suggestions were that within the magnetosphere, average conditions would include an electric field directed away from Saturn [*Blanc et al.*, 2002] assuming nominal conditions (i.e., a dipole magnetic field and exact corotation). This would set up the electric field seen by new pickup ions from Titan's extended atmosphere. However, the data have shown that conditions are rarely nominal, and each encounter has its own geometry. In particular, Saturn's bowl-shaped magnetodisk [*Arridge et al.*, 2008] changes with season and has a direct effect on upstream conditions at Titan [*Arridge et al.*, 2011a]. An additional complexity is that the solar and corotation wake orientations change through Titan's orbit around Saturn [e.g., *Coates*, 2009].

Atmospheric loss rates are large and the subject of some debate [*Johnson et al.*, 2009] although ion loss rates have been measured [*Coates et al.*, 2012]. Magnetospheric energy and composition drive some complex chemistry. Also sunlight is a driver, but Titan's location in Saturn's outer magnetosphere (20 R_S) prevents significant contributions of mass or significant dynamic effects on the magnetosphere.

Chemical complexity in Titan's ionosphere was one of the major new discoveries of the Cassini mission, using in situ measurements from the Cassini Plasma Spectrometer (CAPS) and Ion and Neutral Mass Spectrometer (INMS) instruments. The complexity is seen in neutral and positive species by INMS and CAPS, as well as the newly discovered negative ions seen by CAPS [*Waite et al.*, 2007; *Coates et al.*, 2007b, 2009, 2010a; *Crary et al.*, 2009]. In addition, related 'tholins' are seen using occultation measurements [e.g., *Liang et al.*, 2007]. Negative ions were unexpected at such high altitudes. Cassini found very heavy negative ions up to 13,800 atomic mass units per charge (amu/q) [*Coates et al.*, 2007b, 2009] as well as positive ions up to ~1000 amu/q [*Waite et al.*, 2007; *Crary et al.*, 2009; *Coates et al.*, 2010a], and it was suggested that the linked neutral-cation-anion chemistry plays a key role in haze formation. The low mass negative ions were identified as CN^-, C_3N^- and C_5N^- [*Vuitton et al.*, 2009] while the formation process for higher mass ions is under study. The ion configuration is unconstrained (e.g., chains, rings or even fullerenes are possible), the latter may transport oxygen to the surface [*Sittler et al.*, 2009]. Recent studies show that agglomeration due to charging [*Michael et al.*, 2011] or chemical processes [*Lavvas et al.*, 2013] may be operating.

The maximum mass of negative ions at Titan was studied as a function of altitude, latitude, and solar zenith angle [*Coates et al.*, 2009] finding that the maximum mass is found at the lowest altitudes. Recently, the density variation with these parameters has been examined [*Wellbrock et al.*, 2013] to further constrain the chemical processes.

Negative ions have been confirmed in the Langmuir probe data, initially using observations at the lowest altitude encounter T70 [*Ågren et al.*, 2013] where CAPS was not oriented in the ram direction, and subsequently at other encounters [*Shebanits et al.*, 2013].

Table 21.2 Comparison of plasma interaction conditions at Saturn's moons. In the location row, the letters refer to Inner, Middle, Outer magnetosphsphere, Sheath, Solar Wind, Tail

Moon	Mimas	Enceladus	Tethys	Dione	Rhea	Titan	Iapetus	Hyper-ion
Orbital dist. (R_S)	3.18	4.09	5.07	6.47	9.05	20.99	61.13	25.43
Radius (km)	198	252	531	561	763	2575	735	135
Location	I	I	I	M	M	O/Sh	SW/Sh/T	Sh/O/T
Activity/atmosphere	No?	Active geysers	No?	Tenuous, O_2/CO_S	Tenuous, O_2/CO_2	Thick, N_2/CH_4	No?	No?

Ionospheric photoelectrons at Titan provide a key indication of ionospheric plasma, or of a magnetic connection to Titan's tail [*Coates et al.*, 2007, 2011a; *Wellbrock et al.*, 2012]. Figure 21.6b illustrates ionospheric plasma seen in the tail of Titan at distances up to 6.8 Titan radii (R_T), identified again using distinctive photoelectron peaks. This was used to estimate plasma escape rates [*Coates et al.*, 2012; see also *Westlake et al.*, 2012]. Photoelectrons also provide an ambipolar electric field driving plasma escape [*Coates et al.*, 2007a, 2012]. Plasma escape rates at Titan showed that Titan loses 7 tonnes of material per day [*Coates et al.*, 2012]. Recent work has shown an upper limit for the field aligned potential at Titan of 2.95 eV [*Coates et al.*, 2015b].

21.3.4.2. Rhea and Dione

Saturn's moons Rhea and Dione are additional sources of pickup ions. Analysis of pickup ion trajectories led to the discovery of exospheres at Rhea [*Teolis et al.*, 2010] (using positive and negative pickup ions to identify the near-surface source), and at Dione [*Tokar et al.*, 2012]. The exosphere production is due to magnetospheric particle bombardment of these icy moons, a process that also occurs at Europa, Ganymede, and Callisto.

21.3.4.3. Enceladus

The importance of Enceladus as a source was first found from magnetometer observations of a draped field [*Dougherty et al.*, 2006]. Flow deflection was also seen by the CAPS ion mass spectrometer (IMS), and the derived production rate was ~100 kgs^{-1} [*Tokar et al.*, 2006], second only to Io in gas production rate from a solar system moon. The source was found to be plumes from 'tiger stripes' close to the South Pole of Enceladus.

The concentration of charged particles in the plume is sufficient that a 'plume ionosphere' forms, with a region of stagnant plasma flow immersed in Saturn's rapidly rotating magnetosphere [*Tokar et al.*, 2009]. Saturn's magnetosphere approximately corotates with the planet at 4 R_S. Positive and negative ionospheric ions were found within the plumes [*Tokar et al.*, 2009; *Coates et al.*, 2010b]. The positive ions appeared as water group ions (mass 16–19) and heavier ions. Pickup ions were also seen in a ring distribution, both close to Enceladus [*Tokar et al.*, 2006] and in the magnetospheric region close to Enceladus' orbit [*Tokar et al.*, 2008]. The negative ions appear as multiples of the water or OH mass, with clusters of up to 100 [*Coates et al.*, 2010a, 2010b]. This further identifies Enceladus as a water source and is consistent with a subsurface ocean there.

Cassini established that Enceladus is the main source of water in the inner magnetosphere, with additional sources from the rings. The almost co-rotating inner magnetosphere, which includes hydrogen ions mainly from Saturn's ionosphere, is dominated by water-based neutrals (O, OH). Enceladus, supplemented by the rings and the associated neutrals, populates the outer magnetosphere as well [*Smith et al.*, 2008; *Thomsen et al.*, 2010; *Arridge et al.*, 2011b]. Some of the remarkably complex chemistry at Titan appears to involve particles, oxygen in particular, originally from Enceladus [*Coates et al.*, 2007a; *Sittler et al.*, 2009].

INMS confirmed that the neutral gas is concentrated over the South Pole [*Waite et al.*, 2006]. Composition data from INMS show that in addition to water, carbon dioxide, methane, ammonia, ^{40}Ar and organics are present in the neutral gas in smaller quantities. CAPS measurements also indicate nitrogen, which may be from ammonia, and that Enceladus, rather than Titan, is the dominant nitrogen source at Saturn [*Smith et al.*, 2009; *Thomsen et al.*, 2010; *Arridge et al.*, 2011b]. In addition, the plume appears to be a variable source with gas production ~10^{27}–10^{28} s^{-1} [*Smith et al.*, 2010].

In addition to the population of neutral ice particles, charged nanograins were found by CAPS [*Jones et al.*, 2009]. The timing of the negative and positively charged grain densities were used to trace the trajectories back to particular sources within the tiger stripe regions. In addition to identifying the location of emission, the trajectories of the charged nanograins were different between the charged species, implying separation with respect to each other and the neutral plume. Saturn's magnetic field effectively acts as a huge mass spectrometer for these particles. Ice grain-plasma interactions play a role in Saturn's inner magnetosphere.

Several pioneering discoveries of new populations near Enceladus were possible using CAPS data. These include charged nanograins [*Jones et al.*, 2009], negatively and positively charged water clusters [*Coates et al.*, 2010b; *Tokar et al.*, 2009], magnetospheric photoelectrons from ionization of neutrals throughout the magnetosphere near Enceladus [*Schippers et al.*, 2009] and plume photoelectrons [*Coates et al.*, 2013]. Further detailed study of the charged dust [*Hill et al.*, 2012] has indicated the charging mechanism is likely from the surrounding plasma. It is clear that Enceladus provides a remarkably complex plasma environment. The unexpected species add to the anticipated cold magnetospheric electrons. Enceladus is one of the key locations in the solar system where 'dusty plasma' can be studied (others include comets). The CAPS energy spectral data revealed several unexpected populations. For example, plume photoelectrons provide an ionization source [*Coates et al.*, 2013], which adds to magnetospheric photoelectrons to provide electron impact ionization, which may be a key process in the magnetosphere at this position [e.g., *Fleshman et al.*, 2012].

The plasma environment of Enceladus is determined by the approximately corotating magnetosphere of Saturn and its interaction with (a) mass loading through charge exchange and negative grain charging and (b) the plasma produced from the plumes via ion pickup. The interaction drives field-aligned currents that can reach the Saturn auroral region and produce an auroral spot [*Pryor et al.*, 2011], a weaker version of the auroral spots at Jupiter associated with Io, Europa, and Ganymede.

The overall picture emerging is that Saturn's magnetosphere is filled with water-group atoms, radicals, and molecules (O, OH, H_2O) from the major sources (Enceladus, main rings, others) slowly being turned into water-group ions (O^+, OH^+, H_2O^+, H_3O^+). The ions are picked up by the rapidly rotating magnetosphere and are eventually lost into the solar wind.

21.3.5. Jupiter's Moons

21.3.5.1. Io, Europa, and Callisto

The volcanic moon Io is a source of heavy (S, O based) neutrals, and a major source of particles for Jupiter's magnetosphere (~1 tonne s^{-1}). Io has a plasma torus from ionization of these [*Bagenal*, 1994 and references therein]. The orbit of Io is well inside the Jovian magnetosphere, where corotation of the rapidly rotating magnetosphere is faster than the moon's orbital speed. Io's wake is therefore ahead of Io in its orbit. Io thus presents a partially conducting obstacle to a subsonic magnetospheric flow, resulting in Alfvén wings [*Neubauer et al.*, 1998]. Pickup ions are produced at a rate of ~$3x10^{28}$ s^{-1}.

Initially, the pickup ion distribution is ring-like (in the dipole approximation, v ⊥ B). Pitch angle scattering occurs as elsewhere in solar system, with a timescale of a few days here [*Huddleston et al.*, 1998]. As the speed is sub-Alfvénic, the bispherical shell produces almost perpendicular pickup as shown in Figure 21.7, which schematically shows pickup ion distributions at Io. Note that due to the low flow speed, the centers of the bispherical arcs are outside both the arcs themselves *Huddleston et al.*, [1998].

The effects of ion pickup are also observed at other Galilean satellites (e.g., ion cyclotron waves at Europa and Ganymede as well as Io) [*Russell et al.*, 2000, 2001; *Volwerk et al.*, 2001]. In these cases, the neutrals are from sputtering under plasma bombardment [e.g., *Johnson et al.*, 2009 and references therein]. The JUICE Mission, and Europa Clipper if approved, will study these processes in more detail via measurements of the pickup ions.

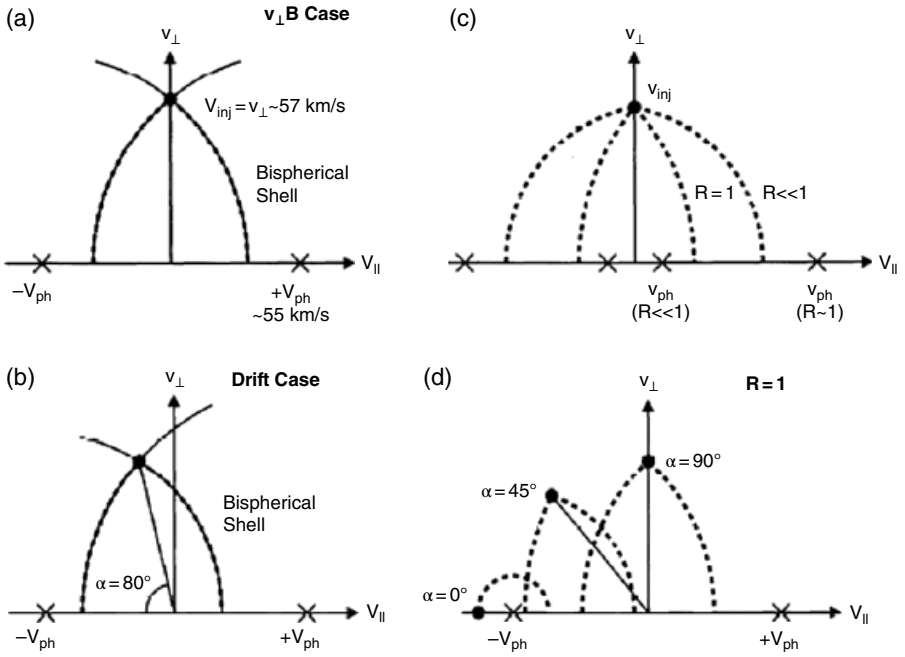

Figure 21.7 Pickup geometry at Io showing bispherical shells [*Huddleston et al.*, 1998]. (a) perpendicular pickup, (b) ~80°, (c) different values of the ratio between the wave phase velocity and the injection velocity $R=V_{ph}/V_{inj}$, and (d) different v-B angles α. All moons in corotating inner magnetospheres of the outer planets will have a similar geometry although V_{ph} and V_{inj} may be different.

21.3.5.2. Ganymede

Ganymede has an intrinsic magnetic field that fundamentally affects its interaction with the plasma environment. This body is unique in the solar system, representing a 'magnetosphere within a magnetosphere' (Jupiter's). Although magnetized, there are common processes with unmagnetized moons such as energetic particle interaction with the surface, exosphere production, and mass loading processes in the surrounding plasma. JUICE will study the interaction in detail from orbit.

21.3.6. Moon

Earth's Moon is usually in the solar wind but spends a fraction of time in Earth's magnetotail. The Moon has some crustal magnetic fields. The plasma interaction is dominated by a wake behind the Moon in the flow direction, as the embedded magnetic field diffuses through the Moon while the particles impact onto the lunar surface. Recent missions have found interesting new kinetic effects. Pickup ions have been detected [*Hilchenbach et al.*, 1992; *Mall et al.*, 1998] and reflected ions also. *Halekas et al.* (2011) summarized some of the new results from recent missions.

Recent results from the Kaguya spacecraft have distinguished four different ion populations produced by solar wind bombardment, including two populations of pickup ions [*Saito et al.*, 2010]: (1) backscattered ions from the surface [*Saito et al.*, 2008], (2) reflected ions from magnetic anomalies, (3) pickup ions (by the solar wind) from backscattered or reflected particles [*Saito et al.*, 2008], and (4) pickup ions (by the solar wind) from the surface or exosphere [*Yokota et al.*, 2009]. Population, (4) above, represents classical pickup ions seen as rings in velocity space. However, the 'self-pickup' process, (3) above, of the reflected proton population (~0.1–1% of the solar wind flux [*Saito et al.*, 2008], provides additional energy beyond the classical pickup process. The particles are also seen as rings.

Self-pickup provides a maximum velocity (for a proton) of up to 3 times the solar wind, and an energy 9 times that of the solar wind [*Saito et al.*, 2008] in the spacecraft frame, due to the 'injection point' being at up to $-u_{sw}$ (see Figure 21.8, which illustrates the pickup ion geometry for both conventional pickup [inner circle] and for self-pickup [outer circle]). In addition, Interstellar Boundary Explorer (IBEX) detected neutral lunar backscattered particles [*McComas et al.*, 2009], while Chandrayaan-1 both confirmed the reflected protons, and found that up to 20% of the incident solar wind flux can be backscattered as neutrals [*Wieser et al.*, 2009; *Bhardwaj et al.*, 2010]. These may then ionize and form part of the 'self-pickup' population. The 'self-pickup' particles may then enter deep into the lunar wake, due to their larger cycloidal trajectories compared to classical pickup [e.g., the particles in (4) above] [*Nishino et al.*, 2009, 2010; *Holmstrom et al.*, 2010].

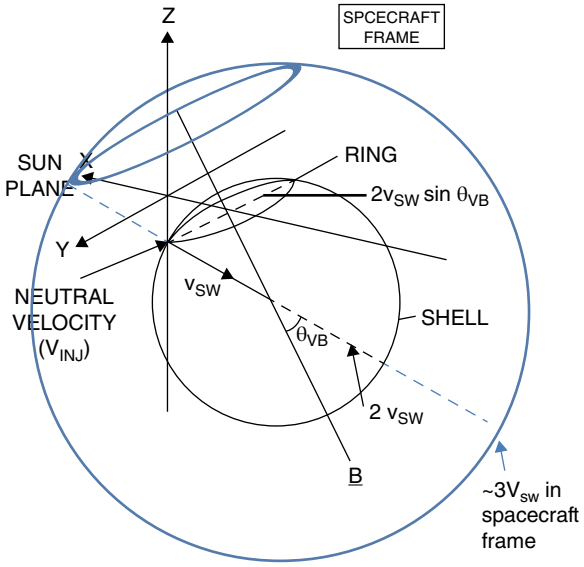

Figure 21.8 Pickup geometry including the effect of reflection from the Moon's surface. The resulting energy is higher [*Coates*, 2012].

21.3.7. Pluto

Our knowledge of Pluto's solar wind interaction will be transformed later this year with the arrival of New Horizons. However, the expectations are that the solar wind Mach number is likely to be high at this location in the solar system [see *Russell et al.*, 1990]. The solar wind interaction is expected to be somewhat comet-like when Pluto is near the Sun and its exosphere is at maximum density. The atmospheric loss rate has been estimated at ~10^{25}–10^{27} s^{-1} [*McNutt*, 1989] and an extended mass loading region is anticipated. The gyroradius of CH_4^+ ions would be 250,000 km and for N_2^+ it would be 658,000 km. The kinetic nature of the interaction, including nongyrotropic distributions as seen at comet Grigg-Skjellerup [*Coates et al.*, 1993b], will make the results very interesting. One aspect that is anticipated is momentum balance between the pickup ions and the solar wind deflection [e.g., *Delamere and Bagenal*, 2004]. This was seen in the AMPTE Lithium and Barium releases [*Coates et al.*, 1986, 1988; *Johnstone et al.*, 1986b], and is also seen in the early data from Rosetta at comet 67P [*Nilsson et al.*, 2015; *Goldstein et al.*, 2015]. Other aspects of the very early pickup interaction as at comet 67P are also possible, although at Pluto, the scale is larger and the neutral particle density is lower near the location where new ions are produced. One aspect is whether a Venus-type ionopause, or a diamagnetic cavity as at Halley, is present [*Cravens and Strobel*, 2015].

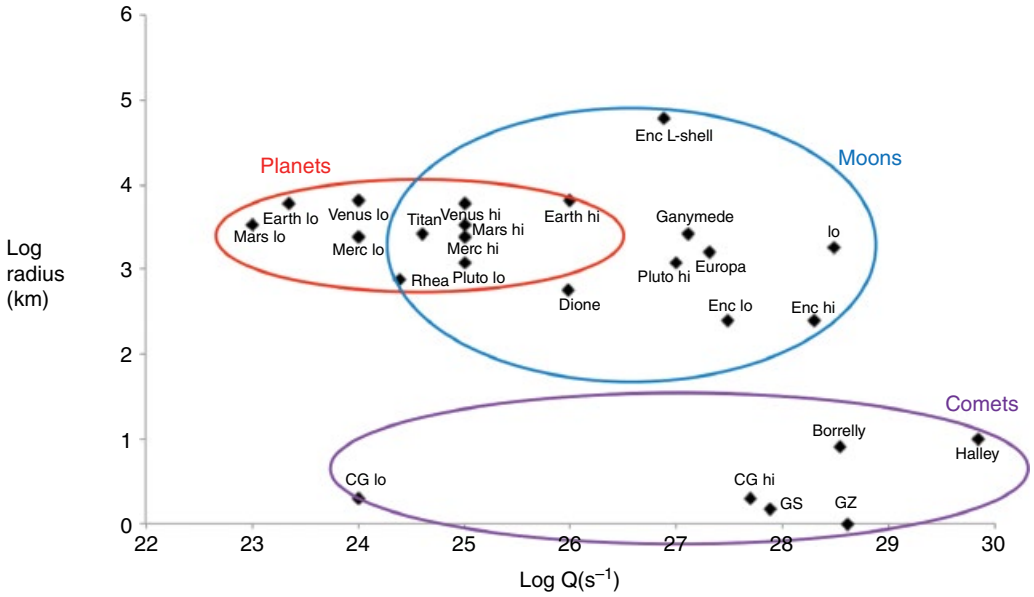

Figure 21.9 Summary of loss rates for solar system objects from Table 21.1 plotted as a function of object radius. [adapted from *Coates et al.*, 2015a]

21.4. ESCAPE: COMPARISON

We have compared the escape rates for the unmagnetized objects in the solar system, and included some magnetized objects in the comparison (see Table 21.1). In Figure 21.9, we show a log-log plot of the loss rates for the solar system objects shown in Table 21.1 against the object radius. We find a remarkable grouping into planets, moons, and comets. There are several different escape processes at work for all objects, including thermal and non-thermal mechanisms, which contribute to all of the rates. Some interesting trends are seen. The smaller objects, such as comets, have generally higher escape rates, due partly to their lower gravity. The moons shown are generally higher escape rates than the planets for similar size objects. In the cases of Io and Enceladus, this is due to their intrinsic activity, and in the other cases shown because of their immersion in hot magnetospheres rather than the solar wind [*Coates et al.*, 2015].

We note that the extremes of the Earth's escape rate are similar to those of unmagnetized objects, and the Pluto points included are based on expectations rather than measurements, but these span the 'planets' and 'moons' areas of the plot.

21.5. SUMMARY AND CONCLUSIONS

We have discussed some of the processes at work and the plasma measurements made so far in the plasma interaction with unmagnetized objects. We discussed the types of interaction, including the effects of upstream conditions and the nature of obstacle. Our tour was organized by objects (comets, Mars, Venus, Titan, Rhea, Dione, Enceladus, Io, Europa, Callisto, Moon, Pluto), but some key processes are common to all these objects, including ion pickup, ionospheric processes such as photoelectron production, and plasma escape processes.

In conclusion, we look forward to the next months of Rosetta operations at comet 67P. This will allow, for the first time, the evolution of the comet-plasma interaction to be followed. Following orbit insertion around 67P at ~3.5 astronomical unit (AU), the activity increases during the approach to perihelion at ~1.24 AU and then subsequently decreases with increasing heliocentric distance during the extended mission.

ACKNOWLEDGMENTS

The data used in this paper are in NASA PDS and ESA PSA. We thank the organizers for the opportunity to present this review, and STFC, UK for financial support. We thank Martin de la Nougerede, UCL-MSSL, for re-drafting Figure 21.3.

REFERENCES

Acuña, M.H., et al. (1998), Magnetic field and plasma observations at Mars: Initial results of the Mars Global Surveyor mission. *Science 279*, 1676–1680, doi:10.1126/science.279.5357.1676.

Ågren, K., et al. (2012), Detection of negative ions in the deep ionosphere of Titan during the Cassini T70 flyby, *Geophys. Res. Lett.*, *39*, L10201.

Angsmann, A., et al. (2011), Magnetic states of the ionosphere of Venus observed by Venus Express, *Planet. Space Sci.*, *59*, 327–337, doi:10.1016/j.pss.2010.12.004.

Arridge, C., et al. (2008), Warping of Saturn's magnetospheric and magnetotail current sheets, *J. Geophys. Res.*, *113*, A08217, doi:10.1029/2007JA012963.

Arridge, C. et al. (2011a), Upstream of Saturn and Titan, Space Sci. *Rev.*, *162*, 25-83, 10.1007/s11214-011-9849-x.

Arridge, C.S., et al. (2011b), Mapping Magnetospheric Equatorial Regions at Saturn from Cassini Prime Mission Observations, *Space Sci. Rev*., *164*, 1–83, 10.1007/s112 14-011-9850-4.

Bagenal, F. (1994), Empirical model of the Io plasma torus: Voyager measurements, *J. Geophys. Res.*, *99*, 11,043–11,062, doi:10.1029/93JA02908.

Barabash, S., et al. (2007a), The loss of ions from Venus through the plasma wake, *Nature 450*, 650–653, 10.1038/nature06434.

Barabash, S., et al. (2007b), Martian atmospheric erosion rates, *Science 315*, 501–503 doi:10.1126/science.1134358.

Bertaux, J.L., et al. (2005), Discovery of an aurora on Mars, *Nature*, *435*, 790–794, doi:10.1038/nature03603.

Bertucci, C., et al. (2008), The Magnetic Memory of Titan's Ionized Atmosphere, *Science*, *321*, 1475–1478, doi:10.1126/ science.1159780.

Bertucci, C., et al. (2015), Titan's interaction with the supersonic solar wind, *Geophys. Res. Lett.*, *42*, 193–200, doi:10.10 02/2014GL062106.

Bhardwaj, A., et al. (2010), Studying the Lunar-Solar Wind Interaction with the SARA Experiment aboard the Indian Lunar Mission Chandrayaan-1, 12th International Solar Wind Conference. *AIP Conf. Proc.*, *1216*, 518–521, doi:10.10 63/1.3395916.

Blanc, M., et al. (2002), Magnetospheric and Plasma Science with Cassini-Huygens, *Space Sci. Rev*., *104*, 253–346, 10.1023/A:1023605110711.

Brace, L.H., et al. (1987), The ionotail of Venus: its configuration and evidence for ion escape, *J. Geophys. Res.*, *92*, 15–26, doi:10.1029/JA092iA01p00015.

Coates, A.J., et al. (1986), AMPTE-UKS ion experiment observations of lithium releases in the solar wind, *J. Geophys. Res.*, *91*, 1311–1319, doi:10.1029/JA091iA02p01311.

Coates, A. J., et al. (1988), Development of the first artificial comet, UKS ion measurements, *Adv. Space Res.*, *8*(1), 15–21, doi:10.1016/0273-1177(88)90337-7.

Coates, A.J., et al. (1989), Velocity space diffusion of pick-up ions from the water group at Comet Halley, *J. Geophys. Res.*, *94*, 9983–9993, doi:10.1029/JA094iA08p09983.

Coates, A.J., et al. (1990), Bulk properties and velocity distributions of water group ions at comet Halley: Giotto measurements, *J. Geophys Res*, *95*, 10249–10260.

Coates, A.J. (1991), Cometary plasma energisation, *Ann. Geophys.*, *9*, 158–169.

Coates, A. J., et al. (1993a), Pickup water group ions at Comet Grigg-Skjellerup, *Geophys. Res. Lett.*, *20*, 483–486, doi:10.10 29/93GL00174.

Coates, A.J., et al. (1993b), Velocity space diffusion and non-gyrotropy of pickup water group ions at comet Grigg-Skjellerup, *J. Geophys. Res.*, *98*, 20,985–20,994, doi:10.1029/ 93JA02535.

Coates, A.J. (2001), *Our Solar System and beyond in the new millennium, in Visions of the Future: Astronomy and Earth Science*. Edited by J.M.T Thompson, p. 85–113, Cambridge University Press, Cambridge, UK, doi:2001vfae/0-521-80 537–6.

Coates, A.J. (1999), The Solar System in the next millennium, *Phil. Trans. Roy. Soc. A*, *357*, 3299–3317, doi:10.1098/ rsta.1999.0495.

Coates, A.J., et al. (2007a), Ionospheric electrons in Titan's tail: plasma structure during the Cassini T9 encounter, *Geophys. Res. Lett*., *34*, L24S05, doi:10.1029/2007GL030919.

Coates, A.J., et al. (2007b), Discovery of heavy negative ions in Titan's ionosphere, *Geophys. Res. Lett.*, *34*, L22103, doi:10.1029/2007GL030978.

Coates, A.J., et al. (2008), Ionospheric Photoelectrons at Venus: Initial Observations by ASPERA-4 ELS, *Planet. Space Sci.*, *56*, 802–806, doi:10.1016/j.pss.2007.12.008.

Coates, A.J. (2009), Interaction of Titan's ionosphere with Saturn's magnetosphere, *Phil. Trans. R. Soc. A*, *367*, 773–788, doi:10.1098/rsta.2008.0248.

Coates, A.J., and G. H. Jones (2009), Plasma environment of Jupiter family comets, *Planetary and Space Science*, *57*, 1175–1191, doi:10.1016/j.pss.2009.04.009.

Coates, A.J., et al. (2009), Heavy negative ions in Titan's ionosphere: altitude and latitude dependence, *Planet. Space Sci.*, *57*, 1866–1871, doi:10.1016/j.pss.2009.05.009.

Coates, A.J. (2010), Ion pickup at comets: comparison with other unmagnetized objects, in Pickup ions throughout the heliosphere and beyond: proceedings of the 9th International Astrophysics Conference, edited by J. le Roux, G. P. Zank, A. J. Coates and V. Florinsky, AIP conference proceedings, 1302, American Institute of Physics, Melville, NY, pp. 213–224, doi:10.1063/1.3529973.

Coates, A.J., et al. (2010a), Negative ions at Titan and Enceladus: recent results, *Faraday Disc.*, *147*(1), 293–305, doi:10.1039/ C004700G2010.

Coates, A.J., et al. (2010b), Negative Ions in the Enceladus Plume, *Icarus*, *206*, 618–622, doi:10.1016/j.icarus.2009. 07.013.

Coates, A.J., et al. (2011a), Ionospheric photoelectrons: comparing Venus, Earth, Mars and Titan, *Planet. Space Sci. 59*, 1019–1027, doi:10.1016/j.pss.2010.07.016.

Coates, A.J., et al. (2011b), Recent results from Titan's ionosphere, *Space Sci. Rev*., *162*, 85–111, doi:10.1007/s112 14-011-9826-4.

Coates, A.J. (2012), Ion Pickup and Acceleration: Measurements From Planetary Missions, in *Physics of the heliosphere: a 10-year retrospective, AIP conference proceedings, 1436, ISBN: 978-0-7354-1026-8, Editor(s): Jacob Heerikhuisen*, Gang Li, Nikolai Pogorelov, Gary Zank, American Institute of Physics, Melville, NY, pp. 89–102, doi:10.1063/1.4723595.

Coates, A.J., et al. (2012), Cassini in Titan's tail: CAPS observations of plasma escape, *J. Geophys. Res.*, *117*, A05324, doi:10.1029/2012JA017595.

Coates, A.J., et al. (2013), Photoelectrons in the Enceladus plume, *J. Geophys. Res.*, *118*, 5099–5108, DOI: 10.1002/jgra.50495.

Coates, A.J., et al. (2015a), Distant ionospheric photoelectron energy peak observations at Venus, *Planet. Space Sci.*, *113–114*, 378-384, doi:10.1016/j.pss.2015.02.003.

Coates, A.J., et al. (2015b), A new upper limit to the field-aligned potential near Titan, *Geophys. Res. Lett.*, *12*, 4676–4684, doi:10.1002/2015GL064474.

Collinson, G.A., et al. (2012), Hot Flow Anomalies at Venus, *J. Geophys. Res.*, *117*, A04204, doi:10.1029/2011JA017277.

Connerney, J.E.P., et al. (2001), The global magnetic field of Mars and implications for crustal evolution. *Geophys. Res. Lett. 28*, 4015–4018, doi: 10.1029/2001GL013619.

Connerney, J.E.P., et al. (2005), Tectonic implications of Mars crustal magnetism, *PNAS*, *102*, 14970–14975, doi:10.1073/pnas.0507469102.

Crary, F.J., et al. (2009), Heavy ions, temperatures and winds in Titan's ionosphere: Combined Cassini CAPS and INMS observations, *Planet. Space Sci.*, *57*, 1847–1856, doi:10.1016/j.pss.2009.09.006.

Cravens, T.E., and D.F. Strobel (2015), Pluto's solar wind interaction: Collisional effects, *Icarus*, *246*, 303–309. doi:10.1016/j.icarus.2014.04.011.

Delamere, P.A., and F. Bagenal (2004), Pluto's kinetic interaction with the solar wind, *Geophys. Res. Lett.*, *31*, L04807, doi:10.1029/2003GL018122.

Delva, M., et al. (2008a), First upstream proton cyclotron wave observations at Venus, *Geophys. Res. Lett.*, *35*, L03105, doi:10.1029/2007GL032594.

Delva, M., et al. (2008b), Proton cyclotron waves in the solar wind at Venus, *J. Geophys. Res.*, *113*, E00B06, 10.1029/2008JE003148.

Delva, M., et al. (2009), Hydrogen in the extended Venus exosphere, *Geophys. Res. Lett.*, *36*, L01203, doi:10.1029/2008GL036164.

Dougherty, M.K., et al. (2006), Identification of a Dynamic Atmosphere at Enceladus with the Cassini Magnetometer, *Science*, *311*, 1406–1409, doi:10.1126/science.1120985.

Dubinin, E., et al. (1993), Cold ions at the Martian bow shock, PHOBOS observations, *J. Geophys. Res.*, *98*, 5617–5623, doi:10.1029/92JA02374.

Dubinin, E., et al. (2006), Hydrogen exosphere at Mars: Pickup protons and their acceleration at the bow shock, *Geophys. Res. Lett.*, *33*, L22103, doi:10.1029/2006GL027799.

Eastwood, J. P., et al. (2008), Evidence for collisionless magnetic reconnection at Mars, *Geophysical Research Letters*, *35*, L02106, doi:10.1029/2007GL032289.

Edberg, N.J.T., et al. (2011), Atmospheric erosion of Venus during stormy space weather, *J. Geophys. Res.*, *116*, A09308 doi:10.1029/2011JA016749.

Fedorov, A., et al. (2008), Comparative analysis of Venus and Mars magnetotails, *Planet. Space Sci.*, *56*, 812–817, doi:10.1016/j.pss.2007.12.012.

Fleshman, B. L., et al. (2012), The roles of charge exchange and dissociation in spreading Saturn's neutral clouds, *J. Geophys. Res.*, *117*, E05007, 10.1029/2011JE003996.

Frahm, R. A., et al. (2006a), Carbon dioxide photoelectron peaks at Mars, *Icarus*, *182*, 371–382, doi:10.1016/j.icarus.2006.01.014.

Frahm, R. A., et al. (2006b), Locations of atmospheric photoelectron energy peaks within the Mars environment, *Space Sci. Rev.*, *126*, 389–402 10.1007/s11214-006-9119-5.

Frahm, R. A., et al. (2010), Estimation of the escape of photoelectrons from Mars in 2004 liberated by the ionization of carbon dioxide and atomic oxygen, *Icarus*, *206*, 50–63, doi:10.1016/j.icarus.2009.03.024.

Goldstein, R., et al. (2015), The Rosetta Ion and Electron Sensor (IES) Measurement of the Development of Pickup Ions from Comet 67P/Churyumov-Gerasimenko, *Geophys. Res. Lett.*, *42*, 3093–3099, doi:10.1002/2015GL063939.

Haaland, S., et al. (2013), Cold Ion Outflow as a Source of Plasma for the Magnetosphere, in *Dynamics of the Earth's Radiation Belts and Inner Magnetosphere*, edited by D. Summers, I. R. Mann, D. N. Baker and M. Schulz, AGU monograph series, vol. *199*, pp. 341–354, AGU, Washington DC.

Halekas, J.S., et al. (2011), New views of the lunar plasma environment, *Planet. Space Sci.*, *59*, 1681–1694, doi:10.1016/j.pss.2010.08.011.

Hansen, K.C., et al. (2007), The plasma environment of comet 67P/Churyumov-Gerasimenko throughout the Rosetta main mission, *Space Science Reviews*, *128*, 133–166, doi:10.1007/s11214-006-9142-6.

Hilchenbach, M., et al. (1992), Detection of singly ionized energetic lunar pickup ions upstream of Earth's bow shock, in Solar Wind Seven, *COSPAR colloquia series 3*, 349–355.

Hill, T.W., et al. (2012), Charged nanograins in the Enceladus plume J. *Geophys. Res.*, *117*, A05209, doi:10.1029/2011JA017218.

Holmstrom et al. (2010), Dynamics of solar wind protons reflected by the Moon, *J. Geophys. Res.*, *115*, A06206, doi:10.1029/2009JA014843.

Huddleston, D.E., et al. (1998), Ion cyclotron waves in the Io torus: Wave dispersion, free energy analysis, and SO2+ source rate estimates, *J. Geophys. Res.*, *103*, 19, 887–19,889, doi:10.1029/97JE03557.

Hundhausen, A.J. (1995), The solar wind, in *Introduction to Space Physics*, edited by M. G. Kivelson and C. T. Russell, pp. 91–128, Cambridge University Press, New York, NY.

Hynds, R.J., et al. (1986), Observations of energetic ions from comet Giacobini-Zinner, *Science*, *232*, 361–365, doi:10.1126/science.232.4748.361.

Johnson, R. E., et al. (2009a), Composition and Detection of Europa's Sputter-Induced Atmosphere, in *Europa*, Eds. R.T. Pappalardo, W.B. McKinnon and K. Khurana, pp. 507–527, University of Arizona Press, Tucson, AZ.

Johnson, R.J., et al. (2009b), *Mass loss processes in Titan's upper atmosphere, in Titan from Cassini-Huygens*, edited by R. H. Brown, J.-P. Lebreton, and J. H. Waite, Springer, Dordrecht, pp. 373–391.

Johnstone, A.D., et al. (1986a), Ion flow at Halley's comet, *Nature*, *321*, 344–347, doi:10.1038/321344a0.

Johnstone, A.D., et al. (1986b), Lithium tracer ion energisation observed at AMPTE-UKS, in *Ion Acceleration in the Magnetosphere and Ionosphere*, Geophys. Monogr. Ser., vol. *38*, edited by T. Chang et al., pp. 186–190, AGU, Washington, D.C., doi:10.1029/GM038p0186.

Johnstone A.D., et al. (1993), Observations of the Solar Wind and Cometary Ions during the Encounter Between Giotto and Comet Grigg-Skjellerup, *Astron. Astrophys.*, *273*, L1–L4.

Jones, G.H., et al. (2009), Fine jet structure of electrically-charged grains in Enceladus' plume, *Geophys. Res. Lett.*, *36*, L16204, doi:10.1029/2009GL038284.

Kallio, E., et al. (2010), Oxygen ion escape at Mars in a hybrid model: High energy and low energy ions, *Icarus*, *206*, 152–163, doi:10.1016/j.icarus.2009.05.015.

Krankowsky, D., et al. (1986), In situ gas and ion measurements at comet Halley, *Nature*, *321*, 326–329, doi: 10.1038/321326a0.

Lammer, H., et al. (2008), Atmospheric Escape and Evolution of Terrestrial Planets and Satellites, *Space Sci. Rev.*, *139*, 399–436, doi:10.1007/s11214-008-9413-5.

Lavvas, P., et al. (2013), Aerosol growth in Titan's ionosphere, *PNAS*, *110*, 2729–2734, doi:10.1073/pnas.1217059110.

Leblanc et al. (2006), Origins of the Martian aurora observed by Spectroscopy for Investigation of Characteristics of the Atmosphere of Mars (SPICAM) on board Mars Express, *J. Geophys. Res.*, *111*, A09313, doi: 10.1029/2006JA011763.

Leblanc et al., (2008), Observations of aurorae by SPICAM ultraviolet spectrograph on board Mars Express: Simultaneous ASPERA-3 and MARSIS measurements, *J. Geophys. Res.*, *113*, A08311, doi: 10.1029/2008JA013033.

Liang, M.-C., et al. (2007), *Astrophys. J. Lett.*, *661*, L199–L202.

Liemohn, M. W., et al. (2006), Mars global MHD predictions of magnetic connectivity between the dayside ionosphere and the magnetospheric flanks, *Space Sci. Rev.*, *126*, 63–76, 10.1007/s11214-006-9116-8.

Luhmann, J.G. (1995), Plasma interactions with unmagnetized bodies, in *Introduction to Space Physics*, edited by M. G. Kivelson and C. T. Russell, pp. 203–226, Cambridge University Press, New York, NY.

Luhmann, J.G., and L.H. Brace (1991), Near-Mars Space, *Rev. Geophys.*, *29*, 121–140, doi:10.1029/91RG00066.

Luhmann, J.G., M. Tatrallyay, and R. O. Pepin (Eds.) (1992), *Venus and Mars: Atmospheres, Ionospheres and Solar Wind Interaction*. American Geophysical Union, Washington, DC, 430 pp.

Luhmann, J.G., W.T. Kasprzak, C.T. Russell (2007), Space weather at Venus and its potential consequences for atmosphere evolution, *J. Geophys. Res.*, *112*, E04S10, doi:10.1029/2006JE002820.

Lundin et al., (2006), Auroral Plasma Acceleration Above Martian Magnetic Anomalies, *Space Science Reviews*, *126*, 333–354, doi: 10.1007/s11214-006-9086-x.

Lundin, R., et al. (1989), First measurements of the ionospheric plasma escape from Mars, *Nature*, *341*, 609–612, doi:10.1038/341609a0.

Lundin, R., et al. (2008), A comet-like escape of ionospheric plasma from Mars, *Geophys. Res. Lett.*, *35*, CiteID L18203, doi:10.1029/2008GL034811.

Lundin, R., et al. (2013), Solar cycle effects on the ion escape from Mars, *Geophys. Res. Lett.*, *40*, 6028–6032, doi:10.1002/2013GL058154.

Mall, U., et al. (1998), Direct observation of lunar pick-up ions near the Moon, *Geophys. Res. Lett.*, *25*, 3799–3802, doi:10.1029/1998GL900003.

Marconi, M.L. (2007), A kinetic model of Ganymede's atmosphere, *Icarus*, *190*, 155–174, doi:10.1016/j.icarus.2007.02.016.

McComas, D.J., et al. (2009), Lunar backscatter and neutralization of the solar wind: First observations of neutral atoms from the Moon, *Geophys. Res. Lett.*, *36*, L12104, doi:10.1029/2009GL038794.

McNutt, R.L., Jr. (1989), Models of Pluto's upper atmosphere, *Geophys. Res. Lett.*, *16*, 1225–1228, doi:10.1029/GL016i011p01225.

Mendis, D.A., et al. (1986), Comet-solar wind interaction: Dynamical length scales and models, *Geophys. Res. Lett.*, *13*, 239–242, doi:10.1029/GL013i003p00239.

Michael, M., et al. (2011), High-Altitude Charged Particles in the atmosphere of Titan, *Planet Space Sci.*, *59*, 880–885, doi:10.1016/j.pss.2011.03.010.

Motschmann, U., and E. Kührt (2006), Interaction of the solar wind with weak obstacles: hybrid simulations for weakly active comets and for Mars, *Space Science Reviews*, *122*, 197–208, doi:10.1007/s11214-006-6218-2.

Neubauer, F.M. (1998), The sub-Alfvénic interaction of the Galilean satellites with the Jovian magnetosphere, *J. Geophys. Res.*, *103*, 19843–19866, doi:10.1029/97JE03370.

Neugebauer, M., et al. (1989), The velocity distributions of cometary protons picked up by the solar wind, *J. Geophys. Res.*, *94*, 5227–5239, doi:10.1029/JA094iA05p05227.

Nilsson, H., et al. (2015), Birth of a comet magnetosphere: A spring of water ions, *Science*, *347*, aaa0571, doi:10.1126/science.aaa0571.

Nishino, M., et al. (2009), Solar-wind proton access deep into the near-Moon wake, *Geophys. Res. Lett.*, *36*, L16103, doi:10.1029/2009GL039444.

Nishino, M., et al. (2010), Effect of the solar wind proton entry into the deepest lunar wake, *Geophys. Res. Lett.*, *37*, L12106, doi:10.1029/2010GL043948.

Parker, E.N. (1958), Dynamics of the interplanetary gas and magnetic fields, *Astrophysics J.*, *128*, 664–676, doi:10.1086/146579.

Pryor, W. R., A. M. Rymer, et al. (2011), The auroral footprint of Enceladus on Saturn, *Nature*, *472*, 331–333, 10.1038/nature09928.

Ramstad, R., et al. (2013), Phobos 2/ASPERA data revisited: Planetary ion escape rate from Mars near the 1989 solar maximum, *Geophys. Res. Lett.*, *40*, 477–48, doi: 10.1002/grl.50149.

Russell, C. T., and R. J.Walker (1995), The magnetospheres of the outer planets, in *Introduction to Space Physics*, edited by M. G. Kivelson and C. T. Russell, pp. 503–520, Cambridge University Press, New York, NY.

Russell, C. T. (2001), The dynamics of planetary magnetospheres, *Planet. Space Sci.*, *49* 1005–1030, doi:10.1016/S0032-0633(01)00017-4.

Russell, C. T., and D. E. Huddleston (2000), Ion-cyclotron Waves at Io, *Adv. Space Res.*, *26*, 1505–1511, doi:10.1016/S0273-1177(00)00090-9.

Russell, C. T., J. G. Luhmann, and R. J. Strangeway (2006), The solar wind interaction with Venus through the eyes of the Pioneer Venus Orbiter, *Planet. Space Sci.*, *54*, 1482–1495, doi:10.1016/j.pss.2006.04.025.

Russell, C. T., R. P. Lepping, and C. W. Smith (1990), Upstream waves at Uranus, *J. Geophys. Res.*, *95*, 2273–2279, doi:10.1029/JA095iA03p02273.

Rymer, A.M., et al. (2009), Discrete classification and electron energy spectra of Titan's varied magnetospheric environment, *Geophys. Res. Lett.*, *36*, L15109, doi: 10.1029/2009GL039427.

Saito, Y., et al. (2008), Solar wind proton reflection at the lunar surface: Low energy ion measurement by MAP-PACE onboard SELENE (Kaguya), *Geophys. Res. Lett.*, *35*, L24205, doi:10.1029/2008GL036077.

Saito, Y., et al. (2010), In-flight Performance and Initial Results of Plasma Energy Angle and Composition Experiment (PACE) on SELENE (Kaguya), *Space Science Rev.*, *154*,. 265–303, doi:10.1007/s11214-010-9647-x.

Schippers, P., et al. (2009), Identification of Photoelectron Energy Peaks in Saturn's Inner Neutral Torus, *J. Geophys. Res.*, *114*, A12212, doi:10.1029/2009JA014368.

Shebanits, O., et al. (2013), Negative ion densities in the ionosphere of Titan-Cassini RPWS/LP results, *Planet. Space Sci.*, *84*, 153–162, doi:10.1016/j.pss.2013.05.021.

Simon, S., et al. (2013), Structure of Titan's induced magnetosphere under varying background magnetic field conditions: Survey of Cassini magnetometer data from flybys TA-T85, *J. Geophys. Res.*, *118*, 1679–1699, doi:10.1002/jgra.50096.

Sittler, E.C. Jr., et al., Heavy Ion Formation in Titan's Ionosphere: Magnetospheric Introduction of Free Oxygen and a Source of Titan's Aerosols?, *Planet. Space Sci.*, *57*, 1547–1557, doi:10.1016/j.pss.2009.07.017.

Smith, H.T., et al. (2008), Enceladus: A potential source of ammonia products and molecular nitrogen for Saturn's magnetosphere,*J. Geophys. Res.*,*113*,A11206,doi:10.1029/2008JA013352.

Smith, H.T., et al. (2010), Enceladus plume variability and the neutral gas densities in Saturn's magnetosphere, *J. Geophys. Res.*, *115*, A10252, doi:10.1029/2009JA015184.

Smyth, W.H. and M.L. Marconi (2006), Europa's atmosphere, gas tori, and magnetospheric implications *Icarus*, *181*, 510–526, doi:10.1016/j.icarus.2005.10.019.

Szego, K., et al. (2009), O^+ ion flow below the magnetic barrier at Venus post terminator, *J. Geophys. Res.*, *114*, E00B26, doi:10.1029/2008JE003170.

Teolis, B.D., et al. (2010), Cassini finds an oxygen–carbon dioxide atmosphere at Saturn's icy moon Rhea, *Science*, *330*, 1813–1815 doi:10.1126/science.1198366. 278.

Terasawa, T., et al. (1986) Detection of cometary pickup ions up to 10^7 km from Comet Halley - Suisei observation, *Geophys. Res. Lett.*, *13*, 837–840, doi:10.1029/GL013i008p00837.

Thomsen, M. F., et al. (2010), Survey of ion plasma parameters in Saturn's magnetosphere, *J. Geophys. Res.*, *115*, A10220, doi:10.1029/2010JA015267.

Tokar, R.L., et al. (2006), *The Interaction of the Atmosphere of Enceladus with Saturn's Plasma Science*, *311*, 1409–1412, doi:10.1126/science.1121061.

Tokar, R.L., et al. (2008), Cassini detection of water-group pick-up ions in the Enceladus torus, *Geophys. Res. Lett.*, *35*, L14202, doi:10.1029/2008GL034749.

Tokar, R.L., et al. (2009), Cassini detection of Enceladus' cold water-group plume ionosphere, *Geophys. Res. Lett.*, *36*, L13203, doi:10.1029/2009GL038923.

Tokar, R.L., et al. (2012), Detection of Exospheric O_2^+ at Saturn's Moon Dione, *Geophys. Res. Lett.*, *39*, L03105, 2012, doi:10.1029/2011GL050452.

Tsang, S.M.E., et al. (2015), Ionospheric Photoelectrons at Venus: Case Studies and First Observation in the Tail, *Planet. Space Sci.*, 10.1016/j.pss.2015.01.019.

Volwerk, M., M. G. Kivelson, and K. K. Khurana (2001), Wave activity in Europa's wake: Implications for ion pickup, *J. Geophys. Res.*, *106*, 26033–26048, doi: 10.1029/2000JA 000347.

Vuitton, V., et al. (2009), Negative ion chemistry in Titan's upper atmosphere, *Planet. Space Sci.*, *57*, 1558–1572, doi:10.1016/j.pss.2009.04.004.

Wahlund, J.-E., et al. (2005), Cassini Measurements of Cold Plasma in the Ionosphere of Titan, *Science*, *308*, 986–989, doi:10.1126/science.1109807.

Waite, J. H., Jr., et al. (2007), The Process of Tholin Formation in Titan's Upper Atmosphere, *Science 316*, 870–875, doi:10.1126/science.1139727.

Waite, J.H., et al. (2006), Cassini Ion and Neutral Mass Spectrometer: Enceladus Plume Composition and Structure, *Science*, *311*, 1419–1422, 10.1126/science.1121290.

Wei, H. Y., and C. T. Russell (2006), Proton cyclotron waves at Mars: Exosphere structure and evidence for a fast neutral disk, *Geophys. Res. Lett.*, *33*, L23103, doi:10.1029/2006 GL026244.

Wei, Y., et al. (2012), A teardrop-shaped ionosphere at Venus in tenuous solar wind, *Planet. Space Sci.*, *73*, 254–261, doi:10.1016/j.pss.2012.08.024.

Wellbrock, A., et al. (2012) Cassini observations of ionospheric photoelectrons at large distances from Titan: Implications for Titan's exospheric environment and magnetic tail, *J. Geophys. Res.*, *117*, A03216, doi:10.1029/2011JA017113.

Wellbrock, A., et al. (2013), Cassini CAPS-ELS observations of negative ions in Titan's ionosphere: Trends of density with altitude, *Geophys. Res. Lett.*, *40*, 1–5, DOI: 10.1002/grl.50751.

Westlake, J.H., et al. (2012), The observed composition of ions outflowing from Titan, *Geophys. Res. Lett.*, *39*, L19104, DOI:10.1029/2012GL053079.

Wieser, M., et al. (2009), Extremely high reflection of solar wind protons as neutral hydrogen atoms from regolith in space, *Planet. Space Sci.*, *57*, 2132–2134, doi:10.1016/j. pss.2009.09.012.

Wood, A.G., et al., The transterminator ion flow at Venus at solar minimum, *Planet. Space Sci.*, *73*, 341–346, doi:10.1016/j. pss.2012.08.006

Yamauchi, M., et al. (2006), IMF Direction Derived from Cycloid-Like Ion Distributions Observed by Mars Express, *Space Sci. Rev.*, *126*, 239–266, doi:10.1007/s11214-006-9090-1.

Yokota, S., et al. (2009), First direct detection of ions originating from the Moon by MAP-PACE IMA onboard SELENE (Kaguya), *Geophys. Res. Lett.*, *36*, L11201, doi:10.1029/2009 GL038185.

Young, D.T., et al. (2004a), Solar wind interactions with Comet 19P/Borrelly, *Icarus*, *167*, 80–88, doi:10.1016/j.icarus.2003. 09.011.

Young, D.T., et al. (2004b), Solar wind interactions with Comet 19P/Borrelly, *Icarus*, *167*, 80–88, 10.1016/j.icarus.2003.09.011.

Zhang, T.L., et al., Magnetic Reconnection in the Near Venusian Magnetotail, *Science 336*, 567–570, doi:10.1126/science. 1217013.

22

Plasma Wave Observations with Cassini at Saturn

George B. Hospodarsky[1], J. D. Menietti[1], D. Píša[1,2], W. S. Kurth[1], D. A. Gurnett[1], A. M. Persoon[1], J. S. Leisner[1,3], and T. F. Averkamp[1]

Video of Yosemite Talk, URL: http://dx.doi.org/10.15142/T3G012

ABSTRACT

Since the Cassini spacecraft arrived at Saturn in 2004, the Radio and Plasma Wave Science (RPWS) investigation has detected a variety of radio and plasma waves in the magnetosphere of Saturn, including whistler mode chorus and hiss, lightning-produced whistlers, high latitude auroral hiss, electrostatic electron cyclotron harmonic (ECH), upper hybrid resonance (UHR) and Langmuir wave emissions, Z- and O-mode narrowband emissions, and Saturn kilometric radiation (SKR). A number of these emissions often exhibit intensity modulations with periods ranging from about 10.6 to 10.8 hours. Plasma waves have also been detected in association with the Saturnian moons, including Enceladus and Rhea. We will review these observations and discuss the properties of the various waves.

22.1. INTRODUCTION

The Cassini spacecraft was launched on October 15, 1997, and, after gravity assist flybys of Venus (twice), Earth, and Jupiter, arrived at Saturn in July 2004. Since that time, the spacecraft has completed over 210 orbits of Saturn. Flybys of the Saturnian moon Titan have been used to change the orbit of the spacecraft, providing good observational coverage in Local Time (LT) and Magnetic Latitude (Lat) of the inner magnetosphere of Saturn. The current plan is to continue the Cassini mission through September 2017, including the time period of the Saturnian northern summer solstice, which occurs in May 2017. In April 2017, Cassini will go into a series of high inclination orbits that cross the equatorial region between the upper atmosphere and the inner edge of the rings (altitudes of few thousand kilometers [km]), providing for the first time comprehensive in situ measurements of this region of Saturn's magnetosphere. During this same time, the Juno spacecraft will be in a highly eccentric polar orbit around Jupiter with a very low periapsis [*Bagenal et al.,* 2014]. Hence, Cassini and Juno will provide near simultaneous measurements of the high latitude regions of two of the giant planets.

The Cassini RPWS instrument has five receivers, three electric antennas, a triaxial search coil magnetometer, and a Langmuir Probe [*Gurnett et al.,* 2004]. The five receivers combined cover a frequency range from ~1 hertz (Hz) to 16 megahertz (MHz) for electric fields, and ~1 Hz to 12 kHz for magnetic fields. The five-channel waveform receiver (WFR) simultaneously collects waveforms from up to five sensors in one of two frequency bands, either 1 to 26 Hz, or 3 Hz to 2.5 kilohertz (kHz). Wave propagation information, including wave normal angle and Poynting vectors, are obtained for various plasma waves when two electric and three magnetic antennas are used.

[1]*Department of Physics and Astronomy, University of Iowa, Iowa City, IA, USA*

[2]*Department of Space Physics, Institute of Atmospheric Physics, Czech Academy of Science, Prague, Czech Republic*

[3]*Arctic Slope Technical Services, Beltsville, MD, USA*

Magnetosphere-Ionosphere Coupling in the Solar System, Geophysical Monograph 222, First Edition.
Edited by Charles R. Chappell, Robert W. Schunk, Peter M. Banks, James L. Burch, and Richard M. Thorne.

The wideband receiver (WBR) provides high time resolution electric or magnetic field waveform data in two possible frequency bands (~60 Hz to 10.5 kHz or 0.8 kHz to 75 kHz), allowing the fine structure of waves to be examined. The High Frequency Receiver (HFR) measures the electric field in the frequency range from ~3.5 kHz to 16 MHz and can provide polarization and direction finding measurements [*Cecconi and Zarka,* 2005].

22.2. WAVE OBSERVATIONS AT SATURN

Voyager 1 and Voyager 2 were the first spacecraft to measure the radio and plasma waves at Saturn [*Gurnett et al.,* 1981; *Warwick et al.,* 1981, 1982; *Scarf et al.,* 1982, 1983, 1984]. The arrival of Cassini at Saturn in 2004 has allowed the RPWS to study these waves in much more detail and also allowed new wave emissions to be detected [see *Gurnett et al.*, 2005; *Mauk et al.*, 2009; *Kurth et al.*, 2009; and *Hospodarsky et al.*, 2012] for overviews of the Saturn magnetosphere and some of the wave observations]. In the solar wind, upstream of the Saturnian bow shock, electrostatic Langmuir waves are often detected [*Hospodarsky et al.,* 2006; *Píša et al.,* 2015]. In the inner magnetosphere (<10 R_S), whistler mode chorus [*Hospodarsky et al., 2008*; *Menietti et al.*, 2013a, 2013b, 2014a, 2014b], quasi-periodic (QP) whistler mode emissions [*Hospodarsky et al.*, 2012], ECH emissions [*Menietti et al.,* 2008a, 2008b, 2012; *Tao et al.,* 2010], and UHR emissions [*Persoon et al.,* 2005, 2006a, 2006b, 2009, 2013] are observed. At higher magnetic latitudes (>~25°), auroral hiss is detected [*Mitchell et al.,* 2009a; *Gurnett et al.,* 2009a; *Kopf et al.,* 2010]. RPWS observations of ion cyclotron waves have also been made in the Saturn downward auroral region. *Menietti et al.* [2011a] showed that these waves can be generated by the observed upward electron beams, and modeling suggested that they can produce significant ion heating as has been observed in the terrestrial auroral region [*Singh et al.,* 1981].

Evidence of lightning in Saturn's atmosphere is shown from observations of lightning whistlers [*Akalin et al.,* 2006] and from observations of Saturn Electrostatic Discharges (SED) [*Kaiser et al.,* 1983; *Zarka* 1985; *Fischer et al.,* 2007, 2011a, 2011b]. The low frequency cutoff of the SEDs has been used to remotely probe the electron density of Saturn's ionosphere [*Kaiser et al.,* 1984; *Mendillo et al.*, 2005; *Fischer et al.*, 2011b; *Moore et al.,* 2012]. A number of radio emissions are also observed, including Z- and O-mode narrowband emissions [*Gurnett et al.,* 1983; *Louarn et al.,* 2007; *Ye et al.,* 2009, 2010, 2011; *Menietti et al.,* 2009, 2010, 2012; *Wang et al.,* 2010], and SKR [*Kurth et al.,* 2005, 2011; *Cecconi et al.,* 2006; *Lamy et al.,* 2008, 2010; *Fischer et al.,* 2009; *Mutel et al.* 2010; *Menietti et al.* 2011b]. Plasma waves have also been detected in association with many of the Saturnian moons, including Enceladus [*Tokar et al.,* 2006; *Gurnett et al.,* 2011; *Leisner et al.,* 2013] and Rhea [*Santolik et al.*, 2011]. The RPWS instrument also detects dust impacts on the Cassini spacecraft, providing information on the properties of dust [*Kurth et al.,* 2006; *Wang et al.*, 2006; *Ye et al.,* 2014a] and sometimes information on the electron density [*Ye et al.,* 2014b]. This paper will review some of these observations and discuss in more detail the properties of the various waves.

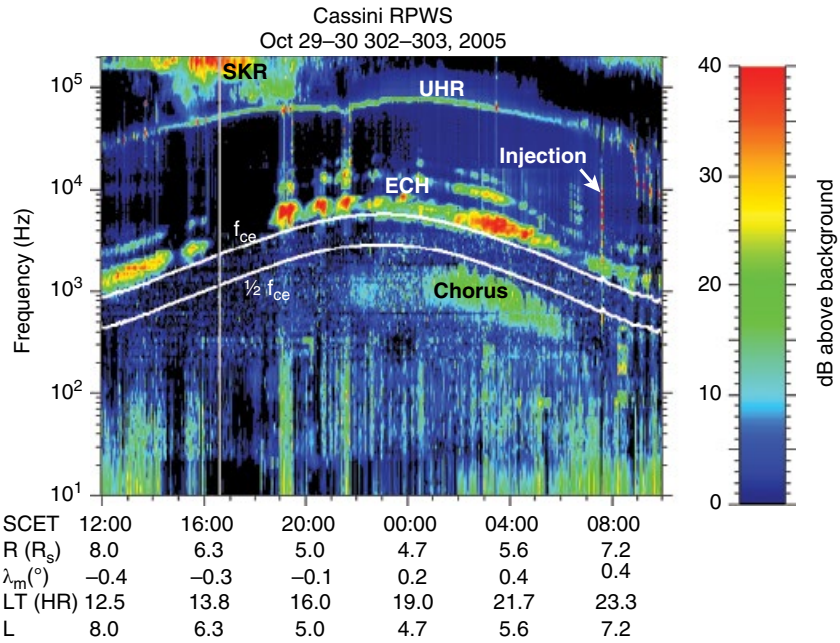

Figure 22.1 Time-frequency electric field spectrogram of the RPWS survey wave data for a near equatorial crossing of the inner magnetosphere. The white lines show f_{ce} and 1/2 f_{ce} determined from the magnitude of the background magnetic field as measured by MAG.

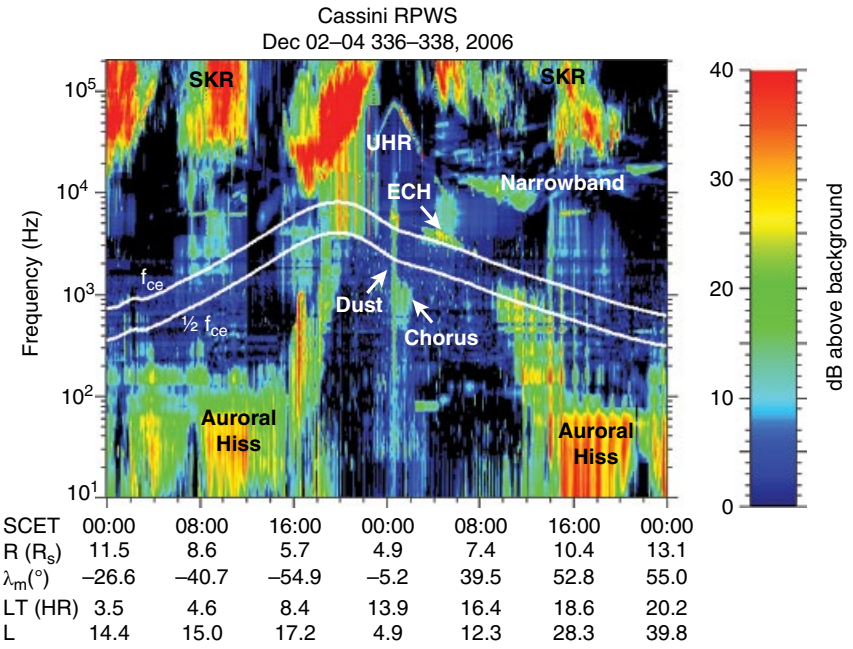

Figure 22.2 Time-frequency electric field spectrogram of the RPWS survey wave data for a high inclination crossing of the inner magnetosphere. The white lines show f_{ce} and 1/2 f_{ce} determined from the magnitude of the background magnetic field as measured by MAG.

Figure 22.1 shows a spectrogram of the electric field intensity of wave emissions measured by RPWS during a near equatorial pass through Saturn's inner magnetosphere. The intensities are plotted in decibels (dB) above background, and the white lines show the electron cyclotron frequency (f_{ce}) and 1/2 f_{ce} derived from the Cassini Magnetometer (MAG) instrument [*Dougherty et al.,* 2004]. During this orbit, a number of plasma and radio wave emissions are observed, including whistler mode, electrostatic ECH, UHR, and SKR emissions. Figure 22.2 shows a spectrogram of the electric field intensity of the wave emissions obtained during a high inclination orbit. Many of the same emissions are detected during this orbit as the one shown in Figure 22.1, including whistler mode emissions, ECH, UHR, and SKR. Additional emissions observed by Cassini at higher latitude include narrowband radio emissions and emissions similar to auroral hiss seen at Earth [*Gurnett*, 1966; *Persoon et al.,* 1988, *Ergun et al.,* 2003]. Figure 22.2 also shows on 3 December 2006 at ~00:40 the broadband signal produced by the impact of dust particles on the spacecraft as Cassini crossed the equatorial plane.

22.3. WHISTLER MODE CHORUS EMISSIONS

Whistler mode emissions are often observed in Saturn's inner magnetosphere with many characteristics similar to chorus detected at Earth and Jupiter. Due to these similar characteristics, we adopt the nomenclature of earlier studies [*Hospodarsky et al.*, 2008; *Menietti et al.*, 2013b, 2014a] and call these whistler mode emissions "chorus." *Hospodarsky et al.* [2008] performed an initial survey of these emissions and characterized them into two types based on their spectral characteristics and where they were observed. The most common type was defined as "magnetospheric" chorus that was observed within ~30 degrees of the magnetic equator between L shells of about 4.5 to 10. Examples of magnetospheric chorus are shown in both Figures 22.1 and 22.2. This emission usually has a bandwidth of a few hundred Hz and is detected below 1/2 f_{ce} as Cassini crosses through the inner magnetosphere. Figure 22.3 shows four spectrograms of "magnetospheric" chorus obtained from the higher resolution RPWS WBR data. A variety of fine structure is associated with the chorus, from a structureless, hiss-like emission (Panel a) to narrowband frequency tones rising in frequency (Panels b, c, and d). The rising tone structure is similar to structures associated with chorus detected at Earth and Jupiter, but the timescales of the structure detected at Saturn are usually longer than those observed at Earth or Jupiter [*Hospodarsky et al.,* 2008].

There is a subset of the "magnetospheric" chorus that have rising tones with periods on the order of many minutes (Panel d of Figure 22.3). These emissions have been referred to as "rising whistler mode emission," "QP whistler emission," or sometimes as "worms," and have been investigated in more detail by *Leisner et al.* [2015]. They are observed about 5% of the time when Cassini is near the magnetic equator within 5.5 R_S of Saturn, and appear to be related to electrons with energies of a few kiloelectron-volts (keV).

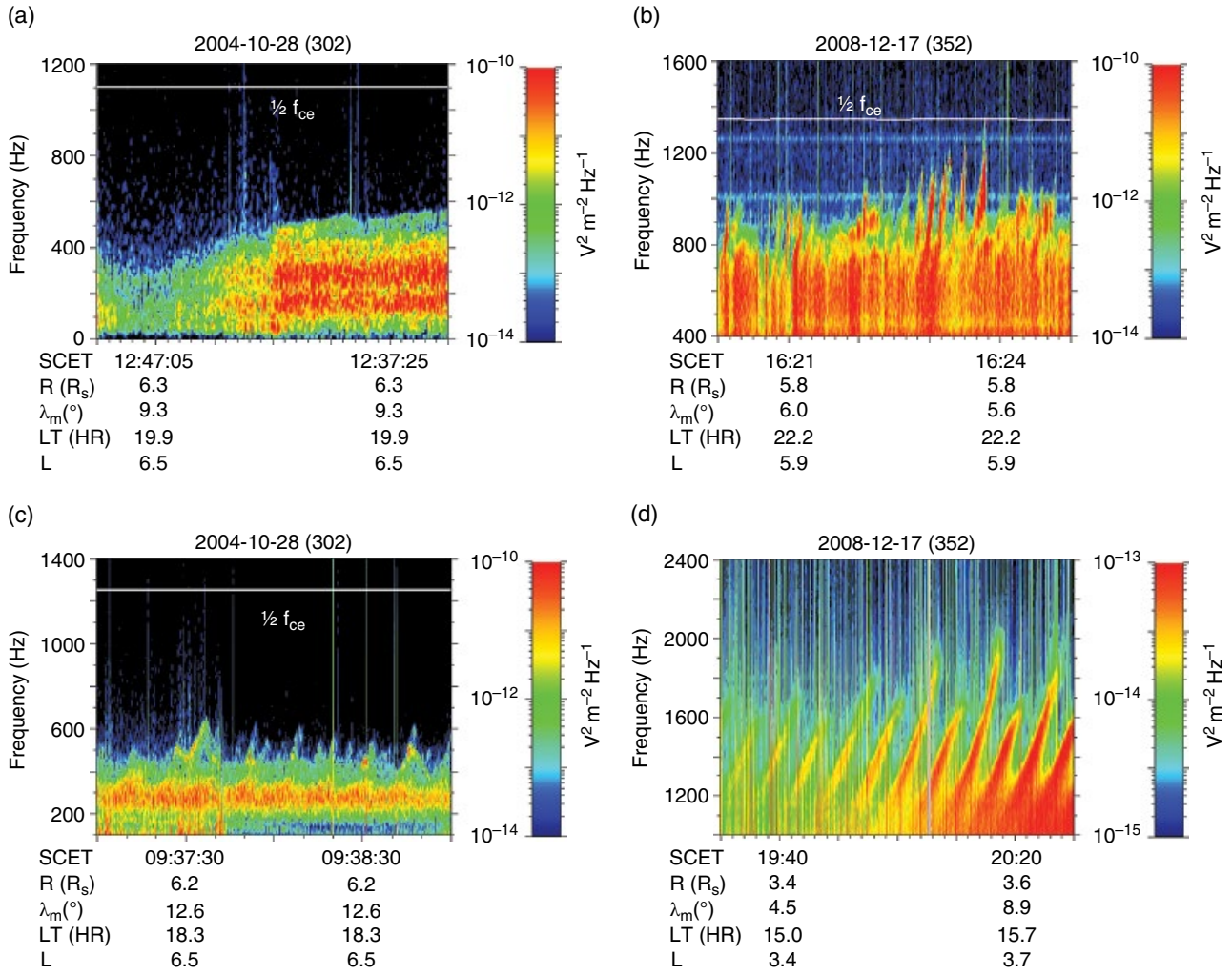

Figure 22.3 Time-frequency electric field spectrograms of the high resolution WBR data showing some of the fine structure associated with whistler mode emissions at Saturn. The white line shows 1/2 f_{ce} determined from the magnitude of the background magnetic field as measured by MAG.

The cause of the many-minute periodicity is not well understood. Although *Hospodarsky et al.* [2008] included these many-minute period rising tone whistler mode emissions with the "magnetospheric" chorus emissions, their spectral characteristics are more similar to the QP whistler mode emissions detected at Earth [*Pasmanik, et al.,* 2004; *Hayosh et al.*, 2013; *Němec et al.,* 2013a, 2013b, 2014]. However, it is currently unclear if the same type of source generation can explain the Earth and Saturn QP emissions.

The second type of whistler mode chorus emission reported by *Hospodarsky et al.* [2008] is detected in association with local plasma injections and were defined as "injection event" chorus. Local plasma injection events are "injections" of hot, less dense plasma produced by the interchange instability in rapidly rotating magnetospheres such as Saturn. These "injections" flow toward the planet while the colder and denser plasma from the inner magnetosphere flows outward [*Burch et al.,* 2005; *Hill et al.,* 2005; *Mauk et al.,* 2005, 2009; *Paranicas et al.,* 2007; *Rymer et al.,* 2007, 2008; *Mitchell et al.*, 2009b]. Young injection events are usually easy to detect with RPWS due to the changes in the spectral properties of the plasma waves associated with the injection compared to the waves detected outside of the events [*Menietti et al.,* 2008a, 2008b; *Hospodarsky et al.,* 2008; *Kennelly et al.,* 2013]. Specifically, the frequency of the UHR usually decreases due to the lower electron plasma density inside of the injection, and the ECH and chorus emissions are enhanced. Figure 22.1 shows an example of an injection event with enhanced ECH waves at about 07:35 Universal Time (UT). The changes in the characteristics of the plasma waves located inside versus outside of an injection event are more easily seen in the higher resolution WBR data shown in Figure 22.4. The top panel of

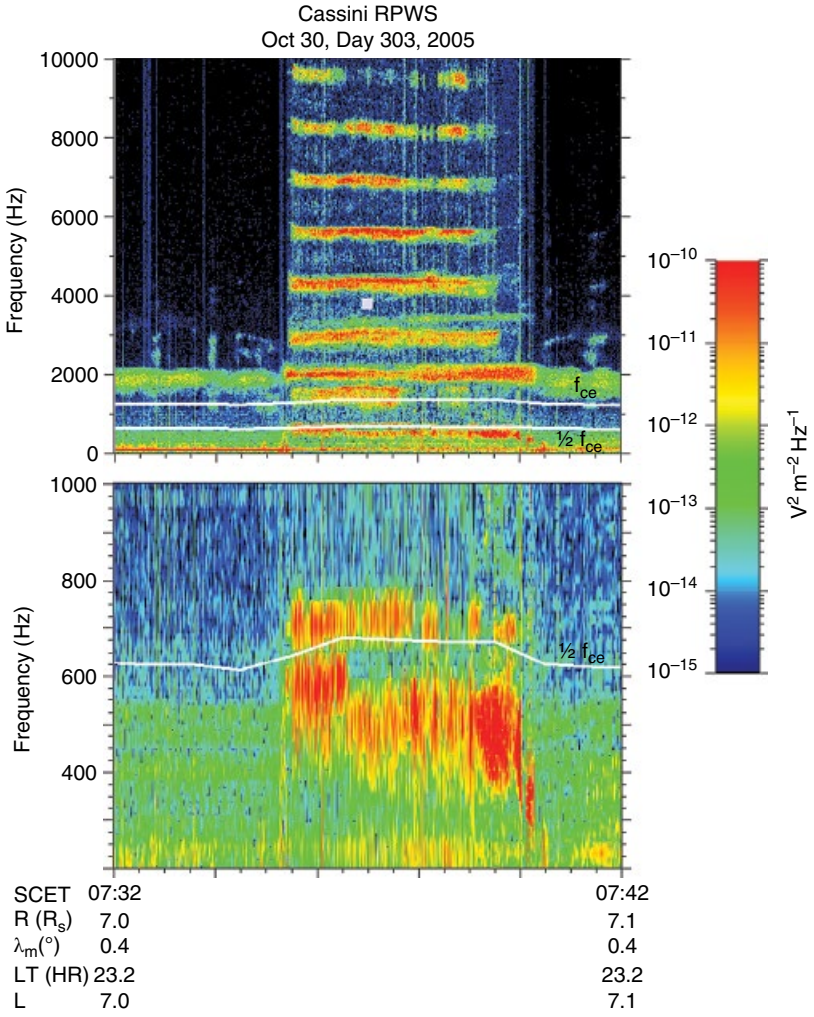

Figure 22.4 Time-frequency electric field spectrograms of the high resolution WBR data showing the change in the plasma wave characteristics inside of an injection event. The white lines show f_{ce} and 1/2 f_{ce} determined from the magnitude of the background magnetic field as measured by MAG. [after *Hospodarsky et al.,* 2008]

Figure 22.4 shows the full frequency range of the event to emphasize the changes in the ECH waves, and the bottom panel shows the typical spectral structure of "injection event" chorus. The white lines in Figure 22.4 show f_{ce} and 1/2 f_{ce} as determined from MAG observations. "Injection event" chorus is often observed in two bands located above and below 1/2 f_{ce}, with a gap in the emission intensity at 1/2 f_{ce}, very similar to chorus detected at the Earth. The "injection event" chorus often contains fine structure (primarily rising tones) at a much smaller timescale (less than a second to a few seconds) than the "magnetospheric" chorus, again more similar to chorus at Earth and Jupiter [*Hospodarsky et al.,* 2008]. *Menietti et al.* [2008a] showed that the chorus emissions observed inside the injection region can be at least partially generated by the measured temperature anisotropies in the electron population.

The occurrence, intensity, LT, and latitude variations of both types of chorus emission at Saturn have been examined by *Hospodarsky et al.* [2008, 2012] and in a series of papers by *Menietti et al.* [2012, 2013b, 2014a, and 2014b]. These studies found that the peak in chorus intensity is detected at about ±5 degrees in magnetic latitude, with the intensity decreasing at the magnetic equator. The emissions are observed at all LT, but display maximum intensity on the nightside between L of 4.5 to 7. The small scale, fine structure is more likely to be observed at higher frequencies and at latitudes greater than ~5°. The "injection event" chorus was typically found to be more intense than the chorus outside of the injection events [*Menietti et al.,* 2014a], and the amplitude and structure of the rising tones was found to reasonably match predictions from non-linear theories of chorus generation [Menietti et al., 2013a]. Calculations

of the wave normal and Poynting vector using the WFR data show that the chorus emissions propagate away from the magnetic equator at Saturn [see Figure 7 of *Hospodarsky et al.,* 2008], similar to results obtained for chorus at Earth [*Ledocq et al.,* 1998; *Santolik et al.,* 2010; *Li et al.,* 2013].

Intense whistler mode waves were also detected in the magnetic flux tube connected to the surface of the Saturnian moon Rhea during a close flyby on 2 March 2010 [*Santolik et al.,* 2011]. The whistler mode emission was observed below 1/2 $f_{ce,}$ had peak amplitudes > 0.5 nT, and was found to be propagating toward Rhea. *Santolik et al.* [2011] showed that these waves could be generated by the loss-cone anisotropy caused by absorption of electrons by the surface of the moon. Strong, bursty electrostatic waves near the electron plasma frequency and broadband electrostatic waves at frequencies well below the ion plasma frequency were also detected during this flyby. The waves near the electron plasma frequency have many of the characteristics of Langmuir waves observed in the solar wind and are believed to be produced by a low energy (~35 electron-volt [eV]) electron beam propagating away from Rhea. The low-frequency waves may be related to the higher frequency waves through a nonlinear three-wave interaction.

22.4. WHISTLER MODE AURORAL HISS EMISSION

Cassini also observes at Saturn a whistler mode emission that has many of the characteristics of auroral hiss detected at magnetic latitudes greater than about 25° [*Mitchell et al.,* 2009a; *Gurnett et al.,* 2009a; *Kopf et al.,* 2010]. Auroral hiss is produced by electron beams and when plotted on a time-frequency spectrogram, usually exhibits a funnel-shaped spectrum [*Gurnett,* 1966]. Figure 22.2 shows examples of auroral hiss observed by RPWS during a high inclination orbit. Auroral hiss has only been detected by Cassini propagating away from the auroral zone of Saturn, and the emission is often observed out to distances of many tens of Saturn radii (R_S). Before 2008, the emission often exhibited a modulation in its intensity with a period of about 10.6 hours in the northern hemisphere and about 10.8 hours in the southern hemisphere, very similar to the periods of the SKR emission [*Gurnett et al.,* 2009a, 2009b]. Shorter scale periodicity on the order of 1 hour is also often detected, and these short scale structures are often correlated with ion conics [*Mitchell et al.,* 2009a]. *Kopf et al.* [2010] analyzed electron beams detected by the Cassini Plasma Spectrometer (CAPS) [*Young et al.,* 2004] during a Cassini high latitude pass and found that the detected beams coincided with observations of auroral hiss emissions. Examination of the predicted emission growth rate demonstrated that each of the measured beams possessed large whistler-mode growth rates, sufficient to produce the observed emission intensities. The planned end of the Cassini mission with high inclination, low altitude orbits should provide an opportunity to further study auroral hiss at Saturn and may encounter source regions of the emission.

Similar auroral hiss-like emissions have also been detected near Saturn's B Ring during the Saturn Orbit Insertion (SOI) period [*Xin et al.,* 2006], and near the Saturnian moon Enceladus [*Gurnett et al.,* 2011]. Using ray tracing and the observed spectral funnel characteristics of the emission observed on seven different Enceladus flybys, *Leisner et al.* [2013] found two possible source regions near the moon, the quadrant upstream of the Saturnward flow terminator and the quadrant downstream of the anti-Saturnward flow terminator. The result of similar source regions for multiple flybys separated by over five years suggests that the electron beam acceleration near the moon is a quasi-time-stationary feature of the plasma interaction. Three more close flybys of Enceladus planned in 2015 and 2016 should provide opportunities to further study the auroral hiss like emissions associated with the moon.

22.5. ELECTROSTATIC ECH AND UHR EMISSIONS

Electrostatic emissions detected in Saturn's inner magnetosphere include ECH and UHR emissions [*Kurth et al.,* 1983] (see examples in Figures 22.1 and 22.2). ECH emissions usually occur in frequency bands at $(n + 1/2)f_{ce}$, where n is an integer. Just like the chorus emissions discussed earlier, the ECH emissions are observed on most orbits when Cassini crosses the inner magnetosphere. The ECH waves also exhibit very different spectral characteristics inside and outside of injection events, as can be seen in the top panel of Figure 22.4. ECH emissions observed outside of injection events are primarily found in the first harmonic band centered at ~1.5 f_{ce}, with higher harmonic bands being weaker and more sporadic. Inside of injection events, the ECH emissions usually increase in both intensity and the number of harmonic bands present. A number of studies have attempted to explain the characteristics of the ECH waves using the electron plasma distributions measured by CAPS [*Rymer et al.,* 2008, 2009] both outside [*Menietti et al.* 2008a] and inside [*Menietti et al.,* 2008b; *Tao et al.,* 2010] of the injection event shown in Figure 22.4. *Menietti et al.* [2008a, 2008b] found that phase space distributions with an assumed narrow, empty loss cone of the lower energy (<100 eV) electron populations both inside and outside the injection event could generate the observed ECH emissions. However, *Tao et al.* [2010] found that inside the injection events, assuming a

non-empty loss cone for electrons with energy near a few hundred eV and a few keV (higher than those predicted by *Menietti et al.* [2008b]) could produce ECH waves with the observed harmonic structure. The precise ECH wave gain in the *Tao et al.* and *Menietti et al.* models is very sensitive to the electron distribution used, which for this event is not measured at the smallest pitch angles. These uncertainties in modeling the "actual" cold electron components may explain the differences in these studies.

The UHR emissions are detected on most orbits in the inner magnetosphere [*Moncuquet et al.,* 2005; *Schippers et al.,* 2013] and during close flybys of Saturn's moons [e.g., *Farrell et al.,* 2009], especially Titan [e.g., *Modolo et al.,* 2007]. Because the frequency of the UHR emissions (f_{uhr}) is related to the electron plasma frequency (f_{pe}) by $f_{uhr}^2 = f_{pe}^2 + f_{ce}^2$, determining f_{uhr} and obtaining f_{ce} from the magnetic field strength provides the electron plasma density (n_e) from $f_{pe} = 8980\, n_e^{1/2}$. By measuring f_{uhr} for each pass through the inner magnetosphere, *Persoon et al.* [2009, 2013] have developed an empirical plasma density model for the Saturnian system.

22.6. NARROWBAND EMISSION

Narrowband emissions at Saturn near 5 kHz were first detected during the Voyager 1 flyby of Saturn [*Gurnett et al.,* 1981]. The Cassini RPWS instrument often observes the 5-kHz emission but also detects narrowband emissions from about 10 kHz to 70 kHz [*Gurnett et al.,* 2005; *Lamy et al.,* 2008; *Ye et al.,* 2009; *Wang et al.,* 2010]. Because the Cassini narrowband emissions usually have intensities peaks in two bands near 5 kHz and 20 kHz, the emissions are referred to as "5 kHz" and "20 kHz" narrowband emissions [*Ye et al.,* 2009]. Examples of these narrowband emissions are shown in Figure 22.2 from about 08:00 to 24:00 on 3 December 2006. *Wang et al*. [2010] examined the occurrence statistics of the Saturn narrowband radio emissions and found that the 5-kHz narrowband emissions are detected by Cassini at all magnetic latitudes, and the 20-kHz narrowband emissions are only observed when Cassini is at higher latitudes. The narrowband emissions are found to be primarily polarized in the left hand ordinary (L-O) mode. However, they are sometimes observed polarized in the right hand extraordinary (R-X) mode and in the Z-mode as discussed by *Ye et al.* [2010] and *Menietti et al.* [2009, 2010]. Recent work by *Gu et al.* [2013] has suggested that this Z-mode emission could be important in energizing Saturn's radiation belt.

22.7. UPSTREAM LANGMUIR WAVES

Observations by Voyager 1 and 2 (*Gurnett et al.,* 1981; *Scarf et al.,* 1982) and more recent observations by Cassini (*Hospodarsky et al.*, 2006; *Píša et al*., 2015) detect Langmuir waves in the foreshock region upstream of the Saturnian bow shock. In planetary foreshocks, electrostatic Langmuir waves at frequencies close to the local plasma frequency (f_{pe}) are generated by electrons reflected from the bow shock via the beam-plasma instability (*Scarf et al.,* 1971). The spectral properties of Langmuir waves depend on the specific electron beam conditions. Close to the upstream foreshock boundary, the electron beams tend to be at higher energies, and intense narrowband emissions at frequencies near f_{pe} are observed [*Etcheto and Faucheux,* 1984]. Further downstream, the beams are lower in energy, and their speed becomes comparable with the thermal speed of the solar wind plasma, resulting in Langmuir waves that spread in a wider frequency range showing upshifted and downshifted electrostatic waves [*Fuselier et al.,* 1985].

Figure 22.5 shows an example of Langmuir wave observations obtained on 1 August 2007 between 08:00 and 10:30 by the WBR onboard the Cassini spacecraft. Typical Langmuir wave amplitudes observed by the RPWS at Saturn are in a range of 0.01 to 1 millivolt per meter (mV/m), with the largest amplitudes detected ~10 mV/m (*Píša el al.,* 2015). The largest observed amplitudes at Saturn are lower by about one order of magnitude than wave amplitudes observed upstream of Earth's bow shock [e.g., *Bale et al.,* 2000]. Cassini's observations at Saturn show that the maximum wave intensity is observed around the upstream foreshock boundary with a slight shift behind the tangent magnetic field line toward the downstream position and with a decrease in intensity along the solar wind direction deeper in the foreshock [*Píša et al.,* 2015]. The wave amplitude also decreases with distance along the tangent field line but decreases more slowly compared to the dependence on the depth. This dependence shows an amplitude decrease of almost one order of magnitude over the distance of 100 R_S. The Langmuir wave amplitude distribution at Saturn for most of the amplitude interval follows a log-normal law as is predicted by the stochastic growth theory [*Robinson,* 1995]. The largest amplitudes deviate from the log-normal distribution and follow a power-law distribution. This deviation can be explained as a result of a combination of many log-normal distributions over a wide range of foreshock positions and during different conditions in the solar wind [*Boshuizen et al.,* 2001]. The possible mechanisms for saturation of the beam instability in planetary foreshocks are still under debate. *Píša et al*. [2015] show that the estimated energy density for the largest measured amplitudes at Saturn does not exceed the threshold for strong turbulence processes, suggesting that weak turbulence saturation processes are more important in the Langmuir wave saturation inside Saturn's foreshock [*Cairns*, 1987].

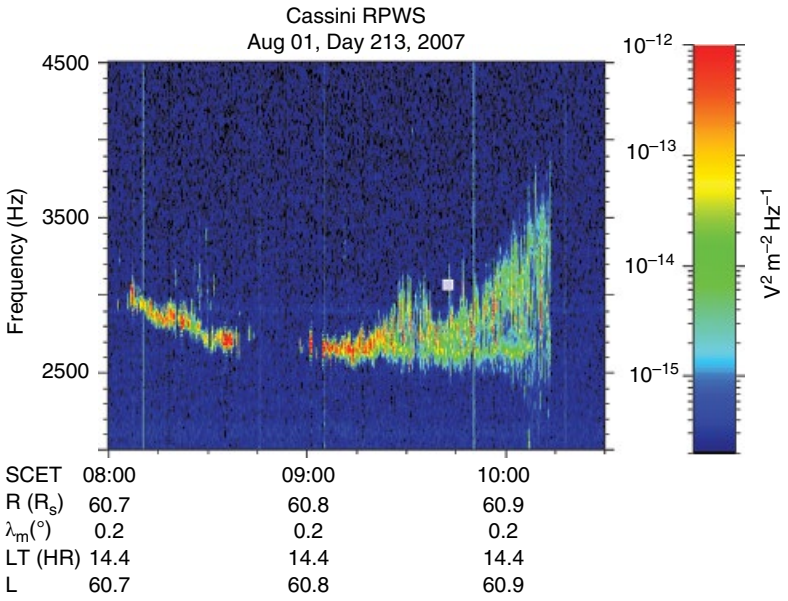

Figure 22.5 Time-frequency electric field spectrogram of RPWS WBR data showing Langmuir waves upstream of the Saturnian bow shock.

22.8. SATURN KILOMETRIC RADIATION AND PERIODICITIES

The rotation periods of the giant planets are usually determined by using the modulation of auroral radio emissions since the rotation period cannot be accurately determined from visual observations due to the lack of a solid surface and uncertainties in the wind speeds. The radio emissions are believed to be tied to the planetary magnetic field that has its source in the deep interior of the planet, so any observed modulation period in the emission should be related to the rotation period of the deep interior. For Saturn, the SKR modulation period was determined from the Voyager 1 data to be 10.6567 hours [*Desch and Kaiser*, 1981], and the "official" rotation rate was later refined to 10.6562 hours [*Davies et al.,* 1996]. However, later observations by the Ulysses [*Lecacheux et al.,* 1997; *Galopeau and Lecacheux*, 2000] and the Cassini spacecraft [*Gurnett et al.,* 2005] have shown that the SKR period varies on the order of ~1%. This variation cannot represent the rotation period of Saturn as this would violate conservation of angular momentum. Furthermore, the SKR was found for the early part of the Cassini mission (2004 to 2009) to exhibit two periods, ~10.6 and ~10.8 hours [*Kurth et al*., 2008]. *Gurnett et al*. [2009b] examined these two periods and found the SKR coming from the northern auroral region exhibited a period of ~10.6 hours and the SKR from the southern auroral region ~10.8 hours. For the more recent observations, the two periods have appeared to converge to a value of ~10.7 hours [*Gurnett et al.,* 2010, *Lamy* 2011; *Fischer et al.*, 2015]. Other wave emissions detected at Saturn have periodicities similar to the SKR period. As mentioned above, *Gurnett et al.* [2009a] showed that auroral hiss often has a modulation in its intensity with a period of about 10.6 hours when Cassini is in the northern hemisphere and about 10.8 hours in the southern hemisphere. This period was found to agree very well with the period determined from the SKR emissions during the same period. Saturn narrowband emissions are also found to be modulated with a period of ~10.8 hours [*Wang et al.,* 2010]. A number of other particle, magnetic field, and auroral observations at Saturn also exhibit modulations with periods similar to the SKR emission. A review of all the different periodicities near 10.6 to 10.8 hours observed at Saturn is beyond the scope of this paper. [See *Carbary and Mitchell*, 2013 for a detailed review of periodicities at Saturn.]

22.9. CONCLUSION

The Saturnian system provides a rich environment to study plasma and wave processes with its rapidly rotating magnetosphere, extensive ring system, and large number of moons, including Enceladus whose plumes provide much of the neutrals and plasma in the magnetosphere. The Cassini mission with its many orbits has greatly increased our understanding of radio and plasma waves in the magnetosphere of Saturn. Plasma waves have also been detected in association with the Saturnian moons Enceladus and Rhea. Many of these emissions are very similar to

emissions detected at Earth, although some of them have different spectral and intensity characteristics. Studying these emissions is important in understanding wave-particle interactions at Saturn and to help understand similar processes at Earth and Jupiter. The Saturn system is also unique in containing a number of wave emissions that exhibit intensity modulations associated with the planetary magnetic field with periods that range from about 10.6 to 10.8 hours. The source of these periodicities is an active area of research and is still not well understood.

ACKNOWLEDGMENTS

The research at The University of Iowa was supported under JPL contract 1415150, National Aeronautics and Space Administration (NASA) grants NNX11AM36G and NNX12AG86G. GBH would like to acknowledge the International Space Science Institute (ISSI) team on "Modes of radial plasma motion in planetary systems." Cassini RPWS data are archived in calibrated, full resolution at the NASA Planetary Data System website: http://pds.nasa.gov/ds-view/pds/viewDataset.jsp?dsid=CO-V/E/J/S/SS-RPWS-3-RDR-LRFULL-V1.0.

REFERENCES

Akalin, F., D. A. Gurnett, T. F. Averkamp, A. M. Persoon, O. Santolik, W. S. Kurth, and G. B. Hospodarsky (2006), The First Whistler Observed in the Magnetosphere of Saturn, *Geophys. Res. Lett.*, *33*, L20107, doi:10.1029/2006GL027019.

Bagenal, F., A. Adriani, F. Allegrini, S. J. Bolton, B. Bonfond, E. J. Bunce, J. E. P. Connerney, S. W. H. Cowley, R. W. Ebert, G. R. Gladstone, C. J. Hansen, W. S. Kurth, S. M. Levin, B. H. Mauk, D. J. McComas, C. P. Paranicas, D. Santos-Costa, R. M. Thorne, P. Valek, J. H. Waite, and P. Zarka (2014), Magnetospheric Science Objectives of the Juno Mission *Space Science Reviews*, doi:10.1007/s11214-014-0036-8.

Bale, S. D., D. E. Larson, R. P. Lin, P. J. Kellogg, K. Goetz, and S. J. Monson (2000), On the beam speed and wave-number of intense electron plasma waves near the foreshock edge, *J. Geophys. Res.*, *105*, 27,353–27,368, doi:10.1029/2000JA900042.

Boshuizen, C. R., I. H. Cairns, and P. A. Robinson (2001), Stochastic growth theory of spatially-averaged distributions of Langmuir Fields in Earth's foreshock, *Geophys. Res. Lett.*, *28*, 3569–3572, doi:10.1029/2000GL012709.

Burch, J. L., J. Goldstein, T. W. Hill, D. T. Young, F. J. Crary, A. J. Coates, N. Andre, W. S. Kurth, and E. C. Sittler Jr. (2005), Properties of local plasma injections in Saturn's magnetosphere, *Geophys. Res. Lett*., *32*, L14S02, doi:10.1029/2005GL022611.

Cairns, I. H. (1987), A theory for the Langmuir waves in the electron foreshock, *J. Geophys. Res.*, *92*, 2329–2342, doi:10.1029/JA092iA03p02329.

Carbary, J. F., and D. G. Mitchell (2013), Periodicities in Saturn's magnetosphere, *Rev. Geophys.*, *51*, 1–30, doi:10.1002/rog.20006.

Cecconi, B. and P. Zarka (2005), Direction Finding and Antenna Calibration Through Analytical Inversion of Radio Measurements Performed Using a System of Two or Three Electric Dipole Wire Antennas on a Three-Axis Stabilized Spacecraft, *Radio Science*, *40*, RS3003, doi:10.1029/2004RS003070.

Cecconi, B., P. Zarka, and W. S. Kurth (2006), SKR polarization and source localization with the Cassini/RPWS/HFR instrument: First results, in *Planetary Radio Emissions VI*, edited by H. O. Rucker, W. S. Kurth, and G. Mann, Austrian Acad. of Sci. Press, Vienna.

Davies, M. E., et al. (1996), Report for the IAU/IAG/COSPAR working group on cartographic coordinates and rotational elements of the planets and satellites: 1994, *Celest. Mech. Dyn. Astron.*, *63*, 127–148, doi:10.1007/BF00693410.

Desch, M. D., and M. L. Kaiser (1981), Voyager measurement of the rotation period of Saturn's magnetic field, *Geophys. Res. Lett.*, *8*(3), 253–256, doi:10.1029/GL008i003p00253.

Dougherty, M. K., et al. (2004), The Cassini magnetic field investigation, *Space Sci. Rev*., *114*, 331–383, doi:10.1007/s11214-004-1432-2.

Ergun, R. E., C. W. Carlson, J. P. McFadden, R. J. Strangeway, M. V. Goldman, and D. L. Newman (2003), Fast auroral snapshot satellite observations of very low frequency saucers, *Phys. Plasmas*, *10*, 454–462, doi:10.1063/1.1530160.

Etcheto, J., and M. Faucheux (1984), Detailed study of electron plasma waves upstream of the Earth's bow shock, *J. Geophys. Res.*, *89*, 6631–6653, doi:10.1029/JA089iA08p06631.

Farrell, W. M., W. S. Kurth, D. A. Gurnett, R. E. Johnson, M. L. Kaiser, J.-E. Wahlund, and J. H. Waite Jr. (2009), Electron density dropout near Enceladus in the context of water-vapor and water-ice, *Geophys. Res. Lett.*, *36*, L10203, doi:10.1029/2008GL037108.

Fischer, G., W. S. Kurth, U. A. Dyudina, M. L. Kaiser, P. Zarka, A. Lecacheux, A. P. Ingersoll, and D. A. Gurnett (2007), Analysis of a Giant Lightning Storm on Saturn, *Icarus*, *190*, 528–544, doi:10.1016/j.icarus.2007.04.002.

Fischer, G., B. Cecconi, L. Lamy, S.-Y. Ye, U. Taubenschuss, W. Macher, P. Zarka, W. S. Kurth, and D. A. Gurnett (2009), Elliptical polarization of Saturn Kilometric Radiation observed from high latitudes, *J. Geophys. Res.*, *114*, A08216, doi:10.1029/2009JA014176.

Fischer, W.S. Kurth, D.A. Gurnett, P. Zarka, U.A. Dyudina, A.P. Ingersoll, S.P. Ewald, C.C. Porco, A. Wesley, C. Go, and M. Delcroix (2011a), A Giant Thunderstorms on Saturn, *Nature*, *475*, 75–77, doi:10.1038/nature10205.

Fischer, G., U. A. Dyudina, W. S. Kurth, D. A. Gurnett, P. Zarka, T. Barry, M. Delcroix, C. Go, D. Peach, R. Vandebergh, and A. Wesley (2011b), Overview of Saturn Lightning Observations, in *Planetary Radio Emissions VII*, eds. H. O. Rucker, W. S. Kurth, P. Louarn, G. Fischer, Austrian Academy of Sciences, Vienna, Austria, 135–144.

Fischer, G., D. A. Gurnett, W. S. Kurth, S. Y. Ye and J. B. Groene (2015), Saturn kilometric radiation periodicity after equinox, *Icarus 254*(0), 72–91, doi:10.1016/j.icarus.2015.03.014.

Fuselier, S. A., D. A. Gurnett, and R. J. Fitzenreiter (1985), The downshift of electron plasma oscillations in the electron foreshock region, *J. Geophys. Res.*, *90*, 3935–3946, doi:10.1029/JA090iA05p03935.

Galopeau, P., and A. Lecacheux (2000), Variations of Saturn's radio rotation period measured at kilometric wavelengths, *J. Geophys. Res.*,*105*,13,089–13,102,doi:10.1029/1999JA005089.

Gu, X., R. M. Thorne, B. Ni, and S.-Y. Ye (2013), Resonant diffusion of energetic electrons by narrowband Z mode waves in Saturn's inner magnetosphere, *Geophys. Res. Lett.*, *40*, 255–261, doi:10.1029/2012GL054330.

Gurnett, D. A. (1966), A satellite study of VLF hiss, *J. Geophys. Res.*, *71*(23), 5599–5615, doi:10.1029/JZ071i023p05599.

Gurnett, D. A., W. S. Kurth, and F. L. Scarf (1981), Plasma Waves near Saturn: Initial Results from Voyager 1, *Science*, *212*, 235, doi:10.1126/science.212.4491.235.

Gurnett, D. A., W. S. Kurth, and F. L. Scarf (1983), Narrowband electromagnetic emissions from Jupiter's magnetosphere, *Nature 302*(5907), 385-388, doi:10.1038/302385a0.

Gurnett, D. A., et al. (2004), The Cassini radio and plasma wave investigation, *Space Sci. Rev.*, *114*, 395–463, doi:10.1007/s11214-004-1434-0.

Gurnett, D. A., et al. (2005), Radio and plasma waves observed at Saturn from Cassini's approach and first orbit, *Science*, *307*, 1255, doi:10.1126/science.1105356.

Gurnett, D. A., A. M. Persoon, J. B. Groene, A. J. Kopf, G. B. Hospodarsky, and W. S. Kurth (2009a), A north-south difference in the rotation rate of auroral hiss at Saturn: Comparison to Saturn's kilometric radio emission, *Geophys. Res. Lett.*, *36*, L21108, doi:10.1029/2009GL040774.

Gurnett, D. A., A. Lecacheux, W. S. Kurth, A. M. Persoon, J. B. Groene, L. Lamy, P. Zarka, and J. F. Carbary (2009b), Discovery of a north-south asymmetry in Saturn's radio rotation period, *Geophys. Res. Lett.*, *36*, L16102, doi:10.1029/2009GL039621.

Gurnett, D. A., J. B. Groene, A. M. Persoon, J. D. Menietti, S.-Y. Ye, W. S. Kurth, R. J. MacDowall, and A. Lecacheux (2010), The reversal of the rotational modulation rates of the north and south components of Saturn kilometric radiation near equinox, *Geophys. Res. Lett.*, *37*, L24101, doi:10.1029/2010GL045796.

Gurnett, D. A., et al. (2011), Auroral hiss, electron beams and standing Alfvén wave currents near Saturn's moon Enceladus, *Geophys. Res. Lett.*, *38*, L06102, doi:10.1029/2011GL046854.

Hayosh, M., D. L. Pasmanik, A. G. Demekhov, O. Santolik, M. Parrot, and E. E. Titova (2013), Simultaneous observations of quasi-periodic ELF/VLF wave emissions and electron precipitation by DEMETER satellite: A case study, *J. Geophys. Res. Space Physics*, *118*, 4523–4533, doi:10.1002/jgra.50179.

Hill, T. W., A. M. Rymer, J. L. Burch, F. J. Crary, D. T. Young, M. F. Thomsen, D. Delapp, N. Andre, A. J. Coates, and G. R. Lewis (2005), Evidence for rotationally driven plasma transport in Saturn's magnetosphere, *Geophys. Res. Lett.*, *32*, L14S10, doi:10.1029/2005GL022620.

Hospodarsky, G. B., W. S. Kurth, D. A. Gurnett, P. Zarka, P. Canu, M. Dougherty, G. H. Jones, A. Coates, and A. Rymer (2006), Observations of Langmuir Waves Detected by the Cassini Spacecraft, in *Planetary Radio Emissions VI*, edited by H. O. Rucker, W. S. Kurth, and G. Mann, Austrian Academy of Sciences Press, Vienna.

Hospodarsky, G. B., T. F. Averkamp, W. S. Kurth, D. A. Gurnett, J. D. Menietti, O. Santolik, and M. K. Dougherty (2008), Observations of chorus at Saturn using the Cassini Radio and Plasma Wave Science instrument, *J. Geophys. Res.*, *113*, A12206, doi:10.1029/2008JA013237.

Hospodarsky, G. B., K. Sigsbee, J. S. Leisner, J. D. Menietti, W. S. Kurth, D. A. Gurnett, C. A. Kletzing, and O. Santolík (2012), Plasma Wave Observations at Earth, Jupiter, and Saturn, in *Dynamics of the Earth's Radiation Belts and Inner Magnetosphere* (D. Summers, I. R. Mann, D. N. Baker and M. Schulz, eds.), American Geophysical Union, Washington, D. C. doi:10.1029/2012GM001342.

Kaiser, M. L., J. E. P. Connerney, M. D. Desch (1983), Atmospheric storm explanation of Saturnian electrostatic discharges, *Nature*, *303*, 50, doi:10.1038/303050a0.

Kaiser, M. L., M. D. Desch, and J. E. P. Connerney (1984), Saturn's ionosphere: Inferred electron densities, *J. Geophys. Res.*, *89*(A4), 2371–2376, doi:10.1029/JA089iA04p02371.

Kennelly, T. J., J. S. Leisner, G. B. Hospodarsky, and D. A. Gurnett (2013), Ordering of injection events within Saturnian SLS longitude and local time, *J. Geophys. Res. Space Physics*, *118*, 832–838, doi:10.1002/jgra.50152.

Kopf, A. J., et al. (2010), Electron beams as the source of whistler-mode auroral hiss at Saturn, *Geophys. Res. Lett.*, *307*, L09102, doi:10.1029/2010GL042980.

Kurth, W. S., F. L. Scarf, D. A. Gurnett, and D. D. Barbosa (1983), A survey of electrostatic waves in Saturn's magnetosphere, *J. Geophys. Res.*, *88*(A11), 8959–8970, doi:10.1029/JA088iA11p08959.

Kurth, W. S., G. B. Hospodarsky, D. A. Gurnett, B. Cecconi, P. Louarn, A. Lecacheux, P. Zarka, H. O. Rucker, M. Boudjada, and M. L. Kaiser (2005), High spectral and temporal resolution observations of Saturn kilometric radiation, *Geophys. Res. Lett.*, *32*, L20S07, doi:10.1029/2005GL022648.

Kurth, W. S., T. F. Averkamp, D. A. Gurnett, and Z. Wang (2006), Cassini RPWS observations of dust in Saturn's E Ring, *Planetary and Space Science 54*(9–10), 988–998,doi:10.1016/j.pss.2006.05.011.

Kurth, W. S., T. F. Averkamp, D. A. Gurnett, J. B. Groene, and A. Lecacheux (2008), An update to a Saturnian longitude system based on kilometric radio emissions, *J. Geophys. Res.*, *113*, A05222, doi:10.1029/2007JA012861.

Kurth, W. S., E. J. Bunce, J. T. Clarke, F. J. Crary, D. C. Grodent, A. P. Ingersoll, U. A. Dyudina, L. Lamy, D. G. Mitchell, A. M. Persoon, W. R. Pryor, J. Saur, and T. Stallard (2009), Auroral Processes, in *Saturn from Cassini-Huygens*, M. K. Dougherty, L. W. Esposito, and S. M. Krimigis, eds, Springer, Dordrecht, 333–374, doi:10.1007/978-1-4020-9217-6_12.

Lamy, L., P. Zarka, B. Cecconi, R. Prangé, W. S. Kurth, and D. A. Gurnett (2008), Saturn kilometric radiation: Average and statistical properties, *J. Geophys. Res.*, *113*, A07201, doi:10.1029/2007JA012900.

Lamy, L., et al. (2010), Properties of Saturn kilometric radiation measured within its source region, *Geophys. Res. Lett.*, *37*, L12104, doi:10.1029/2010GL043415.

Lamy, L. (2011), Variability of Southern and Northern Periodicities of Saturn Kilometric Radiation, in *Planetary Radio Emissions VII*, eds. H.O. Rucker, W.S. Kurth, P. Louarn, G. Fischer, pp. 38–50, Austrian Academy of Sciences, Vienna, Austria.

Lecacheux, A., P. Galopeau, and M. Aubier (1997), Re-visiting Saturnian kilometric radiation with Ulysses/URAP, in *Planetary Radio Emissions IV*, edited by H. O. Rucker, S. J. Bauer, and A. Lecacheux, pp. 313–325, Austrian Acad. of Sci. Press, Vienna.

LeDocq, M. J., D. A. Gurnett, and G. B. Hospodarsky (1998), Chorus source location from VLF Poynting flux measurements with the Polar spacecraft, *rhea*, 4063–4066, doi:10.1029/1998GL900071.

Leisner, J. S., G. B. Hospodarsky, and D. A. Gurnett (2013), Enceladus auroral hiss observations: Implications for electron beam locations, *J. Geophys. Res. Space Physics*, *118*, 160–166, doi:10.1029/2012JA018213.

Leisner, J, S., G. B. Hospodarsky, J. D. Menietti, U. Taubenschuss, and D. A. Gurnett (2015), Rising Whistler-Mode Emissions in Saturn's Inner Magnetosphere, in prep.

Li, W., J. Bortnik, R. M. Thorne, C. M. Cully, L. Chen, V. Angelopoulos, Y. Nishimura, J. B. Tao, J. W. Bonnell, and O. LeContel (2013), Characteristics of the Poynting flux and wave normal vectors of whistler-mode waves observed on THEMIS, *J. Geophys. Res. Space Physics*, *118*, 1461–1471, doi:10.1002/jgra.50176.

Louarn, P., et al. (2007), Observation of similar radio signatures at Saturn and Jupiter: Implications for the magnetospheric dynamics, *Geophys. Res. Lett.*, *34*, L20113, doi:10.1029/2007GL030368.

Mauk, B. H., et al. (2005), Energetic particle injections in Saturn's magnetosphere, *Geophys. Res. Lett*., *32*, L14S05, doi:10.1029/2005GL022485.

Mauk, B. H., D. C. Hamilton, T. W. Hill, G. B. Hospodarsky, R. E. Johnson, C. Paranicas, E. Roussos, C. T. Russell, D. E. Shemansky, E. C. Sittler, Jr., and R. M. Thorne (2009), Fundamental Plasma Processes in *Saturn's Magnetosphere, in Saturn from Cassini-Huygens*, M. K. Dougherty, L. W. Esposito, and S. M. Krimigis, eds, Springer, Dordrecht, 281–331, doi:10.1007/978-1-4020-9217-6_11.

Mendillo, M., L. Moore, J. Clarke, I. Mueller-Wodarg, W. S. Kurth, and M. L. Kaiser (2005), Effects of ring shadowing on the detection of electrostatic discharges at Saturn, *Geophys. Res. Lett.*, *32*, L05107, doi:10.1029/2004GL021934.

Menietti, J. D., O. Santolík, A. M. Rymer, G. B. Hospodarsky, A. M. Persoon, D. A. Gurnett, A. J. Coates, and D. T. Young (2008a), Analysis of plasma waves observed within local plasma injections seen in Saturn's magnetosphere, *J. Geophys. Res.*, *113*, A05213, doi:10.1029/2007JA012856.

Menietti JD, O. Santolik, A. M. Rymer, G. B. Hospodarsky, D. A. Gurnett, and A. J. Coates (2008b), Analysis of plasma waves observed in the inner Saturn magnetosphere. *Annal. Geophys. 26*, 2631–2644, doi:10.5194/angeo-26-2631-2008.

Menietti, J. D., S.-Y. Ye, P. H. Yoon, O. Santolík, A. M. Rymer, D. A. Gurnett, and A. J. Coates (2009), Analysis of narrowband emission observed in the Saturn magnetosphere, *J. Geophys. Res.*, *114*, A06206, doi:10.1029/2008JA013982.

Menietti, J. D., P. H. Yoon, Y. Sheng-Yi, B. Cecconi and A. M. Rymer (2010), Source mechanism of Saturn narrowband emission, *Ann. Geophys*. *28*(4), 1013–1021, doi:10.5194/angeo-28-1013-2010.

Menietti, J. D., P. Schippers, O. Santolík, D. A. Gurnett, F. Crary, and A. J. Coates (2011a), Ion cyclotron harmonics in the Saturn downward current auroral region, *J. Geophys. Res.*, *116*, A12234, doi:10.1029/2011JA017102.

Menietti, J. D., R. L. Mutel, P. Schippers, S.-Y. Ye, D. A. Gurnett, and L. Lamy (2011b), Analysis of Saturn kilometric radiation near a source center, *J. Geophys. Res.*, *116*, A12222, doi:10.1029/2011JA017056.

Menietti, J. D., Y. Y. Shprits, R. B. Horne, E. E. Woodfield, G. B. Hospodarsky, and D. A. Gurnett (2012), Chorus, ECH, and Z mode emissions observed at Jupiter and Saturn and possible electron acceleration, *J. Geophys. Res.*, *117*, A12214, doi:10.1029/2012JA018187.

Menietti, J. D., Y. Katoh, G. B. Hospodarsky, and D. A. Gurnett (2013a), Frequency drift of Saturn chorus emission compared to nonlinear theory, *J. Geophys. Res. Space Physics*, *118*, 982–990, doi:10.1002/jgra.50165.

Menietti, J. D., P. Schippers, Y. Katoh, J. S. Leisner, G. B. Hospodarsky, D. A. Gurnett, and O. Santolik (2013b), Saturn chorus intensity variations, *J. Geophys. Res. Space Physics*, *118*, 5592–5602, doi:10.1002/jgra.50529.

Menietti, J. D., G. B. Hospodarsky, Y. Y. Shprits, and D. A. Gurnett (2014a), Saturn chorus latitudinal variations, *J. Geophys. Res. Space Physics*, *119*, 4656–4667, doi:10.1002/2014JA019914.

Menietti, J. D., T. F. Averkamp, J. B. Groene, R. B. Horne, Y. Y. Shprits, E. E. Woodfield, G. B. Hospodarsky, and D. A. Gurnett (2014b), Survey analysis of chorus intensity at Saturn, *J. Geophys. Res. Space Physics*, *119*, 8415–8425, doi:10.1002/2014JA020523.

Mitchell, D. G., W. S. Kurth, G. B. Hospodarsky, N. Krupp, J. Saur, B. H. Mauk, J. F. Carbary, S. M. Krimigis, M. K. Dougherty, and D. C. Hamilton (2009a), Ion conics and electron beams associated with auroral processes on Saturn, *J. Geophys. Res.*, *114*, A02212, doi:10.1029/2008JA013621.

Mitchell, D. G., J. F. Carbary, S. W. H. Cowley, T. W. Hill, and P. Zarka (2009b), The Dynamics of Saturn's Magnetosphere, in *Saturn from Cassini-Huygens*, eds. M. K. Dougherty, L. W. Esposito, and S. M. Krimigis, Springer, Dordrecht, *257–279*, doi:10.1007/978-1-4020-9217-6_10.

Modolo, R., J.-E. Wahlund, R. Boström, P. Canu, W. S. Kurth, D. Gurnett, G. R. Lewis, and A. J. Coates (2007), Far plasma wake of Titan from the RPWS observations: A case study, *Geophys. Res. Lett*., *34*, L24S04, doi:10.1029/2007GL030482.

Moore, L., G. Fischer, I. Mueller-Wodarg, M. Galand, and M. Mendillo (2012), Diurnal Variation of Electron Density in the Saturn Ionosphere: Model Comparisons with Saturn Electrostatic Discharge (SED) Observations, *Icarus*, *221*, 508–516, doi:10.1016/j.icarus.2012.08.010.

Moncuquet, M., A. Lecacheux, N. Meyer-Vernet, B. Cecconi, and W. S. Kurth (2005), Quasi thermal noise spectroscopy in the inner magnetosphere of Saturn with Cassini/RPWS: Electron temperatures and density, *Geophys. Res. Lett*., *32*, L20S02, doi:10.1029/2005GL022508.

Mutel, R. L., J. D. Menietti, D. A. Gurnett, W. Kurth, P. Schippers, C. Lynch, L. Lamy, C. Arridge, and B. Cecconi (2010), CMI growth rates for Saturnian kilometric radiation, *Geophys. Res. Lett.*, *37*, L19105, doi:10.1029/2010GL044940.

Němec, F., O. Santolík, M. Parrot, J. S. Pickett, M. Hayosh, and N. Cornilleau-Wehrlin (2013a), Conjugate observations of quasi-periodic emissions by Cluster and DEMETER spacecraft, *J. Geophys. Res. Space Physics*, *118*, 198–208, doi:10.1029/2012JA018380.

Němec, F., O. Santolík, J. S. Pickett, M. Parrot, and N. Cornilleau-Wehrlin (2013b), Quasiperiodic emissions observed by the Cluster spacecraft and their association with ULF magnetic pulsations, *J. Geophys. Res. Space Physics*, *118*, 4210–4220, doi:10.1002/jgra.50406.

Němec, F., J. S. Pickett, and O. Santolík (2014), Multispacecraft Cluster observations of quasiperiodic emissions close to the geomagnetic equator, *J. Geophys. Res. Space Physics*, *119*, 9101–9112, doi:10.1002/2014JA020321.

Paranicas, C., D. G. Mitchell, E. C. Roelof, B. H. Mauk, S. M. Krimigis, P. C. Brandt, M. Dusterer, F. S. Turner, J. Vandegriff, and N. Krupp (2007), Energetic electrons injected into Saturn's neutral gas cloud, *Geophys. Res. Lett.*, *34*, L02109, doi:10.1029/2006GL028676.

Pasmanik, D. L., E. E. Titova, A. G. Demekhov, V. Y. Trakhtengerts, O. Santolik, F. Jiricek, K. Kudela, and M. Parrot (2004), Quasi-periodic ELF/VLF wave emissions in the Earth's magnetosphere: Comparison of satellite observations and modelling, *Ann. Geophys.*, *22*, 4351–4361, doi:10.5194/angeo-22-4351-2004.

Persoon, A.M., D. A. Gurnett, W. K. Peterson, J. H. Waite Jr., J. L. Burch, and J. L. Green (1988), Electron density depletions in the nightside auroral zone, *J. Geophys. Res.*, *93*(A3), 1871–1895, doi:10.1029/JA093iA03p01871.

Persoon, A. M., D. A. Gurnett, W. S. Kurth, G. B. Hospodarsky, J. B. Groene, P. Canu, and M. K. Dougherty (2005), Equatorial electron density measurements in Saturn's inner magnetosphere, *Geophys. Res. Lett.*, *32*, L23105, doi:10.1029/2005GL024294.

Persoon, A. M., D. A. Gurnett, W. S. Kurth, G. B. Hospodarsky, J. B. Groene, P. Canu, and M. K. Dougherty (2006a), An electron density model for Saturn's inner magnetosphere, in *Planetary Radio Emissions VI*, edited by H. O. Rucker, W. S. Kurth, and G. Mann, 81–91, Austrian Acad. of Sci. Press, Vienna.

Persoon, A. M., D. A. Gurnett, W. S. Kurth, and J. B. Groene (2006b), A simple scale height model of the electron density in Saturn's plasma disk, *Geophys. Res. Lett.*, *33*, L18106, doi:10.1029/2006GL027090.

Persoon, A. M., et al. (2009), A diffusive equilibrium model for the plasma density in Saturn's magnetosphere, *J. Geophys. Res.*, *114*, A04211, doi:10.1029/2008JA013912.

Persoon, A. M., D. A. Gurnett, J. S. Leisner, W. S. Kurth, J. B. Groene, and J. B. Faden (2013), The plasma density distribution in the inner region of Saturn's magnetosphere, *J. Geophys. Res. Space Physics*, *118*, 2970–2974, doi:10.1002/jgra.50182.

Píša, D., G. B. Hospodarsky, W. S. Kurth, O. Santolík, J. Souček, D. A. Gurnett, A. Masters, and M. E. Hill (2015), Statistics of Langmuir wave amplitudes observed inside Saturn's foreshock by the Cassini spacecraft, *J. Geophys. Res. Space Physics*, *120*, doi:10.1002/2014JA020560.

Robinson, P. A. (1995), Stochastic wave growth, *Phys. Plasmas*, *2*, 1466–1479, doi:10.1063/1.871362.

Rymer, A. M., et al. (2007), Electron sources in Saturn's magnetosphere, *J. Geophys. Res.*, *112*, A02201, doi:10.1029/2006JA012017.

Rymer, A. M., B. H. Mauk, T. W. Hill, C. Paranicas, D. G. Mitchell, A. J. Coates, and D. T. Young (2008), Electron circulation in Saturn's magnetosphere, *J. Geophys. Res.*, *113*, A01201, doi:10.1029/2007JA012589.

Rymer, A. M., B. H. Mauk, T. W. Hill, N. André, D. G. Mitchell, C. Paranicas, D. T. Young, H. T. Smith, A. M. Persoon, J. D. Menietti, G. B. Hospodarsky, A. J. Coates, and M. K. Dougherty (2009), Cassini evidence for rapid interchange transport at Saturn, *Planetary and Space Science 57*(14–15), 1779–1784, doi:10.1016/j.pss.2009.04.010.

Santolík, O., J. S. Pickett, D. A. Gurnett, J. D. Menietti, B. T. Tsurutani, and O. Verkhoglyadova (2010), Survey of Poynting flux of whistler mode chorus in the outer zone, *J. Geophys. Res.*, *115*, A00F13, doi:10.1029/2009JA014925.

Santolík, O., D. A. Gurnett, G. H. Jones, P. Schippers, F. J. Crary, J. S. Leisner, G. B. Hospodarsky, W. S. Kurth, C. T. Russell, and M. K. Dougherty (2011), Intense plasma wave emissions associated with Saturn's moon Rhea, *Geophys. Res. Lett.*, *38*, L19204, doi:10.1029/2011GL049219.

Scarf, F. L., R. W. Fredricks, L. A. Frank, and M. Neugebauer (1971), Nonthermal electrons and high-frequency waves in the upstream solar wind: 1. Observations, *J. Geophys. Res.*, *76*, 5162–5171, doi:10.1029/JA076i022p05162

Scarf, F. L., D. A. Gurnett, W. S. Kurth, and R. L. Poynter (1982), Voyager 2 plasma wave observations at Saturn, *Science*, *215*, 587–594, doi:10.1126/science.215.4532.587.

Scarf, F. L., D. A. Gurnett, W. S. Kurth, and R. L. Poynter (1983), Voyager Plasma Wave Measurements at Saturn, *J. Geophys. Res.*, *88*(A11), 8971–8984, doi:10.1029/JA088iA11p08971.

Scarf, F. L., L. A. Frank, D. A. Gurnett, L. J. Lanzerotti, A. Lazarus, and E. C. Sittler Jr. (1984), Measurements of plasma, plasma waves and suprathermal charged particles in Saturn's inner magnetosphere, in *Saturn*, edited by T. Gehrels, pp. 318–353, Univ. of Ariz. Press, Tucson.

Schippers, P., M. Moncuquet, N. Meyer-Vernet, and A. Lecacheux (2013), Core electron temperature and density in the innermost Saturn's magnetosphere from HF power spectra analysis on Cassini, *J. Geophys. Res. Space Physics*, *118*, 7170–7180, doi:10.1002/2013JA019199.

Singh, N., R. W. Schunk, and J. J. Sojka (1981), Energization of ionospheric ions by electrostatic hydrogen cyclotron waves, *Geophys. Res. Lett.*, *8*(12), 1249–1252, doi:10.1029/GL008i012p01249.

Tao, X., R. M. Thorne, R. B. Horne, S. Grimald, C. S. Arridge, G. B. Hospodarsky, D. A. Gurnett, A. J. Coates, and F. J. Crary (2010), Excitation of electron cyclotron harmonic waves in the inner Saturn magnetosphere within local plasma injections, *J. Geophys. Res.*, *115*, A12204, doi:10.1029/2010JA015598.

Tokar, R. L., R. E. Johnson, T. W. Hill, D. H. Pontius, W. S. Kurth, F. J. Crary, D. T. Young, M. F. Thomsen, D. B. Reisenfeld, A. J. Coates, G. R. Lewis, E. C. Sittler, and D. A. Gurnett (2006), The Interaction of the Atmosphere of Enceladus with Saturn's Plasma, *Science 311*(5766): 1409–1412, doi:10.1126/science.1121061.

Wang, Z., D. A. Gurnett, T. F. Averkamp, A. M. Persoon and W. S. Kurth (2006), Characteristics of dust particles detected near Saturn's ring plane with the Cassini Radio and Plasma Wave instrument, *Planetary and Space Science 54*(9–10), 957–966, doi:10.1016/j.pss.2006.05.015.

Wang, Z., D. A. Gurnett, G. Fischer, S.-Y. Ye, W. S. Kurth, D. G. Mitchell, J. S. Leisner, and C. T. Russell (2010), Cassini

observations of narrowband radio emissions in Saturn's magnetosphere, *J. Geophys. Res.*, *115*, A06213, doi:10.1029/2009JA014847.

Warwick, J. W. et al. (1981), Planetary radio astronomy observations from Voyager 1 near Saturn, *Science 212*, 239, doi:10.1126/science.212.4491.239.

Warwick, J. W. et al. (1982), Planetary radio astronomy observations from Voyager 2 near Saturn. *Science 215*, 582, doi:10.1126/science.215.4532.582.

Xin, L., D. A. Gurnett, O. Santolík, W. S. Kurth, and G. B. Hospodarsky (2006), Whistler-mode auroral hiss emissions observed near Saturn's B ring, *J. Geophys. Res.*, *111*, A06214, doi:10.1029/2005JA011432.

Ye, S.-Y., D. A. Gurnett, G. Fischer, B. Cecconi, J. D. Menietti, W. S. Kurth, Z. Wang, G. B. Hospodarsky, P. Zarka, and A. Lecacheux (2009), Source locations of narrowband radio emissions detected at Saturn, *J. Geophys. Res.*, *114*, A06219, doi:10.1029/2008JA013855.

Ye, S.-Y., D. A. Gurnett, J. B. Groene, Z. Wang, and W. S. Kurth (2010), Dual periodicities in the rotational modulation of Saturn narrowband emissions, *J. Geophys. Res.*, *115*, A12258, doi:10.1029/2010JA015780.

Ye, S.-Y., G. Fischer, J.D. Menietti, Z. Wang, D.A. Gurnett, and W.S. Kurth (2011), An Overview of Saturn Narrowband Radio Emissions Observed by Cassini RPWS, in *Planetary Radio Emissions VII*, eds. H.O. Rucker, W.S. Kurth, P. Louarn, G. Fischer, 99–114, Austrian Academy of Sciences, Vienna, Austria.

Ye, S.-Y., D. A. Gurnett, W. S. Kurth, T. F. Averkamp, S. Kempf, H.-W. Hsu, R. Srama, and E. Grün (2014a), Properties of dust particles near Saturn inferred from voltage pulses induced by dust impacts on Cassini spacecraft, *J. Geophys. Res. Space Physics*, *119*, 6294–6312, doi:10.1002/2014JA020024.

Ye, S.-Y., D. A. Gurnett, W. S. Kurth, T. F. Averkamp, M. Morooka, S. Sakai, and J.-E. Wahlund (2014b), Electron density inside Enceladus plume inferred from plasma oscillations excited by dust impacts, *J. Geophys. Res. Space Physics*, *119*, 3373–3380, doi:10.1002/2014JA019861.

Young, D. T., et al. (2004), Cassini plasma spectrometer investigation, *Space Sci. Rev.*, *114*, 1–112, doi:10.1007/s11214-004-1406-4.

Zarka, P. (1985), Saturn Electrostatic Discharges: characteristics, comparison to planetary lightning and importance in the study of Saturn's ionosphere, in *Planetary Radio Emissions*, edited by H. O. Rucker and S. J. Bauer, 237–270, Austrian Academy of Sciences Press, Vienna.

23

Titan's Interaction with Saturn's Magnetosphere

Joseph H. Westlake[1], Thomas E. Cravens[2], Robert E. Johnson[3], Stephen A. Ledvina[4], Janet G. Luhmann[4], Donald G. Mitchell[1], Matthew S. Richard[5], Ilkka Sillanpää[6], Sven Simon[7], Darci Snowden[8], J. Hunter Waite, Jr.[9], and Adam K. Woodson[10]

Video of Yosemite Talk, URL: http://dx.doi.org/10.15142/T36K5Z

ABSTRACT

Cassini's suite of in situ and remote sensing instruments has sampled Titan's atmosphere and ionosphere during more than 100 close flybys spanning the years from 2004 to 2015. Even with this large number of samples, the coverage in the multitude of geospatial, magnetospheric, solar, and seasonal configurations is rather sparse resulting in an incomplete understanding of the coupling between the complex atmosphere and ionosphere of Titan and Saturn's corotational magnetospheric plasma. This paper reviews the Cassini observations from multiple instruments at Titan to piece together a cohesive picture of the interaction between Saturn's magnetosphere and Titan's ionosphere and thermosphere as it is currently understood.

23.1. INTRODUCTION

Titan orbits at the edge of Saturn's magnetosphere. Aside from a few special cases where Titan is in Saturn's magnetosheath or the solar wind, the moon spends most of its time in Saturn's sub-corotational magnetospheric plasma that consists primarily of ions sourced from the inner moon Enceladus. The interaction of the magnetospheric plasma with Titan's atmosphere and ionosphere is complex and tends to be disordered due to the lack of an intrinsic magnetic field at Titan [*Wei et al.*, 2010]. The moon-magnetosphere interaction is driven by the convergence of the magnetospheric plasma with the extended ionosphere produced by photoionization of Titan's neutral atmosphere. Titan's electrically conducting ionosphere is produced mainly by photoionization of the ambient N_2 and CH_4 atmosphere [*Cravens et al.*, 2006; *Ågren et al.*, 2009]. The plasma is slowed as it encounters the atmosphere, and the frozen-in magnetic field lines become further mass-loaded and mired therein. Far from the moon the field continues to rotate with Saturn faster than Titan orbits so that in the vicinity of Titan it stretches and becomes draped around the moon, slowly convecting through the ionosphere toward Titan's induced magnetotail. A schematic of the Titan moon-magnetosphere interaction is given in Figure 23.1 showing the moon, its atmosphere and ionosphere as well as the orientation of the magnetospheric flow over Titan. The

[1] *Applied Physics Laboratory, Johns Hopkins University, Laurel, MD, USA*
[2] *Department of Physics and Astronomy, University of Kansas, Lawrence, KS, USA*
[3] *University of Virginia, Charlottesville, VA, USA and New York University, New York City, NY, USA*
[4] *Space Sciences Laboratory, University of California Berkeley, Berkeley, CA, USA*
[5] *Department of Physics and Astronomy, Benedictine College, Atchison, KS, USA*
[6] *Finnish Meteorological Institute, Helsinki, Finland*
[7] *Earth and Atmospheric Sciences, Georgia Institute of Technology, Atlanta, GA, USA*
[8] *Central Washington University, Ellensburg, WA, USA*
[9] *Space Science and Engineering, Southwest Research Institute, San Antonio, TX, USA*
[10] *Laboratory for Atmospheric and Space Physics, University of Colorado, Boulder, CO, USA*

Magnetosphere-Ionosphere Coupling in the Solar System, Geophysical Monograph 222, First Edition.
Edited by Charles R. Chappell, Robert W. Schunk, Peter M. Banks, James L. Burch, and Richard M. Thorne.

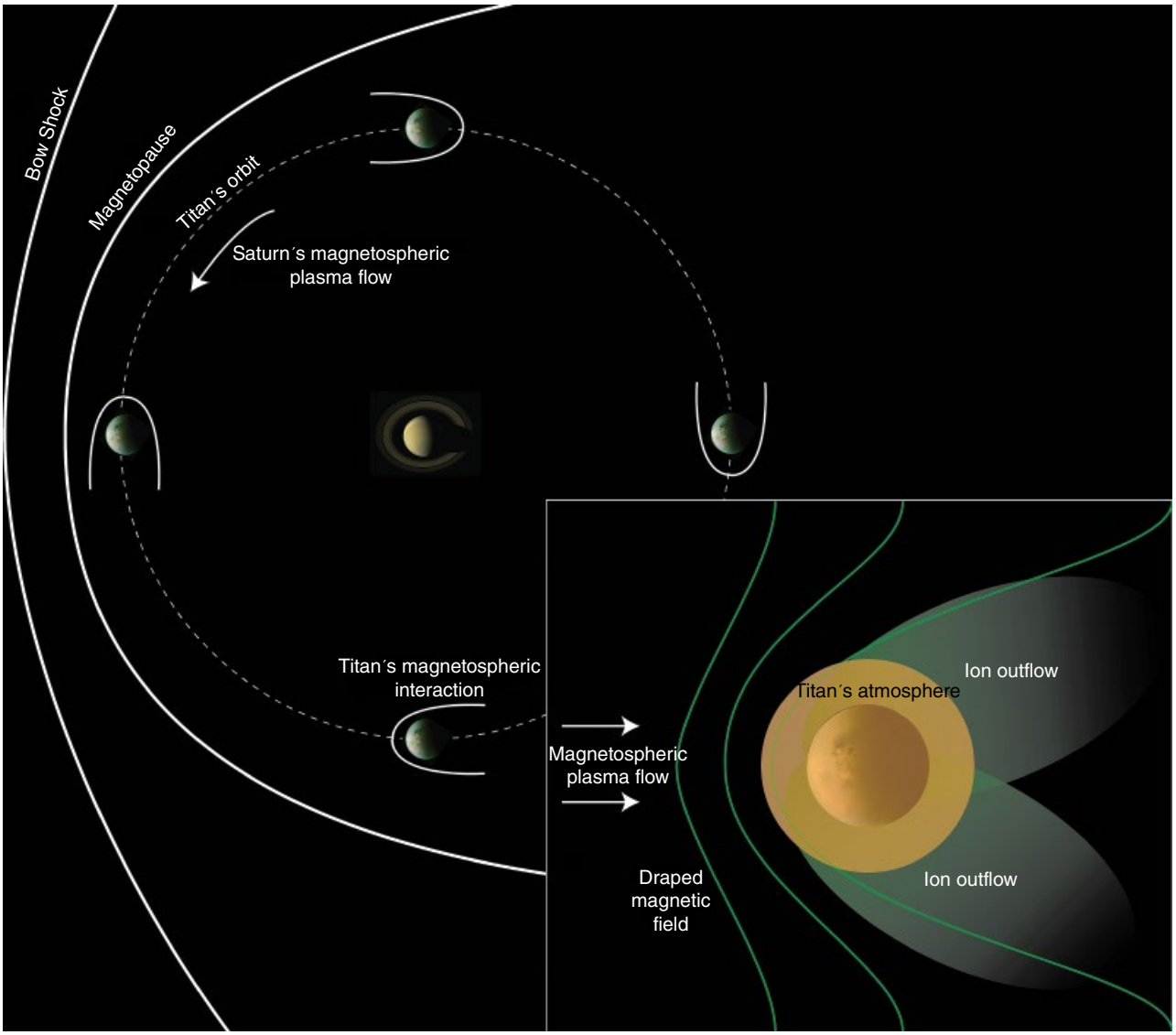

Figure 23.1 The orientation of Titan's sunlit face with respect to the direction of Saturn's magnetospheric flow changes as it orbits Saturn. In addition to the change in orientation of the interaction, the plasma characteristics change as Titan moves through Saturn's magnetosphere with more plasma sheet encounters on the dayside of Saturn and fewer on the nightside where the plasma sheet has thinned and tends to rapidly flap over Titan [*Simon et al.,* 2010]. The inset shows the general structure of Titan's interaction with Saturn's magnetosphere.

Titan interaction is submagnetosonic in general and therefore an upstream bow shock is not present, and the magnetospheric plasma directly interacts with the ionosphere and upper atmosphere. The magnetic field penetrates to a depth in the atmosphere where ionospheric particles are produced creating mass loading as they drag through Titan's ionosphere. This interaction forms a magnetic pileup region upstream of the ionosphere and a bipolar magnetotail in the wake downstream of the interaction [e.g., *Neubauer et al.*, 1984, 2006; *Bertucci et al.*, 2007]. We also note that although Titan is generally immersed in Saturn's magnetospheric plasma, that plasma is dynamic on timescales of roughly three hours presenting a wide range of upstream conditions such as the relatively sparse but hot lobe or the dense plasma sheet [*Rymer et al.*, 2009; *Simon et al.*, 2010]. Figure 23.1 also introduces the important concept of the angle between the magnetospheric plasma flow and the solar incidence angle, which for Titan can vary from 0 to 180 degrees as opposed to say Venus where the solar wind flow is roughly parallel with the flux of solar photons. Saturn's magnetospheric plasma at Titan's orbit is also known to have magnetospheric local time structure with a thicker, more perturbed plasma sheet on the dayside and a thinner, more dynamic plasma sheet on the nightside [*Simon et al.*, 2010].

The Saturn-orbiting Cassini spacecraft makes frequent visits to the large moon Titan, taking measurements as it dives into the atmosphere. The relevant instruments for assessing the moon-magnetosphere interaction are the Cassini Plasma Spectrometer (CAPS), magnetometer (MAG), Radio and Plasma Waves (RPWS), Ion and Neutral Mass Spectrometer (INMS), and the Magnetospheric Imaging Instrument (MIMI). Each of these instruments is described in detailed review papers (Table 23.1).

Several modeling studies have investigated the structure and features of the moon-magnetosphere interaction. We do not present a comprehensive list and description of these studies but instead provide sufficient background information to support the later discussions. MHD models have been pursued for the Titan interaction including those with multiple fluids, time dependence, and Hall effects [e.g., *Cravens et al.*, 1997; *Ledvina and Cravens*, 1997; *Ma et al.*, 2006; 2009]. These models generally roughly replicate the magnetic field structure and have been used to study the interaction behavior under time-dependent upstream conditions and to investigate specific details such as the ion escape fluxes for various species [*Ma et al.*, 2006]. Since the field is relatively weak, hybrid modeling of the interaction adds the effect of the large ion gyroradius and has been used to investigate the energy deposition into Titan's atmosphere and the influence of various species on the interaction structure [e.g., *Brecht et al.*, 2000; *Sillanpää et al.*, 2007, 2011, 2015; *Simon et al.*, 2007, 2009; *Ledvina et al.*, 2012; *Ledvina and Brecht*, 2012]. Hybrid models have been used to investigate Titan's interaction with the solar wind [*Ledvina et al.*, 2004]. Recent models have also included the effects of negative ions near the exobase [*Ledvina and Brecht*, 2012] and ion-neutral collisions on the magnetospheric interaction [*Ledvina et al.*, 2012; *Sillanpää and Johnson*, 2015] showing that these have substantial effects on the spatial distribution of the energy deposited into the upper atmosphere and on the ion escape rates.

Table 23.1 Synopses of the Cassini instruments used to study the moon-magnetosphere interaction

Instrument	Measurement	Reference
INMS	Thermal ions and neutral gas	*Waite et al.*, 2004
CAPS	Plasma ions and electrons	*Young et al.*, 2004
RPWS	Radio and plasma waves and Langmuir Probe	*Gurnett et al.*, 2004
MIMI	Energetic particles, electrons, ions, energetic neutral atoms (ENA)	*Krimigis et al.*, 2004
MAG	Magnetic fields	*Dougherty et al.*, 2004

23.2. OBSERVATIONS OF THE SATURN-TITAN INTERACTION

The structure of the Saturn-Titan interaction has been systematically characterized in several studies. The magnetospheric conditions were characterized by *Rymer et al.* [2009] and *Simon et al.* [2010] by analyzing electron distributions sampled by the CAPS Electron Spectrometer (ELS), magnetometer data, and the MIMI over numerous Titan encounters resulting in four primary magnetospheric plasma types: three corresponding to Titan's position in the plasma sheet, lobe, or magnetosheath, and one bimodal type consisting of hot sheet-like or lobe-like electrons mixed with cold pickup electrons, possibly indicative of freshly ionized neutrals. *Simon et al.* [2013] showed that the magnetic field at Titan generally assumes a steady-state draping configuration (Figure 23.2) but with short-range oscillations as well as significant perturbations in the vicinity of the magnetodisk. They found that the majority of Titan flybys adhered to this draping scenario while a limited subset (some of which will be discussed in the next section) exhibited highly perturbed draping signatures or no discernible draping at all. Moreover, variation in the measured ambient plasma and field draping conditions alludes to the compression of Saturn's magnetosphere and the dynamic warping, or "flapping," of its plasma sheet due to solar wind forcing.

Below the exobase near 1500 kilometer (km), Titan's main ionosphere is sufficiently conductive (ranging from 10^{-3} to 10^{-1} S/m perpendicular to the magnetic field) to couple to the external plasma flow, setting up ionospheric current systems and associated convection electric fields [*Ness et al.*, 1982; *Blanc et al.*, 2002; *Rosenqvist et al.*, 2009; *Cravens et al.*, 2010]. Though the main ionosphere appears solar driven, *Ledvina et al.* (2012) show that the induced magnetosphere is robust against changes in the incident solar ultraviolet (UV) direction. *Crary et al.* [2009] used CAPS's ion beam sensor (IBS) and INMS measurements of the ion temperatures to show that there is a clear warming trend in the ion temperatures above 1100 km suggesting that the ions and neutrals are not closely coupled implying that there exists an ion heating process that could be driven by the interaction of Titan's ionosphere with Saturn's magnetosphere. The ionospheric current systems can introduce energy into the thermosphere through Joule heating or ion collisional heating [e.g., *Ågren et al.*, 2011]. No direct mapping of these current

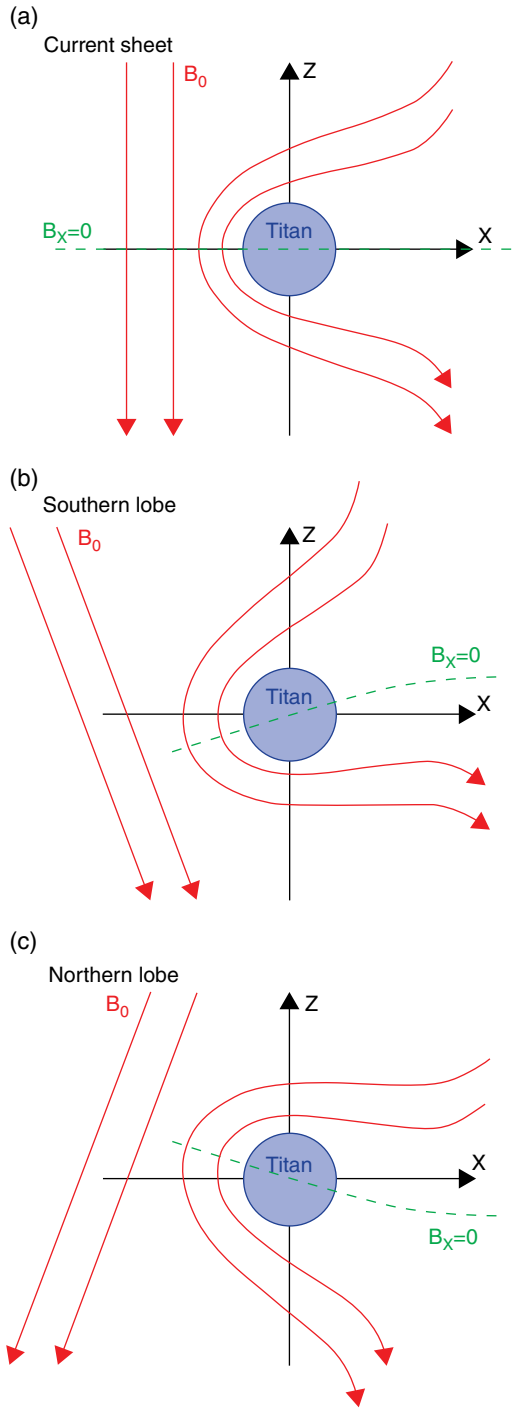

Figure 23.2 Titan's induced magnetosphere at different positions with respect to Saturn's current sheet. [From *Simon et al.*, 2013]

systems exist, though the various conductivities have been measured [*Rosenqvist et al.*, 2009].

Several Cassini instruments have observed that the convection electric fields produce flows of atmospheric ions from near Titan's exobase region. These ions propagate down the tail and eventually merge with Saturn's thermal plasma flow. For several consecutive and geometrically similar flybys, the Langmuir Probe has shown significant enhancements in electron density above the exobase perhaps indicating a steady feature [*Edberg et al.*, 2011]. During several flybys the CAPS ELS has clearly shown the electron energy signature (24.1 electron-volts [eV] electrons produced from N_2 ionization from the solar HeII line) of ionospheric photoelectrons deep in Titan's magnetotail [e.g., *Wei et al.*, 2007; *Coates et al.*, 2012; *Wellbrock et al.*, 2012). This indicates either a direct magnetic connection with the ionosphere or, more likely, recent transport of plasma directly from the ionosphere. *Westlake et al.* [2012] using the INMS and *Woodson et al.* [2015] using the CAPS Ion Mass Spectrometer (IMS) found ion compositions that could only be produced in Titan's ionosphere (Figure 23.3; CH_5^+, $HCNH^+$, etc.) far from Titan in a region where ion-neutral chemistry is inefficient. These measurements indicate that ions are readily removed from Titan's ionosphere, challenging the composition identifications from early Cassini work and the Voyager flybys [*Hartle et al.*, 1982; *Sittler et al.*, 2005]. *Woodson et al.* [2015] also showed that the CAPS observations are consistent with the multi-fluid MHD modeling results of *Ulusen et al.* [2012], specifically the boundaries of the interaction in the model match the locations of the CAPS observations. These observations together reveal that traditional pickup processes in which atmospheric neutrals are ionized and picked up into the magnetospheric flow are inefficient compared to the process of producing a relatively high density of ionospheric ions on the relatively weak field lines.

The INMS observation during the T40 flyby was fortuitous due to a combination of a spacecraft roll and a mismatch between the entrance lens settings and the expected thermal ion velocity resulting in the INMS velocity passband being set for ions with some flow velocity. Following the serendipitous T40 flyby, and the recognition that the energy scans used throughout the mission for in-flight calibrations could be configured to obtain topside ionospheric ions, the INMS was then configured to make use of the ion entrance lens to scan the incoming velocity of the ions. In this mode the quadrupole switching lens is swept in voltage while maintaining a constant mass on the quadrupole mass analyzer. Further observations by the Cassini INMS of Titan's ionospheric outflow during the T95 flyby are shown in Figure 23.4. In this observation ionospheric ions are observed at altitudes above 2000 km with substantial flow velocities (1–5 km/s). Also observed is a mass dependence of the flow velocity with heavier species having less velocity than the lighter species indicating that the acceleration is mass dependent. Also notable is the appearance of masses as high as mass 39 out to the exobase showing that the complex

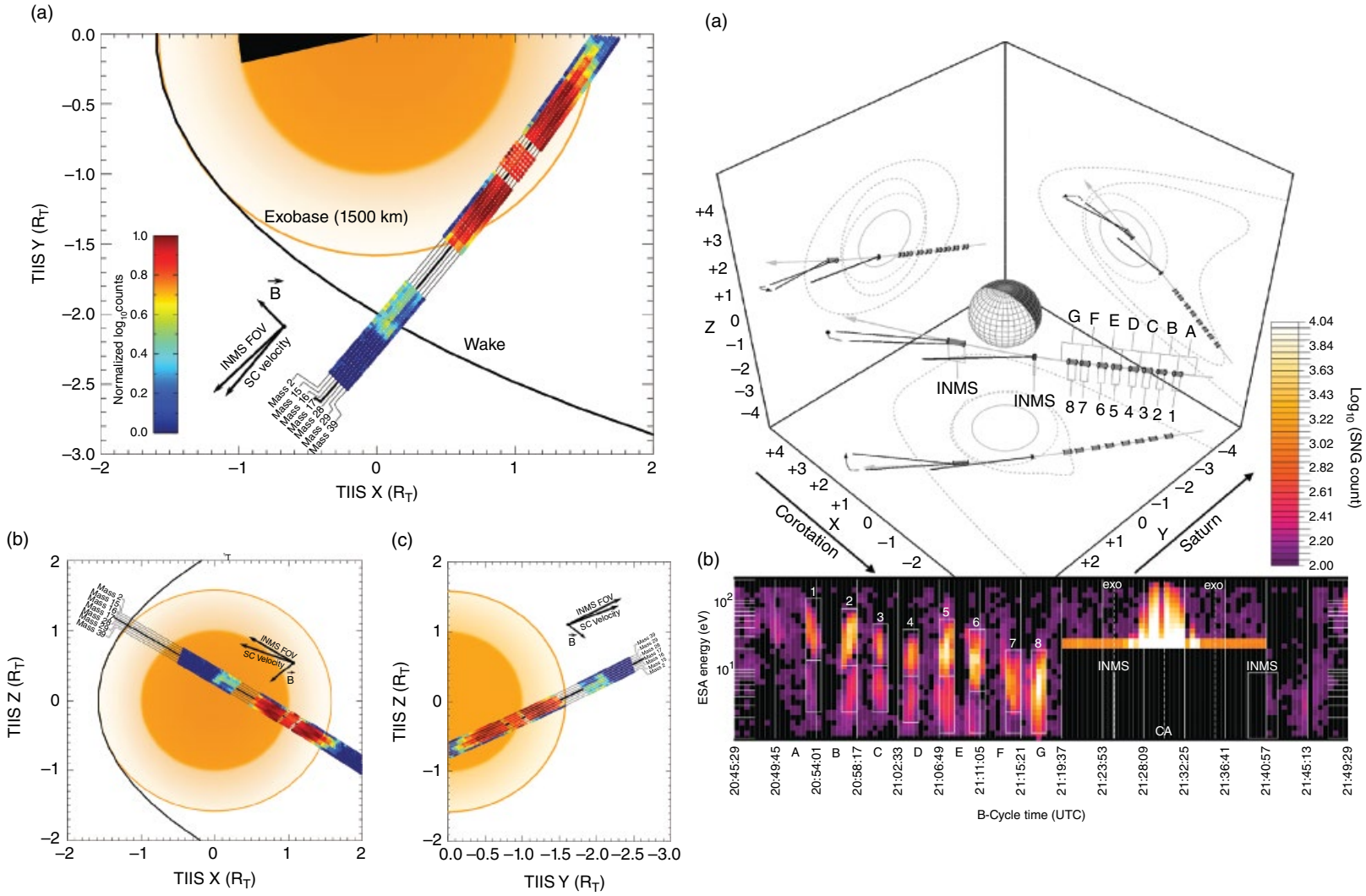

Figure 23.3 Ionospheric outflow observed by the INMS and CAPS instruments during the T40 encounter. The left panels show the Cassini INMS observations during this flyby that show an observation far from the exobase of ions that were produced in Titan's ionosphere [*Westlake et al.*, 2012]. The right panel shows CAPS total ion counts during the same encounter with boundaries shown from *Ulusen et al.* [2012]. The associated mass spectra (not shown) reveal heavy ions down tail from Titan that have a composition consistent with ions produced in the ionosphere [*Woodson et al.*, 2015]. The velocity of the ions observed by the INMS close to the exobase is ~1 km/s for the heavy species and ~7 km/s for H_2^+ with a direction that is consistent with radial or slightly downtail outflow from Titan. The thermal pressure presumably dominates this outflow [e.g., *Ulusen et al.*, 2010]. Farther down tail the ions have been accelerated to 5–25 km/s with ions of Titan origin found as far away as 11,000 km [*Woodson et al.*, 2015].

hydrocarbons created in Titan's ionosphere have sufficiently long lifetimes and acceleration processes to be lifted from the main ionosphere to the exobase.

Ions that originate from Titan are observable in the energy per charge spectrum from the CAPS-IMS. A compilation of the locations where CAPS-IMS has observed these ions (restricted to ions with energies below below 100 eV) is shown in Figure 23.5. The magnetospheric protons and water group ions are generally observed at 1 keV and above [e.g., *Thomsen et al.*, 2010] and thus 100 eV is a good energy constraint for ions escaping from Titan's ionosphere. We can see that ions sourced from Titan are observed significantly down tail (as much as 5–8 Titan radii). The pattern of two lobes identified by Voyager and several cross-tail Cassini flybys is also clearly present in the data [e.g., *Sittler et al.*, 2005; *Coates et al.*, 2012]. It is clear that the outflowing ions are primarily constrained within 2 R_T of the wake midline. We note that some biasing in this data set is present because it is common for Cassini to approach Titan from the downstream side (+X in Titan Interaction System [TIIS] coordinates) and turn just after closest approach so the upstream region is likely undersampled due to the limited field of view of the CAPS instrument.

23.3. MAGNETOSPHERIC PRECIPITATION AND ITS EFFECTS ON TITAN'S THERMOSPHERE AND IONOSPHERE

Titan's moon-magnetosphere interaction also affects the neutral atmosphere and ionosphere through heating and ionization by magnetospheric particle precipitation. Due to the Saturn orbiting nature of the Cassini mission, it is challenging to separate the influence of magnetospheric processes from solar processes on the thermosphere and ionosphere. Here we present the current state of knowledge on the effect of magnetospheric precipitation on Titan's thermosphere and ionosphere that has been gained during the Cassini mission.

Precipitating magnetospheric electrons, protons, and water group ions (largely sourced from Enceladus) ionize, dissociate, and heat Titan's thermosphere and ionosphere. Particle precipitation ionizes and dissociates N_2 and CH_4 starting the chemical scheme that produces complex organic molecules, and oxygen from Saturn's magnetosphere is recognized as the source of oxygen observed in Titan's atmosphere [*Hartle et al.*, 2006; *Hörst et al.*, 2008]. Particle precipitation also heats ionospheric electrons and ions [*Richard et al.*, 2011], affecting electron recombination rates [*Vigren et al.*, 2013, 2015] and the thermal pressure of the ionosphere [*Ma et al.*, 2011]. Energetic ions sputter Titan's atmosphere, creating ENAs [e.g., *Michael et al.*, 2005]. These processes along with the heating and ionization from solar photons create a dynamic thermosphere and ionosphere that quickly responds to changes in the external environment.

Observational evidence of particle precipitation into Titan's atmosphere comes from ENA emissions from the Cassini ion and neutral camera (INCA) instrument, which are essentially photographs of the Titan interaction region at a global scale. These ENA measurements have indicated that the moon-magnetosphere interaction and particle precipitation is highly variable [Figure 23.6; *Mitchell et al.*, 2005]. Hydrogen ENAs from Titan arise

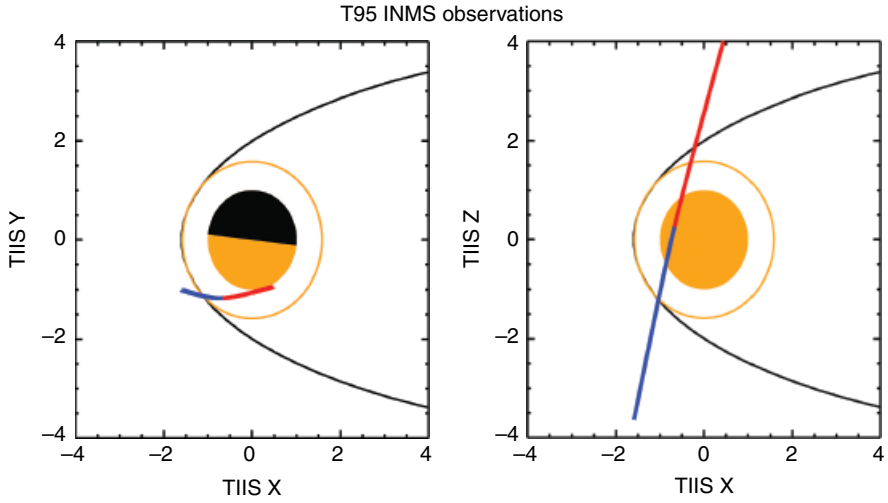

Figure 23.4 Cassini INMS observations of the composition of Titan's ionospheric outflow during the T95 flyby using its new mode, in which the quadrupole switching lens is swept in voltage while mass is kept constant, revealing significant densities of ionospheric ions out to and past 2000-km altitude. The right two columns of spectrograms show the inbound (left) and outbound (right) observations of ions flowing from Titan during the T95 flyby.

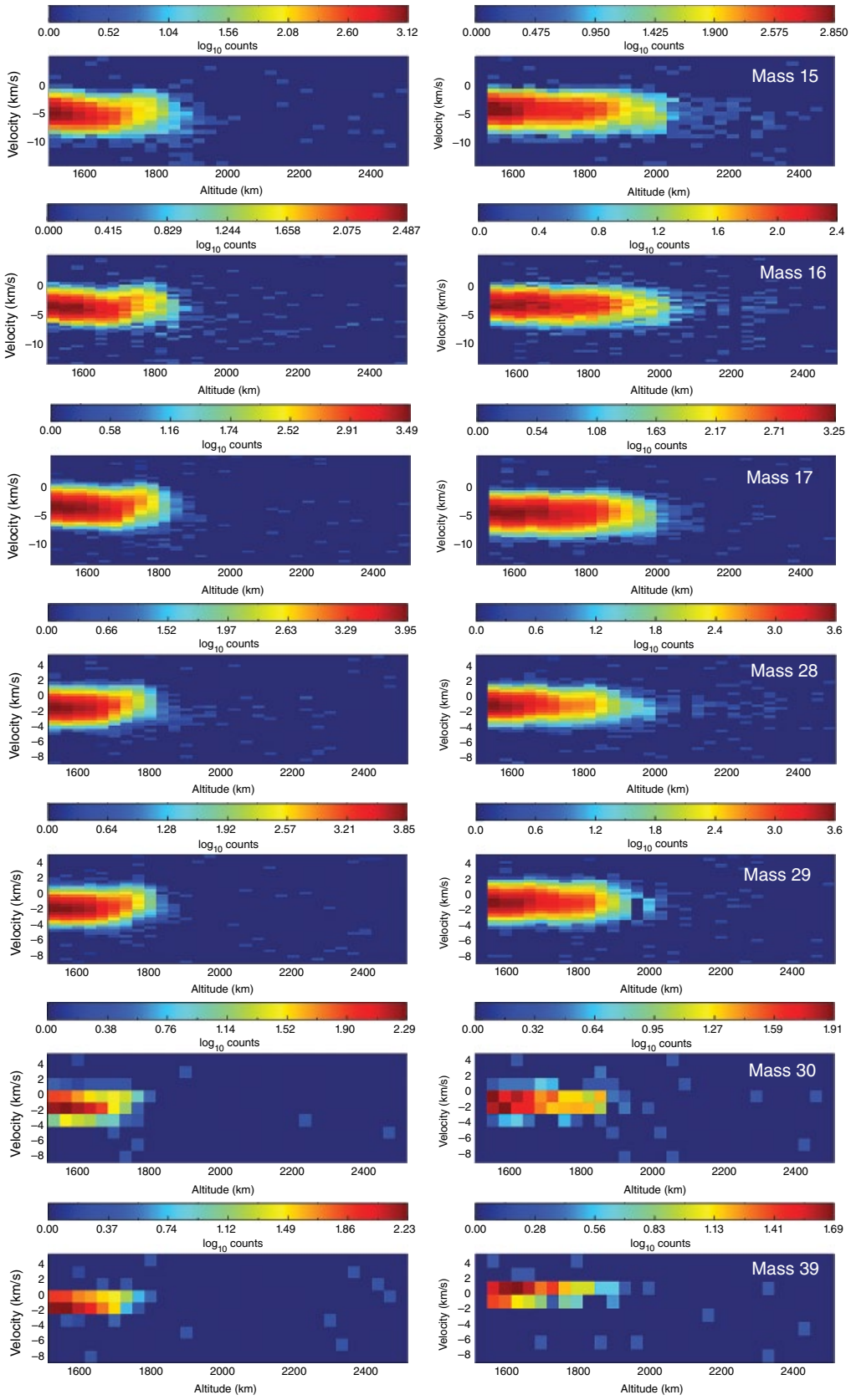

Figure 23.4 (*Continued*)

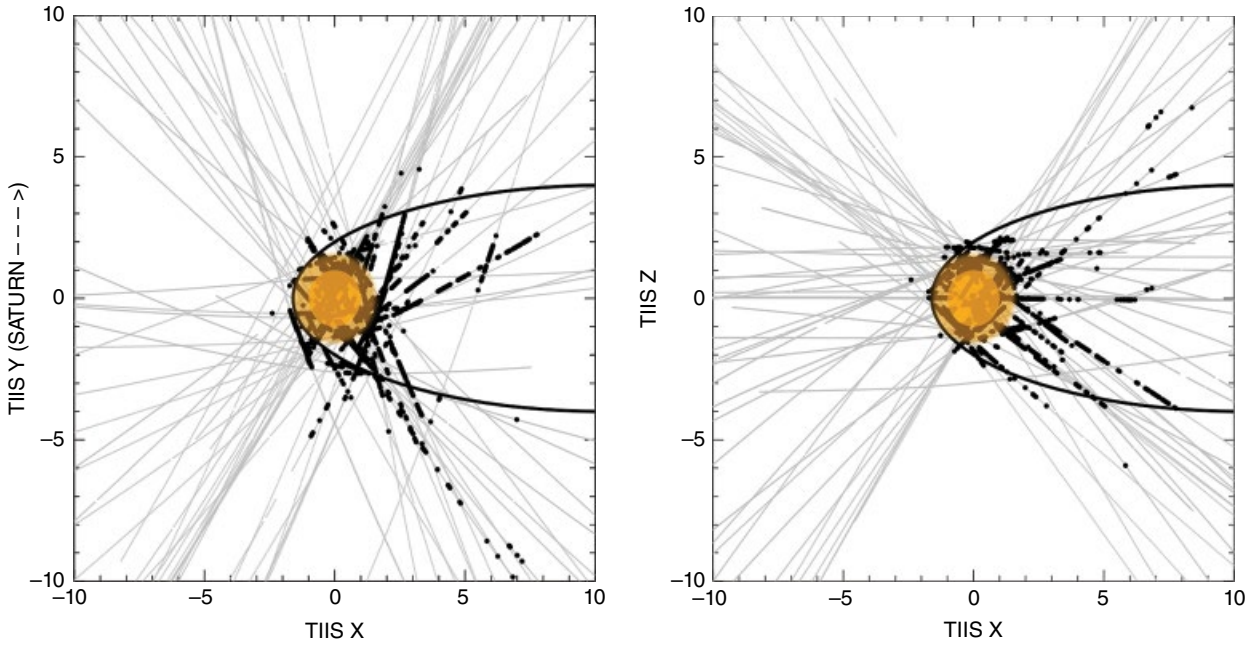

Figure 23.5 Locations of ions sourced by Titan observed by the CAPS IMS in the Titan interaction system coordinates (TIIS). This coordinate system is formed with the flow into the +X direction, Saturn in the +Y, and Z completing the orthogonal set. These locations were selected as having significant count rates and energies below 100 eV. The black dots show the identified regions, and the gray lines show the flyby tracks. A conceptual wake is shown in addition to the exobase at 1500 km.

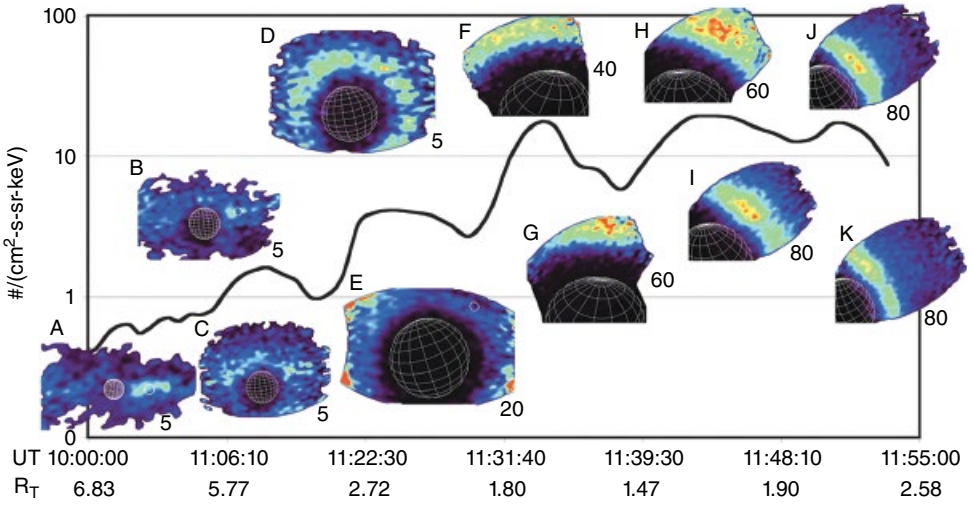

Figure 23.6 Energetic hydrogen images between 20 and 50 keV during the TB flyby. The images are located according to their acquisition time. The color scale for each image is linearly scaled according to the number immediately to the lower right in ENAs cm^{-2} s^{-1} sr^{-1} keV^{-1}. The images are arranged over a timeline of the observed summation of ENA emissions during the flyby. These ENA images reveal both the structure of the magnetospheric particle precipitation at Titan but also the variable nature of the moon-magnetosphere interaction [from *Mitchell et al.*, 2005].

when Saturn's magnetospheric particles impact Titan's dense atmosphere and charge exchange with the ambient atmosphere producing an ENA that no longer follows the magnetic field. These images are therefore clear representations of the spatial structure of the moon-magnetosphere interaction. ENA emission studies have shown that the observed intensities vary according to the magnetic field arrangement [*Wulms et al.*, 2010] and the flux

of particles into the atmosphere [*Mitchell et al.*, 2005]. Furthermore, the ENAs have been used to track the extent of the neutral atmosphere by identifying neutrals out to the edge of the Hill sphere or 50,000 km from Titan [*Brandt et al.*, 2012]. Interestingly, this study also found several flybys with unique asymmetries in the observed ENA fluxes indicating some asymmetries in the interaction.

Due to the dynamic nature of magnetospheric precipitation at Titan, it is difficult to fully characterize the effect that these processes have on the thermosphere and ionosphere. However, comprehensive studies of magnetospheric ion and electron precipitation and the resulting ionization and energy deposition rates have been completed from the multitude of Cassini flybys and Voyager data [*Snowden et al.*, 2013b, 2014a, 2014b; *Gronoff et al.*, 2009; *Cravens et al.*, 2008, 2009; *Richard et al.*, 2011, 2014, 2015; *Shah et al.*, 2009; *Smith et al.*, 2009; *De La Haye et al.*, 2008; *Shematovich et al.*, 2001; *Michael and Johnson*, 2005; *Michael et al.*, 2005). In general, the energy deposition rate from magnetospheric O^+ is the largest of the magnetospheric energy sources [*Snowden et al.*, 2014]. The flux of thermal O^+ into Titan's atmosphere is asymmetric because of the large gyroradius of the O^+ and possibly also deflection due to gradients in the magnetic field [*Hartle et al.*, 2006; *Ledvina et al.*, 2005; *Sillanpää et al.*, 2011], while suprathermal to energetic O^+ is mainly isotropic near Titan [*Sergis et al.*, 2009]. Protons with energies of a few to 10s of keV are observed via ENA imaging to precipitate deep into Titan's thermosphere [*Mitchell et al.*, 2005; *Smith et al.*, 2009]. Suprathermal magnetospheric electrons enter Titan's atmosphere directly along draped magnetic field lines. Much of the modeling of particle impacts into Titan's thermosphere has neglected the isotropic nature of particles in this region of the magnetosphere, especially above a few keV. Many of these models have incorrectly shown exclusion of particles with energies of several keV by only simulating 90° pitch angles and neglecting particles with greater pitch angles.

Cassini radio occultations show that particle precipitation can significantly enhance the electron density in Titan's ionosphere [Figure 23.7; *Kliore et al.*, 2011]. This observation is corroborated by the classification of at least one of the disturbed passes as being within the plasma sheet [*Rymer et al.*, 2009], with high particle fluxes [*Garnier et al.*, 2010] resulting in enhanced ionization near the peak of the ionosphere at 1100 km. Additionally, during some flybys, magnetospheric particle precipitation appears to be necessary to reproduce the observed density and/or temperature of Titan's nightside ionosphere [*Richard et al.*, 2011, 2015]. Other studies have indicated that, compared to solar EUV, typical rates of magnetospheric particle precipitation do not strongly

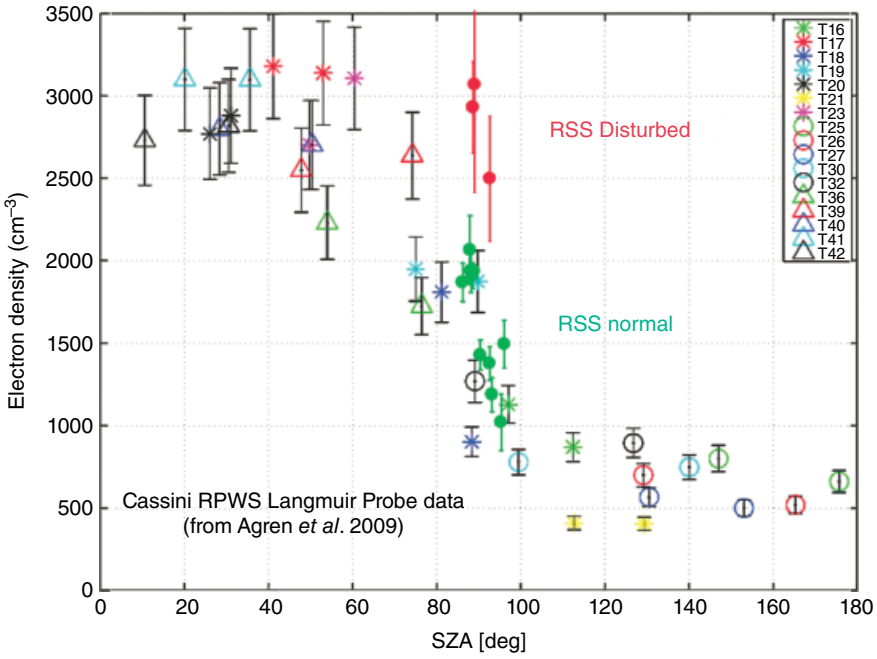

Figure 23.7 A compilation of the peak ionospheric electron density at Titan from several passes using the RPWS-LP [*Ågren et al.*, 2009] and the Radio Science (RSS) occultations [*Kliore et al.*, 2011]. The RPWS-LP densities show a clear dependence on solar zenith angle while the RSS occultations show significant disturbances due to enhanced particle precipitation.

perturb the ionosphere [e.g., *Galand et al.*, 2006, 2010; *Lavvas et al.*, 2011]. *Galand et al.* [2010] showed that a significant additional source of ionization was required in the ionosphere, which they suggest can be provided by magnetospheric electron precipitation. Cassini ultraviolet spectrometer observations indicate that the energy deposited in Titan's thermosphere by magnetospheric particles is less than 10% of solar EUV [*Stevens et al.*, 2011].

The analysis of Cassini INMS data [*Müeller-Wodarg et al.*, 2006; *Müeller-Wodarg et al.*, 2008; *Magee et al.*, 2009; *Cui et al.*, 2009, 2011; *Westlake et al.*, 2011; *Snowden et al.*, 2013; *Tucker et al.*, 2013] indicates that the structure of Titan's thermosphere is highly variable. *Westlake et al.* [2011] showed that Cassini INMS observed higher temperatures when Titan was within Saturn's plasma sheet and lower temperatures in the lobe indicating that the magnetospheric particle precipitation may cause the large variability in the temperature of the upper atmosphere [Figure 23.8; *Westlake et al.*, 2011]. *Bell et al.* [2011] found that magnetospheric particle precipitation can increase the temperature of Titan's thermosphere on timescales of roughly 10 Earth days. *Snowden et al.* [2013] calculated magnetospheric energy deposition profiles from precipitating ions and electrons and compared them to the energy deposition profile of solar EUV [Figure 23.9] finding that the energy deposited by magnetospheric particles is less than 10% of solar EUV and unlikely to cause strong variations in the temperature of Titan's thermosphere. Solar forcing is also not a clear driver, prompting *Snowden and Yelle* [2014] to suggest that large-scale atmospheric waves might be responsible. What is less certain, and has been extensively debated, is whether or not the incident and pick-up plasma has any long-term evolutionary effect on the atmosphere [e.g., *Lunine et al.*, 1999; *Johnson*, 2004; *Penz et al.*, 2005; *Mandt et al.*, 2009].

23.4. TITAN'S INFLUENCE ON SATURN'S MAGNETOSPHERE

Titan is a substantial source of plasma at the edge of Saturn's magnetosphere (Figure 23.10). Wei et al. (2009) suggested that Titan might control the position of Saturn's magnetopause. The dayside magnetopause is typically found to exist inside of Titan's orbit except when Titan is at noon local time and its local pressure enhancement reduces the compressibility of the magnetosphere. *Wei et al.* [2009] suggests that the compressibility of the magnetosphere is reduced either by anchoring the magnetic field to the Titan ionosphere, mass-loading the flux tube, or the action of fast neutrals crossing field lines and transferring momentum from the subsonic magnetospheric plasma.

Near midnight Titan appears to facilitate tail reconnection by mass-loading of the flux tube thus causing additional field stretching [*Menietti et al.*, 2007; *Russell et al.*, 2008; *Wei et al.*, 2009]. Coupled studies of the Saturn magnetosphere with Titan have suggested that periodic signatures in the magnetosphere could be generated by Titan's interaction with centrifugal interchange instabilities [*Winglee et al.*, 2013]. Furthermore, *Menietti et al.* [2009] showed a clear dependence of the Saturn Kilometric Radiation (SKR) on Titan local time where

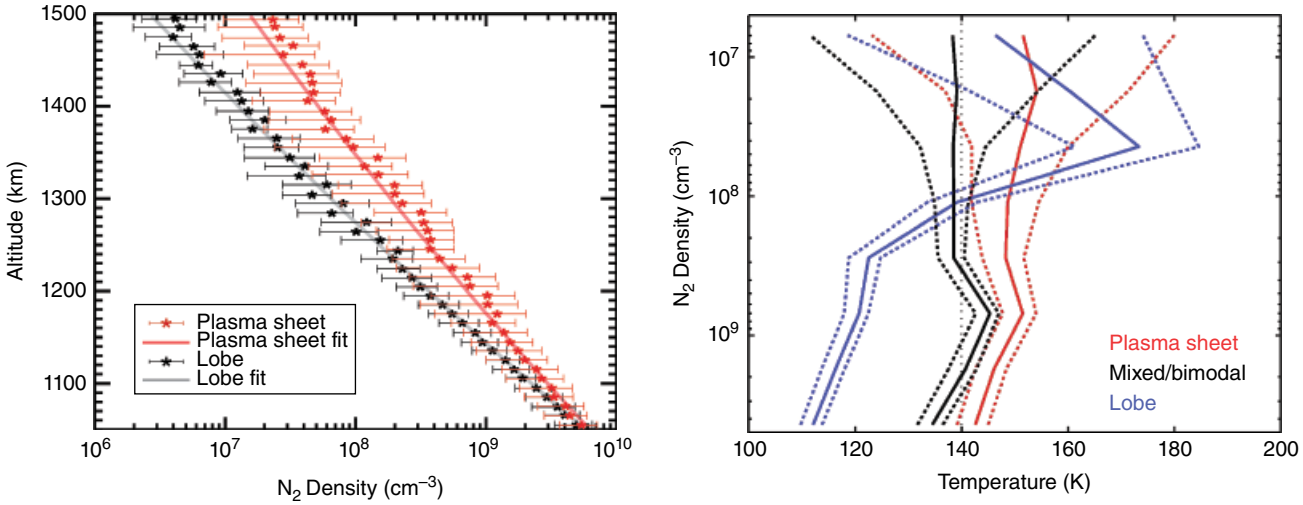

Figure 23.8 Cassini INMS observations of Titan's thermospheric neutral densities and temperatures related to changes in magnetospheric configuration. The left panel shows the differences in the neutral density structure [*Westlake et al.,* 2011], and the right shows the temperature structure [*Snowden et al.,* 2013a]. The temperature profiles shown in the left panel were obtained by fitting the INMS data with an isothermal density profile. The temperatures on the right are produced by top-down pressure integration of the density profiles.

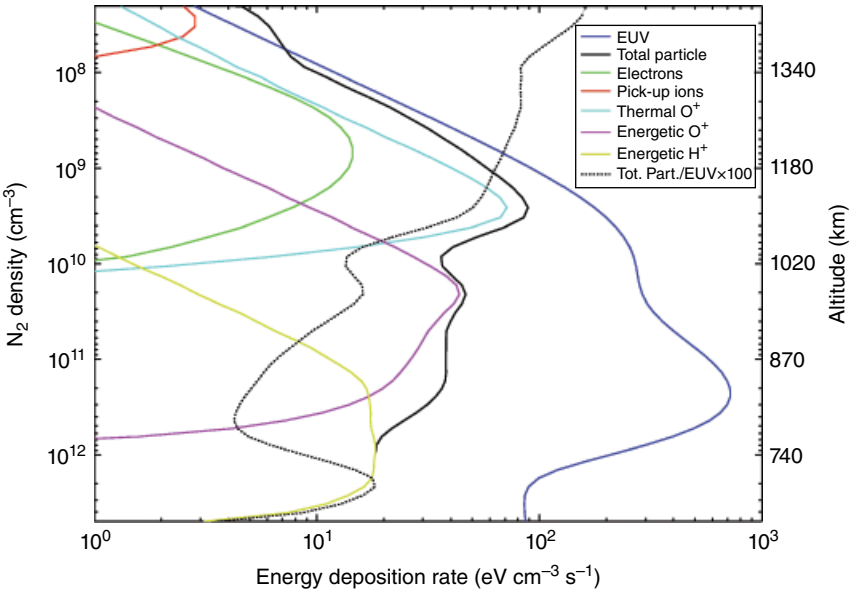

Figure 23.9 Energy deposition rates of various magnetospheric ions and electrons and diurnally averaged solar extreme ultraviolet (EUV) energy deposition rates assuming average EUV fluxes from 2007 [*Snowden et al.*, 2014].

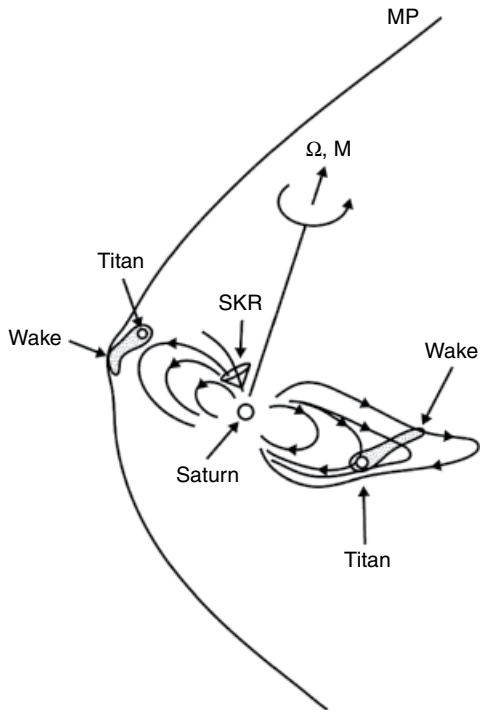

Figure 23.10 A schematic of how Titan's extensive wake influences Saturn's magnetopause and the Saturn Kilometric Radiation (SKR), a strong, periodic, low-frequency radio emission that emanates from Saturn, both on the dayside and nightside [from *Menietti et al.*, 2007].

the occurrence probability of SKR is increased when Titan is near midnight and a decrease when Titan is in the afternoon sector. These observations are supported by the modeling work of *Snowden et al.* [2011a, 2011b] that placed Titan's induced magnetosphere into Saturn's magnetosphere and self-consistently produced some of these features.

23.5. SUMMARY AND DISCUSSION

Titan's interaction with Saturn's magnetosphere is one of the more complex phenomena in our solar system, demonstrating a variety of configurations. Finally after more than 10 years in orbit around Saturn, we are beginning to understand the interaction, which is critical to the understanding of the evolution of its atmosphere. It is clear that the magnetosphere's geometry affects the details of the interaction, with the magnetopause and plasma sheet configurations determining the characteristics of Titan's ambient plasma. Moreover, the moon's convoluted, induced magnetosphere—capable of retaining fossilized magnetic fields—results in variable ion flux into and out of the atmosphere. Saturn's magnetosphere can drive enhanced ionization in Titan's ionosphere and likely also drives chemistry in the lower thermosphere and provides an external source of oxygen for Titan's lower atmosphere as well.

It is also clear that Titan affects Saturn's magnetosphere reducing the compressibility of the magnetosphere on the dayside and promoting reconnection on

the nightside. Titan's atmospheric escape acts as a source of material into the outer magnetosphere. Complex hydrocarbons and nitrogen-bearing compounds are produced through ion-neutral chemistry on field lines in Titan's ionosphere that are then carried into the magnetospheric flow. The ion composition and photoelectrons are clear tracers of these ionospheric sources of plasma. More controversial is the role of neutral escape in populating Saturn's magnetosphere [e.g., *Tucker and Johnson*, 2009; *Tucker et al.*, 2013]. It is clear that Titan's atmosphere is a source of neutral and ionized hydrogen throughout Saturn's magnetosphere [*Tseng et al.*, 2013], but this is not the case for heavier carbon or nitrogen containing species [*Smith et al.*, 2007; *Tucker and Johnson*, 2009]. Therefore, the role of the ambient plasma on the evolution of the Titan's atmosphere [e.g., *Johnson*, 2004] remains a critical problem.

ENA observations at Titan also reveal the dynamic nature of the moon-magnetosphere interaction. ENA images of the moon-magnetosphere interaction also hint at asymmetries in the structure of the interaction. Changes in the upstream flux of energetic particles result in large changes in energy deposition and ionization of atmospheric neutrals. These changes are clearly observed in the ENA observations at Titan and indicate potential asymmetries in the interaction. These images present a unique window into the moon-magnetosphere interaction that have not been available for other missions and will continue to be a wealth of information on the structure and dynamics of the Saturn-Titan interaction.

REFERENCES

Ågren, Karin, J.-E. Wahlund, Philippe Garnier, Ronan Modolo, J. Cui, M. Galand, and I. Müeller-Wodarg (2009), "On the ionospheric structure of Titan." *Planetary and Space Science 57*, no. 14: 1821–1827.

Ågren, K., et al. (2011), Detection of currents and associated electric fields in Titan's ionosphere from Cassini data, *J. Geophys. Res.*, *116*, A04313, doi:10.1029/2010JA016100.

Arridge, C. S., K. K. Khurana, C. T. Russell, D. J. Southwood, N. Achilleos, M. K. Dougherty, A. J. Coates, and H. K. Leinweber (2008), Warping of Saturn's magnetospheric and magnetotail current sheets, *J. Geophys. Res.*, *113*, A08217, doi:10.1029/2007JA012963.

Arridge, C. S., N. André, C. L. Bertucci, P. Garnier, C. M. Jackman, Z. Németh, F. J. Crary, et. al. (2011), Upstream of Saturn and Titan. *Space Science Reviews*, *162*, 25–83.

Bell, J. M., J. Westlake, and J. H. Waite Jr. (2011), Simulating the time-dependent response of Titan's upper atmosphere to periods of magnetospheric forcing, *Geophys. Res. Lett.*, *38*, L06202, doi:10.1029/2010GL046420.

Bertucci, C., F. M. Neubauer, K. Szego, J.-E. Wahlund, A. J. Coates, M. K. Dougherty, D. T. Young, and W. S. Kurth (2007), "Structure of Titan's mid-range magnetic tail: Cassini magnetometer observations during the T9 flyby." *Geophysical Research Letters 34*, no. 24.

Blanc, M., S. Bolton, J. Bradley, M. Burton, T. E. Cravens, I. Dandouras, M. K. Dougherty, et al. (2002), "Magnetospheric and plasma science with Cassini-Huygens." *Space science reviews 104*, no. 1–4: 253–346.

Brandt, Pontus C., K. Dialynas, I. Dandouras, D. G. Mitchell, P. Garnier, and S. M. Krimigis (2012), "The distribution of Titan's high-altitude (out to ~ 50,000 km) exosphere from energetic neutral atom (ENA) measurements by Cassini/INCA." *Planetary and Space Science 60*, no. 1: 107–114.

Coates, A. J., et al. (2012), Cassini in Titan's tail: CAPS observations of plasma escape, *J. Geophys. Res.*, *117*, A05324, doi:10.1029/2012JA017595.

Crary, F. J., B. A. Magee, K. Mandt, J. H. Waite, J. Westlake, and D. T. Young (2009), "Heavy ions, temperatures and winds in Titan's ionosphere: Combined Cassini CAPS and INMS observations." *Planetary and Space Science 57*, no. 14: 1847–1856.

Cravens, T. E, I. P. Robertson, J. H. Waite Jr., R. V. Yelle, W. T. Kasprzak, C. N. Keller, S. A. Ledvina, H. B. Niemann, J. G. Luhmann, R. L. McNutt, W.-H. Ip, V. De La Haye, I. Müeller-Wodarg, J.-E. Wahlund, V. A. Anicich, and V. Vuitton (2006), The composition of Titan's ionosphere, *Res. Lett.*, *33*, L07105, doi:10.1029/2005GL025575.

Cravens, T. E., I. P. Robertson, S. A. Ledvina, D. Mitchell, S. M. Krimigis, and J. H. Waite Jr. (2008), Energetic ion precipitation at Titan, *Geophys. Res. Lett.*, *35*, L03103, doi:10.1029/2007GL032451.

Cravens, T. E., I. P. Robertson, J. H. Waite, R. V. Yelle, V. Vuitton, A. J. Coates, J.-E. Wahlund, K. Agren, M. S. Richard, V. De La Haye, A. Wellbrock, and F. M. Neubauer, (2009), Model-data comparisons for Titan's nightside ionosphere. *Icarus*, *199*, 174–188, doi:10.1016/j.icarus.2008.09.005.

Cravens, T. E., M. Richard, Y.-J. Ma, C. Bertucci, J. Luhmann, S. Ledvina, I. P. Robertson, J.-E. Wahlund, K. Agren, J. Cui, I. Müeller-Wodarg, J. H. Waite, M. Dougherty, J. Bell, and D. Ulusen (2010), Dynamical and magnetic field time constants for Titan's ionosphere, Empirical estimates and comparisons with Venus *J. Geophys. Res.*, *115*, A08319, doi:10.1029/2009JA015050.

Cui, Jun, R. V. Yelle, Véronique Vuitton, J. H. Waite, W. T. Kasprzak, D. A. Gell, H. B. Niemann, et al. (2009), "Analysis of Titan's neutral upper atmosphere from Cassini Ion Neutral Mass Spectrometer measurements." *Icarus 200*, no. 2: 581–615.

Cui, J., R. V. Yelle, I. C. F. Müeller-Wodarg, P. P. Lavvas, and M. Galand (2011), The implications of the H2 variability in Titan's exosphere, *J. Geophys. Res.*, *116*, A11324, doi:10.1029/2011JA016808.

De La Haye, V., J. H. Waite, T. E. Cravens, S. W. Bougher, I. P. Robertson, and J. M. Bell (2008), Heating Titan's upper atmosphere. *J. Geophys. Res*, *113*, A11314, doi:10.1029/2008JA013078.

Dougherty, M. K., S. Kellock, D. J. Southwood, A. Balogh, E. J. Smith, B. T. Tsurutani, B. Gerlach, et al. (2004), "The Cassini magnetic field investigation." In *The Cassini-Huygens Mission*, pp. 331–383. Springer Netherlands.

Edberg, N. J., K. Ågren, J. E. Wahlund, M. W. Morooka, D. J. Andrews, S. W. H. Cowley, M. K. Dougherty, et al. (2011), Structured ionospheric outflow during the Cassini T55–T59 Titan flybys. *Planetary and Space Science*, *59*(8), 788–797.

Galand, M., R. V. Yelle, A. J. Coates, H. Backes, and J.-E. Wahlund (2006), Electron temperature of Titan's sunlit ionosphere. *Geophys. Res. Lett*, *33*, L21101, doi:10.1029/2006GL027488.

Galand, M., R. Yelle, J. Cui, J.-E. Wahlund, V. Vuitton, A. Wellbrock, and A. Coates (2010), Ionization sources in Titan's deep ionosphere, *J. Geophys. Res.*, *115*, A07312, doi:10.1029/2009JA015100.

Garnier, P., I. Dandouras, D. Toublanc, E. C. Roelof, P. C. Brandt, D. G. Mitchell, S. M. Krimigis, N. Krupp, D. C. Hamilton, and J-E. Wahlund (2010), "Statistical analysis of the energetic ion and ENA data for the Titan environment." *Planetary and Space Science 58*, no. 14: 1811–1822.

Gronoff, G., J. Lilensten, L. Desorgher, and E. Flückiger (2009), "Ionization processes in the atmosphere of Titan-I. Ionization in the whole atmosphere." *Astronomy & Astrophysics 506*, no. 2: 955–964.

Gurnett, D. A., W. S. Kurth, D. L. Kirchner, G. B. Hospodarsky, T. F. Averkamp, P. Zarka, A. Lecacheux, et al. (2004), "The Cassini radio and plasma wave investigation." In *The Cassini-Huygens Mission*, pp. 395–463, Springer Netherlands.

Hartle, R. E., E. C. Sittler, K. W. Ogilvie, J. D. Scudder, A. J. Lazarus, and S. K. Atreya (1982) "Titan's ion exosphere observed from Voyager 1." *Journal of Geophysical Research: Space Physics (1978–2012) 87, no. A3* (1982): 1383–1394.

Hartle, R. E., E. C. Sittler, F. M. Neubauer, R. E. Johnson, H. T. Smith, et al., (2006), "Initial interpretation of Titan plasma interaction as observed by the Cassini plasma spectrometer: Comparisons with Voyager 1," *Planetary and Space Science 54*, 1211–1224.

Hörst, S. M., V. Vuitton, and R. V. Yelle (2008), Origin of oxygen species in Titan's atmosphere, *J. Geophys. Res.*, *113*, E10006, doi:10.1029/2008JE003135.

Johnson, R.E. (2004), "The Magnetospheric Plasma-Driven Evolution of Satellite Atmospheres," *The Astrophysical Journal. 609*: L99–L102.

Kliore, A. J., A. F. Nagy, T. E. Cravens, M. S. Richard, and A. M. Rymer (2011), Unusual electron density profiles observed by Cassini radio occultations in Titan's ionosphere: Effects of enhanced magnetospheric electron precipitation? *J. Geophys. Res.*, *116*, A11318, doi:10.1029/2011JA016694.

Krimigis, S. M., D. G. Mitchell, D. C. Hamilton, S. Livi, J. Dandouras, S. Jaskulek, T. P. Armstrong. et al. (2004) "Magnetosphere imaging instrument (MIMI) on the Cassini mission to Saturn/Titan." In *The Cassini-Huygens Mission*, pp. 233–329. Springer Netherlands.

Lavvas, P., M. Galand, R. V. Yelle, A. N. Heays, B. R. Lewis, G. R. Lewis, and A. J. Coates (2011). Energy deposition and primary chemical products in Titan's upper atmosphere. *Icarus*, *213*, 233, doi:10.1016/j.icarus.2011.03.001.

Ledvina, S. A., T. E. Cravens, and K. Kecskeméty (2005), Ion distributions in Saturn's magnetosphere near Titan, *J. Geophys. Res.*, *110*, A06211, doi:10.1029/2004JA010771.

Ledvina, Stephen A., Stephen H. Brecht, and Thomas E. Cravens (2012), "The orientation of Titan's dayside ionosphere and its effects on Titan's plasma interaction." *Earth, planets and space 64*, no. 2: 207–230.

Ledvina, Stephen A., and Stephen H. Brecht (2012) "Consequences of negative ions for Titan's plasma interaction." *Geophysical Research Letters 39*, no. 20.

Luhmann, J. G., D. Ulusen, S. A. Ledvina, K. Mandt, B. Magee, J. H. Waite, J. Westlake, et al. "Investigating magnetospheric interaction effects on Titan's ionosphere with the Cassini orbiter Ion Neutral Mass Spectrometer, Langmuir Probe and magnetometer observations during targeted flybys." *Icarus 219*, no. 2: 534–555.

Lunine, Jonathan I., Yuk L. Yung, and Ralph D. Lorenz (1999), "On the volatile inventory of Titan from isotopic abundances in nitrogen and methane." *Planetary and Space Science 47*, no. 10: 1291–1303.

Ma, Y., A. F. Nagy, T. E. Cravens, I. V. Sokolov, K. C. Hansen, J.-E. Wahlund, F. J. Crary, A. J. Coates, and M. K. Dougherty (2006), Comparisons between MHD model calculations and observations of Cassini flybys of Titan, *J. Geophys. Res.*, *111*, A05207, doi:10.1029/2005JA011481.

Ma, Y. J., et al. (2009), Time-dependent global MHD simulations of Cassini T32 flyby: From magnetosphere to magnetosheath, *J. Geophys. Res.*, *114*, A03204, doi:10.1029/2008JA013676.

Ma, Y. J., C. T. Russell, A. F. Nagy, G. Tóth, M. K. Dougherty, A. Wellbrock, A. J. Coates, P. Garnier, J.-E. Wahlund, T. E. Cravens, M. S. Richard, and F. J. Crary (2011), The importance of thermal electron heating in Titan's ionosphere: Comparison with Cassini T34 flyby. *J. Geophys. Res*, *116*, A10213, doi:10.1029/2011JA016657.

Magee, B. A., J. H. Waite, K. E. Mandt, J. Westlake, J. Bell, and D. A. Gell (2009), INMS-derived composition of Titan's upper atmosphere: Analysis methods and model comparison. *Planetary and Space Science*, *57*(14), 1895–1916.

Mandt, Kathleen E., J. Hunter Waite, William Lewis, Brian Magee, Jared Bell, Jonathan Lunine, Olivier Mousis, and Daniel Cordier (2009), "Isotopic evolution of the major constituents of Titan's atmosphere based on Cassini data." *Planetary and Space Science 57*, no. 14: 1917–1930.

Menietti, J. D., B. Groene, T. F. Averkamp, G. B. Hospodarsky, W. S. Kurth, D. A. Gurnett, and P. Zarka (2007), Influence of Saturnian moons on Saturn kilometric radiation, *J. Geophys. Res.*, *112*, A08211, doi:10.1029/2007JA012331.

Michael, M., and R. E. Johnson (2005, "Energy deposition of pickup ions and heating of Titan's atmosphere." *Planetary and Space Science 53*, no. 14: 1510–1514.

Michael, M., R. E. Johnson, François Leblanc, M. Liu, J. G. Luhmann, and V. I. Shematovich (2005), "Ejection of nitrogen from Titan's atmosphere by magnetospheric ions and pick-up ions." *Icarus 175*, no. 1: 263–267.

Mitchell, D. G., P. C. Brandt, E. C. Roelof, J. Dandouras, S. M. Krimigis, and B. H. Mauk (2005), "Energetic neutral atom emissions from Titan interaction with Saturn's magnetosphere." *Science 308*, no. 5724: 989–992.

Müeller-Wodarg, I. C. F., R. V. Yelle, N. Borggren, and J. H. Waite (2006), Waves and horizontal structures in Titan's thermosphere. *J. Geophys. Res*, *111*, A12315, doi:10.1029/2006JA011961.

Müeller-Wodarg, I. C. F., R. V. Yelle, J. Cui, and J. H. Waite (2008), Horizontal structures and dynamics of Titan's thermosphere.*J. Geophys. Res*,*113*,E10005,doi:10.1029/2007JE003033.

Németh, Z., K. Szego, Z. Bebesi, G. Erdős, L. Foldy, A. Rymer, E. C. Sittler, A. J. Coates, and A. Wellbrock (2011), Ion distributions of different Kronian plasma regions, *J. Geophys. Res.*, *116*, A09212, doi:10.1029/2011JA016585.

Ness, Norman F., Mario H. Acuna, Kenneth W. Behannon, and Fritz M. Neubauer (1982), "The induced magnetosphere of Titan." *Journal of Geophysical Research: Space Physics (1978–2012) 87*, no. A3: 1369–1381.

Neubauer, F. M., D. A. Gurnett, J. D. Scudder, and R. E. Hartle (1984), Titan's magnetospheric interaction. *Saturn*, *1*, 760–787.

Neubauer, F. M., H. Backes, M. K. Dougherty, A. Wennmacher, C. T. Russell, A. Coates, D. Young, et al. (2006), "Titan's near magnetotail from magnetic field and electron plasma observations and modeling: Cassini flybys TA, TB, and T3." *Journal of Geophysical Research: Space Physics (1978–2012) 111*, no. A10.

Penz, T., H. Lammer, Yu N. Kulikov, and H. K. Biernat (2005), "The influence of the solar particle and radiation environment on Titan's atmosphere evolution." *Advances in Space Research 36*, no. 2: 241–250.

Richard, M. S., T. E. Cravens, I. P. Robertson, J. H. Waite, J.-E. Wahlund, F. J. Crary, and A. J. Coates (2011), "Energetics of Titan's ionosphere: Model comparisons with Cassini data." *Journal of Geophysical Research: Space Physics (1978–2012) 116*, no. A9.

Richard, M. S., T. E. Cravens, C. Wylie, D. Webb, Q. Chediak, R. Perryman, K. Mandt, et al. (2014), "An Empirical Approach to Modeling Ion Production Rates in Titan's Ionosphere I: Ion Production Rates on the Dayside and Globally." Journal of Geophysical Research: Space Physics.

Richard, M. S., et al. (2015), An empirical approach to modeling ion production rates in Titan's ionosphere II: Ion production rates on the nightside, *J. Geophys. Res. Space Physics*, *120*, doi:10.1002/2014JA020343.

Rosenqvist, Lisa, J-E. Wahlund, Karin ógren, Ronan Modolo, H. J. Opgenoorth, D. Strobel, I. Müeller-Wodarg, P. Garnier, and C. Bertucci (2009), "Titan ionospheric conductivities from Cassini measurements." *Planetary and Space Science 57*, no. 14: 1828–1833.

Russell, C. T., C. M. Jackman, H. Y. Wei, C. Bertucci, and M. K. Dougherty (2008), Titan's influence on Saturnian substorm occurrence, *Geophys. Res. Lett.*, *35*, L12105, doi:10.1029/2008GL034080.

Rymer, A. M., H. T. Smith, A. Wellbrock, A. J. Coates, and D. T. Young (2009), Discrete classification and electron energy spectra of Titan's varied magnetospheric environment, *Geophys. Res. Lett.*, *36*, L15109, doi:10.1029/2009GL039427.

Sergis, N., S. M. Krimigis, D. G. Mitchell, D. C. Hamilton, N. Krupp, B. H. Mauk, E. C. Roelof, and M. K. Dougherty (2009), Energetic particle pressure in Saturn's magnetosphere measured with the Magnetospheric Imaging Instrument on Cassini, *J. Geophys. Res.*, *114*, A02214, doi:10.1029/2008JA013774.

Shah, M. B., C. J. Latimer, E. C. Montenegro, O. J. Tucker, R. E. Johnson, and H. T. Smith (2009), "The Implantation and Interactions of O+ in Titan's Atmosphere: Laboratory Measurements of Collision-induced Dissociation of N2 and Modeling of Positive Ion Formation." *The Astrophysical Journal 703*, no. 2: 1947.

Sillanpää, I., E. Kallio, R. Jarvinen, and P. Janhunen (2007), "Oxygen ions at Titan's exobase in a Voyager 1–type interaction from a hybrid simulation." *Journal of Geophysical Research: Space Physics (1978–2012) 112*, no. A12.

Sillanpää, I., D. T. Young, F. Crary, M. Thomsen, D. Reisenfeld, J.-E. Wahlund, C. Bertucci, E. Kallio, R. Jarvinen, and P. Janhunen (2011), "Cassini Plasma Spectrometer and hybrid model study on Titans interaction: Effect of oxygen ions." *Journal of Geophysical Research: Space Physics (1978–2012) 116*, no. A7.

Sillanpää, I., and R.E. Johnson (2015), The role of ion-neutral collisions in Titan's magnetospheric interaction, Planetary and Space Science, doi:10.1016/j.pss.2015.01.007, in press.

Simon, S., G. Kleindienst, A. Boesswetter, T. Bagdonat, U. Motschmann, K.-H. Glassmeier, J. Schuele, C. Bertucci, and M. K. Dougherty (2007), Hybrid simulation of Titan's magnetic field signature during the Cassini T9 flyby, *Geophys. Res. Lett.*, *34*, L24S08, doi:10.1029/2007GL029967.

Simon, S., and Motschmann, U. (2009), Titan's induced magnetosphere under non-ideal upstream conditions: 3D multi-species hybrid simulations. *Planetary and Space Science*, *57*(14), 2001–2015.

Simon, S., A. Wennmacher, F. M. Neubauer, C. L. Bertucci, H. Kriegel, J. Saur, M. K. Dougherty, et al. (2010), Titan's highly dynamic magnetic environment: A systematic survey of Cassini magnetometer observations from flybys TA–T62. *Planetary and Space Science*, *58*(10), 1230–1251.

Simon, S., S. C. van Treeck, A. Wennmacher, J. Saur, F. M. Neubauer, C. L. Bertucci, and M. K. Dougherty (2013), Structure of Titan's induced magnetosphere under varying background magnetic field conditions: Survey of Cassini magnetometer data from flybys TA–T85, *J. Geophys. Res. Space Physics*, *118*, 1679–1699, doi:10.1002/jgra.50096.

Sittler, E. C., R. E. Hartle, A. F. Vinas, R. E. Johnson, H. T. Smith, and I. Mueller-Wodarg (2005), "Titan interaction with Saturn's magnetosphere: Voyager 1 results revisited." *Journal of Geophysical Research: Space Physics (1978–2012) 110*, no. A9.

Smith, H. T., D. G. Mitchell, R. E. Johnson, and C. P. Paranicas (2009), "Investigation of energetic proton penetration in Titan's atmosphere using the Cassini INCA instrument." *Planetary and Space Science 57*, no. 13: 1538–1546.

Smith, H. T., R. E. Johnson, E. C. Sittler, M. Shappirio, D. Reisenfeld, O. J. Tucker, M. Burger, F. J. Crary, D. J. McComas, and D. T. Young (2007), "Enceladus: The likely dominant nitrogen source in Saturn's magnetosphere." *Icarus 188*, no. 2: 356–366.

Smith, H. T., and A. M. Rymer (2014), An empirical model for the plasma environment along Titan's orbit based on Cassini plasma observations, *J. Geophys. Res. Space Physics*, *119*, 5674–5684, doi:10.1002/2014JA019872.

Snowden, D., R. Winglee, and A. Kidder (2011), "Titan at the edge: 1. Titan's interaction with Saturn's magnetosphere in the prenoon sector." *Journal of Geophysical Research: Space Physics (1978–2012) 116*, no. A8.

Snowden, D., R. Winglee, and A. Kidder (2011), Titan at the edge: 2. A global simulation of Titan exiting and reentering Saturn's magnetosphere at 13:16 Saturn local time, *J. Geophys. Res.*, *116*, A08230, doi:10.1029/2011JA016436.

Snowden, D., R. V. Yelle, J. Cui, J-E. Wahlund, N. J. T. Edberg, and K. ógren (2013), "The thermal structure of Titan's upper atmosphere, I: Temperature profiles from Cassini INMS observations." *Icarus 226*, no. 1: 552–582.

Snowden, D., R. V. Yelle, M. Galand, Andrew J. Coates, Anne Wellbrock, Geraint H. Jones, and P. Lavvas (2013), "Auroral electron precipitation and flux tube erosion in Titan's upper atmosphere." *Icarus 226*, no. 1: 186–204.

Snowden, D., and R. V. Yelle (2014), "The thermal structure of Titan's upper atmosphere, II: Energetics." *Icarus 228*: 64–77.

Snowden, D., and R. V. Yelle (2014), "The global precipitation of magnetospheric electrons into Titan's upper atmosphere." *Icarus 243*: 1–15.

Stevens, M. H., J. Gustin, J. M. Ajello, J. S. Evans, R. R. Meier, Kochenash, A. J., A. W. Stephan, A. I. F. Stewart, L. W. Esposito, W. E. Mcclintock, G. Holsclaw, E. T. Bradley, Lewis, B. R., and A. N. Heays (2011), The production of Titan's ultraviolet nitrogen airglow. *J. Geophys. Res.*, *116*, 05304, doi:10.1029/2010JA016284.

Thomsen, M. F., D. B. Reisenfeld, D. M. Delapp, R. L. Tokar, D. T. Young, F. J. Crary, E. C. Sittler, M. A. McGraw, and J. D. Williams (2010), "Survey of ion plasma parameters in Saturn's magnetosphere." *Journal of Geophysical Research: Space Physics (1978–2012) 115*, no. A10.

Tseng, W.-L., R. E. Johnson, and W.-H. Ip (2013), "The atomic hydrogen cloud in the saturnian system," *Planetary and Space Science 85*, 164–174.

Tucker, O. J., and R. E. Johnson (2009), Thermally driven atmospheric escape: Monte Carlo simulations for Titan's atmosphere, *Planet & Space Sci. 57*, 1889–1894.

Tucker, O. J., R. E. Johnson, J. I. Deighan, and A. N. Volkov (2013), "Diffusion and thermal escape of H2 from Titan's atmosphere: Monte Carlo Simulations," *Icarus 222*, 149–158.

Ulusen, D., J. G. Luhmann, Y-J. Ma, S. Ledvina, T. E. Cravens, K. Mandt, J. H. Waite, and J-E. Wahlund (2010), "Investigation of the force balance in the Titan ionosphere: Cassini T5 flyby model/data comparisons." *Icarus 210*, no. 2: 867–880.

Ulusen, D., J. G. Luhmann, Y. J. Ma, K. E. Mandt, J. H. Waite, M. K. Dougherty, Jan-Erik Wahlund, et al. (2012), "Comparisons of Cassini flybys of the Titan magnetospheric interaction with an MHD model: Evidence for organized behavior at high altitudes." *Icarus 217*, no. 1: 43–54.

Vigren, E., M. Galand R. V. Yelle, J. Cui, J.-E. Wahlund, K. ógren P. P. Lavvas, I. C. F. Müeller-Wodarg, D. F. Strobel, V. Vuitton, A. Bazin (2013), On the thermal electron balance in Titan's sunlit upper atmosphere. *Icarus 223*, 234–251, doi:10.1016/j.icarus.2012.12.010.

Vigren, E., M. Galand, R. V. Yelle, A. Wellbrock, A. J. Coates, D. Snowden, J. Cui, P. Lavvas, N. J. T. Edberg, O. Shebanits, J.-E. Wahlund, V. Vuitton, and K. Mandt (2015), Ionization balance in Titan's nightside ionosphere, *Icarus*, Volume *248*, 1 March, pages 539–546, ISSN 0019–1035, 10.1016/j.icarus.2014.11.012.

Waite Jr, J. H., W. S. Lewis, W. T. Kasprzak, V. G. Anicich, B. P. Block, Tom E. Cravens, G. G. Fletcher, et al. (2004), "The Cassini ion and neutral mass spectrometer (INMS) investigation." In *The Cassini-Huygens Mission*, pp. 113–231. Springer Netherlands.

Wei, H. Y., C. T. Russell, J.-E. Wahlund, M. K. Dougherty, C. Bertucci, R. Modolo, Y. J. Ma, and F. M. Neubauer (2007), Cold ionospheric plasma in Titan's magnetotail, *Geophys. Res. Lett.*, *34*, L24S06, doi:10.1029/2007GL030701.

Wei, H. Y., C. T. Russell, A. Wellbrock, M. K. Dougherty, and A. J. Coates (2009), Plasma environment at Titan's orbit with Titan present and absent, *Geophys. Res. Lett.*, *36*, L23202, doi:10.1029/2009GL041048.

Wei, H. Y., C. T. Russell, M. K. Dougherty, F. M. Neubauer, and Y. J. Ma (2010), Upper limits on Titan's magnetic moment and implications for its interior, *J. Geophys. Res.*, *115*, E10007, doi:10.1029/2009JE003538.

Wellbrock, A., A. J. Coates, I. Sillanpää, G. H. Jones, C. S. Arridge, G. R. Lewis, D. T. Young, F. J. Crary, and A. D. Aylward (2012), Cassini observations of ionospheric photoelectrons at large distances from Titan: Implications for Titan's exospheric environment and magnetic tail, *J. Geophys. Res.*, *117*, A03216, doi:10.1029/2011JA017113.

Westlake, J. H., J. M. Bell, J. H. Waite Jr., R. E. Johnson, J. G. Luhmann, K. E. Mandt, B. A. Magee, and A. M. Rymer (2011), Titan's thermospheric response to various plasma environments, *J. Geophys. Res.*, *116*, A03318, doi:10.1029/2010JA016251.

Westlake, J. H., et al. (2012), The observed composition of ions outflowing from Titan, *Geophys. Res. Lett.*, *39*, L19104, doi:10.1029/2012GL053079.

Winglee, R. M., A. Kidder, E. Harnett, N. Ifland, C. Paty, and D. Snowden (2013), "Generation of periodic signatures at Saturn through Titan's interaction with the centrifugal interchange instability." *Journal of Geophysical Research: Space Physics 118*, no. 7: 4253–4269.

Woodson, A. K., H. T. Smith, F. J. Crary, and R. E. Johnson (2015), Ion composition in Titan's exosphere via the Cassini Plasma Spectrometer I: T40 encounter, *J. Geophys. Res. Space Physics*, *120*, 212–234, doi:10.1002/2014JA020499.

Wulms, Veit, Joachim Saur, Darrell F. Strobel, Sven Simon, and Donald G. Mitchell (2010), "Energetic neutral atoms from Titan: Particle simulations in draped magnetic and electric fields." *Journal of Geophysical Research: Space Physics (1978–2012) 115*, no. A6.

Young, D. T., J. J. Berthelier, M. Blanc, J. L. Burch, A. J. Coates, R. Goldstein, M. Grande, et al. (2004), "Cassini plasma spectrometer investigation." In *The Cassini-Huygens Mission*, pp. 1–112. Springer Netherlands.

Part VI
The Unified Modeling of the Ionosphere and Magnetosphere at Other Planets and Moons in the Solar System

24

Magnetosphere-Ionosphere Coupling at Jupiter and Saturn

Thomas W. Hill

Video of Yosemite Talk, URL: http://dx.doi.org/10.15142/T3PK59

ABSTRACT

Some aspects of magnetosphere-ionosphere (M-I) coupling are universal from one planet to another, for example, the crucial role played by Birkeland (magnetic-field-aligned) currents that dynamically couple the collisionless magnetosphere to the collisional ionosphere. This chapter emphasizes the rotation-driven magnetospheres exemplified by Jupiter and Saturn, rather than the solar-wind-driven magnetospheres exemplified by Earth and Mercury. Rotational control of the magnetosphere is exerted through the agency of internal plasma sources provided by moons internal to the magnetosphere, primarily Io at Jupiter and Enceladus at Saturn. This chapter focuses on theoretical and numerical modeling studies of the most recently and completely observed rotation-driven magnetosphere, that of Saturn, by the Cassini orbiter spacecraft.

24.1. INTRODUCTION

The phrase "magnetosphere-ionosphere coupling" implies that there are two distinguishable regions, the magnetosphere (largely collisionless) and the ionosphere (largely collisional) that are separate but coupled. This excludes the induced magnetospheres of Venus and Mars because the magnetosphere and ionosphere are not distinguishable regions there. It includes the intrinsic magnetospheres of Mercury, Earth, Jupiter, Saturn, Uranus, and Neptune, where the solar wind is largely excluded from the ionosphere by an intrinsic planetary magnetic field.

Some features of M-I coupling are common to most planetary magnetospheres:

• Birkeland (magnetic-field-aligned) currents transmit electromagnetic stresses between the magnetosphere and the ionosphere, thereby coupling their convective ($\mathbf{E} \times \mathbf{B}$ drift) motions.

• Plasma can be exchanged between the two regions along magnetic-field lines, thereby coupling their chemical compositions.

• Birkeland currents, especially when upward, tend to produce bright auroral emissions and nonthermal radio emissions, making the ionosphere essentially a two-dimensional map of the three-dimensional magnetosphere (although reading this map is sometimes fraught with uncertainty and controversy).

There are, however, important differences from one planet to another. A useful classification scheme follows:

• Solar-wind-driven magnetospheres (Earth and Mercury), versus

• Rotation-driven magnetospheres (Jupiter and Saturn).

There is, in principle, a continuous spectrum spanning both types, but the most extensively studied planetary magnetospheres fall clearly at one end or the other of this spectrum, as listed above. *Brice and Ioannidis* [1970] elucidated the difference: A magnetosphere is solar-wind-driven if

Physics and Astronomy Department, Rice University, Houston, TX, USA

Magnetosphere-Ionosphere Coupling in the Solar System, Geophysical Monograph 222, First Edition.
Edited by Charles R. Chappell, Robert W. Schunk, Peter M. Banks, James L. Burch, and Richard M. Thorne.

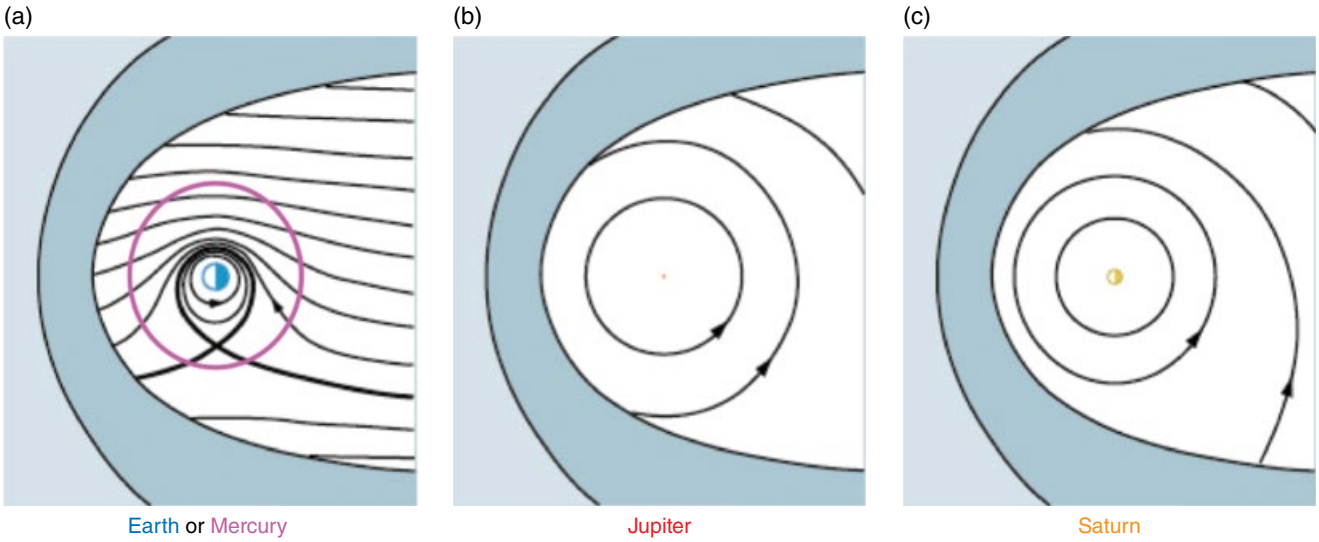

Figure 24.1 Schematic illustration of the plasmapause locations for Earth, Mercury, Jupiter, and Saturn. The size of the planet is scaled to the size of its magnetosphere, which is plotted on the same scale for all planets. At Earth, the plasmapause (heavy curve) lies between the planet and its magnetopause, leaving a large domain available for the return flow of solar-wind-driven convection. At Mercury, the plasmapause is well inside the planet and therefore irrelevant. At Jupiter and Saturn, the plasmapause is well outside the magnetopause and therefore leaves no room for a return flow of solar-wind-driven convection. Based on the idea introduced by *Brice and Ioannidis* [1970].

its plasmapause lies well inside its magnetopause. If not, it is (or at least may be) rotation driven.

The plasmapause [*Nishida*, 1966; *Brice*, 1967] is the topological boundary separating inner-magnetospheric flow, dominated by planetary rotation, from outer-magnetospheric flow, driven by the solar-wind interaction. Figure 24.1 shows equatorial cartoon views of the magnetospheres of Earth and Mercury (a), Jupiter (b), and Saturn (c), with the size of the planet scaled to that of its magnetosphere. In all panels, the equatorial flow is a simple superposition of corotational flow and a uniform Sunward return flow representing that imposed by the solar-wind interaction. In panel (a), the plasmapause is the heavy contour lying between Earth and its magnetopause; Mercury's theoretical plasmapause would lie well inside the planet and is therefore irrelevant. In the other two panels, the plasmapause lies well outside the magnetopause and therefore does not appear on the scale of the figure. The simple (and empirically correct) interpretation is that equatorial flow is dominated by partial corotation in the magnetospheres of Jupiter and Saturn, but by solar-wind-driven convection in those of Earth and Mercury.

The Brice-Ioannidis criterion is a necessary but not sufficient condition for a magnetosphere to be rotation driven. The other requirement is an internal source of plasma that can tap rotational energy from the planet and invest it in driving magnetospheric phenomena. We are fortunate in that Jupiter and Saturn, the two most thoroughly studied of the giant planets, meet this second requirement in abundance. Jupiter's internal plasma source is dominated by the sulfur-dioxide volcanic plumes of the satellite Io at $L \approx 6$, and Saturn's is dominated by the water vapor and ice geyser plumes of the satellite Enceladus at $L \approx 4$. (In this chapter, L is simply r/R_P where r is equatorial distance from the rotation axis and R_P is the planetary radius, R_J for Jupiter and R_S for Saturn.) The outward transport of this internally generated plasma extracts rotational energy from the planetary atmosphere at thermosphere-ionosphere levels [*Dessler*, 1980; *Eviatar and Siscoe*, 1980]. The associated flows of mass and energy are reviewed by *Bagenal and Delamere* [2011] and *Delamere et al.* [2015a].

We have performed numerical simulations of the centrifugally driven interchange process using the Rice Convection Model (RCM). Unlike previous RCM Jupiter simulations [*Yang et al.*, 1994; *Pontius et al.*, 1998; *Wu et al.*, 2007], the RCM Saturn simulations include a continuously active, radially extended source of cool dense water-group (W^+) plasma based on the Enceladus neutral-cloud model of *Johnson et al.* [2006]. The resulting $\mathbf{E} \times \mathbf{B}$ convection takes the form of multiple narrow outflow fingers of cool dense plasma from the imposed internal plasma source, interspersed with even narrower (and hence faster) inflow fingers of hot tenuous plasma from a source external to our modeling region. The alternating inflow-outflow finger structure was present in the earlier Jupiter simulations, but the width disparity between

inflow and outflow fingers is a new feature produced in the Saturn simulations by the presence of an active distributed plasma source. The width disparity is confirmed by observations of the Cassini Plasma Spectrometer (CAPS) as shown by *Chen et al*. [2010].

The RCM logic and numerical procedures are described by *Liu et al*. [2010] and *Liu and Hill* [2012]. Our Saturn simulations to date have spanned the inner magnetosphere ($2 < L < 12$), where the magnetic field is nearly dipolar and nearly time independent. The RCM assumes electrostatic M-I coupling and thus applies to time scales much longer than magnetohydrodynamic (MHD) wave transit times (a few minutes or less). The coupling is enforced by calculating the Birkeland current density produced by the divergence of the magnetospheric current, mapping that Birkeland current down to the ionosphere, and matching it there to an equal and opposite divergence of the ionospheric conduction current. The latter provides the source term of an ionospheric equation for the electrostatic potential Φ.

The planetary ionosphere is represented in the RCM by a thin spherical shell having Pedersen conductance Σ_P and Hall conductance Σ_H. In Saturn simulations to date we have set the physical Σ_P = constant ~ 6 S and the physical $\Sigma_H = 0$, for lack of definitive information to the contrary. The RCM code does, however, include an effective Σ_P* to represent implicitly the pick-up current of newly injected magnetospheric ions and an effective Σ_H* to represent implicitly the Coriolis acceleration of those ions. These effective conductances are employed for numerical stability reasons, as explained in detail by *Liu et al*. [2010].

The simulations of *Liu et al*. [2010] included the effects of the cool dense plasma from the internal source, under a cold-plasma approximation that included the rotation-driven centrifugal, Coriolis, and pick-up currents but not the gradient/curvature drift currents. This approach was generalized by *Liu and Hill* [2012], who included the gradient/curvature drift of the cool plasma and found a ~50% enhancement of the linear growth rate and of the ultimate nonlinear velocity of the interchange cells compared to the cold-plasma approximation. The results shown below are based on the formulation of *Liu and Hill* [2012], as used in the simulation shown in Figure 3c of that paper.

24.2. IONOSPHERIC SIGNATURES OF M-I COUPLING AT SATURN: BIRKELAND CURRENTS

Like the convection pattern, the Birkeland current pattern also exhibits a finger-like structure in the RCM simulations. Figure 24.2a shows the upward Birkeland current density just above Saturn's ionosphere as computed in the RCM simulation of *Liu and Hill* [2012; their Figure 3c] in a late quasi-steady stage of the simulation. Upward currents flow at the boundaries between outflow and inflow channels wherever the inflow channel precedes the outflow channel in the sense of corotation; it is selected for display here because it is the upward current that is most likely to produce detectable ultraviolet (UV) auroral emissions [*Knight*, 1973; *Cowley et al*., 2004]. The finger structure is evident, with maximum current density occurring at the tips of the fingers at the high-latitude simulation boundary ($L = 12$).

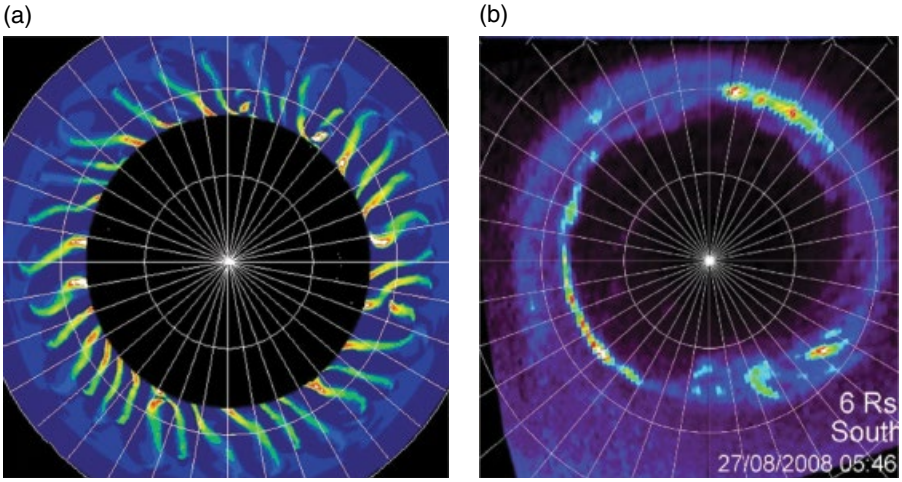

Figure 24.2 Fine structure of upward Birkeland current density in an RCM Saturn simulation (a) and of auroral luminosity in a Cassini UVIS image (b) extracted from Figure 4b of *Grodent et al*. [2011]. White circles mark colatitudes of 10°, 20°, and 30° (dipole $L \approx 33$, ≈ 8.5, and $\equiv 4$, respectively) and longitude sectors are 10° wide. Auroral luminosity is, of course, not the same as upward Birkeland current density, so the correspondence in scale size is merely suggestive, not definitive.

Similar fine-scale longitudinal structure has been reported in Cassini high-latitude magnetometer observations of Birkeland current signatures [*Talboys et al*., 2009a, 2009b; *Bunce et al*., 2010]. These observed Birkeland current structures have previously been attributed to Kelvin-Helmholtz vortices observed at Saturn's magnetopause [*Masters et al*., 2009, 2010; *Delamere et al*., 2013, 2015b] and modeled by *Delamere et al.* [2011] and *Walker et al*. [2011]. Note, however, that the latitude of the observed auroral oval maps to $L \sim 10$–15, well inside the typical dayside magnetopause at $L \sim 20$–25. Thus, we propose an alternative interpretation, that the fine structure of the observed Birkeland currents is attributable, at least in part, to the finger-like structure of centrifugally driven interchange convection.

The most visually compelling signature of the Birkeland current structure is the auroral structure that it produces. High-resolution imaging by the Cassini Ultraviolet Imaging Spectrograph (UVIS) does, in fact, reveal a similar fine structure, as illustrated in Figure 24.2b, extracted from Figure 4b of *Grodent et al*. [2011]. The correspondence between modeled and observed structures is encouraging. The azimuthal wave number m, as in $\Phi \propto \exp(im\varphi)$, lies in the range $m \sim 30$–40 (~10° peak-to-peak separation) for both simulated and observed structures. This is a persistent feature of the RCM Saturn simulations, with a finger spacing that is physically determined by the radial width scale of the imposed plasma source distribution [*Wu et al*., 2007].

The comparison shown in Figure 24.2 is not direct in a quantitative sense because Birkeland current density is not the same as UV auroral brightness; the latter is a monotonic but nonlinear function of the former. In particular, the *Knight* [1973] theory imposes a minimum threshold upward Birkeland current density for production of detectable auroral emissions. The Knight theory has been successfully implemented for the parameters appropriate to the large-scale Saturnian auroral oval [*Cowley et al*., 2004], and we look forward to applying this implementation to the smaller-scale current structures present in the RCM simulations. This will presumably improve the comparison by suppressing the lower latitude tails of the finger structures (green in Figure 24.2a). A Knight-theory algorithm has already been implemented and tested in the RCM code for Earth applications [e.g., *Song*, 2010].

The larger scale local-time (LT) asymmetries of Saturn's observed auroral brightness are well documented not only in Figure 24.2b here but also in previous Hubble Space Telescope (HST) and UVIS observations [*Kurth et al*., 2009; *Carbary*, 2013]. These larger scale LT asymmetries are not included in existing RCM simulation results, by virtue of our simplifying assumptions, but may be included to some extent in future work by planned inclusion of known LT asymmetries of magnetic-field structure and ionospheric conductance. In computing the large-scale $\mathbf{E} \times \mathbf{B}$ flow, the RCM neglects the field-aligned electric potential drop which, although it is responsible for the bright auroral emissions, is a small perturbation to the underlying $\mathbf{E} \times \mathbf{B}$ flow at both Jupiter [*Ray et al*., 2012] and Saturn [*Ray et al*., 2013].

24.3. MAGNETOSPHERIC SIGNATURES OF M-I COUPLING AT SATURN: INJECTION-DISPERSION STRUCTURES

The clearest magnetospheric signature of interchange transport at Saturn is the multitude of hot plasma injection-dispersion structures that are observed on every Cassini pass through the inner magnetosphere ($5 <\sim L <\sim 10$) [*André et al*., 2005; *Burch et al*., 2005; *Hill et al*., 2005; *Mauk et al*., 2005; *André et al*., 2007; *Chen and Hill*, 2008; *Rymer et al*., 2009; *Chen et al*., 2010; *Thomsen*, 2013; *Thomsen et al*., 2014]. These signatures are produced by centrifugally driven interchange injection combined with gradient-curvature drift dispersion of the hot plasma inflow fingers, as illustrated schematically in Figure 24.3. The cool dense plasma flows outward with no visible energy dispersion, while the hot tenuous plasma flows inward and exhibits obvious energy dispersion if and when it reaches the inner magnetosphere (Figure 24.4). Similar injection structures were inferred from Galileo particle and field observations near the Io plasma torus in Jupiter's magnetosphere [*Bolton et al*., 1997; *Kivelson et al*., 1997; *Mauk et al*., 1997; *Thorne et al*., 1997], but the characteristic energy-time dispersion signatures were not evident there because of the much slower gradient-curvature drift speed for particles of a given energy at a given L at Jupiter compared to Saturn. A similar drift dispersion signature is, however, quite evident in substorm-related injections of magnetotail plasma into the geosynchronous orbit region of Earth's magnetosphere [e.g., *DeForest and McIlwain*, 1971].

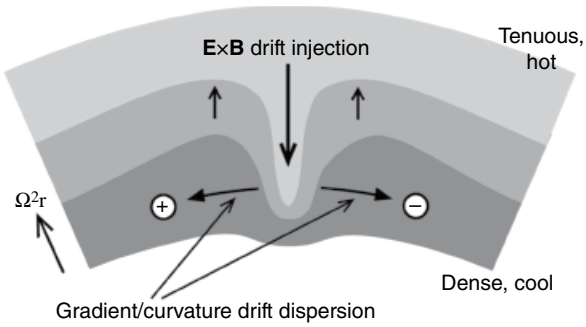

Figure 24.3 Schematic depiction of centrifugally driven interchange convection and gradient-curvature drift dispersion at Saturn, reproduced from Figure 1 of *Hill et al*. [2005].

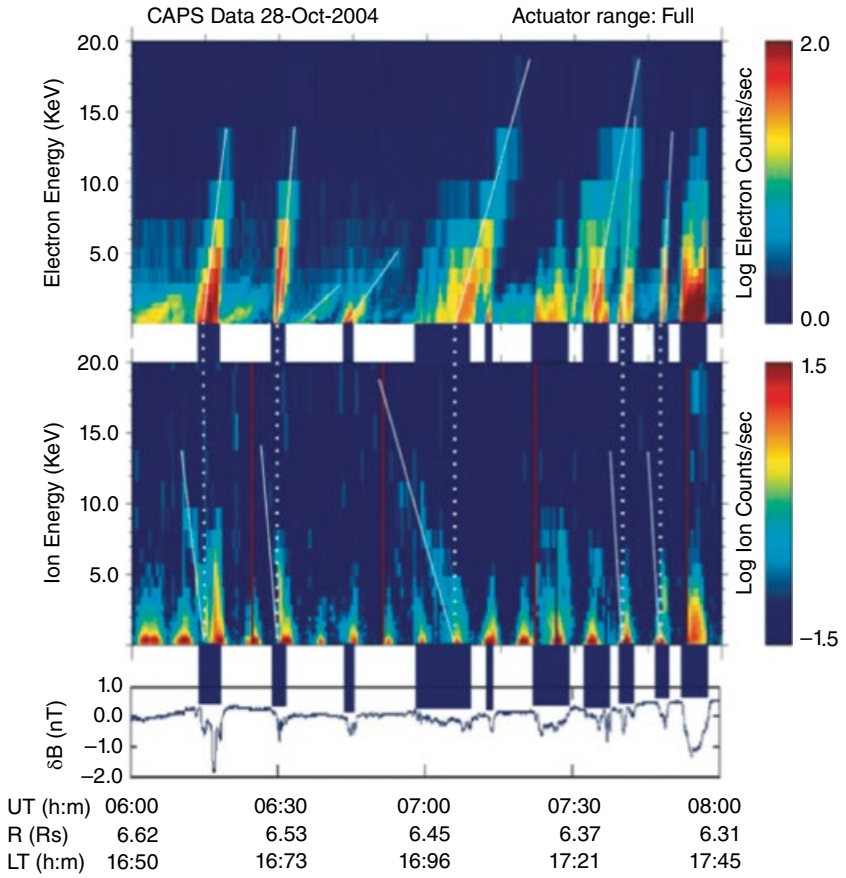

Figure 24.4 CAPS electron (top panel) and W^+ ion (middle panel) count-rate spectrograms, and associated diamagnetic perturbations from Cassini MAG (bottom panel), reproduced from Figure 2 of *Hill et al.* [2005]. The two legs of the V-shaped dispersion signatures (light white lines) share a common apex (dashed white vertical lines) located within the associated diamagnetic perturbations. Since this early Cassini orbit (October 2004), it has been established that similar injection-dispersion structures are observed on every pass of Cassini through Saturn's inner magnetosphere ($5 <\sim L <\sim 10$).

RCM simulations exhibit the same finger-like interchange mode structure that is inferred from the Cassini observations, with about the right azimuthal scale size. In particular, the RCM results agree with the observed (but not predicted) fact that the hot inflow fingers are narrower, and hence faster in their radial motion, than the cool outflow fingers, by an average factor ~10 [*Chen and Hill*, 2008; *Chen et al.*, 2010]. Earlier RCM simulations for Jupiter did not display this width disparity, probably because they solved an initial value problem without a continuously active radially distributed plasma source.

Previous RCM Saturn simulations [*Liu et al.*, 2010; *Liu and Hill*, 2012] included the effects of the cool dense plasma from internal sources, but not of the hot tenuous plasma from external sources. Thus, they could not attempt to simulate the observed energy-time dispersion structures produced by the hot inflow fingers. To simulate these structures, we have now installed a realistic source of hot tenuous plasma at our outer ($L = 12$) simulation boundary and tracked the motions of these particles within several discrete energy-invariant channels [*Liu*, 2013; *Hill et al.*, paper in preparation, 2015]. The hot plasma source is specified in accordance with CAPS measurements made in the region $L >\sim 12$, including the water-group positive ion densities and temperatures reported by *Thomsen et al.* [2010] and the hot and cold electron densities and temperatures reported by *Schippers et al.* [2008]. This hot plasma is convected inward by the inflow fingers that arise as a necessary consequence of the outflow fingers driven by the internal source of cool dense plasma. The addition of this hot tenuous plasma does not materially affect the convection system in our region of interest, which is still driven by the cool dense plasma from interior sources, because the gradient-curvature drift current carried by the hot plasma is a small perturbation to the centrifugal plus gradient-curvature drift current carried by the cool plasma.

When plotted in a linear-energy versus linear-time format, the observed particle spectrograms (e.g., Figure 24.4) consistently display a V-shaped dispersion curve, with electrons forming the right half of the V and W^+ ions (when detectable) forming the symmetrical left half [*Hill et al.*, 2005]. This is because the gradient-curvature drift is westward for electrons, eastward for positive ions, and proportional to energy, and the V-shaped longitudinal dispersion structure rotates quickly past the spacecraft, which is relatively stationary in L for the duration of the event. The apex of the V is located within a narrow density cavity in the cool background plasma [*Burch et al.*, 2005]. This density cavity in the cool plasma is associated with a diamagnetic field perturbation, which is negative when the spacecraft is at relatively high latitudes, as it was during the interval shown in Figure 24.4 (bottom panel), where the hot plasma dominates the plasma pressure but is positive when the spacecraft is near the equatorial plane [*André et al.*, 2007], where the cool background plasma dominates the plasma pressure.

Figure 24.5 shows, for one longitude quadrant, the outflow channels from the interior source (left panel) and the complementary inflow channels from the exterior source (right panel), at a particular time step late in the simulation. The color scale denotes the flux-tube ion content per unit magnetic flux, $\eta = \int nds/B$. The two panels have the same spatial scale but widely differing color scales for η because the hot plasma is far less dense than the cool plasma. The black contours are instantaneous equipotential contours, or $\mathbf{E}\times\mathbf{B}$ drift streamlines. The right panel shows results for injected W^+ ions that attain a kinetic energy of 8.5 kiloelectron-volt (keV) at $L = 6.5$; the result is similar for other ion energy invariants. The motion visible in this plot is dominated by $\mathbf{E}\times\mathbf{B}$ drift within the particle energy range of interest.

Figure 24.6 shows equatorial paths of test particles in eight energy-invariant ranges (four for electrons and four for W^+ ions). The heavy quasicircular arc with arrowheads in the left panel is the path of the Cassini spacecraft in L-ϕ coordinates for a particular interval containing a clear injection-dispersion signature in CAPS data that was selected for analysis. The inset on the right zooms in on the region near $L = 6.5$, showing the longitude separation of particles with different energy invariants resulting from their cumulative gradient-curvature drift since their injection at a common longitude at $L = 12$. Outside $L \sim 8$, the motion of all tracked particles is dominated by their common inward $\mathbf{E}\times\mathbf{B}$ drift, which was persistent for many hours in this case (a selection criterion for this example). The gradient-curvature drift dispersion is clearly evident at $L = 6.5$, the nearly constant radial distance of the spacecraft during this interval.

These longitude displacements, converted to time displacements along the Cassini track, are plotted for different particle energy invariants in Figure 24.7 in the two left panels (electrons top and W^+ ions bottom).

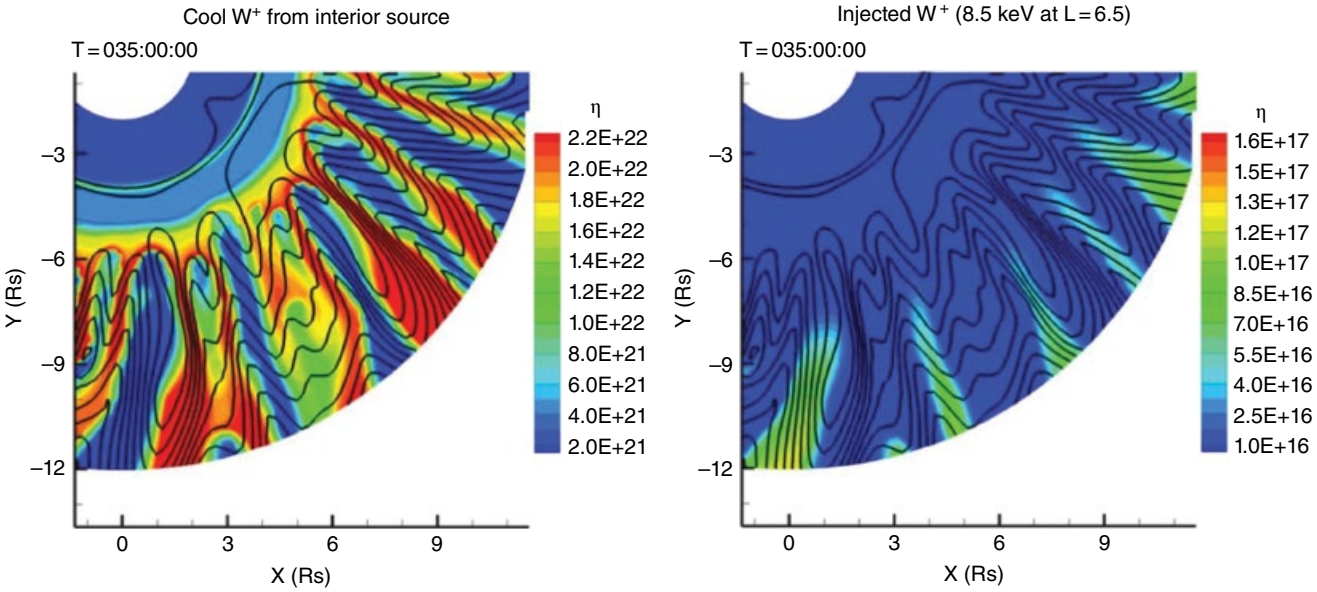

Figure 24.5 One quadrant of longitude is shown at a time step late in an RCM simulation for Saturn. The color bar shows the W^+ ion content per unit magnetic flux, $\eta = \int nds/B$, for cool dense W^+ ions flowing outward from an interior source (left panel) and for hot W^+ ions flowing inward from an external source (right panel). Note the complementarity of the two flow patterns, and note the wide difference between the color bars for the two panels. The black contours are instantaneous electrostatic potential contours = instantaneous **E**×**B** flow streamlines.

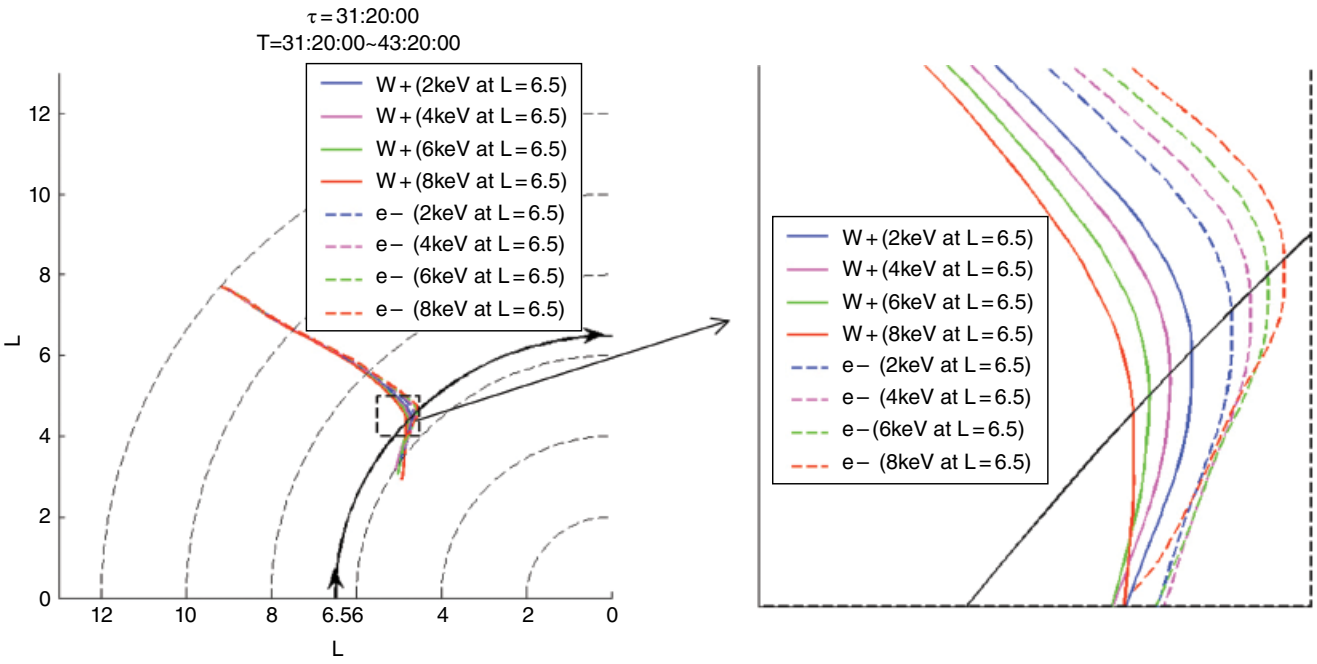

Figure 24.6 Computed trajectories of test particles in time-dependent RCM-simulated fields, in four relevant ranges of the energy invariant corresponding to the stated particle energies at L = 6.5, for electrons (colored dashed lines) and W^+ ions (colored solid lines). All particles share a common injection location and time at L = 12, the outer RCM boundary. The gradient-curvature drift dispersion (inset panel on the right) maximizes for these particles near L = 6.5, the approximately constant distance of Cassini (black solid line) during a particular CAPS-observed dispersion structure selected for comparison in Figure 24.7 below.

The points are color coded with the energies that the particles attain through adiabatic transport from $L=12$ to $L=6.5$. For comparison, the two right panels show observed electron (top) and W^+ (bottom) energy-time dispersion structures observed by CAPS near 06:15 UT on 28 October 2004 (the first of the five structures marked by thin white lines in Figure 24.4 above). The simulated (left panels) and observed (right panels) structures are plotted on the same energy scale and the same time scale for easy comparison. (The time axis on the simulated panels shows elapsed time since the particles' injections at a common injection point at $L=12$ at a common time defined as $T=0$ in the simulation, but both left and right panels span the same 30-min time interval.) Like the observed dispersion curves, the simulated dispersion curves form an almost symmetrical V shape, with W^+ ions forming the left leg of the V and electrons the right leg. The simulated Vs are not perfectly symmetrical because particles with different energy invariants have experienced slightly different $\mathbf{E}\times\mathbf{B}$ drift histories during the course of their inflow from $L=12$ to $L=6.5$, but this slight asymmetry is not discernible on the scale of the figure.

This case demonstrates that the RCM can successfully simulate the production of a typical CAPS-observed injection-dispersion event in Saturn's inner magnetosphere. It is important to note, however, that this "successful" case was unusual among the many test-particle simulations that were attempted, using a trial-and-error process. Most of the injection longitudes and times that were attempted at $L=12$ (the outer RCM boundary) did not transport hot particles coherently inward to $L\sim$6-7 where their gradient-curvature dispersion becomes evident. This is either because most particles injected at $L=12$ drift from their inflow channel into an adjacent outflow channel before reaching the inner magnetosphere, or because the inflow-outflow channel structure itself changes chaotically in time during the inward transit. Physically, we conclude that the many injection-dispersion events observed by CAPS in the inner magnetosphere represent only a small subset of the potential injections from the outer magnetosphere.

24.4. FUTURE WORK

In the near future, we plan to convert the simulated upward Birkeland current patterns (e.g., Figure 24.2a) into patterns of the expected UV auroral brightness, using algorithms developed by *Cowley et al.* [2004], to provide a more definitive comparison with observed brightness patterns (e.g., Figure 24.2b).

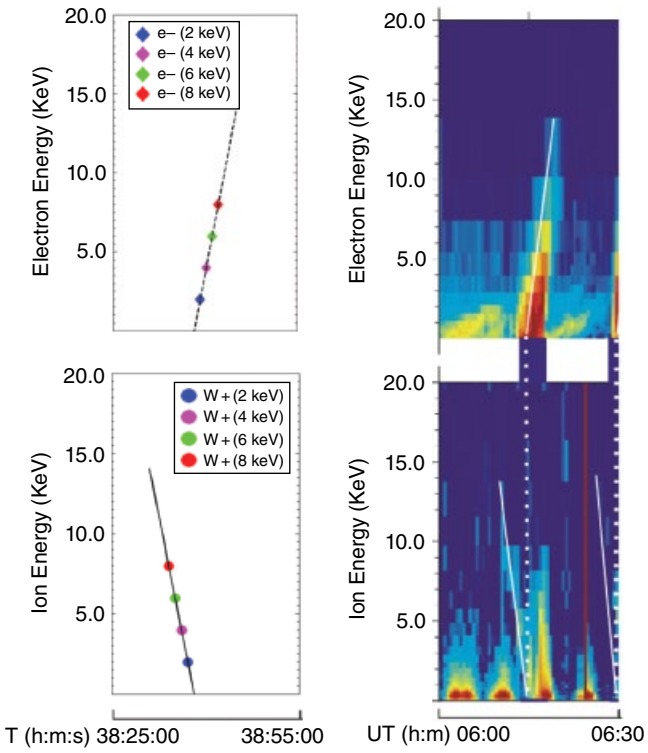

Figure 24.7 Comparison of RCM-simulated (left two panels) and CAPS-observed (right two panels) spectrograms for electrons (top two panels) and W^+ ions (bottom two panels) for a particular observed event selected for comparison. The simulation results are derived from Figure 24.6 above, and the observed results are extracted from Figure 24.4 above. All panels share the same (linear) energy scale and the same (linear) time scale.

On a longer time scale, we plan to incorporate the observed non-dipole distortions of Saturn's magnetic field that become important beyond $L \sim 12$, as well as the expected diurnal asymmetry of the ionospheric conductance. These patterns are fixed in solar local time, and will be represented by time-variable retrograde rotating patterns in the corotating reference frame in which the RCM simulations are carried out. This generalization, although complicated, is perfectly feasible using existing RCM algorithms that have been tested extensively at Earth. This improvement will roughly double the range of L that we are able to simulate reliably, out to the vicinity of the day side magnetopause, typically at $L \sim 20$–25. It will also enable us to investigate, for the first time, the complex interplay between the corotating longitudinal structure of the inner magnetosphere and the local-time-fixed structure of the outer magnetosphere. This interplay may contribute, in unknown ways, to the observed time-variable modulation period of the Saturn Kilometric Radiation (SKR) and of many related magnetospheric phenomena [*Carbary and Mitchell*, 2013, and references therein].

24.5. IMPLICATIONS FOR COMPARATIVE MAGNETOSPHERIC STUDIES

The basic physics of electrodynamic M-I coupling through Birkeland currents is universal from one magnetized planet to another, provided the planet also has a conducting ionosphere. The detailed results of this process, however, differ widely from one planet to another, because they are sensitive to the planetary rotation rate and to the presence and distribution of significant plasma sources interior to the magnetosphere. At Jupiter, the dominant plasma source is dissociation and ionization of volcanic SO_2 ejecta in the orbital vicinity of Io at $L \approx 6$. At Saturn, it is ionization of water-group molecules ejected from the cryovolcanic geysers of Enceladus at $L \approx 4$, although the ionization occurs farther out, in the range $5 <\sim L <\sim 10$, owing to the paucity of ionizing electrons at $L \approx 4$. The spatial overlap of the plasma source region and the plasma interchange transport region has novel consequences at Saturn, including the large disparity between the azimuthal widths of the outflow versus inflow sectors (e.g., Figures 24.4 and 24.5). At Earth, by contrast, the dominant plasma sources are injection from the solar wind and outflow from the ionosphere.

Because of the differing plasma source locations and the differing importance of rotational effects, the criterion for interchange (in)stability differs between Jupiter and Saturn, on the one hand, and Earth on the other hand. At Jupiter and Saturn, the relevant parameter is the radial gradient of the flux-tube mass content $m_i\eta = m_i \int nds/B$, where m_i is the average ion mass. The radial mass distribution is born unstable ($d\eta/dL < 0$ outside the peak of η) by virtue of the internal plasma sources. At Earth, the relevant parameter is instead the radial gradient of the flux-tube entropy content $pV^{5/3}$, where p is the plasma pressure (assumed isotropic and hence constant along a field line) and V is the flux-tube volume per unit magnetic flux ($\propto L^4$ in a dipole field). To the extent that the plasma source is external (the solar wind), the plasma distribution is born stable against interchange on average, but the most interesting dynamical events (substorms, sawtooth events, and storms) apparently occur when this stable gradient is locally and temporarily reversed [e.g., *Sazykin et al.*, 2002; *Lemon et al.*, 2004; *Yang et al.*, 2008; *Wolf et al.*, 2012; *Yang et al.*, 2014]. Despite the differences from planet to planet, interchange motions regulated by M-I coupling provide an important radial transport mechanism in all three of these planetary magnetospheres.

ACKNOWLEDGMENTS

Financial support was provided by National Aeronautics and Space Administration (NASA) grant NNX09AH99G to Rice University and by NASA JPL

contract 1243218 to the Southwest Research Institute. I am indebted to Rice colleagues X. Liu, S. Sazykin, and R. A. Wolf for their important contributions to the work reported here.

REFERENCES

André, N., M. K. Dougherty, C. T. Russell, J. S. Leisner, and K. K. Khurana (2005), Dynamics of Saturnian inner magnetosphere: First inferences from the Cassini magnetometers about smallscale plasma transport in the magnetosphere, *Geophys. Res. Lett*., *32*, L14S06, doi:10.1029/2005GL022643.

André, N., et al. (2007), Magnetic signatures of plasma-depleted flux tubes in the Saturnian inner magnetosphere, *Geophys. Res. Lett.*, *34*, L14108, doi:10.1029/2007GL030374.

Bagenal, F., and P. A. Delamere (2011), Flow of mass and energy in the magnetospheres of Jupiter and Saturn, *J. Geophys. Res. (Space Physics)*, *116*, A05, 209.

Bolton, S. J., R. M. Thorne, D. A. Gurnett, W. S. Kurth, and D. J. Williams (1997), Enhanced whistler-mode emissions: Signatures of interchange motion in the Io plasma torus, *Geophys. Res. Lett.*, *24*, 2123.

Brice, N. M. (1967), Bulk motion of the magnetosphere, *J. Geophys. Res.*, *72*, 5193–5211.

Brice, N. M., and G. A. Ioannidis (1970), The magnetospheres of Jupiter and Earth, *Icarus*, *12*, 173–183.

Bunce, E. J., et al. (2010), Extraordinary field-aligned current signatures in Saturn's high-altitude magnetosphere: Analysis of Cassini data during Revolution 89, *J. Geophys. Res.*, *115*, A10238, doi:10.1029/2010JA015612.

Burch, J. L., J. Goldstein, T. W. Hill, D. T. Young, F. J. Crary, A. J. Coates, N. André, W. S. Kurth, and E. C. Sittler, Jr. (2005), Properties of local plasma injections in Saturn's magnetosphere, *Geophys. Res. Lett*., *32*, L14S02, doi:10.1029/2005GL022611.

Carbary, J. F. (2013), Longitude dependences of Saturn's ultraviolet aurora, *Geophys. Res. Lett.*, *40*, 1902–1906, doi:10.1002/grl.50430.

Carbary, J. F., and D. G. Mitchell (2013), Periodicities in Saturn's Magnetosphere, *Rev. Geophys.*, *51*, 1–30, doi:10.1002/rog.20006.

Chen, Y., and T. W. Hill (2008), Statistical analysis of injection/dispersion events in Saturn's inner magnetosphere, *J. Geophys. Res.*, *113*, A07215, doi:10.1029/2008JA013166.

Chen, Y., T. W. Hill, A. M. Rymer, and R. J. Wilson (2010), Rate of radial transport of plasma in Saturn's inner magnetosphere, *J. Geophys. Res.*, *115*, A10211, doi:10.1029/2010JA015412.

Cowley, S. W. H., E. J. Bunce, and J. M. O'Rourke (2004), A simple quantitative model of plasma flows and currents in Saturn's polar ionosphere, *J. Geophys. Res.*, *109*, A05212, doi:10.1029/2003JA010375.

DeForest, S. E., and C. E. McIlwain (1971), Plasma clouds in the magnetosphere, *J. Geophys. Res.*, *76*, 3587.

Delamere, P. A., R. J. Wilson, and F. Bagenal (2011), Kelvin-Helmholtz instability at Saturn's magnetopause: hybrid simulations, *J. Geophys. Res.*, *116*, A10, 222.

Delamere, P. A., R. J. Wilson, S. Eriksson, and F. Bagenal (2013), Magnetic signatures of Kelvin-Helmholtz vortices on Saturn's magnetopause: global survey, *J. Geophys. Res. (Space Physics)*, *118*, 393–404, doi10.1029/2012JA018197.

Delamere, P. A., F. Bagenal, C. Paranicas, A. Masters, A. Radioti, B. Bonfond, L. Ray, X. Jia, J. Nichols, and C. Arridge (2015a), Solar wind and internally driven dynamics: influences on magnetodiscs and auroral responses, *Space Sci. Rev*., *187*, 51–97, doi10.1007/s11214-014-0075-1.

Delamere, P. A., A. Otto, X. Ma, F. Bagenal, and R. J. Wilson (2015b), Magnetic flux circulation in the rotationally-driven giant magnetospheres, *J. Geophys. Res*. (*Space Physics*), doi10.1029/2015JA021036.

Dessler, A. J. (1980), Mass-injection rate from Io into the Io plasma torus, *Icarus*, *44*, 291–295.

Eviatar, A., and G. L. Siscoe (1980), Limit on rotational energy available to excite Jovian aurora, *Geophys. Res. Lett.*, *7*, 1085–1088.

Grodent, D., J. Gustin, J.-C. Gérard, A. Radioti, B. Bonfond, and W. R. Pryor (2011), Small-scale structures in Saturn's ultraviolet aurora, *J. Geophys. Res.*, *116*, A09225, doi:10.1029/2011JA016818.

Hill, T. W., A. M. Rymer, J. L. Burch, F. J. Crary, D. T. Young, M. F. Thomsen, D. Delapp, N. André, A. J. Coates, and G. R. Lewis (2005), Evidence for rotationally driven plasma transport in Saturn's magnetosphere, *Geophys. Res. Lett*., *32*, L14S10, doi:10.1029/2005GL022620.

Johnson, R. E., H. T. Smith, O. J. Tucker, M. Liu, M. H. Burger, E. C. Sittler, and R. L. Tokar, (2006), The Enceladus and OH tori at Saturn, *Astrophys. J.*, *644*, L137, doi:10.1086/505750.

Kivelson, M. G., K. K. Khurana, C. T. Russell, and R. J. Walker (1997), Intermittent short-duration plasma-field anomalies in the Io plasma torus: evidence for interchange in the Io plasma torus, *Geophys. Res. Lett.*, *24*, 2127.

Knight, S. (1973), Parallel electric fields, *Planet. Space Sci.*, *21*, 741.

Kurth, W. S., E. J. Bunce, J. T. Clarke, F. J. Crary, D. C. Grodent, A. P. Ingersoll, U. A. Dyudina, L. Lamy, D. G. Mitchell, A. M. Persoon, W. R. Pryor J. Saur, and T. Stallard (2009), Auroral processes, Chap.12, *Saturn from Cassini-Huygens* (M. Dougherty, L. Esposito, and S. M. Krimigis, eds.), Springer Verlag, Dordrecht.

Lemon, C., R. A. Wolf, T. W. Hill, S. Sazykin, R. W. Spiro, F. R. Toffoletto, J. Birn, and M. Hesse (2004), Magnetic storm ring current injection modeled with the Rice Convection Model and a self-consistent magnetic field, *Geophys. Res. Lett.*, *31*, L21801, doi:10.1029/2004GL020914.

Liu, X. (2013), *Modeling the Plasma Convection in Saturn's Inner Magnetosphere*, Ph.D. thesis, Rice University, Houston, TX.

Liu, X., and T. W. Hill (2012), Effects of finite plasma pressure on centrifugally driven convection in Saturn's inner magnetosphere, *J. Geophys. Res.*, *117*, A07216, doi:10.1029/2012JA017827.

Liu, X., T. W. Hill, R. A. Wolf, S. Sazykin, R. W. Spiro, and H. Wu (2010), Numerical simulation of plasma transport in Saturn's inner magnetosphere using the Rice Convection Model, *J. Geophys. Res.*, *115*, A12254, doi:10.1029/2010JA015859.

Masters, A., N. Achilleos, C. Bertucci, M. K. Dougherty, S. J. Kanani, C. S. Arridge, H. J. McAndrews, and A. J. Coates

(2009), Surface waves on Saturn's dawn flank magnetopause driven by the Kelvin-Helmholtz instability, *Planet. Space Sci.*, *57*, 1769–1778, doi:10.1016/j.pss.2009. 02.010.

Masters, A., et al. (2010), Cassini observations of a Kelvin-Helmholtz vortex in Saturn's outer magnetosphere, *J. Geophys. Res.*, *115*, A07225, doi:10.1029/2010JA015351.

Mauk, B.H., D. J. Williams, and R. W. McEntire (1997), Energy-time dispersed charged particle signatures of dynamic injections in Jupiter's inner magnetosphere, *Geophys. Res. Lett.*, *24*, 2949.

Mauk, B. H., et al. (2005), Energetic particle injections in Saturn's magnetosphere, *Geophys. Res. Lett*., *32*, L14S05, doi:10.1029/2005GL022485.

Nishida, A. (1966), Formation of plasmapause, or magnetospheric plasma knee, by the combined action of magnetospheric convection and plasma escape from the tail, *J. Geophys. Res.*, *71*, 5669–5679.

Pontius, D. H., Jr., R. A. Wolf, T. W. Hill, R. W. Spiro, Y. S. Yang, and W. H. Smyth (1998), Velocity shear impoundment of the Io plasma torus, *J. Geophys. Res.*, *103*, 19,935.

Ray, L. C., R. E. Ergun, P. A. Delamere, and F. Bagenal (2012), Magnetosphere-ionosphere coupling at Jupiter: a parameter space study, *J. Geophys. Res. (Space Physics)*, *117*, A01205, doi10.1029/2011JA016899.

Ray, L. C., M. Galand, P. A. Delamere, and B. L. Fleshman (2013), Current-voltage relation for the Saturnian system, *J. Geophys. Res. (Space Physics)*, *118*, 3214–3222, doi10.1002/jgra.50330.

Rymer, A. M., et al. (2009), Cassini evidence for rapid interchange transport at Saturn, *Plan. Space. Sci.*, *57*, 1779.

Sazykin, S., R. A. Wolf, R. W. Spiro, T. I. Gombosi, D. L. De Zeeuw, and M. F. Thomsen (2002), Interchange instability in the inner magnetosphere associated with geosynchronous particle flux decreases, *Geophys. Res. Lett*., *29*(10), doi:10.1029/2001GL014416.

Schippers, P., M. Blanc, N. André, I. Dandouras, G. R. Lewis, L. K. Gilbert, A. M. Persoon, N. Krupp, D. A. Gurnett, A. J. Coates, S. M. Krimigis, D. T. Young, and M. K. Dougherty (2008), Multi-instrument analysis of electron populations in Saturn's magnetosphere, *J. Geophys. Res.*, *113*, A07208, doi:10.1029/2008JA013098.

Song, Y. (2010), *Space Weather Event Modeling of Plasma Injection in the Inner Magnetosphere with the Rice Convection Model*, Ph.D. thesis, Rice University, Houston, TX.

Talboys, D. L., C. S. Arridge, E. J. Bunce, A. J. Coates, S. W. H. Cowley, and M. K. Dougherty (2009a), Characterization of auroral current systems in Saturn's magnetosphere: High-latitude Cassini observations, *J. Geophys. Res.*, *114*, A06220, doi:10.1029/2008JA013846.

Talboys, D. L., C. S. Arridge, E. J. Bunce, A. J. Coates, S. W. H. Cowley, M. K. Dougherty, and K. K. Khurana (2009b), Signatures of field-aligned currents in Saturn's nightside magnetosphere, *Geophys. Res. Lett.*, *36*, L19107, doi:10.1029/2009GL039867.

Thomsen, M. F. (2013), Saturn's magnetospheric dynamics, *Geophys. Res. Lett.*, *40*, 5337, doi:10.1002/2013GL057967.

Thomsen, M. F., D. B. Reisenfeld, D. M. Delapp, R. L. Tokar, D. T. Young, F. J. Crary, E. C. Sittler, M. A. McGraw, and J. D. Williams (2010), Survey of ion plasma parameters in Saturn's magnetosphere, *J. Geophys. Res.*, *115*, A10220, doi:10.1029/2010JA015267.

Thomsen, M. F., D. B. Reisenfeld, R. J. Wilson, M. Andriopoulou, F. J. Crary, G. B. Hospodarsky, C. M. Jackman, X. Jia, K. K. Khurana, C. Paranicas, E. Roussos, N. Sergis, and R. L. Tokar (2014), Ion composition in interchange injection events in Saturn's magnetosphere, *J. Geophys. Res. Space Physics*, *119*, 9761–9772, doi:10.1002/2014JA020489.

Thorne, R. M., et al. (1997), Galileo evidence for rapid inward transport in the Io torus, *Geophys. Res. Lett.*, *24*, 2131.

Walker, R. J., K. Fukazawa, T. Ogino, and D. Morozoff (2011), A simulation study of Kelvin-Helmholtz waves at Saturn's magnetopause, *J. Geophys. Res.*, *116*, A03203, doi:10.1029/2010JA015905.

Wolf, R. A., C. X. Chen, and F. R. Toffoletto (2012), Thin-filament simulations for Earth's plasma sheet: Interchange oscillations, *J. Geophys. Res.*, *117*, A02215, doi:10.1029/2011ja016971.

Wu, H., T. W. Hill, R. A. Wolf, and R. W. Spiro (2007), Numerical simulation of fine structure in the Io plasma torus produced by the centrifugal interchange instability, *J. Geophys. Res.*, *112*, A02206, doi:10.1029/2006JA012032.

Yang, J., F. R. Toffoletto, R. A. Wolf, S. Sazykin, R. W. Spiro, P. C. Brandt, M. G. Henderson, and H. U. Frey (2008), Rice Convection Model simulation of the 18 April 2002 sawtooth event and evidence for interchange instability, *J. Geophys. Res*, *113*, A11214, doi:10.1029/2008ja013635.

Yang, J., R. A. Wolf, F. R. Toffoletto, S. Sazykin, and C.-P. Wang (2014), RCM-E simulation of bimodal transport in the plasma sheet, *Geophys. Res. Lett.*, *41*, 1817–1822, doi:10.1002/2014GL059400.

Yang, Y. S., R. A. Wolf, R. W. Spiro, T. W. Hill, and A. J. Dessler (1994), Numerical simulation of torus-driven plasma transport in the Jovian magnetosphere, *J. Geophys. Res.*, *99*, 8755.

25

Global MHD Modeling of the Coupled Magnetosphere-Ionosphere System at Saturn

Xianzhe Jia[1], Margaret G. Kivelson[1,2], and Tamas I. Gombosi[1]

Video of Yosemite Talk, URL: http://dx.doi.org/10.15142/T3JS3C

ABSTRACT

At Saturn's orbital distance of ~9.5 astronomical units (AU), the low solar wind dynamic pressure and weak interplanetary magnetic field (IMF) interact with the planet to create a magnetosphere that dwarfs Earth's magnetosphere. At Earth, the global structure and dynamics of the magnetosphere are controlled primarily by the interaction with the solar wind. In contrast, at Saturn, although the form of the magnetospheric cavity is still the result of solar wind stresses, many properties of the magnetosphere are determined largely by internal processes associated with the planet's rapid rotation and the stresses arising from internal plasma sources dominated by the moon, Enceladus. Coupling between the ionosphere and the magnetosphere through electric currents plays a vital role in determining the global configuration and dynamics of Saturn's magnetosphere. To understand the large-scale behavior of the solar wind-magnetosphere-ionosphere interaction, we have applied the global magnetohydrodynamic (MHD) model, Block Adaptive Tree Solar Wind Roe-type Upwind Scheme (BATS-R-US), to Saturn that self-consistently couples the solar wind, the magnetosphere, and the ionosphere and incorporates important mass-loading processes associated with Enceladus and its extended neutral cloud. Here we present results from our global simulations that have been carried out to understand how the various internally and externally driven processes affect the Saturnian magnetosphere.

25.1. INTRODUCTION

At Saturn's orbital distance of ~9.5 AU, the low solar wind dynamic pressure and weak IMF (smaller by an order of magnitude or more relative to values near Earth) interact with the planetary magnetic field to create a magnetosphere that dwarfs Earth's magnetosphere. At Earth, the global structure and dynamics of the magnetosphere are controlled primarily by the interaction with the external solar wind. In contrast, at Saturn, although the global shape of the magnetospheric cavity is still the result of solar wind stresses, many properties of the magnetosphere are determined largely by internal processes associated with the planet's rapid rotation (rotation period of ~10.7 hours) and the stresses arising from internal plasma sources dominated by the icy moon, Enceladus.

One prominent example of internally driven phenomena is the ubiquitous periodic modulations of particle and field properties observed in Saturn's magnetosphere. Periodic variations at roughly Saturn's rotation period were first identified in the power emitted in Saturn kilometric radiation (SKR). Subsequent studies have found the SKR periodicity in a variety of features of Saturn's magnetosphere including the perturbation magnetic field both near the equator and at high latitudes, the flapping

[1]*Department of Climate and Space Sciences and Engineering, University of Michigan, Ann Arbor, MI, USA*

[2]*Department of Earth, Planetary, and Space Sciences, University of California at Los Angeles, Los Angeles, CA, USA*

Magnetosphere-Ionosphere Coupling in the Solar System, Geophysical Monograph 222, First Edition.
Edited by Charles R. Chappell, Robert W. Schunk, Peter M. Banks, James L. Burch, and Richard M. Thorne.

of the tail current sheet, the location of the magnetopause and bow shock, thermal plasma density, energetic particle fluxes, the intensity of energetic neutral atoms (ENA) fluxes, and auroral properties. The source of the periodicities remains uncertain, but there is little doubt that field-aligned currents (FAC) are required to couple the rotating planet to the magnetosphere and to impose periodic behavior on the entire system.

Although rotational effects appear dominant in Saturn's magnetosphere, there is also considerable observational evidence that indicates external disturbances present in the solar wind, such as the interplanetary shocks, can also produce significant impact on the global magnetosphere. For instance, during Cassini's approach to Saturn in 2004, simultaneous solar wind and auroral observations revealed that Saturn's aurora undergoes dramatic changes following the arrival of solar wind shocks.

To understand the large-scale behavior of the solar wind-magnetosphere-ionosphere interaction at Saturn, we have conducted global MHD simulations of the coupled system by using the MHD model, BATS-R-US [*Powell et al*., 1999; *Gombosi et al*., 2002], that incorporates important mass-loading processes associated with Enceladus and its extended neutral cloud (see Section 25.2 for model description). In this paper, we present results from two sets of global simulations that have been carried out to understand how various internally and externally driven processes affect the Saturnian magnetosphere. In Section 25.3, we show results from a series of simulations that incorporate rotating flow vortices in the ionosphere, which impose periodic perturbations on the entire magnetosphere. We discuss several major aspects of the model runs that demonstrate how periodicity is imposed on different parts of the magnetospheric system. In Section 25.4, we present results from a simulation using a non-steady solar wind input with a range of parameters that allows us to investigate how Saturn's magnetosphere responds to the external forcing. There our focus is placed on magnetotail reconnection and its associated dynamics. We summarize our findings from the MHD simulations in Section 25.5.

25.2. GLOBAL MHD MODEL

Global MHD models have been widely used to simulate planetary magnetospheres including those of the giant planets. Although an MHD model does not model kinetic effects, such as energy-dependent particle drifts and wave particle interactions, it has the advantage of capturing the large-scale behavior of a magnetosphere with reasonably good grid resolution but at lower computational cost compared to kinetic models. In developing a global simulation for the giant planet magnetospheres, it is critically important to include the plasma sources associated with moons. Global models use different approaches to introduce moon-related sources. For instance, the global model by *Fukazawa et al.* [2007a and 2007b] does not explicitly include the plasma sources associated with Enceladus in the simulation domain but rather introduces them by fixing plasma density and pressure in time at the simulation inner boundary, which is placed outside of the main regions in which Enceladus-associated plasmas are added to the system. Similarly, the multi-fluid MHD model by *Kidder et al*. [2012] holds the density of the water-group ion fluid fixed near Enceladus' orbit to mimic the addition of new plasma from the moon. In contrast, the BATS-R-US Saturn MHD model adopts a more direct approach in which source and loss terms are incorporated into the MHD equations to model the various mass-loading processes associated with Enceladus's neutral cloud, such as photoionization and electron impact ionization, charge-exchange, and recombination [*Hansen et al.*, 2005]. With this approach, the mass-loading distribution in the BATS-R-US simulations can be controlled and specified as input based on available observational data and/or inferences from models of Saturn's neutral and plasma distributions. In particular, the published BATS-R-US simulations of Saturn's magnetosphere include an axisymmetric disc-like source centered at ~5.35 R_S (R_S = 60,268 kilometer [km] is Saturn's radius) to represent the main plasma source of water group ions W^+ (H_2O^+, OH^+, O^+) originating from Enceladus according to the neutral and plasma models of *Richardson et al.* [1998], which took into account the fact that the densities of the electrons that produce the ionization of neutrals peak outside of Enceladus's orbit. In addition, the model also includes an axisymmetric torus around Titan's orbit at ~20 R_S representing a secondary plasma source of nitrogen ions N^+ originating from Titan, whose source rate is assumed to be $5x10^{25}$ ions/s (or 1.1 kg/s). The model runs discussed in this paper assumed two different total mass-loading rates of ~85 kg/s (for the simulation of solar wind influences presented in Section 25.4) and ~170 kg/s (for the simulations of magnetospheric periodicities presented in Section 25.3), both of which fall within the range of published estimates [*Jurac and Richardson*, 2005; *Fleshman et al*., 2010; *Smith et al.,* 2010; *Bagenal and Delamere*, 2011].

One noteworthy feature of the BATS-R-US model is that it allows use of generalized curvilinear coordinates, which provide a smooth mapping from a logically Cartesian grid to an arbitrary curvilinear grid [*Tóth et al.*, 2012]. Recent BATS-R-US applications to Saturn have used a non-uniform spherical mesh [*Jia et al*., 2012a, 2012b], which is found to better resolve fine structures of the large-scale electric currents responsible for the magnetosphere-ionosphere coupling compared to a Cartesian mesh with comparable grid resolutions. The computational domain on which the set of MHD equations is

solved covers the region $-576\ R_S < X < 96\ R_S$, $-192\ R_S < Y, Z < 192\ R_S$.

In order to avoid the high Alfvén speed close to the planet that greatly limits the maximum allowable time step, all global MHD simulations applied to Saturn have placed their inner boundaries away from the planet. In BATS-R-US, the inner boundary is located at a radial distance of 3 R_S. The coupling between the magnetosphere and the ionosphere is then handled by using an approach based on mapping of field-aligned currents [*Ridley et al.,* 2004]. Field-aligned currents are calculated in the magnetosphere at 4 R_S, near the inner surface of the magnetospheric domain, and then mapped into the ionosphere at ~1 R_S along dipole field lines. Owing to the continuity of electric currents, field-aligned currents must close through horizontal currents in the ionosphere, which is approximated by a resistive and infinitesimally thin layer located at ~1000 km above the surface of the planet, where the peak ionospheric conductivity typically is [e.g., *Moore et al*., 2010]. Closure currents in the ionosphere are then used to derive the distribution of the electric potential and, in turn, the perturbation in ionospheric convection for an assumed ionospheric conductance. The calculated convection modulation is then superimposed onto the rigid corotation flow pattern to obtain a modified ionospheric convection pattern. Finally, the ionospheric convection pattern, which determines the flow velocity perpendicular to the magnetic field, is mapped back along dipole field lines from the ionosphere to the magnetosphere under the ideal MHD assumption that magnetic field lines are equipotentials. The mapped flows, therefore, set the transverse velocity components at the inner boundary of the global MHD model. In addition, a mass density of 0.1 amu/cm^3 and a temperature of 3 electronvolts (eV) [e.g., *Wolfe et al.*, 1980] are taken as the initial condition and fixed in time at the inner simulation boundary.

25.3. SIMULATIONS OF MAGNETOSPHERIC PERIODICITIES

In this section, we present results from a series of global simulations that have been carried out to understand the origin of Saturn's magnetospheric periodicities, one of the most perplexing phenomena discovered in the Saturnian system [see a recent review by *Carbary and Mitchell*, 2013]. Periodic modulation of SKR was identified first in the data of the Voyager spacecraft in the early 1980s [*Desch and Kaiser*, 1981]. Years later, reexamination of Pioneer and Voyager data by *Espinosa and Dougherty* [2000] and *Espinosa et al.* [2003] revealed periodicity in the magnetometer data. Ulysses measurements demonstrated that the period was not fixed, but changed slowly over time scales of years [*Lecacheux et al.*, 1997; *Galopeau and Lecacheux*, 2000]. With the arrival of Cassini at Saturn, it became clear that the periodicity is present in many aspects of field and particle properties [*Paranicas et al.*, 2005; *Carbary et al*., 2007; *Southwood and Kivelson*, 2007; *Gurnett et al.,* 2007, 2010b; *Kurth et al*., 2007; *Fischer et al.,* 2014; *Andrews et al*., 2008; *Provan et al*., 2009a, 2009b; *Mitchell et al*., 2009; *Khurana et al*., 2009], and in auroral emissions [*Nichols et al*., 2008; *Carbary*, 2013]. Extensive analysis of SKR emissions during the Cassini epoch have established that the frequency drifts at a rate of order 1% per year [*Kurth et al.*, 2007; *Gurnett et al*., 2007], that northern hemisphere sources are modulated at a frequency slightly higher than that of southern hemisphere sources [*Gurnett et al.,* 2009, 2010a; *Lamy*, 2011; *Andrews et al.,* 2010, 2012; *Southwood*, 2011; *Provan et al.,* 2011] and also that the source of SKR emissions drifts in the sense of planetary rotation [*Lamy,* 2011]. On approach to equinox in August 2009, the two distinct periods converged toward 10.7 hours. There was speculation that the northern and southern periods would cross [*Gurnett et al.,* 2010a], but continued monitoring has found the two periods hovering close to 10.7 hours without crossing [*Provan et al.,* 2014].

A number of models have been proposed to account qualitatively for the observed periodic behavior. Some models suggest that the periodicity originates from the equatorial region of the magnetosphere, such as the twin-cell plasma convection model [*Goldreich and Farmer*, 2007; *Gurnett et al*., 2007] and the rotating plasma disk model [*Khurana et al.*, 2009], while other models hypothesize that the driver of the periodicity is located at high latitudes, either in the atmosphere or the ionosphere [e.g., *Smith*, 2006, 2014; *Jia et al*., 2012a; *Southwood and Cowley*, 2014]. Nonetheless, all the models require a rotating field-aligned current system with $m = 1$ symmetry that link the northern and southern hemispheres with each other and with the magnetosphere [*Southwood and Kivelson*, 2007; *Andrews et al.*, 2008]. To understand the response of the coupled magnetosphere-ionosphere system to such a rotating FACs system, *Jia et al.* [2012a] have introduced in their Saturn global MHD model a heuristic pattern of FACs rotating at a prescribed period (taken to be the SKR period in the present simulations). In their model, the FACs that link the ionosphere and the magnetosphere are driven by vortical flows imposed on the ionosphere [*Jia et al*., 2012a; *Jia and Kivelson*, 2012]. While the driver of the vortical flows is unspecified in the model, the imposed flows could arise through coupling to thermospheric winds, such as those that have been explored by *Smith* [2006, 2014] or through instabilities arising from polar cap rotation as proposed by *Southwood and Cowley* [2014]. However they are imposed, the authors argue that the source of the FACs must have sufficient inertia to restore both periodicity and phase of

the perturbations following intermittent magnetospheric reconfigurations.

As shown by *Jia et al.* [2012a] and *Jia and Kivelson* [2012], the simulation model with atmospheric vortex captures numerous properties of the observed periodicity with considerable quantitative fidelity. Here we show examples from the vortex simulations to demonstrate how localized structures in the ionosphere can exert significant global influences on the magnetosphere. We focus on the situation corresponding to Saturn's southern summer (prior to August 2009). To establish how the magnetosphere responds to currents driven by a rotating ionospheric vortex, the simulation has been run for idealized cases in which the solar wind flow is orthogonal to Saturn's rotation axis, the ionospheric Pedersen conductance is 3 S in the south and 1 S in the north to account for the different intensities of the northern and southern SKR emissions during southern summer. A southward-orientation of the IMF (0.5 nT) is used in order to minimize solar-wind-driven perturbations of the magnetosphere in these simulations. The vortical flows in the high latitude ionosphere are specified using a mathematically tractable form based on the spherical harmonics. Here we start with a simulation with only one pair of vortices imposed in the southern ionosphere to examine the system response to the dominant southern source. The rotation period of the ionospheric vortex is set to be 10.8 hr, consistent with the southern SKR period for late 2005 and early 2006 [*Gurnett et al.,* 2009].

The vorticity pattern imposed is shown in Figure 25.1a. Although vortical flows are imposed only in the south, FACs appear throughout the polar regions in both hemispheres after the simulation has stabilized. FACs are more intense in the south than the north and most intense in regions linked to the center of the imposed vortices (Figure 25.1b and 25.1c). The FAC system generated in the south closes in part within the magnetosphere where it imposes periodic variations, but some current flows through the equator and closes in the northern ionosphere. This ionosphere-to-ionosphere current system corresponds to the cam current inferred from Cassini magnetometer data [*Southwood and Kivelson*, 2007]. Interaction with the magnetosphere modifies the directly driven currents in the ionosphere in both hemispheres, although the most intense currents in the south differ little from those imposed.

The assumed ionospheric input drives a host of diverse periodic magnetospheric phenomena. Within the magnetosphere, rotating perturbations arise. Figure 25.2, a snapshot taken after the responses have stabilized, shows the distribution of plasma mass density and azimuthal current density in the equatorial plane, along with unit vectors of the perturbation magnetic field at a phase of rotation indicated by the image of the southern ionosphere in the upper left hand corner. Inside of ~12 R_S, the

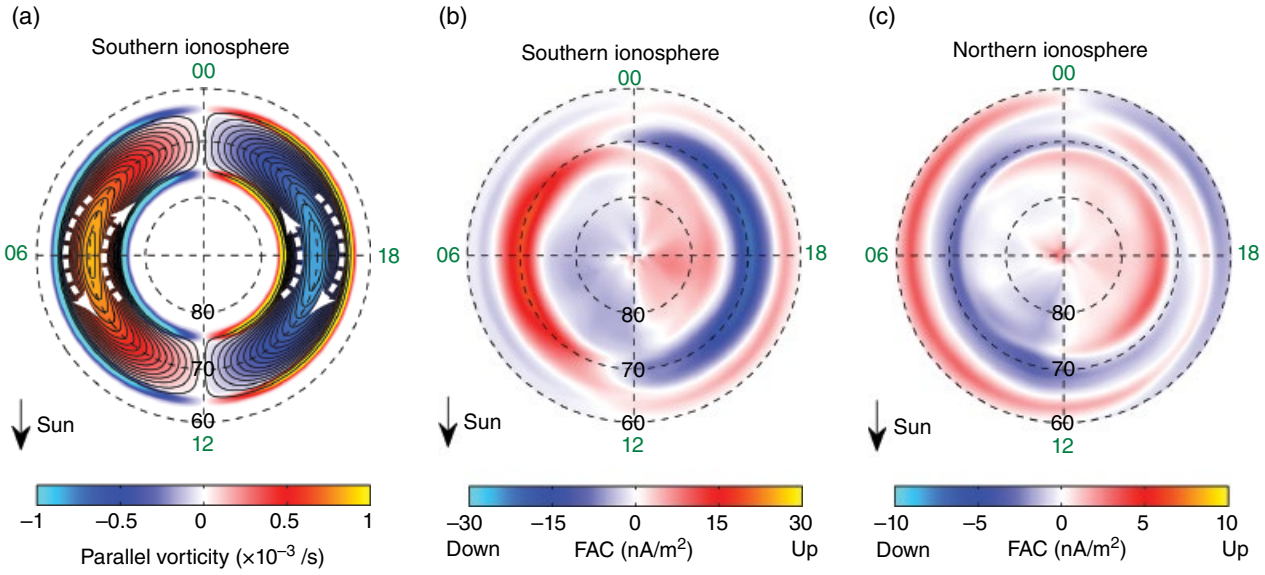

Figure 25.1 Ionospheric conditions from the simulation that imposes an atmospheric vortex [from *Jia et al.,* 2012a]. (a) The imposed flow vortex in the southern hemisphere obtained from one cycle of a spherical harmonic potential of order $l = 15$, $m = 1$. Color indicates the flow vorticity parallel to the local magnetic field, solid lines are flow streamlines, and dashed arrows show local flow directions. (b) Color contours of field-aligned current density associated with the perturbed flow in the southern ionosphere. (c) As for (b) but for the northern ionosphere and with a different color bar. Images are viewed downward from the north.

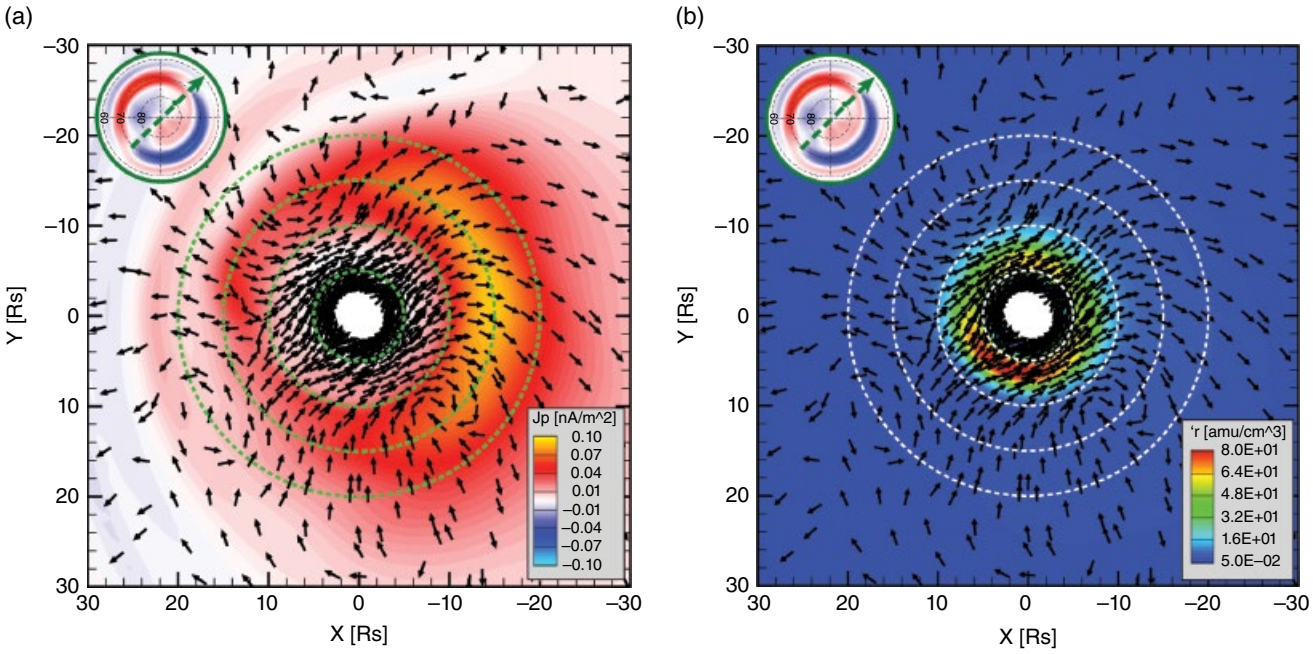

Figure 25.2 Snapshots of the equatorial magnetospheric properties from the simulation with a rotating vortex imposed on the southern ionosphere [from *Jia et al.,* 2012a]. (a) Color represents the azimuthal current density. (b) Color represents plasma mass density. In both panels, the phase of the rotating ionosphere is illustrated in the upper left, and the black arrows represent unit vectors of the magnetic perturbations in the equatorial plane. Circles show multiples of 5 R_S.

rotating field is approximately uniform, modified by diversion around the inner magnetosphere and skewed by magnetopause and magnetotail currents. Outside of ~12 R_S, the flow and field perturbations are dominated by local time (LT)-dependent responses, consistent with Cassini observations reported by *Andrews et al.* [2008, 2010]. Throughout the equatorial magnetosphere, the azimuthal current density, J_p, a ring current, is positive (Figure 25.2a), consistent with outward ballooning of the dipole field. Localized enhancements of J_p form the asymmetric ring current [*Khurana et al.*, 2009; *Andrews et al.,* 2010; *Brandt et al.*, 2010], consisting of two parts, one fixed in LT, one rotating. The fixed component weakens and then intensifies as the rotating component passes through it. An azimuthal variation in plasma density (Figure 25.2b) links closely to the rotation phase of the southern hemisphere vortex. A new density peak forms between 5 and 8 R_S in the afternoon sector once each rotation period. This density enhancement rotates, slowing and dissipating as it reaches the morning sector, just as a new density peak develops near dusk. Periodic density variations observed by *Gurnett et al.* [2007] inside of 5 R_S on Cassini orbits with periapses in the afternoon/dusk sector probably correspond to the periodically recurring density peak in the simulation. The outward shift of the density peak relative to observations arises because, in the simulation, the inner boundary falls at 3 R_S and the mass loading peak near Enceladus's orbit [*Richardson et al.,* 1998; *Sittler et al.,* 2008] has been shifted slightly outward. For the steady solar wind conditions used in this simulation, plasmoid releases occur each time the outflow sector (inward-pointing magnetic perturbations and enhanced plasma density) rotates into the nightside magnetosphere, a prediction that remains to be confirmed by direct in situ observations. Associated with plasmoid release is inward-moving hot plasma, thought to be the source of periodic bursts of ENAs [*Paranicas et al.,* 2005; *Mitchell et al.*, 2009].

Other features consistent with observations include the intensity of the FACs flowing upward from the ionosphere that vary as the source region in the ionosphere rotates. Figure 25.3 (a–f) shows the modeled intensity of upward FACs in the southern ionosphere versus LT at different rotation phases. Following the pattern through a cycle, one sees that the FACs become most intense as the source region (indicated by the magenta dot) rotates through the morning sector. The vortical flows imposed in the southern ionosphere drive a current system fixed in the rotating frame, whereas flows and pressure gradients in the magnetosphere introduce LT asymmetries into the ionospheric current system [*Southwood and Kivelson*, 2009]. Because the SKR emission is generated by downward-moving energetic electrons that are accelerated by parallel electric field associated with intense upward

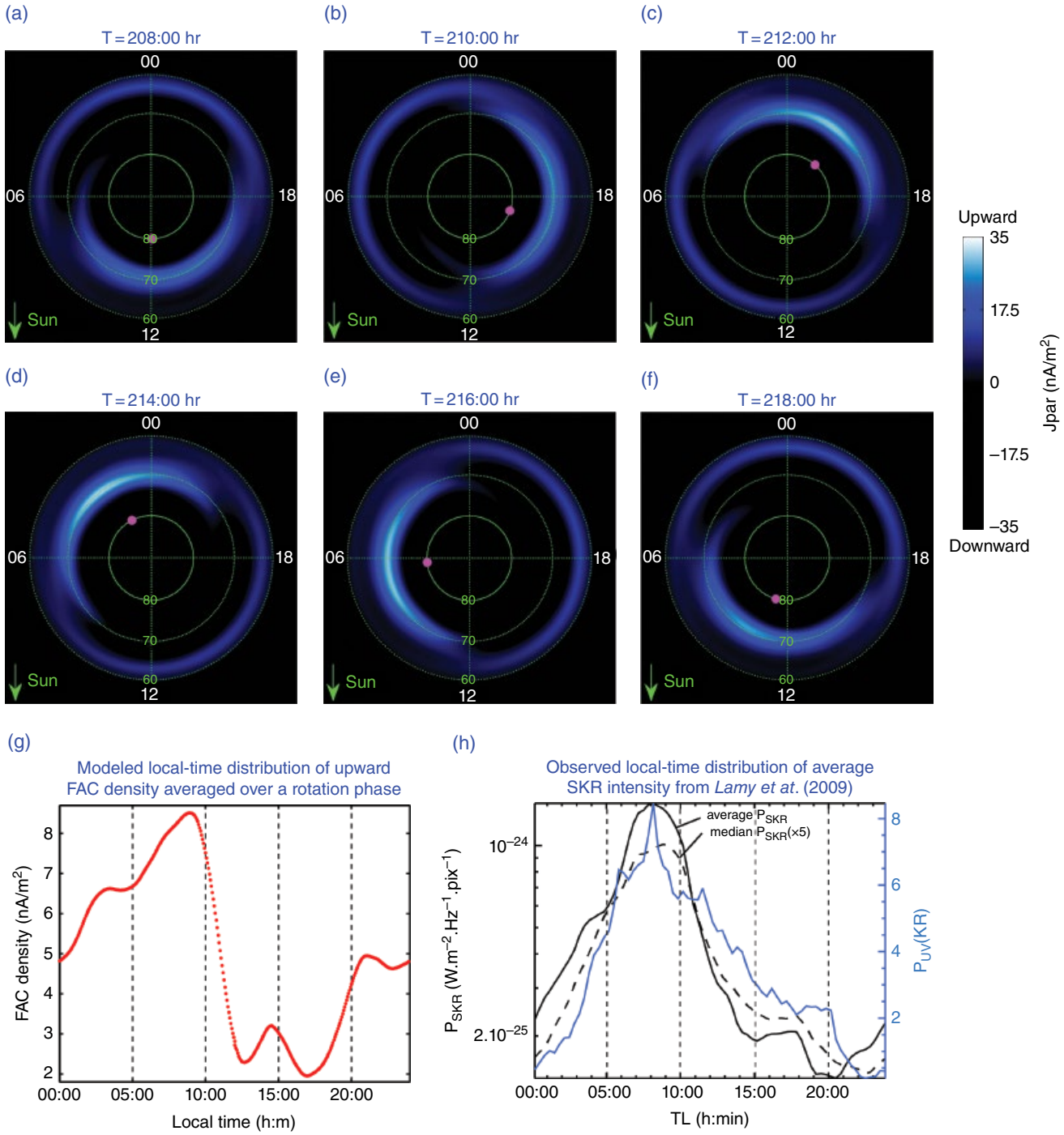

Figure 25.3 Rotational modulation of the FAC intensity in the ionosphere [from *Jia et al.*, 2012a]. (a–f) Upward FAC density from the southern hemisphere at different rotation phases in the simulation. The small pink circle shows the meridian of the center of the vortex driving upward current. (g) Average over a rotation phase of upward FAC density in the south versus LT from the simulation. (h) Ultraviolet (UV) power (blue) and SKR intensity (black) versus LT adapted from *Lamy et al.* [2009]. Dashed curve is the median SKR intensity.

FACs [*Wu and Lee*, *1979*; *Galopeau et al.*, 1989], it is reasonable to identify the intense upward current as the source of SKR. Therefore, asymmetries of the FAC intensity seen in our model can account for the LT variation of the intensity of SKR emissions [*Lamy et al.*, 2009]. This result is further supported by a direct comparison of the LT dependence of FACs between the model and observations as shown by Figure 25.3 g–h. Figure 25.3 g shows the intensity of the modeled current versus LT averaged over a full rotation, and Figure 25.3 h

shows the average of the observed SKR intensity versus LT of the source over many rotation periods [*Lamy et al.,* 2009]. The variation with LT of the FAC intensities is similar in the two plots. The localization of the peak intensity between 06 and 10 LT in the simulation matches the localized peak of the observed intensity variations of SKR, consistent with the idea proposed by *Southwood and Kivelson* [2009] that the rotating FACs drive the most intense SKR emissions as they rotate into the morning sector where the rotating currents are enhanced by magnetospheric currents fixed in local time.

The flow perturbations introduced in the model ionosphere not only generate the field-aligned currents as discussed above, but also impose flow perturbations on the magnetospheric plasma resulting in compressional waves propagating throughout the magnetosphere. *Kivelson and Jia* [2014] further analyzed the simulation run with a pair of vortices in the southern ionosphere focusing on the large scale displacements of the magnetopause and the magnetotail current sheet that occur in response to propagating compressional perturbations. It is found that the compressional waves propagate northward from the southern source and move radially away from the current-carrying L-shell at all LTs, resulting in periodic displacements of the various magnetospheric boundaries. As an example, we show in Figure 25.4 the equatorial magnetopause locations extracted through five rotation cycles from the simulation. The amplitudes of displacements are in good agreement with Cassini observations [*Clarke et al.*, 2010], although, because an MHD simulation does not correctly model properties of energetic particles, wave speeds are underestimated in the simulation compared with reported speeds of fronts in the magnetosphere [*Clarke et al.,* 2010]. There is a notable dawn-dusk asymmetry in the boundary oscillation. In particular, the boundary is found more variable at radial distances near dawn than near dusk and, on average, to be located farthest out near dawn (Figure 25.4). *Pilkington et al*. [2015] have investigated asymmetries of Saturn's magnetopause based on Cassini observations and found that the expressions for dawn-dusk asymmetry of the equatorial magnetopause provided by *Kivelson and Jia* [2014] are consistent with previously unquantified asymmetries of their data set.

The compressional waves launched from the rotating current sources also cause the current sheet in the tail to move up and down periodically, a motion usually referred to as flapping [*Carbary et al.*, 2008; *Khurana et al*., 2009; *Arridge et al.*, 2011; *Provan et al*., 2012]. Here we show in Figure 25.5 a sequence of snapshots of the modeled magnetosphere in the noon-midnight meridian plane extracted from the dual-sources simulation [*Jia and Kivelson,* 2012]. In the dual-sources simulation, a pair of vortices rotating at the northern SKR period (10.6 hr corresponding to the pre-equinox conditions) is added in the

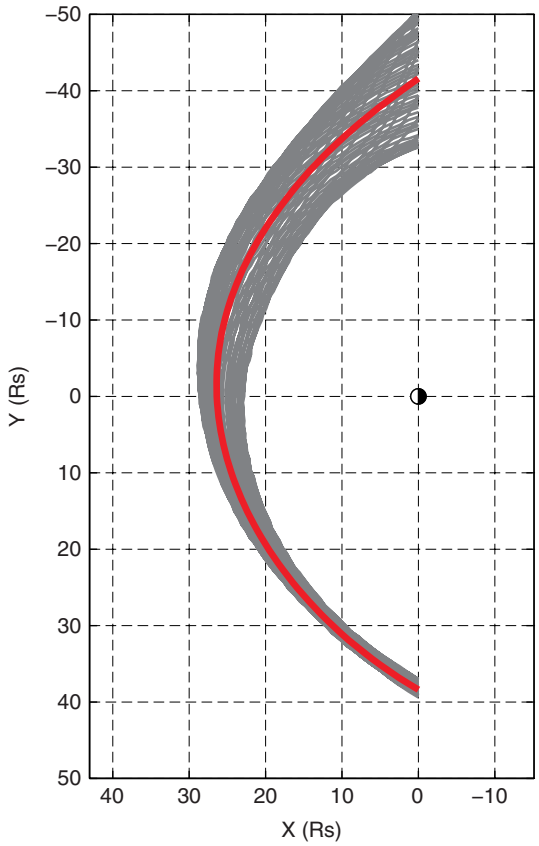

Figure 25.4 Magnetopause boundary every 1 h through five rotation cycles (gray) extracted from the simulation of *Jia et al*. [2012a] and fit to the mean location (red). The figure is from *Kivelson and Jia* [2014].

northern ionosphere in addition to the rotating vortex imposed in the south, allowing us to investigate how the magnetosphere responds to vortical ionospheric anomalies rotating at different rates in the two hemispheres. The images shown in Figure 25.5 reveal the varying configuration of the magnetotail. In particular, the current sheet (defined by the reversal of the polarity of the radial magnetic field) moves northward and back to the equator through a rotation cycle. The plasma sheet is seen to thicken and thin through a rotation cycle, and there is evidence of perturbations propagating tailward (e.g., plasma bulges traveling downtail at the boundary of the plasma sheet). These periodic modulations of the plasma sheet are further illustrated in a more quantitative manner in Figure 25.6, which shows the variations of the central location and thickness of the plasma sheet at $X = -40$ R_S downtail over 33 days. Figure 25.6a confirms that the current sheet moves predominantly up and back, rarely moving below the equator, and the amplitude of the periodic excursions of the sheet is clearly modulated by the beat interaction of the imposed dual sources rotating at slightly different periods. Figure 25.6b shows that the plasma sheet thickness in our simulation has a mean

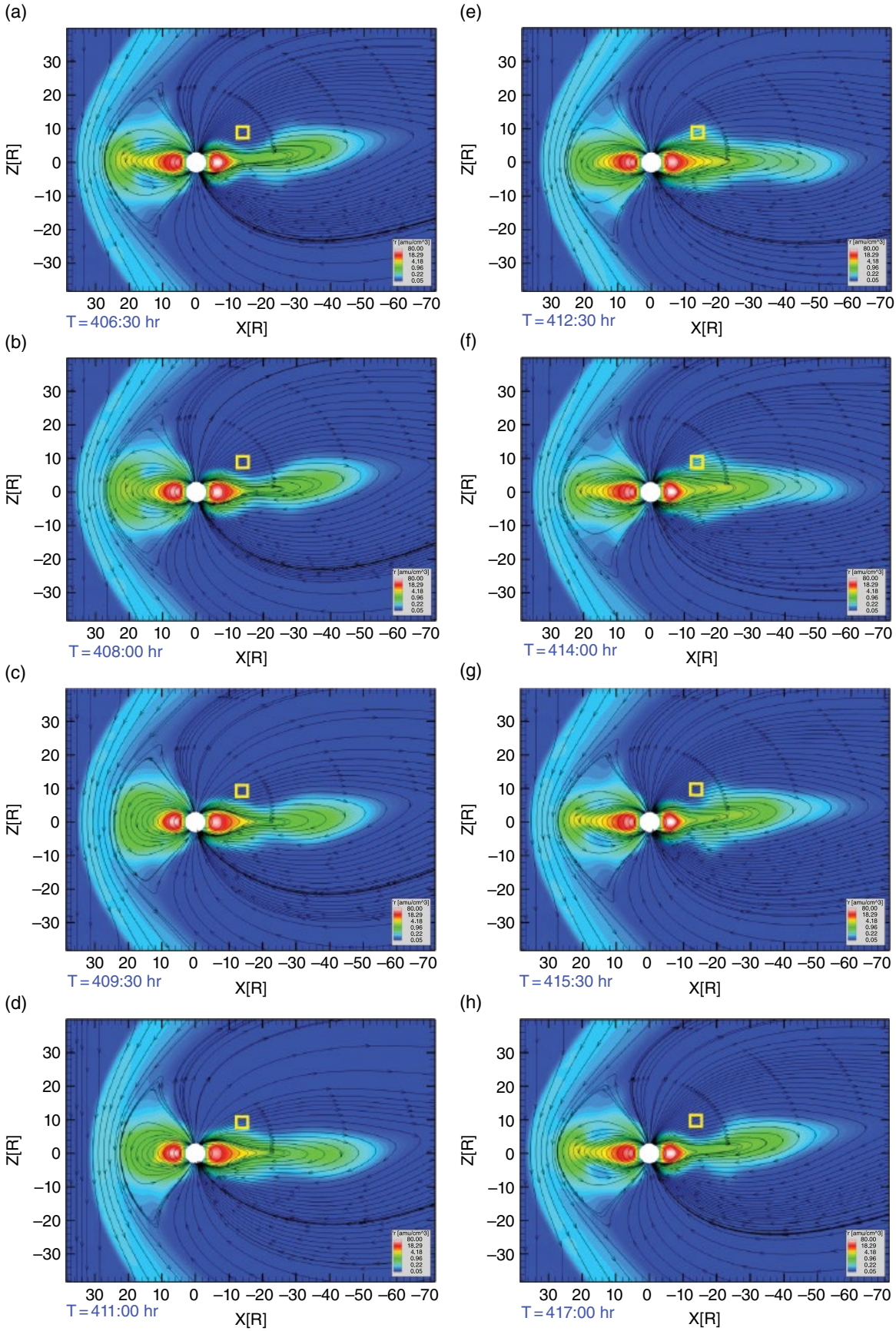

Figure 25.5 The plasma density (color) and field lines on the midnight meridian extracted every 1.5 h through one rotation period from the simulation of *Jia and Kivelson* [2012] that included two pairs of rotating vortices, one in the southern and the other in the northern hemisphere. The field lines are traced starting from fixed locations arbitrarily distributed in this plane.

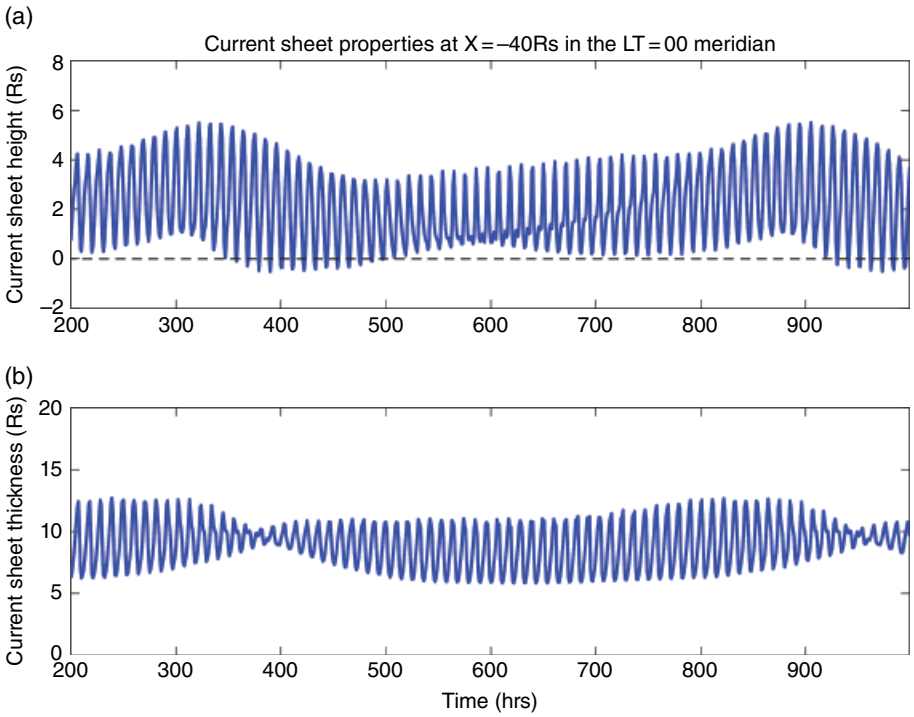

Figure 25.6 Periodic modulation of the plasma sheet central location (a) and thickness (b) extracted from the dual sources simulation [from *Jia and Kivelson,* 2012]. Both properties are measured on the midnight meridian at 40 R_S downtail.

value of about 8 R_S and varies roughly by a factor of 2 when the two rotating sources are in phase. *Jia et al.* [2012a], using only one source in the south, find that displacements of the current sheet in the tail are in accordance with the data reported by *Khurana et al.* [2009]. In that study, we suggest that it is the southern source that provides net northward momentum to the plasma. In this dual-sources simulation, we find that even with dual sources, the stronger source in the south dominates the momentum input to the displacement of the current sheet. While the flapping motions are driven mainly by the stronger southern source, aspects of the variations seen in our model, such as the height of the central current sheet above the equator and the thickness of the plasma sheet, are strongly influenced by the dual sources in ways that are consistent with Cassini observations [*Arridge et al.*, 2011; *Provan et al.*, 2012].

25.4. SIMULATIONS OF SOLAR WIND INFLUENCES

The simulations with atmospheric vortex shown in the previous section demonstrate how localized structures in the ionosphere can exert global influences on the magnetosphere. The solar wind also appears to play an important role in affecting the global magnetospheric configuration and dynamics under certain circumstances. A manifestation of the solar wind influence is Saturn's aurora. Simultaneous observations of the solar wind and the aurora show that both the size and intensity of the main auroral oval are subject to dramatic changes following the arrival of large solar wind disturbances, such as interplanetary shocks [*Clarke et al.*, 2005; *Crary et al.*, 2005; *Bunce et al.*, 2008]. Among the various solar wind parameters, the dynamic pressure and convection electric field appear to be the main controlling factors [*Crary et al.*, 2005].

There is considerable evidence from Cassini in situ measurements indicating that magnetic reconnection occurs in Saturn's magnetotail and plays an important role in driving the global circulation of plasma and magnetic flux [e.g., *Hill et al.,* 2008; *Jackman et al.*, 2007, 2014; *Thomsen et al.*, 2013, 2015; *Mitchell et al.*, 2015]. Occurrence of tail reconnection has also been seen in global MHD simulations. For instance, *Fukazawa et al.* [2012] conducted a simulation study in which a steady solar wind with a northward IMF was used to understand the generation of the large-scale field-aligned currents in Saturn's magnetosphere. Their simulation showed that tail reconnection occurs under such conditions, and the morphology of the tail X-line is such that it starts in the late evening sector and extends into the dawn sector. *Zieger et al.* [2012] carried out a series of BATS-R-US simulations using steady solar wind input with different

dynamic pressures and considering different mass-loading rates. Their simulations suggest that tail reconnection occurs in a quasi-periodic manner under low pressure conditions, and the periodicity appears to depend on both the external pressure and the mass-loading rate. *Kidder et al*. [2012] performed multi-fluid MHD simulations where they considered non-steady solar wind conditions. They found that a pressure pulse in the solar wind or an IMF rotation from southward to northward can trigger reconnection in the tail.

Using the BATS-R-US MHD code, we have carried out a systematic simulation study to examine the role of the solar wind in affecting Saturn's magnetospheric dynamics [*Jia et al.,* 2012b]. The simulation adopts an idealized solar wind input (Figure 25.7a) that has properties representative of Corotating Interaction Regions (CIR), the dominant feature in the solar wind seen at Saturn during solar minimum [*Jackman et al*., 2005]. As shown in Figure 25.7a, the upstream input includes shock disturbances of different strengths as well as rotations of the IMF, allowing us to study the dynamical response of the magnetosphere to a variety of solar wind discontinuities.

Among other things, the simulation study by *Jia et al.* [2012b] specifically examined the role of tail reconnection in driving dynamics in the magnetosphere and how tail reconnection takes place under various external conditions. Two types of reconnection have been identified in their simulation. The first corresponds to the so-called "Vasyliūnas-cycle" reconnection [*Vasyliūna*s, 1983], which occurs on closed field lines as a result of the centrifugal acceleration of mass-loaded flux tubes forced by the planetary rotation. An important consequence of this process is the release of plasmoids, which provides a means for removing plasma added by the internal sources from the magnetosphere. We note that a similar "Vasyliūnas-cycle" reconnection takes place in the atmospheric vortex simulations discussed above, where the release of the plasmoid appears to occur periodically as a result of the flow perturbations imposed by the ionospheric flow anomaly [*Jia et al*., 2012a; *Jia and Kivelson,* 2012]. The second type of reconnection identified in the *Jia et al*. [2012b] simulation refers to the so-called "Dungey-cycle" reconnection [*Dungey,* 1961] that involves open field lines in the lobes. The "Dungey-cycle" reconnection is found to occur in the simulation when the IMF is in an orientation (e.g., northward or along the Parker spiral) that favors dayside magnetopause reconnection, which produces open magnetic flux that is subsequently transported to the tail.

These two types of reconnection appear to yield reconnection products with very different plasma and field characteristics. In particular, the Dungey-type reconnection, which involves the lobe field lines above the plasma sheet, typically results in hotter and more depleted flux tubes with faster flows in the outflows from the reconnection site compared to those produced directly by the Vasyliūnas-type reconnection. Figures 25.7b and 25.7c show the dynamical consequences associated with a modeled tail reconnection event that involves lobe reconnection. The reversal of the magnetic field component (Bz) normal to the tail current sheet serves as a good indicator of where reconnection occurs. Field lines traced in the region of the Bz reversal as shown in Figure 25.7b reveal the presence of a plasmoid with flux rope-like geometry. Following the formation of the plasmoid, reconnection between open field lines in the two tail lobes takes place, producing reconnected field lines with very low plasma densities but high flow speeds (blue field lines) that travel behind the plasmoid. Consequently, the fast flows from the lobe reconnection act to accelerate the plasmoid downtail (Figure 25.7b). Saturnward of the tail X-line, hot, tenuous, and rapidly moving flux tubes are ejected from the reconnection site (Figure 25.7c). On their return from the tail reconnection site to the dayside, those flux tubes can generate significant disturbances in the magnetosphere in the form of particle injections and large blobs of ENA emissions [*Mitchell et al.,* 2009, 2015; *Thomsen et al*., 2015]. Furthermore, the flow shears and pressure gradients between those return flux tubes and the surrounding plasma produce intense field-aligned currents flowing into and out of the ionosphere, especially on the dawnside, that would be expected to cause auroral brightening [e.g., *Mitchell et al.*, 2009]. Recently *Thomsen et al*. [2015] have analyzed Cassini in situ observations acquired along an inclined orbit that enables a fast scan through the dawnside magnetosphere from the lobe to the inner magnetosphere. During this pass, Cassini first encountered a region of hot and tenuous plasma that lies between the lobe with low plasma density and the inner magnetosphere with dense and cold plasma. Given the characteristics of the observed plasma population (low density, high temperature, and a significant water-group ion content), this region is consistent with that expected to be produced of Vasyliūnas-type reconnection. Near the outer edge of this reconnected region, Cassini observed a layer of supercorotating plasma with densities lower than those in the Vasyliūnas-cycle region and more depleted of water group particles, which might be associated with Dungey-type lobe reconnection. Both the reconnection geometry and the particles/fields characteristics observed during this Cassini pass are consistent with the predictions by the MHD simulation.

The time-varying solar wind input used in the *Jia et al*. (2012b) simulation also allows one to investigate how the magnetospheric dynamics varies under different conditions of solar wind dynamic pressure, which is thought to have important effects on Saturn's magnetosphere [e.g., *Cowley et al.,* 2008]. As an example, in Figure 25.8, we

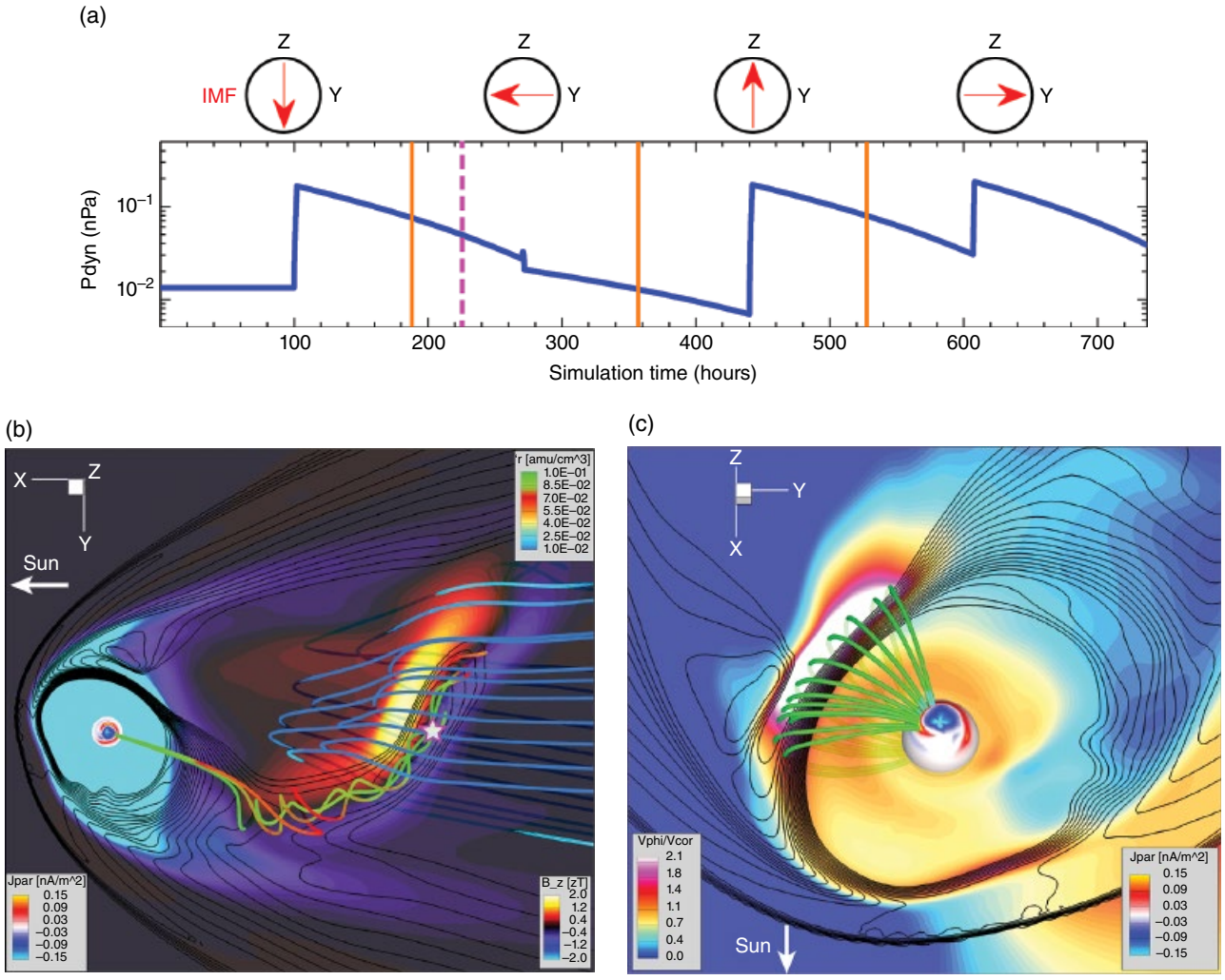

Figure 25.7 Tail reconnection and its impact on the magnetosphere and ionosphere [from *Jia et al.*, 2012b]. (a) Solar wind input used in the simulation. The blue curve shows the solar wind dynamic pressure as a function of time. The simulation is divided into four stages (separated by the orange vertical lines). During each interval of about one week, the IMF of magnitude 0.5 nT is fixed in orientation, either southward, dawnward, northward, or duskward as indicated by the inserts at the top. (b) Three-dimensional structure of a plasmoid formed in the simulation with the IMF roughly aligned with the spiral angle [at T= 225 hr as marked by the magenta dashed line in (a)]. Shown in the background are color contours of Bz (bottom-right color bar) and line contours of plasma density in the equatorial plane. Selected field lines showing the magnetic structure of the plasmoid are color coded with plasma density (top-right color bar). (c) Three-dimensional perspective of the large-scale disturbances associated with the tail reconnection event shown in (b). Plotted in the equatorial plane are the color contours of Vphi/Vcor overlaid with line contours of plasma density. The pattern of field-aligned currents in the ionosphere is also shown (mapped to a sphere of radius 4 R_S for clarity). Green lines show some sample field lines traced from the region of intense upward field-aligned currents in the ionosphere.

compare the tail X-line geometry for low and high solar wind pressure situations. In both panels of Figure 25.8, the tail X-line (marked by the magenta curve) can be readily identified as the flow separatrix from which fast plasma flows with speeds of a few hundred to over a thousand km/s diverge. When the solar wind pressure is relatively low as is the case shown in Figure 25.8a, the tail X-line is located in the midnight-to-dawn sector at a distance of ~40 R_S. When the magnetosphere is compressed by a forward interplanetary shock as shown in Figure 25.8b, the tail X-line not only moves closer to the planet (at ~25 R_S) but also becomes narrower in width with its center shifted toward midnight. Under such circumstances, there appears to be regions in the tail near both the dawn and dusk flanks where closed flux tubes carrying magnetospheric plasma stream down the tail. As

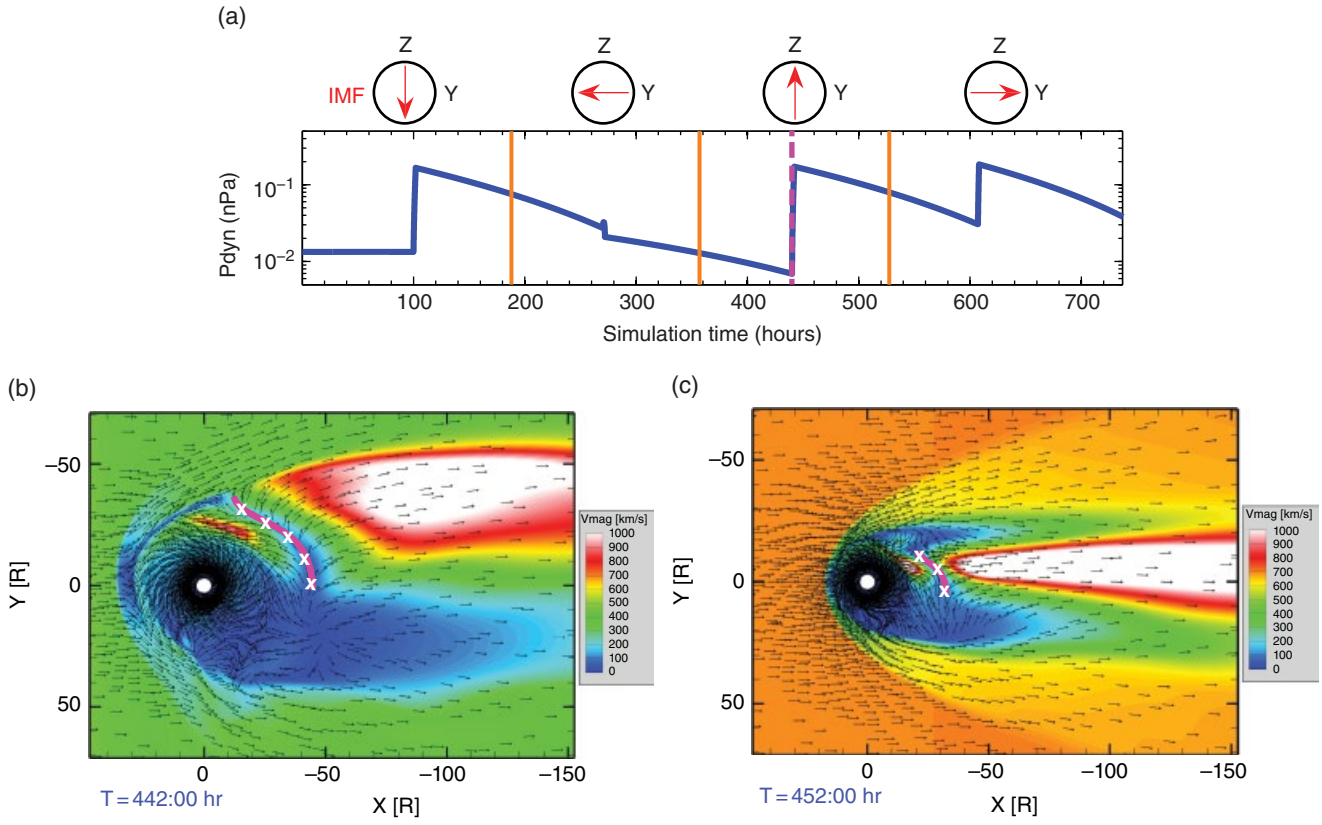

Figure 25.8 Comparison of the tail X-line before and after compression of the magnetosphere induced by an interplanetary shock. (a) Time history of the dynamic pressure of the input solar wind. (b) and (c) Equatorial views of the plasma flow speed (color contours) overlaid with unit flow vectors corresponding, respectively, to times before and after the impact of the shock as indicated by the magenta dashed line in (a). The magenta lines with white crosses in (b) and (c) mark the tail X-lines, out of which fast bulk flows are being ejected. Results are extracted from the simulation described in *Jia et al.* [2012b].

discussed in *Jia et al.* [2012b], these two flanks may play an important role in releasing plasma from the magnetosphere through breaking-off of the closed flux tubes at large distances. *Delamere and Bagenal* [2013] have argued that it is possible that Saturn's magnetospheric dynamics is driven primarily by the viscous interaction at the magnetopause boundary producing two extended wings with closed magnetic flux on the dawn and dusk flanks, similar to that shown in Figure 25.8b. However, it is worth stressing here that such a convection pattern as shown in Figure 25.8b is normally seen in the simulations under strong solar wind driving conditions, for example, high solar wind dynamic pressure. As shown in Figure 25.8a, when the solar wind pressure decreases, the tail configuration appears very different from that in the high pressure case (e.g., only one extended region of closed flux on the dusk flank is present). This comparison from the simulation suggests that characteristics of the tail reconnection, such as its location and geometry, and the resultant global convection can change significantly in response to variations of the external pressure. Similarly, plasmoid release resulting from tail reconnection also depends on the external solar wind conditions. *Jia et al.* [2012b] have found that the solar wind dynamic pressure affects the recurrence rate of plasmoid release in the tail (i.e., the release rate becomes higher as the dynamic pressure increases), a finding similar to that reached by another MHD simulation study by *Zieger et al.* [2012].

25.5. SUMMARY AND CONCLUSIONS

In this paper, we have presented two sets of MHD simulations of Saturn's magnetosphere using the BATS-R-US model that couples the solar wind, the magnetosphere and the ionosphere self-consistently and includes the major plasma sources associated with the moons. The first set of simulations are carried out to investigate how the coupled magnetosphere-ionosphere system responds to rotating FACs with an $m = 1$ symmetry as an attempt to understand the origin of Saturn's mysterious periodicities evidenced by various fields and particles measurements. Vortical flows with an $m = 1$ symmetry are imposed

in the model ionosphere generating a rotating field-aligned current system coupled to the magnetosphere. In the simulations, the solar wind is set at nominal values and kept constant in time so that we can focus on the effects of the internal driver. The simulation model has been run for cases that impose different ionospheric boundary conditions including a single vortex in the southern hemisphere, dual vortices in the southern hemisphere, and dual vortices in both hemispheres. Our objective in studying the MHD simulations is to understand whether an ionospheric source of FACs of the sort that we have assumed can account for the periodic responses observed, and, if it can, to establish the mechanisms through which periodicity is imposed on different parts of the magnetospheric system. Our analysis presented in a series of papers [*Jia et al.*, 2012a; *Jia and Kivelson*, 2012; *Kivelson and Jia*, 2014] has concluded that the model does reproduce a broad range of observed periodic phenomena with good quantitative fidelity.

Several major results from the vortex simulations are discussed in this paper. It is found that the imposed flow vortices in the ionosphere generate rotating perturbations of the magnetic field and plasma density in the near-equatorial regions as well as a rotating asymmetric ring current inside of ~12 R_S, consistent with various Cassini in situ observations (Figure 25.2). The modeled FACs, which are the sources of SKR, have properties that account for key features reported for those radio emissions including rotation of the most intense currents with an amplitude that varies with local time and peaks in the morning meridian (Figure 25.3). Furthermore, the flow anomalies introduced in the model ionosphere impose flow perturbations on the magnetospheric plasma resulting in compressional waves propagating throughout the magnetosphere. The waves launched from the rotating sources lead to large-scale displacements of various magnetospheric boundaries. For instance, the magnetopause moves radially in and out with amplitudes that correspond to observations and its equatorial cross section is asymmetric in the dawn-dusk direction (Figure 25.4). The tail current sheet periodically moves up and down beyond ~15 R_S, and the tail plasma sheet thickens and thins periodically at both the effective rotation period and at the beat period between the northern and southern sources (Figures 25.5 and 25.6), all consistent with in situ observations.

Motivated by various observational studies that have demonstrated the solar wind influences on the Saturnian magnetosphere, we have carried out another global simulation to characterize the dynamical response of the magnetosphere/ionosphere to different types of solar wind disturbances. This simulation adopts a time-varying upstream input with a range of parameters representative of the solar wind at Saturn's orbit. The simulation specifically allows one to investigate the interaction of Saturn's magnetosphere with CIRs and associated interplanetary shocks, which have been regularly observed near Saturn during solar minimum. Of particular interest is the role of magnetic reconnection in driving global dynamics. Our simulation reveals that there are generally two types of reconnection in the tail, that is, the "Vasyliūnas-cycle" reconnection arising from the centrifugal stresses imposed by the planet's rapid rotation on mass-loaded flux tubes, and the "Dungey-cycle" reconnection involving reconnection of open field lines that are produced on the dayside and subsequently convected into the tail lobes. Because of the low densities and high Alfvén speeds of the lobe field lines, the "Dungey-cycle" reconnection typically produces hotter and more depleted flux tubes with faster flows in the outflows from the reconnection site compared to those produced directly by the Vasyliūnas-cycle reconnection, which initiates on closed field lines with relatively high plasma densities and low Alfvén speeds. An important product of the tail reconnection is the formation of plasmoids, which provides a means for releasing magnetospheric plasma supplied by the internal sources from the magnetosphere. However, our analysis of the simulation output indicates that the mass loss through large-scale plasmoids in the tail only accounts for a small fraction (~10% on average) of the total mass added to the magnetosphere by the Enceladus-associated sources, suggesting that it is important to consider other mechanisms that are able to release the magnetospheric plasma (such as small-scale plasmoid release near the flanks). Our simulation also shows that tail reconnection is able to generate global impacts on the coupled magnetosphere/ionosphere system, such as large-scale reconfigurations of the magnetosphere, hot particle injections into the inner and middle magnetospheres that may produce enhanced ENAs emissions, and intensification of FACs in the ionosphere that are expected to cause aurora brightening (Figure 25.7). Consistent with previous observational studies, our simulation study finds that variations of the solar wind pressure can have significant influences on Saturn's magnetospheric configuration and dynamics, including how reconnection operates in the magnetotail (Figure 25.8).

ACKNOWLEDGMENTS

This work was supported by National Aeronautics and Space Administration (NASA) through grants NNX12AK34G at the University of Michigan (XJ and MGK) and NNX10AF16G at UCLA (MGK) and by the Cassini mission under contracts JPL 1409449 (TIG and XJ) and 1416974 (MGK). Data used in this study were obtained from simulations using the SWMF/BATS-R-US

code developed at the University of Michigan, which is available at http://csem.engin.umich.edu/tools/swmf/. The simulation runs were performed on the Pleiades supercomputer managed by the NASA Advanced Supercomputing Division.

REFERENCES

Andrews, D. J., et al. (2008), Planetary period oscillations in Saturn's magnetosphere: Phase relation of equatorial magnetic field oscillations and Saturn kilometric radiation modulation. *J. Geophys. Res. 113*, A09205, doi:10.1029/2007JA012937.

Andrews, D. J., A. J. Coates, S. W. H. Cowley, M. K. Dougherty, L. Lamy, G. Provan, and P. Zarka (2010), Magnetospheric period oscillations at Saturn: Comparison of equatorial and high-latitude magnetic field periods with north and south Saturn kilometric radiation periods, *J. Geophys. Res.*, *115*, A12252, doi:10.1029/2010JA015666.

Andrews, D. J., S. W. H. Cowley, M. K. Dougherty, L. Lamy, G. Provan, and D. J. Southwood (2012), Planetary period oscillations in Saturn's magnetosphere: Evolution of magnetic oscillation properties from southern summer to postequinox, *J. Geophys. Res.*, *117*, A04224, doi:10.1029/2011JA017444.

Arridge, C. S., N. Andre, K. K. Khurana, C. T. Russell, S. W. H. Cowley, G. Provan, D. J. Andrews, C. M. Jackman, A. J. Coates, E. C. Sittler, M. K. Dougherty, and D. T. Young (2011), Periodic motion of Saturn's nightside plasma sheet, *J. Geophys. Res.*, *116*, A11205, doi:10.1029/2011JA016827.

Bagenal, F., and P. A. Delamere (2011), Flow of mass and energy in the magnetospheres of Jupiter and Saturn, *J. Geophys. Res.*, *116*, A05209, doi:10.1029/2010JA016294.

Brandt, P. C. *et al.* (2010), Saturn's periodic magnetic field perturbations caused by a rotating partial ring current. *Geophys. Res. Lett. 37*, L22103, doi:10.1029/2010GL045285.

Bunce, E. J., et al. (2008), Origin of Saturn's aurora: Simultaneous observations by Cassini and the Hubble Space Telescope, *J. Geophys. Res.*, *113*, A09209, doi:10.1029/2008JA013257.

Carbary, J. F., D. G. Mitchell, S. M. Krimigis, D. C. Hamilton, and N. Krupp (2007), Charged particle periodicities in Saturn's outer magnetosphere. *J. Geophys. Res. 112*, A06246, doi:10.1029/2007JA012351.

Carbary, J. F., D. G. Mitchell, P. Brandt, C. Paranicas, and S. M. Krimigis (2008), ENA periodicities at Saturn. *Geophys. Res. Lett. 35*, L07102, doi:10.1029/2008GL033230.

Carbary, J. F., and D. G. Mitchell (2013), Periodicities in Saturn's magnetosphere, *Rev. Geophys.*, *51*, 1–30, doi:10.1002/rog.20006.

Carbary, J. F. (2013), Longitude dependences of Saturn's ultraviolet aurora, *Geophys. Res. Lett.*, *40*, doi:10.1002/grl.50430.

Clarke, J. T., et al. (2005), Morphological differences between Saturn's ultraviolet aurorae and those of Earth and Jupiter, *Nature*, *433*, 717–719.

Clarke, K. E., D. J. Andrews, C. S. Arridge, A. J. Coates, and S. W. H. Cowley (2010), Magnetopause oscillations near the planetary period at Saturn: Occurrence, phase, and amplitude, *J. Geophys. Res.*, *115*, A08209, doi:10.1029/2009JA014745.

Cowley, S. W. H. et al. (2008), Auroral current systems in Saturn's magnetosphere: comparison of theoretical models with Cassini and HST observations. *Ann. Geophys. 26*, 2613–2630.

Delamere, P. A. and F. Bagenal (2013), Magnetotail structure of the giant magnetospheres: Implications of the viscous interaction with the solar wind, *J. Geophys. Res.*, *118*, doi:10.1002/2013JA019179.

Desch, M. D., and M. L. Kaiser (1981), Voyager measurement of the rotation period of Saturn's magnetic field, *Geophys. Res. Lett.*, *8*, 253–256, doi:10.1029/GL008i003p00253.

Dungey, J. W. (1961), Interplanetary field and the auroral zones, *Phys. Rev. Lett.*, *6*, 47.

Espinosa, S. A., and M. K. Dougherty (2000), Periodic perturbations in Saturn's magnetic field, *Geophys. Res. Lett.*, *27*, 2785–2788, doi:10.1029/2000GL000048.

Espinosa, S. A., D. J. Southwood, and M. K. Dougherty (2003), How can Saturn impose its rotation period in a noncorotating magnetosphere? *J. Geophys. Res.*, *108*(A2), 1086, doi:10.1029/2001JA005084.

Fischer, G., Ye, S.-Y., Groene, J. B., Ingersoll, A. P., Sayanagi, K. M., Menietti, J. D., Kurth, W. S., and Gurnett, D. A. (2014), A possible influence of the Great White Spot on Saturn kilometric radiation periodicity, *Ann. Geophys.*, *32*, 1463–1476, doi:10.5194/angeo-32-1463-2014.

Fleshman, B. L., P. A. Delamere, and, F. Bagenal (2010), A sensitivity study of the Enceladus torus. *J. Geophys. Res. 115*, E04007, doi:10.1029/2009JE003372.

Fukazawa, K., T. Ogino, and R. J. Walker (2007a), Magnetospheric convection at Saturn as a function of IMF BZ, *Geophys. Res. Lett.*, *34*, L01105, doi:10.1029/2006GL028373.

Fukazawa, K., T. Ogino, and R. J. Walker (2007b), Vortex-associated reconnection for northward IMF in the Kronian magnetosphere, *Geophys. Res. Lett.*, *34*, L23201, doi:10.1029/2007GL031784.

Fukazawa, K., T. Ogino, and R. J. Walker (2012), A magnetohydrodynamic simulation of Kronian field-aligned currents and auroras, *J. Geophys. Res.*, *117*, A002214, doi:10.1029/2011JA016945.

Galopeau, P., P. Zarka, and, D. Le Queau (2000), Theoretical model of Saturn's kilometric radiation spectrum. *J. Geophys. Res. 94*, 8739–8755, 1989.

Galopeau, P. H. M., and A. Lecacheux, Variations of Saturn's radio rotation period measured at kilometer wavelengths, *J. Geophys. Res.*, *105*, 13,089–13,102, doi:10.1029/1999JA005089.

Goldreich, P., and A. J. Farmer (2007), Spontaneous axisymmetry breaking of the external magnetic field at Saturn, *J. Geophys. Res.*, Vol. *112*, A05225, doi:10.1029/2006JA012163.

Gombosi, T. I., G. Tóth, D. L. DeZeeuw, C. P. T. Groth, K. C. Hansen, K. Kabin, and K. G. Powell (2002), Semi-relativistic magnetohydrodynamics and physics-based convergence acceleration, *J. Comp. Phys.*, *177*, 176.

Gurnett, D. A., et al. (2007), The variable rotation period of the inner region of Saturn's plasma disk. *Science*, *316*, 442–445, doi:10.1126/science.1138562.

Gurnett, D. A., et al. (2009), Discovery of a north-south asymmetry in Saturn's radio rotation period. *Geophys. Res. Lett. 36*, L16102, doi:10.1029/2009GL039621.

Gurnett, D. A., et al. (2010a), The reversal of the rotational modulation rates of the north and south components of

Saturn kilometric radiation near equinox. *Geophys. Res. Lett. 37*, L24101, doi:10.1029/2010GL045796.

Gurnett, D. A., et al. (2010b), A plasmapause-like density boundary at high latitudes in Saturn's magnetosphere, *Geophys. Res. Lett.*, *37*, L16806, doi:10.1029/2010GL044466.

Hansen, K. C., A. J. Ridley, G. B. Hospodarsky, N. Achilleos, M. K. Dougherty, T. I. Gombosi, G. Tóth (2005), Global MHD Simulations of Saturn's Magnetosphere at the time of Cassini Approach, *Geophys. Res. Lett.*, *32*, L20S06, doi:10.1029/2005GL022835.

Hill, T. W., et al. (2008), Plasmoids in Saturn's magnetotail, *J. Geophys. Res.*, *113*, A01214, doi:10.1029/2007JA012626.

Jackman, C. M. et al., (2005), Interplanetary conditions and magnetospheric dynamics during the Cassini orbit insertion fly-through of Saturn's magnetosphere. *J. Geophys. Res. 110*, A10212, doi:10.1029/2005JA011054.

Jackman, C. M., C. T. Russell, D. J. Southwood, C. S. Arridge, N. Achilleos, and M. K. Dougherty (2007), Strong rapid dipolarizations in Saturn's magnetotail: In situ evidence of reconnection, *Geophys. Res. Lett.*, *34*, L11203, doi:10.1029/2007GL029764.

Jackman, C. M., et al. (2014), Saturn's dynamic magnetotail: A comprehensive magnetic field and plasma survey of plasmoids and traveling compression regions and their role in global magnetospheric dynamics, *J. Geophys. Res.*, *119*, 5465–5494, doi:10.1002/2013JA019388.

Jia. X., M. G. Kivelson, and T. I. Gombosi (2012a), Driving Saturn's magnetospheric periodicities from the upper atmosphere/ionosphere, *J. Geophys. Res.*, A04215, doi:10.1029/2011JA017367.

Jia, X., K. C. Hansen, T. I. Gombosi, M. G. Kivelson, G. Tóth, D. L. DeZeeuw, and A. J. Ridley (2012b), Magnetospheric configuration and dynamics of Saturn's magnetosphere: A global MHD simulation, *J. Geophys. Res.*, *117*, A05225, doi:10.1029/2012JA017575.

Jia, X., and M. G. Kivelson (2012), Driving Saturn's magnetospheric periodicities from the upper atmosphere/ionosphere: Magnetotail response to dual sources, *J. Geophys. Res.*, *117*, A11219, doi:10.1029/2012JA018183.

Jurac, S., and J. D. Richardson (2005), A self-consistent model of plasma and neutrals at Saturn: Neutral cloud morphology. *J. Geophys. Res. 110*, A09220, doi:10.1029/2004JA010635.

Khurana, K. K., et al. (2009), Sources of rotational signals in Saturn's magnetosphere. *J. Geophys. Res. 114*, A02211, doi:10.1029/2008JA013312.

Kidder, A. et al. (2012), External triggering of plasmoid development at Saturn, *J. Geophys. Res.*, *117*, A07206, doi:10.1029/2012JA017625.

Kivelson, M. G., and X. Jia (2014), Control of periodic variations in Saturn's magnetosphere by compressional waves, *J. Geophys. Res.*, *119*, doi:10.1002/2014JA020258.

Kurth, W. S., A. Lecacheux, T. F. Averkamp, J. B. Groene, and D. A. Gurnett (2007), A Saturnian longitude system based on a variable kilometric rotation period. *Geophys. Res. Lett. 34*, L02201, doi:10.1029/2006GL028336.

Lamy, L., B. Cecconi, R. Prangé, P. Zarka, J. D. Nichols, and J. T. Clarke (2009), An auroral oval at the footprint of Saturn's kilometric radio sources, co-located with the UV aurorae, *J. Geophys. Res.*, *114*, A10212, doi:10.1029/2009JA014401.

Lamy, L. (2011), Variability of southern and northern SKR periodicities. *Planetary Radio Emissions VII*, edited by H. O. Rucker et al., pp. 39–50, Austrian Acad. of Sci. Press, Vienna, doi:10.1553/PRE7s39.

Lecacheux, A., P. Galopeau, and M. Aubier (1997), Revisiting Saturn kilometric radiation with Ulysses/URAP, in *Planetary Radio Emissions IV*, edited by H. O. Rucker and S. J. Bauer, pp. 313–325, Austrian Acad. of Sci. Press, Vienna.

Mitchell, D. G., et al. (2009), Recurrent energization of plasma in the midnight-to-dawn quadrant of Saturn's magnetosphere, and its relationship to auroral UV and radio emissions. *Planet. Space. Sci. 57*, 1732–1742, doi:10.1016/j.pss.2009.04.002.

Mitchell, D. G., et al. (2015), Injection, Interchange, and Reconnection: Energetic particle observations in Saturn's magnetosphere, AGU Geophysical Monograph Series: *Magnetotails in the Solar System* (eds A. Keiling, C. M. Jackman and P. A. Delamere), John Wiley & Sons, Inc., Hoboken, NJ..

Moore, L., I. Mueller-Wodarg, M. Galand, A. Kliore, and M. Mendillo (2010), Latitudinal variations in Saturn's ionosphere: Cassini measurements and model comparisons, *J. Geophys. Res.*, *115*, A11317, doi:10.1029/2010JA015692.

Nichols, J. D., et al. (2008), Oscillation of Saturn's southern auroral oval, *J. Geophys. Res.*, Vol. *113*, A11205, doi:10.1029/2008JA013444.

Paranicas, C. et al. (2015), Periodic intensity variations in global ENA images of Saturn. *Geophys. Res. Lett. 32*, L21101, doi:10.1029/2005GL023656, 2005.

Pilkington, N., et al. (2015), Significant asymmetries in Saturn's magnetosphere, *Magnetospheres of the Outer Planets meeting*, Atlanta, Georgia.

Powell, K., P. Roe, T. Linde, T. I. Gombosi, and D. L. DeZeeuw (1999), A solution-adaptive upwind scheme for ideal magnetohydrodynamics, *J. Comp. Phys.*, *154*, 284.

Provan, G., D. J. Andrews, C. S. Arridge, A. J. Coates, S. W. H. Cowley, S. E. Milan, M. K. Dougherty, and D. M. Wright (2009a), Polarization and phase of planetary-period magnetic field oscillations on high-latitude field lines in Saturn's magnetosphere, *J. Geophys. Res.*, *114*, A02225, doi:10.1029/2008JA013782.

Provan, G., S. W. H. Cowley, and J. D. Nichols (2009b), Phase relation of oscillations near the planetary period of Saturn's auroral oval and the equatorial magnetospheric magnetic field, *J. Geophys. Res.*, *114*, A04205, doi:10.1029/2008JA013988.

Provan, G., D. J. Andrews, B. Cecconi, S. W. H. Cowley, M. K. Dougherty, L. Lamy, and P. M. Zarka (2011), Magnetospheric period magnetic field oscillations at Saturn: Equatorial phase "jitter" produced by superposition of southern and northern period scintillations, *J. Geophys. Res.*, *116*, A04225, doi:10.1029/2010JA016213.

Provan, G., D. J. Andrews, C. S. Arridge, A. J. Coates, S. W. H. Cowley, G. Cox, M. K. Dougherty, and C. M. Jackman (2012), Dual periodicities in planetary-period magnetic field oscillations in Saturn's tail, *J. Geophys. Res.*, *117*, A01209, doi:10.1029/2011JA017104.

Provan, G., L. Lamy, S. W. H. Cowley, and M. K. Dougherty (2014), Planetary period oscillations in Saturn's magnetosphere: Comparison of magnetic oscillations and SKR modulations in the post-equinox interval, *J. Geophys. Res.*, accepted, doi:10.1002/2014JA020011.

Richardson, J. D., A. Eviatar, M. A. McGrath, and, V. M. Vasyliūnas (1998), OH in Saturn's magnetosphere: Observations and implications. *J. Geophys. Res. 103*, 20245–20255.

Ridley, A., T. I. Gombosi, and, D. Dezeeuw (2004), Ionospheric control of the magnetosphere: conductance. *Ann. Geophys. 22*, 567-584.

Smith, H. T. et al. (2010), Enceladus plume variability and the neutral gas densities in Saturn's magnetosphere. *J. Geophys. Res. 115*, A10252, doi:10.1029/2009JA015184.

Smith, C. G. A. (2006), Periodic modulation of gas giant magnetospheres by the neutral upper atmosphere, *Ann. Geophys.*, *24*, 2709–2717.

Smith, C. G. A. (2014), On the nature and location of the proposed twin vortex systems in Saturn's polar upper atmosphere, *J. Geophys. Res. Space Physics*, *119*, doi:10.1002/2014JA019934.

Southwood, D. J., and M. G. Kivelson (2007), Saturnian magnetospheric dynamics: Elucidation of a camshaft model. *J. Geophys. Res. 112*, A12222, doi:10.1029/2007JA012254.

Southwood, D. J., and M. G. Kivelson (2009), The source of Saturn's periodic radio emission. *J. Geophys. Res. 114*, A09201, doi:10.1029/2008JA013800.

Southwood, D. J. (2011), Direct evidence of differences in magnetic rotation rate between Saturn's northern and southern polar regions. *J. Geophys. Res. 116*, doi:10.1029/2010JA016070.

Southwood, D. J., and S. W. H. Cowley (2014), The origin of Saturn's magnetic periodicities: Northern and southern current systems, *J. Geophys. Res. Space Physics*, *119*, 1563–1571, doi: 10.1002/2013JA019632.

Thomsen, M. F., R. J. Wilson, R. L. Tokar, D. B. Reisenfeld, and C. M. Jackman (2013), Cassini/CAPS observations of dusk-side tail dynamics at Saturn, *J. Geophys. Res.*, *118*, doi:10.1002/jgra.50552.

Thomsen, M. F., D. Mitchell, X. Jia, C. M. Jackman, G. Hospodarsky, and A. Coates (2015), Plasmapause formation at Saturn, *J. Geophy. Res.,* doi: 10.1002/2015JA021008.

Tóth, G. et al. (2012), Adaptive numerical algorithms in space weather modeling. *J. Comp. Phys.*, *231*, 870–903, doi:10.1016/j.jcp.2011.02.006.

Vasyliūnas, V. M. (1983), Plasma distribution and flow, in *Physics of the Jovian Magnetosphere*, edited by A. J. Dessler, pp. 395–453, Cambridge Univ. Press, New York.

Wolfe, J. H., J. D. Mihalov, H. R. Collard, D. D. McKibbin, L. A. Frank, and D. S. Intriligator (1980), Preliminary Results on the Plasma Environment of Saturn from the Pioneer 11 Plasma Analyzer Experiment, *Science*, Vol. *207*, No. 4429, pp. 403–407.

Wu, C. S., and L. C. Lee (1979), A theory of the terrestrial kilometric radiation. *Astrophys. J. 230*, 621-626, doi:10.1086/157120.

Zieger, B., K. C. Hansen, T. I. Gombosi, and, D. L. DeZeeuw (2010), Periodic plasma escape from the mass-loaded Kronian magnetosphere. *J. Geophys. Res. 115*, A08208, doi:10.1029/2009JA014951.

26

Simulation Studies of Magnetosphere and Ionosphere Coupling in Saturn's Magnetosphere

Raymond J. Walker[1] and Keiichiro Fukazawa[2]

Video of Yosemite Talk, URL: http://dx.doi.org/10.15142/T3Z302

ABSTRACT

Auroral images coupled with magnetohydrodynamic (MHD) simulations can provide a global view of magnetosphere and ionosphere coupling. In this paper, we use a global MHD simulation of Saturn's solar wind and magnetosphere and ionosphere system to investigate the structure of field-aligned currents connecting the magnetosphere and ionosphere when the interplanetary magnetic field (IMF) is northward. The emphasis is on the location and source of field-aligned currents directed away from the ionosphere that are thought to be associated with electron precipitation. We find that the largest currents are found at the edge of the polar cap. They occur at the dayside magnetopause, in Kelvin-Helmholtz (K-H) vortices on the flanks of the magnetosphere and in the region of the tail where Saturnward flows diverge around the corotating inner magnetosphere region. In the simulation the currents are primarily generated by the component of flow vorticity parallel to the magnetic field. We also modeled the ionosphere convection system and the energy flux to the ionosphere associated with diffuse aurora and find that the energy flux is largest in the region of the polar cusp and in the flow divergence region.

26.1. INTRODUCTION

Auroral images provide one way to investigate the overall interaction between the magnetosphere and the ionosphere. They are especially important in studies of magnetosphere and ionosphere coupling in planetary magnetospheres, since multi-spacecraft observations are not available. Global simulations provide a complementary approach. In particular simulations allow us to place in situ spacecraft observations in planetary magnetospheres and auroral images in a more global context. In this paper, we will use a global magnetohydrodynamic simulation of the interaction between the solar wind and Saturn's magnetosphere and ionosphere to study magnetosphere and ionosphere coupling in a rapidly rotating magnetosphere. We concentrate on Saturn because recent computing advances enable us to model Saturn with a very high resolution code (a grid spacing of $0.1R_S$), and our studies have shown that this high resolution is necessary to properly resolve features in the magnetosphere and ionosphere system.

Saturn has an intrinsic magnetic field with an equatorial surface magnetic field of 0.2G. Saturn's rotation period is 10 h 39 m, and its magnetic dipole is approximately aligned with its spin axis. Like at Jupiter, a frictional torque in Saturn's ionosphere accelerates plasma toward co-rotation. The ionospheric torque is transmitted to the magnetosphere by field-aligned currents that close through radial currents [*Hill*, 1979; *Vasyliunas*,

[1] *Department of Earth, Planetary and Space Sciences, University of California at Los Angeles, Los Angeles, CA, USA*

[2] *Academic Center for Computing and Media Studies Kyoto University, Yoshidahonmachi, Sakyo-ku, Kyoto, Japan*

Magnetosphere-Ionosphere Coupling in the Solar System, Geophysical Monograph 222, First Edition.
Edited by Charles R. Chappell, Robert W. Schunk, Peter M. Banks, James L. Burch, and Richard M. Thorne.

1983]. In the magnetosphere, $\boldsymbol{J} \times \boldsymbol{B}$ (where $\boldsymbol{J}$ is the current density and $\boldsymbol{B}$ is the magnetic field) is in the direction to accelerate plasma while $\boldsymbol{J} \times \boldsymbol{B}$ in the ionosphere is in the direction to slow the atmosphere's rotation. The dominant source of plasma is from geysers on Enceladus. They provide the magnetosphere with between 12 kg/s and 250 kg/s of water group ions [*Jackman et al.*, 2014].

Saturn's main auroral oval is thought to be related to the boundary between open and closed field lines in Saturn's polar cap [*Cowley and Bunce*, 2003]. This differs from Jupiter's magnetosphere where the main oval is thought to be related to the breakdown of co-rotation in Jupiter's middle magnetosphere. Magnetic reconnection in Saturn's tail is expected to reduce the size of the polar cap and thereby lead to aurora on the dawn side of the magnetosphere, which expands poleward in analogy with aurora at the Earth [*Cowley et al.*, 2005]. *Badman et al.* [2014] used auroral images to estimate the changes in the polar cap size and estimated net reconnection rates of a few tens of kilovolt (kV). *Nichols et al.* [2014] used Hubble Space Telescope observations to suggest that enhancements of dawnside aurora may be related to tail lobe reconnection and estimated a reconnection voltage of 280 kV. *Grodent et al.* [2011] have shown localized enhancements in the dayside aurora that may be related to K-H waves at the magnetopause.

In this paper, we will use a global MHD simulation of Saturn's magnetosphere to investigate magnetosphere and ionosphere coupling. The connection between the magnetosphere and ionosphere is through field-aligned currents. We will use the simulation to calculate the currents, their distribution in space, their connection to the ionosphere, and their time dependence. We will evaluate possible generation mechanisms and compare our results with the systems inferred from observations. In Section 26.2, we briefly describe the simulation code, and in Section 26.3, we describe the resulting magnetospheric configuration and the resulting configuration of currents in the ionosphere. In Section 26.4, we discuss the simulated magnetosphere in the context of the observations.

26.2. THE SIMULATION MODEL

Our model of Saturn's magnetosphere [*Fukazawa et al.*, 2007; *Walker et al.*, 2011] was adapted from a code developed to study Jupiter's magnetosphere [*Ogino et al.*, 1998]. It uses a Cartesian grid with a uniform grid spacing of $0.1R_S$. The overall grid is $1802 \times 1202 \times 602$ corresponding to $60R_S > X > -120R_S$, $60R_S > Y > -60R_S$ and $0 < Z < 60R_S$, where X is positive toward the Sun, Z is northward, and Y completes a right-handed system. Initially, the Kronian plasma is contained in a rotating equilibrium current sheet. There is no model of the Enceladus torus, but the simulation code has an inner magnetosphere source in the current disk at $5R_S$. For the results in this paper, the source rate was 2.75×10^{27} water group ions/s. Initially, a solar wind with velocity of $V_{SW} = 300$ km/s and dynamic pressure of $P_{dyn} = 0.0083$nPa enters the upstream boundary of the simulation at $x = 60R_S$. The temperature of the solar wind is 2×10^5K. There was no initial IMF. After 2 h, a northward IMF of 0.4 nT entered the upstream boundary. Continuous boundary conditions were used at the top, back, and sides of the simulation while symmetry boundary conditions were used at the equator.

The ionosphere of Saturn was modeled by using the current continuity equation

$$\nabla \cdot \sum \cdot \nabla \Phi = j_{\parallel} \sin I$$

where Σ is the conductance tensor, ϕ is the ionospheric potential, $j_{\parallel}$ is the field aligned current density and I is the inclination of the magnetic field. Field aligned currents from the inner boundary of the simulation at $5R_S$ were mapped along field lines to the ionosphere where the continuity equation was solved for $\nabla\Phi$. The ionospheric solution was carried out on a 200×200 point grid. The Pedersen conductance was 1S, and the Hall conductance was set to zero.

26.3. SATURN'S SIMULATED MAGNETOSPHERE

Reconnection at Saturn's dayside magnetopause occurs when the IMF has a northward component. There is much less erosion of the dayside magnetopause in Saturn simulations due to reconnection than is found in simulations of the Earth and Jupiter [*Fukazawa et al.*, 2012; *Jia et al.*, 2012]. In Figure 26.1, we have plotted B_Z in the equatorial plane with color coding while flow vector arrows have been superimposed in white for 10 h, 12 h, and 16 h after the onset of dayside reconnection. Note that the arrows have been drawn along flow streamlines. Only part of the simulation box is shown in order to make the magnetosphere near Saturn easier to see. The white lines at 16 h are contours of $B_Z = 0$. During this interval, the flux transfer gave a voltage of about 80 kV compared with the solar wind potential difference across the magnetosphere of about 580 kV [*Walker and Jia*, 2016].

In the top panel (10 h), linear waves can be seen at the dawn magnetopause. At Saturn, the rotational flows in the magnetosphere are opposite to the magnetosheath flow in the morning sector. Thus, the magnetospheric flows increase the shear at the magnetopause and that can make the boundary unstable to the K-H instability. In general, the magnetospheric flows are in the same direction as the magnetosheath flow in the afternoon. At this time, the magnetic field at the equator points southward everywhere in Figure 26.1, so there is no near-Saturn reconnection in the tail at this time.

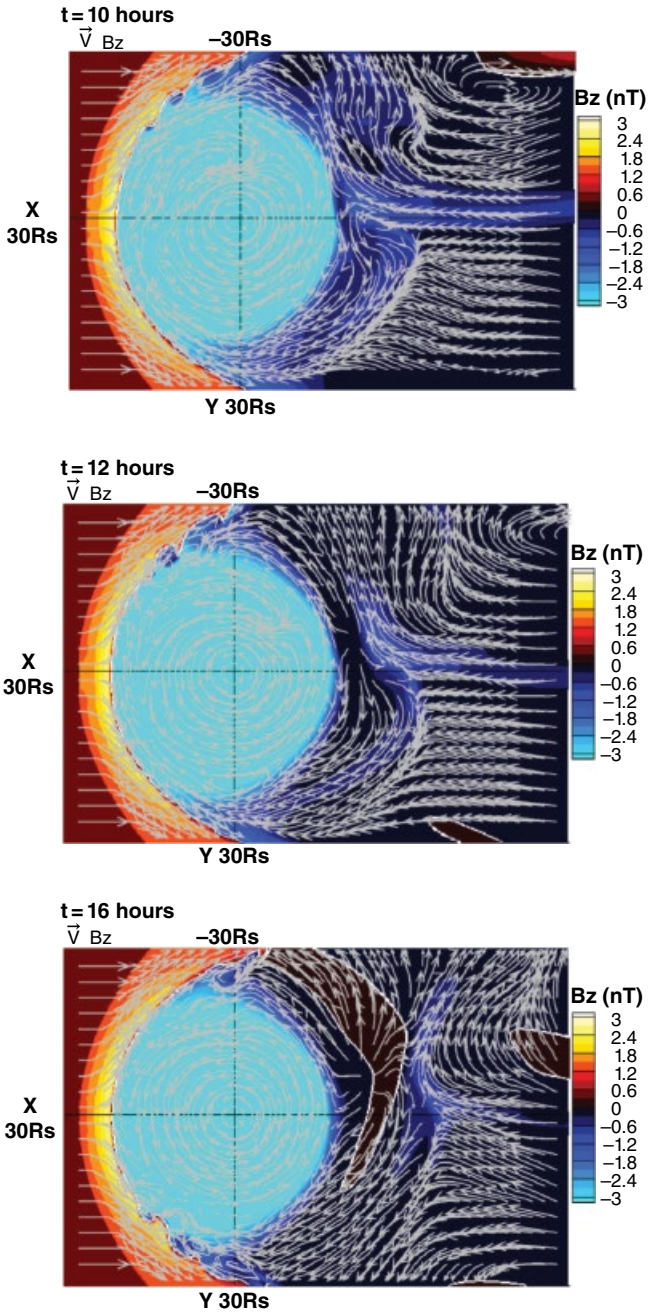

Figure 26.1 The magnitude of the B_Z component of the magnetic field as color contours and plasma flow vectors in the equatorial plane at t=10h, 12h, and 16h after reconnection began at the dayside magnetopause. Contours of B_Z =0 are white. [Adapted from *Fukazawa et al.*, 2012]

At 12 h, the waves at the dawn magnetopause have become larger and non-linear. Clear vortices can be found in the flows near the boundary. They have propagated tailward along the morning magnetopause. There is still no near-Saturn reconnection. By 16 h, vortices like those earlier in the morning have appeared on the afternoon magnetopause. The vortices on the morning magnetopause have moved almost entirely out of the region of the display. In the tail, a near-Saturn neutral line can be seen by the white line where the magnetic field B_Z reverses. Within the white lines the magnetic field is northward. This is the magnetic O (plasmoid) region. At this time, the reconnection is on closed field lines. Later between 20 h and 22 h, the reconnection reaches the lobe field lines [*Walker and Jia*, 2016], and a plasmoid like structure moves down the tail. *Jackman et al.* [2011] examined 34 plasmoids and found that typically they contain about 3 GWb of magnetic flux. *Jia et al.* [2012] reported <1 to 10 GWb in a simulation study with an average of 3.5 GWb. The plasmoid in Figure 26.1 contains about 5 GWb of flux. One of the long-term questions at Saturn is how does the mass from Enceladus leave the system? Both observational studies [*Thomsen et al.*, 2013; *Jackman et al.*, 2014] and simulation studies [*Jia et al.*, 2012; *Walker and Jia*, 2016] find that the plasmoids do not remove sufficient mass from the system to account for the Enceladus source.

In Figure 26.1, we saw very small waves on the magnetopause boundary. We have enlarged the velocity plot in Figure 26.2 at 10 h and 12 h. The dawnside vortices are much easier to see in this format. In the 10 h plot, the first signs of the waves on the boundary have appeared. *Walker et al.* [2011] applied the linear K-H stability criterion to the simulation results. They found that the boundary became unstable to K-H waves at about this time at 0900 local time (LT). By 12 h, the K-H vortices are well formed. The dusk boundary was stable to K-H waves until later in the simulation. The equivalent plots at 12 h and 16 h in the afternoon are shown in Figure 26.3. At 12 h, the boundary is smooth, but by 16 h, there are well-developed vortices on the afternoon magnetopause. Again *Walker et al.* [2011] found that the waves form when the boundary became unstable to the K-H instability. On the afternoon side, the shear was enhanced by flow from Saturn's tail in the direction opposite to co-rotation. This time the boundary became unstable at about 1500 LT. The K-H waves in the morning have propagated down the tail.

Field-aligned currents provide the connection between the magnetosphere and the ionosphere. From current continuity, the field-aligned currents in MHD can be written as

$$\nabla \cdot \mathbf{j}_{\parallel} = \frac{\partial j_{\parallel}}{\partial s} = -\nabla \cdot \frac{1}{B^2}\left(\mathbf{B} \times \left[\rho \frac{d\mathbf{v}}{dt} + \nabla p \right] \right)$$

where $\boldsymbol{j}_{\parallel}$ is the parallel current, the differential element ∂s is along the magnetic field direction, $\boldsymbol{B}$ is the magnetic

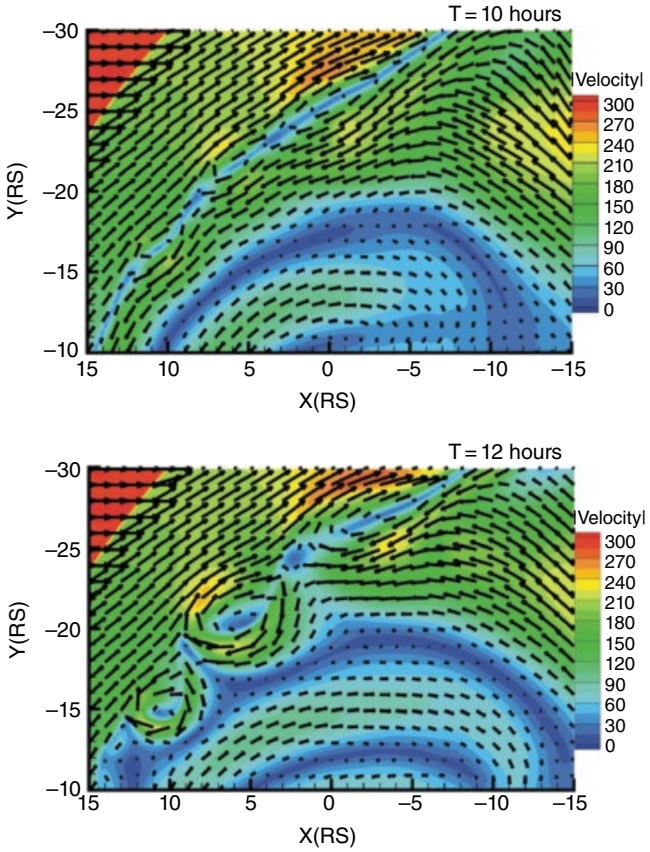

Figure 26.2 Plasma speed as color contours and flow arrows in the equatorial plane at 10h (top) and 12h (bottom).

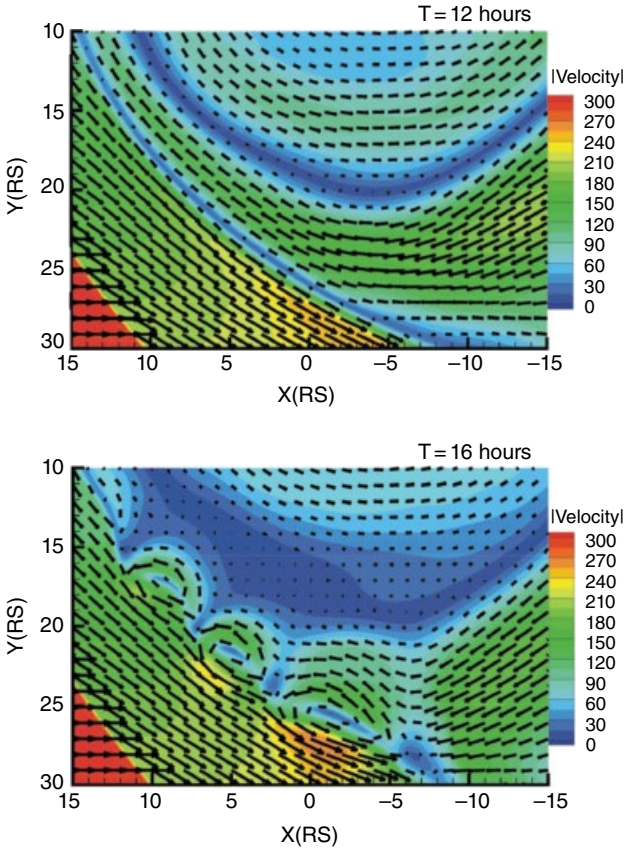

Figure 26.3 Plasma speed as color contours and flow arrows in the equatorial plane at 12h (top) and 16h (bottom).

vector, ρ is the mass density, $\boldsymbol{v}$ is the velocity, and p is the thermal pressure. If the inertial term is small then

$$\frac{j_{\parallel}}{B}(ion) - \frac{j_{\parallel}}{B}(eq) = -\frac{\mathbf{B}_{eq}}{B^2}\cdot\left(\nabla p_{eq}\times\nabla V\right)$$

where the notation "ion" means the quantities are evaluated in the ionosphere, and "eq" means they are evaluated in the equatorial magnetosphere. $V = \int_{eq}^{ion}\frac{\partial s}{B}$ is the flux tube volume. On the other hand, if the pressure term is small then

$$B\frac{\partial}{\partial s}\left(\frac{j_{\parallel}}{B}\right) = -\frac{\rho}{B}\frac{d\Omega_{\parallel}}{dt} \qquad (26.1)$$

where $\Omega_{\parallel}$ is the parallel vorticity. In Figure 26.4, we compare the pressure gradient (top) and the inertial term (bottom) at 12h. Note that the scale of the inertial term is 500 times that of the pressure term. Although there are pressure gradients in the simulation results, the pressure gradient term is everywhere smaller than the inertial term. The inertial term is the largest contributor to the field-aligned currents. It is largest at the magnetopause in the vortices and in the flow diversion region of the tail.

In Figure 26.5, we have plotted the field-aligned currents in the magnetosphere just below the equator ($Z = -0.05R_S$), which were determined by applying the equatorial boundary condition. This makes it easier to compare the magnetospheric currents with the ionospheric currents in the following figures. The top panel is at 12h, and the bottom panel is at 16h. Of special interest are blue colored currents since they are directed away from the ionosphere. This direction is consistent with precipitating electrons. At 12h, the strongest away currents are in the vortices near the morning magnetopause (1), along the magnetopause in the late morning (2), and in the tail region where the flow from the tail diverges (3, 3'). At 16h, there are strong currents near the dawn magnetopause (4), and in the evening flow divergence area similar to those at 12h (5). The away currents in the region of the vortices at dusk are found in a smaller region of the vortices (6) than was the case earlier (1) on the dawnside. In the early morning, the currents earthward of the reconnection site (5') are away from the planet.

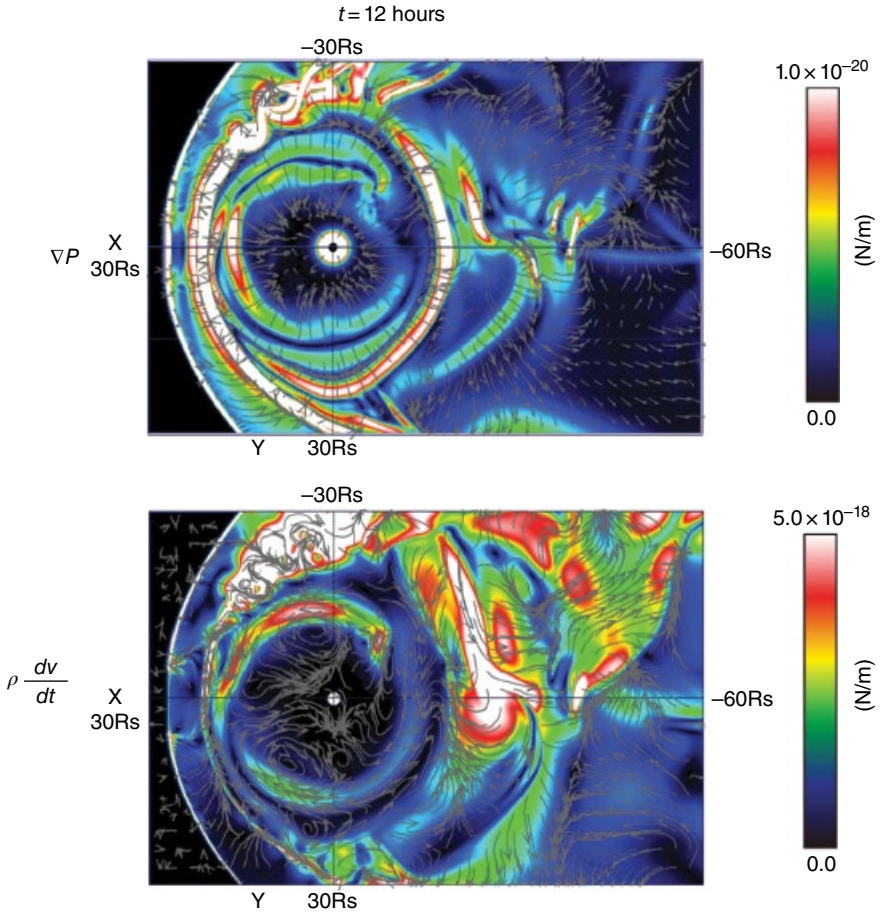

Figure 26.4 The magnitude of ∇p (top) and $\rho \frac{dv}{dt}$ as color contours and their vector representation in the equatorial plane at t=12h. [from *Fukazawa et al.*, 2012]

The parallel currents were calculated at the Saturnward boundary of the simulation and mapped along dipole field lines to the ionosphere. In Figure 26.6, we have plotted the currents in the southern hemisphere in a view from the north looking through Saturn to the south. Again, blue currents are away from the ionosphere. Most observations of aurorae at Saturn are of the southern hemisphere. There are three bands of alternating away and toward currents that are most evident in the morning. The highest latitude dawnside currents (4 at 12 h and 3 at 16 h) are away and are found at the edge of the polar cap. In the late morning, this structure changes into alternating away and toward currents. This is most evident in the 12 h panel in the region marked 1, 2, and 3. A similar structure at 16 h can be found in the afternoon in the region marked 1 and 2. Notice that the regions of away currents are much smaller in the afternoon than they were in the morning at 12 h. The high latitude currents on the afternoon and evening are toward Saturn (7 at 12 h and 6 at 16 h) and away at lower latitudes. If we map the night side currents to the equatorial magnetosphere, they map to the flow divergence region (3, 3' at 12 h and 5, 5' at 16 h).

The structured parallel currents on the dayside in Figure 26.6 (1, 2, 3 at 12 h and 1, 2 at 16 h) are closely related to the vortices at the magnetopause. We have calculated field lines from these parallel currents at the inner edge of the simulation out into the equatorial magnetosphere. The magnetospheric foot prints of selected ionospheric parallel currents are plotted in Figures 26.7 and 26.8. The quantity plotted in the equatorial plane is a qualitative indication of the change in parallel vorticity ($d\Omega_{\parallel}/dt$). Figure 26.7 gives the difference in the parallel vorticity between 12 h and 10 h, and Figure 26.8 gives the difference in the parallel vorticity between 16 h and 12 h. Blue parallel vorticity change corresponds to away currents in the ionosphere. The parallel current plots from Figure 26.7 have been reproduced from 12 h in Figure 26.7 and 16 h in Figure 26.8. In Figure 26.7, currents marked 1', 2', and 3' in the ionosphere map to the K-H vortices in the equatorial magnetosphere and $d\Omega_{\parallel}/dt$ has the correct sign to generate the parallel currents. Similarly in

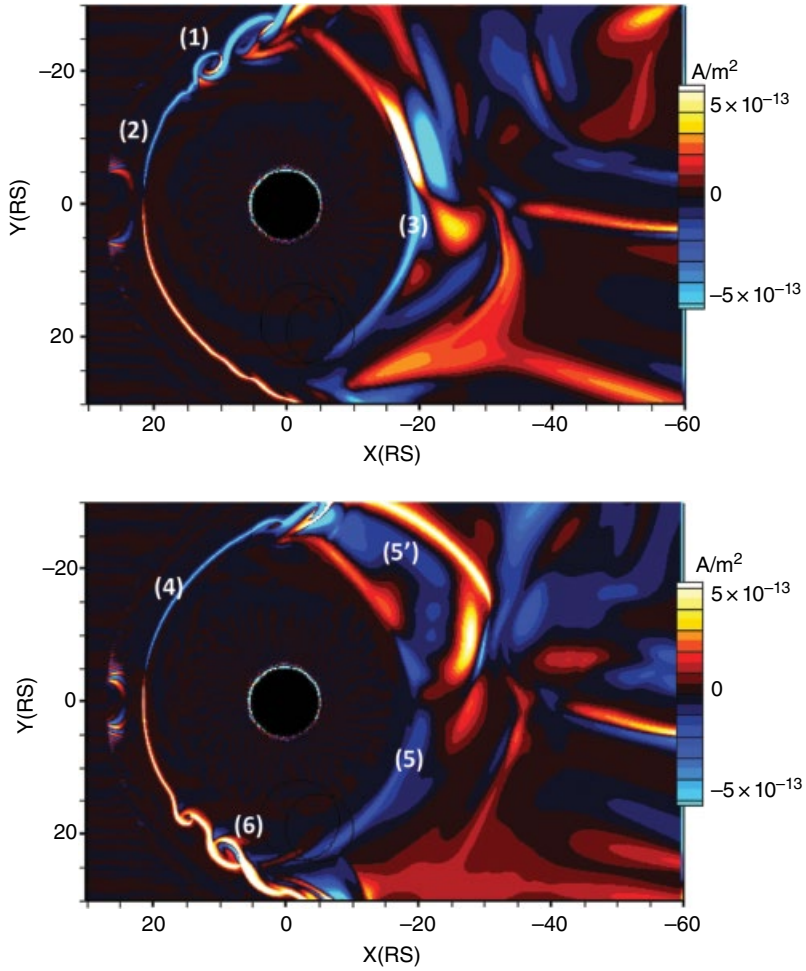

Figure 26.5 Field aligned currents in the plane at Z=-0.5R_E at 12h (top) and 16h (bottom). Blue currents are away from the ionosphere.

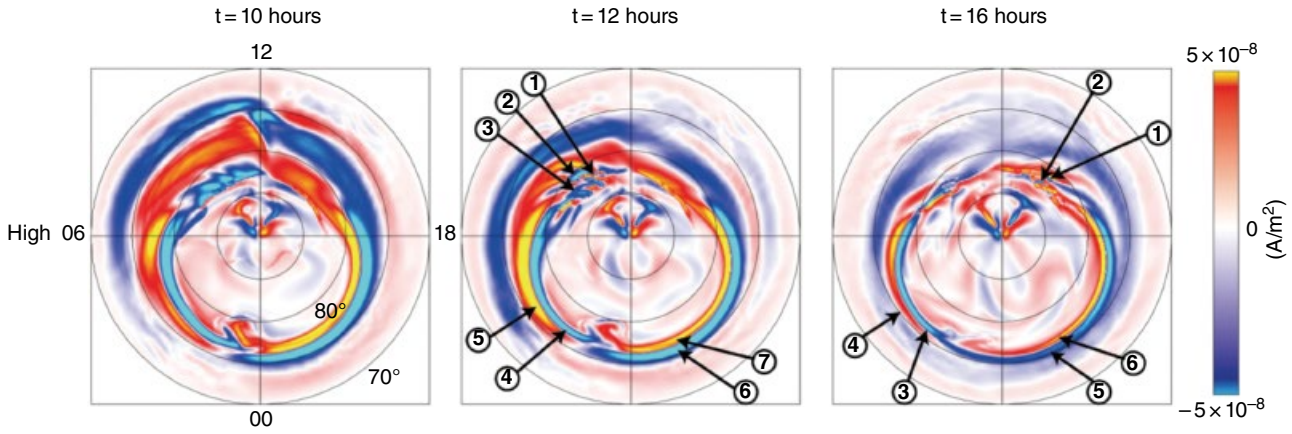

Figure 26.6 Field aligned currents mapped to the ionosphere from the inner edge of the simulation at 10h (left), 12h (center), and 16h (right). Blue indicates currents that are away from the ionosphere. [adapted from *Fukazawa et al.*, 2012]

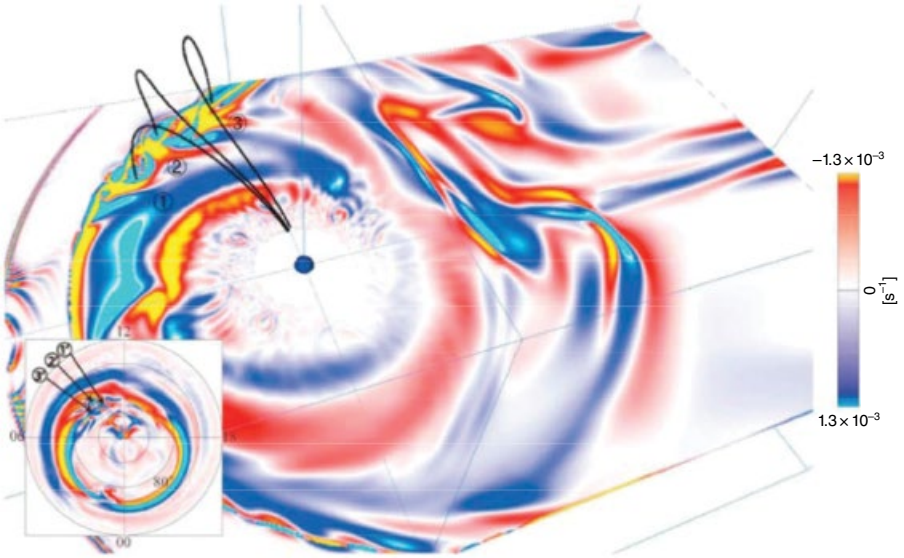

Figure 26.7 The magnetic field connection between the ionosphere and the magnetosphere at 12h (black field lines). The background is the difference in the parallel vorticity between 12h and 10h. The change in the vorticity in blue is consistent with field-aligned currents away from the ionosphere. The polar distribution of field aligned currents from Figure 26.6 is repeated in the insert. The structures in the parallel currents labelled 1′, 2′, and 3′map along field lines to the region of the magnetopause vortices. [from *Fukazawa et al.*, 2012]

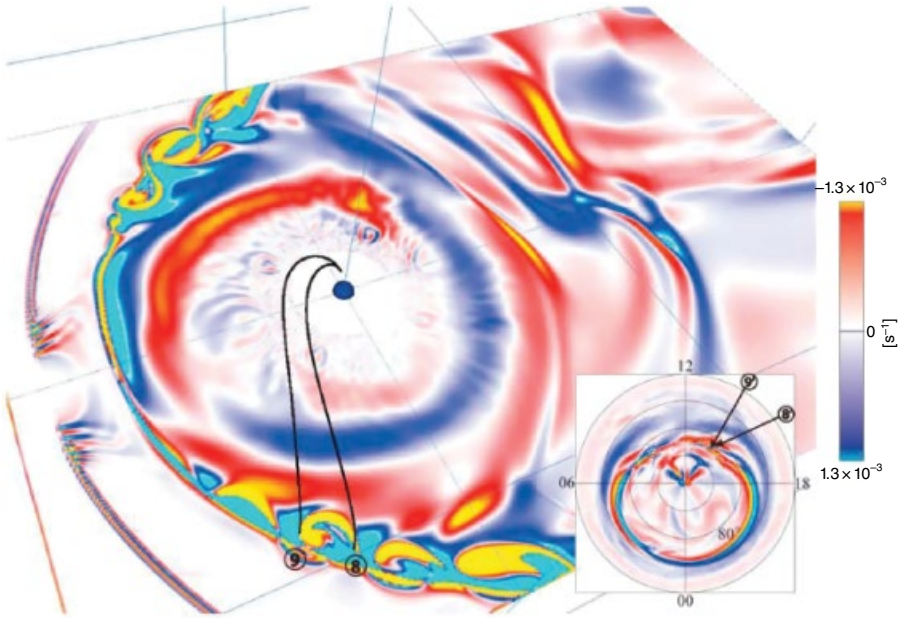

Figure 26.8 The magnetic field connection between the ionosphere and the magnetosphere at 16h (black field lines). The background is the difference in the parallel vorticity between 16h and 12h. The change in the vorticity in blue is consistent with field-aligned currents away from the ionosphere. The polar distribution of field aligned currents from Figure 26.6 is repeated in the insert. The structures in the parallel currents labelled 8′, 9′ map along field lines to the region of the magnetopause vortices in the afternoon. [from *Fukazawa et al.*, 2012]

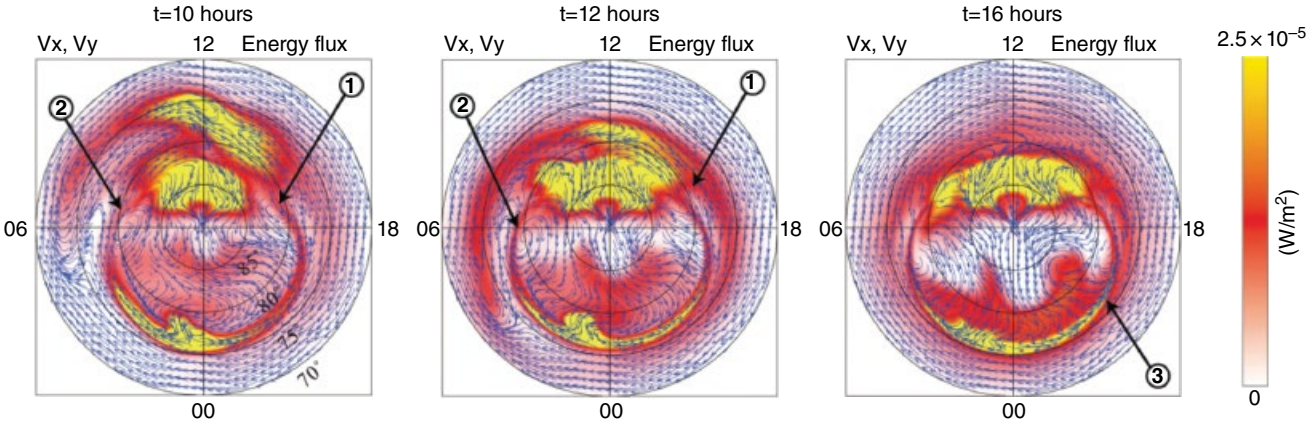

Figure 26.9 Plasma velocity (arrows) and energy flux (colored contours) in the polar ionosphere at 10h, 12h, and16h. The energy flux was mapped from the inner boundary of the simulation. [adapted from *Fukazawa et al.,* 2012]

Figure 26.8, regions of away current marked 8 and 9 in the insert map to blue parallel vorticity consistent with away currents.

In analogy with the Earth's magnetosphere, we can use the energy flux to the ionosphere ($F_E = pv_{th} / \sqrt{\pi}$) where p is the pressure and v_{th} is the thermal velocity to estimate the distribution of diffuse aurora. A polar plot in Figure 26.9 gives the results for 10h, 12h, and 16h. In this calculation, energy flux $F_E > 1 \times 10^{-5}$ Wm^{-2} covers much of the polar cap above ~72°. The largest energy flux (>2.5 × 10 Wm^{-2}) occurs near local noon and in a band (3) about midnight. We estimate about 2 gigawatts (GW) from the simulated energy flux. If the diffuse aurora is 10% efficient, that would be about 0.2 GW.

The arrows in Figure 26.9 give the ionospheric convection pattern. The convection pattern is complex. At lower latitudes (<75°), the flows are in the co-rotation direction. At higher latitudes, there is a two-cell convection pattern but because of the interaction between rotation and the magnetospheric convection pattern, the cells are highly structured. The centers of the two cells are marked 1 and 2 on the 10h and the 12h plots. In the flow diversion region, the flow is opposite to co-rotation pre-midnight (for example in the region marked 3 at 16h).

26.4. DISCUSSION

At Saturn like Jupiter, rotational flows dominate over most of the magnetosphere. Reconnection occurs in our simulations of Saturn's magnetosphere but unlike the case at Earth, it is not the main driver of transport at Saturn. Please see *Walker and Jia* [2016] for a recent review comparing simulation results at Earth, Jupiter, and Saturn. The conclusion that reconnection at Saturn is relatively weak also was reached based on observational studies of the magnetopause boundary layer by *Masters et al.* [2011]. In the simulation presented in this paper, the potential associated with reconnection was about 80kV. As noted in the introduction, *Badman et al.* [2014] found typical values of a few tens of kV, but *Nichols et al.* [2014] found a case with a very large potential 280kV. *McAndrews* [2008] used Cassini magnetopause crossings to estimate 48kV. Overall, the simulation results are consistent with observation-based estimates. For the northward IMF simulation represented here, K-H vortices formed first on the dawn and then on the dusk magnetopause. Several authors [*Masters et al.*, 2009, 2010, 2012; *Walker et al.*, 2011; *Delamere et al.*, 2013] have presented possible K-H observations near Saturn's morning magnetopause. *Masters et al.* [2012] and *Delamere et al.* [2013] find that possible K-H oscillations occur more frequently in the afternoon than in the morning.

The K-H instability is maximally unstable for magnetic fields directed purely northward or southward. *Walker et al.* [2011] carried out a parameter search for cases with northward and southward IMF. K-H waves were found in all of the simulations except two cases with southward IMF. For those cases, the velocity shear was not sufficient for the generation of K-H waves [see Table 1 of *Walker et al.*, 2011]. At Saturn, the magnetic field is mainly in the east-west direction. Recently *Fukazawa et al.* [2014] have simulated a case in which Cassini spacecraft observations provided the solar wind parameters for the MHD simulation. The magnetic field was primarily in the east-west direction with a smaller north-south component. K-H-like waves were found on the boundary. This interval is currently undergoing additional study.

Field-aligned currents provide the connectivity between the magnetosphere and the ionosphere. Alternating bands of toward and away field-aligned currents were found in the simulated ionosphere (Figure 26.6). The

primary generating mechanism in the simulation was the inertial term (1) in the current continuity equation. The largest field-aligned currents corresponded to the K-H vortices on the flanks of the magnetosphere, the dayside magnetopause, and the flow divergence region in the near-Earth tail. If the aurorae at Saturn are associated with away field-aligned currents then the simulation results are consistent with the argument by *Cowley and Bunce* [2003] and observations by *Bunce et al.* [2008] that the dayside aurorae correspond to the flow shear at the open closed field line boundary. This is different than at Jupiter where the main auroral oval is thought to map to the region where co-rotation breaks down. The strongest currents calculated in the simulation ($>10^{-7}$ A/m^2) compare favorably with those (1.7×10^{-7} A/m^2) inferred from observations by *Masters et al.* [2010]. In the simulation the away currents in the morning and afternoon are very structured. These map to the K-H vortices and may be related to dayside auroral spots reported by *Grodent et al.* [2011]. The observed auroral spot are between 1 and 30 kR. According to *Grodent et al.* [2010], an incident energy flux of 0.27 mW m^{-2} corresponds to 1.7 kR of ultraviolet emission. *Fukazawa et al.* [2012] used the simulated energy flux to estimate that the spots in the simulation would give emissions of 5 or 6 kR. In general, the auroral emissions estimated from the simulations are at the low end of the observed range [*Fukazawa et al.*, 2012].

We used the energy flux to the ionosphere as a proxy for diffuse aurora and find a peak at the polar cusps. This yellow region in Figure 26.9 may correspond to the diffuse patches of auroral emissions observed by *Gérard et al.* [2005].

ACKNOWLEDGMENTS

RJW served as the National Science Foundation (NSF) Program Director for Magnetospheric Physics during the period when much of this work was carried out. He gratefully acknowledges the NSF Individual Research and Development Program. He also acknowledges the Natioanl Aeronautics and Space Administration (NASA) grant NNX09AV91G under which this work as completed. Computing support was provided by the Research Institute for Information Technology, Kyushu University.

REFERENCES

Badman, S. V., C. M. Jackman, J. D. Nichols, J. T. Clarke, and J.-C. Gérard (2014), Open flux in Saturn's magnetosphere, *Icarus*, *231*, 137–145, doi:/j.icarus.2013.12.004.

Bunce, E. J., et al. (2008), Origin of Saturn's aurora: simultaneous observations by Cassini and the Hubble Space Telescope, *J. Geophys. Res.*, *113*, A09209, doi:10.1029/2008JA013257.

Cowley, S. W. H., and E. J. Bunce (2003), Corotation-driven magnetosphere-ionosphere coupling currents in Saturn's magnetosphere and their relation to the auroras, *Annales Geophysicae 21*, 1691–1707.

Cowley, S. W. H., S. V. Badman, E. J. Bunce, J. T. Clarke, J. C. Gerard, D. Grodent, C. M. Jackman, S. E. Milan, and T. K. Yeoman (2005), Reconnection in a rotation-dominated magnetosphere and its relation to Saturn's auroral dynamics, *J. Geophys.*, Res. *110*, A0222011, doi:10.1029/2004JA010796.

Delamere, P. A., R. J Wilson, S. Eriksson, and F. Bagenol (2013), Magnetic signatures of Kelvin-Helmholtz vortices on Saturn's magnetopause: Global survey, *J. Geophys. Res. 118*, 393–404, doi:10.1029/2012JA018197.

Fukazawa, K., S. Ogi, T. Ogino, and R. J. Walker (2007), Magnetospheric convection at Saturn as a function of IMF BZ, *Geophys. Res. Lett.*, *34*, L01105, doi:10.1029/2006GL028373.

Fukazawa, K., T. Ogino, and R. J. Walker (2012), A magnetohydrodynamic simulation study of the Kronian field-aligned currents and auroras, *J. Geophys. Res.*, *117*, A02214, doi:10.1029/2011JA016945.

Fukazawa, R. J. Walker, and S. Eriksson (2014), Massively parallel MHD simulation of Kronian magnetosphere convection and auroral emission with solar wind. Paper presented at the fall AGU meeting, San Francisco, 7–12 December.

Gérard, J.-C., E. J. Bunce, D. Grodent, S. W. H. Cowley, J. T. Clarke, and S. V. Badman (2005), Signature of Saturn's auroral cusp: Simultaneous Hubble Space Telescope FUV observations and upstream solar wind monitoring, *J. Geophys. Res.*, *110*, A11201, doi:10.1029/2005JA011094.

Grodent, D. J., A. Radioti, B. Bonfond, and J.-C. Gérard (2010), On the origin of Saturn's outer auroral emission, *J. Geophys. Res.*, *115*, A08219, doi:10.1029/2006JA012110.

Grodent, D., J. Gustin, J.-C. Gérard, A. Radioti, B. Bonfond, and W. R. Pryor (2011), Small-scale structures in Saturn's ultraviolet aurora. *J. Geophys. Res.*, *116*, A09225, doi:10.1029/2011JA016818.

Hill, T. W. (1979), Inertial limit on corotation. *J. Geophys. Res.*, *84*, 6554–6558, doi:10.1029/JA084iA11p06554.

Jackman, C. M., J. A. Slavin, and S. W. H. Cowley (2011), Cassini observations of plasmoid structure and dynamics: implications for the role of magnetic reconnection in magnetospheric circulation at Saturn, *J. Geophys. Res.*, *116*, A10212, doi:10.1029/2011JA016682.

Jackman, C. M., C. S. Arridge, N. André, F. Bagenal, J. Birn, M. P. Freeman, et al. (2014), Large-scale structure and dynamics of the magnetotails of Mercury, Earth, Jupiter and Saturn, Space Science Review, 85–154, doi:10:1007/s112140-014-0060-8.

Jia, X., K. C. Hansen, T. I. Gombosi, M. G. Kivelson, G. Téth, D. L. DeZeeuw, and A. J. Ridley (2012), Magnetospheric configuration and dynamics of Saturn's magnetosphere: A global MHD simulation, *J. Geophys. Res.*, *117*, A05225, doi:10.1029/2012JA017575.

Masters, A., D. G. Mitchell, A. J. Coates, M. K. Dougherty, S. J. Kanani, C. S. Arridge, et al. (2009), Surface waves on Saturn's dawn flank magnetopause driven by the Kelvin-Helmholtz instability, *Planet. Space Sci.*, *57*, 1769, doi:10/1016/j.pss.2009.02.010.

Masters, A., et al., (2010), Cassini observations of a Kelvin-Helmholtz vortex in Saturn's outer magnetosphere, *J. Geophys. Res*., *115*, A07225, doi:10.1029'/2010JA015351.

Masters, A., D. G. Mitchell, A. J. Coates, and M. K. Dougherty (2011), Saturn's low-latitude boundary layer: Properties and variability, *J. Geophys. Res.*, *116*, A06210, doi:10.1029/2010JA016421.

Masters, A. N. Achilleos, J. C. Cutler, A. J. Coates, M. K. Dougherty, and G. H. Jones (2012), Surface waves on Saturn's magnetopause, *Planet. Space Sci*., *65*, 109–121, doi:10.1016/j.pss.2012,02.007.

McAndrews, H. J., C. J. Owen, M. F. Thomsen, B. Lavraud, A. J. Coates, et al. (2008), Evidence for reconnection at Saturn's magnetopause, *J. Geophys. Res.*, *113*, A04210, doi:10.1029/2007JA012581.

Nichols, J. D., S. V. Badman, K. H., Baines, R. H. Brown, E. J. Bunce, J. T. Clarke, et al. (2014), Dynamic auroral storms on Saturn as observed by the Hubble Space Telescope, *Geophys. Res. Lett*., *41*, 3323-3330, doi:/10.1002/2014GL060186.

Ogino T., R. J. Walker, and M. G. Kivelson (1998), A global magnetohydrodynamic simulation of the Jovian magnetosphere. *J. Geophys. Res.*, *103*, 225, doi:10.1029/97JA02247.

Thomsen, M. F., R. J. Wilson, R. L. Tokar, D. B. Reisenfeld, and C. M. Jackman (2013), Cassini/CAPS observations of duskside tail dynamics at Saturn, *J. Geophys. Res*., *118*, 5767-5781, doi:/10/1002/jgra.50552.

Vasyliunas, V. M. (1983), Plasma distribution and flow, in *Physics of the Jovian Magnetosphere*, A. J. Dessler, ed., Cambridge Univ. Press, Cambridge, pp. 395–453.

Walker R. J., K. Fukazawa, T. Ogino, and D. Morozoff (2011), A simulation study of Kelvin- Helmholtz waves at Saturn's magnetopause. *J. Geophys. Res.*, *116*, A03203, doi:10.1029/2010JA015905.

Walker, R. J., and X. Jia (2016), *Chapter 9 Simulation studies of plasma transport at the Earth, Jupiter and Saturn, Magnetic Reconnection-Concepts and Applications*, edited by W. D. Gonzalez and E. N. Parker, Springer, New York, pp. 345–372.

27

Characterizing the Enceladus Torus by Its Contribution to Saturn's Magnetosphere

Ying-Dong Jia, Hanying Wei, and Christopher T. Russell

Video of Yosemite Talk, URL: http://dx.doi.org/10.15142/T3F30D

ABSTRACT

As an essential part of Saturn'ss magnetosphere, the Enceladus torus is located in the region in which the stresses in the plasma are dominated by Saturn's internal magnetic field, and is strongly coupled with the ionosphere. The torus is supplied by the ejecta from the south pole of Enceladus, which travels in a circular orbit, varying with radial distance from Enceladus. The cryovolcanic gas and grains are partly ionized, and thus, interact with the other neutrals, plasma, and field in the inner magnetosphere. These interactions significantly distort the internal magnetic field of Saturn, and thus, can be used to assess the production intensity of new materials. We survey the available Cassini observations for signals of such interactions between 2005 and 2012, and complete the interaction scenario with MHD modeling, to determine the spatial and temporal variation of the Enceladus torus. A wake is seen behind Enceladus, extending along the orbit, with a radial distance that varies with distance from Enceladus, confirming radial flow deflection, possibly caused by charged dust particles.

27.1. INTRODUCTION

The Saturnian magnetosphere is driven more by its rotation than by the solar wind [*Brice and Ioannidis*, 1970; *Kivelson et al.*, 2005], causing the plasma inertia to determine the structure and scale of the magnetosphere. Among the eight major moons around Saturn, Enceladus is smaller than average but nevertheless the most active one, significantly contributing to the magnetospheric inertia of Saturn. The strong plume [*Daugherty et al.*, 2006; *Porco et al.*, 2006] at its south pole sends hundreds of kilograms of dust and gas into Saturn's inner magnetosphere [*Hansen et al.*, 2006; *Waite et al.*, 2006]. This plume intensity, which will be studied at length in this paper, has been investigated by several methods, returning a wide range of values.

University of California at Los Angeles, Los Angeles, CA, USA

Early knowledge of the Saturn system is limited to telescopes from Earth, and three spacecraft passes: Pioneer 11, Voyager 1, and Voyager 2. Starting in 2004, when Cassini began orbiting Saturn, a wealth of measurements was gathered, with numerous discoveries that reveal rich details of this planet-moon system.

For over a hundred passes that flew through the Enceladus torus or through flux tubes that are connected to the torus, Cassini has made 20 close flybys at Enceladus. The coverage of the trajectories is projected onto two-dimensional planes and shown in Figure 27.1. Although the plume intensity is still under debate, the plume itself is found to be long lasting, constantly transporting momentum into the Saturnian magnetosphere.

The injection from the polar region of Enceladus shoots southward into the Enceladus orbit. The injected material is a mixture of grains with radii from micron to nanometers, pushed by gas, which is primarily water vapor. Some of the dust grains fall back onto the Enceladus surface and

Magnetosphere-Ionosphere Coupling in the Solar System, Geophysical Monograph 222, First Edition.
Edited by Charles R. Chappell, Robert W. Schunk, Peter M. Banks, James L. Burch, and Richard M. Thorne.

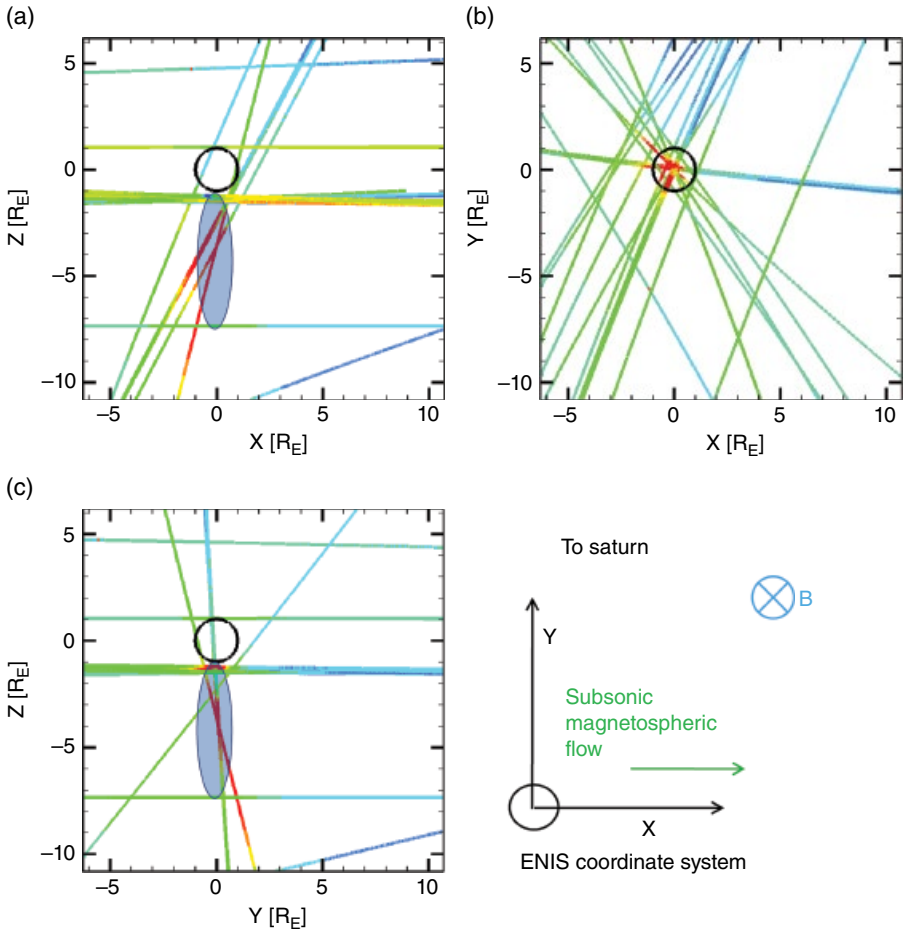

Figure 27.1 Trajectory coverage of Cassini flybys during years 2005 to 2012 projected into two-dimensional planes. The black circles are Enceladus. The color contours along the trajectories represent observed magnetic field perturbations. The shaded oval sketches the plume location.

some travel far enough to replenish the E-ring around Saturn. The water vapor is only partially ionized, forming a gas and plasma torus at the Enceladus orbit. The plasma torus is spun up by the rotating magnetosphere, from an orbital speed of 12 kilometers per second (km/s) to a sub-corotating speed of 30 km/s, which is 78% the corotation speed [*Wilson et al.*, 2009]. The neutral gas extends radially outward, not only by pressure, but also by the significant ionization process. Charge exchange creates hot neutrals, which travel several times faster than the local orbital speed.

Around Enceladus, the intensive ionization process dumps kilograms of ions into the Enceladus magnetic flux tube each second, raising the plasma density by orders of magnitude and stagnating the flow [*Tokar et al.*, 2009]. The large shear in flow speed around Enceladus distorts the magnetic field [*Jia et al.*, 2010a], which was first observed by Cassini in early 2005 [*Dougherty et al.*, 2006]. Such interaction also excites waves and currents that flow into both of Saturn's ionospheres [*Saur et al.*, 2007; *Simon et al.*, 2011].

The strong magnetic field in the inner magnetosphere of Saturn connects the Saturnian ionosphere to the Enceladus plume. The velocity shear between orbiting plume and sub-corotating magnetosphere can be treated as a flow interaction problem with chemical reactions, dust grains, and the moon surface. This study investigates these interaction signals recorded by Cassini, to determine the flow and field in the Enceladus torus. Section 27.2 quantifies this interaction. Section 27.3 discusses the variability of the Enceladus plume. Section 27.4 investigates the Enceladus torus, especially the wake trailing the moon, and Section 27.5 summarizes these findings.

27.2. ENCELADUS AND ITS PLUME IN SATURN'S MAGNETOSPHERE

The Enceladus-magnetosphere interaction system is composed of length scales that are orders of magnitude different. The Saturnian magnetosphere is about 6 million km across, or 100 Saturn radii (R_S). The Enceladus

Table 27.1 Plasma parameters upstream of Enceladus. Values without a source are calculated using the upstream values. The minimum mean-free path λ_{in} is estimated using maximum neutral density 10^{14} m^{-3} [*Smith et al.*, 2010], collision rate 10^{-15} m^3s^{-1} [*Huebner et al.*, 1992], and stagnated velocity 1 km/s^{-1} [*Tokar et al.*, 2009]

Parameters	Value
Ion Temperature, T_i	35 electron volts (eV) [*Tokar et al.*, 2006]
Field strength, B	330 nT [*Daugherty et al.*, 2006]
Plasma Beta, β	0.01
Flow shear, u	18 km/s [*Wilson et al.*, 2009]
Plasma number density, n	50 ~ 100 cm^{-3} [*Tokar et al.*, 2006]
Sound speed, v_s	17 km/s
Alfven speed, V_A	200 km/s
Water ion gyro radius, r_g	15 km
Water ion inertial length, λ_i	100 km
Ion-neutral collision mean free path, λ_{in}	>10 km
Debye length, λ_D	0.004 km

orbit is located in the inner magnetosphere, about 4 Rs from Saturn, or 0.2 million km. The radius of Enceladus (R_E) is barely 250 km, or 0.004 Rs.

Table 27.1 gives the plasma conditions at Enceladus. This interaction is sub-Alfvénic, and the plasma is cold. The chemical reactions are simpler than that around other moons, because water group ions dominate both in the torus and in the plume [*Tokar et al.*, 2006]. The inner magnetosphere of Saturn is relatively quiet with no significant radial flow activities.

In contrast with the solar wind-magnetosphere-ionosphere around the Earth, the Saturn-Enceladus plasma interaction system includes Saturn's ionosphere, Saturn's magnetosphere, and the moon Enceladus and its plume, which is not a typical ionosphere or a magnetosphere. The pickup process in the plume decelerates the flow, creating a region of several Enceladus radii (R_E) with induced magnetic field. The magnetic perturbation propagates along Saturn's magnetic field at the Alfvénic speed. In the plume center where neutral density reaches 10^{14} m^{-3}, the collision mean-free path is comparable with ion gyroradius and ion inertial length, so the Hall effect [*Saur et al.*, 2007] can become important, bringing an ionospheric characteristic to this region with an Enceladus radius in scale.

In summary, the interaction at Enceladus forms an ionosphere-magnetosphere-induced field-ionosphere interaction system. However, the field lines connecting Enceladus to Saturn's ionosphere are about half a million kms long. Assuming only 60,000 km of such flux tubes are populated with dense plasma, it takes the Alfvén wave 10 minutes to reach Saturn's ionosphere and return. Meanwhile, Saturn's magnetospheric flow has passed tens of R_E downstream. For this reason, we neglect the effects of Saturn's ionosphere in the study of magnetohydrodynamic (MHD) structures around Enceladus, and build our local model in the vicinity of Enceladus. The Enceladus Interaction Coordinate System (ENIS) [*Dougherty et al.*, 2006] is sketched in Figure 27.1.

Since Enceladus is a driving force in Saturn's magnetosphere, it is important to determine the secular variation of the plume intensity. Individual hotspots are seen to be active and to cool down during different flybys [*Goguen et al.*, 2013, and references therein]. However, is the total mass production rate from the south pole significantly changing or not? *Melin et al.* [2009] have found little change in the total oxygen torus orbiting within 10 Rs of Saturn. Previous studies on the Enceladus plume have yielded very different conclusions on the plume variability. *Saur et al.* [2008] have found the plume varying by a factor of 8 by using fluid modeling of the interaction in a fixed background magnetic field. This causes an electrical current that induces a magnetic field that matches the magnetic perturbation seen by Cassini. However, *Hansen et al.* [2008] compared their observations in 2007 and 2005, when vents on the surface had evolved, finding the total plume stable. Later on, more studies have yielded results that support one of these two extremes. These studies are based on a single instrument observation, and thus, there are biases due to the methods and assumptions that were used. Beyond this, there are observations of the Enceladus torus, examining longitudinal distribution in neutrals and plasma, still not leading to a settlement of plume variation question. These results are summarized in Table 27.2.

The density of the Enceladus plasma disk is found to be changing between 40 and 110 cm^{-3} [*Gurnett et al.*, 2007]. Thus, to invert the plume intensity from the plasma interaction in this region, this density variation needs to be included. Fortunately, the plasma density is monitored by the Cassini Radio and Plasma Wave Science (RPWS), and we use that data as the upstream condition for our model. We modeled the earlier nine flybys with a MHD model constrained by the Cassini magnetometer observations of the perturbation to the total magnetic field [*Jia et al.*, 2010b]. The inverted plume production rates are listed in Table 27.3.

The upstream density has changed by a factor of two among these flybys, while the plume strength is changed by less than 50%, more stable than some other investigations [e.g., *Smith et al.*, 2010].

Hedman et al. [2013] have found variations in plume brightness of over three times, which can be associated to distance to Saturn. They explained this variation with eruption strength affected by tidal forces. This result is

Table 27.2 Typical previous studies that address plume variation. Variation is defined by min/max

Source	Method	Data	Loss rate	Variation
Saur et al., 2008	E-J modeling	Magnetic field E0, E1, E2	0.2–1.6 ton/s	8
Hansen et al., 2008	Monte Carlo model	UVIS column density	0.2 ton/s	1.3
Kriegel et al., 2009	Hybrid model	Magnetic field E1, E2	N/A	2
Jia et al., 2010b	MHD model	Magnetic field E0–E6	0.6–0.9 ton/s	1.5
Smith et al., 2010	Monte Carlo model	INMS E2, E3, E5	0.03–0.3 ton/s	10
Hansen et al., 2011	Monte Carlo model	UVIS column density	0.2 ton/s	1.3
Kriegel et al., 2011	Hybrid and dust model	Magnetic field E5–E11	N/A	3
Pryor et al., 2011	Aurora footprint	UVIS 2008	N/A	3
Hedman et al., 2013	Infrared brightness	VIMS 2005–2012	N/A	3

Table 27.3 Plume intensity used in a MHD model in agreement with Cassini magnetic field strength observations [*Jia et al.*, 2010b]. CA is closest approach distance; n is the upstream plasma density from RPWS measurements; P is the estimated plume production rate

Flyby	E0	E1	E2	E3	E4	E5	E6	E7	E8
Year	2005	2005	2005	2008	2008	2008	2008	2009	2009
CA(R_E)	6.0	3.0	1.7	1.2	1.2	1.1	1.8	1.4	6.2
n_{up}(cm^{-3})	90	70	70	90	55	90	45	52	44
P ($kg\ s^{-1}$)	900	600	800	900	680	740	740	740	800

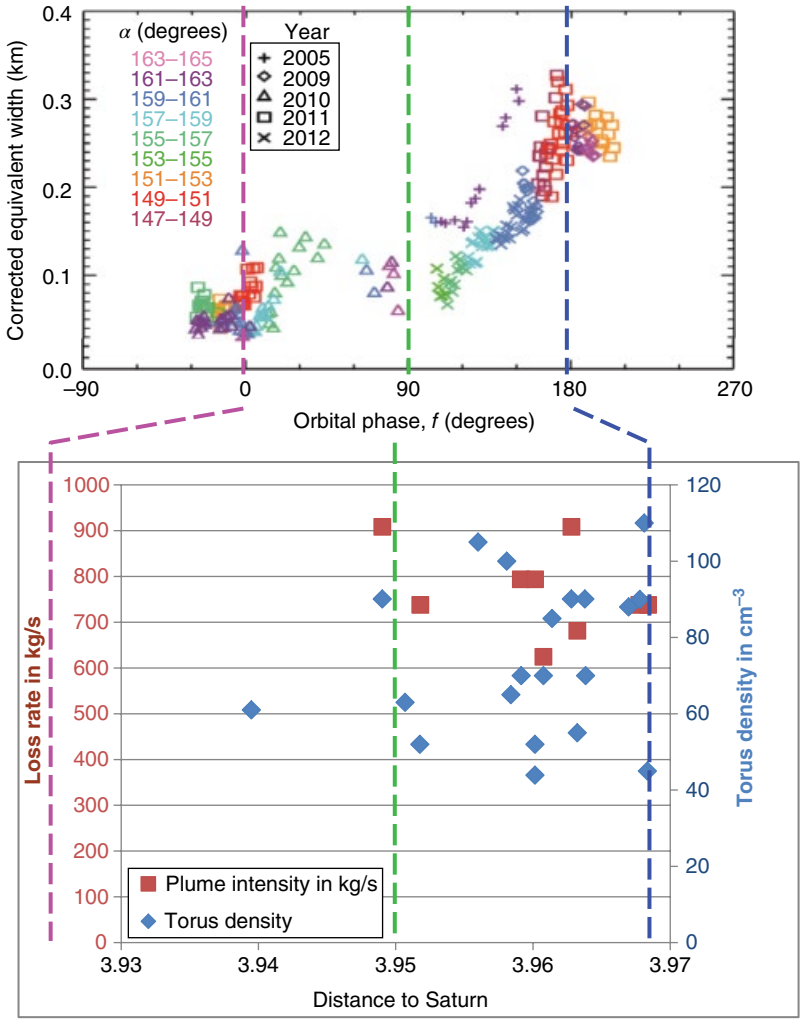

Figure 27.2 The top panel is a reproduction of Figure 4 by *Hedman et al.* [2013]. Three colored dotted lines are added to mark 0°, 90°, and 180° phase angles. The bottom chart plots the gas plume intensity [*Jia et al.*, 2010b] and torus plasma density [*Jia et al.*, 2010b; *Kregel et al.*, 2014] against the distance to Saturn. Three Saturn-centric distances are marked in the bottom panel corresponding to the three phase angles in the top panel, with the same colored lines.

found in agreement with the footprint brightness variation, which is also varying by a factor of a few [*Pryor et al.*, 2011]. We argue that footprint brightness is the effect of plasma interaction at Enceladus, which reflects both the variation in upstream density and the variation in plume strength. As listed in Table 27.3, the upstream density itself varies by a factor of two. It does not take a significant variation in plume intensity to cause a combined effect on the footprint.

There is a more complete measurement of torus plasma density during the Cassini flybys [*Kregel et al.*, 2014]. The bottom panel of Figure 27.2 plots the gas plume intensity and torus plasma density against the distance to Saturn. Hedman's Figure 4 is also plotted in the top panel of Figure 27.2 for comparison. In the bottom panel of Figure 27.2, there is no orbital phase dependence for either modeled production rate or upstream torus density in the upstream.

In years 2011 and 2012, Cassini made four passes at the south pole of Enceladus with very similar trajectories, as shown in Figure 27.3. The sharp jumps in Bx and By at $y = 1\ R_E$ are believed to be surface currents created by the non-conducting surface of Enceladus [*Teolis et al.*, 2014]. In the Bz perturbation, two dotted lines mark the location of the two B_Z minima, which are inside the surface currents. The decrease of B_Z perturbation along E14, E17, and E18, in contrast to that seen along E19, is caused by gas pressure in the plume that becomes strong enough to expel the magnetic field, creating a partial magnetic "cavity." From the Bz data, the size of the cavity is about 1 R_E in the y-direction. On the other hand, this partial cavity is not seen along E19, indicating the cavity is quite small (less than 80 km) in the x-direction at this z-distance of about 60 km.

During the flybys, the orbital distances of Enceladus during E14, E17, and E18 are 3.961, 3.968, and 3.958 R_S, respectively. The torus density measures 85, 110, and 100 cm^{-3}, respectively. However, the perturbation to the field strength, which is similar to that of the Bz component, is not ordered by the orbital distance but by the torus density. The perturbation is smallest along E14, due to its smallest torus density, even though the orbital distance during E14 is in the middle of the three flybys.

Now if the plume has been stable, why does the torus density vary by a factor larger than the plume intensity itself? One explanation is that the inner magnetosphere is not as stable as we had thought. The interaction at Enceladus diverts the flow at the moon and diverts the

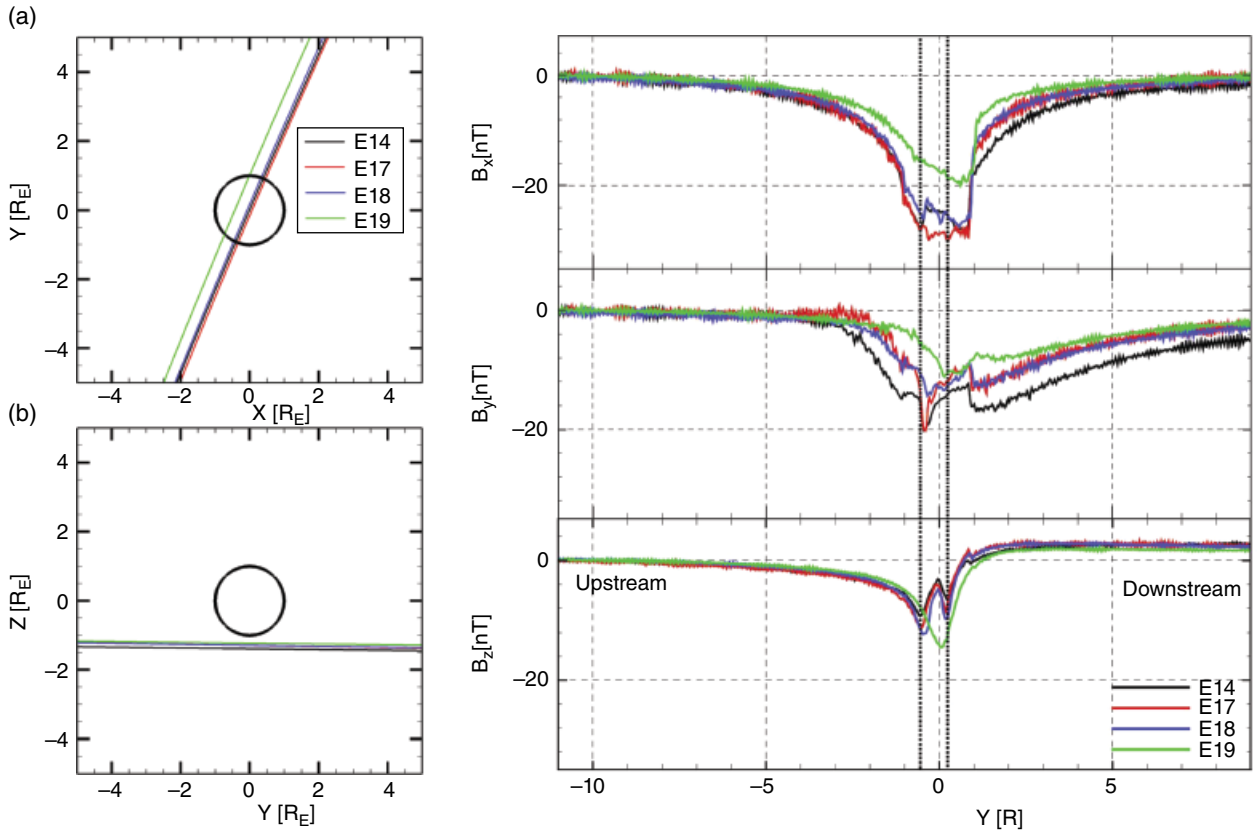

Figure 27.3 Left panels: Cassini trajectories along E14, E17, E18, and E19 flybys. Right panel: Detrended magnetic field perturbation in three components.

flux tubes radially inward as they travel down the Enceladus orbit. These motions are investigated in the next section.

27.3. THE ENCELADUS WAKE

Among the 20 flybys, the E15 flyby on 19 October 2011 is the only wake flyby. As shown in Figure 27.4, the field perturbations are seen in two distances from the Enceladus orbit. In the top panels, the largest B_X perturbation is between y = 2 and 4 R_E, while the minimum B_Z is between y = −1 and −2 R_E. The magnetic field perturbation is also shown in detail in the bottom panel.

As shown in Figure 27.5a, the cold electron density measured by Cassini RPWS, exhibits a 50% drop in electron density between y = −1 and −2 R_E from Enceladus. The energetic electron detector on Cassini-MIMI, as shown in panels b and c, has seen a dropout in electron counts in the same location. However, in contrast to the magnetic Bx and By decrease shown in Figure 27.5d, none of these particle detectors has seen obvious perturbation between y = 2 and 4 R_E.

The particle and field data at y = −1 and −2 R_E indicate the diverted flow from the Enceladus orbit at y = 0 R_E, as sketched in the top panels of Figure 27.4 in dotted lines. The flow diversion is seen by *Jia et al.* [2011], and further explained in a more generalized case by *Jia et al.* [2012b]. As a consequence, the field-aligned current system linking Enceladus to the Saturnian ionosphere is also rotated, as shown in Figure 27.6. While a simple pickup model decelerates the flow and piles up the flux tubes, the magnetic field is enhanced in front of the plume and depressed

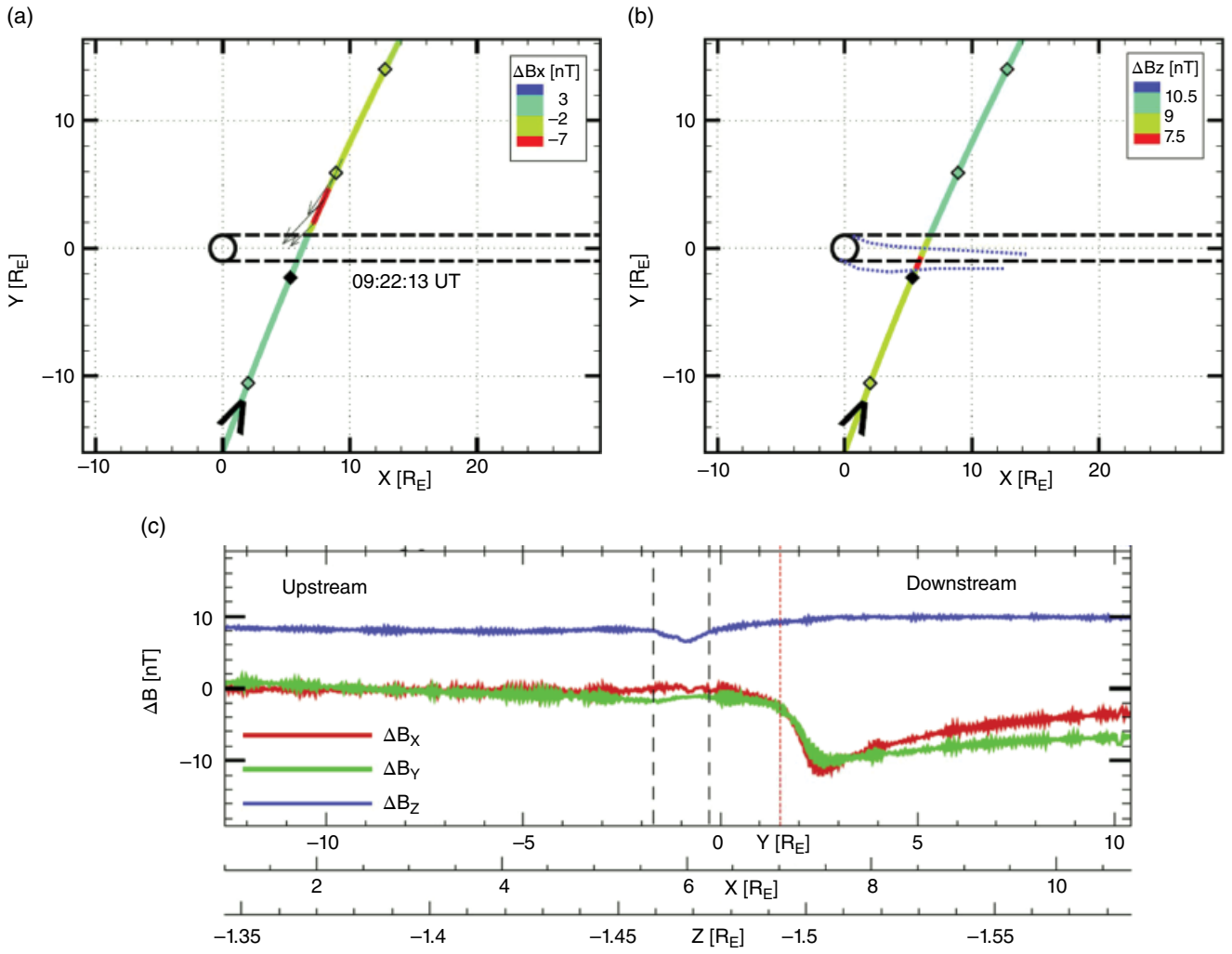

Figure 27.4 Cassini E15 flyby at Enceladus. Top panels show the projected geometry of the spacecraft. The color along the trajectory represents the contour level of B_X and B_Z perturbations, respectively. Bottom panel shows the magnetic field perturbations. The measured values are subtracted by the Saturnian model field [*Khurana et al.*, 2005; *Jia et al.*, 2011]. The original measurement is shown in Figure 27.5d.

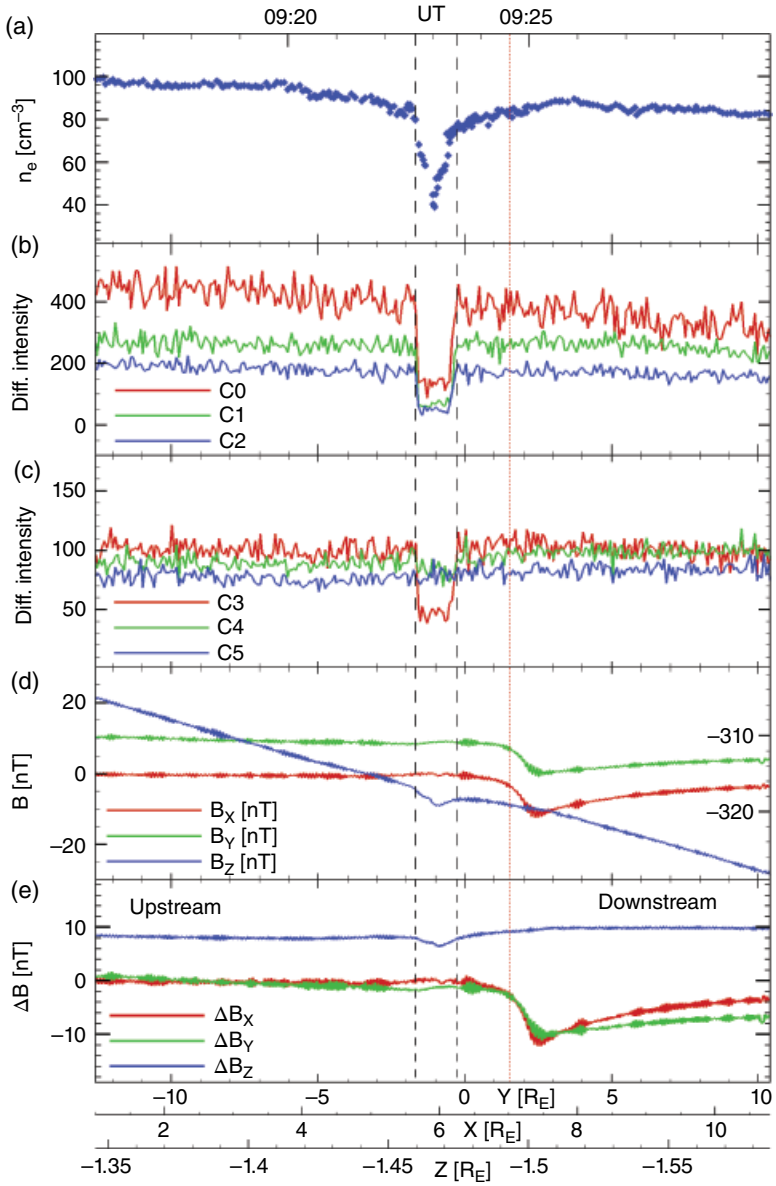

Figure 27.5 The Cassini measurements along E15 reproduced from AGU poster [*Jia et al.*, 2012a]. Panel a shows the cold electron density by RPWS. Panels b and c show hot electron counts in different energy ranges by LEMMS, in units of [cm^{2}sr^{-1}s^{-1}keV^{-1}]. Channels C0–C5 are electron counts. Their energy ranges are 18–40, 27–48, 41–60, 56–100, 92–183, and 175–300 keV, respectively [*Krupp et al.*, 2012]. Panel d shows the magnetic field components, with B_Z labeled on the right. The black dashed vertical lines at y = −1.7 and −0.27 mark the peaks outside the wake in panel b. The red dotted lines mark the start of B_X and B_Y perturbations.

downstream. With charged dust, the water ions are pushed toward −y, adding more pileup of the field in the −y direction, and moves the region with depressed magnetic field toward + y [*Jia et al.*, 2011, 2012b]. We used a simplified model with no moon but used only Saturnian magnetospheric flow and negatively charged dust pickup interaction to reproduce the field diversion in the Enceladus plume. The University of Michigan Block Adaptive Tree Solar Wind Roe-type Upwind Scheme (BATS-R-US) code is used to simulate this two-fluid interaction [*Jia et al.*, 2011]. The flow diversion in the y direction can be seen in the modeled blue stream lines in Figure 27.6d. In addition, the color contour of magnetic field strength in Figure 27.6d shows the modeled orientation of the magnetic field enhancement-depression region due to charged dust, which is supported by both the measured contour colors shown in Figure 27.6b and the measured magnetic field vectors shown in Figure 27.6c.

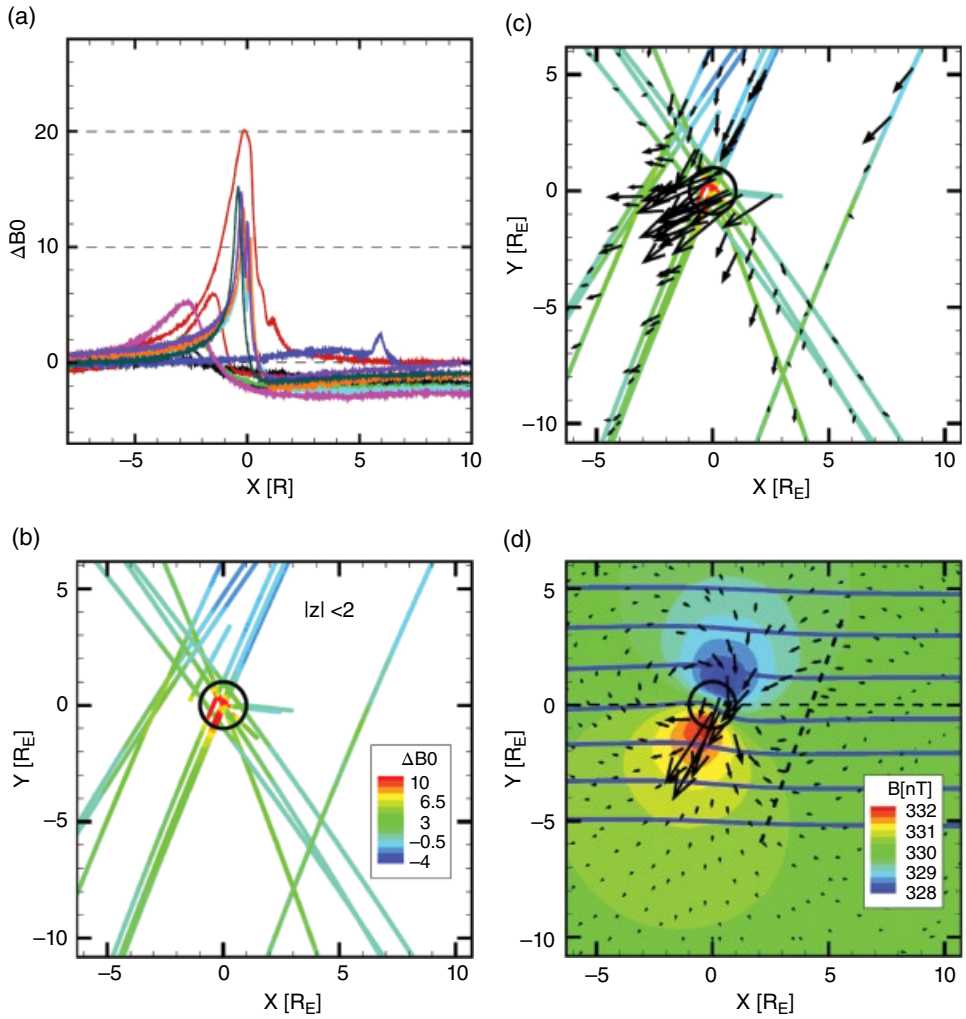

Figure 27.6 Perturbation in the total field measured along flybys E0 to E19. Panel a shows the perturbation along the trajectory. Panel b shows the contour of the perturbation in two dimensions. Panel c shows the arrow of the magnetic field vector over the same color contour of panel b. Panel d show a multi-fluid MHD simulation with charged dust picked up in the plume using the interaction described by *Jia et al.* [2011]. The color contour denotes magnetic field lines, and the blue lines are ion stream lines, while the black arrows are magnetic field vector projected into this X-Y plane. The slant dashed line is a trajectory comparable to E15, but closer to X, because the dust cloud used in this simplified simulation is not as dense as estimated by Cassini measurements.

This region of reduced magnetic strength is the region that the Bx decreases (i.e., at y = +2 R_E to +4 R_E along E15 of Figure 27.4 and 27.5.

The flow diversion in Saturn's radial direction creates oscillations along the Enceladus wake. We looked into the wake signatures in Cassini magnetic field data between latitudes of ±10 degrees. The wake encounters are plotted in Figure 27.7. The wake is seen moving radially all along the Enceladus orbit. This radial motion expedites the radial transport of plasma and magnetic flux and also creates a density variation larger than the plume variation.

27.4. SUMMARY

In summary, the interaction at Enceladus creates a torus of gas, plasma, and dust along its orbit. The new injections from the Enceladus plume then interact and disturb the torus. The plasma in the torus is spun by Saturn's magnetosphere, but the new pickup ions decelerate the plasma torus to about 80% sub-corotation. The local interaction at Enceladus decelerates the torus flow to its orbital speed, while the charged dust diverts the torus flow in the radial direction of Saturn. This flow diversion is carried on along the Enceladus orbit,

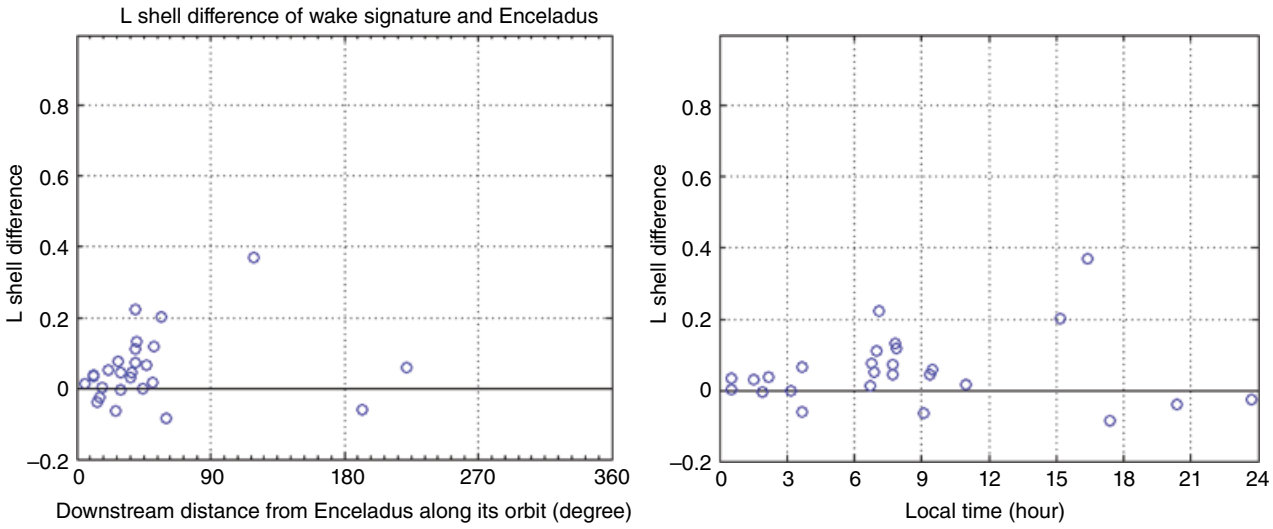

Figure 27.7 L-shell location of the Enceladus wake along its orbit.

making the flux tube that contains the Enceladus wake oscillate about the Enceladus orbit with inward and outward displacements.

REFERENCES

Brice, N. M., and G. A. Ioannidis (1970), The Magnetospheres of Jupiter and Earth, *Icarus*, *13*(2), p. 173–183, DOI:10.1016/0019-1035(70)90048-5.

Dougherty, M. K., K. K. Khurana, F. M. Neubauer, C. T. Russell, J. Saur, J. S. Leisner, and M. E. Burton (2006), Identification of a Dynamic Atmosphere at Enceladus with the Cassini Magnetometer, *Science*, *311*(5766), 1406-1409, DOI:10.1126/science.1120985.

Goguen, J. D., B. J. Buratti, H. Robert Brown, R. N. Clark, P. D. Nicholson, M. M. Hedman, R. R. Howell, C. Sotin, D. P. Cruikshank, K. H. Baines, K. J. Lawrence, J. R. Spencer, and D. G. Blackburn (2013), The temperature and width of an active fissure on Enceladus measured with Cassini VIMS during the 14 April 2012 South Pole flyover, *Icarus*, *226*(1), p. 1128–1137, DOI:10.1016/j.icarus.2013.07.012.

Gurnett, D. A., A. M. Persoon, W. S. Kurth, J. B. Groene, T. F. Averkamp, M. K. Dougherty, and D. J. Southwood (2007), The Variable Rotation Period of the Inner Region of Saturn's Plasma Disk, *Science*, *316*(5823), pp. 442, DOI:10.1126/science.1138562.

Hansen, C. J., L. Esposito, A. I. F. Stewart, J. Colwell, A. Hendrix, W. Pryor, D. Shemansky, and R. West (2006), Enceladus' water vapor plume, *Science*, *311*, 1422–1425.

Hansen, C. J., L. W. Esposito, A. I. F. Stewart, B. Meinke, B. Wallis, J. E. Colwell, A. R. Hendrix, K. Larsen, W. Pryor, and F. Tian (2008), Water vapour jets inside the plume of gas leaving Enceladus, *Nature*, *456*(7221), pp. 477–479, DOI:10.1038/nature07542.

Hansen, C. J., D. E. Shemansky, L. W. Esposito, A. I. F. Stewart, B. R. Lewis, J. E. Colwell, A. R. Hendrix, R. A. West, J. H. Waite Jr., B. Teolis, and B. A. Magee (2011), The composition and structure of the Enceladus plume, *Geophys. Res. Lett.*, *38*(11), L11202, DOI:10.1029/2011GL047415.

Hedman, M. M., C. M. Gosmeyer, P. D. Nicholson, C. Sotin, R. H. Brown, R. N. Clark, K. H. Baines, B. J. Buratti, and M. R. Showalter (2013), An observed correlation between plume activity and tidal stresses on Enceladus, *Nature*, *500*(7461), pp. 182–184, DOI:10.1038/nature12371.

Huebner, W. F., J. J. Keady, and S. P. Lyon (1992), Solar photo rates for planetary atmospheres and atmospheric pollutants, *Astrophys. & Space Sci. 195*(1), p. 1–294, DOI:10.1007/BF00644558.

Jia, Y.-D., C. T. Russell, K. K. Khurana, Y. J. Ma, J. S. Leisner, and M. K. Dougherty (2010a), Time-varying magnetospheric environment near Enceladus as seen by the Cassini magnetometer, *Geophys. Res. Lett.*, *37*(9), L09203, doi:10.1029/2010GL042948.

Jia, Y.-D., C. T. Russell, Y. J. Ma, K. K. Khurana, W. Kurth, and T. I. Gombosi (2010b), The interaction of Saturn's magnetosphere and its moons 3: Time Variation of the Enceladus Plume, *J. Geophys. Res.*, *115*(12), A12243, 10.1029/2010JA015534.

Jia, Y.-D., C. T. Russell, K. K. Khurana, Y. J. Ma, J. S. Leisner, A. M. Persoon, and M. K. Dougherty (2011), Cassini magnetometer observations over the Enceladus poles, *Geophys Res. Lett.*, *38*(19), L19109, DOI:10.1029/2011GL049013.

Jia, Y., C. T. Russell, K. K. Khurana, N. Krupp, J. S. Leisner, A. M. Persoon, and M. K. Dougherty (2012a), The dusty plasma at Enceladus as seen by Cassini and multi-fluid modeling, *AGU Fall Meeting*, abstract #P51A-2023.

Jia, Y.-D., Y. J. Ma, C. T. Russell, H. R. Lai, G. Tóth, and T. I. Gombosi (2012b), Perpendicular flow separation in magnetized counter-streaming plasma, *Icarus*, *218*(2), 895–905, doi:10.1016/j.icarus.2012.01.017.

Khurana, K. K., C. S. Arridge, and M. K. Dougherty (2005), A versatile model of Saturn's magnetospheric field, *EGU poster* #EGU05-A-05970.

Khurana, K. K., M. K. Dougherty, C. T. Russell, and J. S. Leisner (2007), Mass loading of Saturn's magnetosphere near

Enceladus, *J. Geophys. Res.*, *112*(A8), 203, doi:10.1029/2006JA012110.

Kivelson, M. G. (2005), The Current Systems of the Jovian Magnetosphere and Ionosphere and Predictions for Saturn, *Space Sci. Rev.*, *116*(1–2), 299-318, DOI:10.1007/s11214-005-1959-x.

Kriegel, H., S. Simon, J. Müller, U. Motschmann, J. Saur, K.-H. Glassmeier, and M. Dougherty (2009), The plasma interaction of Enceladus: 3d hybrid simulations and comparison with cassini mag data, *Planetary and Space Science*, *57*(14–15), 2113–2122.

Kriegel, H., S. Simon, U. Motschmann, J. Saur, F. M. Neubauer, A. M. Persoon, M. K. Dougherty, and D. A. Gurnett (2011), Influence of negatively charged plume grains on the structure of Enceladus' Alfvén wings: Hybrid simulations versus Cassini Magnetometer data, *J. Geophys. Res.*, *116*(A10), A10223, DOI:10.1029/2011JA016842.

Kriegel, H., S. Simon, P. Meier, U. Motschmann, J. Saur, A. Wennmacher, D. F. Strobel, and M. K. Dougherty (2014), Ion densities and magnetic signatures of dust pickup at Enceladus, *J. Geophys. Res.*, *119*(4), 2740–2774, DOI:10.1002/2013JA019440.

Krupp, N., et al. (2012), The Cassini Enceladus encounters 2005–2010 in the view of 375 energetic electron measurements, *Icarus*, *218*, 433–447, doi:10.1016/j.icarus.2011.12.018.

Melin, H., D. E. Shemansky, and X. Liu (2009), The distribution of atomic hydrogen and oxygen in the magnetosphere of Saturn, *Planetary and Space Science*, *57*(14–15), p. 1743–1753, DOI:10.1016/j.pss.2009.04.014.

Porco, C. C., et al. (2006), Cassini Observes the Active South Pole of Enceladus, *Science*, *311*(373), 1393–1401.

Pryor, W., et al. (2011), The auroral footprint of Enceladus on Saturn, *Nature*, *472*(203), 331, doi:10.1038/nature09928.

Saur, J., F. M. Neubauer, and N. Schilling (2007), Hemisphere coupling in Enceladus' asymmetric plasma interaction, *J. Geophys. Res.*, *112*(A11), DOI:10.1029/2007JA012479.

Saur, J., N. Schilling, F. M. Neubauer, D. F. Strobel, S. Simon, M. K. Dougherty, C. T. Russell, and R. T. Pappalardo (2008), Evidence for temporal variability of Enceladus' gas jets: Modeling of Cassini observations, *Geophys. Res. Lett.*, *35*(20), L20105, DOI:10.1029/2008GL035811.

Simon, S., J. Saur, F. M. Neubauer, U. Motschmann, and M. K. Dougherty (2009), Plasma wake of Tethys: Hybrid simulations versus Cassini MAG data, *Geophys. Res. Lett.*, *36*, L04108, doi:10.1029/2008GL036943.

Simon, S., J. Saur, H. Kriegel, F. M. Neubauer, U. Motschmann, and M. K. Dougherty (2011), Influence of negatively charged plume grains and hemisphere coupling currents on the structure of Enceladus' Alfvén wings: Analytical modeling of Cassini magnetometer observations, *J. Geophys. Res.*, *116*, A04221, doi: 10.1029/2010JA016338.

Smith, H. T., R. E. Johnson, M. E. Perry, D. G. Mitchell, R. L. McNutt, and D. T. Young (2010), Enceladus plume variability and the neutral gas densities in Saturn's magnetosphere, *J. Geophys. Res.*, *115*, A10252, doi:10.1029/2009JA015184.

Tenishev, V., M. Combi, and H. Waite (2007), A numerical study of dust distribution in the Enceladus' atmosphere *American Geophysical Union*, Fall Meeting 2007, abstract #P21B-0538.

Teolis, B. D., I. Sillanpää, J. H. Waite, and K. K. Khurana (2014), Surface current balance and thermoelectric whistler wings at airless astrophysical bodies: Cassini at Rhea, *J. Geophys. Res.*, *119*(11), pp. 8881–8901, DOI:10.1002/2014JA020094.

Tokar, R. L., R. E. Johnson, T. W. Hill, D. H. Pontius, W. S. Kurth, F. J. Crary, D. T. Young, M. F. Thomsen, D. B. Reisenfeld, A. J. Coates, G. R. Lewis, E. C. Sittler, and D. A. Gurnett (2006), The Interaction of the Atmosphere of Enceladus with Saturn's Plasma, *Science*, *311*(5766), 1409–1412.

Tokar, R. L., R. E. Johnson, M. F. Thomsen, R. J. Wilson, D. T. Young, F. J. Crary, A. J. Coates, G. H. Jones, and C. S. Paty (2009), Cassini detection of Enceladus' cold water-group plume ionosphere, *Geophys. Res. Lett.*, *36*, L13203, doi:10.1029/2009GL038923.

Waite, J. H., M. R. Combi, W.-H. Ip, T. E. Cravens, R. L. McNutt, W. Kasprzak, R. Yelle, J. Luhmann, H. Niemann, D. Gell, B. Magee, G. Fletcher, J. Lunine, and W.-L. Tseng (2006), Cassini Ion and Neutral Mass Spectrometer: Enceladus Plume Composition and Structure, *Science*, *311*(5766), 1419.

Wilson, R. J., R. L. Tokar, and M. G. Henderson (2009), Thermal ion flow in Saturn's inner magnetosphere measured by the Cassini plasma spectrometer: A signature of the Enceladus torus? *Geophys. Res. Lett.*, *36*(23), L23104, DOI:10.1029/2009GL040225.

Part VII
Future Directions for Magnetosphere-Ionosphere Coupling Research

28

Future Atmosphere-Ionosphere-Magnetosphere Coupling Study Requirements

Thomas E. Moore[1], Kevin S. Brenneman[1], Charles R. Chappell[2], James H. Clemmons[3], Glyn A. Collinson[1], Christopher Cully[4], Eric Donovan[4], Gregory D. Earle[5], Daniel J. Gershman[1], R. A. Heelis[6], Lynn M. Kistler[7], Larry Kepko[1], George Khazanov[1], David J. Knudsen[4], Marc Lessard[7], Elizabeth A. MacDonald[1], Michael J. Nicolls[8], Craig J. Pollock[1], Robert Pfaff[1], Douglas E. Rowland[1], Ennio Sanchez[8], R. W. Schunk[9], Joshua Semeter[10], Robert J. Strangeway[11], and Jeffrey Thayer[12]

Video of Yosemite Talk, URL: http://dx.doi.org/10.15142/T3988X

ABSTRACT

The Heliophysics community must have a quantitative, predictive understanding of the dynamically variable escape of gravitationally trapped volatile matter from atmospheres, driven by energetic processes. This loss depletes atmospheres of selected constituents, causing dramatic changes in bulk surface pressure as well as composition, as has perhaps occurred most dramatically at Mars. In geospace, the process dissipates solar wind energy to produce ionospheric outflows that feed back on dynamics of the solar wind interaction with Earth. Proposed mechanisms include the upward ambipolar electric field associated with electron heating, Joule heating, wave-particle electron and ion heating interactions, and ponderomotive effects. It is unclear if waves interact with particles primarily in a cyclotron resonant mode, in a lower hybrid exchange of electron and ion energy, or in a bulk ponderomotive mode. Future studies will require observation of magnetospheric and thermospheric boundary conditions applied to the exobase transition region, and the response of atmospheric gas, ions, and electrons to the ensuing battle between energetic forcing, collisional dissipation, and gravity. Such studies will determine the mechanisms of energetic mass escape and the degree to which planetary mass loss is drawn from above by energetic evacuation or driven from below by energetic pressurization.

[1] *NASA Goddard Space Flight Center, Greenbelt, MD, USA*
[2] *Vanderbilt University, Nashville, TN, USA*
[3] *Aerospace Corporation, El Segundo, CA, USA*
[4] *University of Calgary, Calgary, AB, Canada*
[5] *Virginia Technical University, Blacksburg, VA, USA*
[6] *University of Texas at Dallas, Richardson, TX, USA*
[7] *University of New Hampshire, Durham, NH, USA*
[8] *SRI International, Menlo Park, CA, USA*
[9] *Utah State University, Logan, UT, USA*
[10] *Boston University, Boston, MA, USA*
[11] *University of California at Los Angeles, Los Angeles, CA, USA*
[12] *University of Colorado, Boulder, CO, USA*

28.1. MOTIVATIONS

A huge amount of progress has been made since the first Yosemite meetings of 1974 and 1976, in understanding the interface between our upper atmosphere and the atmosphere of the Sun, and the transport of matter between them. At that time, the mission that came to be known as Dynamics Explorer was taking shape as a two-spacecraft exploration of the atmosphere, the ionosphere, and its extensions in the plasmasphere and polar wind, as modified by solar wind interactions with the magnetosphere in the auroral zones. In this paper, we will be

Magnetosphere-Ionosphere Coupling in the Solar System, Geophysical Monograph 222, First Edition.
Edited by Charles R. Chappell, Robert W. Schunk, Peter M. Banks, James L. Burch, and Richard M. Thorne.

surveying the requirements for a contemporary study of atmosphere-ionosphere-magnetosphere (AIM) interactions with a three-point focus on the exobase transition region, across which the atmosphere becomes the magnetosphere, energy is transported downward, and atmospheric mass is transported upward in response.

On the supply side, our atmosphere gains some 40 tons of mainly refractory material per day from incident meteorites and dust. There are of course spikes in that accretion rate, from larger bodies, and the energy deposited in the atmosphere also produces escape of volatiles. On the continuous loss side, mainly volatiles are involved, and of these, a simple Jeans' escape model, evaluated at the exobase around 500 kilometer (km) altitude (defined by equal scale height and collision mean free path), suggests mainly a loss of hydrogen and a lesser amount of helium. At typical thermospheric temperatures, the lighter species escape at approximately the rate they are produced or transported diffusively up to the exobase. Molecular photodissociation of some species liberates binding energy, but this in general is insufficient to produce much loss of heavier species from Earth or Venus, though it may have played a significant role at Mars. Solar wind interactions may be a more important cause of volatile losses [*Luhman and Bauer*, 1992]. The light ion species escape with a flux similar to that of gaseous light atoms, with some enhancement owing to temperatures that generally exceed that of the thermospheric gas, while heavier ion species are expected to escape with much smaller fluxes, owing to their gravitational confinement.

Enhanced ablation of planetary atmospheres by energy deposition from stellar winds [*Moore and Horwitz*, 2007] is a fundamental process that influences the evolution of habitable worlds. The existence and role of a planetary magnetic dynamo is an important variable, as suggested by a comparison with the planet Mars, which has little or no magnetic dynamo at present, and is thought to have been quite wet at one time, presumably with a much thicker atmosphere. The MAVEN mission was conceived to investigate how it is losing atmosphere at present and how this may have evolved over time.

Through space exploration, we have come to appreciate the important role of magnetic connectivity between the Earth and Sun. If the solar wind were incident directly on the upper atmosphere, as it is on the Lunar surface, for example, or the atmosphere of Venus or Mars (with some exceptions), the energy flux would be on the order of 0.1–1 mW/m^2. However, our magnetosphere expands the surface of interaction over 100-fold, at the same time reconnecting and funneling most of the intercepted solar wind energy into the auroral zones, which map magnetically to the boundary layer between the solar wind and the magnetosphere. The energy flux to the auroral ionosphere is observed to be about 100 times greater than the solar wind energy flux at Earth, 10–100 mW/m^2. This energy flux, divided between electromagnetic and kinetic energy, accelerates the light ion outflow, and greatly enhances mass flux of the heavier atmospheric species O+, N2+, NO+, and O2+, with a power law dependence on the energy inflows [*Strangeway et al.*, 2005].

At Earth, in addition to a very prominent intrinsic magnetic dynamo and magnetosphere, we also have a prominent outflow of geogenic volatiles into space around our planet. This outflow is thought to substantially affect the dynamic response of our magnetosphere to solar wind variations [*Brambles et al.*, 2010; *Garcia et al.*, 2010; *Moore et al.*, 2014]. This in turn influences space weather, rendering it unpredictable, given the current lack of understanding of the outflows.

Dating from the 1960s, we have understood that atmospheric gases are dissociated and ionized in the upper atmosphere, forming a partially ionized "ionosphere" with a temperature of a few thousand K (thermal energy of a few tenths of an electron volt). The earliest sounding rocket probes showed that the density scale height was consistent with this, less than 100 km, indicating very rapidly falling densities of ionospheric plasma above the F-region proper. However, higher altitude probes and whistler wave monitoring found substantially higher densities than those projected from such small scale heights, and this gave rise to the concept of a "plasmasphere" that could be understood as the halo of lighter species H+ and He+. A theory of plasmaspheric "filling", emptying and "refilling" was developed more or less hand in hand with a theory of an escaping "polar wind" of light ions at higher latitudes where the plasma attempted to fill flux tubes that were opened to the solar wind every few hours though magnetospheric circulation. A theory of "plumes" of plasmaspheric light ion plasmas, created by bursts of magnetospheric circulation, was a natural outcome of this picture [*Grebowsky*, 1970]. This in turn gave rise to a view of the hot plasmas (kiloelectron-volt [keV] and higher) in the magnetosphere as originating from the solar wind, while the cold plasmas were thought to have originated from the ionosphere, and this view appeared to explain most of the observations available by 1970 [*Chappell et al.*, 1972].

However, in 1972, the Lockheed Palo Alto group published the surprising result that magnetospheric hot plasmas (keV thermal energies) contain substantial amounts of oxygen plasma that could only have come from the ionosphere rather than the solar wind. Fairly soon after that, the same group reported observations of keV ions flowing out of the auroral regions of the ionosphere, either in the form of beams or "conics" indicating a combination of acceleration or heating mechanisms operating parallel to or transverse to the local magnetic field. Others soon reported similar observations from other spacecraft, quickly confirming this

surprising result. This discussion is a much abbreviated overview of the initial indications of the importance of our topic here.

Since the first Yosemite conferences, extensive observations have been obtained of auroral plasma outflows of light and heavy ion plasmas. The highlights can be summarized as follows [*Moore and Horwitz*, 2007; *Lotko*, 2007 and references therein]:

- A pervasive polar wind outflow of light ions exists everywhere outside the plasmasphere (attempting to fill flux tubes that are periodically emptied by convection).
- Heavy ion outflows occur at all local times of the auroral oval.
- The highest heavy ion outflow fluxes occur in the dayside cusp region, and the highest energies are found in the nightside evening aurora.
- A strong solar cycle dependence has been found, with the highest heavy ion fluxes at solar maximum, when the thermosphere is substantially warmed and inflated relative to periods of lower solar extreme ultraviolet (EUV) flux.
- Higher fluxes are found when the internal geomagnetic activity of the magnetosphere is higher, as scaled for example by the planetary K index.
- Incoherent scatter radar (ISR) studies show that upflow is produced by either or both of thermal electron heating and/or thermal ion heating.
- ISR studies have also noted anomalous radar backscatter spectra, interpreted as evidence for "highly nonthermal" (pick-up ring or toroidal) plasma ion velocity distributions.
- Outflow was shown to be associated with solar wind intensity or dynamic pressure, and/or its variability, by correlating solar wind and outflow observations.
- Only a weak correlation of cusp region outflow fluxes was found with the orientation of the interplanetary magnetic field, despite the known relationship to magnetic activity.
- Both kinetic energy inputs and electromagnetic energy inputs were found to be highly correlated with plasma outflow flux.

The polar wind light ion outflow results from the poor gravitational confinement of light ions at typical ionospheric temperatures. Their outflow is also accelerated by an ambipolar electric field set up through the force balance between the dominant heavier ion species O+ and the electron environment created by photoionization. This field is just strong enough to confine the electrons to the vicinity of the heavier ion plasma and also helps to eject the lighter species whose mass is not in balance with it. The heavier O+ remains gravitationally bound for electrons created by solar EUV photons but can be thrown out of balance by more energetic electron environments, as discussed further below.

Figure 28.1 illustrates many of the highlights cited above, from Fast Auroral Snap-shoT (FAST) mission observations at altitudes in the auroral acceleration region, well above the exobase transition region. Regions of strong current sheets are seen to drive strong (superthermal) longitudinal convection, in the presence of electron precipitation enhanced in energy by association with upward currents, or in density by association with downward currents and Alfvén waves, and in the presence of strong broadband plasma waves. Observations like these led to the identification of possibly causal relationships between ion outflow and both electron precipitation and Poynting flux into the ionosphere below [*Strangeway et al.*, 2005].

Electron heating and ion heating create separate paths to plasma up-flows that may cooperate or operate independently in various circumstances, as reported from ISR observations [*Wahlund et al.*, 1992]. This is reasonable, given that plasmas must remain quasi-neutral, so electron escape must be accompanied by corresponding ion escape to maintain overall neutrality. Quasi-neutrality is enforced by the so-called ambipolar electric field that couples electrons to ions. The magnitude of the potential drop must be sufficient to reduce the electron escape flux and enhance the ion escape flux until they yield zero net current. Thus, the magnitude of the potential drop is a measure of the energy distribution of the electrons, which must overcome this potential to escape.

Since the ionospheric electron temperature is typically reported to be 1000 to 3000 K (0.1 to 0.3 electron-volts [eV]), we might expect that the ambipolar potential must be similarly limited. However, a population of superthermal hot tails in the electron energy distribution results from unthermalized photoionization or impact ionization by incident auroral electrons of higher energy. When these hot tail electrons have sufficient fluxes, the associated ambipolar potential rises as high as their characteristic energy, which may be from several to tens of eVs. This important potential is directly controlled by the flux and energy of superthermal electrons.

Theory of ambipolar plasma flows [*Khazanov et al.*, 1998] shows that the ambipolar potential counters and even negates the gravitational potential that binds ions to a planet. The degree to which it does this at a given altitude scales with the electron pressure gradient, which in turn is driven by electron heating. Strong electron heating therefore reduces the effective gravitational binding energy, lowers the ion escape velocity, and reduces the ion temperature required for substantial ion escape. Enhanced superthermal electrons were found capable of producing a ~7 volt (V) ambipolar potential, at which point ion escape rises to limit further growth of that potential. However, recent observations [*Kitamura et al.*, 2012, 2013] have yielded evidence that the mean ambipolar

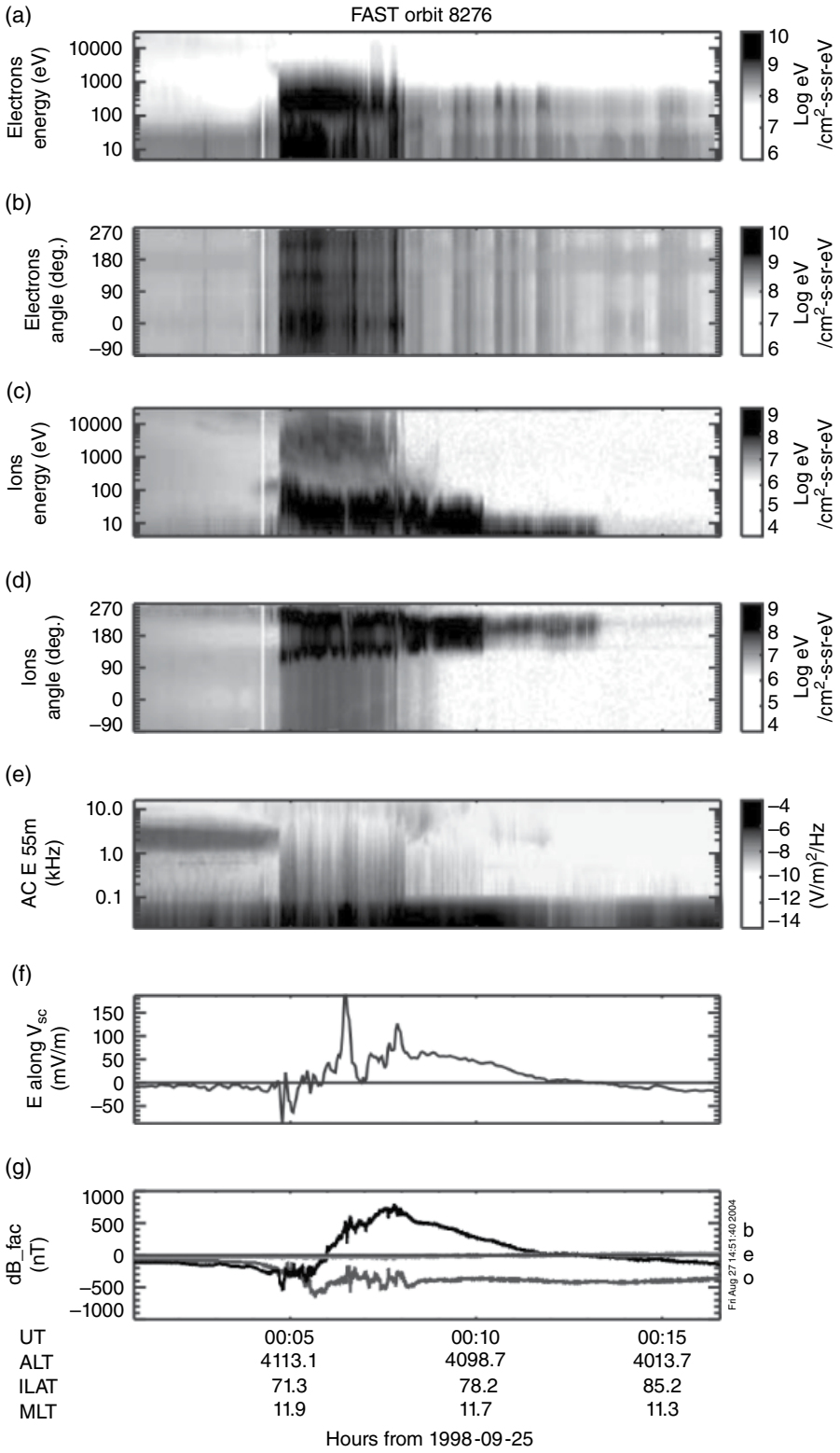

Figure 28.1 FAST measurements [*Strangeway et al.*, 2005] of ion energization and outflow in panels (c) and (d), associated electron precipitation in panels (a) and (b), broadband plasma waves in panel (e), strong convection in panel (f), and field-aligned currents in panel (g).

potential above the auroral zones is ~20 V with a wide variance around that value. A reconciliation between these two values has not yet been accomplished but is likely to involve the effects of auroral processes. In any case, the ambipolar potential is a potent factor that must be understood to accurately predict outflow fluxes of heavier ions.

Our current theoretical models and simulations of ionospheric outflows implement a more or less complete set of mechanisms. *Schunk and Sojka* [1997] have treated the global three-dimensional outflow as a Generalized Polar Wind (GPW), while *Glocer et al.* [2009] have treated it as a Polar Wind Outflow Model (PWOM). The physical mechanisms are summarized in Figure 28.2, which is inspired by the work of *Strangeway et al.* [2005]. Here, the two pathways to the ionosphere of electromagnetic and kinetic energy are indicated, along with their linkage to the dense atmosphere, as well as the ionospheric ions and electrons. The latter influences the former via the ambipolar electric field. However, there are few if any observational constraints on the ambipolar potential derived by such models, or its relationship to the complex superthermal electron environment of the auroral zone, including both photoelectrons, precipitating auroral electrons, and backscatter and secondary populations, not to mention field-aligned currents, all of which are relevant. We currently are unable to routinely observe whether the models are getting the correct ambipolar potential.

An even more serious problem with current models and simulations is that they do not derive resonant plasma wave amplitudes from first principles. Rather the intensity spectrum of resonant waves is an empirically determined free parameter (or a very large number of free parameters, when spatial distribution is considered) of the models. As such it can be and is freely adjusted to optimize the results, defined largely as obtaining a net outflow in "reasonable agreement" with observed escape fluxes. This level of understanding does not adequately support quantitative prediction of outflows in response to specified magnetospheric conditions. One exception to this exists in the area of Alfvén waves propagating into the ionosphere from the global magnetosphere. Here, efforts have been reported [*Zhang et al.*, 2012] in which global circulation models with sufficient time resolution are used to compute the spectrum of waves incident upon the ionosphere, in so-called "Alfvénic aurora."

A virtual zoo of plasma wave modes may be effective and active in producing ionospheric outflows extending from DC to the lower hybrid range for ion heating and much higher for electron heating. Different wave modes have different sources, and it is generally unclear upon which source of waves to focus for purposes of quantifying their growth, propagation, and dissipation. Constraining this problem by identifying the predominant wave modes, sources, and sinks is perhaps the biggest single requirement for a mission to resolve these issues. A treatment is needed that is capable of driving the electron precipitation, deriving the ambipolar potential distribution as well as the Poynting flux, across the entire wave mode spectrum.

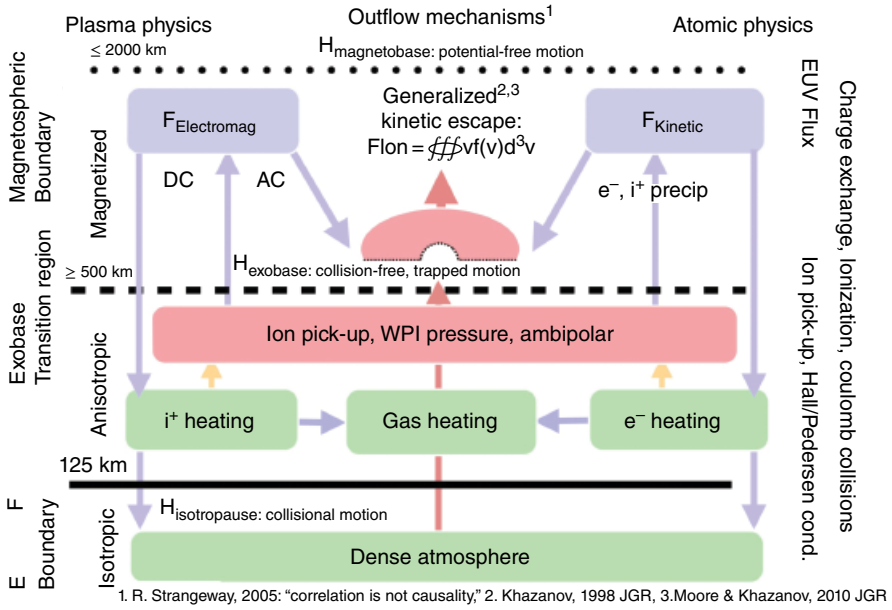

Figure 28.2 Energy flow diagram of the exobase region of transition from collisional to magnetized plasma.

28.2. OUTFLOW HIGHLIGHTS RECONSIDERED

Consideration of the above-mentioned motivations gives rise to certain questions about the basic arguments taken as foundational assumptions in our current understanding of ionospheric outflows.

28.2.1. Must Oxygen Ions Possess at Least 10 eV of Kinetic Energy to Escape the Gravitational Potential of Earth?

This is technically true for free escape from the exobase, above which collisions become negligible. However, depending on the amount of electron heating and the resultant ambipolar potential distribution, heavy ions may not need additional energy to escape from Earth. For typical auroral electron environments, the effective binding energy for ions is substantially reduced or eliminated, lessening the requirement to heat such ions to drive their escape well below 10 eV. Just how much the barrier is lowered can only be assessed through knowledge of the ambipolar potential and its height distribution in relation to the gravitational potential.

28.2.2. Is it True that "Joule Heating" Imparts too Little Energy to Account for Oxygen Escape?

Joule heating occurs in a context of frequent collisions between convecting ions and relatively stationary and massive gas atoms. Each time an ion collides with a gas atom, it is scattered randomly about the neutral gas frame of reference. Each time an ion is created, or exchanges an electron with the slow atom, a slow ion is produced in the neutral frame. Each ion is subsequently picked up by the convection electric field into the convecting plasma frame, having gained equal parts gyration energy and convection energy. For slow convection and light ions, the energy gain is small compared with the thermal speeds of the plasma ions and much smaller than 10 eV. Gas atoms being the dominant species by density, most of the Joule heat energy ends up in the gas and its heating, while a relatively small fraction heats the lower density ions. The result is an expansion of the gas density scale height, which raises the exobase linearly with thermospheric temperature [*Banks and Kockarts*, 1973].

An important relevant result from astrophysical wind theory [e.g., *Leer and Holzer*, 1980] is that energy deposition into such winds below the altitude at which they become supersonic (the critical point) increases the mass flux of the wind with only a minor (negative) effect on velocity. Added energy increases the ionospheric scale height, increasing densities and mass flux, so the mean energy per particle inevitably declines and consequently the outflow speed. Energy deposition into such winds above the critical point increases their velocity or mean energy per particle and decreases their density, with only minor effect on mass flux. Thus, high altitude energy addition evacuates the heating region, reduces density and thermal pressure, and creates a demand for upward flow from below. Whereas, low altitude energy addition increases pressure and density above the heating region and drives flows upward.

It follows in the ionospheric context that the heavy ion mass flux of outflows is controlled by energy inputs at relatively low altitude, near and just above the exobase, where the energy is diluted on a per particle basis by the high density but may be sufficient for escape with sufficient ambipolar reduction of gravitational binding energy (see Section 28.2.1. above).

28.2.3. Are Ions Heated and Accelerated to Escape Energy Primarily Through Interactions with Waves, and if so, is their Source in the Auroral Acceleration Region Above?

Intense waves are often observed in association with ionospheric ion heating, and it is generally assumed that they are dissipating energy derived from a free energy source into the ions. Heating of ions by these waves is widely considered to be the most important process for heating to produce outflows. However, the source of the waves is uncertain, and their intensity and the heating rate or ponderomotive effects they produce cannot be predicted with any confidence in the absence of detailed knowledge of the source region.

Given the association with auroral phenomena, the usual assumption has been that the source of wave energy lies in the strong field-aligned current systems that link the auroral ionosphere with the magnetosphere and emit waves strongly in the auroral acceleration region at mid-altitudes of about 1 R_E. Ion resonant waves have been shown to grow from the ion velocity shear associated with such currents [*Ganguli et al.*, 1994]. The currents are carried by electrons moving along field lines, so a wave mode coupling parallel electron motions with perpendicular ion motions may also be relevant, and lower-hybrid waves have been a candidate for this. Though they do not readily resonate with thermal ions, it is thought [*Retterer et al.*, 1994] that they may raise superthermal tails on the ion distributions and thereby create outflows.

Another important source of waves is the magnetosphere itself, where turbulent processes are launching Alfvén waves sporadically or even continuously along field lines, especially in the auroral zone conjugate regions, which are subject to reconnection with the solar wind magnetic field. A class of aurora identified as "Alfvénic," in recognition of the role played by such waves, is a copious source of ionospheric outflows. These Alfvénic aurora can generate outflow in multiple ways: by

generating soft electron precipitation that creates ambipolar potential; or an ionospheric Alfvén resonator, which generates ultra low frequency-extremely low frequency (ULF-ELF) structure near the edges of the downward current region [*Streltsov and Lotto*, 2008; *Pokhotelov et al.*, 2000], or by resonantly heating the ions more directly. These processes may not be as steady or prevalent as the low frequency energy associated with magnetospheric convection, but the two blend together as a continuum in frequency and wavelength space.

A third wave source in the ionosphere itself is suggested by the importance of DC electromagnetic energy flux, carried again by the auroral field aligned current systems, and appearing as "Joule" heating of the ionosphere, when the ions are forced to flow horizontally through the gas at superthermal speeds (faster than thermal speed). At levels where the ion-neutral collision frequency is comparable with the local ion gyro-frequency, an ion pick-up process results. The ion velocity distributions become toroidal or ring shaped under strong (faster than the thermal speed) convection, because ions colliding with atoms are either randomized in velocity about the neutral atom frame, or created in that frame by ionization, or by charge exchange, forming a new ion in the neutral frame. Either way, the ion pick-up into the convecting frame by the convection electric field imparts to the ion a gyration energy equal to its convective energy, and a toroidal or ring distribution results.

When the majority of ions is affected, this type of distribution is the most unstable in the solar system, with the greatest phase space density gradient in velocity space [*Moore and Khazanov*, 2010]. The instability drives waves that scatter the ring beam in energy and angle, filling and washing out its non-thermal low velocity void. Some theoretical work [*Puhl et al.*, 1993] has accounted for the observation of hot power law tails as a result of pick-up ion thermalization by plasma waves driven by the pick-up velocity distributions. The energy distribution resulting from pick-up ion thermalization has been shown to be an important factor in controlling ionospheric outflow flux [*Moore and Khazanov*, 2010].

Wave-particle-interactions are considered to be critically important mediators of ion heating, and credible candidate sources exist at high altitudes in magnetospheric boundary layers, at intermediate altitudes in the auroral acceleration region, and within the ionosphere proper. We must determine the source of free energy for such waves, the direction of their Poynting flux, and where they are dissipated into resultant plasma heating.

28.3. SCIENCE OBJECTIVES/ACTIONS

The ionospheric outflow arguments outlined above give rise directly to a set of mysteries or questions about outflows that culminate in a single overarching objective for future research in the coupling of atmospheres with magnetospheres, and the resultant escape of atmospheres into space.

- Mystery 1. How does the ambipolar electric field respond to electron precipitation, driving and responding to ion outflow and heating?
- Mystery 2. How is energy transported to the exobase region, raising scale heights and the exobase, and enhancing the escaping flux of heavier ion plasma?
- Mystery 3. Where and how do plasma-resonant waves grow, propagate, and dissipate, transferring energy into electrons, ions, and resultant plasma outflows?
- Objective: Determine whether planetary mass loss is drawn from above by energetic evacuation or driven from below by energetic pressurization by the above effects.

In pursuit of the above objectives, the following actions must be targeted as part of a responsive mission design. Here, the actions to be accomplished by the mission are numbered with respect to the mysteries identified above:

- 1a. Determine the ambipolar potential at multiple conjugate parcels at altitudes from the topside F region to the exobase, and above the exobase by one maximal atmospheric scale height; that is, in the collisional region (ionosphere), the magnetized region (magnetosphere), and in the transition region where collision and gyro frequencies are comparable (exobase region).
- 1b. Determine the electron pressure and energy distribution in the same set of parcels, to constrain, along with 1a., the distribution of ambipolar potential along the field line.
- 2a. Determine electromagnetic and kinetic energy densities and fluxes in the same set of parcels. Map these across the auroral zone in latitude and along the auroral zone a distance exceeding the maximum cross-track plasma convection displacement between F peak altitude and exobase (~1200 km).
- 2b. Determine the source and collisional medium gas density/pressure within the same altitude ranges.
- 2c. Determine the density, pressure, and velocity distribution of core plasma ions by species and electrons in multiple conjugate parcels over the same altitude range.
- 3a. Determine the intensity spectrum of plasma-resonant waves in multiple conjugate parcels spanning the same altitude range.
- 3b. Determine the direction and magnitude of all types of plasma-resonant wave energy flow.

When these actions are completed, a significant closure will be achieved on the overarching objective. When we incorporate the ambipolar effects of electron heating, the flow path of energy to the region driving outflows and the role of waves in that energy flow, it will become possible to properly parameterize our models and simulations of outflow, especially relating to the source, intensity, propagation, and dissipation of plasma waves.

28.4. MISSION/MEASUREMENT REQUIREMENTS

Given the motivations described above, the identification of an overarching objective for future research in this area and of a set of actions that are needed to achieve those ends, how can we resolve them, answer the questions and move forward toward a quantitative physical understanding of atmospheric escape? We wish to move toward a future in which the interaction between the magnetosphere and the thermosphere is as well described and modeled as the interaction between the magnetosphere and the solar wind. To accomplish this end, we must undertake a program to improve upon and undertake new measurements of fundamental processes in the A-I-M system that determine the ambipolar electric field and associated potential, quantify the flow of energy of all types from sources to sinks, and in particular track the growth, propagation, and dissipation of plasma waves of ionospheric, auroral, and ionospheric origin.

What, then, are the requirements for such a program of study of the atmosphere-ionosphere-magnetosphere system? We illustrate the requirements using diagrams of the system to be studied, as shown in Figure 28.3. Here we display our subject in terms of altitude regimes along the vertical axis, and scale lengths (with required time resolution at orbital velocity) along the horizontal axis. Figure 28.3 points to a requirement for observations at three simultaneous levels: in the (collisional) ionospheric F-region proper, at the bottom of the (magnetized) auroral acceleration region, and in the transition region between them where ion-neutral collision frequency is comparable with gyro frequency.

28.4.1. Measurements

The parameters to be measured at multiple levels were identified in the action list above, but let's collect them into a short list:

- Core Plasma Analyzer (CPA), ion and electron velocity distributions; CPAi, CPAe
- Gas pressure; Rapid Atmospheric Neutral Gas Experiment (RANGE)
- Electric and Magnetic Field Probes (EFP and MFP): wave amplitudes and frequency spectra
- Poynting flux (DC to Lower Hybrid Resonance [LHR]); EFP, MFP
- Hot plasma analyzer (HPA); ion and electron pitch angle distributions

An overview example of many of the measurements needed was given in Figure 28.1, however, note that we are adding to the typical list a "core plasma" measurement, where the term "core" refers to the lowest energy

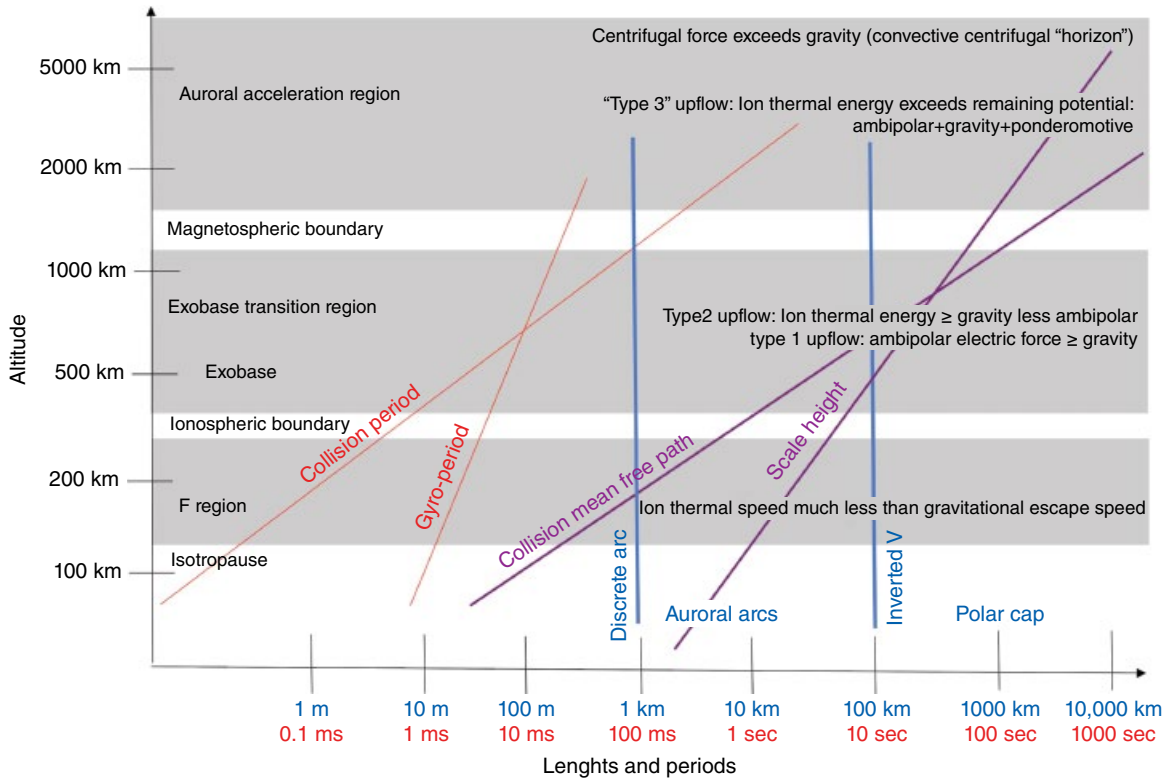

Figure 28.3 Schematic diagram of the altitude regimes and length/time scales to be diagnosed, to serve as a guide to required spatiotemporal resolution and sampling.

component of the plasma, normally referred to as "cold" or "thermal." To make progress, it is essential to relax all assumptions that this plasma has a negligible temperature (relative to escape) and also that it is thermal or Maxwellian in velocity distribution. We also added an atmospheric gas pressure measurement, which is necessary to quantify ion-neutral collision frequencies and mean free path lengths.

28.4.2. Multi-level Sounding and Mapping

The actions identified above emphasize the need for simultaneous measurements at multiple levels of the atmosphere-ionosphere-magnetosphere system. We take this as a requirement, based on the need to observe magnetic and gravity-aligned gradients of a large number of plasma parameters identified in the action list above, and described in more detail below. It is also a prescription for advancement from single spacecraft studies, such as those performed by Freja, Viking, and ePOP. We consider that three levels are the minimum requirement. Observations in the "ionosphere" will determine the lower boundary condition on the region of interest. Observations of the "lower magnetosphere" will determine the upper boundary condition on the region of interest. Observations from the exobase transition region will determine the relationships between the response within this system and the boundary conditions applied by the atmosphere and the magnetosphere.

We define "the ionosphere" as the peak of the F-region, ~125–350 km altitude. The exobase is defined as the height where collision mean free path matches atmospheric scale height, nominally ≥ 500 km altitude, and rising with enhanced atmospheric temperature [*Banks and Kockarts*, 1973]. We define the "lower magnetosphere" as lying one light atom/ion scale height above the exobase, so ~1500 km altitude.

We note that, until we have a constellation of spacecraft spread in both altitude and latitude, it will be useful to sample parcels within the primary region of interest at temporal separations much smaller than a typical orbital period, to distinguish fluctuations from steady features. This can be accomplished readily if two spacecraft pass through the auroral oval at nearly the same altitude in quick succession, a scenario that is readily achieved by the mission orbit plan described below.

The science objectives described above represent key questions at the core of magnetosphere-ionosphere coupling. More specifically, the in situ observations will be designed to answer questions related to how low energy terrestrial plasma is thrown and/or drawn up to the Earth's magnetosphere. By definition, this means observations of the low energy plasma and electric and magnetic fields. This is very different from topside missions that explore phenomena related to higher energy plasma, where the connection between the in situ observations at a spacecraft and related auroral and other features in the ionosphere proper is more direct, by which we mean more directly along the field lines to the ionosphere. In the case of the low energy plasma, ions with pitch angles near the loss cone at the satellite can have convected hundreds of kilometers horizontally as they move up the magnetic field to the altitude of the satellite. Ions with different pitch angles and different energies will have come from differing locations in the ionosphere, as illustrated in Figure 28.4, so in a very real sense, the plasma observed

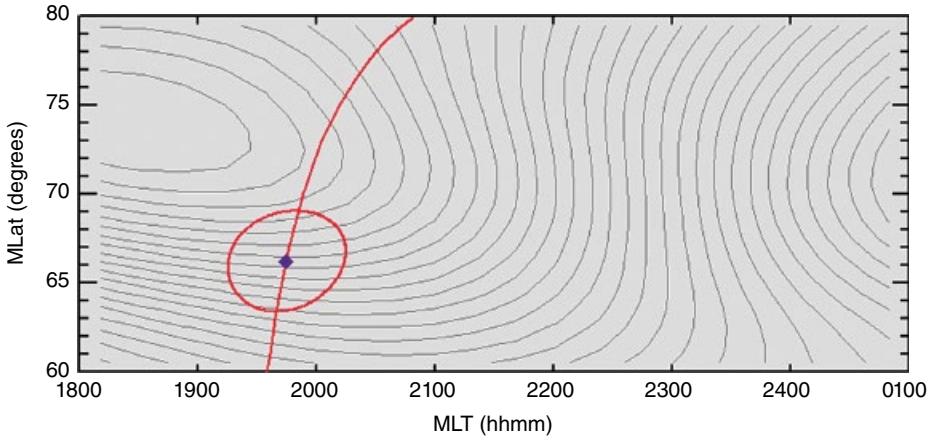

Figure 28.4 Evening sector auroral zone ionospheric electric potential contours, separated by 2 kV, from the *Weimer* [1996] potential model. Low energy ions observed at a polar orbiting satellite transiting above this region (e.g., blue dot along the red trajectory) will have convected to the satellite along paths that are at times oblique to the track. The region of origin will be remote from the observation point up to several hundreds of kilometers as suggested by the red circle around the observing point.

by a spacecraft will have originated from a broad swath around the spacecraft foot-point. As well, these objectives target subtle consequences of the numerous ionospheric processes that affect the superthermal plasmas. For these and other reasons, ground-based remote sensing of auroral luminosity, ionospheric convection, electric currents, and other ionospheric parameters will be important for future AIM science.

Sounding and mapping observations can be grouped into two very different categories. On the one hand, we have well instrumented observatories organized around powerful Incoherent Scatter Radar (ISR). These observatories are designed to "drill deep," providing comprehensive measurements related to the ionosphere, its small-scale dynamics, and its response to forcing from above. ISRs and other co-located instruments will provide for what is effectively a "third satellite." On the other hand, extensive arrays of All-Sky Imagers (ASI), High Frequency (HF) radars, and ground-based magnetometers provide a lower-resolution multi-scale view of the ionospheric and auroral dynamics that control much of ionospheric outflow. In this section, we begin with a brief review of ISR observations of ion outflow of the type that will support future AIM observations. We follow with a brief description of networks of ASIs that we expect will provide data that will support AIM science. We note that the field of view of existing HF radars (the Super Dual Auroral Radar Network [SuperDARN] radars) existing and networks of ground-based fluxgate magnetometers span the region covered by the ASI networks.

28.4.3. Incoherent Scatter Radars

The ionospheric F-region is well diagnosed locally by ISRs. In fact, these radars are the tools with which the important distinction between electron heated up flows and ion heated up flows were discovered. In Figure 28.5, we show examples of the two types of up-flow, termed Type 1 and Type 2 outflow by *Wahlund et al.* [1992]. In general, both types of heating can occur together, but this work established their independence from each other, as well as their capability to cooperate in lifting ionospheric plasmas. From this work, it has become clear that both electron and ion heating are effective in producing up-flows because of the ambipolar coupling of electrons and ions, which prevents one from flowing without a corresponding flow of the other.

We also define another hypothetical type of outflow, which we term as Type 3. By this, we mean outflows of the kind observed at higher altitudes in the auroral acceleration region, in a case where there is neither electron nor ion heating in the conjugate exobase region below, to supply plasma to the auroral acceleration region. Of course all three types of outflow may well operate in combination within specific events, but we seek here to decompose and separately parameterize the outflow flux as driven by these three separate types of energy input.

Photoelectrons have also been cited as a possible driver of up-flows and outflows. They are, after all, the baseline agent that creates new ionization of the ionospheric plasma. But it was soon realized that electron heat conduction greatly moderates the role of residual photoelectrons [*Khazanov et al.*, 1997, 1998]. A bit of reflection tells us that photoelectrons cannot be effective in lifting heavy ions out of the ionosphere. If they were, the plasmasphere would contain a substantial amount of O+ ions, yet it is relatively devoid of them, except in its outer reaches where magnetospheric processes are active. Thus, we must look for more energetic electron heating than is produced by solar EUV at the Earth, to power heavy ion outflows.

Another important result came out of ISR studies of the auroral ionosphere, as shown also in Figure 28.5. *Suvanto et al.* [1989] and others identified distinctly non-thermal backscatter spectra from patches of ionosphere that were rapidly convecting. The strange spectra were interpreted in terms of the toroidal ion pick-up velocity distributions produced by ion neutral coupling [e.g., *St.-Maurice and Schunk*, 1979; *Wilson*, 1994] and are intrinsically unstable to ion resonant waves that will thermalize the distributions. Thus, the exobase region where ions collide with neutrals at approximately their gyro frequency should be an important source emitting ion-resonant waves, whose function is to thermalize these highly unstable pick-up distributions. And ISR is a powerful tool with which to diagnose this region, in conjunction with in situ observations of the actual ion velocity distributions.

ISR observations of the auroral ionosphere and exobase region should be a fundamental baseline for any mission seeking to better understand topside ionospheric response to auroral forcing. These ISR observations are routinely made from multiple high-latitude stations, with fields of view in longitude, latitude, and altitude sufficient to provide excellent coverage of the low-altitude region of interest here.

The ISR observations show that heating and outflow is tightly associated with auroral processes ranging from pure precipitation to strong convection. Thus, it will be a requirement to know auroral conditions in the region where Type 1 and Type 2 heating events are occurring. The most effective way to provide auroral condition diagnostics within the heating region might seem to be from a spacecraft that is observing the up-flow or outflow. However, owing to our interest in the lowest altitude origins of the heating, combined with the slow

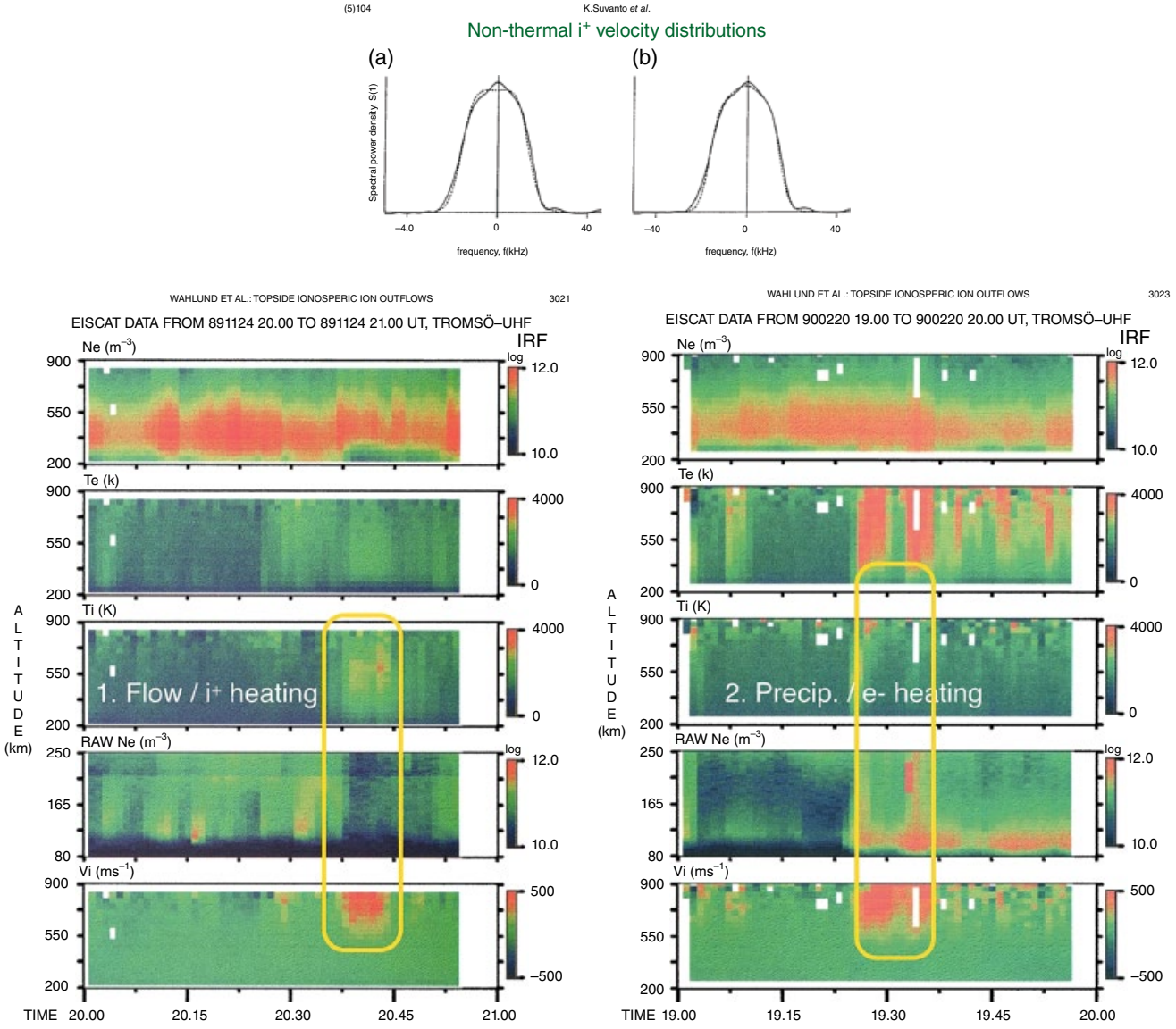

Figure 28.5 European incoherent scatter (EISCAT) discovery of the independent linkage of ionospheric up-flows with ion heating (Type 1) and electron heating (Type 2) [*Wahlund et al.,* 1992]. Top center panel illustrates the inference of non-thermal ion velocity distributions in the rapidly convecting auroral ionosphere [*Suvanto et al.,* 1989].

initial upward acceleration of the up-flow, as well as the association of the heating with intense longitudinal (cross-track) convection jets, the origin of the heating may be quite distant from the location of a satellite observing the up-flow at moderate to high altitudes. This is illustrated in Figure 28.4. For upward flow of less than 1 km/s in a convection jet of 5 km/s, the up-flow will be caught in a crosswind that carries it ~1000 km from its source at 250 km altitude, by the time it is observed at 500 km altitude. Certainly, the vertical profile of the acceleration is relevant here, but it should be apparent that reliable observations of the source region are best obtained from a wide field of view global multispectral auroral mapping capability. This could be provided by a higher altitude imaging spacecraft with sufficiently wide field of view and resolution, or by a ground-based all sky imaging network such as that provided by the Canadian GeoSpace Monitoring (CGSM) network that has supported the Time History of Events and Macroscale Interactions during Substorms (THEMIS) mission and is currently being upgraded by the University of Calgary. For a small Explorer class mission, the latter is the necessary choice, whereas a more ambitious medium Explorer or flagship mission could avail itself of a space-borne

imaging system that would require less data merging and integration work on the ground.

28.4.4. Ground-Based Networks

Extensive networks of ground-based ASIs, SuperDARN radars, and magnetometers will provide an important multi-scale view of the auroral dynamics and ionospheric phenomena that affect and control much of ion outflow. A large number of SuperDARN radars operate in the northern and southern hemisphere [*Chisham et al.*, 2007]. Together, these provide time evolving maps of the ionospheric convection across almost all of the northern and southern hemisphere sub-auroral and auroral zones and polar caps. Extensive networks of ground-based magnetometers across much of the northern and southern hemisphere (land masses) are operated by research and space weather programs in Canada, the U.S., Greenland, across Europe, China, South America, and Antarctica. Data from these multiple arrays are increasingly available through coordinated programs such as SuperMAG [*Gjerlov*, 2011]. The magnetometer data provides information about ionospheric currents, ULF waves, and magnetosphere-ionosphere (M-I) coupling.

The SuperDARN radars and ground magnetometers provide nearly continuous, nearly global information about ionospheric convection and currents. Obtaining information about the multi-scale auroral distribution is more problematic, owing to the fact that imaging the low-light levels of typical aurora is essentially impossible unless the Sun is well below the horizon, a situation that is further exacerbated by poor frequent viewing conditions due to clouds, moonlight, and other confounding factors. Nevertheless, over the last 15 years there has been a dramatic increase in the number of ASIs that are operating worldwide, in the reliability of their operation, and in access to the very large data sets that they produce.

The Finnish MIRACLE and U.S. Antarctic AGO ASI networks were successful early pathfinders in efforts to create mosaics of auroral luminosity from images collected simultaneously by multiple ASIs. The network of ASIs spanning all of Alaska and auroral latitudes across Canada deployed as part of the NASA THEMIS mission has had a profound effect on how ASIs are used in geospace research in general [*Donovan et al.*, 2006; *Mende et al.*, 2008]. This network is now comprised of 21 ASIs that collect simultaneous white light images at a three-second cadence. Software has been developed for mapping the images into geographic coordinates assuming a fixed emission altitude. The data are available online, and access is fully open. The images are only collected at night, a significant fraction of the images are compromised by poor viewing conditions and other factors, there are significant difficulties introduced by assuming all of the auroral luminosity originates from one altitude, and the images are panchromatic so have little if any information about the energy of the precipitating particles. However, for the first time, we have contiguous high time and space resolution auroral images spanning multiple hours of magnetic local time (MLT) and the entire latitude extent of the auroral distribution. This new capability has provided a fundamentally new view of multi-scale geospace dynamics as impressed on the ionosphere [see e.g., *Nishimura et al.*, 2011]. As well, the large number of imagers and their continuous operation during night time has led to a dramatic increase in the number of conjunctions between relevant satellites and magnetically conjugate ASIs.

Looking forward to future missions, we can expect that THEMIS-ASI will either still be operating or will have evolved or been replaced. As well, there are efforts in multiple countries to develop new ASI networks that have the extent of coverage of THEMIS-ASI but that bring additional information via imaging in specific auroral wavelengths. A notable development is the new redline ASI network that has been deployed in Canada. Consisting of eight (soon nine) highly sensitive imagers, REGO (for REdline Geospace Observatory) collects images in the auroral "redline" (630 nm) at the same cadence as the overlapping THEMIS-ASI network. The redline images convey information about lower energy electro precipitation, highly relevant to processes influencing ion outflow. As well, qualitative differences between the THEMIS-ASI white light and simultaneous REGO images enable inferences about the higher energy electron precipitation. In addition, there are multi-spectral ASIs operating in Scandinavia (as part of MIRACLE) and elsewhere, and full-color ASIs operating in Canada, Scandinavia, the Faroe Islands, and Iceland. These, THEMIS-ASI, and REGO represent the minimum auroral coverage we can expect in future studies.

THEMIS-ASI (and the complimentary THEMIS magnetometer program) represented a new development in ground-based instruments for a major geospace satellite mission. A ground-based multispectral observing system was integrated into a major geospace mission at the outset to address required observations that could not be obtained from the satellites alone. Going beyond context information, these ground-based observations provide a point of view, without which the in situ observations would fail to capture the multi-scale complexity of substorms. Thinking about the future, one can envision important roles for ground-based observations. In particular, redline auroral images can provide detailed information about the type of aurora that a spacecraft mission would be flying over (e.g., the Alfvénic aurora discussed above are relatively straightforward to identify in REGO images), and convection information from SuperDARN

will provide critical information in terms of mapping trajectories of particles back from the satellites to their ionospheric origins.

In Figure 28.6, the Fields of View (FoV) of ISRs located at Poker Flat (Alaska), Resolute Bay (Canada), Kangerlussuaq (Greenland), Millstone Hill (Massachusetts), Tromso (Norway), and Svalbard (Norway) are shown with the blue dashed curves. The black circles indicate the FoVs of the THEMIS ASIs in Alaska, Canada, and Greenland, color and other ASIs operating in Iceland and the Faroe Islands, and the MIRACLE network of ASIs operating in Scandinavia. The larger red curve in Canada shows the merged FoV of new redline-dedicated ASIs. The smaller six-imager merged FoV sitting within the redline network indicates full-color ASIs that are currently operating. Funding is being sought to upgrade these six full-color ASIs to high-speed greenline and blueline ASIs. The grid indicates contours of magnetic latitude (50° to 75° in 5° steps) and magnetic longitude (15° or one MLT hour steps). The red and yellow lines indicate magnetic midnight and noon assuming a UT of 0630. The two gray oval-shaped regions indicate a nominal cusp and substorm onset region, again assuming a universal time (UT) of 0630. Note that each ASI FoV is within the collective FoVs of the northern hemisphere SuperDARN network and that magnetometers are deployed near and around all of the ASIs.

28.4.5. Gas

Atmospheric gas is of course the source of all ionization, and its presence is a very fundamental assumption of all ionospheric theory. Auroral primary ionization, charge exchange, and collisional interactions all depend upon the density of the atmospheric gas, which is known to be variable in response to auroral Joule heating, and it is thus a requirement to know its density in the outflow source region.

Figure 28.7 illustrates this requirement for a gas pressure analyzer. The CHAMP drag was correlated with ion outflows observed by the FAST spacecraft in nearly conjugate passes, and it was found that the outflow is directly correlated with the deceleration increase (drag) at ~454 km altitude. Separate relations have been reported between CHAMP drag and the Poynting flux of electromagnetic energy into the ionosphere [*Knipp et al.*, 2011]. Poynting flux is of course also known to

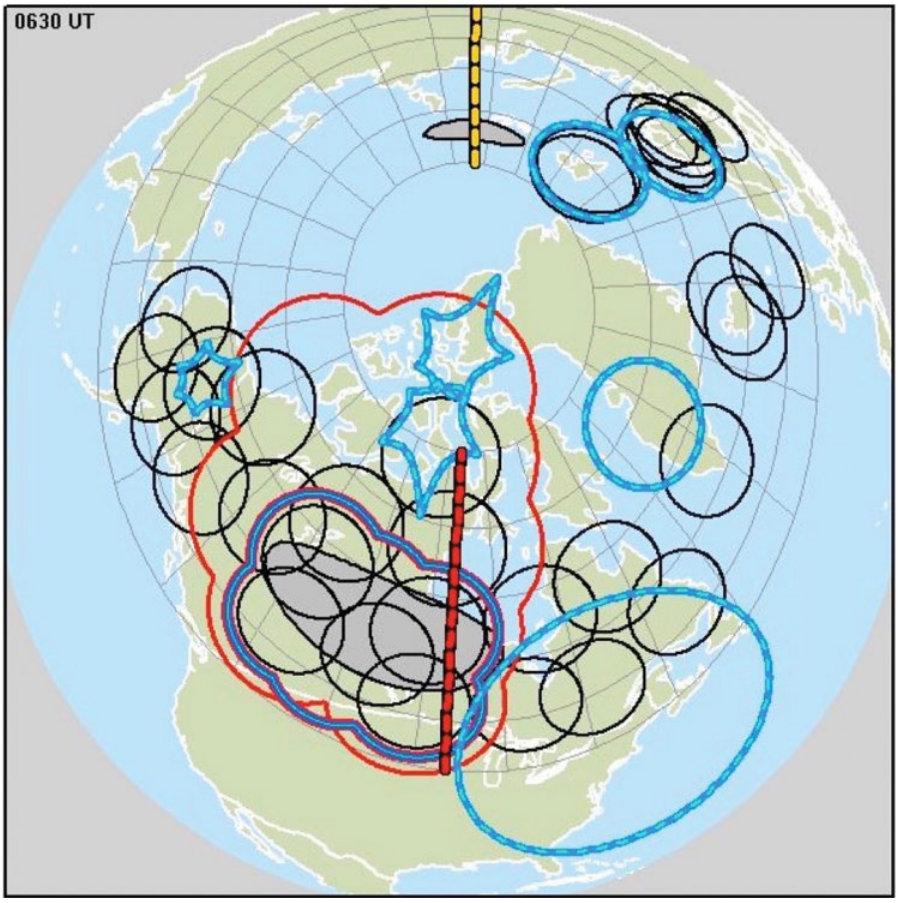

Figure 28.6 Northern hemisphere ASI networks and ISR facilities.

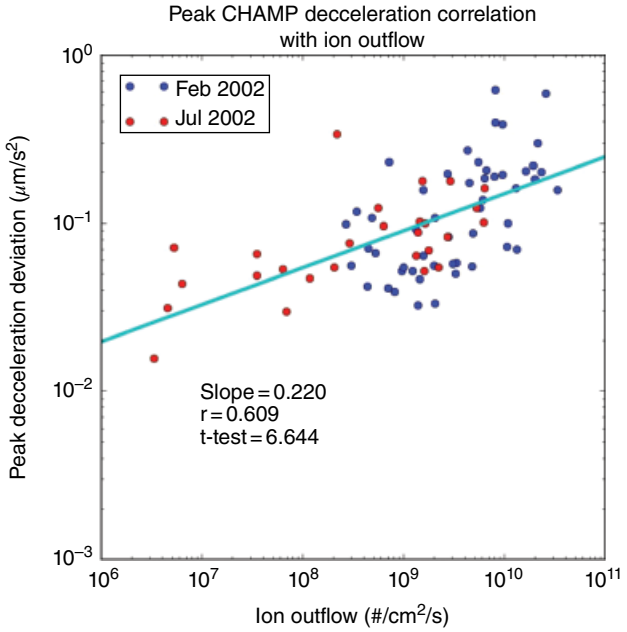

Figure 28.7 Observed correlation between ion outflow flux at the FAST spacecraft, and drag acceleration of the CHAMP spacecraft, when near magnetic conjugacy. [after *D. K. Olson*, 2012, Dissertation, U. MD. College Park]

correlate well with ion outflow [*Strangeway et al.*, 2005]. Incident DC Poynting flux is expected to be dissipated largely into the atmospheric gas, with a small fraction going into processes that heat and lift the ionospheric plasma. The question to be addressed using gas measurements in this region follows: "Is the enhancement of ion outflow in part accounted for by the increased gas that serves as a source of ionization or of enhanced collision frequency or consequent upward motion of the exobase?"

28.4.6. Fields

The electric and magnetic fields are critical parameters that must be measured in order to fully understand the mechanisms of atmospheric escape. These range from quasi-static convection and field aligned current signatures, through Alfvénic and ULF waves to ion-resonant modes in the ELF and very low frequency (VLF). The quasi-static electric fields must be measured with an accuracy and temporal and spatial resolution suitable for determining Joule heating rates and ion drift motion. This is best carried out with a double probe experiment, with spin plane booms of sufficient length (tens of meters), and spin-axis booms that are as long as possible.

Such a double-probe instrument will provide the necessary observations to permit assessment of ion heating rates and also perpendicular convection of plasma as it moves along the field line. This nominally requires a three-axis measurement of the quasi-static electric field, because the magnetic field will take on a range of angles relative to the (spinning) spacecraft body. The third (cross-track horizontal) axis of the electric field vector can potentially be determined from the ram component of the ion flow, as measured by the plasma instruments, if necessary. Spatial scales corresponding to auroral arc widths (1–10 km) must be well resolved in order to make accurate measurements of Joule heating rates, implying sample rates significantly faster than 8 Hz, assuming a spacecraft velocity of 8 km/s. The absolute accuracy must be sufficient to accurately measure ion bulk velocities on the order of 100 m/s, consistent with significant Joule heating rates.

The quasi-static magnetic field will provide information necessary to infer field-aligned current intensities associated with ion energization and outflow. Several models (*Ganguli et al.*, 1994; *Streltsov and Lotko*, 2008) drive ULF and ELF waves unstable in regions of intense velocity shear associated with field-aligned currents. Measuring the field-aligned current (using the infinite current sheet approximation) will permit assessment of the importance and ubiquity of these instabilities. This requires a three-axis magnetic field measurement, with accuracy of a few nT requiring the magnetometer to be mounted on a boom deployed at least a body diameter away from the spacecraft, sampled faster than 10 Hz, in order to resolve small-scale filamentary currents that are often the most intense.

Moving up in frequency, Alfvénic structures require a faster sampling rate, with Alfvén frequencies of a few Hz requiring sample rates of at least several tens of Hz, ideally in all three electric and magnetic field axes, in order to estimate propagation direction and wavelength. Assuming $\mathbf{E} \cdot \mathbf{B} = 0$, a two-axis electric field and three-axis magnetic field measurement could be used to estimate these parameters.

At still higher frequencies, the amplitude, frequency spectrum, and k-vector of ELF and VLF waves that may be ion-resonant must be measured. Again, this is best performed with a three-axis electric and magnetic field measurement. The fluxgate magnetometer technique is most sensitive below a few tens of Hz, and so measurement of higher frequency hiss and other waves is best performed with a sensitive tri-axial search coil. The sensitivity of the instrument must be sufficient to accurately resolve k-vectors, as well as detect weaker wave modes, and provide a spatial sampling rate sufficient to resolve wave modes that may be spatially varying on spatial scales of a few kilometers (requiring both burst mode measurements with burst lengths of a few minutes and onboard power spectra at a cadence of 0.5 to 1 second).

As an example, the VISIONS sounding rocket [*Collier et al.*, 2015] flew through the nightside auroral zone following substorm onset. Two components of the convection electric field and the power spectrum of waves in the ELF to VLF range were observed. Transversely, accelerated ions up to 1 keV were associated with a region of strong plasma convection and enhanced broad band extremely low frequency (BBELF) wave activity. This highlights the need for wave measurements at frequencies that can participate in ion gyro-resonant interactions.

Measurements at still higher frequency are most useful in the electric field domain, to provide secondary measurements of electron wave modes. These will be useful for diagnosing electron number density (from Langmuir oscillations) and for studying instabilities generated by the core and energetic particle distributions, which will be measured by the rest of the mission instrument complement.

28.4.7. Plasma

As important as it is to observe the electromagnetic fields that transmit available energy to accelerate plasma particles, it is even more important to observe the response of those particles to the energy inputs, especially the initially cold, thermal plasma of the topside ionosphere. The "bottom line" for our requirements will be the resultant heating and escape of the electron and ion plasmas, reflected in flow speed, temperature, and pressure values that, for particle instruments, are derived from count rates that translate into velocity distributions of the particles. In addition to providing bulk plasma parameters, the velocity distributions are themselves important measurements, because they reveal anisotropies of the plasma, such as beams (flows), conics, and toroids (magnetic symmetries), and also energy distributions that may be far from thermal equilibrium (hot tails). As described above, all of these bear on the mechanisms that operate in the transfer of energy, understanding of which is the core goal of future AIM studies. For these reasons, we have adopted the name "core plasma" for what has often been referred to as "cold" or "background" plasma. Here, it is in the foreground. The precipitating particles carry kinetic energy into the exobase region, creating new ionization as well as dissipating energy into the thermal electron gas and must therefore also be observed. Thus, comprehensive measurements of both core plasma and precipitating hot plasma particles are relevant and required for AIM science objectives.

Core ion plasma crosswind, headwind, and vertical winds are required, as well as a three-dimensional velocity distribution capability adequate to detect and analyze toroidal pick-up ion velocity distributions. Because nonthermal velocity distributions of the core plasma are implicated by theory and the ISR observations, the core plasma must be measured without assumptions as to its thermal nature; that is, the full three-dimensional velocity distribution is required with angular resolution of <1°–10° over an energy range from <1eV to 10s of eV. Ion composition is a requirement because gyro frequencies, heating mechanisms, and ion pick-up may be mass/charge dependent, and the gravitational binding energy certainly is. Time resolution is of key importance for resolving narrow auroral current sheet or drift channel features, such as those that were not quite resolved from a slowly moving rocket-borne instrument that resolved about 12 sec or 12 km [*Moore et al.*, 1996]. This makes it clear that the real-time resolution requirement is to resolve discrete arc scales ~1 km when traveling at 8 km/s; thus, full distributions are needed every 125 ms.

Low energy plasma observations are compromised of small spacecraft floating potentials, though this is less debilitating in the relatively high-density environment of the exobase transition. Still, it is important to know what energy is being observed and to prevent the floating potential from significantly blocking the core plasma. The CPA is best mounted on a short boom with a programmable aperture bias potential, and a single ended spacecraft potential measurement must be provided by the EFP instrument.

Dynamic range is also a challenge for the CPA in that it must diagnose both the thermal core and its nearby energetic tail distribution, which may be a few to several orders of magnitude lower in energy flux. While low fluxes can be integrated, it is also important to maintain good time resolution for the required measurements.

For the precipitating plasmas, the relevant energy range is 10s of eV to 10s of keV, to cover typical auroral conditions. Local pitch angle distributions are required, with an angular resolution 10–20° for both electrons and ions. Ion composition is highly desirable to identify hot plasma sources, and because ion kinetic energy transport may also be important in heating the ambient ionosphere, and the transfer of such energy via collisions may be mass/charge dependent. Also, energetic precipitating ions have also been suggested as sources of free energy for plasma wave growth, particularly in the magnetospheric cusp region. Because we don't expect hot plasma precipitation to be finely structured by auroral currents and flows, time resolution is relaxed somewhat to resolving tens of km at 8 km/sec, thus ~1–2 sec, or a half spin of a typical small spinning spacecraft.

28.4.8. Mission Orbits

To make the required multi-level sounding measurements, a straightforward orbital solution exists, as illustrated in Figure 28.8. In conjunction with appropriate

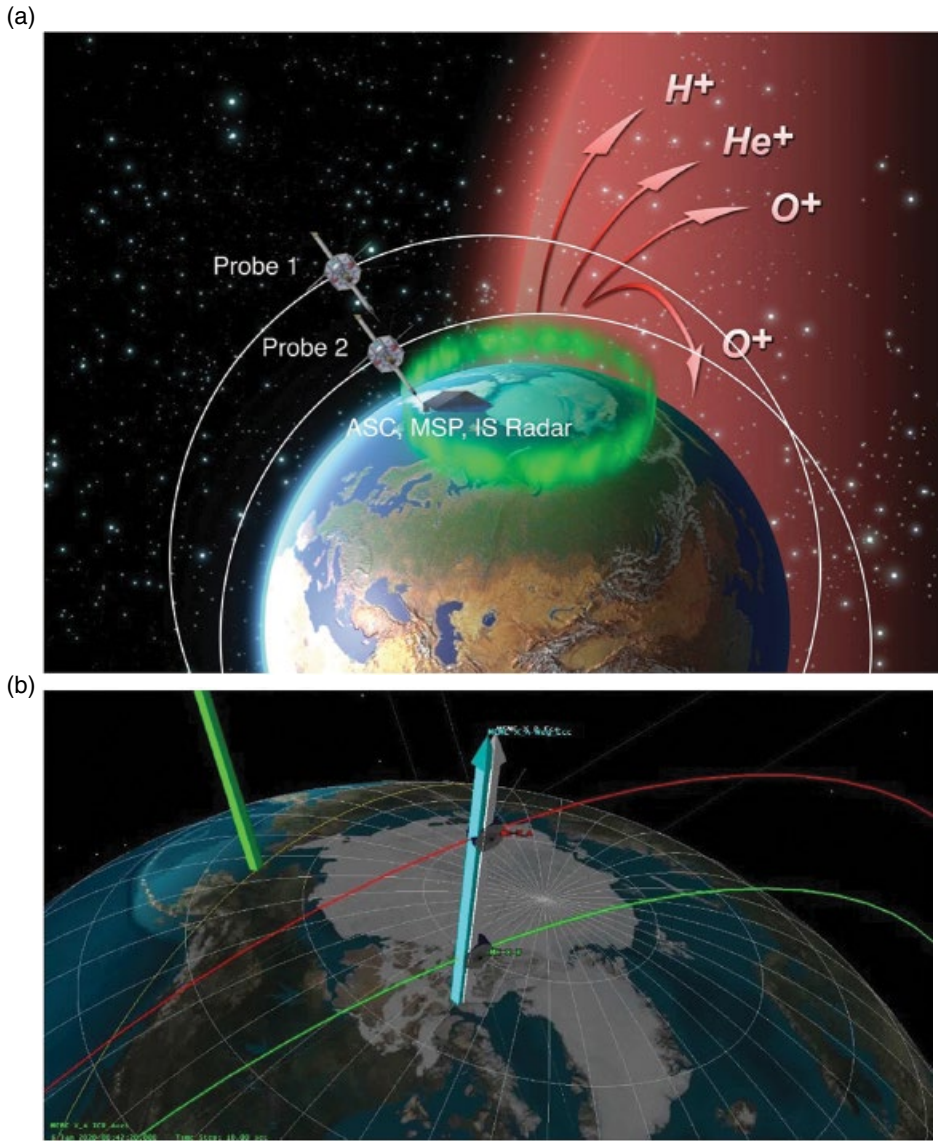

Figure 28.8 (a) Orbit concept for a mission point design to study AIM coupling using two orbiting probes, one or more ISR stations, and the Canadian GeoSpace Monitoring network. (b) Closeup of simulated orbits illustrating the moment when the two spacecraft are magnetically conjugate over the auroral oval in one hemisphere. Half an orbit later, they reverse positions vertically in the opposite hemisphere.

ISR sites, two spacecraft are placed in identical 350 km × 1200 km elliptical orbits at ~85° inclination so that they cross the auroral zones four times each orbit. The spacecraft mean anomalies are held in phase (requiring ~ weekly trimming) while the orbit eccentricities are out of phase, such that one s/c is high while the other is low, and vice versa. They, thus, achieve magnetic near-conjugacy twice per orbit, and the latitude of this conjugacy precesses around the Earth and through the auroral zones roughly once per month, as the orbit also rotates in local time, giving a complete local time sample over the course of six months. In this way, the spacecraft achieve magnetic near-conjugacy with the ISR and ASI arrays ground station periodically, providing a multi-level sounding of dayside, nightside, and dawn-dusk phenomena, as required.

This scheme alternates the magnetic conjugacy at high latitudes with periods when the two spacecraft are in similar altitude ranges (700–1000 km) and crossing the same sets of field lines with a temporal separation of a few minutes. This permits studies of temporal variability of ion outflow responses, to complement the three-point conjugate measurements. Finally, the 350 × 1200 km orbits can be achieved in stages,

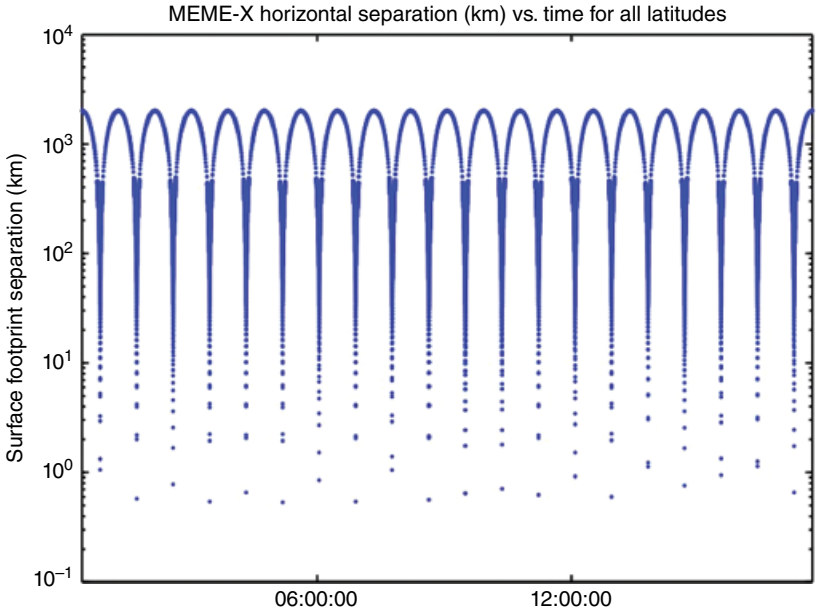

Figure 28.9 Horizontal separation between a pair of spacecraft in the orbits described, for a number of orbits. Vertical separations vary similarly, maximizing when horizontal separation is minimal. Horizontal separations correspond to temporal separations of about 0–5 minutes.

allowing multi-level "sounding" of the region of interest, with the apogee being raised in steps, in order to determine statistically how the ambipolar potential is distributed, as well as the ion response and the wave populations.

Given the inevitable precession of these orbits, the spacecraft periodically pass over the auroral zone and ISR support station at intermediate altitudes, achieving near-conjugacy with ground stations successively in time rather than simultaneously. This provides a double measurement in the exobase region of interest, with a separation in time between conjugacy with a selected ground site. Orbit modeling as shown in Figure 28.9 indicates that the separations vary between near-conjugacy and about 2000 km, or approximately four minutes, with a mean of order two minutes. This somewhat serendipitous feature of this orbit solution satisfies an important requirement to distinguish between steady states and fluctuating conditions, while obtaining conjugate soundings from at least two altitudes, below and above the nominal exobase. Since the exobase rises linearly with thermospheric temperature, for the most interesting events with strong heating and up-flows, the spacecraft will be exploring the disturbed exobase transition region on virtually every pass over the auroral zones, that is four times per orbit, with varying spatio-temporal spacings that will reveal the transient behaviors of the system, as well as its quasi-steady structure.

28.4.9. Spacecraft

A minimalist starting point for the required spacecraft is the THEMIS spacecraft, which supports an outstandingly high ratio of payload to spacecraft system mass in a small package that fits within, for example, a Pegasus fairing [*Harvey*, 2008]. The THEMIS spacecraft are spinners with three axis electric field and magnetic field probes, a plasma instrument (without composition), and an energetic particles instrument.

Figure 28.10 illustrates a point design based on the THEMIS bus dimensions and components. It has been made formally octagonal, and the locations of components have been shifted. However, the most significant changes are in the payload. First, a gas pressure instrument (RANGE) has been substituted for the energetic particles telescope. Second, the core plasma analyzers (CPAi and CPAe) have been placed on short booms sufficient to extend them beyond the nominal Debye sheath of the spacecraft. A Langmuir Probe (LP) has also been added on a second boom similar to the magnetometer boom, as is customary to extend the sensor beyond the spacecraft Debye sheath.

28.5. SUMMARY DISCUSSION

We began this paper with a summary of our current knowledge about the escape of planetary atmospheres into space, driven by these energy inputs from the solar

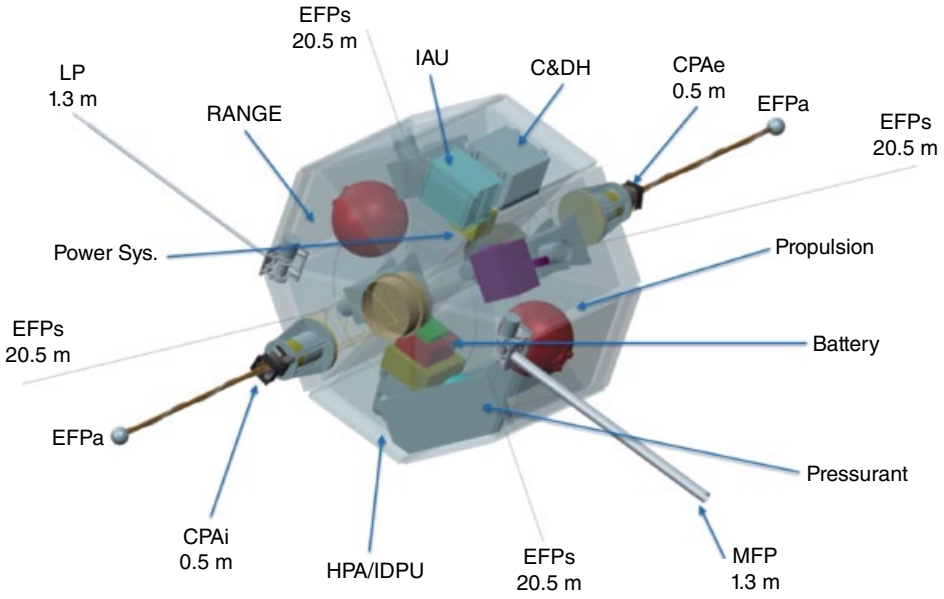

Figure 28.10 A spacecraft point design based on the THEMIS spacecraft bus for a small, efficient probe suitable for atmosphere-ionosphere-magnetosphere coupling studies described herein. EFP, MFP, LP, CPA (core plasma analyzer, e, i), HPA, RANGE (gas pressure).

wind. These are based largely upon isolated single spacecraft and ISR studies. We noted that our knowledge remains clouded and insufficient to support quantitative predictions derived from observations of solar wind conditions, without which our excellent global circulation models must remain qualitative. A huge uncertainty remains in our knowledge of the distribution of the ambipolar potential that couples electrons with ions. Enhanced fluxes of either electron precipitation or electromagnetic energy are effective in producing up-flows and outflows, but current global models do not compute electron heating rates that in turn drive ion flows.

A further huge uncertainty lies in our lack of knowledge of the sources and propagation of ion-resonant waves that are thought to mediate the conversion of energy from various sources into ion heating. Current models of ionospheric outflows must treat the levels of such waves as free parameters that are set mainly according to their ability to produce credible outflows in reasonable agreement with observed levels. To progress beyond this level, we need to measure the distribution of waves along field lines (in a statistical sense) as well as their propagation directions and their modeled effects on the observed ion populations.

We identified certain accepted tenets of our understanding that appear ripe for reconsideration in light of recent work. We noted a dearth of studies involving joint observations by ISR and spacecraft overflights. Those that have been performed have involved excessive separations between the spacecraft and the ionosphere in such a way that plasma flow streamline conjugacy is exceedingly difficult to establish. We concluded that a multilevel sounding of the exobase region is both essential and accessible, beginning with familiar ISR sounding of the topside ionosphere, combined with wide field auroral imaging and diagnostics from the ground, and adding two additional levels sampled by a pair of identical spacecraft with instrumentation suitable to complement the ISR observations.

With this base, we identified a set of detailed open questions that can be organized under a single overarching objective posed as a dichotomy between escape powered by the reduction of pressure in the auroral magnetosphere, or escape powered by the enhancement of pressure in the topside ionosphere.

Is planetary mass loss drawn from above by energetic evacuation or driven from below by energetic pressurization?

From this objective and question, we derived requirements for a mission to resolve that issue, involving the use of multiple observation points in and above the ionosphere, centered on the exobase transition from collision dominated to magnetized plasmas. We derived requirements for a two-spacecraft mission complemented by ISR observations of the ionospheric F layer, and ground-based mapping of global auroras. This would enable diagnosis of conditions within the regions of the ionosphere that are flow streamline conjugate, that is, in a Lagrangian sense, with the spacecraft observations.

28.6. CONCLUSIONS

We conclude that substantial progress toward a quantitatively predictive understanding of global ionospheric plasma outflows can be made by a mission satisfying the requirements outlined above. As a bottom line, such a mission can be mounted at the resource levels of a National Aeronautical and Space Administration (NASA) Small Explorer mission using two highly efficient spacecraft based on the THEMIS bus, and launched to the required orbits by a Pegasus-class launch vehicle. Such a mission would need to operate for a minimum of one year to fully sample terrestrial local times and latitudes.

ACKNOWLEDGMENTS

The authors acknowledge support from the Goddard Space Flight Center Internal Research and Development Program.

REFERENCES

Banks, P. M., and G. Kockarts (1973), *Aeronomy*, Academic, New York.

Burchill, J. K., and D. J. Knudsen (2015), IMF Bz dependence of cusp ion upflow and electron temperature, Geophys. Res. Lett., in press.

Chappell, C. R. (1972), Recent satellite measurements of the morphology and dynamics of the plasmasphere, Rev. Geophys., p. 10, 951.

Chisham, G., et al. (2007), A decade of the Super Dual Auroral Radar Network (SuperDARN): scientific achievements, new techniques and future directions, *Surveys in Geophysics*, Volume *28*, Issue 1, pp. 33–109.

Collier, M. R., D. Chornay, J. Clemmons, J. W. Keller, J. Klenzing, J. Kujawski, J. McLain, R. Pfaff, D. Rowland, M. Zettergren, VISIONS remote observations of a spatially-structured filamentary source of energetic neutral atoms near the polar cap boundary during an auroral substorm, *Adv. Sp. Res.*, V.56, 10, 2015, pp. 2097–2105, http://dx.doi.org/10.1016/j.asr.2015.08.010.

Donovan, E., S. Mende, B. Jackel, H. Frey, et al. (2006), The THEMIS all-sky imaging array, system design and initial results from the prototype imager, *Journal of atmospheric and Terrestrial Physics*, *68*, 13, pp. 1472–1487, doi:10.1016/j.jastp.2005.03.027.

Garcia, K. S., V. G. Merkin, and W. J. Hughes (2010), Effects of nightside ion outflow on magnetospheric dynamics: results of multifluid MHD modeling. *J. Geophys. Res*. *115*, A00J09, http://dx.doi.org/10.1029/2010JA015730.

Ganguli, G., M. J. Keskinen, H. Romero, R. Heelis, T. Moore, and C. Pollock (1994), Coupling of microprocesses and macroprocesses due to velocity shear: An application to the low-altitude ionosphere, *J. Geophys. Res.*, *99*(A5), 8873–8889, doi:10.1029/93JA03181.

Gjerloev, J. W. (2011), A Global Ground-Based Magnetometer Initiative, Eos, *Transactions American Geophysical Union*, Volume *90*, Issue 27, pages 230–231, DOI:10.1029/2009EO270002.

Glocer, A., G. Tóth, T. Gombosi, and D. Welling (2009), Modeling ionospheric outflows and their impact on the magnetosphere, initial results, *J. Geophys. Res.*, *114*, A05216, doi:10.1029/2009JA014053.

Harvey, P., E. Taylor, R. Sterling, and M. Cully (2008), The THEMIS Constellation, *Space Sci. Rev*., *141*, p. 117.

Khazanov, G. V., M. W. Liemohn, and T. E. Moore (1997), Photoelectron effects on the self-consistent potential in the collisionless polar wind, *J. Geophys. Res.*, *102*(A4), 7509–7521, doi:10.1029/96JA03343.

Khazanov, G. V., M. W. Liemohn, E. N. Krivorutsky, and T. E. Moore (1998), Generalized kinetic description of a plasma in an arbitrary field-aligned potential energy structure, *J. Geophys. Res.*, *103*(A4), 6871–6889, doi:10.1029/97JA03436.

Knipp, D., S. Eriksson, L. Kilcommons, G. Crowley, J. Lei, M. Hairston, and K. Drake (2011), Extreme Poynting flux in the dayside thermosphere: Examples and statistics, Geophys. Res. Lett., doi:10.1029/2011GL048302.

Leer, E., and T. E. Holzer (1980), Energy addition in the solar wind, *J. Geophys. Res.*, *85*(A9), 4681–4688, doi:10.1029/JA085iA09p04681.

Lotko, W. (2007), The magnetosphere-ionosphere system from the perspective of plasma circulation: A tutorial, J. *Atmospheric and Solar-Terrestrial Physics*, *69*, 191–211.

Luhmann, J. G., and S. J. Bauer (1992), Solar wind effects on atmosphere evolution at Venus and Mars, in: Venus and Mars: Atmospheres, Ionospheres, and Solar Wind Interactions, Geophys. Monograph #66, Am. Geophys. Un., p. 417.

Mende, S. B., S. E. Harris, H. U. Frey, V. Angelopoulos, C. T. Russell, B. Jackel, M. Greffen, and L. M. Petticolas (2008), The THEMIS array of ground based observatories for the study of auroral substorms, *Space Sci. Revs. 141*, 1–4, p. 357. doi:10.1007/978-0-387-89820-9_16.

Moore, T. E., and J. L. Horwitz (2007), Stellar ablation of planetary atmospheres, *Rev. Geophys.*, *45*, RG3002, doi:10.1029/2005RG000194.

Moore, T. E., and G. V. Khazanov (2010), Mechanisms of ionospheric mass escape, *J. Geophys. Res*., *115*, A00J13, doi:10.1029/2009JA014905.

Moore, T. E., M. O. Chandler, C. J. Pollock, D. L. Reasoner, R. L. Arnoldy, B. Austin, P. M. Kintner, and J. Bonnell (1996), Plasma heating and flow in an auroral arc, *J. Geophys. Res.*, *101*, 5279–5298.

Moore, T.E., et al. (2014), The ionospheric outflow feedback loop, Journal of Atmospheric and Solar-Terrestrial Physics, http://dx.doi.org/10.1016/j.jastp.2014.02.002i.

Nishimura, Y., L. R. Lyons, V. Angelopoulos, T. Kikuchi, S. Zou, and S. B. Mende (2011), Relations between multiple auroral streamers, pre-onset thin arc formation, and substorm auroral onset, *J. Geophys. Res.*, *116*, A09214, doi:10.1029/2011JA016768.

Puhl, P., T. E. Cravens, and J. Lindgren (1993), Ion thermalization in the inner coma of a comet, *Astrophys. J.*, *418*, 899–911. Rowland, D., M. Collier, J. Keller, J. Klenzing, R. Pfaff,

J. McLain, J. Clemmons, and J. Hecht, (2015), Imaging low-energy ion outflow in the auroral zone, in preparation.

Retterer, J. M., T. Chang, and J. R. Jasperse (1994), Transversely accelerated ions in the topside ionosphere, *J. Geophys. Res.*, *99*, 13,189–13,202.

St.-Maurice, J.-P., and R. W. Schunk (1979), Ion velocity distributions in the high-latitude ionosphere, *Rev. Geophys.*, *17*(1) 99–134, doi: 10.1029/RG017i001p00099.

Schunk, R.W., and J. J. Sojka, (1997), Global ionosphere-polar wind during changing magnetic activity, *J. Geophys. Res*. *102*, A6, p. 11, 625.

Strangeway, R. J., R. E. Ergun, Y.-J. Su, C. W. Carlson, and R. C. Elphic, (2005), Factors controlling ionospheric outflows as observed at intermediate altitudes, *J. Geophys. Res.*, *110*, A03221, doi:10.1029/2004JA010829.

Streltsov, A. V., and W. Lotko (2008), Coupling between density structures, electromagnetic waves and ionospheric feedback in the auroral zone, *J. Geophys. Res*., *113*, A05212, doi:10.1029/2007JA012594.

Suvanto, K., et al. (1989), Analysis of incoherent scatter radar data from non-thermal F region plasma, *J. Atmos. Terr. Phys.*, *51*(6), 483–495, doi:10.1016/0021-9169(89)90088-3.

Wahlund, J. E., H. J. Opgenoorth, I. Haggström, K. J. Winser, and G. O. L. Jones (1992), EISCAT observations of topside ionospheric ion outflows during auroral activity: Revisited, *J. Geo- phys. Res.*, *97*, 3019–3037.

Weimer, D. R. (2012), A flexible, IMF dependent model of high-latitude electric potentials having "Space Weather" applications, *Geophysical Research Letters*, Volume *23*, Issue 18, pages 2549–2552, DOI: 10.1029/96GL02255.

Wilson, G. R. (1994), Kinetic modeling of O+ upflows resulting from ExB convection heating in the high-altitude F region ionosphere, *J. Geophys. Res.*, *99*(A9), 17,453–17,466, doi:10.1029/94JA01214.

Zhang, B., W. Lotko, O. Brambles, P. Damiano, M. Wiltberger, and J. Lyon (2012), Magnetotail origins of auroral Alfvénic power, *J. Geophys. Res.*, *117*, A09205, doi:10.1029/2012 JA017680.

INDEX

Magnetosphere-Ionosphere Coupling in the Solar System, Geophysical Monograph 222, First Edition.
Edited by Charles R. Chappell, Robert W. Schunk, Peter M. Banks, James L. Burch, and Richard M. Thorne.

A LISTING OF THE DOI URL VIDEO LINKAGES IN THE ORDER THAT THEY APPEAR IN THE MONOGRAPH

Video or Chapter	DOI URL
Prologue	http://digitalcommons.usu.edu/yosemite_chapman/1974/ http://digitalcommons.usu.edu/yosemite_chapman/2014/
Video—Burch/Chappell	http://dx.doi.org/10.15142/T3C30S
Chapter 1—Burch	http://dx.doi.org/10.15142/T3J01P
Video—Axford/Banks	http://dx.doi.org/10.15142/T35K5N
Chapter 2—Yau et al.	http://dx.doi.org/10.15142/T34S3N
Chapter 3—Haaland et al.	http://dx.doi.org/10.15142/T3MS30
Video—Hanson/Heelis	http://dx.doi.org/10.15142/T31S3Q
Chapter 4—Heelis	http://dx.doi.org/10.15142/T3QG6Z
Chapter 5—Lu	http://dx.doi.org/10.15142/T3T88K
Video—Johnson/Chappell	http://dx.doi.org/10.15142/T3X30R
Chapter 6—Kistler et al.	http://dx.doi.org/10.15142/T3D303
Chapter 7—Kitamura et al.	http://dx.doi.org/10.15142/T33K51
Chapter 8—Liemohn and Welling	http://dx.doi.org/10.15142/T3D596
Video—Thorne	http://dx.doi.org/10.15142/T3HS32
Chapter 9—Thorne	http://dx.doi.org/10.15142/T38G6X
Chapter 10—Hospodarsky et al.	http://dx.doi.org/10.15142/T3W886
Video—Williams/Lanzerotti	http://dx.doi.org/10.15142/T3GW2D
Chapter 11—Lanzerotti et al.	http://dx.doi.org/10.15142/T31011
Chapter 12—Jordanova	http://dx.doi.org/10.15142/T3RG68
Video—Banks/Schunk	http://dx.doi.org/10.15142/T30W22
Chapter 13—Schunk	http://dx.doi.org/10.15142/T3C88J
Chapter 14—Welling et al.	http://dx.doi.org/10.15142/T3V88W
Video—Fairfield/Slavin	http://dx.doi.org/10.15142/T38C78
Chapter 15—Glocer	http://dx.doi.org/10.15142/T33S3B
Chapter 16—Zou et al.	http://dx.doi.org/10.15142/T37G6M
Video—Wolf	http://dx.doi.org/10.15142/T34K5B
Chapter 17—Wolf et al.	http://dx.doi.org/10.15142/T3001Q
Chapter 18—Longley et al.	http://dx.doi.org/10.15142/T3H01C
Video—Park/Carpenter	http://dx.doi.org/10.15142/T3NK50

(*Continued*)

Magnetosphere-Ionosphere Coupling in the Solar System, Geophysical Monograph 222, First Edition.
Edited by Charles R. Chappell, Robert W. Schunk, Peter M. Banks, James L. Burch, and Richard M. Thorne.

Video or Chapter	DOI URL
Chapter 19—Krall et al.	http://dx.doi.org/10.15142/T3KS3P
Video—Nagy	http://dx.doi.org/10.15142/T3RC7M
Chapter 20—Cravens	http://dx.doi.org/10.15142/T32S31
Chapter 21—Coates	http://dx.doi.org/10.15142/T3B887
Video—Coroniti/Kivelson	http://dx.doi.org/10.15142/T3W30F
Chapter 22—Hospodarsky et al.	http://dx.doi.org/10.15142/T3G012
Chapter 23—Westlake et al.	http://dx.doi.org/10.15142/T36K5Z
Video—Hill and Reiff	http://dx.doi.org/10.15142/T37C7Z
Chapter 24—Hill	http://dx.doi.org/10.15142/T3PK59
Chapter 25—X. Jia et al.	http://dx.doi.org/10.15142/T3JS3C
Video—Reid/McPherron	http://dx.doi.org/10.15142/T3S888
Chapter 26—Walker et al.	http://dx.doi.org/10.15142/T3Z302
Chapter 27—Y. Jia et al.	http://dx.doi.org/10.15142/T3F30D
Video—Schmerling/Kavanagh/Banks/Doupnik	http://dx.doi.org/10.15142/T3MK5P
Chapter 28—Moore et al.	http://dx.doi.org/10.15142/T3988X